Advanced Photon Source Upgrade Project

Preliminary Design Report

December 2012

Chapter 1: Project Overview

The Advanced Photon Source, an Office of Science User Facility operated for the U.S. Department of Energy (DOE) Office of Science by Argonne National Laboratory, is supported by the DOE under Contract No. DE-AC02-06CH11357.

Table of Contents

List of Figures

List of Tables

Acronyms and Abbreviations

AE	Acquisition Executive
AES	APS Engineering Support Division
ANSI	American National Standards Institute
APM	Associate Project Manager
APS-U	Advanced Photon Source Upgrade
ASO	Argonne Site Office (DOE)
BES	Basic Energy Sciences
CAS	Contingent Additional Scope
CAT	Collaborative Access Team
CD	Critical Decision
CM	configuration management
DOE	Department of Energy
EIA	Electronic Industries Alliance
ESD	Engineering Specification Document
ES&H	environment, safety and health
EVMP	Earned Value Management Procedure
EVMS	Earned Value Management System
EVMSD	Earned Value Management System Description
FMS	Facility Management and Services
ICD	Interface Control Document
ICMS	Integrated Content Management System
JLAB	Thomas Jefferson National Accelerator Facility
KPP	Key Performance Parameter
LBNL	Lawrence Berkeley National Laboratory
MOA	Memorandums of Agreement
MOU	Memorandums of Understanding

OPM	Office of Project Management
PD	Project Director
PDR	Preliminary Design Report
PEP	Project Execution Plan
PIP	Project Implementation Plan
PM	Project Manager
PMCS	Project Management Control System
PMB	Performance Measurement Baseline
PMO	Project Management Office
PRD	Physics Requirements Document
PSAC	Project Science Advisory Committee
PSC	Photon Sciences
QA	Quality Assurance
rf	radio frequency
SAC	Science Advisory Committee
SC	Office of Science
SPX	Short Pulse X-rays
TPC	Total Project Cost
UC-A	UChicago Argonne
WBS	Work Breakdown Structure
WFI	Wide Field Imaging
XSD	X-ray Science Division

This page intentionally left blank.

1 Project Overview

1.1 Executive Summary

On April 22, 2010, the U.S. Department of Energy (DOE) granted approval of Mission Need, Critical Decision 0 (CD-0) for the Advanced Photon Source (APS) Upgrade Project. Following the CD-0 approval, Argonne National Laboratory prepared a conceptual design for the Project. The Project received CD-1, "Approval Alternative Selection and Cost Range," on September 15, 2011 and this Preliminary Design Report has been prepared to support the completion of the CD-2 milestone. The Project is an upgrade of the existing third-generation APS light source which will enable APS to provide an unprecedented combination of high-energy, high-average brilliance, high flux, and short-pulse x-rays together with state-of-the-art x-ray beamline instrumentation to complement fourth-generation light sources.

1.2 Introduction

The DOE's APS is the largest synchrotron light source in the Western Hemisphere and provides the brightest x-ray beams in the energy range above 25 keV to researchers from around the United States and the world. In fiscal year (FY) 2011, more than 350 universities sent researchers to the APS, as did 65 companies, and better than 140 medical schools and research institutions, both government and private. In total, more than 5,000 researchers participated in over 4,000 experiments at the APS in FY2011, resulting in more than 1,400 peer-reviewed publications. Because the APS has been operational since 1996 and is the leading high-energy synchrotron radiation facility in the nation, the upgrade is essential to provide the scientific community with improved capabilities in high-energy diffraction, *in situ* studies of material synthesis, imaging, ultra-fast diffraction and spectroscopy.

This Preliminary Design Report is presented in five chapters and provides a Project overview, description of the management strategy, and summary of the technical design.

Chapter 1 provides an overview of the Project, summarizes management strategies that are detailed in the Project Execution Plan and the Project Implementation Plan, and provides a detailed summary of the Project scope that is further described in the subsequent chapters of this report.

Chapter 2 summarizes the assessments and processes that the Project is developing including Environment, Safety and Health; Quality Assurance; Risk Management; Value Management; and Systems Integration.

The majority of this document is focused on providing a description of the technical scope. For each of the scope-specific chapters, a scope overview, a discussion on interfaces with other Project elements, as well as brief descriptions of Contingent Additional Scope (CAS) where appropriate is provided.

Chapter 3 describes the Accelerator Systems; **Chapter 4** discusses the Experimental Facilities Upgrades; and **Chapter 5** addresses the Enabling Technical Capabilities. A summary from each of these chapters is included at the end of this overview.

1.2.1 Project Scope Overview

The APS Upgrade Project scope includes the design, procurement, assembly, installation, and testing of the accelerator hardware, beamline instrumentation, and enabling technical capabilities required to upgrade the existing APS synchrotron light source. Specifically, the main scope elements include:

- Upgrade technical equipment to increase the operating current to 150 mA.
- The addition of long straight sections in the APS storage ring lattice in order to accommodate long insertion devices, or to fit into one straight section a combination of a superconducting undulator and a permanent magnet undulator, or a combination of a permanent magnet undulator and a set of superconducting radio-frequency deflecting cavities.
- Superconducting insertion devices that will provide greatly increased brightness in the hard x-ray range (photon energy greater than 20 keV) to APS users.
- New planar, revolver, and variable polarization insertion devices optimized for beamline missions.
- A Short-Pulse X-ray accelerator facility consisting of superconducting radio-frequency deflecting cavities with the capability to produce hard x-ray pulses more than an order of magnitude shorter than those currently available for enhanced time resolution.
- A transformational suite of more than a dozen new and upgraded x-ray beamlines with orders-of-magnitude improvements in performance through advanced optical and detection systems.
- New or upgraded information technology and physical infrastructure.

When completed, the APS Upgrade will provide unique technical capabilities both in the accelerator, and in the beamlines, such that scientists can observe, understand, and ultimately control materials function on the nanoscale through two themes that reflect the scientific power of high-energy x-rays: mastering hierarchical structures through imaging, and understanding real materials under real conditions in real time.

The scope of the APS Upgrade, organized in three technical areas, is summarized below.

Accelerator and X-ray Source Upgrades

- Short Pulse X-rays (SPX) by transverse rf deflection
- Increased beam stability and increased beam current to 150 mA operation
- 2 Superconducting undulators
- 5 Revolver undulators
- 3 Planar undulators
- 3 Polarizing undulators
- 3 Long straight sections (~7.7 m)

Experimental Facilities

- 8 New beamlines
- 6 Beamline upgrades
- 6 Beamline relocations
- High heat load upgrades to beamline optics

Infrastructure and Enabling Technologies

- 15 New front ends
- 7 Renovated front ends
- Physical infrastructure for Wide Field Imaging beamline
- Next generation beam position monitors.

1.2.2 Scientific Program Overview

The overall objective of the APS Upgrade Project is to provide the APS scientific community with new and enhanced experimental techniques to observe, understand, and ultimately control materials function on the nanoscale through two themes that reflect the scientific power of high-energy x-rays: mastering hierarchical structures through imaging, and understanding real materials under real conditions in real time.

1.2.3 Facility Overview

As part of the APS Upgrade scope, eight new and six upgraded beamlines were included in the Conceptual Design Report in May of 2011. However, the APS currently has only three unoccupied sectors (a sector is defined as one insertion device beam line and one bending magnet beamline), sectors 25, 27 and 28. In order to implement the beamline upgrade scope and concomitantly incorporate proposed activities beyond the APS Upgrade Project, a long-term plan for the locations of current and potential future programs/beamlines at the APS was developed. This long-term plan is called the APS Roadmap (www.aps.anl.gov/Upgrade/Forum). One of the main features of the Roadmap is that future expansion of

insertion device beamlines will be through the addition of "cants" that allow two beamlines to occupy one sector. The current version of the Roadmap defers consideration of those beamlines that will be sited on bending magnet sources, since bending magnet ports are much more readily available and siting is not as challenging task.

In developing the Roadmap, a goal was to minimize disruption or relocation of the existing Collaborative Access Team (CAT) or X-ray Science Division (XSD) beamlines. However, some beamlines may have to be relocated. One example is a Magnetic Diffraction program currently in Sector 6 that has to move in order to construct the future Short Pulse Imaging and Spectroscopy beamline there. Another example is the 250-m long Wide Field Imaging (WFI) beamline that can only be built on three potential sites, without affecting existing buildings, parking lots, roads and wet lands, namely Sectors 18, 19, and/or 20. All three sectors currently have programs.

Initially, ten possible Roadmap scenarios were developed for consideration. Subsequently, the Project received advice from the APS Science Advisory Committee (SAC), the Project SAC (PSAC), and Laboratory management, and feedback from the APS user community and APS staff. The Project followed up by meeting representatives of Roadmap-affected programs and discussed impacts of various scenarios. Rough cost estimates of all options were performed and technical limitations were considered. After synthetizing all this input, one scenario was selected as the baseline.

The list of beamlines/programs in the scope of the APS Upgrade, their future locations and whether they are new, upgraded or relocated beamlines is shown in Table 1-1.

Table 1-1: APS Upgrade Scope Overview.

Beamline/Program	**Location**	**New**	**Upgrade**	**Relocation**
Short Pulse X-ray Scattering and Spectroscopy	7-ID		1	
Short Pulse X-ray Imaging and Microscopy	6-ID	1		
High Flux Pump-Probe	14-ID		1	
Wide Field Imaging	20-ID	1		
In Situ Nanoprobe	32-ID	1		
Resonant Inelastic X-ray Scattering	27-ID	1		
Magnetic Spectroscopy - Hard	4-ID		1	
High Energy X-ray Diffraction	1-ID	1	1	
X-ray Interface Science	28-ID	2		
Sub-micron 3D Diffraction	34-ID	1	1	
Advanced Spectroscopy and LERIX	25-ID			2
Magnetic Spectroscopy - Soft	2-ID		1	
Magnetic Diffraction	2-ID			1
Fuel Spray Dynamics	BM			1
Bragg Coherent Diffractive Imaging	9-ID			1
Fluorescence Microscopy	9-ID			1

1.2.4 Capabilities and Performance Goals (KPPs)

The APS Upgrade Project will involve upgrades to the existing APS accelerator including new insertion devices located in the straight sections of the accelerator, the creation of new beamlines, upgrades to existing beamlines, and the creation and installation of new enabling technologies. The APS Upgrade will provide high-energy, high-average-brilliance, short-pulse, penetrating hard x-rays in the energy range above 25 keV; nanoscale focal spots approaching 10 nm above 25 keV; time resolution better than 10 ps; new or improved x-ray beamlines; and the technical capabilities required to fully exploit these upgraded technical components. The combination of these upgrades will provide a more intense beam at all beamline locations and provide capabilities unique among all facilities in the world. The baseline technical parameters of the completed APS Upgrade are captured by the Key Performance Parameters (KPPs) as defined in the Project Execution Plan (PEP).

Table 1-2 provides the preliminary Threshold and Objective KPPs. that will be finalized and approved as part of the CD-2 process. The Threshold KPPs are the parameters against which the Project's performance will be measured at CD-4. The Objective KPPs describe the technical goals of the Project, if project performance is sustained and sufficient contingency is becomes available. Achievement of these parameters will be verified as part of the testing of technical systems. Equipment checkout and testing required to confirm hardware performance will be executed as part of the Project, while final commissioning and optimization of performance will be executed by the APS.

Table 1-2: APS Upgrade Key Performance Parameters.

Key Performance Parameter	**Thresholds (Performance Deliverable)**	**Objectives**
Operating current capability for all front end components	150 mA	150 mA
Undulators installed	12	21
X-ray brightness* at 23.7 keV or above for an installed insertion device	2×10^{20}	2×10^{20}
X-ray brightness* at 70 keV or above for an installed insertion device	1×10^{19}	1.6×10^{19}
New beamlines installed and ready for commissioning with x-ray beam	6	9
Beamlines upgraded and ready for commissioning with x-ray beam	6	8
**Resolution of a delivered x-ray focusing optic at 25keV	20 nm	10 nm

*photon/second/0.1%bw/mm^2/mrad^2. Verification of brightness KPPs will be done by magnetic measurements of the assembled insertion devices based on design lattice parameters. Shastri and collaborators [1] have confirmed that calculated brightness based on magnetic field measurements is in excellent agreement with measurements of the actual x-ray brightness delivered by an undulator.

**Verification of the resolution of a delivered x-ray focusing optic will be done by measuring the transfer function of an optic using either a scanning microscope or a full-field microscope. By observing the spatial frequency at which contrast transfer declines to the noise level, one has a simple and direct measure of the performance of the optic as shown by Jacobsen et al., Ultramicroscopy 47, 55 (1992).

As a result of scope refinement and subsequent cost analysis, the previous Objective of 200 mA has proven to be prohibitively expensive (~$32M) for the incremental performance improvement relative to the threshold value of 150 mA. The 33% flux increase resulting from increasing the current from the 150 mA to 200 mA can be much more effectively realized by an appropriate choice of an insertion device. Furthermore, the APS Science Advisory Committee recommended the 200 mA goal to be in the category of lowest priority. Therefore, the 150 mA is the Objective for the operating current capability of front end components of the Project.

1.3 Project Management Overview

The APS Upgrade Project utilizes a number of systems and procedures to support the overall management of the Project. These systems comply with the requirements of APS, Argonne National Laboratory, and the DOE. The Project Execution Plan (PEP) defines the management of the Project from the DOE perspective. The Project Implementation Plan (PIP) defines the project-level management processes and tools utilized by the Project. A summary of these management systems is provided below, and more detailed information on the Project budget, schedule, and management processes can be found in the PEP and PIP.

The Project Management Control System (PMCS – discussed in section 1.3.4) provides the Project with the systems necessary to manage the cost and schedule of the Project. At the heart of the PMCS is the Work Breakdown Structure (WBS – discussed in section 1.3.3) and associated dictionary that define the Project's scope. From the WBS and associated cost and schedule estimates, the detailed Integrated Project Schedule and cost estimate are developed from the subproject specific work and scope packages. The Project has established the performance baseline and will track accrued value and manage this to the baseline schedule using an ANSI-compliant and Argonne-certified Earned Value Management System (EVMS – also discussed in section 1.3.4). The Project has exercised the use of the EVMS during the development of the Preliminary Design. The APS Upgrade design is controlled and managed through configuration management as described in Chapter 2, Assessments. The Project cost baseline is presented in Table 1-3 and a list of Level 0 and 1schedule milestones is presented in Table 1-4.

Safety is the highest priority of the Project. The primary objective is to systematically integrate excellence in ES&H into the management and work practices of all activities, including integration with ongoing programs at APS, and at all levels so that the Project's mission is achieved while protecting the public, employees, contractors, users, and the environment. The ES&H efforts are summarized in Chapter 2 of this PDR and fully detailed in additional supporting documents.

Table 1-3: Preliminary Cost Estimate for the APS Upgrade.

WBS Element	WBS Description	Total Estimated Cost ($K)
U1	APS Upgrade Project	391,000
U1.01	Project Management	35,536
U1.02	Research & Development	17,786
U1.03	Accelerator Systems	76,347
U1.04	Experimental Facilities	128,927
U1.05	Infrastructure & Enabling Technologies	31,636
	Sub-total (includes escalation)	**290,233**
	Escalation	**27,457**
	Contingency	**100,767**

Table 1-4: Level 0 and Level 1 Project Milestones.

Critical Decision	Milestone	Schedule Date
CD-0	Approve Mission Need	4/27/2010 (actual)
CD-1	Approve Alternative Selection and Cost Range	9/15/2011 (actual)
CD-3a	Approve Long Lead Procurements	8/30/2012 (actual)
CD-2	Approve Performance Baseline	4/2013
CD-3	Approve Start of Construction	4/2014
CD-4	Approve Project Completion	9/2020

1.3.1 Project Organization and Governance

The Project is funded by the DOE and managed through UChicago Argonne (UC-A). It is carried out in collaboration with universities and laboratories in the U.S. and other countries. The responsibilities for managing the Project are shown in the organization chart in Figure 1-1, and are described in greater detail in the PEP and PIP.

DOE has assigned Argonne the responsibility to plan and execute the APS Upgrade Project within an agreed-to scope, cost and schedule in a safe and responsible manner. Argonne provides access to resources, systems, and other capabilities required in the execution of the Project. As the Management and Operating contractor for Argonne, UC-A will be accountable to DOE for carrying out the APS Upgrade Project.

The Project has been designated as the highest priority at the Laboratory, and as such has established a Project Office in the Photon Science Directorate that will be responsible for all R&D, conceptual, preliminary, and final design, fabrication, installation, and acceptance testing; and overall day-to day management of the Project. The Project Office consists of the managers and subproject leaders who have responsibility for the Project to define and execute the Project on budget and schedule, and in accordance with all required rules, regulations and safety procedures. The Project team to Level 3 of the WBS is shown in Figure 1-2 and more complete descriptions of the various Project roles and responsibilities are included in the PIP.

1.3.2 Advisory Committees

The Project retains three independent advisory committees, the Project Scientific Advisory Committee, the Project Machine Advisory Committee, and the Upgrade Project Management Advisory Committee. These committees provide independent advice to the Project on the scientific and machine technical components and progress, and on management, organization, and interactions with stakeholders. Additional advisory and review committees are detailed in the PIP.

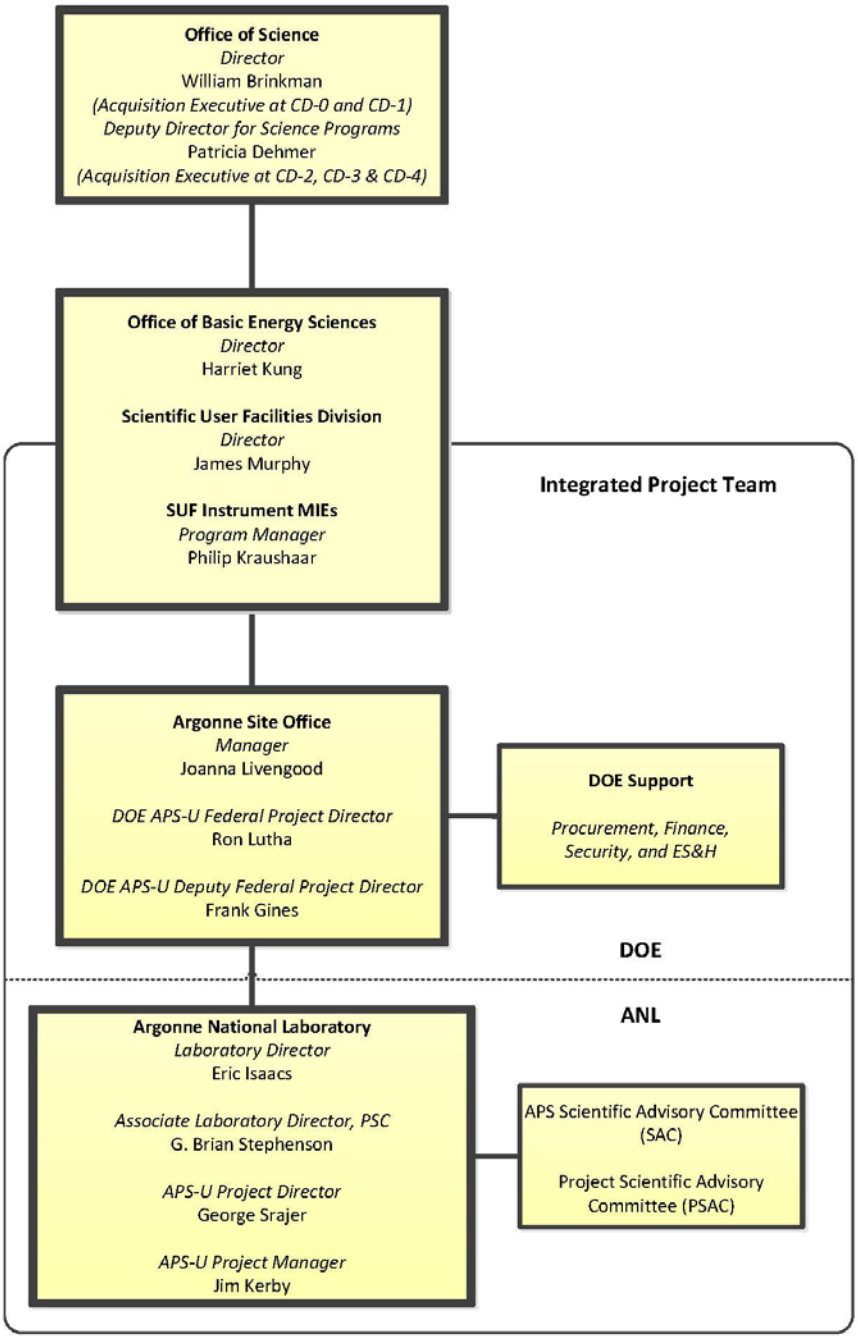

Figure 1-1: DOE Organization Chart of the APS Upgrade Project.

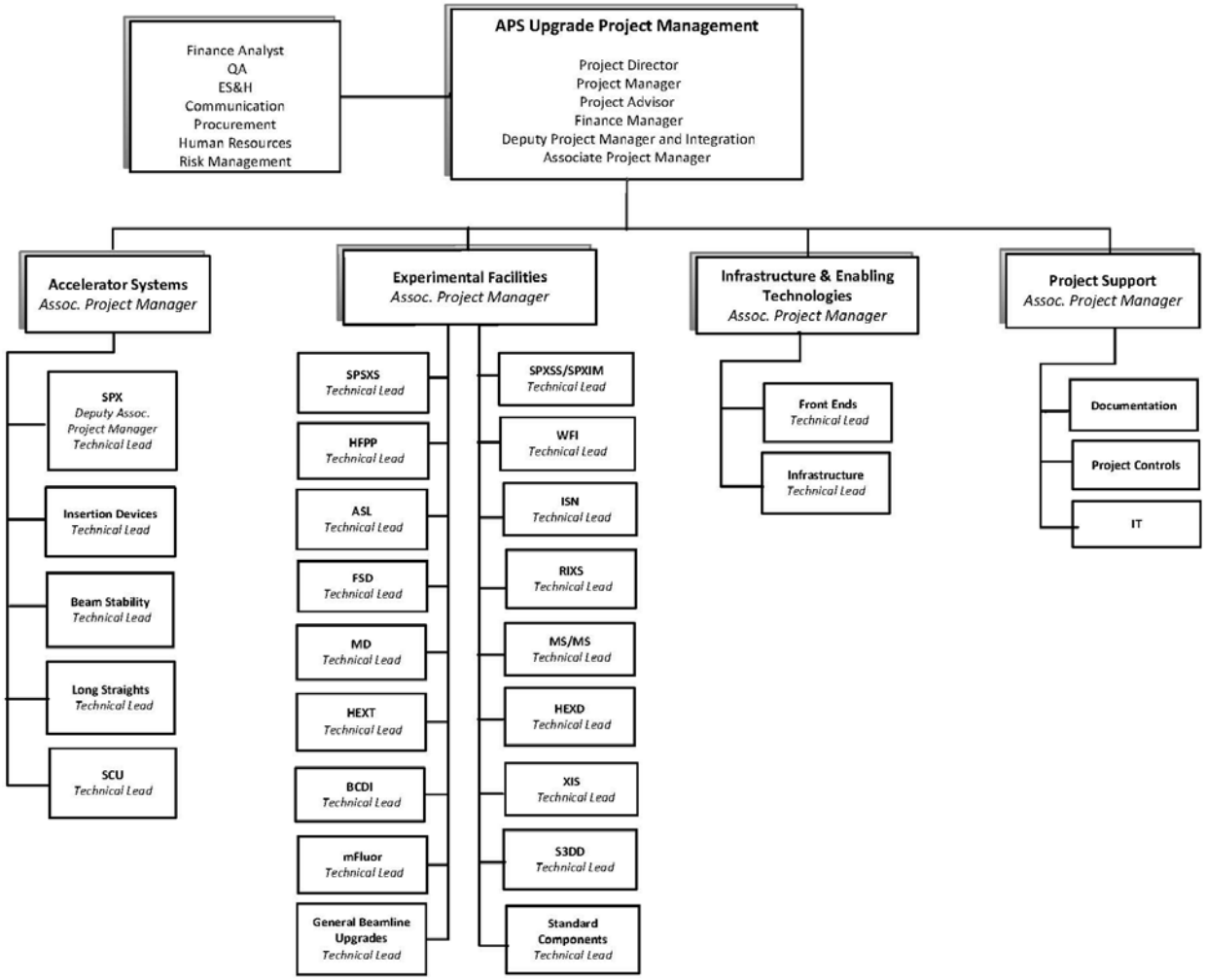

Figure 1-2: Organizational Chart of the APS Upgrade Project to WBS Level 3.

1.3.3 Work Breakdown Structure

The foundation for the scope required for completion of the Project is contained in the Work Breakdown Structure (WBS) and is shown to Level 2 in Table 1-5. The development of the WBS and the WBS dictionary are consistent with the requirements set forth in DOE Order 413.3B, Program and Project Management for the Acquisition of Capitol Assets and ANSI/748a, Earned Value Management Systems. A more complete description of the WBS is available in the PIP; the WBS and WBS Dictionary are available to the Project in SharePoint and are provided at Project reviews as supporting documents.

Each element of the WBS captures all costs, resources, and activities necessary to complete the system with an associated schedule. The detailed activities, defined at the control account level, that have been identified to design, fabricate, construct, and install the Project are described in the WBS dictionary All changes to the WBS must be approved prior to implementation. The approval process is defined in the Project's Configuration Management Plan.

Table 1-5: APS Upgrade Work Breakdown Structure to Level 2 including definitions.

WBS #	WBS Title	WBS Description
U1.01	Project Management Planning and Administration	This WBS element covers the project management, planning and organization function of the APS Upgrade Project.
U1.02	Research & Development	This WBS element covers all R&D required to develop additional technical information before final designs of new accelerator and beamline components can be complete.
U1.03	Accelerator Systems	This WBS element defines the accelerator portion of the APS Upgrade Project, including storage ring components, insertion devices, diagnostics improvements, and superconducting RF deflecting cavities to provide shorter x-ray pulses.
U1.04	Experimental Facilities	This WBS element defines the new x-ray beamlines, upgrades to existing x-ray beamlines, and the move of any existing x-ray beamlines to accommodate Project scope, and optics for existing beamlines to operate at higher current.
U1.05	Infrastructure & Enabling Technologies	This WBS element defines the portion of the Project required to deliver beamline front end renovations or replacements for higher current or new beamlines. The Wide Field Imaging Beamline physical infrastructure, utility upgrades, general engineering, and support services are included.

1.3.4 Project Management Control Systems

As detailed in the PIP, projects performed at Argonne adhere to the requirements in DOE Order 413.B, Program and Project Management for the Acquisition of Capital Assets including compliance with the industry standard for project control systems described in the American National Standards Institute (ANSI) Electronic Industries Alliance (EIA) 748, Earned Value Management Systems.

The Argonne EVMS Description (EVMSD) and supporting EVM Procedures (EVMP) documents the project management processes essential to effective planning, organization, control and surveillance of major projects. Compliance with the EVMSD policies and processes described in the implementing procedures are required for all activities performed within the Project approved baseline. The EVMSD derives its authority from the Argonne Policy Manual and is maintained by the Office of Project Management (OPM).

1.3.5 Resource Support from Argonne (MOUs)

Efficient allocation of resources with critical skills is crucial to the execution of the Project. Identification and utilization of the skills and the collective learning embedded in the APS requires communication and a deep commitment to work across organizational boundaries. To this end, a Memorandum of Agreement (MOA) was signed between the Project and all three divisions in APS. The MOA establishes guidelines to create and maintain cooperative working relationships; to facilitate joint planning and evaluation of

services; to develop efficient management of limited financial and human resources; and to meet and exceed all performance measures established by the Project.

Assignments of individuals to work on the Project are captured in the Effort Request Agreements (ERA) between the Project and each division. In the ERAs, the amount of effort for an individual for a given year is estimated and agreed upon by divisional and Project management. These ERA are discussed further in the PIP.

1.3.6 Other Participating Institutions/Agencies

APS Upgrade has enlisted the services of two other national laboratories to provide portions of the Short Pulse X-ray (SPX) System. Thomas Jefferson National Accelerator Facility (JLAB) is providing the design and fabrication of the cavity and cryomodules. Lawrence Berkeley National Laboratory (LBNL) is providing R&D for the SPX radio frequency (rf) controls and timing system.

Memoranda of Understanding are in place between Argonne National Laboratory and Thomas Jefferson National Accelerator Facility and between Argonne National Laboratory and Lawrence Berkeley National Laboratory for the effort at each lab.

1.3.7 Requirements Management and Controls

The APS Upgrade Project Capabilities and Performance Goals are discussed in Section 1.2.4. Project requirements based on the Key Performance Parameters and overall system requirements discussed in Section 1.2.4 are provided in the APS Upgrade Project Physics Requirements Document (APSU-1.01-PRD-001). These requirements have been developed based on input from the APS Scientific Advisory Committee (SAC) and APS Upgrade Stakeholders and are approved by the Project Director. The goal of requirements management is to ensure that the Project requirements and related system requirements are controlled to establish and maintain a technical baseline for the Project.

Project requirements documents include Physics Requirements Documents (PRDs), Engineering Specification Documents (ESDs), and Interface Control Documents (ICDs). These documents are discussed further in Chapter 2 of this PDR.

1.3.8 Interface Management

Due to the nature of this Project as an upgrade to existing facilities, the interfaces between Project activities and other Argonne organizations, APS operational activities, external Laboratories and inter-Project activities must be carefully managed. This process is critical to develop the Project while minimizing any potential impact on APS operations. A Transition to Operations plan is in development and further detailed in the PIP.

1.3.8.1 Organizational Interfaces

The Project is a matrixed organization within the Photon Sciences (PSC) Directorate. Currently, most Project staff are associated with other APS divisions, the PSC Directorate or Facility Management and

Services (FMS) within the Office of Project Management (OPM). The Project organization is shown in Figure 1-2 above.

Three technical scope-specific Associate Project Managers (APMs) and two cross-Project APMs have been identified. The first three APMs, who are matrixed from other APS Divisions, act as primary interface managers with their respective divisions and division management on a regular basis. All issues with potential impact to either the Project or the operation of the APS facility will initially be addressed by APMs with support from the APM for Integration and the Project Manager. Additional roles and responsibilities are detailed in the PIP.

External Project interfaces, including interfaces with the institutions described above in section 1.3.6 are managed with MOUs while ERAs are used to agree on effort from within the Photon Sciences Directorate.

1.3.8.2 Schedule Development and Integration with Operations

The APS Upgrade will be planned and executed with minimal impact on APS operations. Information provided here is a summary description of the full planning effort provided for contextual reference only. The APS has now been in operation for about sixteen years and through this time, a functional operational schedule has evolved which provides:

- 5000 hours of x-ray beam delivered to the user community,
- sufficient time to perform the needed maintenance and ongoing upgrades to the accelerator facility,
- adequate time to recommission the accelerator after the maintenance periods
- time to perform needed accelerator studies.

This schedule is the result of extensive discussions and negotiations between accelerator staff and the user community, and optimizes the effectiveness of both communities. It has been utilized with little variation over the last ten years, and it is this schedule that is used to plan the integration and coordination of the Project into the APS while successfully maintaining operations.

The schedule for FY2011 is shown in Figure 1-3. It is based around three operational periods, and three extended shutdowns (dark blue shading on schedule). Each shutdown is approximately one month long, with a slightly longer shutdown encompassing the Christmas-New Year Holiday period; it is generally considered less efficient due to extensive use of holiday and vacation time. Following each shutdown is a period of accelerator startup which is typically one week long. From the user perspective, these two periods (shutdown and accelerator startup) are both “dark times”, but from the machine maintenance point of view, are very distinct. The accelerator enclosures are expected to be closed at the end of the maintenance period, and all work, and requisite post-work verification must be complete at this time. The startup time will serve a very important role during Project installation. It allows some schedule contingency if there are problems with maintenance work, and it allows for the startup of the accelerator after both the normal shutdown work, and Project work.

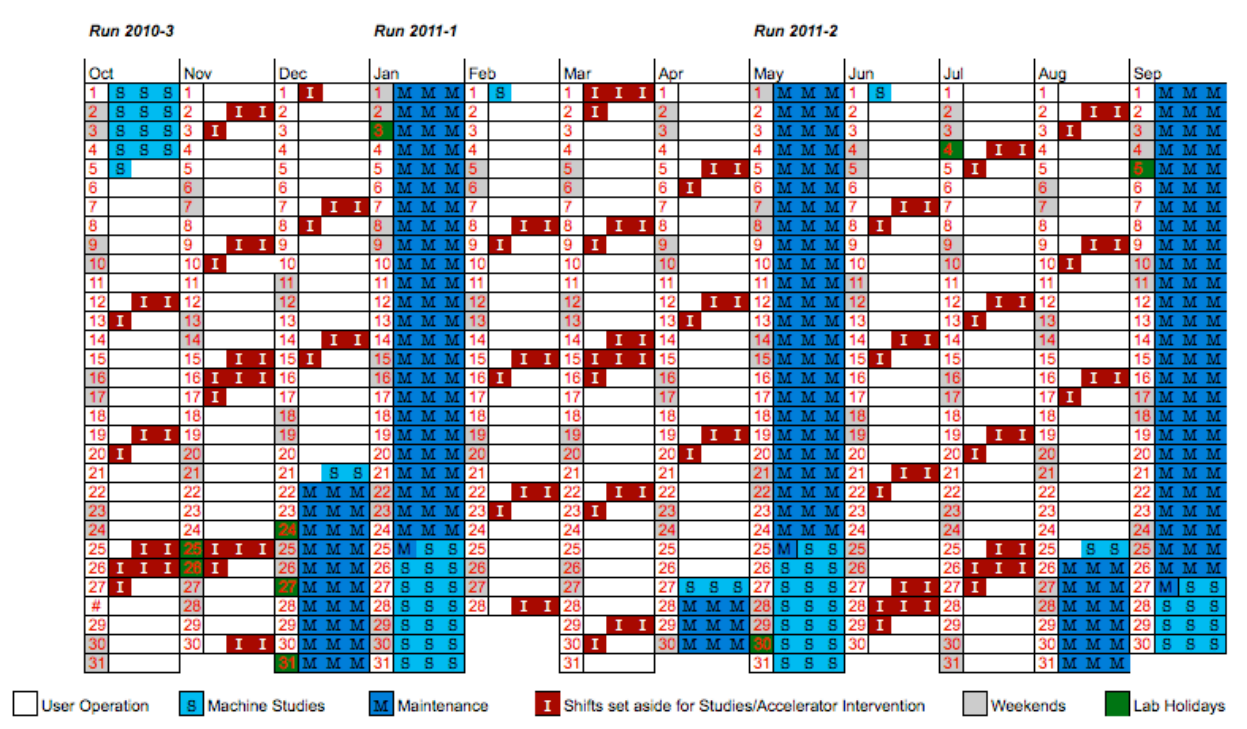

Figure 1-3: Typical APS Operating Schedule.

1.3.9 Related Management Plans

The Project has developed a number of management documents that guide the overall development of the Project. Some of these documents are required by DOE to achieve critical decision milestones, and others are considered best practice. A brief description of each of the key documents developed during Preliminary Design for the CD-2 phase is described below.

The **Project Execution Plan (PEP)** summarizes the information and processes that are essential for successful management of the APS Upgrade Project. The PEP is the primary agreement regarding Project objectives, planning, and execution among DOE Office of Science (SC) / Basic Energy Sciences (BES), the DOE Argonne Site Office (ASO), and Argonne National Laboratory.

The **Project Implementation Plan (PIP)** describes the project management structure, responsibilities, systems, and processes used for managing the Project. The Project provides the management and oversight to achieve the scientific, technical, cost and schedule objectives for the Project. The PIP serves as a supplement to the PEP and provides further details specific to the Project. Any discrepancies between the two should rely on the PEP for clarification. While the PIP is a living document; it is placed under configuration control at CD-2 and will be reviewed and updated throughout the life of the Project as appropriate.

The **Configuration Management Plan** describes the configuration management responsibilities and processes that support the design and implementation of the Project. The purpose of the Configuration Management Plan is to identify the organization responsible for providing the configuration control,

define a configuration-controlled item, describe the change control process, and identify the plan for configuration status accounting and verification.

The **Risk Management Plan** for the Project defines the strategy implemented to manage risk associated with cost, schedule, technical scope, environment, safety and health (ES&H), and Quality Assurance (QA). It is supported by the full Risk Register.

1.4 Scope Summary

The detailed summaries provided below are excerpted and repeated here from the introductory sections of Chapters 3, 4 and 5 of this PDR; this section is provided as a consolidated high-level description of the Project scope. Further details and descriptions of all Project elements can be found in the full version of the corresponding chapters.

1.4.1 Accelerator Upgrades

The APS is the largest accelerator complex in the Western Hemisphere dedicated to the production of synchrotron radiation using electrons stored in a ring. With a 1104-m circumference and a 7-GeV beam energy [2] there are only three other sources in the world with a comparable size and electron beam energy [3, 4, 5]. APS consists of an injector and storage ring. The purpose of the injector is to supply beam to the storage ring. No changes to the injector are planned as part of the APS Upgrade Project. A number of upgrades to the storage ring will be undertaken, as detailed in in Chapter 3 of this PDR. These upgrades are targeted at specific changes that will improve the scientific capabilities of the APS in order to address the Mission Need and Key Performance Parameters (KPPs) described earlier in section 1.2.4.

1.4.1.1 Accelerator Complex and Present Operations

The APS contains 40 largely identical sectors, each of which consists of accelerator components and a 5-m-long straight section. Five of these straight sections are reserved for accelerator systems required for beam injection, replenishing of the electron beam energy, and diagnostics. The remaining 35 straight sections are available for insertion devices, typically undulator magnets that produce x-rays for user experiments. The maximum length available for such devices is 4.8 m. Each sector also contains two bending magnets, one of which is designed for use as an x-ray source.

The most fundamental parameters of the stored electron beam are the energy, current, and emittance. Light sources targeting hard x-ray applications tend to operate with high electron beam energy E, since the energy of x-rays produced in undulators scales like E^2. There is also a tendency to operate with moderate beam current to reduce rf power requirements and x-ray beam power loads on the beamline front ends to more manageable levels. The APS presently operates at 100 mA, which is fairly typical of

sources in this energy range. The APS effective emittance,[1] 3.1 nm, is again typical for high-energy third-generation sources. The normal vertical emittance is 40 pm, which is somewhat higher than typical, resulting both from user requirements and the desire to operate routinely in few-bunch modes (see below). Of these basic parameters, only the beam current and emittance will change as part of the APS Upgrade, as discussed below.

Besides total beam current, the electron beam bunch timing pattern is very important for many applications. For this reason, APS operates with various bunch patterns or modes (depicted in Figure 1-4):

- ***24-bunch mode:*** As the name suggests, this features 24 equispaced bunches. The time between bunches is about 150 ns, with a full width half maximum (FWHM) bunch duration of about 80 ps, which is suitable for certain time-resolved studies. This mode is used about 65% of the time.
- ***Hybrid mode:*** This features a single intense bunch of 16 mA together with a collection of 56 bunches crowded on the opposite side of the ring. There is a space of about 1.6 ms before and after the intense bunch that has a FWHM duration of about 120 ps, which again makes it suitable for certain time-resolved studies. This mode is used about 15% of the time.
- ***324-bunch mode:*** This features 324 equi-spaced bunches. This mode is used about 20% of the time.

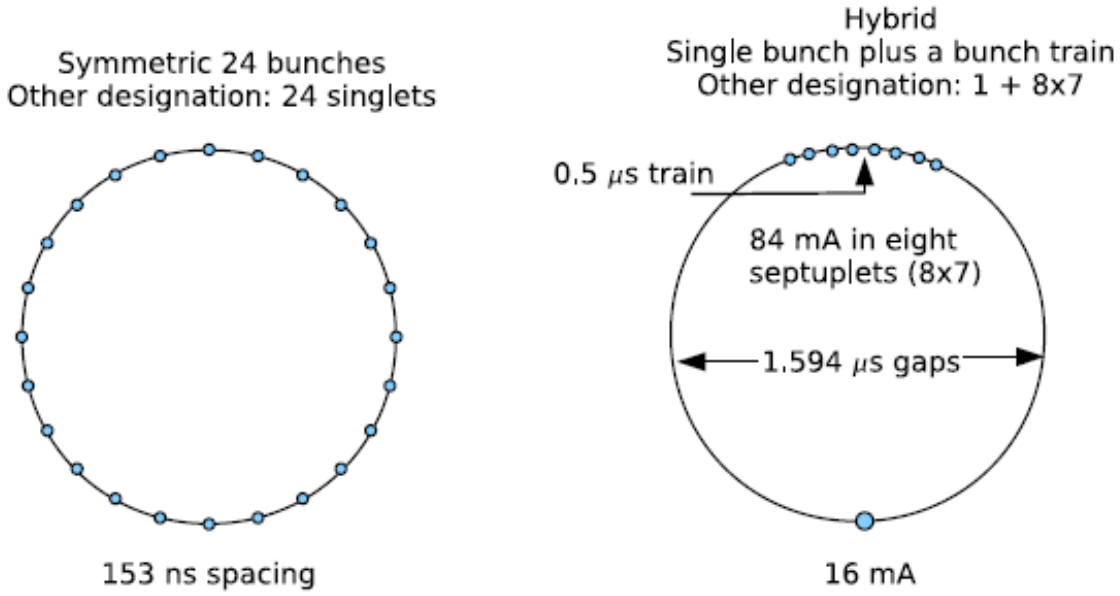

Figure 1-4: Depictions of two bunch patterns at present operating current of 100 mA.

[1] The effective emittance is the emittance including dispersion effects. At the center of a straight section with $\alpha_x = 0$ and $\eta'_x = 0$, it is given by $\sigma_x \sigma_{x'} = \epsilon_0 \sqrt{1 + (\sigma_\delta \eta_x)^2 / (\epsilon_0 \beta_x)}$, where σ_x is the rms beam size, $\sigma_{x'}$ is the rms divergence, ϵ_0 is the raw natural emittance, and α_δ is the fractional rms energy spread.

One goal of the Project is to continue to support operation in all three modes. Another important aspect of the beam is partitioning of the effective emittance into the beam size and divergence in the horizontal and vertical planes. The electron beam size and divergence are nominally identical at all beamlines, a result of the 40-fold symmetry of the accelerator lattice. However, reduced horizontal beam (RHB) size can be delivered to one straight section, while leaving other straight sections unchanged. At present, each APS run includes some time operating with such a lattice. In principle, this can be provided to several sectors when there is demand. At present, there is little impact on machine operation from the broken symmetry. As discussed in subsequent sections, delivering this mode in the APS Upgrade is more challenging because of other lattice changes.

The combination of low emittance and high charge per bunch in the 24-bunch and hybrid modes leads to short beam lifetimes. Even with a vertical emittance of 40 pm, the lifetime in 24-bunch mode at 100 mA is typically 8 hours, while the lifetime of the hybrid bunch is about 3 hours. Because of this, the beam intensity would decay rapidly, resulting not only in loss of x-ray intensity, but perhaps more importantly, in variation in beam-position-monitor (BPM) systematics and heat loads on x-ray optics. This would negatively impact experiments that demand high beam stability. For these reasons, the APS pioneered top-up mode [6], which involves frequent injection of beam to make up for losses. At present, top-up injections occur at 2-minute intervals in 24-bunch mode and 1-minute intervals in hybrid mode. The 324-bunch mode has a sufficiently long lifetime that top-up is not required; instead, the beam is added every 12 hours to restore 100 mA. One additional attraction of this mode is that it provides valuable time for injector development and operator training.

APS operates for users for approximately 5000 hours per year, with typical mean time between faults of 50 to 100 hours and availability of 97 to 99%. There are three runs and three shutdowns per calendar year. During a run, weekly maintenance and study periods are scheduled, lasting for 24 to 48 hours. Much of this time is used to perform necessary repairs or studies that prepare the accelerator for an upcoming change in the fill pattern or lattice.

1.4.1.2 Accelerator Upgrade Components

The APS accelerator upgrade includes a number of components, several of which will be unique. These are driven by Mission Need and Key Performance Parameters, discussed in section 1.2.4, including

- The need for additional beamline capacity
- The need for more stable beams to allow demanding, state-of-the-art experiments to be performed
- The need to provide intense, tunable, few-picosecond x-ray pulses with high repetition rates for time-domain experiments
- The need to provide higher brightness and flux in the hard x-ray regime (above 10 keV), with particular emphasis at 25 keV and above.

Implementation of these upgrades will present many challenges, not the least of which is the intention to continue to operate the APS for 5000 hours per year. This implies that installation of components in the storage ring, as well as commissioning of new systems, will have to take place during existing

maintenance and startup periods. In this introduction, the approach to each of these requirements is briefly described; details are provided in Chapter 3 of this PDR.

By and large, each of these upgrades could be pursued independently. That is, they are complementary, but not tightly linked. If there are links, they are indicated in Chapter 3.

1.4.1.3 Capacity

The need for additional beamline capacity is addressed by provision of additional canted straight sections and long straight sections. At present, each straight section at APS accommodates a total of 4.8 m of insertion devices, which is suitable for canting two devices with a length of 2.1 m each. As described in section 3.2, the Project plans to provide three long straight sections for which the total length of insertion devices is increased to approximately 7.7 m. This allows increased capacity with higher brightness and flux, due to the longer devices that are possible. Provision of long straights is also beneficial in order to implement the Short-Pulse X-ray (SPX) scheme without reducing capacity (i.e., the long straights are helpful in accommodating the SPX hardware and insertion devices in the same straight).

Provision of long straights has a modest negative effect on brightness because the horizontal emittance will increase. However, the increase is less than 10%, which is considered acceptable.

1.4.1.4 Stability

More stable beams will allow demanding, state-of-the-art experiments to be performed. This is addressed by a multipronged approach to improving electron beam stability, as described in section 3.3. The goal is to increase the short- and long-term beam stability by a factor of two to four.

Improved beam stability has essentially no negative impacts on other aspects of the APS Upgrade. Indeed, it is helpful in that it is in some cases equivalent to a brightness increase. The Short-Pulse X-ray (SPX) project has the potential to negatively impact beam stability. As a result, specific steps are taken as part of the SPX project that include setting tolerances on various errors and providing the diagnostics needed for control, feedback, and fine tuning.

1.4.1.5 Short X-ray Pulses

There is a need to provide intense, tunable, few-picosecond x-ray pulses with high repetition rates for time-domain experiments. This is addressed by the use of Zholents' deflecting-cavity scheme [7] for production of short x-ray pulses. This scheme, discussed in section 3.6, addresses one of the major deficiencies of storage ring light sources, namely, the inability to make intense, few-picosecond x-ray pulses.

As stated above and described in detail in section 3.6.3.2, the SPX system has the potential to negatively impact beam stability, both in terms of beam motion and emittance. Hence, upgrades to the beam stabilization systems, in particular the fast feedback system, are highly desirable as a complementary upgrade. In addition, a comprehensive suite of SPX-specific diagnostics are planned.

1.4.1.6 Brightness and Flux

There is a need to provide higher brightness and flux in the hard x-ray regime, above 10 keV, with particular emphasis above 25 keV. This is addressed in part by optimized insertion devices, as described in section 3.4, which includes planar undulators with customized periods, revolver undulators, and short-period superconducting undulators. The need for higher brightness and flux is also addressed by provision of a number of long straight sections, as described in section 3.2, and by increasing the operating electron beam current from 100 mA to 150 mA.

In addition, improved control of the coupling will be implemented, which will also improve x-ray brightness by permitting lower vertical emittance and providing more predictable beam parameters. These changes are described in more detail in section 3.2.

1.4.1.7 Accelerator Systems Upgrade Project Scope and Work Breakdown Structure

The accelerator portion of the APS Upgrade Project scope is detailed in Table 1-6, together with related Work Breakdown Structure (WBS) elements, for ease in correlating the accelerator scope items detailed in Chapter 3 with other Project documentation.

Storage Ring Technical Components, WBS U1.03.02, includes two lower-level WBS areas: improvement by a factor of two to four in beam stability (WBS U1.03.02.01) and design, construction, and installation of long straight sections in the APS storage ring (WBS U1.03.02.02). Beam stability improvements are discussed in section 3.3, while long straight sections and other lattice changes are discussed in section 3.2.

The Short-Pulse X-ray (SPX) System, WBS U1.03.03, includes the design, construction, installation, and checkout verification of all components of the SPX deflecting-cavity system, with the exclusion of the actual buildings that will house the components. SPX and the risk-mitigating SPX0 research and development program are discussed in section 3.6.

Insertion Devices (IDs), WBS U1.03.04, includes both superconducting and conventional permanent magnet and electromagnetic planar and polarizing devices. The devices that will be constructed, installed, and tested by the APS Upgrade are listed in Table 1-6. Insertion devices are discussed in section 3.4.

Planar Undulators, WBS U1.03.04.01, are constructed based on existing designs at the APS. This WBS area includes the construction, installation, and checkout verification of all components of the required number of planar undulator systems. Development of a new magnetic period is included in the baseline, a standard, well-understood activity at the APS. Planar undulators are discussed in section 3.4.2.

WBS U1.03.04.02 includes two types of polarizing undulators. The EMVPU, U1.03.04.02.01, is an electromagnetic device, while APPLE-II devices, U1.03.04.02.01, are based on permanent magnets. The EMVPU and APPLE-II undulators are discussed in sections 3.4.3.3 and 3.4.3.2. These WBS areas include the construction, installation, and checkout verification of all components of the required number of polarizing undulator systems. It is assumed that the EMVPU will be designed and constructed in-house, and that APPLE-II devices will be specified by the APS Upgrade and then procured from industry.

Superconducting Undulators, WBS U1.03.04.03, includes development of an 18-mm-period, approximately 1-m-long engineering prototype device. Development and production of a 2-m-long full-scale device of the same period length is included in the same WBS area. The SCU scope includes design, construction, installation, and checkout verification of all deliverables of the SCU system.

Results of the risk-mitigating SCU0 programmatically supported research and development program are discussed in section 3.5. Revolver Undulators, WBS U1.03.04.04, includes the construction, installation, and checkout verification of all components of the required number of revolver undulator systems. The risk-mitigating revolver-development program is discussed in section 3.4.2.5.

Canted Section Magnets, WBS U1.03.04.05, are required in some sectors, as are corrector magnets. This WBS area includes the construction, testing, installation, and checkout verification of the magnets and power supplies included within this system.

Insertion Device Vacuum Chambers, WBS U1.03.04.07 includes procurement of aluminum extrusions and fabrication and testing of the required number of ID vacuum chambers. All IDs require ID vacuum chambers; however, some of the existing chambers will be re-used. ID vacuum chambers are discussed in section 3.2.7.9.

APS Upgrade Project funding covers all activities up to actual commissioning with beam in the storage ring. Commissioning activities are the responsibility of APS Operations, and are not part of the scope of the APS Upgrade. The Transitions to Operations plans are discussed further in the APS Upgrade Project Execution Plan.

Two of the accelerator upgrades, the improved beam stability and 150-mA operating current (section 3.7) will benefit all APS users, while the impact of others, such as SPX and the new IDs, will be restricted to specific beamlines.

Table 1-6: The APS Upgrade accelerator systems project scope and corresponding WBS elements.

WBS	Description	Quantity	Section
U1.03.02	Storage Ring Technical Components		
U1.03.02.01	Beam Stability		3.3
U1.03.02.02	Long Straight Sections	3	3.2
U1.03.03	Short-Pulse X-ray (SPX) System		
U1.03.04	Insertion Devices	13	3.4
U1.03.04.01	Planar Undulator	3	3.4.2
U1.03.04.02.01	Electromagnetic Variability Polarizing Undulator (EMVPU)	1	3.4.3.3
U1.03.04.02.02	Advanced Planar Polarized Light Emitter (APPLE-II)	2	3.4.3.2
U1.03.04.03	Superconducting Undulator (SCU2)	1	3.5
	Superconducting Undulator Engineering Prototype (SCU1)	1	
U1.03.04.04	Revolver Undulator	5	3.4.2.5
U1.03.04.05	Canted Section Magnets	8	
	Corrector Magnets	2	
U1.03.04.07	Insertion Device Vacuum Chambers (IDVC)	12	3.2.7.9

1.4.1.8 Interdependency

Several key interdependencies exist between the APS Upgrade Project's accelerator systems activities in WBS U1.03 and the APS X-ray Science (XSD) and APS Engineering Support (AES) divisions. Accelerator-related Physics Requirements Documents (PRDs) are developed by Accelerator Systems Division (ASD) personnel and may be approved by ASD, AES, XSD, and APS Upgrade personnel. Funding for the effort required to plan, design, procure, assemble, install, document, and test Project systems and components is provided by the APS Upgrade Project.

Commissioning with x-ray beam is not included in the APS Upgrade scope, but is the responsibility of the X-Ray Science Division. Beam commissioning plans developed by XSD personnel are approved by ASD, AES, XSD, and APS Upgrade personnel, as appropriate.

There are interdependencies between the APS Upgrade accelerator, beamline, and enabling technologies WBS areas. Beamline technical leads write beamline-specific PRDs, listing the required x-ray energies and harmonics. Accelerator scientists develop PRDs for each of the insertion devices to be provided by the APS Upgrade Project.

Interface Control Documents (ICDs), signed by all relevant parties within the three technical WBS areas, formalize technical details, such as the period length of an insertion device.

The building that will house many of the SPX system components is being provided with funding that is external to the Project. SPX relies heavily on collaboration with JLAB and LBNL; Stanford Linear Accelerator Center (SLAC) also provides simulations.

The building in which superconducting undulator development takes place was refurbished by the Laboratory and furnished to the APS Upgrade team for this purpose.

Insertion device research and development is also funded off-Project; however, progress is closely monitored by the Project. Superconducting undulator development relies on a collaboration with the University of Wisconsin for thermodynamic calculations.

1.4.2 Experimental Facilities Upgrades

The Experimental Facilities (WBS element U1.04) consist of all of the beamlines that are being significantly impacted by the APS Upgrade Project, beamline optics and heat-load-component upgrades needed to accommodate the increased storage ring current, and general development of detectors and nanofocusing optics. In this chapter, the preliminary design activities in each of these areas are discussed. In addition, contingent additional scope (CAS) that is under consideration for possible inclusion in the Project is clearly identified and briefly described. If the CAS relates to enhancement of an individual beamline, that discussion occurs in the context of that beamline subsection; if the CAS item is an entire beamline, it will be discussed in section 4.21.

In the baseline plan that is being submitted for Critical Decision 2 (CD-2) approval, there are 20 beamlines that are directly part of the APS Upgrade Project: eight are new beamlines (three on unoccupied ports, five from cants), six are upgrades in place and six are relocations. This does not include

additional beamlines that will get optics or heat load component upgrades due to the increase of the storage ring current to 150 mA (WBS U1.04.04).

1.4.2.1 APS Roadmap and Consequences to the APS Upgrade

An activity with a major effect on the U1.04 Preliminary Design has been the APS Roadmap process [8]. The APS Roadmap is a long-term plan for the locations of current and potential future programs and beamlines at the APS. The plan includes APS Upgrade related beamlines (both in scope and CAS), but also includes proposed beamline activities that are not part of the upgrade Project scope, such as the Dynamic Compression program which has been located at sector 35. After a lengthy development process and numerous interactions with APS stakeholders, a “base” scenario was developed and released on April 30, 2012. The locations of the new, upgraded, and relocated beamlines in the APS Upgrade scope are listed in Table 1-1 above. The Preliminary Design and all costs/schedule described in this document are for this base design. In addition, two optional Roadmap scenarios involving rearrangements of four beamlines have been developed (see Table 1-7).

Some of the key features of the APS Roadmap are:

- No collaborative access team (CAT) program will be relocated.
- The Wide Field Imaging (WFI) program will be placed at 20-ID. This beamline will be the first to extend beyond the boundaries of the APS experiment hall. A consequence is that the current spectroscopy programs on 20-ID (essentially the same as the Advanced Spectroscopy and LERIX [ASL] program) will be relocated.
- The three unoccupied insertion device (ID) locations at the APS will be filled by ASL, Resonant Inelastic X-ray Scattering (RIXS), and X-ray Interface Science (XIS).

A consequence of the Roadmap is that several coordinated moves of beamline programs are required. This "domino" effect is a significant challenge for beamline upgrade scheduling that we have taken into account in developing the Roadmap and the schedule presented in this Preliminary Design.

A simple domino effect is the placement of WFI at 20-ID, which requires that the ASL program moves to 25-ID. This is straightforward because 25-ID is currently unoccupied and the activities at 25-ID for ASL can start as soon ASL is technically ready to move. This gives the Project some flexibility in scheduling the move of ASL, with the major constraint that all WFI activities must have time to finish prior to the end of the Project.

A more complicated domino effect arises from the need to locate the Short Pulse X-ray Imaging and Microscopy (SPXIM) beamline at 6-ID so that it is located between the short-pulse deflecting cavities, providing access to the SPX pulses. As a result, the current MD program at 6-ID must be relocated and the base Roadmap scenario places it at 2-ID. The current 2-ID program, mFluor, is therefore displaced to a cant on 9-ID. The current programs at 9-ID, RIXS and Liquid Surface Scattering (LSS), will move to 27-ID and 28-ID, respectively. This sequence of program moves requires careful attention in the schedule. The initial moves of RIXS and LSS must occur very early in the Project to allow enough time for the subsequent activities.

Table 1-7: Differences Between APS Roadmap Base Scenario and Options.

Program	Definition	BASE Scenario	Scenario Option 1	Scenario Option 2
ISN	*In Situ* Nanoprobe	32-ID-2	9-ID-2	9-ID-2
BCDI	Bragg Coherent Diffractive Imaging	9-ID-2	9-ID-1	32-ID-2
MD	Magnetic Diffraction	2-ID-1	32-ID-2	2-ID-1
XSD mFluor	Fluorescence Microprobes (2-ID-D/E)	9-ID-1	2-ID-1	9-ID-1

NOTE: For notation “n-ID-x”, “x” denotes a cant. The use of "1" or "2" does not indicate which half of the straight section is assigned.

The Roadmap process recognized that in some situations, further design work was needed to assure that the optimal location for a given program was selected. Two scenario options were defined, differing from the base scenario by the placement of the *In Situ* Nanoprobe (ISN), Magnetic Diffraction (MD), Bragg Coherent Diffraction Imaging (BCDI), and Fluorescence Microprobes (mFluor) programs. Detailed design work is still underway to understand the various pros and cons of the siting for each of these programs.

1.4.2.2 Description of Scope

Table 1-8 shows the Experimental Facilities Upgrades WBS for U1.04 down to level 3. Table 1-9 shows the scope of the U1.04.02 area of the Project. Beamlines in the area have a status of: Base, CAS, Partial, or Option. *In Scope* denotes that all aspects of the beamline described in the Project documentation are in the scope for the proposed baseline. *CAS* indicates the beamline is currently considered contingent additional scope, with only design work funded by the Upgrade. *Partial* indicates that some of the activities for that beamline are CAS. *Option* indicates a design activity for an alternate location of a particular program.

Table 1-8: U1.04 WBS Description.

WBS	Name	Comment
U1.04.01	Experimental Facilities Management	
U1.04.02	Beamlines	Includes all beamlines being upgraded by the Project, except those that are only being upgraded for 150-mA operation.
U1.04.03	(Not Utilized)	
U1.04.04	General Beamline Upgrades	

Table 1-9: U1.04.02 WBS Description.

WBS	Acronym	Title	Location	Status	Comment
U1.04.02.01	BGS	Beamline Global Support			Activities in support of beamlines globally.
U1.04.02.02	SPXSS	Short Pulse X-ray Scattering and Spectroscopy	7-ID	In Scope	In-place upgrade.
U1.04.02.03	SPXIM	Short Pulse X-ray Imaging and Microscopy	6-ID	In Scope	New beamline.
U1.04.02.04	HFPP	High Flux Pump-Probe	14-ID	In Scope	In-place upgrade.
U1.04.02.05	WFI	Wide Field Imaging	20-ID	In Scope	New beamline.
U1.04.02.06	HEXT	High Energy X-ray Tomography	Not sited	CAS	Assumes unoccupied site with “superbend”. Preliminary and final design effort in scope.
U1.04.02.07	ISN	In-situ Nanoprobe	32-ID	In Scope	New beamline on cant. TXM remains on other cant.
U1.04.02.08	RIXS	Resonant Inelastic X-ray Scattering	27-ID	In Scope	27-ID currently unoccupied. New beamline, incorporates RIXS programs from 9-ID and 30-ID.
U1.04.02.09	MS-H	Magnetic Spectroscopy-Hard	4-ID	In Scope	In-place upgrade. Assumes MS-S moved from 4-ID. APPLE undulator.
U1.04.02.10	HEXD	High Energy X-ray Diffraction	1-ID	In Scope	New beamline on cant, in-place upgrade on other cant.
U1.04.02.11	XIS	X-ray Interface Science	28-ID	Partial	28-ID currently unoccupied. New beamlines for tunable branch 1 and LSS program from 9-ID on branch 2 are in scope. Rest of branch 2, and branches 3 & 4 are CAS.
U1.04.02.12	S3DD	Sub-micron 3D Diffraction	34-ID	In Scope	New beamline on cant, in-place upgrade on other cant, includes mDiff program from 2-ID.
U1.04.02.13	ASL	Advanced Spectroscopy and LERIX	25-ID	Partial	25-ID currently unoccupied. Relocations of programs from 20-ID are in scope, upgrade items are CAS.
U1.04.02.15	SPSXS	Short Pulse Soft X-ray Spectroscopy	6-BM	CAS	Preliminary and final design effort in scope.

WBS	Acronym	Title	Location	Status	Comment
U1.04.02.16	MS-S	Magnetic Spectroscopy-Soft	2-ID	In Scope	Upgrade of program from 4-ID. Assumes MD on other branch.
U1.04.02.17	MD	Magnetic Diffraction	2-ID	In Scope	Relocation from 6-ID. Assumes MS-S on other branch.
U1.04.02.18	FSD	Fuel Spray Dynamics	BM, not sited	In Scope	Relocation from 7-BM. Assumes unoccupied bending magnet.
U1.04.02.19	BCDI	Bragg Coherent Diffractive Imaging	9-ID	In Scope	Relocation from 34-ID. Assumes mFluor on other branch.
U1.04.02.20	mFluor	Fluorescence Microprobes	9-ID	In Scope	Relocation from 2-ID. Assumes BCDI on other branch.
U1.04.02.21	LSS-1	Liquid Surface Scattering	15-ID	Option	Option for LSS at 15-ID.
U1.04.02.22	MS-S-2	Magnetic Spectroscopy-Soft	4-ID	Option	Option for MS-S remaining at 4-ID.
U1.04.02.23	MS-H-1	Magnetic Spectroscopy-Hard	4-ID	Option	Option for MS-S remaining at 4-ID.
U1.04.02.24	ISN-1	In Situ Nanoprobe (Option 1)	9-ID	Option	Option for ISN at 9-ID with BCDI.
U1.04.02.25	BCDI-1	Bragg Coherent Diffractive Imaging (Option 1)	9-ID	Option	Option for BCDI at 9-ID with ISN.
U1.04.02.26	MD-1	Magnetic Diffraction (Option 1)	32-ID	Option	Option for MD at 32-ID on new cant with TXM. High speed imaging relocates.
U1.04.02.27	mFluor-1	Fluorescence Microprobes (Option 1)	2-ID	Option	Option for mFluor remaining at 2-ID with MS-S on other branch.

The scope for U1.02.02 and U1.04.04 is given in Table 1-10 and Table 1-11. WBS U1.02.02.02 is R&D activities in support of U1.04. WBS U1.04.04.01 and U1.04.04.02 are for upgrading optics and high-heat-load components for beamlines that are not otherwise part of the Project in order to mitigate any heat load issues caused by increasing the storage ring current to 150 mA. WBS U1.04.04.03 is for activities for development and deployment of fast-framing pixel-array detectors and WBS U1.04.04.04 is for the development of nanofocusing optics.

Table 1-10: U1.02.02 WBS.

WBS	Title
U1.02.02.01	High Speed Detection Development
U1.02.02.02	Resonant Inelastic X-ray Scattering Optics R&D
U1.02.02.03	Nanofocusing Optics Development

Table 1-11: U1.04.04 WBS.

WBS	Title
U1.04.04.01	High-Heat-Load Optics
U1.04.04.02	High-Heat-Load Components
U1.04.04.03	Detectors (Closed)

1.4.2.3 Beamline Summaries

1.4.2.3.1 Short Pulse X-ray Scattering and Spectroscopy (SPXSS)

The SPX Facility consists of three independent beamlines: Short Pulse X-ray Scattering and Spectroscopy (SPXSS); Short Pulse X-ray Imaging and Microscopy (SPXIM); and the Short Pulse X-ray Soft X-ray Spectroscopy (SPSXS), which is in contingent additional scope. These three beamlines are located between the two rf deflection cavities that provide chirped electron pulses.

The SPXSS beamline will provide picosecond-duration, high-repetition-rate pulses of tunable, polarized x-ray radiation to enable ground-breaking experiments in chemical dynamics, condensed matter physics, materials science, and atomic physics. The picosecond time scale has unique importance because it is an excellent match for structural dynamics in nanoscale systems and for conformational changes in molecular and supramolecular systems. These areas are of technological relevance, as well as fundamental interest. The maximum repetition rate is ideal for flowing gas- and liquid-phase samples and for emerging nanoscale devices operating in the terahertz domain. Examples of science enabled at the SPXSS beamline include: Photoinduced energy and electron transfer; solvation dynamics; thermal and atomic transport at interfaces; dynamics of fundamental excitations; and laser control of x-ray absorption.

1.4.2.3.2 Short-Pulse X-ray Imaging Microscopy (SPXIM)

The principal goal of the Short-Pulse X-ray Imaging Microscopy (SPXIM) beamline is to provide picosecond-duration, high-repetition-rate pulses of tunable, polarized x-ray radiation for imaging and microscopy experiments in condensed matter physics and materials science. The picosecond time scale has unique importance because it is an excellent match for structural dynamics in nanoscale systems. These areas are of technological relevance as well as fundamental interest.

The facilities described here will facilitate ground-breaking experiments in a range of scientific problems. The SPX facilities will have an important and immediate impact on unresolved problems in these areas. Scattering, imaging, and spectroscopy probes will be particularly valuable in five areas: Dynamics in

ferroic materials, High-frequency materials and devices, Thermal and atomic transport at interfaces, Dynamics of fundamental excitations, Picosecond imaging.

1.4.2.3.3 High Flux Pump-Probe (HFPP)

The High Flux Pump-Probe (HFPP) located on the 14-ID beamline is part of BioCARS, a national user facility for synchrotron-based macromolecular crystallography and an integral part of the multi-disciplinary Center for Advanced Radiation Sources (CARS) at the University of Chicago. The APS Upgrade Project scope for the HFPP beamline consists of two major components: 1) Construction of a larger 14-ID-D experimental station to accommodate complex sample environments, additional x-ray optics, and extend the SAXS/WAXS resolution; and 2) a Kirkpatrick-Baez (K-B) mirror system for secondary focusing. With the ability to isolate a high-flux single x-ray pulse, the 14-ID beamline provides unique capabilities at the APS and in the US. The facility is able to accommodate researchers from the fields of atomic and molecular physics, biology, chemistry, materials science, and materials under extreme conditions. The beamline has the capability to perform small-molecule and macromolecular crystallography; wide angle x-ray scattering (WAXS) in solids, solution, and gas phases; general diffraction; and thermal diffuse scattering.

1.4.2.3.4 Wide Field Imaging (WFI)

The scientific focus for the Wide Field Imaging (WFI) beamline is on dynamics. The goal is to perform two-dimensional (2-D) or three-dimensional (3-D) imaging with ~1-µm spatial resolution, as fast as possible. Based on experience at APS beamline 32-ID, it will be possible to image very- high-speed phenomena with 100-ps exposure time. For tomography, it should be possible to obtain an entire 3-D data set in 10 ms. The scientific drivers for this beamline cover a very broad range of disciplines and requirements. Sample sizes will range from ~1-50 mm, and can be soft-tissue (biomedical applications) or high-Z materials (superalloys). As such, the design of the beamline includes three experiment stations, near, middle, and far. The near station will accommodate experiments that require the highest temporal resolution, while the far station will accommodate experiments that require the highest sensitivity and spatial resolution. The middle station will accommodate experiments between those two.

1.4.2.3.5 *In Situ* Nanoprobe (ISN)

The *In Situ* Nanoprobe (ISN) beamline is aimed at highest-resolution imaging, spectroscopy, and tomography of energy materials and energy devices, as well as of other complex systems. The ISN beamline will provide a spatial resolution of 20 nm using diffractive optics, and of 50 nm using reflective optics. The ISN instrument will provide variable temperature, flow of gases and fluids, and applied electrical fields, towards the study of properties of materials and devices under *in situ* conditions, including materials fabrication and device operation.

The ISN encompasses the study of advanced energy harvesting, conversion and storage systems, approaches to sustainable energy, platforms for advanced electronics, and materials and systems aimed at sustainable construction and carbon capture. All these systems have in common complex, hierarchical structures with nanoscale features often in nonplanar geometries, where small quantities of

inhomogeneously distributed dopants, precipitates, contaminants, and second-phase particles play an increasingly important role in overall system performance.

1.4.2.3.6 Resonant Inelastic X-ray Scattering (RIXS)

Currently the Resonant Inelastic X-ray Scattering (RIXS) program is spread over two time-shared beamlines of varying sophistication. In the context of the APS Upgrade Project, it will be consolidated at one dedicated, optimized, state-of-the-art insertion device beamline at 27-ID. Explicit goals are to optimize x-ray source parameters for this photon-hungry technique, improve the energy-resolution from the ~100 meV to the ~20 meV level or even better, and optimize throughput and momentum resolution by implementing multi-analyzer assemblies. Furthermore, new capabilities will be added including sample stages allowing access to small scattering angles, polarization control and analysis for incident and scattered photons, and a comprehensive suite of sample environments for meaningful *in situ* experimentation.

RIXS, with its small-scattering cross section, has become viable only with the advent of third-generation synchrotron radiation sources and remains somewhat hampered by the relatively coarse energy resolutions (~100 meV) available until recently. In the context of the APS Upgrade, these shortcomings will be remedied and the resulting increased capabilities will dramatically improve the quality of information that may be extracted from a given sample with this already powerful technique.

1.4.2.3.7 Magnetic Spectroscopy Hard X-rays (MS-H)

Beamline 4-ID-D is dedicated to variable-polarization hard x-ray spectroscopic studies of electronic and magnetic materials. The element- and orbital-specificity inherent to the x-ray absorption process, coupled with the high brilliance and penetrating power of hard x-rays, probe changes in valence state, orbital occupancies, hybridization, charge transfer, and electronic ordering under extreme pressures. Furthermore, when coupling high-pressure with magnetic fields, x-ray magnetic dichroism techniques can be used to yield element-specific information on spin-polarization, orbital and spin magnetization, magneto-crystalline anisotropy, and magnetic ordering at high pressures. Beamline 4-ID-D is currently the only facility in the United States for performing magnetic dichroism experiments using hard x-rays. The upgrade includes: installation of an APPLE-II; installation of Kirkpatrick-Baez (K-B) mirrors for high-pressure studies; addition of fine roll adjustment to the second-crystal monochromator for dynamic control of horizontal beam position; new instrumentation for high field (10 T) and high pressure (> 1 Mbar) x-ray magnetic circular dichroism (XMCD) experiments; and expansion of the experimental station to accommodate new instrumentation.

1.4.2.3.8 High-Energy X-ray Diffraction (HEXD)

The high-energy x-ray program at 1-ID will upgrade the existing beamline and add a second beamline by canting the 1-ID straight section. A short-period superconducting undulator (SCU) and increased storage current will provide an order of magnitude more flux at 1-ID than available today at high x-ray energies. The equivalent brilliance increase will be exploited by short-focal-length optics setups in all stations to deliver micro-focused beamlines to experiments. Four experimental stations will permit optimized instruments dedicated to SAXS/WAXS, HEDM, tomography, resonant scattering, fluorescence, and

investigations of surfaces and buried interfaces. Combined SAXS/WAXS enables studies of materials over micron to angstrom length scales. Similarly, near- and far-field HEDM techniques would be merged such that a single sample can be probed on multiple length scales, with application to grain growth, *in situ* deformation of metallic alloys, and stress fields of a propagating crack. Simultaneous tomographic capability can locate voids and cracks. Resonant scattering near heavy-element K-edges enables obtaining high-spatial-resolution pair distribution function measurements of interatomic structure with the added strength of element selectivity, providing insights into the structural disorder in Pt nanoparticle catalysts. The surface instrument, in combination with high-energy x-rays, will allow characterization of systems having important interfaces that lie buried deeply under their exposed surfaces.

1.4.2.3.9 X-Ray Interface Science (XIS)

Four new beamlines are proposed for this facility dedicated to interface science. These beamlines form the core of a broader development plan for a comprehensive interface science "village". The primary beamline and the first station of the first fixed-angle beamline are in the scope of Project. The second station of the first fixed-angle beamline and the other two fixed-angle beamlines are contingent additional scope (CAS). The primary beamline will be widely tunable and will provide a flexible diffractometer instrument that will enable state-of-the-art x-ray interface scattering studies. The two remaining experimental stations on this beamline will used to house customized instruments provided by the user community. The first fixed-angle beamline will be the home of the liquid surface scattering (LSS) instrument and program from 9-ID.

1.4.2.3.10 Sub-Micron Three-Dimensional Diffraction (S3DD)

The Sub-Micron Three-Dimensional Diffraction (S3DD) beamlines include a new beamline and an upgraded beamline to be developed at 34-ID. Dedicated X-ray polychromatic and monochromatic nanofocusing platforms will be constructed. Canted undulators will allow for simultaneous and independent use of microbeam diffraction and nanoscale diffraction facilities.

The S3DD beamlines will provide users with scientific access to a suite of scanning diffraction instruments (both K-B mirror and zone-plate based), which will be unique in the world. These instruments will use highly focused beams to measure the local lattice structure, orientation, and strain tensor with high point-to-point spatial resolution. The size of the focused x-ray beams in the two independently operated stations will range from ~50 nm to ~micron in size, enabling the match of the probe size to the fundamental scale of the materials problem with a minimum of angular divergence in order to provide the highest possible resolution in reciprocal space. The ability to easily alternate between polychromatic and tunable monochromatic diffraction modes will be another key feature unique to 34-ID, enabling studies of a much wider range of randomly oriented or polycrystalline "real" materials.

1.4.2.3.11 Advanced Spectroscopy and LERIX (ASL)

The Advanced Spectroscopy (AS) and Low-Energy-Resolution Inelastic X-ray (LERIX) beamlines are canted undulator relocations of the existing programs from 20-ID. They consist of the Advanced Spectroscopy and LERIX (ASL) branch lines. The Advanced Spectroscopy branch line provides spectroscopy applications based on variable-resolution analysis of the sample fluorescence. The LERIX

branch will support the LERIX spectrometer and the ultra-high vacuum (UHV) component of the advanced spectroscopy techniques. The ASL program is relocated from 20-ID to 25-ID to enable the building of WFI as a long beamline.

1.4.2.3.12 Magnetic Spectroscopy – Soft X-rays (MS-S)

The upgrade of the soft x-ray magnetism beamline seeks to provide magnetic spectroscopy and imaging capabilities with a sensitivity level that is two orders of magnitude better than the current capabilities through a hundred fold increase x-ray flux (x10 in sensitivity), and faster polarization switching and lock-in detection (x10 increase in sensitivity). This improvement will enable XMCD experiments on materials with dilute magnetic dopants, ultra-small induced magnetic moments, and buried interfacial structures. The upgrade includes: the installation of a specialized variable-polarization insertion device with fast switching capabilities (~10 Hz); replacement of the beamline mirrors and monochromator to increase the available flux by two orders of magnitude; installation of new focusing mirrors to provide more flexible flux densities in each experimental station; and installation of a new higher-field, cryogen-free magnet to expand sample environment capabilities.

1.4.2.3.13 General Beamline Upgrades

This component of the Project has been developed specifically to assist those operating beamlines around the ring that are not directly included in the APS Upgrade Project plans. There are twenty-one "non-upgrade" sectors on the standard APS map. These active, mature, R&D producing facilities will continue to operate, uninterrupted, while the APS Upgrade, including new beamlines and beamline relocation projects, are built. The one KPP that does globally affect every research sector, upgrade or not, is the increase in ring-current from 100 mA to 150 mA.

The first beamline components under re-evaluation for increased ring current operation are the high heat load (HHL) optical elements. Historically, each APS sector was developed by independent design/build teams and chose different optical schemes depending on the science mission supported by that beamline. There are a wide variety of mirrors and monochromator designs used throughout the facility; evaluating these disparate mechanical systems and the wide variety of HHL first-crystal designs, with consideration of the sources and power loads incident upon each, is one of the goals of this sub-project.

Another critical set of beamline components under re-evaluation for increased ring current operation are the HHL absorbers. Absorbers are the generic term for the category of beamline components that absorb unneeded x-rays, convert them into heat, and safely dispose of that heat via a cooling process-water stream.

1.4.2.4 Contingent Additional Scope

The contingent additional scope for WBS U1.04 is described in detail below in the sections clearly denoted as CAS. Table 1-12 is a summary of the WBS U1.04 CAS. The Preliminary and Final Design for the CAS activities are included in the scope so that if any CAS items are brought into the Project at a future date, execution of those activities will be more easily integrated into the Project and able to commence in a timely manner.

Table 1-12: U1.04 Contingent Additional Scope.

WBS	Title	Comment
U1.04.02.06	High Energy Tomography	Entire beamline. Associated "superbend" accelerator project is also CAS.
U1.04.02.11.04	X-ray Interface Scattering Fixed Angle Beamline 1	Second station on the first fixed-angle beamline.
U1.04.02.11.05	X-ray Interface Scattering Fixed Angle Beamline 2	Entire beamline branch.
U1.04.02.11.06	X-ray Interface Scattering Fixed Angle Beamline 3	Entire beamline branch.
U1.04.02.13.03	Advanced Spectroscopy & LERIX	Optics and detectors upgrade for the LERIX branch.
U1.04.02.13.04	Advanced Spectroscopy & LERIX	Optics and detectors upgrade for the Advance Spectroscopy branch.
U1.04.02.15	Short Pulse Soft X-ray Scattering	Entire beamline.

1.4.2.5 Interdependencies

An important aspect of the Project is the independencies between the upgraded beamlines, the front ends (U1.05), the insertion devices (U1.03), the rest of the accelerator (U1.03), and APS operations. Physics Requirement Documents (PRDs), Engineering Specification Documents (ESDs), and, especially Interface Control Documents (ICDs) are utilized to manage these interdependencies, along with linkages in the cost/scheduling database. The required approvals for each of these documents include key people in each area to insure that information is robustly distributed throughout the APS. The Project also encourages, and often arranges, face-to-face meetings between key personnel in different areas to resolve or clarify issues.

The APS is the largest scientific user facility in the United States and serious consideration has been given to planning the APS Upgrade Project in such a manner as to avoid unnecessary disruption to user operations. With the exception of the three unoccupied ID beamlines, all of the other beamline activities have an impact on currently operating beamlines. Wherever possible, disruptive installation activities (e.g., the building of a new shielded enclosure) are scheduled for a shutdown (non-user beam) period, and staging of upgrades is sometimes possible to avoid long shutdown of individual beamlines. Close coordination of the front end, storage ring, and insertion device schedules (with linkages in the scheduling database) is required to assure that all aspects of the necessary infrastructure is in place for efficient handover of a beamline to operations.

The technical leads for all beamline projects are matrixed from the X-ray Science Division (XSD) and most still have significant operational responsibilities. Matrixing personnel from other areas to support a project always presents challenges, but a strong advantage is that potential Project/Operations conflicts are often avoided, or at least minimized, when staff have shared responsibilities between the Project and Operations. Because of their experience, the technical leads have usually worked with the front end and accelerator personnel and both sides have some understanding of each other's needs. This also helps to minimize Project/Operations conflicts.

Several beamline design aspects are strongly dependent on the capabilities provided by the accelerator (U1.03; see chapter 3 of this PDR). The choice of ID is key for optimal performance of a beamline and selection of period, length, tunability, polarization, etc. is highly specialized for any given beamline. The selection of the ID also is a key factor in selecting the appropriate front end for a beamline. A beamline/front end/insertion device ICD is required for each ID beamline. These documents are the result of interactive discussions among the key beamline, ID, and front end people and reflect a common agreement on the choices. The process of developing these documents is discussed further in the APS Upgrade Project Implementation Plan.

Two beamline subprojects (WFI and HFPP) have significant physical infrastructure needs. The WFI beamline is the first to extend past the boundaries of the APS experiment hall and will have an experimental station approximately 250 m from the ID. This requires a separate building as described in WBS U1.05 (see Chapter 5 of this PDR). The HFPP beamline program is at 14-ID and is an upgrade of an existing beamline. Part of the current infrastructure is a Biohazard Level 3 facility that will be expanded as a part of the Project scope. The activities related to this are also in WBS U1.05.

1.4.3 Enabling Technical Capabilities

The APS Upgrade Project covers various aspects of the current APS from the accelerator to the beamlines to infrastructure. To fully support the APS Upgrade scope, the enabling technical capabilities section encompasses areas that will supplement the other two technical areas of Project scope, namely the accelerator (X-ray beam position monitors) and beamline (Physical infrastructure and front ends) upgrades.

1.4.3.1 Front Ends

The accelerator in this context is defined as mainly the storage ring, where the electron beam orbits. A beamline is usually defined as the section where the x-ray beam travels to the experiment. The front end, in this context, is the portion of the beamline inside the storage ring enclosure; it is the first element to “see” the x-ray photon beam.

The APS storage ring has been operating at 7 GeV with 100 mA of stored beam since January 1996. There are 70 locations around the ring for beamlines. Of these locations, 35 are for taking a fan of bending magnet (BM) radiation and the remaining 35 are for insertion device (ID) radiation. The BM front end was designed to handle 300 mA of stored beam. The ID front ends were originally designed to handle 100 mA of stored beam from a typical undulator insertion device 2.4-m long with a 3.3-cm period. Over the past few years, newer designs for a 4.8-m-long device capable of handling higher currents of 200 mA were designed and installed in some locations in the storage ring. In addition, over the past few years a new canted undulator (CU) design to handle two beams separated by about 1 mrad was also designed and installed in a few locations around the ring.

The APS Upgrade Project scope calls for operating the storage ring routinely at 150 mA and 7 GeV. This will require upgrading the existing front ends to handle the higher currents. The Project scope also involves converting some beamlines to the aforementioned canted geometry to provide two independent beams from a single location.

One of the goals of the Project is to enhance beam stability by implementing the next-generation x-ray beam position monitor (XBPM). The next-generation XBPM is a component of the front end. The recently designed high-heat-load (HHL) front end and CU front end (CUFE) have been modified to accommodate the next-generation XBPM.

The Project scope calls for replacing some of the front ends with HHL front ends equipped with next-generation XBPMs, and some with CU front ends with next-generation XBPMs. The front ends, which are not affected by the beamline upgrades, will be retrofitted to allow for 150-mA operation. More details of the complete scope for the Project are discussed in Chapter 5.

1.4.3.2 Physical Infrastructure

The APS experiment hall can accommodate a maximum beamline length of ~75 m from the center of a straight section in the storage ring. Most of the beamlines end well before the sector boundary, at about 60 m from the source.

The Project scope includes building a long beamline extending to about 250 m from the source. The wide-field imaging beamline at 20-ID is described in Chapter 4. Construction of the long beamline requires modification to the existing APS experiment hall. In addition, an experimental station building will be constructed to house the experiment station at 250 m from source. This beamline will traverse the experiment hall corridor, enter the laboratory/office module, and exit the APS main building. A new beam transport corridor to connect the APS building with the experimental station building will be constructed.

All activities related to the construction of the experimental station building, the transport corridor, and all modifications to the APS experiment hall are covered Chapter 5. Details of the construction and modification to the existing infrastructure will also be discussed in Chapter 5.

1.4.3.3 Enabling Technical Capabilities Scope and Work Breakdown Structure

The scope for Enabling Technical Capabilities with its associated Work Breakdown Structure (WBS) is listed in Table 1-13.

Table 1-13: Enabling Technical Capabilities Scope.

WBS	PDR Section	Description	Quantity
U1.05.02	5.2	Front End Upgrades	
U1.05.02.02	5.2.1	Front End for High Heat Load Inline Undulators (HHLFE)	7
U1.05.02.03	5.2.2	Front End for Canted Undulators (CUFE)	6
U1.05.02.04	5.2.4.1	Front End for Long Straight Section Canted Undulators (LSSCUFE)	1
U1.05.02.06	5.2.3	Front End v1.2 Retrofit	7
U1.05.02.08	5.2.4.2	Front End for SPX Canted Undulators (SPXCUFE)	1
U1.05.02.11	5.2.1.3	Next Generation X-ray BPM System for HHL	7
U1.05.02.12	5.2.2.3	Next Generation X-ray BPM System for CU	6
U1.05.02.13	5.2.4	Next Generation X-ray BPM System for LSSCU	1
U1.05.02.15	5.2.4	Next Generation X-ray BPM System for SPXCU	1
U1.05.02.20	5.2.5	Front End Installations	23
U1.05.03	5.3	Site Services & Utilities	
U1.05.03.01	5.3.2	Wide Field Imaging Beamline Facility	
U1.05.03.04	5.3.3	Facility Enhancement for High Flux Pump-Probe (Sector 14)	

1.4.3.4 Interdependencies

The APS Upgrade has been divided into three technical areas: accelerator upgrades, beamline upgrades, and enabling technologies. The technical scopes in these three areas have been discussed in Chapters 3, 4, and 5, respectively. There are numerous dependencies between the three areas. In addition, the APS is an operating facility and numerous APS Upgrade activities are dependent on APS Operations.

The dependencies between the areas are described in the Project Interface Control Documents (ICDs). The interdependencies, as and when identified, will be captured in the ICDs. To give a few examples: a front end is a prerequisite for a beamline. The specific beamline needs are taken into consideration for the choice of the front end. In addition, the front end must have the source defined by the type of ID to be installed by the accelerator upgrade. Installations of the front ends are coordinated with the APS accelerator maintenance cycles.

Construction of the experimental station building will meet the requirements for the Wide Field Imaging (WFI) beamline. Physical infrastructure activities rely on close coordination with numerous outside entities, namely external contractors and Argonne Facilities Management & Services. All such activities will be captured in the ICDs.

1.5 Summary

This Preliminary Design Report (PDR) summarizes the design of the proposed upgrades to the Department of Energy's (DOE's) Advanced Photon Source. As summarized in this introductory chapter, and detailed throughout this report, the APS Upgrade will enable the APS to remain a world-leading facility for many years to come by providing the user community with a dozen new or upgraded beamlines with improvement in areas such as high-energy diffraction, *in situ* studies of materials

synthesis, wide-field imaging, ultrafast diffraction and spectroscopy. The scope of the APS Upgrade also includes insertion devices optimized for brightness at high energies (e.g., superconducting or revolver), an electromagnetic variable polarizing undulator that will produce helicity-switching circularly polarized x-rays, long straight sections, superconducting rf cavities to produce picosecond x-ray pulses, higher electron current for 150 mA and enhanced beam stability.

References

[1] S.D. Shastri, R.J. Dejus, D.R. Haeffner, "Experimental Characterization of APS Undulator A at High Photon Energies (50-200 keV)," *J. Synchrotron Rad.*, vol. 5, pp. 67-71, 1998.

[2] J. N. Galayda, "The Advanced Photon Source," *Proc. of PAC 1995*, pp. 4-8, 1996.

[3] J. L. Laclare, "Commissioning and Performance of the ESRF," *Proc. of PAC 1993*, pp. 1427-1431, 1993.

[4] S. Date et al. , "Operation and Performance of the SPring-8 Storage Ring," *Proc.of PAC 1999*, p. 2346–2348, 1999.

[5] K. Balewski et al., "PETRA III: A New High Brilliance Synchrotron Radiation Source at DESY," *Proc. of EPAC 2004*, p. 2302–2304, 2004.

[6] L. Emery and M. Borland, "Upgrade Opportunities at the Advanced Photon Source Made Possible by Top-up Operations," *Proc. of EPAC 2002*, p. 218–220, 2002.

[7] A. Zholents et al. , "Generation of subpicosecond X-ray pulses using RF orbit deflection," *Nuclear Instruments and Methods in Physics Research A*, pp. 425, 385, 1999.

[8] "Developing APS Roadmap Scenarios," 2012. [Online]. Available: http://www.aps.anl.gov/Upgrade/Forum/.

Advanced Photon Source Upgrade Project

Preliminary Design Report

December 2012

Chapter 2: Assessments

Table of Contents

List of Tables

Acronyms and Abbreviations

ACIS	Access Control Interlock Systems
ACS	access control system
AES	APS Engineering Support Division
ALARA	As Low As Reasonably Achievable
APS	Advanced Photon Source
ARSPPC	APS Radiation Safety Policy and Procedures Committee
BSDRSC	Beamline Safety Design Review Steering Committee
CFR	Code of Federal Regulations
CR	continuing resolution
CUFE	Canted-Undulator Front End
DOE	Department of Energy
EA	environmental assessment
EMS	Environmental Management System
ES&H	Environment, safety, and health
ESD	Engineering Specifications Document
EVMS	Earned Value Management System
HAR	Hazards Analysis Report
HHLFE	High-Heat-Load Front End
IBC	International Building Code
ICS	Interface Control Document
ISMS	Integrated Safety Management System
ISO	International Organization for Standardization
LCW	Low Conductivity Water
LMS	Laboratory Management System

LOTO	lockout and tagout
LSSCUFE	Long Straight Section Canted-Undulator Front End
MCFL	Maximum Credible Fire Loss
NEC	National Electrical Code
NEPA	National Environmental Policy Act
NFPA	National Fire Protection Association
OMB	Office of Management and Budget
PEP	Project Execution Plan
PL	performance level
PRD	Physics Requirements Document
PSS	Personal Safety Systems
QA	Quality Assurance
RCRA	Resource, Conservation and Recovery Act
rf	Radio-frequency
RMP	Risk Management Plan
SAD	Safety Assessment Document
SIL	safety integrity level
SPX	short-pulse x-ray
TPC	Total Project Cost
VESDA	Very Early Smoke Detection Apparatus
WHSP	Worker Safety and Health Program
XBPM	x-ray beam position monitor

This page intentionally left blank.

2 Assessments

The Advanced Photon Source (APS) Upgrade Project has implemented a number of assessments and processes to ensure that the Project is carried out according to processes and requirements in place and that comply with the policies and procedures of the APS, Argonne National Laboratory, and the Department of Energy (DOE). These include Environment, Safety, and Heath (ES&H); Quality Assurance; Value Management; Risk Management; and System Integration. The information provided in this chapter summarizes the Project efforts that are managed in respective standalone plans and the Project Implementation Plan (PIP).

2.1 Environment, Safety, and Health

UChicago Argonne, LLC's contract to operate Argonne National Laboratory includes the requirement to manage the Laboratory in compliance with Title 10 of the Code of Federal Regulations (CFR), Part 851, referred to as 10 CFR 851, Worker Safety and Health Program. The purpose of the program is the prevention of injuries and illnesses to workers at the covered sites. This rule is substantively similar to DOE Order 440.1A Worker Protection Management for DOE and Contractor Employees that most sites have been working under as a DOE directive that was incorporated into the operating contract for the site. The rule in turn refers to a number of other Department of Energy orders, policies, and guidelines that provide the framework for Argonne's Worker Safety and Health Program (WSHP) and its Integrated Safety Management System (ISMS), which have been reviewed and accepted by the DOE. Argonne's interpretation of these requirements is defined within Argonne's Laboratory Management System (LMS). It is understood that the APS Upgrade Project will comply with these requirements collectively referred to as the "ESH and QA program."

Argonne also has developed an Environmental Management System (EMS). An EMS description communicates the policies and procedures that together comprise the EMS at Argonne in compliance with DOE Order 450.1A. Argonne has chosen to develop and implement its EMS to meet the requirements of International Organization for Standardization (ISO) 14001:2004, Environmental Management Systems.

Everyone at Argonne is required to comply with the applicable procedures, instructions, and directives in order to perform safe, environmentally compliant work that protects the health and safety of the worker and the public while meeting quality requirements and preserving the integrity of DOE assets.

Existing and mature programs at APS will be followed to ensure that the design, installation, testing, and commissioning phases of the Project are consistent with APS processes.

2.1.1 APS Hazards Analysis Methodology

The hazards associated with the operation of the APS facility and standard x-ray beamline configurations have been addressed in APS Safety Assessment Document (SAD) [1]. A Hazards Analysis Report (HAR) [2] will be developed to address the hazards specific to the APS Upgrade Project. At the conclusion of the APS Upgrade Project the HAR will be incorporated into the APS SAD. (Note: The HAR and SAD are the same document with different nomenclature in the DOE Orders).

The hazard analysis process for the HAR documents the study of potential hazards associated with the proposed modifications to the APS facility and x-ray beamlines. The analysis of each hazard is based on a bounding-event approach in which the most severe case of each hazard category is analyzed to identify the worst-case result. If the result is bounded by the existing hazard analysis in the APS SAD, the only change involved with the SAD will be descriptive text. If the result is not bounded by the existing analysis in the APS SAD, then a new event analysis will be developed that includes the determination of the initiating occurrence, possible detection methods, safety features that could prevent or mitigate the event, probability of occurrence, and the possible consequences.

The APS Upgrade will apply the hazards analysis approach identified in the EN 62061 standard “Safety of Machines,” which addresses functional safety of electrical, electronic, and programmable controls of machines and defines comprehensive requirements. This standard includes recommendations for the development, integration, and validation of safety-related electrical, electronic, and programmable electronic control systems for machines. Since EN 62061 does not specify any requirements on the capacity of non-electrical (e.g., hydraulic, pneumatic, or electromechanical) safety-related control elements for machines, the EN ISO 13849-1 standard “Safety of Machines,” which does address safety-related components of controls and covers the entire safety function with all devices, will be used. EN ISO 13849-1 not only includes the quality approach of the EN 954-1 standard, but it also addresses the safety functions in terms of quantity. Based on the system categories, Performance Levels (PLs), which are discrete category levels that specify the capability of safety-related control components to execute a safety function, and Safety Integrity Levels (SILs), which are discrete category levels for the determination of the safety integrity requirements of safety-related control functions, will be used. The standard addresses the determination of the PL for safety-relevant control components on the basis of designated architectures for the scheduled service life. For the combination of several safety-relevant components into a total system, the standard contains information on the determination of the resulting PL. The standard is applicable to safety-related control components and all types of machines, irrespective of the technology and energy used (e.g., electrical, hydraulic, pneumatic, mechanical).

2.1.2 APS Upgrade Project Safety Design

The design and development of the APS Upgrade Project and its technical components involve an iterative review process. The safety of the design and the effects of the operation of the technical components are included in the conceptual development of the APS Upgrade. This process begins with the identification and evaluation of hazards, development of control or alternative mechanisms to address the identified hazards, and where necessary, a revision of the design to assure that the hazards are eliminated or appropriately mitigated. The safety review and revision process will continue as designs progress and became more detailed. This same process was used for the original APS Project.

2.1.2.1 Safety Design Reviews

The latest version of the APS Design Review Procedure, APS procedure # 3.1.01, is being followed by the APS Upgrade Project. This procedure defines a uniform approach for the APS when designs are being reviewed. The procedure applies to designs for new projects or modifications to existing APS systems, including mechanical, pressure, cryogenic, electrical, electronic, software, safety, and shielding systems. This same procedure is applied to designs brought to the APS by external parties, e.g., partner users. In this case, the review focuses on safety, although recommendations regarding technical issues may be included in the report. APS management uses a graded approach to determine the appropriate level of formality to be applied to design reviews. Any improvements or modifications to an APS safety system must follow a formal review process.

The x-ray beamline review process is currently managed by the Beamline Safety Design Review Steering Committee (BSDRSC). When assembled, the beamline components are inspected by the Beamline Commissioning Readiness Review Team and the appropriate APS safety committees. Comments and guidance from each of these reviews provide input to the iterative process of safety design and procedures improvement.

The BSDRSC conducts its evaluation in a systematic manner using the expertise of the committee members as well as committee advisors. The initial safety analysis for each beamline is prepared by the group managing the beamline. The estimated effect of each hazard is evaluated by the BSDRSC with regard to its potential impact on personnel and on operation of the facility.

Changes to the APS accelerator Access Control Interlock Systems (ACIS) and the experimental beamline Personal Safety Systems (PSS) interlock systems are reviewed by the APS Radiation Safety Policy and Procedures Committee (ARSPPC). This committee also reviews changes to radiation monitoring systems. Any changes approved by the ARSPPC must be approved in turn by the APS Engineering Support Division (AES) Associate Division Director with oversight of the Safety Interlocks Group. If needed, changes to the SAD may be triggered.

2.1.3 Design Criteria

The design and operation of all radiation producing facilities at Argonne are governed by the As Low As Reasonably Achievable (ALARA) policy. APS has historically maintained radiation dose limits below regulatory limits.

2.1.3.1 Safety Systems

An access control system (ACS) consists of electrical interlocks and mechanical barriers whose function is to prevent exposure of personnel to prompt radiation; this is accomplished by controlling personnel access into a beamline/accelerator enclosure and by turning off beam and radio frequency (rf) generators when an unsafe condition is detected.

Two types of access control systems are utilized for the APS:

- The Access Control Interlock System (ACIS) is used for electron beam enclosures (accelerators and storage ring) and is controlled remotely by qualified operators in the Main Control Room;
- The Personnel Safety System (PSS) is utilized for beamline enclosures (instrument stations, first optical enclosures) and is controlled locally by beamline staff or users.

The ACS must also perform the following functions:

- Provide failsafe and redundant interlocks to control access
- Allow for various access and beam travel configurations
- Provide emergency shutoff capabilities

As installation of the APS Upgrade will not require a significant change to the present shielding footprint, the ACIS will undergo only necessary upgrades and enhancements to address the new facility and operating conditions. These upgrades include: additional status and control interfaces to accommodate new rf power sources, access control modules for storage ring zone, and logic upgrades. The PSS will conceptually remain the same as existing PSS installations used for APS in terms of design, functions, and configuration.

Administrative requirements are mandated to ensure reliable operation. This requires that the ACIS and PSS systems be certified, tested, and protected against unauthorized modification.

All additions and changes will conform to Argonne's ESH-5.16 Ionizing Radiation Protection – Radiation Safety Interlock Systems [3] and ESH-5.3 Ionizing Radiation Protection – Access Control [4] documents.

2.1.3.2 Non-Ionizing Radiation, Lasers, and Magnetic Fields

The APS Upgrade rf systems will produce rf radiation in the 2856 MHz and 11424 MHz ranges, which when not controlled could have an adverse health effect on personnel working on or near the system. The APS Upgrade will incorporate safety measures based on present operations. These include interlocked waveguides and vacuum chambers at the rf cavities and strict adherence to procedures for installation, monitoring, and testing of the rf system. Aside from the cavities, the waveguides are interlocked with a positive pressure interlock system as are all APS rf waveguide systems.

As the rf energy is fully contained within the envelope of these waveguides under pressure or vacuum chambers at the rf cavities under high vacuum, opening the system up will trigger the interlock through a pressurization or de-pressurization of the system and effectively prevent the source from being energized. Running the rf in this mode precludes microwave leakage, as failure of the vacuum system will occur before exposure to non-ionizing rf radiation.

Procedures are also in place to ensure: all flange bolts are torqued to a predetermined value, and rf leak testing is completed after all installations and maintenance activities and periodically before start-up of the system after scheduled shutdowns.

APS Upgrade operations and experimental programs utilizing Class 1, 2, 3a, 3b, and 4 lasers will be reviewed and controlled as required by national consensus standards and the Argonne Laser Safety Program. Locations for long-term use of Class 3b and Class 4 lasers will be identified during design, and appropriate safety features (e.g., control of exposed beams) will be incorporated into the design of the facility. Lasers, particularly those in Class 3b and Class 4, will require written procedures for each device to control eye or skin exposure and associated electrical and industrial hygiene hazards, e.g., exposure to solvents, dyes, and halogen gasses. As per APS laser safety procedures, Class 4 laser control areas are required to be interlocked with a failsafe system. The APS Laser Safety Program will define the required interlock systems, training, and signage.

The APS Upgrade will utilize equipment and devices that generate magnetic fields. The concern with all these devices is the strength and extent of the fringe fields and how they may affect persons and equipment in their vicinity. Fringe fields in excess of 5 gauss are of particular concern because they could affect medical electronic devices (pacemakers), while fields over 600 gauss could impact ferromagnetic implants (artificial joints) and other material (tools).

2.1.3.3 Electrical Safety

An accelerator facility by nature has subsystems that either produce or use high voltage or high current, either of which can present an electrical hazard to personnel if not managed properly. The APS Upgrade will operate in a similar mode to other accelerators at Argonne; therefore, control and work procedures for electrical subsystems, as well as entry into the accelerator housing are well understood. Primary mitigation of the hazard will be through de-energizing equipment and placement of barriers, and the effective use of written system Lockout and Tagout (LOTO) procedures and Argonne's ESH-9.3, Rev. 6 Electrical Safety Program – Electrical Systems and Equipment [5] document.

The design, upgrade, installation, and operation of electrical equipment will be in compliance with the National Electrical Code, Title 29 Code of federal Regulations, Parts 1910 and 1926 (as applicable) and NFPA 70E [6]. Various levels of electrical safety training and LOTO training are provided by Argonne for those personnel who may work on or near potential electrical hazards.

2.1.3.4 Natural Phenomena Hazards Mitigation

The design of the APS addressed mitigation of hazards posed by natural phenomena, and the same considerations are being applied to the APS Upgrade Project.

2.1.3.5 Seismic Safety

Seismic risk at Argonne is considered low, as defined by the International Building Code (IBC), and the IBC does not impose any additional seismic design requirements. APS structures are designed and constructed to limit the effects of a major earthquake to acceptable levels. The majority of APS Upgrade components will be installed in facilities where seismic stability is well documented and deemed acceptable. To further ensure and maintain a safe and healthful workplace, the design and construction of new experimental facilities buildings for the APS Upgrade will also be reviewed for seismic safety compliance.

2.1.3.6 Wind Load – Tornado Safety

Wind-loading requirements on the building (per the IBC) are specified in the structural design, calculations, and specifications, as well as being specified for all building exterior enclosure systems. Tornado shelters are designated per Argonne guidelines at interior protected locations of the APS buildings.

2.1.3.7 Flooding

Flooding is not considered to be a likely hazard because the APS is not in a flood zone, is on high ground, and has few subsurface areas, which all have dedicated sump pumps.

2.1.3.8 Lightning Protection

Lightning protection and grounding have been included in the design for the entire APS facility, per IBC, National Fire Protection Association, and National Electrical Code requirements.

2.1.4 Hazardous Material

During the installation and operation phases of the APS Upgrade it is anticipated that minimal quantities of hazardous materials will be used. Examples would be paints, epoxies, solvents, oils, and lead in the form of shielding, etc. There are no current or anticipated activities at the APS Upgrade that will expose workers to levels of contaminants (dust, odors, and fumes) above permissible levels.

Argonne's Industrial Hygiene Program detailed in the Argonne ES&H Manual addresses potential hazards to workers from the use of hazardous materials. The program identifies how to evaluate workplace hazards at the earliest stages of the project and implement controls to eliminate or mitigate these hazards to an acceptable level. Industrial hygiene hazards will be evaluated, identified, and mitigated as part of the hazard assessment process.

Site- and facility-specific procedures are also in place for the inspection, safe handling, storing, transporting, and disposing of hazardous materials. These are contained in the Argonne ES&H Manual, Waste 3.6 Chemical Waste Disposal [7], which describes minimum standards to maintain for compliance with applicable regulations.

2.1.5 Fire Safety

The probability of a fire in the APS Upgrade is very low, similar to that for present operations, as accelerator and beamline components are primarily fabricated out of similar, nonflammable materials, and combustible materials in general are kept to a minimum.

The Maximum Credible Fire Loss (MCFL) at APS, which assumes proper functioning of the smoke detection and mitigation systems and a normal response from the onsite fire department, is limited to isolated components, such as magnets, vacuum chambers, and associated cabling. The most hazardous

"reasonably foreseeable" incident or event with any substantial consequences would be a fire in existing insulating material of the electrical cable plant caused by an overload condition. The hazard of greatest concern in this situation is the production of halogenated gases. The Argonne ES&H Manual 11.2 Fire Protection – General Fire Safety [8] addresses all fire safety issues.

Installation of new cables for the APS Upgrade will meet the current Argonne standards for cable insulation and comply with National Electrical Code (NEC) standards concerning cable fire resistance. A Very Early Smoke Detection Apparatus (VESDA) system, which is an aspiration-type smoke detection system, is in place in the accelerator housing, undulator tunnel, and experiment hall. These areas are protected by automatic heat-activated wet sprinkler systems. Fire extinguishers are located in all buildings and accelerator housings for use by trained personnel. The combination of smoke detection systems, sprinklers, and onsite fire department (response time <5 minutes) affords an early warning and timely response to fire or smoke-related incidents. Burn injuries caused by a fire are not expected. Personnel access areas in both the linac accelerator housing and support buildings are within 150 feet of an exit in both directions. Multiple entry/exit points will aid in keeping personnel emergency egress times and property damage to a minimum. See ESH-19.1, Rev 4, Design Criteria for Facilities – Exit Systems and Life Safety [9].

2.1.6 Environmental Protection

Installation of the APS Upgrade requires the removal of some hardware (magnets and vacuum chambers) and the installation of new components suited to the proposed facility. Electrical distribution systems will be upgraded or installed as appropriate and minor installation and/or modifications to the Low Conductivity Water (LCW) system will be made to accommodate heat transfer needs. Removal of these materials and the subsequent installation activities will produce small quantities of hazardous, nonhazardous, and radioactive waste that will be managed through defined processes. Past history indicates that normal operation of the accelerator does not typically produce waste. However, some hardware may have induced radioactivity associated with it from its proximity and time close to the beam. Other components may contain hazardous materials as part of their design, e.g., mineral oil in electrical components, or have radioactive contamination from the LCW system.

All material removed from within the accelerator housing will be surveyed for residual radioactivity or contamination, labeled, and held onsite for disposal evaluation, as defined in the Argonne Radiation Safety Program. Items that show residual radioactivity or contamination will be stored on the Argonne site for future reuse or ultimate disposal. Any hazardous waste will be disposed of in accordance with Argonne procedures and ultimately to a permitted treatment, storage, and disposal facility under regulations set forth in the Resource, Conservation and Recovery Act (RCRA).

Component manufacturing and system installation may also produce hazardous wastes, such as used solvent from degreasing baths or spent cutting fluids. These wastes are managed and controlled routinely during operations at APS in full compliance with Argonne's policies on the management of hazardous materials and waste minimization.

The addition of a building to house cryogenic systems and the required earth removal, and construction activities were the subject of an Environmental Assessment (EA) under the National Environmental Protection Act (NEPA), for which a Categorical Exclusion was granted.

All activities will be managed to prevent adverse impact on groundwater, storm water, and air quality, and to minimize any ground disturbing activities.

2.1.7 Disassembly and Installation Safety

2.1.7.1 General

During demolition and installation operations, oversight of activities and safety compliance remains a line organization responsibility. Responsibilities of Project personnel include, but are not limited to:

- Apprising individuals working on the APS Upgrade Project of Argonne and DOE safety criteria prior to performing work at the APS
- Conducting periodic inspections of work areas to evaluate safety compliance program and quality of work
- Providing information to the APS Upgrade Project personnel as required or requested
- Communicating and resolving safety deficiencies as identified

Enforcement of subcontractor requirements is carried out by the Argonne Purchasing Department and may involve withholding payment(s) if applicable codes and standards are not met.

2.1.7.2 Equipment Disassembly and Installation

APS Upgrade Project management recognizes that equipment disassembly and installation activities can pose significant hazards. Management will ensure that Project activities and associated hazards are evaluated before work starts, in conformance with the latest revisions of Argonne Laboratory-wide procedures.

The APS Upgrade will require that written procedures for equipment disassembly and installation be developed and followed consistent with LMS-PROC-65, Non-Experimental Skill-of-the-Worker, and LMS-PROC-200, Local Work Planning and Control Implementing Procedures. Storage ring and infrastructure modifications will be performed during scheduled maintenance periods.

APS Upgrade project management also will ensure that installations involving supplier personnel are managed in conformance with the requirements established in Argonne procedures LMS-PROC-221, Technical Representative and Contractor ESH Representative, and LMS-PROC-123, Contractor Safety.

2.1.8 Summary

The APS Upgrade Project involves a variety of facility changes that will be implemented or installed over a multiyear effort involving different portions of the facility. The changes are no different than other facility modifications that must be evaluated for ES&H considerations prior to installation or use. Argonne and APS ES&H procedures will be followed by the APS Upgrade Project. Documents

developed for the APS Upgrade Project related to ES&H include the Hazard Analysis Report and the NEPA determination.

2.2 Quality Assurance

The Quality Assurance (QA) requirements for the APS Upgrade Project originate from DOE Order DOE O 413.3B, Program and Project Management for the Acquisition of Capital Assets, which requires the Project to address the QA criteria in 10 CFR 830 Subpart A and DOE O 414.1D, Quality Assurance. The contractor requirements documents in Attachments 2 and 3 of DOE O 414.1D requires the APS Upgrade Project to develop a QA program that implements 10 DOE QA criteria and suspect/counterfeit item prevention using a graded approach. The 10 DOE QA criteria are as follows:

1. Quality Program
2. Personnel Qualification and Training
3. Quality Improvement
4. Documents and Records
5. Work Processes
6. Design
7. Procurement
8. Inspection and Acceptance Testing
9. Management Assessment
10. Independent Assessment

DOE also recommends following the information in DOE G 413.3-2, Quality Assurance Guide for Project Management; DOE G 414.1-2B, Quality Assurance Management System Guide for Use with 10 CFR 830 Subpart A, Quality Assurance Requirements; and DOE O 414.1C when developing a QA program.

The Project will implement the DOE QA requirements and recommendations using the Argonne Laboratory Management System (LMS), which has been certified to ISO 9001:2008 Quality Management Systems Requirements.

The Project will develop a Project Quality Assurance Plan to manage the quality assurance requirements of the APS Upgrade. Additional quality procedures will be created to afford APS Upgrade staff the specific guidance and clarity for achieving the quality goals of the Project. All processes will integrate with the Argonne LMS and be in concert with the DOE and other regulatory requirements.

Argonne LMS-POL-9, Quality Policy, states that the quality policy of Argonne is to pursue continual improvement in products and services and in relationships internally and with its customers, and that Argonne is committed to the following:

- Providing exceptional products and services in support of the Laboratory's mission, customer requirements, and country
- Providing an environment—through empowerment, training, and recognition—that will challenge and reward employees
- Maintaining a safe and healthy environment for employees and for anyone who may be affected by the employee's organization

DOE Order 413.1B also contains a requirement for the APS Upgrade Project to integrate safety at all levels of the Project, including QA, and use the DOE Integrated Safety Management System (ISMS).

The APS Upgrade will implement the DOE ISMS requirements by following the LMS ISMS Description Document, which addresses how the principles of ISM, and their associated QA requirements, are integrated into the daily processes of the Laboratory.

Department of Energy Order 414.1D requires the APS Upgrade Project to ensure that it performs reviews of their management, technical, and design processes. The expectation for reviews requires internal assessments (performed by qualified staff within the organization but removed from the process under examination), and external reviews, (performed by qualified personnel outside the APS Upgrade organization). The review process is discussed in more detail in the Project's PIP.

The APS Upgrade Management Assessment Schedule is maintained by the APS Integrated Content Management System under content ID number APSU_1421445

The APS Upgrade Project Quality Assurance Representative will also conduct self-assessments of the APS Upgrade Quality Plan, procedures, and related documents.

Further information on the APS Upgrade Quality Assurance program is documented in the Quality Assurance Plan, APSU-1.01-PLN-001-01.

2.3 Value Management

The purpose of this Value Management section of the PDR is to describe the goals and procedures for implementing Value Management, Value Engineering, and Value Analysis during the life cycle of the APS Upgrade Project. The complete Value Management process is defined in the Project's PIP. Utilizing Value Management for the Project helps to:

- Establish cost consciousness in the Project
- Identify cost drivers in the cost baseline
- Develop cost-reduction strategies
- Manage costs within the Project

Value Management, as it applies to the APS Upgrade Project is concerned with defining what value actually means for the Project as well as following through with processes to provide that value.

Value Management is applicable to all organizations performing work on the APS Upgrade Project, and these processes are applied to aspects of the Project, as appropriate.

Applicable documents to Value Management include the Office of Management and Budget (OMB) Circular A-131, "Value Engineering" DOE P 413.2 Subject: VALUE ENGINEERING Approved 1/07/2004; and DOE Order 413.3B dated 11/29/2010, Program and Project Management for the Acquisition of Capital Assets.

2.4 Risk Management

2.4.1 Overview

The need for a formal risk management process is called out by the Department of Energy (DOE) Order 413.3B. This order, in conjunction with DOE Guide 413.3-7A, the Argonne National Laboratory (Argonne) Earned Value Management System (EVMS), and best practices from other large-scale science projects within the DOE complex are the basis for establishment of the APS Upgrade risk management process.

The document that outlines the risk management process is called the Risk Management Plan (RMP), document number APSU-1.01.04-PLN-001. The APS Upgrade RMP formalizes the approach for risk management and analysis, defines and describes the Risk Register, outlines the roles and responsibilities of project personnel performing risk management functions, and delineates the reporting and tracking requirements for risk-related information. This description of the risk management process is a summary of the key components of the Risk Management Plan.

2.4.2 Process

The APS Upgrade Project risk management process consists of the following steps performed on a continuous basis throughout the life of the Project:

1. Plan, implement, and revise the Project's risk management process
2. Identify threats and opportunities to the Project's cost, schedule, and technical scope
3. Analyze the impact of identified threats and opportunities to the Project's cost, schedule, and technical baselines; and develop risk-handling plans to manage and control the risks
4. Monitor risks, mitigation plans, and Management Reserve (MR) and Contingency until the risks are retired or the Project is closed

The objective of the APS Upgrade risk management process is to establish a structured, formal, and disciplined approach to identifying potential threats and opportunities as early as possible in order to evaluate the most critical risks, monitor triggers effectively, and determine the amount of MR and Contingency needed to moderate the risks.

2.4.3 Critical Risks

An overview of the current APS Upgrade risk topics and the associated steps taken to handle these risks are identified below. The APS Upgrade Risk Registry, actively maintained on the Project's SharePoint site, contains the complete set of documented Project risks.

2.4.3.1 Beamline and Other Technical Equipment Risks

Beamline performance goals are predicated on advances in beamline technology and optics continuing at a rate similar to recent progress. If the beamline were built using current technology, it could achieve the technical goals as planned. In some cases, the beamlines might initially operate at lower performance than optimal; but as is common practice with x-ray beamlines, they are being designed to allow performance to improve over their lifetime. The plans, cost estimate, and schedule for the beamlines are based on Argonne's considerable experience with dozens of APS beamlines. To further mitigate risk, Argonne held independent and external reviews of design, plans, cost, and schedule for the various beamlines. These reviews validated the preliminary design plans and estimates. Contingency calculations for the beamlines are based on Argonne's experience with beamlines, the current status of the design, and a subsystem-by-subsystem risk analysis.

2.4.3.2 Civil Construction Risks

The APS Upgrade, as an MIE project, has no major civil construction components. However, there are some small support infrastructure and facilities components that must be in place to support the acquisition and installation of some specific technical equipment. One such component will be built in the vicinity of a wetland area and the location of a planned new building. The APS Upgrade is bound by the current APS Environmental Assessment; however, a categorical exclusion was approved by the DOE NEPA compliance officer in May 2011.

2.4.3.3 Accelerator Risks

The detailed list of risks for the accelerator is provided in the Project Risk Register. In summary, there are low and moderate cost and schedule risks as well as technical scope risks. To proactively mitigate these and other risks, the Project held independent and external reviews of the design, technical, cost, and schedule components of the various accelerator subsystems. Contingency calculations for the accelerator components are based on APS experience with accelerators, the current status of the design, and a subsystem-by-subsystem risk analysis.

2.4.3.4 Cost Risks

There is low risk that the Project will exceed the Total Project Cost (TPC) defined in the Project Execution Plan (PEP). The Contingency is estimated at greater than 30% of all Project costs. Cost estimates are based on vendor quotes, catalog prices, expert opinions, and recent similar purchases. For equipment items manufactured only by foreign firms, fluctuations in foreign exchange rates are another source of cost risk. Cost-reduction strategies include negotiating quantity discounts to procure multiple

units of particular instruments at a lower price and identifying possible early procurements. The performance of internal audits on the cost estimate and the implementation of the formal Risk Management Plan are both efforts that aid in lowering the exposure to many cost-sensitive risks. The process of managing the Project budget is discussed in greater detail in the Project's PIP.

2.4.3.5 Schedule Risks

The preliminary schedule analysis shows significant risks associated with the short-pulse x-ray (SPX) development and construction, and with the installation of beamlines in the existing shutdown windows. To help mitigate these risks, approximately 18 months of schedule contingency is included at the end of the Project schedule for the completion of the last beamlines. Coordination with ongoing facility operations and regular shutdown schedules present a risk in managing the Project schedule during installation, and will be addressed by including it in the baseline planning and coordination of operational and Project tasks.

Secondary risks may develop as a result of the coordination efforts with scheduled operational downtime windows, whereby key resources may be unavailable to adequately perform the Project tasks that can only be performed during a downtime period. The Project is evaluating personnel needs to mitigate this risk. The development of the responsibility assignment matrix and detailed Project schedule will aid in reducing the likelihood of secondary resource-centric risks from occurring. The process of managing the Project schedule is discussed in greater detail in the Project's PIP.

2.4.3.6 Project Funding Risks

There are significant funding risks associated with continuing resolutions (CRs) and not receiving funds as planned given the current federal funding environment. Mitigating approaches will include assuming six months of CR in FY 2013 and three months of CR for the remaining years in the Project budget, planning to award contracts in the third quarter of fiscal years, and utilizing contracting methods with lower initial funding authorization. These contracting methods allow the work to begin prior to receipt of full funds but will require careful management from technical and contracting staff. As long as the Project schedule, budget, and spending plan reflect this mitigation strategy, the impact caused by CRs and other potential funding issues can be reduced. Another method for ensuring funding does not adversely impact the outcome of the Project is for the risk management and project controls Project team to actively communicate Project performance and risk status to the Project Director, who in turn will routinely keep the Federal Project Director informed.

2.5 System Integration

System Integration for the APS Upgrade Project is concerned with:

- Assuring that the Project deliverables meet the Project requirements and quality standards
- Assuring the Project delivery process is performed in a safe, cost-effective, and efficient manner

The Systems Integration process is based on the generation of formal requirements and interface documentation that is reviewed, approved, and controlled at the Project level, and effective communication between project systems representatives.

2.5.1 Requirements Management

Requirements management is an essential part of System Integration and is governed for the APS Upgrade by the Requirements Management Plan (Document No. APSU-1.01.05-PLN-002). This plan establishes a process to manage a common understanding of the technical and non-technical requirements that are used to develop the Project.

Project requirements documents generally fall into three categories: Physics Requirements Documents (PRDs), Engineering Specifications Documents (ESDs), and Interface Control Documents (ICDs). Table 2-1 provides a current partial listing of the requirements documents under development for the Project. The complete list of requirements documents is maintained on the APS Upgrade Integration and Coordination SharePoint site.

The highest-level Project requirements are given in the APS Upgrade Project Physics Requirements document (APSU-1.01.05-PRD-001). The goal of requirements management is to ensure that Project requirements are controlled to establish and maintain a technical baseline for the Project. The Requirements Management Plan establishes an orderly method by which the goals of requirements management will be achieved.

Table 2-1: APS Upgrade Requirements Documents (Partial List).

Document Number	Document Title
APSU-1.01.05-PRD-001	APS Upgrade Project Physics Requirements
APSU-1.05.02.02-PRD-001	APS Upgrade High-Heat-Load Front End (HHLFE) with Next-Generation XBPM Physics Requirement Document (PRD)
TBD	Engineering Specifications for High-Heat-Load Front End
APSU-1.05.02.03-PRD-001	APS Upgrade Canted-Undulator Front End (CUFE) with GRID XBPM Physics Requirements Document (PRD)
TBD	Engineering Specifications for Canted-Undulator Front End
APSU-1.05.02.04-PRD-001	APS Upgrade Long Straight Section Canted-Undulator Front End (LSSCUFE) Physics Requirements Document
TBD	Engineering Specifications for Long Straight Canted Front End
APSU-1.05.02.11-ESD-001	APS Upgrade Engineering Specifications Document Next-Generation X-Ray Beam Position Monitor (XBPM) System for High-Heat-Load Undulator Front End
TBD	APS Upgrade Engineering Specifications Document Next-Generation X-Ray Beam Position Monitor System for High-Heat-Load Canted-Undulator Front End

Requirements Documents are placed under configuration control according to the APS Upgrade Controlled Document Procedure and the APS Upgrade Configuration Management Plan, discussed below.

2.5.2 Configuration Management

Configuration management for the APS Upgrade Project is the process of creating and maintaining Project-related configuration items. Configuration management helps to ensure that any changes or modifications to these items are properly recorded, analyzed, approved, and tracked. Configuration management also helps to prevent unauthorized or uncontrolled physical hardware changes to equipment, changes to controlled documents, and changes to controlled software.

A Configuration Management Plan is employed by the APS Upgrade Project to identify and control relationships with respect to design, fabrication, construction, installation, and testing of Project-supplied systems, subsystems, and components. The Project recognizes the importance of maintaining clear, concise, and accurate records in order to maintain schedule, control costs, and provide as-built information for future (non-APS Upgrade) operation, maintenance, and decommissioning activities. This Configuration Management Plan has been established to ensure that key functional organizations, both internal and external to the APS, are aware of their roles and responsibilities during all of the APS Upgrade Project phases.

The Configuration Management Plan describes the configuration management responsibilities and processes that support the design and implementation of the APS Upgrade Project.

References

[1] "Safety Assessment Document (DOE O 420.2B Safety of Accelerator facilities)".

[2] "The Hazards Assessment Report (DOE O 413.3B 11-Program and Project Management for the Acquisition of Capital Assets)".

[3] "ESH-5.16, Rev 1, Ionizing Rad Protection - Radiation Safety Interlock Systems".

[4] "ESH-5.3, Ionizing Radiation Protection – Access Control".

[5] "ESH-9.3, Rev. 6, Electrical Safety Program - Electrical Systems and Equipment".

[6] "NFPA 70E, Standard for Electrical Safety in the Workplace".

[7] "Waste 3.6, Chemical Waste Disposal".

[8] "ESH-11.2, Rev 2, Fire Protection – General Fire Safety".

[9] "ESH-19.1, Rev 4, Design Criteria for Facilities – Exit Systems and Life Safety".

The Advanced Photon Source, an Office of Science User Facility operated for the U.S. Department of Energy (DOE) Office of Science by Argonne National Laboratory, is supported by the DOE under Contract No. DE-AC02-06CH11357.

rev. 20121120

Advanced Photon Source Upgrade Project

Preliminary Design Report

December 2012

Chapter 3: Accelerator Upgrades

This page intentionally left blank.

CONTENTS

LIST OF FIGURES

LIST OF TABLES

ACRONYMS AND ABBREVIATIONS

ACIS	access control interlock system
ADC	analog-to-digital converter
AFE	analog front end
ALS	Advanced Light Source
AOM	acoustic-optic modulator
APPLE	advanced planar polarized light emitter
APS	Advanced Photon Source
APS-U	APS Upgrade
ASCU	advanced superconducting undulator
ASD	Accelerator Systems Division
ASME	American Society of Mechanical Engineers
ATLAS	Argonne Tandem Linear Accelerator System
BAT	beam arrival time
BLM	beam loss monitor
BM	bending magnet
BPLD	beam position limit detector
BPM	beam position monitor
BPVC	Boiler Pressure Vessel Code
BSP	bunch signal processor
cal-tone	calibration-tone
CAS	contingent additional scope
CBI	coupled-bunch instability
CDF	cumulative distribution function

CF	carbon fiber
CFE	canted front end
CMM	coordinate measurement machine
CNC	computerized numerically controlled
CPRF	connector pressurized rectangular flat
CPU	circularly polarized undulator
CRL	compound refractive lens
CU	canted undulator
DA	dynamic acceptance
DAC	digital-to-analog converter
DI	de-ionized
DSP	digital signal processor or digital signal processing
EHHL	extremely high heat load
EM	electromagnetic
EMVPU	electromagnetic variably polarizing undulator
ESD	engineering specification document
FE	front end
FFT	fast Fourier transform
FNAL	Fermi National Accelerator Laboratory
FPGA	field-programmable gate array
GRID-XBPM	grazing-incidence insertion device x-ray beam position monitor
h	hour
HHL	high heat load
HLRF	high-level rf
HMI	human-machine interface
HOM	higher-order mode
HPM	hybrid permanent magnet
HTS	high-temperature superconducting
HVPS	high-voltage power supply

ID	insertion device
IDVC	insertion device vacuum chamber
IEX	intermediate-energy x-ray
IF	intermediate frequency
ILC	International Linear Collider
IVU	in-vacuum undulator
JLab	Jefferson Accelerator Laboratory
KPP	key performance parameter
LBNL	Lawrence Berkeley National Laboratory
LEP	Large Electron-Positron Collider
LHC	Large Hadron Collider
LHe	liquid helium (He)
LL	low-loss
LLRF	low-level rf
LLS	long straight section
LMA	local momentum acceptance
LMF	low-peak magnetid field
LNDS	liquid nitrogen distribution system
LO	local oscillator
LOM	lower-order mode
LR	load ratio
LSS	long straight section
LTS	low-temperature superconductor
MLI	multi-layer insulation
MOGA	multi-objective genetic algorithm
MPS	machine protection system
MSPS	mega-samples per second
NEG	non-evaporable getter
ODH	oxygen deficiency hazard

OFE	oxygen-free electronic
OFHC	oxygen-free high-conductivity
PA	photon absorber
PID	proportional integral and derivative
PLC	programmable logic controller
PM	permanent magnet
PMT	photomultiplier tube
PMU	permanent-magnet undulator
PRD	physics requirements document
PS	photon shutter
PSD	power spectral density
PSS	personnel safety system
PWD	potential well distortion
QA	quality assurance
rf	radio-frequency
RHB	reduced horizontal beam
RHB	reduced horizontal beta
RRR	residual resistivity ratio
RTD	resistive thermal device
RTDL	real-time data link
RTFB	real-time feedback
RW	resistive wall
SAD	Safety Assessment Document
SCU	superconducting undulator
SFP	small form-factor pluggable
SOM	same-order mode
SOW	statement of work
SPX	short-pulse x-ray
SR	storage ring

SRF	superconducting radio-frequency
SVD	singular value decomposition
TE	transverse electric
TM	transverse magnetic
TMCI	transverse mode-coupling instability
TUV	Technischer +ANw-berwachungsverein
UA	Undulator A
VHHL	very high heat load
VP	vanadium permendur
WBS	work breakdown structure
XBPM	x-ray beam position monitor
XRF	x-ray fluorescence

Chapter 3

Accelerator Upgrades

3.1 Overview

The Advanced Photon Source (APS) is the largest accelerator complex in the Western Hemisphere dedicated to the production of synchrotron radiation using electrons stored in a ring. With a 1104-m circumference and a 7-GeV beam energy [3.1-1], there are only three other sources in the world with a comparable size and electron beam energy [3.1-2–3.1-4]. APS consists of an injector and storage ring. The purpose of the injector is to supply beam to the storage ring. No changes to the injector are planned as part of the APS Upgrade Project. A number of upgrades to the storage ring will be undertaken, as detailed in subsequent chapters of this document. These upgrades are targeted at specific changes that will improve the scientific capabilities of the APS in order to address the Mission Need and Key Performance Parameters (KPPs) described in Chapter 1 of this document.

This section contains an overview of the accelerator complex as it now exists and operates, as well as a brief summary of the accelerator aspects of the upgrade and how these relate to the Mission Need and the KPPs. These aspects are discussed in detail in subsequent sections of this chapter.

3.1.1 Accelerator Complex and Present Operations

The APS contains 40 largely identical sectors, each of which consists of accelerator components and a 5-m-long straight section. Five of these straight sections are reserved for accelerator systems required for beam injection, replenishing of the electron beam energy, and diagnostics. The remaining 35 straight sections are available for insertion devices, typically undulator magnets, that produce x-rays for user experiments. The maximum length available for such devices is 4.8 m. Each sector also contains two bending magnets, one of which is designed for use as an x-ray source.

The most fundamental parameters of the stored electron beam are the energy, current, and emittance. Light sources targeting hard x-ray applications tend to operate with high electron beam energy E, since the energy of x-rays produced in undulators scales like E^2. There is also a tendency to operate with moderate beam current to reduce rf power requirements and x-ray beam power loads on the beamline front ends to more manageable levels. The APS presently operates at 100 mA, which is fairly typical

of sources in this energy range. The APS effective emittance,[1] 3.1 nm, is again typical for high-energy third-generation sources. The normal vertical emittance is 40 pm, which is somewhat higher than typical, resulting both from user requirements and the desire to operate routinely in few-bunch modes (see below). Of these basic parameters, only the beam current and emittance will change as part of the APS Upgrade Project, as discussed below.

Besides total beam current, the electron beam bunch timing pattern is very important for many applications. For this reason, APS operates with various bunch patterns or modes (depicted in Figure 3.1-1):

- *24-bunch mode*: As the name suggests, this features 24 equispaced bunches. The time between bunches is about 150 ns, with a FWHM bunch duration of about 80 ps, which is suitable for certain time-resolved studies. This mode is used about 65% of the time.
- *Hybrid mode*: This features a single intense bunch of 16 mA together with a collection of 56 bunches crowded on the opposite side of the ring. There is a space of about 1.6 μs before and after the intense bunch that has a full width half maximum (FWHM) duration of about 120 ps, which again makes it suitable for certain time-resolved studies. This mode is used about 15% of the time.
- *324-bunch mode*: This features 324 equispaced bunches. This mode is used about 20% of the time.

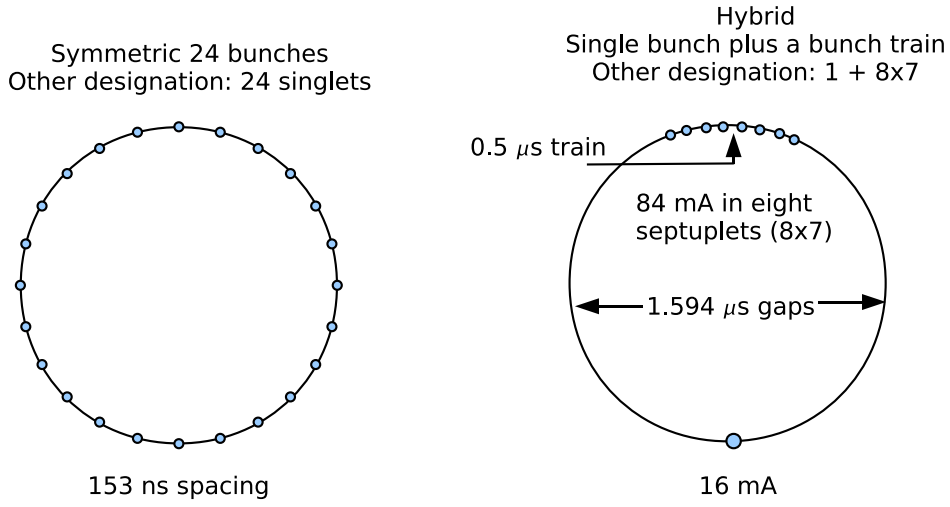

Figure 3.1-1: Depictions of two bunch patterns at present operating current of 100 mA.

One goal of the Project is to continue to support operation in all three modes.

Another important aspect of the beam is partitioning of the effective emittance into the beam size and divergence in the horizontal and vertical planes. The electron beam size and divergence are nominally identical at all beamlines, a result of the 40-fold symmetry of the accelerator lattice. However, reduced horizontal beam (RHB) size can be delivered to one straight section, while leaving other straight

[1]The effective emittance is the emittance including dispersion effects. At the center of a straight section with $\alpha_x = 0$ and $\eta'_x = 0$, it is given by $\sigma_x \sigma_{x'} = \epsilon_0 \sqrt{1 + (\sigma_\delta \eta_x)^2/(\epsilon_0 \beta_x)}$, where σ_x is the rms beam size, $\sigma_{x'}$ is the rms divergence, ϵ_0 is the raw natural emittance, and σ_δ is the fractional rms energy spread.

sections unchanged. At present, each APS run includes some time operating with such a lattice. In principle, this can be provided to several sectors when there is demand. At present, there is little impact on machine operation from the broken symmetry. As discussed in subsequent sections, delivering this mode in the APS Upgrade is more challenging because of other lattice changes.

The combination of low emittance and high charge per bunch in the 24-bunch and hybrid modes leads to short beam lifetimes. Even with a vertical emittance of 40 pm, the lifetime in 24-bunch mode at 100 mA is typically 8 hours, while the lifetime of the hybrid bunch is about 3 hours. Because of this, the beam intensity would decay rapidly, resulting not only in loss of x-ray intensity, but perhaps more importantly, in variation in beam-position-monitor (BPM) systematics and heat loads on x-ray optics. This would negatively impact experiments that demand high beam stability. For these reasons, the APS pioneered top-up mode [3.1-5], which involves frequent injection of beam to make up for losses. At present, top-up injections occur at 2-minute intervals in 24-bunch mode and 1-minute intervals in hybrid mode. The 324-bunch mode has a sufficiently long lifetime that top-up is not required; instead, the beam is added every 12 hours to restore 100 mA. One additional attraction of this mode is that it provides valuable time for injector development and operator training.

APS operates for users for approximately 5000 hours per year, with typical mean time between faults of 50 to 100 hours and availability of 97 to 99%. There are three runs and three shutdowns per calendar year. During a run, weekly maintenance and study periods are scheduled, lasting for 24 to 48 hours. Much of this time is used to perform necessary repairs or studies that prepare the accelerator for an upcoming change in the fill pattern or lattice.

3.1.2 Accelerator Upgrade Components

The APS accelerator upgrade includes a number of components, several of which will be unique. These are driven by Mission Need and Key Performance Parameters, discussed in Chapter 1, including:

- The need for additional beamline capacity.
- The need for more stable beams to allow demanding, state-of-the-art experiments to be performed.
- The need to provide intense, tunable, few-picosecond x-ray pulses with high repetition rates for time-domain experiments.
- The need to provide higher brightness and flux in the hard x-ray regime (above 10 keV), with particular emphasis above 25 keV.

Implementation of these upgrades will present many challenges, not the least of which is the intention to continue to operate the APS for 5000 hours per year. This implies that installation of components in the storage ring, as well as commissioning of new systems, will have to take place during existing maintenance and startup periods. In the remainder of this section, the approach to each of these requirements is briefly described. Details are given in appropriate sections below.

By and large, each of these upgrades could be pursued independently. That is, they are complementary, but not tightly linked. If there are links, they are indicated in the discussion below.

3.1.2.1 Capacity

The need for additional beamline capacity is addressed by provision of additional canted straight sections and long straight sections. At present, each straight section at APS accommodates a total of 4.8 m of insertion devices, which is suitable for canting two devices with a length of 2.1 m each. As described in section 3.2, we plan to provide three long straight sections for which the total length of insertion devices is increased to approximately 7.7 m. This allows increased capacity with higher brightness and flux, due to the longer devices that are possible. Provision of long straights is also beneficial in order to implement the Short-Pulse X-ray (SPX) scheme without reducing capacity (i.e., the long straights are helpful in accommodating the SPX hardware and insertion devices in the same straight).

Provision of long straights has a modest negative effect on brightness because the horizontal emittance will increase. However, the increase is less than 10%, which is considered acceptable.

3.1.2.2 Stability

More stable beams will allow demanding, state-of-the-art experiments to be performed. This is addressed by a multipronged approach to improving electron beam stability, as described in section 3.3. The goal is to increase the short- and long-term beam stability by a factor of two to four.

Improved beam stability has essentially no negative impacts on other aspects of the APS Upgrade. Indeed, it is helpful in that it is in some cases equivalent to a brightness increase. The SPX project has the potential to negatively impact beam stability. As a result, specific steps are taken as part of the SPX project that include setting tolerances on various errors and providing the diagnostics needed for control, feedback, and fine tuning.

3.1.2.3 Short X-ray Pulses

There is a need to provide intense, tunable, few-picosecond x-ray pulses with high repetition rates for time-domain experiments. This is addressed by the use of Zholents' deflecting-cavity scheme [3.1-6] for production of short x-ray pulses. This scheme, discussed in section 3.6, addresses one of the major deficiencies of storage ring light sources, namely, the inability to make intense, few-picosecond x-ray pulses.

As stated above and described in detail in section 3.6.3.2, the SPX system has the potential to negatively impact beam stability, both in terms of beam motion and emittance. Hence, upgrades to the beam stabilization systems, in particular the fast feedback system, are highly desirable as a complementary upgrade. In addition, a comprehensive suite of SPX-specific diagnostics are planned.

3.1.2.4 Brightness and Flux

There is a need to provide higher brightness and flux in the hard x-ray regime, above 10 keV, with particular emphasis above 25 keV. This is addressed in part by optimized insertion devices, as described in section 3.4, which includes planar undulators with customized periods, revolver undulators, and short-period superconducting undulators. The need for higher brightness and flux is also addressed

by provision of a number of long straight sections, as described in section 3.2, and by increasing the operating electron beam current from 100 mA to 150 mA. The accelerator is presently capable of running at 150 mA in all fill patterns, but would require upgrades to run beyond that.

In addition, further improvements to control of the coupling will be implemented, which will also improve x-ray brightness by permitting lower vertical emittance and providing more predictable beam parameters. Options and potential performance are described in more detail in section 3.2

3.1.2.5 The APS Upgrade Project Scope and Work Breakdown Structure

The accelerator portion of APS Upgrade Project scope is detailed in Table 3.1-1, together with related work breakdown structure (WBS) elements, for ease in correlating the accelerator scope items described in this chapter with other project documentation.

As noted above, the Project scope includes operation at 150 mA with all of the attendant changes to the front ends and beam lines. However, this does not require any changes to the accelerator systems and hence does not appear in Table 3.1-1.

Table 3.1-1: The APS Upgrade accelerator systems project scope and corresponding WBS elements.

WBS	Description	Quantity	Section
U1.03.02	**Storage Ring Technical Components**		
U1.03.02.01	Beam Stability		3.3
U1.03.02.02	Long Straight Sections	3	3.2
U1.03.03	**Short-Pulse X-ray System (SPX)**		
U1.03.04	**Insertion Devices**	13	3.4
U1.03.04.01	Planar Undulator	3	3.4.2
U1.03.04.02.01	Electromagnetic Variably Polarizing Undulator (EMVPU)	1	3.4.3.3
U1.03.04.02.02	Advanced Planar Polarized Light Emitter (APPLE-II)	2	3.4.3.2
U1.03.04.03	Superconducting Undulator (SCU2)	1	3.5
	Superconducting Undulator Engineering Prototype (SCU1)	1	
U1.03.04.04	Revolver Undulator	5	3.4.2.5
U1.03.04.05	Canted Section Magnets	8	
	Corrector Magnets	2	
U1.03.04.07	Insertion Device Vacuum Chambers (IDVC)	12	3.2.7.9

Storage Ring Technical Components, WBS U1.03.02, includes two lower-level WBS areas: improvement by a factor of two to four in beam stability (WBS U1.03.02.01) and design, construction, and installation of long straight sections in the APS storage ring (WBS U1.03.02.02). Beam stability

improvements are discussed in section 3.3, while long straight sections and other lattice changes are discussed in section 3.2.

The Short-Pulse X-ray (SPX) System, WBS U1.03.03, includes the design, construction, installation, and checkout verification of all components of the SPX deflecting-cavity system, with the exclusion of the actual buildings that will house the components. SPX and the risk-mitigating SPX0 research and development program are discussed in section 3.6.

Insertion Devices (IDs), WBS U1.03.04, includes both superconducting and conventional permanent-magnet and electromagnetic planar and polarizing devices. The devices that will be constructed, installed, and tested by the APS Upgrade are listed in Table 3.1-1. Insertion devices are discussed in section 3.4.

Planar Undulators, WBS U1.03.04.01, are constructed based on existing designs at the APS. This WBS area includes the construction, installation, and checkout verification of all components of the required number of planar undulator systems. Development of a new magnetic period is included in the baseline, a standard, well-understood activity at the APS. Planar undulators are discussed in section 3.4.2.

WBS U1.03.04.02 includes two types of polarizing undulators. The EMVPU, U1.03.04.02.01, is an electromagnetic device, while APPLE-II devices, U1.03.04.02.01, are based on permanent magnets. The EMVPU and APPLE-II undulators are discussed in sections 3.4.3.3 and 3.4.3.2. These WBS areas include the construction, installation, and checkout verification of all components of the required number of polarizing undulator systems. It is assumed that the EMVPU will be designed and constructed in-house, and that APPLE-II devices will be specified by the APS Upgrade and then procured from industry.

Superconducting Undulators, WBS U1.03.04.03, includes development of an 18-mm-period, approximately 1-m-long engineering prototype device. Development and production of a 2-m-long full-scale device of the same period length is included in the same WBS area. The SCU scope includes design, construction, installation, and checkout verification of all deliverables of the SCU system. Results of the risk-mitigating SCU0 programmatically supported research and development program are discussed in section 3.5.

Revolver Undulators, WBS U1.03.04.04, includes the construction, installation, and checkout verification of all components of the required number of revolver undulator systems. The risk-mitigating revolver-development program is discussed in section 3.4.2.5.

Canted Section Magnets, WBS U1.03.04.05, are required in some sectors, as are corrector magnets. This WBS area includes the construction, testing, installation, and checkout verification of the magnets and power supplies included within this system.

Insertion Device Vacuum Chambers, WBS U1.03.04.07 includes procurement of aluminum extrusions and fabrication and testing of the required number of insertion device vacuum chambers. All insertion devices require insertion device vacuum chambers; however, some of the existing chambers will be re-used. Insertion device vacuum chambers are discussed in section 3.2.7.9.

APS Upgrade Project funding covers all activities up to actual commissioning with beam in the storage ring. Commissioning activities are the responsibility of APS Operations, and are not part of the scope of the APS Upgrade.

Two of the accelerator upgrades, the improved beam stability and 150-mA operating current (section 3.7) will benefit all APS users, while the impact of others, such as SPX and the new insertion devices,

will be restricted to specific beamlines.

3.1.3 Interdependency

Several key interdependencies exist between the APS Upgrade Project's accelerator systems activities in WBS U1.03 and the APS operating organization. Accelerator-related Physics Requirements Documents (PRD) are developed by Accelerator Systems Division (ASD) personnel and are approved by APS Engineering Services (AES), ASD, X-ray Sciences Division (XSD), and APS Upgrade personnel. Funding for the effort required to plan, design, procure, assemble, install, document, and test Project systems and components is provided by the APS Upgrade Project. Weekly meetings of the Operations Directorate, which includes representatives of all APS divisions, APS Upgrade, and the APS user community, are used for discussion of scheduling and operations issues related to changes to accelerator systems.

Commissioning with beam is not included in the APS Upgrade scope, but is the responsibility of the operating organization. Beam commissioning plans developed by the operating organization are approved by AES, ASD, XSD, and APS Upgrade personnel, as appropriate.

There are interdependencies between the APS Upgrade accelerator, beamline, and enabling technologies WBS areas. Beamline technical leads write beamline-specific PRDs, listing the required x-ray energies and harmonics. Accelerator scientists develop PRDs for each of the insertion devices to be provided by the APS Upgrade Project.

Interface Control Documents (ICD), signed by all relevant parties within the three technical WBS areas, formalize technical details, such as the period length of an insertion device.

The building that will house many of the SPX system components is being provided with funding that is external to the project. SPX relies heavily on collaboration with Thomas Jefferson National Accelerator Facility (JLAB) and Lawrence Berkeley National Laboratory (LBNL); Stanford Linear Accelerator Center (SLAC) also provides simulations.

The building in which superconducting undulator development takes place was refurbished by the Laboratory and furnished to the APS Upgrade team for this purpose.

Insertion device research and development is also funded off-Project; however, progress is closely monitored by the Project. Superconducting undulator development relies on a collaboration with the University of Wisconsin for thermodynamic calculations.

3.1.4 References

[3.1-1] J. N. Galayda. The Advanced Photon Source, Proc. of PAC 1995, pp. 4–8, (1996).

[3.1-2] J. L. Laclare. Commissioning and Performance of the ESRF, Proc. of PAC 1993, pp. 1427–1431, (1993).

[3.1-3] S. Date et al. Operation and Performance of the SPring-8 Storage Ring, Proc.of PAC 1999, pp. 2346–2348, (1999).

[3.1-4] K. Balewski et al. PETRA III: A New High Brilliance Synchrotron Radiation Source at DESY, Proc. of EPAC 2004, pp. 2302–2304, (2004).

[3.1-5] L. Emery and M. Borland. Upgrade Opportunities at the Advanced Photon Source Made Possible by Top-up Operations, Proc. of EPAC 2002, pp. 218–220, (2002).

[3.1-6] A. Zholents et al. Generation of subpicosecond X-ray pulses using RF orbit deflection, Nuclear Instruments and Methods in Physics Research A, **425**, 385, (1999).

3.2 Lattice and Accelerator Physics

3.2.1 Introduction

One of the goals of the APS Upgrade Project is to meet the need for higher-brightness x-ray beams, as well as the simultaneous need for additional beamline capacity. Provision of a number of long straight sections is an effective way to meet this need. Long straight sections are needed for long insertion devices (IDs) and in order to be able to fit in one straight section a combination of a superconducting undulator and a permanent magnet undulator or a combination of a permanent magnet undulator and a set of superconducting cavities. Hence, long straights are an important part of providing higher brightness, increased capacity, and short x-ray pulses (see section 3.6).

Specific details for all these goals are discussed throughout this report. This section focuses on the beam dynamics issues pertaining to establishing the APS lattice with long straight sections. The most significant challenge of this task arises from a need for uneven distribution of long straight sections around the ring to meet user demands and practical constraints. The loss of lattice symmetry associated with this presents potentially severe consequences in terms of beam emittance increase, lifetime reduction, and loss of injection efficiency.

In 2003, APS accelerator scientists and engineers, in consultation with interested members of the user community, conducted an extensive study of various options for implementation of long straight sections. Several of these involved replacement of dipole magnets which, while very effective at lengthening the straight section, was determined to be too expensive for the benefit delivered. In the end, it was decided to make a long straight section by removing one quadrupole magnet on each side of the existing straight section.

This is conceptually simple and requires no additional magnets, which greatly reduces the cost. This scheme requires rebuilding the girders on either side of the straight section. These girders presently hold the quadrupole triplets, as well as two sextupoles, two steering magnets, and several beam position monitors. Although no additional magnets are needed, girders must be prepared ahead of time for rapid installation.

Because of the breaking of ring symmetry by the long straight sections, much effort has been spent in mitigating the adverse effects on beam dynamics by making adjustments to the strengths of the quadrupole and sextupole magnets, a unique opportunity offered by the existing power supply arrangement in which all quadrupoles and sextupole magnets have individual power supplies. Taking advantage of this opportunity, a new approach relying on a parallel genetic optimization algorithm for lattice optimization has been developed that allows us to largely regain the performance parameters of the original symmetric lattice. Discussion of the approach developed for the APS appears in the first part of this section. In addition to the arrangement of the long straight sections, a requested special sector with reduced horizontal beam size also reduces the symmetry of the lattice. The method of

recovering the performance of a symmetric lattice is essentially the same as that employed when introducing the long straight sections.

Following the discussion of lattice design, there is a discussion of experimental tests of mock-up lattices, which give confidence in the results. One outcome of these tests, as reported in section 3.2.2.5, is that the extent of beam steering for users will have to be restricted in order maintain good injection efficiency and lifetime.

Issues in correcting the vertical emittance will be discussed next. In the presence of errors, a storage ring produces a somewhat large vertical emittance that can be reduced to reasonable levels using standard techniques used at all light sources. In addition, the nonlinear properties of a lattice are usually worsened by the same errors that cause vertical emittance. Thus when the vertical emittance is corrected, the nonlinear properties are improved.

In the final part of this section, there is a review of collective effects in the storage ring, which are well characterized in the present configuration. They define the practical operating limits for total current and for single-bunch charge. In particular, the potential impact of lattice changes and longer insertion device chambers is examined with a view toward maintaining the existing operating limits and setting requirements for chamber gaps. (Other changes, such as the introduction of rf cavities for the SPX source, will potentially adversely impact collective effects, and are discussed in section 3.6. Requirements for higher current operation will also be discussed in section 3.7.)

After a brief discussion of dependencies on programmatic work in section 3.2.6, section 3.2.7 provides a detailed discussion of the engineering requirements, specifications, and design.

3.2.2 Lattice Design

The APS magnetic lattice consists of 40 double-bend sectors, normally operated in an essentially translation- and reflection-symmetric configuration. (The symmetry is slightly broken by the use of Decker distortion in the user Sectors 1-35 [3.2-1], a feature that any upgrade must retain since it reduces backgrounds on x-ray beam position monitors.) Each sector has ten quadrupoles, seven sextupoles, and eight steering magnets per plane. In anticipation of the need to customize the electron optics, all quadrupoles and sextupoles have independent power supplies [3.2-2]. In addition to permitting optics correction [3.2-3], this feature has allowed provision of special reduced horizontal beam (RHB) size optics for several beamlines. Its importance to the APS Upgrade is twofold: First, it permits entertaining lattice customizations without the expense of additional power supplies and controls. Second, it permits mocking-up many of these customizations before committing to hardware changes.

One of these customizations will be provision of long straight sections (LSSs) to (nominally) four sectors. As described above, this will be accomplished by removing the long Q2 quadrupoles, one beam position monitor (BPM), and one corrector on either side of the target straight section, then moving other components away from the straight section into the empty locations.

Since the APS has 40 sectors and since only three LSSs sections are required, the LSSs cannot be symmetrically placed. In addition, for implementation of SPX, two LSSs separated by a single short straight are required, since this permits accommodating the SPX cryomodules without excessively reducing the space available for undulators.

Based on these evolving considerations and recent progress in optimization of the nonlinear properties

of lattices [3.2-4, 3.2-5], workable nonsymmetric configurations incorporating three, four, and eight LSSs have been developed. The configurations with three LSSs meet the present needs of the Project, so the others will not be discussed further.

There are two other requirements for the lattice design:

- RHB size in Sector 20, in support of the wide-field imaging beamline. The desired horizontal beam size is less than 120 μ, compared to about 280 μ for the standard APS lattice.
- Linear optics and sextupole turning in support of SPX. SPX requires a specific vertical phase advanced (2π) between the sets of cavities, as well as specific sextupole tuning to mitigate the increase in vertical emittance.

Provision of special optics for RHB and SPX does not require new or modified hardware. However provision of an LSS does require hardware modifications. Provision of an LSS is conceptually simple, since it nominally only involves *removing* accelerator components. In practice, this requires pre-assembling new girders to be installed in place of the existing girders (known as girders 1 and 5) on either side of the straight. In addition, a new vacuum chamber must be prepared and installed for the straight section. Analysis of the schedule indicates that a single LSS can be installed during a standard APS shutdown, which lasts approximately one month. Engineering and installation details are discussed in section 3.2.7.

As discussed in section 3.2.2.5, the new lattices are more sensitive to orbit displacement in sextupoles than the existing APS lattices. As a result, it will be necessary to center the orbit in the sextupoles, which is not presently required. This implies the need to improve the alignment of the accelerator and beamlines in those locations where the beamlines are now accommodated by large steering of the electron beam. This can be done gradually (i.e., a few sectors at a time). Steering tolerances are still under investigation, but preliminary estimates indicate that 23 insertion device beamlines and 14 bending magnet beamlines will require realignment. This is not part of the Project scope.

3.2.2.1 Lattice Constraints

Before describing in detail how the new lattices are developed, the properties of the present lattice and constraints that must be satisfied by new lattices are reviewed. The present APS lattice functions are shown in Figure 3.2-1. Constraints on new lattices include:

- Maximum beta functions in the horizontal and vertical planes of 40 m and 30 m, respectively. Ideally, maximum beta functions should be as small as possible, particularly at ID transitions, in order to reduce the effective chamber impedance (see section 3.2.4).
- Horizontal beta functions at the center of ID straights of between 15 and 25 m. In general, values close to 20 m are used now and are preferred.
- Vertical beta functions at the center of the ID straights within 50% of $\beta_{opt} = L/2$, where L is the length of the small gap chamber. ($L \approx 2.5$ m for a normal straight.) This maximizes the vertical acceptance. The beta function β_e at the end of the chamber is relatively insensitive to the exact value $\beta_c = \beta_{opt} + \Delta\beta_c$ at the center, being governed by

$$\frac{\Delta\beta_e}{\beta_e} \approx \frac{1}{2}\left(\frac{\Delta\beta_c}{\beta_c}\right)^2, \tag{3.2-1}$$

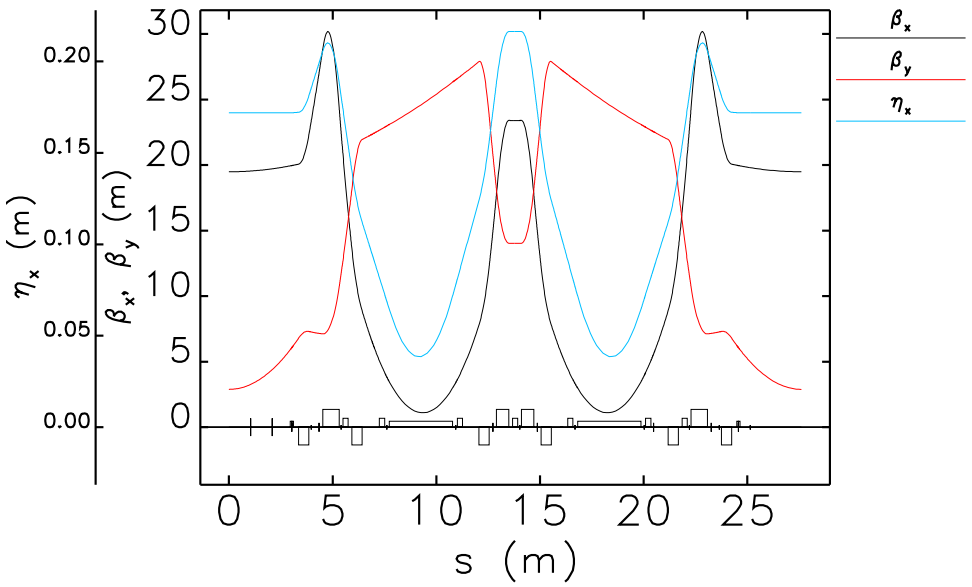

Figure 3.2-1: Present lattice functions for the first sector of the APS.

so that β_e is within 13% of the optimum value.

- At present the APS effective emittance is 3.1 nm, resulting from a 2.5-nm natural emittance combined with the presence of dispersion in the straight sections. Because the effective emittance has been optimized to the present low value, any changes are likely to result in an increase. This increase should be kept to under $\sim$10%. In order to keep the emittance close to its present value, the horizontal integer tune should be 36 (the present value) or higher. There is little reason to raise it above this value, so both tunes were kept close to the present values, $\nu_x = 36.15$ and $\nu_y = 19.25$.

- Because of the need to run with high single-bunch current, APS operates with high chromaticities, which reduces the impact of the transverse mode coupling instability. In 100-mA, 24-bunch mode, it has historically been necessary to have $\xi_x \approx 7$ and $\xi_y \approx 6$, while in hybrid mode $\xi_x \approx \xi_y \approx 11$ was typically required. A newly developed single-bunch feedback system has recently been put into routine operation [3.2-6]. With this system, the requirement for exceeding 16 mA per bunch is reduced to $\xi_x \approx \xi_y \approx 9$, while $\xi_x \approx \xi_y \approx 4$ is needed for 24-bunch mode at 150 mA. The SPX system is incompatible with hybrid mode. Hence, $\xi_x \approx \xi_y \approx 9$ configurations that support hybrid mode do not need to accommodate SPX with its unusual sextupole tuning.

- Neither any main accelerator magnets nor any power supplies will be upgraded as part of the Project. Hence, existing power supply limits must be respected, which gives $K_1 \leq 0.9$ m^{-2} for quadrupoles. For most sextupoles, the present limit is $K_2 \leq 21.6$ m^{-3}. If necessary, inexpensive "noses" can be added to the sextupole poles as was done already for the S2 family, raising the limit to 29.8 m^{-3} [3.2-7].

- As described in detail below, sufficient dynamic acceptance (DA) is necessary in order to have efficient injection. Simulations of the present operating lattice indicate that the dynamic acceptance is -12 to -15 mm on the injection side, as shown in Figure 3.2-2. Hence, this value was the target in optimization of new lattices. The dynamic acceptance on the positive side is

less important, resulting in a target of 7 mm. In the vertical plane, the target was 1 mm, which is quite generous compared to the typical rms beam size of 10 μm for the stored beam and 0.2 mm for the injected beam (assuming 10% coupling in the booster).

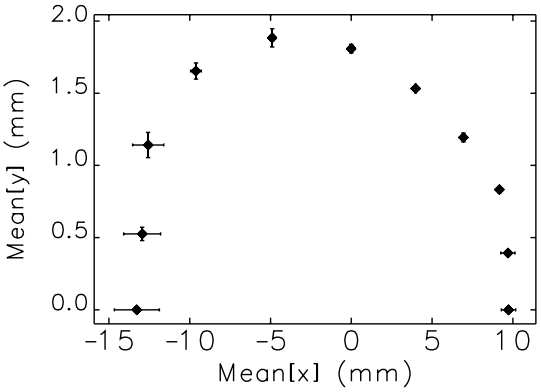

Figure 3.2-2: Nominal dynamic acceptance computed for 50 error ensembles for $\xi_x = 7$ and $\xi_y = 6$. The error bars show the standard deviation of the DA boundary location.

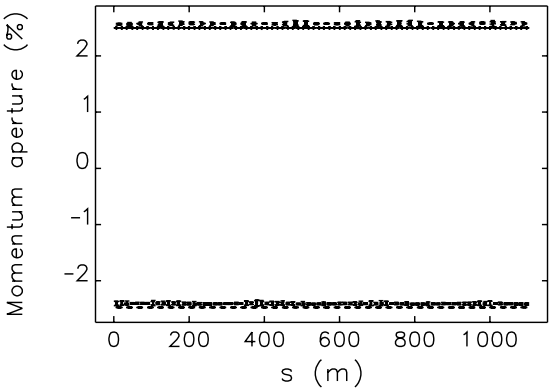

Figure 3.2-3: Nominal momentum acceptance computed for 50 error ensembles for $\xi_x = 7$ and $\xi_y = 6$. The error bars show the standard deviation of the boundary location. An rf voltage of 9 MV is assumed and is the limiting factor in determining the momentum acceptance.

- Although APS runs in top-up mode [3.2-8] and can therefore tolerate a somewhat short beam lifetime, there are limits both in the amount of charge and frequency of injections. Ideally, to avoid disturbing experiments, injection occurs no more frequently than every 120 seconds, although in hybrid mode at present injection occurs every $\Delta T_i = 60$ s. While the injector is nominally capable of delivering $\Delta Q_i = 6$ nC per shot, a value of 3 nC is routinely available. The minimum workable lifetime is

$$\tau_{\min} = \frac{Q_s \Delta T_i}{\Delta Q_i \eta_i}, \tag{3.2-2}$$

where Q_s is the total stored charge, and η_i is the injection efficiency. At 150 mA and 80% efficiency, this gives $\tau_{\min} = 3.8$ h for a 60-second top-up interval.

Another consideration is the droop in the charge in each bunch between injections, which should be kept to a minimum. This is given by

$$D = 1 - e^{\frac{-B\Delta T_i}{\tau}}, \tag{3.2-3}$$

where B is the number of stored bunches. If the lifetime is only 3.8 hours for 24 bunches, $D = 0.1$, i.e., a 10% droop. This is probably acceptable, but clearly having a longer lifetime is desirable, if for no other reason than to prevent radiation damage of components.

The lifetime is strongly affected by the local momentum acceptance (LMA), described in detail below. The reference LMA for the present APS lattice is shown in Figure 3.2-3. This is sufficient to provide lifetimes of 8 to 9 hours at 100 mA in 24 bunches for the nominal vertical emittance of 40 pm.

3.2.2.2 Dynamic and Momentum Acceptance

As alluded to above, in addition to designing appropriate linear optics, the nonlinear dynamics of the lattice must be controlled in order to obtain adequate dynamic and momentum acceptances. This section provides an explanation of the meaning and importance of these quantities.

Dynamic acceptance (DA) is characterized by the area in horizontal and vertical space into which particles may be injected and survive as stored beam. Thus, the importance of the DA is that it is a primary determinant of the injection efficiency. At the APS, injection is performed in the horizontal plane, i.e., with non-zero residual amplitude in the horizontal motion, so the horizontal DA needs to be much larger than the vertical. In addition, since injection is from inside the ring, the horizontal acceptance on the negative side is more important than on the positive side.

DA is determined by tracking particles with increasing initial horizontal (x) and vertical (y) amplitudes until the boundary between survival and loss is found. This process is illustrated in Figure 3.2-4. A series of n line searches are conducted beginning at the origin. The coordinates along the lines are simply

$$x = R\cos\phi_n, \tag{3.2-4}$$

$$y = R\sin\phi_n, \tag{3.2-5}$$

where $\phi_n = n\pi/L$ for an L-line search. For each line, it is desired to find the smallest R, R_{da}, at which a particle will be lost within N turns. To do this, R is increased in small steps ΔR until a loss is seen within N turns. The step interval ΔR is then subdivided to refine the determination of R_{da}. The set of (x, y) points resulting from the determination of R_{da} for each line defines the DA boundary.

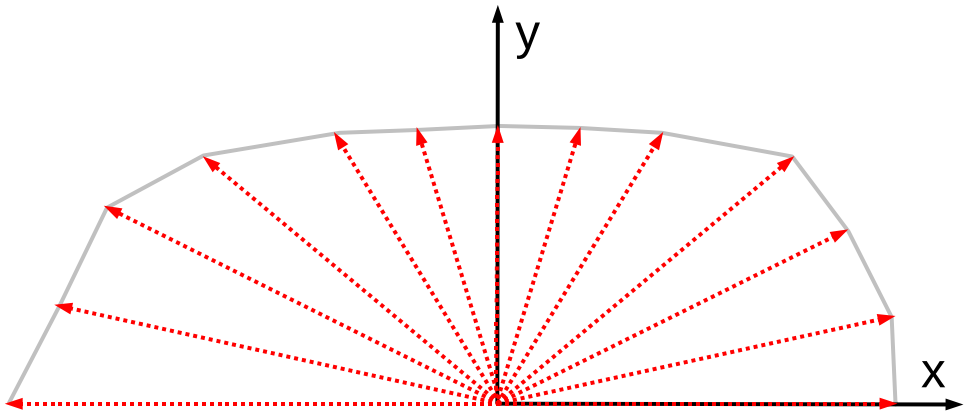

Figure 3.2-4: Illustration of the method used to determine dynamic acceptance. Particles are launched at intervals along a series of lines beginning at the origin. After a loss is seen, interval subdivision is used to refine the determination of the minimum acceptance required for loss. The (x, y) location of first particle loss defines a point on the dynamic acceptance boundary.

Momentum acceptance is characterized by the maximum momentum displacement that a particle can undergo and still survive. In general, this quantity varies as a function of position around the ring, as well as for negative and positive momentum displacements. Hence, the quantity of importance is the *local* momentum acceptance (LMA), characterized by two functions $\delta_n(s)$ and $\delta_p(s)$. These give, respectively, the maximum fractional negative and positive momentum displacements that a particle

may experience at location s and still survive a chosen number of turns. These functions are primary determinants of the Touschek lifetime, which is the dominant lifetime-limiting mechanism in the APS and other third-generation light sources.

The method used to determine $\delta_{n,p}(s)$ [3.2-9] is similar to that used for determining the dynamic acceptance. At the exit of selected elements (i.e., at selected s positions), particles are given increasing positive or negative momentum kicks, then tracked N turns. When a loss is seen, the step size is decreased to refine the determination of the boundary.

For both DA and LMA determination, particle tracking must include not only the effects of the magnets, but also longitudinal motion, radiation damping, physical apertures, and errors.

Longitudinal motion: The need for longitudinal motion (i.e., motion in the rf bucket) in the case of the LMA is clear, since the momentum acceptance may be determined either by transverse dynamics or the rf acceptance $\pm\epsilon_{\text{rf}}$. This is particularly the case with the APS, where the rf voltage is relatively low, giving $\epsilon_{\text{rf}} \approx \pm 2.3\%$. In the case of DA, there is some small sensitivity to longitudinal motion, which results from the small path-length dependence on the betatron amplitude.

Radiation damping: Radiation damping must be included in the model for several reasons. First, it may increase the DA or LMA by damping the growth of particle motion near the stability boundary. Second, it stabilizes the determination of the acceptance by sweeping the particle's amplitude over a small range. This ensures that an unstable amplitude is not "stepped over" in the search. For this reason, in computing the LMA it is advisable to choose a momentum step size $\Delta\delta$ that is smaller than $\epsilon_{rf}(1 - e^{-NT_r/\tau_\delta})$, where T_r = 3.68 μs is the revolution time, and $\tau_\delta = 4.8$ ms is the longitudinal damping time. For APS, taking $N = 400$ is adequate, as it implies that more than 25% of the initial momentum displacement decays away in the course of the simulation. A third reason for including damping in LMA simulations is that this large momentum slew potentially sweeps the particle past many resonances, the effect of which would be missed if radiation damping was omitted. Similar reasoning applies for DA determination, where radiation damping results in a rapid drop in amplitude that may result in sampling resonances due to the tune shift with amplitude.

Physical apertures: Although it is common to speak of the "dynamic aperture," what is in fact of interest is the dynamic acceptance, which is the aperture including both dynamic and physical limits. Often, it is found that the effective aperture is smaller than the physical aperture, which may lead to the erroneous conclusion that the physical aperture is not important. Including small vertical physical apertures is particularly important when there is coupling of horizontal and vertical motion, as it can result in significant reductions in the *horizontal* aperture. All simulations include realistic physical apertures unless otherwise stated. In particular, in the case of the long straight sections, the simulated apertures include the effect of the longer ID chamber.

Inclusion of errors: Inclusion of errors refers not only to multipole errors resulting from magnet imperfections, but, far more importantly in the case of APS, to random errors in the strength and alignment of magnets. For example, without errors the effect even of the half-integer resonance may not be seen in a tracking simulation. Similarly, without errors there would be no coupling between the horizontal and vertical planes, an effect that is well known to strongly influence the dynamic acceptance of light sources with small-vertical-gap insertion devices. Hence, lattice errors must be included in the simulations.

Effective methods exist for correcting linear optics [3.2-10] and coupling (e.g., [3.2-11–3.2-13]), which are important in light sources because of the small insertion-device vertical apertures. In the APS, for example, the lattice function errors are corrected to the 1% rms level [3.2-3] and coupling is corrected

to the 1% level. These are commonly achieved in modern storage rings.

It would seem that in order to be realistic, not only must errors be included, but also correction of those errors using real-world techniques. However, correction is not essential in the simulations. Once correction is performed, what is left are residual errors of a certain level. Instead of modeling relatively large errors with correction, it is sufficient to simply use smaller random errors that give lattice function and coupling errors at post-correction levels. This neatly sidesteps a considerable complication. It has been found that assuming quadrupole and sextupole strength errors at the 0.02% rms level and tilt errors at the 0.05 mrad rms level give lattice errors at or above the desired level. It is then only necessary to apply a coupling correction algorithm to emulate the operational method of setting of the vertical emittance.

3.2.2.3 Optimization Technique

The requirements set down in the previous section are a mixture of linear optics constraints and constraints that depend on nonlinear properties of the lattice. The latter are, of course, controlled through adjustment of the sextupole magnets. A very common approach [3.2-14] to optimization of sextupole settings is to minimize various resonance driving terms, which in turn minimizes tune shifts with transverse amplitude $d^n\nu_{x,y}/dA_{x,y}^n$ and momentum offset $d^n\nu_{x,y}/d\delta^n$. However, as described in the last section, APS operates with chromaticities $d\nu_{x,y}/d\delta$ that are considerably different from zero. Hence, the utility of minimizing the higher-order chromaticities is doubtful. Indeed, very likely there is a need to employ significant higher-order terms to minimize the size of the tune footprint over the desired momentum acceptance.

The issue is less obvious in the case of the amplitude-dependent tune shifts. However, experience has shown that small amplitude-dependent tune shifts are not always optimal, depending on the proximity of the working point to strong resonances. In some cases, it has been found that a large tune shift with amplitude can defuse a resonance by preventing quasi-stable particles from remaining on the resonance.

Even when it is applicable, the traditional method of sextupole optimization does not guarantee good DA and LMA. If it did, tracking simulations would not be needed to validate the sextupole configuration, and yet such simulations are universally used. Informed by these observations, a new technique for sextupole optimization technique was developed [3.2-4, 3.2-5] that relies on tracking simulations directly. It is made possible by the availability of relatively inexpensive computing clusters and fully scriptable accelerator simulations.

Although this method could use any tracking code, the ability to create fully scripted simulations is essential, since matching and tracking must run without human intervention. Thus, the tracking program `elegant` [3.2-15, 3.2-16] was used, together with the SDDS Toolkit [3.2-17] and `geneticOptimizer` [3.2-18]. The latter is a script that implements a multi-objective genetic algorithm (MOGA).

In this method many computers are simultaneously used to evaluate the DA and LMA for various lattice tunings (e.g., tunes and sextupole settings). As described above, DA and LMA computation includes radiation damping, synchrotron oscillations, and physical apertures. After completion of a sufficient number of evaluations, a genetic algorithm is used to "breed" more candidate configurations based on the best configurations seen so far. The process continues until a sufficiently good solution is obtained or until the results stop improving.

As mentioned above, it is important to include errors in the DA and LMA simulations. In order to have a hope that the optimization will converge, it is of course essential that the errors remain unchanged for each evaluation. Hence, optimization is performed with a single, fixed ensemble of errors. It is always possible that an error ensemble may be chosen that happens to provide atypically good results. To guard against this possibility, the optimized configuration is subsequently evaluated with a large number of ensembles.

Any optimization requires one or more penalty functions. In the work reported here, a multi-objective optimization was used. The objectives are derived from the DA and lifetime.

Dynamic Acceptance Penalty Function:

While the DA is frequently computed, quantitative use of the acceptance is uncommon and can be fraught with uncertainty. Typically, the horizontal acceptance is quoted as a single number, which can not quantify the shape of the acceptance. Such a number could well be highly misleading. However, in order to optimize DA, it is necessary to obtain one or a few quantities that clearly indicate how good a solution is. The approach adopted here is to use the area of the DA, but to compute it with certain restrictions that ensure it is a useful quantity.

One potential pitfall of using the DA area is that the optimizer might provide a useless solution with large vertical acceptance and small horizontal acceptance. This can be prevented by simply not scanning the vertical coordinate beyond the minimum requirement. This prevents the algorithm from "seeing" any vertical DA that exceeds requirements.

Another potential pitfall is that the acceptance may not have a smooth shape. In some instances depending, for example, on the strength of coupling resonances, one might find useless protrusions that enlarge the area but that are not useful for injection. This was avoided by applying a clipping algorithm to the DA boundary, as illustrated in Figure 3.2-5.

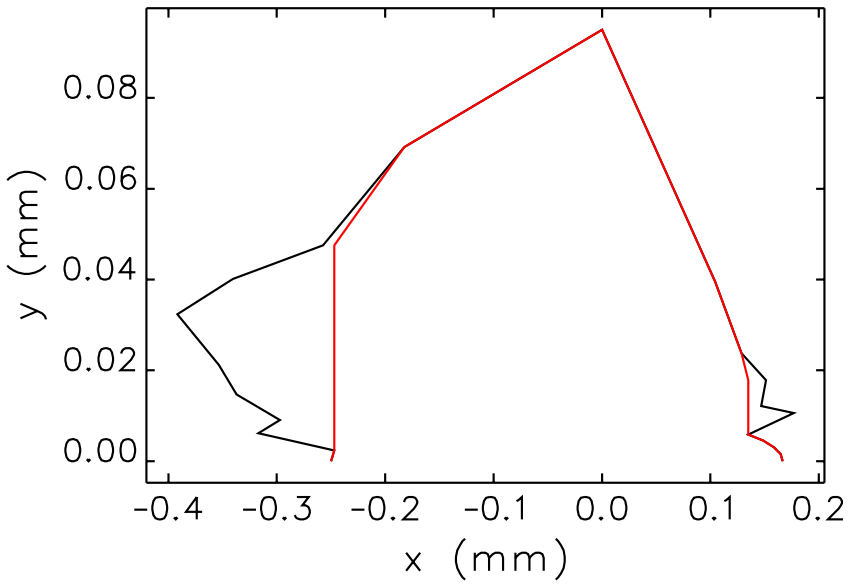

Figure 3.2-5: Illustration of the behavior of the dynamic acceptance boundary clipping method. The black line shows the original dynamic acceptance boundary, while the red line shows the clipped boundary.

A third potential pitfall is that the acceptance may be enlarged at $x > 0$ at the expense of $x < 0$ (at

APS, inject occurs on the $x < 0$ side). This is avoided by clipping off any DA that extends beyond $x = 7$ mm, which provides generous room for oscillation of the stored beam due to the mismatched kicker bump used in APS.

With these restrictions and modifications, it was found that the area of the DA, A_d, is a robust indicator of a good solution. Because the goal is to maximize this area, the related objective function is $-A_d$.

Lifetime Penalty Function:

The Touschek lifetime can be computed from the LMA, the Twiss parameters, the beam emittances, and the bunch charge. This is done using the program `touschekLifetime` [3.2-19], which uses the Twiss parameters and LMA computed by `elegant` and applies Piwinski's formalism [3.2-20].

In order to reduce the computer resource requirements, the LMA is not computed at the exit of every element. Instead, it is computed at the exit of the S1, S3, and S4 sextupoles in (typically) the first eight (of 40) sectors. Experience shows this is representative of the LMA around the ring. In order to compute the Touschek lifetime, it is assumed that the LMA repeats the same pattern in the subsequent 32 sectors. The optimized results are checked in ensemble evaluation by determining the LMA at the exit of all sextupoles.

The objective function related to the Touschek lifetime τ_T is $-\tau_T$, since the goal is to maximize the lifetime.

In many cases, optimization of the lifetime results in a relatively small momentum-dependent tune footprint that avoids major resonances, such as the integer, half-integer, and main coupling resonances. However, in some cases it was found that stable half-integer resonance crossings occurred. These apparently are possible because of strong coupling between the planes and/or large tune shift with amplitude. Observation of phase-space trajectories for such crossings shows an exchange of amplitude between the planes, as well as mitigation of the effects of the resonances due to fairly rapid synchrotron motion and, presumably, large tune shifts with momentum and amplitude.

In spite of this, it was decided to disallow crossing the half integer resonance. This was done by modifying the LMA computation to "cap" the momentum acceptance at the momentum deviation that corresponds to the resonance crossing, if any. This requires first tracking a series of off-momentum particles to determine their tunes. This adds only a small amount of additional running time. The momentum acceptance cap is accepted as an additional parameter by `touschekLifetime`.

Linear Optics Variation

Published work [3.2-4, 3.2-5] indicates that variation of the tunes is important in finding an optimal solution. More recently, it was determined that more detailed linear optics variation is essential, particularly in obtaining solutions for RHB.

In the present APS lattice, there are three types of sectors: ordinary user sectors, which include Decker distortion [3.2-1]; special user sectors with RHB size; and non-user sectors, which do not have Decker distortion. Of the 40 sectors in the ring, a least 33 are ordinary user sectors while 5 are non-user sectors. Changing the working point is thus relatively simple, even using a quadrupole knob for the ordinary sectors, while changing other linear optics parameters is usually not difficult.

When the lattice becomes more complex, this is not true. In particular, with long straights there is a reduced ability to change the tunes and other linear optics parameters while satisfying other constraints, such as maximum beta functions and emittance.

Originally, the approach was to optimize lattices with the tunes as the only linear optics parameters under the control of MOGA. The detailed linear optics solution was considered to be sufficiently constrained by fixed requirements on the maximum lattice functions and the lattice functions at the straight section. However, in the course of developing the RHB lattice, it was determined that this was insufficient. It was observed that two solutions with the same tunes and linear optics constraints could have significantly different performance. Hence, it was concluded that MOGA should be provided with additional "knobs" to allow varying the linear optics constraints in more detail. This implies that for each evaluation, a new linear optics solution must be obtained that differs from previous solutions by more than just the tunes. Examples of the type of additional knobs are maximum lattice functions in different parts of the machine and lattice functions at specific locations, e.g., the vertical beta functions at defocusing sextupoles in the RHB section.

For complex lattices, the most robust approach is to perform simultaneous matching of a model ring that includes one or more instances of every cell. For example, for an LSS the matching would include the sector leading to the long straight and the sector leading away from it. Although this is not as difficult as matching the entire ring, it is still time-consuming. Use of recently added parallel optimization features [3.2-21] in the program [3.2-15] has expedited this work.

Details of the Algorithm:

Having reliable objective functions is perhaps the most important part of any optimization. This has been covered in the previous subsections. Here, several details of the optimization algorithm itself are described. The algorithm, which is implemented in the `geneticOptimizer` Tcl script [3.2-18], is as follows:

1. Create N randomized configurations. Typically, these are "small" perturbations from a reasonable starting point, e.g., a previous similar configuration or the present operational configuration. N varies depending on the computing resources available. Typically, $N \sim 100$, but $N > 1000$ has been used for some of the work reported here.
2. Submit N jobs to a cluster to evaluate the configurations.
3. Wait until at least M (e.g., 4 to 10) configurations are newly completed. (Note that the running time is not the same for all configurations, since a small DA/LMA takes less time to simulate.)
4. Collect information on all completed configurations.
5. If the best configuration is adequate, stop. Otherwise:
   (a) Perform a nondominated sort to find the first- or highest-rank solutions.
   (b) Determine how many open slots P are available.
   (c) For each open slot:
      i. Randomly select two configurations from this group to act as "parents."
      ii. Randomly blend the attributes of the parents to "breed" a new configuration.
      iii. Submit a new job to evaluate this configuration.
6. Wait for at least one job to complete.
7. Return to step 4.

The quantities N, M, and P have been determined in only a rough fashion based on experience, rather than any systematic program of study.

3.2.2.4 Optimization Results

Because experience showed that the RHB configuration was the most challenging, work began with optimization of this configuration by itself, followed by addition of three LSSs. The final step was to incorporate the SPX requirements. Operationally, two lattices are required. The first, "3LSS+RHB", features three LSSs in Sectors 1, 5, and 7, plus RHB in Sector 20, with a chromaticity of 9 in both planes. A total of 69 MOGA knobs are used for this optimization:

- Horizontal and vertical tunes—2 knobs.
- Sextupoles in long-to-short Sector 1, which are duplicated in Sectors 5 and 7—7 knobs.
- Sextupoles in short-to-long Sector 2, which are duplicated in Sectors 6 and 8—7 knobs.
- Five of seven sextupoles in short-to-short Sector 3, which are duplicated all remaining Sectors—5 knobs. (The other two sextupole families in these sectors are used for direct chromaticity adjustment.)
- Sextupoles in RHB Sectors 20 and 21—14 knobs.
- Sextupoles in Sector 36, which are duplicated in the remaining "Zone F" Sectors 37-40—7 knobs.
- Values of β_x, β_y, and η_x at center of LSS and non-RHB, non-Zone-F straights—6 knobs.
- Horizontal beam size and β_y at RHB straight—2 knobs.
- Maximum values of β_x, β_y, and η_x in LSS, non-RHB, and Zone F sectors—9 knobs.
- Values of β_x, β_y, or η_x at strategic locations in Sectors 20 and 21—10 knobs.

The large number of independent sextupoles was used based on experience that showed, for example, that asymmetric distributions of sextupole strength are helpful [3.2-22].

Because of the high chromaticity, this is a challenging lattice for which to obtain good results. Figure 3.2-6 shows the lattice functions for the entire ring, while Figure 3.2-7 shows detail of the RHB section. The horizontal beam size at the RHB sector is 85 μm, well below the 120 μm requirement. This was one of the welcome outcomes of the additional linear optics parameters described above.

It is of interest that the dynamic acceptance in this lattices is enlarged on the negative x side compared to the lattice without long straight sections. Indeed, the dynamic acceptance is larger than the nominal limiting physical aperture (described above), which results from a curious distortion of the phase-space ellipses between the injection point at the end of Sector 40 and the location of the minimum aperture (which is -15 mm in the horizontal at straight section 4). This could only be brought about through adjustment of a significant number of sextupoles between the injection and limiting aperture points, which is what happened in the present case. More detail may be found in [3.2-22].

The second required lattice, "3LSS+RHB+SPX", has three LSSs in sectors 1, 5, and 7, RHB in sector 20, and SPX in sectors 5 through 7, with a chromaticity of at least 4 in both planes. A total of 105 MOGA knobs are used for this optimization. In addition to most of those just listed, they include

- Sextupoles in Sectors 6 and 7—14 knobs.

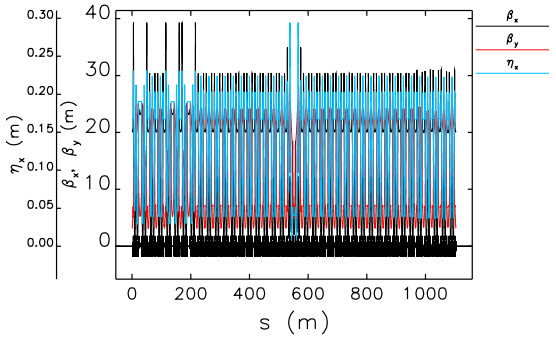

Figure 3.2-6: Optical functions for the full ring with 3 LSSs at nonsymmetric locations and RHB in Sector 20.

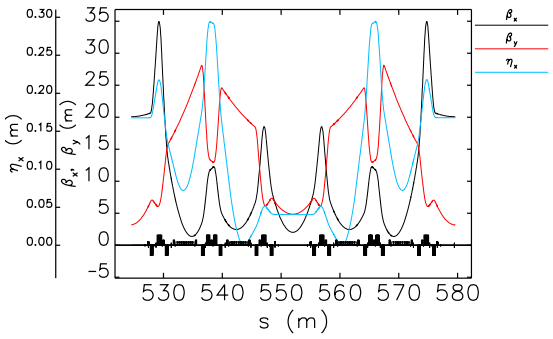

Figure 3.2-7: RHB-area detail of optical functions for solution with three LSSs and RHB.

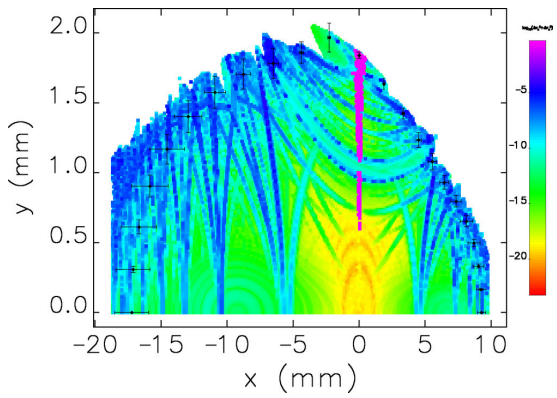

Figure 3.2-8: Dynamic acceptance from 50 ensembles for the lattice with three LSSs, RHB, and $\xi_x = \xi_y = 9$, superimposed on the frequency map for the machine with no errors.

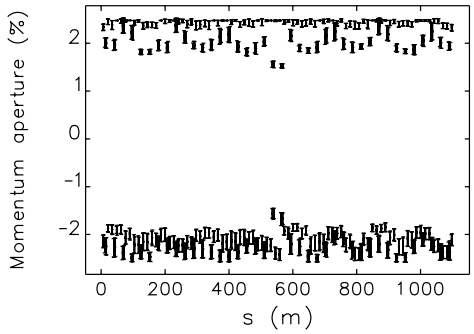

Figure 3.2-9: Momentum acceptance from 50 ensembles for the lattice with three LSSs, RHB, and $\xi_x = \xi_y = 9$.

- Maximum β_x, β_y, and η_x values in Sectors 5 through 8–3 knobs.
- β_x, β_y, and η_x at the center of the Sector 6 straight section—7 knobs.
- Values of β_x, β_y, or η_x at chosen locations in sectors 1, 3, and 36—15 knobs.

An essential requirement is a vertical phase advance of 2π between the centers of the two groups of cavities. There are four possible placement options for the cavities. For example, the cavities could be placed in the upstream half of straights 5 and 7, which is referred to as US+US. Other options are DS+DS, DS+US, and US+DS. Results are shown for the DS+DS configuration, which involves the least significant changes in the optics and minimizes interference between the cryomodules and the bending magnet beamline.

In addition to optimizing the lifetime and DA, it is also necessary to minimize the amount of emittance growth in the vertical plane. (The source of the emittance growth is described in section 3.6.3.2.) Originally, a one-time optimization of the 14 interior sextupoles (i.e., those in Sectors 6 and 7) was

performed, followed by optimization of the rest of the lattice in a fashion similar to that just described. However, it was found that the predicted lifetime was significantly reduced when the deflecting cavities were turned on, but that this could be overcome by including the deflecting cavities in the optimization simulations. At the same time, the 14 interior sextupoles must be under the control of the MOGA algorithm and minimization of the emittance growth due to the cavities must be one of the optimization objectives. The emittance growth is "measured" by tracking a multi-particle beam once through the SPX region, starting with Sector 4 and ending with Sector 8. This has been found to be highly correlated with the vertical emittance growth in equilibrium.

The linear optics for the region surrounding the SPX straight is shown in Figure 3.2-10. Figures 3.2-11 and 3.2-12 show the dynamic and momentum acceptance for 50 ensembles with $\xi_x = \xi_y = 5$. This comfortably exceeds the requirement of $\xi_x = \xi_y = 4$. The horizontal beam size at the RHB straight is 97 μm, comfortably under the 120 μm requirement.

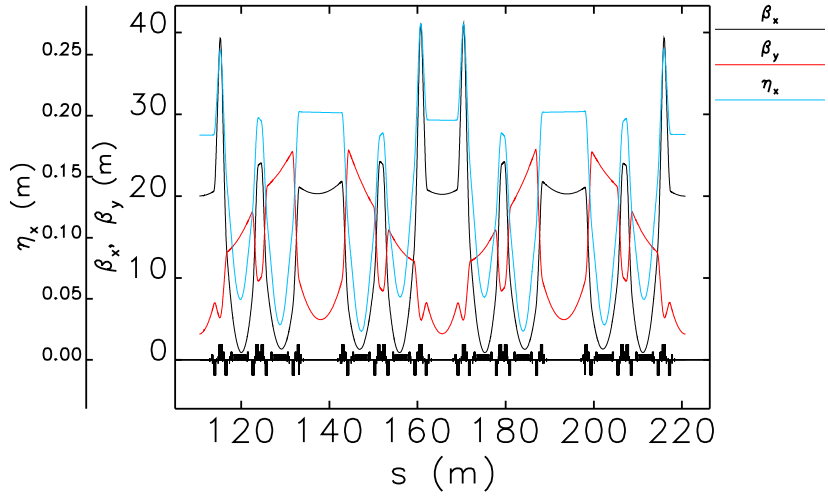

Figure 3.2-10: Detail of optical functions for solution with three LSS, RHB, and SPX. Shown are the functions for the SPX sectors, which start and end with long straights while having a short straight in the center.

Table 3.2-1 compares the parameters of the two lattices. It is seen that the effective emittance increases by less than 10% going from the present lattice to the final lattice. The the horizontal and vertical tunes have been constrained to fall close to the values used in operations, even though this is not the ideal working point in the simulations. (See section 3.2.2.5 for more discussion of this point.)

Table 3.2-2 gives a comparison of the predicted lifetime for the lattices for various fill patterns. For each lattice, the lifetime is computed for each of the 50 ensembles. Variations in lifetime result from variations in the momentum acceptance, as the vertical emittance is held constant at 35 pm. The median gives a prediction of the most likely lifetime in operations, while the 5th percentile gives a prediction of the lowest likely lifetime. That is, the probability is 95% that the lifetime is greater than this value. All the lattices have median and 5th percentile lifetimes above the requirement of 3.8 hours for the 15-mA, 24-bunch patterns.

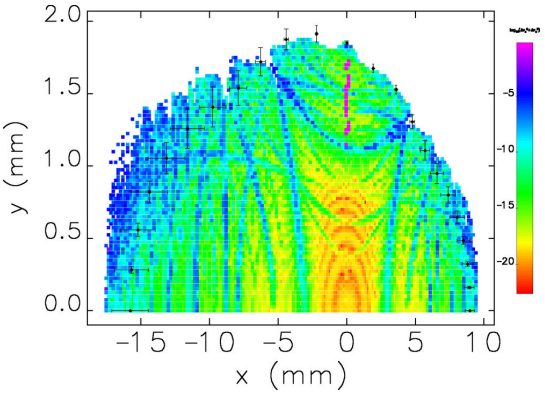

Figure 3.2-11: Dynamic acceptance from 50 ensembles for the lattice with three LSS, RHB, and SPX and $\xi_x = \xi_y = 5$, superimposed on the frequency map for the machine with no errors.

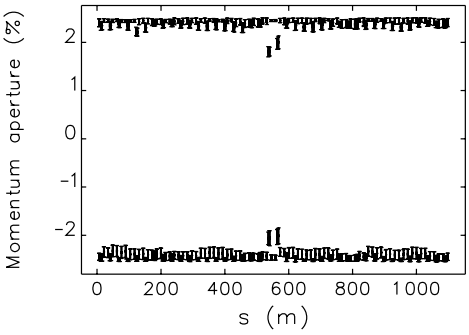

Figure 3.2-12: Momentum acceptance from 50 ensembles for the lattice with three LSS, RHB, and SPX and $\xi_x = \xi_y = 5$.

The achieved lifetime for the 16-mA hybrid bunch in the 3LSS+RHB+SPX lattice is comparable to what is obtained in present operations. However, as noted, the lattice does not have sufficient chromaticity to be workable for 16-mA hybrid mode. Optimization of this configuration is on-going.

The 150-mA, 324-bunch mode was evaluated with the high chromaticity required for the 24-bunch mode. The lifetime is quite long in spite of the excessively high chromaticity, which provides an operational convenience as it obviates the need to change sextupoles when changing between the 24- and 324-bunch fill patterns. Presently, the 324-bunch mode does not require top-up. However, if the vertical emittance was reduced to, say, 10 pm, the lifetime would drop to about 20 hours, which would require occasional top-up. This mode would provide significantly higher brightness than the other modes, owing to the low coupling.

3.2.2.5 Experimental Tests

Because the APS has independent power supplies for all quadrupoles and sextupoles, it is possible to mock up a long straight section. This is done by setting to zero the power supplies for the Q1 magnets on either side of the target straight section. This reduces the quadrupole strength to K_1 = -0.006 m^{-2}, compared to a maximum strength of 0.9 m^{-2} [3.2-7]. Using the same techniques as discussed in the previous section, it is possible to optimize the linear and nonlinear properties of the lattice to obtain a configuration with large predicted dynamic acceptance and lifetime. Such optimizations were carried out for a series of mock-up lattices corresponding to each of the configurations described in the previous subsection. So far, experimental tests were completed for two of the mock-up lattices, known as 4NLSS and 4NLSS+SPX. Tests of lattice 4NLSS+RHB are also close to completion. (The number of mocked-up long straights differs from the present requirement of three because of changes in requirements and the significant time needed to perform experimental studies.)

It is important to mention that it has been APS policy from the beginning of operation to allow large user-requested beam steering. Over time the storage ring and beamlines have settled, and, at many locations, the steering has accumulated to several millimeters of orbit distortion. This orbit is called “user orbit” and deviates from the centers of magnets significantly. This would have been a big problem

Table 3.2-1: Comparison of major parameters of the four lattices.

	Nominal $\xi_{x,y} = 7, 6$	3LSS+RHB+SPX $\xi = 5$	3LSS+RHB $\xi = 9$	Units
Betatron tunes				
Horizontal	36.127	36.141	36.143	
Vertical	19.248	19.230	19.236	
Lattice functions				
Maximum β_x	29.613	37.479	36.175	m
Maximum β_y	25.705	28.755	28.227	m
Maximum η_x	0.224	0.277	0.295	m
Average β_x	13.656	13.469	13.557	m
Average β_y	15.173	14.700	14.543	m
Average η_x	0.156	0.154	0.148	m
Radiation-integral-related quantities at 7 GeV				
Natural emittance	2.479	2.767	2.855	nm
Energy spread	0.096	0.096	0.096	%
Horizontal damping time	9.626	9.626	9.626	ms
Vertical damping time	9.631	9.631	9.631	ms
Longitudinal damping time	4.817	4.817	4.817	ms
Energy loss per turn	5.353	5.353	5.353	MeV
Standard ID straight sections				
Effective emittance	3.186	3.457	3.433	nm
β_x	20.092	20.014	20.077	m
η_x	0.189	0.184	0.167	m
β_y	3.088	3.156	3.154	m

for the storage ring optics, but fortunately the APS has separate power supplies for all quadrupoles (and sextupoles). As long as the optics is regularly corrected, there seems to be no significant negative effects from operating on a significantly non-zero orbit.

When testing of the new lattices started, the first lattice was set up on the "user orbit." Lattice setup includes installing new quadrupole and sextupole setpoints, correcting the orbit, measuring and correcting the beta functions and dispersion, adjusting the coupling, and optimizing the injection efficiency. In this experiment, it proved impossible to improve injection efficiency above 40% or store beam current above 40 mA. A lifetime vs betatron tunes scan was performed and exhibited a strong resonance line at $2\nu_x - \nu_y = 53$. This is a skew-sextupole-type resonance that is excited when large coupling is present.

To reduce this resonance, the lattice was subsequently set up on the "reference orbit," i.e., the orbit going through the centers of the magnets. For this condition, the lifetime vs tunes scan showed that the width of the resonance $2\nu_x - \nu_y = 53$ was reduced, giving significantly improved injection efficiency and lifetime. All other lattice tests have been performed on the "reference orbit."

This result implies that beamlines will have to be realigned to allow elimination of large orbit offsets

Table 3.2-2: Comparison of computed lifetimes for various lattices and fill patterns. For each fill pattern, the median and 5th percentile lifetimes are shown for all lattices. The assumed vertical emittance is 35 pm. Note that SPX will not be operated in hybrid mode. In addition, the 324-bunch mode does not require significant chromaticity, but operationally it is convenient to use the same values as those used for the 24-bunch mode.

	Nominal $\xi_{x,y} = 7, 6$ h	3LSS+RHB+SPX $\xi = 5$ h	3LSS+RHB $\xi = 9$ h
100 mA/24			
median	9.2	9.9	7.3
5^{th} percentile	8.6	9.5	6.8
150 mA/24			
median	-	7.5	5.5
5^{th} percentile	-	7.1	5.1
16 mA (hybrid)			
median	-	-	2.9
5^{th} percentile	-	-	2.7
134 mA/56 (hybrid)			
median	-	-	10.9
5^{th} percentile	-	-	8.0
150 mA/324			
median	43.3	45.7	36.1
5^{th} percentile	40.9	44.1	33.9

in the accelerator magnets. Steering tolerances are still under investigation, but preliminary estimates indicate that 23 insertion device beamlines and 14 bending magnet beamlines will require realignment. This can be done gradually (i.e., a few sectors at a time) and could be started prior to installation of any long straights, in order to save time. This is not part of Project scope, but is already in progress.

The first lattice tested that is relevant to the APS Upgrade was the 4NLSS mockup lattice. After standard lattice setup, a lifetime of 6 hours was achieved with 100 mA stored in 24-bunch fill pattern. Comparing this number to the Table 3.2-2, it is apparent that the achieved lifetime is a little over the expected 5th percentile lifetime. Only very limited time has been devoted to optimizing experimental performance of this lattice due to time constraints. Experience shows that if sufficient time is spent on lattice correction and optimization, it is possible to improve upon initially achieved results. Hence, even though the expected median lifetime was not achieved in the 4NLSS lattice, there is confidence that this lattice is now suitable for user operation.

Although the test was successful, there was one issue: The optimization process suggested betatron tunes of 36.10 and 19.35. After setting up the lattice with such tunes it was found that the lifetime was short. Moving the tunes to the usual APS working point of 36.16 and 19.22 provided for better lifetime. This was not the first time that the optimization suggested tunes that were not optimal for the real machine. Very likely there is some feature in the real machine not included in the model, that makes the usual APS working point better in terms of lifetime than the one suggested by the optimization.

Several steps have or may be taken to investigate this issue:

- Addition of fringe-field modeling for multipoles did not make a significant difference.
- Improvement of fringe-field model for dipoles is under consideration.
- Remeasurement of one quadrupole and sextupole of each type to characterize fringe fields and excitation curves. There is some suspicion that the excitation curves for the S2 sextupole family may be in error. However, preliminary measurement results do not support this suspicion.
- Improvement of the coupling correction algorithm used for the experiments.
- Improvement of the modeling method to include explicit correction of the orbit and optics.

The next step was to test the 4NLSS+SPX lattice, for which a detailed a comparison of simulation and experimental results was performed. As was mentioned before, the lattice was set up on the "reference orbit." The response matrix fit was used to derive the storage ring model (the so-called "calibrated model"). Figures 3.2-13 through 3.2-16 show lattice beta functions and dispersion obtained by the response matrix fit after one iteration of lattice correction. The beating of the lattice functions is typical for the initial lattice correction. Due to time constraints, the lattice was not corrected further. It is not expected that lattice perturbations of this scale would have a large effect on the lattice performance.

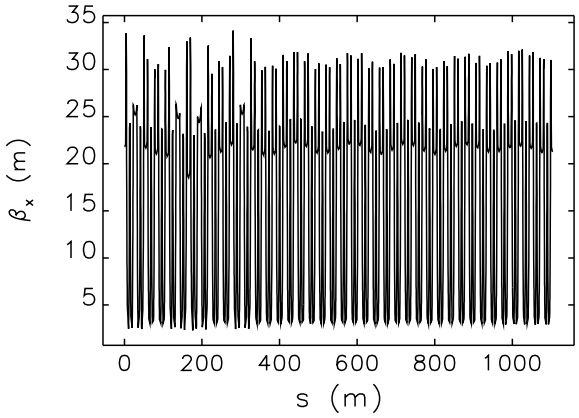

Figure 3.2-13: Horizontal beta function obtained by the response matrix fit.

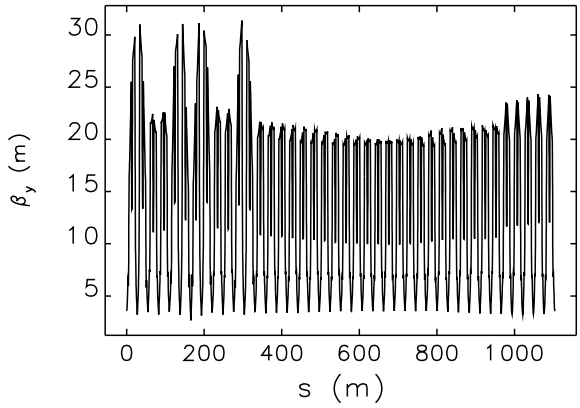

Figure 3.2-14: Vertical beta function obtained by the response matrix fit.

The storage ring model was used to calculate the DA and lifetime, which were then compared to the measured values. DA is measured by kicking a single bunch using one of the injection kickers and recording the fraction of beam that survives as a function of the kick strength. For this measurement, the S39IK3 kicker was used. During every kick, beam motion is also recorded using the BPMs. This procedure was repeated in simulation: a kick was applied to the simulated bunch of particles, which was then tracked for 2000 turns to determine the surviving fraction of the bunch. The kicker strength is calibrated using recorded beam motion and the calibrated lattice model.

Figure 3.2-17 shows results of the DA measurement and corresponding simulations. It is convenient to use that kick amplitude for which 50% of the beam survives as a single-number characterization of the DA. It is seen that the agreement in that sense is very good (not that the x axis is suppressed in the

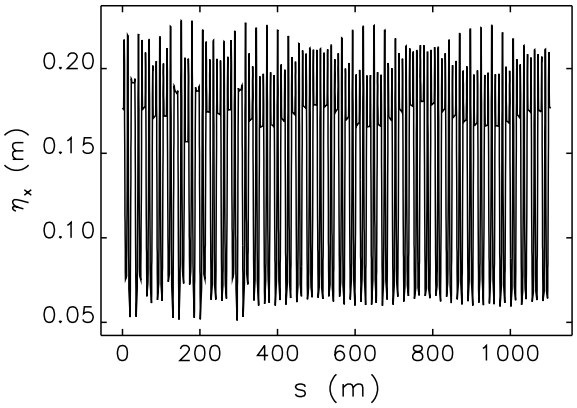

Figure 3.2-15: Horizontal dispersion obtained by the response matrix fit.

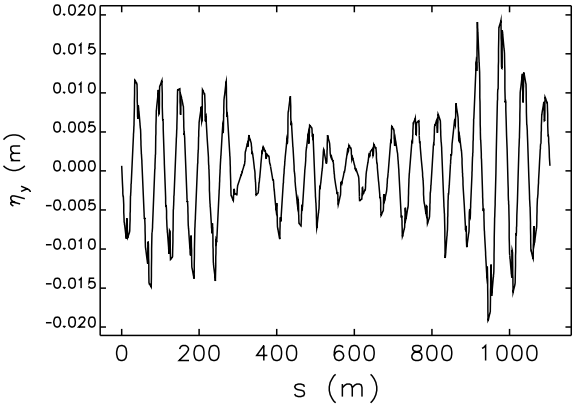

Figure 3.2-16: Vertical dispersion obtained by the response matrix fit.

figure). The simulations show a steeper loss curve than the measurements. This difference, which is common in such measurements, is attributed to collective effects. In particular, it has been found that the lower the single-bunch current at which the DA measurement is done, the steeper the loss curve. The measurement presented here was done with 1 mA single bunch current. Typically measurements are not done below 1 mA because BPM readings become too noisy.

The calibrated model was also used to calculate LMA, as shown in Figure 3.2-18. The LMA was used to calculate lifetime, giving a lifetime of 5.6 hours at 100 mA. The measured lifetime was 6.0 hours, which is in very good agreement. However, this lifetime is slightly shorter than the expected 5th percentile lifetime from Table 3.2-2. One of the reasons might be that the lattice was optimized for higher vertical tune than the one at which it was actually tested (as mentioned above). But in any case, this lattice is acceptable for operations.

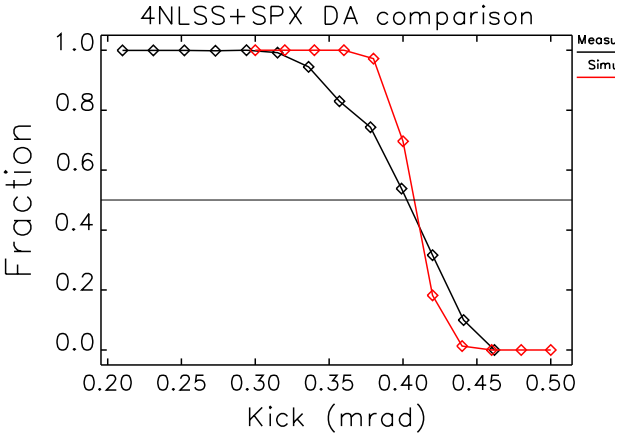

Figure 3.2-17: Comparison of measured and calculated dynamic aperture.

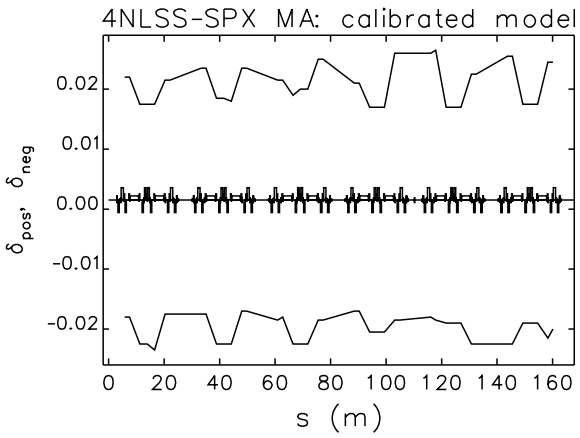

Figure 3.2-18: Calculated momentum aperture.

Table 3.2-3 summarizes test results of the mock-up lattices. It shows that the lifetimes achieved in tests for all lattices are slightly lower than the expected 5th percentile lifetime. This might indicate

some lifetime overestimate in the simulations. It is suspected that the overestimation might come from the fact that in simulations only quadrupole tilts are used as sources of coupling, while in real life vertical orbit in sextupoles also contributes to coupling. This effect will be added to the error ensemble evaluation. In any case, achieved lifetimes are sufficient for operation. Also, experience shows that spending more time on small improvements and corrections of the experimental lattice usually leads to further improvements of the lattice performance.

Table 3.2-3: Comparison of predicted and measured lifetime for mock-up lattices.

	4NLSS	4NLSS+SPX	4NLSS+RHB
Design chromaticity (x and y)	9; 9	8; 8	9; 9
Predicted median lifetime	7.1	8.6	7.9
Predicted 5th percentile lifetime	6.1	6.6	5.9
Measured lifetime	6.0	6.0	5.4

One special issue that has to be addressed during the tests is the changed physical aperture at locations of LSSs. Presently the small-gap vacuum chambers have a length of 5 m; after the APS Upgrade, the small-gap vacuum chambers at LSS locations will have a length of about 7.8 m. Due to the beta-function increase in a drift space, that would lead to decreased acceptance of such vacuum chambers. It is not expected that this will be an important factor because the acceptance of the long vacuum chamber with a gap of 7.5 mm will still be larger than the smallest acceptance of the ring — 5-m-long, 5-mm gap ID vacuum chamber in Sector 4. To test this, the reduced aperture was mocked up moving the orbit closer to the vacuum chamber wall such that the distance from the beam orbit to the wall would be the same in terms of the beam size:

$$D_{new} = G\,\frac{\sigma_{2.5m}}{\sigma_{3.85m}}, \tag{3.2-6}$$

where G is the vacuum chamber half-gap, and σ is the vertical beam size at 2.5 m or 3.85 m from the center of the long straight section. For an 8-mm vacuum chamber, it means moving the orbit towards one of the walls by 0.25 mm. There was no observed effect on the lifetime or injection efficiency. The test was performed with an old upgrade lattice that had eight long straight sections.

3.2.2.6 Remaining Work

The lattice work is well advanced and shows that the desired configuration with three nonsymmetrically placed long straight sections and one RHB insertion, both with and without SPX, are generally workable. Development of lattices will continue as requirements evolve.

In addition, even though the lifetimes achieved in the mock-up studies are sufficient, it is worthwhile to understand why the experimental tests give lifetimes on the lowest edge of the expected range. One reason could be that the experiments use a less sophisticated method for coupling correction, which can be readily improved (see section 3.2.3.2). This reason could also be stated the opposite way: the simulations do not have realistic levels or sources of coupling. Another unresolved issue is why the computer optimization always tends to place vertical betatron tune close to 19.3 while experiments found that a lower tune gives better lifetime; this, again, may be a result of an insufficiently detailed model of the source and degree of coupling.

3.2.3 Coupling Control

3.2.3.1 Introduction

The brightness of a synchrotron radiation source is inversely proportional to the transverse beam emittances. The emittances are defined by the equilibrium between radiation damping and quantum excitation. A great deal of research is devoted to the minimization of the horizontal emittance in storage rings, which largely comes down to a matter of making the horizontal dispersion small. The vertical emittance—typically a small fraction of the horizontal emittance—results from a combination of vertical dispersion and coupling of the horizontal emittance into the vertical plane.

In an ideal planar storage ring, there are no vertical bends and therefore no deliberately produced vertical dispersion or coupling. In a real machine, there are multiple sources of vertical dispersion, including small tilts of the horizontal bending magnets and coupling of the horizontal dispersion via tilted quadrupoles and vertically misaligned sextupoles. The spurious vertical dispersion is usually much smaller than the horizontal dispersion and can be made even smaller using correcting skew quadrupoles. Thus, the impact of quantum excitation and the subsequent emittance in the vertical plane is much smaller than in the horizontal. As mentioned, another source of the vertical emittance is coupling between motion in the horizontal and vertical planes. Both of these effects can be minimized by performing better alignment of the storage ring magnets and by applying beam-based corrections using skew quadrupoles. The smaller these effects, the smaller the vertical emittance, and therefore the higher the brightness of the light source.

In addition to affecting the vertical emittance, coupling of betatron oscillations between the horizontal and vertical planes also affects beam dynamics during injection. In third-generation light sources the vacuum chambers have very small vertical gaps (for installation of various insertion devices such as undulators and wigglers). Since the injection process requires a large aperture, injection is performed in the horizontal plane, where insertion devices do not limit the available aperture. However, due to coupling between planes, large horizontal beam oscillations during injection can transfer into the vertical plane, resulting in loss of beam on small-gap vacuum chambers. Again, skew quadrupoles can be used to reduce these effects, as can improved alignment of quadrupoles and sextupoles.

The coupling between horizontal and vertical planes is introduced by skew quadrupole gradients that can be generated by small tilts ϕ of quadrupoles:

$$K_{sq} = K\phi,$$

or with nonzero vertical orbit y_o in sextupoles:

$$K_{sq} = -\frac{1}{B\rho}\frac{\partial^2 B_y}{\partial x^2} y_o.$$

Some insertion devices can also be sources of coupling. Dedicated skew quadrupole magnets are used to compensate the effect of all unwanted coupling sources. They can also be used, of course, to increase the coupling and vertical dispersion.

Indeed, in a perfect machine it would be necessary to do this in order to avoid extremely small vertical emittance. At the APS and other third-generation sources, the electron-beam lifetime is defined by the Touschek scattering and is proportional to the beam volume. Thus, having very small vertical beam size means having very short lifetime. On the other hand, introducing or allowing excessive x-y coupling

will reduce the lifetime by reducing the local momentum aperture. Even though the APS can tolerate short lifetime due to top-up operation, there is still a limit on how short the lifetime can be. Therefore it is crucial to have good control of both vertical dispersion and coupling of beam motion in order to maintain a careful balance between the contradicting requirements of good injection efficiency, high brightness, and long lifetime.

3.2.3.2 Issues for Upgrade

In order to control the vertical emittance and coupling, one must have a good measurement of both and the ability to control each separately. At the APS the emittance ratio is deduced from the ratio of horizontal and vertical beam sizes measured on the diagnostics beamline in Sector 35. It is controlled using 19 skew quadrupoles located in every second sector (with one missing in the injection area). The present coupling correction algorithm consists of three steps:

1. Minimize the vertical dispersion. This is done using the measured vertical dispersion by computing the required skew quadrupole strengths using singular value decomposition (SVD).
2. Minimize the vertical beam size. This is done by using an optimizer that adjusts the skew quadrupoles in a pattern determined by the two orthogonal phases of the main coupling harmonic ($\nu_x - \nu_y = 36 - 19 = 17$).
3. Add vertical dispersion to achieved desired vertical emittance. This is done by adding skew quadrupole current at the 0^{th} harmonic, which ideally gives the same pattern of vertical dispersion everywhere while driving the coupling resonance as little as possible.

This quick and convenient procedure allows the APS to control the global ratio of emittances but not the local beam tilts in each sector. The goal of the APS Upgrade with respect to coupling is to improve local control of the vertical emittance and beam tilts and to enable lower vertical emittance operation if ever required. In addition, better control of the coupling will improve the injection efficiency and lifetime of challenging lattices, such as the high-chromaticity lattice for hybrid mode (see section 3.2.2.4). Ideally, it will provide the possibility of using lower coupling, presumably in 324-bunch mode where the lifetime will accommodate it, and perhaps coupled with the lattice providing reduced horizontal emittance using modified damping partition numbers, as described in section 3.2.5.5.

Local measurement of the coupling is possible using a response matrix fit [3.2-10]. The response matrix fit detects all skew quadrupole errors in the ring, which then can be put in the storage ring model and used to calculate local beam sizes everywhere. The storage ring model generated by the response matrix fit is referred to as a “calibrated” model.

As discussed above, presently the APS operating orbit has large vertical deviations at many sextupoles. This is the result of beam steering for user beamlines. Such an orbit results in large coupling with significant local variations of vertical beam size that are impossible to compensate using existing skew quadrupoles. Figure 3.2-19 shows variations of vertical beam size at ID locations as calculated using the response matrix fit. Sector 2 has the largest operating vertical orbit, and it also has the largest vertical beam size. Existing skew quadrupoles also do not allow for coupling minimization below emittance ratio of about 1% on the present user orbit.

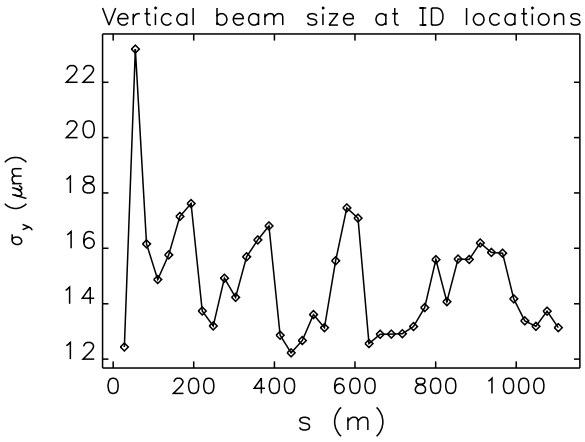

Figure 3.2-19: Variations of vertical beam size at ID locations (middle of ID straight sections) in the present APS.

Tests have shown that steering the orbit through the centers of sextupoles significantly decreases the coupling and beam-size variation while improving the beam dynamics. However, this would not be enough to provide local vertical beam size control in case this capability is ever requested.

As mentioned above, maintaining low coupling is not only important for providing small vertical beam sizes for brighter x-ray beams; it is also required for improving beam dynamics. From experiments, it is known that presently the APS beam dynamics is affected by the skew-sextupole resonance $2\nu_x - \nu_y = 53$. This resonance is driven by a combination of nonzero coupling and sextupoles. Keeping coupling small minimizes the strength of that resonance.

There exist a number of other ways to minimize coupling. Three methods have been experimentally tested. The first is to minimize the measured vertical dispersion and vertical beam size (first two steps in the coupling correction algorithm outlined above). The second is minimization of the calculated cross-plane orbit response and vertical dispersion using the calibrated model. The minimization in this method is done using the inverse derivative of the cross-plane orbit response matrices. The third method is minimization of calculated beam sizes at several locations using the calibrated model. In this method the minimization is done with the simplex technique.

The first method is presently the fastest because it relies on relatively fast dispersion measurement and on-line beam size measurements. The other two methods rely on response matrix measurement, which is more time-consuming, and also on a compute-intensive response matrix fit. The third method also involves a slow nineteen-variable simplex minimization. It was found that with the right combination of parameters, all three methods achieve a reasonably low coupling of about 0.7%. Important parameters here, depending on the method, include the number of singular values used for matrix inversion for correction of measured dispersion and the relative weight of the residual dispersion error during cross-plane response minimization. The minimization results vary with different lattices, minimization parameters, and time spent on minimization. A methodical study of the minimization parameter space or a comprehensive comparison of the methods has not been performed.

To improve local coupling control and to reduce the minimum achievable emittance ratio, the possibility of increasing the number of skew quadrupoles was investigated. The most straightforward way to

increase the number of skew quadrupoles at APS is to convert some of the orbit correctors into skew quadrupoles or change orbit correction magnets into combined-function corrector/skew quadrupole magnets. APS has eight corrector magnets per sector. However, correctors at APS serve various purposes and could not be removed from orbit correction or local orbit steering without sacrificing performance. Only one corrector family is presently not used in orbit correction and local steering – A:HV4. Another possibility is to install additional magnets. In general, almost every sector at APS has room available for installation of a skew quadrupole magnet at two locations. One location is between girders 1 and 2 immediately upstream of corrector A:HV3; this place is presently used for the A:QS skew quadrupoles in every fourth sector with the rest of the sectors being available (with a small number of exceptions). A second location is between quadrupoles B:Q5 and B:Q4. This location is presently occupied by B:HV4 correctors, but these correctors are gradually being moved to a new location between girders 3 and 4. After this move is complete, the location between quadrupoles B:Q5 and B:Q4 will become available for skew quadrupole installation (again with a few exceptions).

Coupling minimization was simulated using different sets of skew quadrupoles for fifty sets of random quadrupole tilt errors. The results are presented in Figure 3.2-20. Several cases were examined:

1. One family of correctors is converted to skew quadrupoles, with existing skew quadrupoles removed (data denoted as AHV2, AHV3, etc.);
2. One family of correctors is converted to skew quadrupoles in addition to existing skew quadrupoles (data denoted as AHV2-QS, AHV3-QS, etc.);
3. Two skew quadrupoles are installed in each sector: one is next to corrector A:HV3 and another is installed in place of the moved corrector B:HV4, with existing skew quadrupoles removed (data denoted as NEWQS);
4. As in the previous case, except only one skew quadrupole per sector is used with location alternating from sector to sector between A:HV3 and B:HV4, existing skew quadrupoles removed (data denoted as NEWQS2).

It is seen that when the number of skew quadrupoles is increased from the present 19 (data set QS in Figure 3.2-20) to 40 that there is no improvement in emittance minimization if the new magnets are installed at the same locations inside the sectors as described in case 1 above. It seems essential to have skew quadrupoles in different locations within sector, as cases 2 through 4 show. One surprising result is that case NEWQS with 80 skew quadrupoles does not give a significant improvement compared to similar case NEWQS2 that has only 40 skew quadrupoles. Based on this result, the most cost effective way to improve coupling correction would be to use one skew quadrupole per sector with the location alternating from sector to sector between A:HV3 and B:HV4 (as in case 4 above). This involves the addition of 21 skew quadrupoles.

As discussed above, having small coupling is beneficial to source brightness and beam dynamics. However, the APS storage ring cannot operate with arbitrarily small coupling due to lifetime limitations, except in 324-bunch mode. In order to improve lifetime, it is advantageous to be able to generate vertical beam size using vertical dispersion without creating too much coupling between the planes. Simulation studies of coupling control were performed using skew quadrupole sources (skew quadrupoles or vertical orbit bumps inside sextupoles) in the area where there are no insertion devices installed (and therefore no small-gap vacuum chambers—in Sectors 36 to 40 [3.2-23]. The idea here is to minimize coupling globally by steering through the centers of magnets and by using skew

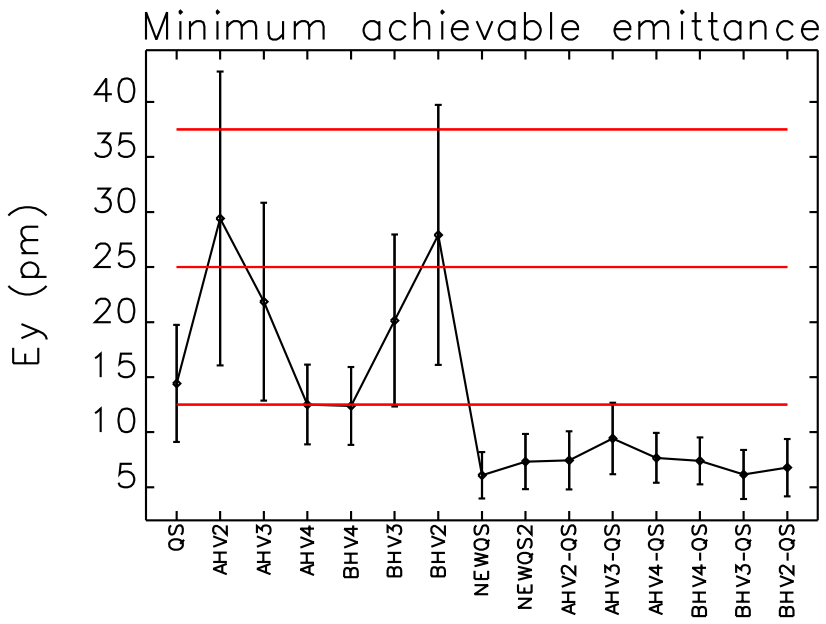

Figure 3.2-20: Minimum achievable vertical emittance for various sets of skew quadrupoles. Statistics is based on fifty random sets of quadrupole tilt errors. Red lines show emittance values corresponding to 0.5%, 1%, and 1.5% emittance ratio. See text for more explanation.

quadrupoles everywhere, then using local coupling sources in Sectors 36 to 40 to increase the global vertical emittance to increase lifetime, without generating global vertical dispersion and coupling.

It was found that it is possible to create a coupling bump in the non-user sectors to control the vertical emittance without creating vertical dispersion and beam tilts all around the ring. Figure 3.2-21 shows the resulting vertical dispersion that generates the required vertical emittance. The dispersion outside of the bump in non-user sectors is very small. This succeeded using 15 skew quadrupoles at the locations of the existing corrector magnets in Sectors 36 through 40. However, there is one drawback to this approach: it was found experimentally that turning off all skew quadrupoles inside the injection orbit bump improves the injection efficiency. The injection bump spans Sectors 39 and 40, therefore limiting the above-described method of coupling control to only Sectors 36 through 38. The combination of the coupling bump and injection bump would need to be studied further. An alternative is to excite the beam using a white-noise source driving the tune measurement striplines [3.2-24].

As discussed in section 3.2.2.5, it was found that in order to improve the beam dynamics, the upgraded lattice will have to operate with the orbit going through the centers of magnets. This will also allow for better control over coupling. Operating on this new orbit will require realignment of some user beamlines. It will also mean that user-requested steering will be limited. No position steering will be allowed, and the preliminary limits on the angle steering are ± 50 μrad in the horizontal and ± 25 μrad in the vertical planes.

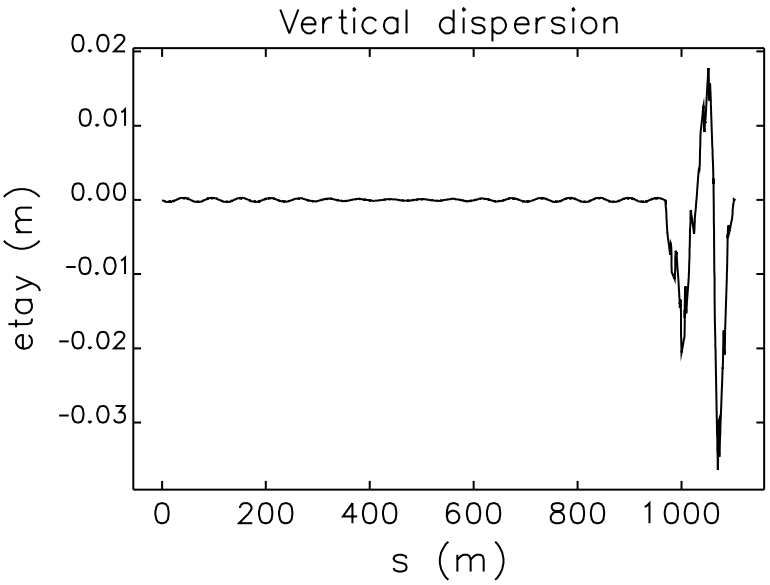

Figure 3.2-21: Vertical dispersion for the coupling bump lattice.

3.2.3.3 Remaining Work

Use of a coupling bump in non-user sectors for vertical emittance could be studied further to minimize its possible effect on the injection efficiency. Using a white-noise source to drive the tune measurement striplines and increase the vertical emittance will be studied as an alternative to introducing vertical dispersion; the combination of this technique with minimization of the x-y coupling, as described above, should improve lifetime results for the new lattices. Limits on user-requested steering will need to be studied in more detail.

3.2.4 Collective Effects

3.2.4.1 Introduction

In the storage ring the limit on the single-bunch current is determined by a combination of the strength of collective effects acting in any plane and the injection process. When the stored current reaches its limit during injection, the amount of charge lost by the stored beam equals the charge of the incoming beam that survives the process. The injection efficiency of the incoming beam decreases with increasing stored bunch charge due to collective effects. Currently the APS delivers 16 mA in the single bunch during hybrid-fill for users. This amounts to 60 nC per bunch, which may be the largest charge producing x-rays per bunch in light sources around the world. APS must deliver the same charge per bunch to the users after the upgrade as it delivers now.

The sources of collective effects may include electron cloud, ions, and impedance elements in the ring. The phenomena caused by the first two were observed in the ring with specially arranged bunch patterns; however, the magnitude of these effects is very small and does not affect nominal operations. On the other hand, the impedance elements in the ring cause various instabilities that often limit the

high-current operation. In the upgrade the same will be true, in that the impedance will dominate the collective effects on the stored beam.

The existing impedance model of the present ring can be used to predict the single-bunch limit, once the additional impedance sources are identified and their contributions are estimated. Hence, this section begins by describing the status of the impedance model that was used to reproduce the various impedance-driven collective effects observed in the ring [3.2-25–3.2-27]. The estimate of impedance and its consequences in the APS Upgrade will be discussed following that.

3.2.4.2 Status of Impedance Model

The microwave instability blows up the longitudinal emittance of the beam not only by lengthening the bunch but also by widening the energy spread. The detailed computation by 3D modeling of impedance elements in the ring gives Z/n close to 0.2 Ω, which gives an estimated threshold of 1 mA. However, careful measurement by an x-ray pinhole camera showed it to be much higher, namely, 7-8 mA. The large discrepancy between theory and experiment was due to the significant bunch shape deformation, the effect of which cannot be fully included in the theory.

In order to overcome this deficiency, the interaction of beam and impedance was modeled as close to reality as possible by simulating macro-particles in longitudinal phase space; tracking includes the impedance up to a few hundred gigahertz, a particularly high range of frequency. One of the results was the anomalous energy spread due to the microwave instability, as shown in Figure 3.2-22. The experimental data and simulation results are in a good agreement, indicating an accurate impedance model.

The longitudinal profile of a bunch measured by the streak camera revealed a non-symmetric distribution in time. The distortion of the bunch was due to the combined effect of potential well distortion and energy loss caused by the imaginary and real parts of impedance, respectively. From the simulation that produced Figure 3.2-22 one can extract a longitudinal profile; this distribution and that of the streak camera overlap each other closely as shown in Figure 3.2-23. Since the only adjustable parameter in the simulation was cavity voltage, which can be estimated very accurately through synchrotron tune measurement, there is confidence not only in the impedance model but also in the simulation method using `elegant`.

The simulation of phase space was extended to 6D including the effect of transverse impedance. It was found that the collective motion of a single bunch was strongly dependent on the sextupole settings.

Historically, it was essential to understand the effect of small-gap chambers on the single-bunch current limit. Initially, with a few 12-mm-gap chambers installed in the ring, it was possible to store more than 20 mA in a bunch with moderate chromaticity (below 5) in the 7.5-nm high-emittance lattice. Eventually more 8-mm-gap chambers were installed, up to 29 in total, in the newly commissioned low-emittance lattice with nonzero dispersion at the straight sections. Following this, it was not possible to store more than 8 mA at moderate chromaticity (around 7), and the chromaticity was limited by the capabilities of the sextupole magnets. After modification of some of the sextupoles, it proved possible to increase the chromaticity to greater than 10, subsequently leading to the present ability to deliver 16 mA in a single bunch. From this it was clear that the single-bunch current was strongly dependent on the chromaticity.

The main purpose of impedance modeling was to predict the single-bunch effects of any proposed new

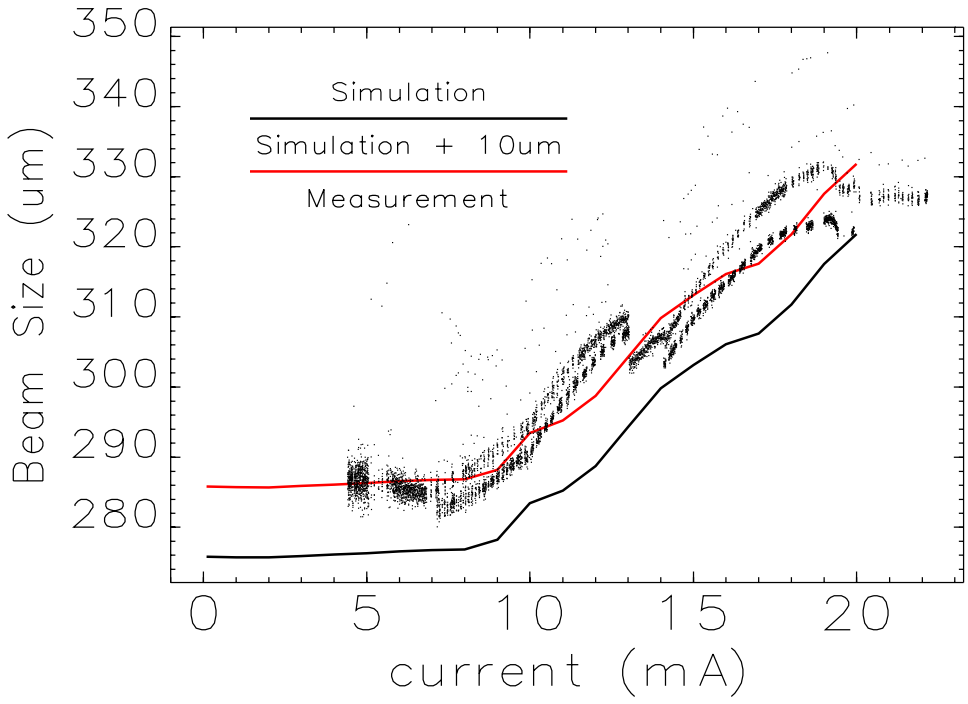

Figure 3.2-22: The dots represent two measurements of the horizontal beam size at an undulator where a dispersion of 17 cm contributes to the energy-dependent beam size. The black curve shows the simulation results with the impedance model. The agreement is very good considering the camera resolution of 40 μm. For better visual guidance the red curve was offset by simply adding 10 μm to the simulation result.

undulator chambers prior to installation in the ring. A practical question is, for example, what would happen to the single-bunch limit if all 8-mm chambers were replaced with 5-mm chambers? In order to answer this question correctly, it is necessary to validate the impedance model with the experimental data at hand or with the measurements specially designed for model validation purposes, prior to applying the model to predict the future performance of the ring.

Through the impedance modeling, several aspects of coherent instability behavior in the transverse planes were anticipated and reproduced experimentally.

- It was found that the transverse mode-coupling instability (TMCI) blows up the beam size in the vertical plane, resulting in scraping on the aperture of the small-gap chambers. During injection, this results in losing a fraction of the stored current in the bunch, which limits the total accumulation. An important prediction of the simulations is that the limits on the stored current and the accumulated current are different. For instance, at a low chromaticity of 3, only 3 mA can be *accumulated*, but it is possible to *store* more current in the bunch. This was verified experimentally by storing 20 mA with a chromaticity of 10, then showing that 5 mA could be retained when the chromaticity was gradually lowered to 3.
- The effect of vertical motion following injection was simulated by kicking the stored beam in the vertical plane, then following the evolution of the centroid and beam size from the tracking data. The same situation was explored experimentally by using the vertical pinger magnet and recording the turn-by-turn beam image with a gated camera. The image was processed to extract

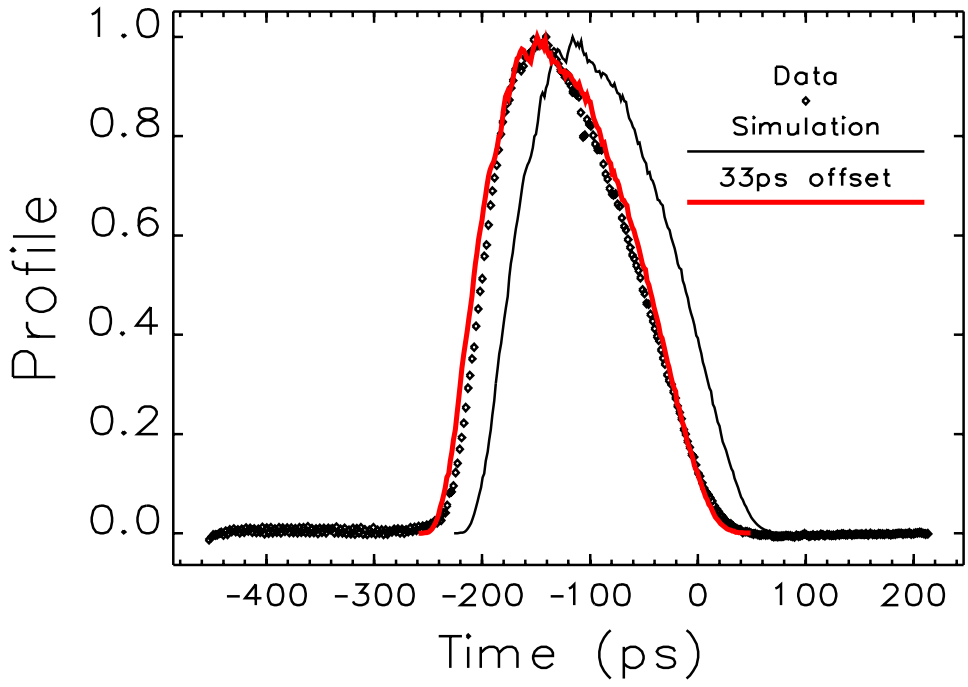

Figure 3.2-23: The open circles represent the streak camera data for 15 mA in the bunch, while the black curve is the simulation result. The red curve is offset by 33 ps from the direct simulation output for better comparison with the streak camera profile, whose reference time was not coincident with the simulation.

the beam size as function of turn. Simulation and experiment were compared, showing good agreement at low current (1 mA) as well as at medium current (5 mA), limited by the available chromaticity at the time of the experiment [3.2-27].

- The observed saw-tooth instability in the horizontal plane was reproduced. The driving impedance was identified in the simulation as the misalignment of the transverse impedance. This effect is similar to the misalignment of a quadrupole magnet except that the dipolar kick is time-dependent instead of static [3.2-25].

- The accumulation limit as a function of chromaticity was measured during two machine studies a week apart. The method was simple: set the highest chromaticity and inject to 20 mA or more in one bunch, using fixed, optimum injection conditions (rf cavity parameters and kicker strengths). Following this, the chromaticity is gradually decreased. For each chromaticity value, inject from zero until the limit is determined. The results of this procedure were compared with the simulation, where the sextupole effects were approximated as the combination of first-order chromaticity and amplitude-dependent tune shift [3.2-28]. (Subsequent work showed that this approximation did not impact the results.) The comparison is shown in Figure 3.2-24.

These tests demonstrated the predictive power of the three-dimensional APS impedance model [3.2-28], though it is still considered a working model in need of continual improvements.

It is possible to utilize the above APS impedance model to predict the single-bunch current limit as a function of hypothetical impedance increase or decrease. Figure 3.2-25 shows the nonlinear change of single-bunch current limit as a function of ring vertical impedance (or wake potential) times a scaling

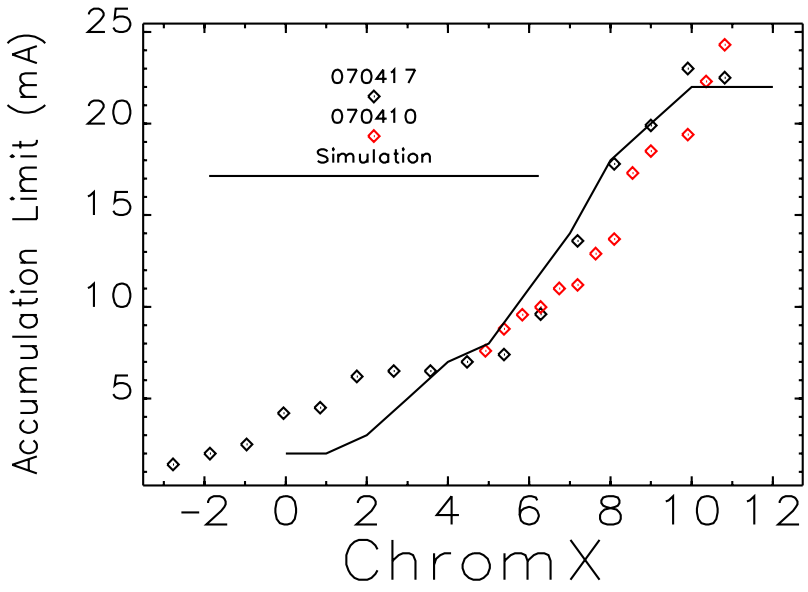

Figure 3.2-24: The symbols represent the measured accumulation limit collected in two machine studies separated by a week; the black curve is the simulation result.

factor Z_t. Actually, one might think that the product of I_{limit} and factor Z_t would be constant, but it is not because the bunch length varies with current.

It is worth noting that, even if the APS can, at times, store as much as 23 mA in a single bunch, the current that can be reliably delivered in operations is found to be about 16 mA—a 2/3 "derating" factor. If this defines the usable limit, it is necessary to minimize or eliminate any impedance increase in the upgrade as discussed in the next section.

3.2.4.3 Issues for APS Upgrade

The APS Upgrade will retain all the present vacuum chambers except new ones for the long straight sections (LSSs), obviously, along with new chambers in undeveloped straight sections. In addition, there will be deflecting cavities used for generating the short x-ray pulses (see section 3.6.3.3). These are the main impedance sources to consider in the upgrade. This section discusses issues related to the impedance of the undulator chambers at the LSSs. The deflecting cavity will be treated separately in section 3.6.3.3.2. Consideration of new chambers is in progress.

There will be four LSSs, each about 8-m long, that will replace the 5-m standard chamber; this immediately increases the impedance of transition by 8/5 because of the increase in β_y at the taper. In order to keep the same accumulation limit, it is necessary to reduce the geometric impedance at the LSSs by 5/8.

Since the impedance of the taper is generated at the transition connecting the regular chamber to the undulator chamber, achieving a smaller impedance will require designing a new transition. Stupakov's [3.2-29] formula for the impedance of a rectangular chamber can be used for this purpose:

$$Z_y = j\frac{Z_0 w}{4}\int_{-\infty}^{\infty} dz \frac{h'(z)^2}{h(z)^3}, \tag{3.2-7}$$

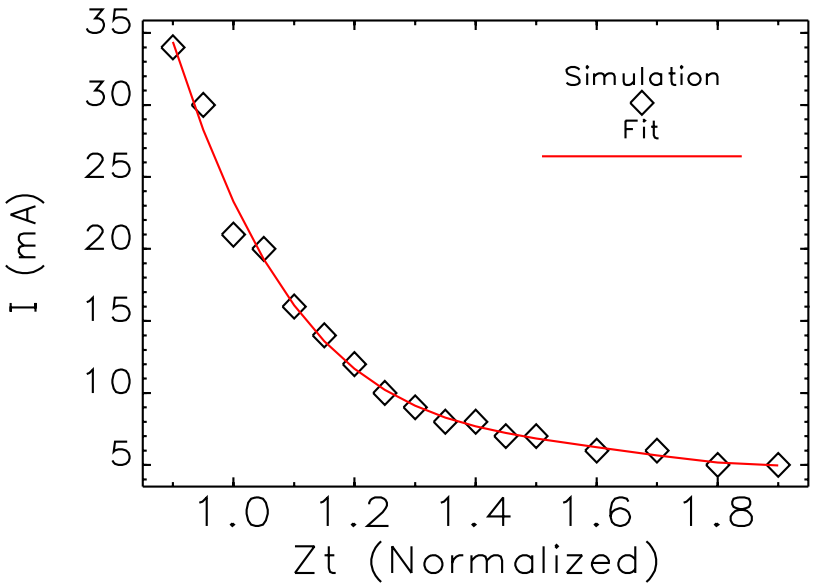

Figure 3.2-25: Single-bunch current limit as a function of vertical impedance. The symbols are simulation results. The line is a fit to guide the eye. The impedance axis is normalized to the value for the current APS storage ring.

where w is a (constant) half-width, and $h(z)$ is the half-height defining the vertical profile. Note that only the tapered section with nonzero $h'(z)$ contributes to the impedance. There are three parameters in the formula, namely, $h(z)$, w, and $h'(z)$. The optimal profile $h(z)$ to minimize the functional Z_y/w was found in [3.2-30] and is

$$h(z) = \frac{h_{\min}}{\left(1 + \left(\beta^{-1/2} - 1\right) z/L\right)^2}, \text{ where } \beta \equiv \frac{h_{\max}}{h_{\min}}. \tag{3.2-8}$$

Note that the profile in Equation 3.2-8 is nonlinear. The ratio of this impedance to that of the linear transition is [3.2-30]

$$\frac{Z_y^{\text{optimum}}}{Z_y^{\text{linear}}} = \frac{8\beta}{(1+\beta)\left(1+\sqrt{\beta}\right)^2}. \tag{3.2-9}$$

Since the theory is developed in the limit of low frequencies, the above impedance expressions have no dependence on frequency, a point which must be kept in mind. For example, it is not expected that there will be any bunch-length dependence in simulations or calculations using such impedances.

For the APS 8-mm-gap chamber where $h_{\max}$ = 21 mm and $h_{\min}$ = 4 mm, the predicted reduction by using a nonlinear taper is, coincidentally, very close to 5/8, which happens to compensate the increased impedance effect caused by the LSS.

In order to verify Equation (3.2-9), the wake potential of the nonlinear taper was numerically computed with `GdfidL` [3.2-31]. For a transition from 21 mm to 4 mm in the vertical plane and flat in the horizontal plane, the optimal profile predicted by Equation (3.2-8), $h(z)$, is shown in Figure 3.2-26.

Kick factors were calculated for bunches of different lengths using the wakefields computed with `GdfidL` for the nonlinear and linear taper. The ratio of kick factors is plotted in Figure 3.2-27. If APS is to benefit from the nonlinear taper then the ratio on this plot should be small. However the

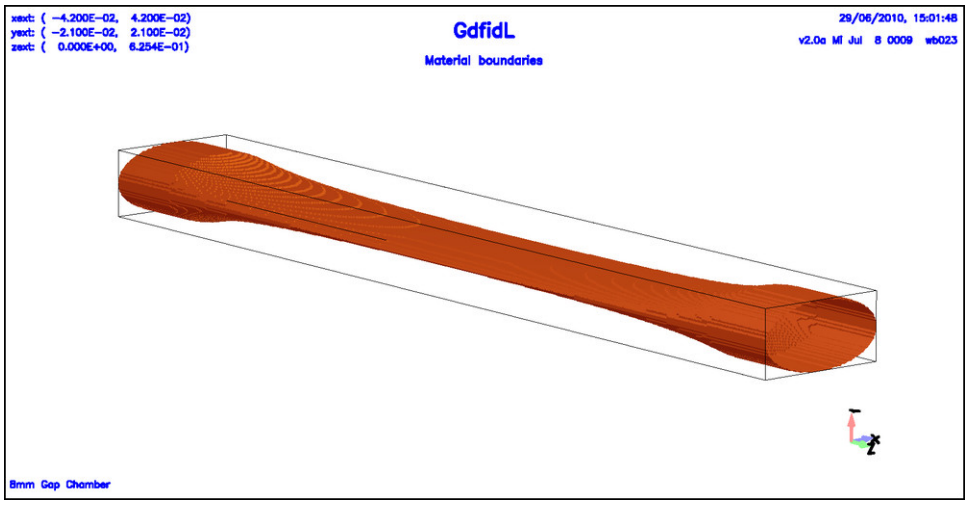

Figure 3.2-26: The vertical profile used in numerical simulation of an optimized nonlinear taper connecting a regular chamber to an undulator chamber with an 8-mm vertical gap.

plot shows a reduction in benefit as the bunch becomes shorter. Thus, using the nonlinear taper only would not provide the required reduction in the impedance from the LSSs. For reference, the expected improvement for the nonlinear taper from the approximate Equation (3.2-9) is shown as a straight line (as mentioned above, there is no frequency or bunch length dependence in this approximation).

It was also found that the reduction could be much less if the horizontal profile was not flat. For the actual APS chamber, where the horizontal profile also varies, the optimization resulted in a reduction of less than 5% of the value for a linear taper, hardly justifying the modification. Hence, it was decided not to adopt a nonlinear taper in the upgrade.

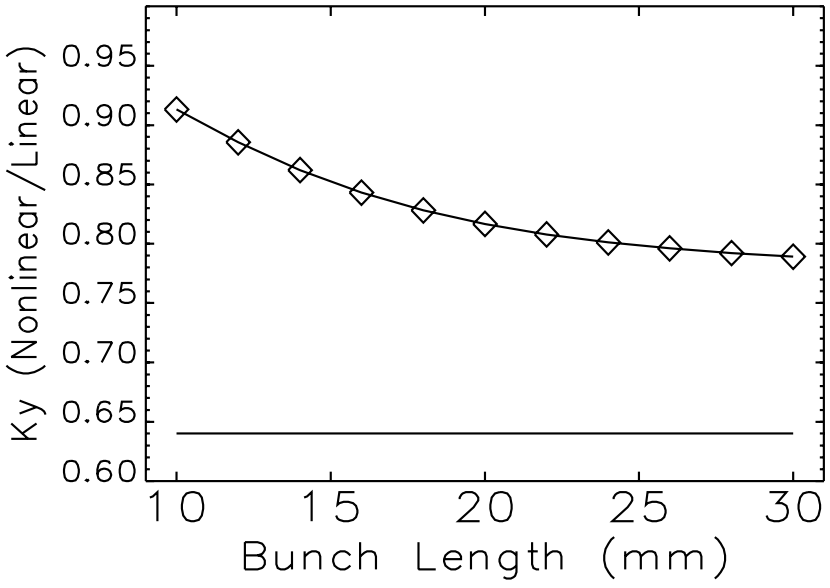

Figure 3.2-27: The ratio of vertical kick factors of nonlinear and linear taper for different bunch lengths. The straight line is the prediction by Equation (3.2-9), i.e., no frequency or bunch-length dependence.

Though an approximate expression, Equation (3.2-7) suggests that the horizontal half-width w strongly controls the vertical impedance. In the long-wave approximation this linear dependence could be correct, but for high frequencies the behavior is unknown. Hence, the quantitative effect of width for the 8-mm-gap chamber was investigated. Figure 3.2-28 shows that widening increases the impedance until it reaches some maximum. This provides an opportunity to estimate the impedance increase of a hypothetical in-vacuum undulator (IVU) chamber if installed (IVUs are noted for their wide chambers).

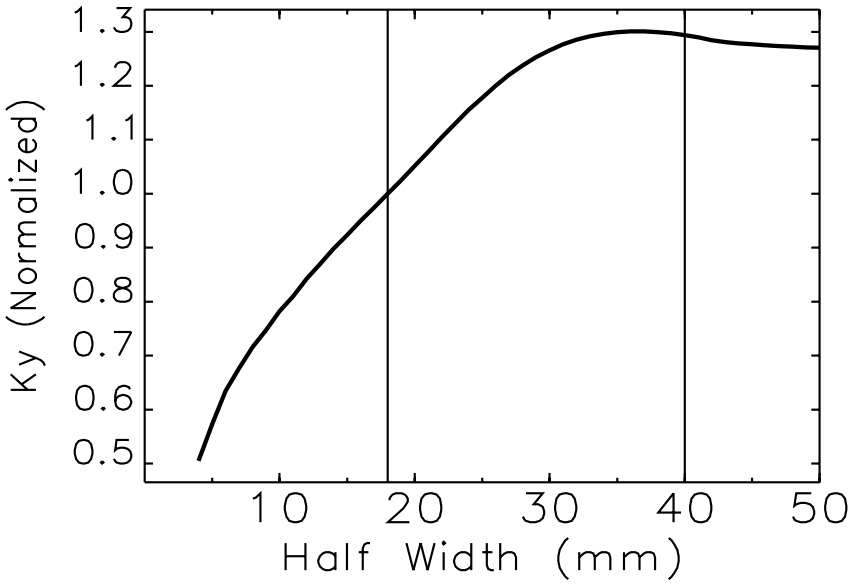

Figure 3.2-28: The vertical kick factor of bunched beam as a function of the half width w of an 8-mm small-gap chamber connected to the regular chamber in the ellipse of (4.2 cm, 2.1 cm).

Conversely, narrowing of the chamber decreases the impedance quite effectively. However, this decrease in aperture might require a smaller horizontal beta function to maintain good injection aperture, which would impose additional requirements on the lattice design.

The last option is to simply make a longer linear transition. A detailed computation of vertical wakes showed that a transition length of over 50 cm is sufficient to achieve the target reduction of 5/8, as shown in Figure 3.2-29.

In order to accommodate this long transition, the area needs to be redesigned as shown in Figure 3.2-30. The downstream will be mirrored with respect to the center of the straight section.

The new transition of the LSS chamber will reduce the effective transverse kick to a level equal to or less than the regular 5-m-long straight section. However, an 8-m LSS chamber will increase the resistive wall impedance (a component of impedance not yet mentioned though important) by 8/5 per sector. Building such a chamber would allow reducing the impact of the resistive wall effect by using a strip of copper on the top and bottom inside surfaces of the chamber. However, in the LSS cases present in the APS Upgrade, this will not be needed. In Sectors 1 and 11, a superconducting undulator with a cryogenically cooled chamber will occupy about 3 m of the straight. In Sectors 5 and 7, a set of superconducting cavities will occupy about 2.8 m of the straight. Due to the low temperature of the cryogenically cooled chamber as well as the large aperture of the SPX chamber, the resistive wall impedance should not increase.

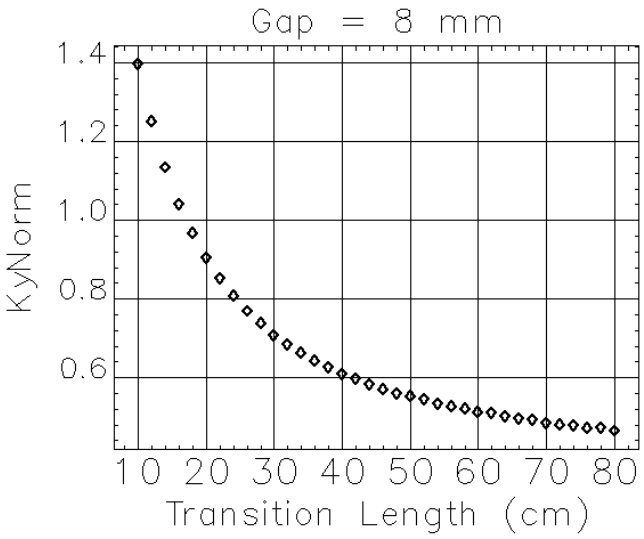

Figure 3.2-29: The vertical kick factor as a function of linear taper length. The values are normalized by the current APS 8-mm gap chamber.

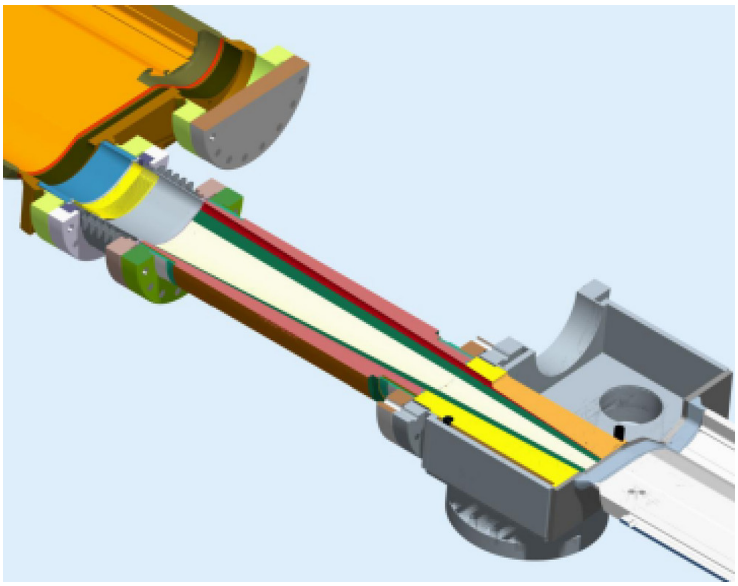

Figure 3.2-30: The new transition designed for the LSS will have 55-cm taper, which is significantly longer than the current taper with 18-cm effective length.

The conceptual layout of the LSS design with a long taper was completed by removing a quadrupole and repositioning the beam position monitor and the radiation absorber; the sector with magnets is shown in Figure 3.2-31.

In summary, in order to make the implementation of LSSs feasible with respect to instabilities it is necessary to control the impedance sources by:

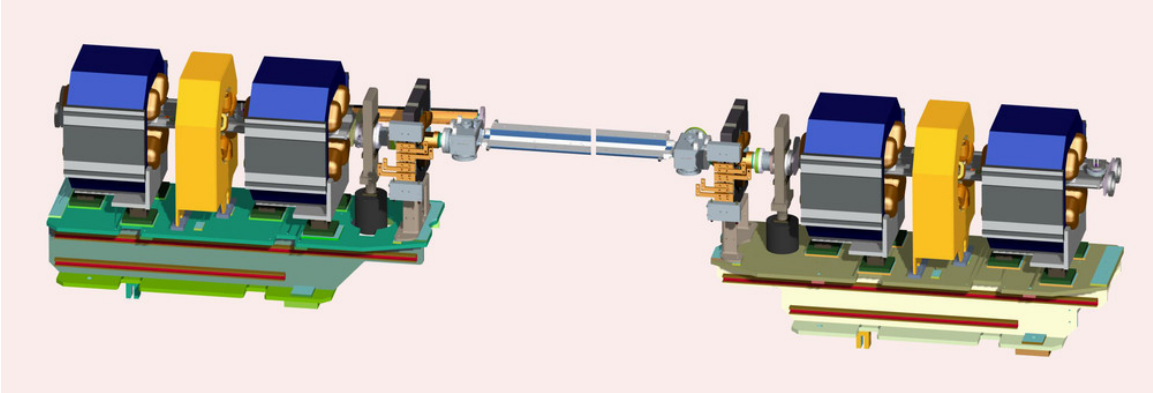

Figure 3.2-31: The conceptual layout of an LSS with components installed on the girder.

- making the taper transition longer at both ends for reducing the geometrical impedance, and
- reducing the resistive wall wake by providing a chamber with a copper-lined beam path or some other configuration that avoids a long, room-temperature chamber.

3.2.5 Lattice Alternatives

A number of alternatives have been considered in detail as possible upgrades for the APS. Many of these are documented in the literature or in internal notes. Among the alternatives considered are:

1. lattices with more than four long straight sections,
2. lattices with lower emittance that require replacing the storage ring,
3. operation at lower energy in order to reduce the emittance,
4. use of damping wigglers to lower the emittance, and
5. changing the damping partition number to reduce the emittance.

In this section, the requirements, advantages, and drawbacks of these options are reviewed.

3.2.5.1 Lattices with More Long Straights

The widespread interest in revolver undulators (see section 3.4.2.5) reduced the demand for long straight sections. However, configurations have been developed for eight long straights, and these appear workable. As might be expected, obtaining acceptable dynamic acceptance and beam lifetime is somewhat harder than for configurations with four LSSs, particularly when both the SPX and RHB insertion are added. Such configurations have also been tested in mock-ups, which largely confirmed their workability. However, at present there is no demand for additional long straights.

3.2.5.2 Replacement Lattices

Two possible replacement lattices were explored, both based on the use of a triple-bend cell and incorporating 10-m-long straight sections. Both require complete replacement of the storage ring magnets, girders, and vacuum system. Only the rf systems and presumably the injection hardware would be retained.

The first of these lattices [3.2-32] was optimized for low effective emittance, with a target of 1 nm. Detailed studies of this lattice indicated that an effective emittance of 0.9 nm should be possible. The magnet strengths were also judged to be possible, provided the bore radius for the quadrupoles and sextupoles was reduced to 20 mm. This would in turn require reducing the chamber size, which was found not to adversely impact instability issues [3.2-33].

In discussing this lattice with users, it emerged that a significant number of users were limited not by beam brightness but by capacity. Hence, the triple-bend concept was further developed to provide the possibility of an additional insertion device beamline [3.2-34]. This was found to be possible by adjusting the relative bend angles of the three dipoles such that the straight section between the second and third dipole was parallel to the existing bending magnet beamline. This new straight section would accommodate a new insertion device with an approximately 1-m length, delivering radiation to an existing bending magnet beamline. Drawbacks of this approach include limitations on the minimum gap imposed by the relatively large vertical beta function at the location of the new insertion device. In addition, the effective emittance increases to 1.7 nm.

As far as the preliminary studies determined, both lattices are feasible. However, because of the relatively small number of quadrupoles in each sector (which results from the desire for long straight sections), it appears to be impossible to replace one sector at a time while maintaining operation of the ring. In other words, the entire ring would have to be replaced at once, which would require a shutdown of at least one year's duration. This was considered unacceptable by the user community.

3.2.5.3 Lower Energy Operation

It is well known that the equilibrium emittance scales as E^2, where E is the electron beam energy [3.2-35]. Hence, in the quest for higher x-ray brightness, one might anticipate some advantage from reducing the electron beam energy. This has been investigated several times at APS and was recently revisited under the assumption that the present low-emittance lattice would be used together with optimized superconducting undulators.

The method of analysis is as follows:

1. Vary the beam energy from 3 GeV to 7.7 GeV in 0.1-GeV steps.
    (a) Vary the device period from 10 mm to 30 mm in 1-mm steps.
        i. Compute the maximum K value available for a NbTi-based device of the chosen period.
        ii. Compute the brightness and flux tuning curves for this device, subject to the high-heat-load front-end limits.
        iii. Multiply the brightness for each harmonic by values that approximately account for the effect of typical phase errors [3.2-36].

iv. Compute the brightness envelope over all harmonics. This eliminates the overlap and gives a single curve of maximum brightness vs photon energy. Gaps in the spectrum are represented by zero values.

2. For a series of 5-keV-wide photon energy bands with starting points from 5 to 95 keV, find the best brightness performance available for each beam energy.

3. For each energy band, find the beam energy that maximizes the brightness performance.

4. For each beam energy, determine the number of photon energy bands for which the brightness performance is within a factor of two of the best available for any energy.

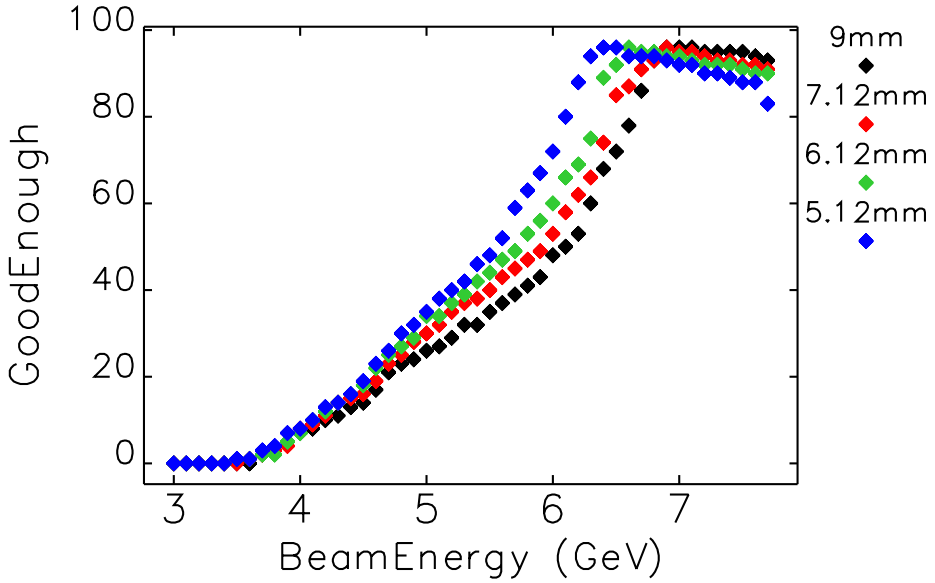

Figure 3.2-32: Number of 5-keV bands between 5 keV and 95 keV for which performance is "good enough," i.e., within a factor of two of the best available result, as a function of the electron beam energy.

Figure 3.2-32 shows the results of the analysis for several different assumed magnetic gaps. For magnetic gaps of 7.12 to 9 mm, operation at 7 GeV is very close to optimal. Indeed, even for the smallest gap explored (5.12 mm), 7 GeV is close to optimal in 90% of the cases. Our conclusion is that large gains in x-ray brightness cannot be obtained by using lower electron beam energy. It is always possible to get a nearly identical gain by simply optimizing the choice of undulator. In addition, higher energy has the advantage of higher instability thresholds, which is important given our emphasis on high single-bunch current for timing experiments.

3.2.5.4 Damping Wigglers

An increasingly popular way to reduce the emittance in a light source is through the use of damping wigglers. This was investigated [3.2-37] for APS from the standpoint of linear optics and rf requirements. The wigglers must be placed in zero-dispersion straight sections, which means that the starting effective emittance will increase from the 3.1-nm value delivered now. (One might imagine that one could use zero-dispersion insertions for the wigglers and retain the distributed dispersion

lattice elsewhere. However, it was found that the increase in energy spread due to the wigglers would significantly reduce the anticipated emittance reduction.) The lowest-emittance zero-dispersion lattice found, irrespective of nonlinear dynamics issues, has an emittance of 4.7 nm. If the three remaining free straight sections were used for (somewhat speculative) 5-T superconducting wigglers with a 60-mm period, the effective emittance would be 1.7 nm.

With such wigglers, the rf voltage requirements increase from about 9 MV to 21 MV. Presently APS has four 5-m-long straight sections available for rf. Analysis of the capabilities of existing superconducting rf systems [3.2-37] indicated that this space is not sufficient. Even conversion of the rf straight sections to a nominal 7.7-m LSS configuration would not suffice. Hence, the use of damping wigglers seems to be ruled out for a number of reasons.

3.2.5.5 Damping Partition Change

Another well-known method for reducing the beam emittance is to increase the horizontal damping partition number J_x. Normally, $J_x + J_y + J_z = 4$, with $J_x = J_y \approx 1$. It is possible to increase J_x at the expense of J_z, which decreases the emittance while increasing the energy spread. Since APS has dispersion in the straight sections, it is important to look at the effective emittance rather than the raw emittance when assessing the effect of such a change. In addition, the direct effect of the energy spread on the brightness may be significant for higher undulator harmonics h.

Adding gradients to the dipoles is one option for changing the damping partition. This can be done either by modifying the cores or adding pole-face windings. Using this method, the effective emittance might be reduced to 1.8 nm. However, this involves very high tunes in both planes (46 in the horizontal and 32 in the vertical), for which no satisfactory nonlinear dynamics solution could be found.

Another approach to changing the damping partition is to change the rf frequency. This results in a systematic orbit in the quadrupole magnets, which can change the damping partition just as the use of a gradient dipole magnet will. The disadvantage of this approach is that, because there is dispersion in the APS straight sections, changing the rf frequency causes significant changes in the orbit, requiring realignment of all the beamlines simultaneously, which simply is not feasible. In addition, the effective emittance can only be decreased by about 20% with this method, because of the large dispersion value at the straight sections.

Since these methods are not satisfactory, another method—producing systematic orbit shifts between the dipoles using a combination of trim coils on the dipoles and steering correctors [3.2-38]—was investigated. Developing this "orbit displacement lattice" is much more difficult than developing a normal lattice, because there is a significant, systematic horizontal orbit in the quadrupoles and sextupoles. Hence, it is necessary to simultaneously optimize linear and nonlinear dynamics. Using the multi-objective optimization techniques described in section 3.2.2.3, a lattice with an effective emittance of 1.5 nm ($J_x = 2.34$, $J_z = 0.66$) was obtained. The brightness increases by over a factor of 2 in the first harmonic, with slightly diminished gains for the higher harmonics. Dropping the coupling from the nominal 1% to 0.3% would further increase the brightness of the first harmonic, by about 50%.

The tunes $\nu_x = 37.34$ and $\nu_y = 18.08$ are not too different from the present values. The chromaticities obtained, $\xi_x = 4.6$ and $\xi_y = 3.8$, are suitable for at least 100 mA in 324 bunches, for which the predicted Touschek lifetime is over 40 hours for a coupling of 1% and about 24 hours for a coupling of 0.3%. More work is needed to improve the dynamic acceptance, which is only 10 mm on the negative side. In addition, the lattice will no doubt be operationally challenging, since quadrupoles,

skew quadrupoles, and sextupoles will be combined-function elements. However, the lattice shows considerable promise as a possible special operating mode. This would require integrating it with a configuration that includes long straight sections, which has not been attempted.

3.2.5.6 Conclusion

Several of the lattice alternatives that were studied as possibilities for the APS Upgrade were reviewed. In general, these suffer from significant drawbacks, including (variously) high cost, inability to implement gradually, and disappointing performance. Only one option, namely the change of damping partition via a systematic orbit, appears to hold much promise. It is being considered as a possible special high-brightness operating mode, provided it can be made workable in the context of the long straight section lattice.

3.2.6 Dependencies on Programmatic Work

Successful completion of the long-straight-section implementation depends on, or will benefit from, several programmatic tasks and resources, which are enumerated here.

1. *Development of lattices.* On-going lattice development and evaluation requires significant computing resources, which are available from APS, Argonne's Laboratory Computing Resource Center, and the Argonne Leadership Computing Facility. Although lattice development is nominally complete, on-going development is anticipated as requirements evolve.

2. *Testing of mock-up lattices.* Testing of mock-up lattices is needed in order to provide confidence that changes will not affect APS operations in unanticipated ways. This is on-going using regular machine studies periods and existing staff. Some results are described in section 3.2.2.5.

3. *Improved collimation.* An improved collimation system is desirable in order to reduce beam losses at insertion devices. This will take on greater importance in the APS Upgrade, since the lifetimes are expected to decrease significantly. Efforts are underway to develop such a system.

4. *Orbit displacement lattice testing.* Development and testing of the orbit displacement lattice, described in section 3.2.5.5, will require use of APS machine studies time and staff. This lattice is not part of the Project scope but represents a potentially worthwhile special operating mode that addresses the requirement for higher brightness.

5. *Alignment of the beamlines.* As discussed in section 3.2.2.5, implementation of non-symmetric lattices requires reduction in the amount of beam steering allowed to accommodate discrepancies in the relative alignment of the ring and beam lines. This effort is on-going, making use of routine machine studies and shutdowns.

6. *Improved coupling control.* As described in section 3.2.3, improved control of coupling will provide benefits in terms of beam lifetime, injection efficiency, and beam properties at source points.

3.2.7 Engineering Specifications

3.2.7.1 Introduction

The storage ring insertion device (ID) straight sections are 5.59 m long and provide space for the installation of 4.8 m of undulators. The goal is to design a longer straight section that can be adapted to any of the existing straight sections. To this end, magnets on girders 1 and 5 will be reconfigured and their respective vacuum chambers and girder weldments modified to create an additional 3.0 meters of space. This design creates 8.0 m of free space with space available to install 7.6 m of undulator or a combination of undulators and cryomodules with superconducting devices.

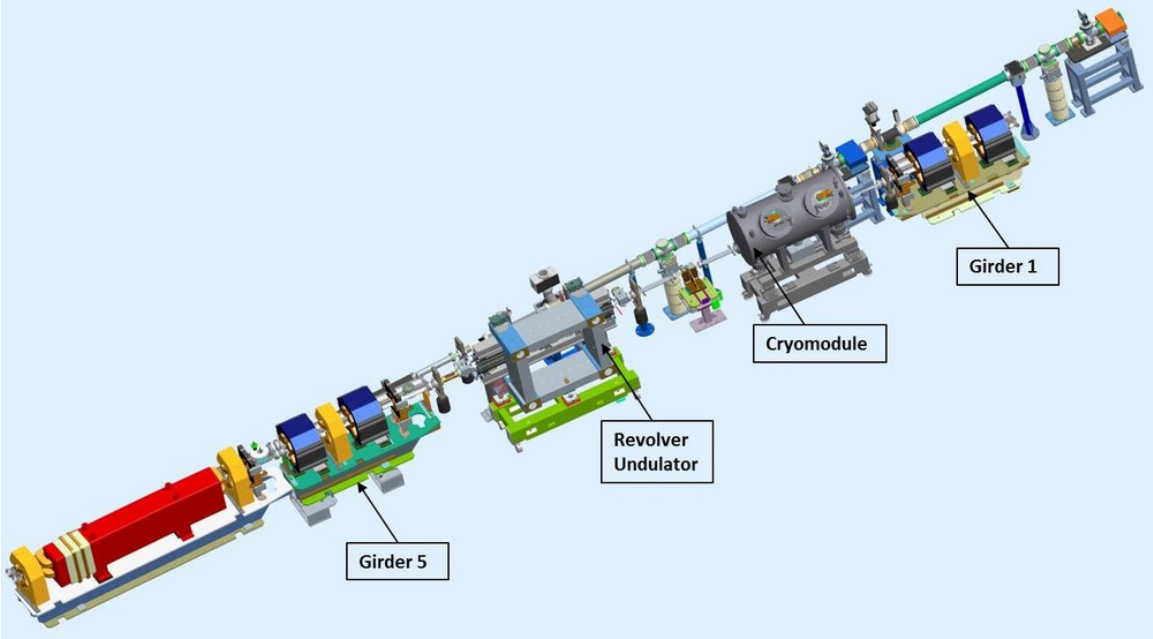

Figure 3.2-33: Typical LSS with reconfigured girders 1 and 5.

3.2.7.2 Technical Description

The LSS engineering specification documents (ESDs) in conjunction with associated fabrication specifications and drawings defines the requirements for the LSS. Sectors 1, 5, and 7 are selected to be converted into long straight sections. Of these three sectors, Sector 1 will be populated with conventional and superconducting IDs while Sectors 5 and 7 will be populated with conventional IDs and superconducting deflecting cavities. Figure 3.2-33 shows a typical long straight section with reconfigured girders 1 and 5.

Deliverables for the LSS include the following assemblies; their sub-assemblies and component parts are described Section 3.2.7.4.

1. Reconfigured Girder 5 Assembly
2. Reconfigured Girder 1 Assembly

3. SCU ID Chamber Assembly
4. SPX ID Chamber Assembly
5. ID Chamber Supports Assemblies
6. Long Taper Transition Absorber Assembly
7. 6.0 in Flanged All-metal Gate Valve—Storage ring ellipse
8. 4.63 in Flanged All-metal Gate Valve—SPX aperture
9. 6.0 in Flanged Bellows Assembly—Storage ring ellipse
10. 4.63 in Flanged Bellows Assembly—SPX aperture
11. SCU Place Holder Vacuum Chamber
12. SPX Place Holder Vacuum Chamber
13. Drift Space Vacuum Chamber
14. SPX Circular Beam Pipe to APS Extrusion Taper Transition
15. SCU Chamber to APS Extrusion Taper Transition

3.2.7.3 Technical Requirements

The technical requirements for the APS Upgrade LSS are derived from the APS Upgrade Long Straight Sections and Lattice Physics Requirements Document (PRD) [3.2-39], which includes the affected sector, lattice, and vacuum system changes. Magnets on girders 1 and 5 are reconfigured such that these existing girders and vacuum chambers can be shortened, creating additional space. A summary of the magnets reconfiguration as derived from the APS Upgrade Long Straight Sections and Lattice PRD is shown in Table 3.2-4.

Girder 5 reconfiguration design is as follows and is shown in Figures 3.2-34 and 3.2-35.

1. Replace 0.8-m quadrupole with 0.5-m-long quadruople
2. Eliminate H2/V2 corrector magnet
3. Eliminate beam position monitor (BPM) BP1
4. New vacuum chamber length = 2.176 m
5. New girder support length = 2.14 m
6. Move EA5 photon absorber upstream 1.46 m

Girder 1 reconfiguration design is as follows and is shown in Figures 3.2-36 and 3.2-37.

1. Replace 0.8-m quadrupole with 0.5-m-long quadruople
2. Eliminate H2/V2 corrector magnet

Table 3.2-4: Long straight section accelerator beamline configuration.

Element Type	Name	Z (m)	Condition
Quadrupole	S1B:Q3	-6.17	Girder 5
BPM	S1B:P2	-5.4	Girder 5 Vacuum Chamber
Sextupole	S1B:S1	-5.62	Girder 5
Quadrupole	S1B:Q2	-5.07	Girder 5
Corrector	S1B:HV1	-4.49	Girder 5
BPM	S1B:P0	-3.59	Upstream-End ID Chamber
BPM	S2A:P0	3.7	Downstream Cryomodule
Corrector	S2A:HV1	4.49	Girder 1
Quadrupole	S2A:Q2	5.07	Girder 1
BPM	S2A:P2	5.4	Girder 1 Vacuum Chamber
Sextupole	S1A:S1	5.62	Girder 1
Quadrupole	S2A:Q3	6.17	Girder 1

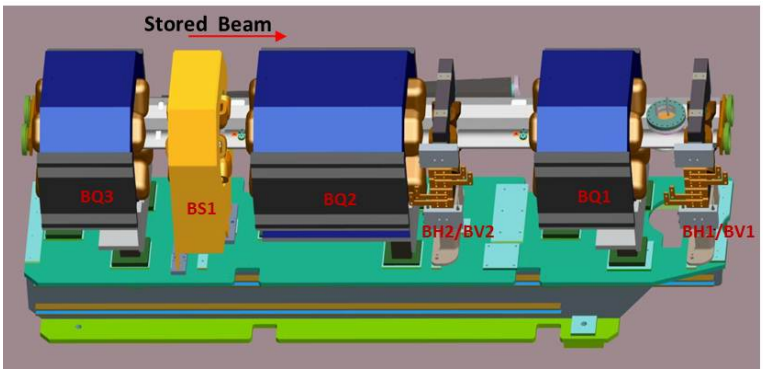

Figure 3.2-34: Existing girder 5 magnets configuration.

3. Eliminate beam position monitor (BPM) AP1
4. New vacuum chamber length = 2.30 m
5. New girder support length = 2.40 m

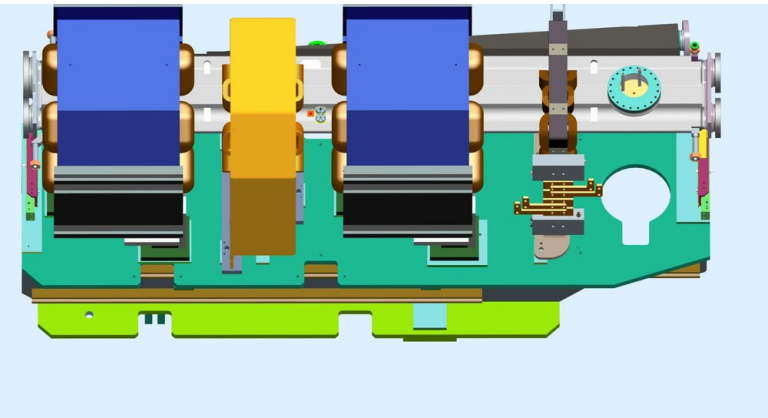

Figure 3.2-35: LSS reconfigured girder 5 magnets.

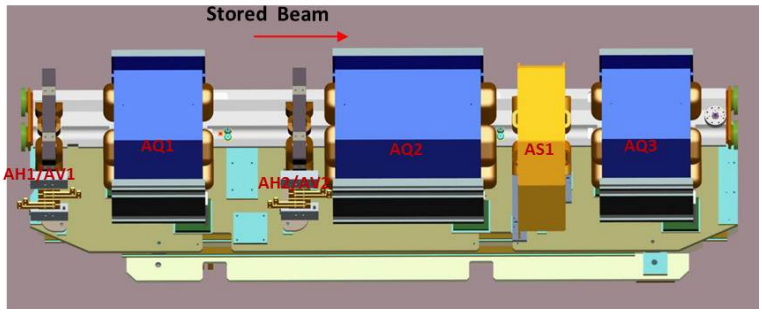

Figure 3.2-36: Existing girder 1 magnets configuration.

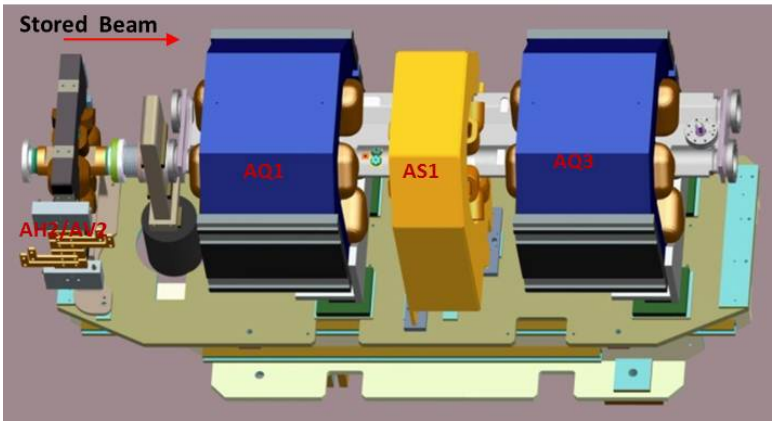

Figure 3.2-37: LSS reconfigured girder 1 magnets.

3.2.7.4 Design and Fabrication Requirements

Detailed drawings and procurement specifications will be provided for the fabrication of girder weldments, girder vacuum chambers, ID vacuum chambers, vacuum chamber supports, and the purchase of catalog items. Vendors shall supply parts in accordance with these documents. Any deviations from these documents must be approved in writing by APS/ANL.

3.2.7.5 General Vacuum Requirements

General requirements for materials, fabrication, cleaning, surface treatment, welding, brazing, handling, assembly, quality assurance, testing, and preparation for delivery will be specified in separate documents. All vacuum components that are to be installed in the LSS must undergo chemical cleaning, leak testing, bake-out, and RGA testing for residual hydrocarbons as detailed in the APS Accelerator Ultra-High Vacuum Guide [3.2-40]. The 220-l/s and 30-l/s ion pumps currently used on girders 5 and 1 vacuum chambers respectively will be reused. New ion pumps as specified by the SCU and SPX groups will be installed on the ID chambers.

3.2.7.6 Girders 5 and 1 Vacuum Chambers

Girders 5 and 1 vacuum chambers shall be machined from existing 6063-T5 aluminum extrusions. In addition to required vendor inspections, machined parts received will undergo quality assurance (QA) inspection per applicable drawings and statements of work (SOWs) by APS technicians and the central shops QA department. Certified machined parts will be delivered to the Vacuum Group for cleaning, assembly and welding, and certification for installation. Each chamber shall be assembled with non-evaporable getter (NeG) systems, as are currently used in the storage ring. Certified chambers will be delivered to the Girder and Magnets Assembly Facility for assembly and alignment.

3.2.7.7 Vacuum Chamber Transitions

A summary of the engineering design specifications for the vacuum chamber transitions is shown in Table 3.2-5, as derived from [3.2-39].

Table 3.2-5: Vacuum chamber transitions parameters.

Transitions Parameter	Specification	Condition
Upstream & Downstream Transitions	$\geq$ 50 cm	LSS with ID Chamber
APS Extrusion to ID Chamber	$\geq$ 50 cm	LSS with SPX & ID Chamber
ID Chamber to SPX Chamber Transition	$\geq$ 20 cm	LSS with SPX & ID Chamber
SPX Chamber to APS Extrusion	$\geq$ 22 cm	LSS with SPX & ID Chamber
APS Extrusion to ID Chamber	$\geq$ 50 cm	LSS with SCU & ID Chamber
ID Chamber to SCU Chamber	$\geq$ 20 cm	LSS with SCU & ID Chamber
SCU Chamber to APS Extrusion	$\geq$ 50 cm	LSS with SCU & ID Chamber

3.2.7.8 APS Extrusion to ID Chamber Long Taper Transitions

A 33.2-cm-long taper transition will be installed immediately upstream of the ID chamber in each LSS. This 33.2-cm-long transition coupled to the 20.0-cm end-box transition will provide a 53.2-cm continuous taper into the ID chamber. Parameters for the 33.2-cm transition design are shown in Table 3.2-6.

Table 3.2-6: APS extrusion to ID chamber long taper transition design parameters.

Parameter	Z (mm)	X (mm)	Y (mm)
Elliptical Aperture	0	41.7	84.68
Elliptical Aperture	242.77	18.04	48.91
Elliptical Aperture	332.33	19.41	55.02
Flanges	6.0 (nom) Conflat	N/A	6.0 (nom) Conflat

3.2.7.9 Insertion Device Vacuum Chambers

Insertion device vacuum chambers shall be machined from 6063-T5 aluminum extrusions. In addition to required vendor inspection, machined parts received will undergo QA inspection per applicable drawings and statements of work by APS technicians and the central shops QA department. Certified machined parts shall be delivered to the Vacuum Group for cleaning, assembly and welding, and certification for installation. ID chamber end boxes shall be designed with tapered transition inserts and photon absorbers to suit the appropriate SCU or SPX long straight section. Design parameters for tapered transitions in the LSS SCU ID chamber end boxes are shown in Tables 3.2-7 and 3.2-8.

Table 3.2-7: LSS SCU ID upstream end box tapered transition design parameters.

Parameter	Z (mm)	X (mm)	Y (mm)	Remarks
Transition Insert	0	19.41	55.02	Elliptical aperture
— ” —	177.67	7.5	Half slot	See current design
Transition End Plate	177.67	7.5	Same as chamber extrusion	See current design
— ” —	200	7.5	— ” —	
Flanges	6.0 (nom) Conflat	N/A	N/A	

Table 3.2-8: LSS SCU ID downstream end box tapered transition design parameters.

Parameter	Z (mm)	X (mm)	Y (mm)	Remarks
Transition End Plate	0	7.5	Same as chamber extrusion	See current design
— ” —	22.33	7.5	Same as chamber extrusion	See current design
Transition Insert	22.33	7.5	Half slot	See current design
— ” —	200	41.7	84.68	Storage ring ellipse
Flanges	6.0 (nom) Conflat	N/A	N/A	

Design parameters for tapered transitions in the LSS SPX ID chamber end boxes are shown in Tables 3.2-9 and 3.2-10.

Table 3.2-9: LSS SPX ID upstream end box tapered transition design parameters.

Parameter	Z (mm)	X (mm)	Y (mm)	Remarks
Transition Insert	0	19.41	55.02	Elliptical aperture
— ” —	177.67	7.5	Half slot	See current design
Transition End Plate	177.67	7.5	Same as chamber extrusion	See current design
— ” —	200	7.5	— ” —	— ” —
Flanges	6.0 (nom) Conflat	N/A	N/A	

Table 3.2-10: LSS SPX ID downstream end box tapered transition design parameters.

Parameter	Z (mm)	X (mm)	Y (mm)	Remarks
Transition End Plate	0	7.5	Same as chamber extrusion	See current design
— ” —	22.33	7.5	Same as chamber extrusion	See current design
Transition Insert	22.33	7.5	Half slot	See current design
— ” —	200	52.0 dia	N/A	
Flanges	6.0 (nom) Conflat	N/A	N/A	

3.2.7.10 SCU Chamber to APS Extrusion Taper Transition

The tapered transition from the SCU vacuum chamber aperture to the storage ring aperture shall be of minimum length 50.0 cm flange to flange. It shall be designed with a screened vacuum pump-out port located on the wall or aisle side of the chamber. Design considerations shall be made for the location of button-type beam position monitors in this chamber. Table 3.2-11 specifies the aperture sizes for the transition.

Table 3.2-11: SCU vacuum chamber to APS extrusion taper-transition design parameters.

Parameter	Z (mm)	X (mm)	Y (mm)
Racetrack Aperture	0	7.2	53
Flange	4.5 (nom) Conflat	N/A	N/A
SR Ellipse	500	41.7	84.68
Flange	6.0 (nom) Conflat	N/A	N/A

3.2.7.11 SPX Chamber to APS Extrusion Taper Transition

The taper transition from the SPX vacuum chamber aperture to the storage ring aperture shall be 51.0 cm long flange to flange. It shall be designed with a shielded vacuum pump-out port located on the

wall or aisle side of the chamber. Design considerations shall be made for the location of button-type beam position monitors in this chamber. Table 3.2-12 specifies the aperture sizes for the transition.

Table 3.2-12: SPX vacuum chamber to APS extrusion taper-transition design parameters.

Parameter	Z (mm)	X (mm)	Y (mm)
Circular Aperture	0	52.0 dia	N/A
Flange	4.63 (nom) Conflat	N/A	N/A
Ellipse	510	41.7	84.68
Flange	6.0 (nom) Conflat	N/A	N/A

3.2.7.12 Magnets Availability

Magnets for the initial installation will be taken from the available spares inventory. Those taken from inventory shall meet the magnetic performance requirements as described in section 2.6 of [3.2-39],the APS Upgrade Long Straight Sections and Lattice PRD. Additional magnets for subsequent installations shall be taken from those removed from the previous installation. Those magnets do not have to be measured.

3.2.7.13 Bellows Assemblies

B2/B4-type bellows assemblies and liners currently installed at both ends of the ID straights will be re-used. Newly designed shielded bellows with 4.5-inch Conflat flanges and aperture to match adjacent SCU or SPX devices will be installed in each of the SCU or SPX long straights.

3.2.7.14 Gate Valves

Gate valves currently installed to isolate the ID straights will be re-used to isolate the LSS. New 4.5-inch flanged gate valves with apertures to match adjacent SCU or SPX devices will be installed as needed in each of the SCU or SPX long straights.

3.2.7.15 Installation

Installation of the LSSs will involve the use of APS technicians, engineers and ANL riggers. Each installation is scheduled to occur over a shutdown / maintenance period. Infrastructure needed to support the SCU or SPX systems at either of the LSSs should be done in prior shutdowns. Girders with magnets and vacuum chamber will be assembled and fiducialized in the Girder and Magnets Assembly Facility prior to transporting them to the storage ring for installation. Each LSS will be installed at least one shutdown prior to the installation of a superconducting device with a place holder vacuum chamber installed in place of the cryomodule. Subsequent shutdowns will allow adequate time for the installation and commissioning of the superconducting device. Figure 3.2-38 shows details of an installation schedule that would allow installation during a typical APS shutdown.

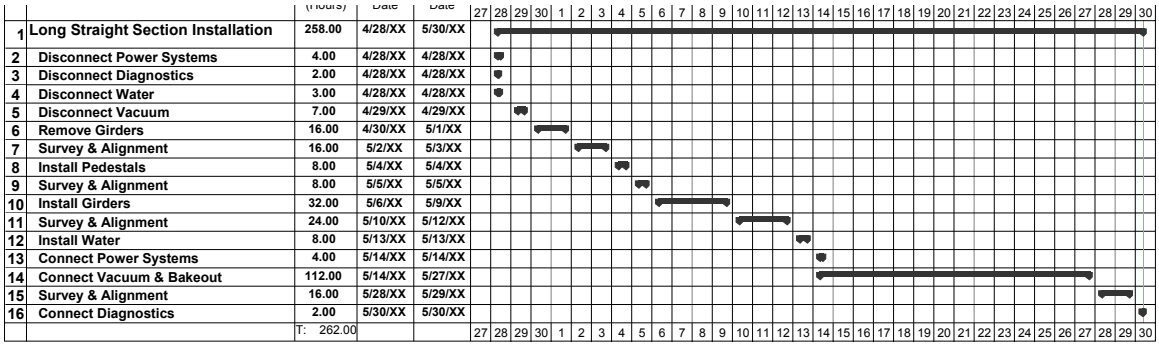

		(Hours)	Date	Date
1	Long Straight Section Installation	258.00	4/28/XX	5/30/XX
2	Disconnect Power Systems	4.00	4/28/XX	4/28/XX
3	Disconnect Diagnostics	2.00	4/28/XX	4/28/XX
4	Disconnect Water	3.00	4/28/XX	4/28/XX
5	Disconnect Vacuum	7.00	4/29/XX	4/29/XX
6	Remove Girders	16.00	4/30/XX	5/1/XX
7	Survey & Alignment	16.00	5/2/XX	5/3/XX
8	Install Pedestals	8.00	5/4/XX	5/4/XX
9	Survey & Alignment	8.00	5/5/XX	5/5/XX
10	Install Girders	32.00	5/6/XX	5/9/XX
11	Survey & Alignment	24.00	5/10/XX	5/12/XX
12	Install Water	8.00	5/13/XX	5/13/XX
13	Connect Power Systems	4.00	5/14/XX	5/14/XX
14	Connect Vacuum & Bakeout	112.00	5/14/XX	5/27/XX
15	Survey & Alignment	16.00	5/28/XX	5/29/XX
16	Connect Diagnostics	2.00	5/30/XX	5/30/XX
		T: 262.00		

Figure 3.2-38: Preliminary schedule showing tasks required for installation of a long straight during a one-month shutdown, assuming eight-hour work days including weekends. (The April shutdown is used only as an example.)

3.2.8 References

[3.2-1] G. Decker and O. Singh. Method for reducing x-ray background signals from insertion device x-ray beam position monitors, Phys. Rev. ST Accel. Beams, **2**(11), 112801, (1999).

[3.2-2] G. Decker. APS Storage Ring Commissioning and Early Operational Experience, Proc. of PAC 1995, pp. 290–292, (1995).

[3.2-3] V. Sajaev and L. Emery. Determination and Correction of the Linear Lattice of the APS Storage Ring, Proc. of EPAC 2002, pp. 742–744, (2002).

[3.2-4] M. Borland et al. Direct Methods of Optimization of Storage Ring Dynamic and Momentum Aperture, Proc. of PAC 2009, (2010).

[3.2-5] M. Borland et al. Application of Direct Methods of Optimizing Storage Ring Dynamic and Momentum Apertures, Proc. of ICAP 2009, (2010).

[3.2-6] C. Y. Yao et al. Recent Progress of the Bunch-by-Bunch Feedback System at the Advanced Photon Source, Proc. of IPAC 2010, p. 2803, (2010).

[3.2-7] V. Sajaev, ANL, (2010). Private communication.

[3.2-8] L. Emery and M. Borland. Top-up Operation Experience at the Advanced Photon Source, Proc. of PAC 1999, pp. 200–202, (1999).

[3.2-9] M. Belgrounne et al. Refined Tracking Procedure for the Soleil Energy Acceptance Calculation, Proc. of PAC 2003, pp. 896–898, (2003).

[3.2-10] J. Safranek. Experimental Determination of Linear Optics Including Quadrupole Rotations, Proc. of PAC 1996, pp. 2817–2819, (1996).

[3.2-11] P. Bagley and D. L. Rubin. Correction of Transverse Coupling in a Storage Ring, Proc.of PAC 1989, pp. 874–876, (1989).

[3.2-12] J. Safranek and S. Krinsky. Plans to Increase Source Brightness of NSLS X-ray Ring, Proc. of PAC 1993, pp. 1491–1493, (1993).

[3.2-13] L. Emery et al. Use of a General-Purpose Optimization Module in Accelerator Control, Proc. of PAC 2003, pp. 2330–2332, (2003).

[3.2-14] J. Bengtsson. The sextupole scheme for the Swiss Light Source (SLS): an analytic approach. Technical Report SLS-TME-TA-1997-0009, SLS, (1997).

[3.2-15] M. Borland. elegant: A Flexible SDDS-Compliant Code for Accelerator Simulation. Technical Report LS-287, Advanced Photon Source, (2000).

[3.2-16] M. Borland et al. Recent progress and plans for the code `elegant`, Proc. of ICAP 2009, (2010).

[3.2-17] M. Borland. A Self-Describing File Protocol for Simulation Integration and Shared Postprocessors, Proc. of PAC 1995, pp. 2184–2186, (1996).

[3.2-18] M. Borland and H. Shang. geneticOptimizer. Unpublished program.

[3.2-19] A. Xiao and M. Borland. Touschek Effect Calculation and Its Application to a Transport Line, Proc. of PAC 2007, pp. 3453–3455, (2007).

[3.2-20] A. Piwinski. The Touschek Effect in Strong Focusing Storage Rings. Technical Report DESY 98-179, DESY, (1998).

[3.2-21] Y. Wang and M. Borland. Exploration of Parallel Optimization Techniques for Accelerator Design, Proc. of IPAC 2011, (2011).

[3.2-22] M. Borland et al. Multi-objective Direct Optimization of Dynamic Acceptance and Lifetime for Potential Upgrades of the Advanced Photon Source. Technical Report LS-319, Advanced Photon Source, (2010).

[3.2-23] M. Borland. Use of a Coupling Bump to Control APS Vertical Emittance. Technical Report OAG-TN-2008-006, APS, (2008).

[3.2-24] A. Franchi et al. Vertical emittance reduction and preservation in electron storage rings via resonance driving terms correction, Phys. Rev. ST Accel. Beams, **14**, 034002, (2010).

[3.2-25] Y. Chae. Impedance Database and Its Application to the APS Storage Ring, Proc.of PAC 2003, pp. 3017–3019, (2003).

[3.2-26] Y. Chae and Y. Wang. Impedance Database II for the Advanced Photon Source Storage Ring, Proc. of PAC 2007, pp. 4336–4338, (2007).

[3.2-27] Y. Chae. The Impedance Database Computation and Prediction of Single Bunch Instabilities, Proc.of PAC 2007, (2007).

[3.2-28] Y. Chae. Study of Impedance and Its Effect on Single-Bunch Instability at the Advanced Photon Source, ICFA Beam Dynamics Newsletter 45, (2008).

[3.2-29] G. V. Stupakov. Geometrical Wake of a Smooth Flat Collimator. Technical Report SLAC-PUB-7167, SLAC, (1996).

[3.2-30] B. Podobedov and I. Zagorodonov. Impedance Minimization by Nonlinear Tapering, Proc. of PAC 2007, pp. 2006–2008, (2007).

[3.2-31] W. Bruns. GdfidL on Massive Parallel Systems, Proc. of LINAC 2002, pp. 418–420, (2002).

[3.2-32] A. Xiao et al. A 1-nm Emittance Lattice for the Advanced Photon Storage Ring, Proc. of PAC 2003, pp. 3447–3449, (2007).

[3.2-33] Y.-C. Chae et al. Single-Bunch Instability Estimates for the 1-nm APS Storage Ring Upgrade with Smaller Vacuum Chamber, Proc. of PAC 2007, Albuquerque, NM, pp. 4330–4332, (2007).

[3.2-34] V. Sajaev et al. New Lattice Design for APS Storage Ring with Potential Tri-fold Increase of the Number of Insertion, Proc. of PAC 2003, pp. 1139–1141, (2007).

[3.2-35] M. Sands. The Physics of Electron Storage Rings: An Introduction. SLAC Report SLAC-121, SLAC, (1979).

[3.2-36] R. Dejus, ANL, (2011). Private communication.

[3.2-37] M. Borland and L. Emery. Evaluation of the Possibility of using Damping Wigglers in the Advanced Photon Source, Proc. of PAC 2003, pp. 1124–1126, (2007).

[3.2-38] M. Borland. Potential Two-fold Reduction of Advanced Photon Source Emittance using Orbit Displacement, Proc. of PAC 2011, p. 2339, (2011).

[3.2-39] M. Borland and Y.-C. Chae. ICMS, APS-U Long Straight Sections and Lattice Physics Requirements Document. https://icmsdocs.aps.anl.gov/docs/groups/aps/@apsshare/@acceleratoroperationsphysics/documents/specification/aps_1423797.pdf.

[3.2-40] C. Liu and J. Noonan. Advanced Photon Source Accelerator Ultrahigh Vacuum Guide. Technical Report ANL/APS/TB-16, Advanced Photon Source, (1994).

3.3 Beam Stability [U1.03.02.02]

3.3.1 Introduction

One of the distinguishing features of third-generation storage ring light sources like the APS are the small beam emittances, which imply small beam size and divergence. Table 3.3-1 shows the typical dimensions for the APS electron beam at the ID location. Any beam motion that is significant compared to these dimensions will impact the ability of users to perform demanding experiments. In essence, fast beam motion washes out the brightness of the beam. Hence, controlling beam motion is effectively a brightness upgrade and serves an important role in delivering the mission requirements.

The values in Table 3.3-1 are typical transverse beam size and divergence values for the particle beam at ID and bending magnet (BM) source points assuming 2.5-nm-rad natural emittance and 1% coupling. Note that for BM sources, the x-ray beam's vertical angular divergence is dominated by the natural synchrotron radiation opening angle, which is approximately $1/\gamma = 73$ μrad.

For the APS, AC beam stability goals have historically been set to be 5% of the x-ray beam's rms phase-space dimensions (both beam size and angular divergence). After discussions with APS X-ray Science Division staff, and considering the fact that x-ray detectors are becoming available with higher bandwidth, the applicable frequency bands for a beam stability specification have been updated. Beam

Table 3.3-1: APS Particle Beam Transverse Dimensions

	Beam Size μm rms		**Angular Divergence** μrad rms	
	ID	BM	ID	BM
Horizontal	275.3	91.6	11.3	56.4
Vertical	8.5	25.5	3.0	1.1

centroid motion as high as 1 kHz may impact x-ray experiments using fast detectors, while motion at higher frequencies produces an increase in effective emittance for most experiments, implying significantly relaxed requirements [3.3-1].

APS Upgrade beam stability goals for ID sources are listed in Table 3.3-2. The most significant change in comparison to the APS Upgrade conceptual design is the addition of AC requirements extending up to 1 kHz. The requirements up to 200 Hz will be retained at the level of 5% of phase space dimensions, while motions from 0.01 to 1000 Hz will be limited to the level of 10% of transverse phase space dimensions. Beam stability at BM sources is already sufficient.

Table 3.3-2: APS Upgrade beam stability present performance and goals.

		AC rms motion 0.01-200 Hz		**AC rms motion 0.01-1000 Hz**		**Long-term drift (One Week)**	
		μm rms	μrad rms	μm rms	μrad rms	μm rms	μrad rms
Horizontal	Present	5.0	0.85	5.0 - 7.0*	NA	7.0	1.4
	Upgrade	3.0	0.53	6.0	1.14	5.0	1.0
Vertical	Present	1.6	0.80	3.7*	NA	5.0	2.5
	Upgrade	0.42	0.22	0.84	0.44	1.0	0.5

* Measurement up to 767 Hz.

3.3.2 Beam Motion Allocation

The above specifications must be met as various systems or devices are added to the ring. To guide these system designs an allocation of beam motion for each is made, though these allocations may change as more is known.

The desire to limit one-week orbit drift with orbit feedback running imposes requirements only on instrumentation drifts (X-ray BPM drifts). If the sources (i.e., ID field perturbations) have drifts, they would be handily compensated by "slow" global orbit feedback. Thus there are no requirements set for drifts of sources of beam motion.

AC beam motion remains to be allocated between perturbing sources. It is assumed that sources perturb the orbit independently of each other and their effects are reduced by orbit feedback individually according to a frequency response. The sources are a mix of existing ones and new ones:

- Ground motion with magnet power supply noise including corrector noise. These are considered together as a storage ring baseline ("SR baseline") orbit motion, i.e., no insertion devices or SPX

running at all.

- SPX, with noise appearing to good approximation only in the vertical plane.
- All permanent-magnet (PM) IDs (i.e., devices that have gaps that move slowly).
- Slowly changing electromagnetic (EM) wigglers (i.e., IEX wiggler).
- Additional EM correctors for PM devices or canted undulator systems.
- Switching electromagnetic devices (i.e., CPU, then its replacement, the electromagnetic variable polarizing undulator (EMVPU), as described in section 3.4.3.3).

The slow-moving IDs are not full-time orbit perturbations. Their configuration (gap or current) changes rarely and usually in relative isolation. Thus all of these IDs are taken as a single perturbations for the budget. If the users make continuous scans of the IDs, then the scans will be slow or over such a small range of gap or current that the orbit feedback will have no problem compensating the slow changes in perturbation to a high degree.

The additional, special EM dipoles for correcting perturbation of certain PM or EM devices may be considered together with the 640 ring steering correctors in the noise budget. The special EM dipoles typically have smaller steering-angle ranges than the SR correctors and are smaller in number.

Table 3.3-2 shows the allowed orbit motion in two frequency bands, expressed in rms terms. In the frequency domain, the orbit motion is quantified by the power spectral densities (PSDs) of the orbit coordinates. The PSD is the square of the Fourier transform of the quantity, which can be obtained experimentally from the control system, or from post-processing a time-history of orbit data. Let $P_x(f)$ be the PSD of the coordinate x with units of, say, $(\mu\text{m})^2$/Hz, and similarly for the other coordinates x', y, and y'. Of interested are the "rms" of the various overlapping bands, which are given by $\int_{f_l}^{f_u} P_x(f)\, df$, where f_l = 0.01 Hz and f_u is 200 Hz or 10000 Hz. The integral can also be referred to as the "power" of the coordinate in an analogy to circuits.

It is assumed that each noise source has contributions to each of the orbit PSDs, e.g., $P_x(f) = P_{x,\text{SR}}(f) + P_{x,\text{SPX}}(f) + P_{x,\text{IDs}}(f) + \ldots$, with each source having different dependency on frequency. The PSDs of each source is unknown and so is the effectiveness of the orbit correction in reducing the motion due to each source. Nevertheless, the individual source's power in the bands 0.01 Hz to 200 Hz or 1000 Hz must be allocated some reasonable values that sum up to the specifications for rms motion in Table 3.3-2. These power requirements can be determined based on experience with existing devices and orbit correction systems.

Table 3.3-3 shows the allocation of power in the two specified bands. The power for the "total" are the squares of the rms values in Table 3.3-2, while the other rows should sum up to the total within rounding error. Some values may seem strangely low since it is not customary to characterize orbit motion with the square of the amplitude. The table values will be explained below row by row.

Note that in the horizontal position power is not derived from the 5%-of-beam-size requirement; it is made lower by some factor 15 because it is thought that APS should be capable of providing this stability. The horizontal divergence power is still derived from the 5%-of-beam-size requirement.

A value of 1 $(\mu\text{m})^2$ was selected for PM IDs for the 0.01-200 Hz band in the x coordinate because it is a reasonably low fraction and most of the power is expected to be in the 0.01-1 Hz range, a tiny slice of the band. This provides a greater allocation to the baseline orbit noise, in which there are many more

Table 3.3-3: Allocations of APS beam stability goals to various system groups. The two values in each table cell are for the 0.01-200 Hz and the 0.01-1000 Hz bands respectively.

System	$\int \mathbf{P_x df}$ $(\mu\text{m})^2$	$\int \mathbf{P_{x'} df}$ $(\mu\text{rad})^2$	$\int \mathbf{P_y df}$ $(\mu\text{m})^2$	$\int \mathbf{P_{y'} df}$ $(\mu\text{rad})^2$
Total	9.0/36	0.33/1.30	0.18/0.71	0.048/0.194
SR baseline	7.0/34	0.27/1.24	0.08/0.34	0.023/0.096
PM and IEX IDs	1.0/1.0	0.03/0.03	0.01/0.01	0.001/0.001
Pulsed EMVPU	1.0/1.0	0.03/0.03	0.01/0.01	0.001/0.001
SPX	0.0/0.0	0.00/0.00	0.08/0.34	0.023/0.096

sources. The power allocated for the 0.01-1000 Hz band is the same, since the IDs do not produce perturbation in the 200- to 1000Hz range.

The divergence power allocated to PM IDs is 0.03 $(\mu\text{rad})^2$, which is one tenth of the total divergence power, a reasonable ratio to pick in order to provide a higher allocation to the baseline orbit noise.

About one tenth of the total power was selected for the vertical plane position power for the same reason. Since the total position power limit is small in the first place, it may be challenging for the PM IDs to meet the requirement.

The vertical divergence power is determined from dividing the position power by β_y^2, because both are derived from a 5%-of-beam-size requirement.

The pulsed EMVPU will have the same behavior as the PM IDs when fast changes are requested with no pulsing, which should be manageable with orbit correction. Hence, in this mode the requirements for the EMVPU are the same as for the PM IDs. The budget for the EMVPU in pulsed mode (nominally 10 Hz) has been set at the same level, even though the spectrum will of course be much different.

Cavity phase regulation of the SPX system is expected to be challenging, as described in section 3.6.3.2. Phase and amplitude noise will produce orbit noise in a large band (up to perhaps 200 kHz). It is expected that, at least in the 0.01- to 200-Hz band, orbit correction will reduce the power density of orbit noise. Since both baseline orbit motion and SPX are very challenging in the vertical plane, it was decided to split the budget approximately in half. Consequences of the SPX beam motion allocation on SPX system specification are shown later in this Chapter in Table 3.6-4.

3.3.3 Beam-Stability Limitations

To arrive at a coherent stability improvement strategy, one must have a clear understanding of the fundamental mechanisms that limit the ability to precisely and accurately measure and correct beam disturbances. These mechanisms fall into a number of broad categories that impact beam stability over a variety of time and frequency scales. At the highest level, one can separate beam instability into three classes:

- Environmental, i.e., true sources of instability that actually disturb the particle beam,
- Systematic, i.e., erroneous readbacks from diagnostic devices, and

- Algorithmic, i.e., errors in how corrections to the particle beam are computed or applied.

The time and frequency scales of primary interest are dictated by the nature of x-ray experiments conducted at the APS. A large proportion of these involve photon counting, which effectively integrate the on-sample x-ray flux over some time period ranging from minutes or hours down to tens of milliseconds. In addition, experiments are conducted in such a fashion that one desires to achieve the same results tomorrow or even next week as were seen today, without performing major beamline adjustments.

Since the inception of the APS real-time orbit correction system c. 1998, one standard measure of AC beam stability has been the amount of rms motion within a frequency band from 0.01 to 30 Hz, averaged over a set of high-resolution rf beam position monitors located nearest to ID x-ray source points. As x-ray experiment integration times continue to fall, this measure needs to be expanded to cover higher frequencies. As shown in Table 3.3-2, the proposed standard measure of AC beam stability for the APS Upgrade will cover motions in the frequency range from 0.01 to 200 Hz.

On longer time scales, a number of difficulties arise, in that it is very difficult to distinguish between long-term drift resulting from electronics, real ground motion, and thermally induced mechanical component motion. In spite of these difficulties, a significant goal of the APS Upgrade is to control long-term beam motion at x-ray source points using the rms motion in microns over a period of one week as a measure.

3.3.3.1 Environmental Disturbances

Major sources and magnitudes of beam motion and their respective amplitudes and time scales are as follows:

- Vacuum chamber water system temperature, 0.1 to 0.2 °F variation over minutes to hours.
- Tunnel air and electronics temperature, 0.8 to 1.2 °F variation over hours to days.
- Diffusive ground motion, 1.7 to 5.5 microns variation over weeks to months.
- Earth tides, tens of microns over hours.
- Girder and magnet vibration, micron-scale, 1 to 100 Hz.
- Power-supply noise, submicron scale, 1 Hz to tens of kHz. This is the result of years of effort to identify and remediate problem components.
- Radio-frequency phase and amplitude noise, micron-scale, 1 Hz to several kHz, but typically narrow-band spectral lines at multiples of 60 Hz, with 360 Hz and 1800 Hz being most prominent.
- Insertion-device field integral variation due to gap changes, 5 to 10 microradians in seconds.

Of these sources, many have already been sufficiently suppressed. ID gap changes are strongly suppressed by the existing 10-Hz orbit correction algorithm, as are the effects of girder vibrations up to 60 Hz. Earth tides are dealt with using feedback of orbit circumference to the master oscillator rf

frequency. Power supply noise has similarly been dealt with, but in addition recent efforts to reduce 20-kHz "chopper noise" affecting fast correctors have been instrumental in the commissioning of a fast multibunch transverse feedback system. In short, sources of environmental noise in the frequency band from 0.01 to 60 Hz have had the most attention, with good success. The challenge to AC noise suppression lies at the higher frequencies up to 200 Hz and beyond. Fortunately technological solutions including outstanding commercially available beam position monitoring electronics and feedback system components provide a clear path forward in this area.

More challenging, and the subject of early R&D efforts, are those sources active in the time frame from hours to days, specifically thermal variation and diffusive ground motion. Research has already begun in these areas.

3.3.3.2 Systematic Errors

The APS has the most diverse set of beam position monitor (BPM) diagnostics used in feedback of any light source in the world. This has had many advantages but has come with its own costs. Among the advantages has been the ability to cross-check readings from different diagnostics, e.g., narrowband rf BPMs near the insertion device source points in comparison with photon BPMs located far downstream. A distinct disadvantage has been maintenance and support of the hardware and software needed to manage all of the different flavors of systematic errors affecting the different systems. The different BPM types and their most significant systematic errors are as follows:

- Narrowband rf BPMs near ID source points have the advantage of having good (micron-scale) long-term drift performance over days. The asynchronous switching between inputs, which underlies their operating principle, results in spurious spectral lines that can occasionally wander below 100 Hz where the real-time feedback system is active. Their AC noise floor is at best some tens of nm /$\sqrt{\text{Hz}}$.
- Broadband rf BPMs used between ID source points have excellent high-frequency performance, but suffer from intensity dependence and fill-pattern dependence, producing several microns of long-term drift and several-micron variations during top-up operation as the fill pattern changes with each shot from the injector. Also, these systems are impacted by a spurious microwave mode present in the large-aperture chambers that mimics a vertical beam position signal.
- Bending magnet photon BPMs are based on photoemission and use pairs of molybdenum blades located above and below the accelerator midplane near bending magnet beamline source points. Bending magnet photon BPMs are the most reliable diagnostics, suffering from very few systematic errors, although they only provide vertical position information. They have excellent AC and DC performance at the submicron level.
- ID photon BPMs, while nearly identical in principle to the bending magnet variety, suffer from the fact that their signal sources, the IDs, are variable. Extensive work to compensate for gap-dependent variations in calibration factor and position offset provide correction only at the level of about 10 microns over the normal range of gap values. Their configuration and compensation has gotten even more complex with the advent of canted undulator beamlines, where cross-talk between BPMs in the same front end result from stray radiation and ID field integral variation. Very careful background subtraction is also necessary to deal with stray radiation from local steering corrector magnets.

3.3.3.3 Orbit-Correction Algorithms

Orbit correction at the APS uses two concurrently operating frequency-band-separated feedback algorithms. Motions slower than about 1 Hz are corrected by a singular value decomposition (SVD) algorithm operating at 10 Hz, with access to the full complement of 278 steering correctors in each plane and over 500 BPMs. Higher-frequency motions are suppressed by the real-time feedback system operating at 1.5-kHz sample rate, which uses a smaller response matrix with at most 38 steering correctors and 160 BPMs.

The 10-Hz algorithm typically uses between 80 and 120 steering correctors per plane and several hundred BPM channels. Performance of the nearly 15-year-old fast feedback is limited by processing power, system bus bandwidth, real-time network throughput, and the availability of fast-steering corrector magnets. All APS steering correctors are identical six-pole magnets wired as combined-function horizontal-vertical steering dipoles. The distinction between fast vs. slow correctors results from the type of vacuum chamber used. Slow correctors are mounted around thick-walled aluminum extrusions which, limit their bandwidth to a few Hz as a result of strong eddy currents, while the 38 fast correctors have steel spool piece chambers.

One consequence of running parallel feedback algorithms is the existence of a frequency dead-band near 1 Hz. This has been compensated reasonably well using a feedforward algorithm that essentially informs the fast system what the slow system is about to do on each 10-Hz sample, to prevent the fast system from fighting against the slow system [3.3-2].

While SVD provides a method for inverting possibly near-singular rectangular matrices, standard practice for the slow feedback has been to restrict the number of steering correctors rather than omit modes with small eigenvalues. For the fast feedback, the number of correctors has necessarily been limited to 38, but in addition, small-eigenvalue modes are eliminated, providing a robust and stable algorithm. Additionally, the capability exists to use weighted SVD that preferentially locks down specific sets of BPMs; however, this capability has not been used during user beam operation.

There are a number of auxiliary algorithms that are independent of the fast and slow feedback. A very slow feedback varies the rf frequency in order to fight Earth tides, which stretch the ring circumference. A fast transient feedforward algorithm drives fast-steering correctors near the injection point to reduce the effects of pulsed injection during top-up operation.

One important element of the APS Upgrade beam stabilization program will be to perform extensive simulations of different feedback system topologies, sample rates, and algorithms to arrive at a system optimized to meet long-term stability goals. Increasing the fast-feedback sample rate by an order of magnitude is expected to extend the closed-loop bandwidth from 60 Hz to 200 Hz or more [3.3-3]. Increasing the number and placement of fast correctors are similarly expected to produce substantially improved stability. These simulations will include the known dynamics of the different BPM systems, steering power supplies, and magnets. In addition, the effects of different lattice functions and errors in the response matrix will be modeled. The effects of SPX will similarly need to be studied.

3.3.4 Beam Stability Developments

Major new developments since the time of the conceptual design are as follows:

- First high-power demonstration and extensive testing of the grazing-incidence ID x-ray beam

position monitor (GRID-XBPM) using radiation from two in-line 3.3-cm-period Undulator A devices [3.3-4].

- New simulation results supporting the strategy for increasing the real-time feedback system sample rate from 1.5 kHz to 20 kHz [3.3-5].
- Installation and commissioning of 22 out of 40 sectors of broadband BPM FPGA-based data acquisition electronics (BSP-100) using programmatic funds.
- Evaluation of x-ray BPM data acquisition methodologies with beam [3.3-6].
- Demonstration of the new BSP-100 data acquisition interface to the present narrowband Bergoz BPM electronics with beam.
- Demonstration of improved vacuum chamber water temperature stability to the level of $\pm$ 0.02 °F by detailed tuning of system regulation parameters.

3.3.5 APS Upgrade Plan

The goals listed in Table 3.3-2 are challenging but achievable in the context of the APS Upgrade. To achieve them, a substantial investment in BPM technology, real-time data networking, mechanical engineering, and high-level software will be required. Specific items addressing beam stability for the APS Upgrade are as follows:

- New BPM electronics — The obsolete BPM electronics for the narrowband rf and photon BPMs will be replaced with modern systems, providing improved resolution and drift characteristics.
- X-ray BPM system enhancement — For new beamline front ends being installed as part of the APS Upgrade, the new x-ray fluorescence-based GRID-XBPM design and ancillary detectors have been integrated into the front-end mechanical design. Existing photon BPMs will continue to be supported for refurbished front ends as needed.
- Storage ring real-time feedback system upgrade — The system will be upgraded to improve the bandwidth from approximately 60 Hz to 200 Hz. The number of fast corrector magnets that can be used will also be doubled.
- BPM mechanical motion sensing system — Critical BPMs will be instrumented with sensors to allow compensation for temperature-induced motion of the monitors.

The scope of the effort and the benefit expected from each of these items are summarized in Table 3.3-4.

3.3.6 New BPM Electronics [U1.03.02.02.01]

Table 3.3-5 is a list of the different types of BPM electronics presently in use to control APS beam stability [3.3-7].

Table 3.3-4: Beam stability upgrades for the APS Upgrade.

Item	Scope	Expected Improvement
New BPM electronics and data acquisition	80 high-resolution rf BPMs, 80 interlocked rf BPMs, 70 ID photon BPMs, 70 BM photon BPMs	Factor of 2, AC noise floor
New hard x-ray BPM systems	14 complete units installed in new front ends	Factor of 2, long-term pointing stability
Real-time feedback system	Complete replacement with modern components	Extend closed-loop bandwidth from 60 to 200 Hz; reduce AC beam motion by a factor of 4
BPM mechanical motion sensing	Install for 14 GRID XBPMs and 68 rf BPMs	Factor of 2, long-term drift

Table 3.3-5: Installed APS BPM electronics.

Type	Location	Advantages	Disadvantages
Narrowband rf	ID source points	Long-term stability	Aliasing; micron-scale drift
Original broadband rf	Ring arcs	Large installed base	Obsolete; intensity dependence
FPGA-based broadband rf	Ring arcs	Low noise	Intensity dependence
Bending magnet photon BPMs	BM front ends	Long lever arm	Vertical only
Insertion device photon BPMs	ID front ends	Long lever arm	Gap-dependent errors

Narrowband rf BPM electronics (Commercial, Bergoz) monitor the particle beam and are attached to capacitive button pickup electrodes mounted on the small-aperture ID vacuum chambers (IDVCs) in pairs (or triplets for canted undulators). Each ID source has an additional pair similarly instrumented but using electrodes mounted on the large 42 $\times$ 80 mm elliptical chambers closest to the insertion devices. These units are used to detect misaligned beams to trigger a fast beam abort (< 1 ms). The best AC performance for the Bergoz receivers using the most advantageous button geometry associated with the IDVCs is no better than about 30 nm /$\sqrt{\text{Hz}}$.

All other rf BPM electronics use the same broadband (10 MHz) rf monopulse receiver front end attached to the large elliptical chambers in the ring arcs. Using operating funds, their obsolete data acquisition is in the process of being replaced to include a modern field-programmable gate array (FPGA) design and fast sampling (14 bits, 88 MS/sec) [3.3-8]. The APS-designed data acquisition board used for this purpose is called the BSP-100 module (bunch signal processor).

Commercially available broadband rf BPM electronics from Instrumentation Technologies, Solkan, Slovenia, have been deployed at the Diamond Light Source among many others. A set of these electronics, called Libera Brilliance+, were procured for evaluation purposes. Shown in Figure 3.3-1 is a comparison of the achievable noise floor for Libera Brilliance vs the APS BSP-100 module. The electronics in this case were attached to opposite ends of the same small-aperture IDVC associated with

the APS 35-ID undulator source point.

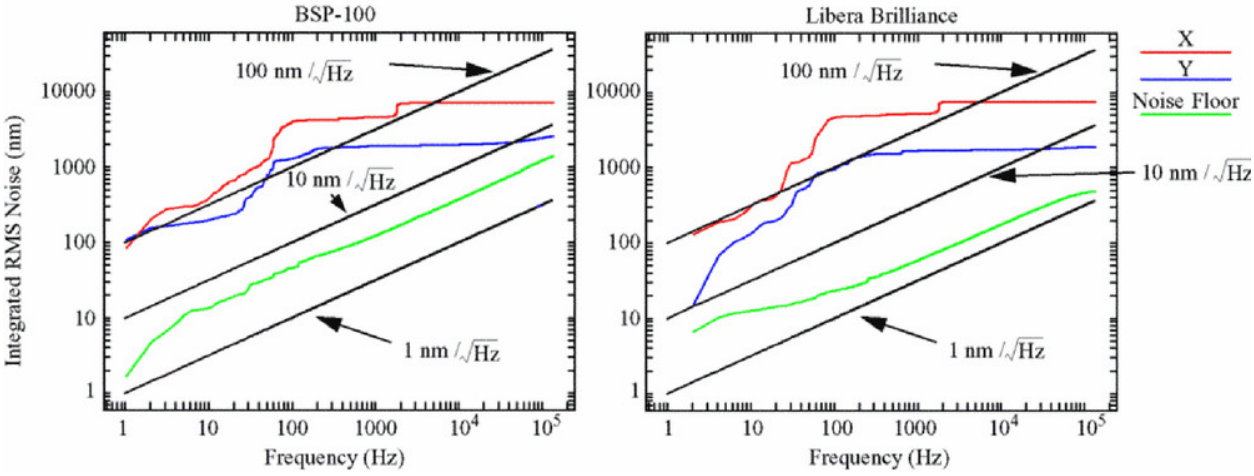

Figure 3.3-1: Comparison of AC performance of BSP-100 (left) and Libera Brilliance (right).

To determine the noise floor (green traces in Figure 3.3-1), a single button was split using a four-way rf splitter. In this case the conversion to microns corresponded to that for the horizontal plane, which in this case has the highest geometric sensitivity. Also shown are the present levels of real beam motion as a function of frequency both horizontally (X) and vertically (Y). The Libera module shows better noise performance, approaching 2 nm /$\sqrt{\text{Hz}}$ and in addition has shown long-term stability at the level of 200 nm p-p over a 24-hour period [3.3-9]. While the BSP-100 modules have the advantage of lower cost and acceptable AC performance, the monopulse rf BPM receivers they sample do not have good enough long-term drift performance and have unacceptably large intensity and fill-pattern dependence.

The Libera solution appears to satisfy the requirements and has been deployed at a large number of light sources but is relatively costly. A new design has been developed for the NSLS-II project at Brookhaven National Laboratory and an example of their design, including an analog front end and a digital front end (cell controller), has been loaned to the APS for evaluation [3.3-10]. At the time of this writing, the NSLS-II design does not yet meet APS requirements: the calibration tone technique for matching channel-to-channel variations has not been demonstrated. Further, NSLS-II uses actively cooled and temperature-regulated electronics racks to meet their requirements, while the Libera solution imposes no such requirement.

Because the ID source points are critically important, a pair of new BPM electronics will be deployed at each of the 35 APS ID sources, with three units for canted undulator straight sections. The Libera Brilliance+ unit has been specified for this purpose in the preliminary design.

It is planned to replace the data acquisition for both the Bergoz system and the photon BPM systems. For the interlocked Bergoz BPM electronics, the APS-designed BSP-100 module will be used for data acquisition. providing the same hardware interface to the new real-time feedback system as for the monopulse BPM system. For the large-aperture (42 mm by 85 mm) vacuum chambers that use 1-cm-diameter capacitive button pickup electrodes, the intrinsic noise performance of the Bergoz receivers is so poor that no dramatic AC improvement was seen. This technique does, however, eliminate known aliasing effects by forcing the internal Bergoz multiplexing to be synchronous with the APS storage ring revolution period. The Bergoz BPM system together with BSP-100 processing will still provide excellent DC performance and its beam missteering interlock function continues to be essential.

The present obsolete photon BPM data acquisition electronics is the same as that used by the installed narrowband Bergoz receivers. Alternatives that have been tested are the BSP-100, the 24-bit National Instruments 9239 digitizer, and a module from Instrumentation Technologies known as the Libera Photon, also 24 bits.

In the evaluation of x-ray BPM data acquisition systems, it is clear that the most challenging requirement will be dealing with the extremely wide dynamic range (4 decades or more) in signal amplitude associated with the exponential dependence of signal strength on ID gap. When sampled directly at a rate of 20 kHz, use of 24-bit resolution shows a clear advantage over 16-bit sampling. Data acquisition hardware from National Instruments and Instrumentation Technologies has been evaluated with beam during machine studies. The use of matched sets of logarithmic amplifiers was briefly considered to handle the wide dynamic range; however, obtaining the necessary level of channel-to-channel matching is deemed impractical at this point. For the remaining photoemission photon BPMs to be used in front ends with no change or simple refurbishment, the APS BSP-100 data acquisition module is planned.

Shown in Table 3.3-6 is a listing of the planned scope for BPM electronics upgrades.

Table 3.3-6: BPM electronics scope.

Location	Present	Replacement	Quantity
IDVC pickups	Bergoz	Libera Brilliance+	80 BPMs
Interlocked P1 pickups outboard of IDVC	Bergoz	Bergoz + BSP-100	80 BPMs
Bending magnet photon BPMs	preamp + digitizer	Preamp + BSP-100	70 BPMs = 140 channels
Unmodified ID XBPMs	preamp + digitizer	Preamp + BSP-100	40 BPMs = 160 channels
GRID-XBPM, IM1,2, XBPM2 for new / upgraded front ends	preamp + digitizer	New electronics	15 sectors = 165 channels

3.3.7 X-ray Beam Position Monitor System Enhancement [U1.05.02.02.10]

The GRID-XBPM lays the foundation for achieving true sub-microradian long-term pointing stability, eliminating many of the deficiencies of the present photoemission-based photon BPMs. Providing a true center-of-mass measurement in the vertical plane, it largely eliminates gap-dependent systematic errors, providing a calibration that is largely independent of gap over a range of gaps from 11 to 40 mm and beyond. This device has been integrated into the design of both the new high heat load (HHL) and canted undulator (CU) beamline front ends. It is one element of an x-ray alignment system built into the front ends, which includes two intensity monitors to track transmission through upstream apertures, and a second x-ray beam position monitor (XBPM) built into the exit mask just outside the shield wall.

A major accomplishment for the GRID-XBPM was the direct detection and compensation of trajectory steering errors internal to the insertion device. This type of error, with amplitude up to 10 microradians, is undetectable using rf BPMS or existing photoemission-based photon BPMs.

Located at a longer distance (18.6 m) from the source, XBPM are well positioned to measure the beam direction. A new generation of hard x-ray BPM using copper K-edge x-ray fluorescence (XRF) from the undulator collimator surfaces are being developed for the APS Upgrade under WBS No. 1.05.02.02.10. Extensive descriptions of the GRID-XBPM and associated systems are given in references [3.3-11] and [3.3-12]. A description of how the GRID-XBPM is to be integrated into the new HHL and canted beamline front-end designs is given in the "Next Generation X-Ray Beam Position Monitors" section of this report. Highlights relevant to beam stability issues are presented here.

The next-generation XBPM consists of four components: (1) the grazing-incidence insertion device x-ray beam position monitor (GRID-XBPM or XBPM-1), (2) beam intensity monitor No. 1 (IM1), (3) the second XBPM (XBPM-2), and (4) the beam intensity monitor No. 2 (IM2). XBPM-1 mainly measures the x-ray beam's angle, IM1 and IM2 are used for beam-based alignment to relate the XBPM position readings to the fixed apertures of Fixed Mask 3 (FM3) and the Exit Mask, respectively. XBPM-2 provides an additional, independent measurement outside of the feedback loop for quality assurance of the beam stability. The diagram shown in Figure 3.3-2 indicates the relationship between the different elements of the enhanced beam stabilization systems, for a specific HHL insertion device beamline.

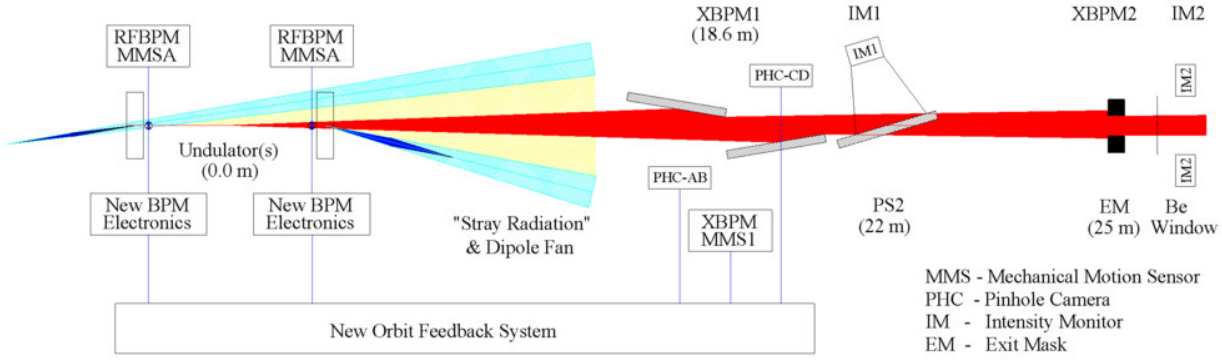

Figure 3.3-2: Diagram indicating the different components of the enhanced beam stabilization systems.

To minimize interference with user operations, the front-end XBPM derives x-ray beam position information entirely from the fringe beam outside of the undulator beam's central cone. In the case of an HHL front end for two inline undulators, the XBPM-1 intercepts the x-ray beam on the left and right sides of the central cone to provide the beam position information. In the case of canted undulators, the XBPM-1 intercepts the x-ray beam above and below the two central cones of the canted undulators to provide information on the beam positions. In normal operations, the beams transmitting through the XBPM-1 will be fully utilized by the XBPM-2 or Exit Mask.

Recently, a GRID-XBPM was designed, fabricated, and tested in the Sector 29 ID beamline (29-IDA). The tests demonstrated several design characteristics of the new XBPM as described below.

Compared to the old photoemission-style XBPMs based on the gold-coated diamond blades, the GRID-XBPM's bending magnet radiation background was reduced by at least 20-fold, as shown in Figure 3.3-3. Plotted are x-ray pickup readbacks as a function of source steering angle for two ID gap settings $G = 29$ mm and $G = 180$ mm, for the photoemission XBPM at Sector 7 (bottom) and the new GRID-XBPM (top). The curves labeled AB are the sum of pickup signals A and B which are offset horizontally from the ID beam center line, while curves CD are the corresponding sum for pickups

diametrically opposite to AB. With the gaps open ($G = 180$) the GRID signals are a factor of 100 smaller than for the photoemission XBPM, and significantly smaller near the ID beam axis ($x' = 0$). When the gaps were closed to 29 mm, the narrow ID beam profiles become visible. The range of the scan had to be limited in this case to avoid tripping the beam missteering interlock. In the case of the GRID-XBPM (top), the $G = 29$ curves have not been multiplied by 100. Although the background signals are still present, they are much smaller than the peak signals from the insertion device and not visible on this scale.

Even if perfect on-axis background subtraction could be performed for the photoemission XBPMs, the horizontal gradient of the background results in a variable calibration factor. This is quantified by the slope ratio defined as the horizontal gradient with gap open ($G = 180$) divided by the gradient with the gap closed. Shown in Figure 3.3-4 is a plot of this ratio for a number of different undulator gap settings. The GRID-XBPM for these tests was located in the first optic enclosure at Sector 29. Three sets of GRID data are shown, corresponding to three different horizontal apertures (2, 3, and 4 mm respectively), and labeled S29-2, S29-3, and S29-4. The same ratio was computed for four photoemission XBPMs with different geometries at Sectors 7, 9, 23, and 32. Even with perfect background subtraction, the signals from the GRID-XBPM are still 10- to 100-fold cleaner than for the photoemission XBPMs.

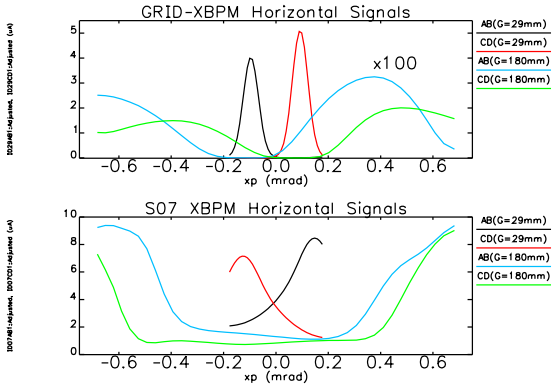

Figure 3.3-3: Measurements of the signal and background levels of the GRID-XBPM (top) and the Au-coated blade (bottom).

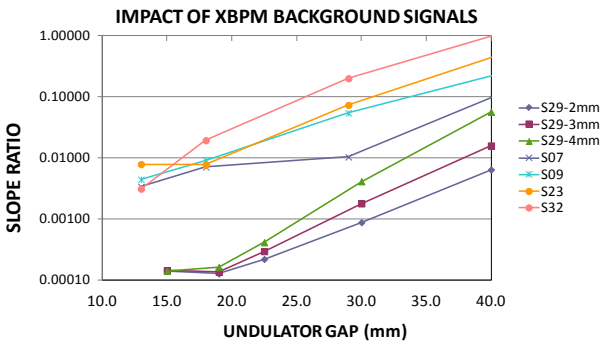

Figure 3.3-4: After background subtraction, the GRID-XBPM signal is approximately 10- to 100-fold cleaner.

For an experiment involving exchanging two inline undulators with different internal steering, the GRID-XBPM correctly monitored changes of the central-cone x-ray beam position where the rf BPM was unable to do so. When the beam was scanned vertically across the entrance slits for these two different undulators, the beamline monochromator measurements agreed with the GRID-XBPM data, showing that the x-ray beam from the upstream and downstream undulators of S29 were different by 4 μrad. Measurements by the rf BPMs at the same time did not register this difference, as shown in Figure 3.3-5. For each configuration, the beam was scanned both upwards and downwards indicating the level of repeatability, e.g., US-UP vs. US-DOWN curves were essentially the same.

Shown in Figure 3.3-6 are data from an experiment where the GRID-XBPM was used to control the orbit feedback system, using an ion chamber downstream of a monochromator as a primary diagnostic, represented by the data labeled 'Mono Flux' in the figure. The monochromator used required frequent optimization, so only the peak values following a machine change (items labeled (1) through (6) in

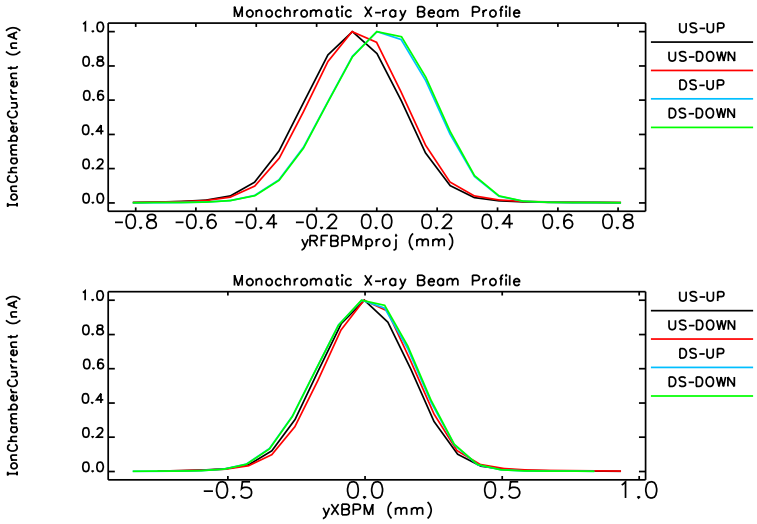

Figure 3.3-5: Monochromatic beam profiles plotted using projected rf BPM position (top) and GRID-XBPM position (bottom). The observed shift in the top plot results from steering internal to the insertion device, which cannot be detected using rf BPMs alone.

the figure) are relevant. Events (1) through (4) represent the closing of one of the two insertion device gaps to the fixed monochromator-set x-ray energy coincident with the opening of the other gap. The data labeled US and DS power indicate gap changes. Feedback using the GRID-XBPM automatically kept the central-cone centered on the beamline's (1 mm x 0.3 mm) entrance aperture and maintained monochromatic flux constant through the four gap exchange events.

If instead the rf BPMs alone were used for orbit control (event (5)), a loss of 10% flux on the entrance slits was observed due to internal steering. Switching back to using the GRID-XBPM (event (6)) recovered the lost flux. This phenomenon had never before been directly observed.

The intensity monitor IM1 will be used during machine studies when the photon shutter (PS) is closed. It uses the XRF and Compton-scattered photons to measure the flux transmitting XBPM-1 and FM3. Using beam-based alignment techniques, the XBPM-1 position readings can be correlated with the FM3 center position or the XBPM-1 aligned with the FM3 immediately downstream of the XBPM.

The intensity monitor IM2 will use elastically and inelastically (Compton) scattered photons to measure the photon flux exiting the front end through the beryllium window into the beamline during user operations. In machine studies when the PS is open, a beam-based alignment technique can correlate the XBPM-2 position readings with the Exit Mask center position, or center the x-ray beam through the Exit Mask using the peak IM2 readings.

An additional x-ray beam position monitor, XBPM-2, will be implemented using the Cu-K XRF from the Exit Mask. When properly set up, a zero XBPM-2 position readout will indicate a centered undulator beam on the Exit Mask, thus allowing quick diagnosis and maintenance of correct beam position.

In addition to replacing XBPM electronics for the entire ring, each new beamline front end to be installed will include a GRID-XBPM, IM1 and IM2 intensity monitors, and XBPM-2. There are 14 new front ends being installed as part of the APS Upgrade.

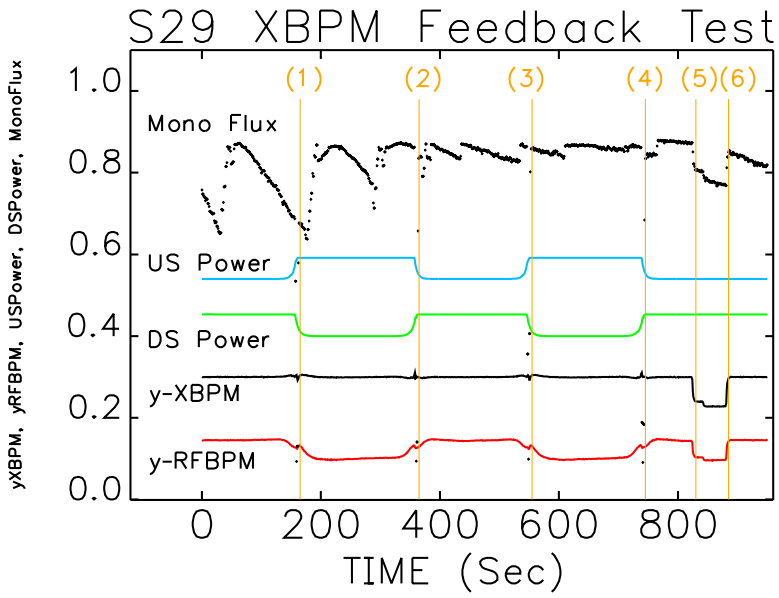

Figure 3.3-6: In a demo experiment, GRID-XBPM was used for orbit feedback and helped maintain constant flux when the upstream and downstream undulators were used as sources.

3.3.8 Storage Ring Real-Time Feedback System Upgrade [U1.03.02.02.03]

One important element of the APS Upgrade beam stabilization program will be to continue the development of extensive simulations of different feedback system topologies, sample rates, and algorithms to arrive at a system optimized to meet stability goals. Increasing the fast-feedback sample rate by an order of magnitude is expected to extend the closed-loop bandwidth from 60 Hz to 200 Hz or more [3.3-5]. Increasing the number and placement of fast correctors is similarly expected to produce substantially improved stability. These simulations included the known dynamics of the different BPM systems, steering power supplies, and magnets. In addition, the effects of different lattice functions and errors in the response matrix will be modeled. The effects of SPX will similarly be studied.

The present APS real-time feedback (RTFB) system operates at a 1.534 kS/sec sample rate and is limited by processing power and data communication bandwidth to use a maximum of 38 steering correctors and 160 BPMs [3.3-13]. It was commissioned in 1997 and has had incremental code patches over the years, but uses many components (digital signal processors, reflective memory) that are 15 or more years old. The closed-loop bandwidth of this system is approximately 60 Hz. To achieve 200-Hz closed-loop 3-dB bandwidth using fast steering corrector magnets, an increase in sample rate by an order of magnitude is needed, to 19.4 kS/sec, which is equivalent to the revolution frequency divided by 14. By using fast digital interfaces to the low-level rf controls of the main 352-MHz and SPX 2815-MHz rf systems, it will be possible to achieve closed-loop 3-dB bandwidth of 1 kHz. Use of modern networking, digital signal processing, and FPGA technology will allow the creation of a reliable system with vastly enhanced capabilities for a modest investment. Details of the engineering specifications are given in reference [3.3-14].

Access to the full complement of rf and photon BPMs, approximately doubling the number of fast-

steering correctors, with real-time access to all steering correctors, slow and fast, should allow reduction of beam motion by a factor of four or more. This implies an increase of required computation power two orders of magnitude beyond that presently available. Simulation efforts to validate this estimation are ongoing.

The solution to the computation bottleneck is field-programmable gate arrays (FPGAs). These devices allow the implementation of highly parallel processing and are capable of clock rates exceeding 300 MHz. This offers a significant performance increase over traditional digital signal processors, which have limited parallel processing capability. For example, dot products, digital filters, and feedback controllers would be computed in parallel rather than sequentially. In addition, the FPGA may be programmed to optimize algorithm implementation to increase performance.

Newer BPM processors such as the APS-developed BSP-100 and the Libera units from Instrumentation Technologies provide high-speed serial data streams via industry-standard small form-factor pluggable (SFP) optical transceivers. Modern FPGAs provide support for these high-speed serial links. It is envisioned that individual high-speed data links would be provided for each BPM processor, connecting the data streams directly to the FPGA. This avoids the system bus bottleneck.

The new system nodes will need to communicate to the APS control system either via an embedded processor running EPICS or a system bus to a modular processor that runs EPICS.

The existing real-time feedback system has a number of useful features, including the “DSP scope,” which is essentially a 40-channel synchronous waveform acquisition system with access to any of the hundreds of available signals. In addition, the AC voltmeter application allows for convenient lock-in type measurements, for example when measuring response to sinusoidal excitations. The DSP scope function that presently is available via the feedback master node could be moved to the FPGA nodes. Other diagnostics, such as AC voltmeter and beam rms motion calculations that operate on BPM vectors spanning all sectors, will need to be computed at a central node.

The RTFB system upgrade block diagram is shown in Figure 3.3-7. The heart of the system is an FPGA-based “double sector” controller that accepts input from two sectors’ worth of BPMs.

For each double sector, the new system needs access to all beam position monitors:

- 16 monopulse BPM channels (four BSP-100 modules)
- 4 narrowband (Bergoz) BPM channels (one BSP-100 module)
- 4, 5, or 6 Libera BPMs depending on canted beamline locations
- 4 ID XBPM channels
- 4 BM XBPM channels

The double sector controller interfaces to the real-time data network and applies the feedback algorithm to the BPM error vector to obtain the corrector error vector, which is then applied. Additional inputs from front-end x-ray intensity monitors will allow automated beamline alignment procedures to be developed using the DSP scope capability.

Additional nodes interfaced to the real-time data network will be available to apply beam-based feedback to the main and SPX rf systems using beam position, tilt, and arrival time errors as feedback signals. Recent experiments using a standard linac S-band phase detector [3.3-15] have shown them to

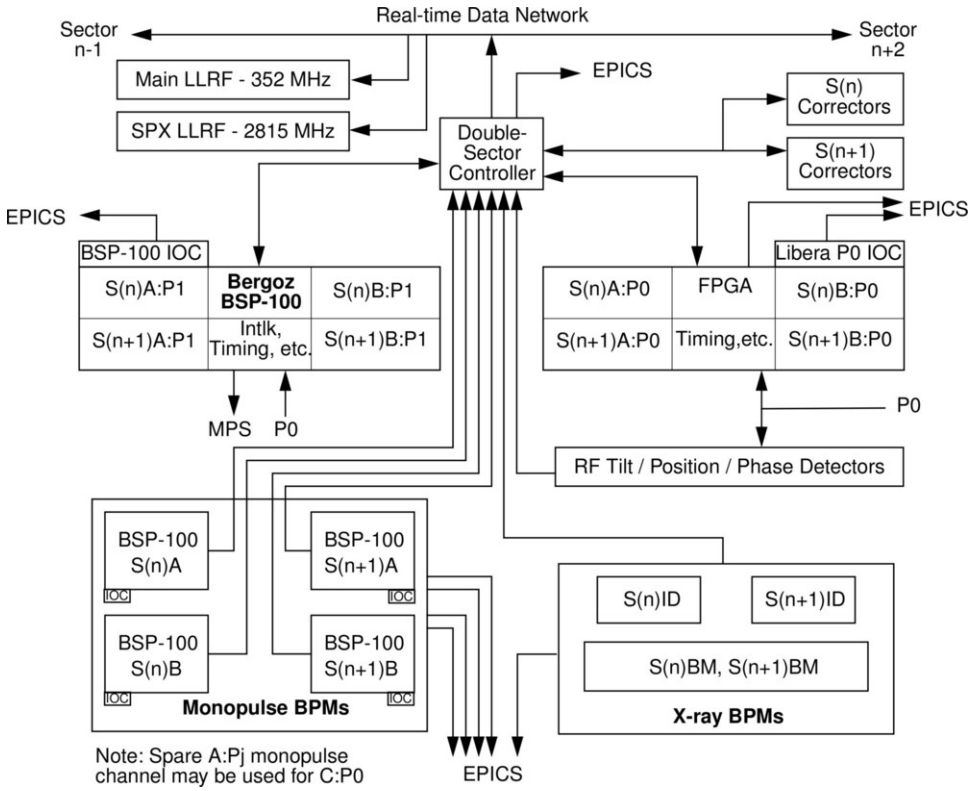

Figure 3.3-7: RTFB system "double sector" block diagram for sector n, where n is odd.

be suitable for measurement of beam arrival time and rf tilt [3.3-16, 3.3-17]. In Sector 5, 1 arrival time and 3 tilt monitors will be interfaced to the high-speed data network using a single standard BSP-100 module.

A significant effort will be required to design, fabricate, and install this system while integrating it incrementally with existing systems that must continue to function at their present level of performance or better through the course of the Project.

A simulator for the feedback system is under development following the original time-domain approach [3.3-18] for a 1995 SPEAR feedback upgrade. The time-domain approach allows analysis not possible or not convenient in the frequency domain, such as quantization noise, slew rate limits, and use of time-series measurement of orbit response of correctors. Also the different BPM types have different frequency responses. Thus depending on which BPMs are predominately used, one would have different loop behavior. In addition the simulator needs to handle mixed discrete and continuous time responses. `Matlab Simulink` [3.3-19] software handles such real-world difficulties, but it was found practical only for low-dimension systems. Our correction system has up to 360 digital inputs and 76 outputs that are coupled, which is cumbersome to enter in a `Simulink` model. Thus the C-program simulator will handle the specific case of orbit correction in the same way `Simulink` would in the general case. Since the software will be Self-Describing Data Sets (SDDS)-compliant, much of the work preparing and analyzing a simulation is offloaded to existing GUIs (e.g., correction matrix creation used in operations) and to standard post-processing tools.

3.3.9 BPM Mechanical Motion-Sensing System [U1.03.02.02.04]

In order to achieve long-term beam stability goals, all sources of mechanical motion of critical in-tunnel beam position monitoring devices must be carefully evaluated and appropriately addressed. This includes the effects not only of water and air temperature, but also Earth tides and diffusive ground motion.

A common measure of diffusive ground motion over extended time periods is the so-called "ATL law" whereby the mean square amount of ground motion taking place over a time period T between two points separated by a displacement L is proportional to their product, with proportionality constant A. This constant takes on values ranging from 10^{-8} to 10^{-4} μm^2/meter/second depending on the site. Research performed at Fermilab in relation to the next linear collider project indicated that a conservative range for A is between 10^{-6} and 10^{-5} μm^2/meter/second [3.3-20].

This means that the relative rms ground motion for 2 BPMs separated by 5 meters (the distance between BPMs mounted on an ID vacuum chamber) is in the range from 1.7 to 5.5 microns over a 1-week period. Dividing by the 5-meter lever arm results in ground-motion-induced angular instability between 350 nanoradians and 1.1 microradians rms. This significantly exceeds the goals stated in Table 3.3-2 for the vertical plane. Horizontally, this level of motion does not violate the stability requirements.

The use of XBPMs in beamline front ends is expected to further improve the ability to stabilize angular motion, being closer to the beamline point of use. The stability of the XBPM is affected by many factors at different time scales: (1) vibration of the XBPM body and its support structure excited by cooling water flow (from milliseconds to seconds), (2) distortion and expansion of the XBPM and its support structure due to temperature changes (from seconds to hours), and (3) diffusive motion of the floor/ground (from days to months). A good part of these changes can be monitored by a real-time position monitoring system that measures the XBPM position relative to a reference surface defined by a hydrostatic level system.

Figure 3.3-8 shows the design for such a position monitor integrated into the GRID-XBPM. Invar posts extending vertically from the granite support have integrated capacitive sensors to detect vertical and horizontal motions of the XBPM brazed assemblies relative to a hydrostatic level system datum vertically, and the granite support block horizontally. An analogous system will be developed for the rf BPM pickup electrodes nearest to the insertion device source points, with capacitive sensors mounted on top of Invar posts having low thermal expansion.

Shown in Table 3.3-7 is a listing of the components planned for the mechanical motion sensing system.

Table 3.3-7: BPM mechanical motion sensing system scope.

Component	Sectors	Channels
GRID capacitive sensors	14	28 V + 28 H
GRID hydrostatic level sensors	14	14 V
RFBPM capacitive sensors	35	70 V + 70 H
RFBPM hydrostatic level sensors	35	70 V

The baseline scope of work for the BPM mechanical motion sensing system will include instrumentation of each of the 14 GRID-XBPMs associated with new x-ray front ends with two pairs of capacitive

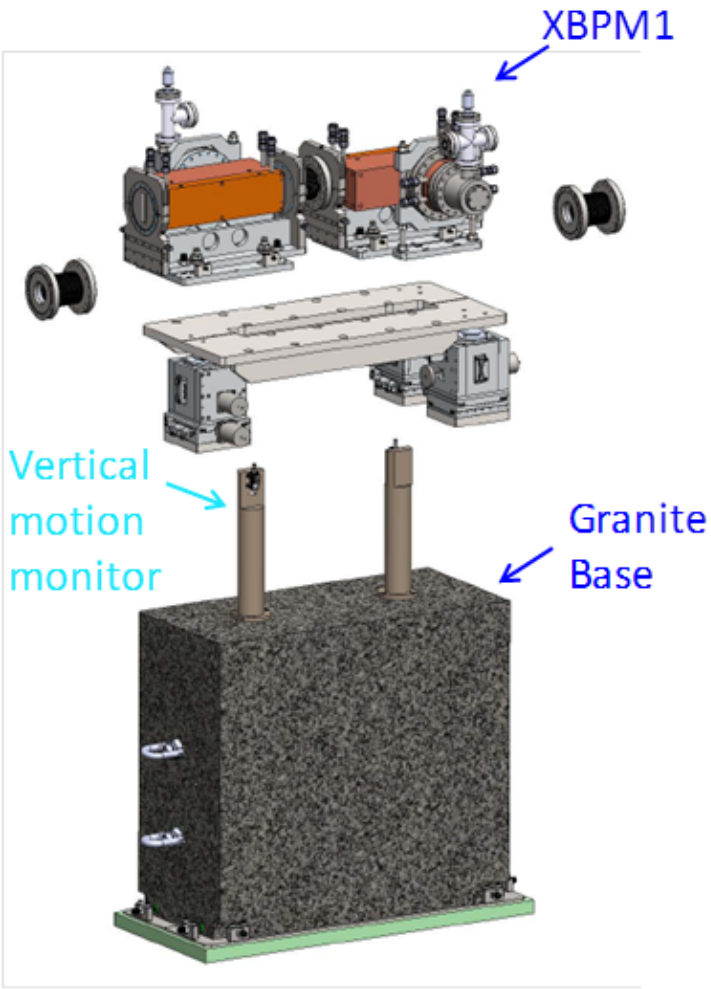

Figure 3.3-8: Mechanical motion sensing concept.

proximity sensors, one pair (horizontal + vertical) for each brazed assembly. Each GRID has two brazed assemblies that are susceptible to thermal motion due to the high levels of incident x-ray power. Ground motion of the floor upon which the GRID granite block is placed will be monitored with a hydrostatic level sensor, which is tied together in a network with the two addition sensors located at the upstream and downstream ends of the associated insertion device straight section, on the floor below the high-resolution rf BPMs.

For those sectors that employ existing or refurbished front ends (i.e., those that will retain the existing photoemission photon BPMs), only the high-resolution rf BPMs mounted on the small-aperture insertion device vacuum chambers will be instrumented with mechanical motion sensors. In any case, a total of 70 high-resolution rf BPMs will have capacitive sensors monitoring horizontal and vertical mechanical motion, and a hydrostatic level sensor on the floor.

In parallel with the mechanical motion sensing system network, ongoing incremental improvements to vacuum chamber water system temperature regulation have already demonstrated the ability to reduce variation to the level of $\pm$ 0.02 °F or better. This is of critical importance for the ID vacuum chambers,

upon which are mounted the high-resolution rf BPM pickup electrodes. Much work remains in this area to assess the relative impact of differential ground motion from Earth tides and diffusive motion, and mechanical distortions resulting from tunnel air temperature stability among other effects. Programmatic work continues on improving tunnel air temperature regulation.

3.3.10 Dependencies on Programmatic Work

There are a number of ongoing projects at various degrees of completion being executed with programmatic funds that directly or indirectly impact the attainment of ultimate beam-stability goals. These include:

- Monopulse BPM data-acquisition system upgrade
- X-ray BPM first article
- Storage ring vacuum chamber microwave mode dampers
- Additional fast steering corrector magnets.

3.3.10.1 Monopulse BPM Data Acquisition System Upgrade

A programmatically funded project was started c. 2005 to upgrade the data-acquisition portion of the aging broadband monopulse rf BPM system. To that end a fast-sampling FPGA data-acquisition board, the BSP-100, was developed. As of May 2012, 22 APS sectors had been upgraded with this new hardware, with hardware in hand for completion of the ring. Since some in-scope BPM electronics are envisioned to use the BSP-100 module, installation and checkout can be integrated in a straightforward fashion between ongoing electronics upgrades and the new APS Upgrade Project scope.

3.3.10.2 X-ray BPM First Article

A first-article grazing-incidence x-ray BPM based on x-ray fluorescence has been constructed using programmatic funding and was tested exhaustively at beamline 29-ID during operating period 2012-1. This test was extremely successful, adding confidence in the design methodology and providing a much-improved basis for cost estimation. Work is ongoing in the area of value engineering, to further improve cost effectiveness of the GRID-XBPM.

3.3.10.3 Storage Ring Vacuum Chamber Microwave Mode Dampers

A long-standing problem associated with the large-aperture APS storage ring vacuum chambers is a spurious microwave mode that mimics vertical beam position signals. Specifically this mode has a vertical component of electric field at the location of the BPM pickup electrodes and has a frequency that falls within the processing bandwidth of the monopulse BPM front-end electronics. A solution involving the insertion of conductive microwave gasket material into the chambers has been arrived at and installed in Sectors 3, 4, 6, and 29. The impact of not completing this work for the whole

ring will be that the affected sectors will have a reduced number of reliable BPMs. In any case, with the proposed BPM electronics upgrades, there will be adequate coverage to provide the desired improvements in beam stability. In addition, the presence of photon BPMs in the bending magnet beamlines provide high-quality vertical position information. Parts to complete this work are in hand and the work will be completed in coordination with other types of vacuum work on the large-aperture chambers as it is scheduled.

3.3.10.4 Additional Fast Steering Corrector Magnets

The 38 existing fast corrector magnets are mounted on steel spool pieces located between girders 1 and 2 in each sector. (Each APS sector comprises five girders plus an ID straight section.) By moving an existing slow corrector magnet downstream by one meter to the spool piece between girders 3 and 4, it will be possible to nearly double the number of available fast correctors with minimal cost. This has already been done in three sectors, with additional sectors funded. Completion of this task will improve the efficiency of the new real-time feedback system, allowing the suppression of orbit disturbances with shorter spatial wavelengths.

3.3.11 References

[3.3-1] L. Young and M. Borland. APS, Email exchange related to beam motion and emittance increase, (2011). APSU_1426487.

[3.3-2] C. Schwartz and L. Emery. Compensating the Frequency Deadband of the APS Real-Time and DC Transverse Orbit Correction Systems, Proc. of PAC 2001, pp. 1234–1236, (2001).

[3.3-3] O. Singh. Characterization of APS Real-Time Feedback, (2007). http://www.bnl.gov/nsls2/workshops/Stability_Wshop_4-18-07.asp.

[3.3-4] B. Yang et al. High-Power Beam Test of the APS Grazing-Incidence Insertion Device X-ray Beam Position Monitor, Proc. of BIW 2012, (2012).

[3.3-5] S. Xu et al. Simulation of the APS Storage Ring Orbit Real-Time Feedback System Upgrade using MATLAB, Proc. of IPAC 2012, pp. 2870–2872, (2012).

[3.3-6] R. Keane et al. Evaluation of a Variety of Photon Beam Position Monitor Data Acquisition Methodologies at the APS, Proc. of BIW 2012, (2012).

[3.3-7] O. Singh and G. Decker. Beam Stability at the Advanced Photon Source, Proc.of PAC 2001, pp. 3268–3270, (2001).

[3.3-8] H. Bui et al. Performance of FPGA-Based Data Acquisition for the APS Broadband Beam Position Monitor System, Proc. of BIW 2008, pp. 80–84, (2008).

[3.3-9] G. Rehm. Recent Development of Diagnostics on 3rd Generation Light Sources, Proc.of EPAC 2008, pp. 1016–1020, (2008).

[3.3-10] K. Vetter et al. NSLS-II RF BPM Update, Proc. of BIW 2012, (2012).

[3.3-11] B. Yang. Engineering Specification Document for the HHL GRID XBPM, (2012). https://icmsdocs.aps.anl.gov/docs/groups/world/documents/specification/aps_1431181.pdf.

[3.3-12] B. Yang. Engineering Specification Document for the Canted Undulator GRID XBPM, (2012). https://icmsdocs.aps.anl.gov/docs/groups/world/documents/specification/aps_1431182.pdf.

[3.3-13] J. Carwardine and F. Lenkszus. Real-Time Orbit Feedback and the APS, BIW98, AIP Conference Proceedings 451, pp. 125–144, (1998).

[3.3-14] G. Decker. Engineering Specification Document for the APS-U Realtime Feedback System, (2012). https://icmsdocs.aps.anl.gov/docs/groups/world/documents/specification/aps_1431171.pdf.

[3.3-15] N. S. Sereno et al. Phase Noise Studies at the Advanced Photon Source, Proc. of IPAC 2012, pp. 2873–2875, (2012).

[3.3-16] N. Sereno et al. Impact of Longitudinally Tilted Beams on BPM Performance at the Advanced Photon Source, Proc. of BIW 2012, (2012).

[3.3-17] N. S. X. Sun, G. Decker. Simulation Studies of Button Pickup Electrode Response to Longitudinally Tilted Beams, Proc. of BIW 2012, (2012).

[3.3-18] J. Corbett et al. Digital Orbit Feedback Compensation for SPEAR, Proc. of PAC 1995, pp. 2714–2716, (1996).

[3.3-19] Simulink by MathWorks. http://www.mathworks.com/products/simulink.

[3.3-20] V. Shiltsev and J. Lach. VLHC/NLC Slow Ground Motion Studies in Illinois, Proc. of PAC 2001, pp. 1470–1472, (2001).

3.4 Insertion Devices [U1.03.04]

3.4.1 Introduction

As described in section 3.1.2, providing higher flux and brightness in the hard x-ray regime, particularly at energies above 10 keV, is a significant aspect of the APS Upgrade mission. The APS is a third-generation light source, so the highest flux and brightness come from IDs. Many existing IDs at the APS are general-purpose devices that are not optimized for particular experiments. Hence, an important aspect of the Project is to provide tailored devices that will maximize performance at the wavelengths of interest to particular experimental programs.

There are many technological options for producing synchrotron radiation, allowing the radiation to be tailored to user requirements to a considerable degree. Immediately below, the present set of IDs is reviewed. Subsequent subsections cover those options that are included as part of the APS Upgrade. In some cases, multiple devices, each with a different period, are indicated, which may be served by a canted configuration (section 3.4.5.5), long straight section (section 3.2), and/or a revolver ID (section 3.4.2.5). Beyond these approaches, which utilize conventional hybrid permanent magnet devices, the Project will develop and deliver two short-period superconducting undulators, as described in section

3.5. These are a key technology for enhancing brightness near and above 20 keV while maintaining other operating characteristics of the APS, such as the maximum single-bunch current.

Table 3.4-1 summarizes the basic device types, their status, their features, and the quantities included in the APS Upgrade scope. In many cases, the period lengths are also known. For a few cases, however, the final period length has only been set tentatively but may still be optimized based on the needs of the individual beamline and to control cost.

Table 3.4-1: Summary of undulator types included in the Project.

Type	Status	Special Features	Number for Upgrade
Planar hybrid permanent magnet (HPM), out-of-vacuum	Many in use at APS	Established technology	3
Planar revolver HPM, out-of-vacuum	In use elsewhere	Selection of periods	5
Superconducting planar	APS Upgrade R&D development	Higher brightness, short period	2
APPLE-II	In use elsewhere	Polarization control, harmonic suppression, on-axis heat load suppression	2
EMVPU (electromagnetic variably polarizing undulator)	New (to be developed as part of the APS Upgrade)	Polarization control, fast switching	1

There is no in-vacuum undulator included in the scope, and the reason for this is explained in section 3.4.4. Accelerator physics requirements and issues related to insertion devices are reviewed in section 3.4.5. Finally, methods for optimizing the choice of undulators for best performance are described in section 3.4.6.

When the APS was originally built and undulators were being chosen for the beamlines, the decision was made to standardize on the 3.3-cm-period Undulator A. Undulator A would be tunable to produce a spectrum of radiation with neither big jumps in brightness nor gaps in the achievable photon energy and so would satisfy most users no matter what specific photon energy they might want. Standardizing on one type of undulator also allowed production efficiencies that lowered the cost per undulator and expedited undulator deliveries. A few users decided that they would be better served by a different period length (e.g., 2.7 cm or 5.5 cm) or a different type of undulator (e.g., an elliptical wiggler, which has since been removed), but most chose Undulator A.

Since then, more focused consideration of individual users' experimental needs has resulted in a greater variety of IDs. Table 3.4-2 shows the range of insertion devices presently installed.

The result of the early standardization on the 3.3-cm-period Undulator A is clear in that a total of 28 Undulators A of various lengths are installed. In addition, a few as-yet-uninstalled Undulators A are on hand, waiting until beamlines whose users have requested another Undulator A are ready for them. Of the other devices, the shorter period lengths were chosen for higher brightness, especially at higher photon energies; this higher brightness came at the cost of the low-energy end of the tuning range,

Table 3.4-2: Breakdown of the 48 presently installed IDs. Device length includes the ends — approximately one period at each end is less than full field strength. The K value is at 10.5-mm gap unless stated otherwise.

Period length	Number	Length (periods)	maximum K_{eff}
33-mm (Undulator A)	20	72	2.74
33-mm	1	70	2.74
33-mm	7	62	2.74
18-mm	1	198	0.46
23-mm	3	103	1.17[a]
27-mm	3	88	1.78
30-mm	2	79	2.20
30-mm	6	69	2.20
35-mm (SmCo)	1	67.5	3.08[b]
36-mm	1	57	3.15
55-mm	1	43	6.57
125-mm (IEX, $K_{x,y} < 2.73$ in Circular Mode)	1	38	$K_x = 3.86, K_y = 5.39$
128-mm (Circularly Polarized Und.)	1	16	$K_{x,y} < 2.8$

Gap set to: [a] 10.6 mm, [b] 9.5 mm.

however. The longer period lengths were chosen to make lower photon energies available.

The 3.5-cm-period undulator was made of SmCo magnets for better radiation resistance. This undulator is installed in the sector with the small-aperture ID vacuum chamber that, as the ring acceptance limit, intercepts a significant fraction of lost particles. The Undulator A previously installed in that sector suffered from an unmanageably high radiation damage rate.

The all-electromagnetic circularly polarized undulator (CPU) has the capability of producing different polarizations—left- or right-handed circular, or vertical or horizontal linear polarization—depending on the needs of the experiment. It can switch between the two circular polarizations at 0.5 Hz, so that more sensitive difference measurements can reveal magnetic states of the sample. It can also go to lower photon energies.

The 1.8-cm-period undulator is a special-purpose device that delivers essentially a single photon energy (and its harmonics) with effectively no tuning range.

Tuning curves for these devices are shown in Figure 3.4-1. Note that, in general, devices with periods shorter than 3.3 cm deliver increasing brightness for 10 keV and above. However, as the period is reduced, gaps appear in the tuning curve. In addition, for sufficiently short periods, the device does not produce sufficient magnetic field to reach the $K \approx 1$ region needed for maximized brightness. (This is particularly evident for the 1.8-cm-period device.) As will be argued in sections 3.4.2, 3.4.4, and 3.5, in the context of APS operations, the use of superconducting technology addresses this issue more effectively than other options, allowing us to deliver on the bright promise of short-period devices.

In addition to these undulators, another type of undulator was just constructed and installed for the intermediate energy x-ray (IEX) beamline. It is an all-electromagnetic, 12.5-cm-period undulator that has quasiperiodic capability for suppression of higher-order harmonics. The device is described in [3.4-1] and the optimization of quasiperiodicity for this application is covered in [3.4-2].

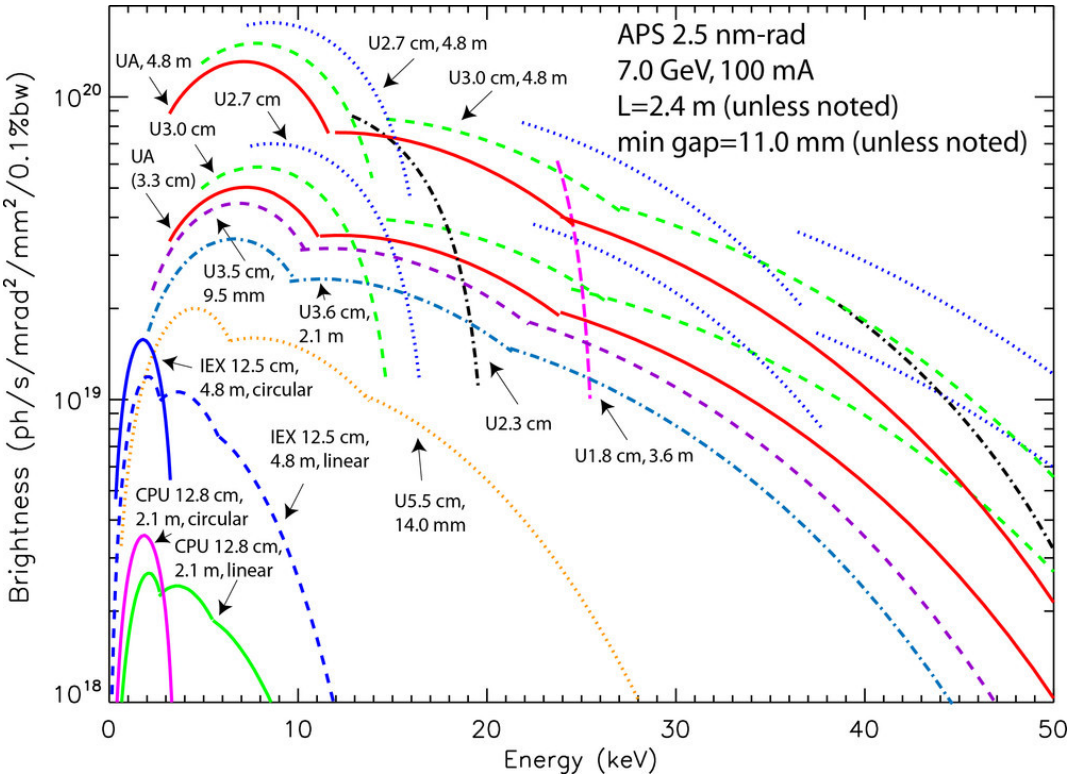

Figure 3.4-1: Tuning curves for the insertion devices presently installed in the storage ring. Different undulator lengths are shown where there are sectors with two in-line undulators installed. All undulators are 2.4-m long unless otherwise noted.

3.4.2 Conventional Planar Devices [U1.03.04.01]

3.4.2.1 Basic Properties

Nearly all of the insertion devices installed at the APS are conventional planar undulators, as can be seen in Table 3.4-2. The magnetic field of the undulator on axis is vertical, the oscillation of the electron beam is horizontal, and the photons that are produced are of horizontal linear polarization, at least on axis. The magnetic field is produced by NdFeB permanent magnets in all of the planar devices (except for the single SmCo-based undulator) with poles between the magnets. The poles are made of vanadium permendur (nominally 2% vanadium, 49% Fe, 49% Co), chosen because it has a higher magnetic permeability than iron when it is properly handled and annealed, leading to a higher on-axis undulator field. This is called a hybrid permanent magnet design.

When assembled, as shown in Figure 3.4-2, the magnetization of the magnet blocks is parallel to the beam axis, with two adjacent magnets being magnetized in opposite directions; the poles between the magnets focus the magnetic flux across the undulator gap. An advantage of this type of design is that the permanent magnet blocks can be sorted so the inevitable variation in magnetic moments between the blocks is averaged somewhat to even out the on-axis variation in magnetic field strength. This is the first step in magnetic tuning.

Occasionally interest is expressed in a planar undulator that produces vertical linear polarization, which

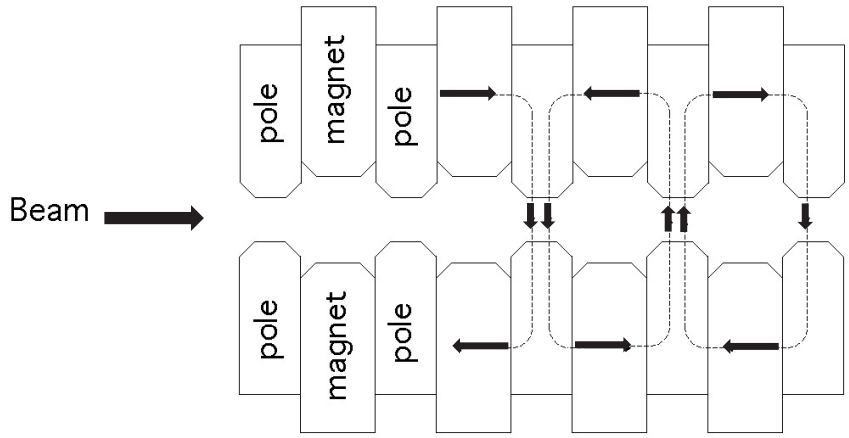

Figure 3.4-2: Diagram showing relative orientation of the electron beam and the planar undulator poles and magnets. The magnetization direction of the magnet blocks is parallel to the beam direction; the poles focus and direct the flux across the gap between the poles.

would require a horizontal planar magnetic field. A planar horizontal field is impractical for a simple conventional planar undulator intended for a storage ring. As discussed in section 3.2.2, relatively large horizontal acceptance is required for injection, so the ID vacuum chamber must be wide, increasing the minimum magnetic gap. The magnetic field strength needed for a reasonable tuning range then becomes out of reach. More complicated pole configurations are possible and are used in circularly polarizing undulators where there is no other choice (see section 3.4.3), but the achievable field strength is still reduced.

3.4.2.2 Choice of Device Parameters

The important characteristics of planar undulators for users are the period length of the magnetic field and the maximum achievable magnetic field strength on the beam axis. In general, a shorter period length means the maximum photon brightness will be higher and will occur at a higher photon energy. This trend can be seen in Figure 3.4-3, which shows the tuning curves for the planar undulators presently installed at the APS, assuming the same beam characteristics and the same overall undulator length. The first, third, and fifth harmonics are shown when they are within the range of the graph. Higher harmonics will also be present in the undulator spectrum but they are not included in the figure. The tuning ranges shown are those that are met by the installed undulators.

As discussed briefly in the introduction to this section, there is a trade-off in shortening the period length in order to increase the brightness, in that the shorter the period length, the weaker the on-axis field of the undulator (at the same gap). The highest field strength that the undulator can produce on-axis, which is at the smallest gap permitted for the undulator, determines the lowest photon energy that can be reached. The implication of this, and the trade-off, can be seen in the figure as the gaps between the first and third harmonics for period lengths shorter than 3.0 cm. For the 2.7-cm period undulator, there is a gap between about 16.5 keV and 22.5 keV that is not covered by either the first or third harmonic. Even with the 3.0-cm-period undulator where there is continuous tunability between the first and third harmonics, there is a discontinuity in brightness slightly below 15 keV as the transition is

made between harmonics. Some users find such a brightness discontinuity problematic, so they might prefer a slightly longer period length, or possibly a different period length so the discontinuity is shifted to a less-troublesome photon energy. Revolver undulators, as described in section 3.4.2.5, will be used by the Project to minimize the effects of discontinuous tunability by providing the tuning range of two different-period undulators in the footprint of one undulator.

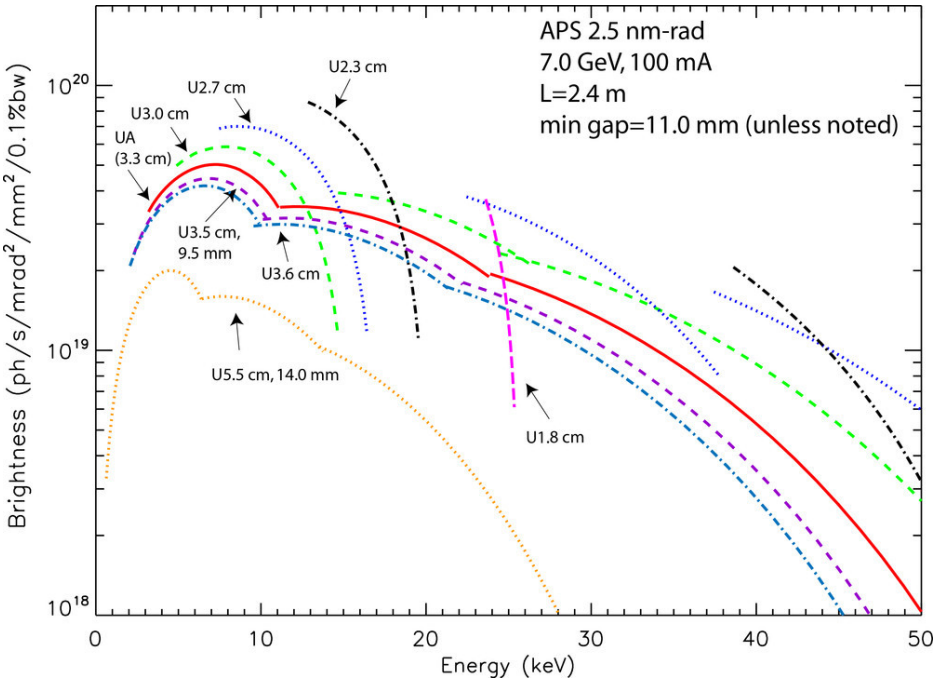

Figure 3.4-3: Tuning curves for undulators with a variety of different period lengths. The same overall magnetic length and beam parameters are assumed for each device to show the effect of just a change in period.

3.4.2.3 Power Load Considerations

The other consideration that must go into the choice of a period length is the power load from whatever undulators will be in the straight section and how that power will be distributed on the front end and beamline components. The total power and power density from planar undulators as a function of the first harmonic energy are shown in Figures 3.4-4 and 3.4-5. Note that even if it is the third (or higher) harmonic that is being used for experiments, the undulator is still producing the first and all other harmonics, and they are all contributing to the overall heat load.

Engineers will continue to work with individual beamlines in order to customize power handling for specific beamline and front-end configurations. As a comparison point, though, the allowable limits for total power and on-axis power density from all the IDs that will be in simultaneous use in the straight section are 21 kW and 590 kW/mrad^2 for the highest-power installed front-end design. Software has been developed for automatic optimization of ID choices, consistent with limits on power handling in the front ends. There could also be a change in design philosophy: instead of requiring the photon shutter to handle the entire heat load of the undulator(s) as is done now, the undulator could be turned off off by stopping the current in an electromagnetic device or by opening the gap in

a permanent-magnet device, as long as the shut-off can be done quickly enough. Such a change in the operations approach might significantly increase the power-handling capability. Both of these points are discussed in greater detail in section 3.4.6.

In the computations shown in Figure 3.4-4, a minimum undulator gap of 10.5 mm is assumed for the variable-gap undulators. This gap is in practice not achievable with the present standard ID vacuum chamber, however. Further information about undulator gaps is given below. A detailed table of the power and power density as a function of gap for various planar IDs can be found in ref. [3.4-3].

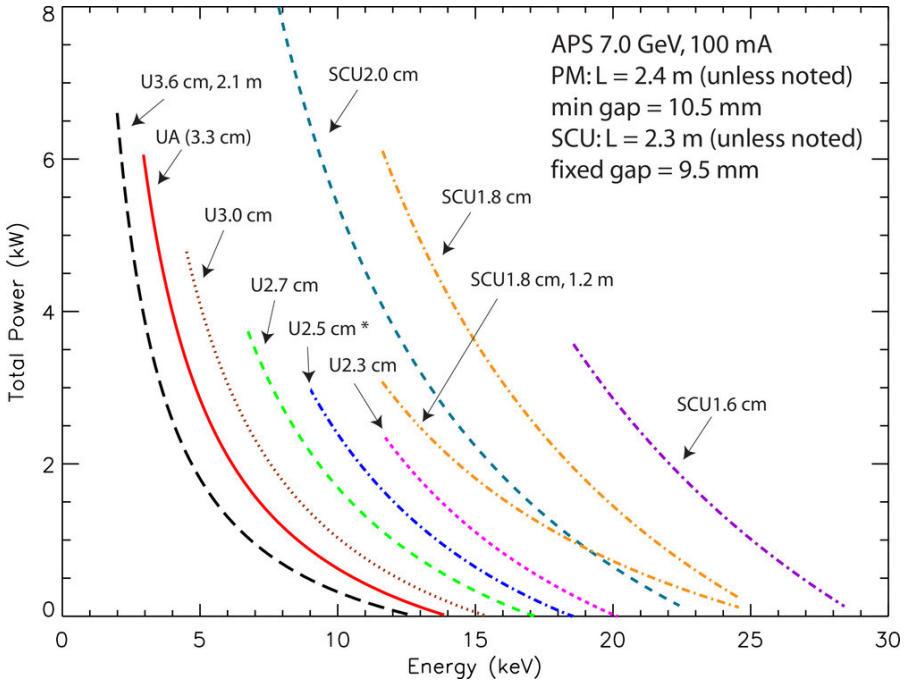

*Figure 3.4-4: Total power from different planar undulators plotted as a function of the first harmonic energy for a beam current of 100 mA. For the permanent-magnet undulators, a device length of 2.4 m (unless noted) and a minimum gap of 10.5 mm are assumed. Power densities for planar superconducting undulators are also included; for those, a magnetic length of 2.3 m is assumed unless noted. Neither the superconducting undulators nor the permanent-magnet undulator with a * has been built (yet), so the calculation is based on estimated magnetic fields.*

Note that the tuning curves given in Figures 3.4-3, 3.4-4, and 3.4-5 are relevant for undulators of a given period length independent of the technology used in the particular undulator. Using a technology that can produce a stronger magnetic field will not change the brightness or power for a given photon energy. What is gained by employing technologies that can produce a higher magnetic field is tuning range — the curves shown will extend to lower photon energies, with the minimum photon energy determined by the maximum field that is achievable.

The minimum gap of an ID is determined by the vacuum chamber that must fit in the gap. The nominal 10-mm outer dimension of today's standard ID vacuum chamber is typically approximately 10.1 mm due to machining tolerances. When the inevitable unevenness along the length of the vacuum chamber, the height variation in the poles, and shims that may protrude slightly are taken into account, the typical minimum operating gap is 11.0 mm. (Height variation in the poles can be due to mechanical tolerances or to deliberate adjustments or tapering of the gap that is done as a part of magnetic

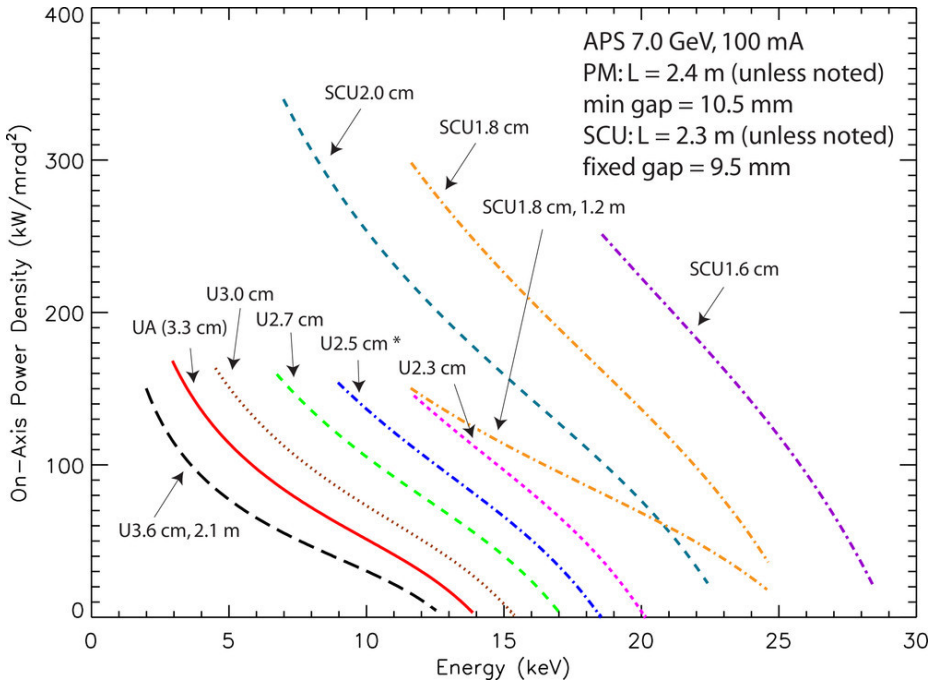

*Figure 3.4-5: On-axis power density from different planar undulators plotted as a function of the first harmonic energy for a beam current of 100 mA. For the permanent-magnet undulators, a device length of 2.4 m (unless noted) and a minimum gap of 10.5 mm is assumed. Power densities for planar superconducting undulators are also included; for those, a magnetic length of 2.3 m is assumed unless noted. Neither the superconducting undulators nor the permanent-magnet undulator with a * has been built (yet) so the calculation is based on estimated magnetic fields.*

tuning.) Occasionally a user asks for extra effort in alignment and adjustment of the undulator during installation, so extra time is taken in eking out the last bit of gap range. The minimum gap may be able to be decreased below 11.0 mm by 0.1 or 0.2 mm, but achieving this is by no means guaranteed and cannot be counted on in the design of a beamline.

Some thought is being given to the design of a new ID vacuum chamber that will permit smaller undulator gaps. One possibility is to add extra internal support so the thinnest part of the vacuum chamber wall can be made thinner without too much additional deflection of the chamber under vacuum. Another possibility is to make the transverse length of the thin part of the wall shorter, but this would require that the magnetic structure become narrower. New magnetic designs with narrower magnets and poles could be developed, but attention would need to be paid to avoiding dynamic multipoles similar to those reported in ref. [3.4-4] that affected operation at SSRL.

3.4.2.4 Available Devices

New undulators with period lengths of 3.6, 3.0, 2.7, and 2.3 cm can be readily provided to users, as these were designed and built at APS. The 3.5-cm SmCo undulator is also an APS design. There are a few as-yet uninstalled 3.3-cm-period undulators on hand at APS, enough to fulfill the anticipated user requests. Undulators with new period lengths that are not very different from the present undulators can

be designed readily.

While new period lengths can be designed and provided, issues can arise around the availability of spares. It is not financially feasible to keep a spare device for every period length when there are so many different period lengths. Such considerations can be factored into the selection of new undulator periods. Spare magnet blocks are kept on hand for each of the period lengths in case an undulator requires replacement of a magnet or magnets, but the time required for such a repair means that, in practice, a spare Undulator A (or another available device) would likely be installed as a temporary substitute while the damaged device undergoes repairs.

It may be helpful to users considering new period lengths to have some guidelines for what the expected minimum-gap field would be. A number of design studies in two dimensions were recently carried out for a variety of period lengths. A good fit for undulators using NdFeB magnets was found with the Equation

$$B_{\mathrm{eff}}(\mathrm{Tesla}) = 3.276e^{-4.51r+1.20r^2}, \tag{3.4-1}$$

where r is the ratio of the gap/period [3.4-5]. This expression can be used with two caveats: 1) the three-dimensional (i.e., real-world) field is slightly lower than the 2-D calculation, possibly by 1%; and 2) various other real-world variables (e.g., construction tolerances, variation in pole heights that affect the accuracy and interpretation of a gap measurement, strength of as-delivered magnet blocks) result in a disagreement in the effective field between calculation and measurement of about 2%. More details of these estimates are given in ref. [3.4-5].

3.4.2.5 Revolver Undulators [U1.03.04.04]

A revolver-type undulator is another possibility for offering greater flexibility to a beamline. (See [3.4-6] and references therein, as well as [3.4-7].) A revolver undulator provides the user with the option to switch between two magnetic structures at will. Each structure can be optimized for a specific requirement or in order to cover a given spectral range with higher average brightness than would be possible with a single device.

The revolver undulators for the APS Upgrade will have two pairs of magnetic structures of different period lengths mounted together in a single undulator support. The upper and lower “jaws” each hold two magnetic structures oriented at 90 degrees with respect to one another. The jaws revolve (at open gap) to select one of the two pairs of magnetic structures, after which the gap may be closed so photons are produced by the selected magnetic structure and period length. Users can change between the two different period lengths as needed, with a cycle time of 5-7 minutes.

Deploying revolver undulators at the APS presents several challenges. The APS ID vacuum chamber design incorporates a small beam section and a large antechamber section. The small beam section allows the undulator poles to be placed in close proximity to the electron beam. The large antechamber section provides bending and torsional rigidity as well as good vacuum conductance and a location for the non-evaporable getter (NEG) strips used for ultra-high vacuum pumping. The vacuum chamber supports are fairly bulky to achieve the strength needed to overcome the bending and torsional rigidity of the vacuum chamber for precise chamber alignment. The ID vacuum chamber design will remain largely unchanged. The existing design accommodates revolver undulators with two magnet arrays, but cannot accommodate three when the third is located between the first two, at a 45-deg. angle. The ID vacuum chamber supports will be revised as part of the APS Upgrade Project to provide clearance for

the lower magnet array that is revolved outward from the ID gap separation mechanism when not in use.

Several revolver undulator prototypes have been designed and are being tested and further developed at the APS. All use the latest APS undulator gap separation mechanism as a basis, which was regarded as desirable but unlikely to be feasible prior to this revolver undulator design work. The key differences between the prototypes are in the strongbacks, which provide bending rigidity to the magnet arrays. One type uses a non-revolving strongback approach, where only the magnet arrays and a minimal support/mounting structure revolve. The other type uses a revolving strongback. Both are shown in Figure 3.4-6. The different prototypes are being evaluated for performance, durability, cost, and reliability. The testing includes single-jaw revolver structures with two magnet arrays of the same period, opposing a fixed jaw with a single magnet array of the same period. Minor changes to the frame of the mechanism were made during a recent revision to better accept the eventual revolver design and to allow more aisle clearance next to an installed planar or revolver undulator for the passage of large components (such as a superconducting undulator cryostat).

The revolver designs incorporate mechanical and control system provisions for ensuring accurate, repeatable, and safe motions, both of the revolver axes and of the gap between the magnet arrays. All of the functionality of the regular, planar undulators is maintained in the revolver, i.e., full user control by gap or energy, gap tapering, selectable gap tolerance (deadband), and synchronous scanning. Some complications arise as the “active” magnet array needs to be sensed for control and gap-energy conversion applications, redundant minimum-gap limit switches need to be provided, and unique revolver axis logic inputs (switches) and control functions are required. Other complications arise from the use of the existing gap separation mechanism, mainly regarding the height available for the magnet structures. The regular, planar undulators use a magnet structure design that has the magnets and poles mounted to a thin, “comb-like” divider plate that is mounted to a thicker baseplate, which is mounted to the strongback. Mechanical shimming between the strongback and the baseplate is an important step in the magnetic tuning of the undulators. The thick baseplates allow for expedient shimming for field uniformity in the initial undulator tuning stages, as their stiffness means that they can be rigidly shimmed with a small number of shims. The absence of these baseplates in the revolver undulator, due to space constraints, means the initial shimming for field uniformity will need to be done between the thin divider plate and the strongback, which will require a greater number of shims to prevent local pole height variation, and in turn, gap and field variation.

Currently, when two undulators are installed in-line in the same sector, the spacing between the undulators in the beam direction is adjusted so the two undulators are in phase at the photon energy specified by the user. The spacing is manually set during installation and cannot be remotely adjusted. With a revolver, the spacing will be adjusted so one of the two revolving magnetic structures is in phase with the other in-line undulator. There is no provision to adjust the relative beam-direction spacing of the two magnet arrays on a revolver undulator, however, so further adjustment of the phasing of the second magnetic array, if desired, will be by means of magnetic tuning of the end fields of the second magnetic structure. The magnetic structures are tuned and installed with magnetic shielding between the in-line undulators.

The cost estimate for the revolver undulator is based on two hybrid, permanent-magnet arrays, each with a length of 2.4 m or less, and a period from 2.2 to 3.8 cm, with a minimum gap of 11 mm. The revolver undulator design will be provided in a version with shortened magnet structures for use in canted undulator sectors. These shorter revolvers will use the same modular undulator magnet structures as the regular planar undulators. The modular structures allow a canted-length magnetic structure to be

assembled from the same parts as a full-length structure with the simple omission of the last module at each end. The shortened strongback will be specific for a canted-length revolver undulator.

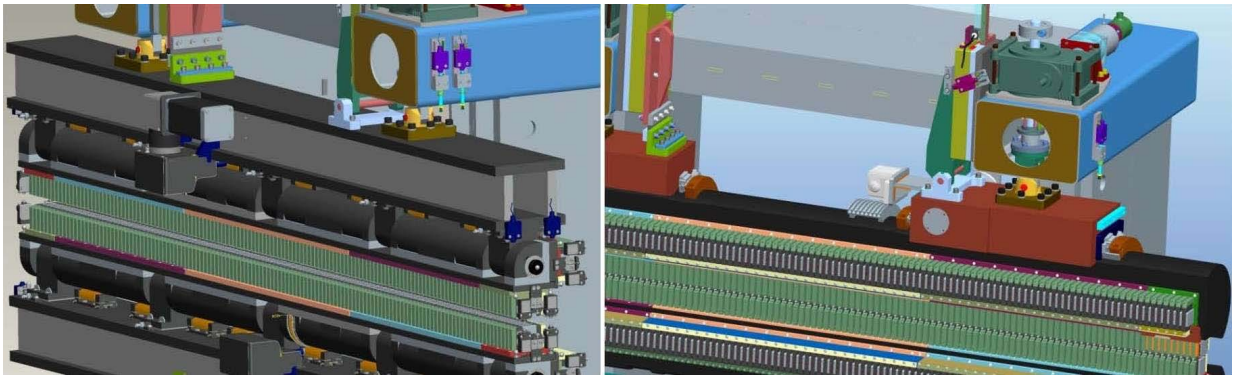

Figure 3.4-6: Revolver prototype designs: non-revolving strongback, left, and revolving strongback, right.

The gap separation mechanisms of the regular planar undulators presently allow the gap of the magnet structure to be tapered; this will be retained in the revolver undulators. The maximum allowed operational taper will be a 5-mm difference between end gaps. Small tapering (on the order of 0.200 mm or less) is useful as an adjustment of magnetic field strength along the length of an undulator. It proved to be essential for expeditiously restoring the performance of radiation-damaged undulators. A linear mechanical taper in the undulator gap was the first, and key, step in correcting for the observed radiation damage. Small tapers are also useful in that they provide some adjustment of the phasing between in-line undulators at photon energies where the undulators are not at the proper separation for ideal phasing. Large tapers (1 to 5 mm) are useful for those users seeking larger spatial and energy distributions of the photon beam produced. This has been desirable historically at the APS, especially for initial beamline commissioning or startup activities following an upgrade. It has been requested as a feature of one of the undulators for the upgrade; one beamline specifically requested the ability to broaden the spatial beam size in order to image a sample as large as a bug or a mouse heart. Calculations of the effect of tapering the undulator found, and measurements confirmed, that the desired spatial broadening can be achieved. While there is some associated loss in flux, it is at a level that is acceptable to the user. Details of the measurement and calculation will be published shortly [3.4-8].

3.4.2.5.1 Optimization of Revolvers

Optimization of the periods on a revolver cannot take place without knowledge of the requirements of x-ray users, which have only recently been defined. However, a methodology and software for choosing revolver periods has been developed, as described in section 3.4.6.

Revolvers are well suited to providing highly tuned performance at a few energies, perhaps coupled with a broad, general-purpose capability. Alternatively, one can use two periods to provide better performance over a broader energy range than is possible with a single period. Two hypothetical cases demonstrate the value of both revolvers and the optimization technique.

1. Operation at 12.4 keV with broad tuning between 5 and 30 keV, shown in Figure 3.4-7. The single-period optimization chooses a U30, which is a very versatile device. With a two-period optimization, a U24 is added, increasing performance at 12.4 keV by a factor of more than 2.

2. Operation with broad tuning between 40 and 100 keV, shown in Figure 3.4-8. The single-period optimization chooses a U25. The two-period optimization adds a U26, significantly improving performance by filling in where the U25 performance falls off.

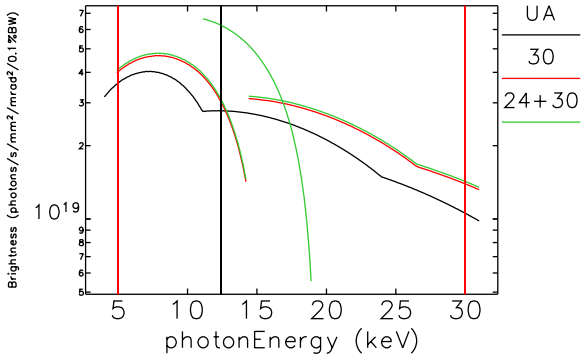

Figure 3.4-7: Comparison of optimized one- and two-period devices to a UA, assuming 2.1-m-long canted devices. The target energy bands were 12.4 keV and 5-30 keV, and are indicated by the vertical lines. The single-period 30-mm curve is offset slightly for visibility.

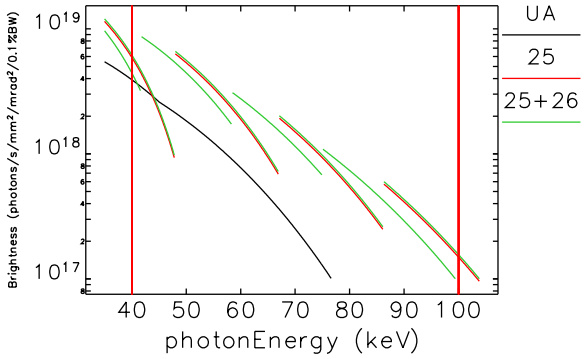

Figure 3.4-8: Comparison of optimized one- and two-period devices to a UA, assuming 2.1-m-long canted devices. The target energy band was 40 keV to 100 keV, as indicated by the vertical lines. The single-period 25-mm curve is offset slightly for visibility.

3.4.3 Devices for Polarized Radiation Production [U1.03.04.02]

3.4.3.1 Introduction

Nearly all of the presently installed insertion devices are conventional planar undulators. On the beam axis, they produce a magnetic field that is vertical and that varies in strength approximately sinusoidally along the axis. Off the beam axis, horizontal transverse and longitudinal field components begin to appear (and of course the inevitable field errors can introduce such small components on axis), but still the electrons that travel through the undulator oscillate in the horizontal plane and produce horizontally linearly polarized photons.

Insertion devices can be built that produce both vertical and horizontal magnetic field components on axis. Often, the maxima in the horizontal field are midway between successive maxima in the vertical field so that the field direction seen by the beam rotates along the length of the device. The resulting trajectory is no longer planar; if the magnitudes of the vertical and horizontal field components are the same, then the beam travels in a circular helix and produces circularly polarized photons. Circularly polarized light is often used in studies of magnetic properties of samples.

There are a number of alternatives available for producing polarized radiation. Those that are included in the APS Upgrade Project are two APPLE-type undulators and an electromagnetic variably polarizing undulator (EMVPU) that can switch polarization rapidly. Their characteristics are discussed below.

3.4.3.2 APPLE Undulator [U1.03.04.02.02]

Probably the most common variably polarizing type of undulator worldwide is the Advanced Planar Polarized Light Emitter (APPLE-style) undulator. Although there are none at APS now, two APPLE undulators are included in the scope of the Project. An APPLE undulator can be used when the period length of the desired undulator is too short to allow space for coils for an electromagnet. A sketch of the magnetic structure scheme is shown in Figure 3.4-9. Four arrays of permanent magnets are combined into two jaws — effectively, one jaw of a standard pure permanent magnet undulator is split in half longitudinally, with the split located immediately above (or below) the beam axis. The longitudinal arrays are then allowed to shift longitudinally with respect to one another. With one phase setting between the magnet arrays, it is a standard planar undulator. At another phase, the combined effect of the arrays produces circular polarization. The motion to change polarization is mechanical, so polarization changes are too slow for lock-in techniques. The gap of an APPLE undulator can also be changed, but since the vertical and horizontal field components change differently with gap, a longitudinal phase shift may be needed to preserve the polarization as the gap is changed.

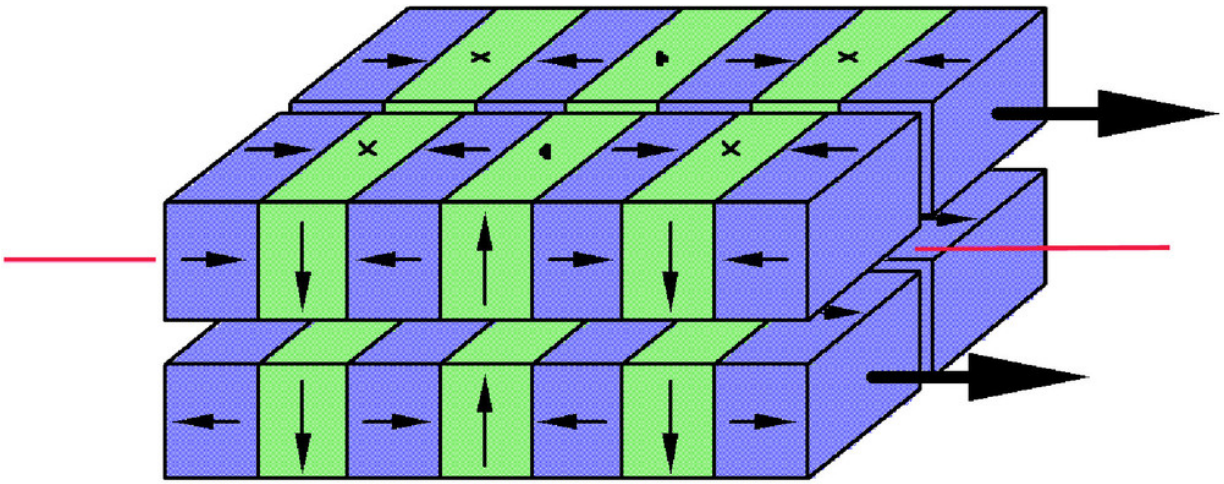

Figure 3.4-9: Magnetic structure scheme for an APPLE-style undulator. The red line represents the electron beam. The magnetic arrays can be shifted longitudinally with respect to one another to change the polarization.

Figure 3.4-9 shows one means of changing the polarization of the light, by the longitudinal shift of two diagonally opposite magnet arrays. This makes available vertical linear, horizontal linear, left- and right-circular, and some types of elliptical polarization. Some APPLE users seek to add to this the option of inclined linear polarization (i.e., linear polarization at any angle, not just horizontal and vertical). This can be accomplished by allowing three (or all four) of the arrays to shift. While inclined linear polarization is often highly desired at lower-energy rings, it may not be as sought-after at the APS. It introduces additional complications in the construction of the APPLE itself, and the effects on the electron beam are more difficult to compensate. Any APPLE-style undulator requires careful attention to compensation of the net effect of its magnetic field on the stored beam because of the strong non-uniformity in the field at the beam axis. Changes in inclined linear polarization result in even greater challenges to magnetic field compensation, but these challenges have been met successfully at other storage rings, including many with electron beams that are lower in energy and less “stiff” than at APS.

APPLE-style undulators are extremely popular at many lower-energy light sources, even becoming the standard undulator type at some labs. As a result, there are several companies that sell APPLEs and have sold enough to have well-tested and successful designs. APPLE undulators for the APS upgrade will be purchased from one of these companies.

Before the procurement process is begun, the anticipated capabilities of the device must be tailored to the needs of the beamline, and fundamental parameters of the undulator selected. This process has begun for one of the two undulators, and a period length of 41.7 mm was tentatively suggested to meet the stated requirement of 2.4-keV minimum photon energy in vertical linear polarization mode. (That same photon energy would then also be reachable in horizontal linear polarization and circular polarization modes.) A magnetic design was completed for use as a guide to what is achievable and as an initial suggestion to the future undulator vendor. It was anticipated that the minimum gap of the device would be 9.8 mm, nominally, but once shims and tolerances are allowed for, the real gap would be 9.5 mm. This would have been compatible with the insertion device vacuum chamber presently installed in Sector 4, where the Magnetic Spectroscopy-Hard (MS-H) beamline is presently co-located with the Magnetic Spectroscopy-Soft (MS-S) beamline. This APPLE device is intended for the MS-H beamline. The undulator for the MS-S beamline (presently a CPU, but will be upgraded to the more rapidly switchable EMVPU as part of the upgrade) absolutely requires a small-gap vacuum chamber. Only one such small-gap ID vacuum chamber (5-mm beam stay-clear) is feasible in the storage ring; a second would reduce the achievable single-bunch beam current and adversely impact experimental programs elsewhere around the ring. When MS-S is moved to Sector 2 as part of the Project, the top priority for a small-gap chamber will move with it.

The possibility remains that with the option of designing an entirely new vacuum chamber for the APPLE, some compromise will be reachable that will allow a gap for the APPLE of less than the standard 11.0 mm. (For example, the long taper design described in section 3.2.4 could be employed.) Obviously, this needs to be investigated before the minimum reachable gap of the APPLE can be set. To ensure that the user requirements can be met, the magnetic design, including the period length, cannot be set until these vacuum chamber issues are settled and the minimum gap is known. Also, a final decision on whether the APPLE undulator will use a standard ID vacuum chamber extrusion with a different machining of the outside contours or have its own specially designed extrusion must wait until the required beam stay-clear aperture is known.

In the reference magnetic design for this APPLE undulator, a quasiperiodic magnetic structure was considered because quasiperiodicity can reduce the “contamination” of a lower harmonic by higher-harmonic contributions to the x-ray spectrum, especially in linear polarization modes (see [3.4-9,3.4-10]). When the degree of residual contamination by higher harmonics was examined more closely, however, it was realized that the degree of residual contamination was quite different in the horizontal and vertical linear modes [3.4-11]. The user feels that this difference in harmonic suppression between horizontal and vertical linear polarization modes would be detrimental to the planned x-ray magnetic linear dichroism measurements. If a means of equalizing the suppression is not found, then the option for quasiperiodicity will be dropped.

The second APPLE-style undulator is intended for the Wide-Field Imaging (WFI) beamline. Discussions with scientists from the WFI beamline to set the requirements of the undulator have not yet begun. The Project cost and schedule data for the second APPLE are based on that device being similar to the first APPLE in scope, but different enough in actual design that the two will not share design and development activities and costs.

3.4.3.3 Electromagnetic Variably Polarizing Undulator (EMVPU) [U1.03.04.02.01]

Another type of variably polarizing undulator will also be provided as a part of the Project. In addition to producing the standard polarizations of left- and right-circular, and horizontal and vertical linear, this undulator will need to switch rapidly between left- and right-circular polarizations. The x-rays produced will be used for magnetic studies of materials; these studies require lower-energy photons, with a requested photon energy range of 400 to 3000 eV. The lowest photon energy was chosen to allow access to the nitrogen edge at 409 eV. The magnetic signals are weak—10^4 or 10^5 times weaker than the main signal—so searching for the small response differences between left- and right-circular polarization is key, and lock-in detection becomes essential for adequate sensitivity. A switching frequency of 10 Hz is requested for effective operation with the lock-in detector; a frequency below 5 Hz is too slow to be useful. The switching requirement means that the device will be all electromagnetic.

It is not enough to require a switching frequency of 10 Hz, however, because the desired circularly polarized photons are produced when the magnetic field of the undulator is constant, not when it is in the process of switching. This leads to the further requirement that the time to complete the handedness switch must be 20% (or less) of the time between switches. For 10-Hz switching, the helicity of the field would change every 50 ms, and the switch must be complete within 10 ms. This refers to the magnetic field seen by the electrons of the stored beam. Careful attention must be paid not only to the settling time in the power supply, but to anything that can affect the on-axis magnetic field, including the AC impedance in the undulator coils and effects of eddy currents in the magnet and in the vacuum chamber.

3.4.3.3.1 Specifications

A general layout of the EMVPU assembly is shown in Figure 3.4-10. Table 3.4-3 lists the requirements for the EMVPU. In the table, two numbers are given for the maximum length; the final value will depend on whether the EMVPU is placed in a canted sector (2.1 m) or a straight (2.4 m) sector.

The horizontal transverse (B_x) component of the undulator field is produced by epoxy-impregnated, indirectly cooled coils around solid vanadium permendur (VP) poles. (The core is water cooled, as explained in section 3.4.3.3.3.) Since the poles are solid rather than laminated, the B_x field will be held constant during active measurements. When the field must be changed to reach a new polarization state or a new photon energy, the current will be ramped slowly in order to avoid eddy currents and stray fields that could affect the stored electron beam.

The vertical (B_y) field component is obtained with single-turn, oxygen-free high-conductivity (OFHC) copper coils around laminated poles. Water cooling channels go through only the back legs of the coils (see section 3.4.3.3.3). The coils are solid copper where they encircle the poles to allow as much current-carrying cross-section surrounding the pole tips as can fit. These are the coils whose current direction will be switched in order to alternate between left- and right-circular polarizations.

Additional coils are planned for the compensation of field errors. Corrector coils, wound around the final set of four B_x poles and the final pair of B_y poles at each end of the device (a total of 12 coils) will be used to correct the electron beam steering and unwanted multipole magnetic fields. Finally, a corrector coil will encircle each magnetic jaw to compensate for Earth's magnetic field.

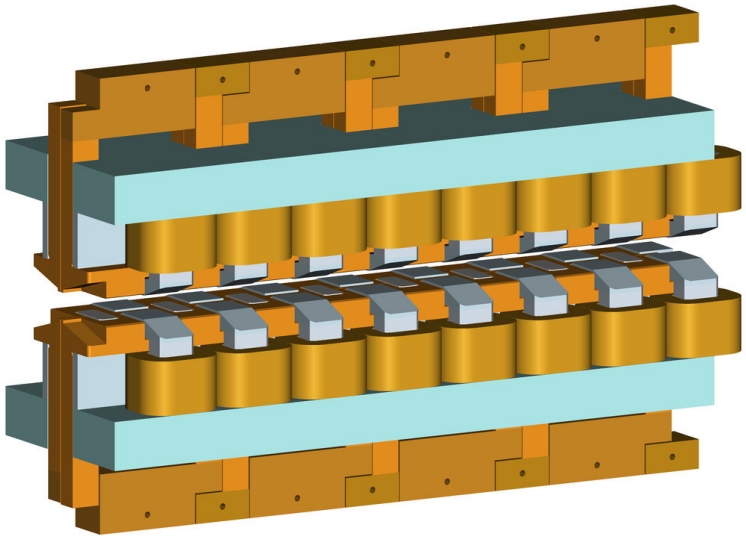

Figure 3.4-10: General assembly layout of the EMVPU. Only four periods are shown.

Table 3.4-3: EMVPU requirements.

Parameter	Value	Unit
Minimum photon energy (horizontal, vertical, or circular)	400	eV
Maximum photon energy (horizontal, vertical, or circular)	3000	eV
Switching frequency between right- and left-handed circular polarization	10	Hz
B_y field switching time (from minus full field to plus full field)	$<$10	ms
Gap	8.5	mm
Maximum length	2.1 to 2.4	m
Maximum coil temperature	100	°C

Table 3.4-4 lists a set of starting parameters for the EMVPU. Shorter period lengths are desirable to increase brightness. Longer period lengths are desirable to reduce the field requirements and to increase the space available for mounting the poles and coils. A 12.5-cm period is a good starting point but may change due to space constraints and/or field requirements as the design is finalized. In any case, the period length will be minimized within the constraints of the requirements.

Table 3.4-4: EMVPU starting parameters.

Parameter	Value	Unit
Period	12.5	cm
Number of periods (including end corrector poles)	16	each
Maximum effective field for linear polarization (horizontal or vertical)	3491	Gauss
Maximum effective field for circular polarization	2469	Gauss

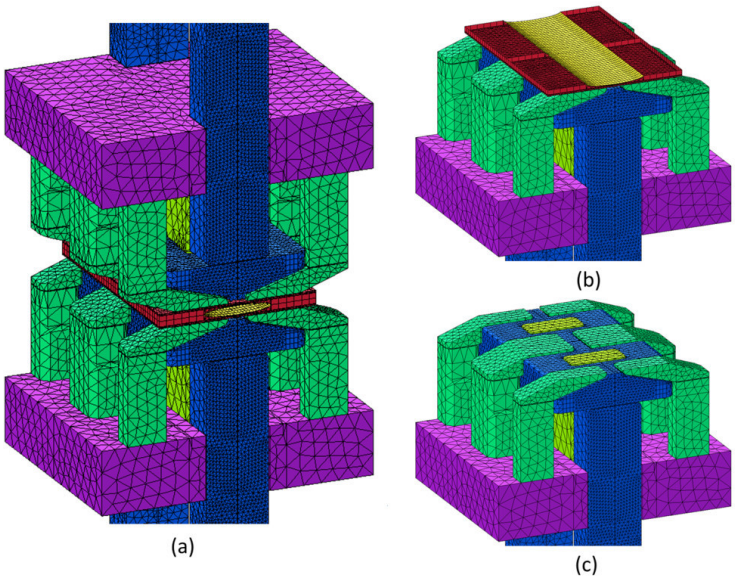

Figure 3.4-11: 3-D OPERA model, shown without B_x coils. (a) One period model. (b) One period bottom jaw with vacuum chamber cut in half. (c) One period bottom jaw.

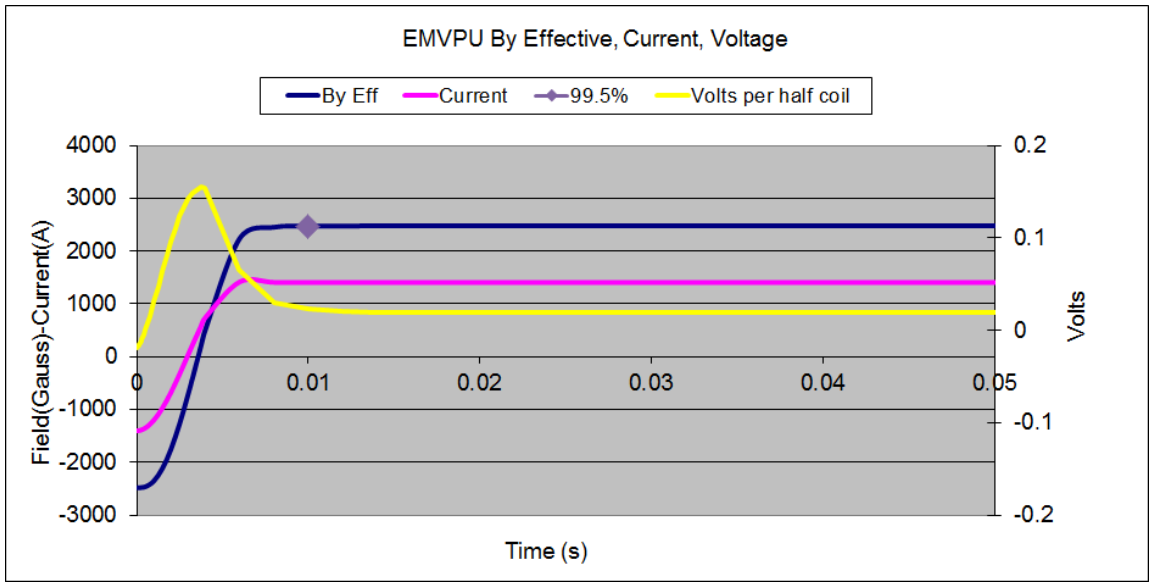

Figure 3.4-12: B_y effective field, current, and voltage in the coils vs. time.

3.4.3.3.2 Magnetic Field Analysis

Magnetic analysis is carried out using the OPERA 3-D suite of codes [3.4-12]. The OPERA/TOSCA finite element code is used for steady state magnetic field analysis, and the OPERA/OPTIMIZER code is used to optimize the coil and pole geometries. The goal of the optimization is to separately maximize the field in each of the x (transverse) and y (vertical) directions to meet or exceed the value listed in Table 3.4-4 for linear polarization, while minimizing the power consumption in the coils. A constraint

is also placed to limit the B_y field roll-off in the x direction. Once the optimum steady state solution is achieved, transient analysis is done using the OPERA/ELEKTRA finite element code. Figure 3.4-11 shows the OPERA model for the EMVPU without the B_x coils.

Figure 3.4-12 shows the effective field, current, and half coil voltage vs. time for the B_y field. (A stainless steel vacuum chamber is assumed in the calculations; see section 3.4.3.3.4.) The current is a half cosine function with a switching time of 6 ms. The B_y effective field reaches 99.5% of full field (shown by the diamond in the figure) within 10 ms. Shortening the current switching time to less than 6 ms will not reduce the B_y field switching time, because the eddy currents in the vacuum chamber are limiting the change. The voltage in the coil is allowed to exceed the steady state value to help overcome the AC impedance in the coil; this over-voltage pulse can be minimized by allowing a current-switching time of 6 ms. A current-switching time longer than 6 ms will result in a B_y switching time greater than 10 ms.

Table 3.4-5 shows the calculated parameters for a possible EMVPU design. Circular mode requires only that the B_x and B_y currents be reduced to provide the effective field for circular polarization listed in Table 3.4-4.

Table 3.4-5: Parameters for a possible EMVPU design.

Mode	Parameter	Value	Unit
Vertical polarization (horizontal field)	Maximum achievable effective field	3500	Gauss
	Peak field at maximum achievable effective field	4003	Gauss
	Ampere-turns per coil at maximum achievable effective field	2405	A-turns
	Power per coil at maximum achievable effective field	40	W
	Total power for 16 period device at maximum achievable effective field (coils only)	5120	W
Horizontal polarization (vertical field)	Maximum achievable effective field	3500	Gauss
	Peak field at maximum achievable effective field	4539	Gauss
	Current at maximum effective field	2000	A
	Power per coil at maximum achievable effective field	106	W
	Total power for 16 period device at maximum achievable effective field (coils only)	6784	W
	B_y inductance for 16 period device (coils only)	113	μH

3.4.3.3.3 Thermal Analysis

The maximum temperature the coils will be permitted to reach is 100°C. The B_x coils are wound with solid copper wire, without an internal water cooling channel. This choice serves to maximize the copper-to-volume packing factor, which ranges from 65.8% to 76.4% [3.4-13]. The 40 watts per coil produced at full current is removed by conduction through the poles and the core to the cooling water channel in the core, shown in Figure 3.4-13. The maximum coil temperature, calculated assuming only conduction as a means of cooling, is 93°C at full B_x current.

This temperature can be reduced by the addition of air cooling. Air from the vicinity of the poles will be drawn into an air-handling system that will be incorporated into the EMVPU support. This

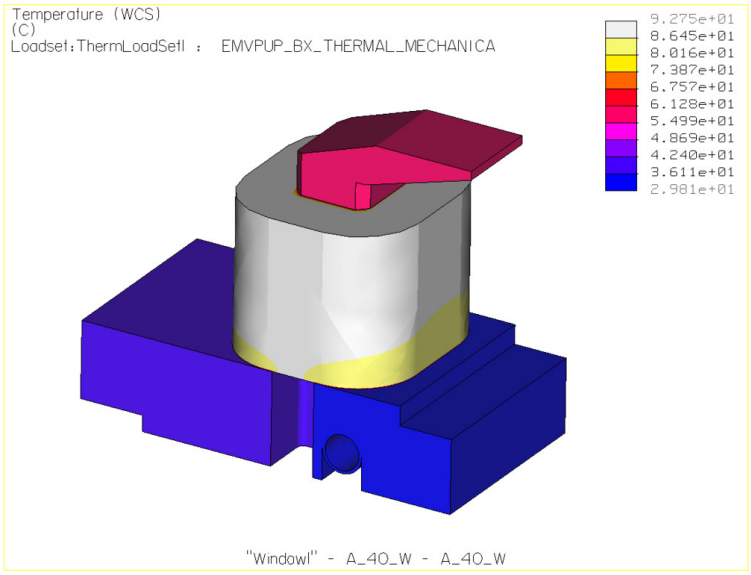

Figure 3.4-13: B_x coil thermal analysis.

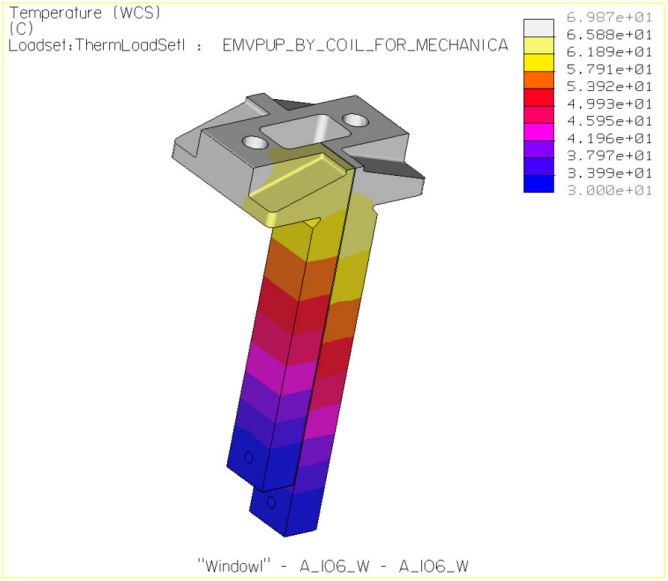

Figure 3.4-14: B_y coil thermal analysis.

air-handling system will be connected to an intake for the air-handling system of the building. This has the advantage of removing the warm air immediately, before it has the opportunity to heat the storage ring tunnel. This air flow over the coils reduces the B_x coil temperature rise by about 10% so the coil temperature will be 86°C.

The single-turn OFHC copper B_y coils have a cooling water channel that crosses through the back ends of the coil legs shown in Figure 3.4-14. The solid-copper section of the coil that circles the pole is cooled by conduction. The 106 watts produced at maximum current result in a maximum temperature of the B_y coils of 70°C. Air flow over the coils is expected to reduce the temperature rise by 10% so

the coil temperature will be 66°C.

3.4.3.3.4 Vacuum Chamber

Typical insertion device vacuum chambers at the APS are made of aluminum because its good electrical conductivity helps reduce the contribution of the vacuum chamber walls to electron beam impedance. That high conductivity, however, makes Al unsuitable for use as the vacuum chamber for the EMVPU—OPERA calculations predict a minimum switching time of 30 ms due to eddy currents in the Al. Switching the B_y field within the required 10 ms means that a lower-conductivity material must be used for the vacuum chamber.

Non-magnetic stainless steel, with its relatively poor electrical conductance, would be a good choice to limit eddy currents. However, the resistive wall impedance, especially for a vacuum chamber with a small vertical aperture, is too high and increases beam instability and loss. Adding a copper coating to the inside of the vacuum chamber reduces effects of the wall impedance on the stored beam [3.4-14–3.4-16] without being so thick as to carry significant eddy currents. The required thickness of the coating based on single-bunch beam stability [3.4-16] is less than 200 μm. A stainless steel vacuum chamber with a 200-micron or thinner copper coating still allows switching of the B_y field within 10 ms. This meets the requirement, so a custom-designed, copper-coated, stainless steel vacuum chamber is planned for the EMVPU.

3.4.3.3.5 Framework Construction

The frame will be designed to mount on a standard APS undulator fixed base and will incorporate casters for easy transport. The lower part of the frame will be constructed of welded tubular steel similar to existing APS undulators. The upper part of the frame will be made of aluminum to reduce the permeability effects that would be present if it were made of steel. Adjustments will be provided for x, y, z, roll, pitch and yaw, and fiducials will be provided to accurately measure the position of the jaws. A transverse (x direction) Acme screw will be provided for use during installation on the storage ring to move the jaws in or out of operating position over the vacuum chamber. The calculated fundamental vibrational frequency of the structure will be as high as reasonably achievable; expected results are above 30 Hz.

3.4.3.3.6 Test Models

The first test model will be a 1-period prototype that will be used to test and confirm the switching speed, assembly, thermal characteristics, field, etc. The design of a subsequent 4-period prototype will be guided by the test results. A 4-period prototype is long enough to incorporate a realistic end configuration. The time-dependent behavior of the field during switching will be measured. Any issues with the quality of the magnetic field will be characterized and means will be found to correct them. The completed 4-period test model could possibly be installed on the storage ring if a location is available and it appears desirable to do so.

The one-turn coils require large solder joints to connect the bus work. The joints will be screwed together, sandwiching a sheet of solder, with spring washers to remove extra space as the sheet of

solder melts. A solder test was developed to prove the concept; further refinement is ongoing.

3.4.3.3.7 Power Supplies

There are no commercial power supplies that can satisfy the unique requirements for the vertical supply: bipolar, 2000-A capacity, and fast switching between positive and negative currents. A suitable circuit topology will be found for this power supply that can switch the EMVPU current between plus and minus 2000 A within 6 milliseconds. Another important part of the development includes designing and developing hardware and control algorithms to ensure the current sharing of the multiple interleaved switching mode DC-to-DC power converters that will together provide 2000 A of operating current for the EMVPU.

3.4.4 In-Vacuum Undulators

At present, all APS undulators are out-of-vacuum. There is no plan to develop or acquire in-vacuum undulators (IVUs) as part of the Project. The explanation for this choice follows.

An out-of-vacuum undulator requires a vacuum chamber in the gap of the device, and means that the undulator magnetic gap will be considerably larger than the beam aperture. For a vertical beam aperture of 8 mm, the minimum undulator magnetic gap is generally 11 mm. Putting the undulator magnetic structure inside the vacuum chamber, however, allows a smaller magnetic gap. Such devices have been installed at other light sources, and technical challenges—such as providing a smooth conducting surface to reduce electron-beam impedance and the need to bake out in-vacuum components, including magnets that are susceptible to thermally induced demagnetization—have been met.

In light of this, it is natural to ask what might be achieved at APS with such devices. The critical issue [3.4-17] is maintaining the same beam impedance as those of out-of-vacuum undulator chambers to allow 16-mA operation in hybrid mode and 150-mA operation in 24-bunch mode. Since the IVUs require a movable taper of higher impedance than that of a fixed taper, the required beam-stay-clear gap for an IVU is 8.75 mm or greater in order to ensure that the impedance does not increase relative to a standard APS chamber. With this constraint, the performance of IVUs is not much different than existing out-of-vacuum devices [3.4-5].

It is partly because of this issue that the APS Upgrade is pursuing the use of superconducting undulators (SCUs), which offer superior performance to IVUs without increasing the impedance. However, if SCUs prove unworkable for some reason, IVUs could be reconsidered for a few locations. To support a beam-stay-clear gap of 7 mm in an IVU while still allowing 16-mA hybrid mode, it will be necessary to modify the straight section to control the impedance. Referring to the long-straight-section work on mitigating the increased impedance effect in section 3.2.4, a long 55-cm transition (Figure 3.2-30) could be combined with a movable taper having a much smaller maximum gap of 12 mm. Since the new movable taper will be of smaller slope and horizontal aperture, the combined impedance would be reduced to that of an 8-mm-gap fixed taper. However, R&D would be required to separate the conductive liner from the IVU when opening the magnetic gap past 12 mm. Though it would seem that an IVU could be installed without increasing the impedance, certainly the cost of an IVU will increase significantly due to the fabrication and installation of a new chamber with a long transition.

Another way to mitigate the impedance issue absent a combination taper design is to lengthen the bunch, either with a dedicated bunch-lengthening cavity or a full complement of (i.e., 16) deflecting cavities in the SPX system (see section 3.6.3.3.2). However, this is not being pursued, for four reasons. First, the full complement of deflecting cavities will not be installed as part of the upgrade, so the effect on bunch length or instability threshold is diminished. Further, installation of dedicated bunch-lengthening cavities is outside the scope of the upgrade. Second, APS does not wish to link the success of one upgrade (insertion devices) to the implementation of another (SPX). Third, in light of the mission need to better serve timing studies, a better use of a lengthened bunch would be to operate at even higher single-bunch current, which requires careful preservation of the transverse impedance. Finally, the potential benefit for APS from IVUs is less than the expected benefit from superconducting devices.

3.4.5 Accelerator Requirements and Issues

Insertion devices (IDs) may have undesired effects on the beam. The effects are normally quantified by two sets of multipole components: one is static field errors, which are measured along a straight-line path, as is done for normal quadrupole and sextupole magnets, and are also dependent on the gap or current settings; and the other one is dynamic field integrals, which are additional nonlinearities that the stored beam experiences because of the amplitude of the oscillation.

The latter come about because in undulators and, to a greater degree, wigglers the stored beam executes relatively large oscillatory trajectories (in one or both planes), which makes the beam experience slightly different peak fields along one full period due to the finite-width poles. This results in a net (small) kick in either or both planes that is nonlinearly dependent on the trajectory of the beam, making a wiggler a nonlinear device.

The actual nonlinearity is complex and cannot be described as a simple multipole or sum of multipole components. Planar undulators have wide poles and the divergence is small in the region of interest (injection aperture) near the beam axis; the multipole components model can be used as a rough approximation. On the other hand, we have the polarizing undulator APPLE, with narrow magnet slits on the center of the top and bottom magnet rows that generate rapid field variation near the beam axis, and we have the electromagnetic wigglers such as the CPU and EMVPU with narrower poles because of interleaving vertical and horizontal poles for alternating B_y and B_x fields. In these two cases the multipole components model is no longer valid in the region of interest (injection aperture). A detailed simulation with a realistic field distribution model is required.

3.4.5.1 Simulation Methods

To evaluate dynamical field integral effects, we start by fitting field-expansion functions (harmonics) to the wiggler 3D field obtained from magnetic model calculations. Fitting provides a certain degree of noise filtering of the data, which is beneficial as this noise can severely overstate the nonlinear effect. Another component of fitting residuals might be the error from an incomplete expansion of the field for high-order transverse spatial harmonics.

Two canonical tracking methods have been implemented in `elegant` [3.4-18]: one was developed by Y. Wu [3.4-19] and added as the CWIGGLER element type, while the other was developed by J. Bahrdt and G. Wüstefeld [3.4-20] and added as the GFWIGGLER element type. CWIGGLER is more

suitable for simulation of electromagnetic wigglers, while GFWIGGLER is more suitable for simulation of APPLE devices. Both elements require field-expansion functions, typically obtained from fits to data from a magnetic model, and both elements can be used for planar undulator simulation.

Y. Wu's method, although accurate, is slow compared to the now-standard kick-map method [3.4-21], which allows for quick modeling of nonlinear effects. The kick map can be obtained directly from the magnet design code RADIA or by tracking a uniform grid of particles of initial $(x, y)_0$ with $(x', y')_0 = (0, 0)$ directly through CWIGGLER. The grid covers all desired trajectories, in this case the vacuum chamber aperture of $\pm$ 17 mm $\times$ $\pm$ 2.5 mm. Only one period needs to be tracked because all periods are generally the same. The resulting kick maps are used as input of a special wiggler element (UKICKMAP) in `elegant`.

Comparisons have been made between these three methods and they agree very well, so one is free to choose the method that is the most convenient for the problem under study.

The shortest length for each wiggler element (CWIGGLER, GFWIGGLER, UKICKMAP) is the period length, and a full ID can be composed by putting periods in series. Static field errors that are not in the magnetic model are simulated by adding thin-lens multipole kicks with random strength to the ends of the wiggler elements.

3.4.5.2 Nonlinear Perturbation

A noted example of a nonlinear wiggler is the SPEAR device analyzed in [3.4-4]. The nonlinearity of this device was partially corrected by end-multipole magnets. Assuming a sinusoidal model of the magnetic field, the nonlinear kick in the x-plane for a horizontally deflecting wiggler is (the simplest case is selected for illustration):

$$\Delta x'(x) = -\frac{L_w}{(E/e)^2}\left(\frac{\lambda_w}{2\pi}\right)^2 B_{y0}^2 \frac{d}{dx}F^2(x), \tag{3.4-2}$$

where L_w is the length of the wiggler, E is the beam energy, λ_w is the period length, B_{y0} is the peak field, $K = 0.934\lambda_w[\text{cm}]B_{y0}[\text{T}]$ and $F(x) = B_y(x)/B_y(0)$. The nonlinearity comes from the roll-off in $F(x)$. The overall strength of the nonlinearity goes as $L_w K^2/E^2$. Fortunately the APS beam energy is high, which mitigates the impact of these effects.

The existing IDs at the APS are mostly hybrid permanent magnet devices (see section 3.4.2.1), which have wide poles (small roll-off in $F(x)$) and moderate K values, and therefore have relatively little higher multipole content in the region of interest. It is highly desirably to keep this particular feature in future planar undulators, including revolvers and superconducting undulators. Both will have similar magnet lengths L_w and K values to existing devices, so this should not be difficult.

The polarizing undulators usually have larger K values in order to reach lower photon energies, giving them the potential to contribute to all linear and nonlinear effects. Also, a strong wiggler that operates in circular or vertical polarization requires narrow B_y poles, which worsens the roll-off in $F(x)$.

Linear perturbing effects are observed in the APS CPU [3.4-22], which operates with specially designed local correction magnets for dipole and quadrupole perturbations. Even stronger effects are expected from the IEX device (now under commissioning), as well as from the APPLE and EMVPU devices described above. Although methods to partially compensate the dynamic field integrals are advancing [3.4-23], we strive to design wigglers such that these would not be necessary. During the

design phase, complete simulation studies with various errors need to be performed as accurately as possible to ensure that the operation of the storage ring is not impaired.

3.4.5.3 Static Field Errors

Even after carefully designing the insertion device to maximize field quality, static field errors still arise from imperfections of the magnet structure. Much effort is spent in reducing these during the magnet-tuning stage. Table 3.4-6 shows the type of magnet errors and their effects on the beam. Limits on these were originally determined in the early stage of the APS [3.4-24] and are reproduced in Table 3.4-7.

The limits on multipole field integrals remain unchanged. However, a new study of ID dipole perturbations that includes the effects of the combined "DC" and "fast" global orbit correction has resulted in improved field integral error specifications [3.4-25]. The main results are that the residual global-orbit error (with orbit correction running) depends on the time rate of change of the ID field integrals and not the absolute field integrals. On the other hand, the absolute ID field integral errors still affect local setting errors, but the requirements can be relaxed if x-ray BPMs are included in global orbit correction.

Table 3.4-6: Effect from ID errors.

Name	Expression	Beam effect
First field integral	$I_{1x,y} = \int B_{y,x} ds$	Beam position
Second field integral	$I_{2x,y} = \int \int B_{y,x} ds' ds$	Beam position
Quadrupole integral	$\int (dB_y/dx) ds$	Tune
Skew quadrupole integral	$\int (dB_x/dx) ds$	Vertical beam size
Higher-order multipole integrals	$\int (d^n B_y/dx^n) ds$, $\int (d^n B_x/dx^n) ds$	Dynamic aperture, lifetime

Table 3.4-7: ID error tolerance specification in 1995.

(a) Steering

Order	Limit[a]
I_{1x}	100 G-cm
I_{1y}	50 G-cm
$I_{2x,y}$	1×10^5 G-cm^2

[a] Superseded by recent study (Tables 3.4-8 and 3.4-9).

(b) Multipole

Order	Normal Component $\mathbf{B_0 Lb_n}$ [a]	Skew component $\mathbf{B_0 La_n}$ [a]
1	50 G	50 G
2	200 G/cm	100 G/cm
3	300 G/cm^2	50 G/cm^2

[a] $\int (B_y + iB_x) dl = B_0 L \sum_{n=0}^{\infty} (b_n + ia_n)(x + iy)^n$

3.4.5.3.1 Global and Local Orbit Stability

With orbit correction and real-time orbit feedback running full-time, the tolerance on ID errors is in terms of rate of change of the perturbations produced by the undulator. For an installed ID this

may set a limit on how fast the gap can be changed. Because of the complex frequency dependence of the correction effectiveness, the actual orbit "ramp" error from IDs has to be modeled with orbit correction simulation (using the parameters used in the present version of orbit correction) to determine acceptability. When ramp errors occur with a short duration, real-time feedback produces a more effective (short-term) correction. Thus Table 3.4-8 provides two sets of field-integral rate-of-change requirements for guidance. The 5-second ramp-error duration was selected because it matches the worst-case behavior of most planar hybrid ID perturbations.

Table 3.4-8: Undulator field integral rate-of-change limit requirements [3.4-25].

Field integral	**Limit for a 5-second duration ramp**	**Unrestricted in duration**	**Driving requirement**
Rate of $\int B_y dz$	21 G·cm/s	5.0 G·cm/s	horizontal orbit stability
Rate of $\int B_x dz$	16 G·cm/s	4.0 G·cm/s	vertical orbit stability
Rate of $\int dz \int B_y dz'$	43,000 G·cm^2/s	10,000 G·cm^2/s	horizontal orbit stability
Rate of $\int dz \int B_x dz'$	4900 G·cm^2/s	1200 G·cm^2/s	vertical orbit stability

Even when the global orbit correction system compensates for the perturbation produced by an ID outside the straight section, there remains the internal orbit error due to first- and second-integral field errors. Thus the photon source position and angle will vary with undulator gap and will depend linearly on these errors. There is no correction or partial correction by the global orbit correction system itself since there are no correctors inside the undulator. However, including the x-ray BPMs in the global orbit correction (as is done at APS) can greatly reduce the photon source and angle error at the expense of nearby rf BPM position errors, which are, after all, not as important as photon beam error.

A model of local steering errors was created with a two-kick perturbation model for IDs in order to set the limit on the absolute first- and second-field integral errors [3.4-25]. An important assumption is that the x-ray BPMs are weighted by a factor 10 more than rf BPMs. (If the x-ray BPMs had infinite weight, e.g., the rf BPM would not "vote," and the beam steering would be entirely subject to the systematics of the x-ray BPMs. Also, there would be issues with orbit control when ID gaps were opened past the point at which the x-ray BPM can produce useful signals.) Note that the requirements for a single, long device are greatly relaxed because the steering magnets are located at the ends of the straight section, i.e., at the ends of the device [3.4-25].

The resulting specifications are given in Table 3.4-9. The requirements depend on the length of undulator and location of nearby beam position monitors (BPMs) and orbit correctors. All typical cases are presented in Table 3.4-9 and described below:

- **Case 1:** Single 5-m-long device surrounded by BPMs right next to it;
- **Case 2:** Single 2.5-m-long device surrounded by BPMs right next to it (for example, canted straight section);
- **Case 3:** One 2.5-m-long device in 5-m-long straight section without a BPM in the middle;
- **Case 4:** Two 2.5-m-long device without a BPM in the middle.

When BPMs are located close to the undulator, the requirements are more relaxed (cases 1 and 2). When BPMs are located at some distance from the undulator, the requirements become very tight and hard to satisfy (cases 3 and 4). These cases can be addressed in several ways: by putting more weight on the x-ray BPMs, by installing additional correctors and BPMs closer to the device, by relaxing the requirements on the orbit stability inside the device, or by some combination of those. Details of requirements for the cases 3 and 4 remain to be worked out.

Table 3.4-9: Requirements for maximum possible change of absolute first- and second-field integral errors over the entire gap range (based on local orbit modeling with x-ray BPMs participating in orbit correction) [3.4-25].

	Case 1	**Case 2**	**Case 3**	**Case 4**
Field Integral	**Single 5-m device**	**Single 2.5-m device**	**One 2.5-m device upstream or downstream**	**Two independent 2.5-m devices[1]**
$\int B_y dz$ (G·cm)	4700	4700	TBD	TBD
$\int B_x dz$ (G·cm)	470	470	TBD	TBD
$\int dz \int B_y dz'$ (G·cm^2)	510,000	130,000	TBD	TBD
$\int dz \int B_x dz'$ (G·cm^2)	170,000	43,200	TBD	TBD

[1] The two undulators are uncorrelated, so we made the tolerance $\sqrt{2}$ tighter than for a single ID.

A misaligned ID could also generate orbit steering from off-centered dynamic-field integrals. The effect is negligible for planar undulators that have wide poles and weak dynamic-field integrals. For polarizing wigglers, due to fast field roll-off, the effect becomes more noticeable and should be reduced by aligning the device properly [2] and applying a local correction scheme to it. The requirements on polarizing wiggler alignment are still under investigation; it is expected that they will be at the same level as that of the ring quadrupole magnets.

A special case for steering stability is that of the fast polarity switch of the EMVPU, which requires a dedicated local time-dependent orbit correction scheme. Detailed studies are ongoing, beam testing with current CPU is also planned.

3.4.5.4 Optics Perturbation

The IDs at the APS are mostly hybrid permanent magnet devices that have little effect on the optical functions of the storage ring because of the high (7-GeV) energy of the stored beam. Normal quadrupole errors, which change the tune of the ring, are generally ignored because their effect is unnoticeable. The edge-focusing effect (affecting only the vertical plane tune) is small as well and is ignored. Skew quadrupole errors, which change the vertical beam size everywhere in the ring, are generally ignored because their effect is small.

[2] Alignment also preserves the effective K value.

Similar effects are expected from revolver and SCU devices as they will have K values and field roll-offs similar to existing planar devices, but detailed field measurements need to be performed.

To simulate perturbations from all planar undulators, the APS Upgrade lattice "NoQ2-4Random1-9-9" (4NLSS, with chromaticity 9 in both plane) was used as the baseline optics, to which was added 25 "U36" type undulators ($L_w = 4.32$ m, $K = 3.1$) in the straight sections. One hundred seeds of random quadrupole-magnet tilt errors (at a level that provides a match to measured optics errors and vertical emittance) and ID field errors (from Table 3.4-7b) were used in our simulations. Statistical simulation results are presented in Table 3.4-10. The dynamic aperture is basically unchanged and beam lifetime is > 3.8 h (12-mm bunch length) for 95% of the random seeds (see Figure 3.4-15). The conclusion is that the perturbations from planar undulators are acceptable.

Table 3.4-10: Tune and coupling perturbations from planar IDs.

	$\overline{\lvert\Delta\nu\rvert}$	$\sigma(\lvert\Delta\nu\rvert)$	$\lvert\Delta\nu\rvert(95\%)$	$\overline{\frac{\Delta\beta}{\beta_0}}$	$\sigma(\frac{\Delta\beta}{\beta_0})$	$\frac{\Delta\beta}{\beta_0}(95\%)$	$\overline{\Delta K}$	$\sigma(\Delta K)$	$\frac{\Delta K}{K_0}(95\%)$
x	1.7×10^3	1.3×10^3	$< 3.6 \times 10^3$	1.5%	0.65%	2.6 %	1.31 %	3×10^4	4.4%
y	2.1×10^2	3.5×10^4	$< 2.2 \times 10^2$	2.8%	0.13%	3.0 %			

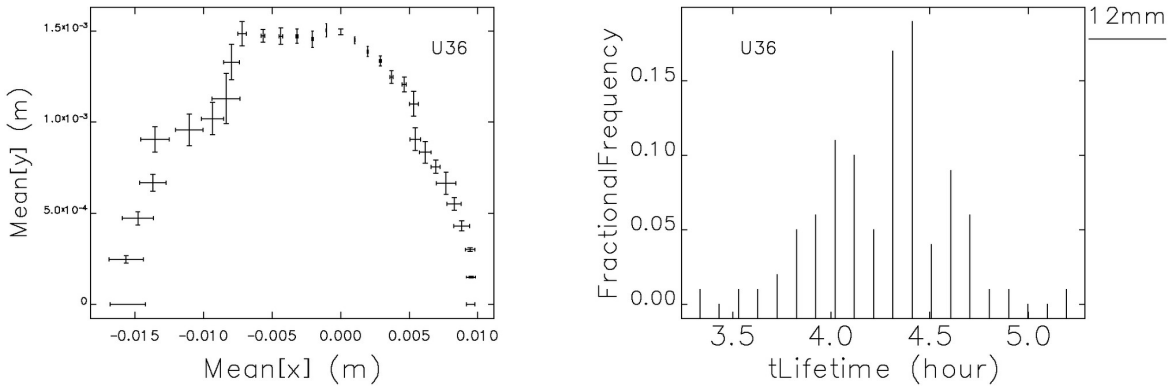

Figure 3.4-15: Simulated dynamic aperture and beam lifetime (12-mm bunch length) from planar ID perturbations.

As discussed in the previous section, effects from polarizing wigglers are much larger due to their generally larger K value and faster field roll-off. Figure 3.4-16 shows the on-axis kick (x=0 or y=0) from the CPU, IEX, and APPLE devices individually in circular polarization mode. The strongest perturbation source is the IEX undulator, which is currently under commissioning. Figure 3.4-17 shows simulated dynamic aperture and momentum aperture from the bare lattice (APS), the lattice with CPU only (CPU), and the lattice with IEX only (IEX). Optical errors are included in the simulation but the static ID-field focusing error is ignored. In this case, there is no noticeable dynamic aperture decrease. IEX magnet measurements show fairly large static field error variation between stored beam (on-axis) and injected beam, and simulation results that include these measured field error indicate a decrease of dynamic aperture (Figure 3.4-18). Preliminary beam testing results show very good agreement with simulation results: in a low-chromaticity lattice, there is no decrease of injection efficiency or beam

lifetime; in a high-chromaticity lattice, some decrease is seen in injection efficiency and beam lifetime. The reduction of dynamic aperture is not very significant, and work is on-going on restoring this machine property by adjusting the local multipole correction coils.

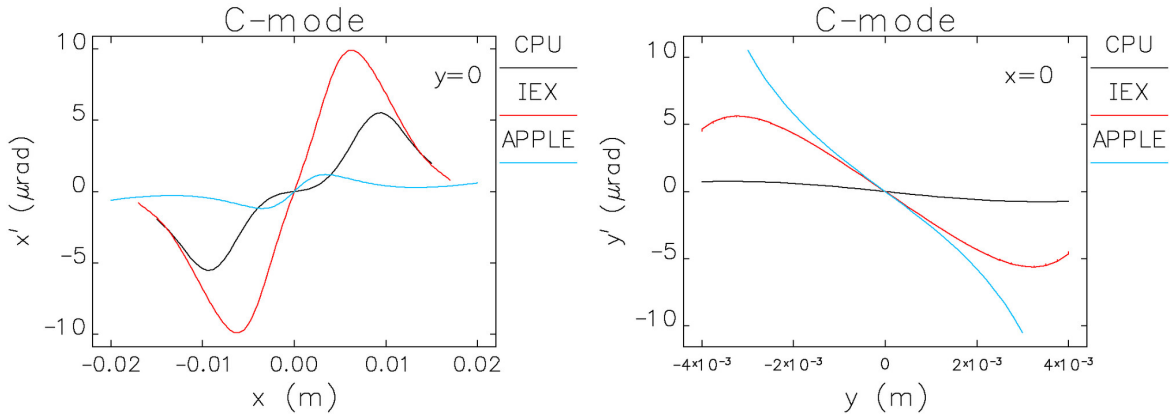

Figure 3.4-16: On-axis dynamic kick of CPU, IEX, and APPLE devices in circular polarization mode.

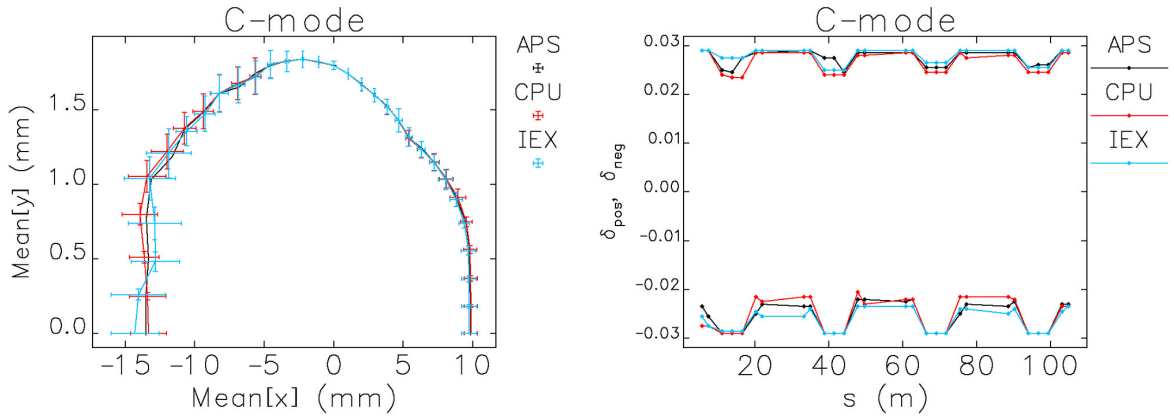

Figure 3.4-17: Simulated dynamic aperture and momentum aperture of bare APS lattice (APS), lattice with CPU (CPU), and lattice with IEX (IEX).

In current APS operation, no noticeable nonlinear effects are seen from the CPU. This ID will be replaced by the EMVPU eventually. Though there is no doubt that the new EMVPU will have better field quality than the CPU, it will have to be checked through simulations when the design is available.

The APPLE device will be the strongest coupling perturbation source when it operates in the inclined mode. Preliminary simulation results show that the effects are quite small for the 7-GeV beam and should not be a concern. There is also no requirement by users for APPLE to work in the inclined mode. For an APPLE working in linear and normal elliptical mode, the perturbation can be largely reduced by properly arranged L-shims. (See [3.4-26] and references therein.)

To reduce the perturbations from the polarizing undulators and confine them locally, extra local correctors are required and feed-forward correction tables need to be built experimentally using beam-based methods. Because the nonlinearities cannot be properly expressed by multipole components,

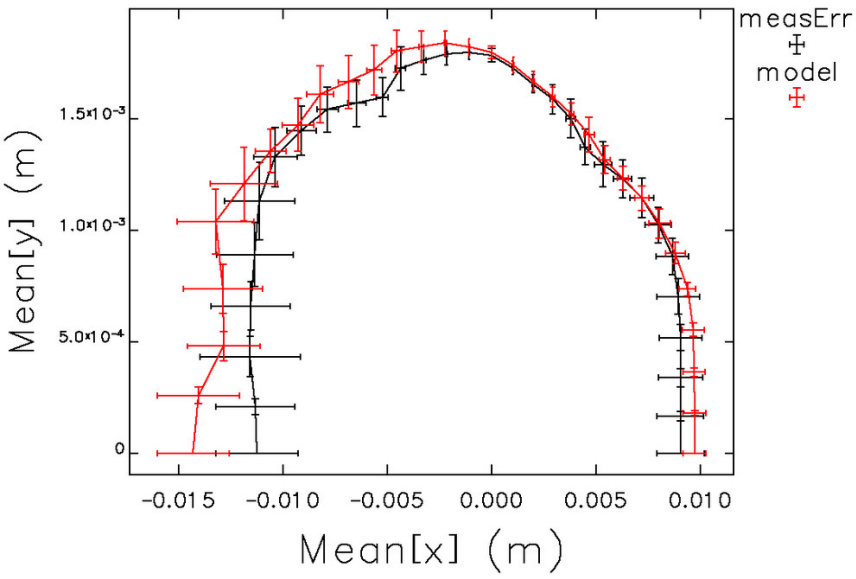

Figure 3.4-18: Simulated dynamic aperture for IEX with (measErr) and without (model) measured field errors.

only the largest optical perturbation term (usually x-tune) can be corrected with local multipole correctors. To completely remove the optics perturbation outside the source ID, at least four-pair independent adjustable quadrupole-magnet knobs are required, which may be realized though adjusting the quadrupole-magnet triplet adjacent to the ID. This correction scheme will be tested in ongoing IEX commissioning.

3.4.5.5 Canted Undulators

In a canted undulator section, two independent undulators separated by a 1-mrad horizontally and inboard-deflecting dipole magnet produce two photon beams separated by the same angle. The photon beams are "canted" by $\pm$ 0.5 mrad with respect to the original beam. Thus the number of possible simultaneous experiments at this sector is doubled.

Presently APS has seven such pairs in 5-m straight sections. The undulators are slightly shorter than the usual 2.4 m because space is needed for additional components: one 1-mrad dipole, one mini-BPM, and one combined function H/V dipole corrector. The required opposite 0.5-mrad angle kicks at the ends are provided by storage ring corrector magnets.

Presently the orbit bump is symmetric with the 1-mrad dipole in the center. It is possible to have an asymmetric bump, in which the two legs are of unequal length. The angle separation would still be 1 mrad. This is applicable in the present $\sim$5-m straight section and in the future $\sim$7.7-m-long straight sections.

If we had an asymmetric bump with 1:2 length ratio, say, then the upstream-to-downstream trajectory angle ratio would be 2:1. The canting angles would be $+0.67$ and -0.33 mrad.

The amount of asymmetry is limited to how close we allow the two photon beams to pass by the dipole-fan photon absorbers located downstream. Presently for the symmetric canted straight section, the photon beam produced by the upstream undulator passes close to the outboard photon absorber, and the steering interlock in place has little margin of error. For any bump with upstream angle larger than +0.5 mrad, a relocation of an absorber or a redesign of the vacuum chamber will be required. For an asymmetric bump with upstream angle smaller than +0.5 mrad, a redesign would not be required.

3.4.6 Optimization Methods and Ultimate Performance

The user requirements that will drive the choice of new insertion devices are not fully defined. However, generally speaking, individual beamlines work within certain bands or ranges of photon energies and desire the highest possible brightness or flux within those bands. This suggests the possibility of automated selection of ID characteristics. In this section, a method is described for automated selection that greatly increases the ease with which the optimal device may be determined. Predictions of ultimate performance for the APS Upgrade and beyond are also shown.

The APS presently operates at 100 mA, but will move to 150 mA as part of the Project. Due to power and power density limits in the front ends, the optimum for one current may well not be optimal for another. Hence, one should optimize for 150 mA. The software described here was configured to allow determining optimal choices for 100, 150, and 200 mA.

Another variable is the type of front end, since that determines the specific power and power density limits. We have investigated a number of possible combinations, as listed in Table 3.4-11. The canted front ends (CFEs) and high-heat-load (HHL) front ends exist now but, as will be seen, they impose significant limits on the performance of advanced devices as the beam current and device length are increased. The VHHL (very high heat load) front end is an extrapolation of the existing HHL design, obtained by simply multiplying the HHL limits by 1.5.

Table 3.4-11: Potential front-end options used in analysis.

Front End	**Power Limit** kW	**Power Density Limit** $\mathrm{kW/mrad^2}$
Canted	20	281
HHL	21	590
VHHL (extrapolation)	32	885
EHHL (new concept)	210	5900

The EHHL (extremely high heat load) case is something altogether different, with assumed power and power density limits that are ten times the HHL values. Analyzing the EHHL front end may seem pointless, since it is an order of magnitude beyond what we are doing today. However, it was realized in the course of this analysis that for SCUs, such high limits may be possible. The power and power density limits for the front ends pertain to the first photon shutter, which must withstand the full power of the beam when the bremsstrahlung stopper is closed. The stopper is closed when the user needs to enter the hutch to change samples, for example. Clearly, there is no need for the device to remain energized when the user is in the hutch. Hence, we realized that the SCU could simply be turned off, in which case the photon shutter will only see the comparatively weak bending magnet radiation. However, if the SCU is always off when the shutter is closed, the front-end limit will be

much higher. The new limits on the front end will presumably originate with the fixed masks, which see the peripheral part of the beam. While these limits are as yet to be determined, it seems clear that they will be much higher than the present HHL limits, particularly if the masks are protected by beam steering interlocks. A factor of 10 was chosen as a working assumption.

Of course, the photon shutter and bremsstrahlung stopper are not necessarily closed in a controlled fashion. One can imagine that the user might erroneously "break into" the hutch without going through proper procedures, causing the shutters to close immediately. In this case, the device needs to be shut off when the closing of the shutters is detected. The photon shutter may briefly see very high heat loads. If this is unacceptable, then the stored beam could be dumped instead.

One might wonder if similar thinking can be applied to HPM devices. While such devices cannot be turned off in the same way as an electromagnetic device, the gap can be opened, giving the same end result. Under controlled conditions, there is no difference. However, in an emergency an SCU can be forced to zero current in about 100 ms, while it may take longer to open an HPM device sufficiently. Even so, emergencies are by design rare. In such cases, one can always resort to dumping the stored beam to protect the shutter, should the opening of the gap be insufficiently rapid.

In addition to the choice of front end, the length of the straight section is potentially variable, as is the length of the device. In all, analysis was performed for six combinations of straight section length and front end:

1. Short canted straight with CFE, which accommodates two devices of up to 2.1-m length each.
2. Long canted straight with CFE, which accommodates two devices of up to 3.55-m length each.
3. Short straight with HHL front end, which accommodates one device of up to 4.8-m length.
4. Long straight with HHL front end, which is assumed to accommodate one device of up to 7.7-m length.
5. Long straight with VHHL front end, which is assumed to accommodate one device of up to 7.7-m length.
6. Long straight with EHHL front end, which is assumed to accommodate one device of up to 7.7-m length.

To provide some flexibility to the algorithm, device lengths were permitted to either take the maximum value, or half of the maximum value. This provided a way to relieve power density limits in the case of the less capable front ends.

3.4.6.1 Optimization Method

The optimization method described in this section can be applied to single- and multi-period devices (i.e., revolvers). This document describes the application of the method to revolvers, since this is the most complicated case. Application to single-period devices is very similar. Results were already shown for two revolver examples in section 3.4.2.5.

The starting point of the method is the assumption that each beamline will be interested in working over a specific set of photon energy bands, and that the desired quantity to optimize is the brightness.

(If flux is the quantity of interest, the same technique can readily be applied.) The analysis has two steps: data preparation and choice of an optimum for a specific requirement.

For data preparation, the following steps are executed for each combination of beam current, front-end type, and straight section length.

1. Vary the device period from 17 mm to 35 mm in 1-mm steps.
   (a) Compute the maximum K value assuming NdFeB magnets according to Equation (3.4-1). A 10.75-mm magnetic gap is assumed. However, this equation is recognized as being somewhat conservative, so the results are valid for a slightly larger gap.
   (b) Run `sddsbrightness` and `sddsfluxcurve` to get power density and total power as a function of K, along with brightness and flux density for harmonics 1 through 9.
   (c) Limit the photon energy range for each harmonic to account for the power and power density limits of the chosen front end.
   (d) Multiply the brightness for each harmonic by values that approximately account for the effect of typical phase errors [3.4-27].
   (e) Compute the brightness envelope over all harmonics. This eliminates the overlap and gives a single curve of maximum brightness vs photon energy. Gaps in the spectrum are represented by zero values.
2. Choose in turn the data for each device period from 17 to 33 mm.
   (a) Loop over all periods that are shorter than or equal to the chosen period.
      i. For each pair of periods, compute the maximum brightness available from either undulator as a function of photon energy.

Following this step, a large set of data files exist for each combination of beam current, front end, and straight section length. Each file describes, for any pair of undulator periods, the maximum brightness available as a function of photon energy when the relevant front-end limits are taken into account.

The next step is to find the optimal pairs of periods for a specific set of photon energy bands. This is performed with another script that accepts the beam current, front-end type, and straight section type, as well as a list of lower and upper limits for any number of energy bands. It produces a list of the top combinations of periods, along with graphs of the performance for each. Because all the data are generated ahead of time, it takes less than 10 s to produce a result. (This algorithm has also been implemented for optimization of three-period revolvers. The amount of data is somewhat larger and, as a result, it takes about 60 s to find the best devices.) The algorithm for choosing the best pairs is as follows:

1. For each period pair p:
   (a) For each band b determine the sum of the widths of any gaps in the brightness tuning curves. Call this W_{bp}.
   (b) For each band b compute the minimum brightness and the average brightness. Call these $B_{bp,m}$ and $B_{bp,a}$, respectively.
2. Perform a nondominated sort [3.4-28] of the results for all p in order to minimize W_{bp} while maximizing $B_{bp,m}$ and $B_{bp,a}$.

3. Select only the first-rank solutions, i.e., the Pareto-optimal set, for further review.

Depending on the number of bands, the algorithm may choose a single period pair or a handful of period pairs. These selections are equivalent in the sense that none is dominated in all performance measures by any other selection. Down-selection from this point requires introduction of an additional decisive criterion, or review by a potential user of the device. When a fully automated selection is desired, a useful criterion to add is maximization of the minimum (for each p) over all bands.

The use of this algorithm for single-period devices is quite straightforward: one simply uses the single-period files instead of the multi-period files. For SCUs and ASCUs (Advanced SCUs), item 1a in the data preparation stage is changed to use the predicted performance curve for the SCUs, with conservative limits for the maximum current as described in earlier sections. In addition, the effective magnetic length of the SCUs is reduced by 0.6 m from that for a HPM device, to account for the cryostat and warm-to-cold transitions. That is, devices are required to have fixed insertion length, not fixed effective length.

3.4.6.2 Optimized Performance Results

To illustrate what can potentially be gained from the APS Upgrade and beyond, six photon energy bands were chosen as examples: 5-15 keV, 15-25 keV, 25-40 keV, 40-100 keV, 25-26 keV, and 75-76 keV. For each, the optimum HPM, two-period revolver, SCU, and ASCU were determined for various combinations of beam current, straight section length, and front end.

The results of the analysis take two forms: first, it shows for any given situation which HPM, two-period revolver, or SCU device is best. The data also show the degree to which, for example, the best SCU exceeds the performance of the best HPM. The easiest way to do this is by showing the ratio of the best SCU or ASCU performance to the best HPM performance. This is seen in Tables 3.4-12 and 3.4-13, which show the ratio of the optimized minimum brightness for a two-period revolver or SCU in the given band to the same quantity for a single-period HPM device. Also shown is the ratio of the optimized minimum brightness for a single-period HPM to the "reference" configuration, which is defined as a 2.1-m-long U33 device in a canted straight at 100 mA. To find the improvement from, say, an optimized ASCU relative to the reference, one simply multiplies the appropriate "Brightness Ratio" by the "HPM rel. reference."

Note that because the ratios are formed from the *minimum* brightness values in each band, the table may tend to understate the improvement. For example, it may well be that the brightness at certain regions in the band increases by a significantly larger factor. Careful definition of the photon bands of interest is thus essential to getting a reliable result.

At 100 mA, the SCU and ASCU are little different except for the 40-100 keV band. For the other bands, improvements over HPM devices are generally factors of 2 to 4, and then only for long devices. In the 40- to 100-keV band, we see improvements of an order of magnitude or more. Two-period revolvers give improvements of less than a factor of two. Section 3.4.2.5 shows additional examples of revolver optimization.

At 150 mA, the current for the APS Upgrade, the results for SCUs generally become less impressive unless we invoke the EHHL front-end concept. For all other front-end choices, long SCUs lose ground compared to 100 mA. The reason is that, at higher current and with long devices, the wide range of K

values available from an SCU is less of an advantage, because the possible tuning range is limited by the front-end power density limit.

In conclusion, it emerges that SCUs and advanced SCUs can provide significant advantages, particularly for high photon energies, but to fully capitalize on this technology requires a new way of thinking about front-end operations.

Table 3.4-12: Results of ID optimization for 100 mA. The "HPM Rel. Reference" column shows the ratio of the optimized minimum brightness for an HPM to the minimum brightness for a U33 device in a short, canted straight at 100 mA. The "Brightness Ratio" column shows the ratio of the minimum brightness for the optimized revolver, SCU, or ASCU to the minimum brightness for the optimized HPM device. The "Lengths" and "Periods" columns list values for HPM, Revolver, SCU, and ASCU, in order.

Band	Front End	LSS	HPM Rel. Reference	Brightness Ratio			Lengths	Periods
				Rev.	SCU	ASCU		
keV							cm	mm
5-15	CFE	0	1.1	1.4	1.2	1.3	210/210/150/150	32/24+30/22/20
5-15	HHL	0	2.8	1.6	1.8	1.8	480/480/420/420	31/24+30/23/23
5-15	VHHL	1	3.7	1.8	1.8	1.8	770/770/710/710	31/24+30/24/24
5-15	EHHL	1	3.7	1.8	2.2	2.5	770/770/710/710	31/24+30/22/18
15-25	CFE	0	1.4	1.3	1.6	2.7	210/210/150/150	30/27+30/21/15
15-25	HHL	0	3.4	1.3	2.0	2.0	480/480/420/420	30/27+30/21/21
15-25	VHHL	1	4.5	1.3	1.9	1.9	770/770/710/710	30/27+30/22/22
15-25	EHHL	1	4.5	1.3	2.1	4.3	770/770/710/710	30/27+30/21/15
25-26	CFE	0	2.1	1.0	1.6	3.0	210/210/150/150	26/26+17/15/13
25-26	HHL	0	5.1	1.0	2.4	3.2	480/480/420/420	26/26+17/15/14
25-26	VHHL	1	6.7	1.0	2.6	3.6	770/770/710/710	26/26+17/15/14
25-26	EHHL	1	6.7	1.0	2.6	4.5	770/770/710/710	26/26+17/15/13
25-40	CFE	0	1.9	1.2	1.9	2.8	210/210/150/150	28/28+23/20/18
25-40	HHL	0	4.4	1.2	2.5	2.5	480/480/420/420	28/28+23/20/20
25-40	VHHL	1	5.8	1.2	2.2	2.2	770/770/710/710	28/28+23/21/21
25-40	EHHL	1	5.8	1.2	2.7	4.4	770/770/710/710	28/28+23/20/17
40-100	CFE	0	250.7	1.2	8.2	18.3	210/210/150/150	25/24+25/18/16
40-100	HHL	0	572.0	1.2	10.3	14.5	480/480/420/420	25/24+25/18/17
40-100	VHHL	1	764.2	1.2	10.7	15.9	770/770/710/325	25/24+25/18/15
40-100	EHHL	1	764.2	1.2	10.7	33.2	770/770/710/710	25/24+25/18/15
75-76	CFE	0	7.9	1.1	5.8	11.0	210/210/150/150	25/26+25/17/13
75-76	HHL	0	18.2	1.1	7.3	7.6	480/480/420/420	25/26+22/17/14
75-76	VHHL	1	24.1	1.1	7.5	8.0	770/770/710/710	25/26+22/17/14
75-76	EHHL	1	24.1	1.1	7.5	14.6	770/770/710/710	25/26+22/17/13

Table 3.4-13: Results of ID optimization for 150 mA. The "HPM Rel. Reference" column shows the ratio of the optimized minimum brightness for an HPM to the minimum brightness for a U33 device in a short, canted straight at 100 mA. The "Brightness Ratio" column shows the ratio of the minimum brightness for the optimized revolver, SCU, or ASCU to the minimum brightness for the optimized HPM device. The "Lengths" and "Periods" columns list values for HPM, Revolver, SCU, and ASCU, in order.

Band	Front End	LSS	HPM Rel. Reference	Brightness Ratio			Lengths	Periods
				Rev.	SCU	ASCU		
keV							cm	mm
5-15	CFE	0	1.6	1.4	1.0	1.0	210/210/150/150	32/24+30/24/24
5-15	HHL	0	4.2	1.6	1.1	1.1	480/480/420/420	31/24+30/26/26
5-15	VHHL	1	5.6	1.8	1.1	1.1	770/770/710/710	31/24+30/28/28
5-15	EHHL	1	5.6	1.8	2.2	2.5	770/770/710/710	31/24+30/22/18
15-25	CFE	0	2.0	1.3	1.3	1.3	210/210/150/150	30/27+30/23/23
15-25	HHL	0	5.1	1.3	1.3	1.4	480/480/420/180	30/27+30/26/15
15-25	VHHL	1	6.8	1.3	1.3	1.8	770/770/710/325	30/27+30/27/15
15-25	EHHL	1	6.8	1.3	2.1	4.3	770/770/710/710	30/27+30/21/15
25-26	CFE	0	3.1	1.0	1.6	2.3	210/210/150/150	26/26+17/15/14
25-26	HHL	0	7.6	1.0	2.4	2.4	480/480/420/420	26/26+17/15/15
25-26	VHHL	1	10.0	1.0	2.6	2.6	770/770/710/710	26/26+17/15/15
25-26	EHHL	1	10.0	1.0	2.6	4.5	770/770/710/710	26/26+17/15/13
25-40	CFE	0	2.8	1.2	1.7	1.7	210/210/150/150	28/28+23/21/21
25-40	HHL	0	6.6	1.2	1.6	1.7	480/480/420/180	28/28+23/23/17
25-40	VHHL	1	8.7	1.2	1.4	1.8	770/770/710/325	28/28+23/24/18
25-40	EHHL	1	8.7	1.2	2.7	4.4	770/770/710/710	28/28+23/20/17
40-100	CFE	0	376.1	1.2	8.2	8.2	210/210/150/150	25/24+25/18/18
40-100	HHL	0	858.0	1.2	4.9	13.9	480/480/420/180	25/24+25/21/15
40-100	VHHL	1	1146.3	1.2	5.1	11.2	770/770/325/325	25/24+25/18/16
40-100	EHHL	1	1146.3	1.2	10.7	33.2	770/770/710/710	25/24+25/18/15
75-76	CFE	0	11.9	1.1	5.8	5.9	210/210/150/150	25/26+25/17/14
75-76	HHL	0	27.2	1.1	3.5	5.8	480/480/420/180	25/26+22/15/13
75-76	VHHL	1	36.2	1.1	3.7	6.9	770/770/710/325	25/26+22/15/13
75-76	EHHL	1	36.2	1.1	7.5	14.6	770/770/710/710	25/26+22/17/13

3.4.7 References

[3.4-1] M. Jaski et al. Magnetic Simulation of an Electromagnetic Variably Polarizing Undulator, Proceedings of PAC 2011, (2011).

[3.4-2] R. Dejus et al. Coil Energizing Patterns for an Electromagnetic Variably polarizing Undulator, Proceedings of PAC 2011, (2011).

[3.4-3] R. Dejus. Power and Power Density of Permanent Magnet Hybrid Undulators and Superconducting Undulators in Support of the APS Upgrade. Technical Report MD-TN-2010-003, ANL, (2010).

[3.4-4] J. Safranek et al. Nonlinear dynamics in a SPEAR wiggler, Phys. Rev. ST Accel. Beams, **5**, 010701, (2002).

[3.4-5] R. Dejus et al. On-Axis Brilliance and Power of In-Vacuum Undulators for the Advanced Photon Source. Technical Report ANL/APS/LS-314, Advanced Photon Source, (2009).

[3.4-6] J. Chavanne et al. Status of the ESRF Insertion Devices, Proc. of EPAC 2004, pp. 372–374, (2004).

[3.4-7] T. Hara et al. Revolver undulator for BL15XU at SPring-8, Nuclear Instruments and Methods A, **467-468**, 161–164, (2001).

[3.4-8] R. Dejus and W.-K. Lee. Undulator Gap Tapering for Manipulation of Radiation Properties. to be published, (2011).

[3.4-9] S. Sasaki et al. Conceptual Design of Quasiperiodic Undulator, Rev. Sci. Instrum., **66**, 1953–1955, (1995).

[3.4-10] S. Hashimoto and S. Sasaki. Concept of a New Undulator that Will Suppress the Rational Harmonics, Nucl. Instrum. Meth. Phys. Res. A, **361**, 611–622, (1995).

[3.4-11] J. Bahrdt. Private communication.

[3.4-12] Cobham Technical Services, Opera 3D Finite Element Code.

[3.4-13] M. Jaski. Design and Fabrication of Magnet Coils, Proceedings of MEDSI 6, volume 1.

[3.4-14] N. Nakamura et al. Reduction in Resistive-Wall Impedance of Insertion-Device Vacuum Chamber by Copper Coating, Proceedings of EPAC98, (1998).

[3.4-15] H. Sakai et al. Development of Copper Coated Chamber for Third Generation Light Sources, Proceedings of PAC05, (2005).

[3.4-16] Y.-C. Chae. ANL, Private communication.

[3.4-17] Y.-C. Chae. How Many IVUs Can We Install without Sacrificing 16-mA Operation? Technical Report ANL/APS/LS-318, Advanced Photon Source, (2009).

[3.4-18] M. Borland. elegant: A Flexible SDDS-Compliant Code for Accelerator Simulation. Technical Report ANL/APS/LS-287, Advanced Photon Source, (2000).

[3.4-19] Y. K. Wu et al. Explicit symplectic integrator for s-dependent static magnetic field, Phys. Rev., **E68**, 046502, (2003).

[3.4-20] J. Bahrdt and Wüstefeld. Symplectic tracking and compensation of dynamic field integrals in complex undulator structures, Phys. Rev. ST Accel. Beams, **14**, (2011).

[3.4-21] P. Elleaume. A New Approach to Electron Beam Dynamics in Undulators and Wigglers, Proc. of EPAC 1992, pp. 661–663, (1992).

[3.4-22] E. Gluskin et al. An Electromagnet Helical Undulator for Polarized X-rays, P. Pianetta, editor, AIP Conf. Proc., volume 521, pp. 344–347. AIP, (2000).

[3.4-23] J. Bahrdt et al. Active Shimming of the Dynamic Multipoles of the BESSY UE112 APPLE Undulator, Proceedings of EPAC 2008, pp. 2222–2224, (2008).

[3.4-24] Y.-C. Chae and G. Decker. Advanced Photon Source Insertion Device Field Quality and Multipole Error Specification, Proc. of PAC 1995, pp. 3409–3411, (1995).

[3.4-25] A. Xiao and L. Emery. ANL, Private communication.

[3.4-26] J. Bahrdt et al. Performance of the PetraIII APPLEII Undulator, IPAC2011 Proceedings, pp. 3254–3256, (2011).

[3.4-27] R. Dejus. ANL, Private communication, (2010).

[3.4-28] K. Deb et al. IEEE TEC, **6**, 182, (2002).

3.5 Superconducting Undulator

3.5.1 Introduction

3.5.1.1 Motivation

A superconducting undulator (SCU) employs a set of superconducting coils to generate a periodic magnetic field. Due to the high current-carrying capacity of superconductors, magnetic flux densities near 1 T can be reached despite undulator period lengths as short as 1.5 to 2.0 cm. (In a conventional permanent magnet or hybrid device, reaching a 1-T field would typically require a period length closer to 3 cm.) Such short-period undulators are becoming very attractive because they produce high brightness at higher photon energies. According to our detailed analysis of various undulator types, including conventional hybrid technology and in-vacuum permanent magnet technology [3.5-1], superconducting undulators have the potential to outperform all other technologies in terms of peak magnetic field for a given period length and magnetic gap, as illustrated by Figure 3.5-1.

On-axis brightness tuning curves for four in-vacuum undulators (1.6-cm, 1.8-cm, 2.0-cm, and 2.5-cm periods, each 2.4-m long) compared to the APS Undulator A for harmonics 1, 3, and 5 in linear horizontal polarization mode for 7-GeV beam energy and 100-mA beam current are shown in Figure 3.5-1. The minimum reachable harmonic energies were calculated for in-vacuum undulators assuming SmCo magnets and a 5-mm beam-stay-clear gap. For comparison, the data for 1.6-cm and 1.8-cm superconducting undulators at the 9.5-mm pole gap have been marked separately by the crosses. As is

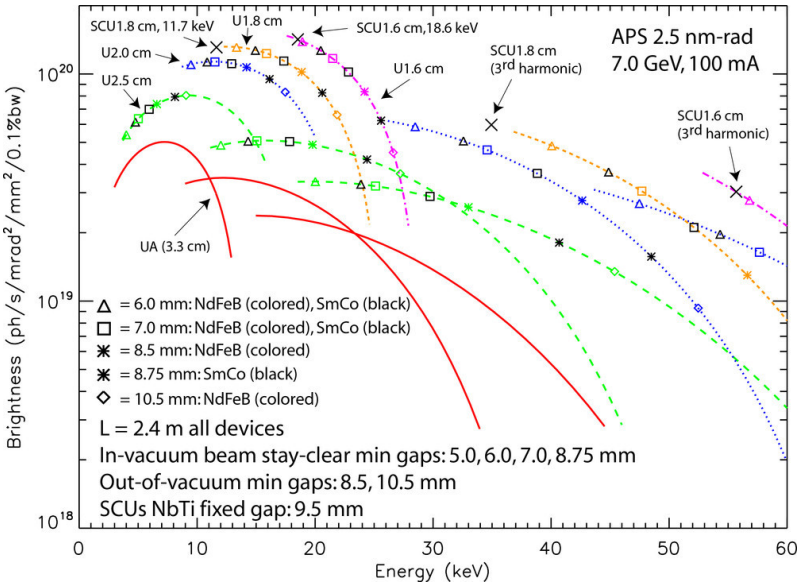

Figure 3.5-1: Comparison of the tuning range from undulators with various period lengths, including hybrid permanent magnet undulators and a superconducting undulators with 1.6-cm and 1.8-cm periods. Beam parameters are for the present APS.

seen from Figure 3.5-1, the 9.5-mm gap and 1.6-cm period SCU at the first-harmonic energy of 18.6 keV nearly overlaps with the 5-mm gap in-vacuum SmCo undulator. A magnetic gap as small as 5 mm is impractical for the APS storage ring, while the 9.5-mm gap of the SCU allows enough room for a beam chamber. This issue is particularly important given the strong desire to continue to run with high single-bunch current, e.g., in hybrid mode (see sections 3.4.4 and 3.2.4).

The magnetic device lengths are fixed in this comparison, which serves to illustrate the improved tuning range but obscures the fact that, for the same insertion length, an SCU has shorter magnetic length (due to the cryomodule) compared to a conventional device. However, the advantage for an SCU persists when this consideration is taken into account, as Figures 3.5-2 and 3.5-3 show. In this example, the SCU magnetic length is 0.9 m shorter than the insertion length, which is a realistic value. The case for the SCU performance advantage is presented more rigorously in section 3.4.6.

3.5.1.2 Worldwide Status

The advantage of applying superconducting technology to undulators has long been recognized by both high-energy physicists and the synchrotron light source community. A superconducting helical undulator was developed at Stanford for the very first free-electron laser experiment in the 1970s [3.5-2]. In the 1980s, the use of such undulators for positron sources in high-energy physics was suggested, and the idea was demonstrated at Budker Institute, Russia [3.5-3]. Recently, a 4-m superconducting helical undulator module was built at the Rutherford Appleton Laboratory, UK, for the International Linear Collider positron source R&D program [3.5-4]. In Europe, a superconducting planar undulator built by ACCEL is in operation at the ANKA light source in Germany [3.5-5], and another device for ANKA is being built by Babcock Noell GmbH [3.5-6]. In Asia, R&D on a superconducting undulator is underway at the National Synchrotron Radiation Research Center, Taiwan [3.5-7]. Presently, there are

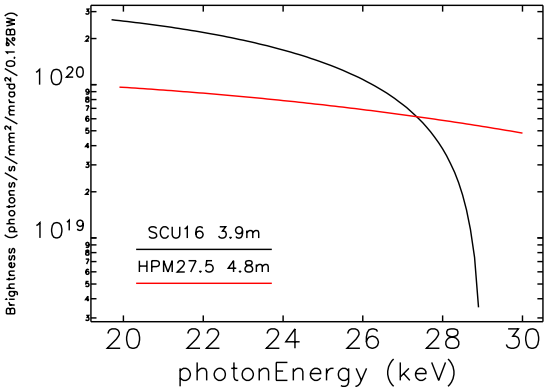

Figure 3.5-2: Comparison of optimal SCU and HPM devices for a 4.8-m straight section targeting 20-25 keV.

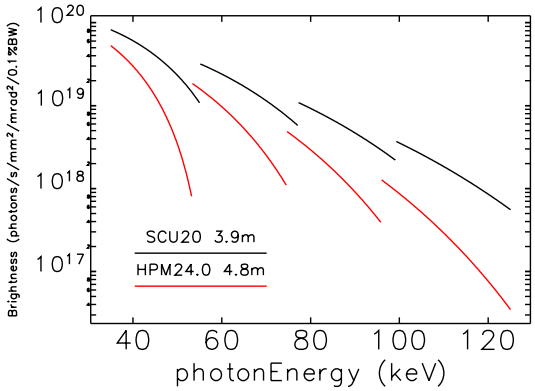

Figure 3.5-3: Comparison of optimal SCU and HPM devices for a 4.8-m straight section targeting 40-120 keV.

no superconducting undulators currently in operation in the U.S.

3.5.2 Research and Development: SCU0

3.5.2.1 Goals

A superconducting undulator is a complex system that includes a precise superconducting magnet operating in the presence of heating by an electron beam. A dedicated R&D program therefore was required to address the following challenging issues:

- Design of the superconducting magnetic structure that produces undulator magnetic field of high quality.
- Development and verification of manufacturing techniques.
- Development of magnetic measurement techniques.
- Building and testing of magnetic structure prototypes.
- Understanding heat sources in the system—both static and dynamic.
- Design of an adequate cooling system.
- Building and testing a full-scale undulator in the storage ring.

The first superconducting undulator, SCU0, is thus a fully functional test device that has been built to be installed into the APS storage ring as a final step of the R&D program. The period length of 16 mm was chosen for this device to deliver 20-25 keV photon energy in the first harmonic. The parameters of the SCU0 are listed in Table 3.5-1.

The design of the SCU0 is based on the experience gained during the feasibility study at the APS that is described in the following section.

Table 3.5-1: Parameters of the SCU0.

1st-harmonic photon energy	20-25	keV
Period length	16	mm
Magnetic gap	9.5	mm
Magnetic length	0.34	m
Cryostat length	2.063	m

3.5.2.2 Feasibility Study at the APS

Since there are no commercial vendors of superconducting undulators in the world except possibly a single company in Germany, an in-house R&D program was started at the APS to develop superconducting undulators. In 2008-09 our activity was focused on developing construction techniques. This phase involved magnetic modeling, developing manufacturing techniques, building, and testing short prototype magnets.

Magnetic simulation of the superconducting undulator was performed using the 2D and 3D OPERA software packages. The issues addressed were the field profile, the undulator peak field value (the maximum field on the undulator axis), design of the magnet ends including correction coils, and calculation of the load line of the superconductor [3.5-8]. The task of magnetic modeling was to find the shortest period length that would give the desired tuning range of 20-25 keV in the first harmonic without violating the APS storage ring beam-stay-clear requirement of 7 mm in the vertical direction. Since the magnetic structure of the planar superconducting undulator consists of two half-magnets separated with a magnetic gap where a beam chamber is located, a magnetic gap of 9 mm was chosen for the modeling, taking into account the thickness of the beam chamber walls.

Despite the opportunities offered by the higher critical current density of a Nb_3Sn superconductor, this project uses the widely used and robust NbTi superconductor. In particular, a round NbTi wire with 0.75-mm outside diameter available from Supercon Inc. was used for the modeling. The superconductor load line was calculated for a period length of 16 mm and a magnetic gap of 9 mm. The calculation showed that the on-axis field of 0.64 T required for the first harmonic energy of 20 keV could be achieved at a wire current of 429 A. At this current the superconductor is at 65% of its critical value at a temperature of 4.2 K. The calculated temperature margin was about 2.1 K. At a magnetic gap of 9.5 mm, the operational current rises to about 500 A, as was found in the tests of the prototype coils (see below).

In the undulator structure, the winding core (or the former) can be made of either nonmagnetic (e.g., an Al alloy) or magnetic material (e.g., a low carbon steel 1006-1010). The effect of a magnetic core on the undulator peak field and the superconductor peak field (the maximum field in the conductor) was analyzed using a 2D OPERA model. It was found that the ratio of the maximum field in the conductor to the on-axis peak field is the lowest for the iron core case, at about 2.8, as compared to 3.3 for the nonmagnetic core case. According to the simulation, the magnetic core increases the undulator peak field value by about 7% as compared to that of the nonmagnetic core. However, only a relatively thin layer of magnetic material around the coil winding is required.

This conclusion has led to the possibility of making the cores using an assembly technique such that magnetic poles are inserted into the grooves precisely cut on a magnetic or nonmagnetic central core part, as opposed to an approach in which the core is machined out of a single block of material. A

number of short prototypes were built in the course of developing these manufacturing techniques, starting with coils about 100 mm in length (10-pole prototypes) and then moving to a length of about 330 mm (42-pole coils), as summarized in Table 3.5-2.

Table 3.5-2: Short undulator prototypes summary.

Prototype	**1**	**2**	**3-5**	**Assembly 1**	**Assembly 2**	**Assembly 3**
No. of poles	10	10	10	42	42	42
Core/pole material	Al/Al	Iron/Iron	Al/Al	Iron/Iron	Al/Iron	Iron/Iron
LHe test status	Tested	Tested	Used for impregnation study	Tested	Tested	Tested
Peak field				0.65 T at 500 A	0.61 T at 500 A	0.65 T at 500 A
Phase error				7.1° at 500 A; 3.3° at 200 A	5.0° at 500 A; 3.0° at 200 A	1.8° at 500 A; 1.6° at 200 A
Expected spectral performance				>75% of ideal in 3rd harmonic (60 keV); >55% of ideal in 5th harmonic (100 keV)		≈100% of ideal in 3rd harmonic (60 keV) ; >97% of ideal in 5th harmonic (100 keV)

It is worth mentioning that the manufacture of superconducting undulators is a technological challenge as it requires precise winding on precisely machined formers. We measured the geometry of the formers and found that a precision in the groove width of 9 μm rms and in the groove depth of 7 μm rms was achieved for a pair of 42-pole assembled cores. The coil winding onto these formers was performed on a specially built winding machine. Finally, the coils were impregnated with epoxy resin. Several small coils were used to develop vacuum impregnation techniques, in collaboration with experts from the Technical Division of Fermi National Accelerator Laboratory (FNAL). This study confirmed that the quality of resin impregnation affects the training of a superconducting coil. Thus, a 42-pole coil with no visible cracks in the resin reached the plateau in tuning curve after only 4 quenches while another coil with cracks required substantial training.

Three 42-pole double-magnet assemblies were built with a 9.5-mm magnetic gap, two with an iron core and iron poles, and one with an Al core and iron poles. All three assemblies were successfully tested in a vertical LHe bath cryostat, as shown in Figure 3.5-4 [3.5-9].

The coils were trained and reached critical currents of 720-760 A, which compares very well to the required operational current between 200 A (for 25 keV in the first harmonic) and 500 A (for 20 keV in the first harmonic). Thus, the design undulator peak field between 0.38 T (at 200 A) and 0.65 T (at 500 A) was successfully achieved.

The magnetic field profile was measured with a cryogenic Hall probe. Results are shown in Figure 3.5-5. It was shown that a design that includes trim coils at each end of the magnet could meet

Figure 3.5-4: Photograph of a 42-pole prototype SCU assembly ready for testing in a vertical LHe dewar.

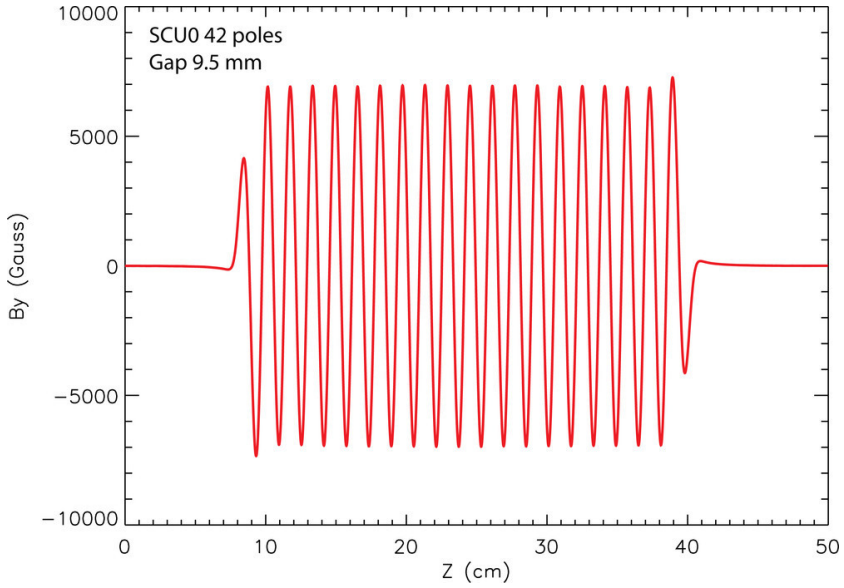

Figure 3.5-5: Measurements for a 42-pole prototype SCU assembly.

magnetic field quality requirements for the first and second field integrals and for phase errors. For the first two test assemblies rms phase errors ranging from 3 to 7 degrees were calculated for the measured field profiles such as those shown in Figure 3.5-5. The third assembly has achieved phase errors below 2 degrees rms without any magnetic shimming. This compares favorably to the original specifications developed for APS construction of Undulator A. The conclusion from this R&D experience is that the superconducting magnetic structure is intrinsically precise as long as it is fabricated accurately.

3.5.2.3 Estimates of Beam-Related Heat Loads

A superconducting undulator employs coils wound with superconducting wire to generate high magnetic field and therefore requires the magnetic structure to be cooled to about 4 K when low-temperature superconductors (LTSs), such as a NbTi and Nb_3Sn, are used. For our first devices, NbTi superconductor was chosen because it is a more established technology and easier to implement. A challenge in successful implementation of low-temperature superconducting technology is the heating caused by the electron beam passing through the undulator beam chamber. Beam image currents and other effects may cause the coil temperature to rise above the critical temperature of the superconductor. Therefore, predictions of the heat load and appropriate design of the cooling system become highly important issues.

It is assumed that the beam-induced heat load in the SCU0 is absorbed on the SCU0 vacuum chamber. As explained in section 3.5.2.4, the central part of the SCU0 vacuum chamber is nominally at 20 K, and is thermally isolated from the magnetic structure. The maximum heat-load handling limit of the cryomodule for the beam chamber corresponds to the total cooling power of the two cryocoolers, which is 40 W at 20 K [3.5-10]. The chamber transitions are in the 300 K-to-60 K temperature transition region, where the heat-load capacity is 224 W. The static non-beam-induced heat load at 60 K is 86 W (see Table 3.5-4). The total heat-load budget for wakefields in the chamber transitions is 50 W and the resistive-wall heat load is 9.7 W (for 100 mA). This leaves a 78W margin in the overall budgeted heat load at 60 K.

Estimates of the various contributions to the heat load due to the stored beam are shown in Table 3.5-3. 24-bunch operation is assumed, which is the worst case for the image current and wakefield heat loads. Where appropriate, the heat loads at 20 K and at 60 K are given separately. Numbers marked with an asterisk refer to the maximum allowed contribution to the heat load budget. “Operations” refers to energizing the undulator coil current in a cold SCU0. “Off” refers to setting the undulator coil current to zero, where the SCU0 is either cold or warm. The heat load at 300 K is included in the unlikely event that the SCU0 chamber is warm while it is installed in the storage ring.

Sources of beam-induced heat load on the SCU beam chamber include wall heating due to beam-induced image currents, synchrotron radiation generated in upstream dipole magnets, wakefield effects, direct beam interception, and electron cloud or multipacting effects. Cw heat loads are present under nominal operation conditions, while specific error or machine study conditions may occur that give rise to individual transient heat loads.

The contribution to the heat-load budget from wall heating from the beam image currents is highest for the 24-bunch mode, followed by the hybrid mode, with the 324-bunch mode being the lowest. The SCU beam chamber is 2.06 m long. The central 1.62 m of the chamber has a vertical aperture of 7.2 mm and is made of extruded Al 6063-T5 alloy that has undergone an abrasive flow polishing procedure [3.5-15]. On either end of the Al chamber is a 220-mm-long 316L stainless steel (SS) cold-to-warm transition. The SS transition vertical aperture varies from 7.2 mm to 25.4 mm at the exit flanges. For calculation of resistive wall heating, temperature-dependent resistivity values [3.5-16, 3.5-17] and numerically-modeled values of the current-dependent bunch length from Figure 3.6-34 were used [3.5-11]. Anomalous skin effects were included in the case of Al at 20 K [3.5-18, 3.5-19].

The surface roughness of the SCU beam chamber has two effects: it can increase the surface resistance and it can increase the synchrotron radiation absorption in the SCU0 chamber, both of which can increase the heat load. With a surface roughness of 0.2 microns rms, the power deposited by the beam on the SCU beam chamber walls increases by 15% [3.5-20]. The surface roughness of the polished

Table 3.5-3: Beam-related heat loads on 2-m-long chamber. Values marked with an asterisk refer to the maximum allowed contribution to the heat load budget.

Heat source	**20 K (60 K), operations 100 mA**	**20 K (60 K), off 150 mA**	**300 K, off 115 mA**
Cw heat loads			
Image current [3.5-11]	4.7 W (9.7 W)	8.8 W (18.2)	31.2 W
Electron cloud [3.5-12]	<2 W	<2 W	<2 W
Wakefields [3.5-13]	<0.5 W (50 W*)		
Injection losses [3.5-14]	2 W (non-top-up mode) 0.1 W (top-up mode)		
Synchrotron radiation	<1 W	<1 W	<1 W
Beam lifetime losses	<< 1 W		
Total cw heat load at 20 K (60 K)	10 W (60 W*)	14 W (70 W*)	
Transient heat loads			
Injected beam loss	13 W	42 W	42 W
Corrector failure	20 W	20 W	20 W
Synchrotron radiation with steering errors	10 W*	10 W*	10 W*
Electron beam steering error	20 W	20 W	20 W
Response matrix measurement		< 1 W	< 1 W
Max. transient heat load	20 W	42 W	42 W

chamber surface is on the order of 0.1 microns rms [3.5-21] and, therefore, the surface roughness effect can be neglected.

Another source of SCU beam chamber heating is a flux of photons from an upstream dipole magnet. Mitigation of the potentially substantial heating is achieved by using a photon absorber (PA) to mask the SCU0 chamber walls, by increasing the horizontal aperture of the SCU beam chamber such that the photon beam passes cleanly through, and by restricting the electron beam steering in the dipole radiation source. The resulting heat load is then reduced to the level of 0.3 W for 100-mA beam current. The heat load on the PA itself from radiation does not exceed 1 kW for beam currents up to 200 mA (such high current is used in machine studies).

The heat load specification includes both primary photons and secondary photons that scatter on the chamber walls. For typical PA angles of 19-30 deg, as measured from the beam axis, the majority of the photons incident on the PA are absorbed. The small fraction that are scattered from the PA surface shall not be incident on the SCU chamber. This criterion is satisfied in the 6-ID layout [3.5-22]. There are no specifications on the surface roughness of the PA.

In addition to the general user orbit stability requirements, the SCU imposes additional requirements: orbit errors must be controlled in the S6B:M dipole magnet for beam currents above about 25 mA. Large orbit displacement and/or angle errors in the dipole can potentially cause a large synchrotron radiation heat load on the SCU0 chamber walls. Specifications for the orbit errors in S6B:M are found

in [3.5-23]. These are derived from calculations of the synchrotron radiation power intercepted by the SCU0 chamber walls including beam steering in S6B:M. Secondary photons were included in the calculations using a diffuse-scattering model and realistic assumptions for the surface roughness of the APS vacuum chamber. The tolerance on vertical angle missteering is the most critical, where an angle error of ± 0.2 mrad is estimated to result in 40 W of heat load [3.5-23]. The heat load budget for vertical S6B:M beam steering will be 10 W (for limited duration).

The synchrotron radiation heat load was also analyzed for the S6B:H1 corrector magnet immediately upstream of the SCU. The corrector produces 20 W of synchrotron radiation power at 100 mA. Under nominal beam orbit conditions, all the synchrotron radiation produced by the corrector passes through the SCU0 chamber without intercepting the walls [3.5-23]. The maximum heat load including orbit errors is within the heat load budget, so there are no specifications for the orbit errors in the corrector. This is also the case for all the other correctors between S6B:M and the SCU.

The SCU beam chamber has a vertical aperture smaller than the aperture of the storage ring chamber. The resulting transitions from the standard chamber height down to the SCU chamber and back cause electromagnetic field perturbations, resulting in wakefield heating. The chamber transitions are included in the 300 K-to-60 K transition of the vacuum layout. The total beam-induced heat load budget for the chamber transitions is 50 W. In the case that a photon mask is installed at the SCU upstream flange, any wakefield-induced heat load shall be computed and shall not exceed 10% of the total SCU heat-load handling limit.

The heat load on the SCU0 chamber due to stored-beam lifetime losses is given by 7 GeV multiplied by the loss current, Q_{stored}/τ, where Q_{stored} = 368 nC is the stored charge per 100 mA and τ is the beam lifetime. A heat load >1 W would require that the beam current loss be >0.14 nA, which implies a beam lifetime <0.7 hr at 100 mA, which is an order of magnitude below typical lifetimes. In terms of beam power, this is also equivalent to assuming that an 8-nC injected bunch is lost on the SCU0 chamber every 1 minute during top-up. Again, this is quite an extreme situation compared to actual experience. Heat load due to beam losses during operations is, therefore, not a concern.

Full loss of the entire injected beam in the SCU, which is possible during machine studies when the SCU0 is turned off, is given by 3 nC $\times$ 7 GeV = 21 J. At a 2-Hz injection rate, this gives 42 W [3.5-24]. This is a conservative upper-limit estimate.

During operation, loss of the entire injected beam on the SCU0 chamber is very unlikely with the 4-ID 5-mm vacuum chamber in place. Without the 4-ID chamber, assuming 2-Hz injection with 70% injection efficiency (i.e., 30% lost), 12.6 W is possible [3.5-24].

Electron cloud heating arises from low-energy background electrons in the vacuum chamber being accelerated into the vacuum chamber wall because of repulsion from a passing beam bunch. When they strike the wall, secondary electrons can be emitted. The secondaries can in turn be accelerated into the wall by the beam. The heating effect is estimated to be <2 W, and multipacting is most likely in the 324-bunch mode [3.5-12]. The heat load due to the generation of an electron cloud and interaction of this cloud with an electron beam and with ions is not well understood. Excessive heat loads observed at the ANKA SCU chamber are consistent with a model that includes the interaction of the beam with an electron cloud and with ions. At this time there is no heat load budget for electron cloud- or ion-induced heating. The vacuum pressure and temperatures near the SCU0 shall be monitored and, based on SCU0 operational experience, a heat load budget for these effects may be developed for the SCU1/2.

The transient heat loads are most likely to happen during machine studies but can be eliminated by

adopting careful procedures for conducting studies. Also, the superconducting undulator magnet should be switched off during machine studies to prevent quenching. The area around the undulator can also be instrumented to allow prompt detection of beam losses, as described in section 3.8.2.

Based on these analyses, the maximum cw heat load during normal operation is estimated to be 10 W. The SCU 20-K cooling system, as described below, has a beam chamber cooling capacity of 40 W, which provides a comfortable margin for normal operation.

3.5.2.4 Cooling Scheme Concept

As indicated in Table 3.5-3, the heat load on the beam chamber from beam-related effects could be as high as about 42 W in the case of an injection accident. In order to prevent this heat from reaching the superconductor, the chamber will be thermally isolated from the superconducting coils and separately cooled by the two lower cryocoolers shown in Figure 3.5-6. These cryocoolers will hold the beam chamber at approximately 20 K and will also be used for cooling two radiation shields to 20 K and 60 K.

The superconducting coils are cooled by liquid He (LHe) that flows through channels in the center of the magnetic cores and is gravity driven in a thermosiphon loop. A cryocooler-cooled recondenser in the LHe tank reliquifies evaporated He, making it a closed system. This and another cryocooler mounted to the top of the cryostat are also used to cool the current lead assemblies.

A listing of the heat loads and the temperatures at which the heat loads occur is shown in Table 3.5-4 along with the total cooling capacity of the four cryocoolers.

Table 3.5-4: Estimated heat loads. All values are in Watts.

Heat source	**Heat load** at 4 K	**Heat load** at 20 K	**Heat load** at 60 K
Beam (100 mA)	—	10	60
Synchrotron radiation	0.0116	0.3	10^{-3}
Thermal radiation	0.012	1.21	4.2
Conduction through:			
beam chamber bellows	—	—	1.4
beam chamber supports	0.08	—	—
He vent pipe bellows	0.006	0.07	0.9
He fill pipe	0.012	—	—
cold mass support	0.005	—	—
radiation shield supports	—	1.2	5.6
Current leads:			
correction coil leads only, 100 A	0.12	—	22
main coil leads only, 500 A	0.45	—	52
Total at I = 500 A	0.696	12.78	146.1
Cooling capacity	3	40	224

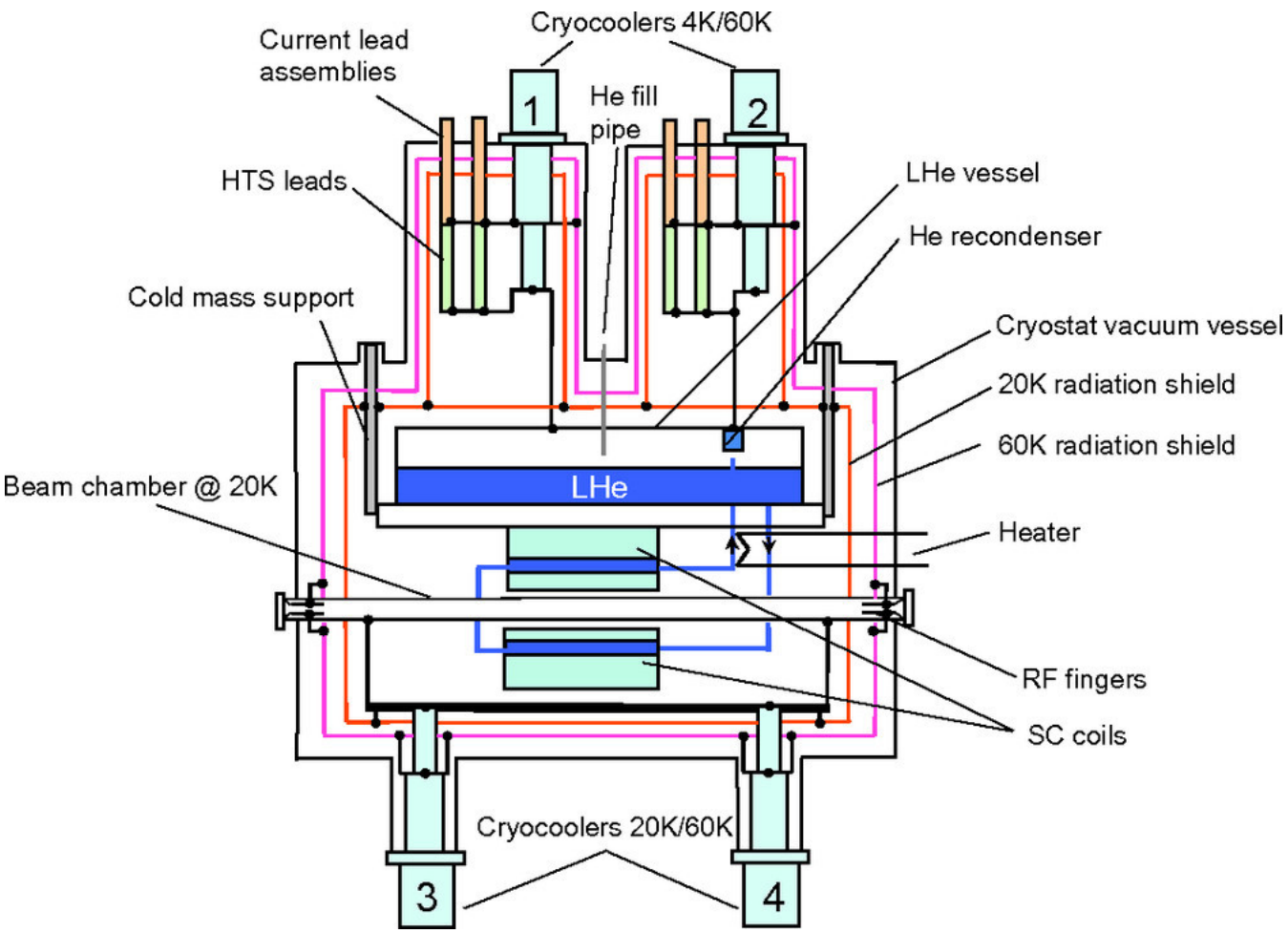

Figure 3.5-6: Superconducting undulator cooling scheme concept.

3.5.2.5 Cryostat Concept

The design of the superconducting undulator cryostat is based on the concept developed at the Budker Institute of Nuclear Physics, Novosibirsk, Russia, and implemented in the superconducting wigglers that have been built for a number of institutions worldwide [3.5-25]. A view of the assembled cryostat is shown in Figure 3.5-7.

A cut-away view of the cryostat is shown in Figure 3.5-8.

The cryostat is designed to hold a 1.15-m-long SCU magnet, but is shown holding the initial 42-pole-long magnetic structure selected for the first test undulator SCU0 that has been built in the R&D phase of the project. The second undulator, SCU1, will use the same 2-m-long cryostat design, provided no flaws are found in testing with SCU0.

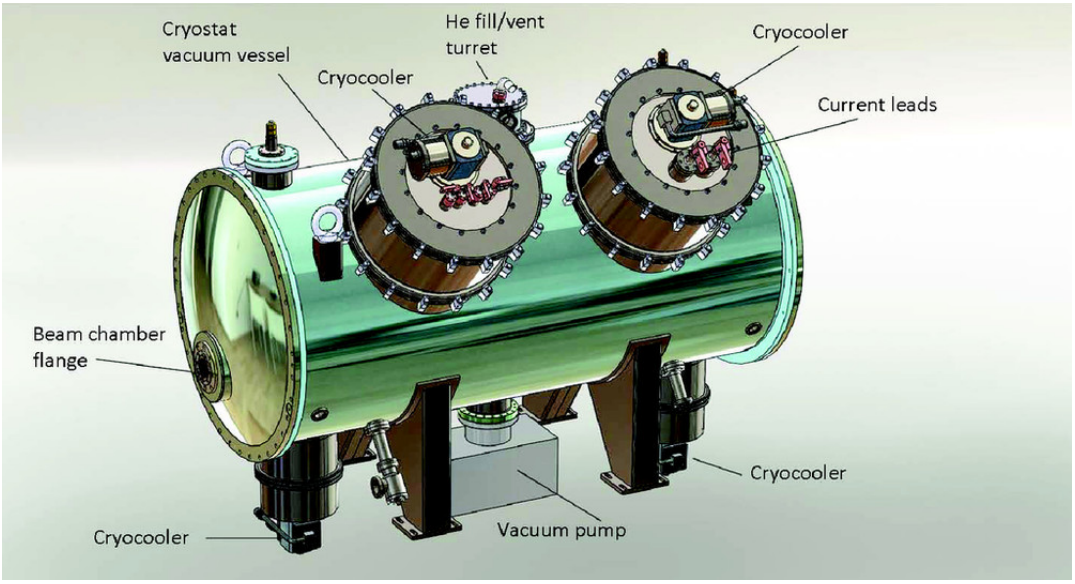

Figure 3.5-7: Drawing of the cryomodule for the superconducting undulator.

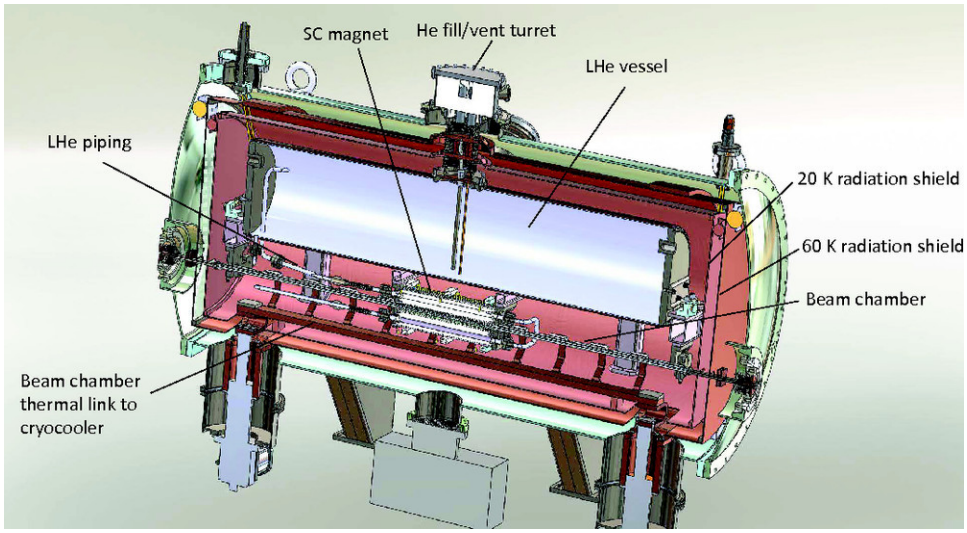

Figure 3.5-8: Cutaway view of the inside of the cryostat.

3.5.2.6 Measurement System

Performance characterization of the SCU is one of the key requirements to be satisfied before installation of the device in the APS storage ring. The procedure includes quality control of superconducting coils after their manufacture and before mounting into the cryostat, as well as final magnetic measurements of the undulator field once the undulator is assembled.

A vertical measurement system was developed for testing SCU magnetic structures up to 1 m long in a vertical LHe cryostat. This system was successfully employed to measure the short undulators listed in Table 3.5-2. It includes a movable Hall probe driven by a precise mechanical stage, power supplies for

the magnets being tested, and a data acquisition system controlled by LabVIEW software. Plans are to use this system for cold tests of superconducting coils for the first two devices. An extended version of such a system will be required for cold tests of 2-m-long structures.

Once assembled into a cryostat, the superconducting undulators will also be measured with a horizontal measurement system that includes a Hall probe assembly to measure magnetic field flux in the vertical and horizontal planes on and off axis. A rotating coil is used for measuring both the field integrals and the multipole components of the magnetic field. The system has been built, is in use, and is described later in the document.

The mechanical concept for the system is based on the idea that a Hall probe is moving inside a vacuum-sealed, warm guide tube located in the cold-bore chamber. The Hall probe assembly is mounted on a carbon fiber rod that is pushed into the SCU by a high-precision mechanical stage located outside the SCU cryostat. Such a rod can also hold a rotating wire coil or even a pair of orthogonal wire coils. In this approach the Hall probe is operating at atmospheric pressure and at close to room temperature and would thus be easily replaceable.

The issue of operating a Hall sensor at various temperatures has already been addressed [3.5-26]. A small cryostat was added to the APS Hall probe calibration facility to measure Hall sensor response at different temperatures including cryogenic temperatures. The measured calibration curves were used in the tests of the SCU magnet prototypes, reported above.

A novel three-sensor Hall probe has been developed for the superconducting undulator measurement system [3.5-27]. It includes a pair of Hall sensors to measure the vertical magnetic field and an additional sensor to measure the horizontal component of the field. The vertical sensors will also be used to find the exact vertical position of the Hall probe assembly by measuring and comparing the field in two different locations. This idea has been successfully tested recently.

In carrying out this work, full advantage will be taken of the extensive experience at APS in magnetic measurements of conventional undulators. Existing methods of undulator field analysis and corresponding software packages are already being implemented into the data acquisition system for the superconducting undulator.

3.5.2.7 Instrumentation and Controls

The successful operation of the superconducting undulator depends upon the status and control of the various subsystems of the cryomodule. These include the cooling circuits, power supplies, internal voltages, pressures, and the liquid He (LHe) level. In order to achieve this, a variety of instrumentation and monitoring equipment needs to be strategically installed within the system.

Initially, each magnetic core is tested in a bath of LHe inside a vertical cryostat in order to perform quench training of the superconducting coils and characterization of the magnetic field quality. This setup requires control and monitoring of the power supplies, monitoring and recording of voltages across the superconducting coils, and monitoring of the LHe bath level.

After the initial testing of the superconducting coils is complete, the coils are installed into the cryomodule for horizontal testing in the lab. The instrumentation required for this setup includes temperature sensors on each of the three cooling circuits, voltage taps on the high-temperature superconducting (HTS) leads and across the superconducting coils, pressure transducers for the insulating vacuum pressure as well as the LHe tank, and a LHe level monitor.

The control system in the lab is required to control the main power supply as well as the end correction coil power supplies, monitor the instrumentation, and log acquired data as necessary. The control system is required to monitor and react to situations that could damage the magnets or the various subsystems, i.e., an increase in the voltages or temperatures should automatically turn the output of the power supplies off.

3.5.2.8 Physics and Beam Commissioning

This section provides physics requirements for the superconducting undulator (SCU) system. Here SCU refers to SCU0, SCU1, or SCU2.

3.5.2.8.1 Photon Beam Performance

This section addresses the requirements of the user regarding SCU performance.

Test device: SCU0

The first superconducting undulator (SCU0) cryomodule will be installed in the downstream end of the 6-ID 5-m-long straight section. A U33 planar hybrid permanent magnet insertion device will be installed in the upstream end.

The SCU0 undulator will be the x-ray source for the 6-ID-D experimental station, which is used for high-energy (50-130 keV) scattering experiments. The device will provide x-rays for experiments in the station at energies near 60 keV and 100 keV using the third and fifth harmonics, respectively. For any one experiment, the device will be operated at fixed current (energy), which maximizes the photon flux in the required spectral range. The device is user-tunable by varying the device current, as long as the criteria in section 3.4.5 are satisfied. Most experiments will take place with the device operating at the maximum design current of 500 A.

The photon flux density at the third harmonic is expected to be at least 80% of the ideal angular flux density and at the fifth harmonic is expected to be at least 60% of the ideal. These requirements are satisfied when the allowable phase error for the SCU0 is defined to be the same as for the U33 devices, given in Table 3.5-5 [3.5-28]. It is noted that the phase error requirement for a short-period SCU is less demanding compared to the standard APS U33 (see next section).

Table 3.5-5: SCU phase error requirements at fixed 9.5-mm gap, variable current.

Quantity	Specification	Driving requirement
Rms phase error	<8 deg	High-harmonic performance

The time required for the SCU0 to achieve its maximum operating current should be no more than 5 minutes after a storage ring beam loss, assuming that the SCU0 has not quenched.

The beam produced by SCU0 should not deviate by more than ± 5 μrad in either the horizontal or vertical planes when the upstream U33 undulator gap is changed. The latter is a requirement on the

upstream U33 device rather than on the SCU0. There is an rf BPM in the middle of the straight section between U33 and SCU0, C:P0; its readback will be used to lock down the orbit.

User devices: SCU1 and SCU2

This section addresses the requirements of the user for operation for SCU1 and SCU2. The HEXD Physics Requirements Document (WBS U1.04.02.10) will provide these requirements in detail. General requirements are discussed below.

The user must define the photon characteristics and the planned operating mode and configuration of all the undulators in the straight section, including the SCU. The SCU installation must allow for sufficient clearance from the bending magnet (BM) dipole beamline, and therefore must be installed in the downstream position in the straight section. The SCU0 cryomodule vessel diameter is 865 mm; the SCU1 or a longer cryomodule is likely to have a similar diameter.

If the user requires that the SCU be used at the same time as an upstream permanent-magnet undulator (PMU), ASD will ensure that operation of the PMU will not steer the electron beam in the SCU by more than the user-provided specification. The SCU device is user-tunable by varying the device current, as long as the criteria in section 3.5.2.8.3 are satisfied.

An SCU installed in a long straight section in the storage ring will be outside the short-pulse x-ray (SPX) insertion after the APS Upgrade, so compatibility issues are not expected.

The phase error specification for the SCU will depend on the period length and the harmonic of interest, as specified by the user. The issue of setting an appropriate rms phase error criterion for the APS undulators, including the SCU, is reviewed in ref. [3.5-28]. The phase error requirement for a short-period SCU is less demanding compared to the standard APS U33. The photon flux at the n^{th} harmonic is proportional to $e^{-n^2\sigma_\phi^2}$ [3.5-29]. Since the SCU will not be used beyond $n = 5$ (in contrast to the standard APS U33 at $n = 11$ or more), the SCU does not need such a small phase error.

3.5.2.8.2 User Operation

The APS storage ring operating parameters that the SCUs must accommodate are given in Table 3.5-6. The operating beam current is the maximum current at which each device is required to operate. All components, including the cryomodule, photon absorbers, and tapers, will be designed to allow the storage ring to operate above 100 mA, up to 200 mA, in machine studies. This is defined as the machine protection limit.

An operating mode of the SCU that is safe during higher-current machine studies is to decrease the SCU current close to 0. This will minimize quenching.

The SCU field-quality specifications are the same as any other planar ID devices installed in the ring. They were originally specified 20 years ago by [3.5-30], reassessed recently in [3.5-31], and are listed in Table 3.5-7. The field quality should ideally be satisfied over a horizontal range of $\pm$12-15 mm in order to preserve good injection efficiency. This defines the good-field region.

Table 3.5-6: APS storage ring parameters that the SCU design must accommodate.

Specification name	Value
Bunch patterns	24-bunch, 324-bunch, hybrid
Operating beam current, SCU0	100 mA
Operating beam current, SCU1 and SCU2	150 mA
Machine protection limit	up to 200 mA (machine studies)
Energy	7 GeV

Table 3.5-7: SCU integrated multipole field quality requirements.

Quantity	Limit	Driving Requirement
Quadrupole	50 G	Tune stability
Skew quadrupole	50 G	Coupling stability
Sextupole	200 G/cm	Nonlinear beam dynamics
Skew sextupole	100 G/cm	Nonlinear beam dynamics
Octupole	300 G/cm^2	Nonlinear beam dynamics
Skew octupole	50 G/cm^2	Nonlinear beam dynamics

3.5.2.8.3 APS Orbit Stability

This section addresses the perturbation of the SCU on the beam trajectory. The SCU field-error tolerance is required to be the same as that for the other planar IDs [3.5-24, 3.5-31].

Global Orbit

With orbit correction and real-time orbit feedback running full-time, the tolerance is in terms of rate of change of the perturbations produced by the undulator (rather than the actual value of the perturbation). This may set a limit on how fast the current can be changed. Because of the complex frequency dependence of the correction effectiveness, the actual orbit "ramp" error from IDs has to be modeled with orbit correction simulation for acceptance (using the present version of orbit correction). When ramp errors have a short duration, real-time feedback produces a more effective correction. Thus Table 3.4-8 provides two sets of field-integral rate-of-change requirements for guidance. The 5-second ramp-error duration was selected because it matches the worst-case perturbation behavior of most planar hybrid IDs, which may or may not correspond to SCU0's.

Local Orbit

When the global orbit correction system compensates for perturbation outside the straight section, there remains the internal orbit error due to first- and second-integral field errors. Thus the photon source position and angle will vary with undulator gap and will depend linearly on these errors. There is no correction or partial correction by the global orbit correction itself since there are no correctors inside the undulator. However, including the x-ray BPMs in the global orbit correction (as is done at APS)

can greatly reduce the photon source and angle errors at the expense of nearby rf BPM position errors, which are not as important as photon beam errors, after all.

A model of local steering errors was created with a two-kick perturbation model for planar IDs in order to set the limit on the absolute first- and second-field integral errors [3.5-31]. The resulting specifications are given in Table 3.4-9. An important assumption is that the x-ray BPMs are weighted by a factor 10 more than rf BPMs. (If the x-ray BPMs had infinite weight, i.e., rf BPM would not "vote," then there would not be a specification for the field integrals based on photon stability.)

For the SCU0, the specification of absolute field-integral errors for a single 2.5-m ID device will be used, as shown in Table 3.4-9), Case 2. For subsequent devices, the specification is to be determined.

Quenches

Quenches can cause a large field disturbance on a time scale that is too fast for the real-time orbit feedback to correct [3.5-32]. If the perturbation is very large, the resulting beam trajectory displacement could exceed the beam position limit detector (BPLD) limits and cause a beam dump. Beam dumps due to a quench should be avoided as much as possible . The maximum allowed deviation at any BPLD is assumed to be 0.5 mm in both transverse planes. The tolerance on the quantity $\sqrt{I_1^2 + (I_2^2/\beta_{\mathrm{U}}^2)}$, where I_1 and I_2 are the first- and second-field integrals, respectively, and β_{U} is the average beta function at the undulator ends, is given in Table 3.5-8 [3.5-32].

Table 3.5-8: Combined field errors during a quench, at fixed 9.5-mm gap.

Quantity	Specification
B_x: $\sqrt{I_1^2 + (I_2^2/\beta_{\mathrm{U}}^2)}$	350 G-cm
B_y: $\sqrt{I_1^2 + (I_2^2/\beta_{\mathrm{U}}^2)}$	2100 G-cm

Figure 3.5-9 shows measured quench data in a vertical test (coils only). Horizontal magnet tests, quench tests, and alignment will be carried out prior to installation.

3.5.2.8.4 Layout

Canting Considerations

The SCUs are planned to be installed in the long straight sections, and the user has expressed interest in a switchable canting scheme [3.5-33]. The design and operation must satisfy the criteria in section 3.5.2.8.3. The impact of the canting scheme on the heat load in the SCU0 beam chamber is discussed below.

The canting angle or switching does not impact the SCU heat load directly; however, the particular configuration of the undulators and cryomodules, i.e., their lengths and placement along the length of the straight section, will have an impact on the placement of photon absorbers (PAs) that shield the SCU chamber(s), and this will impact the specification for the horizontal aperture of the SCU

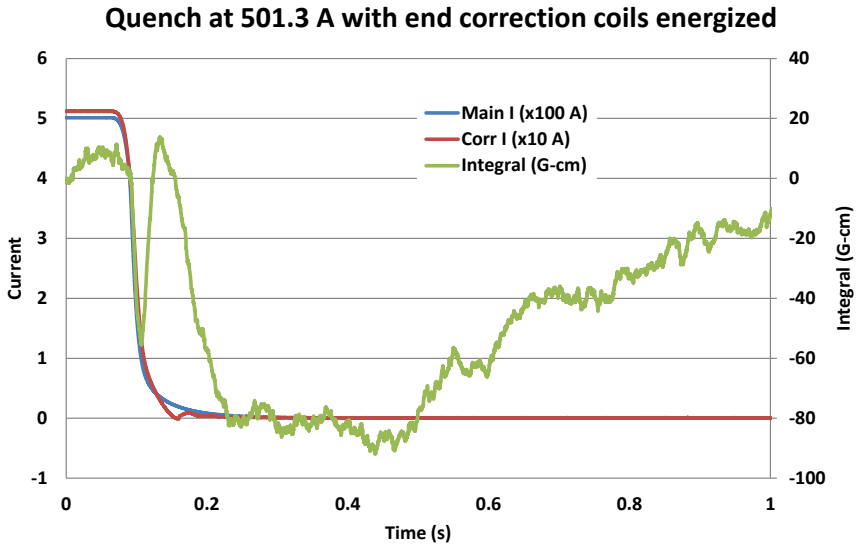

Figure 3.5-9: Measured quench data in a vertical test (coils only). The quench was initiated with a heater. The integrated field is relative to the start of the quench.

chamber(s). For the user-specified configuration, a layout shall be designed and ray tracing shall be performed to ensure that there is sufficient clearance between the SCU chamber(s) and the on-axis (y=0) synchrotron radiation from all bending magnet sources, including the upstream BM magnet and upstream B:H1 corrector magnet.

As a guide, the clearance for the SCU0 chamber is 3 mm [3.5-22]. The clearance for SCU will be 3 mm, but this specification may be modified after gaining operating experience with the SCU0. The clearance can be satisfied either by choosing an appropriate full horizontal aperture, or by displacing the SCU chamber horizontally. Mechanical design considerations also play a role in determining which solution is best. With either design, calculations of the synchrotron radiation heat load including beam orbit errors shall be carried out per ref. [3.5-23, 3.5-34].

Acceptance

The vertical and horizontal acceptance in the region of the SCU shall not define the minimum acceptance of the storage ring. The beam stay-clear requirement shall be at least ± 3.5 mm vertically and ± 18 mm horizontally.

Vacuum System

An aluminum vacuum chamber will be provided to enclose the beam, and the magnetic device will be outside this chamber. The SCU chamber on-axis full aperture is 7.2 mm vertically, with a minimum wall thickness of 0.75 mm. The horizontal aperture is to be specified after the canting configuration is determined per section 3.5.2.8.4. The tolerance is +0.1 mm on the vertical aperture and $\pm$ 0.05 mm on the minimum wall thickness. For reference, the SCU0 chamber shape is shown in Figure 3.5-10.

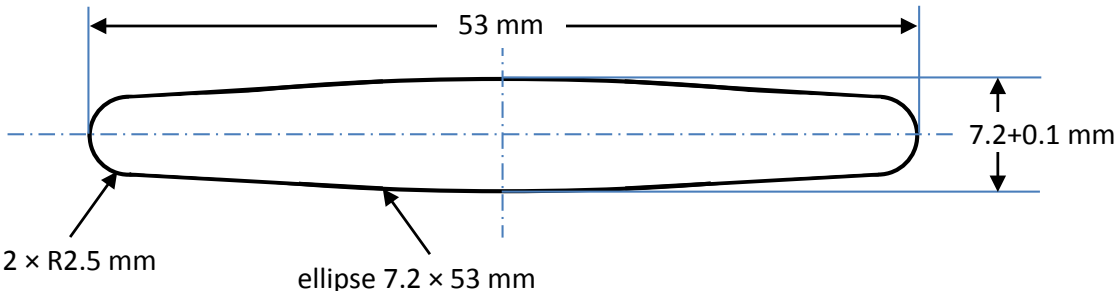

Figure 3.5-10: Schematic of SCU0 chamber cross section. The SCU aperture may require modification.

The vacuum system shall have no surfaces that allow near-normal incidence of the direct synchrotron radiation. Any such surfaces must be shielded from direct synchrotron radiation by a photon absorber or a photon mask.

A photon absorber will be provided upstream of the SCU to shield the SCU chamber walls from direct synchrotron radiation in the horizontal plane. The absorber shall satisfy the beam-stay-clear requirement, and the tolerance on its position is $\pm$ 0.5 mm. The absorber shall be designed to handle the heat load from 200-mA operation in all user bunch modes during machine studies. This heat load shall not exceed 1 kW. This criterion is satisfied with the PA designed for the SCU0 [3.5-22], and this design can be used as a guide.

Impedance Budget

The impedance budget for the SCU insertion is given in ref. [3.5-35]. The photon absorber (upstream of the SCU) is necessary to protect the SCU, and it has no separate impedance specification. The photon absorber impedance is part of the overall impedance budget.

3.5.2.8.5 Alignment

The alignment tolerance for the U33 ID chambers is $\pm$75 microns in x and y, and $\pm$250 microns in z [3.5-36]. This alignment tolerance is based on a $\pm$75-micron tolerance for setting the height of the vacuum chamber and a $\pm$75-micron tolerance for the midplane of the undulator with respect to the midplane of the vacuum chamber (since the undulator is aligned to the vacuum chamber.) The total alignment tolerance is $\pm$150 microns [3.5-37] in y.

In the SCU the magnetic structure is integrated with the beam chamber. The field error specification shall be satisfied and be reproducible when the system is cooled down (allowing for relative motion between the vacuum chamber and the magnetic structure). The alignment tolerance for the magnetic structure relative to the SCU chamber is $\pm$150 microns in y.

One of the issues for the SCU is the relative alignment of the photon absorber, the SCU vacuum chamber, and the upstream dipole source. The alignment specifications are guided by [3.5-36, 3.5-38, 3.5-39]. The photon absorber position tolerance relative to the ID chamber center is $\pm$0.5 mm. The photon absorber is integrated into the U33 ID chamber, whose alignment specification was stated above.

The alignment tolerance of the SCU chamber relative to the U33 ID chamber is ±150 microns in x and y.

3.5.2.8.6 Machine Protection

When the beam position limiting detector (BPLD) system is enabled, the BPLD system limits orbit distortions in the straight sections. An orbit distortion during user operation can be caused, for example, by a single corrector failure [3.5-40]. Orbit errors in the upstream dipole and B:H1 corrector will be minimized by the orbit control system. In the case of SCU0, the 6-BM beamline is not presently in use, therefore orbit error tolerances do not impact the users.

To protect the SCU from excessive synchrotron-radiation-induced heat loads, in particular when the BPLD system and/or orbit control systems are not enabled, a system or procedure shall be developed. The response time of the system/procedure is to be determined based on the estimates of the heat load from mis-steered beam and the risk of quenching. Parameters that will be monitored, possibly with alarms installed to alert the operators, include rf BPMs, x-ray BPMs, the temperature of the vacuum chamber, and/or the local vacuum pressure [3.5-40].

3.5.2.8.7 Commissioning

SCU commissioning will be based on experience gained during SCU0 commissioning. SCU0 commissioning includes an SCU0 cryomodule test followed by an SCU0 beam test [3.5-41]. The first priority during commissioning is to test that beam-induced heat loads do not exceed safe limits for the SCU0. The second priority is to test that user beam can be delivered. A final priority is to operate the SCU0 and deliver photons to the user. In the commissioning plan, each test has prerequisites, operations steps, test pass criteria, test fail actions, and the test duration defined.

The goal of the cryomodule tests is to confirm that the cryomodule integrity and operability have not be compromised during the undulator installation in the storage ring. Once the tests are successfully completed without the electron beam, the SCU0 undulator is ready to be tested with the electron beam. It should be noted that the cool-down test occurs partially in parallel with user beam operation. The duration of this phase is about 10 days.

1. Vacuum test (insulating vacuum space)
2. Cool-down test
3. Power-up test
4. Quench test
5. Operation stability test

Beam tests are preceded by baseline measurements of the storage ring impedance and aperture before installation of the SCU0. Beam tests after the SCU0 is installed include beam-based alignment, transparency tests with the SCU0 powered off (including storage ring impedance), and operations tests

with the SCU0 powered on. The duration of this phase is 8 weeks, to be carried out during the machine intervention/study periods.

The first goal of the beam tests is to confirm that the unpowered SCU0 does not measurably increase the storage ring impedance, decrease injection efficiency, or decrease the beam lifetime. The second goal is to ensure that the SCU0 is sufficiently protected from beam losses and beam-induced heat loads. A minimum set of these tests must be completed prior to user operation, otherwise these tests are continued during machine intervention/studies periods. The final goal is to confirm that the powered SCU0 only perturbs the beam orbit or beam size within the specifications.

1. Baseline measurements
2. Beam-based alignment
3. Transparency tests
   (a) Assess chamber aperture
   (b) Accumulation in a single bunch
   (c) Beam dump test
   (d) Accumulation in 24-bunch pattern
   (e) Accumulation in 324-bunch pattern
   (f) Accumulation in hybrid bunch pattern
4. Operation tests with SCU0 powered
   (a) Accumulation in 24-bunch pattern
   (b) Beam perturbation and field integral test
   (c) Quench test

3.5.3 SCU Engineering Design [U1.03.04]

These sections describe the design of the superconducting undulator based on the test device SCU0. This undulator has been designed and manufactured, and has successfully passed a cold test. The design of this first undulator is considered to be the basis for the design of future devices.

3.5.3.1 User Devices

In addition to the test device SCU0, the APS Upgrade will build and install two longer user devices SCU1 and SCU2 that will deliver the promised enhanced brightness for hard x-rays in the range between 40 keV and 120 keV. The parameters of the user SCUs are listed in Table 3.5-9.

While the period length of the SCU0 is 1.6 cm, the period length chosen for the SCU1 and SCU2 is 1.8 cm for better coverage of the photon region above 40 keV. The calculated brightness of the user devices is shown in Figure 3.5-11 in comparison with the Undulator A.

The magnetic length of the SCU2 will be doubled compared to SCU1 and will reach about 2.3 meters. The cryostat length will correspondingly grow to about 3 meters.

Table 3.5-9: Parameters of the superconducting undulators.

	SCU1	SCU2	
1st-harmonic photon energy	12-25*	12-25*	keV
Period length	18	18	mm
Magnetic gap	9.5	9.5	mm
Magnetic length	1.140	≃ 2.3*	m
Cryostat length	2.063	≃ 3.0*	m

* Preliminary

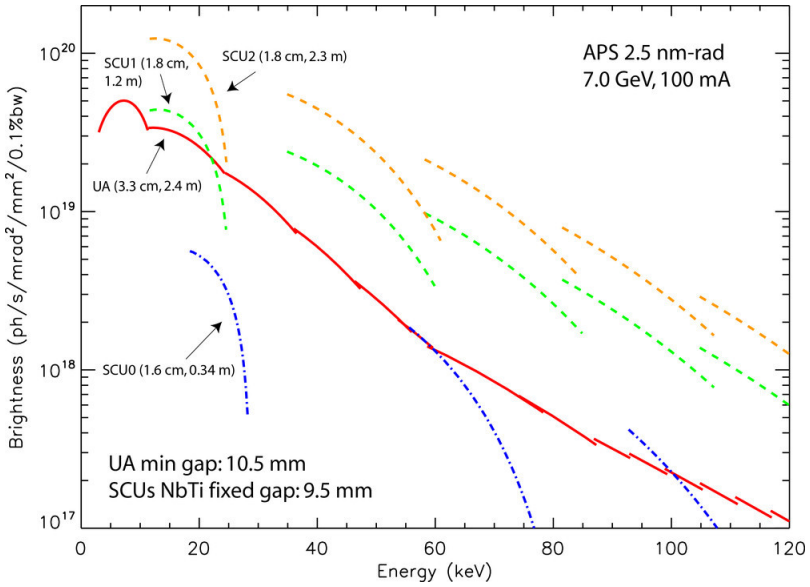

Figure 3.5-11: Calculated brightness of the test undulator SCU0 and the user devices SCU1 and SCU2.

SCU1 will use the existing SCU0 magnetic design, cryostat, cooling scheme, instrumentation, controls, and measurement system. Hence, these systems are described below in more detail than in the previous section on SCU0 development. Commissioning and operating experience with the 1-m-long undulator SCU1 will drive the design of the longer SCU2 device. Additional engineering development may be required before manufacturing.

3.5.3.2 Magnetic Structure Design

As in planar permanent magnet or hybrid undulators, the magnetic field in the superconducting planar undulator is created by a pair of identical magnets, or jaws, separated by a gap where a beam vacuum chamber is accommodated. Each jaw is a series of racetrack superconducting coil packs separated by magnetic poles, with currents flowing in opposite directions in adjacent coil packs.

The magnetic design of the SCU0 magnet is based on the results of magnetic simulations performed with the OPERA and RADIA software packages that have been proven during the R&D phase of the Project. A round 0.75-mm NbTi wire is wound in the rectangular grooves between the poles. An assembled design of the magnetic core was chosen where individual, precisely ground and lapped poles

of low carbon steel are inserted in slots machined in the ground and polished core. In such a design, the coil groove surfaces are very smooth to help avoiding short circuits in the winding process [3.5-42]. A computer model of the SCU core is shown in Figure 3.5-12.

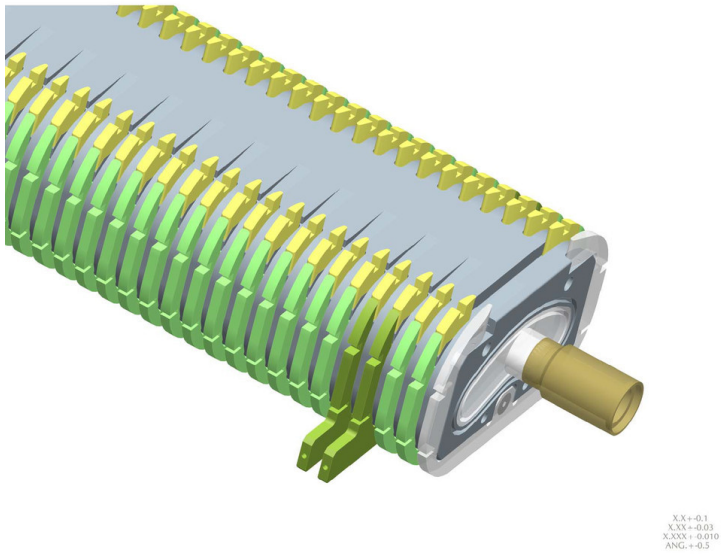

Figure 3.5-12: Design model of the SCU core.

Each jaw has a main coil with 39 turns per winding pack (fewer in the last two grooves at each end of the jaw), and two correction coils that are wound on top of the main coil in the last two end grooves. The correction coils are separately powered and are used for tuning the field integrals.

The technological steps of the magnetic structure manufacture include winding the superconducting wire onto the cores on a computer-controlled winding machine followed by epoxy resin impregnation in a special mold. The completed core is then tested separately or in an assembly in a vertical LHe bath cryostat.

The assembled SCU0 magnetic structure is shown in Figure 3.5-13.

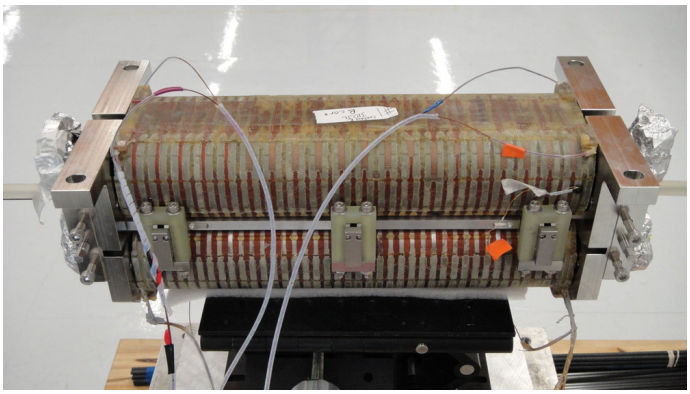

Figure 3.5-13: Photograph of assembled SCU0 magnet.

3.5.3.3 Cooling System Design

This chapter describes design of the SCU0 cooling system, which is used as the model for the SCU system.

The basic cryocooler-based concept and use of a LHe reservoir is proven, while the thermosiphon technique for liquid helium circulation through the undulator magnet cores is a new development. Thermosiphon technology is well established for cryogenic applications [3.5-43], although the horizontal layout of the system and correspondingly small liquid head limit helium circulation. R&D measurements were conducted using a test pipe structure (with the hydraulic properties similar to the ones of a single 42-pole magnet core) mounted horizontally in a test cryostat to evaluate thermosiphon performance. Test results indicated that helium circulation via thermosiphon was enhanced when a heater mounted to the helium return pipe was energized. Provision for such a heater has been implemented into the cryostat design.

The SCU0 cooling system consists of four 2-stage Gifford-McMahon cryocoolers. The first stage of all four units cools the outer thermal radiation shield to a temperature below 60 K. Actual measurements of shield temperature on the SCU0 indicate an operating equilibrium temperature around 40 K. The upper ends of all HTS current leads (two 1-kA-rated leads for the main magnet plus four 100-A-rated leads for the correctors) also receive cooling at this temperature level, primarily from the upper two cryocoolers. The cryocooler second stages operate at different temperatures depending on their connected thermal loads. The upper two coolers are designed with second stages that provide 1.5 W each at 4.2 K. These are connected to the liquid helium reservoir and recondense helium vapor back to liquid. The lower two coolers are designed with second stages capable of 20 W each at 20 K. These are connected to the beam chamber via a copper thermal bus and thermal links. Operational experience with SCU0 indicates that the beam chamber operates close to 10 K while the liquid helium recondensation power is in excess of the static heat load. A 1-W trim heater is operated to balance the load against available cooling power and maintain positive pressure, 4.2 K conditions. Figure 3.5-14 shows a graphical display of the system under cryogenic test.

The 4 K second stages of the upper two cryocoolers are connected to the liquid helium reservoir with aluminum thermal links. One cryocooler is attached directly to the exterior of the reservoir vapor space while the second is attached to a gold-plated hemispherical recondensing bulb, which penetrates through the wall of the reservoir vapor space through a flanged connection. Recondensation of evaporated helium takes place in the LHe reservoir where the vapor contacts both the inside wall of the reservoir and the recondensing bulb. The reservoir shell is fabricated from an explosion-bonded copper/stainless steel sheet. The copper exterior eliminates temperature gradients between the liquid and vapor spaces of the reservoir. Figures 3.5-15 and 3.5-16 show a rolled test section of copper/stainless steel sheet as well as the completed LHe reservoir.

The beam chamber is thermally insulated from the cores, and is conduction cooled by the two lower cryocoolers. In this scheme, the beam chamber is thermally isolated from the magnet system. As a result, the higher cooling capacity of the cryocoolers can be employed. Flexible thermal links are used to connect the cryocoolers to their respective heat loads. These links provide the necessary motion for alignment and assembly as well as provide the necessary heat transfer with minimal temperature difference. Figure 3.5-17 shows a picture of the thermal links between the second stage of one of the lower cryocoolers and the thermal bus, with additional thermal links to the beam chamber also shown. A completed cold mass is shown in Figure 3.5-18.

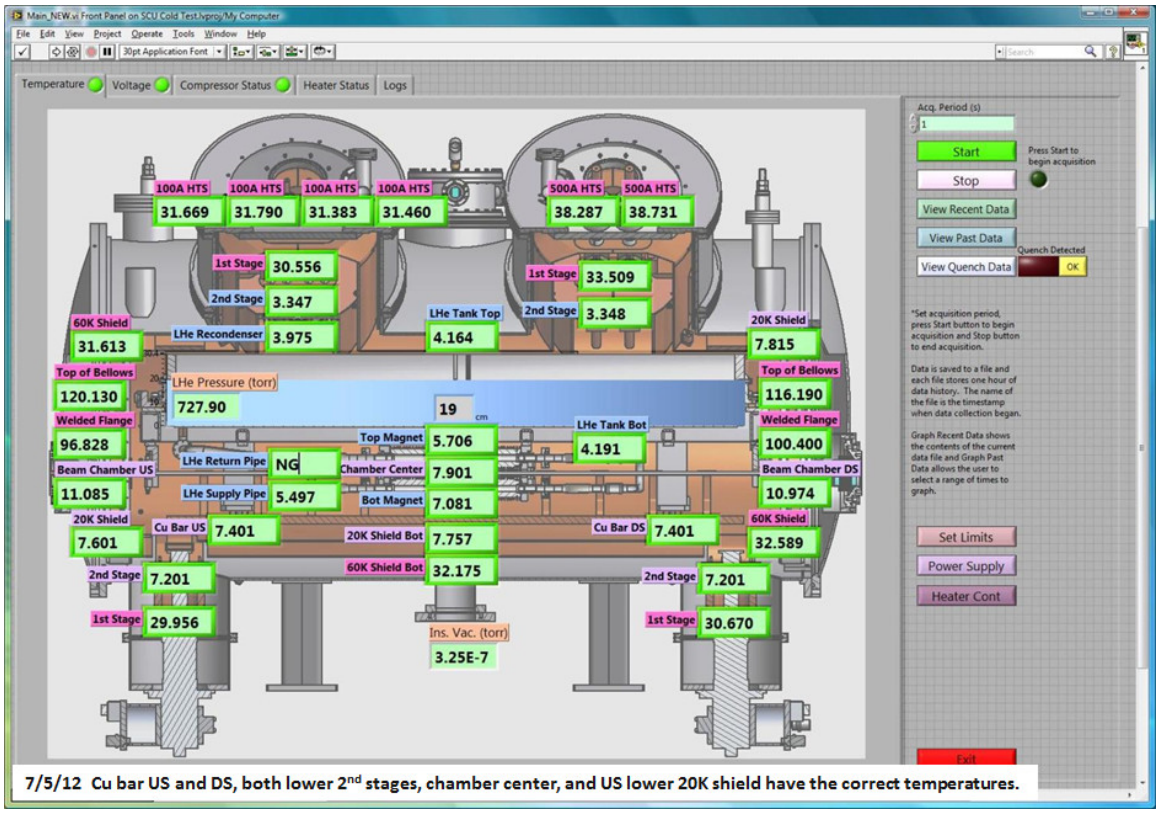

Figure 3.5-14: Thermometry data from initial cryogenic operation of SCU0, July 2012.

Figure 3.5-15: Rolled Cu/SS test piece.

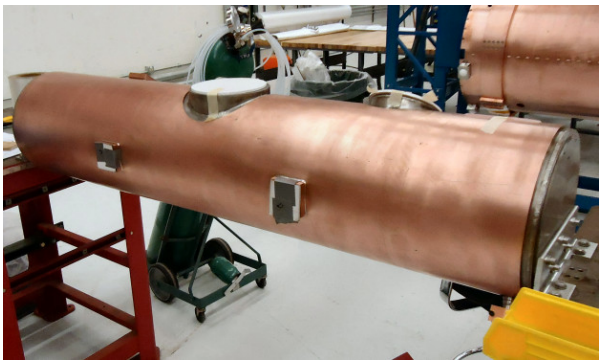

Figure 3.5-16: Closeup of explosion-bonded Cu/SS LHe reservoir shell.

3.5.3.4 Cryostat Design

The cryostat is designed to be compatible with a cryocooler-based cooling scheme. Use of cryocoolers eliminates any permanent connection to a centralized liquid helium cryogenic refrigeration and distribution system and makes it easier to locate superconducting undulators anywhere around the storage ring. The limited cooling power available with existing cryocooler technology requires a correspondingly low heat load, which is achieved by thorough cryogenic analysis and design,

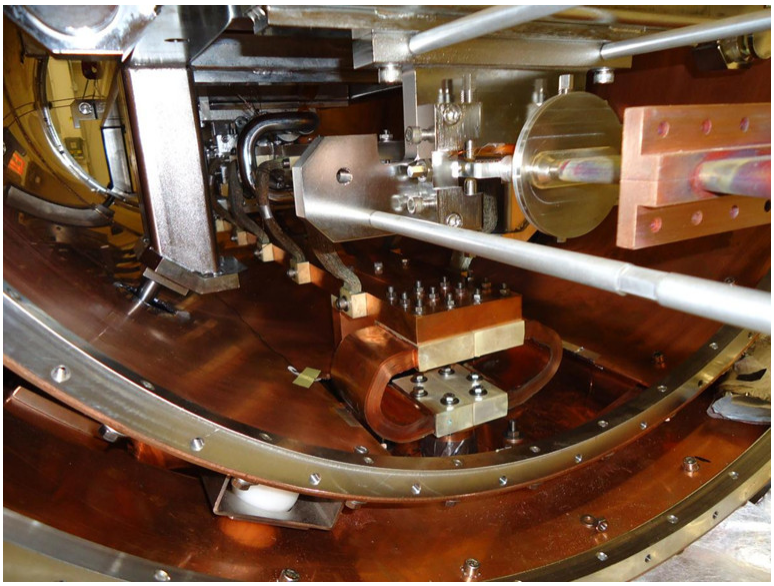

Figure 3.5-17: View of cold mass showing flexible thermal links between the lower cryocooler second stage/thermal bus and the thermal bus/beam chamber.

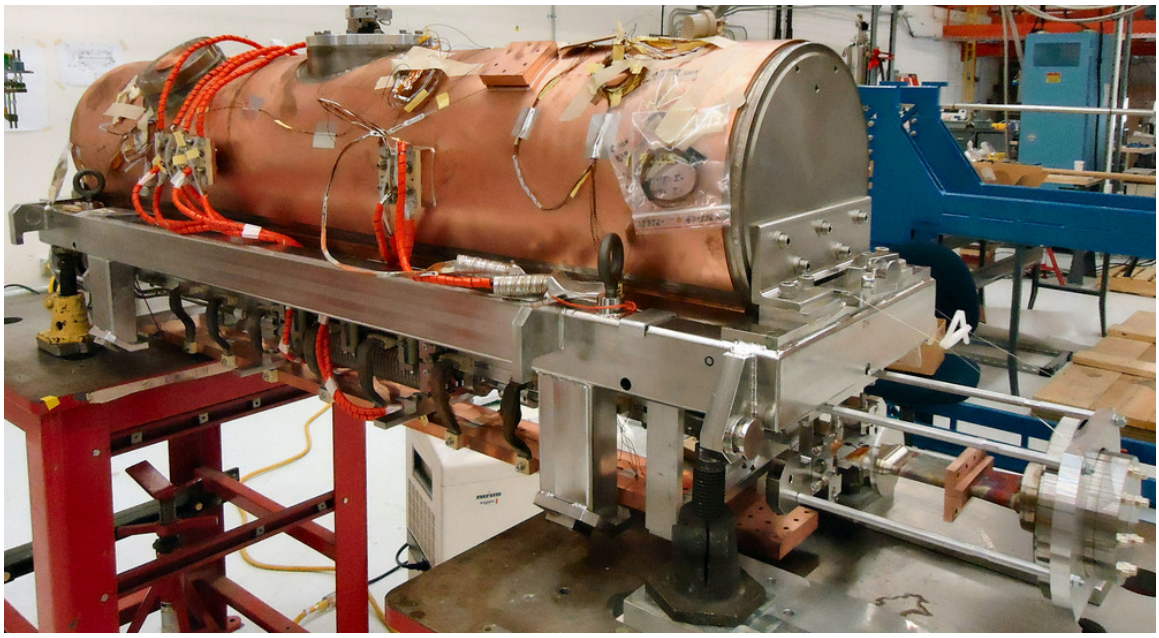

Figure 3.5-18: Completed cold mass ready for installation into the cryostat.

well-conceived fabrication and assembly procedures, and disciplined execution.

The cryostat design includes thermal radiation shields at 60 K and 20 K nominal temperature levels. Elements that cross these thermal barriers (current leads, instrumentation wires, support structures, beam chamber) are thermally intercepted to minimize conduction heat leak. A blanket of multi-layer insulation (MLI) surrounds the outer (60 K) shield to reduce the radiation heat load. Contacts between thermal links and heat sources/sinks were carefully designed and assembled to minimize joint thermal

impedances. This is particularly critical for the current lead assemblies where thin single-crystal sapphire washers are used to provide good thermal contact while preserving electrical isolation.

Major components of the cryostat (vacuum vessel, thermal radiation shields, and liquid helium reservoir) were built-to-print in industry. This contract was successfully carried out on time and on budget. The cryostat assembly/integration was performed in-house. Initial cryostat cooldown was performed in early July 2012 using the cryocoolers and required about three days to reach base temperature. Thermal performance is in good agreement with calculations, with the result that the thermal shields operate at reduced temperatures due to an excess of cryocooler capacity. This provides a generous operating margin for the cryogenic system. Regularly scheduled maintenance of the cryocooler cold heads and compressors is required at 10,000 and 30,000 hours, respectively. Figures 3.5-19, 3.5-20, and 3.5-21 show the cryostat in various stages of assembly.

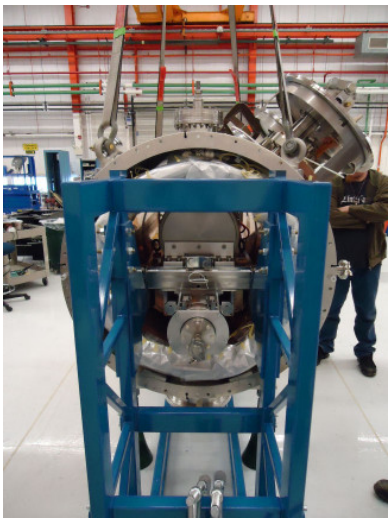

Figure 3.5-19: Cold mass being loaded into the vacuum vessel/thermal shield assembly.

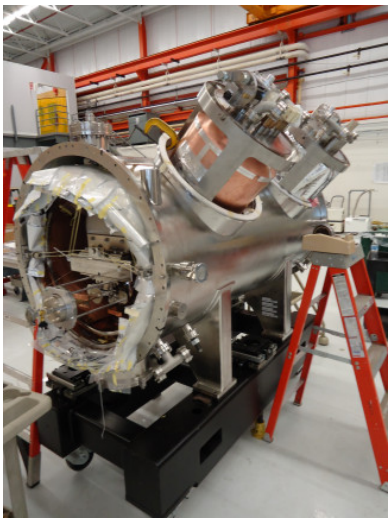

Figure 3.5-20: Cryostat assembly showing cold mass and current lead turrets.

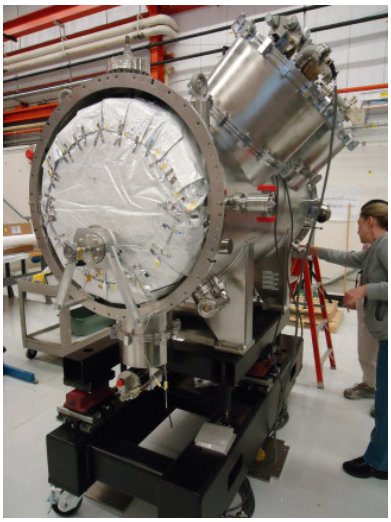

Figure 3.5-21: Cryostat showing completed current lead turrets and insulation blanket.

3.5.3.5 Instrumentation and Controls

The engineering control system, shown in Figure 3.5-22, is used in the lab to control and monitor the various subsystems of the superconducting undulator. The hardware and instrumentation that is used in the system is described below and was chosen to provide the information needed to assess the operation of the undulator and diagnose potential issues with the cryomodule. Figure 3.5-23 is a diagram of the connections between the control system hardware and the cryomodule.

The software interface was developed using National Instruments LabVIEW software. The primary objective of the interface is to display the acquired data in a meaningful way and provide an intuitive interface to control the power supplies and heaters. The software is also capable of logging data at a user-defined interval as well as recording commands sent to the power supplies and heaters. The logged data can be retrieved and displayed in graphical form. The software also monitors the magnet to detect and record when a quench has occurred. The current decay of the power supplies and the voltage across each magnet are recorded during a quench.

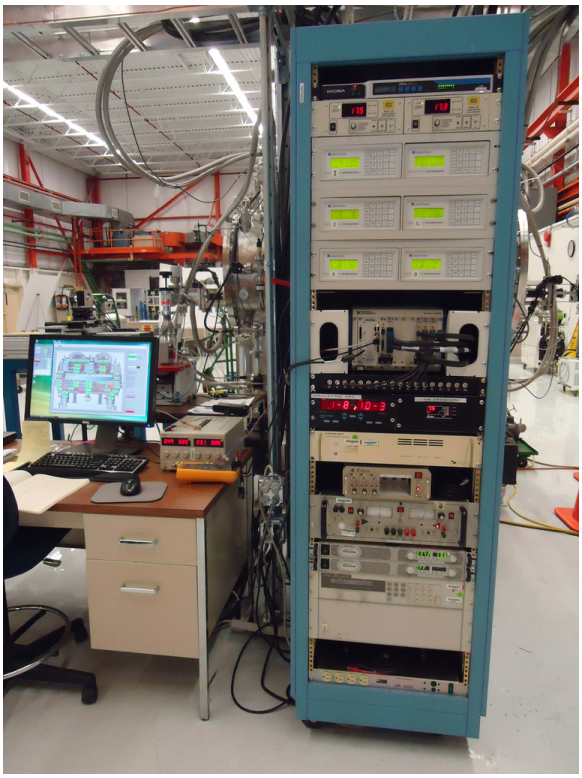

Figure 3.5-22: Control system rack with all components installed.

Several screens were developed to display the instrumentation information. The indicators were placed on the screen to reflect the location of each sensor inside the cryomodule. A screenshot of the temperature display panel is shown in Figure 3.5-14. The panel that displays the voltages can be seen in Figure 3.5-24. A screenshot of the status of the installed heaters can be seen in Figure 3.5-25. The LHe level, cryomodule insulating vacuum, and the pressure inside the LHe tank are displayed in the previously mentioned three screens as well. The panel that shows the status of the compressors can be seen in Figure 3.5-26. The retrieval and display of logged data can be seen in Figure 3.5-27. In the event of a quench, the data can be seen in a display shown in Figure 3.5-28.

The following is a list of the hardware components and instrumentation:

- National Instruments PXI chassis
  - Two 24-bit PXI-4462 DSA modules, one for quench monitoring and recording and one to monitor the voltage across the high temperature superconductors
  - FPGA module with analog outputs for power supply control, analog inputs for power supply and voltage tap monitoring, and digital inputs for monitoring the status of the compressors
  - Switch module for heater control
- Temperature sensors
  - Monitored by Lakeshore 218 temperature monitors
  - Thirty-six Cernox sensors calibrated to 1.4 K or 4.2 K

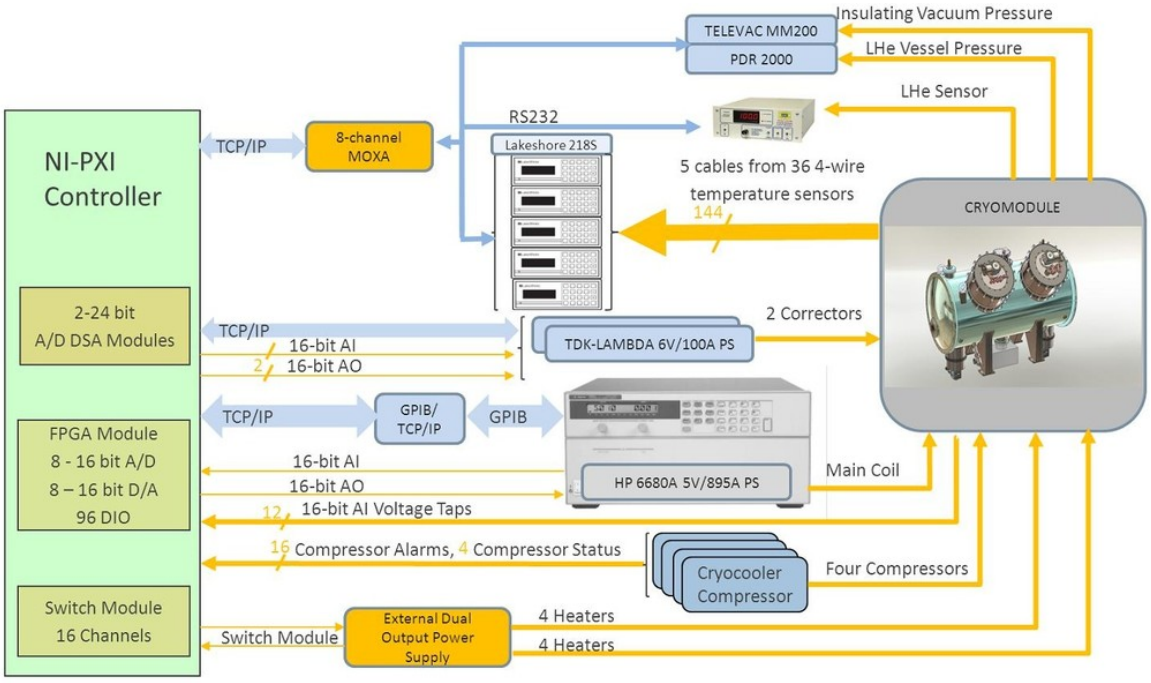

Figure 3.5-23: Diagram of the connections between the controller and the cryomodule.

  - Installed in various locations to monitor the 4 K, 20 K, or 60 K cooling circuits

- Voltage taps
  - Monitored by a National Instruments 24-bit PXI-4462 DSA module and a 16-bit FPGA module
  - Used to monitor the voltages across the high-temperature superconducting leads and the superconducting magnet coils

- Heaters
  - Eight heaters controlled by a National Instruments PXI switch module and external power supplies
  - The thermosiphon heater, located on the LHe return pipe, is used to control the pressure in the LHe tank via a software-based feedback system

- Pressure transducers
  - One transducer from Televac to monitor the insulating vacuum
  - One transducer from MKS to monitor the pressure inside the LHe tank

- Main power supply
  - Agilent 6680-A, 5-V, 875-A power supply
  - Overvoltage protection is used to shutdown the supply in the event of a quench

- Corrector power supplies

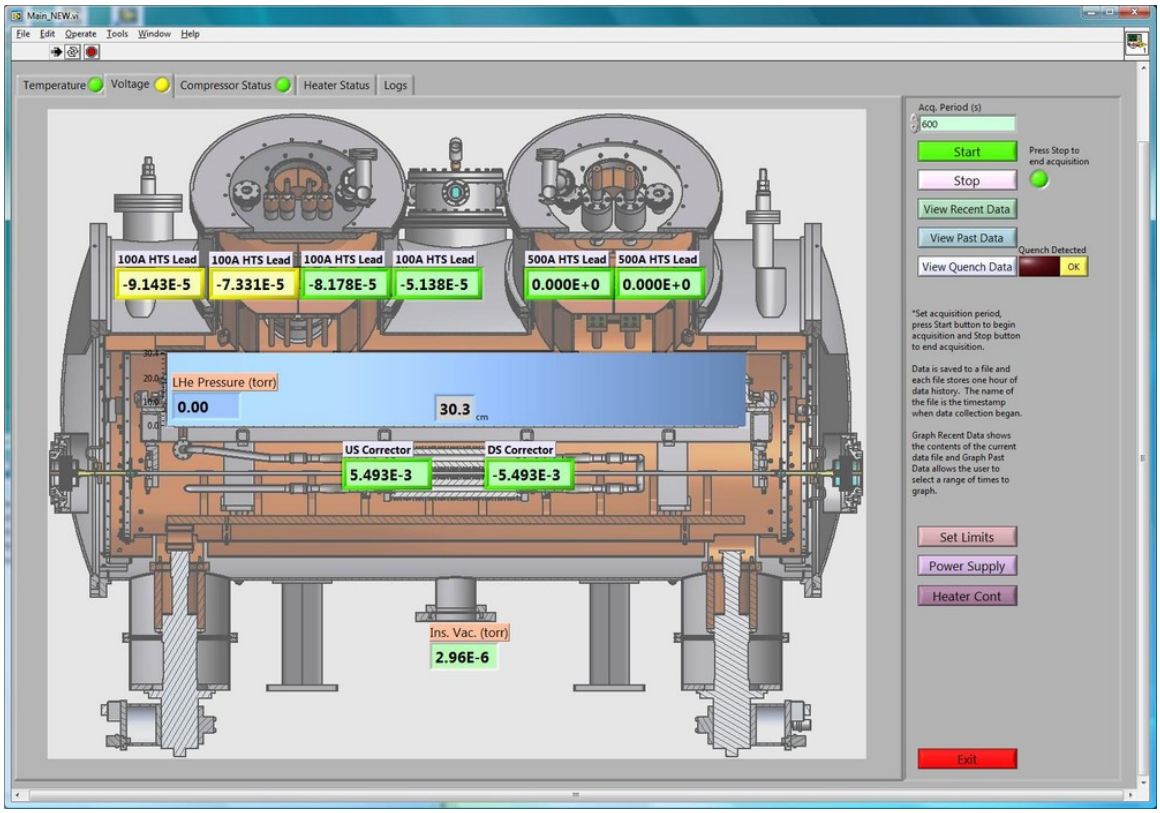

Figure 3.5-24: Control screen developed to display the voltages, LHe level, and pressures within the cryomodule.

  - Two TDK-Lambda, 6-V, 100-A power supplies
  - The corrector power supplies are controlled using a lookup table based on the output of the main power supply

- LHe level monitor
  - AMI model 135 level monitor and a 30-cm probe

It should be noted that the system described above is being used for standalone warm and cold tests of the superconducting undulator before its installation into the APS storage ring. To control the SCU0, SCU1, and SCU2 in the storage ring, an EPICS-based system currently under development will be employed. It will incorporate the features of the existing system as well as any lessons learned.

3.5.3.6 Measurement System Design

This section describes the design of the SCU horizontal magnetic measurement system, which is presently being used for characterization of the SCU0 prototype and which will also be used for the SCU1 and (with modification) SCU2 magnets.

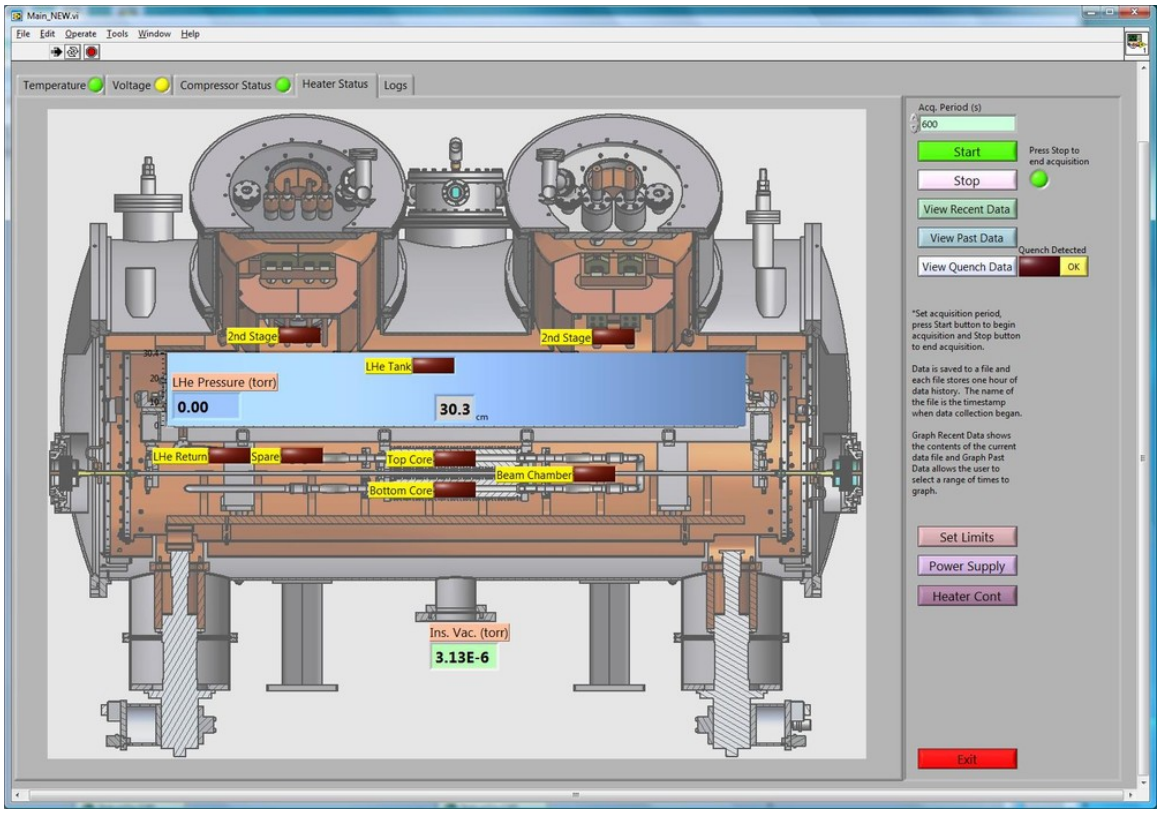

Figure 3.5-25: Control screen developed to display the heater status, LHe level, and pressures within the cryomodule.

Table 3.5-10: Horizontal measurement system requirements.

Measured Quantity	Required Resolution	Peak Signal Level	Achieved Resolution
B Field	0.2 G	10000 G	0.1 G
1st Field Integral	10 G-cm	0.5 mV @ 2 Hz	0.2 G-cm
2nd Field Integral	2500 G-cm^2	2 mV @ 2 Hz	100 G-cm^2

The SCU horizontal measurement system incorporates Hall probe mapping for determining local field and phase errors, and a stretched wire rotating coil for measuring field integrals and integrated multipole coefficients according to the requirements listed in Table 3.5-10.

The mechanical design of the SCU horizontal measurement system is based on a concept developed at the Budker Institute for superconducting wiggler measurement systems. The SCU horizontal measurement system incorporates a heated warm-bore Ti tube inside the cold Al beam chamber as shown in Figure 3.5-29. The guide tube is heated by warm nitrogen gas and by passing a DC current from end to end. It is thermally insulated from the Al beam chamber via a spiral-wrapped Kevlar thread. The Al chamber is also evacuated to minimize heating from the guide tube. The Ti tube serves as a guide for a Hall probe assembly during mapping, and the integral coil rotates inside as well. This design allows the Hall probe and rotating coil to be installed independently of the SCU cryostat temperature. The guide tube can be positioned ± 1 cm horizontally from the magnet central axis. The

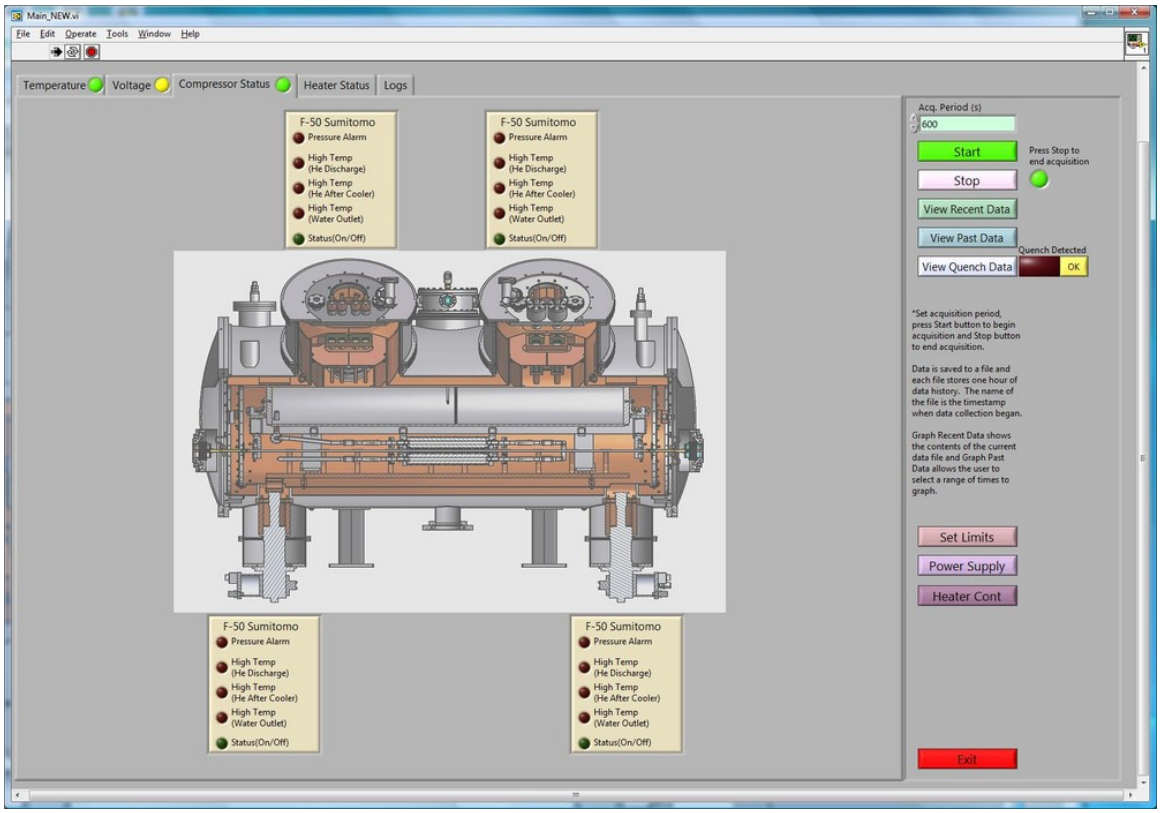

Figure 3.5-26: Control screen developed to display the status of the compressors.

3.5-m long positioning stage is used to drive the Hall probe assembly during field mapping. Figure 3.5-30 shows the 3.5-m linear stage and the upstream-end mechanical components. The measurement system utilizes four linear stages, one for the z-stage longitudinal scanning, and three x-stages for transverse motion. Two rotary stages are used for the rotating coil; one of these is also used for Hall probe mapping. Figures 3.5-31, 3.5-32, 3.5-33, and 3.5-34 show the upstream and downstream stages when configured for rotating coil measurements.

Figure 3.5-35 depicts an overview of the electronics hardware for the measurement system. National Instruments LabVIEW software is used for all data acquisition and control for the measurement system.

3.5.3.6.1 Measurement System Capability

The capabilities of the measurement system are as follows:

- On-the-fly Hall probe measurements (Hall probe speed of 2 cm/s, position precision Δz of 0.1 mm) to determine local field errors and phase errors.
- Three-sensor Hall probe (attached to carbon fiber tubing and driven by linear stage) to measure B_y and B_x simultaneously and determine the mid-plane field regardless of sensor vertical offset from magnetic mid-plane [3.5-27], the technique is described below. The probes can also be rotated through 360 degrees at a fixed z location.

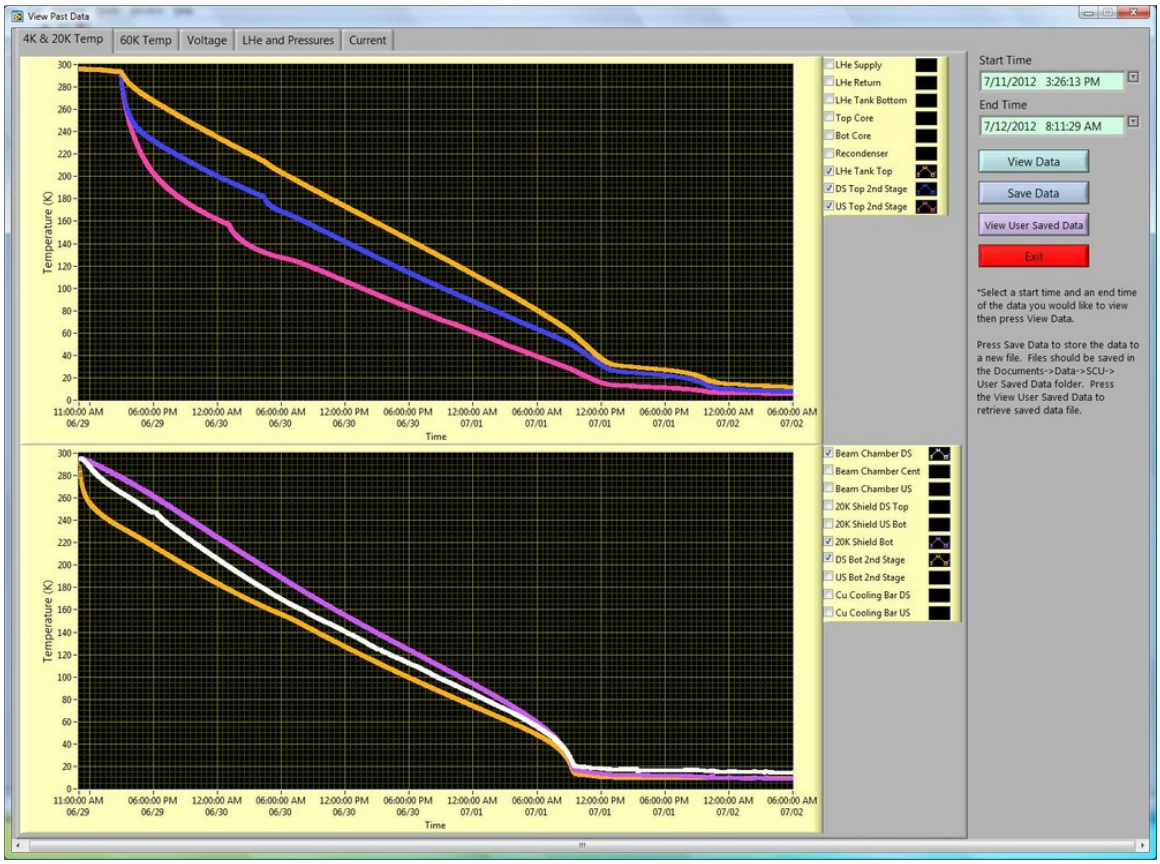

Figure 3.5-27: Control screen developed to display previously logged data. Displayed is temperature data from the 4 K and 20 K cooling circuits during the initial cooldown of the cryomodule.

- Stretched wire rectangular and "figure-8" coils to determine the first and the second field integrals.
- Rotary stages on the upstream end of the cryostat as well as on the z-axis linear stage to provide synchronized rotary motion for stretch coils.
- Integral coil measurements can be done by rotating through 360 degrees and triggering at fixed angular positions, or can be rotated continuously to provide lock-in amplifier capability.
- Coils can be translated along x-axis approximately ± 1 cm to measure integrated multipoles.

3.5.3.6.2 Hall Probe System Details

The Hall probe assembly utilizes three Hall sensors and one thermal sensor mounted to a ceramic substrate. The outer diameter of the ceramic substrate is 3.8 mm and the length is 29 mm. This assembly is mounted inside a carbon fiber (CF) tubing that has a nominal OD of 5 mm. Figure 3.5-36 shows the Hall sensor assembly. The sensor leads are run inside the CF tubing and terminated to a connector on an Al mounting fixture. The mounting fixture couples the Hall probe assembly to a rotary stage. The rotary stage connects to a transverse linear stage with 100-mm travel. The transverse linear

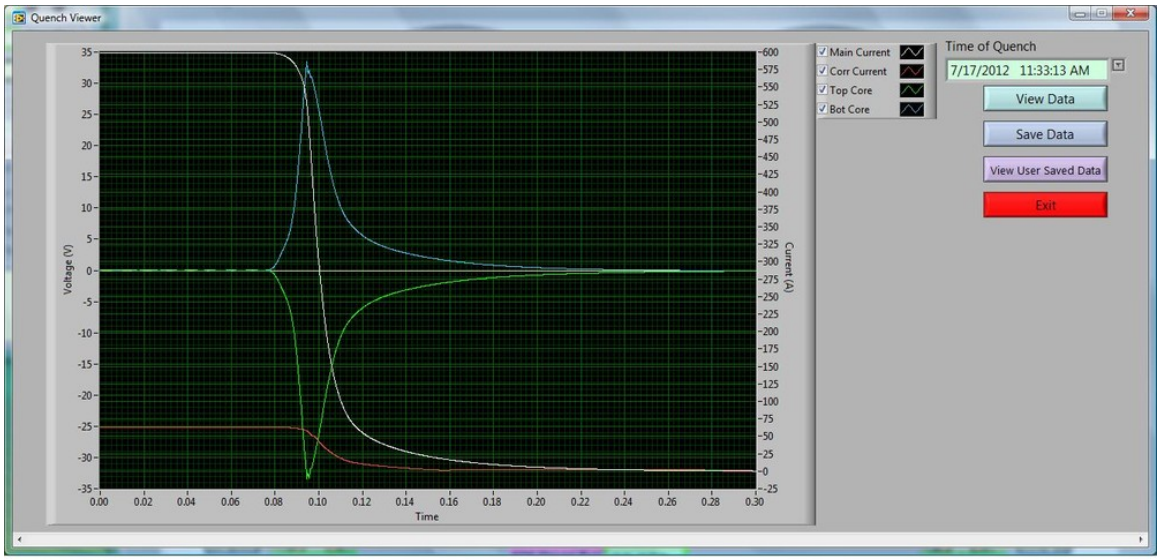

Figure 3.5-28: Control screen developed to display the current decay and voltages recorded by the control system when a quench is detected.

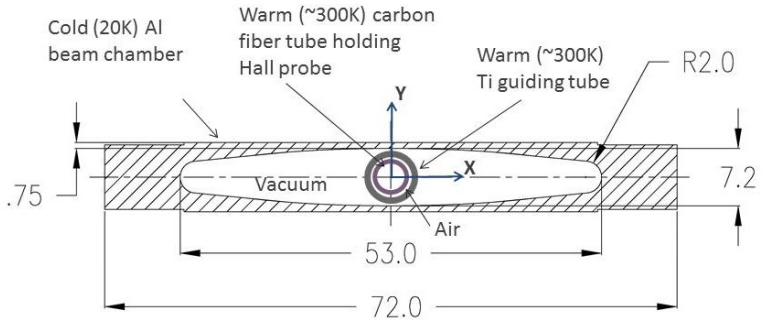

Figure 3.5-29: Cross section of the Al beam chamber with the Ti guide tube and Hall probe carbon fiber tubing.

stage connects to a longitudinal stage with 3.5-m travel, which is used for scanning along the z-axis of the SCU. Typical mapping limits for SCU0 were ±35 cm along the longitudinal axis (z-axis) and ±1 cm along the transverse axis (x-axis). The system is capable of measuring longer devices, up to 2 m.

Mounted to the ends of the SCU cryostat are two stages that allow automated motion in the transverse plane and manual motion in the vertical plane (y-axis), see the Figures 3.5-33 and 3.5-34. These stages provide tension for the guide tube, vacuum sealing between the Al beam chamber and the guide tube OD, and automated positioning along the x-axis. Bellows and O-ring seals provide for motion of the stages relative to the cryostat. The guide tube is manually aligned vertically and horizontally so that it is centered and does not touch the Al beam chamber. This is accomplished by using an alignment telescope that has been aligned to the measurement bench z-axis. This line becomes the fiducial reference for aligning the cryostat and guide tube.

Figure 3.5-30: View of 3.5-meter linear stage on the upstream end of the SCU0 cryostat.

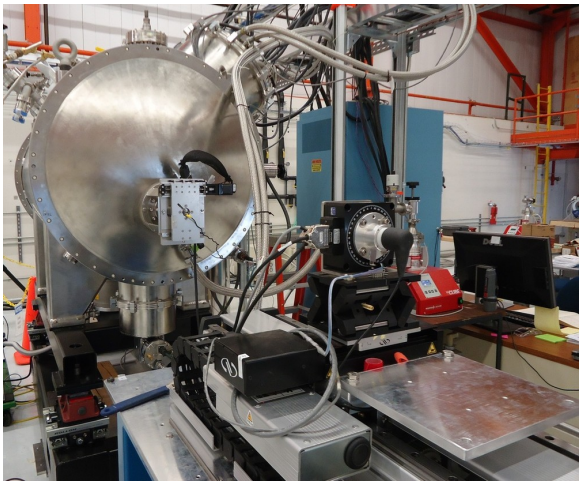

Figure 3.5-31: Upstream end of the cryostat showing horizontal and rotary stages with the coil installed.

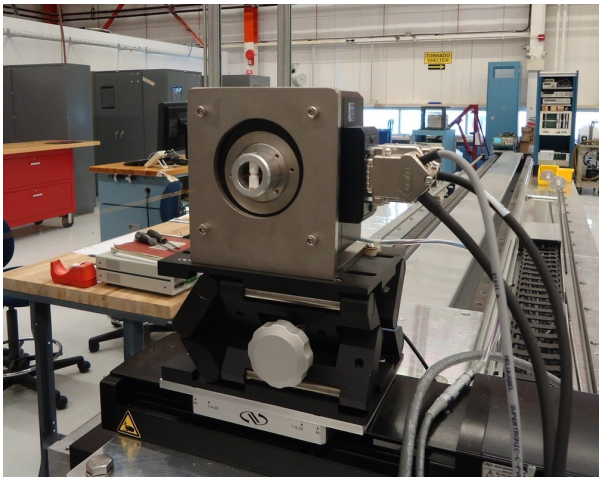

Figure 3.5-32: Closeup of upstream end of the rotary stage with the coil installed.

After the Ti guide tube has been aligned, the CF Hall probe assembly can be inserted into the guide tube and mounted to the rotary stage. Hall probe mapping is automated via a LabVIEW-based program that controls the motion of all axes, as well as the power supplies. Typical scanning velocity is 40 mm/s with the Hall probe position, and the Hall sensor voltages are recorded every 200 µm. Data are saved in various file formats.

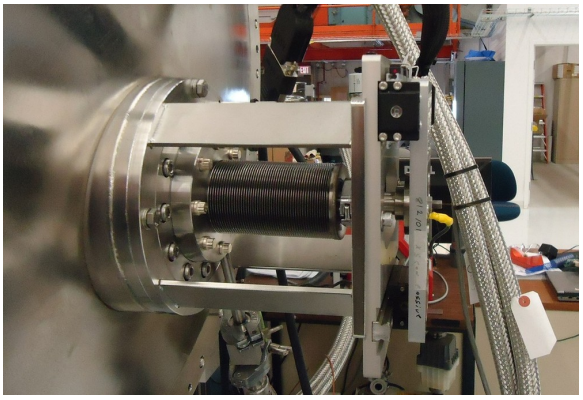

Figure 3.5-33: Upstream end of the cryostat showing the linear stage, bellows, and guide tube.

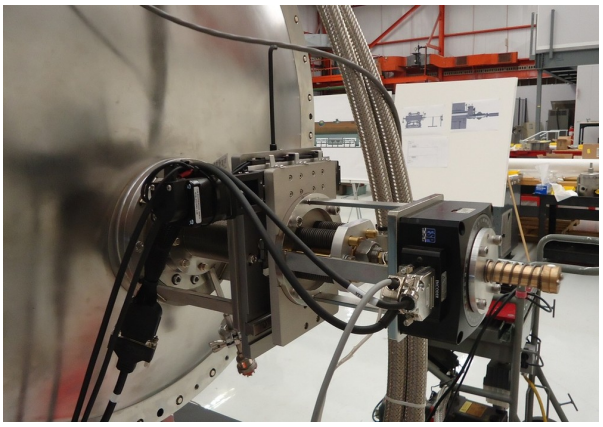

Figure 3.5-34: Downstream end showing the linear and rotary stages with the coil installed.

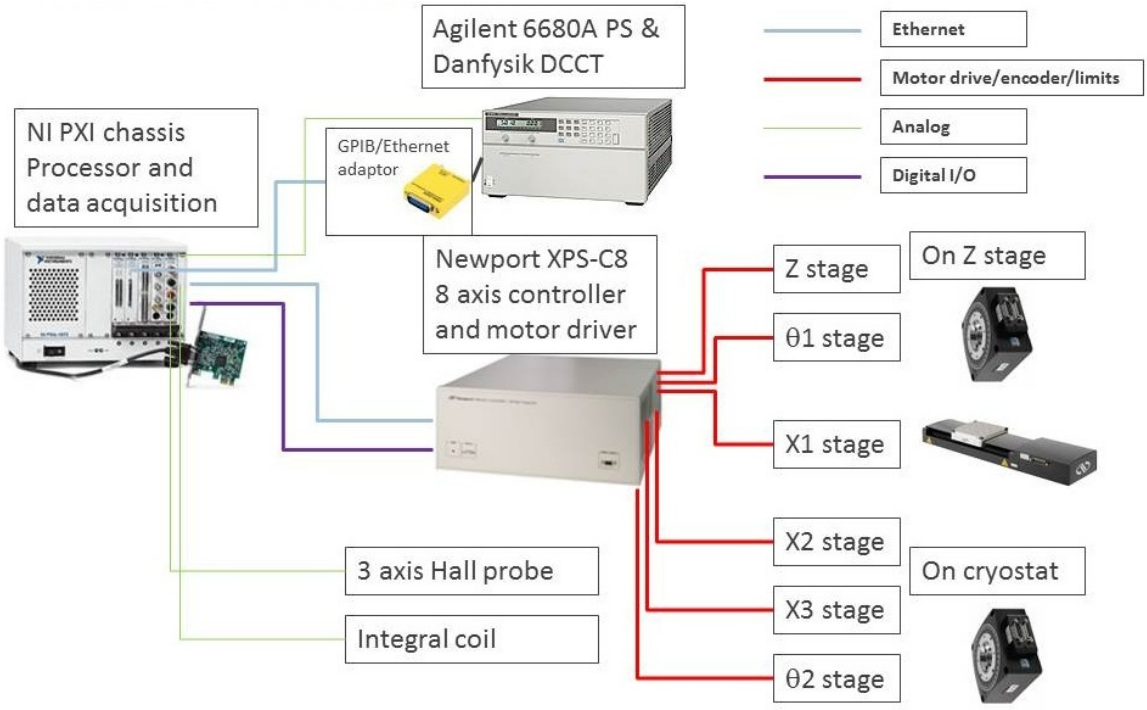

Figure 3.5-35: Diagram of the SCU horizontal magnetic measurement data acquisition system.

3.5.3.6.3 Dual Hall Sensor Method

Since the undulator field along the y-axis varies as the hyperbolic cosine, using two Hall sensors separated vertically by a known dimension allows the calculation of the mid-plane field B_o as well as the offset of the average position of the sensors from the ideal vertical mid-plane. The vertical field of

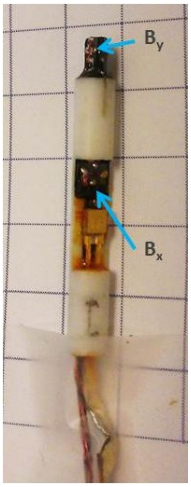

Figure 3.5-36: Three-sensor Hall probe assembly. There are two vertical (B_y) and one horizontal (B_x) field sensors and a temperature sensor.

an undulator as a function of vertical position y, and longitudinal position z, can be described by

$$B_y(z,y) = B_o \cosh ky \sin kz, \tag{3.5-1}$$

where

$$k = 2\pi/\lambda, \tag{3.5-2}$$

and at the field peaks for each Hall sensor by

$$B_{y1} = B_o \cosh ky_1 \tag{3.5-3}$$

and

$$B_{y2} = B_o \cosh ky_2, \tag{3.5-4}$$

where B_{y1} and B_{y2} are the field values from each Hall sensor and B_o is the on-axis field.

With the following definitions

$$\Delta B_y = B_{y2} - B_{y1} \tag{3.5-5}$$

and

$$B_{sum} = B_{y2} + B_{y1}, \tag{3.5-6}$$

and Δy as the vertical separation between Hall sensors, then the average vertical position of the two sensors relative to an ideal mid-plane can be described by

$$y = \frac{1}{k} \tanh^{-1} \left(\frac{\Delta B}{B_{sum} \tanh \frac{k\Delta y}{2}} \right). \tag{3.5-7}$$

The on-axis vertical field can then be calculated by

$$B_{y0} = \frac{B_{y1}}{\cosh k(y - \frac{\Delta y}{2})} = \frac{B_{y2}}{\cosh k(y + \frac{\Delta y}{2})}. \tag{3.5-8}$$

3.5.3.6.4 Rotating Coil System Details

The stretched wire rotating coil consists of a one-turn loop of 125 μm diameter CuBe wire. The width of the coil is 4 mm and length is 3.5 m. The coil is supported at the ends by v-cut ceramic pins. The pins are mounted in fixtures that are connected to rotary stages. The rotary stages can be rotated as master/slave or individually. To measure the first integral, the coil is configured as a normal planar coil; for the second integral, one end is flipped 180 degrees to form a "figure-8" coil.

For measurement of the first field integral, the stages are continuously rotated at 1 rev/s. The coil signal is coupled through a rotatable connector and then to an amplifier with a gain of 1000. The output of the amplifier is then sampled by a National Instruments digital signal analyzer module. A software-based lock-in amplifier is used to determine the amplitude of the fundamental frequency of rotation, and the vertical and horizontal components of the first integral are calculated. (The lock-in amplifier technique was implemented at the suggestion of T. Tanabe during the February, 2010 design review [3.5-44].) The typical resolution of the first integral with this technique is 0.2 G-cm with repeatability of approximately 1 G-cm. See Figure 3.5-32 for a view of the upstream rotating stage and the v-cut ceramic pin.

In order to measure the second field integral with the "figure-8" coil, the first integral needs to be known as well as the angle of the "figure-8" coil [3.5-45].

Recent measurements of the first and second field integrals of SCU0 have shown that the on-axis first integral is less than 50 G-cm for all excitation currents. The second integral is typically less than 1000 G-cm^2 and can be adjusted within a range of $\pm$150 kG-cm by varying the corrector coil current from 0 A to 100 A. These are within the specifications in Table 3.4-7a.

3.5.3.6.5 SCU0 Magnetic Measurement Results

The Hall probe mapping results show that the peak field at 500 A is approximately 6400 Gauss with a first integral of less than 50 G-cm and phase errors of approximately 1 degree rms. Figures 3.5-37, 3.5-38, 3.5-39, and 3.5-40 show the results of a Hall probe scan with the main coils energized to the nominal main-coil design current of 500 A and corrector coil current of 51.8 A.

The SCU horizontal magnetic measurement system has been fully functional since March, 2012 and can accommodate SCU devices up to 2 meters magnetic length. Presently the system is being successfully used to characterize the SCU0 device. It will also be used for the SCU1 device and then adapted for the longer SCU2 device.

3.5.4 References

[3.5-1] R. Dejus et al. On-axis Brilliance and Power of In-Vacuum Undulators for the Advanced Photon Source. Technical Report MD-TN-2009-004, APS, (2009).

[3.5-2] L. R. Elias and J. M. Madey. Superconducting Helically Wound Magnet for the Free-Electron Laser, Review of Scientific Instruments, **50**, 11, (1979).

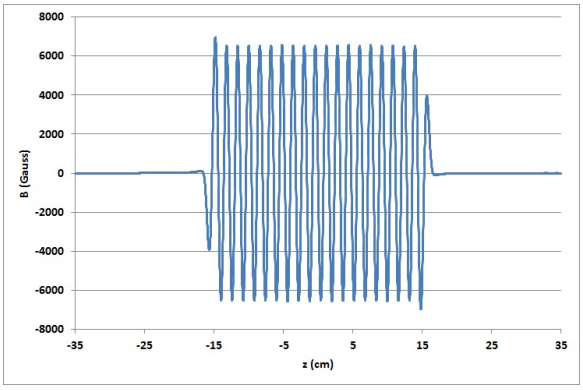

Figure 3.5-37: Plot of the SCU0 on-axis B field with the main coils energized to 500 A and the correction coils to 51.8 A. Peak field is about 6400 Gauss.

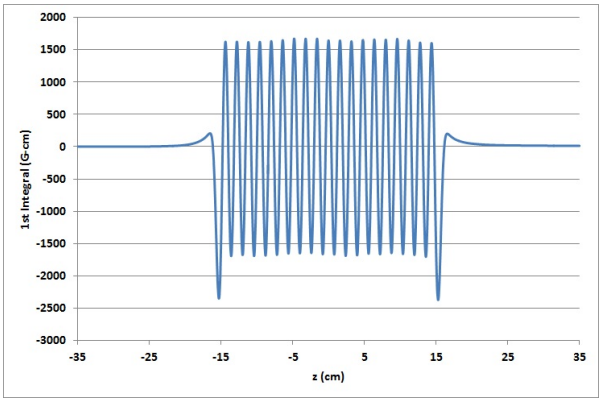

Figure 3.5-38: Plot of the SCU0 first field integral with the main coils energized to 500 A and the correction coils to 51.8 A. Final value is 12 G-cm.

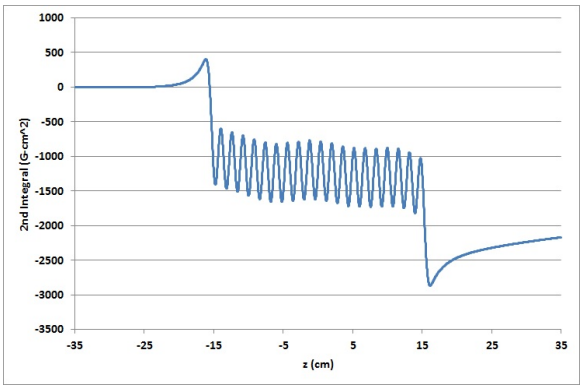

Figure 3.5-39: Plot of the SCU0 second field integral with the main coils energized to 500 A and the correction coils to 51.8 A. Final value is -2170 G-cm^2.

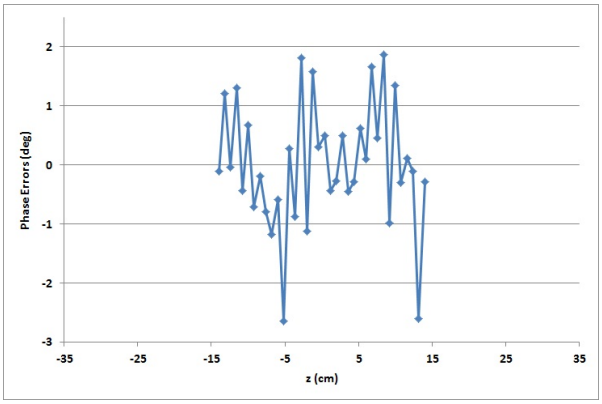

Figure 3.5-40: Plot of SCU0 phase errors with the main coils energized to 500 A and the correction coils to 51.8 A. Rms value is 1.04°.

[3.5-3] G. Y. Kezerashvili et al. Colliding Beam Polarization Measurement Using Superconducting Helical Undulator at the VEPP-2M Storage Ring, Nuclear Instruments and Methods, **A314**, 15, (1992).

[3.5-4] J. Rochford. The Superconducting Undulator for the ILC Positron Source, Proc. of PAC 2009, (2009).

[3.5-5] A. Bernhard et al. Performance of the First Superconducting Cold-Bore Undulator in an Electron Storage Ring, IEEE Transactions on Applied Superconductivity, **17**(2), 1235, (2007).

[3.5-6] C. Boffo et al. Fabrication of the New Superconducting Undulator for the ANKA Synchrotron Light Source, Proc. of IPAC 2010, (2010).

[3.5-7] J. C. Jan et al. Design and Improvement of a Mini-Pole Superconducting Undulator at NSRRC, IEEE Transactions on Applied Superconductivity, **18**(2), 427, (2008).

[3.5-8] Y. Ivanyushenkov. Magnetic Simulation of a Superconducting Undulator for the Advanced Photon Source, Proc. of PAC 2009, p. 310, (2009).

[3.5-9] Y. Ivanyushenkov et al. Status of R&D on a Superconducting Undulator for the Advanced Photon Source, Proc. of PAC 2009, p. 313, (2009).

[3.5-10] Y. Ivanyushenkov et al. A Design Concept for a Planar Superconducting Undulator for the APS, IEEE Transactions on Applied Superconductivity, **21**, 1717–1720, (2011).

[3.5-11] K. Harkay. Total Resistive Wall Heat Load for SCU0 Commissioning. Technical Report APS_1431827, APS, (2012).

[3.5-12] M. Petra and R. Kustom. Sources of Dynamic Heat Load for the Superconducting Undulator (SCU). Technical Report APS_1283081, APS, (2004).

[3.5-13] R. Kustom. ANL, Private communication, (2010).

[3.5-14] V. Sajaev. ANL, Private communication, (2010).

[3.5-15] E. Trakhtenberg et al. Extruded Aluminum Vacuum Chambers for Insertion Devices, Proc. of PAC 2011, p. 2093, (2011).

[3.5-16] R. Powell et al. J. Applied Physics, **31**(3), 496, (1960).

[3.5-17] C.Y. Ho and T.K. Chu. Electrical Resistivity and Thermal Conductivity of Nine Selected AISI Stainless Steels. Technical Report DTIC A129160 CINDAS Report 45, Purdue University, (1977).

[3.5-18] R. Kustom. Preliminary Report on Heat Load due to Image Currents on the Vacuum Liner of a Superconducting Undulator (Version 2). Technical Report APS_1423346, APS, (2011).

[3.5-19] S. Kim. Resistive wall heating due to image currents on the beam chamber for a superconducting undulator. Technical Report APS_1429125, APS, (2012).

[3.5-20] R. Kustom. Effect of Surface Roughness on Power Deposition in the Superconducting Undulator. Technical Report APS_1429078, APS, (2011).

[3.5-21] E. Trakhtenberg. Private Communication, (2011).

[3.5-22] K. Harkay and L. Boon. APS SCU0 Photon Absorber Heat Load Analysis. Technical Report APS_1424713, APS, (2011).

[3.5-23] L. Boon and K. Harkay. SCU Heating from a Steered Beam. Technical Report APS_1429030, APS, (2012).

[3.5-24] V. Sajaev. Private Communication, (2011).

[3.5-25] S. Khruschev et al. Superconducting 63-Pole 2 T Wiggler for Canadian Light Source, Nuclear Instruments and Methods, **A575**, 38, (2007).

[3.5-26] Y. Ivanyushenkov et al. Calibration of Hall Probe at Cryogenic Temperatures, Proc. of IMMW 16th 2009, (2009).

[3.5-27] I. Vasserman. ANL, Private communication, (2010).

[3.5-28] R. Dejus. On the Issue of Setting the RMS Phase Error Criterion for the APS Undulators (Rev 0d). Technical Report APS_1425199, APS, (2011).

[3.5-29] R. P. Walker. Nuclear Instruments and Methods A, **335**, 328, (1993).

[3.5-30] G. Decker. Advanced Photon Source Insertion Device Field Quality and Multipole Specifications. Technical Report APS/IN/ACCPHY/95-1, APS, (1995).

[3.5-31] A. Xiao and L. Emery. APS-U Planar and Revolver Undulator Field Quality Specifications. Technical Report APS_1427506, APS/ASD/AOP, (2012).

[3.5-32] V. Sajaev. Calculation of maximum possible field integrals during an SCU quench. Technical Report APS_1424705, APS, (2011).

[3.5-33] V. Sajaev. Simulation of switchable canted orbit in a 5-kicker bump configuration. Technical Report APS_1424392, APS, (2011).

[3.5-34] K. Harkay et al. Synchrotron radiation heat load on the superconducting undulator SCU chamber for ideal and missteered beam trajectories. Technical Report APS_1424505, APS, (2012).

[3.5-35] M. Borland and Y.-C. Chae. APS-U Long Straight Sections and Lattice Physics Requirements Document. Technical Report APS_1423797, APS, (2011).

[3.5-36] G. Wiemerslage. Installation and Alignment of the Insertion Device Vacuum Chamber. Procedure XF-PI 3, APS, (1995).

[3.5-37] E. Moog. Vertical positioning requirement for APS 33-mm-period undulators. Technical Report APS_1425011, APS, (1999).

[3.5-38] L. Emery. Storage Ring Magnet and Photon Aperture Tolerance Budget for Top-Up Safety. Procedure 3-00055, APS, (2011).

[3.5-39] G. Goeppner. Verify Positions of Storage Ring Vacuum Chambers in the Magnets. Procedure 310301-00411, APS, (2010).

[3.5-40] V. Sajaev. Maximum possible orbit in the dipole upstream of the superconducting undulator. Technical Report APS_1424305, APS, (2012).

[3.5-41] K. Harkay et al. SCU0 Commissioning Plan. Technical Report APS_1423845, APS, (2012).

[3.5-42] E. Trakhtenberg et al. Proc. of MEDSI 2010, (2010).

[3.5-43] B. Badouy. Heat and Mass Transfer in Two-Phase He I Thermosiphon Flow, S. Breon, editor, Advances in Cryogenic Engineering, volume 47B, pp. 1514–1521. AIP, (2002).

[3.5-44] T. Tanabe and H. Kitamura. Journal of Synchrotron Radiation, **5**, 475–477, (1998).

[3.5-45] I. Vasserman and J. Xu. A new magnetic field integral measurement system. Technical Report ANL/APS/TB-49, APS, (2004).

3.6 Short-Pulse X-Rays

3.6.1 Introduction

As part of the upgrade, APS will provide a short-pulse x-ray system (SPX) delivering few-ps x-ray pulses. After consideration of alternatives (section 3.6.2), the use of superconducting deflecting cavities has been selected. This system must meet several operational requirements:

- minimize frequency of interruption of user experiments
- minimize the disturbance of the storage ring beam during user operation
- be transparent to the users with the deflecting cavities detuned and parked at other than 2 K

The SPX performance requirements are specified in section 3.6.3.1, which defines the technical specifications requirement for the SPX technical systems and components. The SPX technical systems and components will be designed to meet these requirements and deliver short-pulse x-rays to a selected number of beamlines.

The SPX technical system comprises:

- Two cryomodules (section 3.6.3.8), each with four superconducting rf deflecting cavities (section 3.6.3.8.2) operated at 2815 MHz, the eighth harmonic of the APS storage ring rf frequency. The cavities are designed to provided 500 kV of deflecting voltage each in the vertical direction, for a total of 4-MV deflecting voltage per cryomodule. Each cavity is equipped with higher- and lower-order mode waveguide dampers (section 3.6.3.9) and slow and fast tuner units (section 3.6.3.8.8).
- Eight 10-kW rf amplifiers operating in continuous wave (cw) mode (section 3.6.3.4).
- Eight low-level rf systems to independently control each cavity field (section 3.6.3.5).
- Timing and synchronization system to provide the phase references (section 3.6.3.6). needed to drive the SPX cavities and to synchronize beam-line lasers to the SPX x-ray beam pulse.
- Beam diagnostics which include beam arrival time (BAT) monitor, vertical beam size monitors, optical beam tilt monitors and beam position monitors (section 3.6.3.10).
- An integrated control system defining the interfaces between the SPX subsystems and the main control room via EPICS, as well as the software tools that must be provided for proper operation of SPX (section 3.6.3.7).
- Fault detection and response system to protect storage ring equipment from potential failure scenarios of the SPX subsystems (section 3.6.3.13).
- Cryoplant with design capacity of 320 Watts at 2 K and 500 watts at 5-8 K and liquefaction of 0.003 kg/s (section 3.6.3.11).
- Deionized water system distribution for SPX rf power systems located in SPX rooms 400A-1 and 400A-4 (section 3.6.3.11).

3.6.2 Approaches to Short X-Ray Pulses

One of the major goals of the APS Upgrade is to address the need for intense, tunable, high-repetition-rate, picosecond x-ray pulses. This is a significant challenge for a storage ring light source, due to the physics governing storage rings. The zero-current rms bunch duration is given by [3.6-1]

$$\sigma_{t,0} = \sigma_\delta \sqrt{\frac{\alpha_c T_r E}{e\dot{V}}}, \tag{3.6-1}$$

where σ_δ is the fractional momentum spread, E is the beam energy, α_c is the momentum compaction factor, T_r is the revolution time, and $\dot{V} = 2\pi(h/T_r)V\cos\phi_s$ is the derivative of the h-harmonic rf voltage V evaluated at the synchronous phase ϕ_s. This gives

$$\sigma_{t,0} = \sigma_\delta T_r \sqrt{\frac{\alpha_c E}{2\pi h e V \cos\phi_s}}. \tag{3.6-2}$$

For the APS, $\sigma_\delta \approx 10^{-3}$, $\alpha_c \approx 2.8 \times 10^{-4}$, $T_r = 3.68\mu$s, $h = 1296$, $V = 9$ MV, and $\phi_s \approx 40°$, giving $\sigma_{t,0} = 20$ ps.

As the current increases, the bunch length also increases due to interaction of the beam with the longitudinal impedance of the vacuum chamber and rf cavities. There are two effects at work. The first is potential well distortion (PWD), which results from the relatively low-frequency part of the impedance (i.e., low frequency compared to the bunch spectrum). As the name suggests, the charge of the electron bunch distorts the potential well created by the rf system. This reduces the effective rf voltage and thus increases the bunch length according to Equation (3.6-1) by, effectively, reducing $\dot{V}$. The PWD has no threshold but lengthens the bunch starting from infinitesimal current. For the APS, measurements [3.6-2] show that

$$\sigma_t \approx 25.1 I^{0.1484+0.0346\log_e I}, \tag{3.6-3}$$

where σ_t is in ps and $I > 0.1$ mA is the bunch current. For the 4.25-mA single-bunch current in 24-bunch mode, this gives about 34 ps. If the beam current is doubled, this will increase to 40 ps.

A second important phenomenon affecting the bunch length is the microwave instability, which depends on the higher frequency part of the impedance. It results in increased energy spread σ_δ, which again increases the bunch length according to Equation (3.6-1). At the APS, the microwave instability threshold is about 7 mA [3.6-3]. At present, it only impacts the intense bunch in hybrid mode operation.

In the face of these phenomena, various approaches have been tried to create shorter x-ray pulses. In this section, a number of these approaches are reviewed, indicating the strengths and weaknesses of each.

3.6.2.1 High-Harmonic Cavity

One approach is to use a high-harmonic rf cavity to increase $\dot{V}$. However, it is difficult to get a significant improvement using this method because of the difficulty of obtaining sufficient voltage. A preliminary study [3.6-4] showed that reducing the bunch length at 4 mA by a mere 50% would require 9 MV at 1.4 GHz. In spite of the marginal benefit, this would take up significant space that could otherwise be used for insertion devices. In addition, it would shorten the Touschek lifetime, which is undesirable given the pressure put on top-up by the shorter lifetime in the upgrade lattices (see section 3.2.2.4).

3.6.2.2 Low-α Operation

A more workable approach [3.6-5] is to reduce the value of α_c in Equation (3.6-1), which can be done by adjustment of the lattice. For example, by reducing α_c by a factor of 100 from the present value of 2.8×10^{-4}, one could reduce the bunch length by an order of magnitude, reaching the few-picosecond regime. However, this causes difficulty in obtaining high bunch current, to the extent that the total stored current is typically reduced significantly. In the first place, single-bunch instabilities are worse for shorter bunches, because the peak current is increased (for fixed-bunch charge) and the frequency spectrum of the bunch is broadened. In addition, as α_c is reduced, the synchrotron tune ν_s also decreases according to [3.6-1]

$$\nu_s = \sqrt{\frac{\alpha_c e \dot{V} T_r}{4\pi^2 E}}. \tag{3.6-4}$$

When ν_s is smaller, the particles in the head and tail of the bunch change positions less frequently, which gives instabilities more time to build up.

For example, the threshold for the important transverse mode-coupling instability (TMCI) is proportional to $\sigma_t \nu_s \propto \alpha$ [3.6-6, 3.6-7]. Hence, the expectation is that threshold would drop 100-fold for a 10-fold reduction in bunch length. While TMCI can be defeated to some extent with feedback and positive chromaticity, these cures have limits. Chromaticity can only be increased so much before other aspects of machine performance like injection efficiency and lifetime suffer. While feedback may be effective in controlling centroid instabilities, beam-size instabilities cannot be controlled.

Another important instability for the APS is microwave instability. In this case, the threshold also goes down as one attempts to shorten the bunch, with a scaling of σ_t^3 [3.6-8]. Although the microwave instability does not result in beam loss, significant increase of the energy spread is problematic in a ring like the APS with nonzero dispersion in the straight sections. Of course, it also fights against the intention to obtain shorter bunch duration.

An additional difficulty with low-α operation for a double-bend lattice is that the emittance increases significantly, since the optics needed for minimum emittance do not accommodate the change in the sign of the dispersion required by low-α optics. For example, in the APS the emittance for a zero-α configure is about 20 nm. For these reasons, the APS has elected not to pursue a low-α mode as it could serve only a small segment of our user community. Although the APS operates in several special fill-pattern modes for timing experiments, these modes remain suitable for almost all users because the APS continues to run at 100 mA.

3.6.2.3 Laser Slicing

Another method of obtaining short x-ray pulses from storage rings is "laser-slicing," in which a laser is used to increase the energy spread of a short slice of the bunch [3.6-9]. This has been successfully used to produce ~100-fs x-ray pulses with repetition rates of hundreds of kHz at the Advanced Light Source (ALS) [3.6-10]. In this concept, a short laser pulse interacts with a section of the electron beam in a wiggler. In order for this interaction to modulate the energy of the electrons, the resonance condition must be satisfied

$$\lambda_w = \frac{2\lambda_l \gamma^2}{1 + K^2/2}, \tag{3.6-5}$$

where λ_w is the wiggler wavelength, λ_l is the laser wavelength, γ is the relativistic factor of the electron beam (1.37×10^4 for APS), and K is the wiggler strength parameter. One readily apparent difficulty is that λ_w increases as γ^2; however, this can be mitigated by making $K = 93.4B[T]\lambda_w[m] \gg 1$, giving

$$\lambda_w \approx 0.077 \sqrt[3]{\frac{\lambda_l \gamma^2}{B^2}}. \tag{3.6-6}$$

A likely candidate for a laser producing a short pulse is a Ti:sapphire laser operating at the wavelength $\lambda_l = 800$. Operating at the fundamental laser wavelength rather than its harmonic is advantageous in terms of available laser power and laser beam quality, since it avoids the use of frequency doubling crystals, which not only reduce the available laser power but also may distort the laser wavefront [3.6-11]. If B = 1.5 T then λ_w = 31 cm and K = 43. No more than 15 periods of such a device can be accommodated in a standard APS straight section. Assuming a 15-period device is placed in a zero-dispersion straight (which would require special optics), it will produce a slight damping effect on the emittance along with a slight increase in energy spread, as well as 34 kW of radiation power distributed into a rather large K/γ angle.

The modulation amplitude of the electron energy is given by equation (9) in ref. [3.6-12]. The rms fractional energy spread of the APS beam is 0.096%, giving an energy spread of σ_E = 6.7 MeV. The peak energy modulation due to the laser as a fraction of the energy spread is shown in Figure 3.6-1. Requiring $p = \Delta E/\sigma_E > 5$ gives $A_l > 3.4$ mJ for a 50-fs FWHM laser pulse and $A_l > 6.3$ mJ for a 100-fs FWHM laser pulse. This is the minimum requirement and will be increased by various factors such as the effect of nonzero electron beam size [3.6-10]. In practice at ALS, a measured laser pulse energy of about twice the minimum value is needed [3.6-11], so it should conservatively require about 12 mJ per pulse. Commercially available lasers can provide 1-kHz pulses with an average power of 20 W [3.6-13]. Hence, at present the repetition rate would be about 1 kHz, which is quite low. Advances in laser technology, e.g., cryogenically cooled Yb:YLF, could possibly allow an increase in the repetition rate by several orders of magnitude in the not-too-distant future [3.6-14].

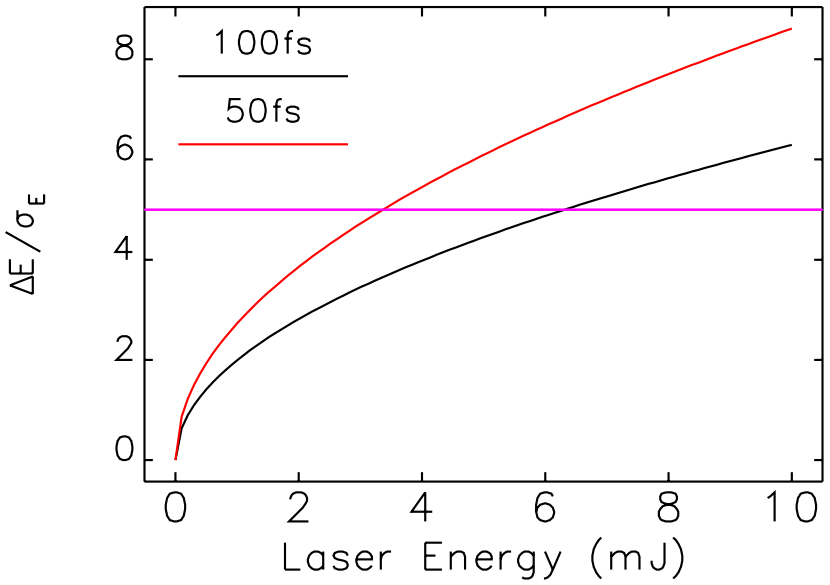

Figure 3.6-1: Energy modulation amplitude normalized to the rms energy spread of the electron beam, for the laser-slicing scheme applied to the APS.

The maximum repetition rate available in this technique when one can alternate electron bunches is determined by the need to limit the beam energy spread increase. To estimate this increase, one first looks at the energy change of an electron during a single turn when the laser hits the bunch. For the i^{th} electron

$$\Delta E_i = (QE)_i + p\sigma_E \sin\omega_l t_i \exp\left\{-\frac{t_i^2}{2\sigma_l^2}\right\}, \tag{3.6-7}$$

where $(QE)_i$ is a random deviate representing quantum excitation, $\omega_l = 2\pi c/\lambda_l$, and σ_l is the laser pulse duration. Averaging this over the electron bunch gives

$$\langle \Delta E^2 \rangle = \mathcal{N}\langle u^2 \rangle T_0 + \frac{p^2\sigma_E^2\sigma_l}{4\sqrt{2}\sigma_t}, \tag{3.6-8}$$

where $\mathcal{N}\langle u^2 \rangle$ is the familiar quantum excitation term [3.6-1], T_0 is the revolution time, and σ_t is the rms electron bunch duration. The effective excitation rate is

$$\frac{d}{dt}\langle \Delta E^2 \rangle = \mathcal{N}\langle u^2 \rangle + \frac{p^2\sigma_E^2\sigma_l}{4\sqrt{2}\sigma_t}\frac{f_l}{n_b}, \tag{3.6-9}$$

where f_l is the laser repetition rate, and n_b is the number of bunches. The equation for the equilibrium energy spread is [3.6-1]

$$\sigma_E^2 = \frac{1}{4}\tau_E \frac{d}{dt}\langle \Delta E^2 \rangle \tag{3.6-10}$$

$$= \sigma_{E0}^2\left(1 + \frac{p^2\sigma_l f_l \tau_E}{16\sqrt{2}\sigma_t n_b}\right). \tag{3.6-11}$$

If σ_E is allowed to grow by 10%, then we have

$$f_l \le \frac{16\sqrt{2}\sigma_t n_b}{5p^2\sigma_l\tau_E}. \tag{3.6-12}$$

For $p = 5$, $\sigma_t = 50$ ps, $n_b = 24$, $\sigma_l = 100/2.35$ fs, and $\tau_E = 4.8$ ms, one has $f_l \le 1$ MHz. This is much larger than the repetition rate of available lasers and is essentially not a limiting factor.

For purposes of calculation, let us assume that a 1-kW laser delivering 10 mJ-pulses will be feasible in the not-to-distant future, giving $f_l = 100$ kHz. Assuming suitable optics between the modulator and the radiator, the effective bunch current for those electrons that contribute to the short pulse is given by [3.6-9]

$$I_b\eta\sigma_l/\sigma_t, \tag{3.6-13}$$

where I_b is the total bunch current and $\eta \approx 0.15$ is the fraction of electrons within the laser pulse that obtain sufficient amplitude to be visible. These parameters (and assuming 200 mA in 24 bunches), yields an effective bunch current of about 1 μA. The flux is reduced by a factor 8×10^3 compared to the full bunch. This low flux may be problematic for many experiments. It could be increased by using a longer, higher-power laser pulse at the expense of a longer x-ray pulse. In addition, ongoing improvements in laser technology should allow an increase in the pulse energy and/or the repetition rate, making this one of the more promising avenues for producing short-pulse x-rays.

3.6.2.4 Non-integer Harmonic Cavities

An idea from G. Wüstefeld et al. [3.6-15] involves the use of multiple-frequency harmonic cavities to produce alternating long and short electron bunches. Their analysis shows the possibility of getting much shorter bunches in Berliner Elektronenspeicherring-Gesellschaft für Synchrotronstrahlung (BESSY) while still maintaining high average current due to the simultaneous presence of long, high-current bunches. This is accomplished by means of two additional rf systems, one at harmonic $h_1 = 3$ and another at $h_2 = h_1 + 0.5$ relative to the main rf system. At even buckets, the three rf systems add, giving an additional voltage slope of $h_1V_1 + h_2V_2$. At odd buckets, the two high-harmonic systems cancel, owing to the imposition of the relationship $h_1V_1 - h_2V_2 = 0$. At zero current, the reduction in bunch length is

$$\frac{\sigma}{\sigma_0} = \sqrt{\frac{V_0}{2h_1V_1}}. \tag{3.6-14}$$

Equivalently,

$$V_1 = \frac{V_0}{2h_1}\left(\frac{\sigma_0}{\sigma}\right)^2. \tag{3.6-15}$$

For BESSY, the main 500-MHz rf system provides 1.5 MV, so a 1.5 GHz ($h = 3$), 25 MV ERL-like cavity could be used, giving $\sigma = 0.1\sigma_0$.

To evaluate this, updated version of the simple impedance model for the APS was used. This includes a resistive term R_s and an inductive term Z/n. The bunch length as a function of current is well characterized by [3.6-16]

$$\sigma_t(ps) = 25.1I^{0.1484+0.0346\ln I}, \tag{3.6-16}$$

where I is the bunch current in mA. For given values of R_s and Z/n for the ring, the program `haissinski` [3.6-17] can be used to solve the Haissinski equation and thus compute the bunch duration vs bunch current. The impedance model parameters can be varied to optimize the agreement between the results from `haissinski` and the experimental fit given by Equation (3.6-16). This was done and results in an excellent fit, as shown in Figure 3.6-2, giving

- R_s = 2.91 kΩ
- Z/n = 0.28 Ω

As in [3.6-15], it is helpful to start by assuming that α is kept at the nominal value of $\alpha_0 = 2.8 \times 10^{-4}$. It is also assumed that $h_1 = 4$, giving a ∼1.4 GHz higher-harmonic system. Given that $\sigma_0 = 20$ ps (48 ps FWHM) for 9 MV on the main rf system, $V_1 = 648MV$ is required to obtain a zero-current bunch duration of 2 ps FWHM (which will match SPX).

This is clearly impractical, which indicates that this scheme is workable only for low-energy rings where the main rf system voltage is relatively low. In [3.6-15], the possibility of running with reduced α is also mentioned. In that case, the goal is to make even shorter bunches. For APS, it is possible to use lower α to reduce the rf voltage requirements. The relevant equations are

$$\frac{\sigma}{\sigma_0} = \sqrt{\frac{V_0\alpha_1}{2h_1V_1\alpha_0}}, \tag{3.6-17}$$

where $\alpha_0 = 2.8 \times 10^{-4}$ is the nominal value of α. If we take $\alpha_1 = \alpha_0/30$, V_1 is reduced by the same factor and becomes a more manageable 21.6 MV.

The next step is to use these values along with the impedance model described in the previous section to compute the bunch duration vs bunch current using `haissinski`. The results are shown in Figure 3.6-3. Unfortunately, the hoped-for reduction in bunch duration does not fully materialize, even for rather low bunch current, because of impedance effects. The conclusion is that this method is not only impractical due to the high voltages required, but it does not provide high-intensity short pulses.

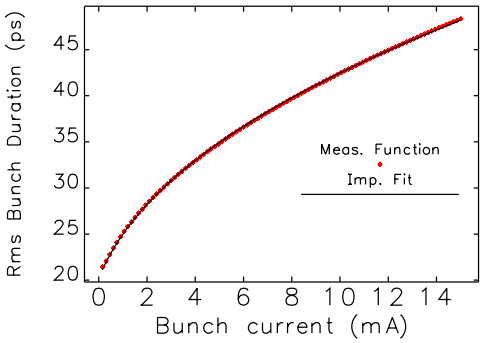

Figure 3.6-2: Results of fitting the impedance model to the experimental bunch length vs bunch current, which is itself described by a fitting function given in Equation (3.6-16).

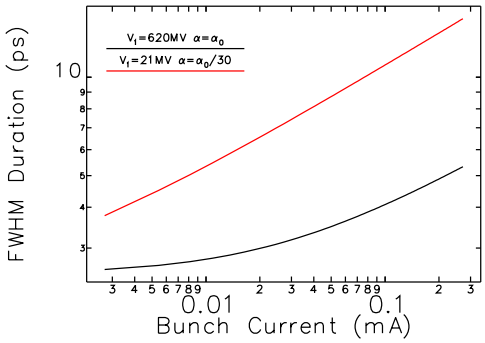

Figure 3.6-3: Predicted bunch duration vs bunch current for Wüstefeld's scheme as applied to APS. See text for details.

3.6.2.5 Deflecting Cavities

In light of the difficulties associated with these existing methods, a method based on the use of deflecting cavities [3.6-18] has been investigated. In this concept, illustrated in Figure 3.6-4, transverse deflecting rf cavities are used to impose a correlation ("chirp") between the longitudinal position of an electron within the bunch and its vertical momentum. The x-rays emitted by each electron tend to travel along the path of the electron itself. Hence, by placing an undulator just downstream of the deflecting cavity (for example), one can produce a chirped x-ray beam. At a sufficient distance (e.g., 30 m) from the undulator, this angular chirp will have evolved into a spatial chirp, so that a strong correlation appears in the x-ray pulse between arrival time and vertical coordinate. Use of vertical slits then permits filtering the pulse in the time dimension, allowing production of an x-ray pulse that is shorter than the electron pulse. This scheme is referred to as the SPX (short-pulse x-ray) scheme.

As shown in Figure 3.6-4, two cavities are required, with the purpose of the second cavity being to cancel the effects on the electron beam of the first cavity. This is necessary in order to avoid extremely large vertical emittance growth. The second cavity must be placed at a vertical betatron phase advance $N \times 180^\circ$ downstream of the first, where N is an integer. Because the APS lattice normally has $\nu_y = 19.2$, or $\Delta\nu_y = 0.48$ per cell, this is readily accomplished by having the cavities separated by N sectors and making slight adjustments to the electron beam optics. If $N > 1$, the time-angle chirp of the electron beam will reappear at all intervening straight sections. This allows for providing chirped pulses to a larger number of beamlines. However, N cannot be increased without limit, due to potential issues with storage ring operation [3.6-19].

The cavities must have a deflecting mode frequency that is a harmonic h of the ring rf frequency, 352

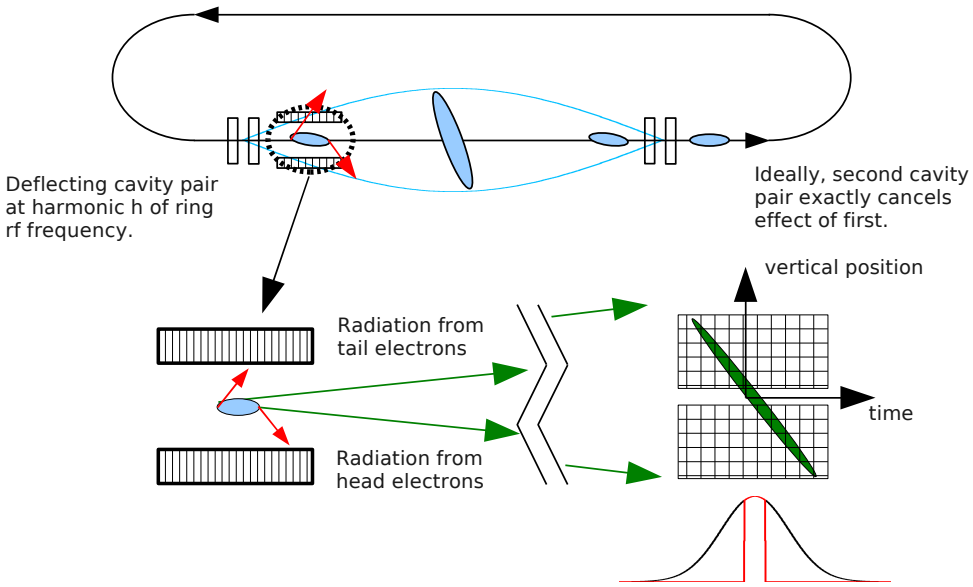

Figure 3.6-4: Illustration of Zholents' scheme for creating short x-ray pulses using deflecting cavities.

MHz. One can characterize the deflecting strength using an effective transverse sinusoidal voltage of amplitude V_t, which can impart a maximum slope change of V_t/E, where E is the electron beam energy. As shown below, $h = 8$ appears to be a workable choice. This corresponds to a deflecting cavity frequency of about 2.8 GHz. This high frequency has implications for the time structure of the x-ray pulses.

As indicated, once the photon beam has drifted a sufficient distance, the pulse can be shortened simply by using vertical slits. This will, of course, discard considerable intensity. Another option [3.6-18] is to use asymmetric-cut crystals to perform pulse compression. Such crystals allow imposing a time-of-flight variation that is proportional to vertical position. In either case, the minimum achievable x-ray pulse duration can be estimated as [3.6-20]

$$\sigma_t \approx \frac{E}{\left(\frac{\partial}{\partial t} V_t \sin \omega_t t\right)_{t=0}} \sqrt{\frac{\beta_{\mathrm{ID}}}{\beta_{\mathrm{rf}}}} \sqrt{\frac{\epsilon_y}{\beta_{\mathrm{ID}}} + \sigma_{y',\mathrm{Rad}}^2} \quad , \tag{3.6-18}$$

where β_{ID} and β_{rf} are the vertical beta functions at the ID and deflecting cavities, respectively; ϵ_y is the vertical slice emittance (i.e., the emittance outside the chirp region); ω_t is the angular frequency of the deflecting mode; and $\sigma_{y',\mathrm{Rad}}$ is the intrinsic vertical divergence of the photons. This is given roughly by [3.6-21]

$$\sigma_{y',\mathrm{Rad}} \approx \sqrt{\frac{\lambda_r}{2L_u}}, \tag{3.6-19}$$

where λ_r is the radiation wavelength and L_u is the length of the undulator. Using 2-MV deflecting voltage with $h = 8$, $\beta_{\mathrm{ID}} = \beta_{\mathrm{rf}} = 3$ m, 10-keV x-rays from a 2.4-m-long device, and $\epsilon_y = 35$ pm, we get $\sigma_t \approx 1.2$ ps. As seen below, this is achievable with 1% transmission through the vertical slits.

Because the cavities are operated continuously, in principle every bunch in the ring is chirped identically and hence produces a short x-ray pulse. The most common operating mode yields a 6.5-MHz bunch rate. Because of the relatively large flux (1% of nominal) and high repetition rate, this

scheme outperforms the others that have been considered and has been chosen as the preferred method for meeting the mission requirement of shorter x-ray pulses.

As mentioned above, an option for the deflecting cavity approach is to use asymmetric-cut crystals to perform x-ray pulse compression [3.6-18]. This does not make the x-ray pulse shorter, but rather permits opening the slits to allow a greater fraction of the x-ray pulse through. This should permit increasing the flux by a significant amount, but the x-ray optics has challenges that would need to be addressed and which are outside the scope of the APS Upgrade. It provides a possible path forward to allow an order-of-magnitude increase in photons per pulse.

3.6.2.6 Alternative Deflecting Cavity Scheme

In the scheme proposed here and illustrated in Figure 3.6-4, the insertion device (ID) is located at a vertical phase advance of $n180^\circ$ from the cavities, where $n \geq 0$ is an integer. As a result, the ultimate x-ray pulse length that is achievable in this scheme is limited by the vertical electron beam divergence and the intrinsic opening angle of the radiation, as well as the deflecting voltage slope.

Another configuration [3.6-22] is possible that makes use of a spatial electron beam chirp. This can be implemented by having a four-cavity bump in a very long straight section, or by placing an undulator at a phase advance of $(2n+1)90^\circ$ from the cavities (where $n \geq 0$). In this case, the relevant comparison is of the size of the chirp to the vertical electron beam size and the intrinsic size of the radiation source. In ID straight sections, the former tends to be small because of the small vertical beta function needed to accommodate the vacuum chamber. The later is given by $\frac{1}{4\pi}\sqrt{2\lambda_r L_u}$. For 1-Å radiation, this is about 10% of the typical vertical beam size at an ID in the APS.

Together, these seem to promise shorter x-ray pulses with less chirp, albeit with lower intensity (since one is still performing slicing). One option for utilization of this scheme requires a long straight section that can accommodate four cavities plus the insertion device. This would have the advantage of eliminating some of the beam dynamics issues described in section 3.6.3.2. If this scheme were implemented in the APS with a nominal 7.7-m-long straight section, it might be possible to fit 6 cavities on either side of a 2.4-m-long ID. The minimum FWHM pulse duration would then be about 3.5 ps with 2% transmission through the slits. As will be seen, shorter pulses are expected with similar transmission using the original scheme. In addition, for approximately the same cost, the original scheme allows providing chirped pulses to several ID and bending magnet beamlines.

Alternatively, one could modify the optics to achieve 90-degree vertical phase advance between three successive straight sections. However, this requires large vertical beta functions in the middle straight section and is not workable.

3.6.2.7 Conclusion

The major methods of achieving short x-ray pulses in a storage ring have been briefly reviewed. The deflecting-cavity-based method has several advantages over the others discussed. The use of a higher-harmonic accelerating cavity compares very poorly as it cannot reach the few-ps scale. The low-α method suffers from low average beam current, which confines it to use as a special, limited operating mode. The laser slicing method suffers from a relatively low repetition rate and at least

10-fold smaller intensity, although it should improve as laser technology improves. Hence laser slicing is the strongest alternative after the chosen approach of using deflecting cavities.

Subsequent sections go into detail about several aspects of this challenging project. First is a discussion of single-particle dynamics, including controlling the impact of the cavities, determination of tolerances, and detailed predictions of performance. Collective effects of the cavities are examined next, which establishes requirements for damping of cavity modes. Following this are discussions of cavity design, cryogenics, low-level rf, and high-level rf. Next, controls are discussed, as are timing, machine protection, and, finally, diagnostics.

As shown below, creation of the deflecting-cavity-based system is challenging. Success will not only create a new capability for APS users and address a key part of the APS Upgrade science mission, it will also show the way forward for other storage ring light sources that seek to create intense, tunable, picosecond x-ray pulses.

3.6.3 Short Pulse X-Ray System

As just demonstrated, the production of short pulse x-rays using deflecting cavities provides ps-level pulses with high repetition rate and a significant fraction of the normal flux. This led to selection of this method for the APS Upgrade. Although it offers high performance, the deflecting-cavity-based Short Pulse X-ray system (hereafter referred to as “SPX”) is challenging in a number of respects. The technical requirements are summarized in section 3.6.3.1.

Damping of cavity modes to ensure beam stability is a particular challenge (section 3.6.3.3), as are tolerances (section 3.6.3.2.3). Plans to meet the cavity impedance budget are discussed in sections 3.6.3.8.2 and 3.6.3.9, which describe the cavity and damper systems. The design goal for the damping system is stability at 200 mA, which provides a safety margin for the 150 mA operation required by the APS Upgrade. The differential phase error tolerance will present many challenges to the low-level rf and timing-synchronization systems. While the common-mode phase tolerance is much more relaxed, storage ring (SR) synchronous phase changes simply due to insertion device (ID) gap changes and due to main SR rf noise [3.6-23, 3.6-24] must be accounted for.

A conceptual system-level design using a beam-based feedback control strategy was developed to address these challenges at a July 2010 SPX Study Meeting by participants from ANL, LBNL, Fermilab, and SLAC [3.6-25], as shown in Figure 3.6-5. In the proposed scheme, beam position monitors outside the SPX zone (section 3.6.3.10) measure orbit distortions caused by differential phase errors between the SPX cavity sectors and feedback to the phase of the second SPX cavity sector via the real-time feedback system (RTFB) (section 3.3). Residual tilt monitors outside the SPX zone can measure tilt caused by differential amplitude errors and correct the amplitude of the second SPX cavity sector. A beam arrival time monitor can be used to measure and feedback to the phase of the main SR rf to correct for common-mode phase errors introduced by main SR rf noise and synchronous phase changes. Beam position monitors within the SPX zone can be used to refine the common-mode phase errors of the SPX system by feeding back on the first SPX cavity sector. Finally, a tilt monitor within the SPX zone can be used to measure and correct for SPX common-mode amplitude errors. Schematics of the SPX 4-cavity string assembly and cryomodule are shown in Figure 3.6-5.

By using beam-based feedback, the inevitable $1/f$ phase noise and long-term drift of the rf system, which ultimately leads to orbit distortions, can be compensated by the RTFB system, at least within its closed loop bandwidth, which is expected to be upgraded from 60 Hz to 200 Hz (section 3.3.8). If

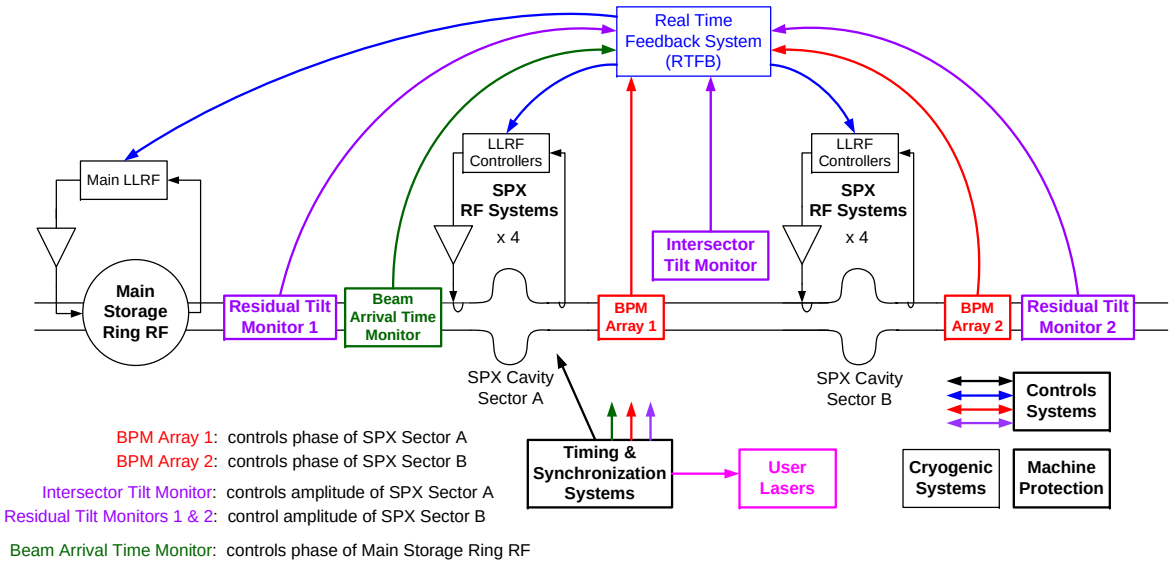

Figure 3.6-5: System block diagram.

the RTFB system is responsible for correcting SPX system amplitude and phase noise in the frequency range of <200 Hz and the low-level rf (LLRF) control system is responsible for regulating noise in the range >10 Hz, an overlap between the two systems in principle [3.6-26] can ensure complete spectral coverage for beam-orbit stability.

A signal synchronized to the first SPX sector cavities, which is indicative of the time of short-pulse x-ray production, will be provided to the user lasers via the timing and synchronization system, which also provides all timing fiducials to the rf and beam diagnostics systems (section 3.6.3.6). Remote control, monitoring, and integration of all SPX subsystems, including within the existing APS storage ring complex, will be provided by the controls systems (section 3.6.3.7). Details of the individual SPX subsystems, including cavity and cryomodule design, cryogenics, low-level rf, high-level rf, machine protection, and diagnostics are given in subsequent sections.

3.6.3.1 Physics Requirements and Issues

A set of physics requirements has been written based on extensive and complex simulations to ensure that the correct deflection is applied to the beam for Sector 6 and 7 users, that no other users will be affected to an unacceptable degree, and that the beam will be, in general, stable during operation of the rf cavities and also during non-operation of the cavities. Many of the simulations will be explained later in this document; here the summary of the requirements will be given. The Project consists of several parts:

- RF system
- Lattice modifications related to the long straight sections (LSSs) needed in Sectors 5 and 7
- Diagnostics
- Undulators and beamlines

3.6.3.1.1 Goals

The goal of the Project is to deliver 1% of the nominal x-ray intensity in a short x-ray pulse, the central 70% of which has a duration of 2 ps, with the long-term goals of achieving 1-ps-long pulses using deflecting cavity approach. This nominal performance assumes a 10-keV photon energy and an undulator with an approximate length of 2.4 m. The cavities will operate only in 24-singlets mode. The cavities should not prevent operation of the storage ring in other bunch patterns. Detailed goals are presented in Table 3.6-1.

Table 3.6-1: Main goals of the SPX project.

Specification name	Goal
Pulse duration (central 70% of the beam)	2 ps
Pulse duration fluctuation	10%
Pulse intensity fluctuation	10%
Pulse timing jitter (fraction of pulse duration)	10%
Maximum vertical emittance outside SPX	40 pm
Vertical emittance variation outside SPX	10%
Rms beam motion outside SPX (as fraction of beam size and divergence)	10%

3.6.3.1.2 Layout

The first deflecting cavity cryomodule will be located in the downstream end of the 5-ID straight section. The second cryomodule will be located in the downstream end of the 7-ID straight section. Both 5-ID and 7-ID straight sections will be long straight sections. The LSS configuration increases the useful length of the straight section from 4.8 m to about 7.7 m. The 6-ID straight section will be unchanged.

3.6.3.1.3 Main Storage Ring and Rf System Parameters

Main storage ring parameters that were assumed during SPX related simulations are given in Table 3.6-2.

Table 3.6-2: Main storage ring and rf system parameters.

Specification name	Value
Current	150 mA
Energy	7 GeV
Revolution frequency	271.55 kHz
Rf frequency	351.93574 MHz
Source tunability	$\pm$ 1 kHz

3.6.3.1.4 Deflecting Rf System

The main parameters of the deflecting cavity system are given in Table 3.6-3.

Table 3.6-3: Main parameters of the deflecting rf system.

Specification name	Value
Rf voltage (stage 1)	2 MV
Number of cavities in a cryomodule (stage 1)	4
Rf voltage (stage 2)	4 MV
Number of cavities in a cryomodule (stage 2)	8
Rf frequency	2815.486 MHz
Cavity tunability	±200 kHz[a]
Source tunability	±1.5 kHz[b]
Operating temperature	2 K

[a] To cover more than one SR revolution harmonic.
[b] SR circumference is not expected to change significantly in the future.

The rf phase and amplitude have to be controlled to sufficient precision to prevent trajectory leakage to the outside of the cavity, bump which could lead to emittance growth and beam motion. The tolerances for the deflecting cavity system are given in Table 3.6-4. The choice of the lower band boundary of 0.01 Hz is dictated by the Beam Stability Physics Requirement Document (PRD) [3.6-27]. The upper band boundary corresponds to the revolution frequency. Separation between beam motion and effective beam size increase is set at 1 kHz [3.6-28].

Differential mode phase variation leads to orbit motion outside of the SPX insertion. BPM-based feedback will be used to compensate the effect of this variation in the band where the orbit correction is effective. The beam motion due to differential phase error with orbit correction running should not exceed the numbers given in Table 3.6-9. In case of orbit correction not running, this beam motion is achieved at phase error values given in Table 3.6-4 (given as an example only). The requirement on the differential mode phase variation with orbit correction running, which will include orbit-based feedback on the phases themselves, will be determined later as a part of the ongoing orbit correction upgrade studies.

EPICS controls will be required that allow common-mode and differential-mode variation of the phase and amplitude of the cavities, as detailed in the Table 3.6-5. In addition to running cavities at the zero crossing (i.e., so that the beam centroid is not kicked), it is also necessary to operate them on crest (i.e., so that the beam centroid is kicked). The on-crest operation is intended for testing the voltage regulation. To support automated control of the rf parameters, a 10-Hz EPICS write capability is required.

Higher- and lower-order modes must be damped to ensure multi-bunch beam stability. Requirements, listed in Table 3.6-6, are calculated taking the bunch form factor into account and assuming synchrotron radiation damping rate only (details of calculations are described in section 3.6.3.3).

Table 3.6-4: Tolerances for SPX deflecting rf system.

Specification name	Rms value	Bandwidth	Driving requirement
Common mode amplitude variation	< 7 %	0.01 Hz – 271 kHz	Keep intensity and pulse length variation under 10% rms
Common mode phase variation	< 10 deg	0.01 Hz – 271 kHz	Keep intensity variation under 10% rms
Differential mode amplitude variation between sectors	< 1.0 %	0.01 Hz – 1 kHz	Keep rms emittance variation outside of SPX under 10% of nominal 35 pm
	< 0.77 %	1 kHz – 271 kHz	Limits effective emittance growth to below 1.5 pm
Differential mode phase variation between sectors	< 0.038 deg[a]	0.01 Hz – 200 Hz	Keep rms beam motion outside of SPX under beam stability requirements
	< 0.078 deg[a]	0.01 Hz – 1 kHz	Same as above
	< 0.28 deg	1 kHz - 271 kHz	Limits effective emittance growth to below 1.5 pm

[a] Given only as an example of what the requirement would be if no orbit correction was running.

3.6.3.1.5 Alignment

Cavity alignment relative to the beam is important both for protecting cavities and for minimizing vertical emittance degradation. A large transverse orbit inside the cavity will generate an excessive amount of rf power while large cavity roll will affect the vertical emittance of the beam. Also, vertical-offset-dependent beam loading perturbations caused by beam arrival jitter can lead to cavity phase noise. Table 3.6-7 lists alignment requirements, based on section 3.6.3.5, section 3.3, and [3.6-29, 3.6-30]. The distance between cavities inside the cryomodule is 0.53 m. Transverse cavity movers might be utilized to allow for beam-based cavity alignment. The requirements on the movers are not set yet.

3.6.3.1.6 Undulators and Beamlines

The trajectory of the beam in the deflecting cavities should pass close to the transverse cavity centers. Once the beam is parked at the center of the cavities, the adjacent ID should not move the orbit significantly. To guarantee that, a corrector and a BPM should be installed between the ID and the cryostat. The ID itself should satisfy the requirements given in the Planar Undulator PRD [3.6-31].

Preliminary analysis shows that increased vertical beam size inside the small-gap ID vacuum chamber does not affect the injection efficiency or lifetime, and therefore modification of the ID vacuum chamber is not necessary.

Table 3.6-5: Phase and voltage control requirements for SPX.

Specification name	Value	Driving requirements
Common mode controls:		
Adjustment range:		
Common mode phase	$>$ 400 deg	To perform scan over one wavelength
Adjustment rate:		
Common mode amplitude	Full range in $<$ 10 s	To apply changes in reasonable time
Common mode phase	Full range in $<$ 10 s	To apply changes in reasonable time
Sector-to-sector controls:		
Amplitude error adjustment range	$>$ 10 %	To compensate for lattice imperfections in full-scale SPX
Amplitude error adjustment step	$<$ 0.1 %	1/10 of requirement from Table 3.6-4
Amplitude error adjustment rate	Full range in $<$ 10 s	To apply changes in reasonable time
Phase error adjustment range	$>$ 5 deg, plus 180 flip	To compensate for lattice imperfections in full-scale SPX
Phase error adjustment step	$<$ 0.005 deg	To be able to demonstrate diff. phase stability requirement
Phase error adjustment rate	Full range in $<$ 10 s	To apply changes in reasonable time
Intra-sector group-to-group:		
Amplitude error adjustment range	$>$ 10 %	To compensate for beta function errors and move effective center of cavity assembly
Amplitude error adjustment step	$<$ 0.1 %	
Amplitude error adjustment rate	Full range in $<$ 10 s	
Phase error adjustment range	$>$ 5 deg	To fine-tune adjustment for beam time-of-flight
Phase error adjustment step	$<$ 0.005 deg	
Phase error adjustment rate	Full range in $<$ 10 s	

3.6.3.1.7 Synchronization of User Laser to the Deflecting Rf

To conduct timing experiments, users will need a synchronization signal for their laser that is tied to the arrival time of the short x-ray pulse. Over the duration of the experiment, the rms deviation between this signal and the photon pulse arrival time should be sufficiently small that the effective pulse duration is not increased significantly. There are also other sources of real or effective pulse length variation,

Table 3.6-6: HOM-LOM requirements for SPX.

Shunt impedance	Limit
Longitudinal	
$(R_s f_{HOM})$ for one monopole HOM/LOM	0.44 MΩ-GHz
R_s for one monopole HOM/LOM at 2 GHz	0.22 MΩ
Transverse	
R_t for one x-plane HOM/LOM	1.3 MΩ/m
R_t for one y-plane HOM/LOM	3.9 MΩ/m

Table 3.6-7: Alignment requirements for SPX cavities (full range).

	Cryomodule alignment	Cavity inside cryomodule
ΔX	±500 μm	±500 μm
ΔY	±200 μm	±200 μm
ΔZ	±1000 μm	±1000 μm
Yaw	±10 mrad	±10 mrad
Pitch	±10 mrad	±10 mrad
Roll	±10 mrad	±10 mrad

e.g., deflecting voltage variation and electron beam vertical orbit angle variation. To keep the total pulse length variation within the required 10%, the synchronization signal jitter should be kept below 270 fs rms over the band of 0.01–1000 Hz. The bandwidth is defined by the typical length of the experiment.

3.6.3.1.8 Effect on/of the Beam

The beam emittance should not be degraded significantly as a result of operating the deflecting mode cavities. Based on an unperturbed emittance, the maximum beam emittance allowed for the beam is listed in Table 3.6-8.

Table 3.6-8: Maximum allowable beam emittances.

Quantity	Unperturbed value	Limit with cavities on
ϵ_x	2.7 nm-rad	2.9 pm-rad
ϵ_y	35 pm-rad	40 pm-rad

Differential mode phase variation leads to vertical orbit motion outside of the SPX insertion. With this orbit motion included, the beam stability goals given in the Beam Stability Physics Requirements Document [3.6-27] still have to be met. Taking into account the suggested allocation of the beam motion budget (see section 3.3), the beam motion caused by the deflecting cavities outside of the SPX insertion should not exceed the numbers given in Table 3.6-9. Requirements on the horizontal motion are not given because it is expected that SPX will not be a source of the horizontal orbit motion.

Table 3.6-9: Maximum allowable vertical beam motion due to deflecting cavities.

Specification name	Bandwidth	Rms value
Vertical position	0.01 Hz – 200 Hz	0.28 μm
	0.01 Hz – 1 kHz	0.57 μm
Vertical angle	0.01 Hz – 200 Hz	0.15 μrad
	0.01 Hz – 1 kHz	0.31 μrad

In addition to the general user orbit stability requirements defined in the Beam Stability PRD, SPX imposes additional requirements: orbit errors must be kept small in the deflecting cavities and in the undulators between the cavities. A large enough vertical orbit in the cavities will generate an unwanted main-mode voltage in the cavities. An orbit angle change in undulators will result in a pulse arrival time change for the experiment. The requirements for orbit stability in the cavities are given in Table 3.6-10. The requirements for orbit stability in the undulator locations are give in Table 3.6-11.

Table 3.6-10: Orbit stability requirements at the cavity locations.

Orbit with cavities on-resonance	$\pm$100 μm
Orbit with cavities off-resonance	$\pm$1000 μm

Table 3.6-11: Beam stability requirements at the SPX ID source [3.6-27].

Quantity	Driving requirement	Rms beam motion	Bandwidth
ΔX	Beam stability	6 μm	0.01 Hz – 1 kHz
ΔY	Timing jitter	4 μm	0.01 Hz – 1 kHz
ΔY'	Timing jitter	1.2 μrad	0.01 Hz – 1 kHz

3.6.3.1.9 Diagnostics

Diagnostics need to:

- ensure that the beam is at the center of the cavities and keep the beam there within $\pm$100 μm;
- characterize the chirp inside and outside the cavity system. Outside the cavity system the permissible beam size increase is $\pm 5\%$;
- ensure the beam outside of the cavities is not disturbed (orbit, beam size, and tilt).

The requirements to BPMs in the deflecting cavity straight sections are given in Table 3.6-12.

Several tilt monitors will be used—one or two inside the SPX zone and one or two outside. Also, a vertical beam size monitor will be used to control the beam size outside the SPX zone. The derivation

Table 3.6-12: Requirements for BPMs in the deflecting cavity straight sections [3.6-32].

	Driving requirement	Resolution (peak-to-peak)	Bandwidth
X	Main-mode power limit	10 μm	1 kHz
Y	Main-mode power limit	10 μm	1 kHz

of the tilt monitor requirements is given in [3.6-32]. The calculation in [3.6-32] used a deflecting voltage of 4 MV, so the numbers shown in Tables 3.6-13 and 3.6-14 were scaled down.

A vertical beam size monitor will be used to control the beam size variations outside of the SPX zone. The requirements are given in the Table 3.6-15.

Table 3.6-13: Requirements for tilt monitors outside the SPX zone [3.6-32].

	Location	Driving requirement	Resolution	Bandwidth
Y	ID	5% beam size increase	0.1 mrad rms	$\leq$ 200 Hz

Table 3.6-14: Requirements for tilt monitors inside the SPX zone [3.6-32].

	Location	Maximum beam tilt/chirp	Resolution	Bandwidth
Y'	ID	0.29 mrad	40 μrad rms	0.1-200 Hz
Y	BM	0.17 rad tilt (dy/dz)	20 mrad rms	0.1-200 Hz

Table 3.6-15: Requirements for the vertical beam size monitor outside the SPX zone [3.6-32].

	Location	Driving requirement	Resolution	Bandwidth
X	ID	5% beam size increase	12 μm rms	0.1-1.0 Hz
Y	ID	5% beam size increase	4 μm rms	0.1-1.0 Hz

3.6.3.1.10 Machine Protection System

As mentioned in the Section 3.6.3.1.8, an electron beam going off-center in the deflecting cavities can deposit rf power in the cavities. At high enough power the cavities and rf source can be damaged. To protect against this, the beam missteering inside the cavities shall be limited to $\pm$500 μm.

During SPX operation, vertical beam size between the deflecting cavities will always be increased. This will change the requirements for the vacuum chamber protection against heating from synchrotron radiation. Careful ray tracing will be required during the final design stage to design the protection system.

In case of a large phase mismatch between deflecting cavities, the vertical beam size can be increased everywhere around the machine. Protection against this event also needs to be considered and designed.

3.6.3.2 Single-Particle Dynamics

Soon after starting simulation of the application of the deflecting cavities at the APS, it was found that the cavities make a large impact on the single-particle beam dynamics in many ways. A lot of effort was devoted to studying the effects and mitigating their consequences. These effects and the ways to control them are described here.

There are many ways in which the deflecting cavities can affect the beam and diminish the operational parameters. As mentioned before, the second cavity is introduced to cancel the chirp produced by the first cavity such that the users outside of the two-cavity system ideally would not see any change in the electron beam parameters. However, many things affect perfect cancellation. Errors, inevitably present in the real machine, can lead to emittance increase and orbit change. But even in the perfect machine, there are many effects that could break the cancellation conditions or affect the beam in other ways.

3.6.3.2.1 Emittance Degradation

There are several effects that result in emittance degradation in the perfect machine. They are described in detail in ref. [3.6-33]; here those effects will be briefly named.

The APS storage ring has 0.1% rms energy spread in the beam. Due to nonzero momentum compaction between the cavities, the energy spread in the beam leads to time-of-flight differences for different particles. The particles arrive at different rf phases and experience only partial kick cancellation. For a particle arriving with a small time delay of Δt, the additional kick after the second cavity would be approximately

$$\Delta y' = -\frac{eV_t\omega\Delta t}{E}, \tag{3.6-20}$$

which leads to emittance increase in a single turn of

$$\frac{\Delta\varepsilon_y}{\varepsilon_y} = \frac{\sqrt{\sigma_{y'}^2 + \frac{V_t\omega_t\sigma_t}{E}}}{\sigma_{y'}} - 1. \tag{3.6-21}$$

Here V_t and ω_t are transverse (or deflecting) voltage amplitude and angular frequency, respectively; E is the beam energy; and $\sigma_{y'}$ and σ_t are the beam divergence and bunch length respectively. Estimations show that this effect is small.

Due to nonzero chromaticity between cavities, the energy spread in the beam leads to different betatron phase advances between the cavities. The closed-bump condition is satisfied only for on-momentum particles. However, if the particle i has an energy deviation of δ_i and the chromaticity between the cavities is ξ_y, then the phase advance of that particle is changed by $2\pi\xi_y\delta_i$. This leads to a particle position change at the second cavity

$$y_2 = \sqrt{\beta_1\beta_2}\; y_1' \sin(2\pi\xi_y\delta_i), \tag{3.6-22}$$

where β_1 and β_2 are vertical beta functions at cavity locations. The rms value of the residual amplitude is

$$\sigma_{y_2} = 2\pi\xi_y\sqrt{\beta_1\beta_2}\;\frac{\omega_t V_t}{E}\sigma_\delta\sigma_t. \tag{3.6-23}$$

Estimations show that in our case for uncorrected chromaticity between cavities the emittance almost doubles. This means that one actually cannot operate without chromaticity correction between the cavities.

To correct the chromaticity between cavities, one needs to install sextupoles. But the sextupoles bring nonlinear fields, betatron phase advance dependence on the kick amplitude, and nonlinear coupling between the horizontal and vertical planes. All these effects together lead to vertical emittance degradation, which then increases the minimal achievable bunch length according to Equation (3.6-18). Figure 3.6-6 shows the vertical emittance increase from 25 pm·rad to 600 pm·rad in just a few turns in the presence of nominal APS sextupoles. This would appear to be a show-stopper, but, as will be shown, a solution is available.

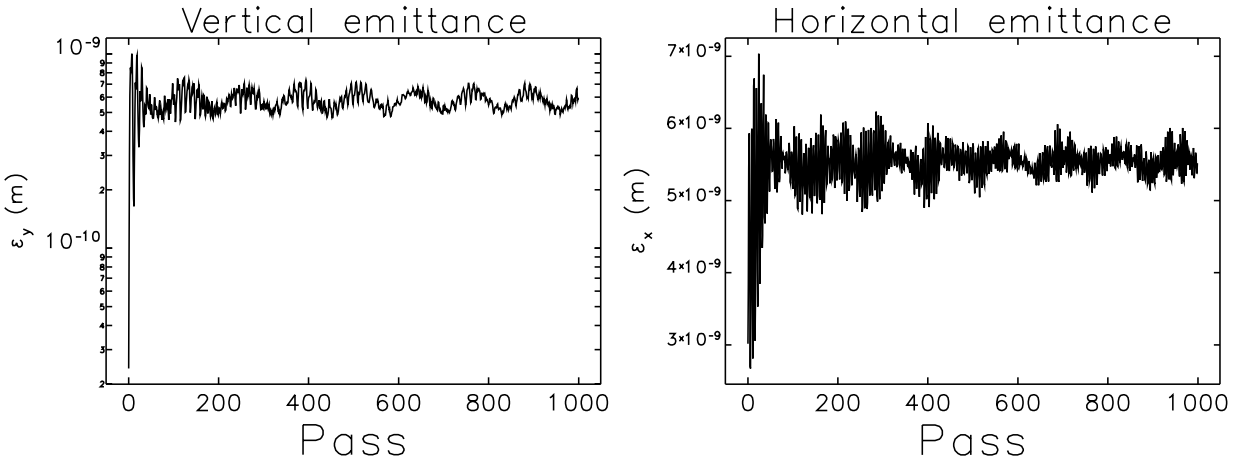

Figure 3.6-6: Emittance blowup with nominal (not optimized) sextupoles. Left plot is vertical emittance, and right plot is horizontal emittance.

3.6.3.2.2 Control of Operational Impact

According to Equation (3.6-18), the minimum achievable pulse length is inversely proportional to the derivative of the deflecting voltage:

$$\left(\frac{\partial V_t \sin \omega_t t}{\partial t}\right)_{t=0} = 2\pi h f_{\mathrm{rf}} V_t, \tag{3.6-24}$$

where f_{rf} is the storage ring rf frequency, and h is the harmonic of the deflecting voltage frequency. The choice of h is dictated by the available rf sources, as will be shown later. The maximum possible deflecting voltage amplitude is defined by the requirement of keeping the beam size smaller than the vacuum chamber. For a 7.5-mm vacuum chamber this gives the following limits: 3.8 MV when the first cavity is placed in the upstream part of the ID straight section and 6.5 MV when the first cavity is located in the downstream end.

High deflecting voltage also leads to vertical emittance increase, and vertical emittance degradation not only undermines the minimal achievable pulse length, it also violates the important requirement of not disturbing the beam for other users that are located outside of the cavity bump. That is why containing the emittance blowup is so important.

In order to understand the processes behind the emittance increase, the effect of an orbit bump produced by a corrector magnet was studied. When an electron is displaced in the sextupole in the

vertical direction, it experiences a kick in the vertical plane,

$$\Delta y' = b_s(y_0 + y)x, \tag{3.6-25}$$

where b_s is the sextupole strength, y_0 is the orbit displacement, and x and y are betatron coordinates. Following ref. [3.6-34] and assuming $y_0 \gg y$, one can obtain the perturbation to the vertical emittance caused by this kick:

$$\Delta\varepsilon_y \approx 2b_s y_0 \sqrt{\varepsilon_x\varepsilon_y\beta_x\beta_y}\sin\phi_x\cos\phi_y = b_s y_0\sqrt{\varepsilon_x\varepsilon_y\beta_x\beta_y}\sin(\phi_x - \phi_y). \tag{3.6-26}$$

One can also calculate an emittance increase due to such a kick in the case of many sextupoles and also including betatron tune dependence on the particle energy through chromaticity:

$$\Delta\varepsilon_y = \sqrt{\varepsilon_x\varepsilon_y}\; e^{-\frac{\theta^2}{2\tau_y^2}} e^{-\sigma_E^2\frac{(C_x-C_y)^2}{Q_s^2}\sin^2\frac{Qs\theta}{2}} \Im\left[\sum_j b_{sj}y_{0j}\sqrt{\beta_{xj}\beta_{yj}}e^{i\Delta\chi_j}\right]\sin(\Delta Q\;\theta + \psi), \tag{3.6-27}$$

where θ is the longitudinal coordinate, τ_y is decoherence time due to tune shift with amplitude, $C_{x,y}$ is chromaticity, Q_s is synchrotron tune, ΔQ is betatron tune difference, $\Delta\chi$ is betatron phase difference, and ψ is the initial phase of the emittance oscillation. Note that the expression inside the bracket is proportional to a coupling coefficient for a linear coupling resonance with $b_{sj}\; y_{0j}$ playing the role of a normalized skew quadrupole gradient. Thus one arrives at the well-known result that vertical orbit distortion in a storage ring with sextupoles produces coupling. The difference between Equation (3.6-27) and an established result is that Equation (3.6-27) also describes transient oscillations found through simulations [3.6-33].

To compare the above expression with simulations, we can rewrite it in a simpler way:

$$\varepsilon_y(\theta) = \varepsilon_{\text{final}} - (\varepsilon_{\text{final}} - \varepsilon_{\text{initial}})\;\; e^{-\frac{\theta^2}{2\tau_y^2}}\;\; e^{-\sigma_E^2\frac{(C_x-C_y)^2}{Q_s^2}\sin^2\frac{Qs\theta}{2}}\sin(\Delta Q\;\theta), \tag{3.6-28}$$

where $\varepsilon_{\text{initial}}$ is the emittance before the kick equation and $\varepsilon_{\text{final}}$ is the final emittance after the emittance oscillations are damped. Thus Equation (3.6-28) describes the oscillation of the vertical emittance after a sudden coupling change. Figure 3.6-7 compares emittance oscillations found in tracking with Equation (3.6-28) for two different chromaticity settings. The red line shows `elegant` tracking simulations, while the black line shows the fit using Equation (3.6-28) with two fitting parameters, $\varepsilon_{\text{final}}$ and τ_y.

Similar calculations can be done for the horizontal plane. When an electron is displaced vertically in a sextupole, it experiences a kick in the horizontal plane:

$$\Delta x' = \frac{b_s}{2}\;(y_0 + y)^2 \approx b_s\; y\; y_0 + \frac{b_s}{2}\;y_0^2. \tag{3.6-29}$$

This kick creates a perturbation to the horizontal emittance

$$\Delta\varepsilon_x \approx -b_s y_0\sqrt{\varepsilon_x\varepsilon_y\beta_x\beta_y}\sin(\phi_x - \phi_y) + b_s y_0^2\sqrt{\varepsilon_x\beta_x}\sin\phi_x. \tag{3.6-30}$$

Here the first term is the same as in Equation (3.6-26), but has the opposite sign. This confirms that the vertical emittance increases at the expense of the horizontal emittance as expected in the case of coupled motion. Since in the case $y_0 \gg \sqrt{\varepsilon_y\beta_y}$, the second term in Equation (3.6-30) dominates.

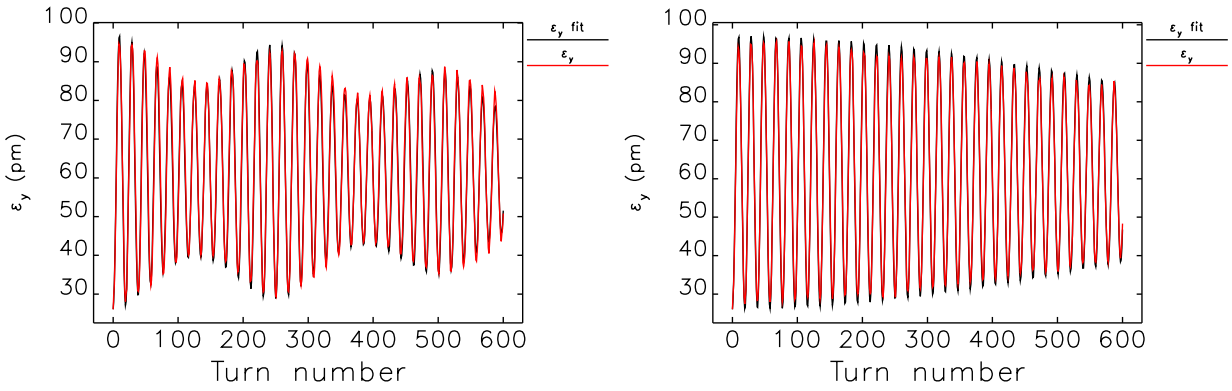

Figure 3.6-7: Comparison of the tracking results (red line) and a fit using Equation (3.6-28) (black curve) due to vertical orbit bump produced by corrector magnets. The left plot is for $C_x = 6$, $C_y = 4$, while the right plot is for $C_x = 6$, $C_y = 6$.

Keeping just the second term and performing calculations for many sextupoles, one can get the following expression for the horizontal emittance oscillations:

$$\Delta\varepsilon_x = \sqrt{\varepsilon_x}\; e^{-\frac{\theta^2}{2\tau_y^2}} e^{-\sigma_E^2 \frac{C_x^2}{Q_s^2}\sin^2\frac{Q_s\theta}{2}} \Im\left[\sum_j b_{sj} y_{0j}^2 \sqrt{\beta_{xj}} e^{i\Delta\chi_{xj}}\right] \sin(Q_x\;\theta + \psi_x). \tag{3.6-31}$$

Long enough after a sudden vertical orbit bump, the emittance oscillations will decay and leave just the lattice with a local vertical orbit bump. Equilibrium vertical emittance will be defined by the coupling on the new orbit, and the horizontal emittance will be unchanged (if the orbit bump is reasonably small). What is the source of the horizontal emittance oscillations in the beginning? To understand that, remember that the vertical orbit bump generates a small kick in the horizontal plane that changes the horizontal closed orbit. But the tracking is done on zero orbit; therefore turning the vertical correctors on is equivalent to a sudden kick in the horizontal plane, which leads to betatron oscillations and emittance growth due to oscillation decoherence. This means that the horizontal emittance will recover due to synchrotron radiation damping in the case of the vertical bump created by correctors.

The difference between the dipole and the deflecting cavity is that, in the case of a deflecting cavity, the kick strength depends on the longitudinal position of the particle in the beam. The beam can be split in many slices in the longitudinal direction, and every slice will see the constant kick as in the case of the dipole (for a few tens of turns until the synchrotron phase is not changed significantly). The slice-to-slice variation of the kick amplitude changes the way the emittance oscillations decay, as can be seen in Figure 3.6-8. Here again the red line shows tracking simulations and the black line shows the fit using the modified expression

$$\varepsilon_y(\theta) = \varepsilon_{\text{final}} - (\varepsilon_{\text{final}} - \varepsilon_{\text{initial}})\;\; e^{-\frac{\theta^2}{2\tau_y^2}} \;\; e^{-\sigma_E^2 \frac{(C_x - C_y)^2}{Q_s^2}\sin^2\frac{Q_s\theta}{2}} e^{-\sin^2\frac{Q_s\theta}{2}} \sin(\Delta Q\;\theta), \tag{3.6-32}$$

where the third exponent was added to account for the amplitude variation (the exact derivation of this term is not available). The agreement between the black and red lines is reasonable though not as good as is in Figure 3.6-7.

The emittance oscillations in the cases of dipoles and deflecting cavities may look different, but the final emittances in both cases are close (around 60 pm, compare Figures 3.6-7 and 3.6-8). (Note that

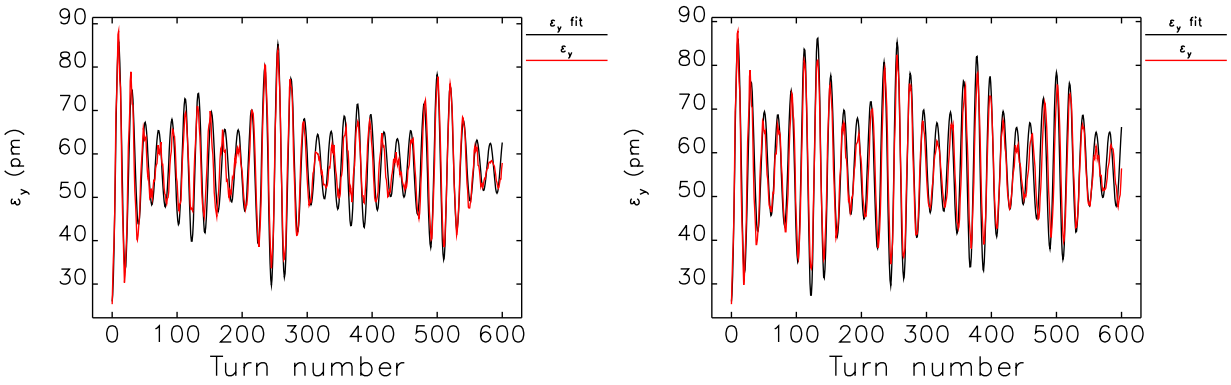

Figure 3.6-8: Comparison of the tracking results (red line) and a fit using Equation (3.6-28) (black curve) for a case of orbit bump produced by rf deflectors. The left plot is for $C_x = 6$, $C_y = 4$, while the right plot is for $C_x = 6$, $C_y = 6$.

the amplitude of the kick in the dipole case corresponds to the cavity kick to a particle at a longitudinal position of one standard deviation.) The exact relation of the emittances for the cases of constant and variable kicks is hard to derive analytically, but simulations were performed for different sets of sextupoles, and the equality of the emittances approximately stands. This fact gives a simple way to predict the equilibrium vertical emittance; however, one should understand that it works only when the coupling is the dominating effect in the emittance increase.

Now it can be stated that the sextupoles between cavities must satisfy the following requirements:

- Compensate natural chromaticity
- Minimize coupling on the vertical bump
- Minimize the total horizontal and vertical kicks that are generated on the vertical trajectory

However, it should be remembered that modern storage-ring-based light sources utilize high symmetry to reduce negative nonlinear effects of strong sextupoles. Local optimization of sextupoles between the cavities breaks global sextupole symmetry and can lead to reduction of the lifetime and injection efficiency. Therefore, to the requirements above should be added:

- Maintain satisfactory dynamic aperture (for injection)
- Maintain satisfactory momentum aperture (for lifetime)

Tracking was used to simulate the effect of the deflecting cavities on the beam. We used `elegant` [3.6-35] and its parallel version [3.6-36], which perform tracking in 6D phase space. Given the large bending radius of the APS dipoles ($\rho = 38.9$ m), first-order matrices were utilized for the dipoles. Quadrupoles and sextupoles were modeled as kick elements up to fourth order. Accelerating cavity harmonic and voltage were chosen to reproduce the measured bunch lengthening per Equation (3.6-3) and the nominal rf acceptance of $\pm 2.35\%$.

In a cavity with open beam pipes, the main deflecting mode is a mixture of transverse-magnetic (TM) and transverse-electric (TE) modes, resulting in a radius-independent deflection [3.6-37]. The

longitudinal electric field was also included to satisfy Maxwell's equations. According to the present design, each cryomodule contains four single-cell cavities. Each cavity was represented as a uniform deflecting field of length $\lambda_t/2$, where λ_t is the deflecting mode wavelength.

Since there are many different requirements on the sextupoles between the cavities, it is important to perform complex sextupole optimization that takes into account both emittance degradation and nonlinear dynamics consequences. The full optimization process consists of the following steps:

- Linear lattice design that ensures proper phase advance between cavities and allows the setting of other parameters, such as beta functions in the cavities;
- Optimization of the sextupoles between the cavities to minimize the emittance growth, which is usually done using single-pass emittance growth;
- Optimization of the sextupoles outside of the cavities to improve dynamic and momentum aperture of the resulting lattice.

The first two steps of the optimization do not take much time, but the last step is time-consuming and can take up to a week on a multiple-core computer (see section 3.2.2.3). The proper sextupole optimization allows one to limit the emittance growth to very reasonable levels [3.6-19], i.e., to about 10%. Figure 3.6-9 shows the resulting vertical emittance as a function of deflecting voltage for bunches with two different lengths. (The lattice was optimized for extremal values of a 4-MV deflecting kick and a 50-ps-long bunch.) The emittance was obtained by tracking 10,000 particles for 10,000 turns through the optimized lattice. The beam moments were averaged over the last 2000 turns to get equilibrium values. Recall that before the sextupole optimization, the vertical emittance increased to 600 pm (see Figure 3.6-6). For the 41-ps case, thought to be appropriate for 150 mA in 24 bunches (see section 3.6.3.3.2), one can approximate the emittance dependence on voltage by the following empirical expression:

$$\Delta\varepsilon_y\,[\text{pm}] \approx 0.76 V_t^2\,[\text{MV}]. \tag{3.6-33}$$

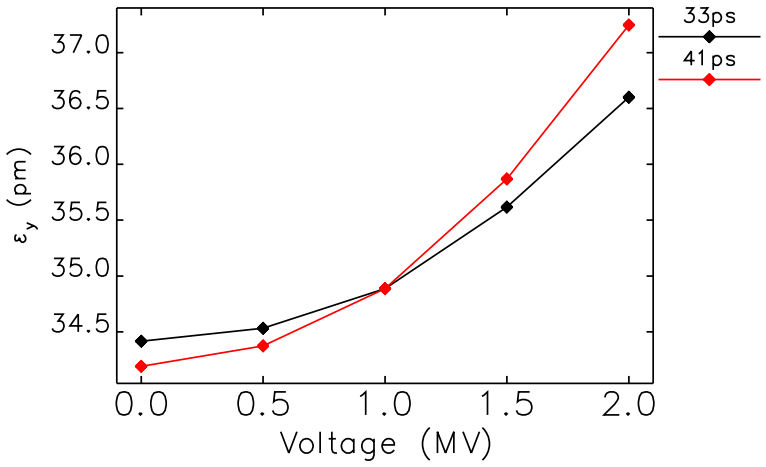

Figure 3.6-9: Dependence of the equilibrium vertical emittance on the deflecting voltage. The 33-ps case is appropriate for 100 mA in 24 bunches, while the 41-ps case is appropriate for 150 mA in 24 bunches (see section 3.6.3.3.2).

3.6.3.2.3 Tolerances

In addition to effects present in an ideal machine, the errors existing in the real machine could further degrade the performance. In this section we will look at the effects that arise in the real machine with errors. We used tracking simulations to determine the sensitivity of the beam orbit, emittance, and other properties to various errors, such as cavity phase or voltage. Based on these sensitivities, we then define the tolerances. Simulations were performed for the optimized sextupoles and always included synchrotron radiation effects.

It is helpful to start by making a catalog of causes and effects related to SPX. For each cause, we list the effect or effects along with the numerical coefficient relating one to the other. Orbit motion is characterized by the square root of the ratio of the orbit invariant $A_y = y^2(1+\alpha_y^2)/\beta_y + 2\alpha_y y y' + \beta_y y'^2$ to the vertical emittance ϵ_y. Emittance variation is characterized as a fraction of the nominal 35-pm emittance. The assumed electron bunch duration is either 33 or 41 ps rms, whichever is most conservative. Table 3.6-16 gives a summary of the results. Details of how the relationships between causes and effects were obtained are given below. The "Rate" column refers to the speed of variation of the cause with respect to the relevant time scale. "Slow" changes are those that users experience as variation or fluctuation. "Fast" changes are those that users average over. In some cases, we have not made the distinction.

Table 3.6-16: Summary of causes and effects related to SPX. See text for details, including derivation of the sensitivities.

Cause	Rate	Effect	Approximate relationship
Common-mode voltage error	All	Intensity variation	1 %/%
	All	Pulse duration variation	1 %/%
Common-mode phase error	All	Intensity variation for SPX	0.063 %/deg^2
Differential voltage error	Slow	Emittance fluctuation	8 %/%^{2}
	Fast	Effective emittance growth	2.8 pm/%^{2}
Differential phase error	Slow	Orbit motion outside SPX	0.13 %/mdeg
	Fast	Effective emittance growth outside SPX	1.9×10^{-5} pm/mdeg^2
Orbit motion at SPX sources	Fast	Pulse duration increase	2.7 %/μrad^2
	Slow	Timing jitter	0.2 fs/nrad
	Fast	Intensity reduction	negligible
	Slow	Intensity variation	negligible

Static Differential Errors

For this analysis, we scanned an offset in phase or voltage for the second cavity and determined the equilibrium change in emittance and orbit. The errors are thus "static" in the sense that they vary slowly compared to the damping time.

To determine rms effects, we used these response curves with a simple SDDS/Tcl script that randomly picks 1000 Gaussian-distributed values of the offset in question. For each random deviate, we determine the corresponding value of the orbit or emittance change. Taking the standard deviation of these values gives the rms variation in the quantity for the chosen random error level. By varying the error level, we can determine the rms response as a function of the rms error.

The orbit response is computed as a fraction of beam size, i.e.,

$$m_{fq} = \sqrt{\frac{A_q}{\epsilon_q}}, \tag{3.6-34}$$

where

$$A_q = \frac{1+\alpha_q^2}{\beta_q}\langle q\rangle^2 + 2\alpha_q\langle q\rangle\langle q'\rangle + \beta_q\langle q'\rangle^2. \tag{3.6-35}$$

In these equations, q is x or y, and angle brackets represent averages over all particles. This is a positive quantity, whereas the actual orbit oscillations are, of course, both positive and negative. Hence, we must look at the rms value of m_{fq} rather than the standard deviation. The emittance response is a positive quantity, hence, using the standard deviation is appropriate.

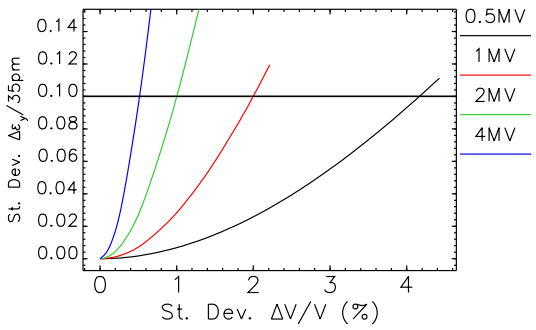

Figure 3.6-10: Fractional standard deviation of the vertical emittance vs standard deviation of the relative voltage error.

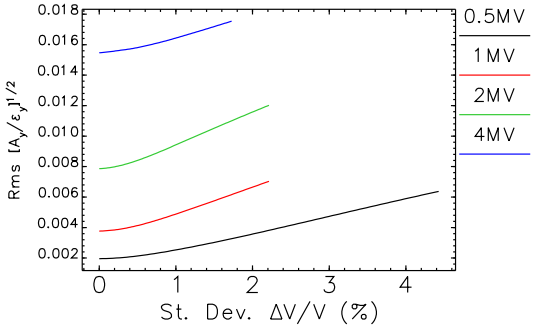

Figure 3.6-11: Fractional rms vertical orbit deviation vs standard deviation of the relative voltage error.

Figures 3.6-10 and 3.6-11 show the effect of differential voltage errors on the emittance and orbit for voltages between 0.5 and 4 MV (the design voltage is 2 MV). As expected, the orbit is insensitive to the voltage error, so this effect is ignored. However, even relatively small voltage errors can cause the emittance to vary by more than 10%. For the 2-MV case, the dependence is approximately characterized by a quadratic dependence, with 8% growth for a 1% error.

Figures 3.6-12 and 3.6-13 show the effect of differential phase errors on the emittance and orbit for voltages between 0.5 and 4 MV (the design voltage is 2-MV). As expected, the emittance is insensitive to the phase error, so this effect is ignored. However, even relatively small phase errors can cause the orbit to vary by more than 10% of the beam dimensions. For the 2 MV case, the dependence is approximately linear, with 0.13% motion per mdeg of phase error.

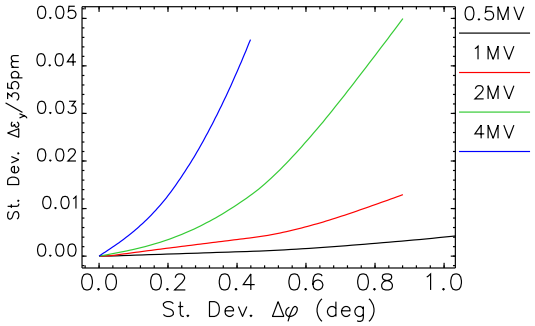

Figure 3.6-12: Fractional standard deviation of the vertical emittance vs standard deviation of the differential phase error.

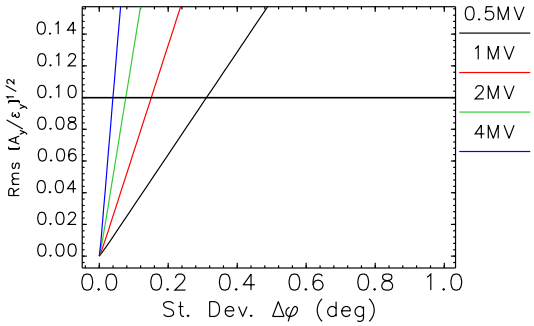

Figure 3.6-13: Fractional rms vertical orbit deviation vs standard deviation of the differential phase error.

Time-Dependent Differential Errors

The results shown above are based on the assumption of static, or slowly varying errors, in that the beam is allowed to find a new equilibrium in the presence of the error. In reality, phase and voltage errors will vary in time. The cavity 3-dB half-bandwidth may be as high as 1.4 kHz if the loaded Q of the rf system is chosen to be as low as 10^6 (see Table 3.6-41). Significant phase and voltage variations may appear at several times at this frequency. Hence, simulations have been used to explore the frequency dependence of the response to phase and voltage errors in a single cavity.

Before proceeding with the simulations, note that, in the simplest picture, phase error modulation will result in a modulation of a centroid kick. One can approach this analytically, following section 7.2.1 of ref. [3.6-38]. The beam displacement due to a kick that occurred k turns ago is

$$\Delta y_k = \sqrt{\beta_1 \beta_2}\theta_k e^{-kT_0/\tau} \sin\left(2\pi\nu k + \Delta\psi_{12}\right), \tag{3.6-36}$$

where $\beta_{1,2}$ is the beta function at the observation (kick) point, $\Delta\psi_{12}$ is the phase advance between the two points, θ_k is the kick delivered k turns ago, T_0 is the revolution time, τ is the damping time, and ν is the betatron tune. If θ_k is modulated with frequency f_m, then $\theta_k = \hat{\theta}\cos(2\pi f_\mathrm{m} k T_0 + \phi)$, where $\hat{\theta}$ is the modulation amplitude, and ϕ is the modulation phase. Since only the frequency dependence is of interest, one can assume the observation point to be the same as the kicker location, so that $\beta_1 = \beta_2 = \beta$ and $\Delta\psi_{12} = 0$. Using some trigonometric identities and Equations (7.13) and (7.14) from ref. [3.6-38], one gets the following expression for the closed orbit:

$$\begin{aligned} y(\phi) &= \sum_{k=0}^{\infty} \Delta y_k \\ &= \frac{\beta\hat{\theta}}{2}\left\{\frac{q\sin A_+\cos\phi}{1-2q\cos A_+ + q^2} + \frac{(1-q\cos A_+)\sin\phi}{1-2q\cos A_+ + q^2} + \right. \\ &\qquad \left. \frac{q\sin A_-\cos\phi}{1-2q\cos A_- + q^2} - \frac{(1-q\cos A_-)\sin\phi}{1-2q\cos A_- + q^2}\right\}, \end{aligned} \tag{3.6-37}$$

where $A_\pm = 2\pi(\nu \pm fT_0)$ and $q = e^{-T_0/\tau}$. The amplitude A of the oscillation is of interest and is given

by

$$\begin{aligned}\frac{A^2}{2} &= \frac{1}{2\pi}\int_0^{2\pi} y^2(\phi)d\phi \\ &= \frac{\beta^2\hat{\theta}^2}{4}\frac{q^2\left(1-\cos 4\pi\nu\right)}{\left(1-2q\cos A_+ + q^2\right)\left(1-2q\cos A_- + q^2\right)}.\end{aligned} \tag{3.6-38}$$

The obvious choice for the damping time τ is the radiation damping time. However, we know that the actual damping time is considerably shorter, due to coherent damping that results from high charge and chromaticity. We have used a value of $1/\tau \approx 500s^{-1}$, based on measurements for the vertical plane with a chromaticity of 7. The result is shown in Figure 3.6-14, where, not unsurprisingly, a resonance behavior at the value of the tune (in this case $\nu = 0.3$) is observed. For the region of interest, up to perhaps 10 kHz, the response is essentially flat.

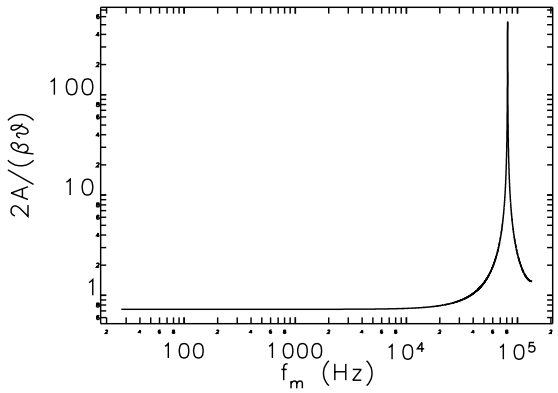

Figure 3.6-14: Frequency dependence of the orbit response to a sinusoidally varying dipole kick.

The effects of phase and voltage modulations were simulated using parallel `elegant` with 30,000 simulation particles to control noise. We imposed sinusoidal modulations on the phase or voltage error in the second set of cavities. The tracking results were then analyzed to determine the frequency variation of the response. The modulation amplitude was chosen to be relatively large (1% in voltage and 0.1 degrees in phase) to further reduce the effects of noise. For the same reason, we used 4 MV for the deflecting voltage, even though 2 MV is the design value. The number of turns we must track depends on the frequency of the modulation. At minimum, we tracked 10,000 turns to allow several damping times. We tracked sufficiently long to have a frequency resolution of about 5% of the modulation frequency, e.g., for a 100-Hz modulation, we tracked 50,000 turns. Transient effects were further reduced by choosing the phase of the modulation such that the modulation is zero at the beginning of the simulation.

To process the centroid data, we subtracted the turn-by-turn centroid data for the case without modulation from the data with modulation, then computed the standard deviation of the value over all turns. For the emittance data, the analysis is more difficult because of significant random fluctuations in the emittance. The approach used here is to compute the PSD of the emittance, then integrate between 0.9 f_{m} and 4.4 f_{m}, i.e., we find the rms variation in the band from 10% below the modulation frequency to 10% above 4 times the modulation frequency. The value of 4 was chosen by looking at the PSDs and noting that 4 harmonics were evident. The signal of interest is the square root of the increase in the integrated PSD relative to the value with no modulation.

As expected, the only significant centroid response is of the vertical centroid to a phase error, whereas other responses are not significantly different from noise. Figure 3.6-15 shows the relevant data. The

value for the 100-mdeg amplitude (70-mdeg rms) modulation is 13.7% rms. From Figure 3.6-13 we would expect a value of 18% rms, which agrees within 30%.

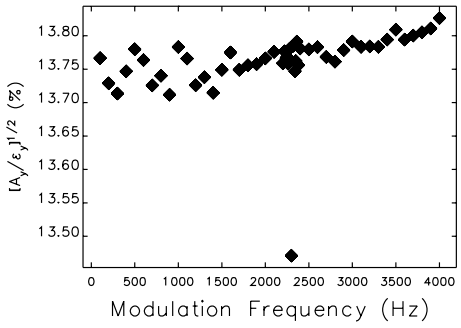

Figure 3.6-15: Response of vertical beam centroid to 100 mdeg differential phase modulation for 4-MV deflecting voltage.

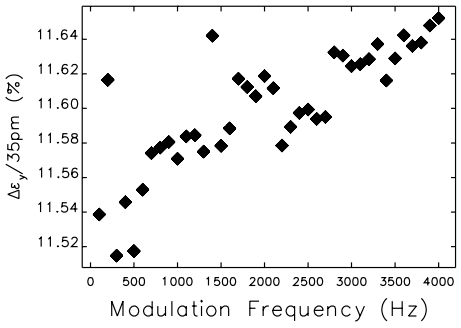

Figure 3.6-16: Response of vertical emittance to 1% differential voltage modulation for 4-MV deflecting voltage.

Also, as expected, the only significant emittance response is of the vertical emittance to the differential voltage error. Other responses are not significantly different from noise. The relevant data is shown in Figure 3.6-16. The value for the 1% amplitude (0.7% rms) modulation is 11.5 % rms, whereas from Figure 3.6-10 we would expect 17% rms, which agrees within 50%.

Effects of Fast Orbit Motion on the Effective Emittance

One of the tightest tolerances for SPX is the differential phase specification, which originates in the desire to control orbit motion. However, orbit motion above a certain frequency is seen by the non-SPX users as an increase in emittance. At first thought, one might imagine that one can somehow add the invariant amplitude A_y of the orbit and the emittance in order to get an effective emittance. This is not correct, particularly when the orbit motion results from a few discrete sources.

Thus, we need to simulate the vertical centroid beam position y_c and slope y_c' variation from differential phase errors. The concept of a closed orbit is somewhat nebulous when a corrector is varying on a time scale shorter than the damping time $\tau = 9.8$ ms. Hence, we performed simulations of driving the beam at different frequencies starting from 10 Hz up to 10 kHz. For each simulation, we recorded the beam position turn-by-turn at each BPM, after allowing the simulation to run for 8000 turns (29 ms, about 3 damping times). Sufficient turns were tracked after this to record at least 10 oscillations.

For each frequency and at each location s we computed a sigma matrix using data from the data after the settling period:

$$\Sigma_c = \begin{pmatrix} \langle y_c^2 \rangle & \langle y_c y_c' \rangle \\ \langle y_c y_c' \rangle & \langle y_c'^2 \rangle \end{pmatrix} = \epsilon_c \begin{pmatrix} \beta_c & -\alpha_c \\ -\alpha_c & \frac{1+\alpha_c^2}{\beta_c} \end{pmatrix}, \tag{3.6-39}$$

where the averages are over turns. Figure 3.6-17 compares the results for 10 Hz and 10 kHz, which differ very little outside the region between the two cavities. This is not surprising, since, as Equation (3.6-38) indicates, what is relevant is the damping time relative to the revolution time. The modulation frequency only matters when it approaches the tune.

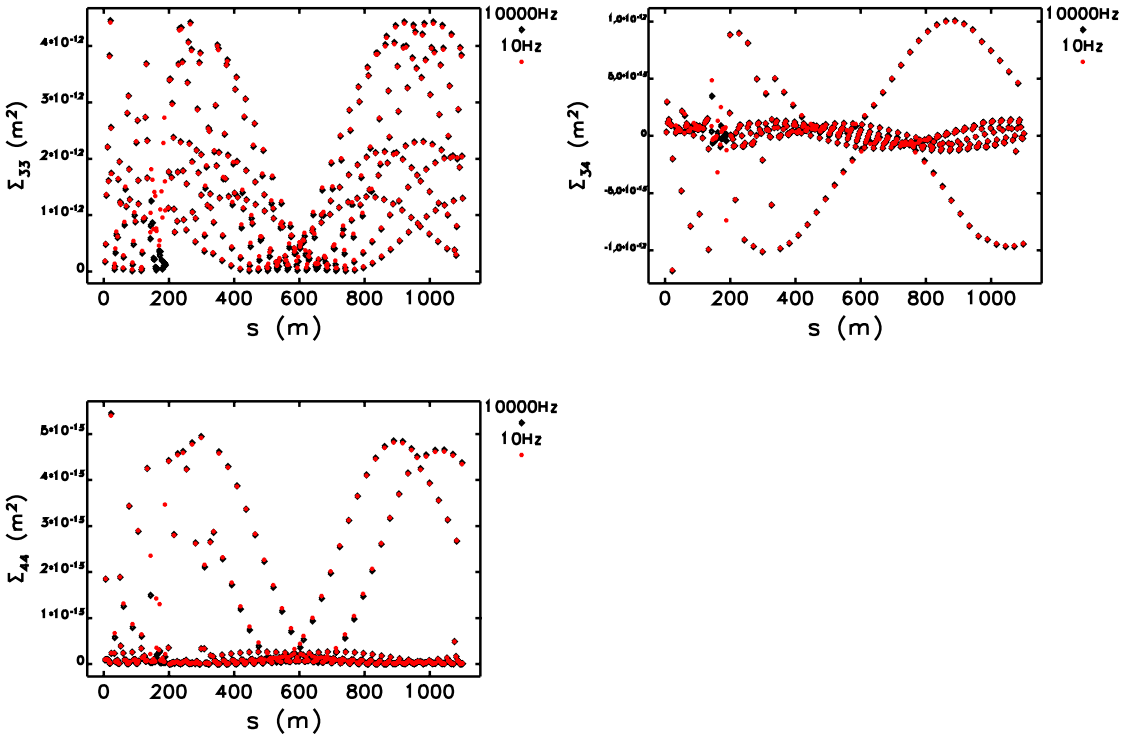

Figure 3.6-17: Comparison of the vertical-plane sigma matrix elements for the beam orbit for modulation of deflecting cavity phase at 10 Hz and 10 kHz.

For the lowest-frequency results, at 10 Hz, we clearly expect that the beam follows the instantaneous mathematical closed orbit as the kick varies. Since the result is essentially the same as for 10 kHz, we conclude that we do not need to concern ourselves with the oscillation frequency, but can simply look at closed orbits for random static phase errors. Once we have simulated many orbits, we compute the centroid sigma matrices as in Equation (3.6-39). This is to be compared to the ordinary beam sigma matrix

$$\Sigma_y = \epsilon_y \begin{pmatrix} \beta_y & -\alpha_y \\ -\alpha_y & \frac{1+\alpha_y^2}{\beta_y} \end{pmatrix}. \tag{3.6-40}$$

In general, we expect $\beta_c \neq \beta_y$ and $\alpha_c \neq \alpha_y$. Hence, we cannot simply add the "orbit emittance" ϵ_c to the emittance ϵ_y. Instead, we must convolve the particle distribution at each s location with the closed orbit distribution at that location. Since there is no correlation between individual particle coordinates relative to the beam center and coordinates of the beam center itself, we perform this convolution by adding the sigma matrices. The determinant of the combined sigma matrix gives the effective emittance. We can also use the elements of the combined sigma matrix to compute the effective lattice functions.

The above discussion is valid regardless of the source of the beam motion. To specifically simulate the effect of differential phase error on emittance, we replaced the four deflecting cavities in both sectors with vertical correctors and ran simulations of closed orbits for various rms kick error levels, given by

$$\sigma_{\Delta y'} = \frac{V}{4E}\frac{\sigma_{\Delta\phi}}{2}\exp\left(-\frac{(\sigma_t\omega)^2}{2}\right), \tag{3.6-41}$$

where $\sigma_{\Delta\phi}$ is the equivalent rms differential phase error, V is the total voltage per set of four cavities, and the exponential factor reflects the effect of the bunch duration relative to the rf period. All four cavities in a single sector are assumed to move together, while cavities in different sectors move in precisely the opposite direction in phase. We performed simulations of 3000 error ensembles for various values of $\sigma_{\Delta\phi}$ and analyzed the data as indicated above, using $\epsilon_y = 37$ pm as the starting emittance (see Figure 3.6-9).

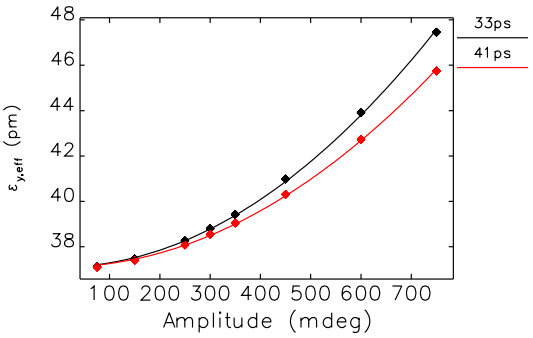

Figure 3.6-18: Effective vertical emittance, combining the beam emittance and the effects of fast orbit motion due to differential phase errors, as a function of the rms differential phase error for two different values of the rms bunch duration.

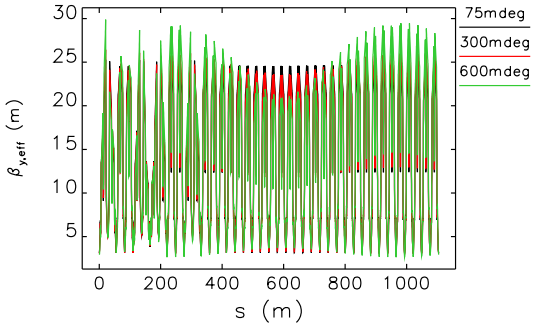

Figure 3.6-19: Effective vertical beta function, combining the beam emittance and the effects of fast orbit motion due to differential phase errors, assuming a 33 ps rms bunch duration. The legend gives the assumed rms differential phase error.

Somewhat surprisingly, we find that the effective vertical emittance is a constant around the ring, increasing as $\sigma_{\Delta\phi}$ increases, as shown in Figure 3.6-18. However, the effective beta function is not constant, as shown in Figure 3.6-19. So the relative orientation of the beam and orbit ellipses changes, but the effect on the emittance is constant, a surprising result. As an aside, we can make a naive estimate of the emittance increase for comparison. Assuming $\sigma_\Delta\phi = 750$ mdeg, the *total* rms kick to the beam centroid is $8\sigma_{\Delta y'} = 3.15\mu$rad, where $\sigma_{\Delta y'}$ is given by Equation (3.6-41). The rms orbit displacement is $\sigma_{\Delta y} = 8\sigma_{\Delta y'}\sqrt{\beta_0\beta_{max}}/(2\sin\pi\nu_y)$, or 19.5 μm. Taking $\sigma^2_{\Delta y} = \epsilon_{y,eff}\beta_{max}$ gives $\epsilon_{y,eff} = 15$ pm, which is 50% higher than the simulation result of 10 pm.

From the data represented in Figure 3.6-18 we find that the effective emittance increases quadratically with phase error. For $\sigma_t = 33$ ps, where the growth is most rapid, the coefficient is $1.9 \times 10^{-5}\mathrm{pm/mdeg}^2$, where the phase error is an rms value.

However, some of the allowance for effective emittance increase must also be assigned to fast-varying differential voltage errors, since they will be viewed as an emittance increase rather than a fluctuation. From Figure 3.6-16 we know that the response is insensitive to the modulation frequency. Hence, we can use the data from the static error simulations (i.e., the data represented in Figures 3.6-10 and 3.6-11) to find the average emittance increase for a particular rms voltage error:

$$\langle\Delta\epsilon_y\rangle[pm] = 2.8\left(\frac{\Delta V}{V}\right)^2_{rms}. \qquad (3.6\text{-}42)$$

Effects of Orbit Motion at SPX Sources

Orbit motion at SPX sources can result in timing and intensity variation. We define anything faster than 0.01 Hz as "fast" in this case, since SPX users are expected to average over time scales of seconds. Anything slower than 0.01 Hz is defined as "slow."

The linking of orbit motion to timing is simple to derive. The central photon passing through the slits a distance L from the undulator must have vertical coordinate $y_s = 0$:

$$y_s = y_u + \left(y'_u + \frac{V}{E}\omega\Delta t_u \right) L, \tag{3.6-43}$$

where u subscripts refer to values at the undulator in the absence of cavity voltage. At the undulator sources inside SPX, vertical beam motion from any source manifests primarily as an angle error. In addition, the angular component dominates at the slits, some 30 m distant from the insertion device. Hence, we ignore y_u and set $y_s = 0$ (to select x-rays going through the slits), giving

$$\Delta t_u = -\frac{y'_u E}{V\omega}. \tag{3.6-44}$$

Assuming that SPX users average over many pulses using an integration time of 1 s or longer, the apparent pulse duration will increase according to

$$\sigma_{txu}^2 = \sigma_{tx}^2 + \sigma_{tu}^2, \tag{3.6-45}$$

where σ_{tx} is the nominal rms duration and σ_{tu} is the orbit motion contribution, obtained from Equation (3.6-44). Assuming that the orbit motion contribution is small and expanding to first order gives

$$\frac{\Delta\sigma_{txu}}{\sigma_{tx}} \approx \frac{1}{2\sigma_{tx}^2}\left(\frac{E}{V\omega}\right)\sigma_{y'}^2, \tag{3.6-46}$$

implying a sensitivity of 2.7%/μrad^2.

The intensity variation resulting from orbit motion originates in the electron beam timing jitter, which we examine in section 3.6.3.2.3. Rewriting Equation (3.6-52) by substituting

$$\sigma_{\Delta\phi} = \omega\sigma_{\Delta t_u} = \frac{E}{V}\sigma_{y'_u} \tag{3.6-47}$$

gives

$$\left(\frac{\Delta I}{I}\right)_{SD} = \frac{(E\sigma_{y'_u})^2}{\sqrt{2}(\omega\sigma_t)^2}, \tag{3.6-48}$$

where $\sigma_t = 33$ ps is the assumed electron bunch duration. For an orbit motion of 1.9 μrad (much larger than we expect, but consistent with a 10% increase in effective pulse duration as discussed below), we infer intensity variation of about 4×10^{-5}, which is negligible.

Next, we look at the timing drift that results from slow beam motion. The sensitivity is simply given by Equation. (3.6-44) and is 0.2 fs/nrad.

Common-Mode Errors

A common-mode voltage error changes the chirp seen by the target beamlines and therefore the pulse duration and intensity. The variation is directly proportional to the voltage variation, so the sensitivity is 1%/%. Unlike most tolerances, this is independent of the deflecting voltage, and hence does not become easier as we lower the voltage.

An additional effect is that the vertical emittance will vary as the common-mode voltage varies. Using tracking results for a 33-ps rms bunch duration, shown in Figure 3.6-9, we can characterize this as

$$\epsilon_y\,[\text{pm}] \approx \epsilon_{y0}[\text{pm}] + 0.19V^2\,[\text{MV}]. \tag{3.6-49}$$

Using this, we can estimate the rms emittance variation due to a voltage variation,

$$\frac{\sigma_\epsilon}{\epsilon} \approx \frac{0.38V^2}{\epsilon_{y0}}\frac{\sigma_V}{V}. \tag{3.6-50}$$

Even for a 1% rms common-mode voltage error at 4 MV, the variation in emittance is less than 0.2%, which is negligible.

Common-mode phase error changes the portion of the bunch that receives zero kick. That means that the optical slits cut out different parts of the pulse, which leads to arrival time change and to pulse intensity change. It also changes the interior orbit, but that can be ignored due to the large beam size between the cavities. Assuming a Gaussian bunch, the intensity variation can be written as

$$\sqrt{\frac{\Delta I}{I}} \approx \frac{\Delta\phi}{2\sqrt{2}\pi f_t \sigma_t}. \tag{3.6-51}$$

where f_t is the deflecting rf frequency, σ_t is the electron bunch length, and I is the pulse intensity. In terms of standard deviations, we have

$$\left(\frac{\Delta I}{I}\right)_{SD} = \frac{\sqrt{2}\phi_{SD}^2}{(2\sqrt{2}\pi f_t \sigma_t)^2}. \tag{3.6-52}$$

Assuming the worse case of a 33-ps rms electron bunch duration, we find a sensitivity of 0.063 %/deg^2.

Conversion of Sensitivities to Tolerances

With the sensitivities in hand, the performance goals listed in Table 3.6-1 can be translated into the tolerances listed in Table 3.6-4. Each performance goal may impact several tolerance requirements, typically through quadrature addition of several effects. Hence, the analysis proceeds by working through the goals in Table 3.6-1 and determining the tolerance implications. Since several performance goals may impact a given tolerance, the final tolerances are the minimum values obtained over all goals.

Tolerances cannot be set without consideration of the bandwidth. In light of this, the words “slow” and “fast” are used to refer to the time scales that users average over. For non-SPX users, it is assumed that 1 kHz is the boundary between fast and slow variation [3.6-28]. For SPX users, it is assumed that 0.01 Hz is the boundary between fast and slow variation [3.6-39].

Effective pulse duration increase (for SPX users) results from fast common-mode voltage variation, fast orbit motion, and fast timing error in the beam-line pump laser. The requirement is 10% increase

relative to the nominal 2-ps FWHM value. This allowance is apportioned in quadrature among the three causes, with a total budget of $1.1^2 - 1 = 0.21$. Assigning 7% to the common-mode voltage and 32% to the other causes keeps the increase within the budget. This corresponds to 1.4-μrad rms fast orbit motion and 270-fs rms laser timing jitter.

Pulse duration fluctuation (for SPX users) results from slow common-mode voltage variation. The requirement is 10% rms fluctuation, which implies a 10% tolerance for common-mode voltage error.

Pulse intensity fluctuation (for SPX users) results from slow common-mode voltage variation and slow common-mode phase error variation. The requirement is 10% rms fluctuation, which is apportioned in quadrature fashion to the two causes, giving an allowance of 7% rms for each. This implies a 7% tolerance for common-mode voltage error. It also implies a 10.5 deg tolerance for common-mode phase error.

Pulse timing jitter (for SPX users) results from slow variation in the beam orbit. The requirement is 10% of the 0.85-ps rms pulse duration, which translates to a tolerance of 425 nrad.

Vertical emittance increase results from the operation of the cavities as well as from fast variation in the differential voltage error between the cavities in the two sectors and fast variation in the differential phase error between the cavities. These contributions do not add in quadrature. With the cavities operating, the expected emittance is 37 pm, leaving a margin of 3 pm, which is divided between the two remaining causes. This implies an 0.7% tolerance on fast differential voltage error and a 280 mdeg tolerance on fast differential phase error.

Vertical emittance variation outside of SPX results from slow variation in differential voltage error between the cavities in the two sectors. The requirement for the emittance variation is 10%, which implies a 1.1% tolerance on the differential voltage.

Orbit motion outside of SPX results from slow differential phase error variation. The allowance for SPX-caused motion is $\sigma_y = 0.28\mu$ m and $\sigma'_y = 0.15\mu$ rad in the band from 0.01-200 Hz, which increases to 0.56 μ and 0.31 μrad, respectively, in the band from 0.01-1000 Hz. Using $\beta_y = 3.5$ m and $\epsilon_y = 40$ pm, these correspond to 5.0% and 10.3% of rms beam divergence, respectively. The tolerances are thus 38 and 79 mdeg, respectively. As mentioned in section 3.6.3.1, this assumes no use of orbit feedback to stabilize the phases. Use of orbit feedback should allow increasing these values by perhaps a factor of three, and is the subject of ongoing simulations (see section 3.3.8).

Combining these numbers with consideration of the different bandwidths for SPX- and non-SPX users gives the tolerances in Table 3.6-1.

3.6.3.2.4 Beam Injection and Aperture Considerations

Vertical aperture limitations play major role in particle losses due to linear and nonlinear coupling. Since vertical beam size between the deflecting cavities is greatly increased, injection efficiency could suffer during SPX operation.

We can perform injection efficiency simulation by tracking a bunch of particles with initial amplitude and beam parameters corresponding to the injected beam from the booster. We used a storage ring model as measured by the response matrix fit for these simulations. The model includes both linear optics distortion and coupling. The injected beam enters the storage ring vacuum chamber with amplitude of -24 mm. After passing through one sector of storage ring optics and two kicker magnets,

it experiences free betatron oscillations with the typical residual amplitude of about 6 mm, which also can be changed in the range between 4 and 7 mm depending on the kicker magnet settings. To simplify the simulations, we tracked the beam with the initial amplitude corresponding to the residual injection oscillations. Initial vertical amplitude was set equal to the measured vertical oscillation amplitude during injection. The particles are tracked for a number of turns, and the fraction of survived particles gives the injection efficiency. Figure 3.6-20 shows the results of the simulations. At the deflecting voltage of 2 MV, the injection efficiency is not significantly affected for the 6- to 7-mm initial oscillation level.

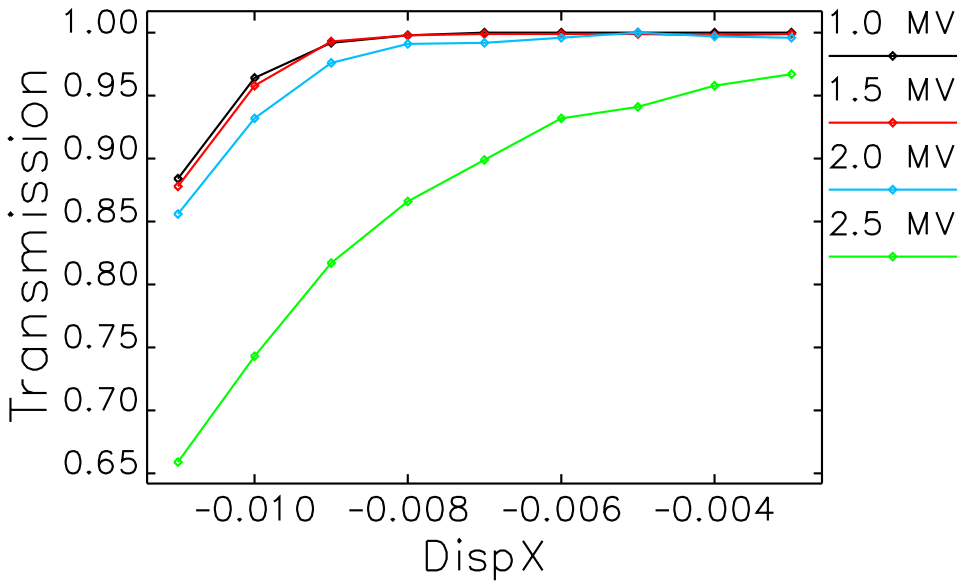

Figure 3.6-20: Particle transmission as a function on initial amplitude for different deflecting voltages. Typical oscillation amplitude is 6 mm. Horizontal emittance of the injected beam is 100 nm·rad and coupling is 5%.

3.6.3.2.5 Effect of Insertion Devices

Next, we looked at the effects of insertion devices on beam properties and injection. First, we repeated the simulations of the equilibrium condition with the addition of kick maps for undulators between the SPX cavities. In Sector 6, which is free of cavities, we placed two 2.4-m-long undulators. In Sector 7, which has a cryomodule at the downstream end, we placed a single 2.4-m-long undulator. This device was approximately centered in the long straight section. Hence, a total of three 2.4-m-long undulators where placed between the cavities, in agreement with the present plans for the beamlines. Two sets of simulations were performed, the first using three devices with a period of 28 mm, the second using three devices with a period of 30 mm. These are devices in the range of interest to the users. Even with all gaps closed to 11 mm, the only definite effect was an increase of the vertical emittance by less than 0.8 pm. To further test this conclusion, we lengthened the device in Sector 7 to 4.8 m and repeated the simulations for the 30-mm undulator period, which previously showed the largest effect. An increase in the vertical emittance of about 1.3 pm was observed. Hence, we conclude that effects on the equilibrium beam properties are not significant.

We also looked at the effect of the insertion devices on injection efficiency. This involved repeating the analysis of the previous subsection with undulator kick maps. No significant change was seen in the results.

3.6.3.2.6 Predicted Performance

To simulate what pulse length and what intensity can be achieved, detailed modeling was performed using electron distributions from tracking and photon distributions from `sddsurgent` [3.6-40]. A 24-bunch mode was assumed, with a 33-ps or 41-ps rms electron bunch length. After tracking 10,000 particles to find the equilibrium for a series of voltages, the particle properties were averaged over 2000 turns. Using these averaged parameters, a single turn was tracked with 1 million particles to get the phase space at the undulator. The undulator was placed 1.2 m from the center of the straight section, as would be typical. This means that the electron beam phase space has about twice as much spatial chirp as it would if the ID was centered on the straight section.

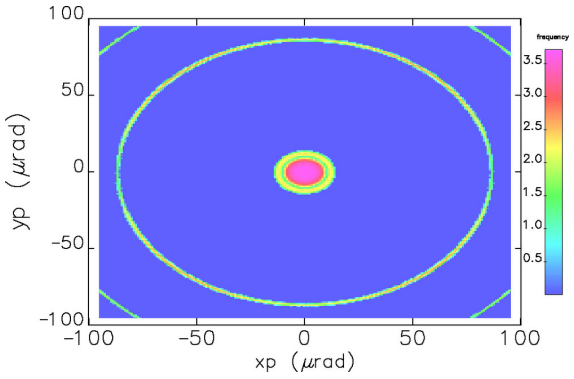

Figure 3.6-21: Angular radiation pattern from 2.4-m-long U33 undulator at 10-keV first harmonic. Relative intensity is shown on a log scale.

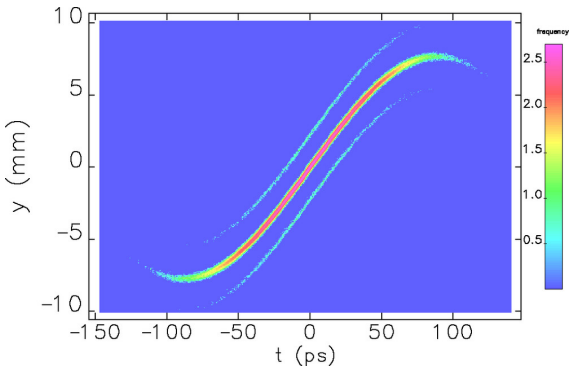

Figure 3.6-22: Radiation phase space at 26.5 m from the source, for 41-ps electron bunch and 2-MV deflection voltage. Relative intensity is shown on a log scale.

`sddsurgent` can calculate the detailed distribution of the central cone radiation and off-axis higher-order harmonics. This distribution was used for convolution with the electron distribution. Photon coordinates generated this way were then read by `elegant`. `elegant` does not specifically recognize these particles as photons, but it can still track them if only drift spaces and slits are used. In modeling the slicing process, an additional ± 0.25-mm horizontal slit at 26.5 m from the source point was used (that slit is used to decrease the intensity of the second harmonic).

Figure 3.6-21 shows the angular flux distribution of the radiation from the Undulator A at 10-keV photon energy. The second harmonic radiation is the large ring at a divergence of about 80 μrad. Use of horizontal slits allows one to attenuate the effect of the second harmonic; however, it cannot be eliminated completely. Figure 3.6-22 shows the radiation distribution at 26.5 m from the source for a 41-ps electron bunch duration. It clearly illustrates the effect of the second harmonic. (For longer bunches, a "back-chirped" portion will also appear.)

Figure 3.6-23 shows the details of time structure of the radiation pulse. The second harmonic presents itself as two pulses around the main pulse with intensity of 1 to 2% of the main pulse at a distance of

several tens of ps from the main pulse. The exact numbers depend on the undulator parameters. For the 41-ps bunch duration, the back-chirped pulses (which would appear at ± 178 ps) are very weak and are neglected here.

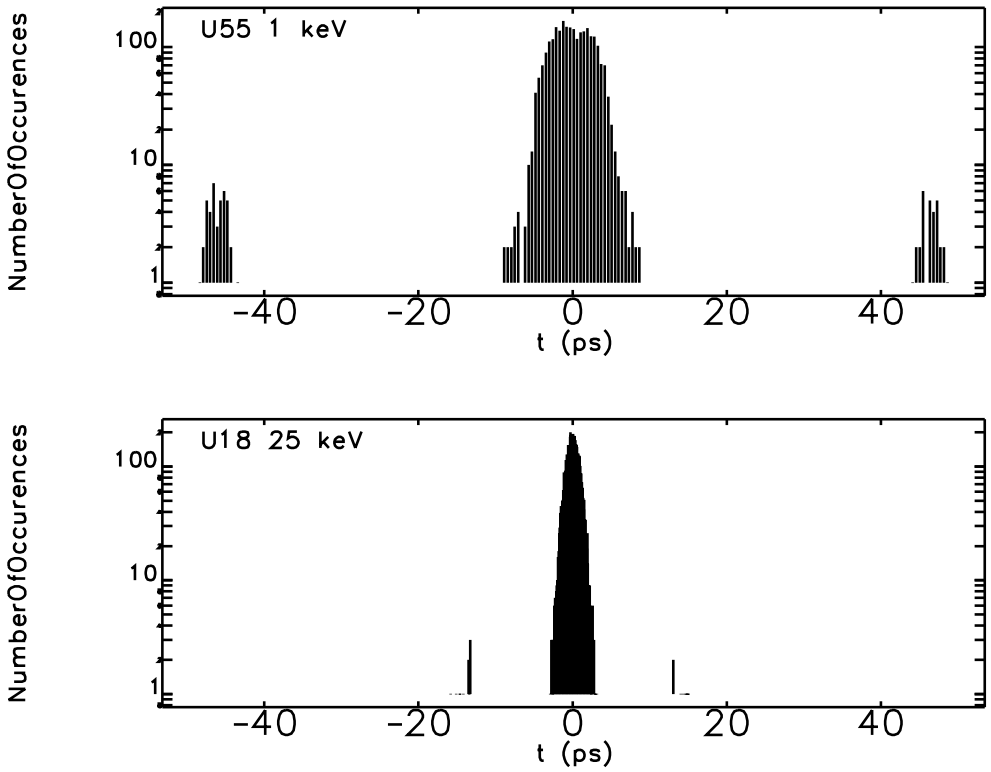

Figure 3.6-23: Time structure of the radiation pulse. The top plot shows 25-keV radiation from undulator U18, while the bottom plot shows 1-keV radiation from undulator U55. The second harmonic presents itself as two pulses around the main pulse with intensity of 1 to 2% of the main pulse at distance of several tens of ps.

The achievable pulse duration for a particular rf voltage depends on photon energy and undulator length because they change radiation divergence $\sigma_{y',\mathrm{Rad}}$ (Equation (3.6-18)). Figure 3.6-24 (left) shows pulse length as a function of the deflecting voltage for 10-keV first-harmonic radiation from the 2.4-m-long U33 undulator. Figure 3.6-24 (right) shows the dependence of the pulse length on the photon energy for the same undulator. One can see that the results improve for harder x-rays, as expected from Equations (3.6-18) and (3.6-19).

In addition to the above calculations, we also investigated two additional factors, using the program SPECTRA [3.6-41] in place of `sddsurgent`. First, we looked at the effect of beam energy spread on the radiation distribution. `sddsurgent` only includes the effect of the beam energy spread on the beam size, whereas SPECTRA includes the effect on the radiation distribution. Second, we investigated the effect of detuning the monochromator from the exact harmonic. We looked at detuning by $\Delta\lambda/\lambda = -1/N$ and $\Delta\lambda/\lambda = -1/(2N)$, i.e., the nominal undulator line width and half the nominal undulator line width. Figure 3.6-25 shows the results for a 41-ps rms electron bunch duration as a function of deflecting voltage. Only in the case of "full" detuning, $\Delta\lambda/\lambda = 1/N$, is a significant effect seen.

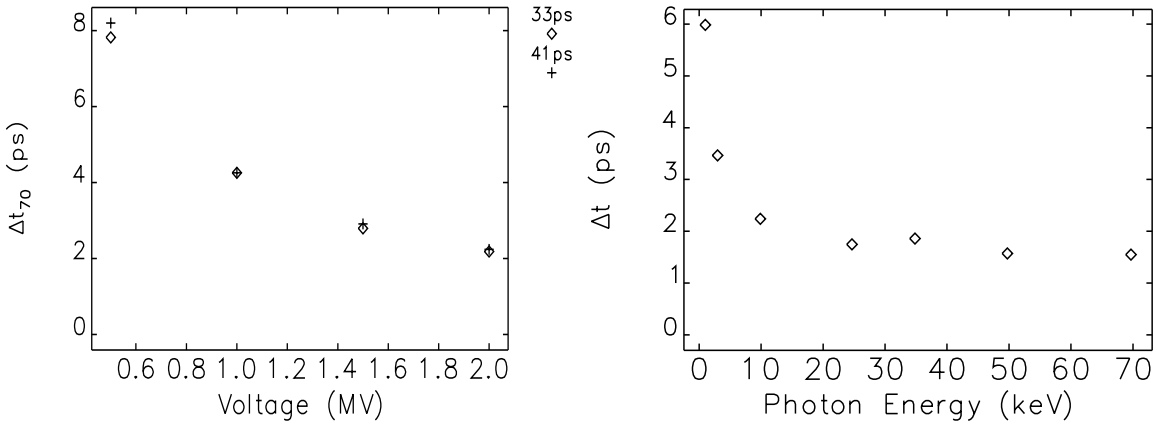

Figure 3.6-24: Predicted pulse duration. Right plot: as a function of deflecting voltage for 10-keV photons and a 41-ps electron bunch duration; left plot: as a function of the photon energy for 2-MV deflection and 41-ps electron bunch duration. The points above 30 keV are for the third harmonic.

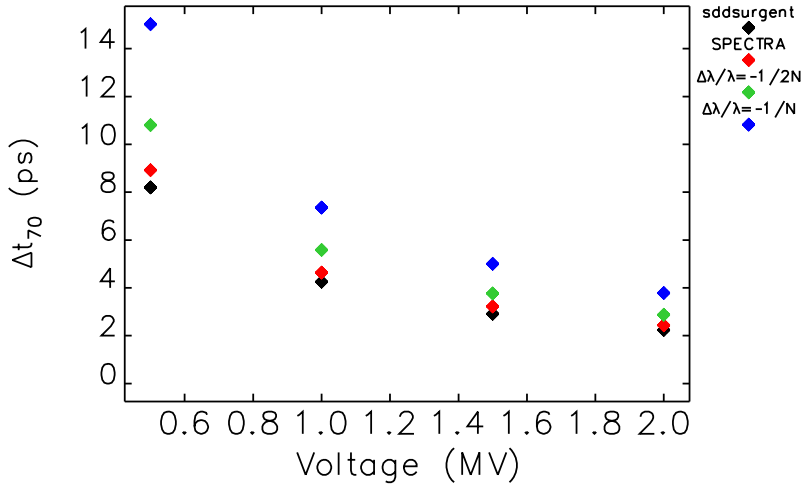

Figure 3.6-25: Predicted pulse duration for 41-ps rms electron bunch duration as a function of deflecting voltage, for four cases: Using `sddsurgent` *to compute the radiation distribution. Using SPECTRA to compute the radiation distribution, which includes broadening due to the beam energy spread. Using SPECTRA with* $\Delta\lambda/\lambda = -1/N$ *and* $\Delta\lambda/\lambda = -1/(2N)$.

3.6.3.2.7 Work Remaining

The beam-dynamics simulations for SPX are highly developed and are believed to give accurate predictions. However, additional tasks suggest themselves, including:

- Perform tolerance estimates with dynamic errors including the effects of orbit feedback and a realistic model of the cavity feedback systems.
- Perform analysis of sensitivity to orbit in interior sextupoles and methods of compensation, including possible additional skew quadrupole elements.

3.6.3.3 Collective Effects

Collective effects related to the deflecting cavities can be separated into short- and long-range effects. The former act within a single bunch, whereas the latter act over one or more turns.

Depending on the detailed resonant properties (i.e., frequencies and shunt impedance) of the cavities, there may or may not be an undesired beam oscillation known as coupled-bunch motion. Calculation methods can determine the safe range of cavity properties for an arbitrary bunch pattern against this instability. One only needs to specify the cavity resonant properties required for stability for all desired bunch patterns. This is discussed in section 3.6.3.3.1.

The single-bunch limit is determined by the sum total of all short-range wakefields produced in the storage ring vacuum chamber components. The deflecting cavities and the pipes connecting them to the standard chamber thus contribute additional short-range wakefields. The goal is to make an accurate estimation of the impact of the SPX cavities on single-bunch properties, including the single-bunch current limit. This is discussed in section 3.6.3.3.2.

3.6.3.3.1 Coupled-Bunch Effects and Requirements

The analysis of multi-bunch stability consists of determining whether it is possible for an oscillation of a multi-bunch beam to grow or to be sustained because of the cavity wakefields. This would occur if an HOM[3] frequency happens to be in resonance with one of the beam modes. If that is likely to happen, even for short periods of time, then the cavity design must be modified or rejected. The bunch motion in the longitudinal and two transverse planes must be considered separately as they depend on cavity resonant modes of different symmetries. The inputs to the calculation are essentially the cavity resonator parameters, the bunch pattern, and the total current.

There are three methods of various complexity (and accuracy) to determine the stability of the beam: explicit tracking of the beam with full optical and wakefield effects, normal mode analysis of bunch motion, and simple worst-case calculation from one cavity HOM.

In addition, these methods must somehow include the randomness of the HOM frequency values, as they are not known to sufficient accuracy in advance. The HOM frequencies change from design (and initial measurement) because of construction tolerances, and they also change during operation (changes in tuner position and temperature). In general the calculations are done with an assumed set of HOM frequencies, which are repeatedly randomized from the ideal design values (also known as a Monte Carlo approach). Statistics are done on the results to determine the likelihood of stability (or instability).

In superconducting cavities, the quality factor Q of a HOM can be very high, i.e., the resonator response is very sharply peaked in frequency and in general not close to any beam-mode frequency. This appears to be a good thing. However, if the HOM frequency varies due to temperature or operational change, the frequency might coincide with a beam mode frequency and the resulting beam instability would be very strong and cause beam loss. Another situation to consider is several cavity HOMs of much different frequency but resonant with the same beam-mode frequency through aliasing. Thus, a Monte Carlo simulation with sufficient sampling would cover operational conditions in one run.

[3] In this section we use for simplicity the term HOM for the resonator modes that are not the driving mode of the cavity — thus HOM means any of the Higher Order Modes, Same Order Modes, and Lower Order Modes defined in subsequent subsections.

The bunch pattern affects the type of beam mode that may occur, thus a Monte Carlo simulation has to be done for each operational bunch pattern.

The Monte Carlo method on HOM frequencies was first applied [3.6-42] for a superconducting cavity application at Cornell, then for LEP [3.6-43]. It was used in the design of the APS to determine the required deQing of the HOMs in the original (normal conducting) 352-MHz cavities [3.6-44, 3.6-45]. The method was applied again on the 2.815-GHz normal-conducting cavities in an earlier proposed SPX project [3.6-46, 3.6-47].

The most complex (and time-consuming) calculation method would be an exact multiparticle tracking of all bunches with an assumed set of HOM frequencies, where phases of all HOM wakefields are advanced in time and where wakefield forces are applied at every bunch passage. Such tracking would include helpful damping effects (at least in transverse planes) from chromaticity and short-term wakefields, which, at the APS, can result in damping at least twice as strong as that of synchrotron radiation. Since the tracking run takes some time to complete, repeating this hundreds of times for Monte Carlo sampling would be very time consuming.

For a general parameter investigation the normal-mode analysis approach is preferred because it takes much less time and can be executed in a conservative way. The centroid-motion-only normal-mode approach by Thompson and Ruth is employed [3.6-48] because it allows analysis of arbitrary bunch patterns. While this method will not include the coherent damping that comes from multiparticle effects, one could compare the result with either the synchrotron radiation damping rate (more conservative) or the expected coherent motion damping rate (more realistic), as deemed appropriate. The code `clinchor` [3.6-45, 3.6-49] was written to implement this normal-mode analysis.

Before reporting on this normal-mode Monte Carlo simulation, one can make an even simpler estimate of the worst growth rate assuming only one "bad" HOM that is resonant with a beam mode, and where the bunches are equally spaced. Calculations under these strict conditions should only be used as a guide of the possible growth rates.

One assumes N bunches equally spaced and equally charged. An unstable mode would have each bunch follow an oscillation of the same amplitude but with a fixed phase difference between them. For example, in the V-plane the centroid motion of the j^{th} bunch detected at a position monitor would be $y_j = A\exp\{i2\pi jm/N\}\exp\{i\Omega_m t\}$, where A is some complex number constant, m is the mode number (0 to $N-1$), and Ω_m is the coherent frequency of mode m. Successive bunches have $\exp\{i2\pi m/N\}$ phase difference. Ω_m is very close to $\nu_y f_0$ in value for all modes, having small differences in real and imaginary parts proportional to the resonator strengths. The imaginary part gives the growth or damping rate. The resonant condition is $f_{\text{HOM}} = -f_0\nu_y + mf_0$, that is, the HOM frequency must be equal to a harmonic of the beam frequency plus an offset given by the betatron frequency. Obviously one does not want a resonance to occur, but we do not have control over the HOM frequencies to sufficient accuracy during the design or tuning stage and during operation. To be conservative, one must assume that the frequency has the worst value, the resonant condition.

The instability growth rates depend on three properties of the cavity modes: the resonance frequency, the Q, and the shunt impedance. Before continuing, the definition of the term shunt impedance must be clarified. There are two conventions that differ by a factor of two. One is the "circuit" model, which is used in ring impedance and instability calculations, and the other is the "accelerator" model, which is used in specifying power requirements for driving a cavity. To avoid confusion, Table 3.6-17 gives the definitions of shunt impedance for the circuit model and related quantities.

Table 3.6-17: Definitions for circuit-model shunt impedance. Definitions are given for both monopole and dipole resonators with frequency ω_r and other related quantities.

Quantity	Longitudinal	Transverse
Voltage integral [a]	$V = \int_{-L/2}^{L/2} E_z(r,z)\ \exp\{-i\omega z/c\}dz$	$V(r) = \int_{-L/2}^{L/2} E_z(r,z)\ \exp\{-i\omega z/c\}dz$
Shunt impedance[b,c]	$R_s = \frac{\lvert V\rvert^2}{2P_c}$	$R_t = \frac{1}{\kappa_r a^2}\frac{\lvert V(a)\rvert^2}{2P_c}$
Impedance	$Z_\parallel(\omega) = \frac{R_s}{1+jQ(\omega/\omega_r-\omega_r/\omega)}$	$Z_\perp(\omega) = \frac{\omega_r}{\omega}\frac{R_t}{1+jQ(\omega/\omega_r-\omega_r/\omega)}$
Wake coefficient	$W_{\parallel 0} = \omega_r R_s/Q$	$W_{\perp 0} = \omega_r R_t/Q$
Wake function[d]	$W_\parallel(z) = W_{\parallel 0}\exp\left\{-\frac{\kappa_r z}{2Q}\right\}\cos(\kappa_r z)$	$W_\perp(z) = W_{\perp 0}\exp\left\{-\frac{\kappa_r z}{2Q}\right\}\sin(\kappa_r z)$

[a] For dipole modes (transverse plane) the integral is performed with a radial offset $r \neq 0$.
[b] P_c is the power needed to maintain the E_z fields, including power dissipated in dampers.
[c] κ_r is the wave number ω_r/c of resonator frequency; a is radius of E_z integration.
[d] Used for time-domain calculations, e.g., mode analysis and tracking.

The growth rates for a single HOM resonator with worst-case frequency are

$$\alpha_s = \frac{\alpha_c I_{\text{total}}}{2(E/e)\nu_s}(R_s f_{\text{HOM}})\exp(-\omega_r^2\sigma_t^2) \tag{3.6-53}$$

for the longitudinal plane and

$$\alpha_{x,y} = \frac{f_0 I_{\text{total}}}{2(E/e)}(\beta_{x,y}R_t)\exp(-\omega_r^2\sigma_t^2) \tag{3.6-54}$$

for the transverse planes. A bunch form factor was added, which is sometimes overlooked in the literature. The quantities besides shunt impedance are explained in Table 3.6-18. The table refers to two values of total current. Although the APS Upgrade requirement is 150 mA, the design requirement for stability purposes is 200 mA, for which all stability calculations are done.

Each growth rate must be compared with the natural damping time of the centroid of the bunch, which we could take as either the synchrotron radiation damping rate ($1/\tau$) of the given plane or the coherent damping rate in that plane (which includes synchrotron radiation damping effects). A bunch-by-bunch feedback is available and can potentially give a strong damping contribution (shown in figures below), for which we will not take credit here. As mentioned above, assuming only the synchrotron radiation damping rate in setting stability conditions is more conservative.

The coherent damping rate is determined by other beam dynamics and is much larger in magnitude than the synchrotron radiation damping rate. To assess the transverse coherent damping rate for the APS Upgrade lattice for various bunch patterns and chromaticities, the damping rate was measured using the pinging method in the current APS 24-bunch reduced horizontal beta function (RHB) lattice. For low bunch currents, I_b, we expect the damping rate to follow the simple model $\alpha_u = \alpha_{u,\text{rad}} + \alpha_{u,\text{fb}} + C_u I_b \xi_u$, where u is either x or y, $\alpha_{u,\text{rad}}$ is the synchrotron radiation damping rate, $\alpha_{u,\text{fb}}$ is the damping provided by feedback, ξ_u is the chromaticity, and C_u is some constant that depends of transverse impedance in plane u. The results are shown in Figures 3.6-26 and 3.6-27. In the current 24-bunch RHB lattice with a chromaticity of 3 and bunch current of 4.5 mA, the maximum damping rates (with bunch-by-bunch feedback on) are 6.3 $\times$ 10^3 s^{-1} and 15 $\times$ 10^3 s^{-1} in the x- and y-plane, respectively. The damping rate contributions from the feedback system saturate to around 4.0 $\times$ 10^3 s^{-1} and 11 $\times$ 10^3 s^{-1} in the x- and y-planes, respectively. Obviously the rate is a nonlinear function of the feedback gain.

Table 3.6-18: Beam and cavity parameters.

Quantity	Value	Comment
Longitudinal plane ring parameters		
Current I_{total}	200 mA	Design requirement
APS Upgrade operational current	150 mA	Not used in stability calculations
Energy E	7 GeV	
Revolution frequency f_0	271.55 kHz	
Synchrotron frequency f_s	2.1 kHz	Incoherent value
Momentum compaction α_c	2.8×10^{-4}	
Longitudinal single-particle damping time τ_s	4.8 ms	
Longitudinal single-particle damping rate $1/\tau_s$	208 s^{-1}	Maximum tolerable growth rate of instability
Transverse plane ring parameters		
Average β_x in cavity	22 m	20 m in standard-length straight section
Average β_y in cavity	7.5 m	Value at end of long straight section.
Transverse single-particle damping time $\tau_{u,\text{rad}}$	9.6 ms	u is either x or y
Transverse single-particle damping rate $1/\tau_{u,\text{rad}}$	104 s^{-1}	*Nominal* maximum allowed growth rate of instability
Coherent damping	2500 to 8000 s^{-1}	Charge- and chromaticity-dependent, and includes synchrotron radiation damping rate[a]
Chromaticity	$+3$ to $+7$	Major contributor to coherent damping
Form factor parameters		
rms bunch length σ_t	23 ps	Shortest bunch length in operational bunch patterns (324 bunches)
Form factor for 2.0 GHz and 2.8 GHz	0.92, 0.85	$\exp(-\omega_r^2\sigma_t^2)$

[a] Range of values in both transverse planes for a chromaticity range of 3 to 7 for a 4-mA bunch. Bunch-by-bunch feedback gain is set to minimum setting for stability.

The contributions from chromaticity are linear with chromaticity with an average rate of 1.17×10^3 s^{-1}/unit and 0.67×10^3 s^{-1}/unit in the x- and y-planes, respectively. This contribution is expected to scale with bunch current; thus we can calculate this contribution for bunch patterns with smaller bunch currents, such as hybrid mode bunch pattern. If there is no significant impedance change in the storage ring vacuum chamber for the future APS Upgrade lattice with similar chromaticity, confidence is high that similar damping rates can be achieved.

In some accelerator applications taking credit for this extra damping would make cavities design easier, such as not requiring HOM dampers. In the present case of superconducting cavities, natural Q's are so

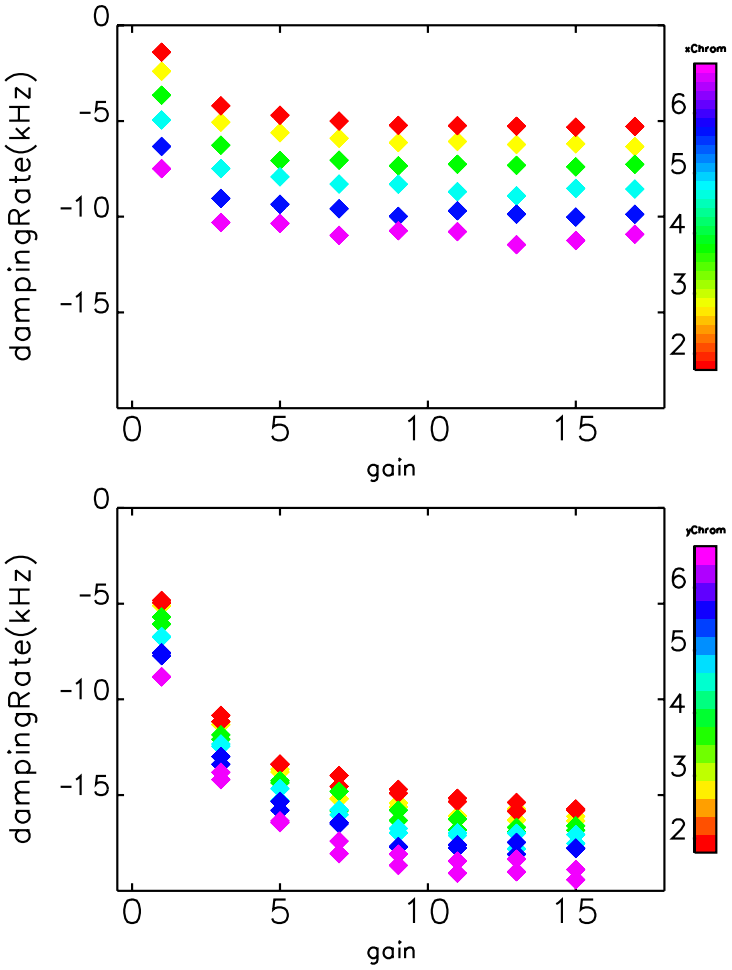

Figure 3.6-26: Damping rate versus feedback system gain for different chromaticities. Top: x-plane, Bottom: y-plane.

high that we need HOM dampers whether or not we take credit for the higher coherent damping rate. The benefit of not assuming the coherent damping rate is that we have a fallback for stabilizing new bunch patterns that have higher growth rates than those presently studied (e.g., unexplored variations of the hybrid bunch pattern).

With the ring parameters listed above, the largest allowed resonator impedances are then determined and are given in Table 3.6-19. The beneficial effect of the bunch form factor is included. These give guidance to the rf cavity designer for target shunt impedances.

The next step is to perform the Monte Carlo calculation using resonator parameters from HOMs provided by the rf cavity designer and with the number of cavities desired. The design of the rf cavities is not finalized at this time, so the resonator parameters used here only allow making an estimate of growth rates. A single-cell design with dampers in each cavity will produce very low Qs for all HOMs. Each of the HOMs will almost certainly satisfy Table 3.6-19 by themselves. However the present design calls for a total of eight cavities to be installed eventually, many of which will have overlapping HOM impedance functions. With a statistical model of how the HOM resonant frequencies may vary from cavity to cavity, one may use a Monte Carlo method to estimate the growth rates.

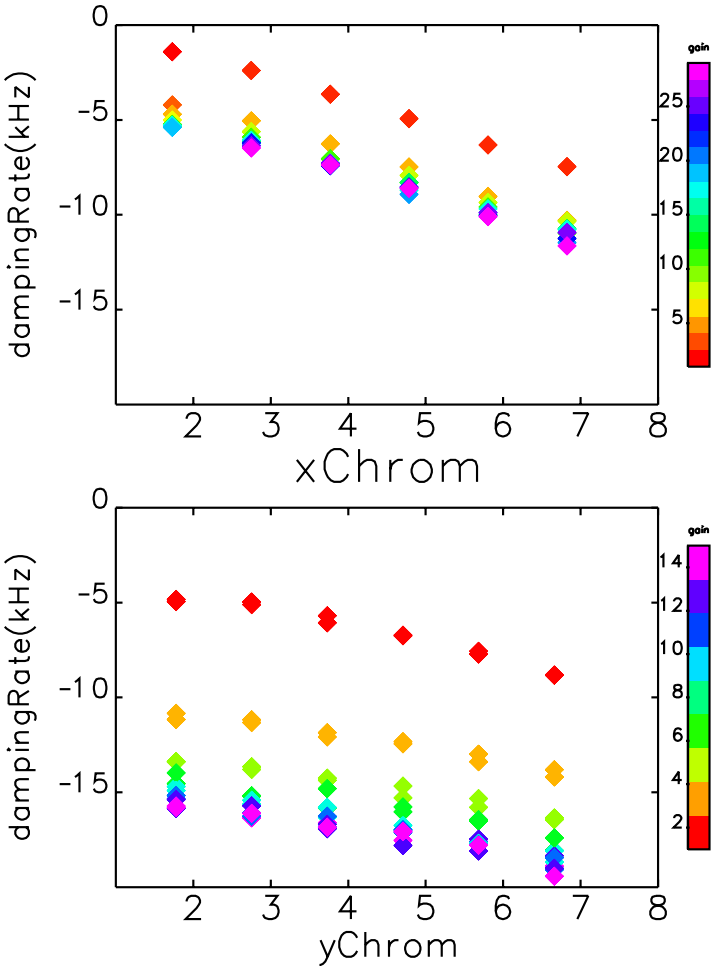

Figure 3.6-27: Damping rate versus chromaticities for different feedback system gains. Top: x-plane, Bottom: y-plane. This is the same data found in Figure 3.6-26.

Table 3.6-19: Simple estimates of largest allowed resonator impedances.

Quantity	Limit on Quantity[a]
$(R_s f_{\mathrm{HOM}})$ for one monopole HOM	0.44 MΩ-GHz [b]
R_s for one monopole HOM at 2 GHz	0.22 MΩ
R_t for one H-plane HOM	1.3 MΩ/m
R_t for one V-plane HOM	3.9 MΩ/m

[a] Estimates include the bunch form factor.
[b] Assumes a conservative bunch form factor for a 2-GHz HOM in all cases.

The utility of the Monte Carlo method can be demonstrated with a concrete example of a design reported in section 3.6.3.8.2 on single-cell superconducting cavities. The V-plane dipole HOMs (Table 3.6-20) are used to calculate the possible transverse instabilities for the 24-bunch fill pattern. Only a few of the HOMs are listed. Others were omitted for brevity because they have much lower R_t.

Table 3.6-20: V-plane HOM parameters used for Monte Carlo simulation.

Frequency (GHz)	R_t/Q (Ω/m)	Q_L [a]
3.02	878	68
3.06	240	797
3.43	449	144

[a] HOM dampers are included.

A calculation for eight cavities was performed with `clinchor`. The modal analysis uses the actual βs at the cavities and a bunch lengthening table (σ_z versus I_b) provided by the user. The frequencies can be randomized uniformly over an interval given by the user. We usually choose the default interval of f_0, giving a chance for any HOM to be centered on a beam frequency. The user can also vary the Qs for a given HOM data set, while maintaining the value of R_t/Q. This feature could be used in other projects, say, to provide a target for HOM damper designs. For the SPX project, the HOM Qs are considered as a given for a particular design, rather than adjustable. One could also specify a "target" staggering step for any of the HOM frequencies, as was done for the APS 352-MHz cavities for preventing overlap between resonators of different cavities. For now, we do not consider such staggering since the Q are expected to be so low that it would be difficult to avoid overlap.

One may ask whether, for a complete calculation, one should include all resonators in the ring, specifically those of the accelerating 352-MHz cavities. We do not presently have a good model of the HOMs of the as-built 352-MHz cavities that explains the observed lack of multi-bunch instabilities (up to 245 mA) that were generally expected. (There was one longitudinal HOM observed early on in one of the 16 cavities; this is now damped with a HOM damper.) It is possible that the resonator Qs in general are much smaller than those calculated earlier in the APS development, since the calculations did not (and could not) take into account damping through the coupler and waveguide network. Other factors not included are coherent damping from chromaticity and other de-coherence effects. It is assumed for the moment that the accelerating cavity HOMs do not contribute to multi-bunch instability when deflecting cavities are added.

The Monte Carlo results are presented as a histogram of the most unstable beam mode for each instance of randomized HOM frequencies in eight cavities. By way of example, Figure 3.6-28 gives such a histogram for the case where only the worst mode is used in the calculation of beam mode growth rates. In addition we plot the cumulative distribution of the most unstable beam mode growth rate, which is just the integral of the histogram. The cumulative distribution can be used to determine the probability of instability for a given natural damping rate, and thus is more useful to consider.

Note that the distribution in growth rates is quite small. This is due to the low Q values of the resonators and the absence of (large) staggering of frequencies. Randomizing the HOM frequencies for low-Q resonators does not have much effect but we performed it anyway to avoid surprises.

The cumulative distribution plot in Figure 3.6-28 also marks the 95th percentile of the distribution, a useful scalar quantity (less noisy than, say, the 100th percentile) that characterizes the distribution when doing scans of parameters.

The simulation with all HOMs is presented in Figure 3.6-29 for the 24-bunch and the hybrid bunch patterns, showing that the growth rates in the hybrid pattern are of the greatest concern.

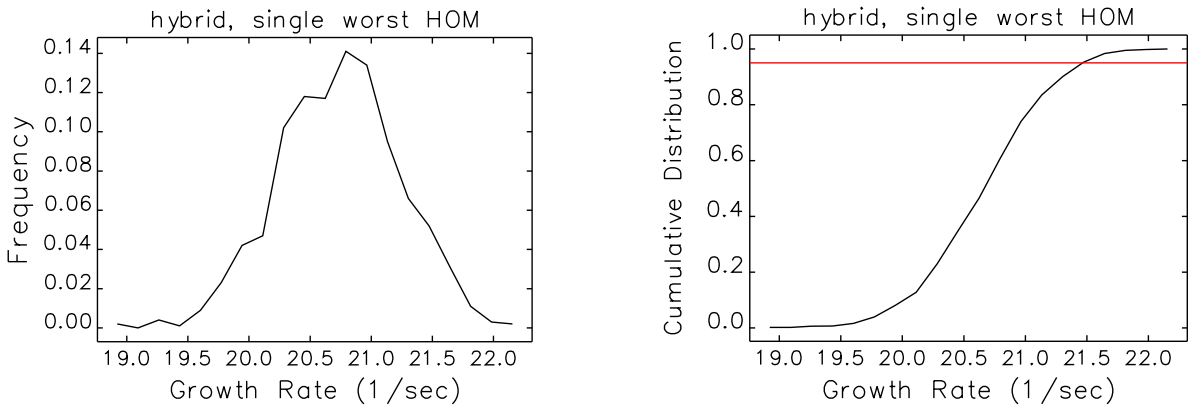

Figure 3.6-28: Distribution of growth rates of instability in the V-plane assuming only the worst dipole HOM. The red line marks the 95th percentile of cases. 1000 samples were calculated.

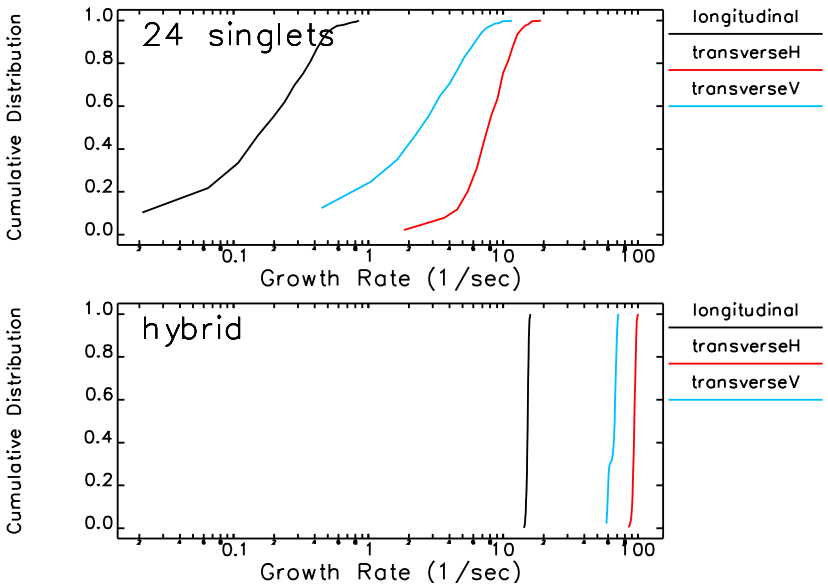

Figure 3.6-29: Distribution of growth rates of instability in the V-plane from an example set of dipole HOMs. The red line marks the 95th percentile of cases. 1000 samples were calculated.

The growth rates must be compared with the natural damping rates of single bunches, which is, at minimum, the synchrotron radiation damping rate, or depending on plane and the optics setting, the coherent damping rate. Data for the hybrid bunch pattern (the worst case) is collected in Table 3.6-21, from which we conclude stability for all planes and bunch patterns.

It was mentioned earlier that the cavity design has not been finalized and, in addition, that the real Qs will not be known until they are measured on the real cavities. If it turns out that the Qs for the as-built system are a little higher (and if the present accelerating 352-MHz cavities might contribute along with deflecting cavities to multi-bunch instabilities) then we might be transversely unstable if only synchrotron radiation damping was present.

The coherent damping rate, which we nominally do not need to invoke in order to conclude that we

Table 3.6-21: Summary of Monte Carlo simulation of instability assuming eight cavities.

Plane	Growth Rate[a] s^{-1}	Synch. Rad. Damping Rate s^{-1}	Coherent Damping Rate[b] s^{-1}	Comment
Longitudinal	15	208	Not applicable	Stable
Horizontal	98	104	4000	Stable
Vertical	70	104	6500	Stable

[a] Worst cases are all hybrid bunch pattern.
[a] Values for chromaticity of +7 and for bunch current of 2.5 mA, and minimum bunch-by-bunch feedback gain setting.

are transversely stable, provides a margin against such changes. The transverse damping rate in both planes were recently measured to be up to 8000 s^{-1} for a range of bunch current and chromaticity settings corresponding to what might be used in hybrid "mode," the bunch pattern for which we predict the highest growth rate. Also, other work has demonstrated the possibility of adjusting the hybrid bunch pattern to reduce the estimated worst-case growth rate by an additional factor of two if need be. In conclusion, we have a high level of confidence that we will not have an issue with multi-bunch instabilities.

3.6.3.3.2 Single-Bunch Effects and Requirements

The layout of the long-straight section (LSS) where the SPX system will be installed is shown in Figure 3.6-30. The SPX system in the storage ring will have a short-range wakefield effect on the beam very much like other impedance sources. The system has two different impedance elements, namely, nonuniform chamber (SPX chamber) and deflecting cavities. Compared to the standard LSS, the SPX chamber[4] will have extra transitions connecting the deflecting cavity pipe to the regular chamber.

The detailed 3-D computation by GdfidL shows that the vertical wake of the SPX chamber excited by a bunched beam is almost the same as for the LSS chamber, as shown in Figure 3.6-31.

The additional impedance source is the deflecting (or crab) cavity itself. The 3-D model of a cavity used in the wakefield computation is shown in Figure 3.6-32. The cavity aperture is 50 mm, a compromise between the desire to minimize wakefields and maximize the effectiveness of waveguide HOM damping (motivating a larger aperture) and the desire to improve deflecting performance (motivating a smaller aperture). With this aperture choice, four cavities at each end of the SPX zone will be needed to generate 2 MV for a total of eight cavities.

The vertical wake potential of a set of four cavities computed by GdfidL is compared with the SPX and LSS chambers in Figure 3.6-31, which shows that the cavity can significantly impact the vertical kick to the beam in the SPX zone in addition to the one from the SPX chamber.

Following the same simulation method used in establishing the APS impedance model, 200,000 macro particles were tracked using `elegant` [3.6-35] with the deflecting cavity impedance included. We compared the injection loss simulation with three different configurations: 1) ring without SPX cavities,

[4]When we refer to the "SPX chamber," we do not include the cavities, just the extrusion for IDs, a straight round pipe where the cavities would go and three taper transitions

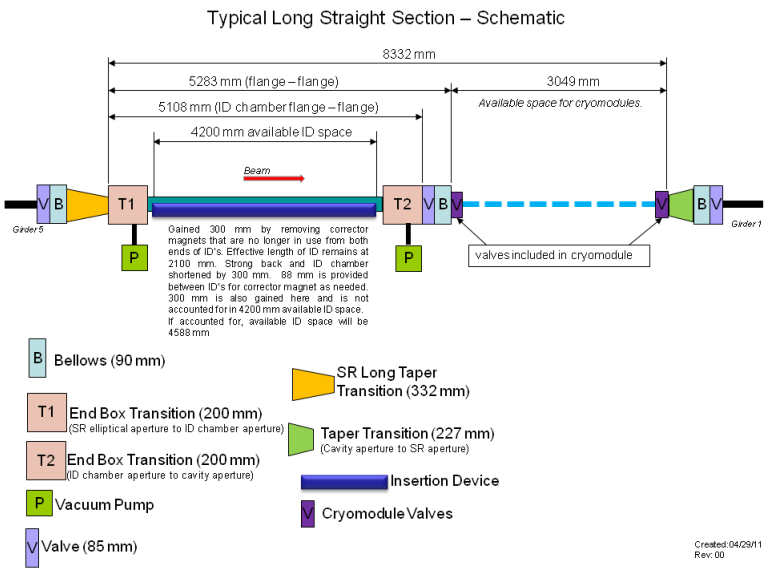

Figure 3.6-30: A long-straight section for the SPX system.

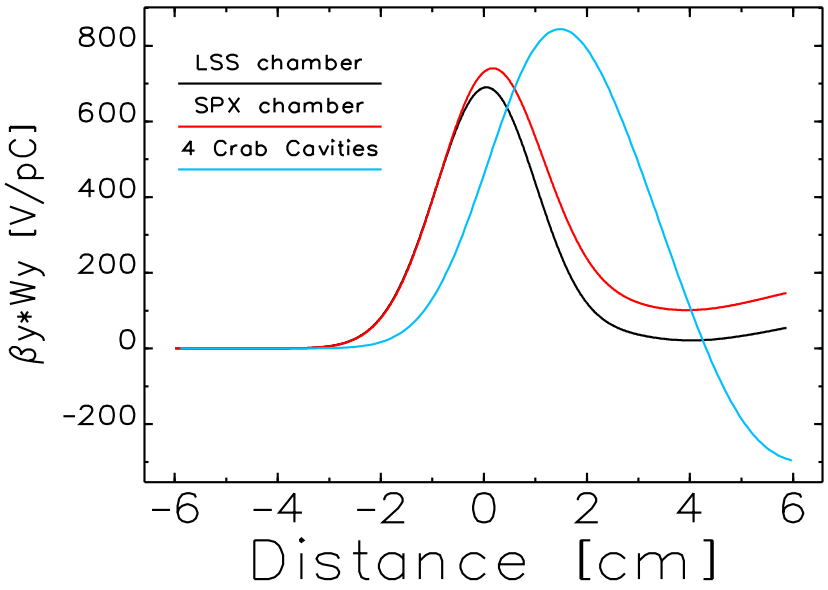

Figure 3.6-31: The vertical wake potential of four deflecting cavities excited by a bunched beam of σ_z = 1 cm compared with those of the LSS and SPX chambers.

2) ring with two sets of four SPX cavities totaling 2 MV, and 3) ring with two sets of eight SPX cavities totaling 4 MV of deflecting voltage. The circles in Figure 3.6-33 indicate the accumulation limit of single bunch at the chromaticity set at 9 in both planes. Interestingly the more SPX cavities installed in the ring, the higher the accumulation limit, as shown in Figure 3.6-33, which is opposite to the result reported for the pulsed crab cavity [3.6-50].

In the previous study [3.6-50], we investigated the effect of transverse impedance only. When the same method was applied to the SPX system, we observed a similar current reduction. However, as shown

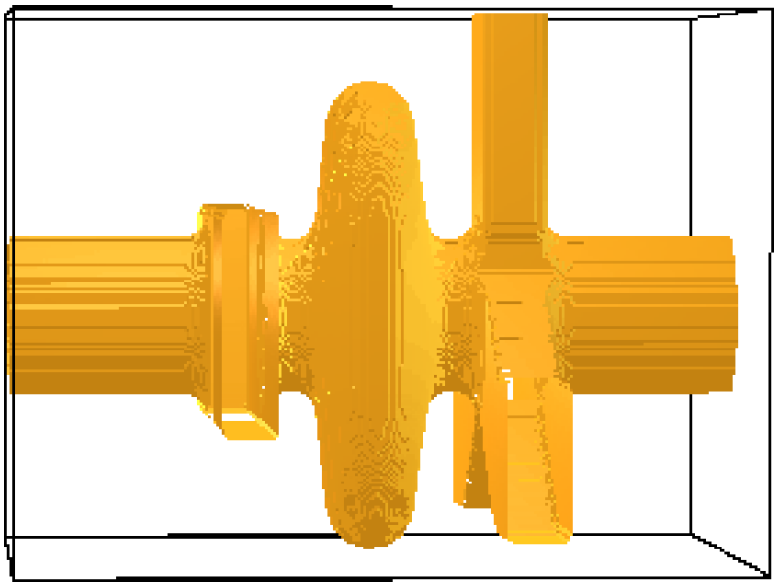

Figure 3.6-32: A GdfidL model of a superconducting deflecting cavity with input/output couplers for the wake potential computation.

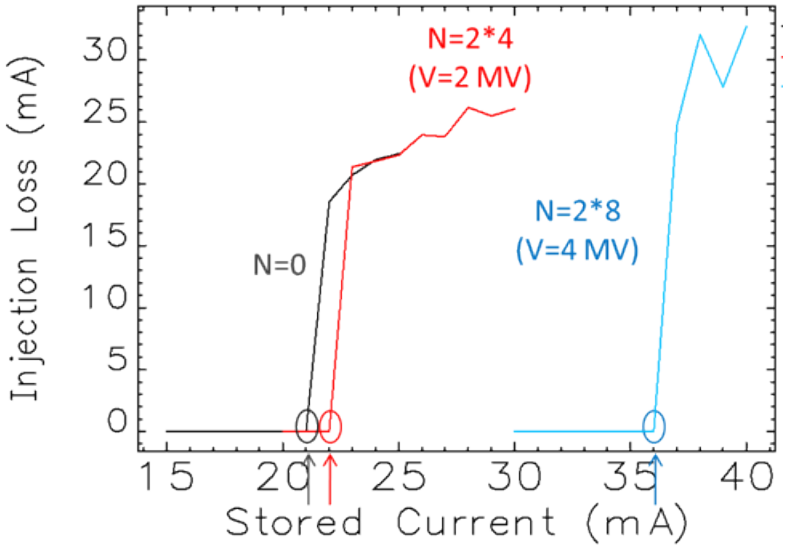

Figure 3.6-33: Injection loss simulation result that determines the single-bunch current limit.

in Figure 3.6-34, with the full 3D impedance including the longitudinal impedance, we found that the bunch was lengthened, which reduces the peak current. As a result, the transverse mode-coupling instability (TMCI) in the vertical plane was reduced in strength, leading to a small net increase in the single-bunch current for the 2-MV cavity system envisioned for the APS Upgrade. Thus, 16 mA can be delivered in a hybrid fill with the SPX system installed in the ring.

In the low-current regime below 6 mA, the increase in bunch length by deflecting cavities is not significant (Figure 3.6-34). This is compatible with the short-pulse operation of the SPX system in the

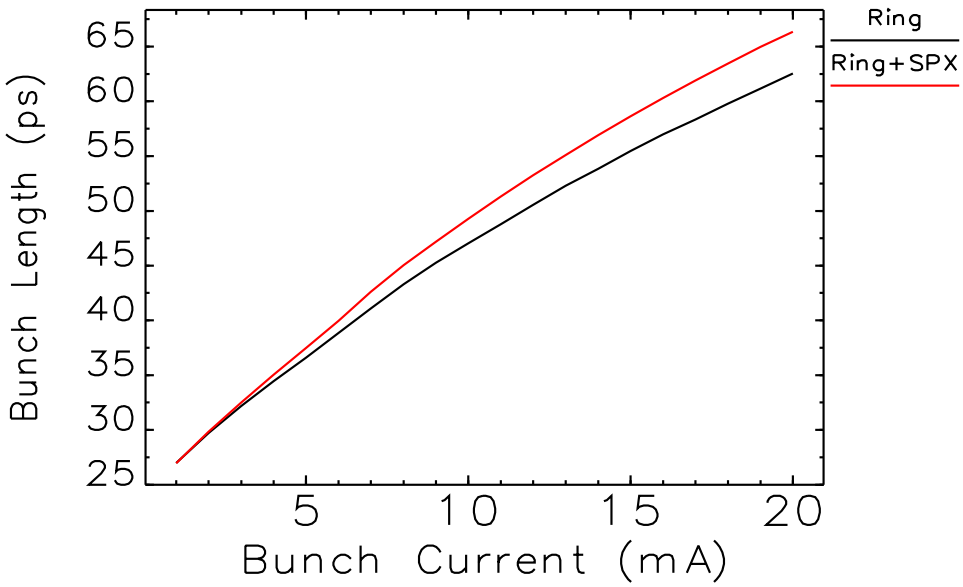

Figure 3.6-34: Bunch lengthening with and without deflecting cavities in the ring, assuming a total of eight deflecting cavities.

24-bunch mode, in which each bunch has 4-6 mA, below the microwave threshold.

Hence, the intensity of short pulses available in 24-bunch mode from SPX will not be affected much by collective effects introduced by the cavities. On the other hand, 16-mA operation in hybrid-fill mode may not be compatible with SPX operation because the coherent motion excited by the microwave instability will make it difficult to produce a precise chirp along the bunch. There are other challenges for SPX operation in hybrid mode, including the phase slew along the 56-bunch train. For these reasons, operation in hybrid mode is not contemplated.

In summary, with up to eight deflecting cavities installed in the ring, more than 16 mA can be stored in a single bunch. Hence, installation of the cavities will not jeopardize hybrid-mode operation. Collective effects with the presence of the cavities should not degrade SPX performance in 24-bunch operation at 150 mA.

Because the deflecting cavities lengthen the bunch, they might be seen as having a helpful effect for other upgrades. For example, we might be able to make other changes in the ring that increase the transverse impedance, without jeopardizing the ability to achieve 16-mA single-bunch current. One obvious possibility would be inclusion of several in-vacuum undulators (IVUs). However, we have elected not to pursue this possibility, for three reasons. First, the lengthening is not significant for the eight cavities included in the Project scope. Only with a much larger number of cavities would an appreciable benefit be seen. Second, we do not wish to link the success of one portion of the Project scope (insertion devices) to the implementation of another (SPX), since in principle the SPX component of the Project scope could be removed. Third, operation at higher single-bunch current would be a significant benefit to timing experiments, which are emphasized in the mission needs statement.

Hence, the APS Upgrade mission would benefit from any improvement resulting from the combination of SPX installation and careful preservation of the transverse impedance.

3.6.3.3.3 Emittance Degradation Due to Impedance

The performance of deflecting cavities generating short x-ray pulses has been investigated based on the single-particle dynamics. However, collective effects occurring within these two sectors may alter the beam dynamics in all planes in a significant way.

The vertical betatron phase, for example, may need to be readjusted because the (small) transverse impedance will detune the phase advance somewhat depending on the charge and shape of bunched beam. Such consideration will make simulations more realistic.

A preliminary simulation of multiparticle dynamics was performed using `elegant` [3.6-35] with an emphasis on vertical emittance degradation. The transverse impedances were added to the otherwise magnet-only lattice (the same one used in section 3.6.3.2) in three stages. At each stage the effect was assessed:

- Impedance of two sets of SPX cavities, each consisting of four deflecting cavities at Sectors 5 and 7. Each cavity impedance kicks the beam in both the x and y planes.
- In addition, chamber impedance of Sector 6 and Sector 7 between the SPX cavities, where the sector impedance was lumped at S6A:Q1 and S6B:Q1 for Sector 6 and at S7A:Q1 and S7B:Q1 for Sector 7.
- In addition, the chamber impedance of remaining sectors outside SPX, where the sector impedance was lumped at the center of each straight section.

Inside the SPX, the bunch will get an impedance kick proportional to the slice offset in the deflecting plane y. Outside the SPX there will be no impedance kick to the beam in an ideal machine because of the cancellation. However, if there will be any residual oscillation in the transverse plane, the emittance may be further degraded because of the impedance. In order to see such effects quantitatively, we tracked 30000 particles over 5000 turns following the same method described in section 3.6.3.2. We used the same lattice with 2-MV deflecting voltage. The current was 6.25 mA with 41-ps rms bunch length. The result was compared with the reference emittance, which was obtained over the 5000 turns without impedance; any increase in emittance then was attributed to the impedance effect.

The emittance with various impedance elements in the ring is plotted in Figure 3.6-35 together with the one without impedance. For the simulation parameter consistent with the APS Upgrade, we could not resolve any impedance effect on the vertical emittance.

3.6.3.3.4 Work Remaining

In the work just reported, we did not include the effect of longitudinal impedance, which would require a nominal simulation condition of 200,000 particles and 10,000 turns, taking a week on a 100-core cluster. However, we believe that the self-consistent simulation is important in predicting the SPX performance, so we plan to continue these simulations using larger computing resources. This study will use the lattice with full magnets and impedances, exploring the effect of closed orbit distortion, different injection kicker settings, feedback operation, and SPX cavity errors along with other operational conditions of the ring.

The collective effect simulations for SPX were mainly developed in the context of instability modeling and are believed to give accurate predictions on single- and coupled-bunch effects. Usually, the study

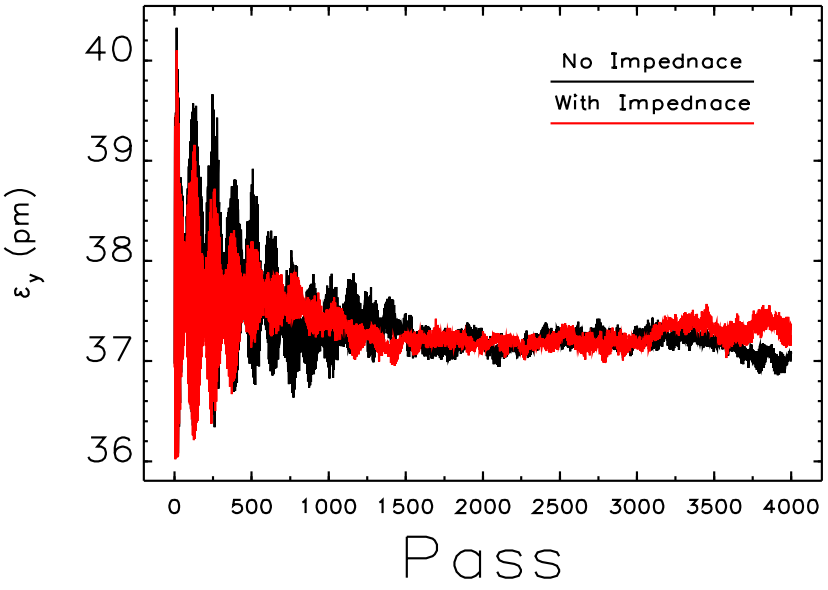

Figure 3.6-35: Vertical emittance with various impedance elements in the ring. See text for explanation.

of collective effects stops here. However, for unconventional situations, such as the APS Upgrade with SPX, the performance-related simulation of emittance degradation is an important issue. For this purpose we will need to simulate the ring as closely as possible to the situation found in realistic operation, which will require large-scale computation on 1000s of cores.

3.6.3.4 High-Power RF System [U1.03.03.01]

This section describes the technical requirements and preliminary design of the SPX high-level rf (HLRF) system. The HLRF system encompasses all rf drive line components and support hardware between the output of the low-level rf control system and the rf input flanges of the deflecting cavity cryomodules, including equipment and personnel protection interlock systems.

3.6.3.4.1 HLRF System Specifications

The SPX HLRF system is required to produce and deliver sufficient rf power at a nominal operating frequency of 2815.44 MHz to the rf input flanges of the eight rf-cavity cryomodules in the SPX rf system in order to generate a nominal deflecting voltage of 500 kV per cavity. Eight 2,815.44-MHz/10-kW cw rf amplifier systems provide rf power to the SPX deflecting cavities, arranged one amplifier per cavity. These amplifier systems are composed of numerous components and sub-systems to provide amplification of the low-level rf drive signal to a maximum continuous output of 10 kW cw, as well as a slow and fast hardware protection interlock system, a personnel safety system, an ACIS/rf interface, a local programmable logic controller (PLC)-based control and monitor system providing local and remote control of each HLRF amplifier system, 8 waveguide transmission systems to provide low-loss power transmission between the amplifier outputs and cavity-cryomodule rf inputs, and remotely located slow and fast rf interlock systems providing equipment protection for the cavity-cryomodule assembly. Each amplifier system also provides process variable readback for the amplifiers as well as for the

cavity-cryomodule system, and personnel safety-related interlock functionality to control rf radiation, high-voltage, and storage ring tunnel radiation hazards. All amplifier components and sub-systems are contained within an aluminum enclosure that is 53.75 inches wide, 77.25 inches tall, and 36 inches deep. The enclosure is designed with one full-height 19-inch equipment rack, and one 30-inch wide compartment housing the klystron, high voltage box, isolator, output waveguide system and water manifolds. Each amplifier system is cooled by de-ionized (DI) water provided by the APS main DI water plant, at a total flow of approximately 40 GPM. The DI water supply shall have a nominal temperature of 90°F, resistivity of 10 MΩ-cm, a pH of 7, and be delivered at a maximum supply and return pressure of 120 psig and 30 psi, respectively.

3.6.3.4.2 HLRF System Topology

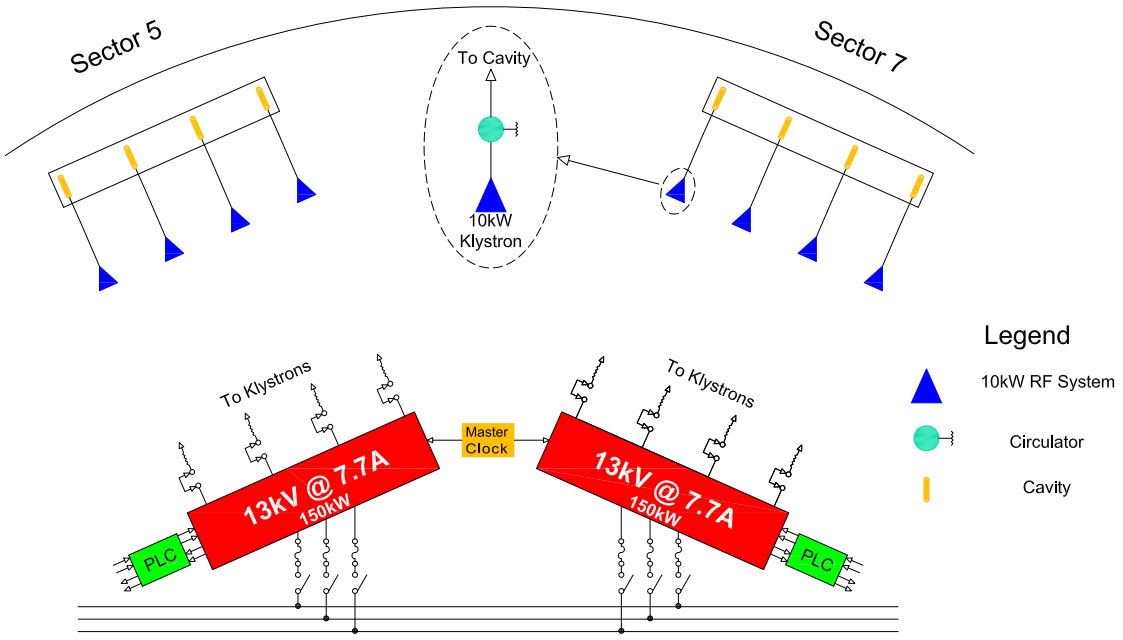

Figure 3.6-36: SPX HLRF system block diagram showing 10-kW rf amplifiers, 150-kW klystron power supplies, and waveguide feeds to cavities located in Sectors 5 and 7.

The SPX HLRF system is comprised of eight 2815.44-MHz/10-kW cw rf amplifier systems, four located in Building 400A-1 for driving rf cavities in Sector 5, and four in Building 400A-2 for driving rf cavities in Sector 7 (see Figure 3.6-36). Two 150-kW high-voltage power supplies (HVPSs) will be utilized to provide klystron beam power, arranged with one HVPS supplying beam power to all of the 10-kW amplifiers in each sector in parallel. Eight separate WR284 waveguide transmission systems are utilized to transmit rf power from the output of each 10-kW amplifier to its respective rf cavity input flange in the storage ring tunnel. Two cavity-cryomodule equipment interlock systems are located on the APS storage ring mezzanine, directly above the cryomodule.

3.6.3.4.3 10-kW Amplifiers

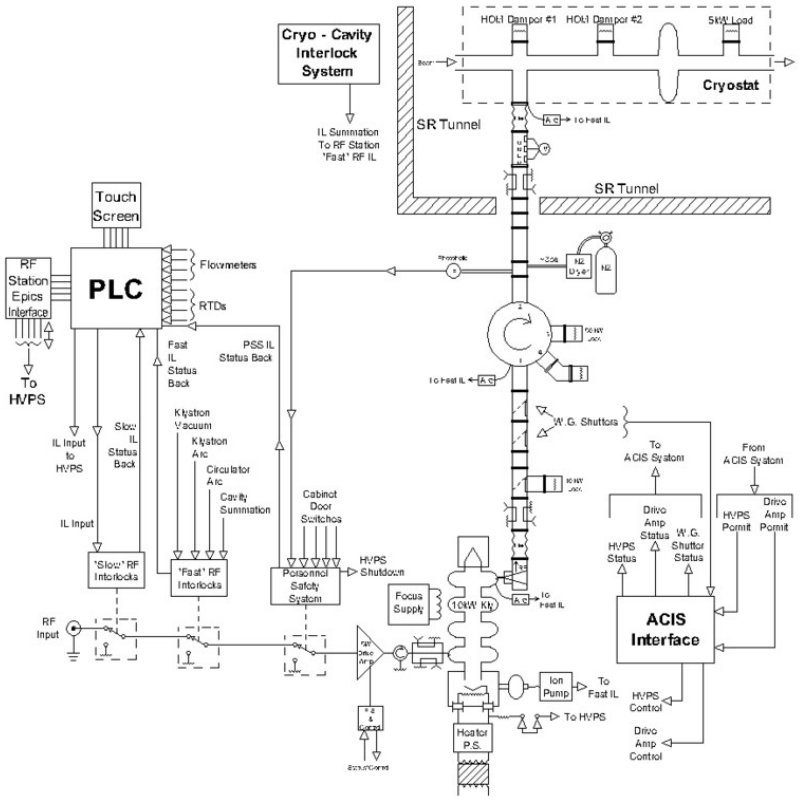

Figure 3.6-37: SPX 10-kW rf system diagram showing internal amplifier subsystems, cavity equipment interlock systems, and details of the waveguide transmission system from the klystron to the deflecting cavity.

Each 10-kW amplifier consists of a 2,815.44-MHz klystron and associated heater power supply; an output waveguide assembly that includes a 50-kW isolator; supply and return water distribution manifolds with flow and temperature sensing instrumentation; and self-contained sub-assembly chassis units providing specific control and monitoring functions for the amplifier. These sub-systems include a personnel safety interlock system; an Access Control Interlock System (ACIS)/rf interface; a klystron rf driver amplifier; master fast and slow rf equipment protection interlock systems; and a control PLC for implementing master slow rf interlock functionality, local touch screen monitoring and control, and providing a network gateway for EPICS remote control and monitoring of the amplifier. A block diagram of the 10-kW rf amplifier system is shown in Figure 3.6-37. A 4-port waveguide isolator is utilized at the output of the klystron to minimize reflected power at the klystron output window, and to maintain a terminating load for rf power propagating back from the deflecting cavity. The isolator is required to maintain a minimum of 30-dB return loss at the klystron output flange over a bandwidth of $\pm$ 5MHz centered on the SPX operating frequency, and has a maximum power handling capability of 50-kW cw. The isolator utilizes two integral water-cooled rf loads, and is fitted with WR284 flat flanges at port #1 (klystron output) and port #2 (amplifier output). The klystron drive amplifier is a solid state S-band cw power amplifier that provides a minimum of 40-dB rf gain to amplify the low-level rf drive signal to a level sufficient to drive the klystron to full power. It is powered by 120 VAC/60

Hz delivered by a dedicated connector on the rear of the chassis to insure that AC line input power is supplied only by the ACIS rf interface chassis. The driver amplifier includes an internal 28-V power supply, output circulator, an output directional coupler that provides a -20-dB sample of the rf drive signal to the klystron, and an internal electromechanical rf relay that is controlled by the master slow rf interlock system PLC and provides a terminating series rf switch to disable rf output of the amplifier in response to rf interlock trips. The ACIS/rf interface provides functionality for the SPX ACIS to disable each SPX rf amplifier and associated high-voltage power supply by redundant methods in order to disable the x-ray radiation hazard created by the SPX deflecting cavities when the storage ring tunnel is open to personnel access. Control and monitoring of the amplifier system is achieved by an internal PLC system that provides a front-panel touchscreen for local control of amplifier functions and parameter monitoring, and also interfaces to EPICS to provide remote control functions and readback of amplifier parameters. The control PLC also provides master slow rf interlock functionality related to amplifier internal hardware interlocks, and also to the cavity/cryomodule rf interlock systems through external inputs.

3.6.3.4.4 Waveguide Transmission System

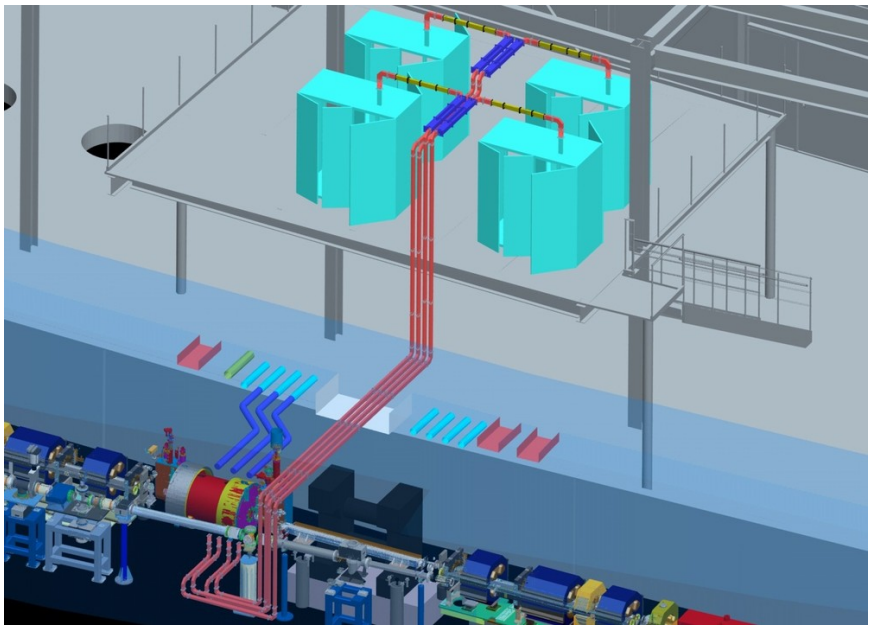

Figure 3.6-38: Pictorial diagram showing the installation of four 10-kW SPX rf amplifiers (green) and associated waveguide installations (red) in Building 400A-1. The low-pass LOM waveguide filters are shown in dark blue.

The waveguide transmission system provides a low-loss rf transmission path between the klystron output flange and the rf input waveguide flange on the cryomodule assembly. A pictorial of the SPX rf amplifiers and waveguide installations in relation to the storage ring and cryomodule is shown in Figure 3.6-38. The waveguide system consists of aluminum WR284 waveguide components fitted with connector pressurized rectangular flat (CPRF) flanges. Internal to the 10-kW amplifier cabinet the waveguide system includes a 6-inch flex section, dual directional coupler, a 2-position waveguide switch and associated 10-kW test load, 2 waveguide shutters, and a 4-port isolator. Two WR284

waveguide shutters are included in the output waveguide transmission line between the klystron rf output flange and the input (port #1) of the isolator to provide a method of administrative control to control rf radiation hazards when the amplifier is under test. The shutters are rated for a power handling capability of 10-kW cw in both open and closed positions, and each shutter provides a minimum of 70-dB isolation in the closed position. The shutters are fitted with auxiliary contacts to provide remote position indication in order to interlock rf power when the shutter is not fully in the open or closed position. A 10-kW water-cooled WR284 rf test load and 3-port, H-plane WR284 waveguide switch are included in the output waveguide transmission line between the klystron rf output flange and the first waveguide shutter. The load and switch comprise a switchable full-power test load that will provide the ability to troubleshoot and test the amplifier at full output power without opening any part of the waveguide transmission system. The waveguide switch is fitted with auxiliary contacts to provide remote position indication to the amplifier control PLC to interlock rf power when the switch is not fully in either selectable position.

Waveguide components external to each amplifier cabinet include a low-pass absorptive waveguide filter for attenuation of lower-order mode (LOM) power generated by the deflecting cavity, 2-directional couplers dedicated to diagnostics and low-level rf use, and a motorized waveguide tuner for adjusting cavity loaded Q. For personnel protection against rf radiation hazards, the waveguide system is pressurized with dry nitrogen to approximately 5-psi from a gas port on the isolator. This positive gas pressure is used to detect openings in the waveguide system that could be potential rf radiation hazards. The internal waveguide pressure is monitored by a Photohelic® gauge that provides an interlock contact to the personnel safety interlock chassis, which will disable the rf drive and high voltage to the klystron if the waveguide pressure drops below a pre-determined trip point. A loss of nitrogen pressure in any of the SPX rf system waveguides will also open an auxiliary nitrogen pressure interlock contact, which is connected to an input of the existing Waveguide Air Interlock System, located in Building 420. This contact will disable all of the 352-MHz rf systems in order to remove beam power from the storage ring as a source of rf power that could leak from an open SPX waveguide system. The expected transmission loss of the waveguide system between each 10-kW amplifier and its respective rf deflecting cavity is approximately 1 dB, resulting in a maximum deliverable rf power of 7.9 kW to the cavity flange.

3.6.3.4.5 Klystrons

The klystron is designed for continuous operation at a center frequency of 2,815.44 MHz at a maximum continuous rf power output of 10-kW cw, with an absolute maximum rf power output capability of 12-kW cw. The klystron will utilize a WR284 CPRF flange output port, diode gun, full-power collector, and permanent magnet focusing. The klystron will be fitted with all shielding necessary to limit ionizing radiation to no more than 0.50 mrem/hour at any point 1 meter from any part of the klystron at rated power output. Other critical specifications for klystron include a 1-dB bandwidth of 7 MHz, a minimum operating efficiency of 50%, 20-kV maximum beam voltage, and a maximum physical length of 32 inches.

3.6.3.4.6 High-Voltage Power Supplies

Two 150-kW, very low ripple, low stored energy, high voltage power supplies will be used to provide beam power for the SPX klystron amplifiers, one located in Building 400A-1 and one in Building

400A-4. Each power supply is designed to provide sufficient beam power for up to four 10-kW amplifier cabinets, and will utilize de-ionized water for cooling. Both power supplies are fed primary input power from a common 480-VAC/3-phase bus to correlate the effects of Ac line noise, and will operate at a minimum of 90% efficiency. Each power supply will provide continuous 150-kW output power at a maximum output voltage of 20 kV, no greater than 5-V peak-to-peak output ripple at all ripple frequencies out to 10 kHz from 25-100% nominal load, and a maximum stored energy of 10 J. Each power supply is designed with eight individual fused outputs with manual disconnect switches in order to provide lock-out/tag-out isolation of individual rf amplifier systems to expedite maintenance or repair.

3.6.3.4.7 Equipment Protection Interlocks

The SPX rf equipment protection interlock system consists of master slow and fast interlock sub-systems located in each 10-kW amplifier, each of which is connected to companion slave slow and fast interlock sub-systems remotely located on the storage ring mezzanine at the cryomodule locations in Sector 5 and Sector 7. A block diagram of the equipment protection interlock system is shown in Figure 3.6-39. The Cryomodule RF Interlock System includes all hardware necessary to implement equipment protection interlocks for the cryomodule and rf cavity components within. It consists of a PLC-based slave slow interlock and an electronic slave fast interlock system, both of which communicate with the main slow and fast interlock chassis in each amplifier system through dedicated wire and optical links in order to form two separate slave-master configurations. The slow interlock PLC system also serves as a gateway to the network-based EPICS control system. The Slow Cryomodule Interlock System provides monitoring and interlock functions for multiple system parameters including LOM and HOM damper water flow rates, return temperatures, infrared monitors on rf windows, thermal diode outputs, thermocouple temperature readbacks, and damper waveguide heater status and control. The detection of any fault conditions by the PLC will result in a latching trip command that is relayed to an external input to the master slow interlock in the rf amplifier system using a single-pair copper circuit. The trip command will cause the master slow interlock in the amplifier to interrupt rf drive to the klystron and latch in the rf-off position if any of the designated interlock alarm limits are exceeded.

Operator-adjustable alarm limits on all interlocked parameters are manually entered into the PLC system using the operator interface touchscreen. The PLC also performs calorimetric power calculations on all cooling-water circuits and displays the calculated power value on both the local touchscreen and as a process variable in EPICS. The response time of the system from first detection of a fault condition to removal of rf drive to the klystron is 20 milliseconds. The Fast Cryomodule Interlock System provides interlock functions for multiple fault conditions including arc detectors on forward power coupler and damper waveguide rf windows, vacuum pressure in the cavities and waveguides, cavity overpower and over-field conditions, and a cavity quench detection signal provided by the low-level rf system The detection of any of these fault conditions will result in a latching fault signal trip command that is relayed to an external input of the master fast rf interlock chassis in the rf amplifier system using a fiber optic link. The trip command will cause the master fast interlock in the amplifier to interrupt rf drive to the klystron and latch in the rf-off condition until a manual reset command is issued by the system operator. Trip points for all fast interlock signals are manually adjusted by potentiometers in the fast interlock chassis. The response time of the system from first detection of a fault condition to removal of rf drive to the klystron is 10 microseconds.

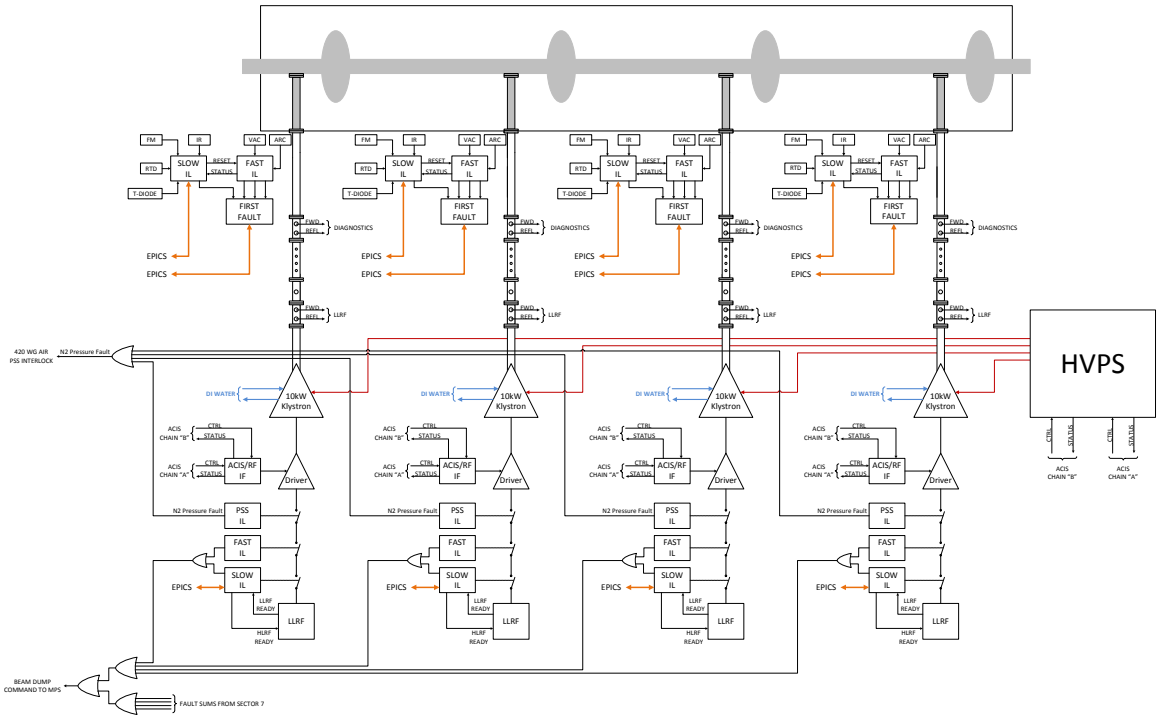

Figure 3.6-39: Block diagram of the SPX rf equipment protection interlock system.

First fault detection is provided by the interlock systems to aid in system troubleshooting when interlock system trips occur in response to multiple simultaneous fault conditions. A first-fault indication will be available on both the local touchscreen and as a status indicator in EPICS. First-fault detection in the Cryomodule RF Interlock System will be implemented by providing individual channel status outputs from the fast interlock electronics chassis to a multiple-input time stamp module that will determine the order in which fault signals occurred. The time stamp module will also interface to EPICS and provide a remote indication of relative fault timing.

3.6.3.4.8 SPX Personnel Safety Interlocks

Each 10-kW amplifier system contains a personnel safety system (PSS) that consists of a single chassis that provides personnel protection against known personnel safety hazards of the SPX rf systems, including exposure to high voltage within the amplifier enclosure and rf radiation hazards from openings in the waveguide transmission system anywhere between the klystron output window and the cryomodule rf waveguide input flange. The chassis also provides two spare contact inputs for connection to future personnel safety devices that provide a contact closure fault output, and includes all relay logic necessary for PSS interlock functionality, a waveguide nitrogen pressure meter, an operator key switch, an emergency stop button, an internal electromechanical rf relay to inhibit rf drive to the klystron in the event a PSS fault condition is detected, and a dedicated relay to generate a dry interlock contact that is used to shut down the klystron HVPS. Upon detection of a PSS fault condition, the PSS chassis will latch in the fault state and interrupt rf drive to the klystron by opening the electromechanical rf relay internal to the PSS chassis and shut down the klystron HVPS by opening the relay contact that is providing an interlock contact closure to the klystron HVPS. A block diagram

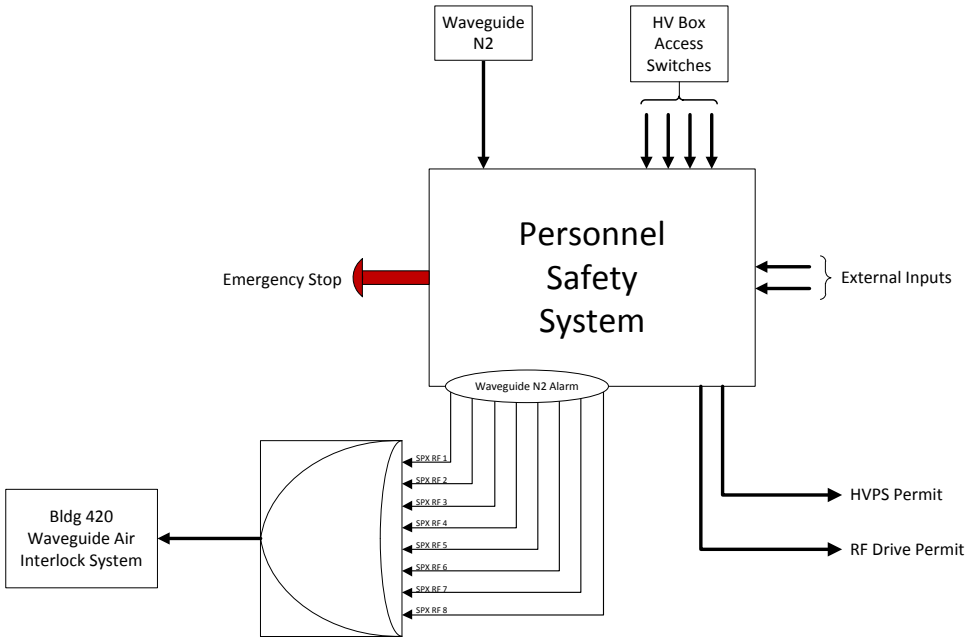

Figure 3.6-40: SPX personnel protection interlock system block diagram.

of the SPX PSS is shown in Figure 3.6-40.

3.6.3.4.9 ACIS/RF Interface

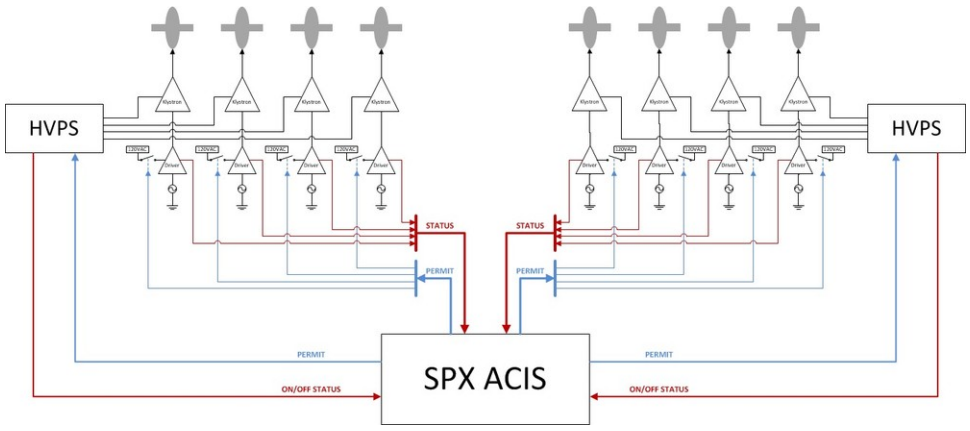

Figure 3.6-41: Diagram showing method used for ACIS to control and monitor the SPX rf systems.

The ACIS/rf interface provides functionality and system interconnection necessary for the SPX ACIS to disable each of the SPX rf amplifier systems by redundant methods in order to control the x-ray radiation hazard created by the SPX deflecting cavities when the storage ring tunnel is open to personnel access. The interface provides the hardware connectivity necessary for the SPX ACIS to independently inhibit operation of both HVPS units and all SPX klystron rf driver amplifiers when the storage ring tunnel is not in beam-permit mode. The interface chassis is controlled and monitored by

redundant interlock chains that are part of the SPX ACIS hardware. HVPS operation is inhibited by de-energizing a contactor supplying 480-VAC/3-phase primary input power to the HVPS inverters, and the driver amplifiers are inhibited by de-energizing a relay that is in series with the 120-VAC primary power input of each amplifier. The interface also provides hard-wired dry-contact signaling to the SPX ACIS from both HVPS units and all driver amplifiers to verify that they are in a safe state. A block diagram of the system is shown in Figure 3.6-41.

3.6.3.4.10 SPX Rf Machine Protection System Interface

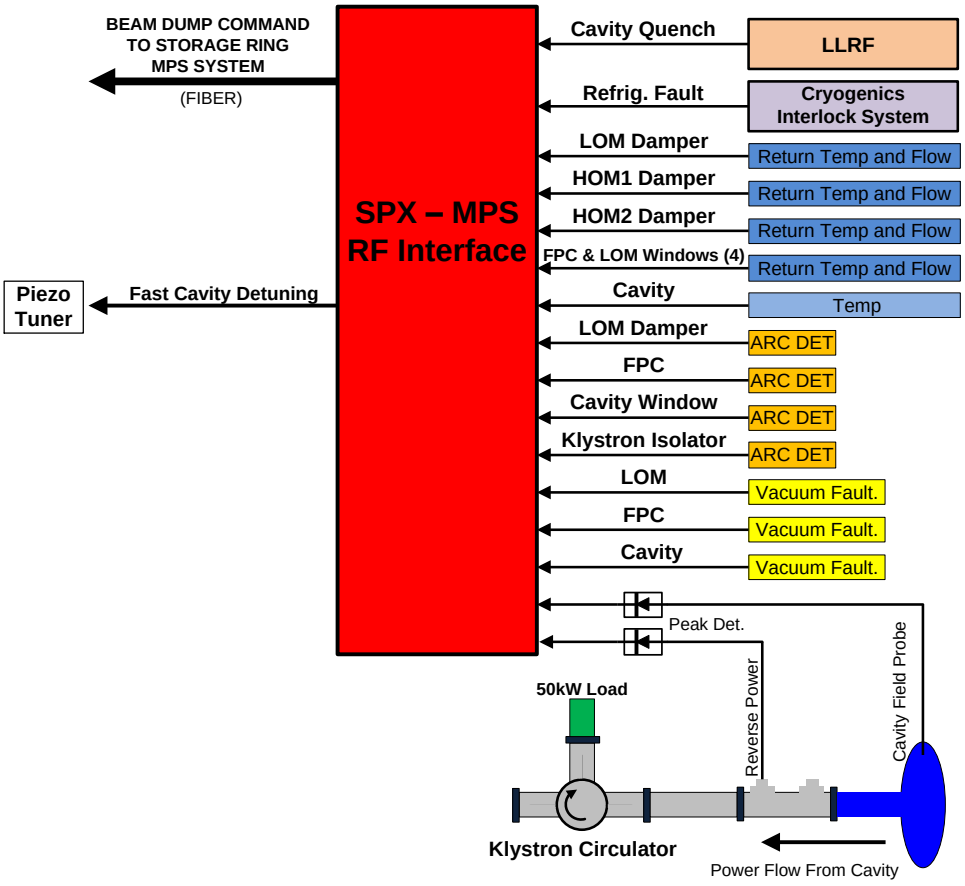

Figure 3.6-42: Block diagram of the SPX rf machine protection system interface.

The SPX rf cavities and HLRF system are protected from damage due to rf power generated by a beam-cavity interaction by decoupling the rf cavities from the beam when a fault condition is detected. A select group of interlock system faults are monitored to detect fault conditions related to power coupled from the storage ring beam. A block diagram of the interface is shown in Figure 3.6-42. These interlock faults include overpower events involving the rf cavity, LOM and HOM dampers, rf amplifier output circulator, and rf windows, and other fault conditions relating to cryogenic systems, vacuum pressure, quench detection, and rf arcing events at the cavity rf windows and the rf amplifier isolator. If such fault conditions are detected, a fast cavity detune command is initiated, which will employ rf cavity piezo tuners to rapidly shift the cavity resonant frequency and decouple the cavity from the beam. If detuning rf cavities does not clear the fault condition, an optical beam-permit signal generated

by the SPX rf interlock systems signals the APS machine protection system (MPS) to initiate a beam dump command.

3.6.3.5 Low-Level Rf [U1.03.03.02]

The purpose of the low-level rf (LLRF) system is to provide amplitude and phase control at the most basic level of individual cavity control while interfacing to the the deflection controller (see section 3.6.3.7), which provides vector-sum type control using beam-based feedback strategies.

3.6.3.5.1 LLRF System Architecture

The SPX rf system will consist of a total of 8 individually driven single-cell superconducting radio-frequency (SRF) cavities. There will be a total of two cryomodules with four cavities in each crymodule. The cryomodules will be separated by two storage ring sectors, or approximately 50 meters. The LLRF system will be partitioned into two separate sector-level LLRF systems as depicted in Figure 3.6-43. At each sector the LLRF system will consist of:

- Four individual LLRF controllers, each of which provides an intermediate frequency (IF) digital front end, FPGA-based individual cavity closed-loop control, a real time data link (RTDL) set point and waveform monitoring interface to the control system, interlock signal interface to the SPX equipment protection system, a slow digital-to-analog converter (DAC) output as the programmable DC bias voltage to the cavity piezo tuner driver, and trigger inputs from the timing/event system to support time-stamping and correlated system measurements.
- Four analog front ends (AFEs) to up/down-convert to/from S-band from/to the IF.
- The LLRF sync head provided by the timing and synchronization system (see section 3.6.3.6). This contains the passive cal-tone summation hardware that provides phase-drift compensation of the LLRF receiver chain as well as the fiber optic components used for the timing/synchronization phase reference.
- A phase reference splitter chassis to distribute the single sync head phase reference output to each of the four LLRF receiver chains.
- A local oscillator (LO) distribution chassis to distribute the timing and synchronization system-supplied LO signal to the LLRF AFEs for down-conversion and to the LLRF controllers for a clock reference.
- A cal-tone amplifier chassis to provide adequate cal-tone signal level to the sync head. Only one cal-tone signal will be required per sector; thus the cal-tone will be taken from only one of the four AFEs.
- A single 4-cavity JLab 12-GeV upgrade-style slow tuner driver chassis to drive the cavity slow-tuner stepper motors. The slow tuner driver electronics are considered to be part of the LLRF system, while the motors and tuners themselves are considered part of the cavity/cryostat system.

- The SPX cavities may have a piezo tuner option for fast detuning purpose. Therefore, provisions will be made for a slow DAC output on the LLRF controller.

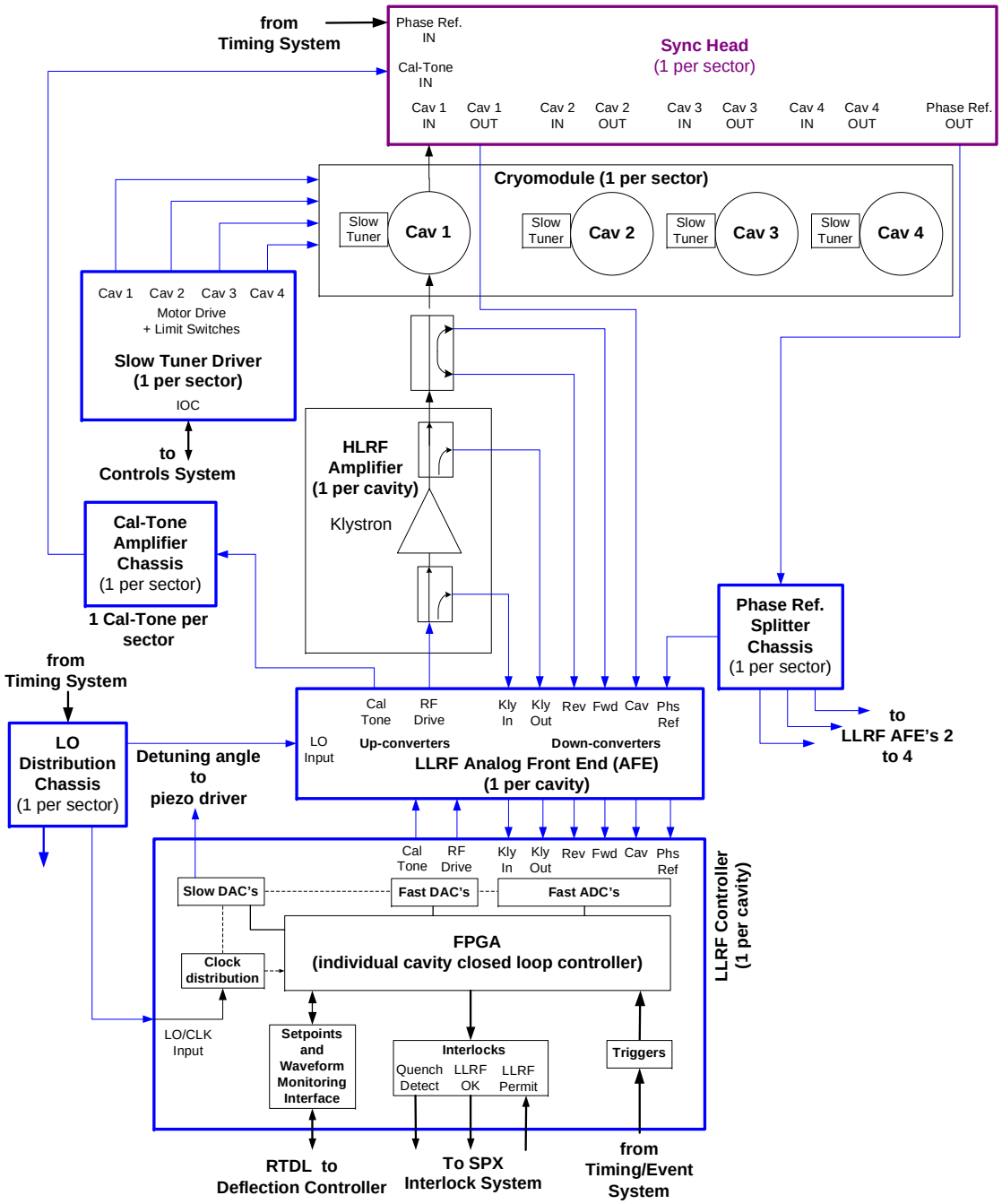

Figure 3.6-43: Sector-level LLRF system block diagram.

The LLRF system in general will provide the following functionality:

- Individual cavity amplitude, phase, and tuning control.

- Klystron drive and output signal monitoring, and optionally a klystron loop if klystron noise performance warrants the use of feedback around the klystron.
- Drift compensation of the LLRF cabling and receivers at the individual cavity level as described in section 3.6.3.5.2.
- Output of a piezo tuner drive voltage from a slow DAC to facilitate piezo-based cavity tuning.
- Interfacing to the RTDL used to communicate to the deflection controller as described in section 3.6.3.7. It has been generally agreed that Controls will undertake the responsibility of the development of the required RTDL interface card as the host interface to the LLRF system while the LLRF system will provide the LLRF local bus as described in section 3.6.3.5.3.
- Interfacing to the SPX equipment protection as described in section 3.6.3.4 to provide cavity quench protection and allow removal of LLRF drive signals.

3.6.3.5.2 Calibration-Tone-Based LLRF Control Scheme

The stringent SPX rf phase stability requirement extends down to 0.01 Hz, which is almost DC. Achieving the required phase control precision relies on an effective method of measuring and compensating the inevitable phase drifts in the rf signal channels to be measured. For this reason, an rf pilot-tone (or "calibration-tone")-based rf calibration scheme is adopted in the SPX LLRF control system to meet the challenge. A successful implementation of such a pilot-tone calibration scheme in accelerator timing and instrumentation was developed at Lawrence Berkeley National Laboratory, and promising results were reported [3.6-51]. Its principle of operation is to have a temperature controlled "sync-head" installed at the origin of the critical signals where they are to be transmitted across the rf signal channels to the digital vector signal receivers. In the case of the SPX LLRF, the critical signals are the cavity probe signal and the rf phase reference signal, and the origin of the signals where the sync-head is installed is at the cavity/cryomodule. A double-sideband rf calibration tone is mixed into the cavity probe ("CAV") and the phase reference signal ("REF") in the sync-head, as illustrated in Figure 3.6-44.

Upon the reception of the rf signals by the digital receiver, the phase of the carrier frequency signal CAV and REF, as well as that of the calibration-tone in the rf signals CAL-U and CAL-L are measured in real time, and the amount of phase drifts in the rf signal paths (from the sync-head to the ADCs of the digital receiver) are also computed in real time by a simple algorithm:

$$\phi_{\text{REF,SIG}} = (\phi_{\text{RF,REF}} - \phi_{\text{RF,SIG}}) - (\phi_{\text{CALU,REF}} - \phi_{\text{CALU,SIG}})/2 - (\phi_{\text{CALL,REF}} - \phi_{\text{CALL,SIG}})/2. \quad (3.6\text{-}55)$$

A more specific SPX LLRF system configuration with the phase drift calibration on the critical signal paths is shown in Figure 3.6-45. It is important to note that the calibration-tone of LLRF only captures the phase drifts in the critical rf signal paths from the sync-head to the LLRF digital receiver. The rf phase reference is delivered to the sync-head from the SPX timing and synchronization system through an optical fiber. The phase drift in the optical fiber is detected by the LLRF phase stabilizer in the SPX timing and synchronization system as described in section 3.6.3.6 and passed on to the LLRF system as a correction term.

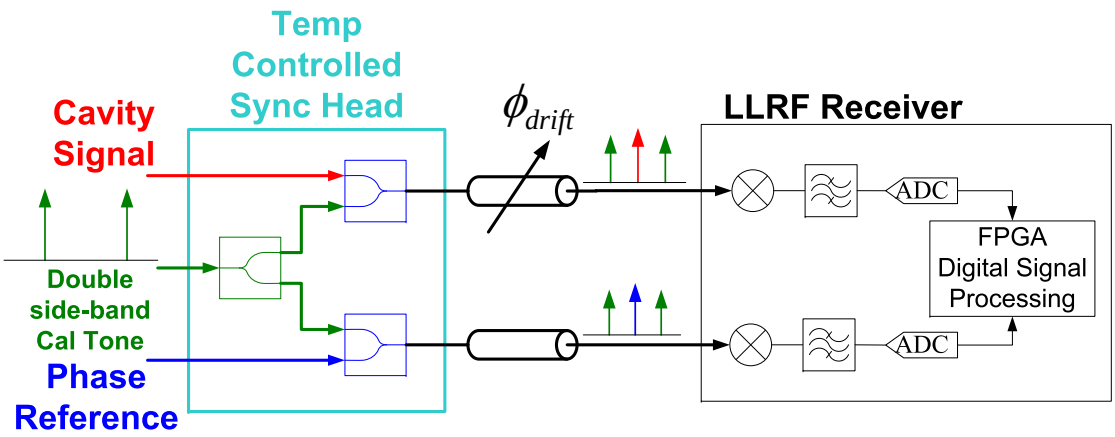

Figure 3.6-44: Principle of operation of rf channel phase drift calibration scheme with "Cal-tone."

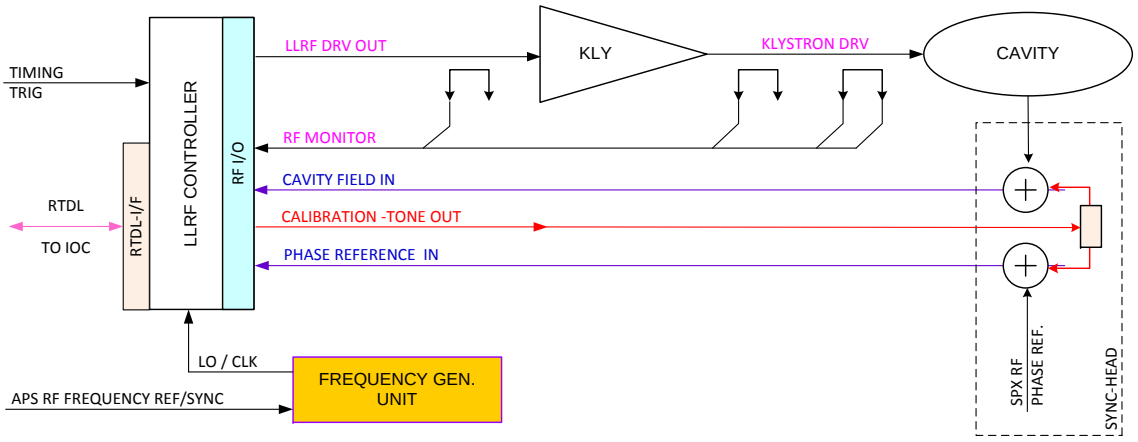

Figure 3.6-45: Conceptual design of a calibration-tone-scheme-based LLRF system for SPX. Only one LLRF sub-system for one cavity is shown here. There are a total of eight instances of the LLRF sub-system in the SPX rf system for the eight cavities.

3.6.3.5.3 LLRF Field Controller Implementation

The high-speed and real-time digital signal processing (DSP) and concurrent execution of the control algorithms in the SPX LLRF cavity field controller require that the digital hardware of the LLRF controller be implemented in field-programmable gate array (FPGA) devices with analog-to-digital converter (ADC) sampling of the rf signals at an IF via an analog down-converter. The controller will output individual klystron rf drive signals to each cavity via an up-converted IF output from a DAC. The LLRF controller hardware will have an architecture as shown Figure 3.6-46 to ensure sufficient hardware resources for implementing the LLRF DSP. The channel phase drift correction scheme with calibration tones is the key feature of the core functionality of LLRF field control. The implementation of this feature requires a multi-channel digital transceiver with frequency-division multiplexing.

The field controller will interface to the control system through an RTDL. Both the RTDL and its

required interface card will be provided by Controls (see section 3.6.3.7). The purpose of interfacing through an RTDL card is to allow the LLRF and RTDL hardware to independently evolve during the development, as long as the LLRF local bus interface standard is maintained. The overall system integration scheme of the SPX LLRF into the accelerator controls infrastructure from the LLRF system's perspective is illustrated in Figure 3.6-47 (also see Figure 3.6-56 in section 3.6.3.7).

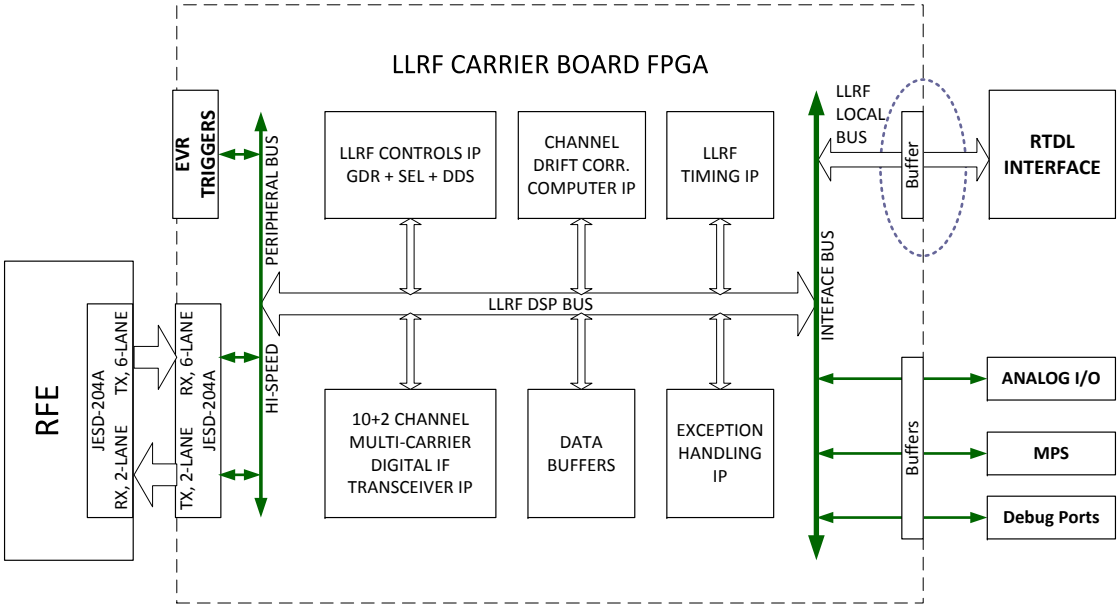

Figure 3.6-46: The required functionality and IP implementation in the LLRF controller.

3.6.3.5.4 LLRF R&D

The R&D plan for SPX LLRF is described in the SPX0 section 3.6.4.8.3.

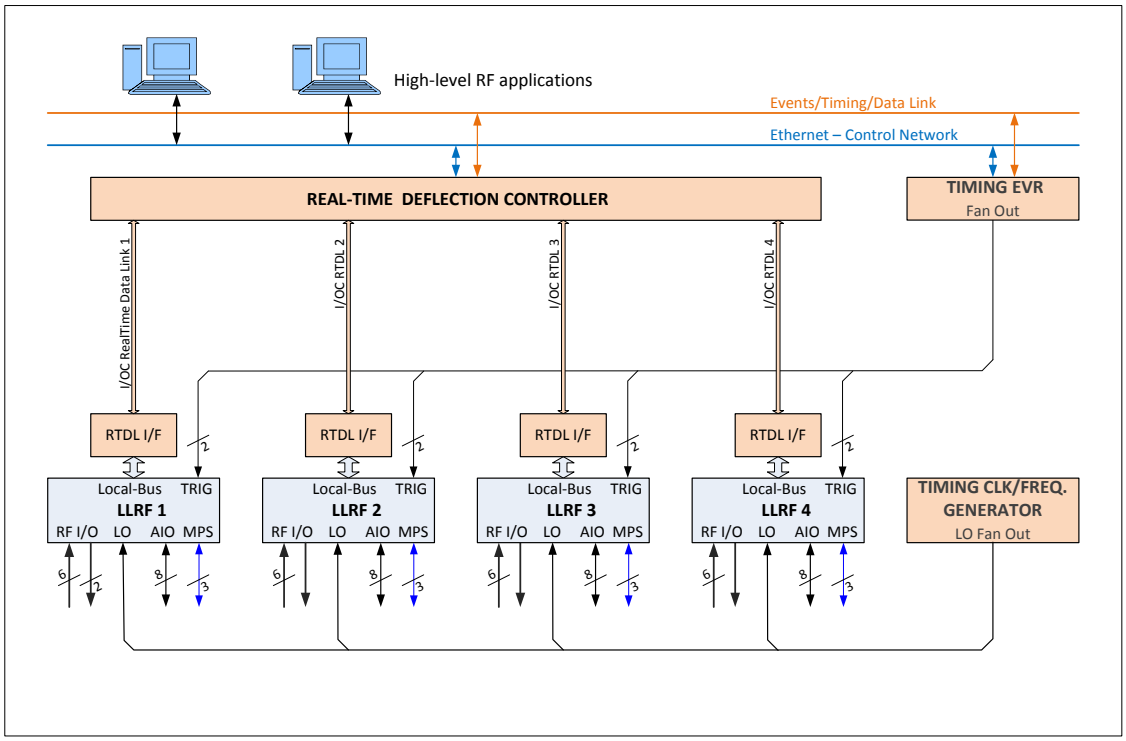

Figure 3.6-47: The interface scheme of SPX LLRF system with the accelerator controls infrastructure.

3.6.3.6 Timing and Synchronization [U1.03.03.03]

3.6.3.6.1 Scope

The timing and synchronization system will provide the information and phase references needed to drive the crab cavities and measure the effects on the electron beam both within the SPX region and the residual effects outside the SPX region. In addition, phase references will be provided to sector beamline lasers for synchronization to the x-ray beam pulses.

3.6.3.6.2 Key Specifications

The SPX rf cavity phase and amplitude need to be controlled to a sufficient precision to prevent excessive orbit motion and maintain a stable short x-ray pulse. Table 3.6-22 lists the phase tolerances for the SPX cavity fields and beamline laser-to-x-ray pulse synchronization that drive the timing and synchronization design.

Table 3.6-22: Key SPX timing and synchronization specifications.

Specification Name	RMS Tolerance	Bandwidth
Common-Mode Phase Variation	< 10 °S	0.01 Hz - 271 kHz
Phase Mismatch Between Cavities	< 0.038 °S	0.01 Hz - 200 Hz
Phase Mismatch Between Cavities	< 0.077 °S	0.01 Hz - 1 kHz
Phase Mismatch Between Cavities	< 0.280 °S	1 kHz - 271 kHz
Beam Line Laser synchronization to X-Ray Pulse	< 270 fs	0.01 Hz - 1 kHz

Note that the degrees units listed in the table are at the SPX cavity frequency of 2815 MHz. At this frequency each degree of phase corresponds to 1 picosecond. These specifications, in particular the phase mismatch between cavities specification of 77 millidegrees, are very demanding and require extraordinary measures to achieve. For example, 1 meter of fiber cable with a temperature coefficient of 7 ppm and a velocity of propagation of 67% of the speed of light will experience a change in delay of 50 femtoseconds per degree C change in temperature. However, it should be noted that the phase mismatch tolerances assume no use of beam-based feedback. It is expected that these tolerances will be relaxed significantly through use of beam-based feedback that will directly control the cavity phases. This will be determined in concert with in-progress modeling of the upgraded orbit control system.

Below 0.01 Hz, beam-based feedback will be used to track and compensate for phase drifts. This is within the capability of the existing orbit feedback systems.

3.6.3.6.3 Approach

To achieve the demanding requirements, the APS has entered into collaboration with the Beam Technology Group of Lawrence Berkeley National Laboratory (LBNL) to assist with the LLRF and timing/synchronization development. This team has many years of experience in LLRF controllers and precision synchronization systems. They have expended a great deal of effort over the years in

developing a system capable of delivering a phase reference stable to the 10s of femtoseconds level. Their fiber link stabilization scheme forms the basis for SPX phase reference distribution [3.6-52].

Figure 3.6-48 shows a block diagram of the phase reference distribution system. Actively stabilized fiber optic links will be used to distribute a 2815-MHz phase reference to each location. The active phase stabilization will correct for drifts due to environmental effects. The LBNL scheme precisely measures the optical phase delay through a fiber using a heterodyne interferometer [3.6-52]. As shown in the figure, each stabilized link consists of two fibers, the reference fiber and the beat fiber. The heterodyne process, in which the original optical frequency is mixed with an optical frequency offset by a 110-MHz radio frequency, results in changes in optical phase being translated into identical phase changes in the 110-MHz rf beat note. One degree of phase change in the 1560-nm optical domain, which corresponds to 21 attoseconds, translates to 1 degree of phase change in the rf domain or 25 picoseconds. This results in approximately 6 orders rf magnitude leverage over direct measurement in the rf domain. The phase changes in the 110-MHz beat note are measured and used to correct for changes in fiber cable delay due to environmental effects, such as temperature.

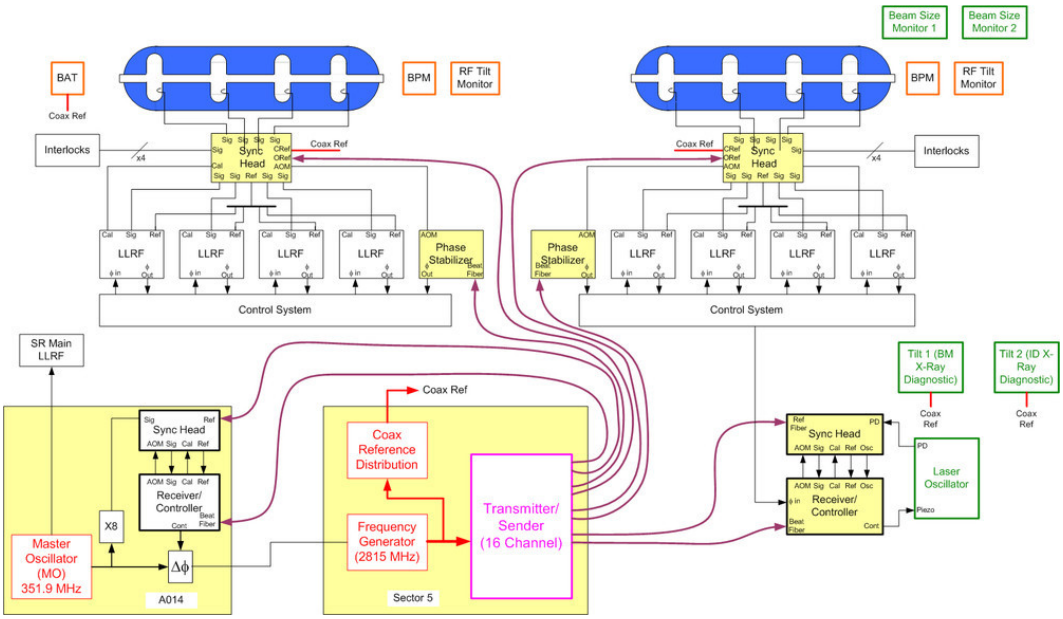

Figure 3.6-48: SPX timing/synchronization block diagram.

LBNL has reported measured results of 19.4-fs rms for a 2.2-km fiber over 60 hours and 8.4-fs rms for a 200-m fiber over 20 hours [3.6-52]. The 19.4-fs measurement for the 2.2-km fiber was a reduction by a factor of approximately 1000 compared to no correction.

The 2815-MHz reference and the local oscillator reference for LLRF will be generated from a 351.9-MHz reference by a frequency generation chassis located at the SPX area. As shown in Figure 3.6-48, the 351.9-MHz reference will be transported from the APS master oscillator in A014 to the SPX area via a phase-stable coax cable.The frequency generation chassis multiplies the 351.9-MHz reference by eight. One of the optical links with a receiver/controller will be used to compensate for drifts in the coax cable by controlling a phase shifter.

The fiber transmitter cw laser output is modulated by the 2815-MHz signal from the frequency generation chassis. The resulting amplitude-modulated optical signal is fanned out for distribution to

the SPX LLRF systems and the beamline laser hutches. Each of the optical links is an independent heterodyne interferometer transporting the 2815-MHz reference as an amplitude modulation on the optical carrier.

At each receiving end, the receiver measures changes in optical phase and uses this measurement to correct the phase of the received 2815-MHz signal.

Each stabilized link receiver consists of two components, the link stabilizer and the sync head. The sync head contains the acousto-optic frequency shifter, which shifts the optical frequency. The sync head is mounted as close as physically possible to the source of the signal to be stabilized, for example, the cavity field probe or laser oscillator. In the case of the SPX cavities, the sync head will be mounted inside the APS tunnel on top of the cryomodule.

3.6.3.6.4 Timing and Synchronization for LLRF

LLRF requires a phase stable 2815-MHz reference. The LLRF phase stabilization consists of two units, the phase stabilizer and the sync head. The sync head is mounted on the cryostat to minimize the cable length from the cavity field probe to the sync head.

Figure 3.6-49 is a block diagram of the phase stabilizer. The beat fiber is received by a photodiode on the fiber optic (FO) board to produce the beat signal. The phase of the beat signal is compared to the phase of the signal that is used to generate the acousto-optical modulator (AOM) drive. This phase difference is a measure of the change in fiber propagation delay and is fed to the LLRF receivers to correct the phase reference received by the LLRF for phase drifts. The diagram shows a separate input for phase set point. In actuality, this input will be driven by the control system via the monitoring/control port.

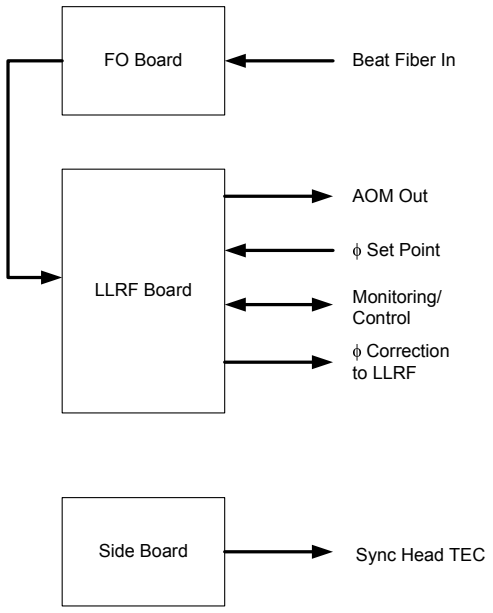

Figure 3.6-49: LLRF phase stabilizer block diagram.

Tables 3.6-23 and 3.6-24 list the input and output connections.

Table 3.6-23: LLRF phase stabilizer signal input and outputs.

Signal	Level	Connector
Beat Fiber In	TBD	APC
AOM Out	TBD	N
Monitoring/Control	TBD	TBD

Table 3.6-24: LLRF phase stabilizer multi-pin (DB25) connector pin-out.

Pin	Signal	Signal	Pin
1	GND	GND	14
2	GND	GND	15
3	GND	GND	16
4	+5V Power	GND	17
5	+15 V Power	GND	18
6	TEC +12V Power	TEC +12V Power GND	19
7	TEC +12V Power	TEC +12V Power GND	20
8	Thermistor +	Thermistor -	21
9	NC	NC	22
10	TEC +12V Power	TEC Set Point GND	23
11	TEC Set Point	TEC Temp Monitor GND	24
12	TEC Temp Monitor	PD Bias GND	25
13	PD Bias		

Figure 3.6-50 is a diagram of the LLRF sync head. This sync head provides inputs for four cavities and inputs for both a fiber reference and a coax reference. General specifications for the LLRF sync head are:

1. Signal inputs and outputs are specified in Tables 3.6-25 and 3.6-26.
2. All internal fiber components are to be fusion spliced.
3. The interior of the sync head will be temperature controlled to $\pm$ 0.01°C via TEC devices and a TEC controller.
4. The entire sync head will be thermally insulated to aid temperature regulation of the interior. Type and thickness of insulation will be determined later in the design.

3.6.3.6.5 Timing and Synchronization for Diagnostics

Diagnostics for SPX include a beam arrival time monitor, vertical beam size monitors, and beam position monitors (BPMs).

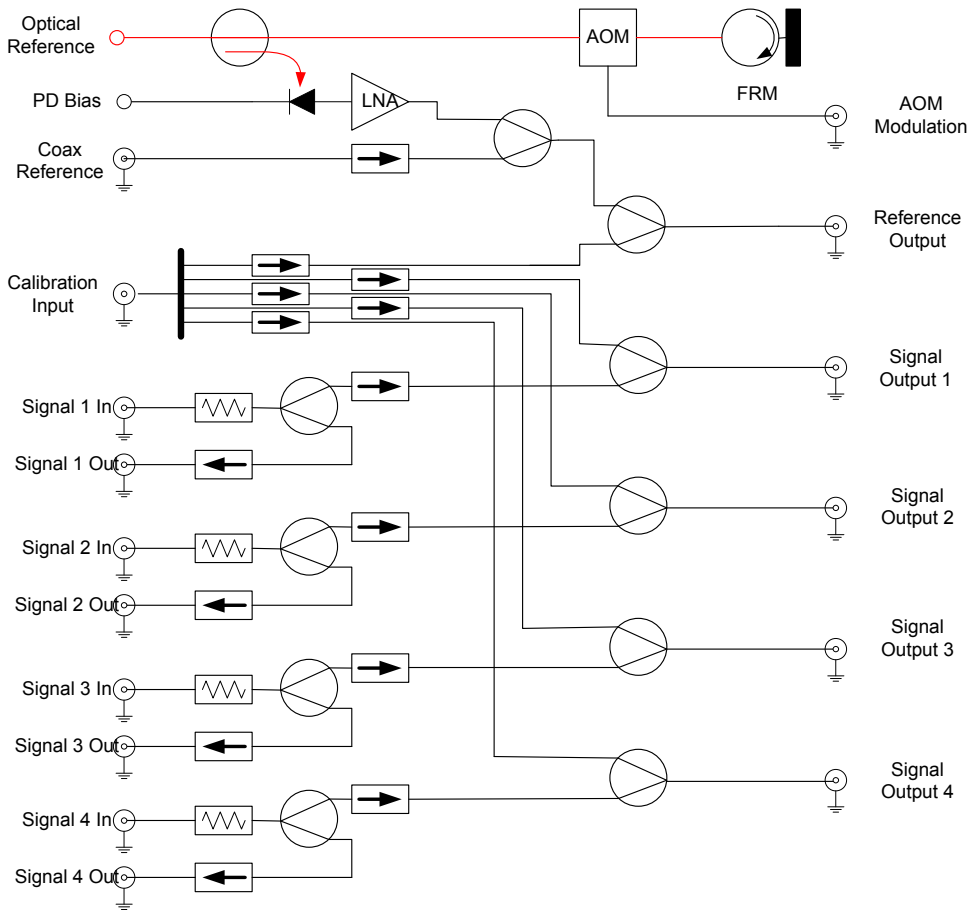

Figure 3.6-50: LLRF sync head block diagram.

Beam Arrival Time Monitor

The beam arrival time (BAT) monitor will require a phase reference. The BAT is not specified for stable operation below 0.01 Hz so a phase stabilizer is not required. The BAT phase reference requirements are given in Table 3.6-27.

Vertical Beam Size Monitor

No timing/synchronization requirements.

Beam Position Monitors

For existing BPM electronics, timing is already in place and existing requirements are adequate. For any new BPM electronics, timing requirements will be determined later in the design process.

Table 3.6-25: LLRF sync head signal inputs and outputs.

Signal	Level	Connector
Fiber Reference In	TBD	APC
Coax Reference In	TBD	N
Cal Tone In	TBD	N
Reference Out	0 dBm	N
Field Out	0 dBm	N
AOM In	TBD	TBD
Field Probe 1 In	20 dBm	N
Field Probe 1 Out	0 dBm	N
Field Probe 2 In	20 dBm	N
Field Probe 2 Out	0 dBm	N
Field Probe 3 In	20 dBm	N
Field Probe 3 Out	0 dBm	N
Field Probe 4 In	20 dBm	N
Field Probe 4 Out	0 dBm	N

Table 3.6-26: LLRF sync head multi-pin (DB25) connector pin-out.

Pin	Signal	Signal	Pin
1	GND	GND	14
2	GND	GND	15
3	GND	GND	16
4	+5 V Power	GND	17
5	+12V Power	GND	18
6	TEC +12V Power	TEC +12V Power GND	19
7	TEC +12V Power	TEC +12V Power GND	20
8	Thermistor +	Thermistor -	21
9	NC	NC	22
10	TEC +12V Power	TEC Set Point GND	23
11	TEC Set Point	TEC Temp Monitor GND	24
12	TEC Temp Monitor	PD Bias GND	25
13	PD Bias		

3.6.3.6.6 Timing and Synchronization for the SPX Beamline

The beamline laser oscillator must be tightly synchronized to the x-ray pulse. To accomplish this a laser controller will be provided that accepts a phase stable 2815-MHz reference and compares the phase of that reference to a harmonic of the laser oscillator to generate an error signal to control the phase of that oscillator.

Figure 3.6-51 shows a diagram of the laser controller consisting of a sync head and receiver controller.

Table 3.6-27: SPX beam arrival time phase reference.

Signal	Frequency	Level	Connector
BAT Phase Reference	351.9 MHz	TBD	TBD

The sync head receives the reference fiber input and an input from the laser oscillator. The receiver controller drives the laser oscillator piezo-actuators to lock the phase to the distributed reference.

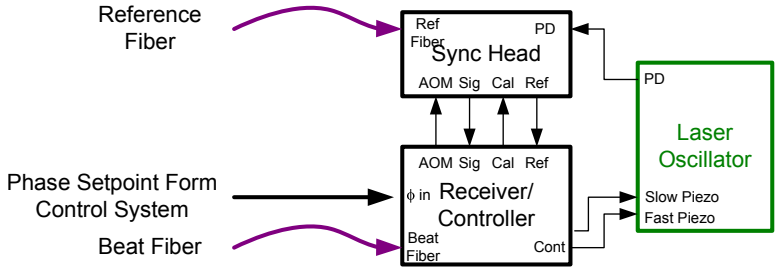

Figure 3.6-51: Laser control block diagram.

Figure 3.6-52 is a block diagram of the laser receiver controller. The beat fiber is received by a photodiode on the FO board to produce the beat signal. The phase of the beat signal is compared to the phase of the signal that is used to generate the AOM drive. This phase difference is a measure of the change in fiber propagation delay and is used by the receiver controller to correct the received phase reference for phase drifts. The reference and signal inputs are down converted by the analog front end. These two signals are phase compared and the resulting phase error signal drives the laser oscillator piezo-actuators to lock the oscillator phase to the reference.

The diagram shows a separate input for the phase set point. In actuality, this input will be driven by the control system via the monitoring/control port.

Table 3.6-28 lists the receiver inputs and outputs and Table 3.6-29 shows the pin out of the multi-pin connector for the sync head TEC.

Table 3.6-28: Laser receiver/controller inputs and outputs.

Signal	Level	Connector
Beat Fiber In	TBD	APC
AOM Out	TBD	SMA
Signal In	TBD	N
Cal Tone Out	TBD	N
Reference In	0 dBm	N
Oscillator Piezo Control	TBD	TBD
Phase Set Point In	TBD	TBD

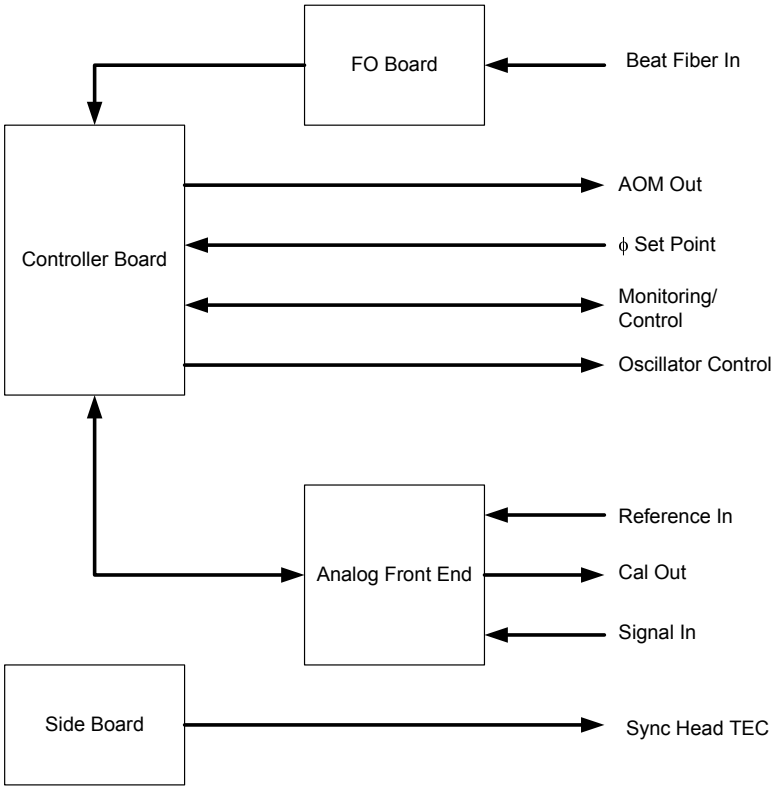

Figure 3.6-52: Laser receiver controller block diagram.

Table 3.6-29: Laser receiver/controller multi-pin (DB25) connector to sync head.

Pin	Signal	Signal	Pin
1	GND	GND	14
2	GND	GND	15
3	GND	GND	16
4	GND	GND	17
5	GND	GND	18
6	TEC +12V Power	TEC +12V Power GND	19
7	TEC +12V Power	TEC +12V Power GND	20
8	Thermistor +	Thermistor -	21
9	NC	NC	22
10	TEC +12V Power	TEC Set Point GND	23
11	TEC Set Point	TEC Temp Monitor GND	24
12	TEC Temp Monitor	PD Bias GND	25
13	PD Bias		

Figure 3.6-53 is a block diagram of the optical sync head used for laser stabilization. Following are general specifications:

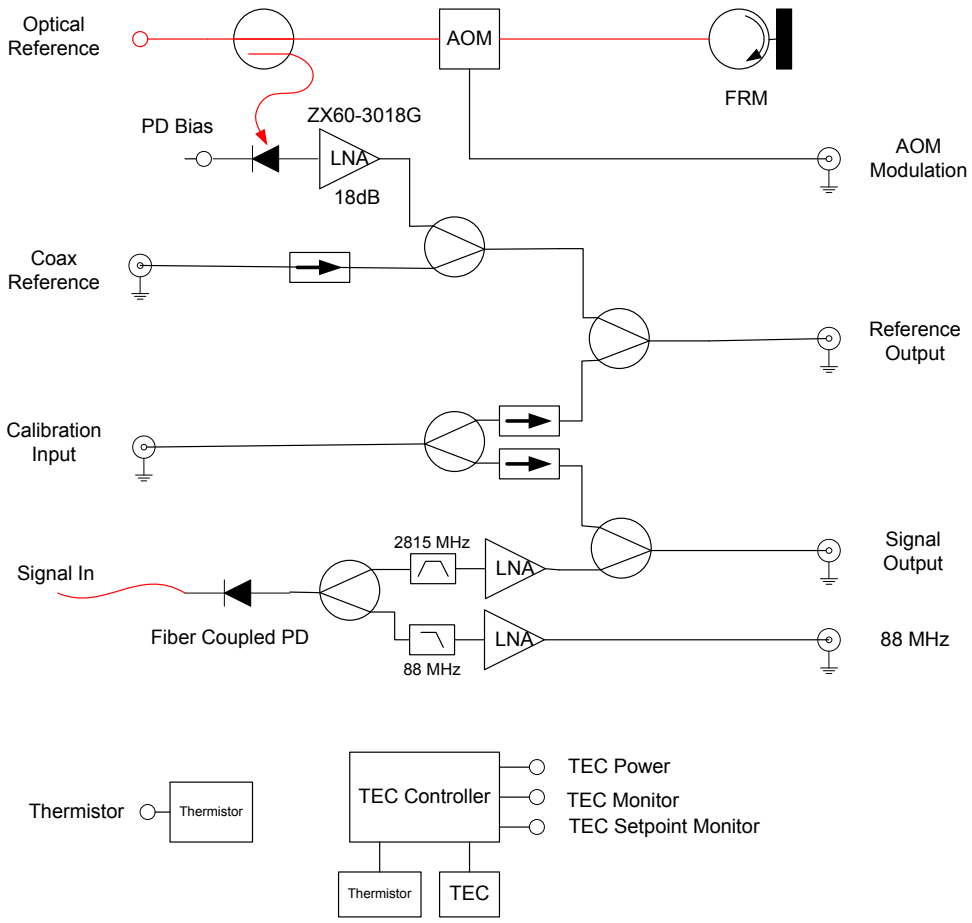

Figure 3.6-53: Optical sync head block diagram.

1. Signal inputs and outputs are specified in Tables 3.6-30 and 3.6-31.
2. All internal fiber components are to be fusion spliced.
3. The interior of the sync head will be temperature controlled to $\pm$ 0.01°C via TEC devices and a TEC controller.
4. The entire sync head will be thermally insulated to aid temperature regulation of the interior. Type and thickness of insulation are to be determined.

The optical reference is passed through an acoustical optical modulator that shifts the optical carrier frequency by 110 MHz total. A portion of the optical reference is coupled to a photodiode that recovers the 2815-MHz amplitude modulation.

An optical signal from the laser oscillator is optically coupled to a fiber-coupled photodiode. The output of the photodiode is split to a bandpass filter and a low-pass filter. The bandpass filter selects a harmonic of the oscillator corresponding to the 2815-MHz reference. This would be the 32nd harmonic in the case of an 88-MHz laser oscillator. The phase of this harmonic is locked to the reference phase by feedback to the piezo in the laser oscillator. The low-pass filter output is used by the laser controller to set the phase of the oscillator to correspond to the storage ring revolution fiducial.

Table 3.6-30: Optical sync head signal inputs and outputs.

Signal	Connector
Optical Reference In	APC
Coax Reference In	N
Cal Tone In	N
Reference Out	N
Signal Out	N
AOM In	SMA
Signal In	APC
88 MHz Out	N

Table 3.6-31: Optical sync head multi-pin (DB25) connector pin-out.

Pin	Signal	Signal	Pin
1	GND	GND	14
2	GND	GND	15
3	GND	GND	16
4	+5V Power	GND	17
5	+15V Power	GND	18
6	TEC +12V Power	TEC +12V Power GND	19
7	TEC +12V Power	TEC +12V Power GND	20
8	Thermistor +	Thermistor -	21
9	PD Bias #2	PD Bias #2 GND	22
10	TEC +12V Power	TEC Set Point GND	23
11	TEC Set Point	TEC Temp Monitor GND	24
12	TEC Temp Monitor	PD Bias #1 GND	25
13	PD Bias #1		

The 2815-MHz reference signal and the 2815-MHz harmonic of the laser oscillator are passed to the laser controller for processing.

3.6.3.6.7 Frequency Generation Chassis

The frequency generation chassis accepts a 351.9-MHz input and multiplies that by 8 to generate the 2815-MHz SPX cavity frequency. In addition, it generates a LO signal by dividing the 351.9 MHz by 6 and mixing that with the 2815 MHz. The 2756.8-MHz upper sideband is passed through a bandpass filter to generate the LO. A block diagram is shown in Figure 3.6-54. Table 3.6-32 lists the input and output signals of the frequency generation chassis.

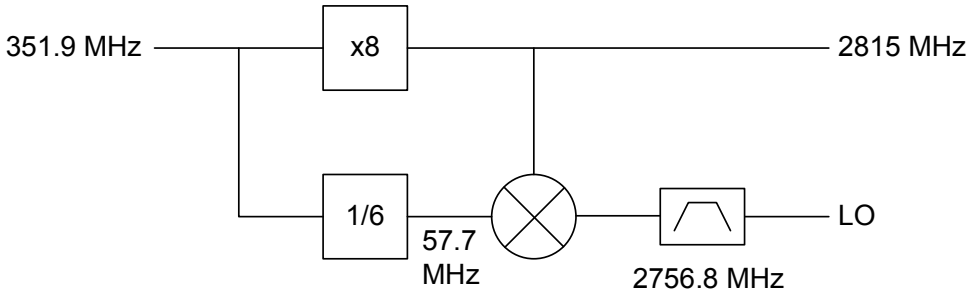

Figure 3.6-54: Frequency generation chassis block diagram.

Table 3.6-32: Frequency generation chassis signals.

Signal	Frequency	Level	Connector
RF Input	351.9 MHz	TBD	N
RF Output	2815 MHz	TBD	N
LO Output	2756.8 MHz	TBD	N

3.6.3.6.8 Transmitter/Sender

A key component of the phase stabilization system is the transmitter/sender, which provides a cw laser whose output is amplitude-modulated by the 2815 MHz for transport to remote locations such as LLRF controllers and beamline laser oscillators. Each channel of the transmitter/sender provides two fibers—a reference fiber and a beat fiber. The reference fiber provides the phase reference to the remote locations. The beat fiber transports information on the reference fiber's change in propagation delay to the remote locations to be used for correcting the reference fiber's phase.

A block diagram for the transmitter/sender is shown in Figure 3.6-55. The transmitter/sender consists of a laser source, EDFA, Modulator, RB locker and 16 channel sender all mounted within a relay rack. Specifications are given in Table 3.6-33.

Laser Safety

All laser light is to be fully contained within chassis or fiber cables. Unused optical outputs are to be capped to prevent escape/leakage of laser light.

3.6.3.6.9 Cable Plant

Fiber Plant

The following requirements have been established for the fiber plant.

1. All fibers shall be single-mode SMF28e fiber.

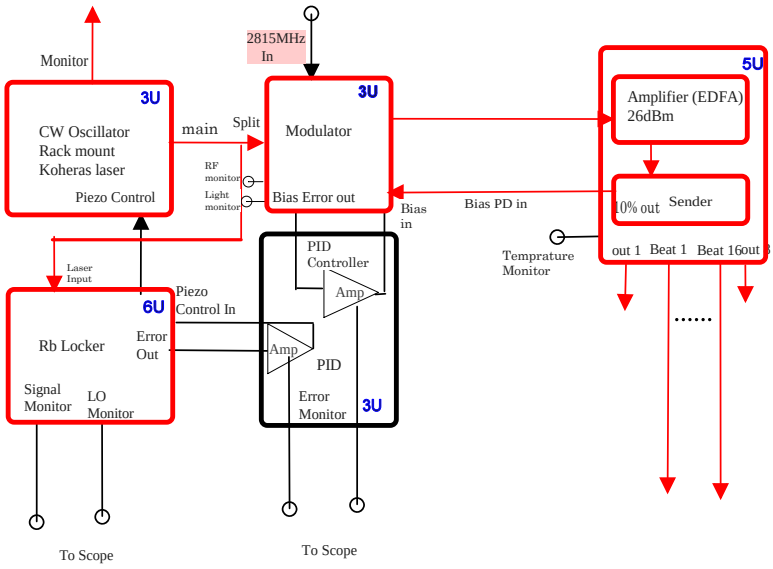

Figure 3.6-55: SPX transmitter/sender block diagram.

Table 3.6-33: Transmitter/sender specifications.

Feature	Specification
Number of channels	16
Number of outputs per channel	2
Signal output power	$\leq$ 10 mW
Wavelength	1560nm
Optical frequency stability	$<$1MHz
Modulation frequency	2815MHz
Input RF power	+15dBm
Beat output modulation frequency	100 $\pm$ 10MHz
Modulation depth	70 $\pm$ 10%
Output optical connectors	FC/APC
Digitally controlled/monitored devices	PID controllers, EDFA
Rack space required	19 inch rack by 6’ high

2. All fiber connectors shall be APC.

3. All fiber splices shall be fusion spliced.

Coax Plant

The following requirements have been established for the coaxial cable plant.

1. All timing coax shall be phase-stabilized Andrew's $\frac{1}{2}$" Heliax.
2. All connectors shall be type N.

3.6.3.7 Controls [U1.03.03.04]

The entire SPX system must be thoroughly integrated with existing APS storage ring controls, timing, and diagnostics. Since instability in the operation of the SPX cavities may impact all APS users, thorough instrumentation and diagnostics are required to detect any operational abnormalities. The primary functions required of SPX controls are to:

- Provide remote monitoring and control to all SPX subsystems.
- Provide interfaces to other APS systems to obtain necessary real-time storage ring information.
- Provide a real-time data processing environment where control algorithms can be executed at high speeds to ensure well-integrated control with the APS storage ring.
- Provide thorough diagnostic information and tools to assist in quick determination of performance problems and postmortem fault analysis.

3.6.3.7.1 SPX Subsystem Interfaces

Each SPX subsystem must be interfaced to the EPICS-based APS Control System for supervisory control and monitoring. Figure 3.6-56 illustrates the required connections between the EPICS IOCs and the SPX subsystems.

The IOCs to be used for SPX controls will be a mixture of soft IOCs (running on Linux servers) and traditional VME-based IOCs located in Bldg 400A. By providing VME-based IOCs, the large selection of VME modules currently used at APS can be utilized for SPX.

In most cases, the required interfaces are well understood and many of the necessary types of interfaces have already been implemented in existing APS systems. Controls support for the SPX LLRF, however, is quite challenging and is discussed separately in a later section.

Table 3.6-34 gives general details about the subsystem requirements for remote control and monitoring.

3.6.3.7.2 SPX LLRF Controls

Figure 3.6-57 illustrates the primary components and interfaces required of the SPX LLRF controls. The list of functions on the right side of the diagram represents end-to-end functionality required for operation. These functions are divided into the different levels and blocks to depict where these functions will be implemented. Such a diagram assists in describing interfaces and functionality at each block.

The Cavity Control layer represents the functions performed by the LLRF controllers. These controllers are provided by the RF Group, and the functions they perform are described in section 3.6.3.5.

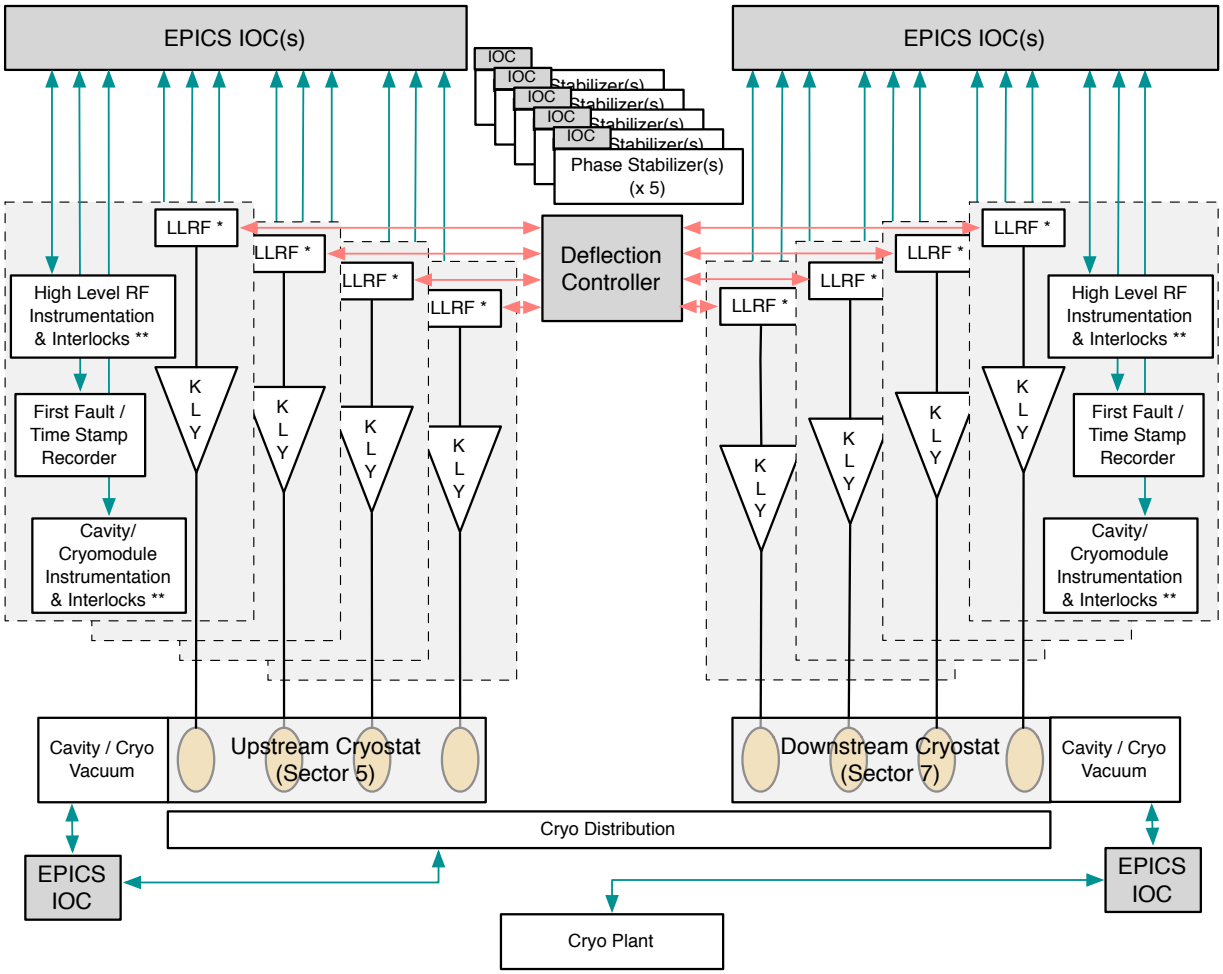

Figure 3.6-56: SPX controls and interfaces to other systems.

Table 3.6-34: Subsystem requirements for control and monitoring.

Subsystem	Devices to Interface	Interface to IOC	Parameters to Monitor/Control	Default Monitoring Rate
LLRF	see Table 3.6-35			
HLRF * Amplifier Control * Slow RF Interlocks * Fast RF Interlocks	PLC (x8)	Ethernet	200 / 50 (x8)	5 Hz
Cavity / Cryomodule * Instrumentation * Slow Interlocks * Fast Interlocks	PLC (x8)	Ethernet	200 / 100 (x8)	10 Hz
Fault/Time Stamp Recorder	VME Module	VME	32 Fault Inputs per module	5 Hz
Cryomodule Vacuum	MM200, MPC, VVC210	Ethernet	50 / 20 (x2)	5 Hz
Cryogen Distribution	PLC (x3)	Ethernet	150 / 30	5 Hz
Cryoplant	PLC	Ethernet	500 / 50	5 Hz
Phase Stabilized Timing * LLRF x 2 * A014 x 1 * User Laser x 1	LBL LLRF4 (x4)	USB	50 / 10 (x5)	5 Hz

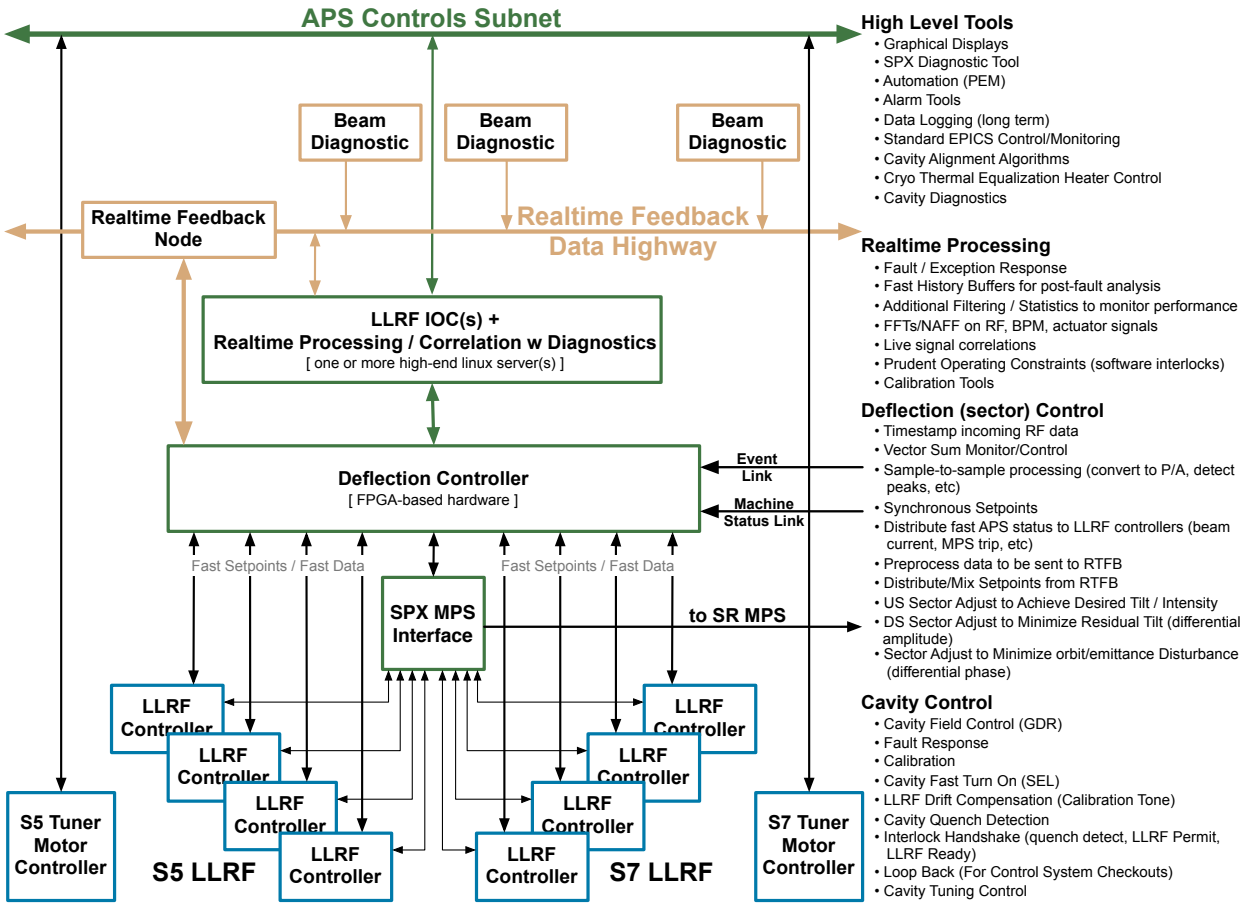

Figure 3.6-57: LLRF signal processing and hierarchical control functions.

Each LLRF controller will interface to the Deflection Controller through a real-time data link (RTDL). This is a full-duplex link that passes rf measurements and other parameters from the LLRF controller and transmits rf setpoints and control data to the LLRF controller. The Deflection Controller provides the capability of dealing with the cavities individually, by a group of two cavities (Group A/B), by sector (four cavities), or all eight together. Additionally, the Deflection Controller will perform sample-by-sample processing of rf data (conversion from I/Q to phase/amplitude, statistics, vector sums, etc.) before passing it on the next layer for additional processing. Ultimately, the cavities will be used as beam actuators whose control signals are derived from the upgraded RTFB system and sent to the SPX LLRF by the Deflection Controller, hence the communication path connecting the Deflection Controller and the RTFB processor.

The data that the Deflection Controller receives from each LLRF controller is ultimately passed on to a Linux server, referred to in the diagram as the IOC/real-time processing unit. This is a high performance multi-core computer that will capture the LLRF data at the required rates (see Table 3.6-35), execute additional data processing routines, and make it available to a soft IOC that will serve the data up via Channel Access. Calculations such as signal calibration, fast Fourier transforms (FFTs), fast-history buffers, and live signal correlations are performed at this level.

Real-time and Near Real-time Functions: The combination of the Deflection Controller hardware (an FPGA-based module), the SPX LLRF IOCs, and dedicated server platforms provide a powerful environment for rf signal processing. Functions can be distributed across this hardware to implement significant capabilities ranging from sample-to-sample calculations in the Deflection Controller to the execution of complex scripts on the dedicated server. Such a flexible environment is necessary as additional functionality continues to be defined for the SPX rf subsystems.

Monitoring/Control of LLRF Data: Each LLRF controller will control a single cavity. An estimate of the data transfer required between each controller and the Deflection Controller is described in Table 3.6-35.

Table 3.6-35: Data rates for LLRF data.

Signal Type	Number	Data Size	Nominal Rate	Data Rate
Rf measurements[a]	10 I/Q pairs (20 total)	20 bits	272 kHz	13.6 MBytes/s
Rf setpoints[b]	2 I/Q pairs	20 bits	20 kHz	200 kBytes/s
Rf parameters (read)	200	32 bits	10 Hz	8 kBytes/s
Rf parameters (write)	200	32 bits	10 Hz	8 kBytes/s

[a] In normal operation, the rf measurements may be decimated to a much lower sample rate. However, for thorough performance and/or fault analysis, the nominal rate must be supported.

[b] In the operational system, the rf setpoints will be derived from the real-time feedback system at the nominal rate. Slower set point changes will continue to be necessary for testing and other operational modes. These slower setpoints are included in the rf parameters (write).

Time-stamping LLRF Data: The rf measurement data and rf parameters read from the LLRF controller must be time-stamped to allow them to be correlated with data from other APS systems. This time-stamp must either be a wall-clock time with sufficient resolution (i.e., less than 3.6 μs) or an integer that represents a revolution (P0) counter. If the rf measurement sample rate changes, this information must be passed along with the data to allow it to be properly interpreted.

I/Q to Phase/Amplitude Conversion and Calibration Factors: For several algorithms and/or operator displays, the I/Q data will be converted to the polar coordinates of phase and amplitude. This

calculation must be done at the full data rate. Calibration factors must also be applied and recorded such that the raw data may be recovered if necessary.

Vector Sum Monitoring / Control / Statistics: For some algorithms and operator displays, the vector sum of pairs of cavities and the vector sum of all four cavities in a cryomodule will be required. This calculation must be done at the full data rate, so it may best be done in the Deflection Controller. A subset of calculated parameters will be provided to the RTFB link for global distribution.

Fault / Exception / Interlock Monitoring and Response: To ensure proper operation and sensible responses to faults, detection of a variety of faults and off-normal conditions will be required. Many critical conditions and responses will be implemented within the interlock systems (not part of this section), and other less critical conditions will be detected within the control system.

To minimize trips that would interfere with beam operation, certain interlock conditions will be shadowed in software with a lower trip threshold, possibly allowing a preventive response to correct the situation.

Fault Analysis: To preserve the admirable availability and MTBF statistics of the APS, the ability to diagnose SPX faults and trips as quickly as possible is imperative. The control system, having access to all synchronous data, will be a key component of the postmortem analysis. All SPX subsystems, however, must be designed to ensure that trip data is appropriately time-stamped for correlation with other data after a fault.

For the rf measurements, this will require fast history buffers that are captured when a fault occurs. Present technology allows for several seconds of full-rate data to be captured on a fault condition.

Additional Real-time Processing: The combination of the FPGA-based Deflection Controller and the server-grade workstation provides a powerful environment to implement any additional real-time or near real-time needs that are identified during the design and operation of the SPX.

3.6.3.7.3 High Level Tools

A number of high-level tools will be needed for the SPX system. Considerations related to these tools include the following.

- **Existing Tools:** The SPX controls will be implemented within the existing accelerator controls framework. This will allow the entire suite of high-level tools (those typically used by accelerator operators, machine physicists, and technical staff) to be applied to the SPX subsystems. Tools that will likely be utilized include graphical operator displays, PEM tools for automation, alarm tools and data logging. MEDM screens that allow subsystem experts to interact with their equipment will be provided.
- **Additional Tools:** Additional high-level tools specific to the deflecting cavities, the control of superconducting rf cavities, and precision LLRF systems will also be required. Such tools may be available from collaborators or similar projects and some may need to be developed here.
- **Rf Phasor Plot:** An application already identified as beneficial for operation of the SPX rf is a graphical plot for the representation of the rf detected phasors as a function of time. Based on an application developed at LBL (called “xgui”) this tool will provide a 2D mode that plots the individual I/Q values as a function of time. A 3D mode (I, Q, time) will also be available. By

providing a rotation knob for each axis, one can view the signals from multiple perspectives to easily visualize signal changes in the various dimensions (I, Q, amp, phase, time). For example, by looking down the time axis, it allows one to view the phasor location at all time instances to visualize signal stability and to visually convert from I/Q to amp/phase. An example plot of the LBL version is shown in Figure 3.6-58.

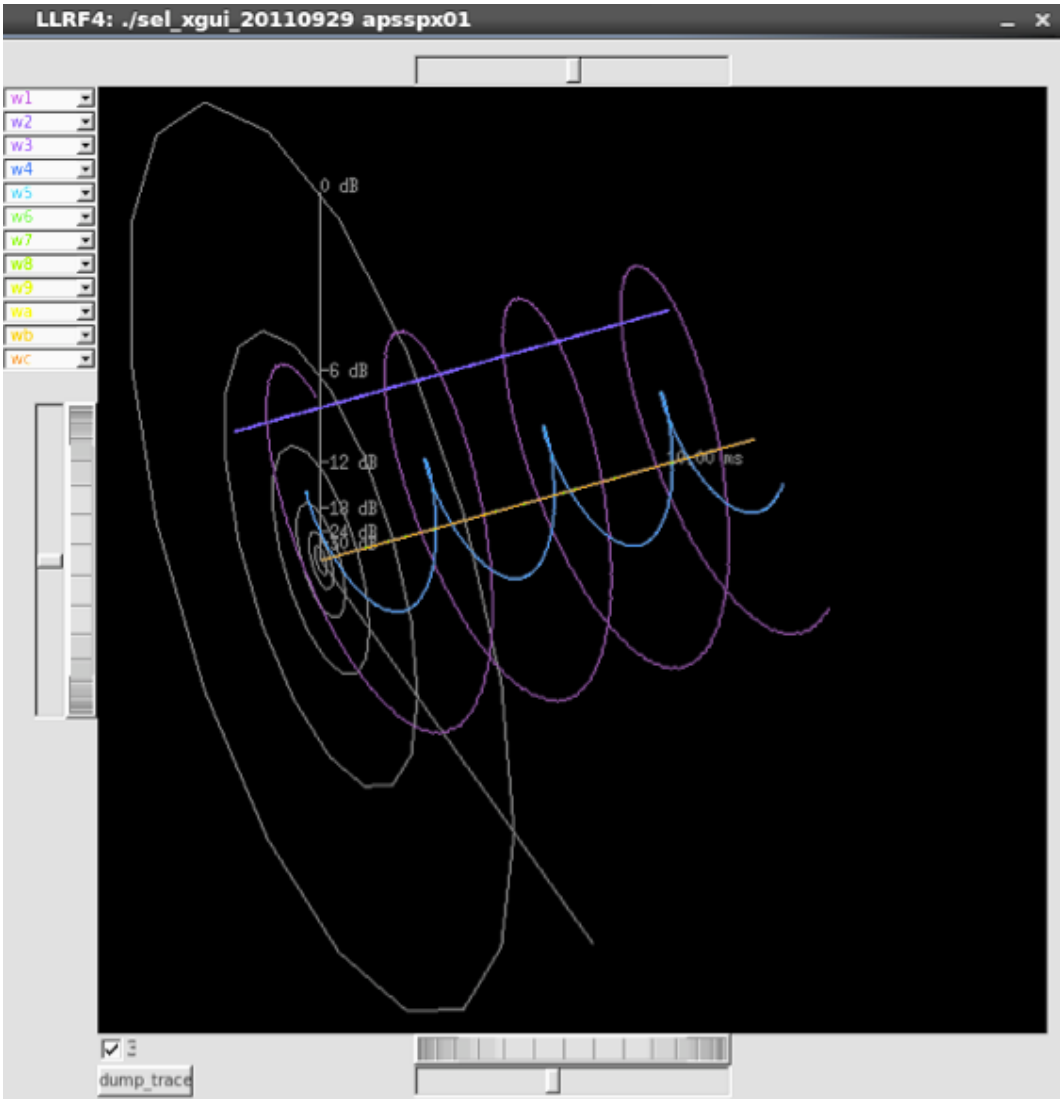

Figure 3.6-58: Phasor plot tool.

- **Live Data Correlation:** It is a requirement that the SPX cavities do not disturb the beam for the APS users. To monitor performance and diagnose anomalies, a tool for live correlation of beam properties (orbit, emittance, etc.) with SPX rf properties will be provided.
- **Data Processing Environment:** APS staff will make extensive use of Octave (a free alternative to Matlab) and the SDDS tools in the development, deployment, commissioning, and operation of the SPX LLRF subsystem. A convenient environment and utility libraries will be provided for Octave to minimize the learning overhead of using this tool with Channel Access and SDDS.

An index of SPX-specific scripts will be maintained to minimize redundant development of algorithms.

3.6.3.7.4 R&D Plan

The R&D plan for SPX Controls is described in the SPX0 section 3.6.4.8.3.

3.6.3.8 Cavity and Cryomodule

3.6.3.8.1 Introduction

Deflecting rf structures (cavities) operate in a mode where the center of the bunch experiences no net Lorentz force while the head and tail of the bunch are deflected in opposite directions. These structures are mainly single-cell or multi-cell superconducting cavities operating in a polarized TM_{110} mode with electromagnetic fields as shown in Figure 3.6-59. As the dipole mode has two polarizations, the undesired polarization, known as the same-order mode (SOM), may cause large deflection to the beam due to its high R/Q. In addition, the fundamental accelerating mode, known as the LOM, strongly couples to the beam and must be damped to avoid any degradation to the beam quality.

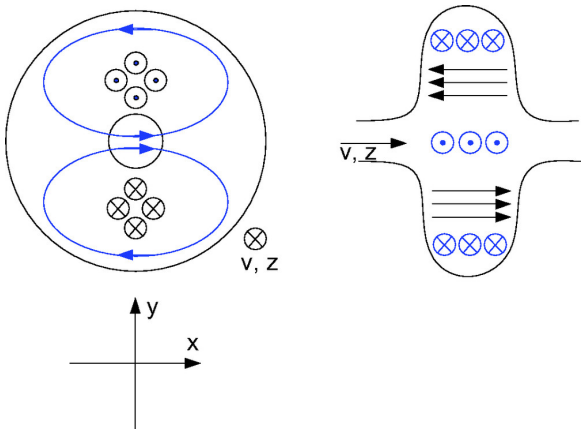

Figure 3.6-59: Polarized TM_{110} mode fields (magnetic [blue], electric [black]) drawn for an electron traveling in the +z-direction receiving a vertical kick up. The magnetic fields lead the electric fields by 90 degrees.

For the APS SPX project, superconducting rf (SRF) structures are chosen since they are best suited for high-repetition-rate applications envisioned for time-resolved experiments at the APS. The initial operating deflecting voltage for the APS SPX deflecting cavities is 2 MV, which will provide x-rays on the order of a few picoseconds. In the long term, additional cavities and rf systems may be added to provide a total deflecting voltage of 4 MV, which will produce shorter x-ray pulses. The APS SPX superconducting rf deflecting cavities are designed to operate at a frequency of 2815 MHz (the eighth harmonic of the APS storage ring rf frequency). It is critical that all HOMs and LOMs are effectively suppressed in the presence of beam in order to meet the APS storage ring beam-stability

and vertical-emittance-growth requirements up to the design requirement of 200 mA. (Note that this is higher than the 150 mA required by the APS Upgrade in order to provide a safety margin.)

Various design options have been evaluated for the APS deflecting cavities based on existing and proposed cavity designs in the superconducting community. The most recent and successful application of the deflecting cavity is at the KEK-B collider in Japan, where a pair of single-cell 500-MHz SC crab cavities were installed and commissioned at the low-energy and high-energy rings (LER and HER, respectively) for the luminosity upgrade [3.6-53]. The KEK-B crab-cavity design uses a squashed cavity geometry to separate the degenerate dipole modes and a coaxial insertion in the beam pipe to effectively damp the LOMs.

In recent years a new collaboration was formed between Argonne National Laboratory, Jefferson Accelerator Laboratory (JLab), Lawrence Berkeley National Laboratory (LBNL), Stanford Linear Accelerator Center (SLAC), and Tsinghua University in Peking, China, to develop SC-deflecting rf cavities suitable for high-energy light sources. Through extensive numerical and analytical studies, a new optimized squashed geometry deflecting cavity with waveguide damping has been designed.

In the following sections, we discuss the cavity design, cryomodule and mechanical design, the cryogenic system, the low- and high-level rf systems, and the control-system requirements.

3.6.3.8.2 Cavity Design [1.03.03.07]

The APS deflecting cavities will operate cw at 2815 MHz, using the TM_{110} cavity mode, to produce a head-tail chirp of the beam. A 2-MV deflecting voltage will be applied to achieve 2-ps x-ray pulses. Four single-cell cavities, each supplying 0.5-MV deflection, will be located in a long straight section (LSS) in Sector 5 to chirp the beam, with another set of four cavities located in Sector 7 to reverse the chirp and return the beam to its nominal orbit. The Mark-I cavity design shown in Figure 3.6-60 represents the original SPX cavity concept and consists of a squashed single-cell cavity with waveguide dampers and input coupler. The Mark-II design shown in Figure 3.6-61 uses a similar cavity shape but relocates the horizontal waveguide damper to the body of the cavity and utilizes a dog bone-shaped coupling iris for enhanced damping; it is the preferred cavity design due to its greater damping and lower beam loss factor. The racetrack cross section of the cavities is similar to the KEK deflecting cavity. It was adopted due to its minimization of the peak surface magnetic fields and frequency relocation of the same-order mode (SOM). The damping features of the KEK design, however, were found to be unsuitable for the SPX cavities, as will be discussed later in this section.

The cavity design was guided by various beam-interaction requirements, including the single-bunch current limit and coupled-bunch instabilities. The single-bunch current limit in the APS must exceed the requirements of the 16-mA intense bunch in hybrid-mode operation by limiting the transverse broadband impedance of the APS. This limit will be maintained in the deflecting cavities by assigning a minimum beam-pipe radius, as well as designing low-impedance beam-pipe transitions. Coupled-bunch instabilities were addressed by ensuring strong coupling of HOMs and LOMs in the cavity to external damping elements.

The coupled-bunch instability requirements for 200 mA are given, very roughly, by

$$\begin{aligned} R_\mathrm{s} \times f_\mathrm{n} &< \text{0.44 M } \Omega\text{-GHz (longitudinal)} \\ R_\mathrm{t} &< \text{1.3 M } \Omega\text{/m (horizontal dipole)} \\ R_\mathrm{t} &< \text{3.9 M } \Omega\text{/m (vertical dipole)} \end{aligned} \tag{3.6-56}$$

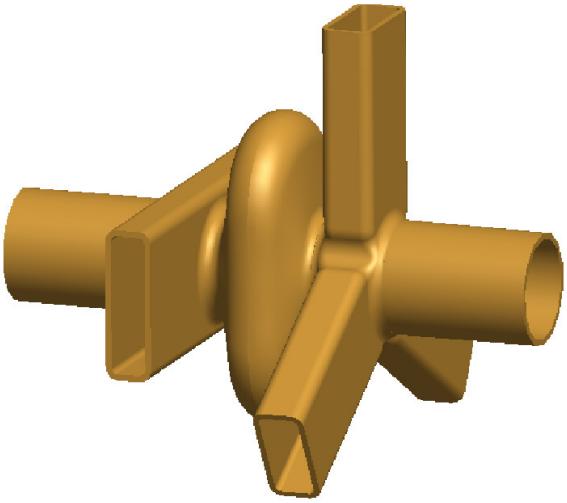

Figure 3.6-60: Mark-I design of the single-cell deflecting cavity with waveguide end groups.

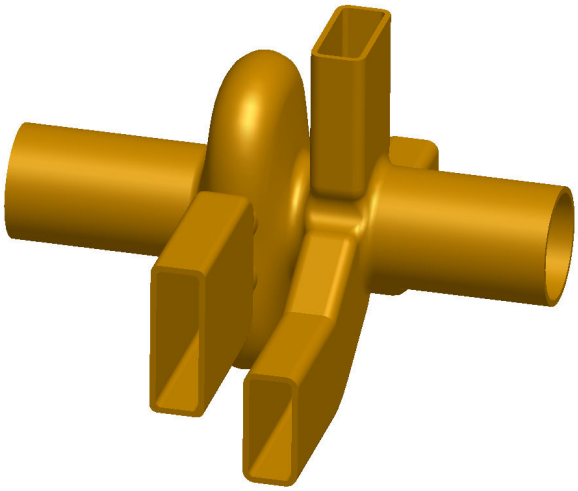

Figure 3.6-61: Mark-II design with on-cell waveguide damping.

where $R_s = V^2/2P_l$, $R_t = \kappa_r V_t^2/2P_l$, $V_t = V/\kappa_r r_o$ is the deflecting voltage, f_n is the LOM/HOM frequency, κ_r is the wave number, P_l is the total loss, and r_o is the radial offset of the voltage integration. The limits in Equation (3.6-56) are based purely on synchrotron radiation losses and do not consider other damping effects in the storage ring. These limits do not depend on the loaded quality factors explicitly, but the corresponding R is linearly related to the Q of a particular LOM/HOM.

The LOM damping is inherently a more difficult task in a deflecting cavity due to its lower frequency compared with the operating mode and subsequently to the greater containment of its modal fields in the interior of the cavity. Damping methods have been devised to extract the LOM using techniques that are invasive to the cavity fields and interact with both the LOM and the deflecting mode without degrading the deflecting mode. Various options have been proposed for the International Linear Collider (ILC) and Large Hadron Collider (LHC) [3.6-54], but KEK [3.6-55] is the first to successfully demonstrate the operation of superconducting deflecting cavities. An adjustable coaxial insert with a rejection filter is utilized in the KEK design to heavily damp the LOM and ensure minimal effect on the deflecting mode at 500 MHz. Scaling this design to 2815 MHz and applying it to the APS deflecting cavity has been considered, but it was found to be difficult due to manufacturing issues, as well as requiring excessive length. Additionally, the coaxial insert must be included in the cold mass, which has proven to be problematic.

The APS has pursued a design that utilizes selective mode coupling into the LOM waveguide in order to simplify the mechanism for damping. In the Mark-II design, a rectangular waveguide is mounted horizontally off the body of the cavity, which couples to both the deflecting mode and the LOM [3.6-56]. The cavity LOM couples strongly to the waveguide TE_{10} fundamental mode, while the deflecting mode couples as a higher-order TE_{20} mode and is rejected by the natural high-pass filtering of the waveguide, as shown for the LOM waveguide on the beam pipe in Figure 3.6-62. The waveguide LOM damper effectively damps the cavity monopole modes, as well as horizontal TM dipole modes (electric fields polarized in the horizontal plane). Vertical dipole mode damping, and additional damping of HOMs, are performed with a Y-end group consisting of three waveguides oriented symmetrically at 120-degree intervals (see Figure 3.6-60).

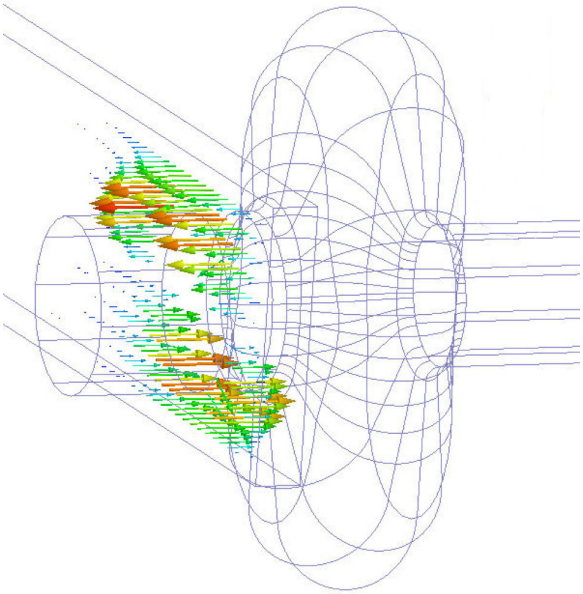

Figure 3.6-62: Field configuration of the deflecting mode coupling to the lower-order mode waveguide.

The level of damping due to the proposed scheme can be seen in Figures 3.6-63 - 3.6-65, where the impedance was calculated using the wake potential generated by a beam located on-axis for the longitudinal modes and a beam radially displaced by 10 mm for the transverse modes. Ideal damper ports on each waveguide termination were assumed for extracting the HOM/LOM power. The APS coupled-bunch stability threshold for 200 mA is shown for reference in the figures and is calculated using Equation (3.6-56). Eight cavities have been assumed where the impedance of each mode is assumed to add constructively in each of the cavities since the Q_{ext} of the LOMs/HOMs is on the order of 10s to 1000s.

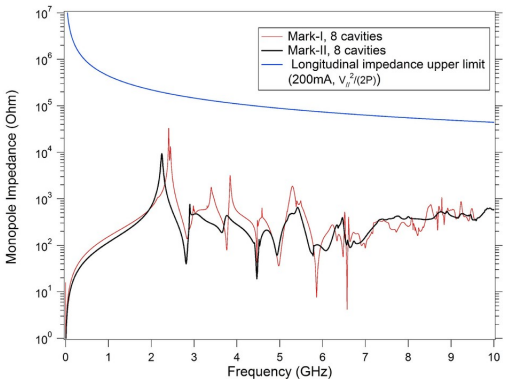

Figure 3.6-63: Longitudinal impedance spectrum of Mark-I and Mark-II deflecting cavity designs with APS beam stability limits for 200-mA beam current.

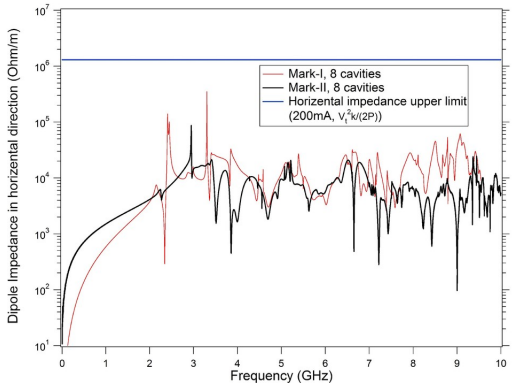

Figure 3.6-64: Horizontal impedance spectrum of Mark-I and Mark-II deflecting cavity designs with APS beam stability limits for 200-mA beam current.

The total power deposited in the dampers due to the beam has been calculated using the cavity loss factor. Additionally, narrow-band impedance or resonant buildup of LOM/HOM power has been

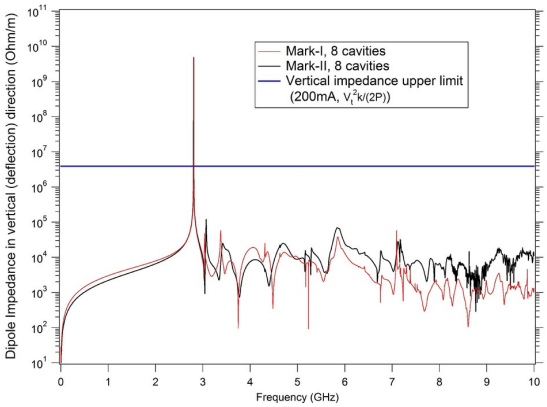

Figure 3.6-65: Vertical impedance spectrum of Mark-I and Mark-II deflecting cavity designs with APS beam stability limits for 200-mA beam current.

estimated by utilizing the fundamental theorem of beam loading and tracking the steady-state rise and decay of the cavity voltage due to periodic bunch trains [3.6-57, 3.6-58]. The average power absorbed by the dampers is calculated from the resultant transient voltage in the cavity and is a function of the bunch pattern, the Q_{ext}, and the frequency of the LOM/HOM. Figure 3.6-66 shows the average power P_b, normalized by the R/Q, for the 324 and 24 uniform bunch fill patterns for Q_{ext}'s of 100 and 1000, where the effects of the bunch form factor have been included. The longitudinal impedance of the SPX cavity is overlaid to show the overlap of the cavity modal structure with the Fourier components produced by the beam. The average power deposited by the beam into the damper is calculated as a sum of $R/Q * P_b$, for all cavity modes. As an example, the lowest-order monopole mode in the Mark-II cavity resonates at approximately 2.3 GHz. For the 24-bunch mode and a LOM Q_{ext} of 100, which is typical for the monopole modes, P_b is 23.2 W/Ohm, as seen in the plot. The damper load is 1.04 kW due to this single mode. The total power loss from the beam in each cavity for all monopole modes is 1.8 kW for the Mark-II cavity and 2.5 kW for the Mark-I cavity, but it is ultimately dependent upon the actual Q_{ext} of the LOMs/HOMs. As seen in the plots, there is no predicted resonant enhancement of the LOM power at the expected Q_{ext} values of 100.

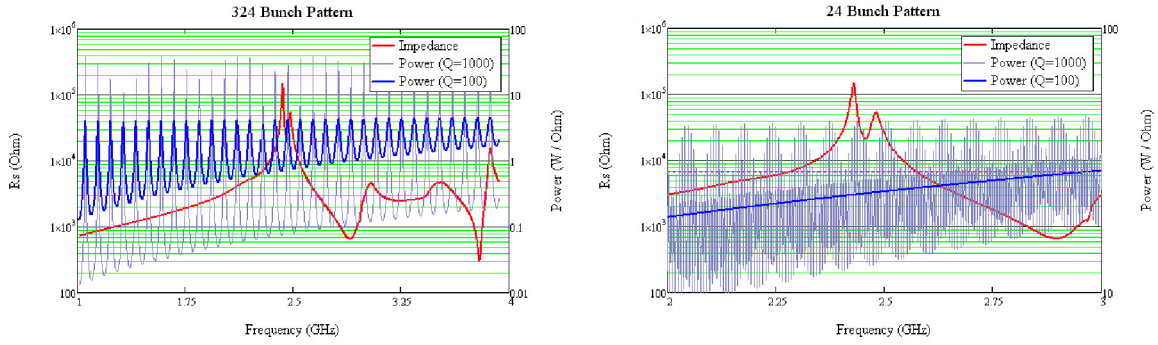

Figure 3.6-66: Longitudinal shunt impedance of the deflecting cavity overlaid on the Fourier spectrum produced by the beam in each of the cavities for the uniform 324- and 24-bunch fill patterns.

While the beam physics design of the deflecting cavity was predicated on fulfilling the cavity/beam-interaction requirements, the rf design optimized various rf performance parameters. Two variations

for the SPX cavity design were evaluated consisting of a low-loss (LL) and a low-peak magnetic field (LMF) options. Both designs anticipated improved rf performance from a reduction of the cavity iris diameter; however, in order to meet the single-bunch current requirements, a minimum diameter of 50 mm was chosen.

The LL design was based on optimizing the transverse $(R/Q)'$, which is related to the ohmic cavity losses P_c of the deflecting mode as follows:

$$\begin{aligned} \left(\frac{R}{Q}\right)' &= \frac{V_t^2}{2\omega U} \\ P_{\mathrm{c}} &= \frac{V_t^2}{2\left(\frac{R}{Q}\right)' Q_{\mathrm{u}}} \end{aligned} \tag{3.6-57}$$

where U is the cavity energy, and Q_{u} is the unloaded quality factor. Within constraints, the LL design was optimized by increasing the slope of the end walls and creating a cylindrically symmetric cavity geometry, as opposed to the squashed cell. An improvement of approximately 20% for the $(R/Q)'$ was made relative to the LMF variant.

Table 3.6-36: Comparison of low-loss and low-peak-magnetic-field cavity designs.

Design	Frequency (GHz)	$(\mathbf{R/Q})'$	$\mathbf{P_c}$ @ 0.5 MV (W)	$\mathbf{B_p/V_t}$ (mT/MV)	$\mathbf{E_p/V_t}$ (MV/m/M)
LMF	2.815	17.8	6.9	182	88
LL	2.815	21.25	5.6	208	79

The LMF design was intended to minimize the peak surface magnetic field in order to create a higher operating gradient thereby producing a more compact cryomodule design. The process of optimizing the LMF design resulted in a squashed racetrack shape, similar to KEK's design. Other modifications, such as increasing the radius of the blend in the high magnetic field region on the cavity iris, as well as creating a vertically oriented elliptical iris to distribute the magnetic field over a larger area, were not attractive due either to inadequate mode damping or the reduction of deflecting voltage for a given peak magnetic field.

A comparison of the LL and LMF designs for a cavity iris diameter of 50 mm can be seen in Table 3.6-36. Note that the peak surface electric field is elevated in the LMF design while the peak magnetic field is reduced by 12%. It will be shown that field emission at high gradients, which is a symptom of high-surface electric fields, does not appear to be a significant limiting factor in the single-cell cavity. Since a peak surface magnetic field not exceeding 100 mT has been specified as a design objective and since the cavities will be integrated into limited available space in the APS storage ring, the LMF design offers preferred rf parameters and has been selected over the LL design. The Mark-I and Mark-II cavities are manifestations of the LMF design. Parameters for the Mark-II deflecting cavity are shown in Table 3.6-37.

The damping elements of each of the SPX cavities will be required to cumulatively dissipate up to 2.5 kW of power with the LOM damper receiving the largest percentage due to strong coupling to the cavity monopole modes. The LOM damper design has been rated for 2-kW power loading to handle either the Mark-I or Mark-II designs. As a result, high-power damper designs are being investigated that are capable of dissipating kilowatts of power. The dampers are required to have a good match across a wide bandwidth in order to meet the stability requirements outlined in Figures 3.6-63 - 3.6-65.

Table 3.6-37: Mark-II deflecting cavity parameters. Note that 200 mA is the design requirement, providing a safety margin relative to the 150 mA operations requirement.

Quantity	Value	
Frequency	2815	MHz
Q_{u}	10^9	
V_{t}	0.5	MV
Energy	0.38	J
k_{ll}	0.28	V/pC
σ	40	ps
$(R/Q)'$	18.6	Ohm
E_{peak}	41	1/m
B_{peak}	100	mT/MV
P_{loss} @ $Q_{\mathrm{u}} = 10^9$	7	W
I_{beam}	200	mA
No. cavities	4×2	

Based on design work and experimentation for low-power dampers [3.6-59], SiC in-vacuum dampers are shown to be broadband and well-suited for ultrahigh vacuum environments. Preliminary numerical analysis of high-power waveguide dampers using a similar material has been performed [3.6-60], where a network of metal posts brazed to the lossy dielectric has been designed as a possible stress relief for the critical brazing operation. A detailed description of dampers development can be found in later sections of this chapter.

The Mark-II cavity design offers improved parasitic mode damping, reduced damper loading, and improved cavity packing factor as compared with the Mark-I design. However, the perturbation on the surface of the cavity body is not routinely attempted in order to prevent enhancement of the peak surface magnetic field. Due to the magnetic field null on the horizontal center plane of the cavity for the TM_{110} mode, a waveguide damper with a careful design of the coupling iris at this location is not expected to produce a detrimental effect on the cavity rf performance. Since the cavity interior of the alternate design is only slightly modified as compared with the Mark-I design, the rf performance at the operating frequency is not significantly altered.

Although the Mark-II cavity has improved damping, any susceptibility to field enhancement and multipacting has to be carefully considered. The peak surface magnetic field is controlled by adjusting the dimensions of the coupling iris and utilizing the rounded dog-bone shape. The potential to suffer from multipacting, on the other hand, is a phenomenon that typically occurs in high magnetic field regions especially near parallel surfaces, conditions which exist near the coupling iris of the LOM waveguides. Multipacting analysis was performed on the Mark-I and Mark-II designs using the parallel 3-D code Omega-3P and Track-3P, where the impact number during 40 rf cycles for electron impact energies between 25 eV and 1.5 keV is shown in Figure 3.6-67. It was found that signs of multipacting occur in both designs along the cavity blend to the end groups with second-order multipacting occurring at a deflecting voltage of approximately 0.3 MV. However, the simulation results do not show any enhancement of multipacting in the Mark-II cavity as compared with the Mark-I design. In fact, experimental results at JLab of a simplified on-cell damper without end groups has not shown significant signs of multipacting.

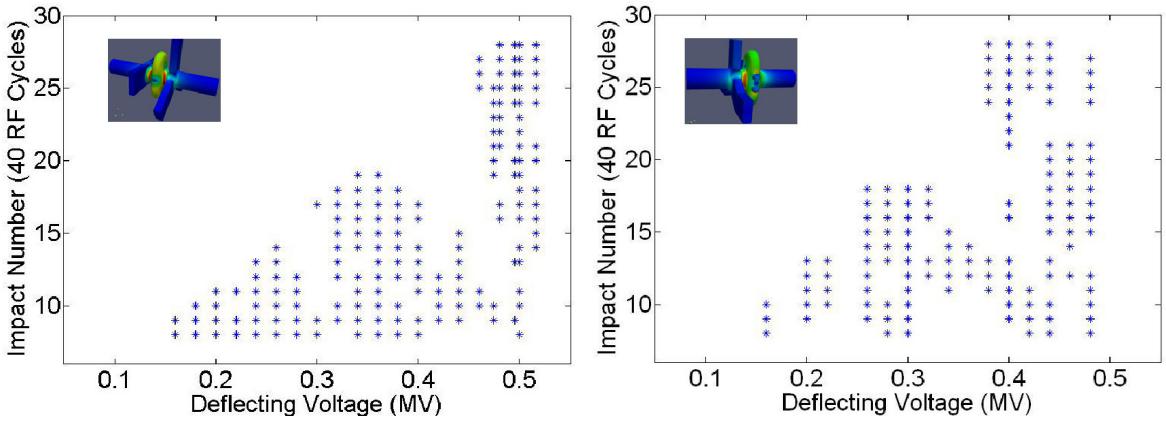

Figure 3.6-67: 3-D multipacting simulation results from SLAC codes Omega3P/Track3P for the Mark-I and Mark-II cavity designs. Forty rf cycles were monitored for resonant electron impacts with energies ranging from 25 eV to 1.5 keV.

Multi-cell options have also been explored including a two-cell cavity, a novel three-cell cavity with a central damping cell for same-passband modes [3.6-61], and a two-cell and a five-cell superstructure [3.6-62]. However, each of these cavities suffer from some combination of peak magnetic surface field enhancement, manufacturing and processing limitations, or insufficient mode damping.

An unloaded quality factor of 10^9 has been assumed for the SPX deflecting cavities based on experimental test data at JLab as shown in Figure 3.6-68 for a single-cell cavity and for the Mark-I cavity prototype. As a result, the anticipated total cryogenic load at 2K due to static and dynamic losses for eight cavities is approximately 80 W. A modest Q-slope at high gradients can be seen, implying that field emission is not a significant factor.

Experiments on prototype Mark-I and Mark-II have shown Mark-II is a viable choice for SPX cavity design based on design parameters and the achieved field and anticipated improvements in Q. Details can be found in section 3.6.4.9.

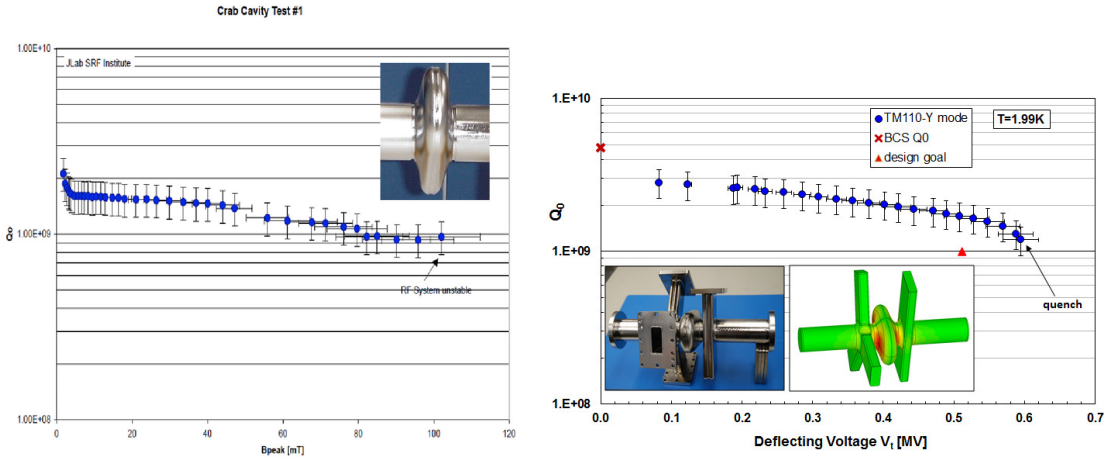

Figure 3.6-68: Experimental data of the Q vs. peak magnetic deflecting field for a single-cell cavity without waveguide end groups (left) and for the prototype Mark-I cavity (right).

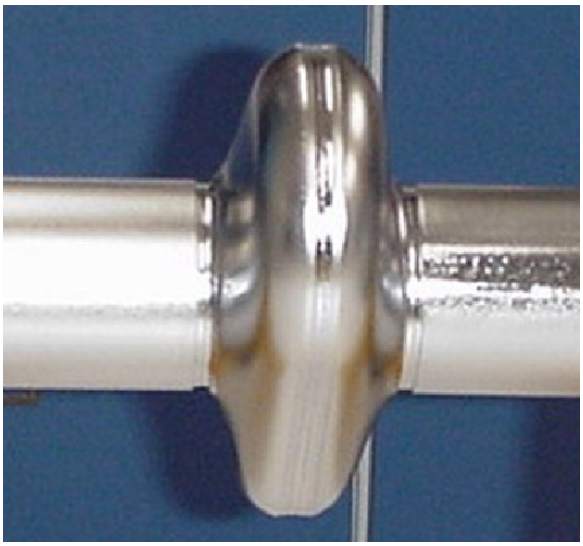

Figure 3.6-69: Single-cell (without end groups) prototype deflecting cavity.

Figure 3.6-70: On-cell damper prototype deflecting cavity.

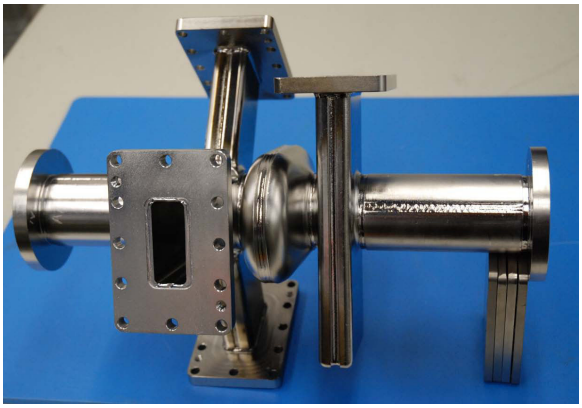

Figure 3.6-71: Mark-I prototype deflecting cavity.

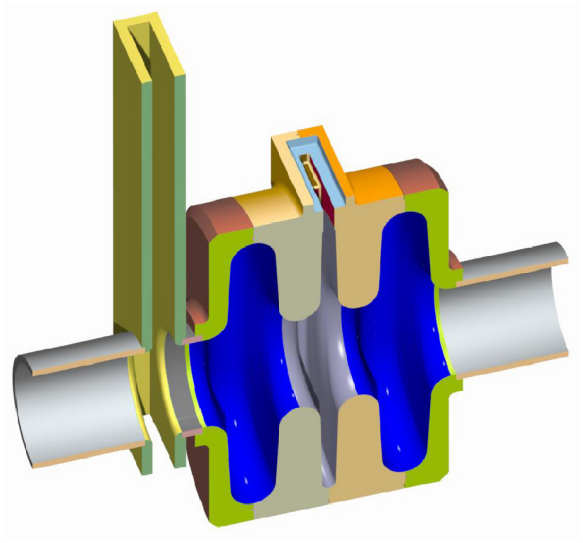

Figure 3.6-72: 3-cell with damping cell model of deflecting cavity.

3.6.3.8.3 Cavity Material

Cavity material is high purity niobium. Its residual resistivity ratio (RRR) must be greater than 300. Cavity wall thickness is recommended to be 3.5 mm. Large-grain niobium disks are sliced from ingot. Table 3.6-38 lists the allowed levels of impurities in the niobium.

Table 3.6-38: Niobium material specification.

Element	Weight ppm
Metallic element	
Ta	500
W	70
Ti	40
Fe	30
Si	30
Mo	50
Ni	30
All others	<30
Light element	
O	10
N	10
C	10
H	2

3.6.3.8.4 Cavity Fabrication

Standard niobium cavities are deep drawn in half-cells from niobium thin sheet before they are joined to form a closed cavity using electron beam welding. Their round shape makes the trimming relatively easy. The SPX deflecting cavity has an oval shape and is unusually narrow along the beam axis direction. Such a shape makes it a perfect candidate for direct machining of half cells instead of forming. The direct machining method can use niobium materials sliced from a niobium ingot, a practice that avoids the formed fine-grain niobium sheet material that sometimes exhibits non-ideal crystal grain distribution or inclusion of foreign materials.

For SPX cavities, large-grain billets are sliced from a large-grain niobium ingot with sufficient thickness. Half cells are then machined out from niobium billet using a high-precision computerized numerically controlled (CNC) machine. Such practice ensures the highest accuracy for parts geometry, which otherwise can change cavity resonance modes and field distribution dramatically. Once half cells are machined, they need to be chemically etched to remove at least 25 microns of surface material before proceeding to electron beam welding. The chemical etching removes potential foreign material inclusion that is common after machining. The final joining of cavity half cells and other components requires electron beam welding. The base vacuum of the electron beam welding equipment should be better than 10^{-5} Torr.

Upon finishing cavity fabrication, optical inspection is required to investigate the integrity of e-beam weld joints and general surface quality. Results are to be documented and any apparent defects are to be repaired before cavity processing.

3.6.3.8.5 Cavity Processing

SPX cavities should be processed with the following procedures once they are fabricated.

1. Visual inspection of all the sealing surface and optical inspection of internal surfaces, particularly the weld areas
2. 90-μm BCP, DT<10°C, 1-μm/min etching rate, inlet to outlet DT<1.5 °C
3. Ultrasonic degrease
4. HPR 1 hour
5. 600°C/10-hour bake out with furnace vacuum $< 5x10^{-6}$ Torr
6. Mechanically tune the cavity to a resonance frequency of 2809.300 MHz, which will produce the desired frequency of 2815 MHz at cryogenic temperature.
7. 10-μm BCP, DT<10°C, 1-μm/min etching rate, inlet to outlet DT<1.5 °C
8. Ultrasonic degrease
9. HPR 1 hour

Large-grain niobium is known to be "soft," i.e., to have a low yield strength. For this reasons, a 600°C hydrogen bake-out for 10 hours is preferred instead of the 800°C, 2-hour bake-out commonly used in other SRF applications, since large-grain niobium could be potentially further softened by an 800°C bake-out.

After processing, the cavities are tested in a vertical Dewar at 2K to check the frequency. Past experience shows that the SPX deflecting cavity resonance frequency shifts by around 6 MHz compared to room temperature. Based on this, additional tuning may be performed to reach the desired frequency.

3.6.3.8.6 Cavity Vertical Test

Cavity vertical tests are needed to ensure cavity internal surfaces are of sufficiently high quality before proceeding with helium vessel attachment, since it is generally difficult to apply additional chemical processing after the helium vessel is attached to the cavity. This is, first, because the helium vessel enclosure prevents easy cooling of the cavity wall, which is needed during processing as the chemical process generates heat. Any temperature change exceeding 15°C will create a run-away chemical process that could etch away more niobium material than anticipated. The high cavity-wall temperature will also drive excessive hydrogen into the niobium. Secondly, the helium vessel prevents attachment of diagnostic temperature sensors that can identify cavity defects.

The cavity vertical test should measure the cavity Q value at various field gradients at 2K. Measurements should be taken at different temperatures for further cavity performance analysis, notably 1.8 K and lower temperatures, down to 1.6 K.

Cavities that achieve 120 mT with a Q greater than 10^9 are considered qualified for helium vessel attachment.

A vertical cavity test facility is being adapted for the SPX deflecting cavities at Argonne, in collaboration with the Argonne Tandem Linear Accelerator System (ATLAS), a heavy-ion superconducting facility. The deflecting cavities manufactured and tested at JLab will be tested in this facility in October 2012 to benchmark results and to perform high-power testing of a fully dressed single-cell cavity.

Additional processing of the cavities may also be performed at ATLAS using the ILC clean room and chemistry facilities.

3.6.3.8.7 Helium Vessel

The Boiler and Pressure Vessel Code (BPVC) is an American Society of Mechanical Engineers (ASME) standard that the Department of Energy adopted for all the future accelerator projects. The SPX cryomodule uses a titanium helium vessel to enclose the niobium cavity to provide liquid-helium cooling of the niobium cavity. The volume of this helium reservoir is considered a pressure vessel, since liquid helium can expand and become pressurized when heated. This pressure vessel includes material of titanium, niobium, and inter-joining niobium-titanium (NbTi) alloy. The ASME BPVC standard requires the vessel internal pressure be no higher than 5 atm and the external pressure no higher than 3 atm. The maximum allowable stress of titanium would be 12.1 kpsi. Since Nb and NbTi are unlisted materials, they cannot be evaluated by the BPVC standard. Practices adopted by DOE national labs have been to use 2/3 of the measured yield stress or 1/3.5 of the tensile stress, whichever is lower, as the maximum allowable stress for these two materials. For an SPX cavity with helium vessel, the weakest material is the niobium. Hence the maximum stress is set at a conservative 6,310 psi. The current helium vessel design uses a flat head at the cavity end compared to other SRF projects to conserve space as shown in Figure 3.6-73. The titanium vessel thickness is set at 0.58 in. for the head while the shell is set to 0.125 in. The titanium bellows is at a reduced diameter of 5.5 in. The end plate of the helium vessel retains the same size as the opposite vessel heads to allow the attachment of the tuner and nitronic rods. Electron beam welding in a butt joint style is planned to join the niobium beam pipe and NbTi transition, while the NbTi transition and titanium vessel head will be joined using a standard weld. The weld joint between titanium head and shell follows BPVC recommendations, as shown in Figure 3.6-74.

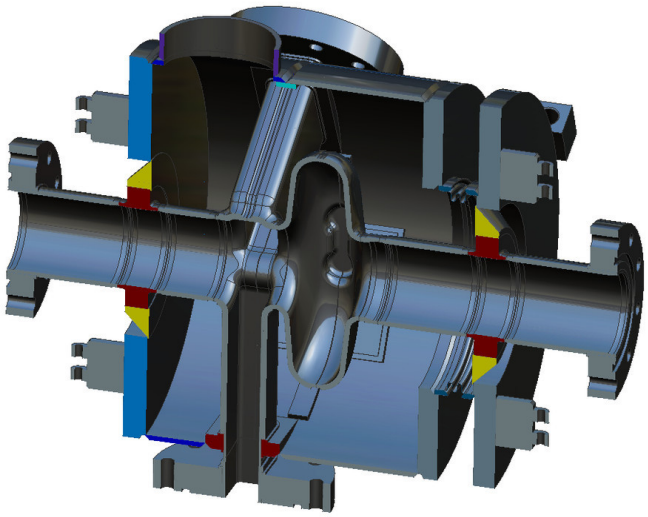

Figure 3.6-73: Helium vessel sectional view.

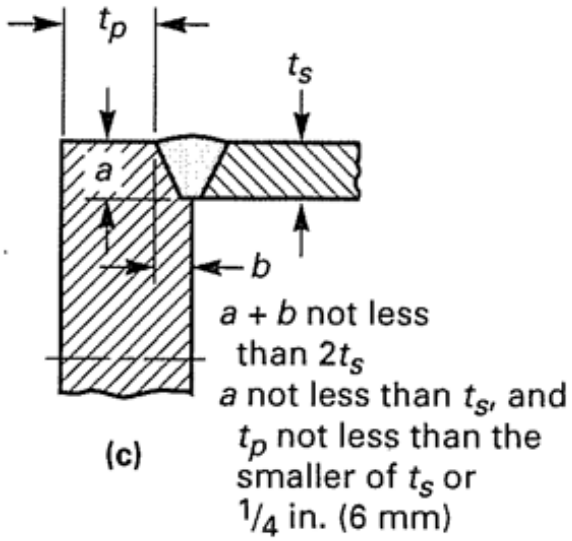

Figure 3.6-74: BPVC recommended weld joint.

The joint between titanium shell and the cavity waveguide uses “saddle” geometry as shown in Figure 3.6-75.

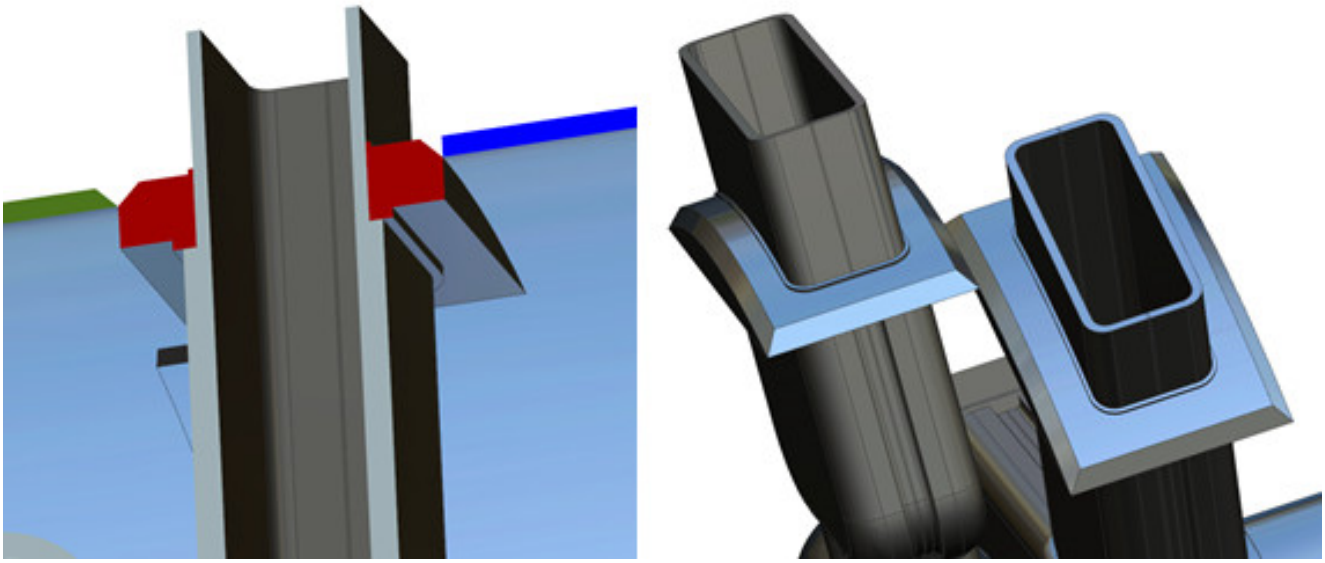

Figure 3.6-75: Saddle joints of waveguide and helium vessel shell.

A “shell joint” refers to a longitudinal and circumferential (categories A and B in BPVC) joint in a titanium vessel. All shell joints must be either double-welded butt joints or single-welded butt joints with backing strip as shown in Figure 3.6-76.

A stress analysis with the above-described helium vessel geometry showed that the niobium cavity has a maximum stress of 6,100 psi under 2.2 atm of expected vessel pressure during cryogenic cool down,

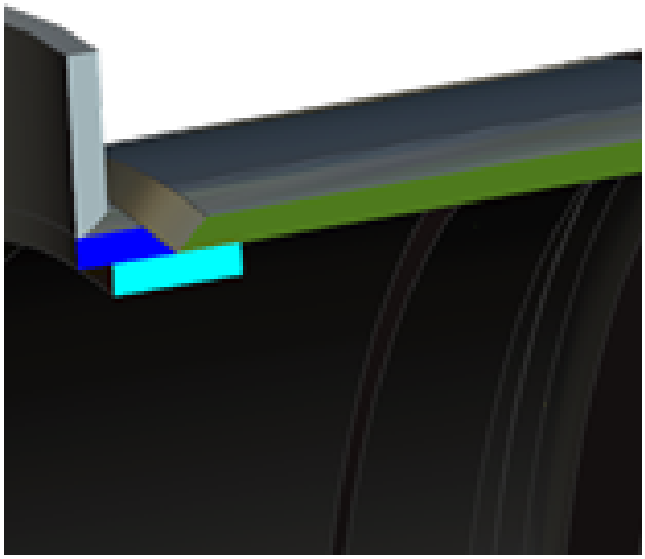

Figure 3.6-76: Shell joints of titanium vessel.

when cold helium gas expands as it flows through the helium supply line to the helium vessel. The maximum stress location was where the cavity LOM waveguide meets the cavity equator, as shown in Figure 3.6-77. This calculation shows that the cavity and helium vessel satisfy the pressure vessel requirement dictated by the BPVC standard. This also suggests that the cryogenic cool down of the cryomodule must be controlled to be slow enough so that the helium pressure does not exceed 2.2 atm.

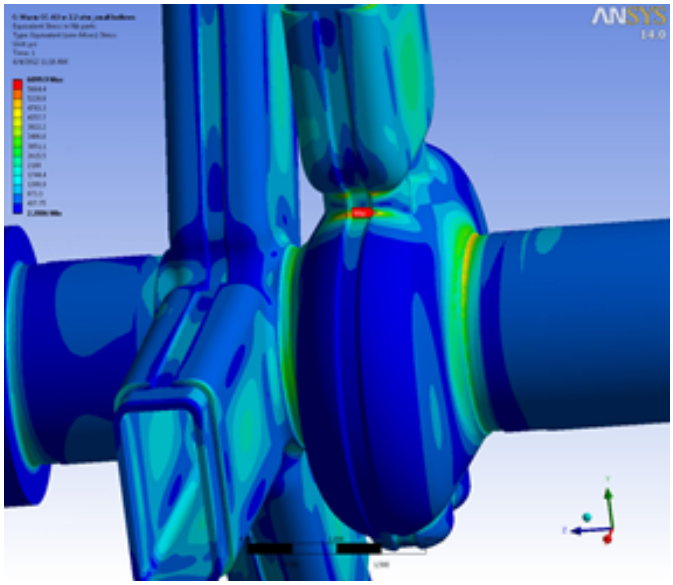

Figure 3.6-77: Stress analysis of the cavity and helium vessel shows maximum stress of 6.1 ksi when the helium vessel is under 2.2 atm pressure.

Figure 3.6-78 shows an SPX0 deflecting cavity fitted with a titanium shell as a mock-up for dimensional checks for interference. Figure 3.6-79 shows a complete cavity helium vessel with different

parts explained in detail.

Current analysis of system stress did not include the attachment of tuner and nitronic rods. Further analysis is in progress while the prototype is being fabricated for actual measurement at cryogenic temperatures.

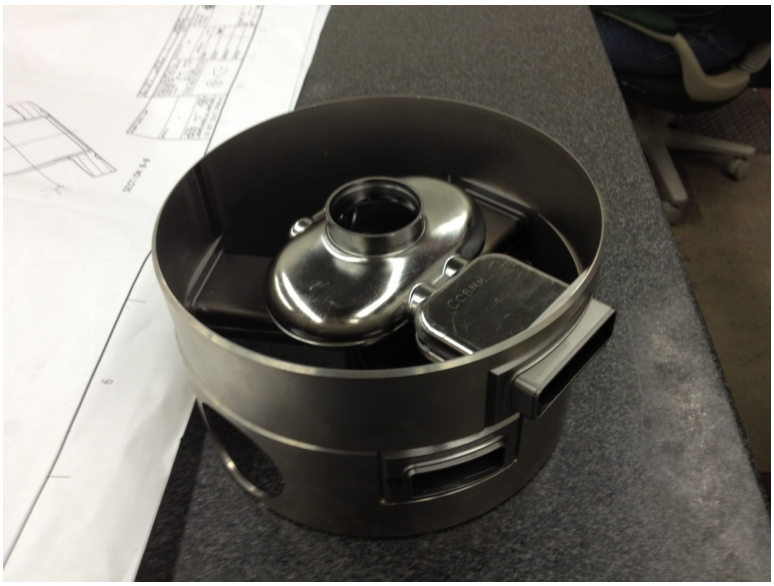

Figure 3.6-78: A SPX0 deflecting cavity enclosed by helium vessel components for a dimensional check.

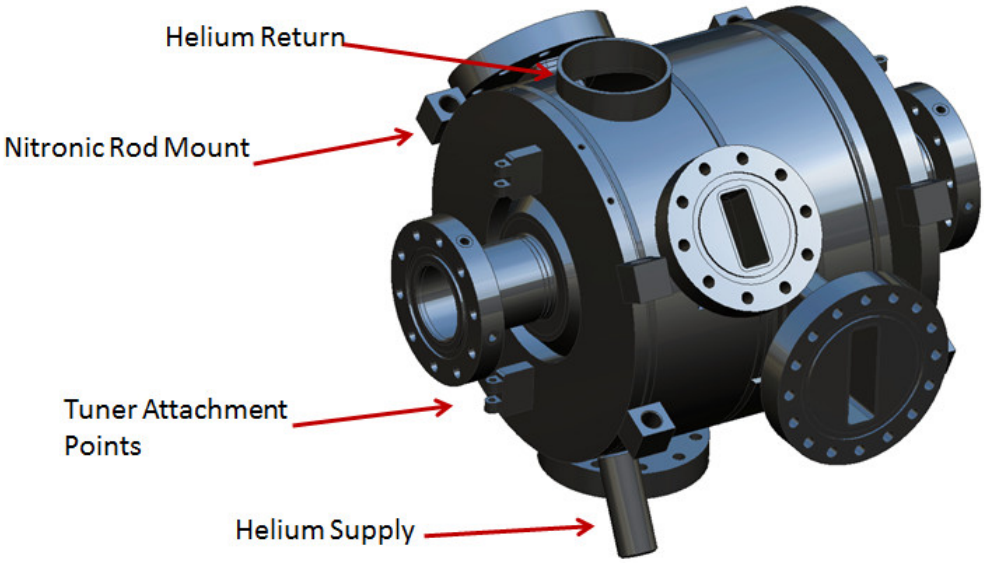

Figure 3.6-79: A complete model of the cavity helium vessel.

3.6.3.8.8 Tuner

The helium-vessel-dressed SPX cavities will be fitted with a CEBAF-style scissor jack tuner. Slow tuning will be realized by a stepping motor. Fast tuning will be accomplished through a piezo-electric actuator, which is optional. Both the stepping motor and the piezo actuator will be located outside of the cryostat. The tuner will be set to tension during initial installation. The tuning range needs to be $\pm$200 kHz with a fine adjustment range of $\pm$25 kHz. The tuning resolution needs to be at least 40 Hz. The optional fast tuner functions mostly for a machine protection (see section 3.6.3.4.10), rather than being used for microphonics compensation as is commonly practiced in other SRF accelerators. The benefit of such tuners may be that they allow the SPX cavities to detune quickly enough to maintain stored beam operation while the cavities are decoupled from the beam. For SPX cavities with loaded Q around 1×10^6, the frequency detuning needs to be 30 kHz to drop the cavity stored energy driven by the beam to a safe level of 1% of the nominal on-resonance stored energy. A 60-kHz tuning range should provide sufficient margin for quick cavity detuning. The resolution of such fast tuning is not critical. The response time should be less than 1 ms, which is close to the decay time of the SPX cavities.

Based on the Mark-II cavity design, the tuner design shown in Figure 3.6-80 was completed. Its parameters are listed in Table 3.6-39.

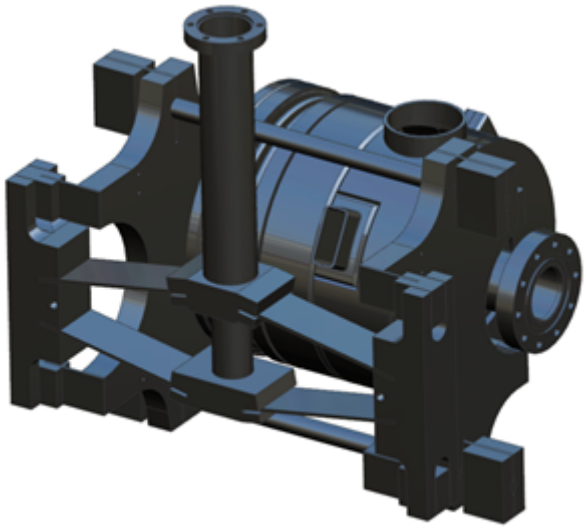

Figure 3.6-80: A dressed cavity is attached with a tuner.

Stress analysis has been conducted to investigate the integrity of tuner components. In the case of a 0.5-mm tuner movement, the maximum stresses are all well within the yield stress. Figure 3.6-81 shows maximum stresses for different tuner components. Their percentages relative to the material yield stress are listed in Table 3.6-40. As the cavity will be stretched or compressed by an amount much less than 0.5 mm, it is concluded that the tuner mechanical design is sound.

Table 3.6-39: Cavity tuner parameters.

Quantity	Value	
Tuning sensitivity	9,000	KHz/mm
Stiffness	170,000	lbs/in
Deflection required for 200kHz shift	22	μm
Force required for 200kHz shift	149	lbs
Step motor resolution	800	steps/rev
Harmonic drive ratio	100	
Ball screw pitch	2	mm/rev
Full step resolution	31.6	Hz/increment
Half step resolution	15.8	Hz/increment
Quarter step resolution	3.4	Hz/increment
Piezo range in displacement	60	μm
Piezo range in frequency	75.8	kHz
Piezo resolution in displacement	0.13	nm
Piezo resolution in frequency	0.16	Hz

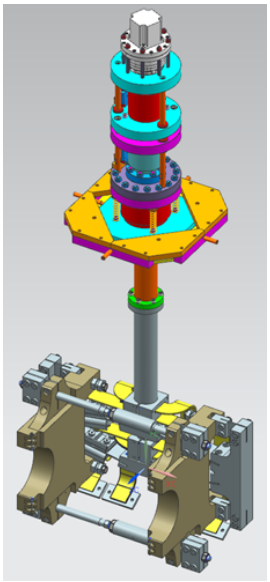

Figure 3.6-81: A complete tuner assembly.

3.6.3.8.9 Fundamental Power Coupling

For use in SPX, a double-window design consisting of two commercially available ceramic pillbox windows, designed to transmit 10-kW rf power, was developed. The ceramic window material is pure Al_2O_3. The window mating flange is a round flange with a rectangular rf seal inside a round vacuum seal. This design allows the power coupling waveguide to extract some of the HOM power along with the other two HOM waveguides in the same Y end group.

Table 3.6-40: Maximum stress in tuner components (% of yield).

Components	Cold	Warm
Pivot arm	23%	26%
Jack arm	25%	45%
Hinge arm	18%	32%
Fulcrum bar	9%	16%

3.6.3.8.10 Cavity Microphonics

Microphonics can adversely affect the cavity frequency and requires extra rf power to compensate the frequency shift. Excess frequency shift may increase the cavity voltage and phase noise.

Vibrations can be introduced through cryomodule connections such as helium pipes, nitronic rods, power coupler, LOM coupler, tuner mount, and cooling water channel that are connected to HOM dampers.

Measurement of these vibration sources will be conducted in various stages as soon as they become available to test. Simulation of a full-system vibration response is in progress. The piezo actuator provided in the warm tuner assembly can be utilized to suppress excessive microphonics when needed.

3.6.3.8.11 Cavity Horizontal Test

The horizontal test of a dressed cavity requires the helium to be contained in the helium vessel only. Such a test typically introduces high-power rf through the power coupler at the nominal external Q compared to a near unity coupling in vertical testing. The horizontal cavity test serves to verify the integrated system performance, which includes the helium vessel, tuner, and power coupler. Cavity performance can degrade during cavity helium vessel attachment, a process usually called cavity dressing. Hence, the horizontal test also serves to verify the cavity and coupler performance after cavity dressing.

As a part of the R&D plan for the SPX0 cryomodule, a new design for the helium vessel and tuner is being prototyped at JLab. ANL is expected to test an SPX0 cavity with the helium vessel and tuner to verify the design specifications of the cavity, helium vessel, and tuner assembly before SPX0 cryomodule production can start. During the horizontal test of the SPX0 cavity, the LLRF system will also be tested. Statistics of rf phase noise and amplitude noise will be measured.

Figure 3.6-82 illustrates a Dewar insert that holds a dressed cavity with the tuner and power coupler attached for a horizontal test.

3.6.3.8.12 Cavity Alignment

The electrical center lines of the SPX cavities have to be precisely aligned to the beam within a certain offset for optimized rf power coupling to the beam. In some cases, although not common, alignment can be utilized to reduce the LOM energy transferred from the beam to the cavity rf field. The requirements, listed in Section 3.6.3.1, are that the electric center of the SPX cavities must be within

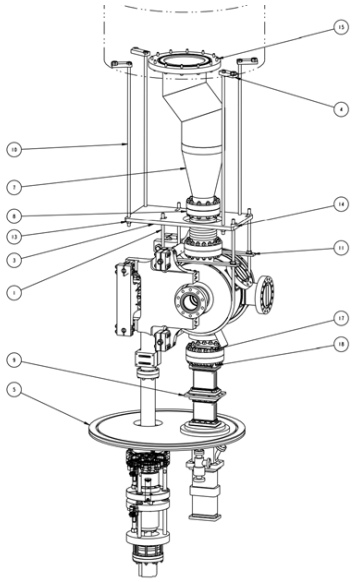

Figure 3.6-82: TC2 dewar insert for horizontal test setup at ATLAS test area.

$\pm 200\ \mu m$ of the beam center line in the Y direction. The X and Z misalignments are less critical at $\pm 500\ \mu m$ and $\pm 1000\ \mu m$, respectively.

The SPX cavity's long radius points along the Y-axis, which is the direction of the intended electron beam tilt. The alignment of this direction is important for proper operation of the system. As listed in section 3.6.3.1, the overall SPX cryomodule shall have roll misalignment of less than 10 mrad, while the yaw and pitch misalignments can be no more than 10 mrad.

Since cavities are paired together with a solid connection, extra care must be taken during assembly of cavity pairs. Cavities will be subjected to a rigorous process of fiducialization and measurement. During cavity fabrication, tooling ball receptacles will be machined onto the cavity, typically on the beam pipe flanges. Stretched-wire measurements will then be used to locate the cavity electrical centers and to monitor excessive cavity center deviation between cavity processing steps, which includes helium vessel dressing and rf tuning. Coordinate measurement machine (CMM) measurements will pre-determine potential flange misplacement. Once the cavity's electric centers are located relative to the tooling balls, cavities can go to their final qualification, and cavity pairs can be assembled. At this stage, the cavity tooling balls serve to locate the cavity electrical centers, which can then be transferred to alignment "rabbit ears" on the space frame and out to the cryostat vacuum shell. These rabbit ears can then be used to align a cryomodule to the beamline during tunnel installation.

3.6.3.8.13 Bellows

The SPX cryomodule requires a flexible bellows at two temperature zones. Figure 3.6-83 shows a schematic of an SPX cryomodule. It includes two deflecting cavity-pairs joined by a flexible bellows, and the cavities are operated at 2 K. The bellows connecting the cavities is cooled by thermal conduction. Its cooling can be enhanced by extra thermal anchoring in the middle of the bellows. The other two bellows will be in the transition sections from 2 K to 300 K. These bellows are in close proximity to the cavities, and they are required to have minimal particulate generation during bellows

flexing. A bellows at the end of the cryomodule will be completely at room temperature. Since its location is far away, its particulate-free requirement can be relaxed; hence, a shielded bellows can be used.

Bellows are used to connect neighboring cavity pairs to each other and to room-temperature valves. The heat generation from wakefields deposited in these bellows has to be minimized, in order to avoid excessive load on the cryogenic budget. For an SPX cryomodule, the heating of the bellows itself would be less than 0.5 W. It is preferable for the inter-cavity bellows to have high thermal conductivity to allow thermal strapping to be effective in removing heat from the bellows. For the transitional bellows, a lower thermal conductivity would be preferred to reduce the static heat flow from high-temperature components to cryogenic components. This suggests a copper-based inter-cavity bellows and a stainless steel-based transitional bellows with a copper inner coating.

Alignment parameters require that the bellows be flexible enough to allow transverse skew motion of 0.5 mm. Thermal contraction requires the bellows to allow a longitudinal motion of 1.0 mm. The SPX cryomodule plans are to employ the same physics design for both inter-cavity bellows and thermal transition bellows.

The bellows design shown in Figure 3.6-84 has been adopted. Six shallow convolutions are divided into two groups to increase mechanical flexibility. The bellows convolution starts inward from a 52-mm inner diameter and is symmetrical, so that the spatial volume of the bellows is equal to the volume of a pipe with 52-mm inner diameter. These careful considerations are important to keep the beam-loss factor low while providing sufficient mechanical flexibility.

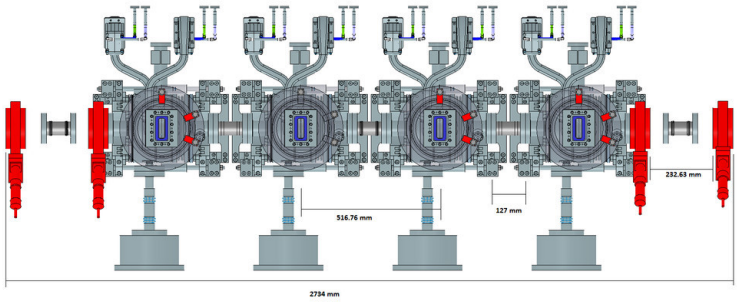

Figure 3.6-83: Four cavity string assembly of a SPX cryomodule.

The prototype bellows has been fabricated and a test with storage beam is planned in January 2013. A backup bellows of the same length with an aperture similar to the APS shielded bellows is also being fabricated.

3.6.3.8.14 Magnetic Shielding

It is well known that a DC residual magnetic flux inside of the cavity can be trapped in the niobium material when it cools below transition temperature. For 2.815 GHz, each additional milligauss of trapped magnetic field increases the cavity residual resistance by 0.5 nΩ. Vertical tests of the deflecting cavity where residual magnetic field is known to be negligible showed its surface resistance was dominated by a residual resistance of 120 nΩ. Any additional increase of residual resistance will decrease the operating Q_0 below 1×10^9. To insure the surface resistance is low when the cavities are

in the cryomodule, the residual DC magnetic field needs to be maintained at less than 20 mG. For the SPX cryomodule, the cavity string magnetic shield will be realized using two layers. The first layer of the magnetic shield encloses the cavity string outside of the helium vessels. Due to the large number of port openings associated with waveguides of the SPX deflecting cavities, a second layer of magnetic shielding will be inserted inside of each helium vessel to provide a direct encapsulation of the niobium cavities. Engineering analysis is being pursued to verify that this is a practical shielding solution.

3.6.3.8.15 Helium Circuit and 4K thermal intercepts

A conceptual compact helium circuit design based on the SNS cryomodule design has been developed instead of following the CEBAF cryomodule design, which uses separate end can technology. In this conceptual design, a helium heat exchanger sits inside of the SPX cryomodule at the upstream location. The unit cools the incoming liquid helium stream with the boil off helium gas. The return gas pipe travels to the downstream end of the cryomodule and provides an anchor line for the 4K thermal intercepts.

3.6.3.8.16 Cryomodule Instrumentation and Control

Cryomodule internal instrumentation provides monitoring of helium, thermal conditions, RF, and vacuum. Helium instrumentation includes the helium level and pressure sensors, as well as temperature diodes for the helium heat exchanger, helium supply line, and return gas manifold. Thermal instrumentation includes thermal diodes and thermocouples at various locations to provide a complete thermal profile of the cavity string, tuner, alignment fixtures, fundamental power coupler, LOM coupler, HOM coupler, beam pipes, and bellows. RF instrumentation includes field probes from the beam pipe and HOM waveguides to provide cavity field and HOM power spectra. Vacuum pressure of both the cavity and the insulating space are monitored. Heaters are attached to the HOM waveguide dampers to prevent cooling water from freezing in case, for example, the HOM damper receives no HOM power when beam is off.

Cryomodule external instrumentation includes the window IR detectors and arc detectors for FPC windows and LOM windows, as well as water flow and temperature monitoring for cooling water for HOM dampers, FPC windows, and LOM windows. LOM field probes monitor the LOM power amplitude and HOM power spectra.

Additional cryogenic instrumentation that maybe closely related to cryomodule operation is covered in the cryogenics section.

3.6.3.8.17 Particulate Consideration

The SPX cryomodule is an SRF cryomodule being integrated with an existing particle accelerator for which particulate control was not originally a concern. Such a legacy accelerator beamline poses a significant challenge for SRF cavities, where particulates can cause cavity performance degradation when they migrate to the cavity high field surfaces.

Guidelines for maintaining a particulate-free environment are being categorized into three areas related to work on beamline components near the SPX cryomodule. The first area is that of initial beamline

component design and fabrication. Internal vacuum surfaces are required to be free of large recesses that are hard to clean or that may easily trap particulates. Electropolishing of internal surfaces is recommended to further eliminate particulate trapping. The second area is that of installation. Parts are to be ultrasonically cleaned and dried in a clean area. Installation requires clean assembly in a local clean room wherever it is possible. The third area is that of post-installation maintenance. Subsequent opening of the vacuum space requires filtered clean nitrogen purging in a laminar flow to prevent particulate movement.

Additional steps are under consideration. Controlled purging using filtered clean nitrogen can be applied from time to time to clean up nearby beamline components as a preemptive measure. Electrostatic trapping next to the SPX cryomodule is also being considered to intercept any charged, floating particulates inside the beamline vacuum space.

3.6.3.8.18 Cryomodule and Mechanical Design [1.03.03.05 / 1.03.03.07]

A total of two cryomodules will be utilized for the SPX project. One will be located in Sector 5 to produce a 2-MV beam chirp, while the other, located in Sector 7, will reverse the chirp to return the beam to its nominal orbit. Each cryomodule will contain four cavities at 2 K operating at 2815 MHz to produce a 0.5-MV deflecting voltage in each cavity. To provide a safety margin for 150 mA operation, the cryomodule will be designed to support a beam current up to 200 mA, and as a result, it must incorporate features to support heavy parasitic-mode damping. It will accommodate high cryogenic loads from dynamic losses, as well as from static losses due to numerous waveguide penetrations from the dampers and power couplers. Alignment tolerances are also critical to maintain LLRF tolerances. Parameters for the engineering design of the cryomodule are shown in Table 3.6-41.

Two deflecting cavities will be connected by a solid beam pipe to form a cavity pair. Each cavity pair will be connected by a low-impedance flexible bellows and supported and aligned using assembly techniques that routinely achieve 500-μm alignment accuracy at JLab. A cylindrical cryomodule geometry has been chosen for the deflecting cavities due to the availability of proven designs for elliptical cavities [3.6-63–3.6-65] and for the anticipated mechanical advantages in achieving tight alignment tolerances due to the symmetric radial forces during cool down. The overall diameter of a typical cryomodule at JLab is 1.0 m and supports a cold mass with transverse dimensions that are comparable with the SPX TM_{110} squashed-cell deflecting cavity.

An R&D effort is being undertaken at JLab to achieve an alignment of the electrical center of the cavities with the beam axis with a goal of 100 μm when installed and adjusted in the cryomodule. The alignment mechanism will consist of actuators to adjust the vertical offset of each cavity. The final alignment will necessarily be beam-based where techniques such as those used by BNL and SLAC will be utilized. The cavity will be adjusted using the TM_{110} dipole mode excitation in the cavity until the signal is nulled, such as during alignment of dipole-mode BPMs. Wire position monitors will be utilized to monitor the alignment during and after cool down.

A view of the cavity string mounted within a conceptual cryomodule is shown in Figure 3.6-83. Each cavity requires four waveguide penetrations with thermal transitions from the cold mass to room temperature with a flexible waveguide assembly to compensate for thermal contraction.

Table 3.6-41: Selected SPX cryomodule design parameters.

Quantity	**Value**
Cavity Frequency	2.815 GHz
Operating Mode	TM_{110}
Cavity Iris Radius	25 mm
Cavity Active Gap	53.24 mm
Number of Cells per Cavity	1
Unloaded Q	$> 10^9$
Deflecting Voltage per Cavity	0.5 MV
Coupler Type	Waveguide
External Q	1×10^6
Number of HOM+FPC/LOM Waveguide Coupler	4
Cryogenic Temperature	2.0 K
2K Heat Load due to Waveguide/Tuners per Cavity	2.4 W
2K Dynamic Heat Load Due to Wall Losses per Cavity $@Q_{\mathrm{u}} = 10^9$	7.0 W
2.0K Static Heat Load Due to Miscellaneous Losses per Cryomodule	2.0 W
Total 2.0K Heat Load $@Q_{\mathrm{u}} = 10^9$	79 W
Slow Tuner Range	$\pm$ 200 KHz
Number of Cavities per Cryomodule	4 (8)
Total Number of Cryomodules	2
Cavity Offset Alignment Tolerance	0.1 mm

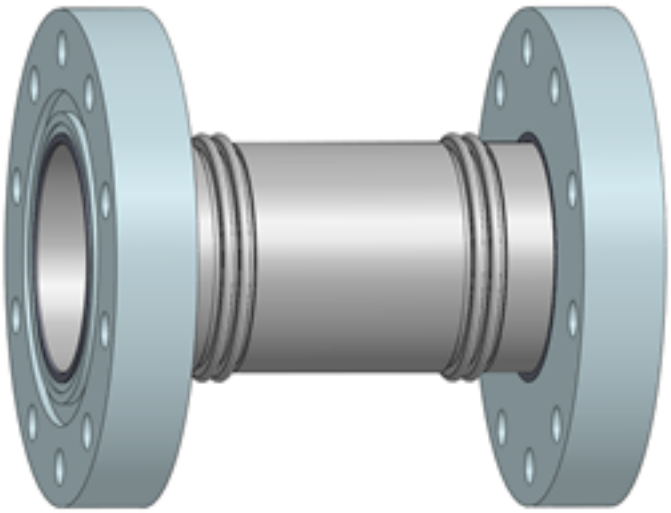

Figure 3.6-84: A prototype low-impedance bellows.

3.6.3.8.19 Heatload

The heat load to 2.0 K for each of the waveguide penetrations has been estimated to be approximately 0.5 W based on an average loading of the HOM and LOM waveguides and input coupler where dynamic losses have been roughly estimated [3.6-66]. The maximum transmission power through the input coupler will be less than 10 kW, while the LOM and HOM dampers may see a cumulative load up to 2.5 kW. Additional 2.0 K thermal loads of 0.4 W due to the static heat leak of the slow tuner and 2.0 W due to the helium distribution, cryomodule supports, and external beam pipe transitions have been included for a total 2 K static heat load of 23 W for two cryomodules. A 1-D model of a waveguide thermal transition from the cryomodule to the warm environment is shown in Figure 3.6-85. A total thermal loss at 2.0 K of 0.26 W was calculated, where 0.21 W loss is attributed to static

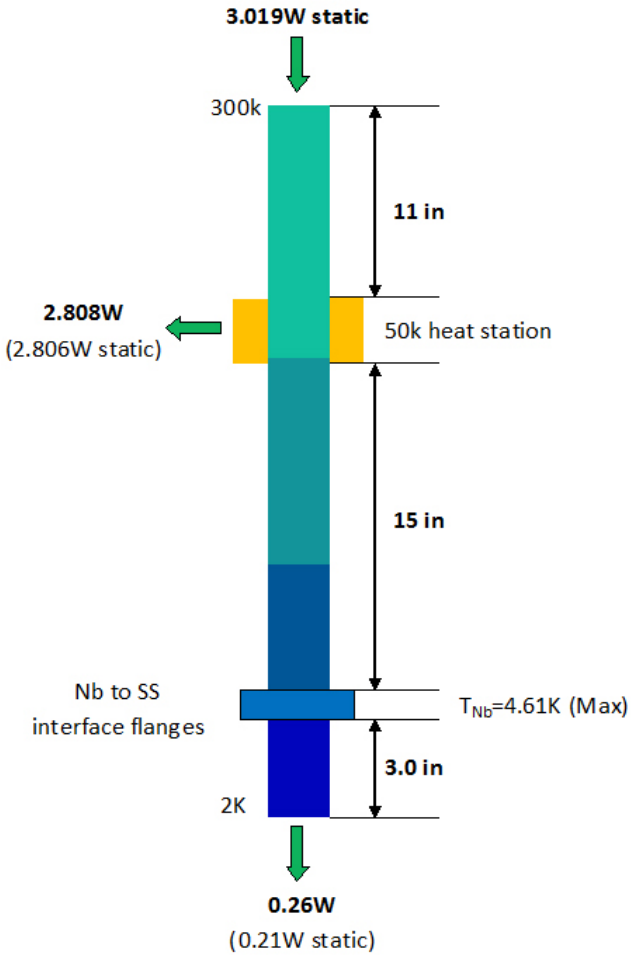

Figure 3.6-85: 1-D thermal model of waveguide transition from 2 K to room temperature.

losses [3.6-62] and where a 15-inch thermal transition and 50 K heat station were assumed. Based on preliminary measurements of prototype deflecting cavities at JLab, an unloaded quality factor of 10^9 has been assumed for dynamic losses in the cavity per section 3.6.3.8.2. This corresponds to a dynamic heat load of 7.0 W. As a result, eight cavities situated in two cryomodules produce a cumulative static and dynamic 2.0 K heat load of 79 W.

3.6.3.8.20 Vacuum

The cavity string will be evacuated through the connecting beam pipe between the warm gate valves and cold gate valves via an attached ion pump. A particle-free mechanical pumping system with controllable filtered dry nitrogen will be used to evacuate the vacuum space before turning on the ion pump. The pressure in the superconducting cavities should be <1 x 10^{-7} Torr at the time the cavities are cooled down to avoid degradation due to vacuum contaminants. An initial pump-down of the cavity vacuum should result in no more than 5 Torr per minute of pressure change. This is to avoid migration of particulates generated during assembly into the niobium cavity through turbulent molecule flow. (A careful calculation is needed to determine the acceptable pressure drop to ensure a molecular laminar flow, which could be lower than 5 Torr per minute.) Another indicator, based on a 1.5-inch vacuum pipe, is the fore-line pressure between the mechanical pump and control valve, which should be no more than 1 Torr to achieve turbulence-free evacuation. A cryostat insulation vacuum of 10^{-4} Torr at the beginning of cool down will provide sufficient insulation, provided there is no appreciable partial pressure of helium. The evacuation of the cryostat is not required to be as slow as evacuation of the cavity. Venting of the cavity vacuum should use filtered dry nitrogen at a peak rate that does not cause the rate of change of pressure in the cavity to exceed that of the evacuation process. The inlet gas filter should have a rating better than 0.01 micron.

3.6.3.9 Dampers and Windows

Implementation of the full SPX project requires eight cavities to provide the deflecting voltage specifications defined in section 3.6.3.1. As a result, sixteen HOM dampers, input coupler windows, and LOM windows will be required for the SPX, as well as eight LOM dampers.

The SPX0 dampers and windows were designed based on power handling and beam stability limits defined for the SPX. As a result, the SPX dampers and windows are not expected to change significantly from the SPX0 designs. The SPX0 damper design criteria are described in section 3.6.4.10.1 where the fabrication process, discussed in section 3.6.4.10.2, outlines the current manufacturing steps for the SPX0 dampers. Experimental results of the dampers and windows, as well as anticipated experimentation, are summarized in section 3.6.4.10.4

During operation of the SPX0 cryomodule, the dampers and windows will be carefully monitored to determine design enhancements that may be implemented, such as the reduction of possible thermal stressing of the input coupler ceramic, or the enhancement of coupling of the HOMs and LOMs to the lossy damper material. Lessons learned from the SPX0 project will be applied to the designs of the SPX dampers and windows, as well as to the outfitting of diagnostics that will be used to monitor power loading, failure modes, and beam-generated field levels in the damper waveguide.

3.6.3.10 SPX Beam Diagnostics [U1.03.03.08]

3.6.3.10.1 Requirements

The short-pulse x-ray source (SPX) presents a new set of beam-diagnostic challenges. Two ensembles of diagnostics are needed, one set inside the SPX zone between the superconducting deflecting cavities, and the other set outside of it to assure that SPX operation does not negatively impact other APS user

experiments. As presently envisioned, deflecting cavities will be located within the insertion device straight sections in Sectors 5 and 7, and beamlines 6-ID and 7-ID will be upgraded to take advantage of the short x-ray pulses generated. Extensive use will be made of existing diagnostic hardware in order to minimize the material and effort cost of the overall SPX project.

The goals of the diagnostics within the SPX zone (Sectors 6 and 7) are to:

- Provide transverse beam-centroid coordinates so the electron bunch can be put through the cryomodules sufficiently close to the centers of the cavities. Rf beam position monitors are to be used for this task.
- Provide beam-position readbacks at both ends of the 6-ID chamber so that the electron beam trajectory through the 6-ID straight section can be stabilized, minimizing timing jitter that orbit changes (primarily angular) may cause. Both rf beam position monitors and x-ray beam position monitors (XBPMs) are to be used.
- Quantify the effect of the deflecting cavities by measuring the beam tilt angle at a location downstream of the first cryomodule. Rf tilt monitors composed of existing S-band phase detector hardware will be used. (The originally planned x-ray optical tilt monitors have been removed from the project scope.)
- The SPX beamlines 6-ID and 7-ID will be instrumented in such a way as to accurately determine the properties of the delivered x-ray beams in terms of pulse duration and arrival time.

The goals of the diagnostics external to the SPX zone are to:

- Measure the beam arrival time with respect to a phase reference and provide this information to a real-time data network for use in the low-level rf controls associated with the deflecting cavities and main rf systems.
- Measure the residual tilt of the electron bunch due to the deflecting cavities. This will require up to two sensitive tilt monitors at two locations outside the SPX, separated by 90 degrees in the vertical betatron phase. Existing S-band phase detector hardware and data acquisition will be used for this purpose.
- Measure the residual emittance increase, mostly in the vertical plane. This will require a vertical-beam-size monitor located at a specific vertical betatron phase relative to the SPX deflecting cavities.
- Due to the loss of diagnostic beamline 35-ID resulting from the construction of the DCS beamline, use will be made of existing beam position monitors to assure minimal impact of SPX on other beamlines.

Table 3.6-42 lists the beam-diagnostic devices needed to support SPX commissioning and operation.

Table 3.6-42: Diagnostics supporting the short-pulse x-ray effort.

Location	Parameter	Diagnostic	No. of Units
Diagnostics within the SPX zone	Beam position	Rf BPM	16 existing, 6 new
	Longitudinal beam tilt	Rf tilt monitor	1, existing
Diagnostics external to the SPX zone	Beam arrival time	Rf BAT monitor	1
	Longitudinal beam tilt	Rf tilt monitor	2, existing
	Vertical emittance	Beam size monitors	1

3.6.3.10.2 Beam Position Monitors within the SPX Zone [U1.03.03.08.01]

At least three pairs of low-drift rf BPMs are needed within the SPX zone: upstream and downstream of the first cryomodule, upstream and downstream of the 6-ID chamber, and upstream and downstream of the second cryomodule.

Alignment of the particle beam vertically as it passes through the superconducting deflecting cavities must be done with a high degree of absolute accuracy, implying a vertical orbit stability requirement of less than $\pm$ 100 μm at the cavity locations (see Table 3.6-10). Vertical offsets drive the cavity deflecting modes, potentially resulting in large amounts of beam-driven rf power being coupled back out to the rf generators as well as difficulty maintaining precise phase regulation.

It is expected that space in the straight sections where the cryomodules are located will be at a premium, so it is planned to use standard pickup electrodes that are normally used for APS operation, but with improved electronics. In both Sectors 5 and 7 the cryomodules will be bracketed by an insertion device on one side and a large-aperture standard APS storage ring vacuum chamber on the other. The 4-mm-diameter capacitive button pickup electrodes mounted on the small-aperture insertion device vacuum chambers will provide more than adequate long-term stability to meet the specification, even using existing electronics. For the large-aperture chambers, the geometric position sensitivity is smaller by up to a factor of 6 in comparison to the insertion device chambers. For this reason, improved electronics such as the Libera Brilliance/Brilliance+ boxes from Instrumentation Technologies will be used. All new electronics are included as part of the beam stability portion of the APS Upgrade.

In the 6-ID and 7-ID straight sections, angular jitter in the centroid trajectory through the straight sections will translate directly into timing jitter for the short-pulse experiments being conducted on the beamline (see section 3.6.3.2.3). While the beam tilt in the center of this straight section should be zero, there will be detectable tilt at the ends of the straight section where the position monitors likely will be located. Similarly, near the cryomodules the beam tilt should be relatively small. First measurements and calculations of the performance of BPM electronics in the presence of beam tilt have been performed [3.6-67], with promising results.

3.6.3.10.3 Beam Arrival Time Monitor [U1.03.03.08.05]

The arrival time of the particle beam with respect to the deflecting cavity fields is an important parameter that must be carefully controlled. For this purpose a phase detector that measures the phase of the particle beam relative to a stable phase reference will be developed. This detector will be located

near the upstream cryomodule in Sector 5. It will require access inside the accelerator enclosure to a stable phase reference signal. This beam arrival time (BAT) detector will ultimately be integrated into the SPX low-level rf control system. The data provided by the BAT detector will be used to control common-mode phase errors, which may result either from longitudinal motion of the beam relative to the reference or common-mode phase changes of the deflecting cavities. The specification (Table 3.6-4) on common-mode phase error is 10 deg S-band. For this reason, the phase reference stability for the BAT monitor should be at the level of 1 ps or below.

The BAT monitor development will leverage off of the present APS linac phase detection and stabilization system. The APS linac phase-stabilization system uses phase detectors to measure the S-band accelerating-structure drive phase relative to the beam arrival phase [3.6-68]. The drive phase is measured at a high-power directional coupler located at the furthest upstream accelerating structure and is compared to beam signals from a strip-line BPM. Their difference is used in a low-bandwidth feedback loop implemented with EPICS to control input klystron drive phase [3.6-69]. The phase detection system operates at 2856 MHz and has a resolution of 0.1 degree (approx. 100 fs). This diagnostic is used routinely for maintaining optimal performance since it was commissioned in 2005, significantly enhancing system stability and reliability.

The BAT monitor will be arranged in a fashion similar to that shown in Figure 3.6-86, taken from the present linac phase-stabilization system. The phase-detector system will compare the phase of a BPM sum signal to a reference phase signal derived from the 352 MHz main rf control and timing system. The phase detector receiver is composed of a summing network, phase detector, and control and regulation boards. External to the receiver are power supply, data acquisition, digital I/O boards, and input filtering components.

The input signals are first fed into matching networks and then into a summing network front-end board that combines four signals from the BPM button pickup electrodes, summed to minimize position dependence. The sum together with a reference rf phase signal are then sent to an Analog Devices AD8302 RF/IF gain and phase detector chip. The AD8302 integrates two closely matched wide-band logarithmic amplifiers, a wide-band linear multiplier/phase detector, a precision 1.8-V reference, and analog output scaling circuits. The gain and phase video output signals are then filtered and scaled to $\pm$ 1.0 volts. The AC-coupled input signals can range from -60 dBm to 0 dBm in a 50-ohm system, and from low frequencies up to 2.7 GHz. The system is capable of bandwidths up to 30 MHz, which can easily meet our requirements of 1-kHz video output bandwidth.

Data acquisition will be performed using an existing design, the BSP-100 module presently being used for the broadband rf BPM upgrade. This allows straightforward integration of data from the BAT monitor into the new fast data-distribution network being developed as part of the real-time closed-orbit feedback system upgrade.

3.6.3.10.4 RF Beam Tilt Monitor [U1.03.03.08.03]

One rf tilt monitor is proposed to be included inside the SPX zone, with two additional monitors outside, located 90 degrees apart, in vertical betatron phase. The requirements inside vs. outside are significantly different, since the tilt is very large inside but, by design, needs to be as small as possible outside the zone. For example, outside the SPX zone, a 40-ps rms bunch (24-bunch mode) with a tilt of 1 mrad adds 12 μm rms in quadrature to the vertical beam size, which will be noticeable. Two sensitive tilt monitors with < 1 mrad resolution will be needed to monitor the residual tilt outside of the SPX

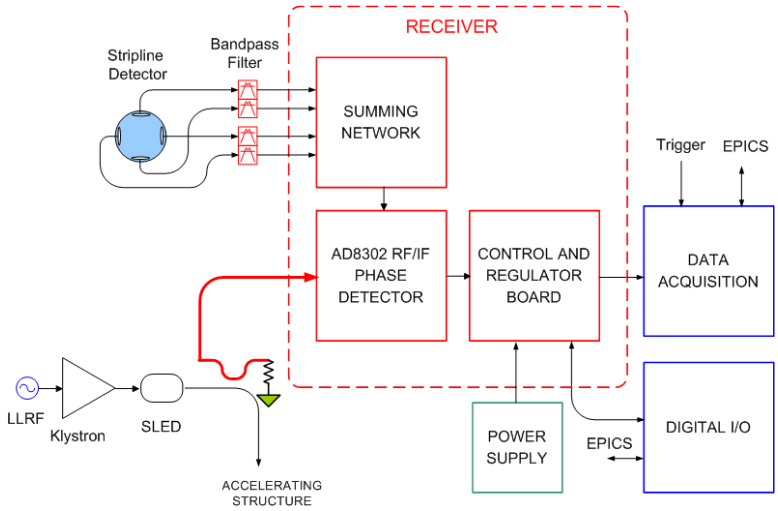

Figure 3.6-86: APS linac beam phase detector block diagram.

zone. Readbacks from these detectors will be used to correctly set the relative phase and amplitude of the deflecting cavities.

The use of capacitive button pickup electrodes together with S-band phase-detection electronics to resolve the relatively large beam tilt inside the SPX zone has been demonstrated [3.6-67]. The tilt monitor concept using buttons was investigated using the present machine coupled with a method to excite a beam-tilt transient [3.6-70]. The electronics design is essentially identical to that used for the beam arrival time monitor, with the exception that the relative phase between top and bottom BPM button electrodes is measured vs. the BAT monitor, which measures the phase between BPM electrodes and an external phase reference. Data acquisition will use an existing BSP-100 module to digitize data from one BAT monitor and three rf tilt monitors. A total of four existing APS S-band phase detectors will be used.

3.6.3.10.5 X-ray Vertical Emittance Monitor [U1.03.03.08.06]

During SPX operation, the x-ray pulse length is directly correlated with the vertical emittance of the electron beam. Furthermore, for most APS users operating outside the SPX zone, the main concern is the impact of SPX operations on their beam stability and effective emittance. Since a typical experiment takes between 10 ms and 10 seconds to register a data point, fast beam motions above 1 Hz to 1 kHz appear like beam size increases. One vertical beam size monitor, operating at least 1 Hz, will be used to assure these users that the SPX operations will have minimal impact on their experiments. The physics requirements [3.6-71] of these monitors are listed in Table 3.6-43.

Table 3.6-43: Requirements for the vertical (BM) beam size monitor for the SPX

Plane	Location	Requirement	Resolution	Bandwidth
X	AM/BM	Tilt induces less than 5% source size increase	27 μm rms	> 1 Hz
Y	AM/BM	Tilt induces less than 5% source size increase	9 μm rms	> 1 Hz

Three techniques are commonly in use for vertical beam size measurements using synchrotron radiation: x-ray pinhole imaging [3.6-72], projection detection [3.6-73], and x-ray imaging with zone plate or compound refractive lens (CRL) [3.6-74, 3.6-75]. In the APS storage ring, the resolution of the pinhole camera is typically 12-15 μm at a bandwidth of 0.1-1 Hz, which does not satisfy the physics requirement. The projection detector uses the synchrotron radiation in the wings of the vertical fan to infer beam sizes. It is sensitive to relative changes of the vertical beam sizes, but requires reliable calibration for the data to obtain absolute beam sizes. We choose x-ray imaging with a CRL as our baseline technique for the vertical beam size monitor. If more detectors are required, we will use the CRL diagnostics to calibrate the low-cost projection detectors and deploy the latter around the ring.

The vertical beam size monitor will be located in the S37 AM source, downstream of the Sector 36 rf cavity. In addition to using the vertical beam size for evaluating the impact of SPX operations, its horizontal beam size may be used, in combination with the 35-BM pinhole camera image, to obtain information on the e-beam energy spread. The sketch of the x-ray imaging diagnostic is shown in Figure 3.6-87. and its components are listed in Table 3.6-44:

- A fixed mask, replacing the existing absorber, allows some bend radiation to pass through a 1 mm (H) × 3 mm (V) aperture, with a maximum power throughput of 26 W.
- A beryllium window brazed on the fixed mask aperture isolates the storage ring vacuum from the beam size monitor components.
- An array of water-cooled apertures, ranging from 0.3 mm to 1 mm, select the rays used for imaging and further limits the transmitted power to below 11 W.
- A beryllium CRL is selected as the main imaging component since it is more robust than zone plates under the high-power synchrotron radiation.
- A single-crystal monochromator selects the imaging x-ray wavelength at the downstream end of the monitor.
- A YAG screen and CCD camera acquire the x-ray image.

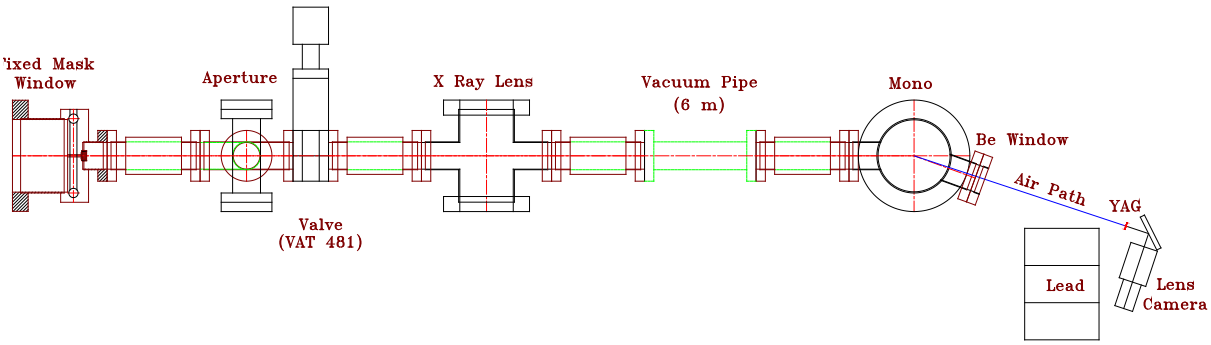

Figure 3.6-87: Sketch of the x-ray vertical beam size monitor (side view).

Table 3.6-45 lists the aperture sizes and estimated diffraction-limited resolution using Rayleigh criterion for perfect lenses. Here we have assumed an operational wavelength of 12.4 keV. Considering the

Table 3.6-44: Major components of the APS high-resolution beam size monitor.

Component	Location	Notes
Fixed mask	8.5 m	Horizontal aperture < 0.2 mrad, power < 26 W at 150 mA
Be window	8.5 m	Absorbed power < 5 W
Aperture	8.8 m	Water-cooled aperture array and beam stop
Valve	8.9 m	40-mm all-metal valve
Be lens	9.1 m	Imaging wavelength $\sim$ 12.4 keV, focal length $\sim$ 3.8 m
Monochromator	14.0 m	Silicon (111)
Camera detector	14.5 m	Lead shielded

small-angle scattering from the beryllium window, aberrations of imperfect lenses [3.6-76] and finite resolution of the x-ray imaging readout (typically several micrometers), we expect the mid-range apertures (0.3-0.7 mm) to be good candidates for routine operations and for meeting the physics requirements.

Table 3.6-45: List of apertures and their performance impact.

Aperture	Transmitted Power	Diffraction Limit	Theoretical resolution
1.0 mm	10.8 W	0.12 μrad	1.1 µm? (vertical aperture not filled)
0.7 mm	6.1 W	0.17 μrad	1.5 µm
0.5 mm	2.8 W	0.24 μrad	2.2 µm
0.3 mm	1.3 W	0.41 μrad	3.7 µm

3.6.3.11 Mechanical Systems Infrastructure

Mechanical systems infrastructure deliverables to the SPX project include deionized water supply and distribution systems, a cryogenic plant and cryogenic distribution system, and accommodations in Building 400A for preparing and testing SRF cryomodules and cavities. Significant effort will be allocated to not only specify, design, and install these systems, but also to coordinate the design of all major SPX mechanical systems to ensure physical compatibility, proper mechanical integration of SPX cryomodules into the APS storage ring, and adequate conventional facility provisions.

3.6.3.11.1 Mechanical Design Integration

A project like SPX that requires a large number of independently designed, yet critically interacting, subsystems requires engineering coordination on a global scale if the design work is to proceed efficiently and confidently. To facilitate the design process and minimize iterations, an integrated 3D CAD model has been built that incorporates all major subsystems, including the new 400A building, into one large assembly. APS survey and alignment personnel have contributed to the effort by making detailed measurements inside the storage ring tunnel, which are then input into the model. As an example, using this model SPX engineers will be able to visually study how the SPX production

cryomodules will be installed into the storage ring, and any potential physical interferences with existing equipment will be immediately obvious.

3.6.3.11.2 Deionized Water Supply and Distribution

A deionized water supply is required for cooling of various SPX subsystems and will be delivered in significant quantities to five primary locations. In each of rooms 400A-1 and 400A-4, it is anticipated that four 10-kW rf amplifier systems, including power supplies, will require no more than 264 gpm. This value is scaled from known water requirements for existing 5-kW amplifier system designs with an additional safety factor of 20 percent. In room 400A-1, rf test stands are expected to require no more than 125 gpm. In room 400A-3, it is anticipated that cryogenic plant components will require no more than 120 gpm. Therefore, the total deionized water flow capacity delivered to the four rooms from APS deionized water supply systems shall be at least 773 gpm. Pre-existing supply capacity to Building 400A is approximately 300 gpm, 50 gpm of which is required for conventional facilities use. Therefore, an additional supply capacity of 523 gpm must be added. This additional water supply will be drawn from the existing APS deionized water system by a new pump located in the storage ring mechanical mezzanine and delivered to Building 400A by new pipes installed on the Building 400 ceiling. A preliminary design of the new supply pump and piping is shown in Figure 3.6-88. Inside the storage ring, each of the two SPX 4-cavity cryomodules will require a total of approximately 28 gpm of deionized water flow. This flow will be drawn from the existing storage ring distribution mains and distributed at each sector among 16 circuits (4 circuits per cavity).

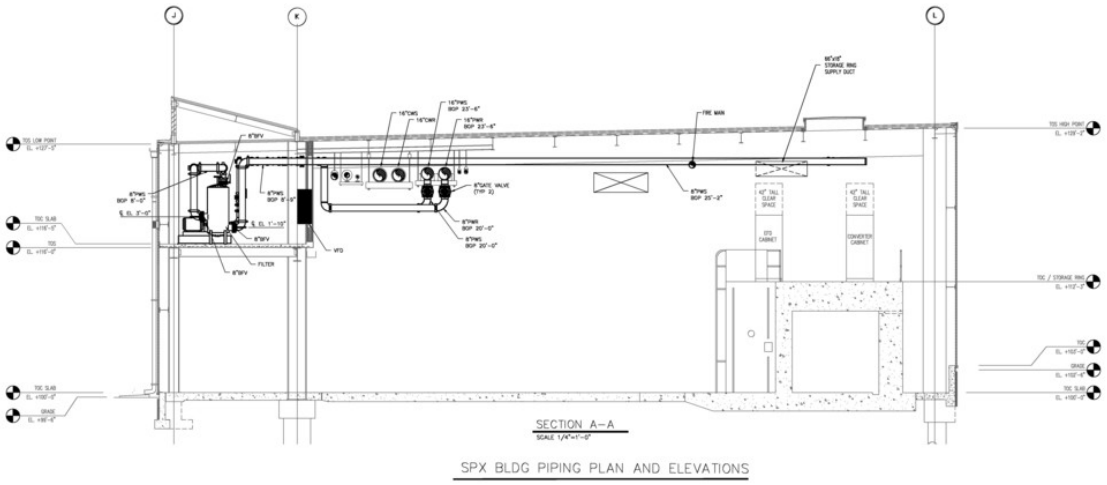

Figure 3.6-88: SPX DI water supply system to Building 400A.

Each water header installed will include supply and return shut-off valves, supply and return dial-indicating pressure gauges, and a drain port. Each circuit installed onto new water headers in 400A will be provided with its own pair of supply and return shut-off valves. Provisions for flow metering and calorimetry will be included in the high-power rf cabinets being served. Each circuit in the storage ring connected to new water headers there will include supply and return shut-off valves, a differential pressure-based flow meter, and a resistance temperature detector. In addition, water circuits in the storage ring will utilize plastic tubing to minimize water flow-induced vibration and to ease installation. This tubing will be a radiation-resistant type known from experience to be adequate for use in the

APS storage ring. Storage ring water circuit flows for each of the eight SRF cavities are given in Table 3.6-46.

Table 3.6-46: Storage ring water circuit flows and heat loads.

Circuit No.	Components	Min. Flow (gpm)	Max. Flow (gpm)
1	Waveguide Windows	1	2
2	LOM Damper	3	4
3	HOM Dampers - Inner Channels	1	2
4	HOM Dampers - Outer Channels	1	2

The SPX systems shall generally require that water is supplied at, or slightly below, room temperature to ensure that condensation does not form on water lines. APS water systems provide water at 78 deg F so no additional temperature adjustment will be needed. SPX systems shall anticipate supply-side pressures of 150 psi and return-side pressurizes of 50 psi, as typically supplied by APS DI water systems. The APS deionized water system supplies water with a resistivity of 10 MΩ-cm. Corrosivity of the water is limited by the APS through oxygen removal. Outside of this, none of the SPX systems utilizing deionized water require special control or monitoring of water chemistry. Therefore, all supplied water temperature, pressure, and chemistry will conform to existing APS conventions.

3.6.3.11.3 Cryogenic Plant and Distribution System

The SPX cryogenic refrigeration and distribution system provides cooling to the crab cavities sufficient to maintain a stable operating temperature under all operating conditions. The system provides saturated liquid helium at 2.0 K via a low heat leak distribution system and must accommodate the static heat loads presented by the cryomodules and distribution system as well as the dynamic load imposed by cavity operation. Figure 3.6-89 shows a block diagram of the system.

The refrigerator provides helium at 300 kPa, 4.6 K to the distribution system. Within each cryomodule the helium is cooled to 2.2 K by heat exchange with the 2.0 K saturated vapor return stream. The 2.2 K, 300 kPa supply is throttle to 2.0 K, 3.13 kPa and supplied to the rf cavities. The vapor space above the cavity bath is maintained at 3.13 kPa (the saturation pressure for LHe at 2.0 K) by a hybrid gas pumping system consisting of one or two stages of cold compression and one stage of vacuum screw compression. The cold compressor(s) generate a pressure ratio of about 4, providing a suction pressure of 13 kPa for the vacuum screw compressor bank. Figure 3.6-90 shows a simplified flow schematic of the refrigeration system. The cryoplant also supplies refrigeration at 4.5 K and 80 K for thermal intercept and thermal shield cooling within the cryomodules and distribution system.

Dynamic heat load estimates vary greatly depending on achieved cavity performance. The plant should be designed with a substantial margin in 2.0 K capacity and also possess a reasonable upgrade path sufficient to handle unforeseen dynamic and/or static loads as well as future capacity increases.

There are many elements that inform the design of a cryogenic system for SRF cavities. These include:

- Pressure stability criteria: The 2.0 K LHe superfluid bathing the SRF cavities must maintain a stable pressure of 23.5 Torr (3.13 kPa) to keep the cavities on frequency. Considering the

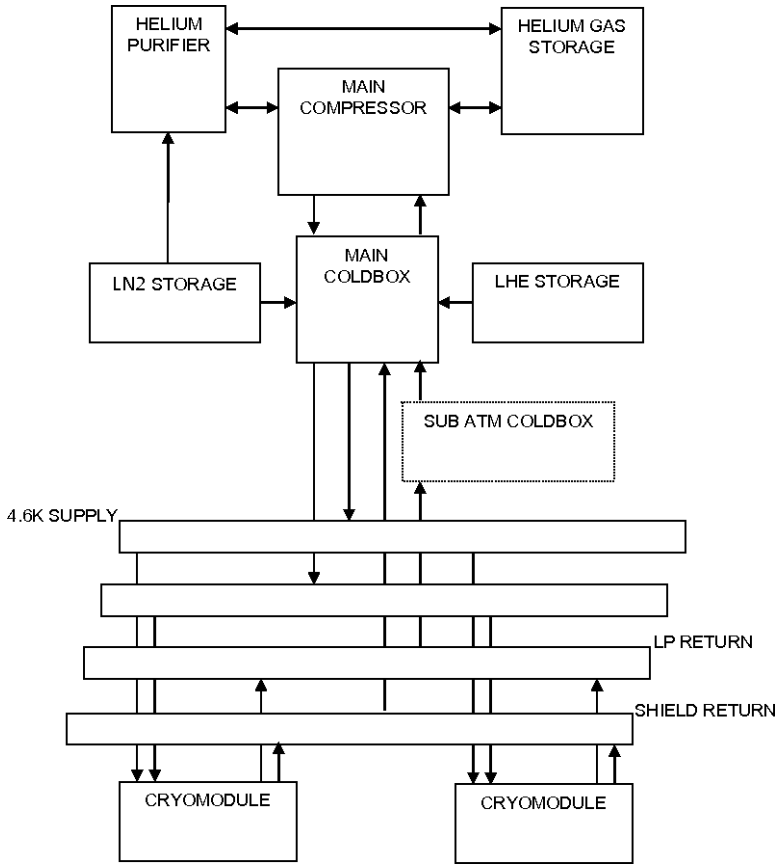

Figure 3.6-89: Refrigeration system block diagram.

performance of typical slow tuners, a pressure stability of $\pm$ 0.5 Torr is adequate and readily achievable with existing cryoplant technology.

- Vibration effects on cavities: Vibrations from the cryoplant (particularly the warm compressor systems) cannot exceed the LLRF specifications. This likely means isolating the compressor skids from the facility through a combination of remote location, isolated concrete pad, and/or isolation mounts.

- Off-design operation: The plant must operate efficiently not only at design load but also at reduced load. A thorough understanding of the cavity operating profile, including time spent at reduced or zero gradient, is necessary to properly specify the off-design operating requirements.

- System margin: Some amount of overcapacity will be designed into the system to mitigate the risks associated with uncertain cavity dynamic heat load and the possibility that the completed plant underperforms. The latter can also be mitigated with an incentive-based procurement contract tied to actual measured capacity during commissioning.

- Upgradability: If the accelerating gradients are increased or cavity performance is well below specification, the cryogenic load may increase beyond that provided by the system margin. In this case, a low cost, efficient capacity upgrade will be required. Provision for such an upgrade should be part of the original system design.

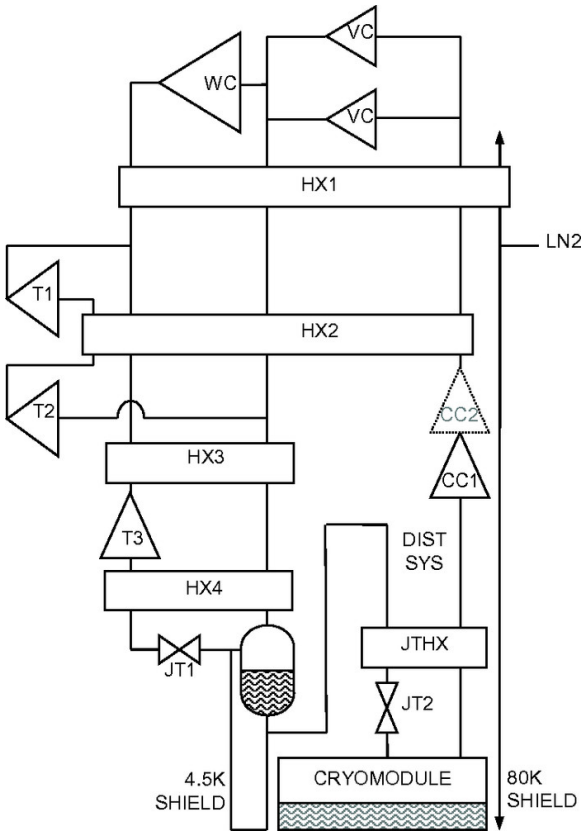

Figure 3.6-90: Refrigeration system flow schematic.

- Safety (pressure, cryogenics, oxygen deficiency hazard, system venting, etc.): Safety analyses are a fundamental aspect of cryoplant design. Vendors will be held to applicable codes and standards with regard to pressure system safety. Oxygen deficiency hazard (ODH) analyses will be conducted for all cryoplant enclosures as well as the regions of the APS tunnel containing cryomodules and distribution system components.

- System reliability: The cryoplant availability must meet overall APS beam-to-user requirements. This may be achieved via on-line spares, modular design, and system margin. A robust control system is an integral part of this aspect of performance. Any control/monitoring systems supplied by the cryoplant vendor must integrate effectively with the APS control system.

- Wall plug power requirements: Modern hybrid 2.0 K cryogenic systems have a load ratio (LR) of about 2.7, where the LR is the ratio of equivalent capacity at 4.5 K to actual capacity at 2.0 K. It is useful for comparison purposes to normalize the capacity of a cryogenic system containing multiple heat loads at a variety of temperatures to a single refrigeration capacity at 4.5 K. In turn, wall plug power requirements for modern systems in this size range are typically 240 W per watt of refrigeration at 4.5 K, plus additional overhead and losses. For the expected capacity range of 160-320 W at 2.0 K, the estimated wall plug power requirement is about 0.3-0.5 MW.

- Similar systems: The ELBE facility at TU-Rossendorf (see Figures 3.5-44 and 3.5-45) operates a cryogenic system capable of 220 W at 1.8 K, upgradeable to 380 W with additional compressors and LN2 precooling. Note that the LR for 1.8 K refrigeration is more like 3.6 compared to 2.7

for 2.0 K. As an example of another similar system, Fermilab has recently purchased a new cryoplant with a design capacity of 500 W at 2.0 K, plus shield loads. Both these systems are based on the hybrid concept, which uses both cold compression and warm screw compressors operating in vacuum to generate the subatmospheric pressure required to produce saturated vapor at 2.0 K or 1.8 K.

- Delivery schedule: Delivery of a cryoplant in this size range is expected to be about 30 months from order to commissioning and final acceptance. The procurement may include on-site startup, commissioning, and training as part of the deliverables. The plant will be capable of operation using the vendor-supplied control system (independent of the master machine control system). Acceptance tests are typically performed by making refrigeration into a storage Dewar and measuring capacity via an electric heater.

A cryogenic transfer line will be designed, built, and installed to support the APS Upgrade superconducting SPX systems. The transfer line will transport cryogenic fluids between the refrigeration plant cold box and the SPX cryomodules. The transfer line will deliver to the cryomodule 4.5 K liquid helium at 3 atm with a flow of 3 g/s. Liquid nitrogen will be used to provide 80 K shield cooling for the cryomodules and distribution system. Each cryomodule is budgeted for a maximum estimated heat load of 60 W at 2 K. Shield heat load is estimated at 180 W. An additional heat load of 500 W at 4.5 K is budgeted for the transfer system.

The transfer line will be installed within the existing Advanced Photon Source Building 400 structure. The transfer line originates at the cold box bayonet box in room 400A-2, branches into two nominally equal length 30-m lines, and terminates at the cryomodule bayonet boxes in Sectors 5 and 7 of the storage ring tunnel. Ventilation penetrations in the tunnel wall limit the transfer line diameter to 8 inches maximum. An expansion joint will be near the penetrations in the tunnel wall. Expansion anchor will be at the T branch at the cold box exit (see Figure 3.6-91). The cold box and cryomodule end-of-line bayonet box will be based on JLab designs.

Connections to the cold box and cryomodule end can are to be with U-tubes of JLab design. The bayonet/U-tube connections are designed for installation or removal under pressure (or vacuum) without system contamination. The design and size is dependent on the flow circuit. The transfer line will be composed of a stainless steel vacuum jacket housing four internal lines inside of a 80 K thermal shield. Transfer line circuits will be insulated with super insulation made of aluminized Mylar separated by layers of nylon fabric. Nominal insulation is 24 layers per cm. The vacuum jacket will use 60 layer of insulation and the internal lines will have 20 layers of insulation (see Figure 3.6-92).

3.6.3.11.4 Accommodations in Building 400A for Cryomodule Preparation and Test

A clean room will be provided for clean assembly of SRF cavity assemblies. After the APS Upgrade Project has been completed, additional facilities are planned for this space to validate required performance and support SRF cavity and cryomodule development. The general arrangement is shown in Figure 3.6-93.

A 14 foot by 10 foot clean room work area and an additional 6 foot by 10 foot clean room vestibule will be located in room 400A-1. Both the clean room and the vestibule will satisfy Federal Standard 209E (ISO 5 meeting ISO 14644-1), which describes requirements for what is commonly referred to as

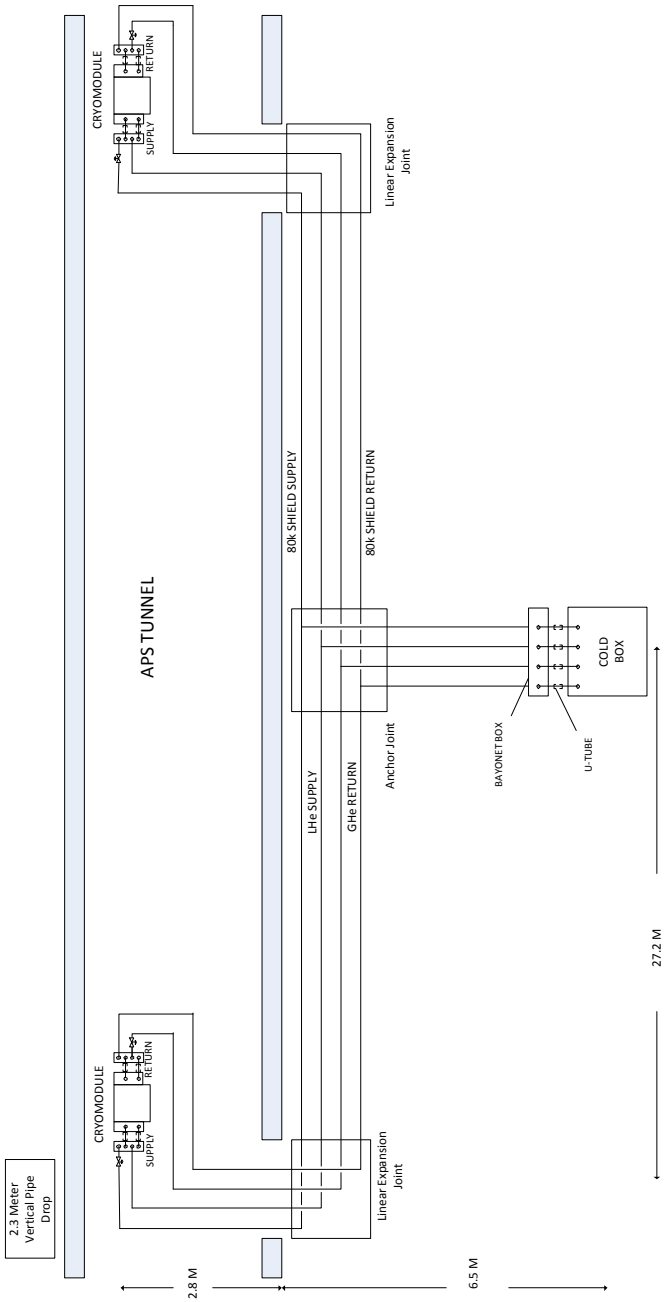

Figure 3.6-91: Cryogenic distribution system schematic.

a class 100 clean room. Ceilings will be 12 feet high to provide adequate work clearance. An additional 8-foot-wide roll-up door located on the wall opposite the vestibule will permit a complete SPX 4-cavity cryomodule into be easily moved in and out of the work area from an adjoining open cryomodule staging area. All walls will be constructed of static-dissipative vinyl. The floor of the clean room, vestibule, and cryomodule staging area will be coated with an easily cleaned, static-dissipative epoxy. Inside the clean room, overhead lighting and standard 100-VAC receptacles will be provided. Design,

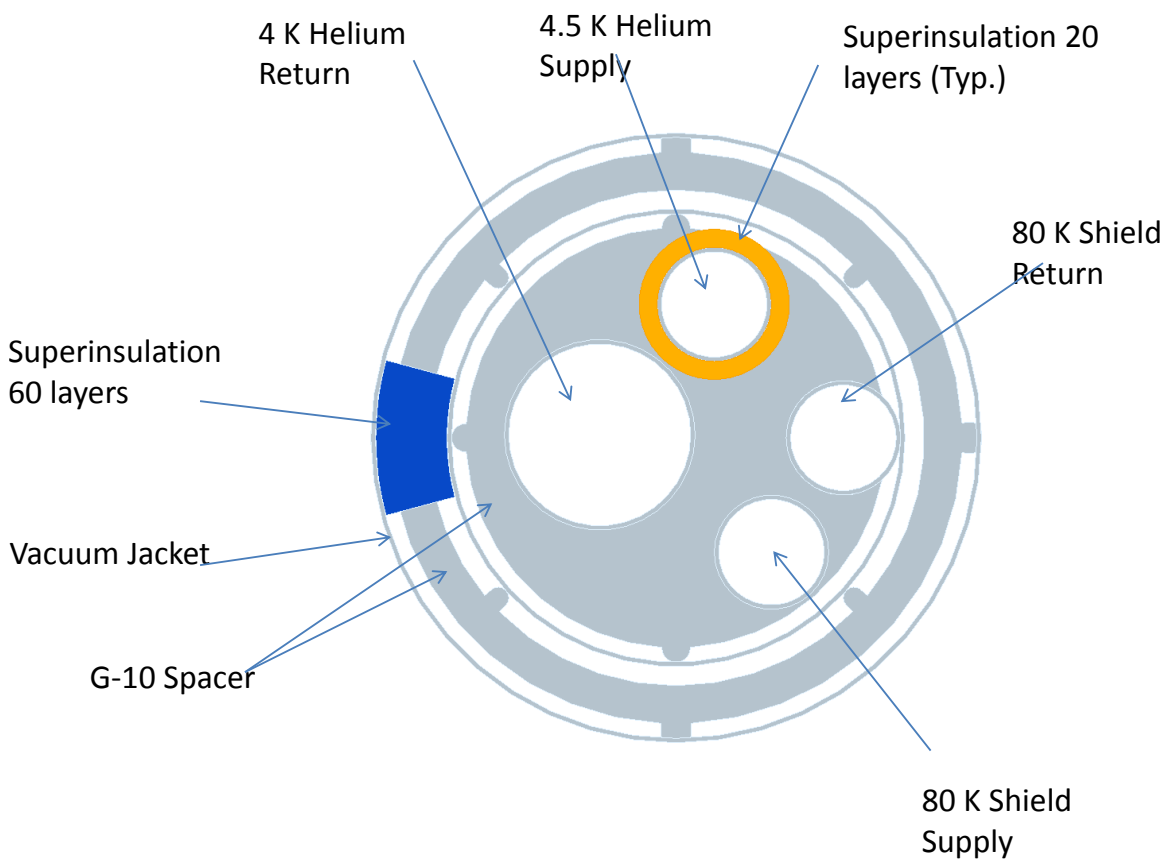

Figure 3.6-92: Cryogenic distribution system transfer line cross section.

fabrication, and installation will be contracted to an outside vendor.

3.6.3.12 Beam Commissioning

The main objective of the SPX commissioning is to safely turn on the storage ring and deflecting cavities without causing any damage to the cavities or storage ring. This has to be done in a planned and timely manner without disrupting APS user operations. The specific goals of the SPX commissioning are as follows:

- Confirm that the APS user operation is possible with installed cavities;
- Confirm that the cavities are protected from damage by the beam;
- Turn on the cavities and confirm that user operation is possible with the cavities on;
- Deliver tilted photon beam to user beamlines.

The first two items above need to be completed during start-up studies, before the beginning of the user run. The other two items could be worked on during storage ring studies.

Cavities may affect APS user operation in many ways:

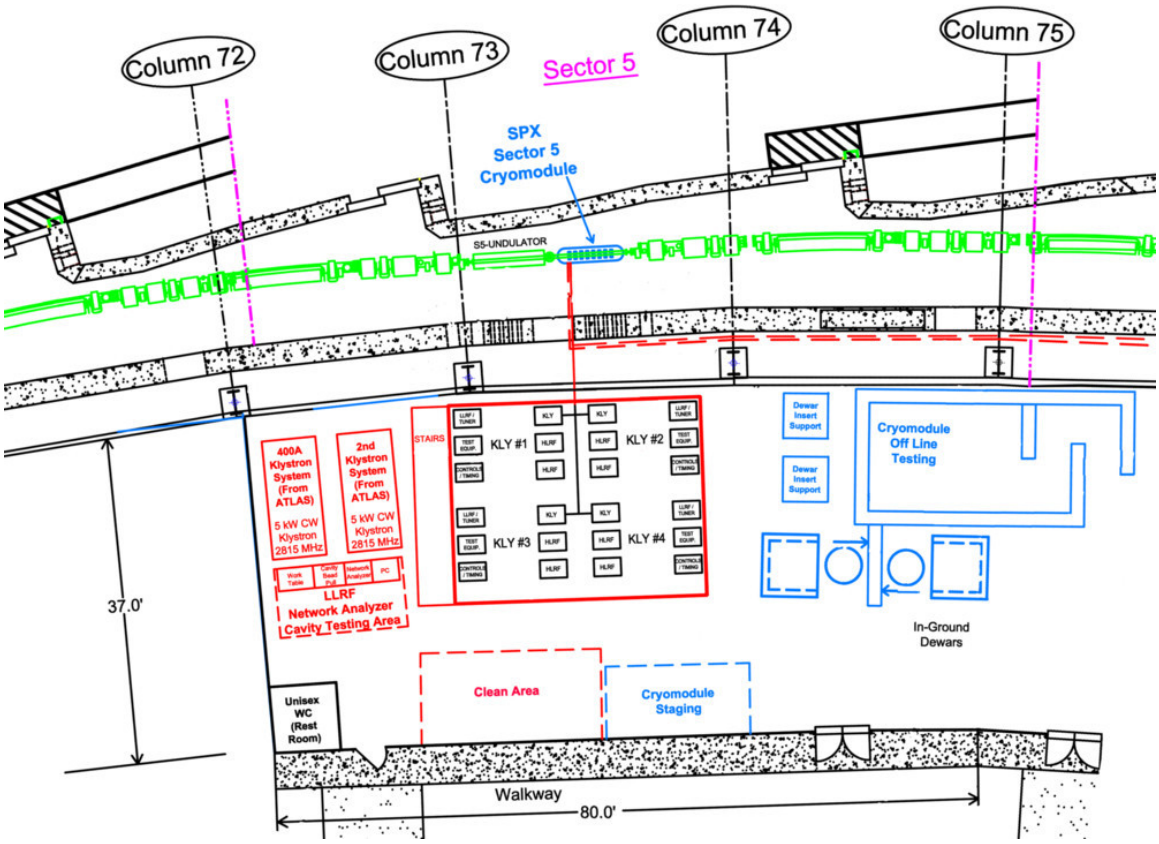

Figure 3.6-93: Cryomodule preparation and test facilities in Building 400A.

- Cavities can change the accumulation limit due to additional impedance;
- Cavities can affect vertical beam size due to deflecting fields inside cavities;
- Cavities can affect injection due to linear and nonlinear coupling on deflected trajectories or due to some combination of deflecting fields and large beam oscillations;
- Cavities can affect lifetime through some linear and nonlinear coupling on deflected trajectories or if an increase of chromaticity is required due to decreased accumulation limit.

To ensure that APS user operation is possible with installed cavities, one needs to check the following items in all fill patterns that are used for operation:

- Injection efficiency is not decreased below the level that prevents top-up operation;
- Lifetime is not decreased below the level that prevents maintaining the desired beam current with top-up interval of 60 s or more;
- Horizontal beam size is not affected by more than five percent;
- Vertical beam size corresponding to 1.5% emittance ratio is achievable;

- Single-bunch accumulation limit is not affected above the level that prevents hybrid fill pattern operation;
- Orbit stability is not affected above established APS alarm limits.

Cavities can also affect SR beam studies. For example, they could prevent machine physicists from creating the large orbits required during orbit response matrix measurement, or prohibit high-current studies. These effects, though important, do not prevent APS user operation and could therefore be tolerated to some degree. For example, response matrix measurement could be done with low current.

3.6.3.12.1 Commissioning Plan

The major items of the commissioning plan are briefly summarized here, then described in more detail below.

1. Perform a set of measurements and preparations in the run preceding the shutdown during which cavity installation will take place. This sets baseline performance parameters that should be recovered after installation of the cavities.
2. Perform cavity tests after installation in the tunnel (without electron beam), including cool-down, low-power rf measurements, and high-power operation. This ensures that the cavities and related systems, such as controls, low-level rf, high-power rf, timing, machine protection, and so forth are functioning as expected.
3. Perform cavity tests at low beam current with unpowered and detuned cavities. This validates the installation and ensures that no obvious problems, such as aperture restrictions, are present.
4. Perform electron beam tests with unpowered and detuned cavities to ensure that normal user operation is possible. This will involve a gradual ramping of the beam current while monitoring cavity signals and beam parameters.
5. Perform electron beam tests with powered and on-resonance cavities. When successful, this step results in a functioning SPX system.

Pre-installation Measurements

The following measurements are required before the cavity installation shutdown to document the machine status:

- Single-bunch accumulation limit in 24 bunches and in hybrid fill modes, with P0 feedback on and off;
- Beam size as a function of current from minimum to 150 mA in 24 singlets;
- Beam size at 150 mA in all fill patterns;
- Beam size in 324 bunches when scraping down from 150 mA to 120 mA;

- Beam size in hybrid when only 16 mA single bunch is injected;
- Spectrum of the beam motion.
- Set-up and saving of 24-bunch lattice with and without P0 feedback, to ensure a working configuration is in hand for start-up.

Other preparations should include girder alignment in Sectors 5 through 8 (if required) to have straight beam orbit, reduction of corrector strengths in those sectors, and measurement of beam position monitor offsets to ensure straightness of the orbit around the cavities. The girder alignment would have to be completed at least one shutdown prior to the installation of SPX.

Checkout without Beam

After cavity installation but before the beginning of the beam tests, the cavities will be tested for mechanical integrity, vacuum conditions, and alignment. Cryogenic performance will also be tested. Following low-power rf measurements, the cavities will be gradually raised to full power. Various rf components will be tested as well. A detailed plan of these tests without beam will be written later.

Checkout with Low-Current Beam

- Perform first injection – 1 to 4 mA in a single bunch, roughly correct beam orbit, establish acceptable injection efficiency;
- Test of HOM/LOM power damping efficiency at low current;
- Test of diagnostics and controls;
- Check beam dump when beam orbit exceeds allowable limits in cavities;
- Check that cavities are not struck by synchrotron radiation during normal operation and during studies with large orbit errors by recording temperature rise;
- Measure cavity centers relative to the beam orbit, move orbit to the cavity centers.

The current in these tests should be limited to 5 mA in a single bunch.

Checkout with Full-Current Beam

- 24 singlets, P0 feedback off:
  - Increase stored beam to 30 mA in 24 singlets
  - Correct orbit using standard orbit correction, save, then dump the beam
  - Perform injection efficiency optimization on the new orbit
  - Check single-bunch accumulation limit, compare it with the measurements before the shutdown

  - Perform rf conditioning (slow increase of stored current from 30 mA to 150 mA over about 20 hours), have beam size measurements available during conditioning
  - Compare beam size measurement to the one before the shutdown
  - Run top-up
- 24 singlets, P0 feedback on:
  - Perform injection efficiency optimization, if necessary
  - Check single-bunch accumulation limit, compare it with the measurements before the shutdown
  - Inject 150 mA, run top-up, compare beam sizes
- 324 bunches, P0 feedback off:
  - Inject 150 mA
  - Slowly (within 1 hour) scrape down beam to 120 mA to check that no instability occurs during beam decay when operating in non-top-up mode. Record beam sizes during the scrape down and compare it with the measurements before the shutdown
- Hybrid fill pattern, P0 feedback on:
  - Inject first beam – 4-mA single bunch
  - Roughly correct orbit
  - Increase stored beam to 30 mA in 24 singlets
  - Correct orbit using standard orbit correction, save, then dump the beam
  - Perform injection efficiency optimization
  - Check single-bunch accumulation limit, compare it with the measurements before the shutdown
  - Compare the beam size at 16 mA with the measurement before the shutdown
  - Inject 150 mA in hybrid mode pattern, run top-up, compare beam sizes

Tests with Powered Cavities

The goal of these tests is to finally commission the generation of short x-ray pulses. We will need to turn the cavities on with the beam and on resonance. If there is not enough time to do this during the start-up, it can be done during weekly machine studies. The approximate sequence of steps will be the following:

- With low current beam, turn first cavity on, leave at some intermediate voltage, and perform deflecting voltage phase scan to synchronize the rf waveform with the beam, then turn the cavity off;
- Repeat the same with the second through eighth cavities until all cavities are individually phased;
- Turn all cavities on and measure their effect on injection and lifetime as a function of deflecting voltage;

- Measure vertical beam sizes and beam tilts between the cavities and outside of the SPX zone (inject more current if necessary for optical measurements), confirming that the beam is tilted between the cavities and undisturbed outside;
- Confirm that the APS operational parameters are not affected by the deflecting cavities.

In these tests, the overall performance of the rf system will be characterized. This includes tuner tests, low-level rf regulation tests under various conditions, cryogenics characterization, high-level rf performance, etc. Also, effects on the electron beam parameters will be characterized on every step. A complete list of tests will be developed after experience with the SPX0 system.

3.6.3.13 Safety Interlock System

3.6.3.13.1 Personnel Protection Interlocks

Potential hazards to personnel from the SPX rf system hardware include rf radiation leakage from open waveguide flanges (non-ionizing radiation), contact with high-voltage conductors (electrical hazard), and exposure to ionizing radiation generated by the klystrons. The personnel safety system (PSS) controls personnel exposure to these hazards by simultaneously disabling both the LLRF drive to the klystron and the HVPS by dedicated hardware interfaces when unsafe conditions are detected. The PSS interface chassis is designed using simple relay logic for maximum reliability and fail-safe modes.

Gas pressure meters are used to monitor positive nitrogen pressure inside the waveguide in order to detect leaking or open waveguide flanges. Loss of waveguide pressure below a minimum set point will constitute a potential hazardous condition and will result in an open contact signal at the PSS main chassis and immediate shutdown of the rf system by two independent and redundant methods. Personnel exposure to high voltage and ionizing radiation is prevented by monitoring klystron amplifier cabinet and HVPS door switches. All access doors and covers on the klystron amplifier cabinet and HVPS must be closed and secured before the PSS system will allow system operation.

3.6.3.13.2 Access Control Interlock System

The SPX ACIS will consist of dual-redundant programmable logic controllers (PLCs), each configured to a TUV-certified SIL2 configuration in accordance with IEC 61508, Functional Safety of Electrical/Electronic/Programmable Electronic Safety-related Systems.

The SPX ACIS will include all hardware, software, and control systems to interface between the storage ring access control interlock system (SR ACIS) and the SPX ACIS to enable the two sets of rf systems, each consisting of one HLRF HVPS and four klystron rf driver amplifiers (see Figure 3.6-94). The SR ACIS will issue a permit signal to the SPX ACIS only when the SR Zone A is in Beam Permit mode. This will require modifications to the SR ACIS, which currently does not separate the SR Zone A from SR Zone B-E. The SPX ACIS will included this permit signal from the SR ACIS in its logic to enable all the SPX HVPSs and klystron rf driver amplifiers. SPX ACIS will return feedback signals to the SR ACIS to provide the status of the SPX ACIS-controlled rf equipment and its own hardware/software.

The SPX ACIS PLC processors and Operator human-machine interface (HMI) will be located at the SR ACIS Operator Panel in the APS MCR (see Figure 3.6-95). Communication cabling, approved for

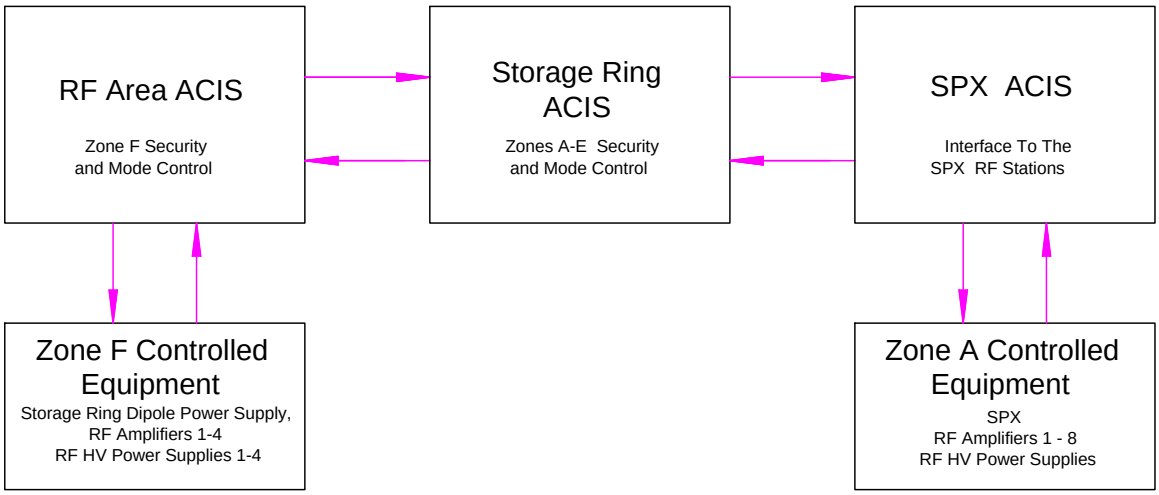

Figure 3.6-94: SPX ACIS's functional relationship to other ACISs.

safety networks, will connect the PLC processors with remote PLC chassis installed in two racks in Building 400A. One rack, in room 400-A1, will interface to one HVPS and four rf klystron amplifiers driving superconducting rf deflecting cavities near sector 5, and a second rack, in room 400-A4, will interface to one HVPS and four rf klystron amplifiers driving superconducting rf deflecting cavities near Sector 7 (see Figure 3.6-96).

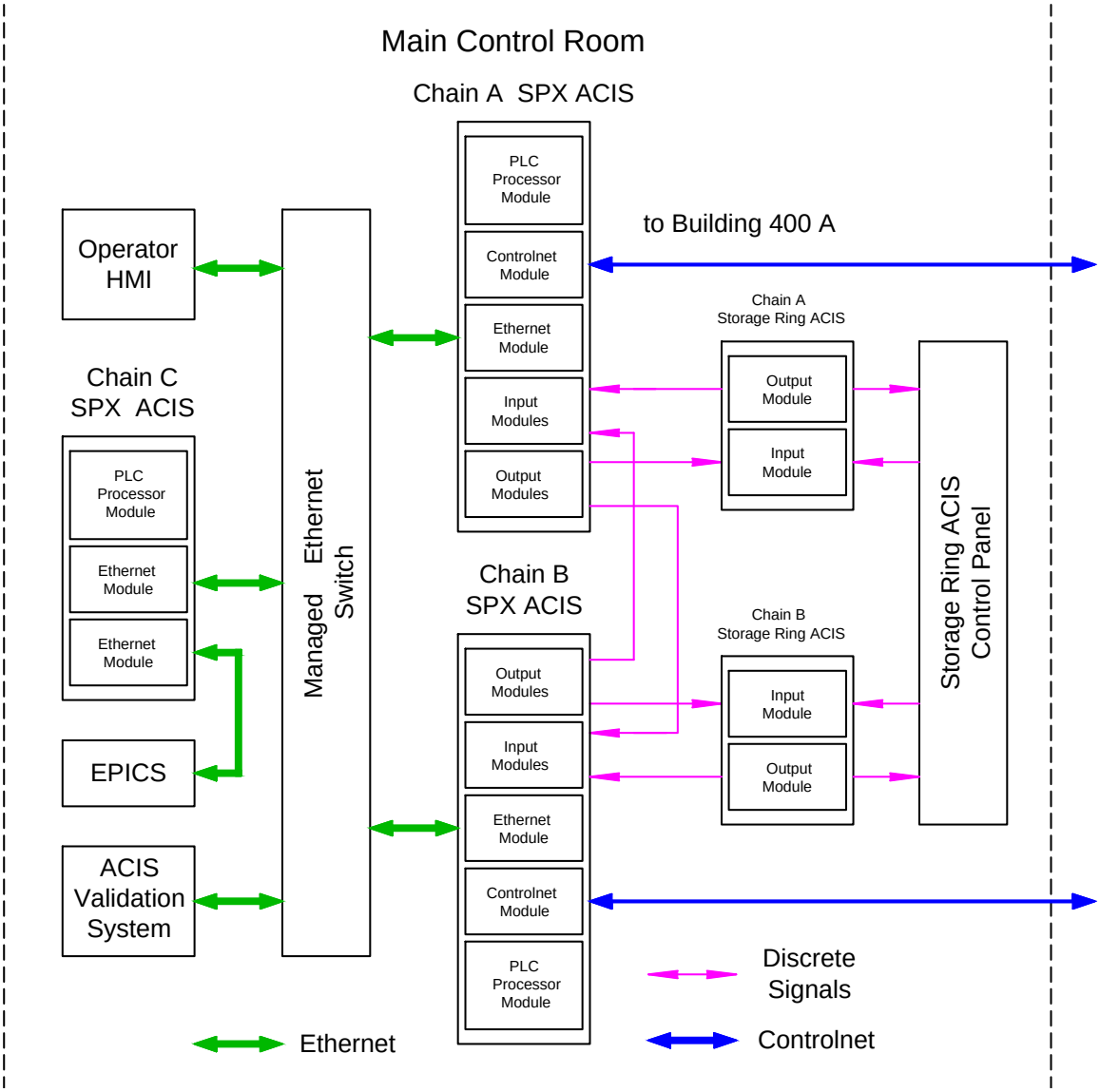

Figure 3.6-95: SPX ACIS MCR equipment block diagram.

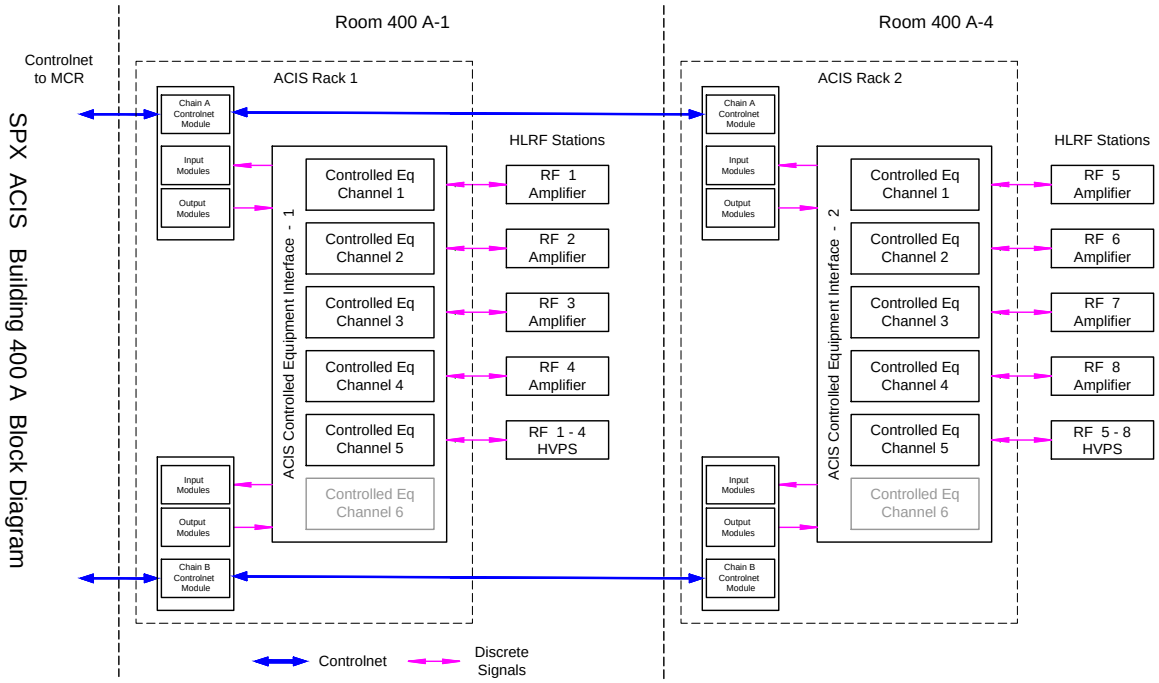

Figure 3.6-96: SPX Building 400A equipment block diagram.

3.6.4 Short Pulse X-Ray System R&D Program (SPX0)

3.6.4.1 Introduction

The proposed SPX system design and its integration into the existing accelerator complex while maintaining beam stability will be challenging. To address these challenges, we plan to install a two-cavity cryomodule into the APS storage ring for a proof-of-concept demonstration and also to mitigate as many technical risks as possible before the SPX construction phase. This first phase (R&D) is referred to as SPX0. Details of the R&D status and plans for individual subsystems are included in their respective discussions in subsequent sections.

The objectives of SPX0 are:

- Demonstrate that SPX system is transparent to the storage ring operation with cavities detuned.
- Test and evaluate deflecting cavities and rf component performance, which includes testing and evaluation of LOM and HOM dampers design.
- Demonstrate cavity voltage regulation and control to the required SPX tolerances.
- Demonstrate cavity differential phase control to the required SPX tolerances.
- Demonstrate fs-level synchronization.
- Provide an opportunity for possible user experiments with $\sim$10-ps x-ray pulse.

In this section, we briefly describe the plans for the two-cavity storage ring test.

The two-cavity cryomodule will be delivered by Jefferson Lab (JLab) fully assembled and under vacuum. Initial high-power cavity tests will be done at JLab with a 5-kW, 2815-MHz cw rf amplifier and two LLRF controllers provided by Argonne. As an option, we may choose to do subsequent high-power tests at the ATLAS facility at ANL's Physics Division, if time permits before its installation in the APS storage ring for in-ring tests.

The optional tests at the ATLAS facility down to 2 K would allow us to do system checks of the SPX0 cryomodule mechanical integrity, vacuum condition, and alignment variation. Additional tests will include cryogenic performance, rf power distribution and conditioning, tuner verification, cavity performance, low-level rf control and microphonics, low-power rf performance of the dampers, and alignment performance. The tests may also include the evaluation of potential dark current.

In the event that there would be no test at ATLAS, the cavities will be functionally checked at low power in Bldg 400A. Final cavity testing will be performed in the SR as part of SPX0 system installation and check out. This testing will be performed just prior to their turn over to Operations.

Once the two-cavity cryomodule is installed and checked out in the storage ring, we will establish normal storage ring operation for users with the cavities detuned (off resonance frequency) and parked at an intermediate temperature. A slowly ramped electron beam will be introduced with the unpowered, detuned cavities at room temperature, liquid-nitrogen temperature, liquid-helium temperature, and finally sub-λ helium temperature. The performance tests will include assessing beam quality and stability, higher- and lower-order mode (HOM/LOM) power damping efficiency, alignment, and diagnostics under passive conditions. We will then apply power to the cavities in a controlled manner until the operating

field is reached and the low-level rf (LLRF) and tuner functionally are tested and verified. During each step, we will test and evaluate performance of SPX0 subsystems including LLRF, high-level rf, slow and fast cavity tuning, timing and synchronization, diagnostics, alignment and HOM/LOM dampers, cryogenic heat load, and machine protection system until full fields are established in the cavities at 2 K. These will be done without stored beam.

Finally, beam will be introduced, and ramped slowly to full current for beam studies with the deflecting cavities. This will be discussed in detail in the SXP0 beam commissioning plan.

Here we will provide a description of the SPX0 technical system and components.

3.6.4.1.1 Cavity and Cryomodule

In the 2-cavity cryomodule each cavity is equipped with a JLab scissor-style tuner. Each cavity will produce an equivalent deflecting voltage of 500 kV. The cavity quality factor Q is specified to be 1×10^9 with an external Q of $\sim 5 \times 10^6$. Schematics of the SPX0 2-cavity string assembly and cryomodule are shown in Figures 3.6-97 and 3.6-98. Three prototype cavities have been fabricated at JLab. After vertical tests, the two cavities with the best performance (deflecting voltage and quality factor) will be selected to be integrated and packaged into the SPX0 cryomodule. Each cavity will be equipped with a JLab-style tuner that will allow for slow and fast tuning of the cavities. Each cavity's field (amplitude and phase) will be controlled by its own dedicated LLRF controller to compensate and correct for microphonics disturbance and beam-loading effect.

3.6.4.1.2 High-Power Waveguide Dampers

The APS Upgrade requires operation at 150 mA. To provide a safety margin, the SPX system is being designed with a requirement of 200 mA. In order to meet the APS storage ring beam stability requirement with 200 mA, we need to ensure that the damping of spurious modes of the SRF deflecting cavities are sufficient without impacting the cavities deflecting mode frequency operating at 2815 MHz. Because of the asymmetric cavity geometry for deflecting-mode operation (versus accelerating mode), both HOMs and LOMs must must be damped. This is a key performance parameter that is being evaluated in the SPX R&D phase (SPX0). We are currently developing several waveguide dampers prototypes that are capable of handling a few kWs of LOM power and hundreds of watts of HOM power. Technical issues such as damping material selection based on rf performance, waveguide geometry, surface bonding, thermal and mechanical stability properties, and particulates are being thoroughly investigated.

3.6.4.1.3 High-Power RF

We are fabricating two 2815-MHz, 5-kW cw rf amplifiers. Each rf amplifier has an internal high-voltage power supply, slow and fast hardware protection interlock systems, an rf personnel safety system (detection and protection against non-ionizing radiation), a PLC-based system for monitoring and control, and a waveguide distribution between the amplifiers and the cavities cryomodule.

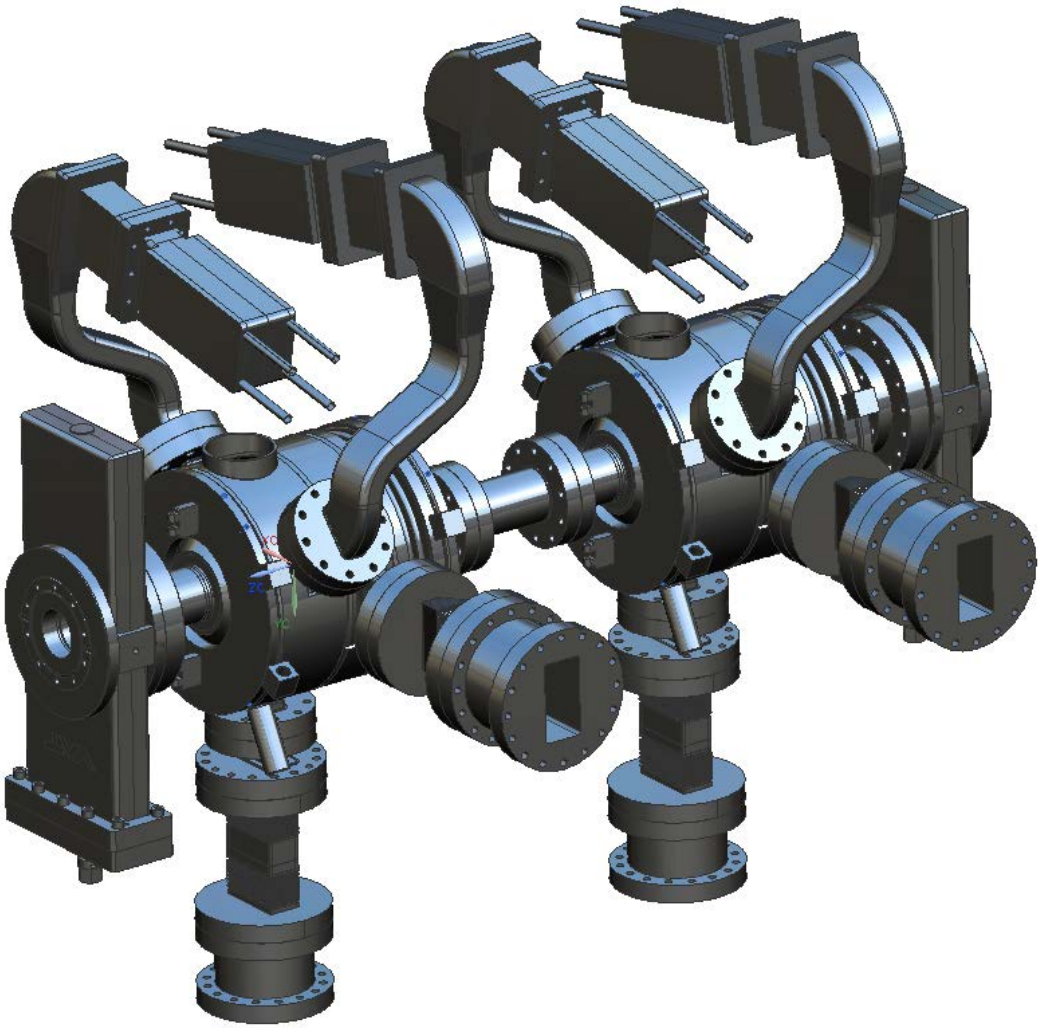

Figure 3.6-97: SPX0 2-cavity assembly.

3.6.4.1.4 Low-Level rf

The primary goal of the low-level rf (LLRF) system for SPX0 is to design and develop an LLRF system that will deliver the rf control performance in precision, stability, and bandwidth that meets the extremely high performance requirements as specified in the SPX PRD. This system is designed to regulate the amplitude and phase of the cavity fields to demonstrate that SPX differential and common mode phase and amplitude specifications can be achieved. For the in-ring test, cavities will be operated in three modes:

- Cavities will be cross-phased operating on rf zero crossing. In this mode, we will determine if we can achieve and maintain <5° common-mode phase variation in the 0.1 Hz-1 kHz bandwidth to keep beam emittance variation distinguishable from differential voltage effect for SPX0. We will also determine if a differential-mode phase variation of <0.077° in 0.1Hz-1 kHz can be

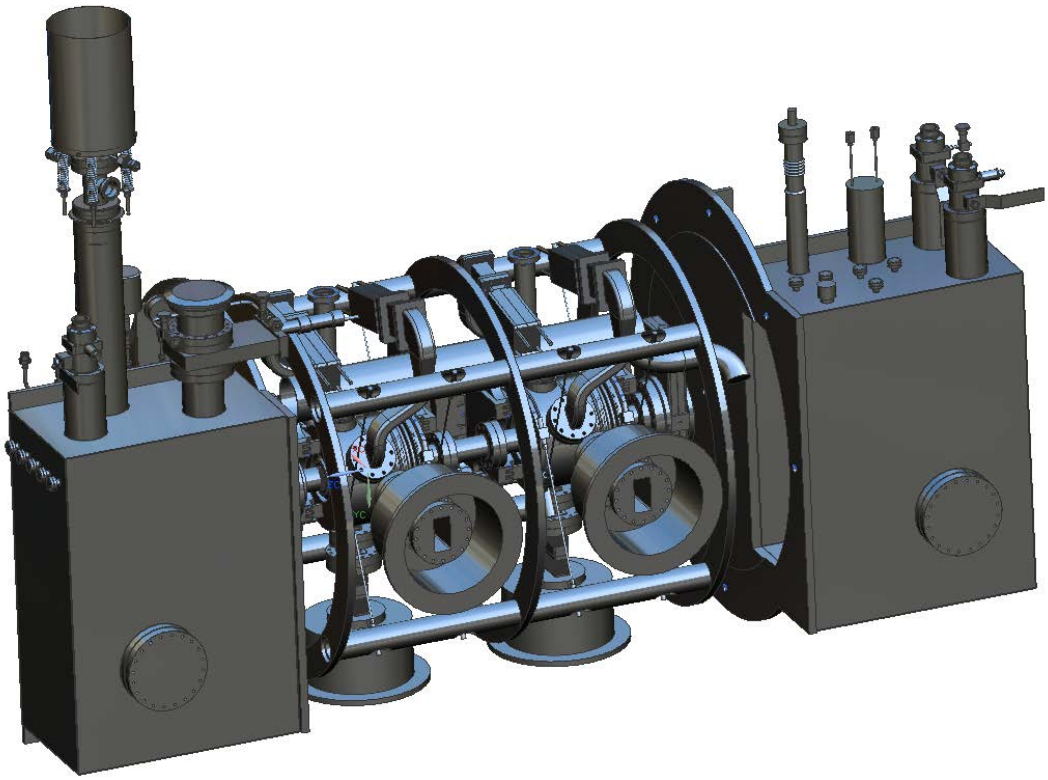

Figure 3.6-98: SPX0 cryomodule.

achieved to see if phase regulation for SPX (to keep global rms orbit motion under 10% for beam size/divergence) can be maintained.

- Cavities will operate in-phase on zero crossing to demonstrate the ability to keep beam emittance variation under 10%, to control arrival time jitter, to control pulse duration increase, and to keep rms beam motion under 10% of beam size and divergence
- Finally, cavities will operate in cross-phase mode on rf crest. In this mode, we will confirm the SPX common- and differential-mode voltage and phase variation requirements.

3.6.4.1.5 Timing and Synchronization

The timing and synchronization system will provide the information and phase references needed to drive the deflecting cavities and measure the effects on the electron beam within the SPX region and the residual effects outside the SPX region. In addition, phase references will be provided to the beamline lasers for synchronization to the x-ray beam pulses.

The primary objective for timing/synchronization SPX0 (R&D phase) is to provide the phase references to the LLRF to demonstrate that the common mode and differential phase tolerances specified in the SPX Physics Requirement Document (PRD) can be achieved.

For this purpose, we formed a collaboration with the LBL Beam Instrumentation Group to adopt their femtosecond timing/synchronization system to SPX requirements.

This system is currently under development, is being built to SPX requirements and will be used for SPX0 to provide phase references to the SPX0 LLRF. Along with this, the technology, including documentation to reproduce the LBL system, will be transferred to ANL so that it can be implemented to meet final SPX timing/synchronization requirements including beamline laser synchronization.

3.6.4.1.6 Diagnostics

No specific R&D is planned for SPX0. We plan to utilize existing diagnostics devices that have been evaluated and determined to be adequate for SPX0. See section 3.6.4.11.

3.6.4.1.7 Controls

The primary goal of controls is to provide support for the SPX0 LLRF and timing tasks. In the R&D phase, will will evaluate platform options for the real-time data processing requirements, demonstrate inter-system communication, and identify additional tools/software required to meet SPX requirements. Controls will be provided to support deflecting cavities tests at the ATLAS SRF facility and in 400A during the R&D phase.

3.6.4.1.8 Mechanical System

Several mechanical systems are needed for installation and operation of the SPX0 cryomodule. The most significant of these include a special storage ring straight section vacuum system, deionized water supply and distribution systems, and a cryogenic supply and distribution system. Significant effort will be allocated to not only specify, design, and install these systems, but also to coordinate the design of all major SPX mechanical systems to ensure physical compatibility, proper mechanical integration of SPX cryomodules into the APS storage ring, and adequate conventional facility provisions.

3.6.4.1.9 Water System

Deionized water distribution systems will be provided for cooling of the high-power rf systems in Building 400A-1, a high-throughput vacuum pumping system in room 400A-3 used for evaporative cooling of the cryomodule liquid helium bath, and rf dampers and waveguide windows located on the cryomodule itself.

3.6.4.1.10 Cryogenics

The cryogenic supply and distribution system for SPX0 is envisioned as a temporary source of 80 K and 2 K cooling for the SPX0 cryomodule. The system is designed for simplicity and low capital cost, consistent with both SPX0 studies and APS storage ring operation.

3.6.4.2 SPX0 Physics Requirements and Issues

As mentioned above, under the SPX0 project, one cryomodule containing two cavities will be installed at the downstream part of the ID5 straight section. The undulator presently installed there will be moved to the upstream part of the straight section. A set of physics requirements was derived based on extensive and complex simulations.

The primary goals of the SPX0 project are as follows:

- To demonstrate operation of two fully powered independently controlled superconducting deflecting cavities with beam, including quantitative measurements of their impact on the beam. This test will require low-level rf control, high-power rf, interlock systems, timing and synchronization systems, cavity alignment, beam diagnostics, controls, and beam feedback.
- To demonstrate synchronization of a beamline laser with the deflecting cavities at the sub-ps level.

When operated in-phase, the two cavities will increase vertical beam size everywhere around the ring, and therefore in this configuration will not be compatible with normal user operation. The tests will only be conducted during weekly storage ring intervention and study periods. When operated in opposite phases with zero net deflecting voltage, no significant effect on the beam is expected, so that the cavities could be operated and tested during user operations. However, this mode of operation will first need to be confirmed as acceptable for user operations.

Many of the requirements here originate in those for the full SPX project, in that SPX0 is intended to test some of the concepts and technology behind the full project.

3.6.4.2.1 Technical Requirements

The main parameters of the deflecting cavities are listed in Table 3.6-47

Table 3.6-47: Main parameters of the SPX0 deflecting cavities.

Quantity	Specification
Electron beam current	100 mA[a]
Number of cavities	2
Total voltage	1 MV
RF Frequency	2815.486 MHz
Cavity tunability	$\pm$200 kHz[b]
Source tunability	$\pm$1.5 kHz[c]
Operating temperature	2 K

[a] When turned off, cavities should not prevent 150-mA beam studies.
[b] To cover more than one SR revolution harmonic.
[c] SR circumference is not expected to change significantly in the future.

The rf phase and amplitude have to be controlled to sufficient precision to prevent excessive orbit motion and to demonstrate the level of control required for the full project.

Simulations of the amplitude and phase control errors were performed (see section 3.6.4.3) for an rms bunch length of 33 ps, corresponding to a total beam current of 100 mA in 24 bunches. The resulting tolerances are listed in Tables 3.6-48, 3.6-49, and 3.6-50. We chose 0.1 Hz for the lower limit of the bandwidth for SPX0 assuming that extension to 0.01 Hz for the full-scale SPX is straightforward. Separation between beam motion and effective beam size increase is set at 1 kHz [3.6-28].

Table 3.6-48: Tolerances for SPX0 for cross-phase operation on zero crossing.

Specification Name	Rms Value	Bandwidth	Driving Requirement
Common-mode voltage amplitude variation	$< 7\%$	0. 1Hz – 271 kHz	Keep beam emittance variation distinguishable from the differential voltage effect for SPX0
Common-mode phase variation	< 5 deg	0.1 Hz – 1 kHz	Keep global orbit motion distinguishable from differential phase for SPX0
	< 18 deg	1 kHz – 271 kHz	Keep rms emittance variation distinguishable from differential phase for SPX0
Differential-mode voltage variation	$< 1\%$	0.1 Hz – 1 kHz	Check regulation required for full-scale SPX: Keep rms emittance variation outside of SPX under 10% of nominal 35 pm
	$< 0.77\%$	1 kHz – 271 kHz	Check regulation required for full-scale SPX: Effective emittance growth under 1.5 pm for SPX
Differential-mode phase variation	< 0.077 deg	0.1 Hz – 1 kHz	Check regulation required for full-scale SPX: Keep global rms orbit motion under 10% of the beam size/divergence for SPX
	< 0.28 deg	1 kHz – 271 kHz	Check regulation required for full-scale SPX: Keep emittance growth outside of SPX under 10% of nominal 35 pm

Orbit motion due to phase mismatch in the low frequency range (lower than 60 Hz) can be corrected by the orbit feedback with orbit correction effectiveness varying with the frequency. In the high frequency range, the phase noise is amplified due to resonance with the betatron frequency. The phase mismatch requirements shown in Tables 3.6-48 and 3.6-49 do not take orbit correction into account. The phase mismatch noise density integrated from 0.1 Hz to 1 kHz and multiplied by the orbit correction effectiveness and the orbit motion transfer function should not exceed the values in Tables 3.6-48 and 3.6-49.

Table 3.6-49: Tolerances for SPX0 for in-phase operation on zero crossing.

Specification Name	Rms Value	Bandwidth	Driving Requirement
Common-mode voltage amplitude variation	$< 6.9\%$	0.1 Hz – 271 kHz	Keep beam emittance variation under 10%
Common-mode phase variation	< 2.5 deg < 3.6 deg	0.1 Hz – 60 Hz 60 Hz – 271 kHz	Control arrival time jitter Control effective pulse duration increase
Differential-mode voltage variation	$< 10\%$	0.1 Hz – 271 kHz	Common sense
Differential-mode phase variation	< 10.7 deg	0.1 Hz – 1 kHz	Keep rms beam motion under 10% of beam size/divergence

Table 3.6-50: Tolerances for SPX0 for cross-phase operation on crest.

Specification Name	Rms Value	Bandwidth	Driving Requirement
Common-mode voltage amplitude variation	$< 5\%$	0.1 Hz – 1 kHz	Support confirmation of full-scale SPX differential voltage requirement
Common-mode phase variation	< 7.2 deg	0.1 Hz – 1 kHz	Support confirmation of full-scale SPX voltage requirement
Differential-mode voltage variation	$< 1\%$ $< 0.77\%$	0.1 Hz – 1 kHz 1 kHz – 271 kHz	Confirm full-scale SPX requirement Confirm full-scale SPX requirement
Differential-mode phase variation	< 2.3 deg	0.1 Hz – 1 kHz	Support confirmation of full-scale SPX voltage requirement

EPICS controls will be required that allow common-mode and differential-mode variation of the phase and amplitude of the cavities, as detailed in Table 3.6-51. In addition, it will be necessary to have a means of changing the phase of one of the cavities by 180 degrees relative to the other, so that the cavities can be run either in phase or out of phase. Note that in addition to running cavities at the zero crossing (i.e., so that the beam centroid is not kicked), we will also need to operate them on crest (i.e., so that the beam centroid is kicked). The on-crest operation is intended for testing the voltage regulation. The tolerances for on-crest operation are shown in Table 3.6-50.

To support automated control of the rf parameters, a 10-Hz EPICS write capability is required.

Table 3.6-51: Phase and voltage control requirements for SPX0.

Specification Name	Value	Driving Requirements
Common-mode controls:		
Adjustment range:		
Common-mode phase	$>$ 400 deg	Perform scan over one wavelength
Adjustment rate:		
Common-mode amplitude	Full range in $<$ 10 s	Apply changes in reasonable time
Common-mode phase	Full range in $<$ 10 s	Apply changes in reasonable time
Cavity-to-cavity controls:		
Amplitude-error adjustment range	$>$ 10%	Compensate for lattice imperfections in full-scale SPX
Amplitude-error adjustment step	$<$ 0.1%	1/10 of requirement from Table 3.6-48
Amplitude-error adjustment rate	Full range in $<$ 10 s	Apply changes in reasonable time
Phase-error adjustment range	$>$ 5 deg, plus 180 flip	Compensate for lattice imperfections in full-scale SPX
Phase-error adjustment step	$<$ 0.005 deg	Demonstrate 0.077-deg stability
Phase-error adjustment rate	Full range in $<$ 10 s	Apply changes in reasonable time

Higher- and lower-order modes must be damped to ensure multi-bunch beam stability (see section 3.5.6.2 of the CDR). Requirements, listed in Table 3.6-52, are calculated taking the bunch form factor into account and assuming synchrotron radiation damping rate only.

Table 3.6-52: HOM/LOM requirements for SPX0 cavities.

Shunt impedance	Limit
Longitudinal	
$(R_s f_{HOM})$ for one monopole HOM/LOM	0.44 MΩ-GHz
R_s for one monopole HOM/LOM at 2 GHz	0.22 MΩ
Transverse	
R_t for one x-plane HOM/LOM	1.3 MΩ/m
R_t for one y-plane HOM/LOM	3.9 MΩ/m

3.6.4.2.2 Alignment

Cavity alignment relative to the beam is important both for protecting cavities and for minimizing vertical emittance degradation. Large transverse orbit inside the cavity will generate an excessive amount of rf power while large cavity roll will affect vertical emittance of the beam. Also, vertical-offset-dependent beam loading perturbations caused by beam arrival jitter can lead to cavity phase noise. Table 3.6-53 lists alignment requirements, based on section 3.6.3.5, section 3.3, and [3.6-29, 3.6-30]. The distance between cavities inside the cryomodule is 0.53 m.

Table 3.6-53: Alignment requirements for SPX0 cavities (full range).

	Cryomodule Alignment	**Cavity Inside Cryomodule**
ΔX	$\pm$500 μm	$\pm$500 μm
ΔY	$\pm$200 μm	$\pm$200 μm
ΔZ	$\pm$1000 μm	$\pm$1000 μm
Yaw	$\pm$10 mrad	$\pm$10 mrad
Pitch	$\pm$10 mrad	$\pm$10 mrad
Roll	$\pm$10 mrad	$\pm$10 mrad

3.6.4.2.3 Diagnostics

To support cavity tests with beam, diagnostics are needed to:

- Ensure that the beam is kept at the center of the cavities;
- Characterize the effect of cavity operation on the beam orbit.

In addition, the ability to impart a beam tilt will provide the opportunity to characterize existing and new diagnostic instrumentation performance with tilted beams. To be able to conduct user experiments, a certain beam stability is also required that is shown in Table 3.6-54. The numbers related to the timing jitter are derived from the expected pulse length of 7 ps FWHM and the required pulse length variation of 10% of that value [3.6-77].

Table 3.6-54: Beam stability requirements at the radiation source location [3.6-27, 3.6-77].

Quantity	**Rms Beam Motion**	**Bandwidth**	**Driving Requirement**
ΔX	3 μm	0.1-200 Hz	General beam stability
ΔY'	$<$1.2 μrad	0.1-60 Hz	Timing jitter
ΔY	$<$4 μm	0.1-60 Hz	To satisfy ΔY' requirement

To control the beam position at the location of the deflecting cavities, the BPM resolution shown in Table 3.6-55 is required. These numbers are routinely achievable with present devices.

Table 3.6-55: Requirements for BPM in the deflecting cavity straight section.

	Resolution	Bandwidth	Driving Requirement
X	10 μm	1 kHz	Beam-Cavity Alignment
Y	10 μm	1 kHz	Beam-Cavity Alignment

An electron beam can drive HOM fields in the deflecting cavity, which in turn can excite electron beam instability. The cavity is designed such that these HOM fields are extracted and absorbed in HOM dampers. Monitoring the HOM power is important to verify the quality of the cavity design and construction, as well as to help identify the source of any multi-bunch instabilities that might be observed. Therefore, a HOM monitor suitable for spectral measurements is required.

3.6.4.2.4 Synchronization of Laser to the Deflecting Rf

To conduct pump-probe experiments, users at 7ID will need synchronization signal for their laser tied to short-pulse arrival time. The rms deviation between this signal and the photon pulse should be sufficiently small that the effective pulse duration is increased by 10% or less. Expected FWHM pulse duration at 7ID for SPX0 is 7 ps (see section 3.6.4.3). Hence, the jitter shall be maintained at 3 ps FWHM, or 1.4 ps rms [3.6-78].

3.6.4.2.5 Machine Protection System

As mentioned in the stability section, an electron beam going off-center in the deflecting cavities can generate rf power. At high enough power the cavities and rf source can be damaged. The electrical center of the cavities will be determined using beam-based methods by observing reflected power as a function of beam position, following which the usual orbit control methods will be used to maintain (but not guarantee) the beam position. The requirements for determining and maintaining the beam position relative to the electrical center are listed in Table 3.6-56.

To protect against damage due to excessive beam offsets that may occur due to uncontrolled orbit excursions, the signal from the cavity field probe will be interlocked. Passive means of protecting the rf sources (i.e., circulators) and interlocks on excessive reflected power will be employed. Finally, protection of the circulators will include monitoring circulator load temperature and using arc detectors.

Table 3.6-56: Maximum desired orbit errors in vertical plane for operation of SPX0 [3.6-29].

Orbit with cavities on-resonance	$\pm$100 μm
Orbit with cavities off-resonance	$\pm$1000 μm

During SPX0 operation, vertical beam size will be increased everywhere. Operation with ID gaps closed will need to be carefully considered.

3.6.4.2.6 Effects on Machine Operation

When not in operation, the SPX0 system must not adversely impact user operations. That is, there should be no significant increase in beam emittance or motion when SPX0 is present in the unpowered condition, where we take "significant" to mean more than 10%.

SPX0 must also not adversely impact machine studies. A primary implication of these requirements is the ability to detune the cavities from resonance (see Table 3.6-47). In addition, all present operational bunch patterns (24 bunch, 324 bunch, and hybrid mode) must be possible up to 150 mA, which has implications for the cavity impedance (see Table 3.6-52). Also, regular response matrix measurements, which may entail significant orbit distortion through the cavities, should be possible with the cavities detuned. This has implications for the allowed orbit displacement that is tolerable in the unpowered cavities (see Table 3.6-56).

Because of interference issues between the SPX0 cryostat and the nearby bending magnet beamline in the radial direction, the SPX0 cryostat will be installed in the downstream end of the 5ID straight section. This will necessitate moving the existing insertion device to the upstream end. This movement will be scheduled in one of shutdowns prior to the cryostat installation in order to separate possible consequences of ID movement from the effects of the cryostat installation.

3.6.4.3 Single-Particle Dynamics

In this section, we show the results of single-particle beam dynamics modeling of SPX0. Using simulated cavities located in Sector 5, we compute relevant beam properties including the achievable x-ray pulse duration for several beamlines, as well as some quantities that may be of interest for computing beam loading or designing diagnostics. We also look at the effects of the SPX0 cavities on injection and beam lifetime. Finally, we analyze tolerances in light of what we need to learn from SPX0.

3.6.4.3.1 Ideal Results

The simulation techniques are the same as those used above (see section 3.6.3.2). We assumed a 33-ps rms bunch duration, which is appropriate for 100-mA, 24-bunch mode. The operational lattice for this mode was also used. We performed simulations for vertical emittances of 35 pm (close to present-day value of 40 pm) and 20 pm (likely minimum we can deliver without additional equipment [3.6-79]).

Figures 3.6-99 and 3.6-100 show the "visibility parameter," defined as

$$\alpha_{45} = \frac{\sigma_{45}}{\sqrt{\sigma_{44}\sigma_{55} - \sigma_{45}^2}}, \tag{3.6-58}$$

where $\sigma_{ij} = \langle x_i x_j \rangle$, $x_4 = y'$, and $x_5 = t$. (This quantity is analogous to α_x and α_y for ordinary transverse phase space characterization.) We see that the visibility is near the maximum value at 7ID, which is why Sector 5 is the ideal location for the SPX0 cavities. In addition, there is interest from 11ID and 14ID [3.6-39]. 11ID will enjoy almost the same visibility as 7ID, while 14ID will be down by only 15%. Reducing the vertical emittance to 20 pm makes only a small difference, and is not likely to affect pulse duration significantly. Figures 3.6-101 and 3.6-102 show the rms beam size and divergence at the straight sections.

Next, we simulated x-ray pulse slicing for each sector, assuming a 2.4-m-long insertion device set for 10 keV and a slit at 26.5 m. As usually, a ± 0.25 mm horizontal slit was used to reduce the size of the side pulses. The achievable pulse duration at Sector 7 is about 7.5 ps FWHM, as shown in Figure 3.6-103.

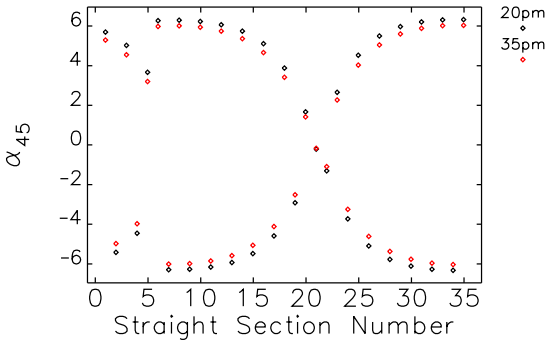

Figure 3.6-99: Chirp visibility function at straight sections for two in-phase 0.5-MV crab cavities in the downstream end of Sector 5.

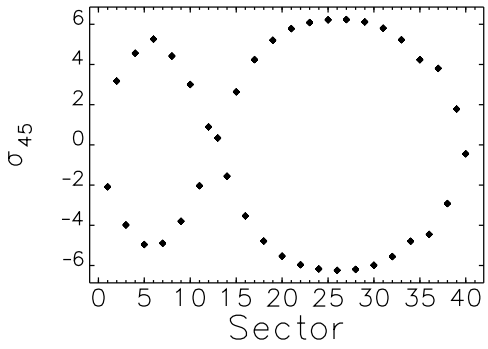

Figure 3.6-100: Chirp visibility function at BM source points for two in-phase 0.5-MV crab cavities in the downstream end of Sector 5.

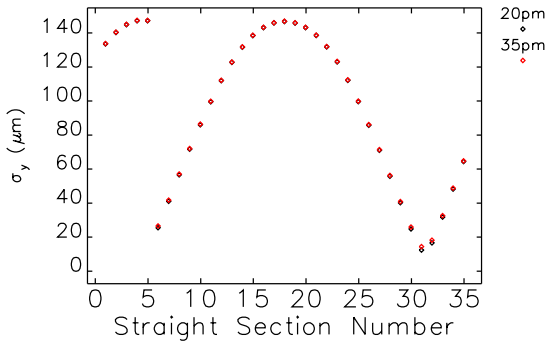

Figure 3.6-101: Rms vertical beam size for each straight section for two in-phase 0.5-MV crab cavities in the downstream end of Sector 5.

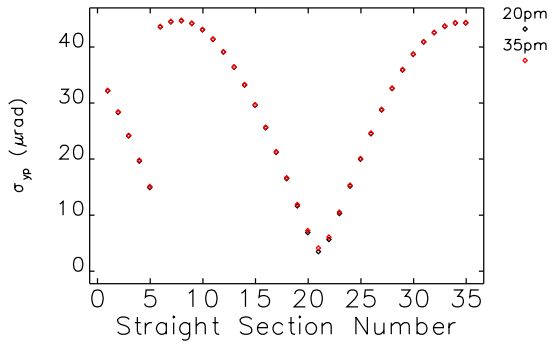

Figure 3.6-102: Rms vertical beam divergence for each straight section for two in-phase 0.5-MV crab cavities in the downstream end of Sector 5.

3.6.4.3.2 Effects on Beam Lifetime

To study the effects of SPX0 on beam lifetime, we used a previously optimized lattice with $\nu_x = 36.13$, $\nu_y = 19.25$, $\xi_x = 7$, and $\xi_y = 6$. These values roughly match what is used now, although the chromaticities are a bit higher than used now that P0 feedback is in routine operation. This will probably tend to understate the difference, in that it will lower the baseline lifetime.

As usual, the main rf voltage and frequency are chosen to mock up potential well distortion [3.6-33]. We chose values appropriate to an rms bunch duration of 33 ps, which ends up giving an rf bucket

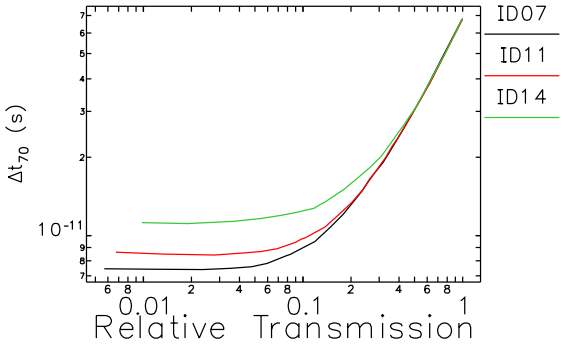

Figure 3.6-103: Results of slit scan for three sectors. The transmission is relative to the situation with the vertical slits completely open.

half-height of about 2.48%, somewhat lower than the 2.55% we have now in operation with 9.5 MV. This will slightly decrease the lifetime of the reference configuration.

Our first step was to compute the local momentum acceptance (LMA) using `elegant` [3.6-35] for the case with the deflecting cavities off. This made use of a set of 50 ensembles of errors and corrections, giving a median vertical emittance of 40 pm. Using `touschekLifetime` [3.6-80] and assuming 100 mA in 24 bunches with a fixed coupling of 1.5%, we found that the median lifetime is about 11.6 hours. This is significantly longer than we have in present operations for the same beam parameters, which calls into question whether rf voltage is really as large as thought. To normalize the results to the measurements, we capped the LMA at $\pm 2.325\%$, which gives a median predicted lifetime of 10.0 hours.

For the case with SPX0 on, we used a method developed by V. Sajaev: The 2000-turn LMA was computed for each ensemble, but with the SPX0 cavities on at 0.5 MV each. For each ensemble, we then computed the difference in lifetime between the case with SPX0 off and on. In all cases, the lifetime decreased, as might have been expected. Figure 3.6-104 shows the cumulative distribution of the lifetime decrease, which has a median of about 0.1 hour, which is perhaps measurable. From this result, we conclude that we are more likely than not to see a measurable lifetime decrease from SPX0 operation. The effect on lifetime could presumably be exaggerated by moving the tunes closer to the $\nu_x - \nu_y$ or $2\nu_x + \nu_y$ resonances.

3.6.4.3.3 Effects on Injection Efficiency

Next, we simulated injection efficiency using `elegant`, using a method similar to V. Sajaev's: In particular, we simply displaced the horizontal bunch centroid at the beginning of tracking by 6 mm and determined the difference between having SPX0 on or off. 6 mm was chosen because it gives >95% capture for almost all ensembles with SPX0 off and corresponds to what we think we have for an injected beam oscillation. Tracking was performed with 1000 particles for 2000 turns, including full synchrotron radiation effects. The initial beam parameters were 100-nm horizontal emittance, 5-nm vertical emittance, 0.115% momentum spread, and 82-ps rms bunch duration, using APS booster

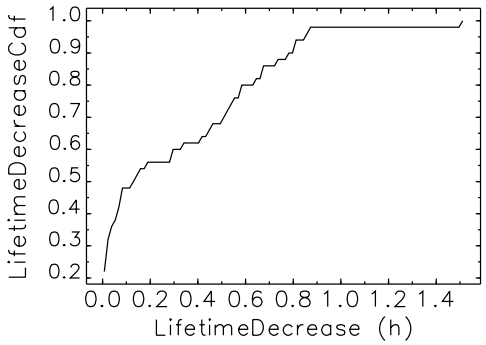

Figure 3.6-104: Cumulative distribution of decrease in lifetime due to two SPX cavities at 0.5 MV each. 50 ensembles were used.

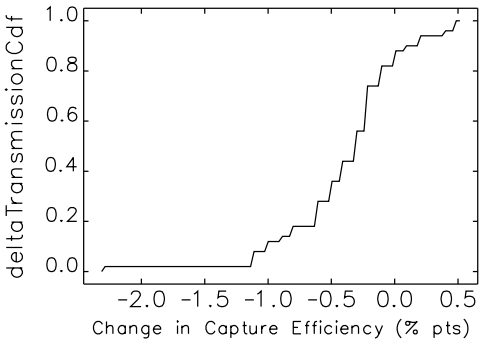

Figure 3.6-105: Cumulative distribution of change in capture percentage due to two SPX cavities at 0.5 MV each. 50 ensembles were used.

parameters from V. Sajaev and C. Y. Yao. [5]

For each ensemble, we performed tracking for 0 MV and 0.5 MV/cavity, then took the difference in capture efficiency. The cumulative distribution function (CDF) of this difference is shown in Figure 3.6-105. We see that little change in capture efficiency is expected. At most we might expect a reduction of 1 percentage point. Again, if we *want* to see something in order to confirm learn about the beam dynamics, we can try moving the working point closer to the resonances noted above.

3.6.4.3.4 Error Sensitivity

One of the primary goals of SPX0 is to test our ability to achieve the exacting tolerances required by the full SPX system. However, it is not a foregone conclusion that we will have sufficient sensitivity to determine whether these tolerances have in fact been achieved. Hence, we have simulated the effects of phase and voltage errors on SPX0, with an eye toward whether we can use beam-based methods to verify the error levels.

First, we look at determination of the differential phase error. If we operate the two SPX0 cavities at opposite zero-crossings, then a differential phase error will produce primarily a change in the slope of the beam trajectory, while a common-mode phase error will produce primarily a change in the offset of the beam trajectory. If we can distinguish between the orbit patterns produced by these trajectory changes, then we can measure the amount of differential and common-mode phase error.

Making use of the fact that statistics of orbits and trajectories are the same (see section 3.6.3.2.3), we performed closed-orbit simulations to try to quantify these considerations and determine whether it will be possible to differentiate between the two types of phase error. For simplicity, the deflecting cavities were modeled as vertical steering elements, with the kick error given by

$$\Delta y' = v\Delta\phi \exp\left(-\omega^2\sigma_t^2/2\right) \tag{3.6-59}$$

[5]The bunch length is probably a few ps longer than this, but that information came after we ran the simulations and is unlikely to impact the results

for a phase error $\Delta\phi$, cavity frequency $\omega = 2\pi f$, normalized deflecting voltage $v = V/E$, and electron bunch length $\sigma_t = 33$ ps. We included other noise sources, namely, vertical correctors. However we deactivated most of the vertical correctors in order to improve our ability to see the desired signals. Powering as few as 10 correctors is consistent with stored beam [3.6-79], so we chose to keep every fourth B:V1 corrector on, using Sectors 3, 7, 11, etc. (for the missing S39B:V1 corrector we substituted S39B:V2). The slow corrector noise up to 500 Hz is about 6 nrad [3.6-81], however, to be conservative we used instead the bit resolution, which is 33 nrad.

In addition to random corrector errors, we separately included 77 mdeg rms errors in differential mode or 1 deg rms errors in common mode, in two separate simulations. We performed two analyses on the orbit data. In the first analysis, we simply compared to patterns of the rms BPM readings. The results, shown in Figure 3.6-106, indicate that we could not detect the differential phase error in this fashion if the error levels are those specified for SPX. Either another method is needed, or the common-mode error level must be reduced to allow visibility of the effects of the differential phase error.

The second analysis involves using the inverse response matrix and assumes that we can perform synchronized data acquisition from the BPMs, which will be possible using the FPGA BPMs now being installed. To explain the technique, we assume again that we can think about orbits as opposed to trajectories. In principle, we can then compute the strength of the 10 corrector magnets and the two steering kicks from the cavities using the inverse orbit response matrix. If we can accurately determine the cavity kicks, we can deduce the differential and common-mode phase errors.

We want to test whether this method can measure the magnitude of a low-level differential phase error when large common-mode errors are present. In addition, we must include corrector noise, BPM noise, and optics errors. BPM noise at the non-source-point BPMs is expected to be 400 nrad rms up to 1 kHz, assuming that all BPMs are upgraded to use BSP-100 units [3.6-82]. Optics errors were simulated by assigning errors to the quadrupole strengths that resulted in a 1% rms vertical beta beat [3.6-83], then using the ideal response matrix in the recovery process. The response matrix for phase errors is shown in Figure 3.6-107, where we see that the response to differential errors is much larger than the response to common-mode errors.

We performed a series of simulations with different magnitudes for the rms common-mode error, while keeping the rms differential error fixed at 77 mdeg. For each common-mode error level, we simulated 2000 cases and used the response matrix to determine the differential and common-mode phase error. As we can see from Figure 3.6-108, we are able to accurately determine the differential error level even in the presence of rather large common-mode errors. There is a slight overestimate of the error level, resulting from the BPM noise. If the BPM noise is increased to 1 μm rms, the inferred differential phase error increases to 87 mdeg rms. We performed this analysis again assuming deflecting voltages of 0.35 MV per cavity, instead of the nominal 0.5 MV. The results were essentially identical to Figure 3.6-108, except that the inferred differential error increased slightly over 80 mdeg.

We noted at the beginning of this section that turn-by-turn trajectories due to time-varying kicks are not the same as closed orbits, even though when analyzed over many turns or seeds they have the same statistics. For fast motion, we need to refine the analysis, which we did as follows: Because we are interested in the beam-centroid effects of phase errors up to 1 kHz, we can assume that turn-by-turn BPM data will be averaged over 1 ms, or 271 turns. Our next simulation thus consists of 1000 runs in which the beam is subjected to 1000 different random values for the cavity phases. After tracking for 271 turns, we compute for each BPM the average value of the beam centroid over those turns, which is a simulation of a single reading from each BPM. What we find, perhaps not surprisingly, is that averaging over 271 turns is sufficient to determine the closed orbit about which the beam is oscillating.

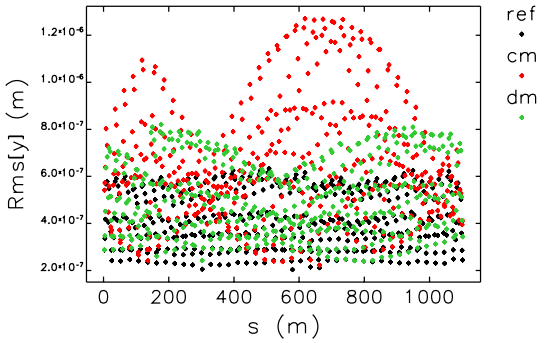

Figure 3.6-106: Comparison of the normalized orbit response to differential and common-mode phase errors in SPX0.

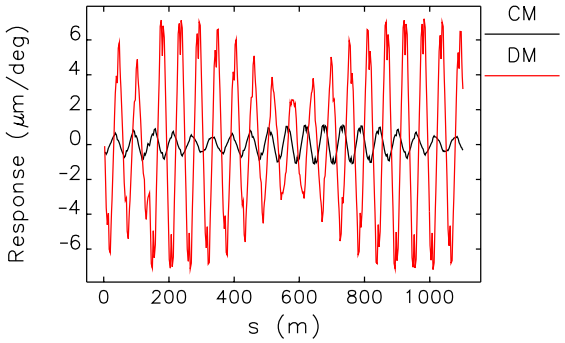

Figure 3.6-107: Vertical orbit response patterns for differential- and common-mode phase errors.

Hence, we can expect that using the response matrix will yield similar results to those just described.

To confirm this, we performed simulations with random common- and differential-mode phase errors, plus random corrector errors. All errors were at the levels determined just above. For each ensemble, we tracked for 271 turns to obtain the "closed orbit." (In reality, of course, the correctors cannot vary this quickly, a fact that may enhance our ability to detect the patterns of interest.) We simplified the simulation by replacing the cavities with equivalent kick elements. Assuming a common-mode phase error level of 5 deg rms, the inferred differential mode error was 82 mdeg rms, which is very close to the expected value of 77 mdeg.

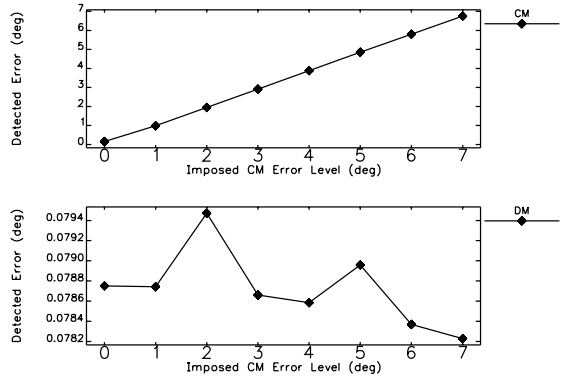

Figure 3.6-108: Inverse response matrix analysis of closed orbits under the influence of 0.077 deg rms differential phase errors and varying common-mode phase error levels, for cross-phase zero-crossing mode. 400-nm BPM noise and 33-nrad corrector noise (on ten correctors) is also included, along with quadrupole strength errors.

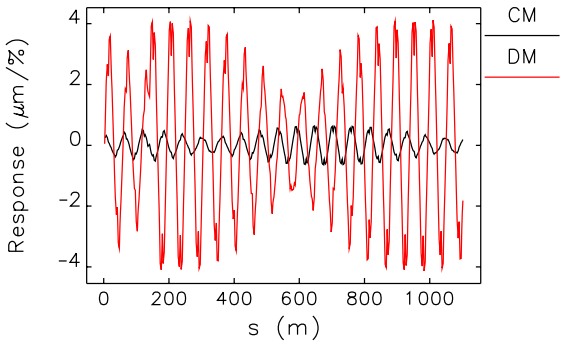

Figure 3.6-109: Vertical orbit response to differential and common-mode voltage errors in cross-phase on-crest condition.

In SPX proper, voltage errors lead to variation in emittance, pulse duration, and intensity. As seen in

section 3.6.3.2, this results in somewhat tight tolerances on differential voltage errors, but more relaxed tolerances on common-mode voltage errors. For SPX0, we seek to verify that these tolerances can be met. By running the two SPX0 cavities on opposite crests, we can create a situation in which we are sensitive to differential voltage errors, but relatively insensitive to common-mode voltage errors.

Following the results in the previous section, we used response matrix analysis to attempt to recover the differential and common-mode error levels in this situation. Figure 3.6-109 shows the response to the two types of error. Once again, we see that the response to a differential error is much larger.

Next, we performed simulations of 2000 orbits, including differential and common-mode voltage errors as well as errors in the ten vertical steering correctors listed above. We then used the response matrix, as above, to deduce the differential and common-mode error levels. The results, shown in Figure 3.6-110 demonstrate that even for fairly large common-mode voltage errors, the differential-mode error level is reliability determined. We performed this analysis again assuming deflecting voltages of 0.35 MV per cavity, instead of the nominal 0.5 MV. As was the case for phase errors, we saw no significant change in our ability to distinguish between the two sources of motion.

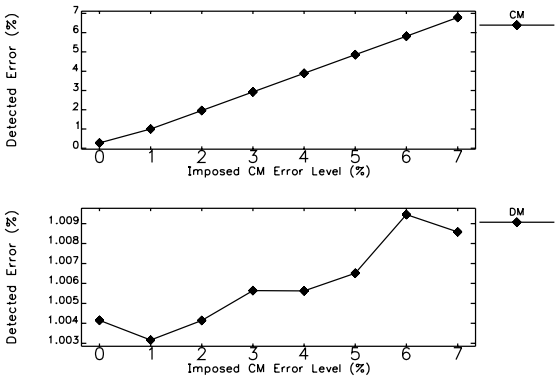

Figure 3.6-110: Inverse response matrix analysis of closed orbits under the influence of 1% rms differential voltage errors and varying common-mode voltage error levels, for cross-phase on-crest mode.

Sufficiently fast beam motion is seen by the users as an emittance increase. Hence, there is a tolerance on the differential phase error above 1 kHz for SPX that is related to how much the emittance is allowed to grow. We would like to confirm the achievement of this tolerance in SPX0 in cross-phase mode, but must consider that common-mode phase errors will create a similar perceived emittance growth. Rf BPMs can of course read the beam position turn-by-turn, but it is unclear whether we can tell the difference between the two types of phase errors if we do not average over many turns to find the closed orbit.

To investigate this, we repeated the above simulations, but instead of averaging over 271 turns, we averaged over 27 turns (i.e., 10 μs). We repeated the above analysis, increasing the BPM noise a factor of $\sqrt{10}$ to 1.3 μm rms. The inferred differential-mode error increased to 96 mdeg. The increase is almost entirely a result of the large BPM noise By using 10,000 “orbits” instead of 1000, this result dropped to 91 mdeg.

We next tried cleaning up the data by using singular-value decomposition (SVD) to filter out the noise.

We performed SVD, removed all but the 12 largest singular values, then reconstructed the data. (Recall that there are 10 correctors and two cavities as orbit sources, which explains the choice of 12 singular values.) Using the reconstructed data, we obtained a result of 78 mdeg using only 1000 "orbits." Hence, we should be able to detect differential phase errors up to 10 kHz in the presence of common-mode errors provided the ratio of the error levels is the same as for slower motion.

3.6.4.3.5 Tolerances

We now wish to determine the SPX0 tolerances with consideration of the bandwidth within which each tolerance applies.

Cross-Phase Operation

In cross-phase operation we attempt to emulate actual SPX operation by having the cavities largely cancel each other's effects. This includes having the two cavities at opposite zero-crossings and at opposite crests. We have analyzed phase tolerances for zero-crossing operation and voltage tolerances for on-crest operation above.

For zero-crossing operation, the signal of interest is the differential phase error, which results primarily in a net kick to the beam centroid. We have seen that we can recover a supposed differential phase error level of 77 mdeg in the presence of large common-mode errors. We somewhat arbitrarily set the common-mode requirement to 5 deg rms.

The SPX requirement for differential phase errors above 1 kHz is 280 mdeg, 3.6 times the 77 mdeg requirement for 0.01 Hz to 1 kHz. Hence, the SPX0 requirement for common-mode phase errors above 1 kHz is 18 deg (3.6×5).

For on-crest operation, the signal of interest is the differential voltage error, which results (primarily) in a net kick of the beam. Again, we were able to recover a supposed 1% rms differential error in the presence of large common-mode errors. We again somewhat arbitrarily set the common-mode requirement to 5%.

The phase error sensitivity in on-crest mode can be analyzed analytically. Consider that the net deflection due to the two cavities is

$$\Delta y' = \frac{V_1}{E}\left(1 - \frac{1}{2}\Delta\phi_1^2\right) - \frac{V_2}{E}\left(1 - \frac{1}{2}\Delta\phi_2^2\right), \tag{3.6-60}$$

where V_i is the voltage of the i^{th} cavity and $\Delta\phi_i$ is its phase error. Writing $V_{\frac{1}{2}} = V + \Delta V_c \pm \Delta V_d/2$ and $\Delta\phi_{\frac{1}{2}} = \Delta\phi_c \pm \Delta\phi_d/2$, where the 'c' and 'd' subscripts refer to the common-mode and differential errors, it follows that

$$\Delta y' \approx \frac{\Delta V_d}{E} - \frac{2V}{E}\Delta\phi_c\Delta\phi_d, \tag{3.6-61}$$

and thus

$$\langle \Delta y'^2 \rangle \approx \left\langle \left(\frac{\Delta V_d}{E}\right)^2 \right\rangle + \frac{4V^2}{E^2}\langle \Delta\phi_c^2 \rangle \langle \Delta\phi_d^2 \rangle . \tag{3.6-62}$$

The phase errors must be small enough that the first term dominates, implying

$$\left\langle \left(\frac{\Delta V_d}{E} \right)^2 \right\rangle \gg \frac{4V^2}{E^2} \left\langle \Delta\phi_c^2 \right\rangle \left\langle \Delta\phi_d^2 \right\rangle . \tag{3.6-63}$$

The differential voltage requirement is about 1%. If we choose, somewhat arbitrarily, $\left\langle \Delta\phi_c^2 \right\rangle = 10 \times \left\langle \Delta\phi_d^2 \right\rangle$, then we require

$$\sqrt{\left\langle \Delta\phi_d^2 \right\rangle} = 2.3^\circ \tag{3.6-64}$$

and

$$\sqrt{\left\langle \Delta\phi_c^2 \right\rangle} = 7.2^\circ . \tag{3.6-65}$$

The specifications, summarized in Table 3.6-57, are at least as demanding as those for SPX operation, since we are attempting to verify SPX levels of performance.

Table 3.6-57: Cross-phase tolerances for SPX0.

Error	Bandwidth	Driving Requirement	Tolerance (rms)
Cavities at opposite zero crossings:			
Differential phase	$<$ 10 Hz	Confirm SPX requirement	Orbit feedback
	10 Hz to 1 kHz	Confirm SPX requirement	77 mdeg
	$>$ 1 kHz	Confirm SPX requirement	280 mdeg
Common-mode phase	$<$ 10 Hz	Support confirmation of SPX	Orbit feedback
	10 Hz to 1 kHz	differential phase requirement	5 deg
	$>$ 1 kHz		18 deg
Cavities at opposite crests:			
Differential voltage	$<$ 1 kHz	Confirm SPX requirement	1.0%
	$>$ 1 kHz	Confirm SPX requirement	0.77%
Common-mode voltage	Full	Support confirmation of SPX differential voltage requirement	5%
Differential phase	10 Hz to 1 kHz	Support confirmation of SPX voltage requirement	2.3 deg
Common-mode phase	10 Hz to 1 kHz	Support confirmation of SPX voltage requirement	7.2 deg

In-Phase Operation

This mode will be used simply to give x-ray users some early exposure to chirped pulses. Since there is no cancellation of chirps between the two cavities, tolerances are relatively relaxed. The values, listed in Table 3.6-58, are identical to those for SPX, with one exception: the common-mode phase tolerance has been specified separately for low- and high-frequency bands. Common-mode phase variation will result in kicks to the beam centroid and variation in arrival time.

Experiments show that a factor of 5 reduction in vertical orbit motion is achieved up to 60 Hz [3.6-84], with reduced effectiveness at higher frequencies. Hence, it is appropriate to separate low- and

high-frequency bands at 60 Hz, assuming that below 60 Hz real-time orbit control is effective, whereas above 60 Hz it is non-existent.

Presumably, any beamline that will use this mode is using relatively narrow vertical slits. Hence, variation in the slope of the orbit affects primarily the arrival time of the slitted pulse. It also affects the intensity of the pulse by selecting a different part of the Gaussian bunch. The following criteria are adopted:

- Below 60 Hz:
  - Worst-case intensity reduction is less than 10% on any pulse.
  - Pulse arrival time rms variation is less than 10% of 8 ps FWHM minimum duration.
  - Vertical orbit motion invariant is less than 10% of beam emittance.
- Above 60 Hz:
  - Worst-case intensity reduction is less than 10% on any pulse.
  - Effective pulse duration is increased by less than 20% from minimum rms value of 3.4 ps.
  - Effective vertical emittance increase is less than 10% of 35 pm.

The x-ray pulse duration and intensity are both impacted by orbit motion, in particular, the slope of the beam trajectory at the source point. Relating these quantities to the trajectory slope requires the coefficient S between slope y' and arrival time t within the pulse. This is shown in Figure 3.6-111 and can be computed from the quantity α_{45} defined by Equation. (3.6-58) using

$$S = \frac{\alpha_{45}}{\sqrt{1+\alpha_{45}^2}} \frac{\sigma_{y'}}{\sigma_t}. \tag{3.6-66}$$

The maximum value is $1.7 \times 10^6 s^{-1}$.

To set the tolerances related to duration and intensity also requires knowing the rms slope of the closed orbit for each band, the magnitude of which is proportional to the rms common-mode phase error. For the $> 60Hz$ case, we simulated this by simply computing 1000 closed orbits and taking averages. For the $< 60Hz$ case, we added orbit correction, using a single-step correction with a gain of 0.8, implying a reduction of a factor of 5 (similar to the improvement seen from the existing system). Figure 3.6-112 shows the results at the P1 BPMs.

To avoid reducing the intensity by more than 10%, we must have

$$e^{-\frac{\Delta t^2}{2\sigma_t^2}} \geq 0.9, \tag{3.6-67}$$

giving $\Delta t < 15$ ps or $\Delta y' < 26$ μrad. This corresponds to a 24-degree rms phase error for the case without correction and a 46-degree error for the case with correction.

A 0.8-ps arrival time change requires a slope change of 1.4 μrad. Hence, for the case with correction (below 60 Hz) the rms common-mode phase error must be under 2.5 deg rms. A 20% increase in effective pulse duration starting for a nominal pulse duration of 3.4 ps corresponds to rms arrival time jitter of 2.3 ps, or rms slope jitter of 3.9 μrad, implying phase jitter of less than 3.6 deg rms.

In addition to affecting the time duration, the timing jitter, and the intensity, both common-mode and differential phase errors can affect the orbit, while both common-mode and differential voltage errors

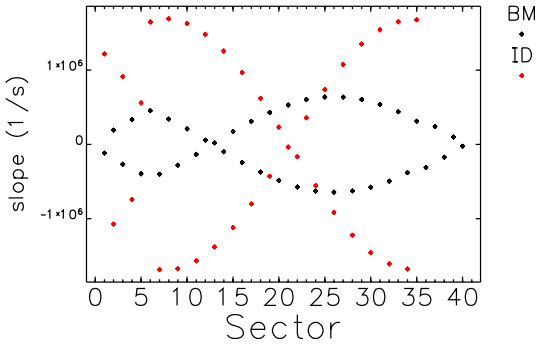

Figure 3.6-111: Slope of y' within a bunch vs t when SPX0 cavities are powered in phase.

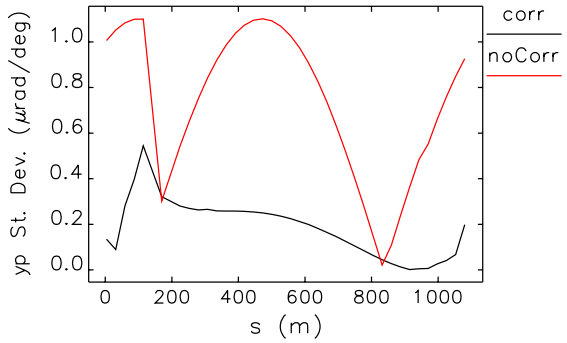

Figure 3.6-112: Vertical orbit slope standard deviation per unit common-mode phase error for the in-phase condition, with and without orbit correction.

can affect the emittance. Separate tracking simulations were performed with varying amounts of each type of error in order to assess these effects. Figure 3.6-113 shows the results for common-mode phase and voltage errors. As expected, phase error impacts the orbit while voltage error impacts the emittance. The orbit response is about 11%/deg of phase error, while the emittance response is about 1.4% per % of voltage error. The former is fairly large, resulting in 20 to 40% beam motion (as a fraction of size or divergence) for the common-mode phase error levels determined above. However, this is acceptable because those using this mode are by assumption using narrow vertical slits in order to create short pulses. The common-mode voltage tolerance is set to a level, 6.9% rms, that gives 10% rms emittance variation.

Figure 3.6-114 shows results for differential phase and voltage errors. The primary effects are orbit motion and emittance growth created by the phase errors. For phase errors at the 10% rms levels, the effects will be less than 10%. Using the same argument as in the previous paragraph, this is negligible. A “common-sense” tolerance for the differential errors is 10 deg for the phase and 10% for the voltage.

Table 3.6-58 summarizes the tolerances.

Table 3.6-58: In-phase tolerances for SPX0.

Error	**Bandwidth**	**Driving Requirement**	**Tolerance (rms)**
Common-mode phase	$<$ 60 Hz	Control arrival time jitter	2.5 deg
	$>$ 60 Hz	Control effective pulse duration increase	3.6 deg
Common-mode voltage	Full	Control emittance variation	6.9 %
Differential phase	Full	Common sense	10 deg
Differential voltage	Full	Common sense	10 %

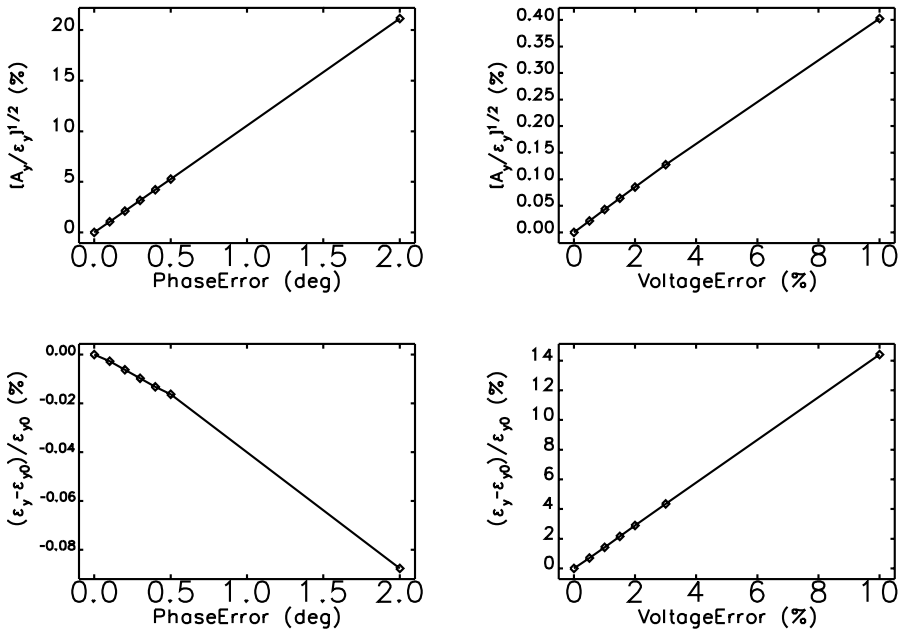

Figure 3.6-113: Emittance increase and orbit motion relative to emittance as a function of common-mode phase and voltage errors for in-phase operation of SPX0.

3.6.4.3.6 Effect of Insertion Devices

We evaluated the impact of operating the circularly polarized undulator (CPU) when SPX0 is in operation. The CPU is presently our most disruptive single device in terms of impact on beam motion and vertical emittance. In this analysis, we examined the sensitivity of injection efficiency and local momentum acceptance to the operation of the CPU. Tracking was performed using `elegant` with the CPU modeled by a kick map [3.6-85]. Three kick maps were used, corresponding to maximum strength in horizontal polarization, vertical polarization, and circular polarization. Fifty ensembles were used for the simulations. Figure 3.6-115 shows the effect on injection efficiency, which was modeled using the technique described in section 3.6.4.3.3. Figure 3.6-116 shows the effect on momentum acceptance, displayed as a histogram of the local momentum acceptances around the ring for all 50 ensembles. In both cases, the effects are negligible.

3.6.4.4 Collective Effects

The main objective of modeling the collective effect was to demonstrate that the SPX system is transparent to the storage ring with cavities detuned. The same will be true for the SPX0 R&D program. As long as the impedance of SPX0 does not make the beam unstable in delivering the various fill patterns up to 150 mA, the situation is acceptable.

The growth rates for a single HOM resonator with worst-case frequency are

$$\alpha_s = \frac{\alpha_c I_{\text{total}}}{2(E/e)\nu_s}(R_s f_{\text{HOM}})\exp(-\omega_r^2\sigma_t^2), \tag{3.6-68}$$

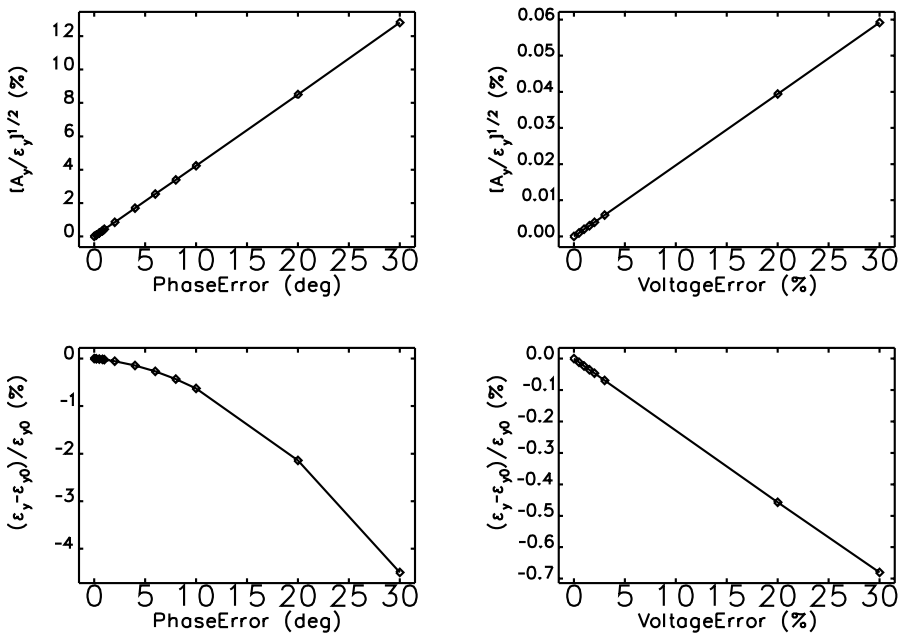

Figure 3.6-114: Emittance increase and orbit motion relative to emittance as a function of differential phase and voltage errors for in-phase operation of SPX0.

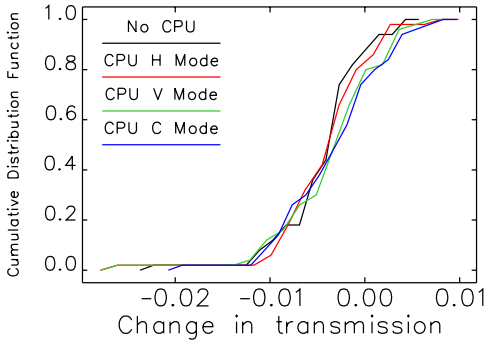

Figure 3.6-115: Effect of SPX0 cavities on injection efficiency for three CPU modes plus the case with the CPU off.

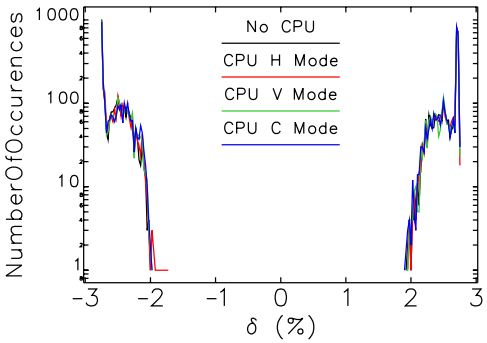

Figure 3.6-116: Effect of SPX0 cavities on local momentum acceptance for three CPU modes plus the case with the CPU off.

for the longitudinal plane and

$$\alpha_{x,y} = \frac{f_0 I_{\text{total}}}{2(E/e)} (\beta_{x,y} R_t) \exp(-\omega_r^2 \sigma_t^2), \tag{3.6-69}$$

for the transverse planes. A design that is stable for the large shunt impedance will certainly be stable for the small shunt impedance.

In section 3.6.3.3.1, the coupled-bunch instability was investigated where the source of HOMs is the eight cavities used for SPX. The beam was found to be stable up to 200 mA. Since the SPX0 utilizes

only two cavities, the HOMs are reduced by a factor of four; hence, the motion will be stable.

In section 3.6.3.3.2, the single-bunch effect was investigated where the current limit was above 16 mA and the emittance degradation due to the impedance was minimal for the 8-cavity SPX. A similar simulation for SPX0 was not specifically performed because the results of SPX will serve as the upper bound. Since the upper bound was acceptable, so will be the SPX0 system in the single-bunch collective effect.

In summary, with up to eight deflecting cavities installed in the ring, more than 16 mA can be stored in a single bunch. Hence, installation of the two cavities for SPX0 will not jeopardize hybrid-mode operation. Collective effects with the presence of the two cavities should not degrade SPX performance in 24-bunch operation at 150 mA.

3.6.4.5 High-Power Rf System [U1.03.03.01]

This section describes the technical requirements and preliminary design of the SPX0 high-level rf (HLRF) system. The SPX0 HLRF system encompasses all rf drive-line components and support hardware between the output of the low-level rf control system and the rf input flanges of the deflecting cavity cryomodule, including equipment and personnel protection interlock systems.

3.6.4.5.1 HLRF System Specifications

The SPX0 HLRF system includes all hardware and specified functionality necessary to amplify the nominal milliwatt-level controlled output of the low-level rf control systems to a maximum output power of 5 kW cw per amplifier system, and deliver this rf power to the rf input waveguide flanges of the rf cavity cryomodule. The HLRF system also includes hardware for providing process variable readback and equipment protection interlocks for the amplifiers and also for the cavity-cryomodule system, and personnel safety interlocks for control of rf radiation and high-voltage hazards. The SPX0 HLRF system consists of two 2,815.44 MHz, 5-kW cw rf power amplifiers, each of which includes an internal high-voltage power supply, slow and fast hardware protection interlock systems, a personnel safety system, local programmable logic controller-based control and monitor system providing local and remote control of the HLRF system, two waveguide transmission systems to provide low-loss power transmission between the amplifier output and cavity-cryomodule rf input, and a remotely-located slow and fast interlock system for the cavity-cryomodule assembly. The SPX0 HLRF rf amplifier systems are located in Building 400A-1. WR284 waveguide transmission systems connect each amplifier output flange to the cryomodule rf input flanges located in the APS storage ring tunnel at Sector 5. A cavity-cryomodule equipment interlock system is remotely located above the cryomodule on the APS storage ring mezzanine.

3.6.4.5.2 HLRF System Topology

This section describes the technical requirements and preliminary design of the HLRF system portion of the SPX0 deflecting cavity rf system. The HLRF system encompasses all rf drive-line components and support hardware between the output of the SPX0 low-level rf control system and the rf input flanges of the deflecting cavity cryomodule, including equipment and personnel protection interlock systems.

3.6.4.5.3 5-kW Rf Amplifiers

Two 2,815.44-MHz/5-kW cw rf amplifier systems will provide rf power to the SPX0 deflecting cavities. Each of these amplifiers is composed of an rf amplifier chain to provide amplification of the low-level rf drive signal to the 5-kW cw level, and multiple self-contained sub-systems that include a personnel safety interlock system, an ACIS/rf interface, a klystron rf driver amplifier, master fast and slow rf equipment protection interlock systems, and a control PLC for implementing master slow rf interlock functionality, local touch-screen monitoring and control, and providing a network gateway for EPICS remote control and monitoring of the amplifier. A block diagram of the 5-kW rf amplifier system is shown in Figure 3.6-117. A four-port waveguide isolator is utilized at the output of the klystron to minimize reflected power at the klystron output window, and to maintain a terminating rf load for rf power propagating back from the deflecting cavity. The isolator is required to maintain a minimum of 30-dB return loss at the klystron output flange over a bandwidth of ± 5 MHz centered on the SPX0 operating frequency, and has a maximum power handling capability of 50-kW cw. The isolator utilizes two integral water-cooled rf loads, and is fitted with WR284 flat flanges at port #1 (klystron output) and port #2 (amplifier output). The klystron drive amplifier is a solid state S-band cw power amplifier that provides a minimum of 40-dB rf gain to amplify the low-level rf drive signal to a level sufficient to drive the klystron to full power. It is powered by 120 VAC/60 Hz delivered by a dedicated connector on the rear of the chassis to insure that ac line input power is supplied only by the ACIS/rf interface chassis. The driver amplifier includes an internal 28-volt DC power supply, output circulator, an output directional coupler that provides a -20-dB sample of the rf drive signal to the klystron, and an internal electromechanical rf relay that is controlled by the master slow rf interlock system PLC and provides a terminating series rf switch to disable rf output of the amplifier in response to interlock trips. The ACIS/rf interface provides functionality for the SPX ACIS to disable each SPX0 rf amplifier and associated high-voltage power supply by redundant methods in order to control the x-ray radiation hazard created by the SPX0 deflecting cavities when the storage ring tunnel is open to personnel access. Control and monitoring of the amplifier system is achieved by an internal PLC system that provides a front-panel touchscreen for local control of amplifier functions and parameter monitoring, and also interfaces to EPICS to provide remote control functions and readback of amplifier parameters. The control PLC also provides master slow rf interlock functionality related to amplifier internal hardware interlocks, and also to the cavity/cryomodule rf interlock systems through external inputs. All amplifier components and sub-systems are contained within an aluminum enclosure that is 74.25 inches wide, 82.25 inches tall, and 36 inches deep. The enclosure is designed with two full-height, 19-inch equipment racks, and one 30-inch wide compartment housing the klystron, high voltage box, isolator, output waveguide system and water manifolds. Wheels are attached to the enclosure to allow easy transport when the amplifier is used as a test stand rf power source. Primary power to each amplifier is fed from a single 480-V/3-ph/4-wire receptacle located on the right side of the amplifier cabinet. At full rated rf power output, the amplifier will require approximately 55 A per phase input current. The amplifier system is cooled by DI water provided by the APS main DI water plant, at a total flow of approximately 40 GPM. The DI water supply shall have a nominal temperature of 90° Fahrenheit, resistivity of 10 MΩ-cm, a pH of 7, and be delivered at a maximum supply and return pressure of 120 psig and 30 psig respectively.

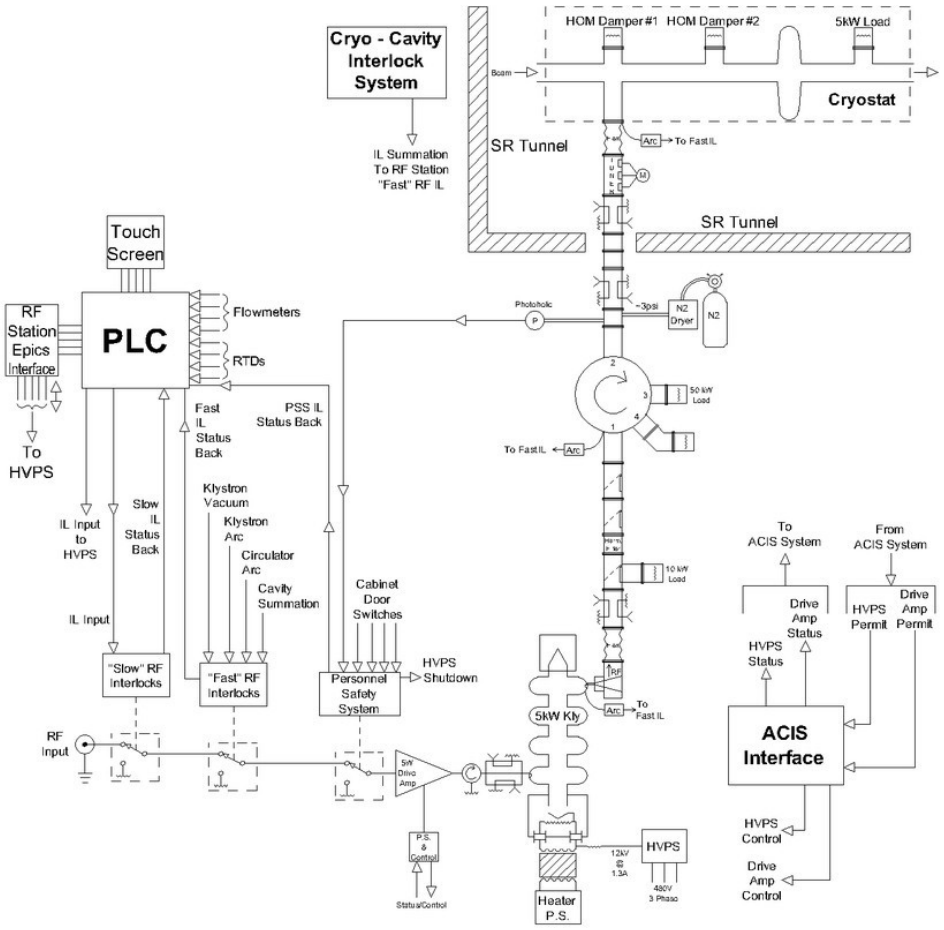

Figure 3.6-117: SPX0 5-kW rf system diagram showing internal amplifier subsystems, cavity equipment interlock systems, and details of the waveguide transmission system from the klystron to the deflecting cavity.

3.6.4.5.4 Waveguide Transmission System

The waveguide transmission system provides a low-loss rf transmission path between the klystron output flange and the rf input waveguide flange on the cryomodule assembly. A pictorial of the SPX0 rf amplifiers and waveguide installations in relation to the storage ring and cryomodule is shown in Figure 3.6-118. The waveguide system consists of aluminum WR284 waveguide components fitted with CPRF flanges. Internal to the 5-kW amplifier cabinet the waveguide system includes a 1-5/8-inch EIA coax-to-WR284 waveguide transition, a six-inch flex section, dual-directional coupler, a two-position waveguide switch and associated 5-kW test load, two waveguide shutters, and a four-port isolator. Two WR284 waveguide shutters are included in the output waveguide transmission line between the klystron rf output flange and the input (port #1) of the isolator to provide a method of administrative control to address rf radiation hazards when the amplifier is used for powering rf test stands. The shutters are rated for a power handling capability of 10-k W cw in both open and closed positions, and each shutter provides a minimum of 70-dB isolation in the closed position. The shutters are fitted with auxiliary contacts to provide remote position indication in order to interlock rf power when the shutter is not fully in the open or closed position. A 5-kW cw water-cooled WR284 rf test load and 3-port, H-plane

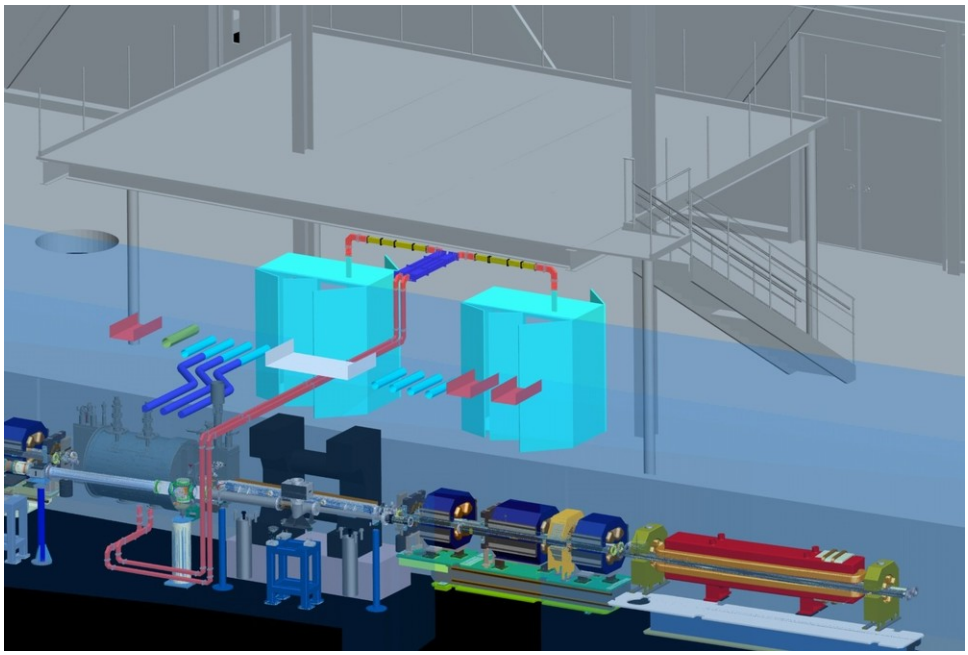

Figure 3.6-118: Pictorial diagram showing the installation of two 5-kW SPX0 rf amplifiers (green) and associated waveguide installations (red) in Building 400A-1. The low-pass LOM waveguide filters are shown in dark blue.

WR284 waveguide switch are included in the output waveguide transmission line between the klystron rf output flange and the first waveguide shutter. The load and switch comprise a switchable full-power test load that will provide the ability to troubleshoot and test the amplifier at full output power without opening any part of the waveguide transmission system. The waveguide switch is fitted with auxiliary contacts to provide remote position indication to the amplifier control PLC to interlock rf power when the switch is not fully in either selectable position.

Waveguide components external to each amplifier cabinet include a low-pass absorptive waveguide filter for attenuation of lower-order mode (LOM) power generated by the deflecting cavity, two directional couplers dedicated to diagnostics and low-level rf use, and a motorized waveguide tuner for adjusting cavity loaded Q. For personnel protection against rf radiation hazards, the waveguide system is pressurized with dry nitrogen to approximately 5 psi from a gas port on the isolator. This positive gas pressure is used to detect openings in the waveguide system that could be potential rf radiation hazards. The internal waveguide pressure is monitored by a Photohelic® gauge that provides an interlock contact to the personnel safety interlock chassis, which will disable the rf drive and high voltage to the klystron if the waveguide pressure drops below a pre-determined trip point. A loss of nitrogen pressure in any of the SPX rf system waveguides will also open an auxiliary nitrogen pressure interlock contact, which is connected to an input of the existing waveguide air interlock system, located in Building 420. This contact will disable all of the 352-MHz rf systems in order to remove beam power from the storage ring as a source of rf power that could leak from an open SPX waveguide system. The expected transmission loss of the waveguide system between each 5-kW amplifier and its respective rf deflecting cavity is approximately 1 dB, resulting in a maximum deliverable rf power of 3.9 kW to the cavity flange.

3.6.4.5.5 Klystrons

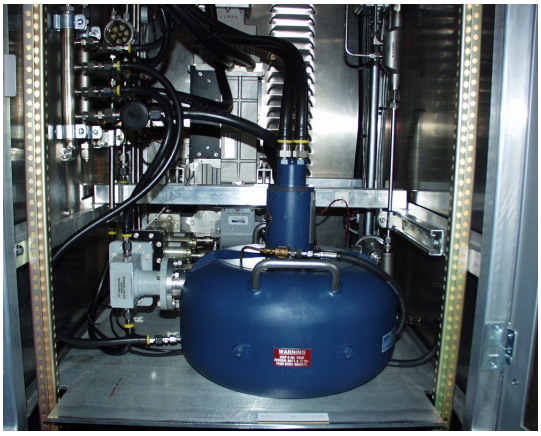

Figure 3.6-119: Photo of L-4442 S-band 5- kW cw klystron as installed in the Building 400A SPX test stand amplifier system.

Figure 3.6-120: Photo of TDK-Lambda high voltage power supply used to supply beam power for the SPX-0 klystrons.

The klystron is the L-4442 S-band cw klystron produced by L-3 Communications Electron Devices Division (see Figure 3.6-119). The klystron is tuned for continuous operation at 2,815.44 MHz at a maximum continuous rf power output of 5-kW cw, resulting in an rf gain of approximately 41 dB. The klystron operates at a nominal beam voltage and current of 12 kV and 1.33 A, respectively, and utilizes permanent magnet beam focusing. De-ionized water is used to cool the collector, body, and output window, and the collector is rated for full beam power. The klystron is fitted with a mod-anode electron gun, but for SPX0 uses the mod-anode terminal grounded to achieve diode-gun operating characteristics.

3.6.4.5.6 High-Voltage Power Supplies

The high-voltage power supply (HVPS) provides beam power for the klystron, and is manufactured by TDK-Lambda Americas. It will deliver a maximum DC output power of 30 kW, and utilizes quadrature dual-switching regulator technology to achieve continuously variable output voltage from 0 to 15 kV DC, and less than 5 V p-p output ripple in order to minimize the phase and amplitude noise that would be generated by the klystron in response to variations in beam voltage. A photograph of the power supply system is shown in Figure 3.6-120.

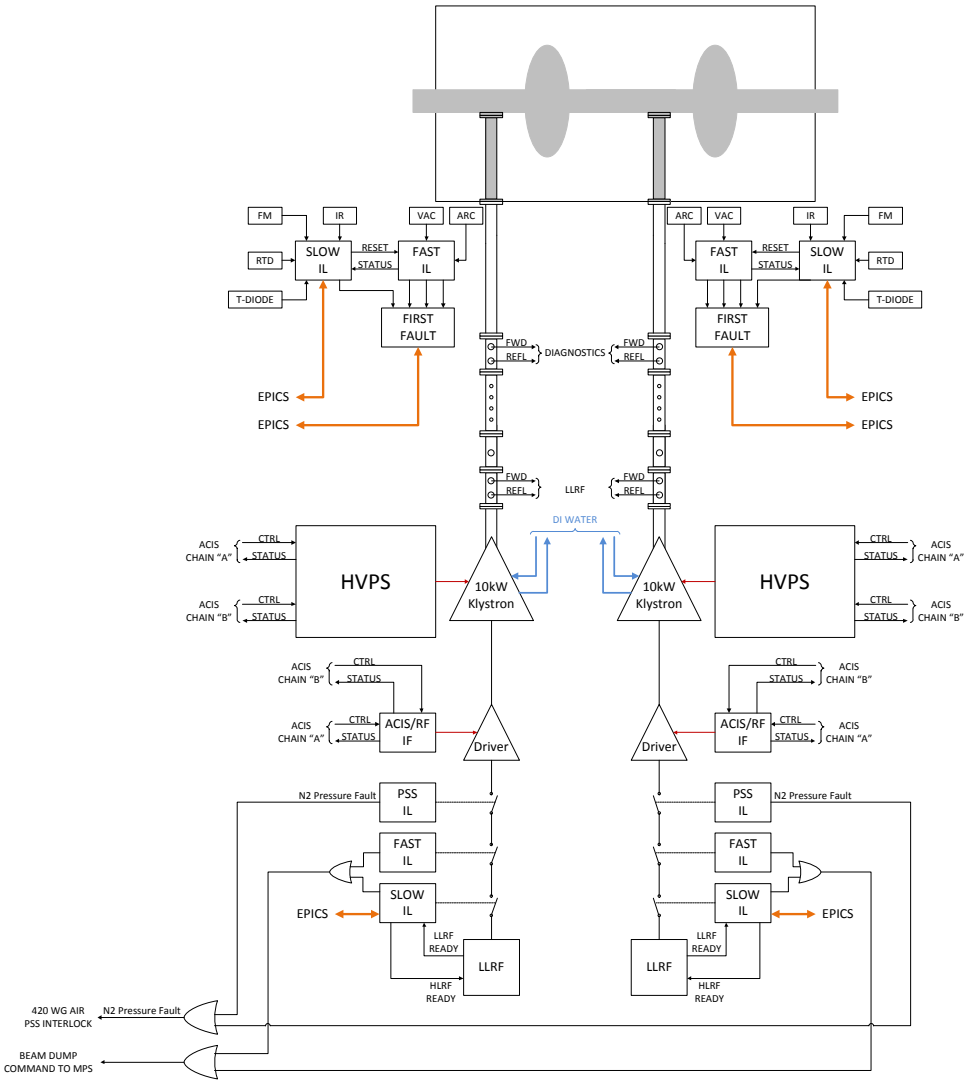

Figure 3.6-121: Block diagram of the SPX0 rf equipment protection interlock system.

3.6.4.5.7 Equipment Protection Interlocks

The SPX0 rf equipment protection interlock system consists of master slow and fast interlock subsystems located in each 5-kW amplifier, each of which is connected to companion slave slow and fast interlock subsystems remotely located on the storage ring mezzanine at the cryomodule location in Sector 5. A block diagram of the equipment protection interlock system is shown in Figure 3.6-121. The cryomodule rf interlock system includes all hardware necessary to implement equipment protection interlocks for the cryomodule and rf cavity components within. It consists of a PLC-based slave slow interlock and a discrete-electronic slave fast interlock system, both of which communicate with the main slow and fast interlock chassis in each amplifier system through dedicated wire and optical links in order to form two separate slave-master configurations. The slow interlock PLC system also serves as a gateway to the network-based EPICS control system. The slow cryomodule interlock system provides monitoring and interlock functions for multiple system parameters including LOM and HOM damper water flow rates, return temperatures, infrared monitors on rf windows, thermal diode outputs,

thermocouple temperature readbacks, and damper waveguide heater status and control. The detection of any fault conditions by the PLC will result in a latching trip command, which is relayed to an external input to the master slow interlock in the rf amplifier system using a single-pair copper circuit. The trip command will cause the master slow interlock in the amplifier to interrupt rf drive to the klystron and latch in the rf-off position if any of the designated interlock alarm limits are exceeded. Operator-adjustable alarm limits on all interlocked parameters are manually entered into the PLC system using the operator interface touchscreen. The PLC also performs calorimetric power calculations on all cooling water circuits and displays the calculated power value on both the local touchscreen and as a process variable in EPICS. The response time of the system from first detection of a fault condition to removal of rf drive to the klystron is 20 milliseconds. The fast cryomodule interlock system provides interlock functions for multiple fault conditions including arc detectors on forward power coupler and LOM damper waveguide rf windows, vacuum pressure in the cavities and waveguides, cavity overpower and over-field conditions, and a cavity quench detection signal provided by the low-level rf system The detection of any of these fault conditions will result in a latching fault signal trip command, which is relayed to an external input of the master fast rf interlock chassis in the rf amplifier system using a fiber optic link. The trip command will cause the master fast interlock in the amplifier to interrupt rf drive to the klystron and latch in the rf-off condition until a manual reset command is issued by the system operator. Trip points for all fast interlock signals are manually adjusted by potentiometers in the fast interlock chassis. The response time of the system from first detection of a fault condition to removal of rf drive to the klystron is 10 microseconds.

3.6.4.5.8 Personnel Safety Interlocks

Each 5-kW amplifier system contains a personnel safety system (PSS) that consists of a single chassis that provides personnel protection against known personnel safety hazards of the SPX rf systems, including exposure to high voltage within the amplifier enclosure and rf radiation hazards from openings in the waveguide transmission system anywhere between the klystron output window and the cryomodule rf waveguide input flange. The chassis also provides two spare contact inputs for connection to future personnel safety devices that provide a contact closure fault output, and includes all relay logic necessary for PSS interlock functionality, a waveguide nitrogen pressure meter, an operator key switch, an emergency stop button, an internal electromechanical rf relay to inhibit rf drive to the klystron in the event a PSS fault condition is detected, and a dedicated relay to generate a dry interlock contact that is used to shut down the klystron HVPS. Upon detection of a PSS fault condition, the PSS chassis will latch in the fault state and interrupt rf drive to the klystron by opening the electromechanical rf relay internal to the PSS chassis and shut down the klystron HVPS by opening the relay contact that is providing an external interlock contact closure to the klystron HVPS. Refer to Figure 3.6-122 for a general block diagram of the SPX0 PSS.

3.6.4.5.9 ACIS/Rf Interface

The ACIS/rf interface provides interface functionality to allow the SPX0 ACIS to independently inhibit operation of the HVPS and klystron rf driver amplifier when the storage ring tunnel is not in beam-permit mode. The interface chassis is controlled and monitored by redundant interlock chains that are part of the SPX0 ACIS hardware. HVPS operation is inhibited by de-energizing a contactor supplying 480-VAC/3-ph primary input power to the HVPS inverters, and the driver amplifier is inhibited by

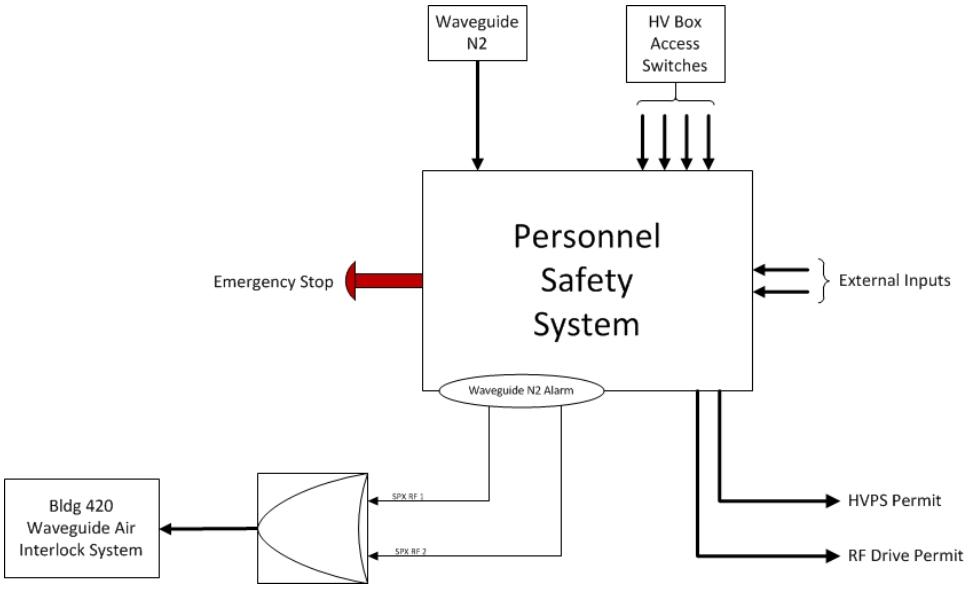

Figure 3.6-122: SPX-0 Block diagram of a personnel protection interlock system.

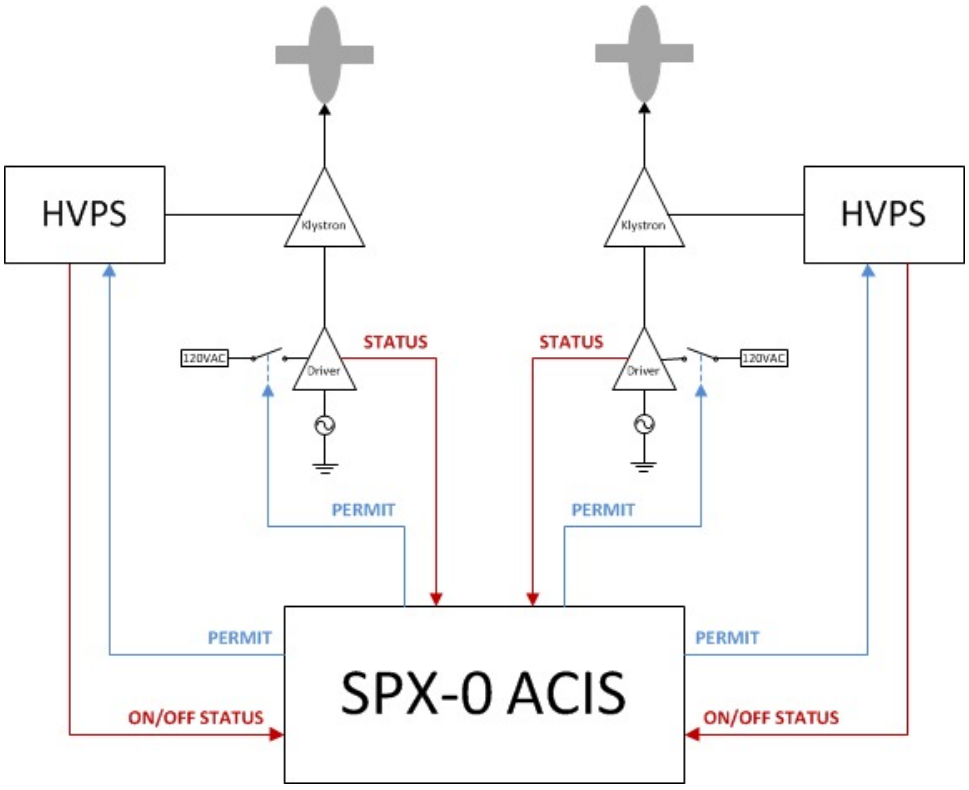

Figure 3.6-123: Block diagram of the SPX0 MPS interface showing beam dump command inputs.

de-energizing a relay that is in series with the 120 VAC primary power input of the klystron driver amplifier. The interface also provides feedback signals to the storage ring ACIS from both the HVPS and driver amplifier to verify that they are in a safe state. A block diagram of the SPX0 ACIS/RF

Interface is shown in Figure 3.6-123.

3.6.4.5.10 SPX0 RF Machine Protection System Interface

The SPX0 rf cavities and HLRF system are protected from damage due to rf power generated by a beam-cavity interaction by decoupling the rf cavities from the beam when a fault condition is detected. A select group of interlock system faults are monitored to detect fault conditions related to power coupled from the storage ring beam. A block diagram of the interface is shown in Figure 3.6-42. These interlock faults include overpower events involving the rf cavity, LOM and HOM dampers, rf amplifier output circulator, and rf windows, and other fault conditions relating to cryogenic systems, vacuum pressure, quench detection, and rf arcing events at the cavity rf windows and the rf amplifier isolator. If such fault conditions are detected, a fast cavity detune command is initiated that will employ rf cavity piezo tuners to rapidly shift the cavity resonant frequency and decouple the cavity from the beam. If detuning rf cavities does not clear the fault condition, an optical beam-permit signal generated by the SPX rf interlock systems signals the APS Machine Protection System (MPS) to initiate a beam dump command.

3.6.4.6 Low-Level rf [U1.02.01.03.02]

The purpose of the SPX0 LLRF R&D is to develop and deliver two individual cavity LLRF controllers with necessary ancillary equipment that will be used to demonstrate the common mode and differential mode amplitude and phase specifications for SPX0, as listed in section 3.6.4.2.

3.6.4.6.1 SPX0 LLRF System

The LLRF system block diagram for a single SPX0 cavity is depicted in Figure 3.6-124 The SPX0 LLRF controller will use the Lawrence Berkeley National Laboratory (LBNL) LLRF4 board. The controller will be housed in a chassis that is shared between LLRF and timing/synchronization in order to contain a second LLRF4 board that is used to provide the phase reference correction as discussed in combination with the sync head in section 3.6.4.7 The analog front end, which converts to/from S-band from/to the IF frequency, will be based upon a custom ANL design as discussed in section 3.6.4.6.3. The slow tuner driver will be a JLab 12GeV upgrade-style chassis purchased directly from JLab. The local oscillator (LO) distribution will be derived from the timing/synchronization frequency generation chassis (see section 3.6.4.7).

3.6.4.6.2 SPX0 LLRF Controller

The LLRF4 controller will provide the following functionality:

- Monitoring of the rf signals as shown in Figure 3.6-124.
- Generation of the rf drive signal and the calibration tone signal.

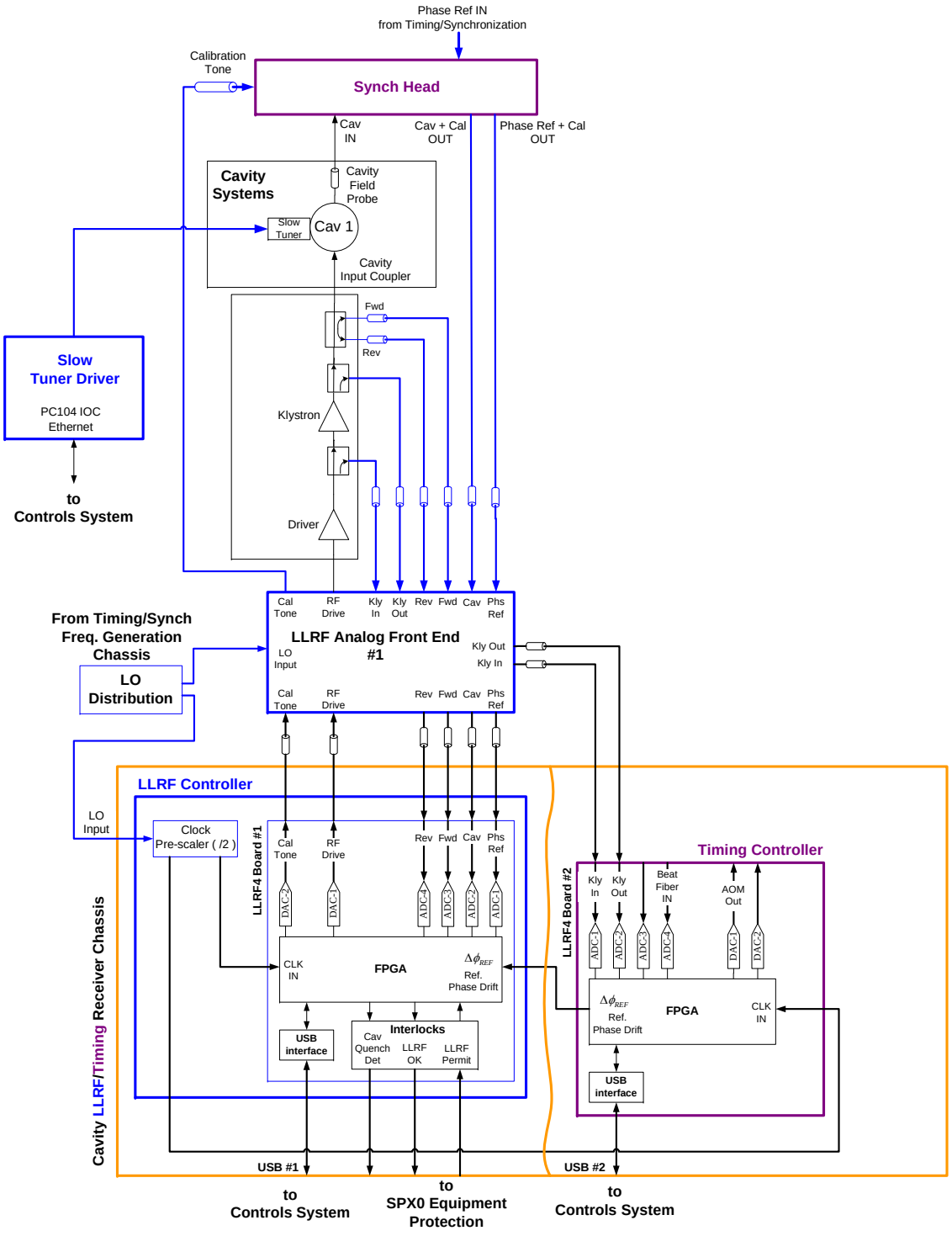

Figure 3.6-124: Single SPX0 cavity LLRF system block diagram.

- Conversion from analog-to-digital (ADC) and digital-to-analog (DAC) at the intermediate frequency (IF).

- Multi-channel digital down-conversion from the IF to baseband including frequency-division multiplexed channels used for the cal-tone (see section 3.6.3.5.2) process.
- The core LLRF in-phase and quadrature control loop FPGA digital signal processing with proportional integral and derivative (PID) control, including phase locking to the phase reference.
- USB communication to the controls system as discussed in section 3.6.4.8.
- Interfacing to the SPX0 equipment protection system including cavity quench detection via a cavity field rate of change.
- Interfacing to the timing/synchronization LLRF4 board to acquire the phase reference drift compensation term.

The SPX0 LLRF4 controller will use a non-I/Q sampling scheme. The ADC clock will be derived by dividing the LO signal by 36 resulting in a nominal ADC clock frequency of ∼76.6 mega-samples per second (MSPS). The output DAC will be clocked at twice this rate. The nominal ADC sample rate results in convenient synchronization to other storage ring devices since it is 282 times the storage ring revolution frequency.

3.6.4.6.3 SPX0 Analog Front End

SPX R&D (SPX0) will provide an opportunity to develop a low-intermodulation-distortion analog front end (AFE) that is compatible with the double-sideband calibration tone scheme discussed in section 3.6.3.5.2. A prototype has already been developed and fabricated using low-intermodulation-distortion Marki Microwave triple-balanced mixers to support laboratory measurements and the SPX0 cavity test program as pictured in Figure 3.6-125.

3.6.4.6.4 LLRF Bench-Top Demonstrations

To begin development of a prototype LLRF system a collaboration with Lawrence Berkeley National Lab's (LBNL) Beam Technology Group (BTG) was formed for the SPX0 program. LBNL has been responsible for supplying the LLRF4 based controllers with accompanying FPGA LLRF control gateware, USB communications, and initial software support.

LLRF bench-top demonstrations were pursued using two high-Q cavity emulator circuits, as depicted in Figure 3.6-126, which allowed for LLRF development independent of any cavity production schedule. By mixing the rf input down to the center frequency of a narrow-bandwidth crystal bandpass filter, the effective Q of the circuit is given by the ratio of the rf frequency to the crystal bandwidth; thus allowing simulation of a high-Q SRF-type resonance.

These bench-top tests ultimately resulted in measurements of the differential phase noise between two high-Q cavity emulators controlled by two separate LLRF systems as depicted in Figure 3.6-127 in order to quantify the phase noise that the LLRF system could be expected to contribute to the SPX0 system (not including other system disturbances such as beam loading, microphonics, and klystron noise). The results of these two system bench-top tests showed that the LLRF4-based system could be expected to contribute ∼20 mdeg rms [0.1 Hz - 100 kHz] (or ∼20 fs jitter) of differential phase noise.

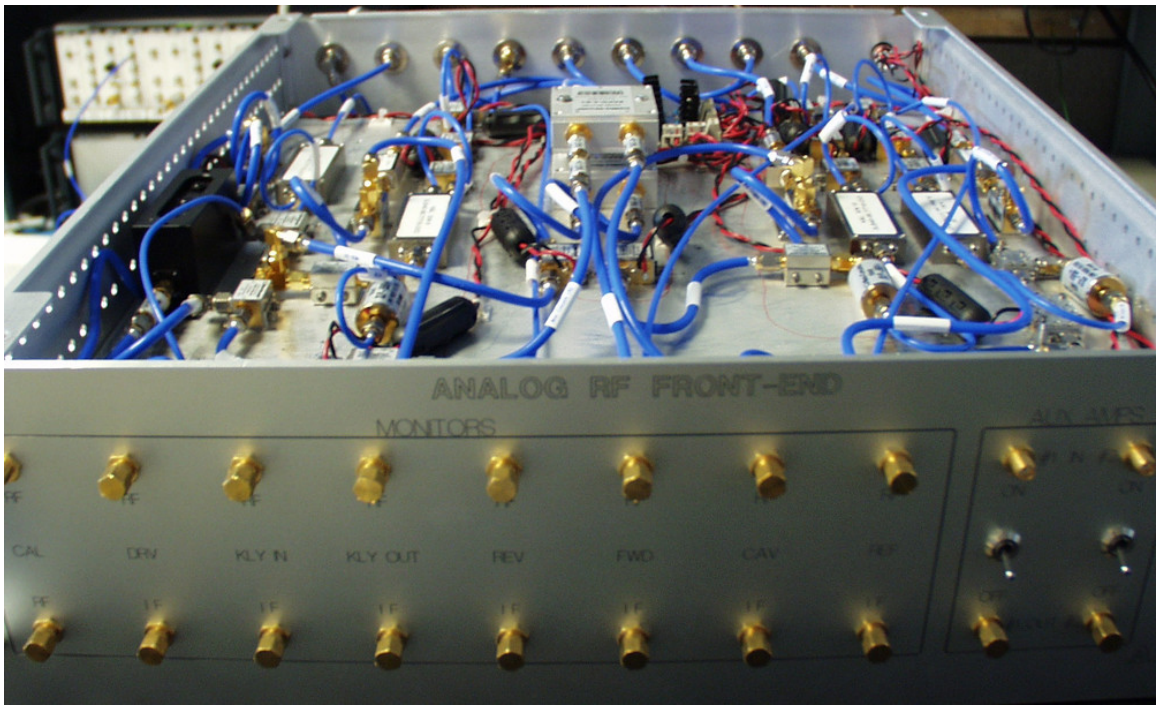

Figure 3.6-125: SPX0 analog front end prototype.

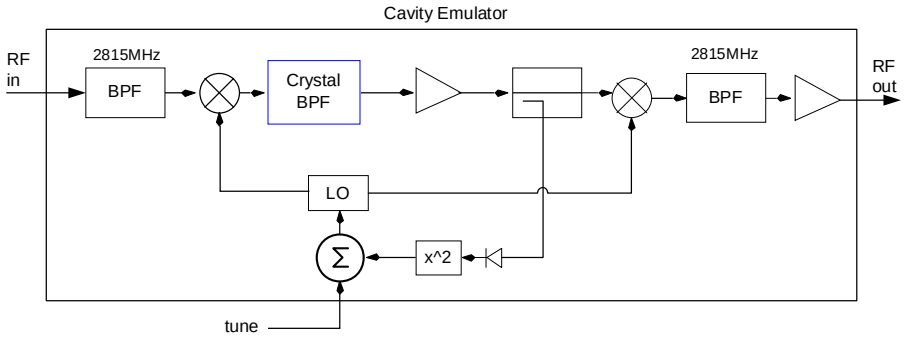

Figure 3.6-126: High-Q cavity emulator concept for LLRF development.

Further tests are being pursued to include the calibration tone process, to fully understand the dynamics of the closed-loop behavior, and to investigate LLRF system noise floor limitations.

3.6.4.6.5 Current Status

The R&D of SPX/SPX0 LLRF is actively taking place in the LLRF development Labs at both the ANL and LBNL sites (Figures 3.6-128 and 3.6-129). The LLRF FPGA IP firmware and software for SPX0 is being developed, and the bench tests of the early code release with just the cavity field control algorithm showed good results. The first release of the code package containing the calibration tone process is currently in development with delivery expected before the ATLAS tests (Figure 3.6-130).

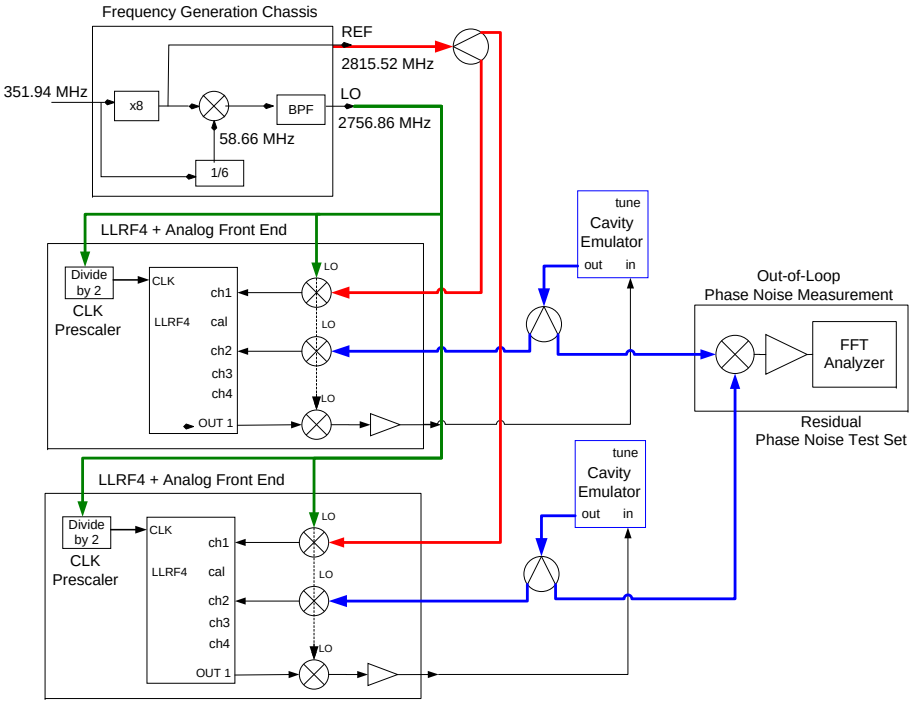

Figure 3.6-127: LLRF two-system bench-top test setup.

A self-contained, complete SPX0 LLRF system has been built as shown in Figure 3.6-131 and is ready to be shipped to the ANL/ATLAS site to participate in the upcoming first field test with the high-power klystron and SPX superconducting cavity. This test will provide first-hand data of the LLRF performance with the presence of the perturbations in the HLRF and SRF cavity system.

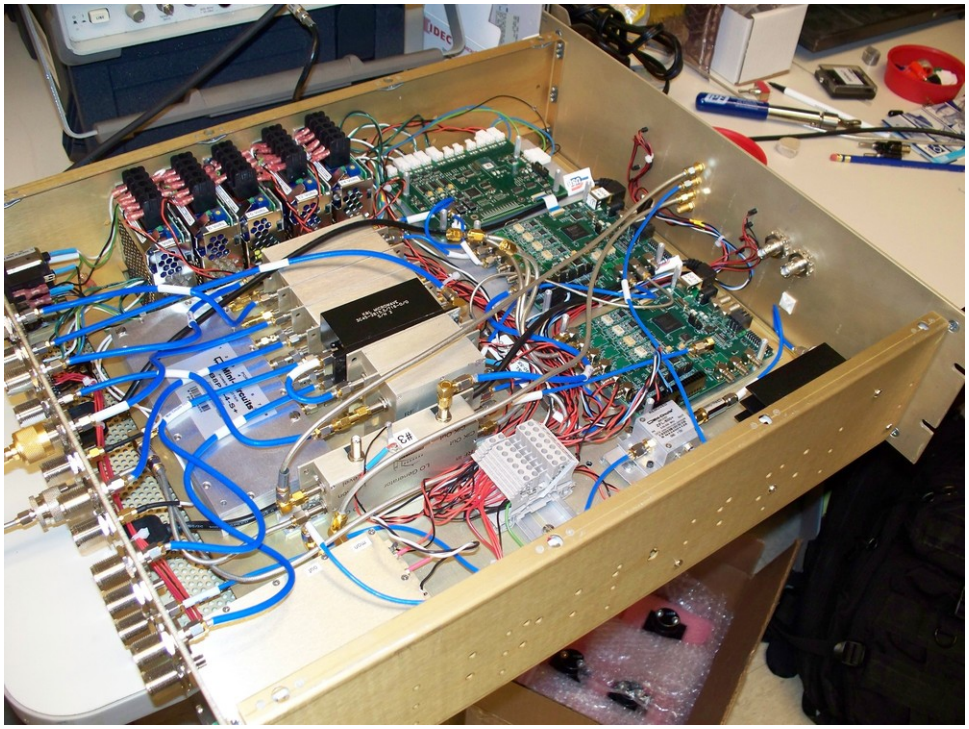

Figure 3.6-128: LLRF4-based digital cavity rf field controller.

Figure 3.6-129: Four SPX0 digital cavity field controllers have been constructed and are under tests at LBNL.

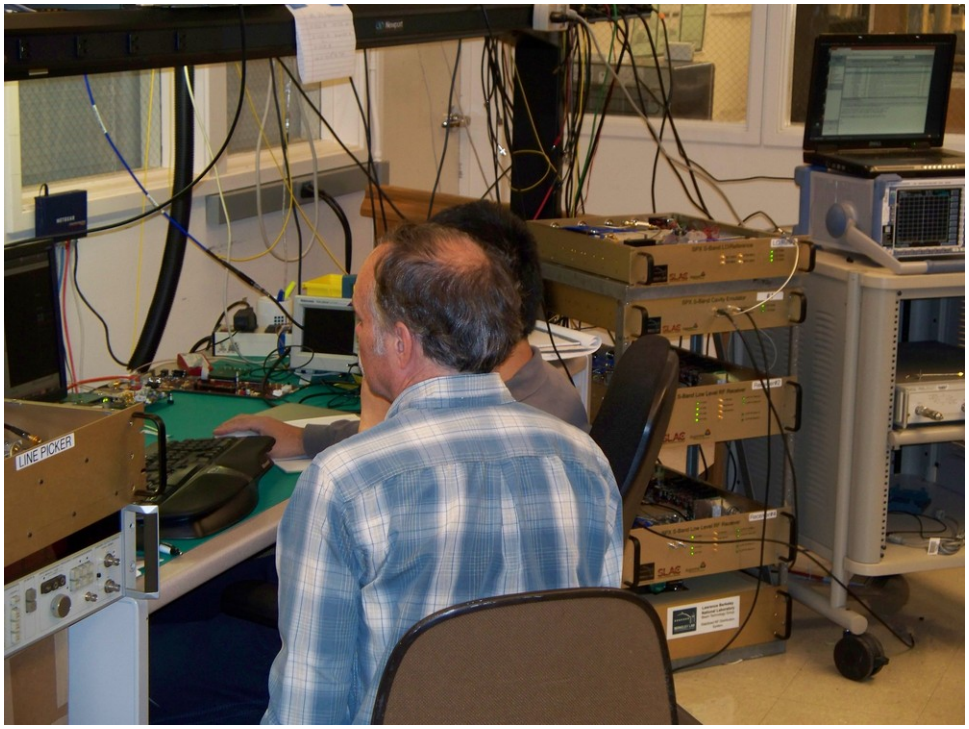

Figure 3.6-130: The SPX0 LLRF FPGA firmware and software developed for supporting the field tests at ATLAS are currently being tested in the LLRF labs.

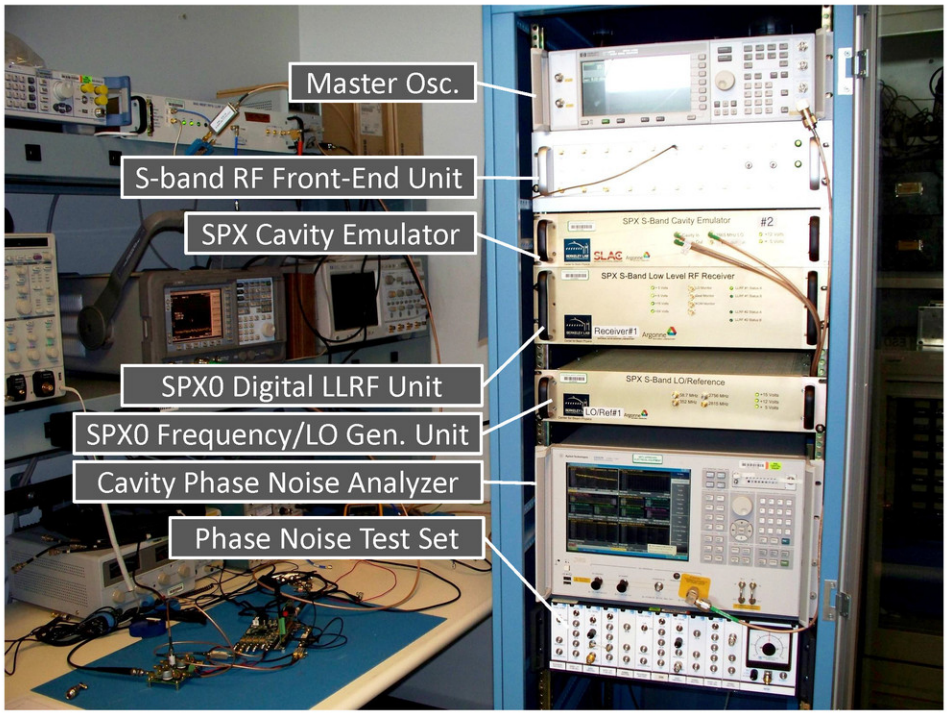

Figure 3.6-131: LLRF lab at ANL.

3.6.4.7 Timing and Synchronization [U1.02.01.03.03]

3.6.4.7.1 Scope

The primary objective for timing/synchronization R&D is to provide the phase references to LLRF that will achieve and demonstrate the common mode and differential phase tolerance specified in the SPX PRD.

To this end a collaboration with LBNL as been entered into to adopt their femtosecond timing/synchronization system to SPX requirements.

Their system will be built to SPX requirements and used for SPX0 to provide phase references to LLRF. In addition, the technology including documentation to reproduce their system will be transferred to ANL so that it may be implemented to meet final SPX requirements for timing/synchronization including beamline laser synchronization.

3.6.4.7.2 Key Specifications

Tables 3.6-59, 3.6-60 and 3.6-61 list key specifications for SPX0 timing/synchronization.

Table 3.6-59: SPX0 phase tolerance requirements for cross-phase operation at zero crossing.

Specification Name	RMS Tolerance	Bandwidth
Common-Mode Phase Variation	< 5 °S	0.1 Hz - 1 kHz
Common-Mode Phase Variation	< 18 °S	1 kHz - 271 kHz
Phase Mismatch Between Cavities	< 0.077 °S	0.1 Hz - 1 kHz
Phase Mismatch Between Cavities	< 0.28 °S	1 kHz - 271 kHz

Table 3.6-60: SPX0 phase tolerance requirements for in-phase operation at zero crossing.

Specification Name	RMS Tolerance	Bandwidth
Common-Mode Phase Variation	< 2.5 °S	0.1 Hz - 60 kHz
Common-Mode Phage Variation	< 3.6 °S	60 Hz - 271 kHz
Phase Mismatch Between Cavities	< 10.7 °S	0.1 Hz - 1 kHz
Jitter Between X-Ray Pulse and Laser	< 1.4 ps	0.1 Hz - 1 kHz

Table 3.6-61: SPX0 phase tolerance requirements for cross-phase operation on crest.

Specification Name	RMS Tolerance	Bandwidth
Common-Mode Phase Variation	< 7.2 °S	0.1 Hz - 1 kHz
Phase Mismatch Between Cavities	< 2.3 °S	0.1 Hz - 1 kHz

3.6.4.7.3 Approach

The timing and synchronization system will provide the phase references needed to drive the SPX0 deflecting cavities. Actively stabilized fiber optic links will be used to distribute a 2815-MHz phase reference to each location. The active phase stabilization will correct for drifts due to environmental effects. John Byrd's group at LBNL has expended a great deal of effort over the years in developing a system capable of delivering a phase reference stable to the tens-of-femtosecond level. Their fiber link stabilization scheme forms the basis for SPX phase reference distribution.

The timing/synchronization system consists of three types of components: a central multichannel transmitter/sender and distributed receivers and synchronization heads. Each channel of timing requires a receiver and a synchronization head. The synchronization head is mounted as close as possible to the signal of interest—cavity field probe for the LLRF and laser oscillator for a beamline.

A key component of the phase stabilization system is the transmitter/sender that provides a cw laser whose output is amplitude-modulated by the 2815 MHz for transport to remote locations such as LLRF controllers and beamline laser oscillators. Each channel of the transmitter/sender provides two fibers—a reference fiber and a beat fiber. The reference fiber provides the phase reference to the remote locations. The beat fiber transports information on the reference fiber's change in propagation delay to the remote locations to be used for correcting the reference fiber's phase.

The LBNL scheme precisely measures the optical phase delay through a fiber using a heterodyne interferometer [3.6-52]. The heterodyne process in which the original optical frequency is mixed with an optical frequency offset by a 100-MHz radio frequency results in changes in optical phase being translated into identical phase changes in the 100-MHz rf beat note. One degree of phase change in the 1560-nm optical domains which corresponds to 21 attoseconds, translates to 1 degree of phase change in the rf domain or 25 ps. This results in approximately 6 orders of magnitude leverage over direct measurement in the rf domain. The phase changes in the 100-MHz beat note are measured and used to correct for changes in fiber cable delay due to environmental effects such as temperature.

Figure 3.6-132 is a block diagram of the SPX0 phase reference distribution system. The fiber transmitter cw laser output is modulated by the 2815 MHz from the frequency generation chassis. The resulting amplitude-modulated optical signal is fanned out for distribution to the SPX LLRF systems, the beamline laser hutches, and diagnostics. Each of the optical links is an independent heterodyne interferometer transporting the 2815-MHz reference as an amplitude modulation on the optical carrier. At each receiving end the receiver measures changes in the optical phase and uses this measurement to correct the phase of the received 2815 MHz signal.

3.6.4.7.4 Measurements

A coax has been installed between room A014—the location of the APS master oscillator—and 400A (SPX building). The length of this cable is 300 meters. This cable will be used to transport the 351.9-MHz master oscillator reference to the SPX area. Phase drift caused by temperature changes is of interest. To that end a network analyzer was used to measure the S11 parameter at the A014 end with the 400A end terminated in a short. Figure 3.6-133 is a plot of the data. The data were taken over a period of five days.The measurement was made at 176 MHz, which is the 16th subharmonic of 2815 MHz. As indicated in the figure, over a period of a few hours, the equivalent phase drift at 2815 MHz was 5.28 degrees. The rate of phase change at 176 MHz was 0.35e-5 degrees/sec, which is equivalent

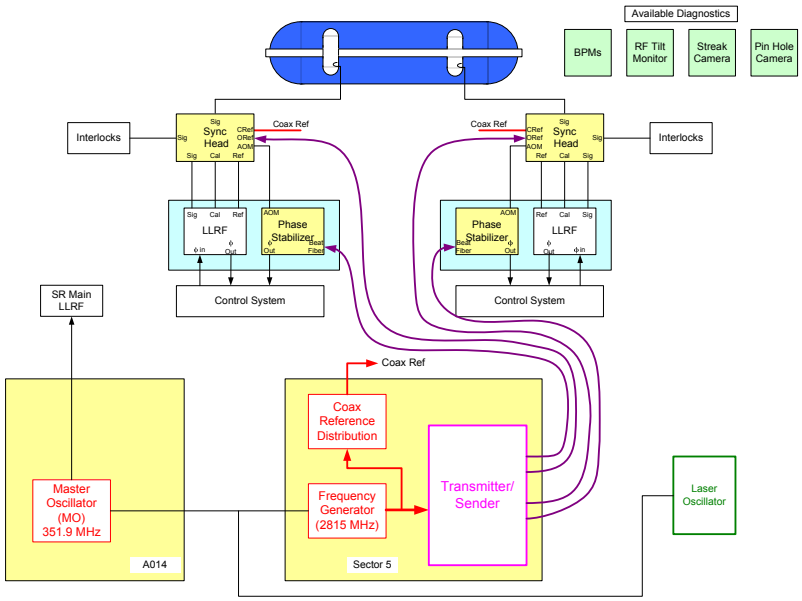

Figure 3.6-132: SPX0 timing/synchronization block diagram.

to 3.36 millidegrees per minute at 2815 MHz. From this one may infer that low bandwidth feedback is all that is required to compensate for cable drifts to the 10-millidegree (10-femtosecond) level.

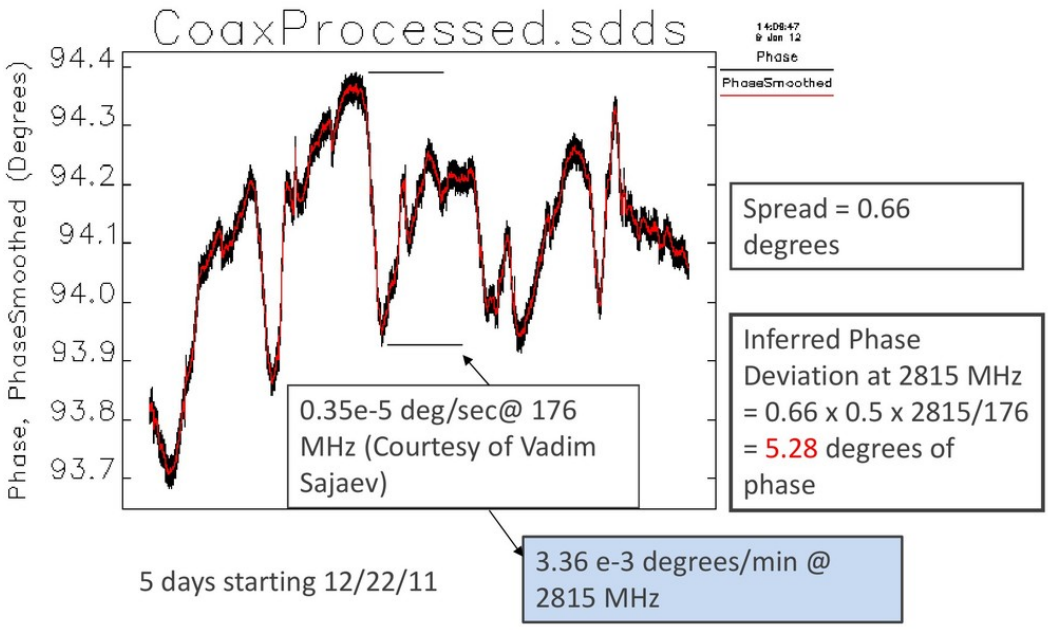

Figure 3.6-133: Phase drift measurement of A014 to 400A coax.

3.6.4.7.5 Transmitter/Sender

A key component of the phase stabilization system is the transmitter/sender, which provides a cw laser whose output is amplitude-modulated by the 2815 MHz for transport to remote locations such as LLRF controllers and beamline laser oscillators. Each channel of the transmitter/sender provides two fibers—a reference fiber and a beat fiber. The reference fiber provides the phase reference to the remote locations. The beat fiber transports information on the reference fiber's change in propagation delay to the remote locations to be used for correcting the reference fiber's phase. A block diagram for the transmitter/sender is shown in Figure 3.6-134.

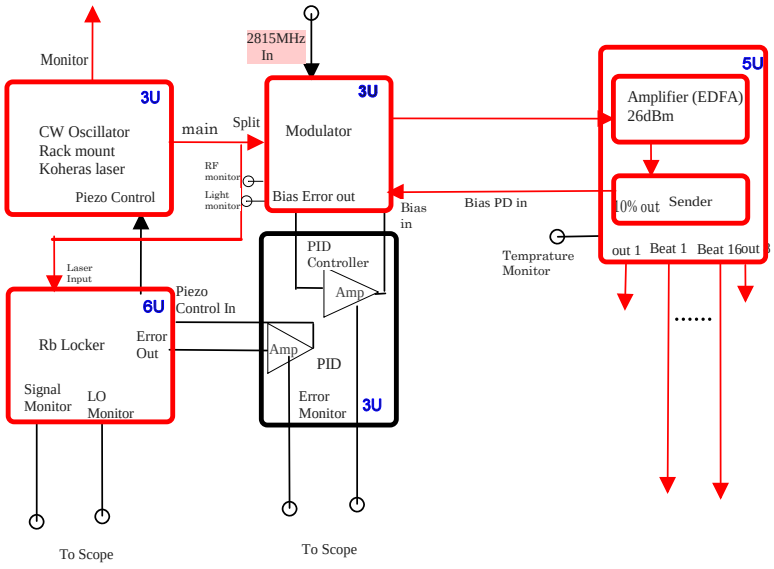

Figure 3.6-134: SPX0 transmitter/sender block diagram.

Specifications

1. Number of channels: 16
2. Laser wavelength: 1560 nm
3. Per channel optical power output: 10 mW max
4. Fiber connectors: APC
5. Modulator input frequency: 2815 MHz
6. Modulator input power: TBD
7. Includes laser source, EDFA, modulator, RB locker, 16 channel sender
8. Entire unit is to be packaged in a relay rack
9. Indicators: TBD

10. Interfaces: TBD

Table 3.6-62: Transmitter/sender units.

Feature	Specification
Number of channels	16
Number of outputs per channel	2
Signal output power	$\leq$ 10 mW
Wavelength	1560 nm
Optical frequency stability	$<$1 MHz
Modulation frequency	2815 MHz
Input rf power	+15 dBm
Beat output modulation frequency	100 $\pm$ 10 MHz
Modulation depth	70 $\pm$ 10%
Output optical connectors	FC/APC
Digitally controlled/monitored devices	PID controllers, EDFA
Rack space required	19 inch rack by 6’ high

Laser Safety

All laser light is to be fully contained within a chassis or fiber cables. Unused optical outputs are to be capped to prevent escape/leakage of laser light.

3.6.4.7.6 Receiver

Figure 3.6-135 is a block diagram of the SPX0 receiver, which includes both an LLRF control and a phase stabilizer in a common chassis. The phase stabilization functions are performed by a second LLRF board located in the receiver This board implements the interferometer, which measures the phase changes in the reference fiber. This error signal is transported to the LLRF controller board for phase correction.

3.6.4.7.7 Synchronization Head

The synchronization head is a key component of the timing/synchronization system. It is mounted as close as possible to the signal of interest to minimize the cable length for the signal of interest. For rf cavities, the signal of interest is the cavity field probe and for beamline lasers the signal of interest is the laser oscillator optical signal. The sync head has two variants—the rf sync head and the optical sync head. Figure 3.6-136 is a block diagram of the sync head. As shown in the figure, the two variants—rf and optical sync heads—are based on a common design. The components in the blue box box are specific to the rf sync head while the components in the yellow boxes are specific to the

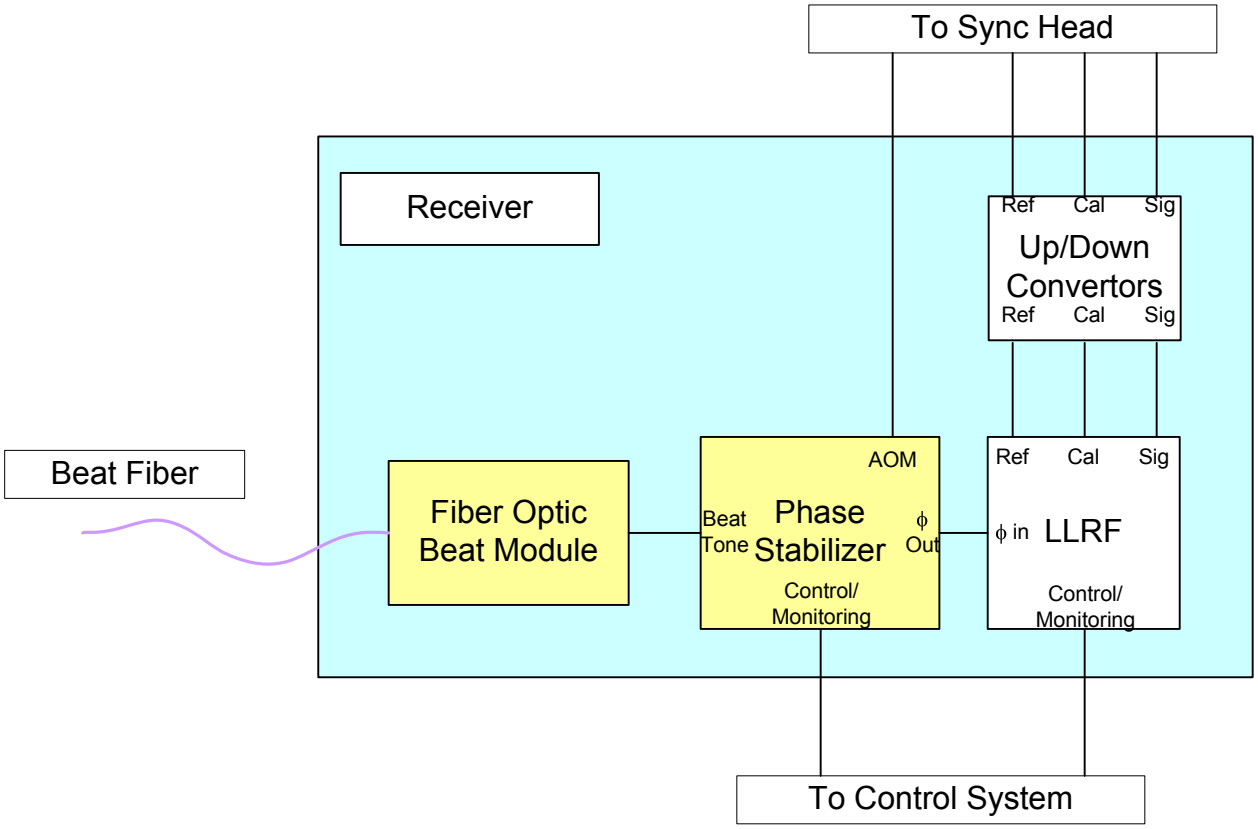

Figure 3.6-135: SPX0 receiver.

optical sync head. Items within the green box, such as the TEC controller, are external to the sync head temperature-controlled interior.

The sync head provides the following functions:

1. Extraction of the 2815-MHz phase reference signal from the modulated fiber carrier.
2. Shift the frequency of the optical carrier through the use of an acousto-optic modulator (AOM).
3. Combine calibration tone signal from the calibration input with the reference and signal inputs.
4. The interior of the sync head will be temperature controlled to $\pm$ 0.01°C via TEC devices and a TEC controller.
5. The entire sync head will be thermally insulated to aid temperature regulation of the interior.

Specific requirements for each variant are listed below.

For rf sync heads:

1. Provide a coaxial signal input for a cavity field probe.
2. Provide an auxiliary signal output.

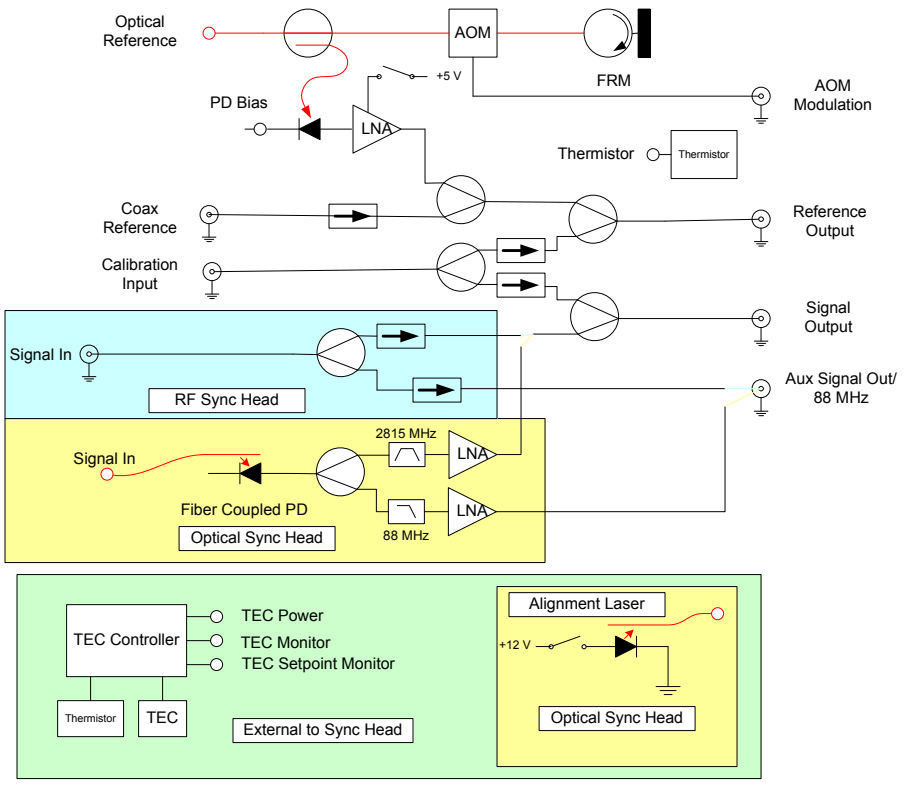

Figure 3.6-136: SPX0 synchronization head.

For optical sync heads:

1. Provide a fiber-coupled photodiode signal input for a laser oscillator signal.
2. Provide a bandpass-filtered 2815-MHz output from the photodiode.
3. Provide a low-pass-filtered 88-MHz output from the photodiode.
4. Provide an external (to the sync head envelope) low-power laser to aid in aligning the optical input to the sync head photodiode.
5. Power the alignment laser by the same 12-V power as the sync TEC.

The input/output connections are listed in Tables 3.6-63, 3.6-64 and 3.6-65.

3.6.4.7.8 Timing and Synchronization for Diagnostics

Diagnostics does not require any additional timing/synchronization for SPX0.

Table 3.6-63: Rf sync head signal inputs and outputs.

Signal	Connector
Optical Reference In	APC
Coax Reference In	N
Cal Tone In	N
Reference Out	N
Signal Out	N
AOM In	SMA
Signal In	N
Aux Signal Out	N

Table 3.6-64: Optical sync head signal inputs and outputs.

Signal	Connector
Optical Reference In	APC
Coax Reference In	N
Cal Tone In	N
Reference Out	N
Signal Out	N
AOM In	SMA
Signal In	APC
88-MHz Out	N

3.6.4.7.9 Timing and Synchronization for SPX Beamline

Because of the larger x-ray beam-pulse width and shorter running time, no extraordinary synchronization is needed for the beamline laser. The existing phase reference will be used to synchronize the laser to the x-ray pulse.

3.6.4.7.10 Frequency Generation Chassis

The frequency generation chassis accepts a 351.9-MHz input and multiplies that by 8 to generate the 2815-MHz SPX cavity frequency. In addition, it generates a local oscillator (LO) signal by dividing the 351.9 MHz by 6 and mixing that with the 2815 MHz. The 2756.8-MHz upper sideband is passed through a bandpass filter to generate the LO. A block diagram is shown in Figure 3.6-137. Table 3.6-66 lists the signals related to this chassis.

3.6.4.7.11 Cable Plant

Fiber Plant

1. All fibers shall be single-mode SMF28e fiber.

Table 3.6-65: SPX0 sync head multi-pin (DB25) connector pin-out.

Pin	Signal	Signal	Pin
1	GND	GND	14
2	GND	GND	15
3	GND	GND	16
4	+5V Power	GND	17
5	+15V Power	GND	18
6	TEC +12V Power	TEC +12V Power GND	19
7	TEC +12V Power	TEC +12V Power GND	20
8	Thermistor +	Thermistor -	21
9	PD Bias #2	PD Bias #2 GND	22
10	TEC +12V Power	TEC Set Point GND	23
11	TEC Set Point	TEC Temp Monitor GND	24
12	TEC Temp Monitor	PD Bias #1 GND	25
13	PD Bias #1		

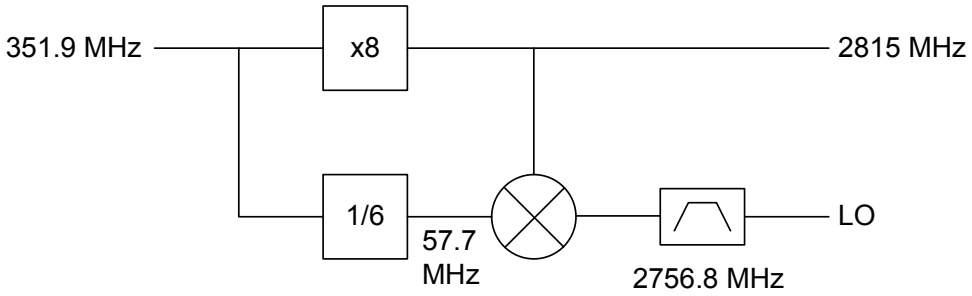

Figure 3.6-137: Frequency generation chassis block diagram.

2. All fiber connectors shall be APC.

3. All fiber splices shall be fusion spliced.

Coax Plant

1. All timing coax shall be phase-stabilized Andrew's $\frac{1}{2}$" Heliax: part number TBD.

Table 3.6-66: Frequency generation chassis signals.

Signal	Frequency	Level	Connector
RF Input	351.9 MHz	TBD	N
RF Output	2815 MHz	TBD	N
LO Output	2756.8 MHz	TBD	N

2. All connectors shall be type N.

3.6.4.8 Controls [U1.03.03.04]

SPX0 will provide an opportunity to prototype several of the concepts that will be required for SPX. Even though there is substantial overlap with section 3.6.3.7, the controls support for SPX0 will be described in this section for completeness.

3.6.4.8.1 SPX0 Subsystem Interfaces

Each SPX0 subsystem must be interfaced to the EPICS-based APS control system for supervisory control and monitoring (see Figure 3.6-138). In most cases, the required interfaces are well understood and many of the necessary types of interfaces have already been implemented in existing APS systems. Controls support for the SPX0 LLRF subsystem, however, requires unique interfacing and must handle high speed measurements. Its implementation is covered in more detail in section 3.6.4.8.2.

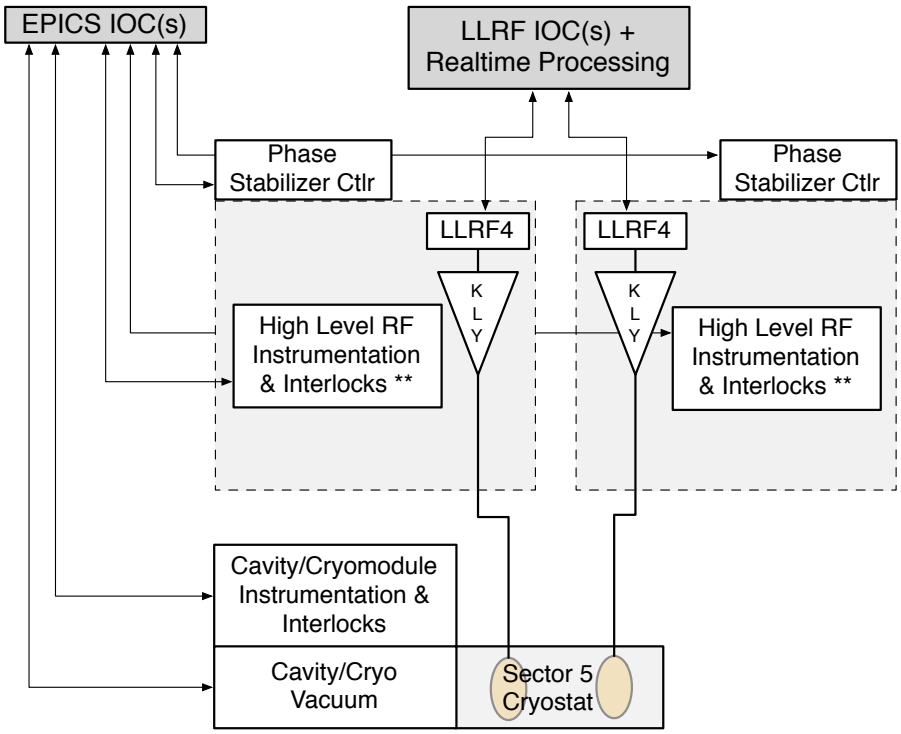

Figure 3.6-138: SPX0 controls and interfaces to other subsystems.

The IOCs to be used for SPX0 controls will be a mixture of soft IOCs (running on Linux servers) and traditional VME-based IOCs located in Building 400A. By providing VME-based IOCs, the large selection of VME modules currently used at APS can be utilized for SPX0. Table 3.6-67 gives the general details about the subsystem requirements for remote control and monitoring for SPX0.

Table 3.6-67: SPX0 subsystem requirements for control and monitoring.

Subsystem	Devices to Interface	Interface to IOC	Parameters to Monitor / Control	Default Rate
LLRF				
* LLRF measurements	BNL LLRF4	USB	6 I/Q waveforms (x2)	272 KHz sample rate
* LLRF setpoints	BNL LLRF4	USB	2 I/Q pairs (x2)	10 Hz
* LLRF parameters	BNL LLRF4	USB	200 / 200 (x2)	5 Hz
HLRF	PLC (x2)	Ethernet	200 / 50 (x2)	5 Hz
* Amplifier control				
* Slow rf interlocks				
* Fast rf interlocks				
Cavity / Cryomodule	PLC (x2)	Ethernet	200 / 100	10 Hz
* Instrumentation				
* Slow interlocks				
* Fast interlocks				
Cryomodule Vacuum	MM200, MPC, VVC210	Ethernet	50 / 20	5 Hz
Phase Stabilized Timing	LBL LLRF4 (x2)	USB	50 / 10 (x2)	5 Hz

3.6.4.8.2 SPX0 LLRF Controls

Figure 3.6-139 illustrates the primary components and interfaces required of the SPX0 LLRF controls. The list of functions on the right side of the diagram represents end-to-end functionality required for operation. These functions are divided into the different levels and blocks to depict where these functions will be implemented. Such a diagram assists in describing interfaces and functionality at each block.

The Cavity Control layer represents the functions performed by the LLRF controllers. These controllers are provided by the RF group and the functions they perform are described in section 3.6.4.6.

Each LLRF4 controller (LBL design) will interface to a Linux-based workstation through a USB link. This high performance multi-core computer will capture the LLRF data at the required rates (see Table 3.6-67), execute additional data processing routines, and make it available to a “soft” IOC that will make the data available via Channel Access.

Without the FPGA-based deflection controller planned for the final SPX system, the real-time performance of the SPX0 controls will be limited. Several algorithms will be prototyped in an effort to understand which are most important for the final system. Calculations such as vector-sum, I/Q to phase/amplitude, mean/max/min/standard deviation, and calibration routines will be implemented although it is unlikely they can be performed on a continuous basis in real time.

3.6.4.8.3 High Level Tools

- **Existing Tools:** The SPX0 controls will be implemented within the standard framework as the

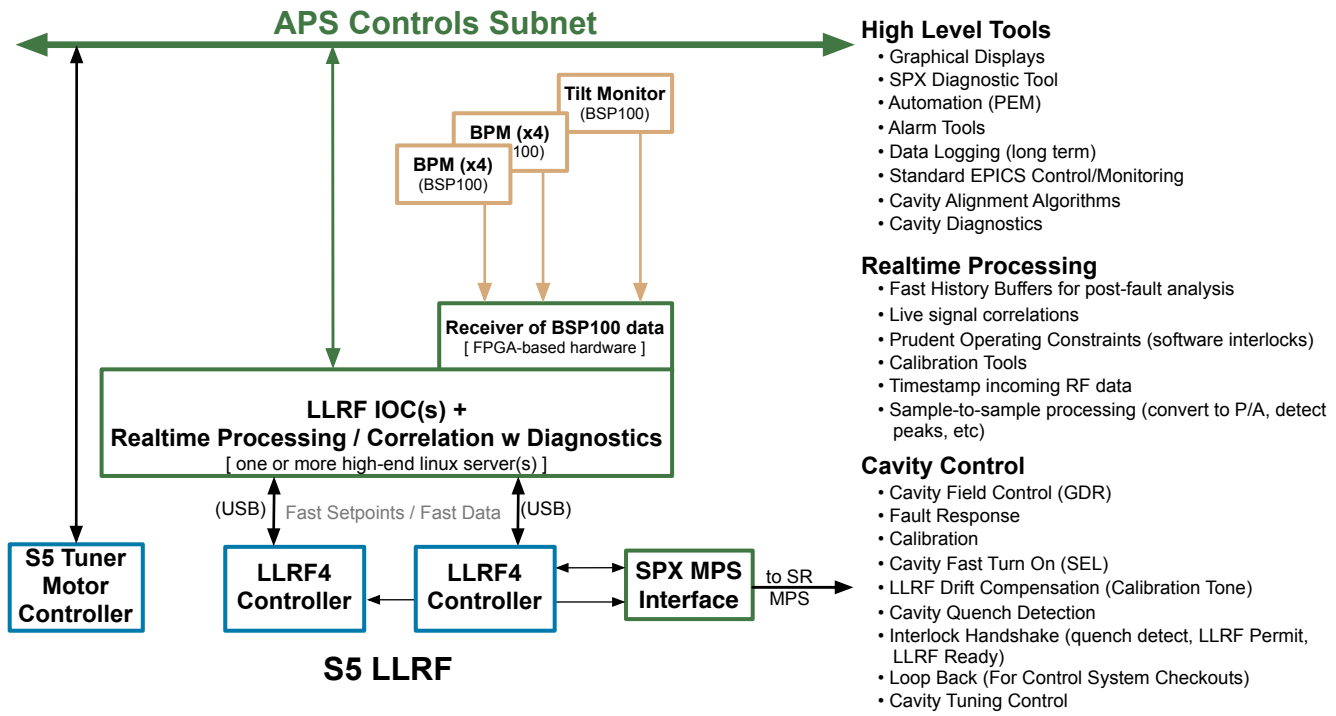

Figure 3.6-139: LLRF signal processing and hierarchical control functions.

existing accelerator controls. This will allow the entire suite of high-level tools (those typically used by accelerator operators, machine physicists, and technical staff) to be applied to the SPX subsystems. Tools that will likely be utilized include graphical operator displays, PEM tools for automation, alarm tools and data logging. MEDM screen, which allow subsystem experts to interact with their equipment will be provided.

- **Additional Tools:** Additional high-level tools specific to the deflecting cavities, the control of superconducting rf cavities, and precision LLRF systems will also be required. Such tools may be available from collaborators or similar projects and some may need to be developed here.
- **Rf Phasor Plot:** The rf phasor plot described in the SPX Controls section 3.6.3.7.3 is planned to be available for use for SPX0.
- **Live Data Correlation:** In the final SPX control system, an interface to the upgraded real-time feedback data highway will make all the diagnostic data (e.g., BPMs, beam size monitors, tilt monitors) available to the SPX subsystem to perform live data correlation. For SPX0, direct links from several BPMs and an rf tilt monitor will be implemented in order to prototype some live data correlation algorithms.
- **Data Processing Environment:** APS staff will make extensive use of Octave (a free alternative to Matlab) and the SDDS tools in the development, deployment, commissioning, and operation of the SPX0 LLRF subsystem. A convenient environment and utility libraries will be provided for Octave to minimize the learning overhead of using this tool with Channel Access and SDDS. An index of SPX0-specific scripts will be maintained to minimize redundant development of algorithms.

3.6.4.8.4 R&D Plan

There are several areas where the work on SPX0 will be used to clarify and guide the design of the final SPX system. These tasks are outlined below:

- Evaluate platform options for the real-time processing requirements
  - Prototype a method of acquiring rf and diagnostic data (from LLRF4, BPMs and tilt monitors) at the revolution frequency (273 kHz), perform real-time statistics, and pass data to a dedicated server. Evaluate what processing must be done within FPGAs or within servers. Evaluate performance bottlenecks.
  - Evaluate the benefits of embedded computer cores within the FPGA.
  - Use above information to direct the implementation of the "Deflection Controller" for the final SPX design.
- Demonstrate inter-system communication
  - Prototype an appropriate real-time data link (RTDL) to pass data between the LLRF controller and the deflection controller.
  - Quantify FPGA resources required for the RTDL.
  - Quantify additional cost if higher bandwidth links are requested/required.
- Identify additional tools/software required to meet requirements
  - Prototype methods to present real-time statistics and data correlations of rf and diagnostic measurements to the operators.
  - Determine if any new technologies (e.g., real-time Linux OS, cluster computation, multiple cores, etc.) will be required to accomplish the required processing.

3.6.4.9 Cavity and Cryomodule

3.6.4.9.1 Introduction

The SPX0 cryomodule is a short cryomodule that accommodates two deflecting cavities. The SPX0 cryomodule is a prototype cryomodule in which many SPX cryomodule components and technologies will be developed and tested. It retrofits existing JLab cryogenic end cans and thus provides a quick path for prototyping.

The following sections describe the cavity prototyping effort, cryomodule and mechanical design for the SPX0 cryomodule, and a dewar-fed cryogenic system.

3.6.4.9.2 Cavity

The design criteria for the SPX0 cavities are the same as those for SPX and are described in section 3.6.3.8. A prototype Mark-II cavity with end groups was constructed at JLab for evaluation of field emission, peak magnetic field, and unloaded quality factor in July 2011. Test results shown in Figure

3.6-140 indicate that the Mark-II cavity can reach the required operating gradient. Its quality factor has yet to achieve the required 10^9, but it is anticipated that upon further cavity processing, the cavity Q can meet the required operating value. Hence, a final determination was made in August 2011 that the Mark-II design would be adopted for SPX0 cavities, in order to take advantage of the superior damping and lower beam loss factor (see section 3.6.3.8.2).

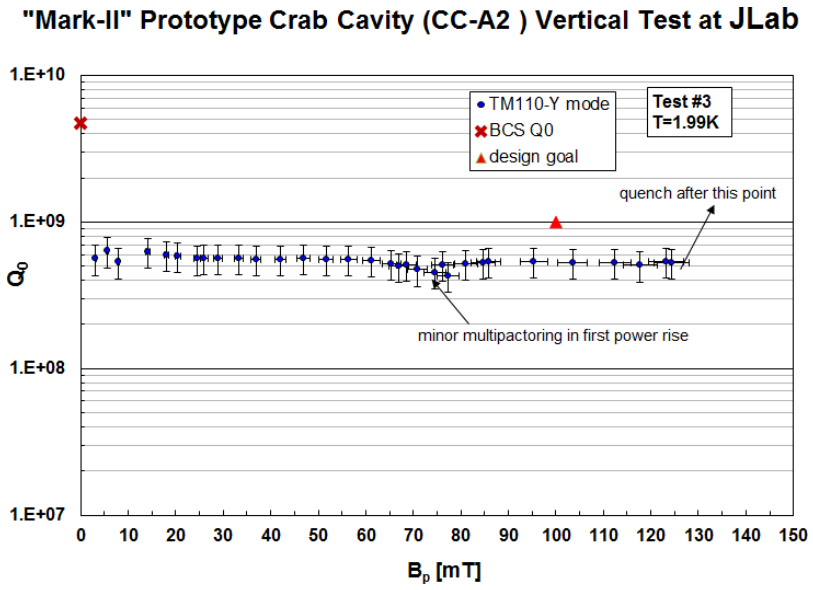

Figure 3.6-140: Experimental data of the Q vs. peak magnetic field for a prototype Mark-II cavity.

Three Mark-II cavities have been fabricated, two of which are shown in Figure 3.6-141. The cavity flanges use the ILC-style vacuum seals with an addition of an rf seals to keep rf field off the flange surfaces.

Figure 3.6-141: Two of the three SPX0 cavities fabricated at JLab.

3.6.4.9.3 Tuner

It is important to measure the cavity stiffness and sensitivity before one can finalize the tuner design. Cavity CCA3-1 was measured at JLab using CEBAF's C100 tuner test stand as shown in Figures 3.6-142 and 3.6-143.

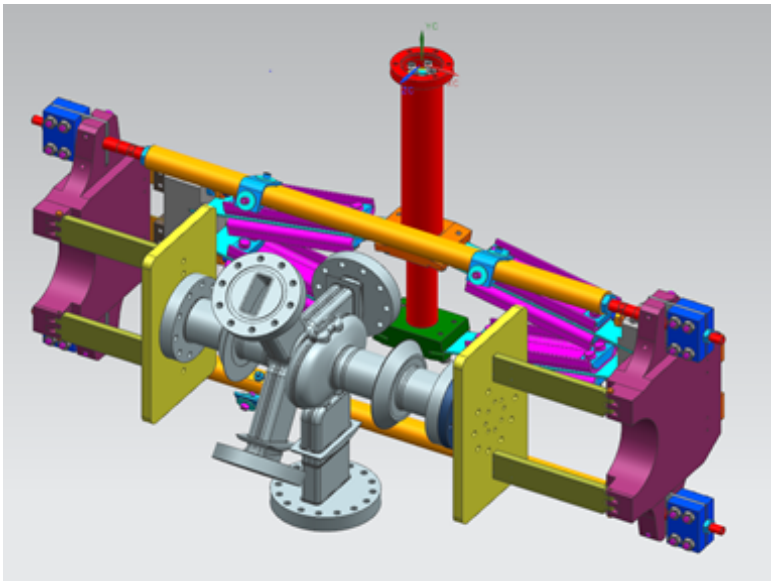

Figure 3.6-142: A CAD model for the CEBAF C100 tuner.

Figure 3.6-143: Cavity CCA3-1 being measured in CEBAF C100 tuner test stand.

The cavity frequency, axial force, and axial length were measured as the cavity was stretched. Figure 3.6-144 shows the measured frequency and force data vs. the cavity stretch. Cavity stiffness and tuning sensitivity were at 13.0 MHz/mm and 10160 lbs/in. Those numbers match the numbers predicted by a

computer simulation of a bare cavity. These numbers are expected to change after the helium vessel is attached and are expected to remain within the design parameters listed in Table 3.6-39.

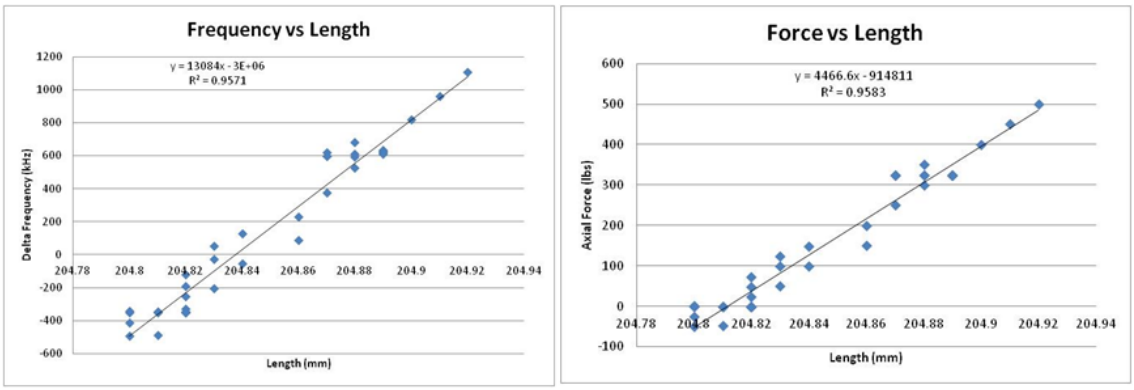

Figure 3.6-144: Cavity CCA3-1 tuning sensitivity and tuning force.

With the successful verification of the design and simulations with the actual cavity, two prototype tuners are being fabricated. They will be used in both the horizontal cavity test and the SPX0 cryomodule assembly.

3.6.4.9.4 Cryomodule and Mechanical Design [1.03.03.05 / 1.03.03.07]

One cryomodule with two deflecting cavities will be tested as part of the SPX0 R&D program. It will be located in Sector 5 and will produce a 1-MV peak deflection. The cryomodule will be required to support a beam current up to 150 mA and, as a result, it must incorporate features to support heavy parasitic mode damping. It will accommodate high cryogenic loads from dynamic losses, as well as from static losses due to numerous waveguide penetrations from the dampers and power couplers. Alignment tolerances are also critical to maintain LLRF tolerances. Parameters for the engineering design of the cryomodule are kept as close to the SPX parameters as possible. They are listed in Table 3.6-68.

SPX0 cryogenics uses liquid Dewars to supply liquid helium and uses a vacuum pump to maintain 2 K operation. The vacuum pump has been measured at 64 W at 23 Torr to keep 2 K operation. The total heat load thus cannot exceed 64 W. An 80 K thermal shield will use LN2 with heat load capacity of 250 W. Table 3.6-69 shows total heat loads are within the SPX0 capacity for both 2 K and 80 K heat loads.

The cavity offset alignment in Table 3.6-68 refers to the offset in the Y-direction. The two cavities in the SPX0 cryomodule will be connected by a rigid beam pipe. A low impedance bellows at each side of the cavity will connect a cold gate valve to a warm gate valve. Alignment of two rigidly connected cavities will be verified under warm conditions using a stretched wire technique. The cavity will be aligned to the beamline flanges within 0.5 mm. This alignment will be transferred to the string assembly and space frame integration such that after cryomodule completion, the cavities will be aligned to beam pipe flanges of cryomodule ends within $\pm$0.5mm. The cryomodule will be supported by an adjustable girder to allow further alignment of the cavity to within $\pm$0.2 mm of the beamline.

R&D: Additional R&D work includes:

Table 3.6-68: Selected SPX0 cryomodule design parameters.

Quantity	Value
Cavity Frequency	2.815 GHz
Operating Mode	TM_{110}
Cavity Iris Radius	25 mm
Cavity Active Gap	53.24 mm
Number of Cells per Cavity	1
Unloaded Q	$> 10^9$
Deflecting Voltage per Cavity	0.5 MV
Coupler Type	Waveguide
External Q	2×10^6
Number of HOM+FPC/LOM Waveguide Coupler	4
Cryogenic Temperature	2 K
2 K Heat Load due to Waveguide/Tuners per Cavity	2.4 W
2 K Dynamic Heat Load Due to Wall Losses per Cavity @$Q_u = 10^9$	7.0 W
2 K Static Heat Load Due to Miscellaneous Losses per Cryomodule	2.0 W
Total 2 K Heat Load @$Q_u = 10^9$	50 W
Slow Tuner Range	$\pm$ 200 kHz
Number of Cavities per Cryomodule	4 (8)
Total Number of Cryomodules	1
Cavity Offset Alignment Tolerance	0.5 mm

Table 3.6-69: Heat estimation for SPX0 cryomodule.

SPX0 Heat Load Components		2 K				Shield			
Heat loads per item	#	per Static	per Dynamic	per Total	Total	per Static	per Dynamic	per Total	Total
Cavity	2		7		14				0
HOM	4	1	1.3	2.3	9.2	0.37	0.72	1.09	4.36
LOM	2	1.36	0.21	1.57	3.14	12.05	0.35	12.4	24.8
FPC	2	1.14	0.48	1.62	3.24	5.09	0.45	5.54	11.08
Beam Tubes	2	0.14	0.16	0.3	0.6				
Component Totals		9.28	20.9		30.18	35.76	4.48		40.24
Static cryostat estimate		12			12	144			144
Total					42.18				184.24

1. High-power testing will be performed on the power coupler waveguide, primarily to evaluate multipacting and arcing. The input coupler rf windows will be tested up to 5 kW and should have sufficient bandwidth for possible HOM transmission.

2. The scissor-tuner design will be further investigated to determine its resolution and performance on an SPX cavity.

3. Water cooling of the dampers in the insulating vacuum will be investigated to determine

construction and assembly details, as well as issues regarding vibrations and microphonics.

4. The internal cryomodule features will be definitively sized and located including the helium distribution system, vacuum vessel, magnetic and thermal shielding, cavity string, waveguides, cryomodule supports, and alignment components. The cryomodule design and assembly sequence must be compatible with the requirement for clean-cavity rf surfaces. This includes a suitable concept for mounting the cryomodule in the beamline without contaminating the clean-string assembly.

5. A measurement of the ground vibration *in situ* will need to be done in order to determine the driven frequencies in the APS tunnel. Numerical analysis of mechanical modes in the cavity string will be undertaken to ensure there are no issues.

6. Flanges in the cavity string in close proximity to the cavity will be analyzed for losses and compatibility.

7. Evaluation of shielded and low-impedance bellows will be performed to determine beam impedance, bellows durability, and the effect on the cryogenic system.

8. Further simulations of the thermal transitions in the cryomodule will be performed including the waveguide penetrations, beam-pipe transitions, and incidental thermal loads between the cavities in the cavity string.

Cryogenics: The SPX0 cryogenic system and distribution system will be similar to the SPX cryogenic system except the liquid helium will not be provided through a dedicated cryoplant. Instead, it will be supplied by a series of liquid helium transfer Dewars that can be replenished at a frequency that satisfies the operational needs of the SPX0 cryomodule. Details of this cryogenic system can be found in section 3.6.4.12.

3.6.4.10 Dampers and Windows

The SPX0 waveguide dampers are intended to absorb rf parasitic mode power from the SPX0 cavities in order to satisfy the beam stability requirements of the APS storage ring. The dampers will operate in conjunction with the cavities to extract and absorb LOM and HOM power by means of waveguides located on the body of the cavity and on the beam pipe. The damper design is based on multiple considerations including rf requirements to ensure beam stability, mechanical requirements to ensure the physical integrity of the dampers during manufacturing and operation, and cleanliness requirements to prevent degradation of the performance of the SPX cavities due to contamination.

The LOM damper waveguide is coupled to the SPX0 cavity through a dog-bone-shaped iris on the body of the cavity along the median plane, as shown in Figure 3.6-145. Two HOM damper waveguides are assembled as part of the upper fork of the Y-end group on the beam pipe. The vertical branch of the Y-end group serves the dual purpose as an input coupler and as a limited-bandwidth HOM damper. The SPX0 project consists of two cavities located in a single cryomodule. As a result, four HOM dampers and two LOM dampers are required for installation.

Rf windows will be utilized for both the input coupler and the LOM waveguides. Double-window designs have been adopted to increase redundancy and reduce the possibility of a vacuum-related failure. Hence, a total of four input coupler windows and four LOM windows will be required, where

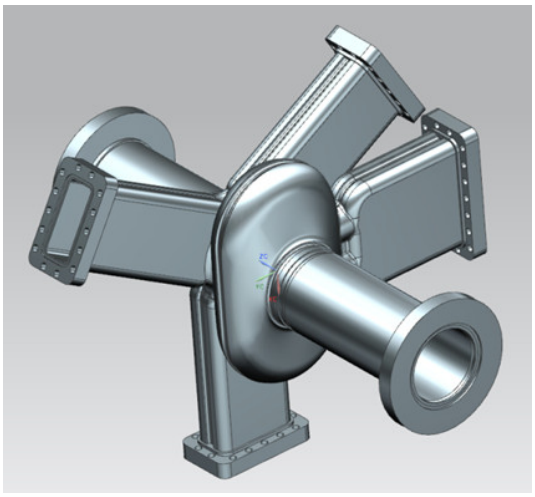

Figure 3.6-145: Mark-II cavity geometry with HOM and LOM waveguides and vertically oriented input coupler.

two of each will be installed during the clean assembly, with the remainder being installed after the insertion of the cavity string into the vacuum vessel.

3.6.4.10.1 Damper Design Criteria

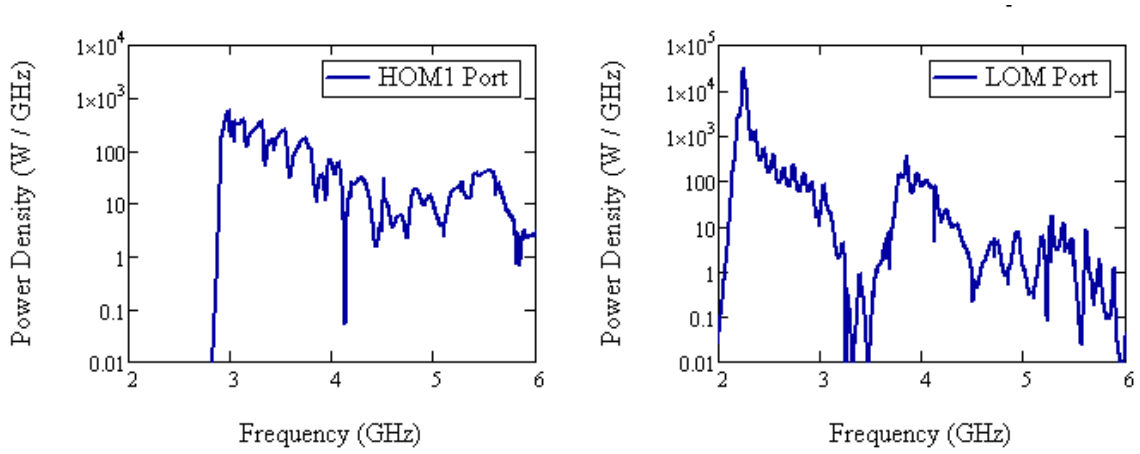

Figure 3.6-146: Power spectrum due to beam-generated power in the SPX0 dampers: (a) HOM and (b) LOM.

The damper system specifications are based on 200-mA beam current in the APS storage ring, which provides a safety margin compared to the 150 mA operating requirement for the APS Upgrade. The HOM damper is expected to absorb about 300 W across a wide bandwidth from 2.9 to 8 GHz. Additional rf loading of the HOM dampers occurs at the operating frequency of 2815 MHz due to evanescent decay in the below-cutoff waveguide but is expected to be limited to less than 10 W. The LOM damper, on the other hand, is expected to absorb approximately 1.4 kW over a comparatively

narrow band where the majority of power is localized at 2.3 GHz, as shown in the plot of the power spectrum in Figure 3.6-146. Ideally, additional loading of the LOM damper at 2815 MHz should be negligible based on the cavity-dogbone geometry and the intentional coupling of the 2815-MHz mode to a higher-order TE20 waveguide mode. However, a vertical offset of the electrical center of the cavity, asymmetries in the LOM coupling geometry due to manufacturing and processing tolerances, or mode conversion from the Y-end group would permit coupling to the fundamental waveguide mode, thereby allowing traveling wave power to create an additional load in the LOM dampers. In order to account for additional loading and to provide a safety margin for each of the dampers, the HOM and LOM dampers are designed to absorb 500 W and 5 kW, respectively.

The LOM damper will operate outside of vacuum since the spectrum of power of the LOM damper is primarily narrowband. An out-of-vacuum load reduces the risks inherent in a high-power rf vacuum load that must be compatible with the vacuum environment, must not negatively impact the operation of superconducting rf components, and is more difficult to maintain. As a result, a high-power, out-of-vacuum load was adapted by Mega Inc., as shown in Figure 3.6-147, with a peak-power specification that is well in excess of the expected load. The load has been procured and successfully tested at the APS. However, results of the testing precipitated design improvements regarding thermal management issues to reduce the temperature of the external waveguide and the lossy material in order to improve the expected reliability of the load.

Due to the broadband requirements of the HOM damper, on the other hand, a high-power rf window was not feasible. As a result, the HOM waveguide dampers are located within the cryomodule where a common vacuum environment is shared with the SPX0 cavities. This requirement necessitates additional design considerations for the damper assembly. The damping material and bonding alloys must be vacuum-compatible with the APS storage ring, as well as meet cleanliness standards for rf components in a superconducting environment. The damper assembly, including SiC tiles, must be cleanable, withstand high-pressure rinsing, and have no more than low levels of particulate generation to prevent contamination of the surface of the superconducting cavity.

Figure 3.6-147: 5 kW out-of vacuum LOM damper.

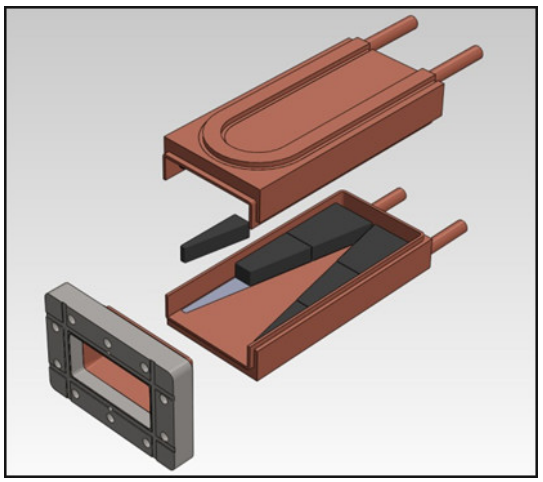

Figure 3.6-148: CAD model of the HOM damper assembly with damper waveguide body, SiC tiles, and rf flange.

Due to the limited accessibility of the HOM dampers, as well as their integration with cavity vacuum,

the reliability and life expectancy of the dampers are critical factors in their design. A wedge-shaped waveguide damper was adopted based on its relative simplicity and its proven performance at PEP-II [3.6-86] and KEK [3.6-87]. At PEP-II, a two-wedge waveguide damper was used for power levels up to 10 kW at a frequency range from 700 to 2500 MHz. Due to the reduced size of the SPX dampers, the high-frequency operation, and the near mono-chromaticity of the LOM damping, the local power density was higher for a similar geometry [3.6-88]. As a result, a four-wedge design, with two wedges on each broadwall of the dampers, was initially adopted for the LOM dampers and was standardized for use with the HOM dampers as shown in Figure 3.6-148. In this way, the temperature gradient across the dampers was reduced as shown in Figure 3.6-149, and peak stresses were minimized. A further benefit of the four-wedge design was the expected mitigation of particulate generation due to temperature-dependent effects at higher rf loads. Following the determination of the four-wedge design, the LOM damper was subsequently redefined for out-of-vacuum operation and was procured from an outside vendor, as described previously. However, the HOM damper retained the features of the design and is being manufactured for SPX0.

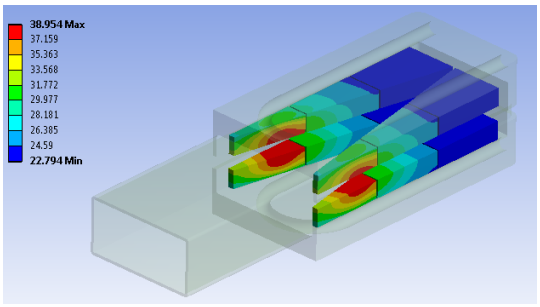

Figure 3.6-149: HOM damper thermal profile.

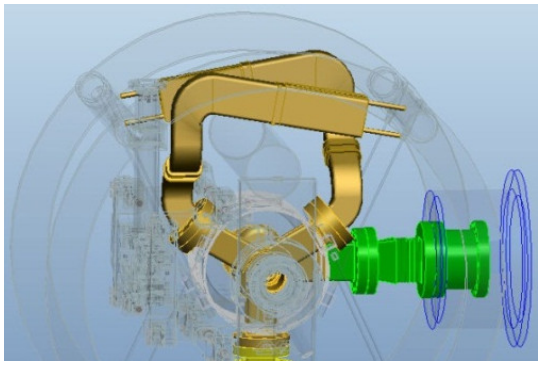

Figure 3.6-150: Layout in the SPX0 cryomodule with cavity and HOM waveguides.

A CAD model showing the layout of the HOM waveguide inside the cryomodule is shown in Figure 3.6-150, where two copper-colored HOM dampers associated with each cavity are angled slightly downward to help prevent the gravitation of particulates onto the surface of the cavity. A bellows, not shown in the figure, is inserted just prior to the dampers as a thermal impedance and to permit lateral and longitudinal motion of the HOM waveguide assembly. The dampers are located outside the 80 K thermal shield, in the warm region of the cryomodule, where water cooling is plumbed directly into the cryomodule to cool the dampers. The length of the HOM waveguide in the cryomodule was adjusted to accommodate packaging and to ensure minimal loading of the damper from 2815 MHz power. A ridge was also designed along its broadwall to reduce the effective cutoff frequency of the HOM waveguide and to improve its low-frequency rf performance at critical higher-order modes.

3.6.4.10.2 SPX0 HOM Dampers

The SPX0 HOM dampers are based on damper prototypes that were recently fabricated, as shown in Figures 3.6-151 and 3.6-152. The damper prototype waveguide was constructed from oxygen-free electronic (OFE) copper. It was initially constructed as two halves with cooling channels machined into the outer broadwall surfaces. Lossy SiC ceramic material was soldered to the copper body with a

Figure 3.6-151: Half of a prototype HOM damper prior to electron-beam welding.

Figure 3.6-152: Full HOM damper without rf flange.

high-temperature, vacuum-compatible solder and will be cleaned for SPX0 using plasma etching. Sets of two waveguide-halves, with waveguide flange and joining neck, were electron-beam welded to form the ultra-high-vacuum-tight WR284 waveguide damper. Prior to packaging into the SPX0 cryomodule, the entire assembly will be processed for the superconducting environment.

Hexoloy SiC was chosen as the rf lossy material due to its optimal combination of rf, thermal, and structural properties, as well as its proven performance at other accelerator facilities. The SiC bulk material is produced from sintered slabs that have been simultaneously fired by the vendor to produce consistent material properties including permittivity and loss tangent. The tiles are cut from the bulk material using a diamond cutter, and each surface of the tile is ground to improve bonding with the solder and to reduce loose material that may result in particulate generation.

An R&D program had been undertaken for the reliable brazing and soldering of the SiC damper tiles to the copper waveguide body. Due to its low coefficient of thermal expansion and chemical inertness, SiC is very challenging to braze to copper. Numerous brazing tests were performed with independent companies who specialize in brazing. During the studies, SiC material vendors, brazing alloys, SiC tile sizes, stress-relieving features, and substrate thicknesses, as well as intermediate bonding layers of molybdenum, were varied to determine an optimal combination. None of the parameter combinations achieved a satisfactory success rate, and in a significant number of cases, pull test results showed minimal strength of the brazed SiC tiles, as shown in Figures 3.6-153 and 3.6-154. As a result, a parallel R&D program involving high-temperature, S bond soldering was selected for the SPX0 dampers. Although soldering possesses a lower threshold for its melting temperature, its 100% bonding success rate and preliminary strength tests offer a much more reliable and robust damper design. The solder, as well as the SiC material, have been tested and validated with an RGA scanner for ultra-high vacuum usage in the APS storage ring.

Prior to electron-beam welding, plasma etching of the damper assembly will be performed for SPX0, while the tiles are easily accessible, in order to remove residue due to the manufacturing processes, especially soldering. Fixturing during the soldering process for the damper prototypes was done with the aid of graphite spacers that will be plated with titanium for SPX0 to minimize contamination from graphite residue, which is difficult to remove even with ultrasonic cleaning and high-pressure rinsing. Electron-beam welding was selected to reduce the heat load on the soldered SiC tiles, as compared with

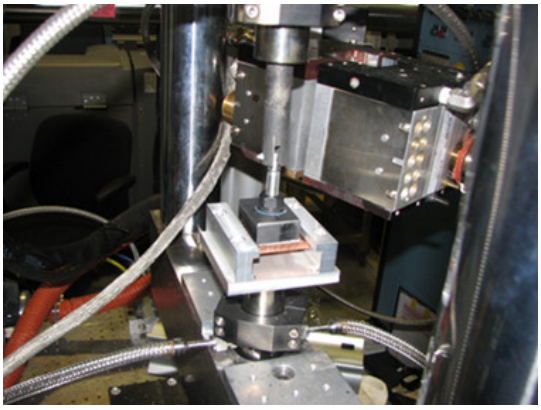

Figure 3.6-153: Pull test apparatus for the determination of initial strength of sample brazing/soldering trial pieces.

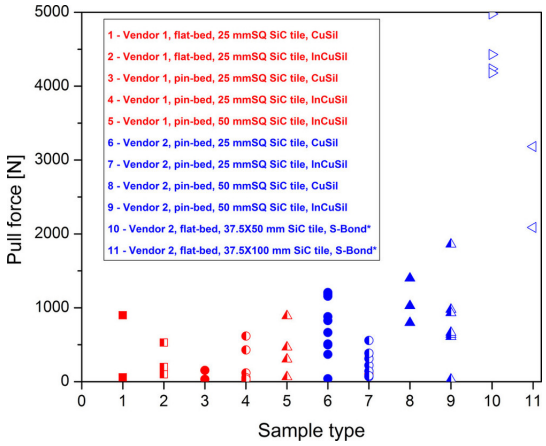

Figure 3.6-154: Pull test results for two vendors with various SiC tile sizes and brazing / soldering alloys.

traditional brazing and welding techniques. The welding joint of the damper assembly was designed to reduce the required input energy to prevent compromise of the solder joints. To protect the SiC tiles during the electron-beam welding process, a copper backing plate with a thin aluminum covering for the tiles was designed to isolate the tiles from the full impact of the electron beam as well as copper splatter.

3.6.4.10.3 Window Design

The LOM damper will be separated from the cavity vacuum by two WR340 warm windows to simplify the packaging of the cryomodule and to eliminate the risk associated with a higher-power in-vacuum load. Although the LOM damper loading is primarily narrowband, it was necessary to implement a quasi-broadband window to prevent new resonances from being generated that violated the APS stability requirements. In order to transition from the LOM cavity waveguide to the WR340 windows, a taper was designed to optimize the return loss of the window for broadband performance.

The input coupler and LOM windows will operate as warm windows and are rated for greater than 40-kW average power by the vendor. Both windows utilize a pillbox design for the WR284 and WR340 waveguide. The locations of the first windows are fixed due to constraints imposed by internal packaging of the cryomodule. The second window locations are optimized for improved performance at critical frequencies. The layout of the LOM windows and waveguide is shown in Figure 3.6-155, while the rf return loss of the LOM double-window design is shown in Figure 3.6-156.

The window assemblies are made from OFE copper with a 99.5% pure, titanium-coated alumina ceramic disk. Custom flanges and waveguide extensions have been designed for the input coupler and LOM windows to produce a compact window design to accommodate waveguide components in the cryomodule such as transition waveguide and bellows, and to optimize thermal impedances to reduce the heat leak to the 2 K helium circuit. All the windows are mounted externally to the vacuum shell of the cryomodule and will rely on water-cooling circuits.

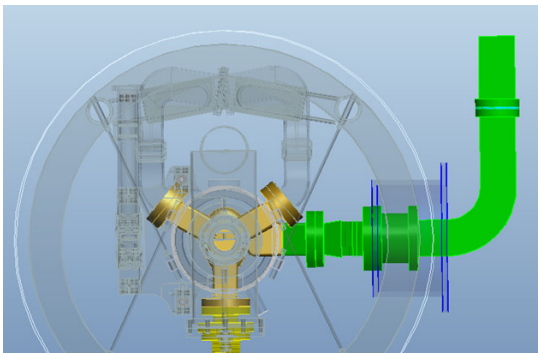

Figure 3.6-155: Layout of the double-window design for the LOM waveguide with the cryomodule.

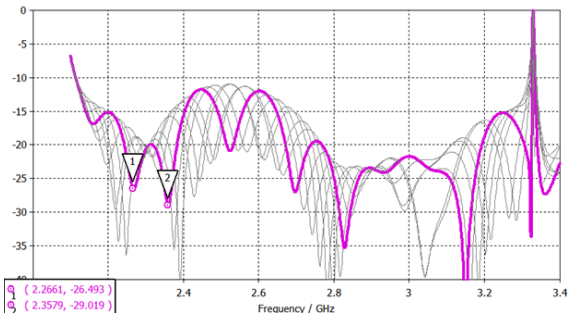

Figure 3.6-156: Return loss of the double-window design for the LOM waveguide.

3.6.4.10.4 Experimental Results

Preliminary testing of the damper material has included ultrahigh vacuum compatibility testing, SiC material property variability testing between samples, re-melting temperature analysis of S-bond solder, and pull tests. The Building 400A facility has also been outfitted for the testing of dampers and rf windows, as shown in Figure 3.6-157. A klystron amplifier, shown in Figure 3.6-158, is capable of producing 4 kW at 2815 MHz. Low- and high-power tests have been performed and are in the process of being performed, to verify the rf performance and mechanical integrity of the components used for SPX0.

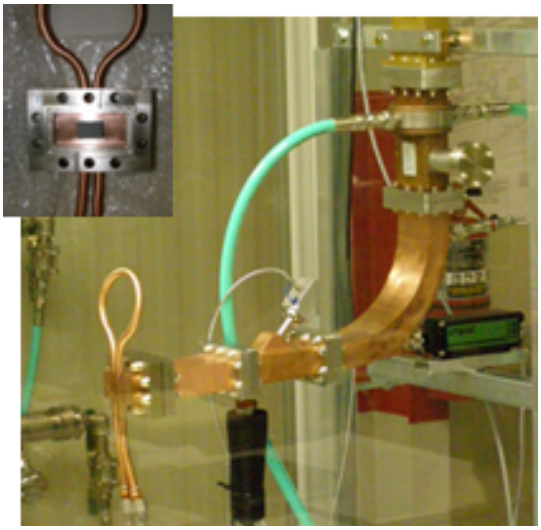

Figure 3.6-157: Particulate test setup with SiC tile soldered to cooling flange (inset).

Figure 3.6-158: High-power klystron components for particulate and window tests.

High-power tests include conditioning of the HOM and LOM dampers up to 500 W and 2 kW, respectively, and up to 4 kW for both the input coupler and LOM windows. The rf windows are further tested using a shorted transmission line with the peak standing-wave electric field located directly on the alumina window to maximize losses and thermally induced stresses. Test data of the average

temperature across the damping material of the LOM damper during conditioning are shown in Figure 3.6-159.

High-power particulate tests are performed to determine the particulate generation of the SiC tiles and solder as a function of temperature. Preliminary results using the particulate test setup shown in Figure 3.6-157 were obtained from SiC sample tiles soldered directly to cooling flanges as shown in the inset. During the particulate test, SiC is heated from rf losses and particulates are forced into a particle counter using positive nitrogen pressure in the waveguide. The resultant particulate count is documented as a function of surface temperature, as shown in Figure 3.6-160. High-power lifetime tests were also performed to evaluate the durability of the mechanical design of the damper. Up to 25,000 cycles were applied, using pulsed rf, to produce thermal gradients across the SiC sample that were comparable to that expected during normal beam operations. The results of the repetition of the stresses induced during the cycling were evaluated to determine the suitability of the damper materials over the anticipated lifetime of the permanent SPX project installation.

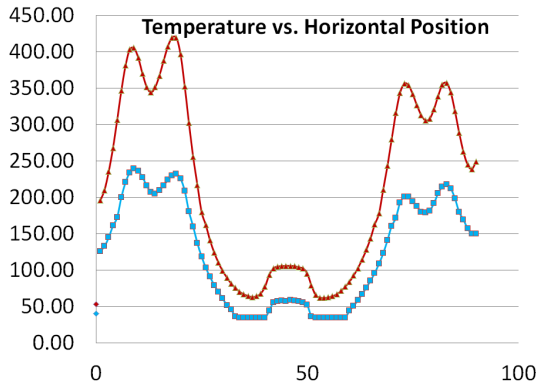

Figure 3.6-159: LOM out-of vacuum load temperature profile at 1 kW and 2 kW.

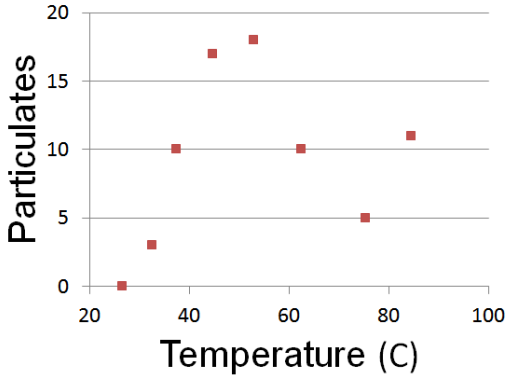

Figure 3.6-160: Particulate count vs. temperature of SiC sample tile.

The high-power tests were successfully completed on the single SiC tiles to qualify the damper materials prior to construction of damper assemblies. In the meantime, full HOM damper prototypes have been received and are in the process of being tested. More accurate thermal distributions and stress profiles will be generated within the damper prototypes, thereby producing a more realistic assessment of particle generation and lifetime effects.

For the SPX0 installation, diagnostics will be installed at the cryomodule to monitor the condition of the dampers and windows and to evaluate the interaction of the damper with beam-generated rf power. Calorimetry will be used to evaluate the power loading of the dampers and windows. Additionally, arc detectors and IR cameras will monitor the rf windows, and field probes in the LOM and HOM waveguides will monitor the spectrum of power being absorbed by the dampers. Redundant heaters have also been designed for each of the HOM damper assemblies, as well as the LOM and input coupler windows, to prevent freezing of the water circuits.

3.6.4.10.5 Off-Normal Conditions

The mechanical integrity of the HOM dampers is critical due to their location within the cryomodule. Since access is difficult for repair and maintenance and since a common vacuum environment is shared with the cavity, off-normal conditions are carefully considered. Issues include freezing of the water cooling lines, the integrity of the solder given a melting temperature of 220°C, and the strength of the solder joint.

As a result of the heat-stationing of the HOM waveguide transmission line to 80 K, freezing may occur when rf loading of the dampers is absent, such as during cool-down of the cryomodule or during a beam loss. Heaters on the windows and HOM dampers will compensate for any loss of damper heating. However, in the event of a total power loss, including loss of emergency backup power, the heaters would be inoperable and the damper assemblies would begin cooling to 80 K. Assuming a conservative estimate of 5 W of power flow from the dampers to the 80 K circuit, the temperature of the cooling channel would drop from 28.8°C to 23.1°C in approximately 18 minutes, or at a rate of 0.3°C/min, as shown in Figures 3.6-161 and 3.6-162. Freezing of the channels would not occur for well over an hour, during which time the cooling lines could be evacuated with compressed air.

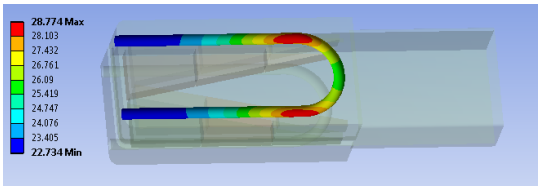

Figure 3.6-161: Simulated water-channel temperature at t=0 following a loss of water flow.

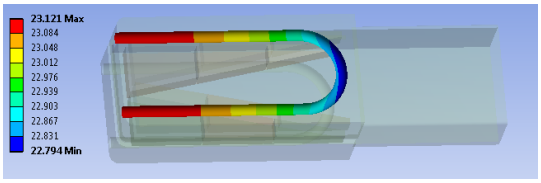

Figure 3.6-162: Simulated water-channel temperature at t=1100 s following a loss of water flow.

Since a high-temperature solder is used for bonding the SiC tiles, the temperature in operation must not exceed the melting temperature of 220°C. During normal rf loading of the HOM dampers, the maxmimum temperature of the dampers, as shown in Figure 3.6-149, is well below the melting temperature. However, a failure of one of the two cooling circuits on the HOM damper would leave one of the damper broadwalls without direct cooling. Rather, conductive cooling would occur through the copper from the uncooled broadwall to the opposite broadwall. The temperature profile, after steady-state is reached, is shown in Figure 3.6-163, where the temperature equilibrium is predicted to be achieved in less than 10 minutes. The maximum temperature on the damper body is 63.6°C, which is still well below alarm thresholds. On the other hand, if both cooling channels failed, an interlock would be required to force a beam dump.

Bonding of the SiC to copper using high-temperature S-bond solder was chosen due to its success rate for bonding, as well as due to preliminary strength measurements as shown from its pull test data. As a result, its bonding strength appears to be more than adequate. However, further experimentation is planned to characterize its bonding integrity during vibration and shock incidents.

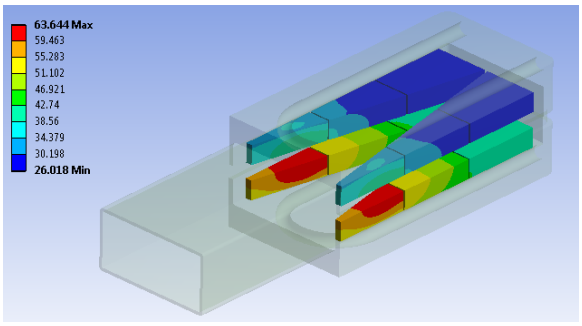

Figure 3.6-163: Steady-state damper temperature due to complete blockage in bottom water channel.

3.6.4.11 Beam Diagnostics [U1.03.03.08]

Existing diagnostics, primarily the APS storage ring beam position monitor systems, will be used to quantify performance of the SPX0 cryomodule including two superconducting deflecting cavities. In addition, a number of spare APS linac S-band phase detectors will be used to quantify arrival time phase noise and beam tilt at select BPM pickup electrode locations. Only beamline 35-BM will be available, including the streak camera and x-ray pinhole camera, to assess large amounts of beam tilt expected around the ring circumference.

3.6.4.12 Mechanical Systems Infrastructure

Several mechanical systems are needed for installation and operation of the SPX0 cryomodule. The most significant of these include a special storage ring straight section vacuum system, deionized water supply and distribution systems, and a cryogenic supply and distribution system. Significant effort will be allocated to not only specify, design, and install these systems, but also to coordinate the design of all major SPX mechanical systems to ensure physical compatibility, proper mechanical integration of SPX cryomodules into the APS storage ring, and adequate conventional facility provisions.

3.6.4.12.1 Mechanical Design Integration

A project such as the SPX0 storage ring test with a large number of independently designed, yet critically interacting, subsystems requires engineering on a global scale if the design work is to proceed efficiently and confidently. To facilitate the design process and minimize iterations, an integrated 3D CAD model has been built that incorporates all major subsystems, including the new 400A building, into one large assembly. APS survey and alignment personnel have contributed to the effort by making detailed measurements inside the storage ring tunnel, which are then input into the model. As an example, using this model SPX engineers will be able to visually study how the SPX0 cryomodule will be installed into the storage ring, and any potential physical interferences with existing equipment will be immediately obvious. An image from this model is shown in Figure 3.6-164.

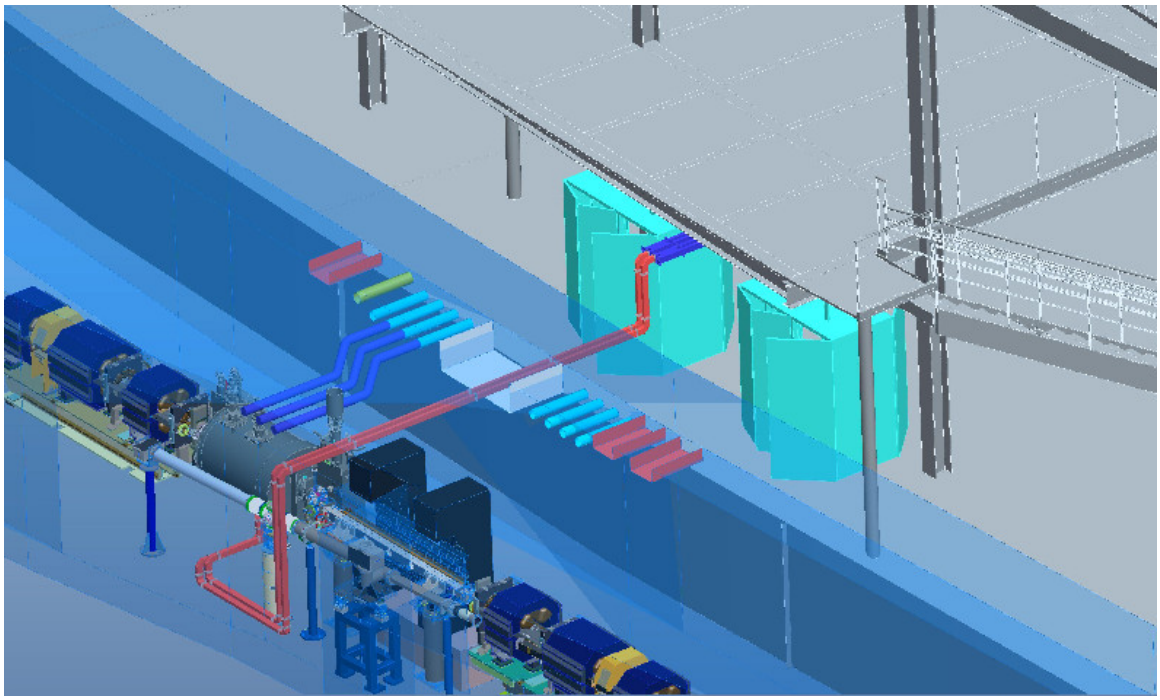

Figure 3.6-164: SPX0 integrated CAD model.

3.6.4.12.2 Straight-Section Vacuum System

The SPX0 straight-section vacuum system includes all vacuum chambers, spools, bellows assemblies, vacuum pumps, gauges, valves, and supporting mechanical hardware required to integrate the SPX0 cryomodule in the downstream half of the Sector 5 straight section in the storage ring and to accommodate an APS Undulator A in the upstream half of the straight section for uninterrupted user operations on the 5-ID beamline. The straight-section vacuum system will bridge the vacuum spaces between the SPX0 cryomodule and adjacent sections of the APS storage ring, provide vacuum pumping for these spaces, and monitor associated vacuum pressures. Figure 3.6-165 depicts a preliminary CAD model of the SPX0 straight-section vacuum system.

Specifically, the SPX0 straight section vacuum system will consist of:

- One insertion device vacuum chamber assembly for a single 2.4-m-long APS Undulator A, complete with end-boxes, aperture transitions, and boot absorber.
- One rf-shielded bellows.
- Three substitute spool pieces to be used when the SPX0 cryomodule is not installed and for experimental bellows testing.
- One standalone aperture transition chamber with pump-out port.
- Six ion pumps and controllers.
- Two UHV vacuum gauges and controllers.

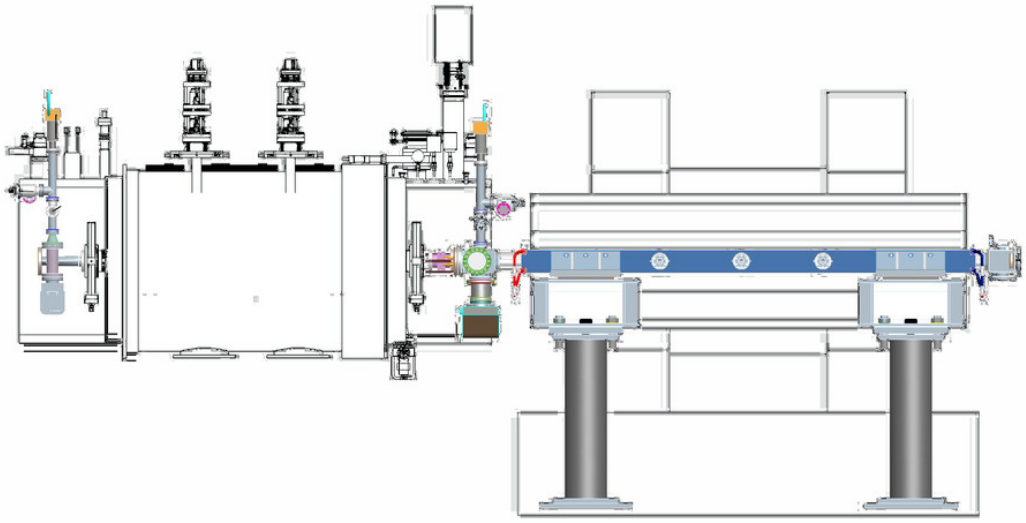

Figure 3.6-165: SPX0 straight-section vacuum system.

- Two NEG cartridge pumps.
- Two insertion device vacuum chamber support stands.
- Two vacuum 'T's.
- Two manually operated angle valves.
- Two mechanical support stands for substitute spool pieces.
- One mechanical support stand for vacuum pumping and pressure monitoring assembly attached to standalone aperture transition.

The SPX0 straight vacuum system utilizes existing, proven APS storage ring vacuum system designs with the following exceptions:

- The insertion device vacuum chamber shall be shortened to accommodate a full-length (2.4-m) Undulator A as provided by STI Optronix. In particular, 2460-mm clearance shall be provided in the beam direction for magnet structures and limit switches.
- The middle insertion device vacuum chamber support stand shall be removed.
- NEG pumping strips inside the insertion device vacuum chamber antechamber shall not be used so as to limit the production of particulates that may migrate to the superconducting cavities. The insertion device vacuum chamber will be modified so that three small ion pumps may be used instead.
- An additional pair of ConFlat flange connections for rf button-type beam position monitors shall be added at the downstream end of the insertion device vacuum chamber.

- The absorber in the downstream end box of the insertion device vacuum chamber shall be moved inboard so that its tip is 18 mm from the beam axis to adequately protect downstream components.
- The aperture transition in the downstream end box of the insertion device vacuum chamber shall adapt to a 52-mm diameter round opening to match the SPX0 cryomodule beam tube aperture.
- A standalone transition chamber will be provided that adapts between the 52-mm diameter SPX0 cryomodule beam aperture and standard storage ring aperture.

3.6.4.12.3 Deionized Water Distribution Systems

Deionized water distribution systems will be provided for cooling of: high-power rf systems in Building 400A-1, a high-throughput vacuum pumping system in room 400A-3 used for evaporative cooling of the cryomodule liquid helium bath, and rf dampers and waveguide windows located on the cryomodule itself. These systems will include piping, valves, pressure gauges, flow meters, thermometry, and minor hardware required for the physical installation. The flow rates required for the three locations are 100 gpm, 60 gpm, and 14 gpm respectively. In addition, approximately 50 gpm must be reserved for conventional facilities' use in 400A. An existing deionized water pump serving Building 400A has a capacity of 300-400 gpm, so all circuits in 400A will be sufficiently served by this pump, and no additional pumping capacity will be provided.

Each water header installed will include supply and return shut-off valves, supply and return dial-indicating pressure gauges, and a drain port. Each circuit installed onto new water headers in 400A will be provided with its own pair of supply and return shut-off valves. Provisions for flow metering and calorimetry will be included in the high-power rf cabinets being served. Each circuit in the storage ring connected to new water headers there will include supply and return shut-off valves, a differential pressure-based flow meter, and a resistance temperature detector. In addition, water circuits in the storage ring will utilize plastic tubing to minimize water flow-induced vibration and to ease installation. This tubing will be a radiation-resistant type known from experience to be adequate for use in the APS storage ring. Storage ring water circuit flows for each of the two cavities in the experimental cryomodule are given in Table 3.6-70.

Table 3.6-70: Storage ring water circuit flows and heat loads.

Circuit No.	Components	Min. Flow (gpm)	Max. Flow (gpm)
1	Waveguide Windows	1	2
2	LOM Damper	3	4
3	HOM Dampers - Inner Channels	1	2
4	HOM Dampers - Outer Channels	1	2

SPX systems shall generally require that water is supplied at, or slightly below, room temperature to ensure that condensation does not form on water lines. APS water systems provide water at 78 deg F so no additional temperature adjustment will be needed. SPX systems shall anticipate supply side pressures of 150 psi and return side pressurizes of 50 psi, as typically supplied by APS DI water systems. The APS deionized water system supplies water with a resistivity of 10 mΩ-cm. Corrosivity of the water is limited by the APS by oxygen removal. Outside of this, none of the SPX systems utilizing

deionized water require special control or monitoring of water chemistry. Therefore, all supplied water temperature, pressure, and chemistry will conform to existing APS conventions.

3.6.4.12.4 Cryogenic Supply and Distribution Systems

The cryogenic supply and distribution system for SPX0 is envisioned as a temporary source of 80 K and 2 K cooling for the SPX0 cryomodule during its operational lifetime, which is expected to last a few months. The system is designed for simplicity and low capital cost, consistent with both SPX0 studies and APS storage ring operation.

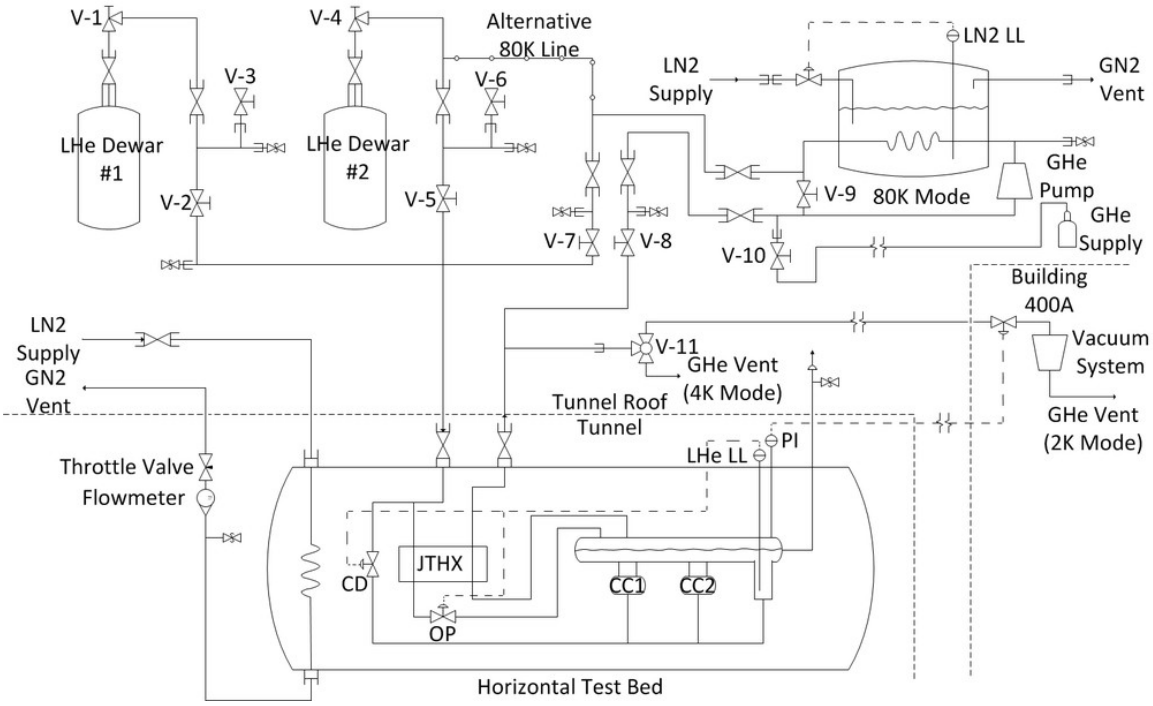

Figure 3.6-166: Flow schematic for the SPX0 cryogenic supply and distribution system.

Figure 3.6-166 shows a schematic of the system. Liquid helium is purchased in portable storage Dewars and fed to the cryomodule at 4.3 K via a simple vacuum-insulated transfer line routed from the tunnel roof down to the cryomodule. The 2 K operating temperature of the SPX cavities is achieved by lowering the pressure of the saturated helium bath surrounding the cavities to 3120 Pa (23.4 Torr) using a room-temperature vacuum system. Efficient operation is achieved by cooling the incoming 4.3 K liquid down to about 2.2 K via heat exchange with the 2 K vapor exhaust before throttling the incoming liquid to 3120 Pa, 2 K at a liquid fraction of about 90 percent. Shield cooling for the cryomodule is provided by liquid nitrogen supplied from the existing APS liquid nitrogen distribution system (LNDS) via a simple vacuum-insulated transfer line routed from the tunnel roof down to the cryomodule. The system is designed to accommodate multiple supply Dewars, which are used sequentially, and allow empty Dewars to be replaced without interrupting system operation. A provision for circulating liquid nitrogen-cooled 80 K helium gas through the liquid helium circuit is also envisioned for possible standby operation.

3.6.4.12.5 High-Performance Waveguide Seals

The performance of a waveguide flange seal serving a high-field superconducting, radio-frequency (SRF) cavity is determined by several characteristics. Ideally, a seal is ultrahigh-vacuum leak tight, electrically bridges the inner surfaces of connecting flanges for optimum rf transmission and minimal heating due to trapped modes, acts as a thermal impedance, and is not prone to generate particulate matter during assembly and disassembly. A commercial sealing technology known as VATSEAL may neatly address all of the above requirements.

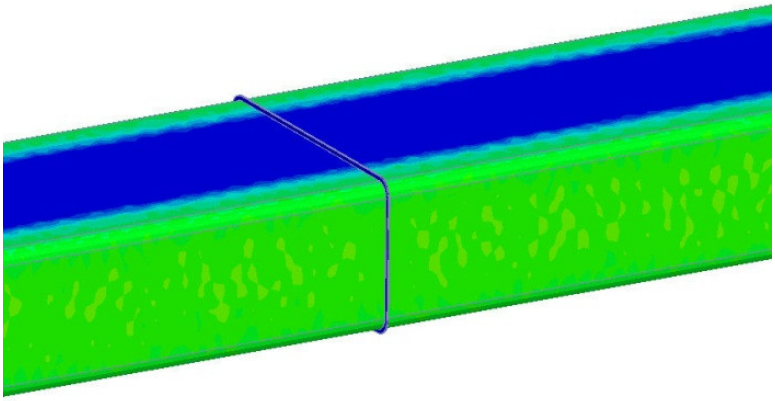

Figure 3.6-167: VATSEAL power loss density.

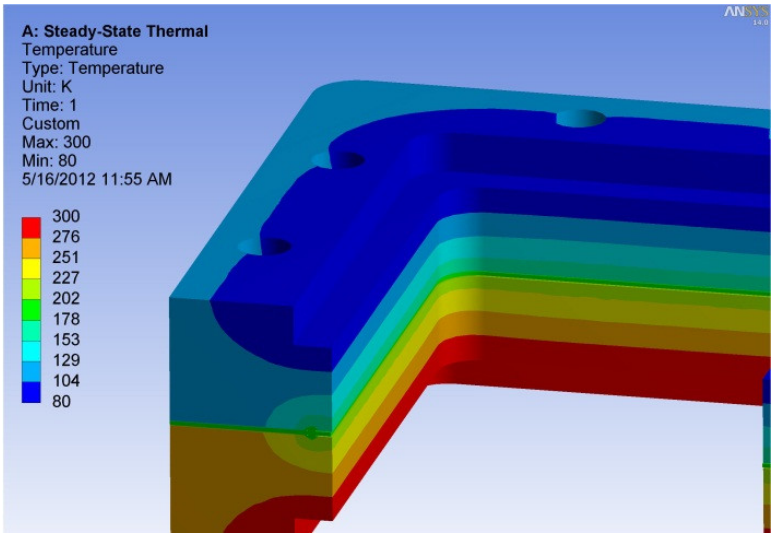

Figure 3.6-168: VATSEAL heat transfer.

Simulations of rf power and conductive heat transfer have been conducted to evaluate the performance of this technology for use in the SPX systems. Figure 3.6-167 is a qualitative depiction of rf power loss density on the surfaces adjoining the interior vacuum space of a WR-284 copper waveguide interrupted by a VATSEAL gasket when provided with 1 kW of power at 2815 MHz. One can see that the losses on the VATSEAL gasket surfaces are similar to those on the broad wall of the waveguide. Of the 4.67

W/m of total calculated losses, only 0.0047 W are deposited on the VATSEAL gasket. Furthermore, reflection due to the VATSEAL was determined to be much less than -30 dB at this frequency. Figure 3.6-168 shows heat transfer through a WR-284 flange connection given fixed waveguide temperatures of 80 K and 300 K on either side, a very conservative assumption. Heat flow through the seal is calculated to be 266 W. One can see that the minimal contact area made by the gasket compensates for the thinness of the material, which is desirable for rf performance.

3.6.4.13 Beam Commissioning

The main objective of the SPX0 commissioning is to perform deflecting cavity tests in a planned and timely manner without disrupting APS user operations. The specific goals of the SPX0 commissioning are as follows:

- Confirm that the APS user operation is possible with installed cavities;
- Confirm that the cavities are protected from damage by the beam;
- Perform beam dynamics experiments in support of the SPX0 project goals.

The first two items above need to be completed during start-up studies before the beginning of the user run. Beam dynamics experiments can be performed later during machine study periods.

Cavities may affect APS user operation in many ways:

- Cavities can change accumulation limit due to additional impedance;
- Cavities can affect vertical beam size due to deflecting fields inside cavities;
- Cavities can affect injection due to combination of some deflecting fields and large beam oscillations;
- Cavities can affect lifetime through some nonlinear fields inside cavities or if increase of chromaticity is required due to decreased accumulation limit.

To ensure that the APS user operation is possible with installed cavities, one needs to check the following items in all fill patterns that are used for operation:

- Injection efficiency is to a degree that prevents top-up operation;
- Lifetime is not affected to a degree that prevents top-up operation;
- Horizontal beam size is not affected by more than 5% ;
- Vertical beam size corresponding to 1.5% emittance ratio is achievable;
- Single-bunch accumulation limit is not affected to a degree that prevents hybrid fill pattern operation;
- Orbit stability is not affected above established APS alarm limits.

Cavities can also affect SR beam studies. For example, they could prevent the creation of large orbits required during orbit response matrix, or prohibit high-current studies. These effects, though important, do not prevent APS user operation, and therefore could be tolerated to some degree.

3.6.4.13.1 Commissioning Plan

The major items of the commissioning are as follows:

1. Perform a set of measurements and preparations before the cavity installation shutdown;
2. Cavity tests after installation in the tunnel without electron beam;
3. Cavity tests with low-current beam and unpowered and detuned cavities;
4. Electron beam tests with unpowered and detuned cavities to ensure that normal user operation is possible;
5. Full-current electron beam tests with powered and on-resonance cavities;
6. Physics experiments to support the SPX project.

The following measurements are required before the cavity installation shutdown to document the machine status:

- Single-bunch accumulation limit in 24 bunches and in hybrid fill modes, with P0 feedback on and off;
- Beam size as a function of current from minimum to 115 mA in 24 singlets;
- Beam size at 102 mA in all fill patterns;
- Beam size in 324 bunches when scraping down from 100 mA to 80 mA;
- Beam size in hybrid when only a 16-mA single bunch is injected;
- Spectrum of the beam motion.

Other preparations include girder alignment in Sectors 5 and 6 (if required) to have straight beam orbit, reduction of corrector strengths in Sectors 5 and 6 and beam position monitor offset measurements to ensure straightness of the orbit around the cavities.

After the cavities are installed but before beginning the beam tests, the cavities will be tested for mechanical integrity, vacuum conditions, and alignment. Cryogenic performance will be tested. Various rf components will be tested as well.

Cavity tests with low-current beam and unpowered and detuned cavities

- Perform first injection—1 to 4 mA in a single bunch, roughly correct beam orbit, establish acceptable injection efficiency;
- Test of HOM/LOM power damping efficiency;
- Test of diagnostics and controls;

- Check beam dump when beam orbit exceeds allowable limits in cavities;
- Check that cavities are not irradiated by SR during normal operation and during studies with large orbit errors by recording temperature rise;
- Measure cavity centers relative to the beam orbit, move orbit to the cavity centers.

The current in these tests is limited to 5 mA in a single bunch.

Electron beam tests with unpowered and detuned cavities to ensure that the user operation is not affected beyond unacceptable limits

- 24 singlets, P0 feedback off:
  - Increase stored beam to 30 mA in 24 singlets
  - Correct orbit using standard orbit correction, save, then dump the beam
  - Perform injection efficiency optimization
  - Check single-bunch accumulation limit, compare it with the measurements before the shutdown
  - Perform rf conditioning (slow increase of stored current from 30 mA to 115 mA over about 20 hours), have beam size measurements available during conditioning
  - Compare beam size measurement to the one before the shutdown
  - Run top-up
- 24 singlets, P0 feedback on:
  - Perform injection efficiency optimization if necessary
  - Check single-bunch accumulation limit, compare it with the measurements before the shutdown
  - Inject 102 mA, run top-up, compare beam sizes
  - 324 bunches, P0 feedback off:
  - Inject 102 mA
  - Slowly (within 1 hour) scrape down beam to 80 mA to check that no instability occurs during beam decay when operating in non-top-up mode. Record beam sizes during the scrape down and compare them with the measurements before the shutdown
  - Hybrid fill pattern, P0 feedback on:
  - Inject first beam—4 mA single bunch
  - Roughly correct orbit
  - Increase stored beam to 30 mA in 24 singlets
  - Correct orbit using standard orbit correction, save, then dump the beam
  - Perform injection efficiency optimization
  - Check single-bunch accumulation limit, compare it with the measurements before the shutdown
  - Compare the beam size at 16 mA with the measurement before the shutdown
  - Inject 102 mA, run top-up, compare beam sizes

Full-current electron beam tests with powered and on-resonance cavities

In these tests, the overall performance of the rf system will be characterized. This includes tuner tests, low-level rf regulation tests under various conditions, cryogenics characterization, high-level rf performance, etc. A complete list of tests will be written later. The tests could be performed during weekly machine studies.

3.6.4.14 Safety Interlock System

3.6.4.14.1 Personnel Protection Interlocks

Potential hazards to personnel from the SPX rf system hardware include rf radiation leakage from open waveguide flanges, contact with high-voltage conductors, and exposure to ionizing radiation generated by the klystrons. The personnel safety system (PSS) controls personnel exposure to these hazards by simultaneously disabling both the LLRF drive to the klystron and the HVPS by dedicated hardware interfaces when unsafe conditions are detected. The PSS interface chassis is designed using simple relay logic for maximum reliability and fail-safe modes. Gas pressure meters are used to monitor positive nitrogen pressure inside the waveguide in order to detect leaking or open waveguide flanges. Loss of waveguide pressure below a minimum set point will constitute a potential hazardous condition and will result in an open contact signal at the PSS main chassis and immediate shutdown of the rf system by two independent and redundant methods. Personnel exposure to high voltage and ionizing radiation is prevented by monitoring klystron amplifier cabinet and HVPS door switches. All access doors and covers on the klystron amplifier cabinet and HVPS must be closed and secured before the PSS system will allow system operation.

3.6.4.14.2 Access Control Interlock System

The SPX0 ACIS will consist of dual redundant programmable logic controllers (PLCs), each configured to a TUV-certified SIL2 configuration in accordance with IEC 61508, Functional Safety of Electrical/Electronic/Programmable Electronic Safety Related Systems.

The SPX0 ACIS will include all hardware, software, and control systems to interface between the storage ring access control interlock system (SR ACIS) and the SPX0 ACIS to enable the two sets of rf systems, each consisting of one HLRF HVPS and one klystron rf driver amplifier (see Figure 3.6-169). The SR ACIS will issue a permit signal to the SPX0 ACIS only when SR Zones A-E are in Beam Permit mode. The SPX0 ACIS will include this permit signal from the SR ACIS in its logic to enable all the SPX0 HVPSs and klystron rf driver amplifiers. The SPX0 ACIS will return feedback signals to the SR ACIS to provide the status of the SPX0 ACIS-controlled rf equipment and its own hardware/software.

The SPX0 ACIS PLC processors and Operator HMI will be located at the SR ACIS operator panel in the APS MCR (see Figure 3.6-170). Communication cabling, approved for safety networks, will connect the PLC processors with a remote PLC chassis installed in one rack in Building 400A. This rack, in room 400-A1, will interface to two HVPS and their associated rf klystron amplifiers driving the superconducting rf deflecting cavities near Sector 5 (see Figure 3.6-171)

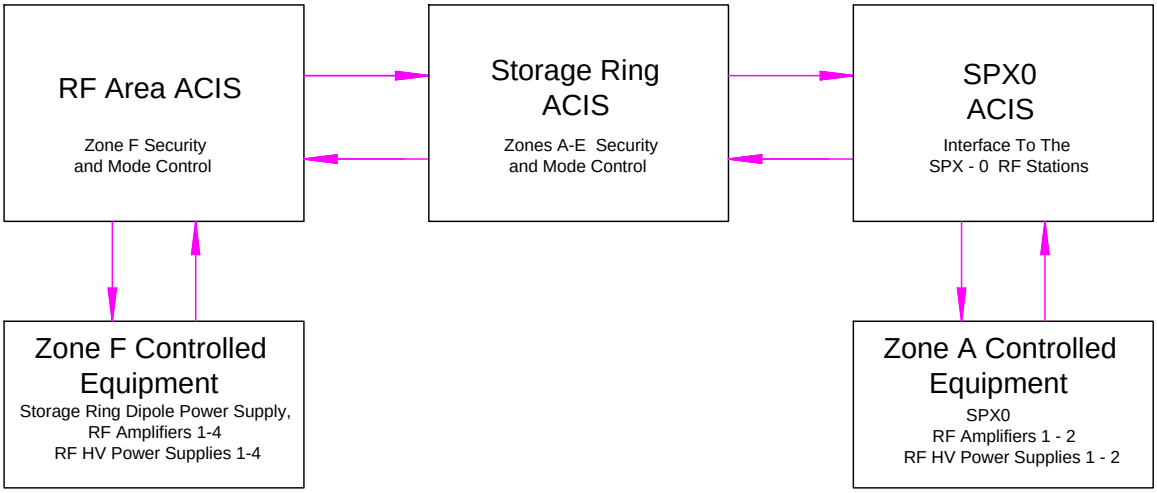

Figure 3.6-169: Functional Relationship to other ACISs.

3.6.5 References

[3.6-1] M. Sands. The Physics of Electron Storage Rings: An Introduction. SLAC Report SLAC-121, SLAC, (1979).

[3.6-2] V. Sajaev. Longitudinal bunch profile. APS web site, (2008). http://www.aps.anl.gov/asd/oag/SRparameters/node6.html.

[3.6-3] Y.-C. Chae et al. Measurement of the Longitudinal Microwave Instability in the APS Storage Ring, Proc. of PAC 2001, pp. 1817–1819, (2001).

[3.6-4] M. Borland. A Very Preliminary Analysis of Using a Harmonic Cavity in the APS. Technical Report OAG-TN-2004-003, APS, (2004).

[3.6-5] J. Feikes et al. Sub-picosecond electron bunches in the BESSY storage ring, Proc. of EPAC 2004, pp. 1954–1956, (2004).

[3.6-6] K. Satoh and Y. Chin. Transverse mode coupling in a bunched beam, Nuclear Instruments and Methods in Physics Research A, **207**, 309–320, (1983).

[3.6-7] M. Bei et al. The Potential of an Ultimate Storage Ring, Nuclear Instruments and Methods in Physics Research A, **622**, 518, (2010).

[3.6-8] C. Limborg. *Ultimate brilliance of storage ring based synchrotron facilities of the* 3^{rd} *generation*. PhD thesis, University Joseph Fourier, Genoble, France, (1996).

[3.6-9] A. A. Zholents and M. S. Zolotorev. Femtosecond X-Ray Pulses of Synchrotron Radiation, Phys. Rev. Lett., **76**(6), 912–915, (1996).

[3.6-10] R. W. Schoenlein et al. Generation of Femtosecond Pulses of Synchrotron Radiation, Science, **287**(5461), 2237–2240, (2000).

[3.6-11] A. A. Zholents, ANL, (2010). Private communication.

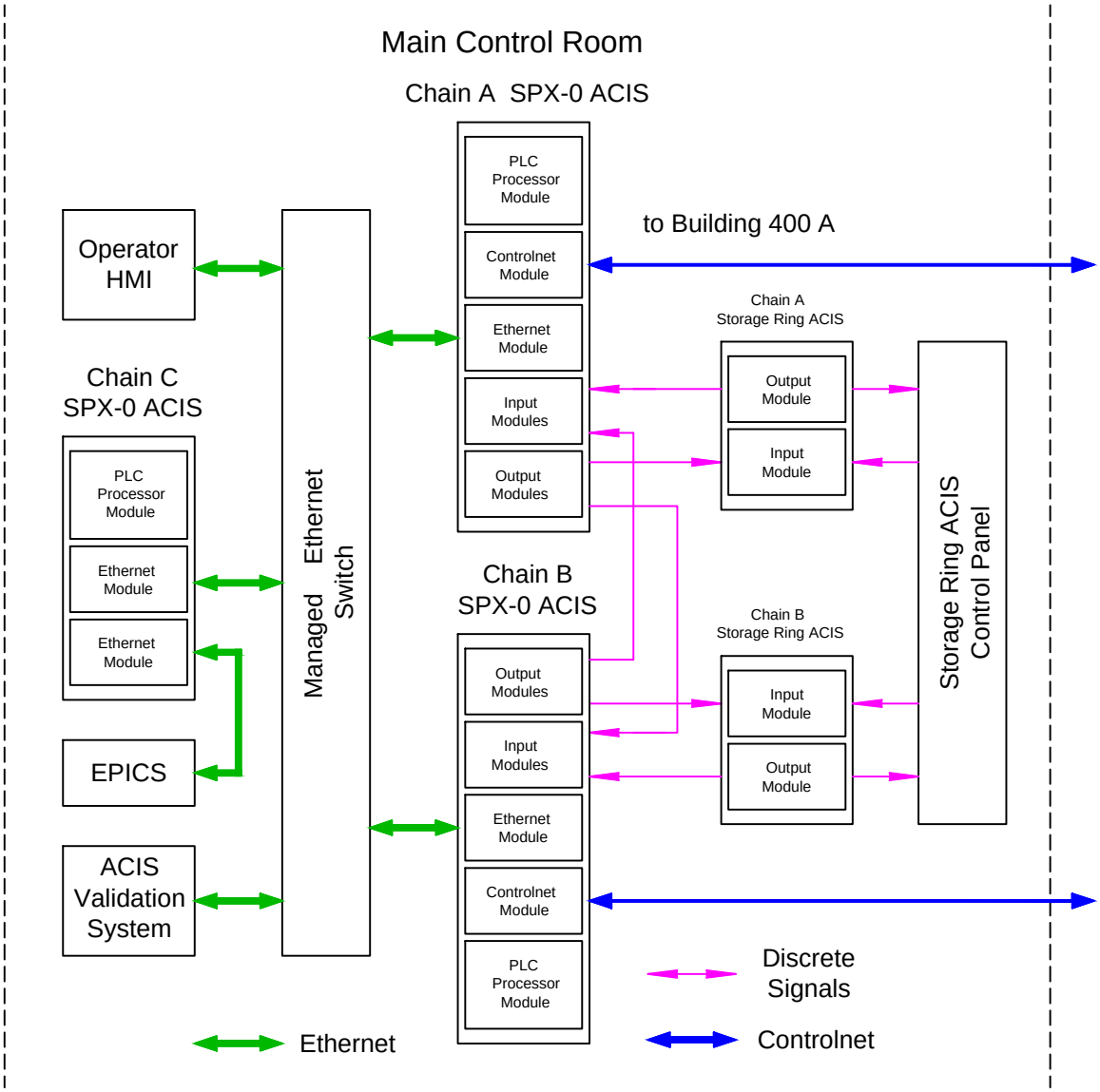

Figure 3.6-170: SPX0 ACIS MCR equipment block diagram.

[3.6-12] A. Zholents and K. Holdack. Energy Modulation of the Electrons by the Laser Field in the Wiggler Magnet, Proc. of FEL 2006, pp. 725–727, (2006).

[3.6-13] Y. Li, ANL, (2010). Private communication.

[3.6-14] T. Y. Fan, (2009). Private communication.

[3.6-15] G. Wüstefeld, A. Jankowiak, J. Knobloch, and M. Ries. Simultaneous long and short electron bunches in the BESSY II storage ring, Proc. of IPAC2011, pp. 2936–2938, (2011).

[3.6-16] V. Sajaev. http://www.aps.anl.gov/asd/oag/SRparameters/SRparameters.html, (2009).

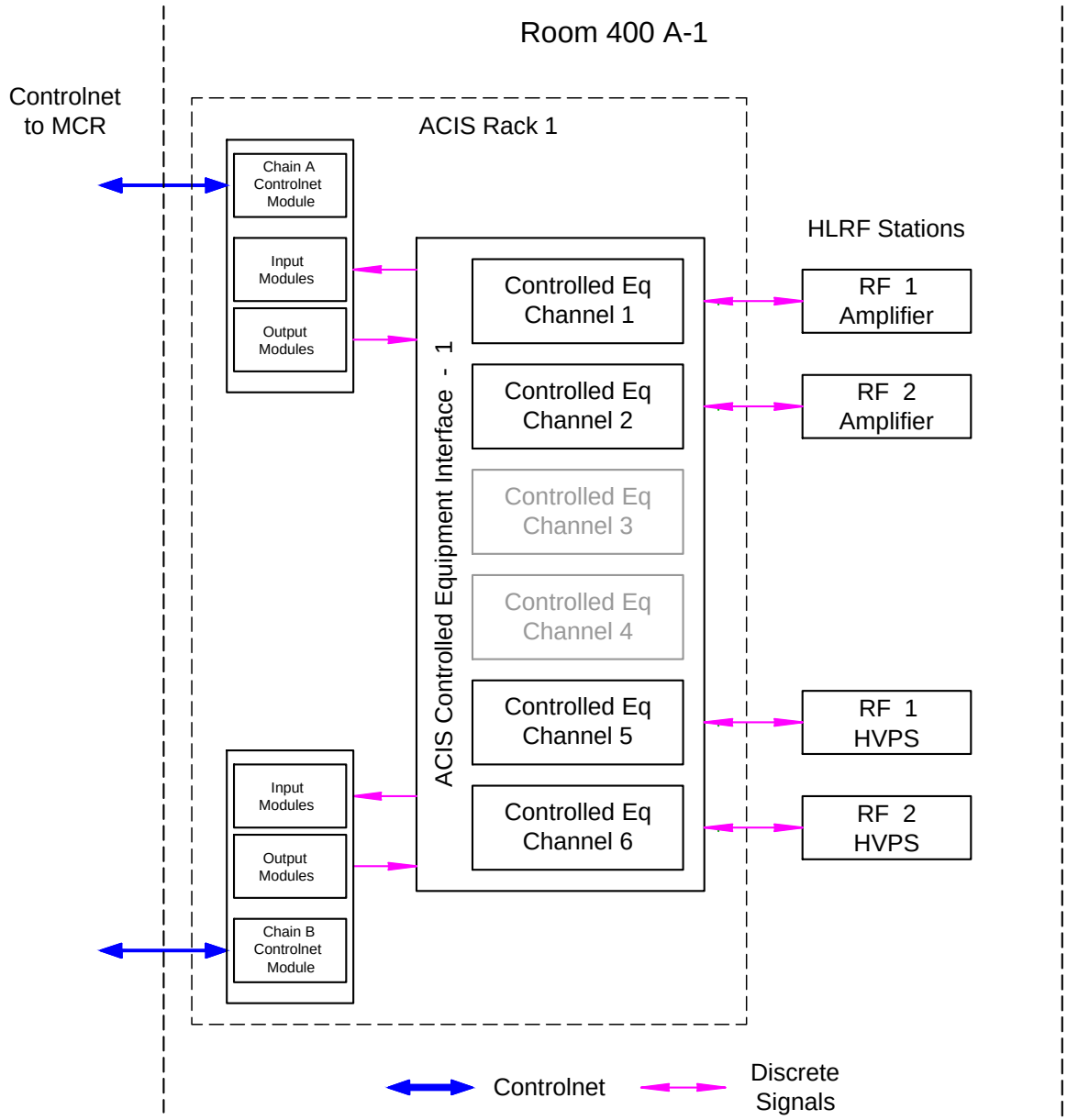

Figure 3.6-171: SPX0 Building 400 A equipment block diagram.

[3.6-17] M. Borland et al. SDDS-Based Software Tools for Accelerator Design, Proc. of PAC 2003, pp. 3461–3463, (2003).

[3.6-18] A. Zholents et al. Generation of subpicosecond X-ray pulses using RF orbit deflection, Nuclear Instruments and Methods in Physics Research A, **425**, 385, (1999).

[3.6-19] M. Borland and V. Sajaev. Simulations of x-ray slicing and compression using crab cavities in the Advanced Photon Source, Proc. of PAC 2005, pp. 3886–3888, (2005).

[3.6-20] M. Borland. Effect of Increased Beta Functions for Closed Chirp Bump. Technical Report OAG-TN-2005-026, APS, (2005).

[3.6-21] K. J. Kim. Characteristics of Synchrotron Radiation. M. Month and M. Dienes, editors, AIP Conference Proceedings 184, pp. 565–632. AIP, (1989).

[3.6-22] T. Fujita et al. Overview of Short-Pulse X-ray Generation Using Crab Cavities at SPRING-8, Proc. of ICAP 2010, pp. 39–41, (2010).

[3.6-23] T. Berenc. Storage Ring RF System Phase Noise Studies. Technical Report ICMS-APS-1414611, APS, (2010).

[3.6-24] T. Berenc. Storage Ring RF System AM & PM Noise Studies Report. Technical Report ICMS-APS-1416636, APS, (2010).

[3.6-25] SPX Study Meeting. APS web site, (2010). http://www.aps.anl.gov/Accelerator_Systems_Division/SPX_Meeting.

[3.6-26] T. Berenc. Introduction to RF System Noise Propagation for SPX. Technical Report ICMS-APS-1412274, APS, (2010).

[3.6-27] G. Decker. APS-U Beam Stability Physics Requirements Document. Technical Report APS_1427507, APS, (2012).

[3.6-28] L. Young and M. Borland. APS, Email exchange related to beam motion and emittance increase, (2011). APSU_1426487.

[3.6-29] T. Berenc. An Equivalent Circuit Model and Power Calculations for the APS SPX Crab Cavities. Technical Report ICMS-APS-1405978, APS, (2011).

[3.6-30] T. Berenc, et. al. Recommendation for SPX0 Cavity Vertical Alignment Tolerance. Technical Report ICMS-APSU_1427530, APS, (2012).

[3.6-31] V. Sajaev. APS-U Planar Undulator Physics Requirements Document. Technical Report APS_1423843, APS, (2012).

[3.6-32] R. L. B. Yang, G. Decker. Physics Requirements of the SPX Electron Beam Diagnostics - An Initial Discussion. Technical Report DIAG-TN-2010-012, APS, (2010).

[3.6-33] M. Borland. Simulation and analysis of using deflecting cavities to produce short x-ray pulses with the Advanced Photon Source, Phys. Rev. ST Accel. Beams, **8**(7), 074001, (2005).

[3.6-34] A. Piwinski. Synchrotron sidebands of betatron coupling resonances. Technical Report DESY 93-189, DESY, (1993).

[3.6-35] M. Borland. elegant: A Flexible SDDS-Compliant Code for Accelerator Simulation. Technical Report LS-287, Advanced Photon Source, (2000).

[3.6-36] Y. Wang et al. Recent Progress on Parallel ELEGANT, Proc. of ICAP 2009, pp. 355–358, (2009).

[3.6-37] M. Borland et al. Beam Dynamics, Performance, and Tolerances for Pulsed Crab Cavities at the Advanced Photon Source for Short X-Ray Pulse Generation, Proc. of PAC 2007, pp. 3429–3431, (2007).

[3.6-38] H. Wiedemann. *Particle Accelertor Physics*, 2nd ed., volume I. Springer, (1998).

[3.6-39] E. Dufresne, (2011). Private communication.

[3.6-40] H. Shang. sddsurgent software based on US by R. Dejus and URGENT by R. Walker, http://www.aps.anl.gov/Accelerator_Systems_Division/Operations_Analysis/manuals/elegant_latest/node89.html.

[3.6-41] T. Tanaka and H. Kitamura. J. Synch. Rad., **8**, 1221–1228, (2001).

[3.6-42] R. Siemann. Instability Growth Rate Calculations for High Energy Storage Rings, Proc. PAC 1981, pp. 2437–2439, (1981).

[3.6-43] J. Hagel and B. Zotter. PC-BBI, A Program to Compute Bunch Beam Instabilities on a PC. CERN SL-AP 90-62, CERN, (1990).

[3.6-44] L. Emery. Coupled-Bunch Instabilities in the APS Ring, Proc. of PAC 1991, p. 1713, (1991).

[3.6-45] L. Emery. Required Cavity HOM DeQing Calculated from Probability Estimates of Coupled Bunch Instabilities in the APS Ring, Proc. of PAC'93, p. 3360, Washington DC, (1993); http://www.JACoW.org.

[3.6-46] L. Emery. Instability Estimates for Three-Cell Deflecting Mode Cavities. Technical Report OAG-TN-2007-023, APS, (2007).

[3.6-47] L. Emery. Monte Carlo Instability Calculations for Three-Cell Deflecting Mode Cavities. Technical Report OAG-TN-2007-024, APS, (2007).

[3.6-48] K. Thompson and R. D. Ruth. Transverse coupled bunch instabilities in damping rings of high-energy linear colliders, Phys. Rev., **D43**, 3049–3062, (1991).

[3.6-49] L. Emery. User's Guide to Program clinchor. http://www.aps.anl.gov/Accelerator_Systems_Division/Operations_Analysis/manuals/clinchor_V1.0/clinchor.html.

[3.6-50] Y.-C. Chae et al. The Wakefield Effects of Pulsed Crab Cavity at the Advanced Photon Source for Short X-ray Pulse Generation, Proc. of PAC 2007, p. 4339, (2007).

[3.6-51] J. M. Byrd et al. Femtosecond synchronization of laser systems for the LCLS, Proc. BIW 2010, pp. 58–62, (2010).

[3.6-52] R. Wilcox et al. Stable transmission of radio frequency signals on fiber links using inteferometric delay sensing, Optics Letters, **34**(20), 3050–3052, (2009).

[3.6-53] T. Abe et al. Beam Operation with Crab Cavities at KEKB, Proceedings for the 1997 Particle Accelerator Conference, pp. 1487–1489, (2007).

[3.6-54] G. Burt. New Cavity Shape Developments for Crabbing Applications. Technical Report EuCARD-CON-2009-016, European Coordination for Accelerator Research and Development, (2010).

[3.6-55] K. Hosoyama et al. Development of the KEK-B Superconducting Crab Cavity, Proc. of EPAC 2008, pp. 2927–2931, (2008).

[3.6-56] G. Waldschmidt. SC Deflecting Cavity LOM/HOM Dampers. Technical Report RF-TN-2008-001, APS/ASD/RF, (2008).

[3.6-57] S. Kim et al. Higher-order-mode (HOM) Power in Elliptical Superconducting Cavities for Intense Pulsed Proton Accelerators, NIM, **492**, 1–10, (1991).

[3.6-58] H. Padamsee. *RF Superconductivity for Accelerators*. John Wiley & Sons, Inc., (1998).

[3.6-59] F. Marhauser. Investigations on Absorber Materials at Cryogenic Temperatures, Proc. of PAC 2009, pp. 2799–2801, (2009).

[3.6-60] B. Brajuskovic et al. Thermomechanical Design of Normal-Conducting Deflecting Cavities at the Advanced Photon Source for Short X-ray Pulse Generation, Proc. of PAC 2007, pp. 3827–3829, (2007).

[3.6-61] G. Waldschmidt. Variations of the Three-Cell SC Deflecting Cavity With a Comparison of a Single-Cell Cavity Design. Technical Report RF-TN-2008-002, APS/ASD/RF, (2008).

[3.6-62] H. Wang et al. Crab Cavity and Cryomodule Prototype Development for the Advanced Photon Source, Proc. of PAC 2011, (2011).

[3.6-63] N. Ohuchi et al. Plan of the S1-Global Cryomodules for ILC, Proc. of PAC 2009, pp. 2790–2792, (2009).

[3.6-64] R. A. Rimmer et al. JLAB CW Cryomodules for 4th Generation Light Sources, Proc. of SRF 2007, pp. 288–292, (2007).

[3.6-65] M. Liepe et al. The Cornell High-Current ERL Injector Cryomodule, Proc. of SRF 2009, (2009).

[3.6-66] T. Hiatt et al. Cryogenic Testing of the RF Input Waveguide for the CEBAF Upgrade Cryomodule, Proc. of PAC 2001, pp. 1155–1157, (2001).

[3.6-67] N. Sereno et al. Impact of Longitudinally Tilted Beams on BPM Performance at the Advanced Photon S ource, Proc. of BIW 2012, (2012).

[3.6-68] S. J. Pasky et al. LINAC Automated Beam Phase Control System, Proceedings of LINAC 2006, pp. 241–243, (2006).

[3.6-69] N. S. Sereno et al. Automated correction of phase errors in the Advanced Photon Source linac, Phys. Rev. ST Accel. Beams, **11**(7), 072801, (2008).

[3.6-70] W. Guo et al. Generating Picosecond X-ray Pulses with Beam Manipulation in Synchrotron Light Sources, Proc. PAC 2005, pp. 3898–3900, (2005).

[3.6-71] V. Sajaev, (2011). Physics Requirement of the SPX Systems.

[3.6-72] L. E. B.X. Yang, A. H. Lumpkin and M. Borland. Recent developments in measurement and tracking of the APS storage ring beam emittance, Proceedings of the 2000 Beam Instrumentation Workshop, pp. 622–624, (2000).

[3.6-73] B. K. Scheidt. Measurement of Vertical Emittance with a System of Six In-Air-X-Ray Projection Monitors at the ESRF, Proc. of DIPAC 2007, pp. 72–74, (2007).

[3.6-74] H. Sakai et al. Phys. Rev. STAB, **10**, 042801, (2007).

[3.6-75] F. Ewald et al. Vertical emittance measurement at the ESRF, Proc. of DIPAC 2011, pp. 188–190, (2011).

[3.6-76] B. Lengeler et al. Nucl. Instr. and Meth. in Phys. Res. A, **467-468**, 944–950, (2001).

[3.6-77] V. Sajaev. Orbit angle jitter effect on pulse arrival time in SPX/SPX0. Technical Report AOP-TN-2012-015, APS, (2012).

[3.6-78] E. Dufresne. Acceptable Jitter for the 7ID Beamline Laser and SPX Cavity Synchronization. Technical report, APS/XSD, (2012). APSU_1427902.

[3.6-79] V. Sajaev, (2011). Private communication.

[3.6-80] A. Xiao and M. Borland. Touschek Effect Calculation and Its Application to a Transport Line, Proc. of PAC 2007, pp. 3453–3455, (2007).

[3.6-81] L. Emery, (2012). Private communication.

[3.6-82] G. Decker, (2012). Private communication.

[3.6-83] V. Sajaev and L. Emery. Determination and Correction of the Linear Lattice of the APS Storage Ring, Proceedings of the 2002 European Accelerator Conference, pp. 742–744, (2002).

[3.6-84] V. Sajaev, (2012). Private communication.

[3.6-85] P. Elleaume. A New Approach to Electron Beam Dynamics in Undulators and Wigglers, Proc. of EPAC 1992, pp. 661–663, (1992).

[3.6-86] R. Pendleton et al. Broadband, Multi-Kilowatt, Vacuum, HOM Waveguide Loads for the PEP-II RF Cavity, Proc. of EPAC 1994, pp. 2013–2015, (1996).

[3.6-87] S. Sakanaka. Development of a Broadband HOM Load for the 714-MHz HOM-Damped Cavity, Proc. of PAC 1997, pp. 2983–2985, (1998).

[3.6-88] G. Waldschmidt et al. Superconducting Cavity Design for Short-Pulse X-Rays at the Advanced Photon Source, Proc. of PAC 2011, pp. 2516–2518, (2011).

3.7 Higher-Current Operation

3.7.1 Introduction

The nominal APS operating current is 100 mA. The brightness and flux are directly proportional to the beam current, which provides a clear path to delivering higher-brightness hard x-rays, an important component of the mission.

The planned operating current after the upgrade is 150 mA. The high-current threshold in the ring has been explored, and it was determined that no accelerator upgrades are required for 150-mA operation. High current (150 mA) is routinely scheduled 2-3 times a year during machine intervention/study periods to optimize storage ring operating parameters for the upgrade.

To establish the performance margin above 150 mA, storage ring components have been identified that either drive collective instabilities through the interaction of wakefields with the beam, or are subjected to excessive beam-driven wakefield heating. Two components, the higher-order mode (HOM) dampers and the vertical diagnostic scraper chambers, presently limit higher-current operation above 150 mA, especially in 24-bunch mode. One of the vertical scraper chambers will be removed in Sept 2012.

The accelerator could operate today at 150 mA, but the front ends (FEs) and x-ray beamlines must be upgraded to overcome present thermal limitations. Details on the FEs are discussed in Chapter 6.2.

In this section, we review the safety envelope, present accelerator capabilities, relevant past work, and related on-going operations-funded efforts. The performance margins are also discussed for the different standard user operating modes.

3.7.2 Safety Envelope

Operation at 150 mA is within the operating envelope, which is itself within the safety envelope, as defined in the APS Safety Assessment Document (SAD) [3.7-1]. The SAD operating envelope gives a maximum stored beam current of 300 mA at 7.0 GeV and a maximum top-up injection charge per cycle of 10 nC. Presently, the top-up injection charge is 3 nC. It is expected that in the upgraded lattice, 3 nC will be sufficient to maintain the stored current with top-up injection. Top-up safety tracking will be repeated per the SAD and Accelerator Systems Division procedures.

3.7.3 Present Capabilities and Configuration

First, the present capabilities and configuration of the APS systems are described. Also included is background on how the present capabilities were developed. This helps to set the stage for discussion of the accelerator performance margin in the various user operating modes above 150 mA.

For nominal, 100-mA operation, two 1.1-MW, 351.93-MHz klystrons are required to drive the 16 radio-frequency (rf) cavities, with each klystron delivering approximately 650-kW rf output power. Operation at 150 mA can be achieved with two klystrons operating at nearly full-rated power output, approximately 800 kW to 1 MW each, depending on the total gap voltage required. Alternatively, up to four klystrons can be used at lower power when operated in a parallel configuration [3.7-2]. The average individual klystron output power and average cavity input power were measured for high current with ID gaps open; these data are shown in Figure 3.7-1. For user operation, the rf power is higher due to the additional ID radiation energy loss; the amount depends on the ID gaps. The ID reference gaps are a standardized set of ID gaps that are used regularly to reproduce user beam alignment. The average measured klystron and cavity power at 100 mA with the ID reference gaps are shown at the maxima of the solid gray bars, respectively, on the figure. The ID power increment was scaled by 50 percent to estimate the power at 150 mA, shown at the maxima of the a broken gray bars.

The rf system is expected to handle 150-mA operation within the design limits of 1.1-MW klystron power and 180-kW coupler power (based on the original LEP design [3.7-3]). The overall reliability of the rf systems will be reduced to some degree when operating at greater than 100-mA stored beam. Reasons for this reduced reliability include operation of the cavity input couplers closer to their design power rating and operation of the klystrons at or near their maximum rf power output. Alternately, more than two klystrons can be operated in a parallel configuration with partial or total loss of rf

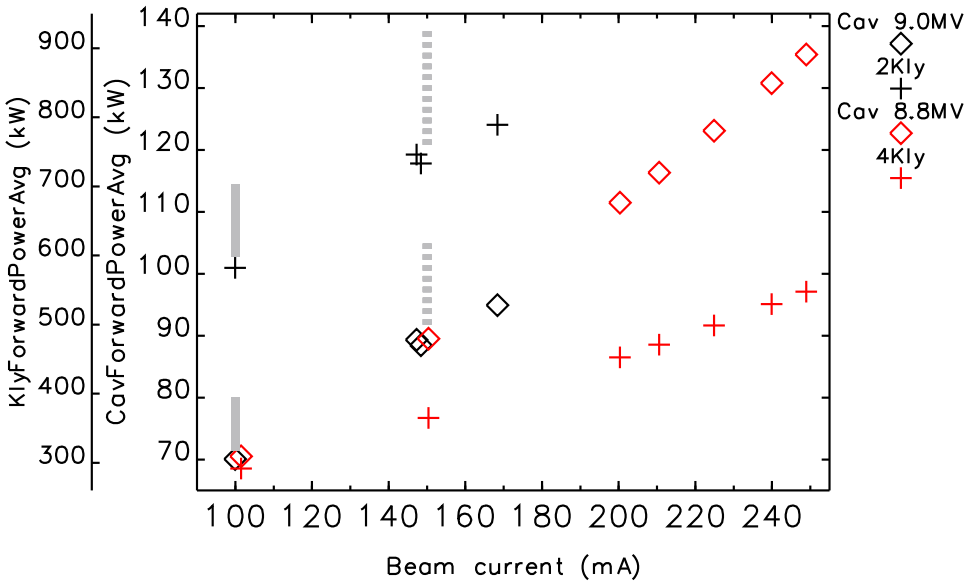

Figure 3.7-1: Average cavity input power (with 16 cavities) and average klystron output power (with 2 or 4 klystrons) for high current and ID gaps open (symbols, see legend). The 4-klystron data shown were with 324 bunches, and the 2-klystron data were with 24 bunches or hybrid mode. The rf power with ID reference gaps is shown with the solid gray bars; the estimated rf power at 150 mA with ID reference gaps is shown with the broken gray bars.

system redundancy, but this is not required for 150 mA. Ongoing or planned programmatic efforts to address rf system reliability are discussed later.

As described in section 3.1.1, the APS presently operates in various fill patterns, all of which will be retained for 150-mA operation. Higher-current operation has been tested using four klystrons with beam stored in the 24-bunch and 324-bunch user operating modes, both of which have uniform bunch current and bunch spacing. Top-up injection was operated several times for up to 90 min with 24 bunches. Higher-current operation has also been tested for the hybrid bunch mode using only two klystrons. In all these tests, the ID gaps were open, the chromaticity was high (i.e., 10 units in each plane) and the bunch-by-bunch feedback system was off. The maximum current and the reason for the limitation at maximum current are summarized in Table 3.7-1. The vertical scraper chamber in Sector 36, whose temperature rise is the main limitation at higher current in 24-bunch mode, is scheduled to be removed in September 2012. For a complete description of the operating modes, see reference [3.7-4].

The high-current thresholds are dominated by longitudinal effects, either rf-cavity longitudinal HOM-driven coupled-bunch instabilities (CBIs) or heating by longitudinal wakefields in various accelerator components, e.g., the vertical scraper chamber. HOM dampers are installed on 4 of the 16 rf cavities to damp the dominant CBI modes. With 324 bunches, the CBI threshold is 245 mA. CBIs were not observed at the current limit with 24 bunches but could occur at higher current. With 24 bunches, several components are approaching temperature limits above 160 mA, including the rf couplers and the HOM dampers themselves. In the hybrid mode, higher current was limited by klystron power in two-klystron operation. The performance margin of <15 mA is smallest for 24 bunches; this margin is expected to increase with the removal of the Sector 36 vertical scraper chamber. The margin is >20 mA for hybrid mode (with two klystrons), and is highest for 324 bunches, at 95 mA. The heating issues are

Table 3.7-1: Maximum stable total current for all operating modes. These results are with high chromaticity and HOM dampers installed, using four klystrons in parallel, unless noted.

Operating mode (no. bunches)	Current limit (mA)	Performance margin (mA)	Limitation at maximum current
24	164	< 15	Heating[a]
324	245	95	CBI (longitudinal)
hybrid	170[b]	> 20	–[c]

[a] Rf coupler, vertical scraper chamber, and rf cavity HOM damper (1 of 4).
[b] Tested with two klystrons only near maximum output power.
[c] To be determined using all four klystrons.

discussed later in more detail.

Transverse multibunch instabilities are driven by the long-range wakefields such as that produced by the resistive wall impedance, while single-bunch instabilities are driven by the short-range wakefields such as that produced by the ID chamber geometric impedance. A transverse bunch-by-bunch feedback system is used in combination with positive chromaticity to stabilize the beam transversely [3.7-5]. The nominal storage ring operating parameters for transverse stability at 100 mA are summarized in Table 3.7-2. The feedback system is not required for the 324-bunch mode because of the low bunch current. In anticipation of higher-current operation, the feedback system amplifier power was recently increased. Studies show that after increasing the amplifier power, stable beam with a single-bunch accumulation limit above 9 mA was achieved with a chromaticity of 3 in both the x- and y-planes. This is sufficient to support the planned 150-mA 24-bunch mode operation of the APS Upgrade.

Table 3.7-2: Nominal storage ring operating parameters for transverse stability at 100 mA.

Operating mode (no. bunches)	Chromaticity (each plane)	Transverse feedback operation status
24	3.5	ON
324	3.5	OFF
hybrid	9	ON

A number of improvements have already been implemented to address heating and/or impedance issues, namely, redesign of the ceramic injection kicker magnet chambers [3.7-6] and installation of HOM dampers in the rf cavities [3.7-7]. After a brief summary of these past improvements, the present high-current limits are discussed with these improvements in place.

3.7.3.1 Past Improvements

3.7.3.1.1 Ceramic Kicker Vacuum Chambers

The four pulsed-injection kickers are mounted over ceramic vacuum chambers. With high-bunch currents like the 24-bunch mode, elevated temperatures were measured on the flanges, vacuum chambers, and attached bellows. The original resistive paste coating was found to be inadequate or damaged, resulting in heating effects that are proportional to the square of the bunch current [3.7-8]. Improvements in the design included improving the rf finger contact and metalizing the inner surface with moly-manganese to a thickness of about 10 microns [3.7-6]. The improvement can be seen in Figure 3.7-2, showing 324-bunch non-top-up operation followed by 24-bunch top-up operation before and after the redesign. The plot on the left includes blowers and water cooling of the flanges.

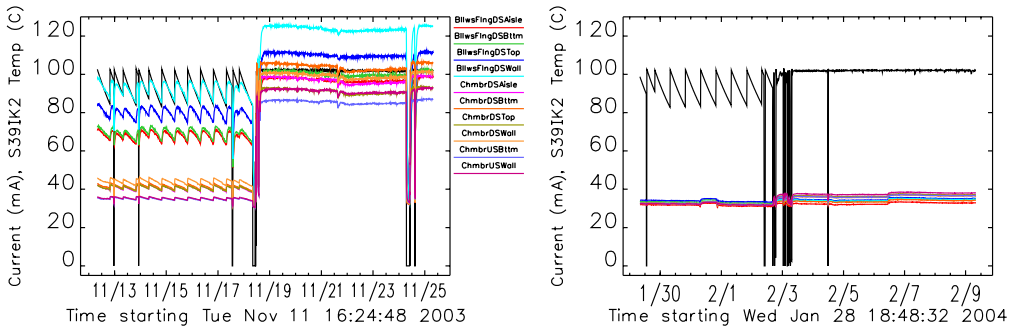

Figure 3.7-2: Kicker chamber temperatures before (left) and after (right) redesign, each showing a one-week period of non-top-up, 324-bunch operation followed by a one-week period of top-up, 24-bunch operation (nominal 100 mA). The black curve is the beam current.

3.7.3.1.2 HOM Dampers

Rf cavity HOMs have long been known to potentially drive longitudinal CBIs in the APS storage ring [3.7-9–3.7-11]. To reduce the effects of the HOMs, the physical lengths of each of the rf cavities were staggered by 0.3 mm during initial construction.

Operationally, the instability threshold was found to be strongly bunch-pattern dependent [3.7-12, 3.7-13]. In 24-bunch operation, the lowest monopole HOM near 538 MHz was found to drive a CBI with a threshold of about 85 mA. This threshold is consistent with a predicted threshold of 80 mA for this HOM for a uniformly filled ring [3.7-9]. Initially, the beam was stabilized for 100-mA operation through a combination of adjusting the cavity cooling water temperature (regulated in sets of four cavities) and, if necessary, detuning the offending cavities. These are standard methods to shift the HOM frequency by changing the cavity volume, which can shift the HOM out of resonance with the beam.

A program (1999–2005) to move storage ring straight-section girders inboard in order to minimize bending magnet radiation pollution of the insertion device x-ray BPMs [3.7-14] had an unanticipated effect on CBI mitigation. The girder displacements were accompanied by an rf frequency evolution to

compensate for the circumference change. As a greater number of girders were displaced, it became more and more difficult to mitigate the CBIs using the standard methods. The total frequency shift was almost 10 kHz, which is many times the synchrotron frequency. It was also found that in some bunch patterns, e.g., the 324-bunch mode, instabilities were observed at certain values of the rf voltage, which is typically set to a value between 8.5 MV to 9.5 MV to optimize the momentum aperture and lifetime.

The situation led to the design and installation of HOM dampers on four of the 16 cavities to damp the 538-MHz mode. Design and manufacturing considerations for the rf cavity HOM dampers are discussed in refs. [3.7-15, 3.7-16], and details of the damper testing and installation can be found in ref. [3.7-7]. The 538-MHz HOM has a strong electric field component along the equatorial plane of the cavity, and a standard coaxial electric-probe damper with a ceramic lossy load was chosen for the design, shown schematically in Figure 3.7-3, left. Since the radial component of the fundamental accelerating mode is zero along the mid-plane, no rejection filter was needed to prevent excessive deQing of the fundamental. The ceramic load is made of AlN with 40% SiC.

Low-power testing of the dampers agreed well with the simulation models. High-power testing of the dampers, as well as conditioning of the damper ceramic load, were performed at the APS 352-MHz rf test stand. During the conditioning process, multipacting was detected on the surface of the damper probe and occurred along the length of the probe that passed through the cavity port (see Figure 3.7-3, right). This multipacting issue was resolved by coating the probes with approximately 10 nm of titanium.

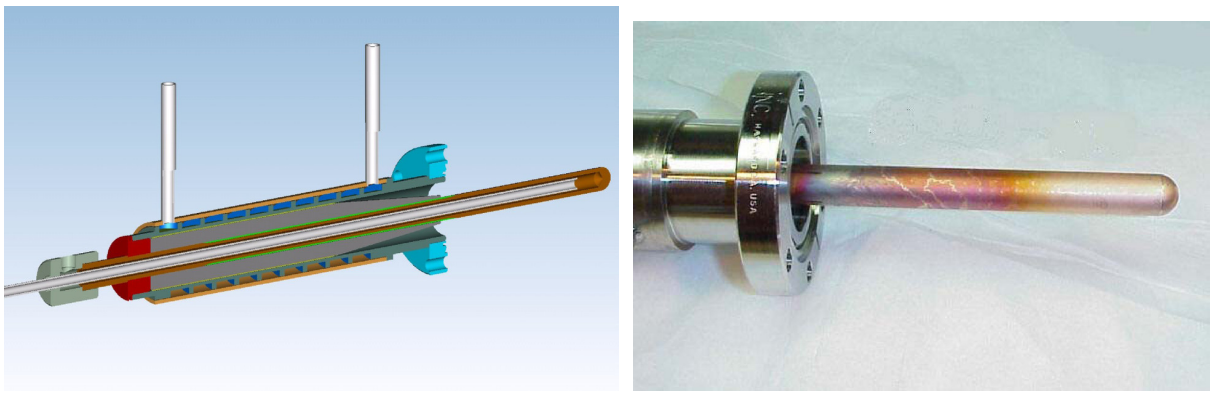

Figure 3.7-3: (Left) Mechanical design of present damper. (Right) Coaxial damper with probe discoloration due to multipacting during high-power conditioning.

Separate flow meters and resistive thermal devices (RTDs) were attached to each water circuit for each of the dampers to monitor the heat load. The flow rates, RTD temperature readings, and the calculated power absorption levels are continuously monitored by a Kyoto programmable logic controller (PLC) that is remotely accessed by EPICS [3.7-17].

Once installed, the dampers performed as expected. With 100-kW fundamental input power, there was no detectable power loss in the damper ceramic. The damper center probe dissipated 240 W, which compares closely with the calculated values [3.7-7]. Since the installation of the dampers, instabilities resulting from the 538-MHz HOM are rarely observed up to 100 mA with the nominal bunch patterns (exceptions are generally for nonstandard machine conditions). However, due to the frequency shift of the HOM by the insertion of the damper, the operating conditions that previously produced the instability cannot be recreated and directly compared.

Many studies have been performed, and it is believed that the dampers have increased the storage ring CBI threshold current by at least 60% over undamped cavities for nominal machine conditions, at which point either other HOMs dominate, or the 538-MHz HOMs in other cavities contribute to driving the beam. The HOM dampers have enabled stable 100-mA operation with greater flexibility (i.e., over a range of rf voltages and without cavity detuning) for the standard bunch patterns for the nominal operating conditions.

There are a number of issues with the present HOM damper configuration. Instabilities are sometimes observed when operating at 100 mA with fewer than the nominal 16 cavities, or with 324 bunches at lower values of the rf voltage. Some nonstandard bunch patterns, such as 14 bunches, have a CBI driven by a HOM near 920 MHz, which is not damped. Exploration of high beam current or other nonstandard bunch patterns has shown that the HOM dampers themselves can be subjected to excessive heating.

3.7.3.2 Longitudinal Limits

A total current of at least 164 mA can be stored stably in 24 bunches. CBIs are not observed up to this current; the HOM dampers appear to have raised the threshold by at least 60 percent compared to undamped cavities. However, several storage ring components approach their temperature or absorbed-power limits above about 160 mA (see Table 3.7-1 and Figure 3.7-4). In the figure, 324 bunches were stored in the period up to 8:00 hours (h) and between 15:45 h and 17:15 h; otherwise 24 bunches were stored. Beam stability was monitored as were the temperatures of hundreds of accelerator components as higher current was stored. The highest-temperature components are included in the figure. The Sector 36 vertical diagnostic scraper chamber body temperature is shown in red. The green and blue curves show the power absorbed by the Sector 38 cavity 3 and cavity 4 HOM dampers, respectively.

The Sector 36 vertical scraper chamber reached high temperatures with high current in 24 bunches. The cavity 4 damper absorbed higher power with 24 bunches, whereas the cavity 3 damper absorbed higher power with 324 bunches. The Sector 37 cavity 4 rf power input coupler downstream/upstream temperatures (turquoise/magenta) showed a large differential of almost 50°C in high-current 24-bunch operation; it is expected that the coupler heating can be mitigated with rf conditioning. It is noted that the ceramic kicker chambers did not reach high temperatures during this test.

The Sector 36 vertical scraper chamber, whose temperature rise is the main limitation at higher current in 24-bunch mode, is scheduled to be removed in September 2012. During a recent 150-mA high-current study (April 2012), the temperature of this scraper chamber body reached temperatures higher than that shown in Figure 3.7-4. The temperatures of the second vertical diagnostic scraper chamber in Sector 38 remain below the limits specified for this component at high current.

With 324 bunches, the beam is stable up to about 245 mA. Above the instability threshold, the beam spectrum clearly shows a CBI signature. The CBI can also be induced with nonstandard operating conditions even at lower current: for example, at 100 mA and reduced rf voltage of 8.5 MV.

For the latter case, an analysis of the CBI modes can determine which cavity HOMs are responsible for driving the beam. Since the bunch spacing is four rf buckets, the beam spectrum has a four-fold degeneracy, as if the rf frequency were $f_{\mathrm{rf}}/4$. Thus the frequency range of any spectrum measurement only needs to be $f_{\mathrm{rf}}/4$ (or $f_{\mathrm{rf}}/8$ since the upper half of the $f_{\mathrm{rf}}/4$ spectrum is a reflection of the lower half). The coupled-bunch mode numbers are determined by dividing the rf frequency span by 4, and renormalizing each reduced frequency span to $N_b = 324$. The longitudinal spectrum for unstable beam

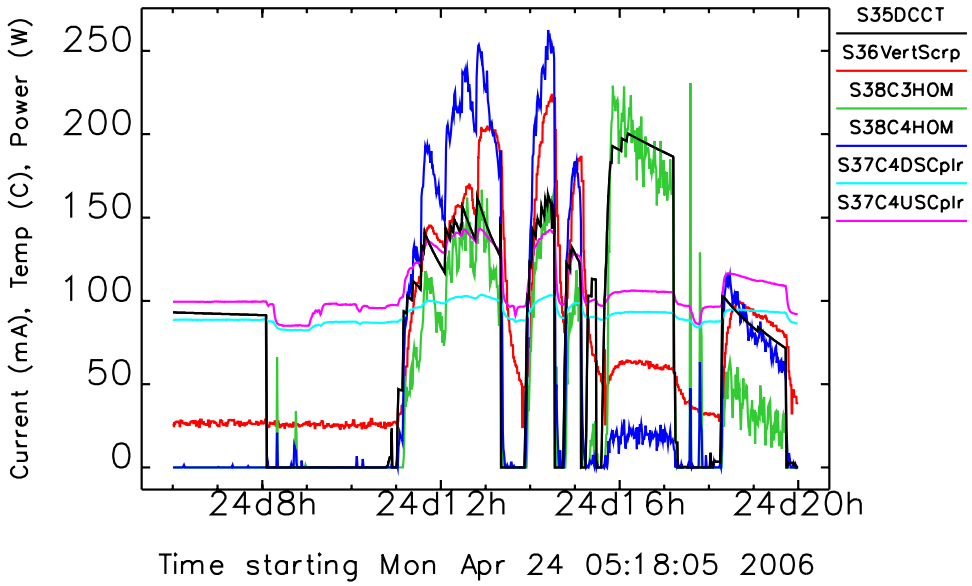

Figure 3.7-4: Temperature excursions for high-current studies. The beam current is shown in black, and the operating modes are described in the text.

as a function of mode number n is shown in Figure 3.7-5. The actual spectrum displayed is the rms average of the measured spectra minus the stable beam spectra to retain the phase-modulation signal (coupled-bunch motion) and remove the amplitude-modulation signal (from uneven bunch population).

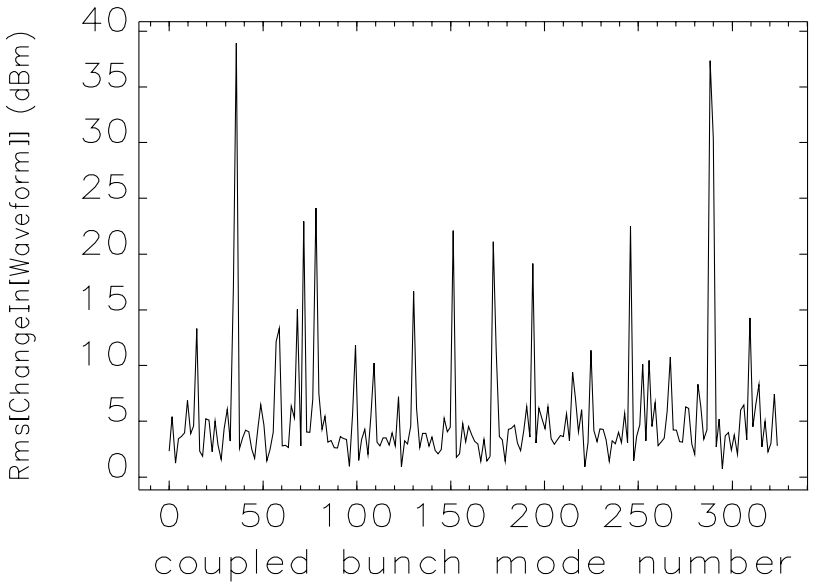

Figure 3.7-5: Dominant longitudinal CBI modes for unstable beam, 324 bunches, 100-mA, 8.5-MV rf voltage (nonstandard conditions), corresponding to monopole HOMs near 538 MHz, 915 MHz, and 1211 MHz.

The dominant mode numbers n, in decreasing strength, are 36, 78, 151, and 130 (and the mirror-symmetric mode numbers $(324 - n)$). The phase shift between oscillations of adjacent bunches is given

by $2\pi n/N_B$. To drive the beam at mode n, the HOM frequency must be equal to

$$f_{\text{HOM}} = \frac{f_{\text{rf}}}{h}(N_b p + n + m\nu_s), \tag{3.7-1}$$

where $h = 1296$ is the harmonic number, p and m are positive indices, and ν_s is the synchrotron tune. Using $f_{\text{rf}} = 351.936$ MHz, the computed CBI mode frequencies are closest to the measured monopole cavity HOMs 538 MHz, 1211 MHz, and 915 MHz. When the beam is unstable, the cavities in Sectors 38 and 36 show relatively strong HOM signals, and thus make good candidates for future HOM dampers.

3.7.3.3 Transverse Limits

The transverse multibunch instabilities are driven by long-range wakefields such as that produced by the resistive-wall (RW) impedance. There is little evidence that the main rf cavity dipole HOMs contribute to the instabilities observed in the APS [3.7-18], despite predictions of low transverse CBI thresholds [3.7-9, 3.7-11]. A similar observation is reported at the European Synchrotron Radiation Facility [3.7-19].

The transverse bunch-by-bunch feedback system is used in combination with positive chromaticity to stabilize the beam transversely [3.7-5]. The feedback system damps beam-centroid oscillations of single-bunch or coupled-bunch motion up to a bandwidth of 117 MHz. In anticipation of high-current operation, the feedback system amplifier power was recently increased from 300 W to 500 W per stripline blade (there are two stripline blades each for the x- and y-plane).

The impact of high chromaticity on beam lifetime is most critical for the 24-bunch mode. Without transverse feedback, the required chromaticity for stable beam for 150 mA in 24-bunch mode was measured to be about 9.5 units in each plane. The transverse feedback system further stabilizes the beam, significantly reducing the chromaticity required for stability. Figure 3.7-6 shows the single-bunch accumulation limit as a function of x- and y-chromaticity, with the feedback system operating and after increasing the amplifier power. Stable beam is achieved with a single-bunch limit of over 9 mA with a chromaticity of 3 in the x- and y-plane. This provides sufficient margin—given the expected increases in the transverse impedance—to support the planned 150-mA 24-bunch-mode operation of the APS Upgrade. This result is also consistent with the assumptions and requirements for chromaticity and beam lifetime discussed in section 3.2.2.4.

Although the transverse feedback system is used operationally, it is useful to review the transverse multibunch instability thresholds without the feedback system [3.7-18]. It is also useful to review the measurements of the long-range transverse impedance.

When the transverse feedback system is off, in the horizontal plane a steady-state instability is observed at the instability threshold, characterized by emittance growth, a self-excited betatron tune signal, and bunch centroid oscillations with constant amplitude. The bunch phases are coupled with a bunch-to-bunch phase corresponding to a transverse mode number of 0.8, which is consistent with an RW-driven transverse CBI. At lower chromaticity, a bursting instability is observed, characterized by a semi-periodic variation in the bunch centroid oscillation amplitude. The multibunch bursting phenomenon is qualitatively similar to the single-bunch instability observed in the APS.

At the instability threshold in the vertical plane, x-y coupling growth is typically observed before a self-excited vertical tune or centroid oscillations can be seen. The bunch phases do not appear to

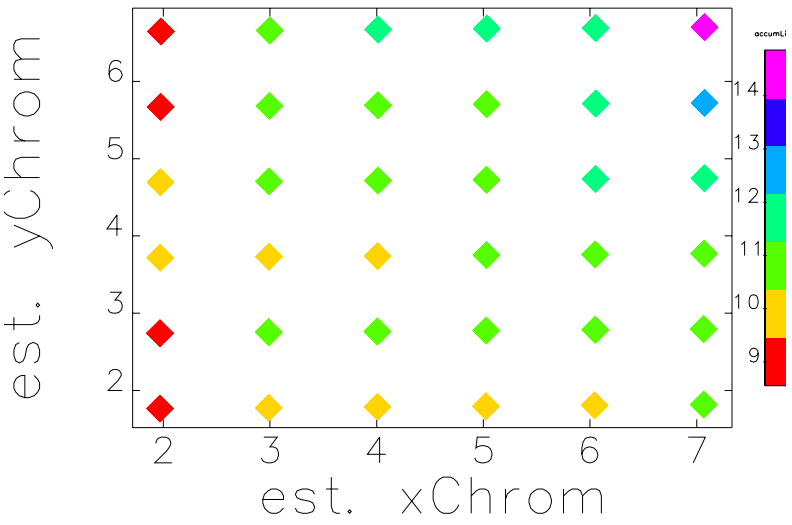

Figure 3.7-6: Single-bunch accumulation limit (mA) as a function of x- and y-chromaticity, with transverse bunch-by-bunch feedback system operating (after the feedback system amplifier power was increased). The chromaticity values are calculated from the lattice model.

be coupled, at least for the standard 24-bunch operating mode; rather, individual bunches become unstable—this might be a coincidental occurrence of single-bunch and multibunch instability for this bunch pattern. Also, vertical bursting is often but not always observed. For reference, the single-bunch TMCI threshold is about 4 mA in the horizontal plane and 2 mA in the vertical plane [3.7-20].

Figure 3.7-7 shows the chromaticities corresponding to the instability onset and the bursting instability threshold in both planes for 100 mA total beam current. These measurements are without the bunch-by-bunch feedback system. Note that the operating chromaticities of 3.5 units in each plane are sufficient for stability for the 324-bunch mode without feedback (cf. Table 3.7-2).

By convention, the instability threshold is given as the current at which the onset of collective motion is observed. In practice, however, it is difficult to determine the current threshold for transverse instabilities because the injection process mixes linear and nonlinear single-particle beam dynamics with impedance (collective) effects. Instead, the threshold is determined by filling the ring starting with high chromaticities (stable conditions), then slowly lowering the chromaticity in each plane separately until collective motion is observed.

The relationship between the chromaticity and the current threshold is not strictly linear, but the threshold expressed as a chromaticity can be useful for relative comparisons. In the range of 324 to 1296 bunches, the threshold in both planes is inversely proportional to the bunch current. This is consistent with the increased head-tail damping for higher bunch current. In the 24- to 54-bunch range, the threshold appears to be dominated by another mechanism, likely single-bunch effects. The horizontal onset is consistently 1-2 units above the vertical. There is a curious deviation from these trends for 72-162 bunches. The reason for this behavior is not understood.

Measurement of the betatron tune shift as a function of current is used to estimate the transverse impedance. The tune shift as a function of single-bunch current was measured for different uniform bunch patterns. For each bunch pattern, the current was scanned from 100 mA down to 10 mA

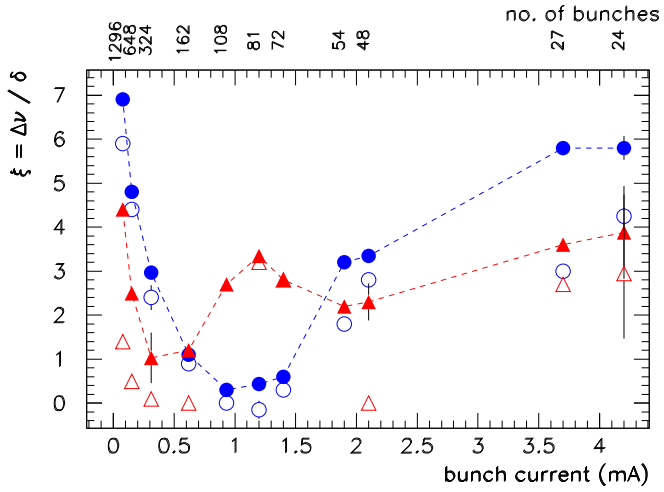

Figure 3.7-7: Horizontal (circles) and vertical (triangles) chromaticity thresholds as a function of uniformly spaced bunch number and bunch current (100 mA total). The closed symbols give the instability onset and the open symbols the bursting threshold.

except for two- and one-bunch fills where current was limited by a single-bunch limit. The results are presented in Figure 3.7-8.

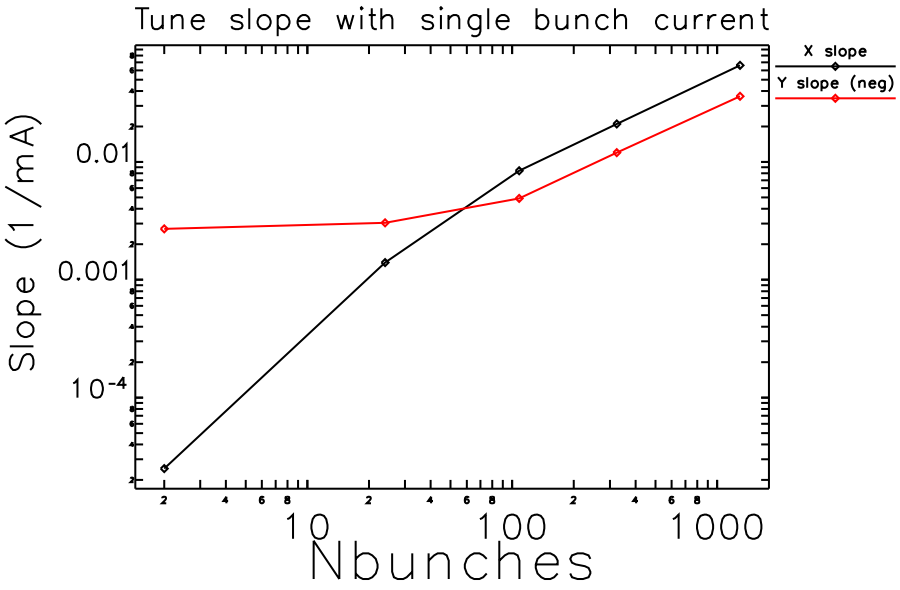

Figure 3.7-8: Tune slope with single-bunch-current dependence on the number of equally spaced bunches (or bunch spacing). The black curve shows the horizontal tune slope, and the red curve shows the vertical tune slope multiplied by -1 to present on a log scale.

One can see that the horizontal tune slope is positive. This was recently observed at several rings [3.7-19, 3.7-21] and is explained by a quadrupolar wakefield of asymmetric vacuum chambers.

The APS has a large number of small-gap insertion device vacuum chambers that are essentially open on one side in the horizontal plane. In the APS, the insertion device chambers dominate the transverse

impedance. One might assume that the vertical RW impedance is orders of magnitude larger than the horizontal due to the 1:2 to 1:5 aspect ratio and inverse cubic dependence on the chamber radius. However, the horizontal and vertical multibunch instability thresholds are comparable (horizontal is actually slightly higher), which implies that the impedance is also comparable. Thus the chamber asymmetry is highly suspected to be the source of a significant impedance in the horizontal case.

An alternative solution to multibunch feedback or high chromaticity for high current may be to reduce the beta functions in the IDs. To study the latter, an all-ID reduced-horizontal beta lattice was tested. The horizontal multibunch instability threshold was increased roughly in proportion to the betatron function reduction factor, as expected [3.7-22]. This solution may be limited in practice by other lattice constraints.

3.7.4 Performance Margin

For 150-mA operation, the performance margin in the 24-bunch mode is relatively small. The margin is higher in the other user modes. The accelerator limitations at the maximum current are understood, and confidence is high that 150-mA operation can be achieved in all user modes without the need for upgrades. In this section, the accelerator limitations and programmatically funded effort and improvements that are related to reliable 150-mA operation are discussed.

3.7.4.0.1 Rf Coupler

The storage ring rf cavity input couplers have been a significant contributor to rf system downtime since the start of APS operation [3.7-23, 3.7-24]. On going improvements have been implemented and further improvements are planned under programmatic funding that are expected to meet the reliability goals for 150-mA operation.

In the past, coupler failures caused by arcing, excessive ceramic heating, and the sudden appearance of pinhole vacuum leaks in ceramics have been analyzed in order to improve coupler performance. Improved fabrication methods, minor design changes, and improvements in the coupler conditioning process have been utilized to reduce coupler failures for operation up to 100 mA. New couplers are routinely conditioned up to 100-kW input power [3.7-23]. In the ring, the rf couplers are conditioned with 115-mA beam at the beginning of every run and operated at 80-90 kW for 100 mA, depending on the ID gaps and rf voltage.

It is expected that operation at beam currents greater than 100 mA will place additional stress on the existing input couplers by operating them closer to their original rf power design limit of 180 kW [3.7-3]. In studies, the measured cavity input power for 200 mA was about 110 kW (ID gaps open, Fig. 3.7-1). This power is similar to what is estimated at 150 mA with ID reference gaps (gray broken bar in Figure 3.7-1). Heating of the coupler ceramics (due to HOM power, which is dependent on the HOM frequency and power level) places additional stress on the input couplers. The additional stress can result in an increased risk of coupler failures. Several design changes and the implementation of an automated conditioning script show promise in improving the power-handling capability and operational lifetime of the couplers. Details are discussed in ref. [3.7-23].

3.7.4.0.2 Parallel-Klystron Operation

Presently, APS operates at 100 mA with two of the four klystrons delivering power to the cavities. Two klystrons are sufficient for 150-mA operation. The klystron power can be reduced by operating three or four klystrons in an alternate mode known as "parallel mode," albeit with a loss of redundancy. Some LLRF changes and software development are needed to improve this mode for use in routine operation. It is expected that these improvements will be funded programmatically.

The present parallel-klystron scheme utilizes one existing phase-control loop at two of the four rf storage ring stations for parallel-klystron phase control, which results in an increase in AC power line-related phase-noise sideband levels of approximately 10 dB over the existing single-ended rf system performance. The existing low-level rf systems will require some level of modification to maintain 60-Hz power-line-related phase-noise sidebands at a level of -50 dBc or better, thereby matching the existing rf system performance when operating in single-ended mode. Also, due to the more complex operator involvement required for the parallel-klystron configuration, automation scripts will need to be developed to assist machine operators in consistent and rapid rf system start-up and reset.

3.7.4.0.3 Scraper Chamber

Presently two double-bladed vertical diagnostic scrapers and two single-bladed horizontal diagnostic scrapers are installed in the APS. For several years, a third horizontal scraper was inserted during operation to help localize beam losses [3.7-25], but it has since been removed. During nominal APS operation and high-current studies the blades of all the diagnostic scrapers are retracted to the full-out position. In early high-current operation in 24-bunch-mode (2006), a temperature rise to greater than 200°C was observed in the Sector 36 vertical scraper body above 164 mA (red curve in Figure 3.7-4); this is considered serious and defined the current limit in 24-bunch mode. During a recent high-current study (April 2012), the same scraper body temperature rose to greater than 300°C. The Sector 36 vertical scraper chamber will be removed in September 2012. The second vertical scraper and two horizontal scrapers do not exhibit excessive heating at higher current.

Simulations show that the transverse force exerted on the beam by wakefields induced by the vertical scraper is small compared to other components, but the energy lost by the beam due to the longitudinal wake could result in a serious heat-load problem [3.7-26]. The longitudinal loss factor k_{z0} is computed to be 1.2 V/pC, assuming a zero-current rms bunch length σ_{z0} of 5 mm, and the loss factor scales approximately with bunch length as $(\sigma_z/\sigma_{z0})^{-1.5}$. The power dissipated by the beam can be estimated using $I^2 k_z/(N_b f_{\text{rev}})$, where I is the total beam current, N_b is the number of bunches, k_z is scaled to the bunch length, and $f_{\text{rev}} = f_{\text{rf}}/h$ is the revolution frequency [3.7-27].

An estimated power scaling can be carried out for 24 bunches. The rms bunch length for 100 mA is 35 ps (10.5 mm), which gives a loss factor of 0.33 V/pC. For the high-current test, the current was 160 mA with an rms bunch length of 40 ps (12 mm), giving a loss factor of 0.27 V/pC. The dissipated power is about 570 W for 100 mA and would be expected to be about 1.1 kW for 160 mA. If this power is dissipated in the small volume between the scraper and the housing, undesired heating can result. The scraper tube temperature rise due to this beam power has not been simulated, but from Figure 3.7-4, the temperature rise is about a factor of two from 100 mA to 160 mA in 24 bunches. This appears to be consistent with the rough estimate of the beam-induced power.

Preliminary work has been carried out on a new conceptual design for the vertical diagnostic scrapers

that mitigates the heating effects. Simulations show that a reduction of k_z by a factor of six can be achieved [3.7-27]. No further work is planned at this time to develop a mechanical design.

A collimating horizontal scraper was installed from 2005-2011 in Sector 37 to localize beam losses. The scraper was instrumented with a built-in electric-field pickup. Beam-driven HOMs in the pickup spectrum are observed as a function of scraper position, shown in Figure 3.7-9. The HOM spectra show about five peaks with moderately high quality factors; such diagnostics would be valuable to directly measure the HOM spectrum in vertical scraper chambers where heating is critical. A new design for a scraper is in progress using programmatic funds, as discussed below.

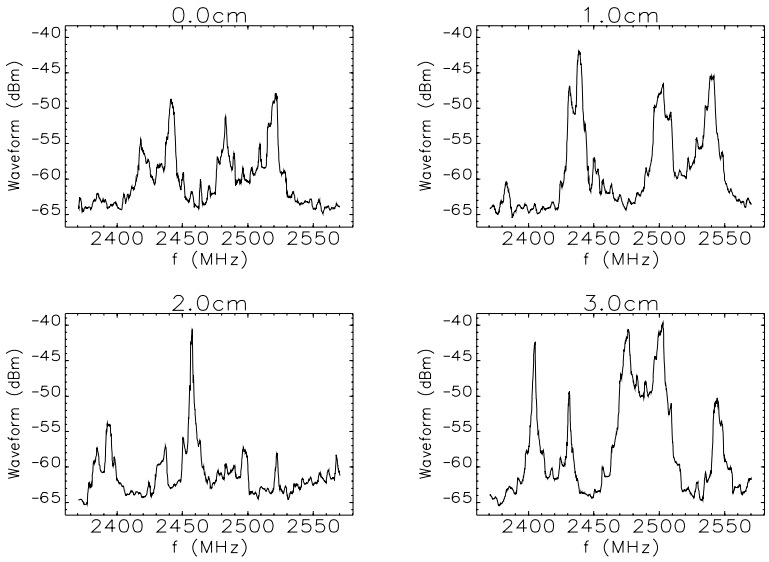

Figure 3.7-9: Horizontal scraper HOMs vs. inserted position.

3.7.4.0.4 HOM Damper Power Dissipation

New HOM dampers are not needed for 150-mA operation. However, the present design exhibits beam-induced heating in one of the four dampers above about 164 mA in 24-bunch mode. There are no heating issues for the 324-bunch or hybrid user operating modes at 150 mA.

Since the coaxial damper is inherently a broadband device and its power measurements are made using calorimetry, it is difficult to evaluate the frequencies of the modes that are being absorbed or to measure their power levels to a precision greater than tens of watts. During typical operation with a 24-bunch fill pattern, the damper ceramic dissipates roughly 100 W of power. In the high-current studies, the damper ceramic dissipated over 250 W of power, which has been designated as the limit to protect the damper.

The HOM damper power dissipation is reproducible over time, as shown in two sets of data acquired several years apart (see Figure 3.7-10). It can be expected with high confidence that 150-mA operation will keep the HOM damper power below their limits under otherwise normal machine conditions.

Preliminary work on a new HOM damper design has been carried out under programmatic funding that addresses the heating issues, and its design goal would be to enable beam operation up to 200 mA, which would provide a generous safety margin for 150 mA operation. The new damper designs are

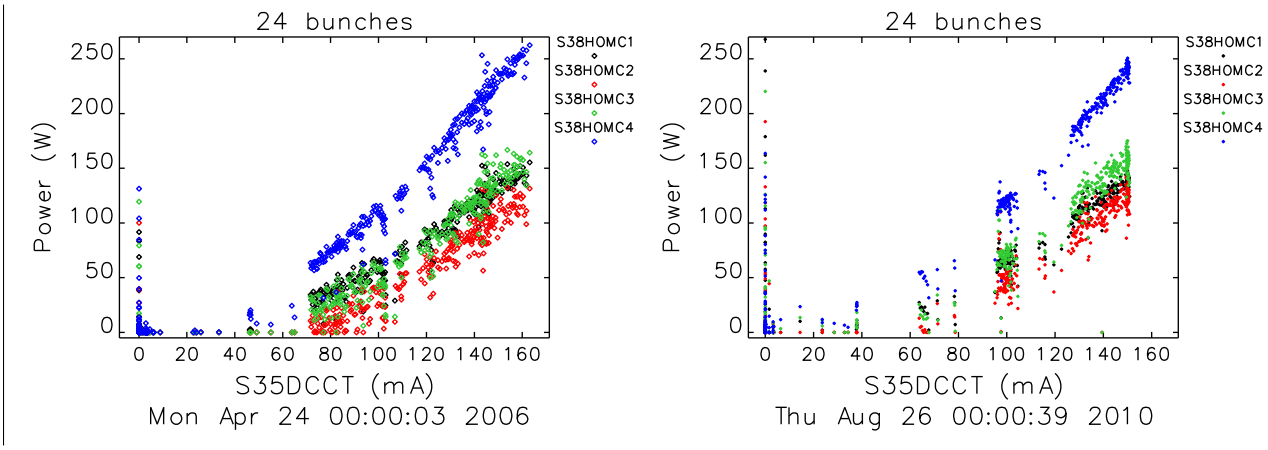

Figure 3.7-10: Power dissipated in a HOM damper ceramic body for 24-bunch-mode as a function of current. The data are reproducible, as acquired on different dates, four years apart.

inductively coupled and include a detachable rf load that enables mode spectral data to be extracted to address the rf diagnostics limitations of the present HOM dampers. A full discussion is beyond the scope of the APS Upgrade; details on the new HOM damper design can be found in ref. [3.7-28].

3.7.4.0.5 Transverse Bunch-by-Bunch Feedback

An upgrade of the transverse bunch-by-bunch feedback system is planned and is underway under programmatic funding. The plan includes the following: upgrade the sample rate from the present 117 MHz to 352 MHz to allow the loop to be closed on all possible bunch patterns; new FPGA firmware to support bunch-by-bunch gain variation; a Linux-based embedded EPICS database that provides more diagnostic information; a 250-MHz bandwidth, 500-Watt stripline device for both planes; and on-line passive tune monitoring and instability mode analysis.

3.7.4.0.6 Other Considerations

The HOM dampers are expected to stabilize the beam against longitudinal coupled-bunch instabilities at 150 mA in all user modes. Wakefield heating is possible in other, non-rf system components. Long periods of storing 150 mA with top-up injection are planned in order to monitor wakefield heating at longer times scales, to condition the rf system, and to study overall accelerator reliability. This effort will be carried out under programmatic funding.

An improved collimation system is planned under programmatic funding. When the collimating horizontal scraper was removed in 2011, damage was observed on the copper and tungsten surfaces that intercepted the electron beam. Simulations of the beam loss distribution and energy deposition suggested that the melting temperature of the tungsten was exceeded [3.7-29]. The original horizontal scraper design was copied (without the electric-field pickup) and re-installed from January-April 2012. Systematic beam dump tests were carried out at specific locations on the scraper surface. When the scraper was removed, damage was again observed for some of the beam dump locations, but the correlation of damage and beam dump conditions is not yet completely understood. The simulations

and experimental data are guiding an ongoing design effort for a new collimation system that takes into consideration both the beam-loss heating of the surface as well as mitigating the wakefield-induced heating in the scraper chamber [3.7-30, 3.7-31].

3.7.5 References

[3.7-1] Advanced Photon Source Safety Assessment Document. Technical Report APS-3.1.2.1.0, Rev. 3, APS, (2012).

[3.7-2] D. Horan and E. Cherbak. Parallel Klystron Operation at the Advanced Photon Source Storage Ring, Proc. of PAC 2001, p. 990, (2001).

[3.7-3] P. Brown et al. Status of the LEP Accelerating Structure, Proc. of PAC 1989, p. 1128, (1989).

[3.7-4] http://www.aps.anl.gov/Facility/Storage_Ring_Parameters.

[3.7-5] C.-Y. Yao et al. Recent Progress of the Bunch-by-Bunch Feedback System at the Advanced Photon Source, Proc. of IPAC 2010, p. 2803, (2010).

[3.7-6] L. Morrison et al. Proc. of MEDSI 2002, p. 34, (2002).

[3.7-7] G. Waldschmidt et al. Proc.of PAC 2005, p. 2443, (2005).

[3.7-8] C. Doose et al. Proc.of PAC 1997, p. 3577, (1998).

[3.7-9] L. Emery. Proc. of PAC 1991, p. 1713, (1991).

[3.7-10] T. Smith. Mode Identification and Cavity Stretching for the Prototype Storage Ring Cavity. Technical Report LS-194, ANL, (1992).

[3.7-11] L. Emery. Proc. of PAC 1993, p. 3360, (1993).

[3.7-12] K. Harkay. Proc.of PAC 1997, p. 1575, (1998).

[3.7-13] K. Harkay et al. Recent measurements of coupled-bunch instabilities and higher-order modes (HOMs) in the APS storage ring. Technical Report ASD/APG/2005-13, Argonne Accelerator Systems Division, (August 11, 2005).

[3.7-14] G. Decker and O. Singh. Method for Reducing X-ray Background Signals from Insertion Device X-ray Beam Position Monitors, Phys. Rev. ST Accel. Beams, **2**(11), 112801, (1999).

[3.7-15] P. Matthews et al. Storage Ring Cavity Higher-Order Mode Dampers for the Advanced Photon Source, Proc. of PAC 1995, p. 1684, (1995).

[3.7-16] Y. Kang. Damping with Coaxial Dampers in the Storage Ring Cavities of the Advanced Photon Source, Proc. of EPAC 1994, p. 2149, (1994).

[3.7-17] Experimental Physics and Industrial Control System, http://www.aps.anl.gov/epics.

[3.7-18] K. Harkay et al. Transverse Multibunch Bursting Instability inthe APS Storage Ring, Proc. of PAC 2007, pp. 4360–4362, (2007).

[3.7-19] R. Nagaoka et al. Observation, Analysis, and Cure of Transverse Multibunch Instabilities at the ESRF, Proc. of EPAC 2000, p. 1158, (2000).

[3.7-20] K. Harkay et al. Impedance and the Single-Bunch Limit in the APS Storage Ring, Proc. of PAC 1999, p. 1644, (1999).

[3.7-21] A. Chao et al. Phys. Rev. ST Accel. Beams, **5**, 111001, (2002).

[3.7-22] K. Harkay and V. Sajaev. Transverse Instability Thresholds for the All-ID RHB Lattice and Its Relation to Tune Slope. Technical Report AOP-TN-2008-058, ANL, (2008).

[3.7-23] D. Horan et al. Improvements to the Rf Cavity Input Couplers at the Advanced Photon Source, Proc. of PAC 2009, p. 1005, (2010).

[3.7-24] D. Horan and D. Bromberek. Technical Report RFTN-2008-10-13, ANL, (2008).

[3.7-25] M. Borland and L. Emery. Touschek Lifetime and Undulator Damage in the Advanced Photon Source, Proc. of PAC 2005, pp. 3835–3837, (2005).

[3.7-26] Y.-C. Chae. The Impedance Database and its Application to the APS Storage Ring, Proc. of PAC 2003, p. 3017, (2003).

[3.7-27] Y.-C. Chae. Wakefield consideration on the design of new vertical scraper. Technical Report ASD/APG/2004-02, ANL, (June 30, 2004).

[3.7-28] G. J. Waldschmidt et al. Inductively Coupled, Compact HOM Damper for the Advanced Photon Source, Proc. of 2011 PAC, (2011).

[3.7-29] J. C. Dooling and M. Borland. Beam Energy Deposition in the Sector 37 Scraper. Technical Report AOP-TN-2011-055, APS_1425090, APS, (2012).

[3.7-30] J. C. Dooling and M. Borland. Beam Energy Deposition in a Modified Scraper. Technical Report AOP-TN-2011-039, APS_1426668, APS, (2012).

[3.7-31] Y.-C. Chae. ANL, private communication, (2012).

3.8 Contingent Additional Scope

3.8.1 Introduction

The systems and components that are included in the APS Upgrade Project baseline are well defined; however, other systems or specific equipment may be considered for inclusion in the baseline should funds become available. The items described in this section are the Contingent Additional Scope (CAS).

Within the accelerator systems, CAS items include beam loss monitors for undulator protection; skew quadrupole magnet systems for improved coupling control; design, simulation, and implementation of a superbend in one area of the storage ring; an additional APPLE-II undulator; an additional revolver undulator; and two additional superconducting undulators.

The loss monitors and skew quadrupoles are described below; however, the revolver, APPLE-II, and superconducting undulators were previously described in sections 3.4.2.5, 3.4.3.2, and 3.5.

3.8.2 Management of Insertion Device Irradiation

Undulators, like other in-tunnel components of the APS complex, are subject to damage by ionizing radiation. This radiation originates from beam losses that occur during injection, beam dumps, and particles lost from the beam due to the finite lifetime. Although losses are generally well controlled in the APS, there have been issues with undulator damage, particularly in the location of the smallest chamber gaps. It is desirable to enhance the instrumentation used to monitor radiation losses at undulators and to better understand the mechanisms behind radiation damage.

3.8.2.1 Beam Loss Monitor Upgrade

The primary goals of the beam loss monitor (BLM) upgrade are: (1) developing detectors suitable for dosimetry measurements at the insertion devices; (2) implementing FPGA-based detector electronics to provide sector-specific loss data to aid optimization of the injection and minimization of losses; and (3) instrumenting several detectors per sector to enable meaningful integration of lost charge during user runs. The secondary goals of the upgrades are to provide: (4) turn-by-turn and bunch-by-bunch loss information after injection; (5) turn-by-turn and bunch-by-bunch loss information during major beam loss events; and (6) spatial information on the local losses within an ID chamber in all three dimensions.

The current APS BLM system consists of 36 sets of Cherenkov detectors and VME signal-processor boards built in house [3.8-1]. Both the detectors and signal processor boards are based on the PEP-II B-Factory design by A. Fischer [3.8-2]. A calibration program for the system was started in 2008. After calibrating all detectors from sector to sector, the absolute loss rate at each ID chamber can be derived by normalizing the count rate with the total charge loss rate deduced from the storage ring current monitor readout [3.8-3]. While these studies validated a methodology for dosimetry measurements, they also showed serious limitations of the system: (1) the detector does not respond to electrons lost in the downstream end of the chamber; and (2) steering the electron beam has strong effects on the detector sensitivity to local losses. One way to mitigate these problems is to experimentally search for new locations where the detectors are less sensitive to steering. However, a better solution is to add more detectors per sector to better integrate the losses in all directions and at both ends of the chamber.

At present, more than 90% of the electrons lost in the storage ring during top-up operations are from the stored-beam lifetime losses, which are dominated by post-Touschek scattering processes. The remaining losses are from injections and infrequent beam dumps. Of all the beam losses in the ring, about 40% occur at the narrow-gap chamber ID-4, the limiting aperture of the storage ring. Unlike the steady-state loss from the stored beam during user runs, the injection losses vary more widely in direction when hitting the chamber, making it more important to have multiple detectors for proper integration of losses. To handle the case of beam dumps, when the entire stored beam is lost in a very short time, the electronics must have a dynamic range of more than nine orders of magnitude.

The existing Cherenkov signal processing board supports only one photomultiplier tube (PMT) and does not have the dynamic range nor the timing circuit for recording beam dumps. Its components are out of date and a new design is needed. The new design will be based on an FPGA to allow a gradual path to increased processing capabilities through firmware upgrades [3.8-4].

Table 3.8-1 lists proposed beam loss monitors in the storage ring tunnel, covering all installed insertion devices. Due to the larger vertical beam deflection by the deflecting cavities, the beam losses inside the

SPX region and downstream sectors are expected to increase. More discussion on the use of beam loss monitors is found in SPX diagnostics section 3.6.3.10.

Table 3.8-1: List of Beam Loss Monitors.

Device monitored	Location	Total number	Notes
Undulator	S1 - S4	4	
Deflecting Cavity	S5, S7	2	SPX[a]
Undulator	S6 - S15	10	SPX
Undulator	S16 - S35	19	

[a] Additional BLMs are proposed for monitoring local losses due to SPX operations.

3.8.3 Improved Control of Coupling

As described in section 3.2.3, addition of skew quadrupoles to the storage ring will allow improved control of x-y coupling, which is beneficial for beam dynamics. Doing so would provide additional assurance that the demanding lattice optics requirements for the long straights, the reduced horizontal beam size insertion, and the short-pulse x-ray system can be met without excessive reduction in beam lifetime. Skew quadrupoles will also provide improved control of beam properties at insertion device locations.

The studies described in section 3.2.3 indicate that addition of 21 skew quadrupoles, for a total of 40 (one per sector), provides coupling control that is nearly as good as having a total of 80 skew quadrupoles. Hence, addition of 21 skew quadrupoles is a very cost effective way to improve coupling control. These would be added in the location of existing steering magnets, some of which are unused and others of which are being relocated in order to improve control of beam stability. Hence, a six-pole design is probably required, which is different from the four-pole design of the existing skew quadrupoles. The required integrated skew strength is 0.4 T based on preliminary analysis.

In addition to the magnets themselves, funding for power supplies, controls, interlocks, cooling water, and cabling would be required, as well as effort toward design, integration, and installation.

3.8.4 References

[3.8-1] A. Pietryla et al. A Cerenkov Radiation Detection System for the Advanced Photon Source Source Storage Ring, Proc. of PAC 2001, pp. 1622–1624, (2001).

[3.8-2] A. Fischer. Diagnostics Development for the PEP-II B Factory, Proc. of BIW 1996, pp. 248–256, (1996).

[3.8-3] B. Yang. APS-SR Cherenkov Detector Pulse Counter Initial Calibration. Technical Report DIAG-TN-2008-012, APS/ASD/DIAG, (2008).

[3.8-4] B. Yang et al. Specification of an FPGA-based Cherenkov Detector Signal Processor. Technical Report DIAG-TN-2008-010, APS/ASD/DIAG, (2008).

The Advanced Photon Source, an Office of Science User Facility operated for the U.S. Department of Energy (DOE) Office of Science by Argonne National Laboratory, is supported by the DOE under Contract No. DE-AC02-06CH11357

Advanced Photon Source Upgrade Project

Preliminary Design Report

December 2012

Chapter 4: Experimental Facilities Upgrades

Table of Contents

List of Figures

List of Tables

Acronyms and Abbreviations

Θ_B	Bragg angle
0-D, 1-D, 2-D	zero-dimensional, one-dimensional, two-dimensional, etc.
ADC	analog-to-digital converter
AES	APS Engineering Support (division at Argonne) Auger electron spectroscopy
AGIPD	Adaptive gain integrating pixel detector
ALD	Atomic layer deposition
ALS	Advanced Light Source
AMO	Atomic, Molecular, and Optical
APD	avalanche photodiode
APS	Advanced Photon Source
ASD	Accelerator Systems Division (of the APS)
ASIC	Application-specific integrated circuit
ASL	advanced spectroscopy and LERIX
BCDA	Beamline Controls and Data Acquisition
BCDI	Bragg coherent diffraction imaging
BCS	Beam conditioning system
BDA	beam-defining aperture
BLA	beam limiting apertures
BLEPS	beamline equipment protection system
BM	Bending magnet
BPM	beam position monitor
BSL	Biosafety level
CARS	Center for Advanced Radiation Sources

CAS	Contingent Additional Scope
CAT	Collaborative access team
CCD	charge-coupled device
CDS	Collimation-Dispersion-Selection
CMOS	complimentary metal-oxide semiconductor
CNM	Center For Nanoscale Materials
CP	circularly polarized
CRL	compound refractive lens
CTR	Crystal truncation rod
CVD	Chemical vapor deposition
DAC	diamond anvil cell
DCM	double-crystal monochromator
DCS	Dynamic compression sector
DESY	Deutsches elektronen-synchotron
DMM	double-multilayer monochromator
DPC	Differential Phase Contrast
EBL	Electron beam lithography
EDS	energy-dispersive x-ray spectroscopy
EMVPU	electromagnetic variable polarization undulator
EPICS	Experimental Physics and Industrial Control System
EPS	equipment protection system
ESD	Engineering specification document
ESRF	European Synchrotron Radiation Facility
EuXFEL	European x-ray free electron laser
EXAFS	Extended x-ray absorption fine structure
F-WT	Fast white-beam tomography
FE	Front end
FEA	finite element analysis
FEL	Free-electron laser
FOE	first optical enclosure

FPCA	Field-programmable computing array
FPGA	Field-programmable gate array
FSD	fuel spray dynamics
FWHM	full width at half maximum
FZP	Fresnel zone plates
GI-SAXS	Grazing-incidence diffraction in small angle x-ray scattering
GI-WAXS	Grazing-incidence diffraction in wide angle x-ray scattering
GPU	Graphics processing unit
GUI	graphical user interface
HEDM	High-energy diffraction microscopy
HEXD	High-energy x-ray diffraction
HEXT	High-energy x-ray tomography
HFPP	High Flux Pump-Probe
HHL	high heat load
HRM	High-energy-resolution monochromator
HVAC	Heating, Ventilation, & Air Conditioning
IBC	Institutional Biosafety Committee
ICD	Interface control document
ICE	Interfaces in complex environments
ID	insertion device
IEX	intermediate energy x-ray
IOC	input/output controller
ISN	*in situ* nanoprobe
K-B	Kirkpatrick-Baez
KPP	Key performance parameter
LCLS	Linac coherent light source
LDRD	Laboratory Director's Research and Development
LERIX	Lower Energy Resolution Inelastic X-ray
LN2	liquid nitrogen
LOM	Laboratory/office module

LSS	Liquid surface scattering
LSSCUFE	Long-straight-section canted-undulator front end
MBE	Molecular beam epitaxy
MD	Magnetic Diffraction
MEMS	Microelectromechanical systems
MERIX	medium energy resolution inelastic x-ray scattering
mFluor	Fluorescence Microprobes
MLL	multilayer Laue lens
MOCVD/ALD	Metal organic chemical vapor deposition/atomic layer deposition
MS-S	Magnetic Spectroscopy – Soft X-ray
NIXS	non-resonant inelastic x-ray scattering
NRTL	Nationally Recognized Testing Laboratories
OFC	oxygen free copper
OFE	oxygen free electronic (copper)
OFHC	oxygen free high conductivity (copper)
OPT	Optics Group
PAD	pixel array detector
PBS	pink-beam slit
PDF	Pair distribution function
PDR	Preliminary design report
PLC	programmable logic controller
PLD	Plasma layer deposition
PMU	Permanent magnet undulator
PRD	Physics requirement document
PSI	Paul Scherrer Institute
PSS	Personnel Safety System
PT	Phase-contrast-enhanced tomography
PZT	piezoelectric transducer
R&D	research and development
RE	rare earth

rf	Radio frequency
RHB	Reduced Horizontal Beam size
RIXS	resonant inelastic x-ray scattering
RMS	root mean square
RSS	radiation safety system
RXES	resonant XES
S3DD	sub-micron three-dimensional diffraction
SASE	Self-amplified spontaneous emission
SAXS	Small-angle x-ray scattering
SBCA	spherically bent crystal analyzer
SCU	Superconducting undulator
SD	Standard deviation
SE	Slope error
SMS	Sample-manipulation system
SOE	second optics enclosure
SOP	Standard operating procedures
SPSXS	Short Pulse Soft X-ray Spectroscopy
SPX	short-pulse x-ray project
SPXIM	Short Pulse X-ray Imaging and Microscopy
SPXSS	Short Pulse X-ray Scattering and Spectroscopy
SQUID	superconducting quantum interference device
SSG	Software Services Group
STM/AFM	Scanning tunneling microscope/atomic force microscope
STXM	scanning transmission x-ray microscopy
SXRS	Soft x-ray resonant scattering
TB	Technical bulletin
TM	transition metal
TOE	third optics enclosure
TXM	transmission x-ray microscope
UF-WT	Ultrafast white-beam tomography

UHV	ultrahigh vacuum
UNS	unified numbering system for metals and alloys
VLS	varied line spacing
VLSPG	varied line spacing plane grating
VLSPGM	varied line spacing plane grating monochromator
VME	Versa Module Europa
WAXS	Wide angle x-ray scattering
WBEE	white-beam experiment enclosure
WBS	white-beam slit work breakdown structure
WFI	wide-field imaging
WP&C	work planning and controls
X-BPM	X-ray beam position monitor
X-PEEM	x-ray photoelectron microscopy
XAFS	x-ray absorption fine structure
XANES	x-ray absorption near edge structure
XAS	x-ray absorption spectroscopy
XES	x-ray emission spectroscopy (nonresonant)
XHF	X-ray High Field
XIS	x-ray interfacial science
XMCD	x-ray magnetic circular dichroism
XMLD	x-ray magnetic linear dichroism
XRIM	x-ray reflection interface microscopy
XRMS	X-ray Resonant Magnetic Scattering
XRR	x-ray reflectivity
XRS	x-ray Raman spectroscopy
XSD	x-ray science division
YAG	Yttrium aluminium garnet
ZP	zone plate

4 Experimental Facilities Upgrades

4.1 Experimental Facilities Overview

The Experimental Facilities (WBS element U1.04) consist of all of the beamlines that are being significantly impacted by the APS Upgrade Project, beamline optics and heat-load-component upgrades needed to accommodate the increased storage ring current, and general development of detectors and nanofocusing optics. In this chapter, the preliminary design activities in each of these areas are discussed. In addition, contingent additional scope (CAS) that is under consideration for possible inclusion in the Project is clearly identified and briefly described. If the CAS relates to enhancement of an individual beamline, that discussion occurs in the context of that beamline subsection; if the CAS item is an entire beamline, it will be discussed in section 4.21.

In the baseline plan that is being submitted for Critical Decision 2 (CD-2) approval, there are 20 beamlines that are directly part of the APS Upgrade Project: eight are new beamlines (three on unoccupied ports, five from cants), six are upgrades in place and six are relocations. This does not include additional beamlines that will get optics or heat load component upgrades due to the increase of the storage ring current to 150 mA (WBS U1.04.04).

4.1.1 APS Roadmap and Consequences to the APS Upgrade

An activity with a major effect on the U1.04 Preliminary Design has been the APS Roadmap process [1]. Dynamic Compression program which has been located at sector 35. After a lengthy development process and numerous interactions with APS stakeholders, a “base” scenario was developed and released on April 30, 2012. The locations of the new, upgraded, and relocated beamlines in the APS Upgrade scope are listed in Table 4-1. The Preliminary Design and all costs/schedule described in this document are for this base design. In addition, two optional Roadmap scenarios involving rearrangements of four beamlines have been developed (see Table 4-2).

Table 4-1: APS Upgrade scope overview.

Beamline/Program	Location	New	Upgrade	Relocation
Short Pulse X-ray Scattering and Spectroscopy	7-ID		1	
Short Pulse X-ray Imaging and Microscopy	6-ID	1		
High Flux Pump-Probe	14-ID		1	
Wide Field Imaging	20-ID	1		
In Situ Nanoprobe	32-ID	1		
Resonant Inelastic X-ray Scattering	27-ID	1		
Magnetic Spectroscopy - Hard	4-ID		1	
High Energy X-ray Diffraction	1-ID	1	1	
X-ray Interface Science	28-ID	2		
Sub-micron 3D Diffraction	34-ID	1	1	
Advanced Spectroscopy and LERIX	25-ID			2
Magnetic Spectroscopy - Soft	2-ID		1	
Magnetic Diffraction	2-ID			1
Fuel Spray Dynamics	BM			1
Bragg Coherent Diffractive Imaging	9-ID			1
Fluorescence Microscopy	9-ID			1

Table 4-2: Differences between APS Roadmap Base Scenario and Options.

Program	Definition	BASE Scenario	Scenario Option 1	Scenario Option 2
ISN	*In Situ* Nanoprobe	32-ID-2	9-ID-2	9-ID-2
BCDI	Bragg Coherent Diffractive Imaging	9-ID-2	9-ID-1	32-ID-2
MD	Magnetic Diffraction	2-ID-1	32-ID-2	2-ID-1
XSD mFluor	Fluorescence Microprobes (2-ID-D/E)	9-ID-1	2-ID-1	9-ID-1

NOTE: For notation “n-ID-x”, “x” denotes a cant. The use of "1" or "2" does not indicate which half of the straight section is assigned.

The Roadmap process recognized that in some situations, further design work was needed to assure that the optimal location for a given program was selected. Two scenario options were defined, differing from the base scenario by the placement of the *In Situ* Nanoprobe (ISN), Magnetic Diffraction (MD), Bragg Coherent Diffraction Imaging (BCDI), and Fluorescence Microprobes (mFluor) programs. Detailed design work is still underway to understand the various pros and cons of the siting for each of these programs.

4.1.2 Description of Scope

Table 4-3 shows the Experimental Facilities Upgrades WBS for U1.04 down to level 3. Table 4-4 shows the scope of the U1.04.02 area of the Project. Beamlines in the area have a status of: Base, CAS, Partial, or Option. *In Scope* denotes that all aspects of the beamline described in the Project documentation are in

the scope for the proposed baseline. *CAS* indicates the beamline is currently considered contingent additional scope, with only design work funded by the Upgrade. *Partial* indicates that some of the activities for that beamline are CAS. *Option* indicates a design activity for an alternate location of a particular program.

Table 4-3: U1.04 WBS description.

WBS	Name	Comment
U1.04.01	Experimental Facilities Management	
U1.04.02	Beamlines	Includes all beamlines being upgraded by the Project, except those that are only being upgraded for 150-mA operation.
U1.04.03	(Not Utilized)	
U1.04.04	General Beamline Upgrades	

Table 4-4: U1.04.02 WBS description.

WBS	Acronym	Title	Location	Status	Comment
U1.04.02.01	BGS	Beamline Global Support			Activities in support of beamlines globally.
U1.04.02.02	SPXSS	Short Pulse X-ray Scattering and Spectroscopy	7-ID	In Scope	In-place upgrade.
U1.04.02.03	SPXIM	Short Pulse X-ray Imaging and Microscopy	6-ID	In Scope	New beamline.
U1.04.02.04	HFPP	High Flux Pump-Probe	14-ID	In Scope	In-place upgrade.
U1.04.02.05	WFI	Wide Field Imaging	20-ID	In Scope	New beamline,.
U1.04.02.06	HEXT	High Energy X-ray Tomography	Not sited	CAS	Assumes unoccupied site with superbend. Preliminary and final design effort in scope.
U1.04.02.07	ISN	In-situ Nanoprobe	32-ID	In Scope	New beamline on cant. TXM remains on other cant.
U1.04.02.08	RIXS	Resonant Inelastic X-ray Scattering	27-ID	In Scope	27-ID currently unoccupied. New beamline, incorporates RIXS programs from 9-ID and 30-ID.
U1.04.02.09	MS-H	Magnetic Spectroscopy-Hard	4-ID	In Scope	In-place upgrade. Assumes MS-S moved from 4-ID. APPLE undulator.
U1.04.02.10	HEXD	High Energy X-ray Diffraction	1-ID	In Scope	New beamline on cant, in-place upgrade on other cant.

WBS	Acronym	Title	Location	Status	Comment
U1.04.02.11	XIS	X-ray Interface Science	28-ID	Partial	28-ID currently unoccupied. New beamlines for tunable branch 1 and LSS program from 9-ID on branch 2 are in scope. Rest of branch 2, and branches 3 & 4 are CAS.
U1.04.02.12	S3DD	Sub-micron 3D Diffraction	34-ID	In Scope	New beamline on cant, in-place upgrade on other cant, includes mDiff program from 2-ID.
U1.04.02.13	ASL	Advanced Spectroscopy and LERIX	25-ID	Partial	25-ID currently unoccupied. Relocations of programs from 20-ID are in scope, upgrade items are CAS.
U1.04.02.15	SPSXS	Short Pulse Soft X-ray Spectroscopy	6-BM	CAS	Preliminary and final design effort in scope.
U1.04.02.16	MS-S	Magnetic Spectroscopy-Soft	2-ID	In Scope	Upgrade of program from 4-ID. Assumes MD on other branch.
U1.04.02.17	MD	Magnetic Diffraction	2-ID	In Scope	Relocation from 6-ID. Assumes MS-S on other branch
U1.04.02.18	FSD	Fuel Spray Dynamics	BM, not sited	In Scope	Relocation from 7-BM. Assumes unoccupied bending magnet.
U1.04.02.19	BCDI	Bragg Coherent Diffractive Imaging	9-ID	In Scope	Relocation from 34-ID. Assumes mFluor on other branch.
U1.04.02.20	mFluor	Fluorescence Microprobes	9-ID	In Scope	Relocation from 2-ID. Assumes BCDI on other branch.
U1.04.02.21	LSS-1	Liquid Surface Scattering	15-ID	Option	Option for LSS at 15-ID.
U1.04.02.22	MS-S-2	Magnetic Spectroscopy-Soft	4-ID	Option	Option for MS-S remaining at 4-ID.
U1.04.02.23	MS-H-1	Magnetic Spectroscopy-Hard	4-ID	Option	Option for MS-S remaining at 4-ID.
U1.04.02.24	ISN-1	In Situ Nanoprobe (Option 1)	9-ID	Option	Option for ISN at 9-ID with BCDI.
U1.04.02.25	BCDI-1	Bragg Coherent Diffractive Imaging (Option 1)	9-ID	Option	Option for BCDI at 9-ID with ISN.
U1.04.02.26	MD-1	Magnetic Diffraction (Option 1)	32-ID	Option	Option for MD at 32-ID on new cant with TXM. High speed imaging relocates.

WBS	Acronym	Title	Location	Status	Comment
U1.04.02.27	mFluor-1	Fluorescence Microprobes (Option 1)	2-ID	Option	Option for mFluor remaining at 2-ID with MS-S on other branch.

The scope for U1.02.02 and U1.04.04 is given in Table 4-5 and Table 4-6. WBS U1.02.02.02 is R&D activities in support of U1.04. WBS U1.04.04.01 and U1.04.04.02 are for upgrading optics and high-heat-load components for beamlines that are not otherwise part of the Project in order to mitigate any heat load issues caused by increasing the storage ring current to 150 mA. WBS U1.04.04.03 is for activities for development and deployment of fast-framing pixel-array detectors and WBS U1.04.04.04 is for the development of nanofocusing optics.

Table 4-5: U1.02.02 WBS.

WBS	Title
U1.02.02.01	High Speed Detection Development
U1.02.02.02	Resonant Inelastic X-ray Scattering Optics R&D
U1.02.02.03	Nanofocusing Optics Development

Table 4-6: U1.04.04 WBS.

WBS	Title
U1.04.04.01	High-Heat-Load Optics
U1.04.04.02	High-Heat-Load Components
U1.04.04.03	Detectors (Closed)

4.1.3 Contingent Additional Scope

The contingent additional scope for WBS U1.04 is described in detail below in the sections clearly denoted as CAS. Table 4-7 is a summary of the WBS U1.04 CAS. The Preliminary and Final Design for the CAS activities are included in the scope so that if any CAS items are brought into the Project at a future date, execution of those activities will be more easily integrated into the Project and able to commence in a timely manner.

Table 4-7: U1.04 Contingent Additional Scope.

WBS	Title	Comment
U1.04.02.06	High Energy Tomography	Entire beamline. Associated Superbend accelerator project is also CAS.
U1.04.02.11.04	X-ray Interface Scattering Fixed Angle Beamline 1	Second station on the first fixed-angle beamline.
U1.04.02.11.05	X-ray Interface Scattering Fixed Angle Beamline 2	Entire beamline branch
U1.04.02.11.06	X-ray Interface Scattering Fixed Angle Beamline 3	Entire beamline branch
U1.04.02.13.03	Advanced Spectroscopy & LERIX	Optics and detectors upgrade for the LERIX branch
U1.04.02.13.04	Advanced Spectroscopy & LERIX	Optics and detectors upgrade for the Advance Spectroscopy branch
U1.04.02.15	Short Pulse Soft X-ray Scattering	Entire beamline.

4.1.4 Interdependencies

An important aspect of the Project is the independencies between the upgraded beamlines, the front ends (U1.05), the insertion devices (U1.03), the rest of the accelerator (U1.03), and APS operations. Physics Requirement Documents (PRDs), Engineering Specification Documents (ESDs), and, especially Interface Control Documents (ICDs) are utilized to manage these interdependencies, along with linkages in the cost/scheduling database. The required approvals for each of these documents include key people in each area to insure that information is robustly distributed throughout the APS. The Project also encourages, and often arranges, face-to-face meetings between key personnel in different areas to resolve or clarify issues.

The APS is the largest scientific user facility in the United States and serious consideration has been given to planning the APS Upgrade Project in such a manner as to avoid unnecessary disruption to user operations. With the exception of the three unoccupied ID beamlines, all of the other beamline activities have an impact on currently operating beamlines. Wherever possible, disruptive installation activities (e.g., the building of a new shielded enclosure) are scheduled for a shutdown (non-user beam) period, and staging of upgrades is sometimes possible to avoid long shutdown of individual beamlines. Close coordination of the front end, storage ring, and insertion device schedules (with linkages in the scheduling database) is required to assure that all aspects of the necessary infrastructure is in place for efficient handover of a beamline to operations.

The technical leads for all beamline projects are matrixed from the X-ray Science Division (XSD) and most still have significant operational responsibilities. Matrixing personnel from other areas to support a project always presents challenges, but a strong advantage is that potential Project/Operations conflicts are often avoided, or at least minimized, when staff have shared responsibilities between the Project and Operations. Because of their experience, the technical leads have usually worked with the front end and accelerator personnel and both sides have some understanding of each other’s needs. This also helps to minimize Project/Operations conflicts.

Several beamline design aspects are strongly dependent on the capabilities provided by the accelerator (U1.03; see chapter 3 of this PDR). The choice of ID is key for optimal performance of a beamline and selection of period, length, tunability, polarization, etc. is highly specialized for any given beamline. The selection of the ID also is a key factor in selecting the appropriate front end for a beamline. A beamline/front end/insertion device ICD is required for each ID beamline. These documents are the result of interactive discussions among the key beamline, ID, and front end people and reflect a common agreement on the choices. The process of developing these documents is discussed further in the APS Upgrade Project Implementation Plan.

Two beamline subprojects (WFI and HFPP) have significant physical infrastructure needs. The WFI beamline is the first to extend past the boundaries of the APS experiment hall and will have an experimental station approximately 250 m from the ID. This requires a separate building as described in WBS U1.05 (see Chapter 5 of this PDR). The HFPP beamline program is at 14-ID and is an upgrade of an existing beamline. Part of the current infrastructure is a Biohazard Level 3 facility that will be expanded as a part of the Project scope. The activities related to this are also in WBS U1.05.

4.2 Short-Pulse X-ray Scattering and Spectroscopy (SPXSS) Beamline

The Short-Pulse X-ray (SPX) Facility is designed to take advantage of the unique features of the SPX source, the most important of which is the production of short-duration x-ray pulses at the full 6.5-MHz repetition rate of the APS. The high average x-ray flux is conveniently parceled in bunches of 10^4-10^6 photons in each picosecond (ps)-duration pulse. The x-ray probe thus offers the opportunity to view dynamics on an atomic-length scale with minimal x-ray induced perturbation of the system. The SPX can produce variable x-ray pulse durations, controlled by the magnitude of the radio frequency (rf) deflection, or, alternatively by the vertical slit size, independently at different beamlines. The photon energy and x-ray spot size can be readily adapted to experiments at the beamlines within the SPX Facility. The advantageous timing structure of the APS storage ring makes it straightforward to select a variable repetition rate as required for different systems.

The experimental facilities associated with the short-pulse x-ray (SPX) source will combine picosecond temporal resolution with atomic-scale spatial resolution, elemental and chemical specificity, and nanoscale spotsizes to enable an understanding of the relationship between structure and function in complex systems. Dynamics are typically initiated with optical laser pulses, which can be used to generate radiation from the terahertz through the extreme ultraviolet for excitation of electronic states and lattice degrees of freedom. Such excitations can heat systems through phase transitions (e.g. melting, ferroic, and superconducting transitions) in complex systems and can create metastable states not present in thermal equilibrium. Excitations can also be initiated with pulsed electrical fields applied on microscopic devices, or via optically induced mechanical transients.

The SPX Facility, as documented in this PDR, consists of three independent beamlines: Short Pulse X-ray Scattering and Spectroscopy (SPXSS); Short Pulse X-ray Imaging and Microscopy (SPXIM); and the Short Pulse X-ray Soft X-ray Spectroscopy (SPSXS), which is included in contingent additional scope. These three beamlines are located between two rf deflection cavities [2, 3] which provide chirped electron pulses, where a correlation is imposed between the longitudinal position of a particle in the bunch and its vertical phase space. The x-ray radiation emitted during traversal through an undulator or bending

magnet preserves the correlation and a short pulse can be selected out simply with a pair of slits. In a bend magnet beamline, the x-ray time correlation is between the vertical source position and time, while on an insertion device beamline, it is between the vertical divergence and time [2]. The source pulse duration on a bend magnet is independent of the x-ray energy (See SPSXS section 4.21.2). As such, it is an attractive source of soft x-rays or white hard x-ray radiation with ps duration.

The SPXSS beamline described in this section is uniquely versatile in that it will allow continuous energy tunability between 4.7 and 35 keV, variable bandwidth with the choice of a double-crystal monochromator ($\Delta E/E \sim 10^{-4}$) or multilayer monochromator ($\Delta E/E \sim 10^{-2}$), variable x-ray repetition rate with the use of a mechanical chopper and variable spot size down to a few microns with Kirkpatrick-Baez (K-B) mirrors to enable time-resolved diffraction and spectroscopic capabilities with few ps resolution at two independent experimental stations.

The SPXSS beamline will provide picosecond-duration, high-repetition-rate pulses of tunable, polarized x-ray radiation to enable ground-breaking experiments in chemical dynamics, condensed matter physics, materials science, and atomic physics. The picosecond time scale has unique importance because it is an excellent match for structural dynamics in nanoscale systems and for conformational changes in molecular and supramolecular systems. These areas are of technological relevance, as well as fundamental interest. The maximum repetition rate is ideal for flowing gas- and liquid-phase samples and for emerging nanoscale devices operating in the terahertz domain. Examples of science enabled at the SPXSS beamline follow.

Photoinduced energy and electron transfer. Understanding energy and charge transport on the atomic scale, processes which span multiple timescales, can inform the engineering of efficient artificial photosynthetic systems [4, 5, 6].

Solvation dynamics. Understanding at an atomic level the process of reorganization of a solvent shell upon electronic changes in a solute is critical for liquid phase chemistry and biology as the solvent shell can hinder or assist chemical reactions [7, 8, 9].

Thermal and atomic transport at interfaces. Many critical processes in the transport of heat across interfaces and the motion of solid-liquid interfaces occur at timescales that have previously been inaccessible to precise x-ray structural probes [10, 11, 12].

Dynamics of fundamental excitations. The structural features associated with the fundamental excitations of solids and the cascade of energy between these excitations are presently difficult to probe because appropriate time-resolved structural techniques do not exist [13, 14].

Laser control of x-ray absorption. Electromagnetic fields of the order of an atomic unit in field strength, newly accessible with the shorter x-ray pulse duration, can control x-ray absorption probabilities and thus alter the x-ray damage mechanisms in matter [15, 16].

4.2.1 Scientific Objectives

Beamline 7-ID, with SPX and new higher-repetition rate lasers will provide striking new capabilities at the APS for the study of thin epitaxial films, multilayers, bulk single crystals, nanoparticles, molecular

switches, and isolated molecules. The higher repetition rate for rapidly reversible processes (e.g. GHz switching) or replenishable samples (e.g. flowing liquid or gas jets) will enable superior statistics compared with standard kilohertz excitation schemes [17]. The addition of a high speed chopper will allow isolation of single x-ray pulses at the storage ring revolution frequency 271.6 kHz for data collection flexibility for samples that recover at slower rates. A block diagram for this beamline is shown in Figure 4-1.

7-ID-C: Time-resolved diffraction experiments. With a tight vertical slit, scattering experiments currently done on 7-ID-C will have nearly 2 orders of magnitude improvement in time resolution while preserving the high wavevector resolution of the 7-ID beamline. The addition of two vertical mirrors also enables a much longer focal distance than the current focusing optics in 7-ID-C, while retaining focal spot sizes around 20 μm. A refurbished six-circle diffractometer will be provided with a pixellated area detector.

7-ID-D: Scattering and spectroscopy experiments will study the evolution of short-lived quantum states from 1 ps – 150 ns following the photoexcitation of light-sensitive molecules in solution or gas phase. Absorption, fluorescence, and emission spectroscopy will be possible, as well as simultaneous diffuse scattering measurements with an area detector, as has been demonstrated already at the 100 ps timescale on a model system [18].

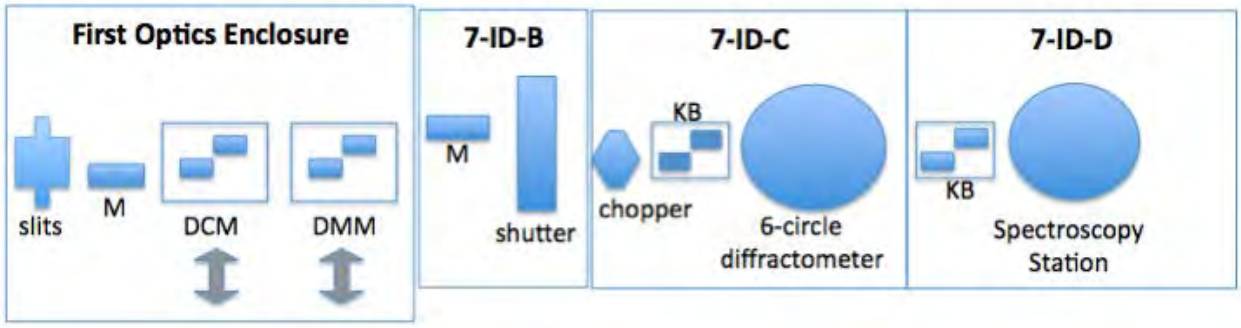

Figure 4-1: Block diagram showing major optical components for the SPXSS beamline. The first optics enclosure, 7-ID-B, 7-ID-C and 7-ID-D enclosures all currently exist. M = mirror, DCM = Double Crystal Monochromator, DMM = Double Multilayer Monochromator, KB = Kirkpatrick-Baez mirror pair.

4.2.2 Source Requirements

Experiments planned for the SPXSS beamline require energies from the Ti K-edge covering all the second-row transition metals up to 35 keV. Section 4.2.2.1 describes the selection of the undulator for the beamline, while section 4.21.2 describes the required SPX accelerator infrastructure.

4.2.2.1 Spectral Requirements

The SPXSS beamline has a spectral range coverage from about 4.7 to 35 keV, covering elements from the Ti edge at 4.966 keV to 35 keV. In order to optimize the flux in this energy range, one revolver undulator

with 2.7 and 3.0 cm periods of 2.4 m length is in scope (see its anticipated brilliance in Figure 4-2). A second but shorter undulator could be designed to fit the ~4.5-m available space [19] and is a potential future upgrade.

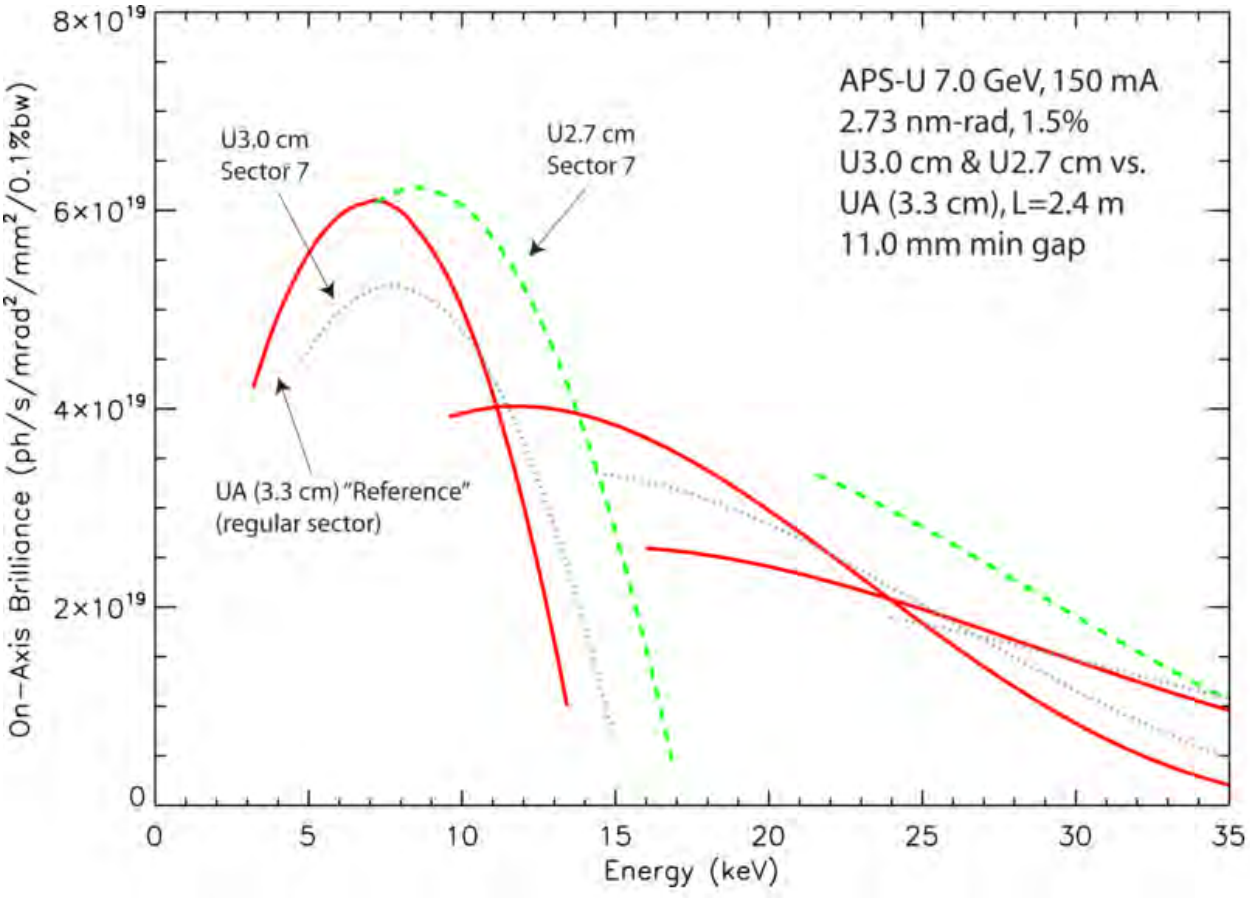

Figure 4-2: The proposed revolver undulator performance for the SPXSS beamline with the crab-cavities off.

4.2.2.2 Source Properties – Unique features of the SPX Source

The chirped electron beam of the SPX source will be unique. Extensive ray tracing was performed from the source through the optics in order to assure the quality of the beam at the sample location and understand the subtleties of the time-angle correlation. For the SPXSS beamline it was assumed that the source of the radiation is a 2.7-cm period undulator tuned to 10 keV (k=1.2) and located 0.3 m upstream of the center of the 7-ID straight section. The distribution of 10^6 electrons (on horizontal and vertical phase space and time) at the center of the undulator was obtained using the elegant code [20] and was subsequently convoluted with the undulator radiation obtained using spectra [21]. 24-bunch mode with a 41 ps rms electron bunch length were assumed.

Figure 4-3 shows the correlation between time and the vertical angle of the radiation emitted over the full horizontal fan of almost ±100 μrad. Figure 4-4 shows the same correlation when the horizontal acceptance is limited to 50 μrad, which contains 23% less "particles" than Figure 4-3. As seen in Figure

4-4, and less clearly in Figure 4-3, there are three bands. The central one corresponds to the radiation emitted by the undulator in the first harmonic whereas the other two bands correspond to the off-axis radiation due to the second harmonic which is shifted from the central one by $\pm\gamma^{-1}\ (1+k^2/2)^{0.5} = \pm 96\mu rad$. Figure 4-4 demonstrates that the correlation between time (t) and vertical angle is linear for the first harmonic radiation over approximately ±170 µrad and |t|<40 ps with a slope of -0.2 ps/µrad. The percentage of "particles" with |t|>40 ps in the ±170 µrad vertical angle range, due to the electrons in the "back-chirped" pulse is less than 0.1%.

The linear dependence between time and vertical angle was used to separate the contributions of the first and second harmonic radiation over the ±170 µrad vertical angle range. From this data one obtains 2.8 ps for the time resolution in the limit of zero vertical divergence for the first harmonic radiation. The individual first and second harmonic contributions were then propagated as a function of the longitudinal position relative to the center of the insertion device. Figure 4-5 shows the standard deviation (SD) of the vertical photon size as a function of the longitudinal position for the three bands. The minimum of the three bands is 22 µm and its location is at 2.89 m downstream the center of the undulator. Actually, the vertical waist of the photon beam, at 2.89 m - 0.3 m = 2.59 m from the center of the straight section, coincides with that of the electron beam, which is at 2.59 m downstream the center of the 7 ID straight section. Therefore, the plane at 2.59 m from the center of the straight section is the vertical source position. It should be noted that the SD of the photon beam size along the vertical direction is larger than that of the electron beam (16 µm). This is expected since at 2.9 m from the center of the ID the photon beam RMS size due to a single electron at the resonant energy $(2.9\ m\ (\lambda/(2\ L))^{0.5}$, where λ is the wavelength and L the undulator length) should be around 16 µm which when added in quadrature to the electron beam size gives 22 µm. A similar calculation yields a horizontal SD size equal to 302 µm, which is that of the horizontal SD of the electron beam located at the center of the 7-ID straight section.

The time distribution of the three bands at the position of the vertical focus (Figure 4-6) demonstrates that the center of the second harmonic contributions are at ± 96 µrad × 2.89 m= ±277 µm from the first harmonic radiation and that they are reasonably well separated. This means that a slit located at a vertical image plane of the photon beam will allow to significantly reduce the radiation of the second harmonic which arrives at a different time for the same divergence.

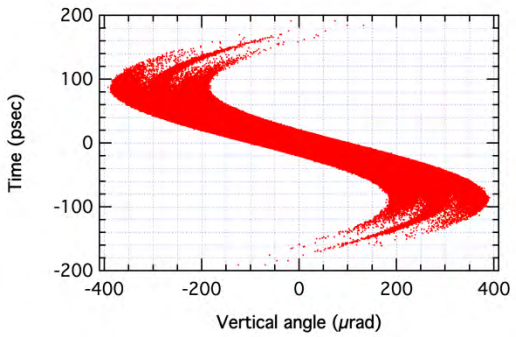

Figure 4-3: Correlation between time and vertical angle when accepting the full horizontal fan.

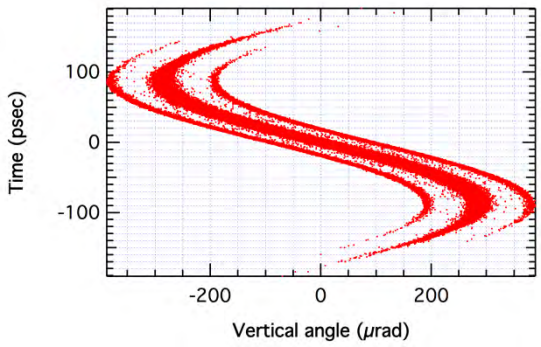

Figure 4-4: Correlation between time and vertical angle when accepting 50 μrad horizontally.

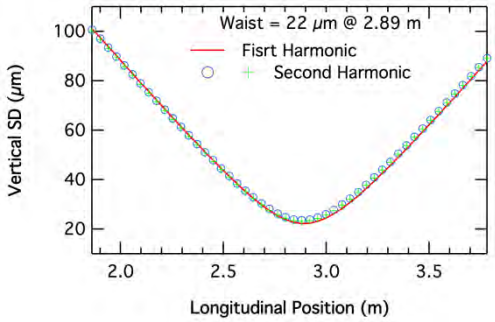

Figure 4-5: Vertical SD of the photon beamsize as a function of the longitudinal distance. Zero meter corresponds to the center of the undulator. The longitudinal dependence of the vertical size of the first (red line) and second (green + and blue o) harmonic is identical.

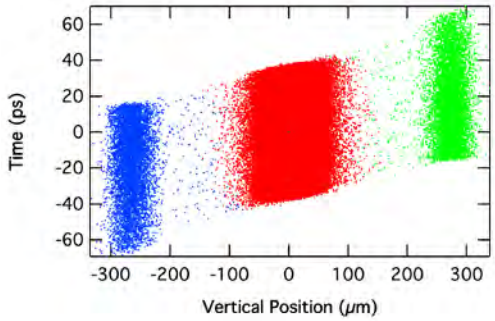

Figure 4-6: Time vs vertical position at the vertical source plane (2.89 m downstream the center of the undulator) for the first (red dots) and second (green and blue dots) harmonic.

4.2.3 X-ray Optical Layout

The primary optical elements in the 7-ID beamline are listed in Table 4-8 and shown, partially, in Figure 4-7. An engineering drawing is shown in Figure 4-8.

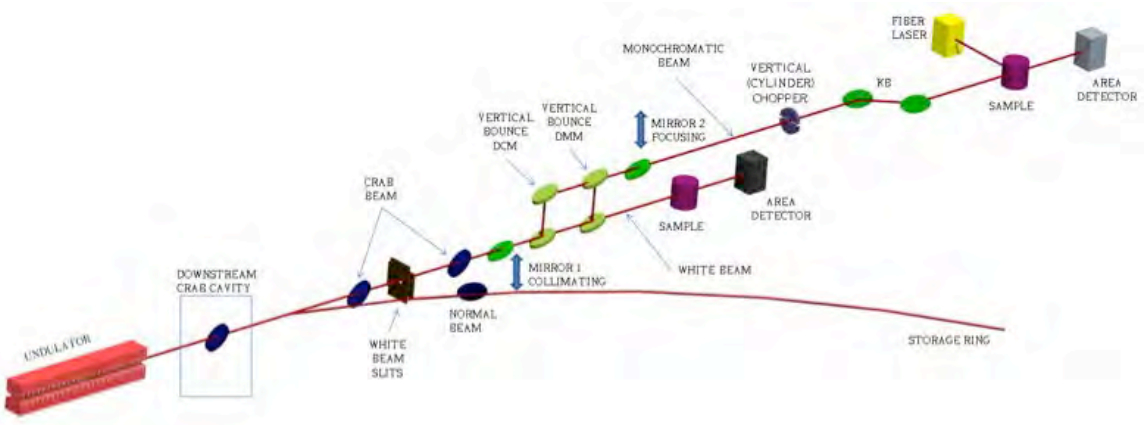

Figure 4-7: Schematic of the optics and instrumentation for the 7-ID beamline SPXSS. Only the optical elements and instrumentation in the 7-ID-C experimental station are shown. The 7-ID-D experimental station will house a K-B mirror and spectroscopy experimental station.

Figure 4-8: Current layout of SPXSS. The currently existing enclosures will be used in the SPXSS. The 7-ID-B enclosure is one of the few white-beam enclosures available around the APS storage ring.

Table 4-8: Beamline components in the 7-ID-C/D beamline.

Component	Distance to Center of Straight (m)	Notes
Pb Collimator	25.75	To limit the bremsstrahlung, opening TBD per ray traces. The collimator is part of the front end.
White-Beam Slits	26.5	Maximum beam size: 2 mm (V) x 3 mm (H)
White-Beam Mirror	27.5	Collimating, vertically deflecting (up bounce), water cooled, 1.2-m Si substrate, Pt, Ni (or Rh), and Si coatings, 2-mrad incidence angle, dynamic bender (4-point), 2-Å surface roughness, and 1-µrad slope error
YAG:Ce diagnostics	29	For mirror alignment, 5-mm field of view
Double-Crystal Monochromator	29.5	Commercial, diamond <111>, or Si <220> crystals, 24-mm vertical offset, liquid nitrogen cooled
Double Multilayer Monochromator	31.5	24-mm vertical offset, liquid nitrogen cooled, multilayer d-spacing and bandwidth TBD
Filters	32	Diamond, Be, Al, thickness TBD
YAG:Ce Diagnostics	32.5	For monochromator alignment, 5-mm field of view.
Pink-Beam Mask	33.5	To prevent singly reflected pink beam from striking unwanted downstream components
Pink-Beam Mirror	34	Focusing, vertically deflecting (down bounce), 1.2-m Si substrate, Pt, Ni (or Rh), and Si coatings, 2-mrad incidence angle, dynamic bender (4-point), 2-Å surface roughness, and 1-µrad slope error
YAG:Ce Diagnostic	34.75	For mirror alignment, 5-mm field of view
Be Window	35	Two openings, white-beam height and 50-mm vertical offset
Vacuum Pipe	35-41	Removable vacuum pipe through 7-ID-B experiment station
Be Window	41	Two openings, white-beam height and 50-mm vertical offset
Integral Shutter	42	Shutter/beamstop for mono and multilayer beams
Beam transport	43-49	Existing UHV-shielded monochromatic beam transport
YAG:Ce diagnostics with x-ray BPM, ending with Be window	49	To image the focus with 5-mm FOV and monitor the beam position
Chopper	50	Isolates single pulses in 24-bunch mode, up to P0 repetition rate (271.6 kHz), 10-W power
Kirkpatrick-Baez (K-B) Mirror Pair	53.5	Long (0.5 m) K-B pair, Si substrate, 2-Å roughness, 1 µrad slope error.
6-Circle Diffractometer	55	Existing instrument, refurbished
Pink Stop	56.5	About 7 W of pink-beam power, assuming 1% BW multilayer and 50% combined reflectivity; the beam can be vertically focused by the pink-beam mirror.
K-B Mirror Pair	58	Long (0.5-m) K-B pair Si substrate, 2-Å roughness, 1-µrad slope error

Component	Distance to Center of Straight (m)	Notes
Spectroscopy Experimental station	58.75	Existing instrumentation refurnished
Pink Stop	63	About 7 W of pink-beam power, assuming 1% BW multilayer and 50% combined reflectivity; the beam can be vertically focused by the pink-beam mirror

4.2.3.1 Simulated Beamline Performance

The novel nature of the chirped electron beam source mandated a complete optical ray tracing for the SPXSS beamline in order to understand the required slope errors for the optical components and the tradeoffs with respect to the pulse duration. The ray tracings described below were performed with the SHADOW code [22, 23]. The source used in the ray tracings consisted of the 10^6 rays described in Section 4.2.2.2 having a continuous distribution of photon energies between 9.998 and 10.002 keV. In the first sets of ray traces an aperture 26.5 m downstream of the source was set to accept 2 mm × 1.5 mm (H×V). In the second set, the aperture was set to accept only 0.3 mm × 1.5 mm (H×V). The pulse duration of this beamline is determined by the convolution between its vertical acceptance and the pulse duration of the source.

The first optical element in this beamline is a vertically deflecting meridional cylinder which collimates the photon beam. The mirror is located at 27.5 m from the source. The collimated beam is then monochromatized by a vertically diffracting double crystal monochromator using Si <220> crystals tuned to 10 keV. Figure 4-9 shows that the energy resolution derived from the ray tracings is practically that of two Si <220> s reflections with collimated light (0.61 eV). Including RMS meridional slope errors of 1 μrad on the collimating and focusing mirrors does not impair the energy resolution.

The meridional cylindrical mirror focuses the vertically collimated beam exiting the monochromator onto a slit located 16 m downstream of the mirror center at the chopper position. The vertical demagnification onto the slit is close to 1.7. The image at the slit in the case of the large vertical acceptance shown in Figure 4-10 shows a clear separation between the radiation from the first and second harmonic. No slope error (SE) is included in this figure. As seen in Figure 4-11, 1 μrad RMS meridional slope error on the collimating and focusing mirrors broadens the individual features.

The relatively large separation between the first and second harmonic along the vertical direction at the focus of the cylindrical mirror means that a slit should be able to separate most of the time "contamination" due to the second harmonic. This is seen in Figure 4-12 which shows the correlation between time and vertical divergence including the slope errors for two cases: with and without a 120 μm slit. The histograms derived from Figure 4-12 are shown in Figure 4-13. As seen in this figure, the FWHM in both cases is 17 ps but the slope errors reduce the first harmonic intensity transmitted by the slit by ~25%. Without slope errors on the optics the transmitted intensity in the first harmonic is almost 100%.

Shorter pulse duration can be obtained at the expense of flux by reducing the vertical acceptance of the beamline. With a 0.3 mm vertical aperture (11 μrad) the pulse duration should be given approximately by $((11\ \mu\text{rad} \times 0.2\ \text{ps}/\mu\text{rad})^2+(2.8\ \text{ps})^2)^{0.5}=3.6$ ps. Figure 4-14 displays the pulse duration simulated with the

0.3 mm aperture and meridional RMS slope error of 1 µrad and 0.2 µrad on the collimated and the focusing mirrors. Both slope errors give practically the same pulse duration, but the larger slope errors reduce the transmitted intensity by 25%. The FWHM of the first harmonic spot along the vertical direction at the slit plane with 0.2 µrad RMS slope errors is 36 µm.

The first element of the K-B pair [24] for the experiments in the D enclosure is the vertical focusing mirror which demagnifies the vertical slit by a factor of 7.7. The next element of the K-B pair is the elliptical cylinder imaging the source along the horizontal direction onto the sample position with a geometrical demagnification of 116. The spot at the sample position for a 0.3 mm vertical aperture, a 120 µm slit and including 1 µrad meridional RMS slope errors on all mirrors is shown in Figure 4-15. The divergence at the sample for the same conditions is in Figure 4-16. The expected spot size under the above mentioned conditions is 7×10 μm^2 (H × V) with a pulse duration of 3.5 ps (See Figure 4-14). Increasing the vertical aperture to 2 mm in 7-ID-A increases the spot to 7×12 μm^2 (H × V) and the pulse duration to 17 ps with 6.6 times more flux.

The K-B pair in the C enclosure produces a spot of less than 15 µm (FWHM) in both directions with a 0.3 mm vertical aperture at the front end, a 60 µm slit, 0.2 µrad RMS slope errors in the first two mirrors and 1 µrad in the K-B mirrors. The divergences at the sample under the same conditions are 2.2×0.06 $mrad^2$ (H × V).

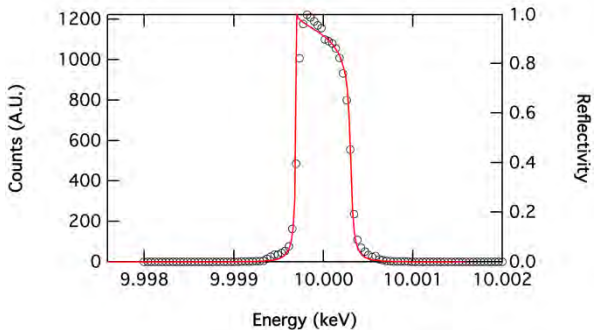

Figure 4-9: Energy resolution obtained from the ray tracings (black circles). Right axis and red trace: Reflectivity of two flat <220> Si with collimated light.

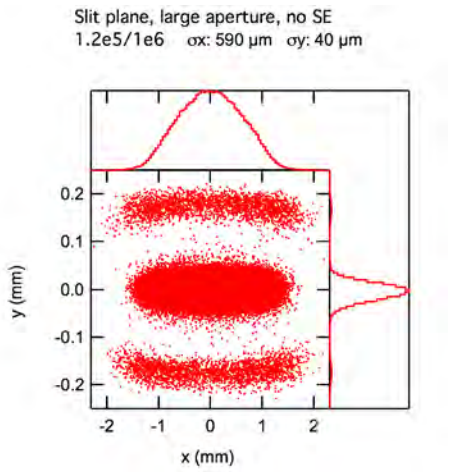

Figure 4-10: Ray tracings at the vertical slit plane. The captions above the figure show the transmitted and total number of rays and the RMS values along the horizontal and vertical directions. Large aperture, no slope errors.

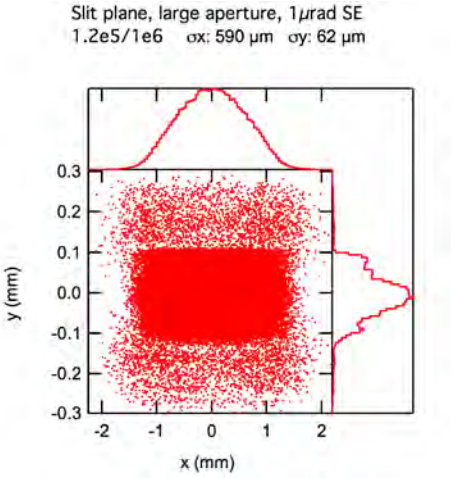

Figure 4-11: As Figure 4-10 assuming 1 μrad RMS meridional slope errors on the collimating and focusing mirrors.

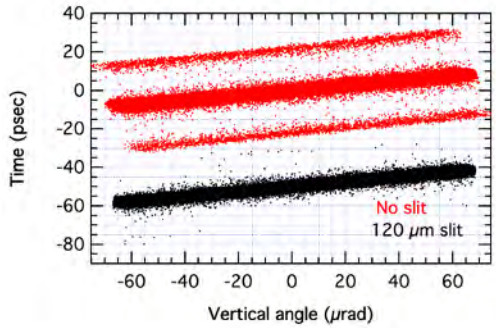

Figure 4-12: Correlation between time and vertical angle at the slit plane assuming 1 μrad RMS slope error on the collimating and focusing mirrors. Red points: no slit; Black points: with 120 μm slit, displaced by -50 ps for clarity.

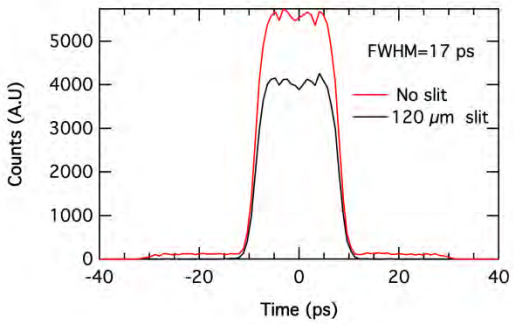

Figure 4-13: Pulse duration with (black trace) and without (red trace) a 120 μm slit. 1 μrad RMS slope error on the first two mirrors, 2 mm vertical acceptance.

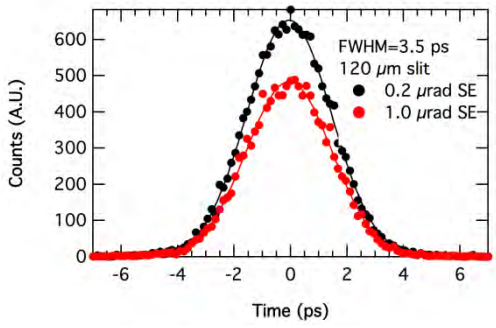

Figure 4-14: Pulse duration with RMS slope errors of 1.0 μrad (black circles) and 0.2 μrad (red circles) on first two mirrors. 0.3 mm vertical acceptance. The lines are Gaussian fits.

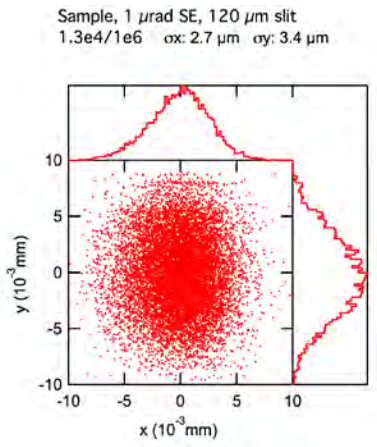

Figure 4-15: Spot pattern at sample plane in 7-ID-D. 120 μm slit. 1 μrad RMS slope error on all mirrors. 0.3 mm vertical acceptance.

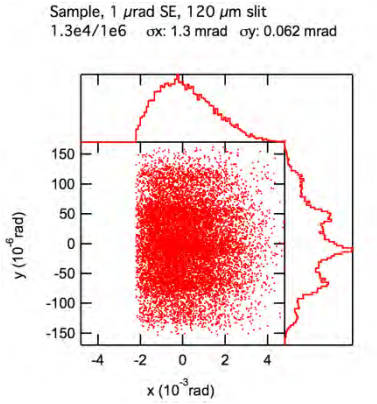

Figure 4-16: Spot pattern of divergence at sample plane. 120 μm slit. 1 μrad RMS slope error on all mirrors. 0.3 mm vertical acceptance.

4.2.3.2 Mirrors

A collimating white-beam mirror provides a nearly parallel beam of x-rays to the monochromators and other optical components. The SPX beam has a reduced power density compared to a standard APS undulator beamline, but if the cavity voltages are off, the cooled mirror must be able to handle the full beam power. Detailed power density calculations and thermal calculations with the cavity on at 2 MV and off will be performed during the Final Design phase. These calculations will guide the mirror cooling scheme.

An uncooled focusing mirror, similar to the collimating white-beam mirror described above but in bounce-down geometry, will follow the monochromators. Ray tracing calculations show a 36-μm focus is achievable at the current planned location of the chopper at the upstream end of 7-ID-C. This would be adequate to isolate a singlet in 24-bunch mode. Placement of the monochromators before the focusing mirror in a collimated beam preserves the energy resolution of the monochromatic beam expected from dynamical diffraction calculations (see Figure 4-9).

4.2.3.3 Monochromators

A double-crystal monochromator is planned, with diamond <111> or Si <220> crystals, such as the Kohzu monochromator currently in use at 7-ID. It will provide monochromatic x-rays with energy resolution $\Delta E/E$ of 6×10^{-5} (see Figure 4-9). A double-multilayer monochromator with a 24-mm vertical offset follows the crystal monochromator and will provide x-rays with a larger $\Delta E/E$ of $\sim 1 \times 10^{-2}$. The design of the monochromator and multilayer takes into consideration the energy range required for experiments and the details of the mechanical design.

4.2.3.4 Focusing Elements

A large vertically reflecting mirror system collimates the beam in 7-ID-A so the monochromators can produce their ideal bandwidth. The second large, vertically reflecting mirror system in 7-ID-B focuses the beam through the chopper aperture in 7-ID-C. Two K-B mirror systems will be located in 7-ID-C and 7-ID-D to provide few-μm beams for experiments.

4.2.4 Beamline Physical Layout

This section describes the beamline physical layout including the front end, first optical enclosures, the three experimental enclosures, and their respective instruments.

4.2.4.1 Front End

A standard APS high-heat-load front end with a 2 mm (H) x 2 mm (V) mask is required. This front end may be equipped with timing and beam-tilt diagnostics to ease cavity operation.

4.2.4.2 Overall Beamline

The 7-ID beamline is part of Sector 7 where a bending magnet (BM) and ID beamlines were implemented. There are no plans in the scope that call for use of the BM beamline for experiments. The sector is equipped with a 2.5-W, 1- or 5-kHz femtosecond Ti:Sapphire system in 7-ID-E that is the workhorse of the current 7-ID program. The next section describes the scope of the APS Upgrade 7-ID beamline.

4.2.4.3 General Description

The SPXSS beamline inludes a first optics enclosure (FOE) (7-ID-A) and three experimental enclosures (7-ID-B, C, D) that already exist. The FOE will house white-beam slits, a collimating mirror, fixed-offset double-crystal and double-multilayer monochromators, and an x-ray filter unit. A vertically deflecting focusing mirror will be placed at the entrance of 7-ID-B. The 7-ID-B enclosure will continue to house an existing phase contrast imaging set-up, followed by a monochromatic shutter/white-beam stop in the 7-ID-B mini-enclosure. An x-ray chopper, an existing streak camera (not shown in the layout), a K-B mirror, and a 6-circle diffractometer will be housed in 7-ID-C. The 7-ID-D enclosure will house a K-B mirror system and a spectroscopy experimental station.

4.2.4.3.1 Radiation Safety Aspects

The two mirrors in their current location produce a vertical beam offset of 26 mm. Both monochromators will be designed for 24-mm offsets allowing for straightforward bremsstrahlung mitigation. Preliminary synchrotron and bremsstrahlung ray traces have been completed already and promise safe operation.

The crab cavities (2-MV design) will most likely be unable to operate during APS hybrid fill mode, thus precluding ultrafast experiments. On the other hand, hybrid fill mode is in high demand for the existing 7-ID-B phase-contrast imaging program [25]. This program requires white beam, so this capability will be retained in 7-ID-B. Access to white beam will also be convenient for beamline commissioning. The use of the white-beam 7-ID-B enclosure for experiments is a change in scope from the conceptual design.

4.2.4.3.2 Vacuum System

A new equipment protection system (EPS) and additional vacuum controllers are required for 7-ID. The current EPS is not supported by the APS Safety Interlocks Group. For the new optics, new vacuum controllers will be purchased and integrated into the Experimental Physics and Industrial Control System (EPICS) and the EPS. The beamline vacuum design will comply with the APS beamline vacuum policy.

4.2.4.3.3 Data Acquisition and Motion Control

The current motion control infrastructure of beamline 7-ID will be used to control the new optics. Additional motion control equipment will be added to the existing infrastructure.

4.2.4.4 First Optics Enclosure and Infrastructure

This section describes the first optics enclosures (FOE), its components and infrastructure in eight subsections. It includes windows, slits, radiation safety components, x-ray optics, and diagnostics.

4.2.4.4.1 Windows

The standard front end 0.5-mm-thick Be window significantly reduces the beamline performance at energies below 6 keV, transmitting only about 60% of the beam at the low-energy limit of the monochromator (4.7 keV). The 26-ID nanoprobe beamline had a 0.2-mm-thick chemical vapor deposition (CVD) diamond window, with only about 20% transmission at 4.7 keV, so Be is preferable to CVD diamond. In conversation with ASD management, front ends with windows rather than with only differential pumps were preferred to prevent particulates from reaching and damaging the cavities in the case of a beamline vacuum failure. A Be window in the front end is planned in the Preliminary Design, but windowless operation will be re-evaluated in the Final Design.

Keeping white-beam experiments in the B enclosure requires double-vacuum windows to fulfill the APS vacuum policy, and thus will further reduce the throughput at low energy. Removing two white-beam, water-cooled Be windows and adding a UHV beam transport is not practical during beamline operation due to the significant labor involved and the risk in damaging these windows. The current 7-ID beamline

with its many Be windows has recently been used successfully at 5 keV, so this is not viewed as a serious limitation.

4.2.4.4.2 Slits

The latest-design, standard water-cooled, undulator white-beam slits are adequate for this beamline.

4.2.4.4.3 Collimators

A collimator will be integrated after the front end to ease the bremsstrahlung shielding. Its location and aperture will be chosen following engineering ray traces.

4.2.4.4.4 Shutters/Stops

A white-beam stop and monochromatic shutter will reside in the existing mini-enclosure downstream of 7-ID-B. Beam from the multilayer monochromator, with an energy of 8 keV, 1% bandwidth, and 50% combined reflectivity can carry about 7 W of power. With the crab cavity on at 2 MV, the front end mask only accepts 19% of the flux; thus, the power of the monochromatic beam will be reduced to 1.4 W. The beam stops and shutters will need appropriate cooling to dissipate the power in the white and monochromatic beams.

4.2.4.4.5 Monochromators

The double-crystal monochromator (DCM) using diamond <111> is designed to operate between 4.7 and 35 keV. It will be a commercial monochromator with a vertical offset of 24 mm and a maximum angle of 40°, which gives a minimum energy of 4.7 keV. A 24-mm offset provides a maximum energy of 35 keV. Diamond crystals presently in use at the APS will diffract only about 40% of the full 2 mm of vertical beam at 35 keV because the beam footprint is larger than the crystal at this photon energy. Recent reports of larger crystals promise to make higher energies more efficient. Diamond crystals with a length of 25 mm are required for the maximum proposed beam height. Depending on the availability of long diamonds, it may be preferable to operate with Si crystals of similar lattice spacing. Indirectly-cooled cryogenic Si crystals should readily work with the crab cavity on or off. Detailed finite-element thermal calculations for water-cooled Si at room temperature will be performed with the crab cavity on and off in the final design.

A double-multilayer monochromator (DMM) will be located downstream of the DCM and will be able to accept the pink bean when the first crystal of the DCM is translated out of the beam. The DMM will have a higher throughput at the expense of a wider bandwidth. This will be also at the expense of a longer pulse duration. Similar calculations as the ones described in section 4.2.2.2 showed that the red shifted radiation emitted by the undulator at 9.95 keV when tuned to 10 keV increases the time resolution from 2.8 ps to 3.6 ps. For the DMM to be tunable over a wide energy range, several coatings with different d-spacings will be available. The DMM will likely require liquid nitrogen cooling due to the large power density incident on the first crystal. It will also have the same vertical offset as the DCM. Simulations will be performed in the final design to guide the selection of the multilayer design bandwidth.

4.2.4.4.6 Mirrors

The coatings for both long mirrors will be three stripes of Pt, Ni (or Rh), and Si. With a 2-mrad incidence angle, the three coatings allow the mirror to match the energy range of the beamline, 4.7-35 keV, and to discriminate against higher harmonics. The white-beam collimating mirror at 27.5 m is water-cooled, using single-crystal Si substrates with dimensions of about 10 cm x 10 cm x 1.2 m. It will absorb 700 W of power when the gap of the U30 undulator is tuned to emit 4.5 keV in the fundamental and the crab cavity voltage is off. This is the power that the Si mirror would absorb with white beam slits set to 3 mm x 1 mm (H x V), containing practically all of the undulator cone.

Mirrors as first optical elements are already used in a horizontal reflecting geometry at beamlines 2-ID and 12-ID. Similar mirror systems are employed in a vertical geometry at the APS as part of a long K-B mirror pair (up to 1 m) at 13-ID, 14-ID, and 16-ID. Both mirrors will produce cylindrical figures with tangential radius of curvature in the range 15-30 km. The mirrors will have surface roughness less than 2-Å RMS and slope errors less than 1-μrad RMS.

4.2.4.4.7 Miscellaneous Optics

A water-cooled filter unit will be available for initial focusing of the beam at the chopper location. Low-Z materials are preferable as they can survive the large power density of the APS. Diamond, Be, and Al foils will be considered, with thickness to be determined. The existing filter unit F2-30 located in 7-ID-A will be utilized.

4.2.4.4.8 Diagnostics

Three standard APS Upgrade YAG:Ce fluorescent screens equipped with EPICS-supported CCD cameras will be located in the 7-ID beamline. They provide high spatial resolution (few μm) and large field of view (5 mm) for alignment and diagnostics of the optics. These screens were not included in the conceptual design report. One screen is placed after the first mirror, another after the second monochromator, and a final one after the second mirror as shown in Figure 4-8.

In 7-ID-C, a diagnostics screen is also needed near the chopper to optimize the focus. The existing x-ray BPM will need an upgrade as it currently uses fluorescence from a Ti foil as the main source of signal for a quad-diode detector. Since Ti spectroscopy is envisioned, a foil of lower-Z material is also required. Since the crab cavity beam reduces the flux of the beamline, new electronics with higher current gain are required to work at high energy (above 10 keV). Commercial designs are also available for x-ray BPMs with selection of several foils. Calculations and projection from current experience will guide the final design.

4.2.4.5 7-ID-C Diffraction Experimental Station

This section describes the x-ray optical components and instruments planned for the 7-ID-C experimental station. Items in scope and located in 7-ID-C are the x-ray chopper to select variable repetition rate, a K-B mirror pair to focus at the sample to few micron spotsize, a refurbished general purpose 6-circle x-ray

diffractometer that will have an enhanced cryostat translation stage, and a pixel array detector (Pilatus 100k) for diffraction experiments.

4.2.4.5.1 X-ray Beamline Components

An x-ray chopper able to isolate a singlet in 24-bunch mode at 271.6 kHz is necessary for reducing sample damage for many experiments. It will be located after the x-ray BPM and will be on an X-Y translation stage to move it in and out of the beam. It will likely be based on current air-bearing technology in use at APS sectors 7-ID, 26-ID, and 32-ID, but with more slots and narrower ones than the existing chopper [26]. These have been found to operate very reliably. The chopper will serve both 7-ID-C and D stations.

The dynamically bent K-B flats are 0.5-m-long Si substrates, with 2-Å RMS roughness and 1μrad RMS slope error. The vertical mirror can accept all the vertical fan delivered through the front end at all design energies. The horizontal mirror acceptance will depend on its angle of incidence which will be optimized to reject higher harmonics. Diffraction experiments in 7-ID-C typically do not run above 15 keV, so this optics can accept 85% of the horizontal source. As mentioned in section 4.2.3.1, the spot at the sample will be less than 15 μm in both directions with a divergence of 2.2×0.06 mrad^2 (H × V).

4.2.4.5.2 Instrumentation

In 7-ID-C, the existing 6-circle diffractometer (Huber Psi 5021), with refurbishment, will be used in conjunction with the advanced area detectors described below. The 6-circle Huber diffractometer in the 7-ID-C enclosure has served with distinction as an instrument for collecting high-quality time-resolved x-ray diffraction data. The six angular degrees of freedom (4 for the sample and 2 for the detector) allow great freedom of scattering geometry as well as freedom in laser-delivery geometry. The standard sample stage has high-resolution XYZ motions, allowing precise positioning of the sample in the beam. An Advanced Research Systems Displex DE202 cryostat (with an ARS-4HW compressor) and an ADC x-ray oven are currently available, allowing base temperatures from 10 K to several hundreds of K. Special covers have been designed and fabricated to allow laser access and large range of x-ray diffraction angles. Common detectors include an avalanche photodiode (APD), with angular resolution defined either by slits or by an analyzer crystal; a Pilatus digital pixel-array detector (loan from the APS Detector Pool, upon request); and occasionally user supplied CCDs. APDs and Pilatus detectors can be gated at the repetition rate of the laser for pump-probe measurements with a gate width of 50 ns [27]; both are about equally popular with 7-ID users.

There are two improvements for the Huber 6-circle diffractometer that will immediately expand the capabilities of the diffractometer by reducing set-up time and therefore increase the speed with which users move from alignment to measurement.

The first improvement is to procure a motorized XYZ stage for the existing Displex cryostat. With the development of a reliable cryostat cover that permits both x-ray and laser beams to reach the sample, the cryostat is a popular accessory to the diffractometer, used with about 25% of recent diffraction experiments. A significant drawback is that only manual translation is available for adjusting the cryostat's position. It is thus very difficult to move the sample to the center of rotation, requiring a trial-

and-error method of going in and out of the enclosure several times to see if the manually adjusted position is satisfactory. Such adjustments are needed every time the sample temperature is changed as the various parts of the cryostat undergo thermal expansion or contraction. A motorized stage would reduce this tedious work to a few simple, automated scans. Each direction has a range of ±2 mm with 1 micron precision. It may also make time-resolved, low-temperature microdiffraction measurements feasible. A commercial solution is included in the scope (Huber 512.12M cryostat carrier).

The second improvement is a rebuilt detector arm for the diffractometer. A dual-detector arm that can hold two detectors, offset in angle, will eliminate significant time spent in installation and alignment. Every time the detector is switched between, say, a Pilatus and an APD, effort (and beamtime) are needed to mount the detector and its equipment on the detector arm, attach cables, align slits, etc. Some of this work can be done between experiments (although some users wish to swap detectors mid-beamtime), but parts (such as fine alignment of slits) must be done with the x-ray beam. A dual-detector arm will allow a switch from one detector to another with a simple rotation of the Two-Theta circle. The dual detector arm will have two dovetail rails, instead of the current single rail, precisely aligned and offset from each other by perhaps 20 or 30°, upon which the different detectors can remain mounted. Heavier counterweights will be required, and stronger motors may also be necessary. It is conceivable that under special circumstances, some experiments may be able to make use of detectors on both arms simultaneously. This will be custom made by Huber.

State-of-the-art excitation (see laser section 4.3.5) and detection schemes will be necessary for experiments at the SPX facilities. For SPX operation at the full-repetition rate of 6.5 MHz, or at lower-repetition rates selected by the chopper, standard detectors are suitable. Advanced pixellated photon counting detectors, e.g., Pilatus, are required at both 7-ID-C for diffraction and at 7-ID-D for detection of fluorescence and scattering from dilute samples. For these pixelated photon-counting detectors, two additional features are desirable: an upper- and lower-level discriminator; and multiple, independently-gateable count registers. Complementary, advanced pixelated integrating detectors with large dynamic range and fast readout are desirable for diffraction studies, especially for time-dispersed diffraction. Since these are not available commercially, the Project will procure a Pilatus 100K for the 7-ID-C enclosure to satisfy the spatial resolution and collection area requirements.

4.2.4.6 7-ID-D Spectroscopy Experimental Station

This section describes the x-ray optical components and instruments planned for the 7-ID-D experimental station specializing in flowing liquid and gas jet targets. The two items in scope located in the 7-ID-D experimental station are: 1) a set of K-B mirrors for focusing to few micron spot size, and, 2) a pixellated array detector for x-ray emission spectroscopy or x-ray diffuse scattering (Eiger 1M). There are no requests for other auxilliary user equipment; the purpose-built liquid and gas targets are user-supplied and mounted on existing 5-degree-of-freedom tables with micron precision in motion.

4.2.4.6.1 X-ray Beamline Components

The x-ray chopper serving 7-ID-C will also be used for 7-ID-D to isolate a singlet in 24-bunch mode at 271.6 kHz when necessary. It will be located after the x-ray BPM and will be on an X-Y translation stage to move it in and out of the beam.

Atomic physics chambers and liquid jets use a working distance of ~0.25 m from the end of the K-B mirror. This implies a mirror-image distance of about 0.5 m, and thus limits the length of the mirror to 0.5 m. Therefore, a K-B mirror system, identical to the one for 7-ID-C, will be located in 7-ID-D. At an angle of incidence of 1.8 mrad, a 0.5-m Rh-coated mirror has a reflectivity of about 80% at 35 keV. At this angle of incidence the vertical mirror will collect 86% (100%) of the vertical beam defined by the 2mm (0.3 mm) aperture and the horizontal mirror will collect half the horizontal radiation fan. As seen in Figure 4-15 and Figure 4-16, the spot size and divergence at the sample are 7×10 μm^2 (H × V) and 4×0.15 $mrad^2$ with the 0.3 mm vertical aperture and pulse duration of 3.5 ps.

4.2.4.6.2 Instruments

In 7-ID-D, user-provided liquid- and gas-phase jets and x-ray emission spectrometers will be used for spectroscopy and scattering. Facility-provided instrumentation will include sample positioning to 1-μm precision, and advanced detectors.

State-of-the-art detection and excitation schemes will be necessary for experiments at the SPX facilities. For SPX operation at the full-repetition rate of 6.5 MHz, or at lower-repetition rates selected by the chopper, standard detectors are suitable. Advanced pixellated photon counting area detectors are required for fluorescence and resonant inelastic x-ray scattering from dilute samples [4, 7, 8, 28]. For the 7-ID-D experiments, an Eiger 1M (with 75 micron pixels) will be procured to satisfy the spatial resolution and collection area requirements for the proposed experiments.

4.2.5 Optical Laser Systems and Infrastructure

High power (up to 20 W), high-repetition-rate (up to 6.5 MHz) and high peak power (up to 50 GW) laser systems will be procured and installed to support the time-resolved experiments. The details of the laser systems and their infrastructure including beam transport, timing diagnostics, and safety ancillaries are described in Section 4.3.5, in the section describing the SPXIM beamline. Table 4-9 summarizes the performance parameters of the laser systems.

Table 4-9: Performance parameters of the laser systems.

	Wavelength	**Duration**	**Rep Rate**	**Power** **Energy per Pulse**	**Remarks**
High-power, high repetition rate laser	1 μm	<0.5 ps	6.5 MHz variable	20 W <10 μJ	
High-peak power laser	800 nm	50 fs	10 kHz	25 W 2.5 mJ	
High-peak power laser	800 nm	50 fs	10 kHz	10 W 1 mJ	Upgraded 7-ID laser
Optical parametric amplifiers	0.2-20 μm			Varied	Pumped by above lasers

4.2.6 Additional

4.2.6.1 Safety Requirements

See SPXIM Safety Requirements in section 4.3.5.5.

4.2.6.2 Control Room

A new enclosed control area is planned for 7-ID on the outboard side of 7-ID-C, as shown in Figure 4-3. It will house workstations and some control equipment. Its requirements are similar to other control areas.

4.3 Short-Pulse X-ray Imaging and Microscopy Beamline

The experimental facilities associated with the Short-Pulse X-ray (SPX) source will combine picosecond (ps) temporal resolution with atomic-scale structural precision, elemental and chemical specificity, and nanoscale spatial resolution to enable an understanding of the relationship between structure and function in complex systems. Dynamics are typically initiated with optical laser pulses, which can be used to generate radiation from the terahertz through the extreme ultraviolet for excitation of electronic states and lattice degrees of freedom. Such excitations can heat systems through phase transitions (e.g. melting, ferroic, and superconducting transitions) in complex systems and can create metastable states not present in thermal equilibrium. Excitations can also be initiated with pulsed electrical fields applied on microscopic devices, or via optically induced mechanical transients.

The SPX Facility is designed to take advantage of the unique features of the SPX source, the most important of which is the production of short-duration x-ray pulses at the full 6.5-MHz repetition rate of the APS. The high average x-ray flux is conveniently parceled in bunches of 10^4-10^6 x-rays in each ps-duration pulse. The x-ray probe thus offers the opportunity to probe dynamics on an atomic-length scale (via diffraction) with minimal x-ray induced perturbation of the system. The SPX can produce variable x-ray pulse durations, controlled by the magnitude of the radio frequency [rf] deflection, or, alternatively by the vertical opening of the slit used to select the fan. The method using the slit aperature has the advantage of allowing the pulse duration to be set independently at different SPX beamlines. The photon energy and x-ray spot size can be readily and independently chosen for specific experiments at the beamlines within the SPX facility. The advantageous timing structure of the APS storage ring makes it straightforward to select a variable experimental repetition rate as required for different systems. In particular, the shorter pulse duration and maximum repetition rate is ideal for the study of emerging nanoscale devices operating in the terahertz domain.

The second independent beamline in the SPX Facility is the Short Pulse X-ray Imaging and Microscopy (SPXIM) and as noted earlier, the SPX Facility is located between the two rf deflection cavities [2, 3] that provide chirped electron pulses. The propagation of the APS storage ring's electron beam through the cavities imposes a correlation between the longitudinal position of an electron in the bunch and its vertical momentum. The x-ray radiation emitted during the electron propagation through an undulator or bending magnet preserves the correlation and a short pulse can be selected out simply with a pair of slits. The SPXIM beamline described in this section is unique in that it will also allow the capture and

refocusing of the entire vertical fan of radiation to provide time-dispersed capabilities with few picosecond resolution.

The principal goal of the SPXIM beamline is to provide picosecond-duration, high-repetition-rate pulses of tunable, polarized x-ray radiation for imaging and microscopy experiments in condensed matter physics and materials science. The picosecond time scale has unique importance because it is an excellent match for structural dynamics in nanoscale systems. These areas are of technological relevance as well as fundamental interest.

The facilities described here will facilitate ground-breaking experiments in a range of scientific problems. The SPX facilities will have an important and immediate impact on unresolved problems in these areas. Scattering, imaging, and spectroscopy probes will be particularly valuable in five areas [29]:

1. ***Dynamics in ferroic materials***. In nanomagnetic, ferroelectric, and multiferroic systems the competition of multiple long-range order parameters leads to new opportunities to manipulate remnant electrical polarization and magnetic order and to drive materials into structural states far from equilibrium [30, 31, 32].
2. ***High-frequency materials and devices***. Structural phenomena have a large impact on optical and mechanical properties in the 10 GHz to 1 THz range, but the detailed origins of these phenomena are only beginning to be understood and exploited. [33, 34, 35]
3. ***Thermal and atomic transport at interfaces.*** Many critical processes in the transport of heat across interfaces and the motion of solid-liquid interfaces occur at timescales that have previously been inaccessible to precise x-ray structural probes [10, 11, 12].
4. ***Dynamics of fundamental excitations.*** The structural features associated with the fundamental excitations of solids and the cascade of energy between these excitations are presently difficult to probe because appropriate time-resolved structural techniques do not exist [13, 14].
5. ***Picosecond imaging.*** The SPX facilities provide the capability to form picosecond duration images of ultrafast processes and, via the divergence of the SPX source, single-shot images of long-length-scale 1-D phenomena including the dynamics of fluid jets and fluid-interface interactions [36, 37].

The SPXIM beamline uses x-ray radiation produced by a hard x-ray insertion device (ID) and consists of two experimental stations; one that uses the full vertical fan to enable novel time-dispersed diffraction capabilities and to record a time history of ~100 ps with few-ps resolution; and a second that houses a zone-plate-based microscope capable of focusing the monochromatic radiation to approximately 100 nm. The SPX facility will be equipped with high-power and high-repetition rate femtosecond lasers, similar to those already existing at the APS [17] that will deliver beams to the SPXIM beamline and SPXSS beamlines. This section describes the x-ray optics, instrumentation, and lasers planned for the SPXIM beamline.

4.3.1 Scientific Objectives

The SPXIM facility will be located at beamline 6-ID. Two set-ups will be developed in independent experimental stations; a 6-circle diffractometer in 6-ID-B and a zone-plate based microscope in 6-ID-C. A block diagram is shown in Figure 4-17.

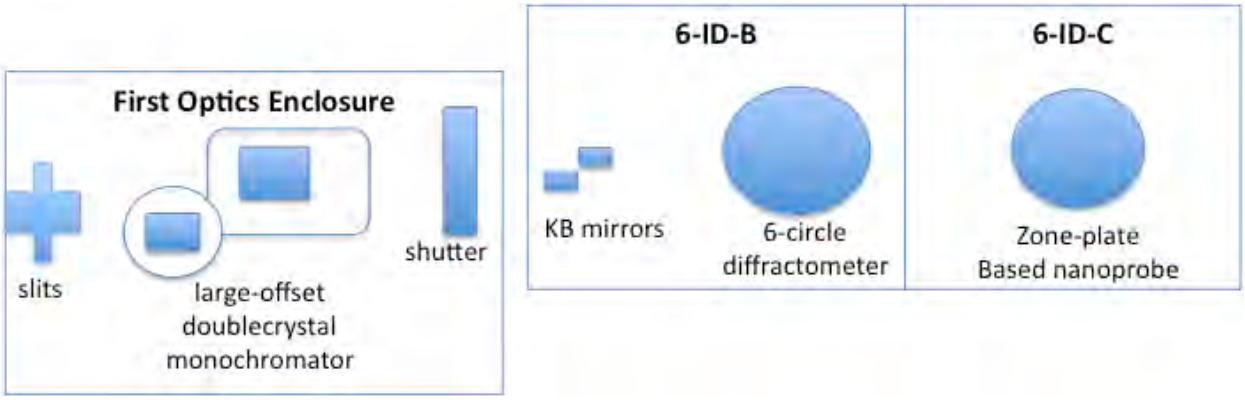

Figure 4-17: Block diagram of SPXIM beamline showing x-ray optical enclosures and location of major components.

The unique operating mode of the 6-ID-B diffractometer involves operating the 6-ID beamline with a large vertical white-beam slit. An angle-time correlation is then established in the incident x-ray beam by refocusing. When such a beam is diffracted by the sample, the entire time histotry can be captured. This effect can be used to improve the throughput of experiments because this diffractometer will provide picosecond time resolutoin but with all the monochromatic flux of a typical beamline. Diffraction experiments in 6-ID-B will be done with moderate angular resolution on single-crystal and epitaxial films by diffracting in the horizontal plane. Here the horizontal source divergence (0.05 mrad) and size will limit the angular resolution and the monochromator energy resolution, but the Bragg diffracted beam will preserve the vertical-time correlation, which can be imaged by an area detector. A laser-pump x-ray probe experiment set up to diffract in the vertical plane will modify the SPX beam's time-angle correlation, as shown in Figure 4-18.

The nanoprobe facility will be located in station 6-ID-C. Here, a tight vertical white-beam aperture is employed. The SPX does not change the vertical source size of the APS undulator x-ray source and it will be possible to focus the hard x-ray radiation to spot sizes comparable to other nanoprobe beamlines with an anticipated focal spot size of 100 nm. Experiments on complex oxides and nanoscale devices will be pumped with high-repetition-rate lasers and probed with picosecond-resolution x-rays on length scales established by the focused beam. The time-resolution gained by the SPX causes each pulse to be reduced in total flux by a factor of 40 in comparison with the full 100 ps duration of present pulses. The reduced intensity can be regained in many systems by increasing the repetiton rates of experiments from the relatively low 1-5 kHz rates presently employed. Increasing the repetition rate up to 6.5 MHz could provide large improvements in the average scattered flux, with 40 times better time resolution.

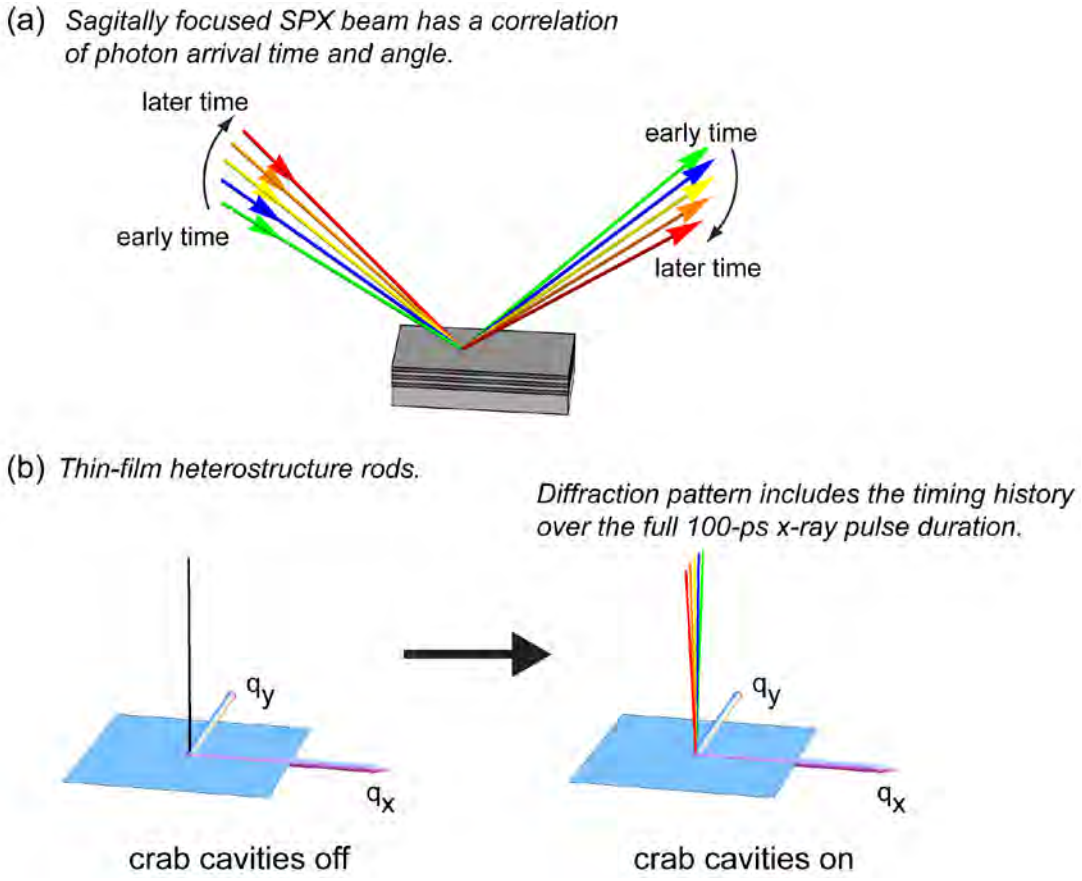

Figure 4-18: Time-dispersed diffraction. (a) Time vs. angle dispersion of the incident x-ray beam. (b) Timing information is imprinted in the angular distribution of diffracted intensity from a thin-film heterostructure.

4.3.2 Source Properties and Requirements

Section 4.3.2.1 describes the selection of the undulator for the beamline, while section 4.3.2.2 describes the correlation between the timing and spatial properties of the SPX source.

4.3.2.1 Spectral Requirements

The SPXIM beamline on 6-ID requires a spectral range coverage from approximately 7 keV to 14 keV in order to provide adequate resolving power in diffraction experiments. To optimize the flux in this energy range, a 2.1-m-long revolver undulator with 27-mm and 30-mm periods was selected. The beamline may be canted in the later stages of its development, following the APS Upgrade, and the selection of the revolver undulator rather than two independent devices keeps that option open. The 27-mm period gives continuous tuning over the entire energy range, and the 30-mm period provides enhanced brightness below 7 keV and above 16 keV with Si <111> as one of the monochromator crystals (see Figure 4-2). It is assumed the minimum gap available for the undulators is 11 mm.

4.3.2.2 Source Properties – Unique Features of the SPX Source

The chirped electron beam of the SPX source is unique. Therefore, extensive ray tracing was performed from the source through the optics in order to assure the preservation of the timing and to understand the subtleties of the time-angle correlation for the time-dispersed diffraction capabilities. The electron beam and x-ray sources were simulated by the Accelerator Systems Division with the source of the radiation as the 2.7 cm period undulator tuned to 10 keV (k=1.2) located 1.2 m downstream the center of the 6-ID straight section. The distribution of 10^6 electrons (on horizontal and vertical phase space and time) at the center of the undulator was obtained using the elegant code [20] and was subsequently convoluted with the undulator radiation obtained using spectra [21]. 24-bunch mode with a 41 ps rms electron bunch length were assumed.

Figure 4-19 shows the correlation between time and the vertical angle of the radiation emitted over the full horizontal fan of almost 200 µrad. Figure 4-20 shows the same correlation when the horizontal acceptance is limited to 50 µrad, which contains 25% less particles than Figure 4-19. As seen in Figure 4-20 and less clearly in Figure 4-19, there are three bands. The central one corresponds to the radiation emitted by the undulator in the first harmonic whereas the other two bands correspond to the off-axis radiation due to the second harmonic which is shifted from the central one by $\pm\gamma^{-1}\,(1+k^2/2)^{0.5} = \pm 96\mu\text{rad}$. Figure 4-20 demonstrates that the correlation between time (t) and vertical angle is linear for the first harmonic radiation over approximately ±200 µrad and |t|<40 ps with a slope of 0.18 ps/µrad. The percentage of particles with |t|>40 ps in the ±200 µrad vertical angle range, due to the electrons in the back-chirped pulse is slightly less than 0.1%. It is interesting to note that the time-angle correlation in Figure 4-20 is inverted from Figure 4-4 on SPXSS because of the different beta functions in the two SPX straight sections.

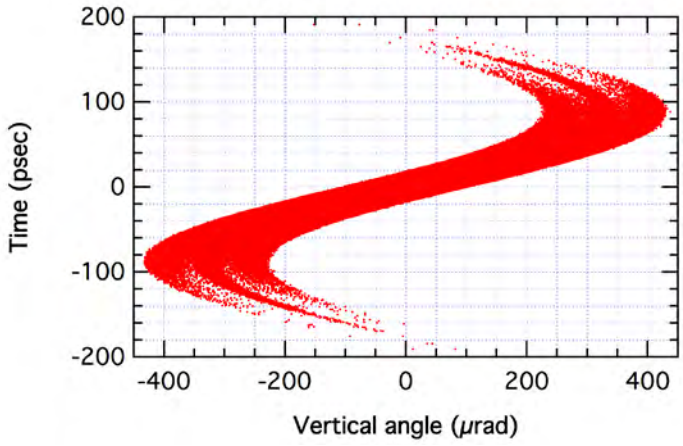

Figure 4-19: Correlation between time and vertical angle when accepting the full horizontal fan.

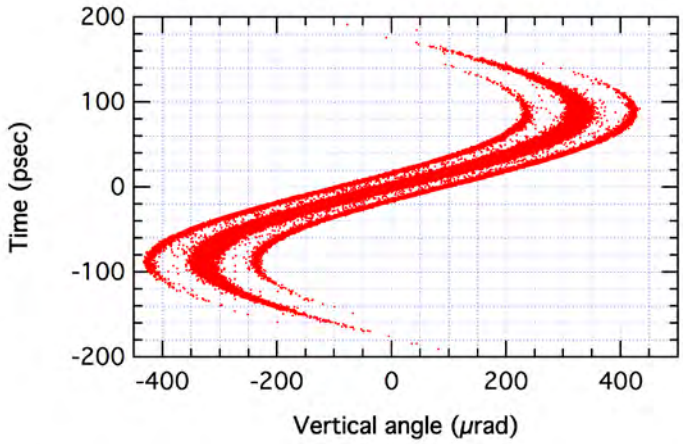

Figure 4-20: Correlation between time and vertical angle when accepting 50 μrad horizontally.

The linear dependence between time and vertical angle was used to separate the contributions of the first and second harmonic radiation over the ±200 μrad vertical angle range. The individual distributions were then propagated as a function of the longitudinal position relative to the center of the insertion device. Figure 4-21 shows the standard deviation (SD) of the vertical photon size as a function of the longitudinal position for the three bands. The minimum of the three bands is 15 μm and its location is at 0.76 m downstream from the center of the undulator. Actually, the vertical waist of the photon beam coincides with that of the electron beam, which is at 1.96 m downstream the center of the 6-ID straight section. Therefore, the plane at 1.96 m from the center of the straight section is the vertical source position. It should be noted that the SD of the photon beam size along the vertical direction is slightly larger than that of the electron beam (14 μm). A similar calculation yields a horizontal SD size equal to 272 μm, which is equal to the horizontal SD of the electron beam located at the center of the 6-ID straight section.

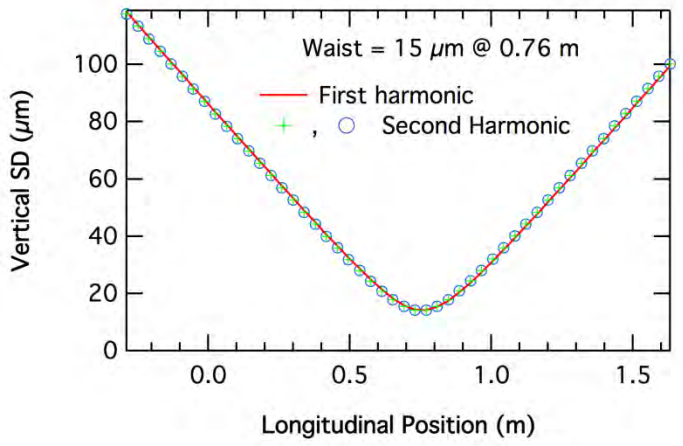

Figure 4-21: Vertical SD of the photon beamsize as a function of the longitudinal distance. Zero meter corresponds to the center of the undulator. The longitudinal dependance of the the vertical size of the first (red line) and second (green + and blue o) harmonic is actually the same.

The time distribution of the three bands at the position of the vertical focus (Figure 4-22) demonstrates that the center of the second harmonic contributions are at ± 96 µrad × 0.75 m= 72 µm from the first harmonic radiation and that they are reasonably well separated. This means that a slit located at a vertical image plane of the photon beam will allow to significantly reduce the radiation of the second harmonic which arrives at a different time for the same divergence.

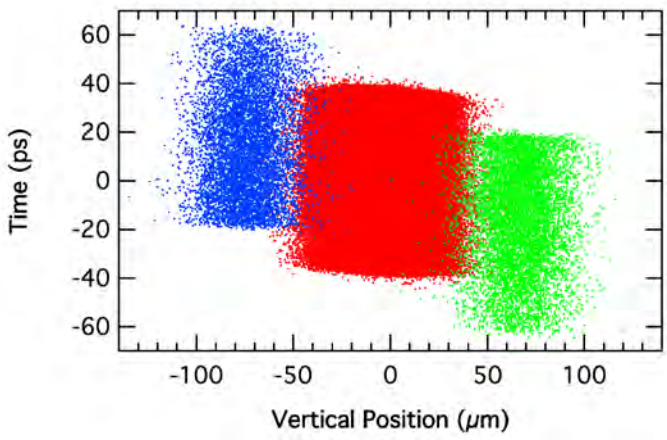

Figure 4-22: Time vs vertical position at the vertical source plane (0.76 m downstream the center of the undulator) for the first (red dots) and second (green and blue dots) harmonic.

4.3.3 X-ray Optical Layout

The primary optical elements in the 6-ID beamline are shown in Figure 4-23 and listed in Table 4-10.

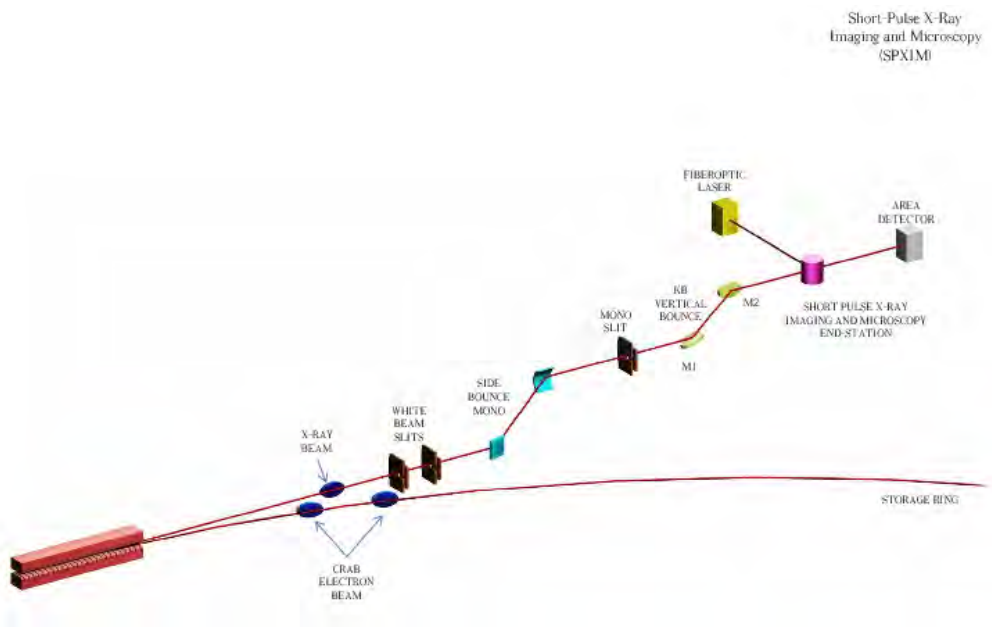

Figure 4-23: The x-ray optical layout for SPXIM experiments. A large offset double-bounce monochromator deflects the beam horizontally and the second crystal focuses the beam vertically with a sagittal bender. The K-B mirror located at the front of the 6-IB-B enclosure can be used to focus either in the 6-ID-B or 6-ID-C experimental station. The zone-plated based microscope planned for the 6-ID-C experimental station is not shown in this figure.

Table 4-10: Beamline components in the 6-ID beamline.

Component	Distance to Center of Straight (m)	Notes
White-Beam Slits	32	Maximum beam size 25 mm (V) x 3 mm (H)
Side-Bounce Double-Crystal Monochromator	35	Large-offset Si <220> and Si <111> crystals, first crystal liquid N2 cooled, second crystal vertical focusing with sagittal bender similar to European Synchrotron Radiation Facility design; energy ranges: Si <111> 4.5-8.3 keV, Si <220> 7.2-14 keV, Si <333> 13.5-24.9 keV
YAG:Ce Diagnostics Cross	35.25	For alignment of the monochromator first crystal
White-Beam Stop	36	With mask and Lead bremsstrahlung stop
YAG:Ce Diagnostic	37	For alignment of the monochromator second crystal
Monochromatic Shutter	40	Accommodates full vertical fan
Secondary Focusing Enclosure	54	Observe the vertical focus at ~2:1 demagnification for the sagittal bender with the YAG:Ce diagnostic cross
Beam Transport	40-55	New UHV-shielded, monochromatic beam transport
Timing slit	54	Vertical slit to isolate fundamental radiation
YAG:Ce Diagnostics with X-ray BPM, Ending with Be Wndow	55	In-enclosure beam diagnostics and feedback signal for the monochromator
K-B Mirror Pair	57	Long (0.5 m) K-B pair, Si substrate, 1-Å roughness, 1-μrad slope error, dynamically bent
6-Circle Diffractometer	60	New instrument for using the time-angle correlation in diffraction experiments.
Zone-Plate Microscope	65	Nanoprobe station with 100-nm focus for imaging and diffraction

4.3.3.1 Simulated Beamline Performance

The novel nature of the chirped electron beam source and x-ray focusing required for the time-dispersed diffraction method mandated a complete optical ray tracing for the SPXIM beamline. It was questioned as to whether the sagittal focusing by the second crystal of the offset monochromator would smear the time resolution. The ray tracings described below were performed with the SHADOW code [22, 23]. The source used in the ray tracings consisted of the 10^6 rays mentioned in section 4.3.2.2 having a continuous distribution of photon energies between 9.997 and 10.003 keV. An aperture 31 m downstream of the the source was set to accept 50 μrad × 200 μrad (hor.×ver.).

The first optical element is a horizontally diffracting Si <220> crystal tuned to 10 keV. The second crystal in the double crystal monochromator (DCM) is also a Si <220> crystal. This crystal is sagittally bent (to a radius of 7.6 m) to focus the 10 keV beam along the vertical direction at the slit which, is positioned at a distance of 54 m from the source. The vertical demagnification is approximately 2:1; not the conventional 3:1 used when a sagittal crystal focuses a much larger divergence [38]. Figure 4-24 shows the intensity as function of the incident energy obtained using SHADOW for three cases: a) after a single flat crystal; b) after a flat crystal followed by the sagittally bent crystal; and c) after the flat crystal followed by a second

flat crystal instead of the sagittally bent one. As seen in the figure, the results for cases b) and c) are practically identical; i.e., neither the energy resolution nor the total intensity are affected by the use of a sagittal cylinder. The figure also compares the resolution obtained using SHADOW with the resolution after two Si <220> p reflections with collimated light. The full width at half maximum (FWHM) with collimated light is 0.49 eV, half the value obtained from the SHADOW results since the latter include the broadening of the energy resolution due to horizontal divergence.

The ray tracings at the vertical slit plane are presented in Figure 4-25. The figure shows a central illuminated zone containing most of the rays as well as two weaker zones separated from the main and above and below it. The correlation between time and vertical angle at the slit plane (see Figure 4-26) shows the main band due to the first harmonic and the two weaker bands due to the second harmonic radiation. As demonstrated in Figure 4-27, a 25 μm slit almost completely eliminates the bands due to the second harmonic. However, the slit does not remove, or decrease, the radiation emitted by the electrons in the "back-chirped" pulses, corresponding to approximtately 0.1% of the intensity of the beam. The time resolution obtained from Figure 4-27 is 2.4 ps (FWHM). Ray tracings performed with preliminary results of finite element analysis of the bent crystal show that the anticlastic bending of the crystal does not affect the vertical size of the beam at the exit slit.

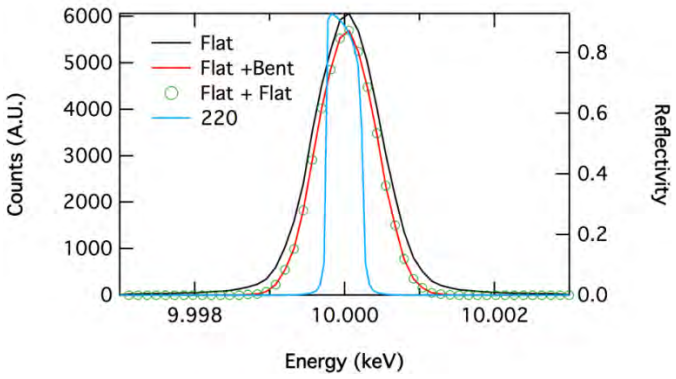

Figure 4-24: Energy resolution of a single flat <220> Si crystal (black trace); a flat followed by the sagittally bent crystal (red line); two flats (green circles). Right axis: Reflectivity of two flat <220> Si with collimated light.

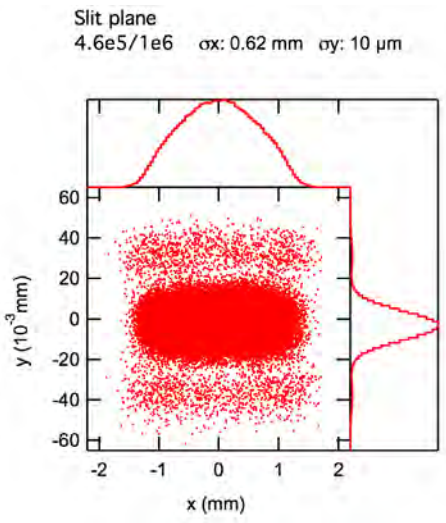

Figure 4-25: Ray tracings at the vertical slit plane. The captions above the figure show the transmitted and total number of rays and the RMS values along the horizontal and vertical directions. The numbers of rays were reduced in this figure for clarity.

The first element of the K-B pair [39] is an elliptical cylinder imaging the source along the horizontal direction onto the sample position with a demagnification of 19. The next element of the K-B pair is the vertical focusing mirror which demagnifies the vertical slit by a factor of 1.6. The spot at the sample position with a 25 μm at the slit plane is seen in Figure 4-28. Based on the results presented in Figure 4-25 and Figure 4-28, a 25-μm slit is required to eliminate the second-harmonic contribution. The 25-μm slit also reduces the total flux by 15% because it intercepts the main beam. The divergence of the beam at the sample position is seen in Figure 4-29. The divergence distribution is 1.3 mrad wide along the vertical direction and approximately 0.8 mrad wide along the horizontal direction.

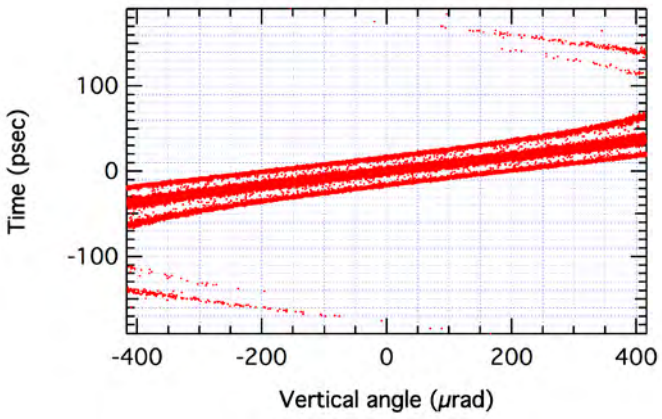

Figure 4-26: Correlation between time and vertical angle at the slit plane.

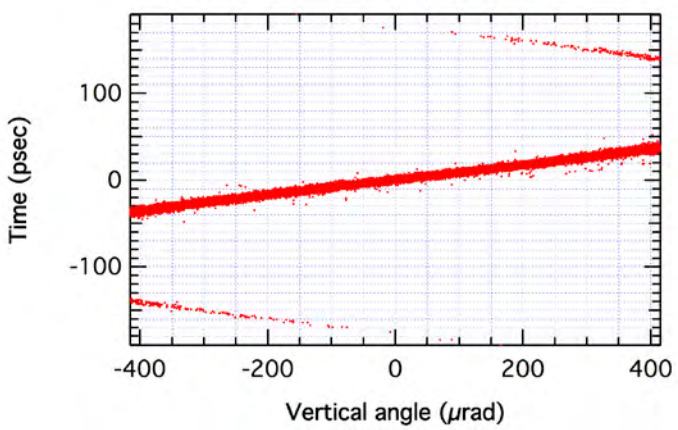

Figure 4-27: Correlation between time and vertical angle with a 25 μm vertical slit as seen behind the slit plane.

Slope errors of 0.5 μrad RMS along the vertical direction on the K-B pair will result in a spot size equal to $2 \times 0.5 \times 10^{-6} \times d$, where d is the distance between the mirror and the sample. For the horizontal mirror d=3 m and the resulting slope error does not have a major influence on the spot size. The vertical mirror is 2.3 m from the sample and the slope error will enlarge the spot to around 5 μm RMS.

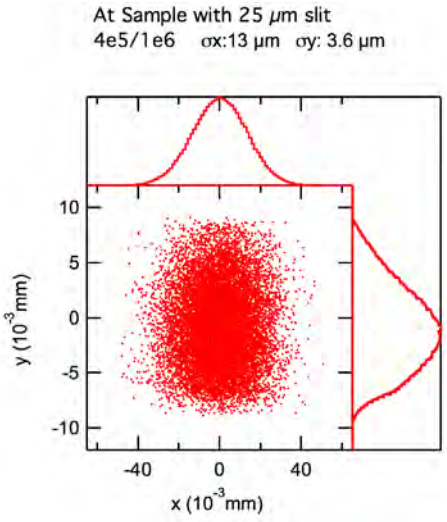

Figure 4-28: Ray tracings at the sample position after a 25 μm slit. The numbers of rays were reduced in this figure for clarity.

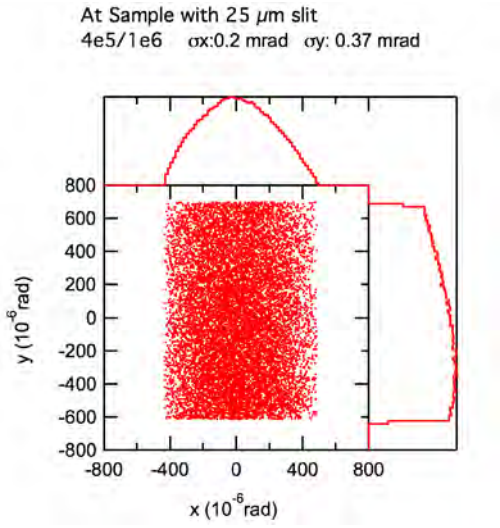

Figure 4-29: Divergence at the sample position after a 25 μm slit. The numbers of rays were reduced in this figure for clarity.

4.3.3.2 Monochromators

A double-crystal monochromator with cryogenically cooled Si <111> and <220> crystals is planned. A similar ACCEL monochromator is currently in use at 12-ID. The diffraction plane is horizontal and the monochromator will have a 0.86-m horizontal offset. It will provide monochromatic x-rays with an energy resolution ΔE/E of 1 x 10^{-4} for Si <220>. The design of the monochromator takes into consideration the energy range required for experiments and the details of the mechanical design. The current design of the similar monochromator at station 12-ID allows it to cover the photon energy range from 7.2-14 keV with Si <220> crystals. The second crystal of the SPXIM monochromator has a commercial sagittal bender that enables vertical focusing of the full SPX vertical fan. Two different crystal orientations will be outfitted to extend the range of photon energies. Energies below 7 keV will be reached using Si <111> crystals. To reach energies up to 24.9 keV, one will use the Si <333> reflection of the monochromator. The energy ranges for each crystal are shown in Table 4-10. The lower energy range will be useful in accessing a wider ranges of elemental edges for resonant scattering, e.g. the Fe K-edge relevant to some multiferroic materials. Higher energies with Si <333> crystals allow higher wavevector coverage and shorter x-ray pulses [3]. Two Si flats <220 and 111> will also be included to bypass the bender for imaging experiments that require preservation of the time-angle correlation [36].

4.3.3.3 Focusing Elements

A K-B mirror system, discussed in section 4.3.3.1 above, will be located in the 6-ID-B enclosure to provide a focused beam of a few microns. A microscope based on zone-plate optics discussed in 4.3.4.6 will be available in the 6-ID-C enclosure.

4.3.4 Beamline Physical Layout

Figure 4-30 shows the preliminary design layout of the SPXIM beamline. The sections below describe in more detail the beamline optics, laser facilities, and user instruments.

4.3.4.1 Front End

With an rf voltage of 4 MV, the root-mean-squared vertical divergence is 0.33 mrad in 24-bunch-mode operation, so a 1-mrad vertical acceptance would accept three standard deviations of the flux, or 86.6% of the total available flux. Although the installation plan for the SPX facility will have a total deflection voltage amplitude of only 2 MV, it may be possible to customize the beta functions of the undulator and cavity to achieve picosecond duration [40]. It is thus worth planning for 1 mrad acceptance. Transporting the full vertical fan of radiation will be challenging for the front-end design, i.e., the vertical mask at 25.5 m will be 25.5 mm. A front end with a 3-mm (H) by 25-mm (V) mask is thus required. The design of the canted SPX front-end is described in section 5.2.2. The energy range of this beamline allows the use of a thin Be window to separate the beamline and machine vacuum. A canted front end will be installed on 6-ID to enable the possibility of a future expansion of 6-ID to be a canted beamline. The upgrade to a canted beamline is not in Project scope.

4.3.4.2 Overall Beamline

The existing x-ray enclosures for Sector 6 of the APS are shown in Figure 4-30. The current 6-ID beamline uses four enclosures (6-ID-A, B, C, D) for a program focused on magnetic studies. The 6-ID beamline will be relocated as part of the APS Upgrade roadmap before the SPXIM beamline is installed. The 6-BM SPSXS beamline, aspart of the APS Upgrade contingent additional scope, is described in section 4.21.2. The Sector 6 facilities also include two bending magnet enclosures that were built but in which no beamline was installed.

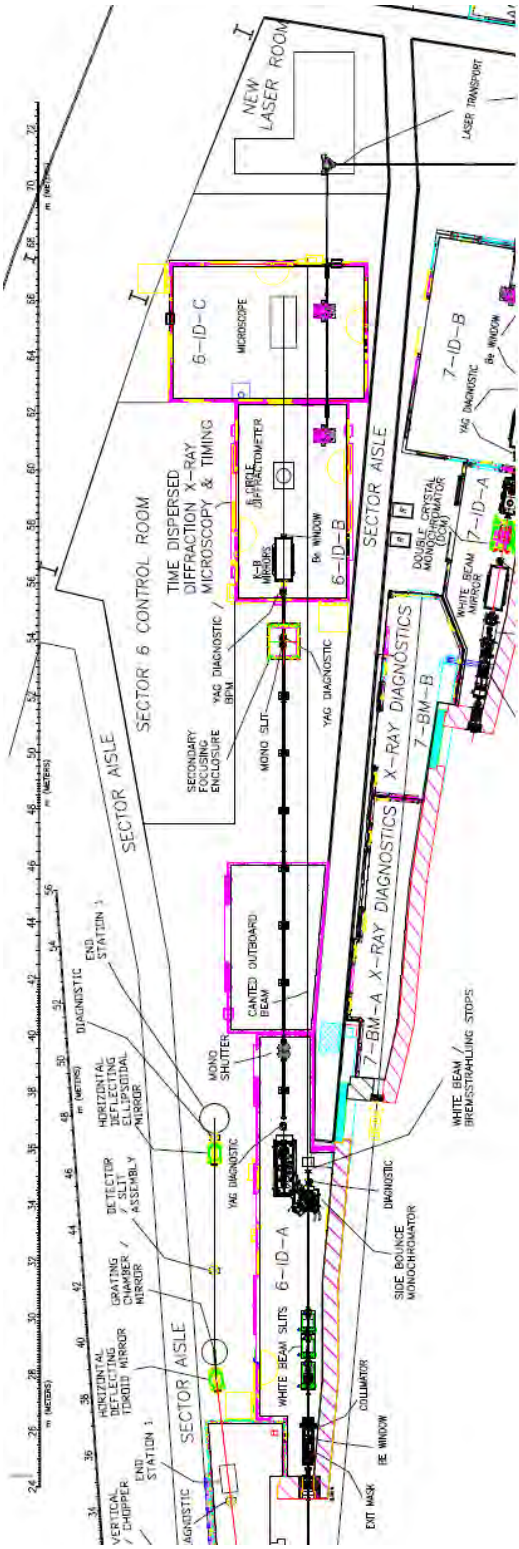

Figure 4-30: Preliminary design layout of the SPXIM beamline. The existing empty station after the monochromatic shutter will not be used for optics.

4.3.4.3 General Description

The SPXIM beamline consists of three x-ray enclosures and one laser enclosure. The 6-ID-A First Optics Enclosure (FOE) houses white-beam slits, a side-bounce monochromator, diagnostics, an x-ray shutter, and a white-beam stop. The 6-ID-B enclosure contains a 6-circle diffractometer and and 6-ID-C contains the zone-plate-based microscope. Both the diffractometer and the zone plate-based microscope can use the upstream K-B mirror system for focusing and/or harmonic rejection. A laser laboratory and a laser transport infrastructure is specified to deliver high-repetition-rate femtosecond laser beams on samples for the SPXSS, SPXIM, and potential SPSXS (contingent additional scope) beamlines.

4.3.4.3.1 Radiation Safety Aspects

The two Si crystals produce a horizontal beam offset of 0.86 m. This offset makes the shielding requirement from the bremsstrahlung straightforward. The monochromator will be followed by a Cu photon absorber and a bremsstrahlung beam stop on the white-beam path, and a monochromatic shutter on the offset beam. The downstream enclosures are designed for monochromatic beam only, thus the white beam is only present in 6-ID-A.

4.3.4.3.2 Vacuum System

A new equipment protection system (EPS) and vacuum controllers are required for 6-ID because it is a new beamline. These are designed with the best current practices; the controllers would reside on the roof of 6-ID-A, on a platform.

4.3.4.3.3 Data Acquisition and Motion Control

A new motion-control infrastructure will be developed to control the beamline. New Experimental Physics and Industrial Control System (EPICS) supported Versa Module Europa (VME) infrastructure will allow monitoring of the beamline and control of experiments. All equipment will be specified and installed by the APS Beamline Controls and Data Acquisition (BCDA) Group.

4.3.4.4 First Optics Enclosure and Infrastructure

This section describes the components and infrastructure housed in the FOE. Windows, slits, radiation safety system components, x-ray optics, and diagnostics are described below.

4.3.4.4.1 Windows

A Be exit window after the 3-mm x 25-mm mask separates the beamline and machine vacuum.

4.3.4.4.2 Slits

A large vertical opening, water-cooled undulator white-beam slit is specified. After contacting a reliable and well-known supplier of synchrotron radiation optics, it appears that the slits can be part of a canted beamline assembly, so that when the future canted beamline is put online, the slits can be used immediately.

4.3.4.4.3 Collimators

A collimator will be integrated after the front end to ease the bremsstrahlung shielding. Its location and aperture will be chosen following engineering ray traces performed in the final design.

4.3.4.4.4 Shutters/Stops

A white-beam stop, bremsstrahlung stop and a separate monochromatic shutter will reside in 6-ID-A.

4.3.4.4.5 Monochromators

The double-crystal, cryogenically cooled monochromator equipped with Si <111>, <220> and <333> crystals is designed to operate between 4.5 and 24.9 keV as described in Table 4-10. It will be a commercially available monochromator with a horizontal offset of 0.86 m. Because of the large vertical fan, the absorbed power will be significantly higher, although if the cavities are on, the power spatial density will be reduced significantly [41]. Indirectly-cooled cryogenic Si crystals are expected to work with higher heat load generated with the cavity off and will definitely work with the cavity on. Detailed finite-element thermal calculations for Si will be performed during the final design for the conditions with the rf-deflection cavities on and off to ensure that the detailed thermal design is compatible with the full power of the beam. A closed-loop cryogenic liquid nitrogen pump is required as well for the cooling of the first crystal.

4.3.4.4.6 Mirrors

There are no mirrors envisioned for the A enclosure.

4.3.4.4.7 Miscellaneous Optics

There are no other optics envisioned for the A enclosure.

4.3.4.4.8 Diagnostics

Several standard APS Upgrade YAG:Ce fluorescent screens equipped with EPICS supported charge-coupled device cameras will be located in the 6-ID-A enclosure. They provide high spatial resolution (10 μm) and a large field of view (25 mm) for alignment and diagnostics of the optics. One camera is needed after the first monochromator crystal and another after the second crystal.

To optimize the curvature of the sagittal bender, a YAG:Ce diagnostic screen is located after 6-ID-A at the 2:1 distance from the mid-travel point of the second monochromator crystal. The exact location was determined following x-ray optical ray traces covered earlier. The camera and diagnostic cross will be housed in a small Pb enclosure.

In 6-ID-B, a diagnostic screen is also needed near the virtual focus to optimize the focus. A new x-ray beam position monitor (BPM) will be procured; this BPM will use fluorescence from Ti foils as the main source of signal for a quadrant diode detector. A Ti foil has been in use for several years at 7-ID and works well for this energy range. Commercial designs are also available for x-ray BPMs with a selection of several foils. Calculations and projection from current experience will guide the final design.

4.3.4.5 6-ID-B Experimental Station

The next sections describe the x-ray optical components and instruments planned for the 6-ID-B experimental station.

4.3.4.5.1 Components

One K-B mirror system will be located in 6-ID-B. The dynamically bent K-B flat mirrors are 0.5-m-long Si substrates, with 1-Å RMS roughness and 1-µrad RMS slope error. Because of the upstream focusing monochromator, the vertical beam size at the K-B location in 6-ID-B will be a fraction of 1 mm, much smaller than the unfocused 50-mm high beam. The focal profile and beam size at the optics were determined by ray-tracing simulations using the SHADOW software package as described earlier. At an angle of incidence of 2.5 mrad, a 0.5-m Rh-coated flat has a reflectivity of approximately 64% at 25 keV and a beam acceptance of 1.25 mm. The full vertical beam in 6-ID-B will be collected with this optic over the full energy range of the monochromator. The horizontal mirror throughput will depend on the choice of undulator, x-ray energy, and distance from the source, but for 10 keV, the mirrors accept the full horizontal source. Ray traces demonstrate that these mirrors will be able to focus vertically to about 10 µm at the sample. The combination of the K-B system and the sagittal bender provide a variety of focusing configurations. A secondary vertical source will be created at the ~2:1 demagnification for sagittal focusing in the shielded enclosure in Figure 4-23. Spatial filtering with the slit as shown in Figure 4-27 cleans up the pre- and post-pulses from the second harmonic of the undulator. It will be the preferred mode of operation. The K-B mirror can then refocus the x-rays on the sample. If instead, one chooses to focus vertically closer to the K-B mirror on the Yttrium aluminium garnet (YAG) diagnostic screen at 55 m shown in Table 4-10, then one might compound focus the full source. This would be beneficial in some experiments working with x-rays above 20 keV where the K-B mirror angle must be reduced to optimize the reflectivity. Another option would be to focus sagittally at the sample, keeping the vertical K-B mirror flat. A slit just upstream of the sample would then remove the pre- and post pulses from the second harmonics.

4.3.4.5.2 Instruments

Specialized instrumentation is required for imaging, scattering, and diffraction experiments. At the 6-ID-B beamline, imaging and scattering experimental stations will be developed using new instruments. A new 6-circle diffractometer with several detectors will be used in conjunction with the advanced area

detectors described below. This diffractometer sits on an optical table to align it in the beam, and a table is present in front of the diffractometer for visible optics.

Excitation schemes will be necessary for experiments at the SPX facilities. For SPX operation at the full-repetition rate of 6.5-MHz, standard detectors can be used. When lower repetition rates are selected to match the sample relaxation, standard gated detectors will be used. Advanced pixelated photon counting detectors, e.g., Pilatus, are required at 6-ID-B for detection of both fluorescence and diffuse scattering. For these pixelated photon-counting detectors, two additional features are desirable: upper- and lower-level discriminators; and multiple, independently-gateable count registers. These features are not currently available in commercial detectors, but groups worldwide are developing detectors which may become available before the SPXIM final design is completed. The Project will review the available detectors during Final Design, and modify plans accordingly.

The choice of the detector for the time-dispersed diffraction mode is crucial and remains challenging. Complementary, advanced pixelated integrating detectors with large dynamic range and fast readout are desirable for diffraction studies, especially for time-dispersed diffraction. The baseline design includes a dedicated Pilatus 100 K. The challenges in using this instrument become apparent when the angular resolution necessary to make use of the timing information is estimated. With a sagittal focusing of approximately 2:1 demagnification and refocusing with the vertical mirror of the K-B pair (also approximately 2:1 demagnification), the vertical divergence on the sample is 1.3 mrad when the SPX cavities are operated at 2-MV. The total duration of the pulse is 72 ps (see Figure 4-29). To achieve 1 ps resolution in a pixelated detector, one must use an intensified gated Charge-Coupled Device CCD camera which images the visible fluorescence from a fast scintillator like LSO:Ce [42]. This scintillator is capable of isolating a single x-ray bunch in 24-bunch mode due to its 28 ns decay time. A gated camera is prefered to average data coincident with the laser frequency. One should be able to achieve 10 μm spatial resolution in such a gated CCD. When the detector is located 2 m from the sample, the pixel size corresponds to a 5 μrad angular resolution or 0.3 ps time sampling. It will clearly not be possible to mount the Pilatus detector at a sufficient distance to permit similar time resolution with its larger 170 μm pixel sizes. A gated CCD will also be included in the baseline scope, pending possible improvements in detector technology.

4.3.4.6 6-ID-C Experimental Station

The 6-ID-C experimental station will include an x-ray nanoprobe instrument providing experimental capabilities in scanning probe transmission diffraction microscopy, Bragg diffraction microscopy, full-field transmission x-ray microscopy, and x-ray nanotomography. As discussed in the introduction, the scientific case for this instrument includes a series of emerging issues in condensed matter physics, materials science, and other fields in which the dynamics occur at 50 nm-scale lengths and with picosecond-scale characteristic times.

4.3.4.6.1 Nanoprobe Instrument Sample Rotation, Positioning, and Sample Environments

The nanoprobe instrument will include degrees of freedom for sample rotation around at least three Euler angle with a fine-step highly reproducible scanning capability in the horizontal angle. The angular

rotation stages will include a full (or nearly full) circle for the horizontal angle, either circles or arcs for the other directions. A key design issue is that vibration of the sample relative to the beam focusing optics must be minimized. In order to do the sample rotation and positioning stages will be mounted on the granite block. The focusing optics in Figure 4-31 will be mounted on the same block in order to minimize the size of the mechanical loop between the sample and the focusing optics. The restrictions on the relative motion of the sample and detector, however, are much less stringent. The detector rotation stages (see section 4.3.4.6.3) will be mounted separately on the experimental floor, and thus mechanically decoupled from the optics-sample mechanical loop.

The nanoprobe will use two stages of sample positioning. A coarse sample translation XYZ stage capable of moving the sample in three dimensions will carry another XYZ piezoelectric stack. The combination of stages will allow translation of the sample over millimeter ranges, with incremental step sizes of 10 nm or less. The piezoelectric stage will be removable to allow heavier sample environments (e.g. furnaces and cryostats) to be used. The absorption tomography mode of the instrument will use a precision rotation stage that replaces the top XYZ piezoelectric stack.

An example staging solution combining a rotation range of approximately 200°, nanoscale motion in two dimensions, and arcs with limited angular range in the orthogonal rotation axes in collaboration with X-Ray Microscopy Group of Argonne's Center for Nanoscale Materials (CNM) is shown in Figure 4-31b. The development of control systems stabilizing the sample position is a key aspect of the design. The instrument shown in Figure 4-31 is compatible commercially available lock-in nanopositioning measurement (Natana, Inc.). Also note that the top cube of Figure 4-31a can be kinematically removed to mount a heating/cooling module or other engineered environments.

4.3.4.6.2 Nanofocusing

The defining feature of the microscope is a robust small mechanical loop between the x-ray optics used to focus the beam and the sample. One possible arrangement is shown in Figure 4-31b. For simplicity, Figure 4-31a shows only the zone plate and not the other required optical elements, including an order-sorting aperture and center stop. The mechanical loop will be designed to ensure long-timescale stability of the relative positions of the zone plate and sample. With proper mechanical design drift rates on the order of 50 nm per hour should be possible, based on recent developments at the CNM.

Progressing from the exit of the flightpath delivering the x-ray beam to the sample, the required optical elements are:

1. A flight path extending to approximately 10 cm from sample.
2. Slits to limit the beam to the size of the zone plate, or to coherently illuminate only a fraction of the area of the zone plate.
3. Ion chamber to monitor the intensity of the incident beam.
4. Central stop on stage with 0.2 μm positioning resolution and stablility in XY. (Z points along the incident beam direction).

5. Zone plate on accurate and stable XYZ stage. The distance from the zone plate to the sample must be adjustable over a range of 5 cm to 15 cm to accommodate varying zone plate diameters and x-ray photon energies.
6. Order sorting aperture on XYZ stage with 0.2 μm positioning. Located 5-20 mm from the sample. OSA stage will be engineered with configurable mounts for background reduction schemes appropriate to each imaging mode and easy access to parallel beam for sample alignment and diffraction topography.
7. Sample. The same elements, with varying degrees of mechanical precision, are also found in the zone plate microfocus instruments at 7ID-B, 2ID-D and at the 26-ID nanoprobe.

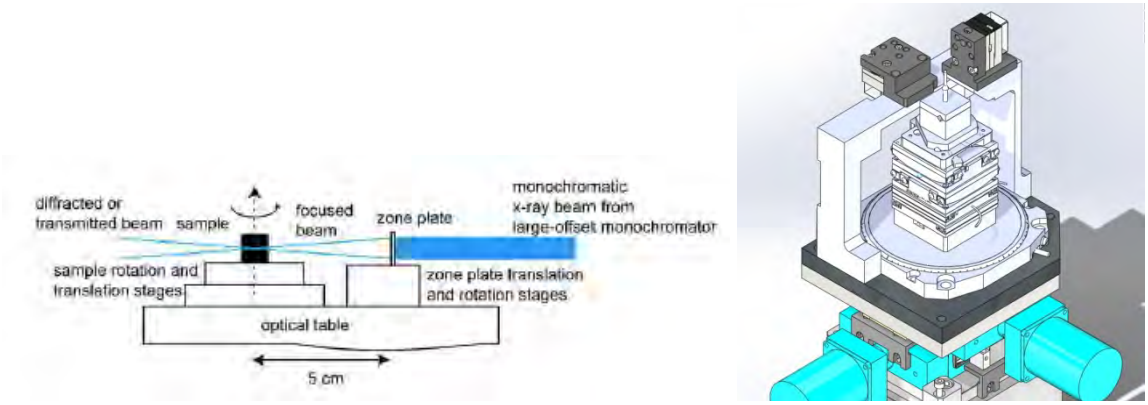

(a) (b)

Figure 4-31: (a) Arrangement of sample rotation stages and x-ray optics. (b) Rendering of sample stage for diffraction, imaging, and tomography.

Optical alignment requires the ability to image the transmitted beam (e.g. with a fluorescent crystal, microscope, and video camera) and to measure its intensity. The transmitted beam imaging instrument can be located sufficiently downstream from the sample position that it does not interfere with the detectors.

4.3.4.6.3 Detection and Imaging

The diffracted or transmitted x-ray intensity will be measured using detectors mounted on a two-circle detector arm. This geometry will permit vertical and horizontal diffraction. The detector will be decoupled from the sample rotation and translations. The detector arm will include the capability to mount the detector at a distance of at least 1 m from the sample in order to resolve the zone plate image in the far field. Because the focused beam is typically somewhat larger in the horizontal axis, the horizontal diffraction geometry is key for nanodiffraction because in this geometry the vertical resolution is not reduced due to footprint effects.

The far field diffraction detection will use a configurable gated pixel array detector. The detector will be used in either Bragg diffraction geometry or in scanning transmission geometry. A separate CCD will be available for transmission imaging with higher spatial resolution. For the transition geometry the two

detectors will share a flight-path. An additional objective zone plate will be available for tomography and imaging experiments.

The precise scanning of the nanoscale focusing optics in principle enables ultrahigh resolution coherent imaging of both periodic and non-periodic extended materials. Iterative phase retrieval imaging techniques using partially coherent illumination have been shown to be both appropriate and necessary for analyzing diffraction data generated by high numerical-aperture focusing optics, motivating a modular detection scheme explicitly allowing for low-noise high-speed far-field imaging at both transmission and Bragg geometries.

4.3.4.6.4 Ultrafast Excitation for Nanodiffraction and Imaging

Two excitation strategies for nanoprobe experiments are shown in Figure 4-32. The electric-field driven approach (Figure 4-32a) delivers GHz-bandwidth electrical signals to the sample for studies of ferroic materials and microelectromechanical devices. A separate arrangement in which a fiber-coupled microscope objective delivers laser pulses is shown in Figure 4-33b. An important capability of the optical excitation arrangement is shown in Figure 4-33. Here, the optical pump and x-ray probe are at different positions on the sample, and the spatial resolution of the microcope is used to map the time- and position-evolution of the mechanical excitation induced by the optical pulse.

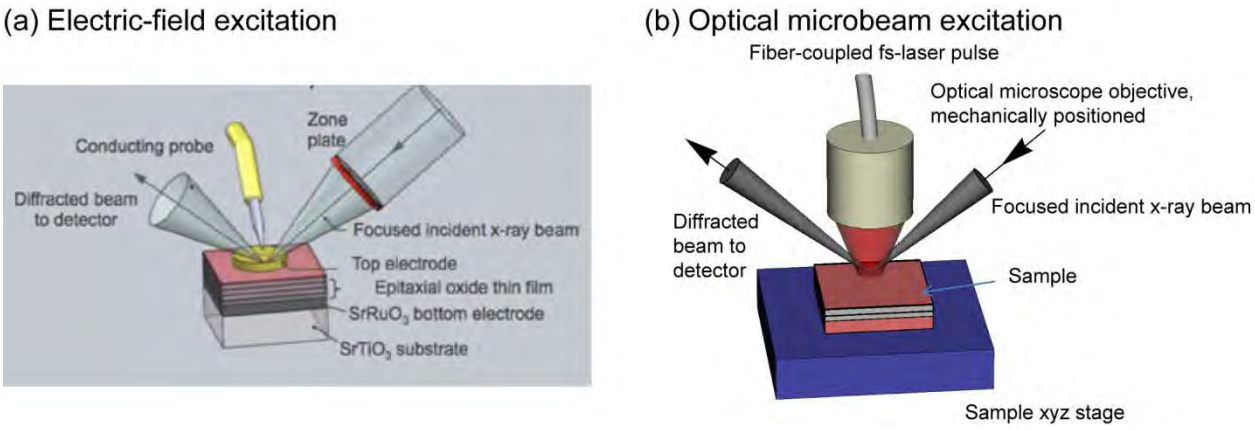

Figure 4-32: Examples of sample excitation mechanisms for ultrafast x-ray nanodiffraction experiments. (a) Electric field excitation via a conducting probe tip. (b) Optical microbeam excitation via an fiber-coupled optical microscope objective translated with the sample.

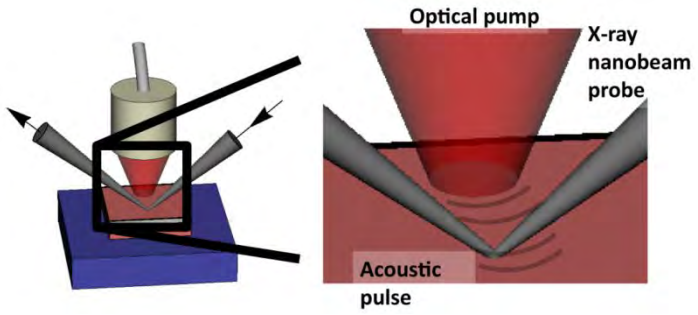

Figure 4-33: Optically driven mechanical excitation using a focused fs-laser beam. The optical pump system must be capable of being precisely positioned on the sample surface at an arbitrary offset with respect to the focused x-ray beam.

4.3.5 Optical Laser Systems and Infrastructure

The laser systems described in this section provide pump sources to accommodate the scientific needs of the SPXIM experiments. The lasers provide a broad range of photon energies, as well as high repetition rates that will allow the signal-to-noise ratio of experiments to be maximized. These laser systems serve both 7-ID and 6-ID x-ray stations in the SPX Facility. The performance parameters for the laser systems are summarized in Table 4-11.

Table 4-11: The SPX Facility lasers.

	Wavelength	**Duration**	**Rep rate**	**Power Energy per Pulse**	**Remarks**
High-power, high repetition rate laser	1 μm	<0.5 ps	6.5 MHz variable	20 W <10 μJ	
High-peak power laser	800 nm	50 fs	10 kHz	25 W 2.5 mJ	
High-peak power laser	800 nm	50 fs	10 kHz	10 W 1 mJ	Upgrade of the 7-ID laser
Optical parametric amplifiers	0.2-20 μm			Varied	Pumped by lasers in table

4.3.5.1 High-Repetition-Rate, Mobile Laser Systems

High-repetition-rate time-resolved experiment require lasers for sample excitation that have: high repetition rates, tunable wavelength ranging from 0.2 micron to 20 microns, fluence on the order of 100 mJ/cm^2, and synchronization of better than 200 fs with respect to the x-ray pulse arrival. Two mobile laser systems with pulse duration of 0.5 ps or shorter, repetition rate ranging from 50 kHz to 6.5 MHz, and power of 20 W will be procured for the SPX facilities in the scope of the APS Upgrade. The performance parameters are based on several state-of-the-art commercial laser systems, including the

Pharos system from Light Conversion Ltd [43], Tangerine from Amplitude Systems [44] and Impulse from Clark-MXR, Inc. [45]. These systems have been installed at other synchrotron light sources. A Pharos system has been procured by the Atomic, Molecular, and Optical (AMO) group in 2012 for installation at the APS.

4.3.5.2 High Peak Power Laser Systems

A Ti: Sapphire laser with a 10-kHz repetition rate, 50-fs pulse duration, and 25 W will be housed in a new laser room at Sector 6 as shown in Figure 4-23. An existing Ti: Sapphire laser system located at station 7-ID-E (Coherent Legend, 2.5 W up to 5 kHz) will be upgraded to produce 1 mJ per pulse at a 10 kHz repetition rate. These new laser systems will produce a broad band of laser energies from 200 nm to 20 μm using an optical parametric amplifier and high THz fields. These laser system performance parameters are based on Coherent Inc.'s current Legend Elite and Legend Elite-Cryo-HE systems [46].

4.3.5.3 Laser Transport System

Transport of the high intensity beams while preserving the beam fidelity is critical for the Ti: Sapphire laser system. An evacuated laser beam transport system will feed the 6-ID-B, C, and 7-ID-B, C, D stations from the Sector 6 laser enclosure. The design of the transport is based on current laser transport from 7-ID-E to 7-ID-C and D stations. The vacuum beam transport system will have beam viewing screens, power monitor, polarization control, and flip and steering mirrors to send the laser beam to a given enclosure. Transform-limited pulses of duration longer than 50 fs would be useful for high-efficiency frequency conversion into the far-infrared. Transport of uncompressed pulses over distances of 10-15 m followed by recompression in the enclosure is routinely done at the LCLS. To best preserve the longitudinal and transverse beam profile before delivering to the sample/OPA/THz generator, standalone compressors will be installed in the x-ray enclosure. The laser can be delivered before compression, thus preventing beam degradation due to nonlinear effects. In addition, active beam stabilization systems will be installed for laser beam pointing stability.

4.3.5.4 Laser Synchronization and Diagnostics

The beamline lasers will require clock signals phase-locked to the cavity voltage. The synchronization will be accomplished using the same techniques as at LCLS and is described in detail in Chapter 3 of this PDR, *Accelerator Upgrades*, section 3.6.3.6, *SPX Timing and Synchronization*. Four synchronization units are needed to accommodate all the laser systems. The jitter between the laser pulse and the x-ray pulse will be smaller than 270 fs over the bandwidth of 0.01-1000 Hz. An array of diagnostics will be devoted to measure and correct the laser and x-ray timing, including a portable picosecond x-ray streak camera, fast photodiodes, and high speed oscilloscopes. Shot-to-shot time stamping of the laser and x-ray beams on the sample at 6.5 MHz is not necessary since the expected jitter of 270 fs is adequate for the SPX time resolution of ~2 ps. Drift will be monitored with a fast diode and an oscilloscope, and should be compensated by the accelerator timing system. Other standard diagnostics such as power meters, optical cameras, and autocorrelators will be procured to ensure the proper operation of the lasers.

4.3.5.5 Laser Safety Systems

Laser safety is key to the success of the programs on the SPXIM beamline. The laser power will be a factor of 10 higher than currently available in 7-ID-E, so special care will be needed for beam alignment and transport. Laser safety enclosure and interlock systems are designed based on existing systems at multiple laser laboratories and enclosures at 7-ID, complying to the Argonne laser safety procedure. These will include a suite of laser eyewear to cover the wider wavelength range and higher laser power, new interlock systems and laser enclosures for 7-ID-B, 6-ID-B, 6-ID-C, and the new laser enclosure at 6-ID. A comprehensive standard procedure will be developed before operating these laser systems before operating these systems in consultation with Argonne's Laser Safety Officer.

4.3.6 Additional

4.3.6.1 Laser Enclosure

The laser enclosure is the only conventional facility on the SPXIM beamline. This room will require < 1° F air temperature stability; chilled clean-water circuits for the laser cooling; clean, dust-free air supply; and a low floor vibration environment.

4.4 High Flux Pump-Probe (14-ID)

The High Flux Pump-Probe (HFPP) located on the 14-ID beamline is part of BioCARS, a national user facility for synchrotron-based macromolecular crystallography and an integral part of the multi-disciplinary Center for Advanced Radiation Sources (CARS) at the University of Chicago. The APS Upgrade Project scope for the HFPP beamline consists of two major components:

1. Construction of a larger 14-ID-D experimental station (replacing the current 14-ID-B experimental station) to accommodate complex sample environments, additional x-ray optics, and extend the SAXS/WAXS resolution.
2. A Kirkpatrick-Baez (K-B) mirror system for secondary focusing.

This section describes only those items that are within the baseline scope of the APS Upgrade Project. For a detailed description of the entire beamline, see Graber et al. [47].

4.4.1 Scientific Objectives

With the ability to isolate a high-flux single x-ray pulse, the 14-ID beamline provides unique capabilities at the APS and in the US [47], and is one of three synchrotron beamlines with similar capabilities around the world. (Beamline ID-09 at the European Synchroton Radiation Facility (ESRF) [48] in France and beamline NW14 at the Photon Factory in Japan [49] are the two other beamlines). The user community for this resource is large and highly multidisciplinary. The facility is able to accommodate researchers from the fields of atomic and molecular physics, biology, chemistry, materials science, and materials under extreme conditions. Technically, the beamline has the capability to perform small-molecule and macromolecular crystallography; wide angle x-ray scattering (WAXS) in solids, solution, and gas phases;

general diffraction; and thermal diffuse scattering. A single 100-picosecond (ps) pulse at 14-ID contains ~4×10^{10} photons. At a 1 kHz repetition rate, the time-averaged flux at beamline14-ID is comparable to the Linac Coherent Light Source (LCLS). Unlike self-amplified spontaneous emission (SASE) free-electron laser (FEL) sources, such as LCLS, the 14-ID beam is also spectrally stable—a characteristic of mature storage ring sources—and affords data that can be quantitated accurately. The combination of high flux and spectral stability makes Sector 14 suitable for measurements on systems with dynamics slower than 100 ps.

A critical factor in the future success of the sector will be the ability to perform experiments under different environmental conditions. However, the current 14-ID-B experimental station was designed and built in the mid-1990s and is small by current beamline standards (3×4.5 m^2 with a 2.6-m ceiling). This makes it very difficult to accommodate complex setups. A larger station (4×8 m^2 with a 3.3-m ceiling) with two separate access doors and an overhead crane, similar to more conventional APS enclosures at other sectors, will facilitate the installation of these complicated setups and make more efficient use of beam time. Additionally, a larger station will accommodate the proposed new large-area detectors and secondary focusing optics for micro-beam experiments, providing a significant enhancement to the current beamline capabilities.

The ability to provide a smaller x-ray focus is very beneficial to many experiments. For example, crystallography will benefit from a small x-ray spot size. The standard crystal size continues to get smaller; therefore, having a small x-ray spot that matches crystal size will increase the signal-to-noise ratio in this case as well. Also, large crystals that have poor crystallinity can be composed of near-perfect microdomains. Probing the microdomains of larger crystals will be beneficial to time-resolved crystallography, particularly for irreversible reactions.

4.4.2 X-ray Optical Layout

4.4.2.1 Mirrors

The Project will install a small K-B mirror system for secondary focusing that images the virtual source created by the existing large, meter-long K-B mirror system, thereby further demagnifying the source. While a smaller x-ray spot size could be achieved by placing an aperture in the x-ray beam, this would significantly reduce the flux at the sample position, and high flux is essential for time-resolved measurements. The proposed K-B mirror system will provide the capability to reduce the spot size and increase the flux density at the sample by a factor of ~10.

To accommodate the footprint of the x-ray beam produced by the virtual source (image produced by the primary mirror system), the horizontal and vertical secondary mirrors will both be 320 mm long. To achieve a 6- to18-keV energy range at 3 mrad incident angle, the mirrors will be made of silicon with a single rhodium stripe on each mirror. To achieve a focal spot size < 10 μm vertically and < 20 μm horizontally, the tangential slope errors must be less than 1-μrad rms and sagittal slope errors must be less than 20 μrad, before coating, and roughness errors of less than 1 Å rms. The mirrors will have a coating of 50-nm rhodium on 10-nm chromium.

4.4.3 Beamline Physical Layout

4.4.3.1 Overall Beamline

Figure 4-34 presents a schematic view of the beamline; the scale indicates the distance from the source point (i.e., the center of the straight section). The current beamline is designed to switch rapidly between three modes of beam delivery: white beam, focused pink beam, and focused monochromatic beam. The focused beams offer strong demagnification of 8.3 to 1 horizontally and 5.2 to 1 vertically to yield a minimum beam size of 20 μm vertically by 90 μm horizontally. In pink-beam mode, x-ray heating of beamline components is reduced by a high heat load (HHL) chopper. The rotor of the HHL chopper is located downstream of the HHL slits at 29.2 m, where the maximum power intercepted by the chopper when both undulators are tuned to 12 keV is 520 W. For most experiments the duty cycle of the HHL chopper is 0.2%, which drops the downstream x-ray power to 1.04 W. This power is easily dissipated without significant heating of beamline components or experimental apparatus. In monochromatic mode, the HHL chopper is translated to a white-beam bypass position, and the monochromator intercepts the full white-beam power. For more details regarding the beamline see Graber et al. [47].

4.4.3.2 General Description

From right to left in Figure 4-34, the components are: 1.5-mm-diameter power-limiting mask (25.5 m), high-heat-load (HHL) slits (28 m), HHL chopper (29 m), Si <111> monochromator (31 m), equipment safety beam stop, primary vertically focusing mirror (47 m), primary horizontally focusing mirror (49.5 m), equipment safety beam stop, pink-beam slits (52.5 m), secondary vertically focusing mirror (57 m), secondary horizontally focusing mirror (57.35 m), and the white-beam stop (61.8 m).

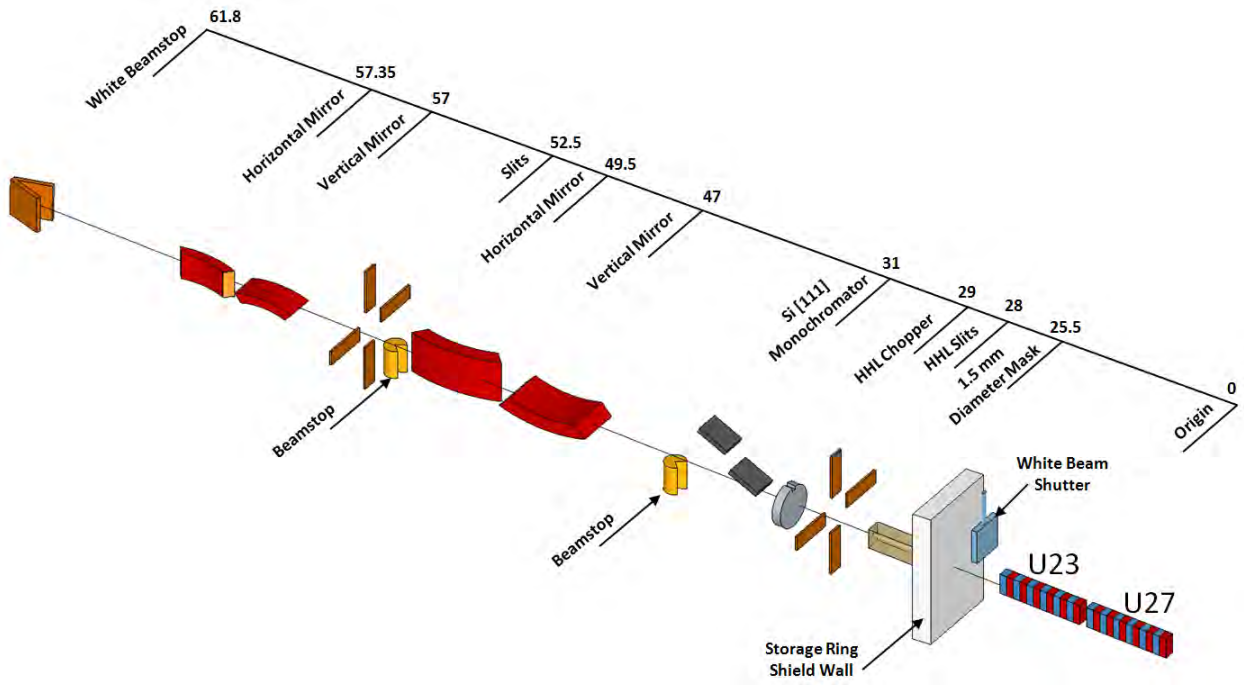

Figure 4-34: Layout of the upgraded 14-ID beamline.

4.4.3.2.1 Radiation Safety Aspects

The 14-ID-A and 14-ID-C radiation enclosures on the BioCARS sector are unchanged by the Project. A new enclosure, 14-ID-D will replace the existing 14-ID-B enclosure, and the beam stop at the end of 14-ID-B will be moved downstream on the back wall of the new enclosure. The radiation safety issues are discussed below.

White-beam Station 14-ID-D

All stations on the beamline are white-beam compatible. The new 14-ID-D station being built as part of the Project and described in this document is designed to APS white-beam specifications.

Thermal Stop 14-ID-D

The current 14-ID-B thermal stop design is intended to stop the white beam as well as focused pink beam (see Figure 4-35). This stop is located in front of the downstream wall of the current 14-ID-B station and is supported by a pipe stand not shown in Figure 4-35. It was manufactured using GlidCop®, which has been shown to resist stress fracturing due to thermal cycling. Since it is possible to focus the 14-ID-C K-B mirror pair on the surface, several angles of incidence to the beam are used to reduce the power density to safe and manageable levels. The current location of the stop is at 58.5 meters but the new location of the stop in the extended enclosure will be at 61.8 meters. Although the ring current increases by 50%, the distance from the large K-B mirror increases; thus it increases significantly the focal spot sizes on the stop and reduces the power density on the stop. The synchrotron ray-trace diagrams will need to be updated for

this new location as well as the thermal loading calculations, but it is expected that the existing stop will be reusable. Compatibility with 150-mA operation will be verified by finite- element analysis (FEA) calculation during final design.

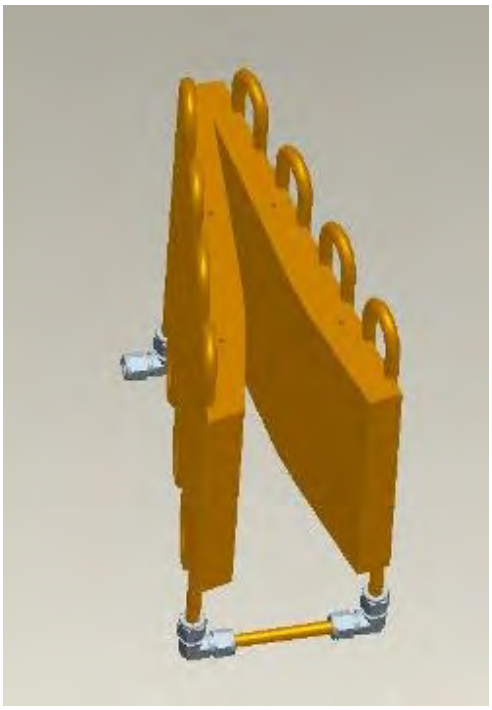

Figure 4-35: High-heat-load thermal stop in 14-ID-B.

4.4.3.3 Experimental Station

Designed and built in mid-1990s, the current 14-ID-B experimental station is rather small (3×4.5 m^2). Considering the expanding scope of the time-resolved experiments conducted at 14-ID that require additional customized equipment to be located in the experimental station and the proposed new K-B mirror system for secondary focusing (section 4.4.1), a larger experimental station is required. The new experimental station will be large enough to accommodate the additional infrastructure necessary to host complicated sample environments and house a large-area detector system, a laser light delivery system, and secondary focusing to afford focused pink and mono beams with ~10 μm in diameter. Time-resolved small-angle x-ray scattering (SAXS) and WAXS measurements will also benefit from an expanded q-range that is made possible by the larger sample-to-detector distances. The proposed size of the new experimental station is roughly 4×8 m^2. Figure 4-36 shows the new layout.

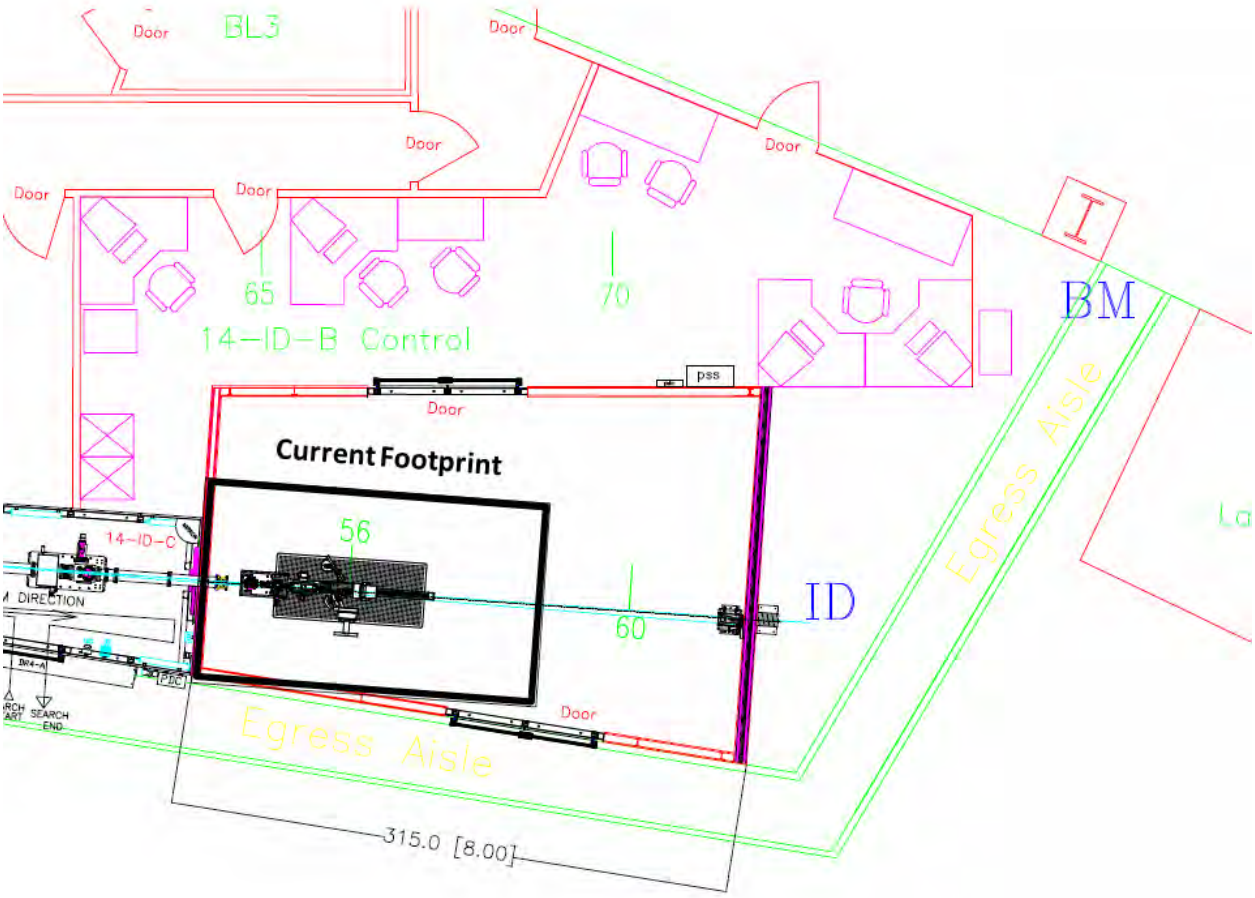

Figure 4-36: This figure shows the current station footprint with a bold black outline. The new experimental station will allow the use of an overhead crane and will have two sets of double doors. The current maximum sample-to-detector distance is 0.8 m. The new station will allow distances as large as 4.5 m, greatly expanding the accessible q-range for SAXS/WAXS measurements.

The existing experimental setup in 14-ID-B is represented in Figure 4-37 by a 3-D solid model. Starting from the right, a large-aperture 0.5-mm-thick beryllium (Be) window (Brush Wellman Electrofusion Products) separates the K-B mirror vacuum segment from the experimental apparatus. The components in Figure 4-37 are mounted on an optical table that is motorized with 6 degrees of freedom. The position of the monochromatic beam is measured by a fluorescence-based beam position monitor (BPM). An attenuator box is located downstream of the BPM, followed by the millisecond shutter. The Jülich chopper is mounted on two Huber mechanical stages that provide horizontal and vertical motion. The vertical motion changes the chopper open time in tunnel-less mode, and the horizontal motion selects the chopper mode: bypass; tunnel-less; or tunnel chopping modes. A rigid pedestal downstream of the Jülich chopper supports an in-vacuum 4-blade JJ-X-ray slit assembly (http://www.jjxray.dk/home) and non-invasive diagnostic x-ray detectors. A 10-mm-diameter beryllium window separates the vacuum segment required by the Jülich chopper from atmospheric pressure on the detector side. Two x-ray-sensitive detectors are located downstream of the beryllium window.

The goniometer is a standard Huber 515.2 kappa model in which a motorized XYZ-translation stage mounted on the phi-stage facilitates centering of the crystal. Two microscope charge-coupled device (CCD) cameras with 1- and 6-μm resolution are mounted to the rigid pedestal and are used to aid in crystal centering. Diffracted x-rays are imaged on an area detector (presently a MAR165 CCD) mounted on a 0.8-m-long Velmex dovetail translation stage used to adjust the crystal-to-detector distance.

The thermal beam stop currently installed in the current 14-ID-B station will be reused, as discussed in section 4.4.3.2.1 above.

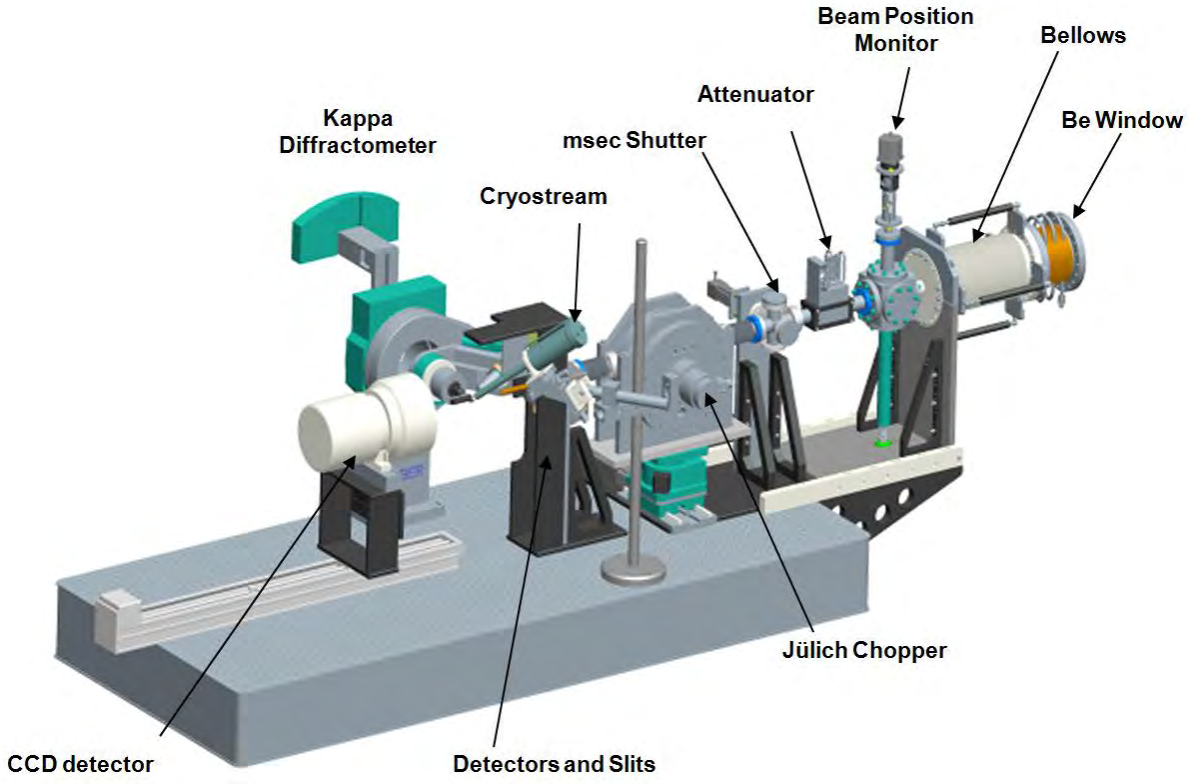

Figure 4-37: The table and experimental apparatus in the 14-ID-B enclosure. These are shown as a 3-D solid model for clarity. The center of the Kappa diffractometer is located 56 m from the source point.

4.4.3.4 Instruments (Physical Description of Major Experimental Instruments)

With the addition of the new 14-ID-D station, the experimental apparatus will be redesigned to accommodate several new modes of operation made possible by the larger station. Flexibility and ease of reconfiguration are both highly desirable capabilities that are incorporated into the design. Figure 4-38 illustrates the proposed layout of the Sector 14 experimental apparatus. The Jülich chopper will be mounted on a fixed table located approximately at the 55-m location along the beam path. The diffractometer table and the detector table will translate along the x-ray beam direction on a set of rails that will be grouted to the floor. This motion will not be motorized and will be used primarily to set the detector distance and increase the demagnification of the secondary K-B mirror system. The

diffractometer table will also support the secondary K-B mirror system. The K-B mirror system will be moved in or out of the beam path on a set of rails. Since both of the mirrors that make up the secondary K-B mirror system have their own translations, the motion of the K-B mirror chamber will not be motorized. This table will also hold the collimator support and *in situ* detectors for monitoring the x-ray beam. The CCD detector will be supported by a third table that is moveable on the rail system. The HFPP project will supply a new optical table to support the K-B and diffractometer as well as the rail system. BioCARS will provide the other two tables and the existing experimental apparatus. All three tables must track the beam from the primary K-B mirrors. This will require a vertical and horizontal translation capability that allows access to the white beam and all pink beams deflected by the primary K-B mirrors. The primary K-B mirror system was designed to cover mirror angles from 2 to 4 mrad, therefore the tables must have the ability to pitch and yaw through twice this value, or 4 to 8 mrad. A conceptual layout with 3D drawings has been completed during the preliminary design.

The first mode in Figure 4-38 essentially replicates the current setup. The second mode shows the current setup with the new short K-B mirror inserted in the beam path. The mirror tank will be inserted into the beam on a set of rails. The second mode is the lowest demagnification mode producing, as drawn, demagnifications of 0.8 to 1 horizontally and 0.25 to 1 vertically which effectively magnifies the original focal spot sizes of the beamline. In an actual use of this mode, the primary K-B focus will be moved slightly upstream of the chopper and the K-B table will be moved downstream slightly to increase the demagnification making it close to unity. Mode three shows a high-resolution SAXS setup with the detector placed approximately 4-m downstream of the sample position. The closest distance for WAXS is 0.18 m. Finally, the fourth mode will produce a highly demagnified secondary focus (5.1 to 1 horizontally and 3.2 to 1 vertically) with a spot size of 7 μm vertically by 18 μm horizontally as shown in Figure 4-39. This will be a significant improvement for all the programs using BioCARS because it will enable tighter laser focus for strong field experiments, and enable studies of smaller biocrystals. Another operation mode based on mode 2 or 4 is not shown in Figure 4-38. If the primary horizontal K-B mirror were flattened, the secondary K-B mirror in the path could be used to achieve even higher horizontal demagnification at the expense of losing some flux. Focal spots with full-width at half-maximum (FWHM) as low as 3 μm (V) x 5 μm (H) have been achieved recently at 7-ID-D with a similar mirror system. One would expect to transmit about 50 % of the horizontal beam in 14-ID-D at 12 keV.

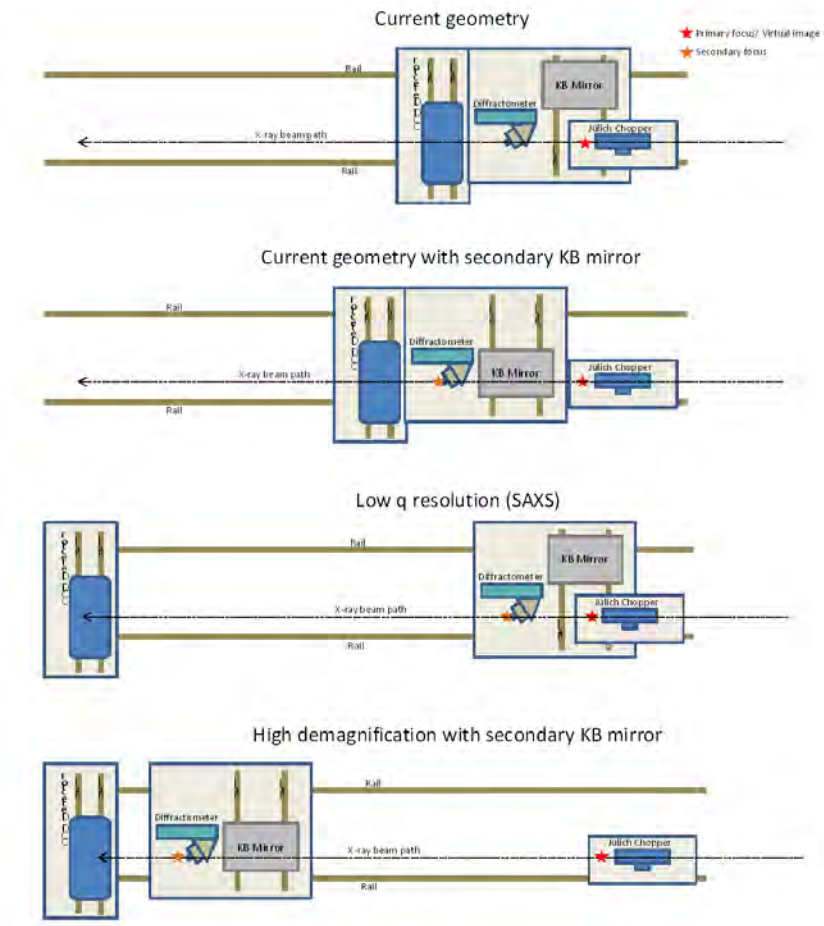

Figure 4-38: This figure shows a schematic representation of four modes of operation 14-ID-D instrument. Mode 1 is at the top while mode 4 is at the bottom of the figure. The Jülich chopper will be stationary while the table that holds the secondary K-B mirror system will move along the beam direction on a set of rails. Similarly, the detector table will also move on the same set of rails.

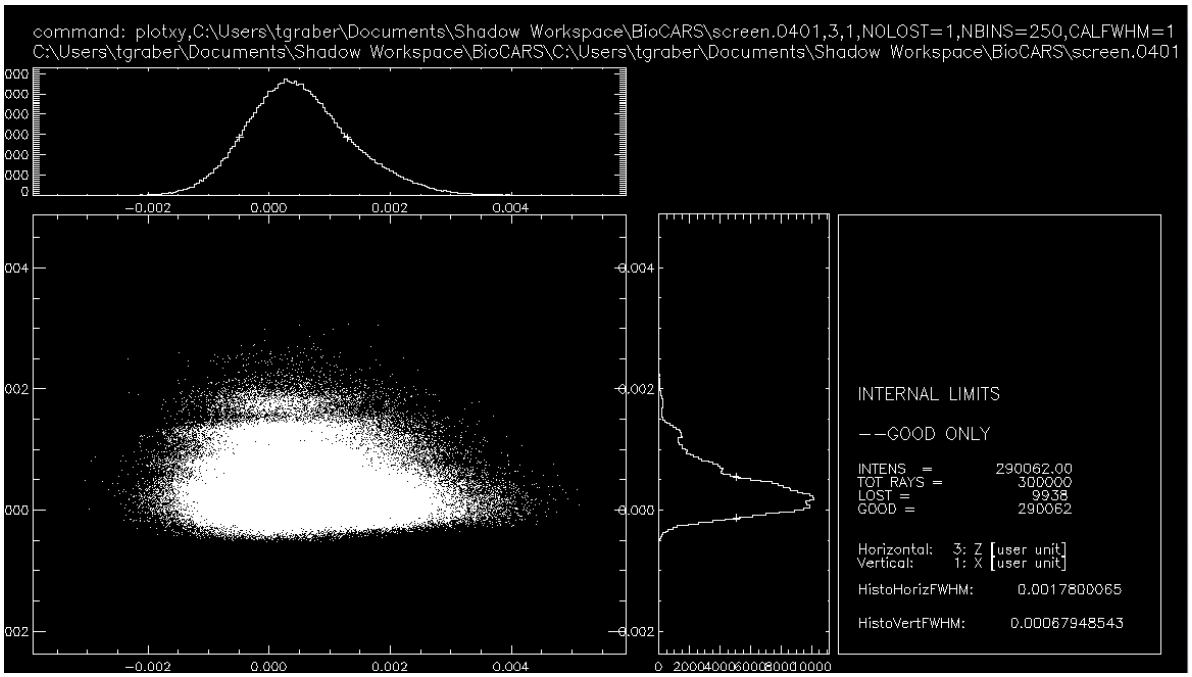

Figure 4-39: SHADOW simulation of the focal spot size expected for mode 4 in Figure 4-38, the mode with the highest demagnification ratio. The simulation includes realistic RMS slope errors of 0.4 µrad (V) and 0.9 µrad (H) on the primary K-B mirror system The FWHM is 7 µm vertically and 17.8 µm horizontally.

4.4.4 Additional

4.4.4.1 Safety Requirements

The 14-ID beamline is equipped with several laser systems. The lasers are housed in an existing enclosure and operate under standard operating procedures (SOPs) approved by Argonne's Laser Safety Officer. The existing 14-ID-B enclosure is equipped with a laser transport and conditioning system mounted on an optical breadboard above the diffractometer table. This optical equipment will be attached to the diffractometer table shown in Figure 4-38. Since the laser goes through a labyrinth, the laser transport is fixed on the enclosure, thus a selection of pipe lengths will be designed to enclose the laser beam for the different locations of the table. This work is integrated in the instrument design discussed in section 4.4.3.4. The SOP will be revised to include these changes and the new enclosure.

4.4.4.2 Retaining BSL-3 Capability

The experimental stations at 14-ID and their associated control areas are embedded in a biohazards facility whose hardware, air handling, and control systems are designed and constructed to permit the safe conduct of experiments on biohazards classed at the Biosafety Level (BSL) BSL-2/3 level. The ability to conduct structural studies of biohazards at the BSL-3 level at this synchrotron facility is currently understood to be one of two worldwide (one station at the new Diamond synchrotron source in the UK has recently implemented it). Closely linked to the hardware is an elaborate set of SOPs that describe

exactly how samples will be introduced to the facility, how experiments will be conducted, how samples and waste will be removed, what procedures must be followed in the event of incidents, and so forth. The hardware and SOPs were rigorously reviewed and approved by Argonne's Institutional Biosafety Committee (IBC)—with whom APS staff work very closely—and by APS management. APS staff actively participated with BioCARS staff in a recent hardware upgrade that improved the air handling system and its control and monitoring capabilities.

The BSL3 capability will be retained and integrated into the standard APS heating, ventilation, and air conditioning (HVAC) system. This will simplify the certification and maintenance of the system. Additionally, the new 14-ID-B station will be designed to meet all BSL-3 requirements. In the current 14-ID-B station, all labyrinths exit to a BSL-3 area. The new station roof will be equipped with wall labyrinths that exit to the experiment hall. Engineering controls and procedures will be developed to seal these during BSL-3 operation.

4.4.4.3 Conventional Facilities Requirements

The data acquisition area adjacent to the 14-ID-B station will be reconfigured to accommodate the new station footprint. Two doors and two walls will need to be removed and reconfigured. The entire facility, including the 14-ID-B station, will be sealed and recertified for BSL-3 use upon completion of the Project. This work is described in Chapter 5, section 5.3.3, *Infrastructure Enhancement for High Flux Pump Probe Beamline* (BSL3, Sector 14).

The deconstruction work also includes removal of some adjacent walls of the conventional facility. The construction work includes installation of associated utilities (electric, water, air), and of the APS-supplied Personnel Safety System (PSS) related equipment. Section 5.3.3 describes the scope of the new conventional facilities construction, i.e., attachment of the existing control room to the new 14-ID-D enclosure, and modification of the existing conventional facility configuration and utilities to achieve BSL-3 certification. The HVAC system will be integrated into the APS building system. Before the deconstruction of 14-ID-B begins, the HVAC control electronics will be integrated into the APS environmental control system.

4.5 Wide-Field Imaging Beamline

The goal of the Wide-Field Imaging (WFI) beamline is a world-class micron-level-resolution, full-field imaging facility with emphasis on phase-contrast and dynamic studies. There are three key parameters for this beamline:

1. The source penumbral angle, defined as the source size/distance
2. Beam size at the sample position
3. Photon density (ph/s/mm^2) at the sample position.

The source penumbral angle affects the achievable spatial resolution and phase sensitivity. The beam size limits the size of the sample that can be imaged, especially for tomography. The photon density affects the exposure time needed per image. Thus, in general, the WFI requires:

1. A small source penumbral angle
2. A few-cm sized beam
3. as high a photon density as possible

A long beamline is the most efficient way of achieving these requirements.

4.5.1 Scientific Objective

The scientific focus for the WFI beamline is on dynamics. The goal is to perform two-dimensional (2-D) or three-dimensional (3-D) imaging with ~1-μm spatial resolution, as fast as possible. Based on experience at APS beamline 32-ID, it will be possible to image very- high-speed phenomena with 100-ps exposure time. For tomography, it should be possible to obtain an entire 3-D data set in 10 ms. The scientific drivers for this beamline cover a very broad range of disciplines and requirements. Sample sizes will range from ~1-50 mm, and can be soft-tissue (biomedical applications) or high-Z materials (superalloys). As such, the design of the beamline includes three experiment stations, near, middle, and far. The near station will accommodate experiments that require the highest temporal resolution, while the far station will accommodate experiments that require the highest sensitivity and spatial resolution. The middle station will accommodate experiments between those two.

4.5.2 Source Requirements

4.5.2.1 Spectral Requirements

The key parameter in determining the length of the beamline is the horizontal photon source size. The goal is to achieve a full width half maximum (FWHM) penumbral opening angle of ~1 μrad ±10%. At 250 m from the source, this translates into a FWHM source size of 250 μm ±10%. In the 10-60 keV range of the beamline, the photon source size is dominated by the electron source size. Therefore, the electron source size will be FWHM 250 μm ±10%, during the APS reduced horizontal beam size (RHB) mode.

Because the beamline will have three experiment stations that are optimized for different set-ups (i.e., maximum spatial resolution or maximum temporal resolution), the source size requirement only needs to be achieved for ~30% of the time. The ability is needed to switch from the APS normal beam size (currently at ~28 μm [V] x 635 μm [H] FWHM) to the reduced horizontal beam size (RHB) mode at least once during each run cycle. The RHB mode has a smaller horizontal source size at the expense of a larger horizontal opening angle, which results in a larger beam size but a corresponding lower photon density. Currently, the beam size at 32-ID during the RHB mode is ~40 μm (V) x 275 μm (H) FWHM. At 250 m, this will translate into a source penumbral angle of 1.1 μrad, which is acceptable.

The beamline will rely on tapering the undulators to increase the beam size as needed. Thus, the design of the undulator support is compatible with tapering. Current calculations require a taper of <2 mm over a 2.4-m device.

The beamline requires as high a photon density as possible on the sample. Therefore, the WFI will be located on an insertion device (ID) beamline. The chosen location is 20-ID. The scope of the WFI project at Preliminary Design requires a switchable canted geometry. Simulations [50] show that 1-mrad

asymmetric canting is doable with the current optics in the APS storage ring (no additional research and development [R&D] required). It is possible to have the undulators in-line and still be able to cant one of them inboard upon request. This gives the added unique possibility to develop high-speed, white-beam stereo imaging in the upstream enclosures (B, C) without compromises in the overall goals of the WFI project. It is thus planned to have a canted front end, shifted inboard.

Dynamic gap control (software that sets a lower limit to the changing gap, given the value of the gap at rest) will be implemented to not exceed the allowable heat load on the front end when two undulators are utilized at once. One undulator will be the existing U3.0, which will provide the spectral coverage between 10-60 keV. The other undulator will be a single-line undulator that has significantly reduced higher harmonics and less heat load. The single-line undulator will be utilized mostly for white-beam imaging, where higher harmonics reduce the image contrast and the high-heat-load limits the possibilities for high-speed imaging. The WFI beamline will have an APPLE II device with a 2.6-cm period [51] as a single-line undulator. An advantage of the APPLE II is that when utilized as a planar device, it will more than double the available photon flux at higher energies (25-60 keV) compared to a planar U3.0. This is helpful because the monochromator and detector efficiencies are poor at high energies. Figure 4-40 shows the spectral output of the different options.

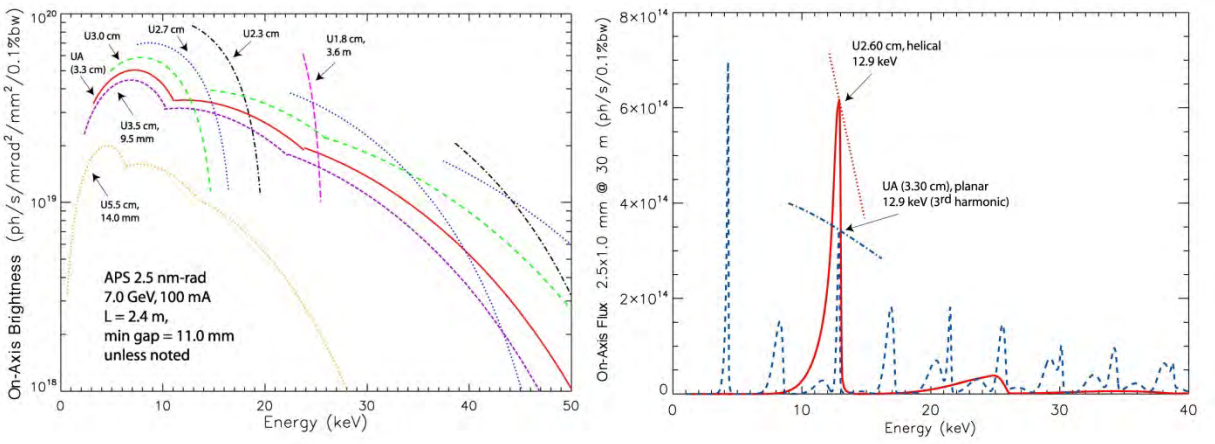

Figure 4-40: Brightness of different planar undulators (left) and flux comparison of helical 2.6 and planar 3.3 (right).

4.5.3 X-ray Optical Layout

Operationally, there are two basic requirements for optical elements on the WFI beamline.

1. Preservation of beam coherence. This is important for quantitative imaging as discussed in the next section. All windows or filters must be made from high-quality polished materials that do not impart structure to the beam. For example, beryllium windows must be made from the highest available quality and polished to the best possible finish. Other materials options (such as chemical vapor deposition [CVD] diamond) are also being considered for all windows.

2. Beam stability and control. The beam motion at the experiment stations must be minimized. The monochromators in the first optics enclosure (FOE) must have the necessary motion resolution to steer the beam into the E station, which is ~240-m away.

4.5.3.1 Monochromators

In many cases, the imaging technique at the WFI beamline does not require a high level of beam monochromaticity. Qualitative edge-enhancement can be achieved using white beam. However, in some cases, such as K-edge absorption subtraction, a high level of monochromaticity ($\Delta E/E \sim 10\text{-}4$) is needed. Table 4-12 shows the double-crystal monochromator (DCM) parameters.

In other cases, quantitative phase retrieval can be performed using multilayers with ~1% bandwidth. Unfortunately, the current generation of multilayers is imperfect and significantly degrades the beam coherence. This is not a major problem for absorption-based contrast, but can be highly detrimental for phase-contrast. At this time, the only monochromators capable of maintaining beam coherence are single-crystal monochromators. Thus, the design includes a silicon DCM in the first optical enclosure.

Table 4-12: Crystal monochromator parameters.

Crystalline Planes	Si<111>
Energy Range	10-60 keV
Geometry	Bragg
Monochromatic Beam Offset	20 mm

The monochromatic beam offset was determined from preliminary ray-tracings for bremsstrahlung protection and a consideration of the size of the beam. In general, a smaller beam offset is preferred.

The planned insertion devices (U1.8 and A2.6) will provide single lines at various energies (13 keV, 24 keV, and harmonics) with natural bandwidths similar to those of a double-multilayer monochromator (DMM). This translates into a highly homogeneous beam with higher flux density that can be utilized instead of a DMM at some discrete energy values.

The development of the multilayer technology is being closely followed, led by the optics group at the European Synchrotron Radiation Facility (ESRF). As such, the option of installing a DMM is still included in the design and cost estimates.

Since the E station will be ~230 m from the FOE, there is a concern regarding the monochromatic beam motion at the E station due to vibrations from the monochromators in the FOE. An angular stability better than 1μrad is required for the monochromators in the FOE. To mitigate this concern, it is planned to have a monochromator in the D station, which is just upstream of the E station. Due to the large beam size at the D station, multilayer monochromators will not be feasible if the full beam is needed. Thus, the preliminary design includes only a silicon crystal DCM in the D station.

4.5.3.2 Windows

All windows on the beamline must be mono/white-beam compatible and preserve the beam coherence as much as possible.

4.5.4 Beamline Physical Layout

The beamline layout is described below. All stations (including B) will be designed to be wide enough (~5 m) to accommodate large experimental setups from users. The location is 20-ID. The FOE can be utilized as is for WFI, but the other stations will be new given that the current stations at 20-ID are not white-beam compatible. The exact shape, size, and location of the stations are still being explored and will be finalized during Final Design.

4.5.4.1 Front End

The front end will be of canted geometry. It will be shifted inboard to accommodate the WFI-specific requirement for asymmetric canting. Most of the time, the beams from both undulators will go through the same port. The second port will be utilized for one of the beams when stereo imaging is planned. Preliminary calculations show that the front end can handle the heat loads of the planned in-line undulators (U3.0 + APPLE 2.6, or U3.0 + U1.8) at 150 mA. No dynamic control protocol will be necessary. Furthermore, the requested undulators are specialized and serve unique purposes; there are no plans to utilize them at the same time.

4.5.4.2 General Description

The beamline layout is schematically shown in Figure 4-41. There are two optical stations (A and D) and three experiment stations (B, C and E).

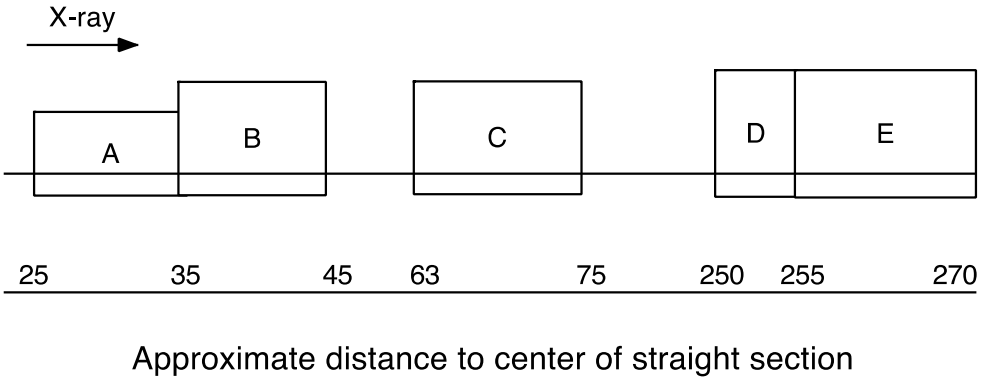

Figure 4-41: Beamline station layout schematic.

Station A will house a silicon DCM (and possibly a DMM). Station D will house a secondary monochromator to serve the E station. Station B will be for experiments that require the highest temporal resolution. Station E will be for experiments that require the highest spatial resolution and phase

sensitivity. Station C is for experiments that require intermediate spatial and temporal resolutions, and for the development of new imaging capabilities such as high-speed stereo imaging. All stations are white-beam compatible. Table 4-13 describes the main components and their respective locations within the beamline. The section of the beam transport crossing the experimental hall will be designed to be removable, to allow traffic of heavy equipment when necessary and/or during shutdown periods. People with light equipment will use the stairs and/or small lifts that will be built to go around the beam transport during normal operations as described in Chapter 5 of this PDR.

Table 4-13: Main beamline components.

Component	**Approximate distance to center of straight section (m)**	**Notes**
Be Window	25.5	Isolation from storage ring
Filter Box	26.0	To reduce heat load on optics
White Beam Slits	27	
Double Multilayer Monochromator	29	LN2 cooled, multi-striped.
Double-Crystal Monochromator	32	LN_2-cooled, Si <111>, Kohzu-type
White/Mono Shutter	34	Shutter/beamstop white/mono
Window	35.5	
White-Beam Choppers	36	Millisecond and microsecond opening times; utilized for very-high-speed and single-hot white-beam imaging
Movable White/Mono Beam Stop	44.5	
Window	45	
Temporary Vacuum Pipe	35.5-45	For downstream experiments
Shielded Vacuum Pipe	45 – 63.5	White/mono beam transport between B & C stations; must carry both canted beams
Window	63.5	
Movable White/Mono Beam Stop	74	
Window	74.5	
Temporary Vacuum Pipe	63.5 – 74.5	For downstream experiments
Shielded Vacuum Pipe	74.5 – 250.5	White/mono beam transport between C and D stations
Window	250.5	
White-Beam slits	251	
Secondary DCM	252-254	LN_2 cooled Si<111>
White/Mono Shutter	254	
Window	255.5	
Beam Stop	269	

Table 4-14 shows the beam size at 60 keV with a tapered U3.0 undulator at various locations along the beamline. These represent the largest beam sizes that will be utilized for the WFI beamline. The required taper is <2 mm over the length of the 2.4-m device.

Table 4-14: Maximum beam size at various locations along the beamline.

Distance from source (m)	Horizontal size (mm)	Vertical size (mm)
35	7	2.5
70	14	5
250	50	18

4.5.4.2.1 Radiation Safety Aspects

Shielding design for the WFI beamline is complicated by the large beam sizes required, high power density resulting from in-line undulator operation, and the option of dual canted beam geometry. Nevertheless, a straightforward and economical scheme for radiation shielding components has been identified. Shielding apertures are determined by required beam sizes and three possible geometries: -centered white-beam, inboard-canted white-beam, and vertically-offset monochromatic beam. Vertical apertures are largely determined by the monochromatic beam offset. The WFI beamline will utilize a monochromatic beam offset of 15 mm, which is essentially the smallest value that will permit a dual silicon-crystal monochromator to be utilized in the D station where the vertical size of the white beam is expected to be as large as 18 mm. An implication of this offset is that all integral shutters and manual beam stops will operate in only two modes: all beams off and all beams on. However, this is not a problem from a radiation safety perspective because all enclosures and beam transports will be rated for white beam. The minimum horizontal synchrotron beam missteering envelope is determined by the required beam size and additional accommodation for the optional inboard canted beam where necessary.

Several water-cooled photon masks and stops will be utilized to control the synchrotron beam missteering envelope. In addition to the mask provided on the front end exit table, photon masks and stops are utilized in the WFI beamline at four additional locations. Upstream of the B-to-C white-beam transport, a pair of masks will be utilized, one for each of the two possible white beams in canted mode. Upstream of the C-to-D transport, another mask will be utilized to control the beam missteering envelope of the in-line beam as much as possible prior to entry into the 175-m-long whit- beam transport. In the same location, a white beam stop will also terminate the optional inboard-canted beam. In roughly the center of the C-D transport, another mask will be utilized in conjunction with an in-vacuum collimator to help keep both possible radiation fans inside the 4 inch diameter vacuum pipe. Finally, at the upstream end of the D station a mask will be utilized to protect the in-vacuum collimator present in the integral shutter.

In general, the masks described above protect an array of nine bremsstrahlung collimators, including those incorporated in integral shutters. The collimators contain the possible bremsstrahlung fan to a size that may be completely stopped at all of the integral shutter and beam stop locations. In addition, the bremsstrahlung collimators are sufficient to contain any transported bremsstrahlung radiation to the inside of vacuum beam pipes in both the B-to-C transport line and the C-to-D transport line, avoiding any potential questions of secondary scattering in the transports. White-beam transports will utilize APS coffin-style lead-clad boxes because lead-wrapped pipes are neither practical nor economical for the large beam-pipe size that is required. The thickness of the lead in these transports will be sufficient to shield for air scattering but not solid scattering of x-ray photons; therefore, careful collimation of both synchrotron and bremsstrahlung radiation fans through these transports is essential.

Integral shutters will be utilized at the downstream ends of the A and D stations so that the heat load on the monochromators in those stations may be kept constant while beam is switched on and off for the experiment stations. These shutters are followed by a length of lead-wrapped beam pipe and a guillotine so as to minimize the amount of secondary scattering that is allowed to pass through the penetration in the downstream wall. At the downstream ends of the B and C stations, manual moveable beam-stops will be utilized because these are only necessary for switching between setups in the three experiment stations.

The WFI beamline will utilize a typical APS personnel safety system (PSS), which will force station searches prior to enabling shutters to permit beam, control and monitor station doors, and monitor the states of radiation shielding components such that, in the event of a potentially unsafe configuration, the front end beam shutter will immediately close.

4.5.4.2.2 Equipment Protection System

The WFI beamline will utilize a typical APS beamline equipment safety system (BLEPS), which will monitor beam-shutter status, monitor vacuum pressures, control and monitor gate valves, and monitor liquid cooling flow to x-ray windows and monochromators such that, in the event of a configuration that could cause equipment to be damaged, the front end beam shutter and/or vacuum gate valves will immediately close.

4.5.4.2.3 Vacuum System

The WFI vacuum system is primarily optimized for user flexibility in the experiment stations. Beryllium windows designed to pass both white and monochromatic beams terminate the beamline vacuum as far upstream or downstream as is practical in the experiment stations. Windows will be water-cooled to remove heat deposited by white beam and coated for protection against oxidation. Users are therefore free to build additional sections of vacuum beam transport in the experiment station or to operate in air. In addition to the segmentation provided by the beryllium windows, gate valves will be placed so that complete isolation of all monochromator sections is available.

Common 4-in. diameter beam pipe with 6-in., CF-type flanges is utilized almost exclusively through the beamline for simplicity and to minimize outgassing in the long beam-transport sections. Beam pipes to be installed in the A and D stations will be electro-polished, thoroughly cleaned, and baked so that pressures of $10E^{-9}$ torr or better may be expected for compatibility with monochromator requirements.

Ion pumps will be located on monochromators, shutters, and periodically elsewhere along the beamline. At each ion pump a vacuum tee will be utilized to install additional accessories into the beamline. These will include an angle valve for rough pumping, a thermocouple gauge for rough vacuum pressure measurement, and a cold cathode gauge for UHV vacuum pressure measurement. The tees will also provide a spare blanked-off port to allow for future expansion.

4.5.4.2.4 Data Acquisition and Motion Control

The data acquisition and motion control system for the WFI beamline will be based on the current system at 32-ID and 2-BM, with advice from the APS Beamline Control and Data Acquisition and Information

Technology groups. The system will closely resemble that of the high-energy tomography beamline because most of the equipment will be quite similar.

4.5.4.2.5 Utilities

All the experiment stations will have the following utilities:

1. Water to cool the windows and other user equipment
2. 120-V and 208-V three-phase electrical outlets on both inside and outside walls
3. Compressed air for air-bearing stages
4. Ventilation fans on the roof.

In addition, an emergency power supply will be required near the A and D stations for the liquid nitrogen pumps and monochromator ion pumps.

Liquid nitrogen will be needed near the A and D stations for the liquid nitrogen pumps. These will be hooked into the central APS LN_2 lines.

4.5.4.3 First Optics Enclosure and Infrastructure, Major Components

Figure 4-42 shows the schematic layout of the first optics enclosure.

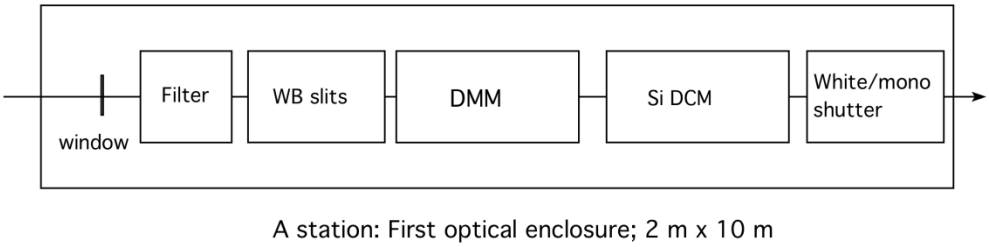

Figure 4-42: Schematic layout of A station.

4.5.4.3.1 Windows

All windows on the beamline will be white- and monochromatic-beam compatible. Preliminary ray tracings indicate that a 15-mm offset of the monochromatic beam is needed due to the large beam size.

In order to preserve the beam coherence as best possible, all the windows will be made from the highest available quality polished low-Z materials (beryllium or CVD diamond, for example). A windowless front end will also be considered during the final design.

4.5.4.3.2 Filters

Because the WFI beamline requires large beams (i.e., larger than the typical central cone of the undulator radiation) there is a substantial increase in total power incident on the beamline optics. Thus, a filter bank is needed to help ameliorate potential heat load issues on the downstream beamline optics. To reduce filter-related phase effects, the filters will be mirror-polished and homogeneous.

4.5.4.3.3 Slits

Two sets of white-beam slits are included, one in each of the optical stations (A and D). Each will be sized to handle the full beam from two in-line undulators at 150 mA. The slits in the A station will be compatible with the canted design to let both beams through when needed.

4.5.4.3.4 Collimators

Collimators will be integrated into the front end and along the long beam pipe that leads to the far station, based in the detailed engineering ray traces.

4.5.4.3.5 Shutters/Stops

Two remote controlled white/monochromatic-beam shutters are required, one at the back of station A and one at the back of station D. There will be a movable beam and bremsstrahlung stops at the back of the B and C stations, and a fixed beam and bremsstrahlung stop at the back of the E station.

4.5.4.3.6 Monochromators, Physical Description

The DCM in the A station will be LN_2-cooled Si<111>, covering the 10-60 keV range in the Bragg geometry. It should be fairly similar to the DCM now in operation at 32-ID and there are several commercial options available that will suffice.

The optional DMM in the A station will also require LN_2 cooling. The exact specifications are not yet determined, but it will be similar to the DMM in operation at 2-BM. State-of-the-art DMMs are also in use at ESRF and a few material pairs are available commercially to choose from (W, Mo, Pd, and Si, B4C). The best quality multilayers will be utilized. The period will be chosen with a large bandwidth in mind, but also with access to the highest energy possible while keeping the substrate size reasonable.

4.5.4.3.7 Diagnostics

For beam diagnostics, there will be a moveable fluorescent screen and camera just downstream of the monochromator.

4.5.4.4 Station B

Figure 4-43 shows the schematic layout of the first experiment station.

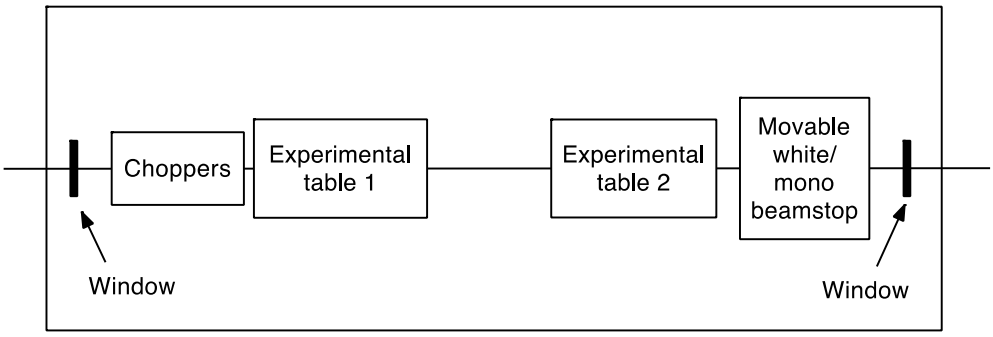

Figure 4-43: Schematic layout of B station.

4.5.4.4.1 Windows

There will be polished Be (or diamond) windows at the front and back of the station. These windows will be white-beam compatible, as described earlier.

4.5.4.4.2 Choppers

Two white-beam choppers are included in the design of the B station. One will be a millisecond-opening device and the other will be a microsecond-opening device. These are modeled after the choppers that are currently operating at 32-ID. The millisecond chopper (5-10-ms opening time for ~1-mm vertical opening) is a pair of cooled copper blocks mounted on leaf springs and driven by a solenoid. The microsecond chopper (~10-μs opening time for 1-mm vertical opening) can either be a fast rotating wheel type or a dual fast solenoid/galvanometer based device. Both will be available for different applications.

4.5.4.4.3 Instruments

There will be two experiment tables in the B station; one dedicated for instrumentation and user-oriented developments, and one for standard ultra-high-speed imaging. The instrumentation will be similar to the current 32-ID-B station. The width of this enclosure will be maximized so that the empty space between the two tables can accommodate large experiment setups. The upper limit will be set by the available space on the experiment hall floor at the 20-ID location.

4.5.4.4.4 Movable White/Monochromatic Beam Stop

A manual, movable white/mono beam/bremsstrahlung beam stop is located at the end of the station. This stop will be in the closed position when the beam is not required downstream, e.g., when experiments are running in the B station.

4.5.4.5 Station C

Figure 4-44 shows the schematic layout of the second experiment station.

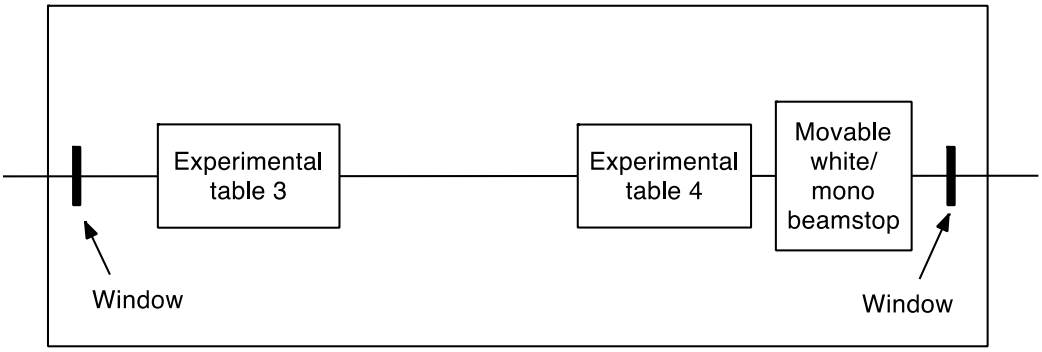

Figure 4-44: Schematic of C station.

4.5.4.5.1 Window

Polished Be windows are included at the front and back of the station. The windows must be able to pass both monochromatic and white beams.

4.5.4.5.2 Instruments

There will be two experiment tables in the C station. One will be a work-horse setup capable of tomography and fast radiography. The other will be utilized for prototypes (e.g., Talbot imaging, white-beam stereo imaging). The instrumentation for the work-horse setup will be the standard tomography/imaging setup currently implemented at 2-BM and 32-ID.

4.5.4.5.3 Movable White/Monochromatic Beam Stop

This is to stop the monochromatic or white beam when experiments are done in the C station. The canted beam will not be transported beyond station C, because the flux density drops by an order of magnitude at 250 m from the source. Also, the 65-mm separation of the two beams in station C is large enough to insert optics.

4.5.4.6 Station D

Figure 4-45 shows the schematic layout of the second optical enclosure.

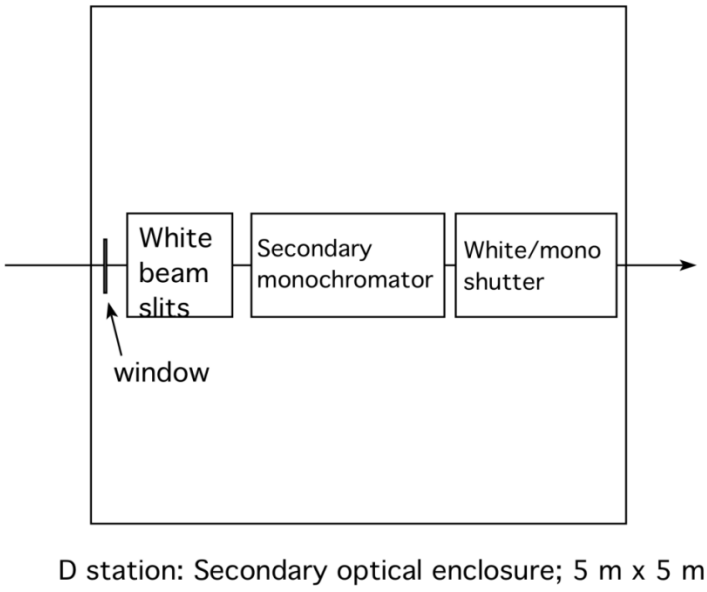

Figure 4-45: Schematic layout of D station.

4.5.4.6.1 Window

A polished Be window is included at the front of the station. The window will pass both white and monochromatic beams.

4.5.4.6.2 White/Monochromatic Beam Slits

These slits must be usable for both white and monochromatic beams.

4.5.4.6.3 Monochromator

The monochromator in the D station serves to provide monochromatic beam to the E station. Because the beam size at the D station will be quite large (see Table 4-14), it is anticipated that it will be larger than monochromators that are normally situated in the FOE.

4.5.4.7 Station E

Figure 4-46 shows the schematic layout of the third experiment station.

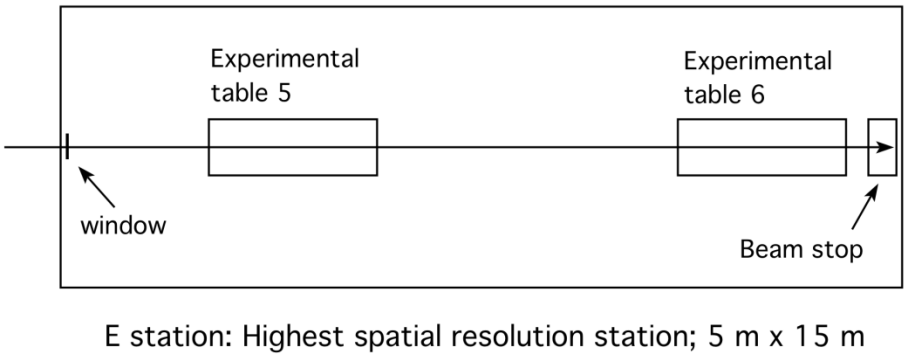

Figure 4-46: Schematic layout of E station.

4.5.4.7.1 Window

There will be a white/monochromatic-beam window at the upstream end of the station.

4.5.4.7.2 Instruments

There will be two experimental tables in the station. One is a work-horse setup, located toward the end of the station. Another is a prototype table; the main focus will be to take advantage of the large source distance and beam size to develop new techniques. The majority of the instruments are readily available and will be purchased from commercial sources. Prices in the cost baseline reflect recent purchases of similar products utilized at 32-ID and 2-BM.

4.5.4.7.3 Beam Stop

There will be a mono/white/bremsstrahlung-beam stop at the downstream end of the station.

4.5.4.8 Conventional Facilities Requirements

See Chapter 5, section 5.3.2 for a detailed description of the conventional facilities requirements.

4.6 *In Situ* Nanoprobe Beamline

The *In Situ* Nanoprobe (ISN) beamline is aimed at highest-resolution imaging, spectroscopy, and tomography of energy materials and energy devices, as well as of other complex systems. The ISN beamline will provide a spatial resolution of 20 nm using diffractive optics, and of 50 nm using reflective optics. The ISN instrument will provide variable temperature, flow of gases and fluids, and applied electrical fields, towards the study of properties of materials and devices under *in situ* conditions, including materials fabrication and device operation.

The ISN beamline will operate with hard x-rays with photon energies between 4 keV and 30 keV, and will have beamline optics designed to allow adjustment of the lateral coherence length and bandpass of

the x-rays. The beamline uses mirror optics for beam steering, higher harmonics rejection, and power management; monochromators to select photon energy and bandpass; diagnostic systems such as beam position monitors and diagnostic screens to align and monitor the beam position; standard components such as shutters and masks; radiation shielding components; equipment and beamline protection systems; and experimental enclosures. The most downstream experimental enclosure will house the ISN instrument.

The ISN instrument will use elliptically figured mirror optics to focus x-rays with large bandpass to a spot size of 50 nm, and diffractive optics such as zone plates or multilayer Laue lenses (MLLs) to focus x-rays with small bandpass to a spatial resolution of 20 nm or below. Both reflective optics and MLL optics are capable of providing high focusing efficiency, between 30% and 80% at high photon energies. The ISN will further integrate components designed to provide *in situ* environments: a heating/cooling stage to provide temperatures between 70 K (with option to go to 40K) and ~500°C, a high temperature stage to provide temperatures of 1000°C or above, sample cells that accommodate flow of gases and fluids, and cells optimized for application of electric fields. The ISN will be optimized for x-ray fluorescence detection. Towards that purpose, the design calls for simultaneous use of two fluorescence detectors with large solid-angle capability, with the goal of achieving a total solid-angle coverage of π st. rad. Complementary to fluorescence detection, the ISN will provide phase contrast as well as coherent diffractive imaging capabilities to allow simultaneous mapping of low-Z matrices using hard x-rays and provide an avenue towards super resolution. To optimize characterization of hierarchically organized systems, the ISN will aim to allow operating at different length scales, by switching between a high-flux configuration that uses partially coherent x-rays with large bandwidth, and a high-resolution configuration that uses spatially coherent x-rays with a small bandpass. The ISN will furthermore deploy “fly scanning techniques”, i.e. data acquisition while the sample moves, in fluorescence mode. This will allow acquisition of high-resolution maps with a large number of pixels in 2D and 3D.

The ISN beamline is designed as a canted beamline and will be implemented as a new branch line at APS Sector 32. The ISN beamline is designed to maximize the coherent photon flux on the sample, by combining spatial filtering design with nanofocusing optics that match the lateral coherence length of x-rays, and to maximize the working distance between optics and sample, as described below.

To maximize the working distance of the focusing optics and accommodate various *in situ* sample cells, it is important that the lateral coherence length in the experimental station be as large as possible, which in turn requires positioning of the ISN as far as possible from the source. A position of at least 72 m from the source is required. This corresponds to a focal length of 22 mm and a working distance of ~ 7.5 mm at photon energies between 6 keV and 30 keV, using diffractive optics with a resolution of 20 nm. The working distance of reflective optics with a spatial resolution of 50 nm is 25-27 mm. Table 4-15 shows working distances for optics with resolution limits of 50 nm, 20 nm, and 10 nm for a distance of the ISN instrument at 72 m from the x-ray source. To position the ISN instrument at sufficient distance from the source, pairing of the ISN beamline, in canted configuration, with a program that requires only a short distance from the source (less than 65 m) is required. This is can be achieved by partnering with the Transmission X-ray Microscope at sector 32, by positioning the TXM instrument at ~ 60 - 62 m from the source, and the ISN instrument in the downstream area of the sector, at ~ 72 m - 75 from the source. This position allows optimum positioning of fluorescence detectors around the sample area of the ISN instrument, and allows maximizing the solid angle of detection and thereby the optimum utilization of brightness from the APS source.

Table 4-15: Working distances for nanofocusing optics with resolution limits of 50 nm, 20 nm, and 10 nm for a distance of the ISN instrument of 72 m from the x-ray source 10 keV photons. For reflective optics, the working distance is independent of the photon energy.

Spatial Resolution limit [nm]	50 nm	20 nm	10 nm
Nanofocusing Optic	Focusing mirror	Zone Plate/MLL	MLL
Working distance	27 mm	7.5 mm	3.7 mm

4.6.1 Scientific Objectives

Efficient, affordable, and scalable systems for energy harvesting, energy conversion, and energy storage are major components of a secure energy future for the United States (U.S.) and the world. Concurrently, it is vital to minimize the environmental impact of energy technologies around the globe, providing sustainability for energy production and usage. For instance, the rise of data centers and personal computing has continued to increase the fraction of energy usage dedicated to computing and related infrastructure, which makes increasing the efficiency of electronics—with the dual purpose of improving energy efficiency and enabling future supercomputing capabilities—an important goal.

The ISN encompasses the study of advanced energy harvesting, conversion and storage systems, approaches to sustainable energy, platforms for advanced electronics, and materials and systems aimed at sustainable construction and carbon capture. All these systems have in common complex, hierarchical structures with nanoscale features often in nonplanar geometries, where small quantities of inhomogeneously distributed dopants, precipitates, contaminants, and second-phase particles play an increasingly important role in overall system performance.

In many cases, the scientific inquiry seeks to understand and control material properties that determine system performance, system efficiency, and environmental impact. Examples of materials systems and devices to be studied include solar cells, fuel cell components, and advanced battery concepts. The science of nanoelectronics will include the study of complementary metal-oxide semiconductor (CMOS) devices designed for 22-nm node technologies and below, with a view to increased performance, speed, and power efficiency. Approaches to sustainable energy will include the study of advanced building materials that reduce CO_2 emissions, research on understanding natural carbon sinks and development of artificial carbon sinks, and biogeochemical cycling of metal contaminants. In most cases, very high spatial resolution, imaging at trace-level sensitivities in complex 2-D or 3-D geometries, and imaging under real operation conditions are required.

4.6.2 Source Requirements

The ISN beamline uses the spatially coherent beam from the APS to achieve diffraction-limited focusing. As such, it takes advantage of the high brightness of the APS. To maximize focused flux, the source must be optimized to provide good brightness throughout the energy range of 4-30 keV. Since the coherent flux scales with the square of the wavelength, $F_{coh} \sim \lambda^2$, the source must be configured to maximize the coherent flux in particular at high photon energies, where both brightness falloff and small wavelength reduce the coherent flux rapidly. A revolver-type undulator is well suited to satisfy the ISN's needs.

4.6.2.1 Spectral Requirements

The ISN beamline provides x-rays with photon energies between 4 keV and 30 keV, to allow spectroscopy at and imaging close to the binding energy of most elements in the periodic table. For example, spectroscopy at the K absorption edge of Ti, aimed at understanding the chemical state of novel battery electrodes based on TiO_2-nanorods, requires a photon energy of just below 5 keV. Access to absorption edges of technologically important materials such as Sb and Te, related e.g. to switching fatigue in novel, chalcogenide-based memory elements, requires photon energies as low as of 4 keV for L-edge studies, or of 27-30 keV and above for K-edge spectroscopy. Spectroscopic studies of catalyst materials such as Pd and Ag require access to their K edges at 24.3 keV and 25.5 keV, respectively, and measurement of the chemical state of Cd, relevant for environmental studies, requires a photon energy of 26.7 keV.

The ISN will use x-rays with bandwidths ranging from $\Delta E/E = 10^{-2}$ to $\Delta E/E = 10^{-4}$. Use of mirror optics, with a focal spot size as small as 50 nm, allow utilization of the full undulator bandwidth of $\Delta E/E = 10^{-2}$, thus maximizing the coherent flux on the sample. To achieve a smaller spot size, diffractive optics such as zone plates and multilayer Laue lenses will be deployed. The bandwidth requirements of diffractive optics range from $\Delta E/E = 10^{-3}$ to $\Delta E/E = 10^{-4}$ in most of the targeted range of spatial resolutions of 50 nm to 20 nm. For photon energies above 6 keV, this can be satisfied by the use of silicon <111> crystals as monochromator optics. For energies below 6 keV, for a resolution of 20 nm, the bandwidth requirement becomes more stringent. Reduction in resolution can be avoided by using zone plates with an acceptance of 320 μm or less, thereby not accepting the full coherent flux.

The ISN is expected to operate most of the time at very high spatial resolution, requiring spatially coherent illumination to achieve diffraction-limited resolution in the range of 20-50 nm. This requires maximizing the coherent flux, in particular at high photon energies where the coherent flux F_{coh} is relatively small due to its dependence on the energy, $F_{coh} \sim B \cdot \lambda^2$, where B is the brightness and λ the wavelength. To reach low photon energies of 4 keV, as well as to provide maximum brightness at high energies, we request a revolver-type insertion device as x-ray source, as discussed below.

The ISN beamline requires continuous tuning of the photon energy throughout the energy range of operation, with particular emphasis on maximizing the coherent flux at high energy. Figure 4-47 shows an example of tuning curves for a revolver-type device, with a combination of periods of 3.3 cm for lower energies and 2.7 cm for higher energies. The larger-period structure (3.3-cm-period structure or similar) will provide continuous energy coverage and good brightness for lower photon energies, where coherent flux is large, while the lower-period structure (2.7-cm-period or similar) can provide higher brightness at high photon energies. A brightness of more than 6×10^{19} phot/s/mm^2/mrad^2 will be delivered by the 2.7-cm structure for photon energies between 7 keV and 12 keV. It is anticipated that continued development of optimized insertion device structures and vacuum chambers will yield more optimized combinations of periods, and plans are to use the configuration best suited to provide maximum brightness across the 4- to 30-keV energy range.

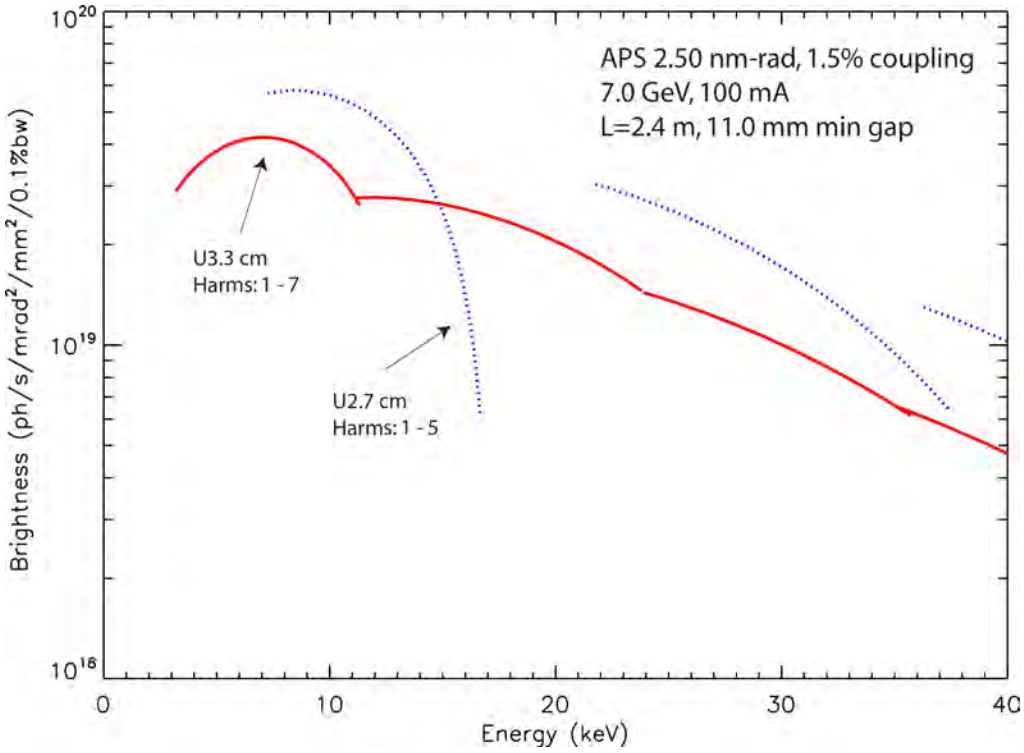

Figure 4-47: Brightness of a revolver-type insertion device. The ISN requires a large-period structure (e.g., 3.3 cm or 3.0 cm) for continuous tuning through the 4- to 30-keV range, and a smaller-period structure (e.g., 2.7 cm) for higher brightness at the 7- to 15-keV and 22- to 30-keV energy regimes. The graph shows the brightness for a 2.4-m-long device (courtesy R. Dejus).

4.6.2.2 Other Source Requirements

The ISN beamline will be placed at a canted sector and will share the sector layout with the transmission x-ray microscope (TXM) program at Sector 32. Therefore, only one straight section is available to house the source for the ISN beamline. To allow effective energy coverage and good brightness throughout the required range of photon energies, the ISN calls for a revolver undulator as source and for maximizing the length of the insertion device. The specifications for the focusing optics are based on an x-ray source with a vertical source size of σ_y = 11 μm. Reduced vertical source size would yield larger lateral coherence length at the experimental station, and therefore longer working distance. This is desirable to add flexibility for *in situ* stages in the experimental station.

4.6.3 X-ray Optical Layout

The ISN beamline optical layout is based on spatial filtering of the x-ray beam in the horizontal and vertical directions (Figure 4-48). A beam-defining aperture (BDA) is placed at a position 42.2 m downstream of the source. The size of the BDA can be adjusted in the horizontal and vertical directions. The lateral coherence length at the position of the nanofocusing optics can be tuned by changing the size of the BDA, as required by the acceptance of the nanofocusing optics.

The BDA is illuminated horizontally by monochromatic beam deflected by a plane, horizontally deflecting mirror and a horizontally deflecting monochromator. It is illuminated vertically by a vertically deflecting, vertically focusing mirror. This design provides coherence preservation in both directions

In the horizontal direction, the BDA may be closed to a size of 10-15 μm to provide a spatially coherent source for illumination of nanofocusing optics with an acceptance of 170 μm. The BDA can be adjusted to accommodate nanofocusing optics with smaller or larger acceptance. In the vertical direction, a pink-beam mirror is used to refocus the source into a spot with a size of 5 μm FWHM at the BDA. The BDA may be closed vertically to a size of 4 μm to provide coherent illumination for nanofocusing optics with acceptance up to 350 μm, such as the upstream optic of a Kirkpatrick-Baez (K-B) mirror system. It may be opened to accommodate optics with smaller acceptance. The size of the BDA can be changed in both vertical and horizontal directions to utilize partially coherent beam, allowing operation at increased flux, at a cost of reduced spatial resolution.

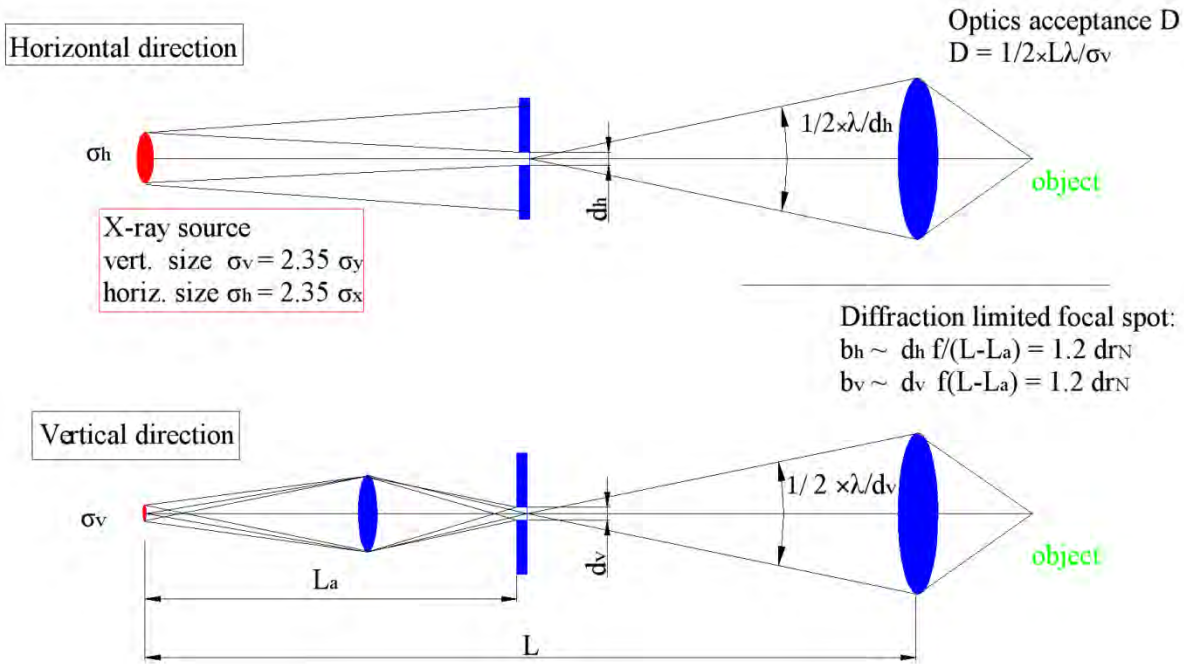

Figure 4-48: Optical layout of the ISN beamline. σ_h and σ_v are the horizontal and vertical source sizes, respectively. L is the distance of the nanofocusing optics from the source, and L_a is the distance of the beam defining aperture from the source. d_h and d_v are the sizes of the beam defining aperture in the horizontal and vertical direction. D is the acceptance of nanofocusing optics.

4.6.3.1 Mirrors

High-heat-load mirrors are required for higher harmonics rejection, power handling, and for providing physical separation of the two branches of a canted beamline in the horizontal direction. To achieve sufficient separation between the TXM branch and the ISN branch, a total of three plane, beam-deflecting mirrors, each providing an angular deflection of 5-6 mrad, is required. The total lateral separation of the canted beams from these mirror systems corresponds to 420 mm at a position 62 m from the source. In

addition, the ISN beamline requires a vertically focusing pink-beam mirror to focus incident x-rays into an intermediate focus at the BDA at 42.2 m from the source, and thereby provide spatial filtering in the vertical direction. Such a mirror system will allow matching of the lateral coherence length of x-rays to focusing mirrors in both Montel and K-B geometry.

The ISN branch will use a plane, water-cooled, horizontally deflecting mirror with a grazing angle of ~2.5 mrad (M1) as high-heatload optic. The mirror will have three reflective stripes (combinations Si/Cr/Pt or Si/Rh/Pt) to provide good higher-harmonics rejection across the full energy range at fixed grazing angle. The mirror will have an optical length of approximately 800 mm to accept 2 mm of one canted undulator beam.

To provide spatial filtering in the vertical direction, a bent, water-cooled, vertically deflecting and vertically focusing mirror with a grazing angle of ~ 2.5 mrad will be used (M2). The mirror will have three reflective stripes (combinations Si/Cr/Pt or Si/Rh/Pt) to match the stripes of the M1. The mirror will focus beam from M1 into a spot with a size of 4-5 μm on the BDA at 42.2 m.

The TXM branch will use two consecutive plane, water-cooled, horizontally deflecting mirrors with a grazing incident angle of ~ 2.5 mrad, as high-heatload optics. These provide a total outboard deflection of ~10 mrad. The mirror will have an optical length of approximately 800 mm each, to accept 2 mm of one canted undulator beam.

4.6.3.2 Monochromators

Monochromators are required to select the photon energy and to define an energy bandwidth. A double-crystal monochromator (DCM) using Si <111> crystals is required to provide the small bandwidth needed to achieve diffraction-limited resolution with nanofocusing diffractive optics and to allow spectroscopic studies. A double-multilayer monochromator (DMM) is required to provide a flux of roughly 25 times more at increased bandwidth for operation with reflective optics.

To minimize any effects the mirror optics or monochromator optics have on the uniformity of the wavefront in the vertical direction, horizontally deflecting geometry as opposed to vertically deflecting geometry will be used for the monochromators. Wavefront aberrations caused by the monochromators will be corrected by spatial filtering using a BDA at 42.2 m. In horizontally deflecting geometry, some intensity will be lost due to reduced reflectivity of the π polarized component of the incident x-ray beam. The reflectivity of the π component is 54% for a photon energy of 4 keV ($\theta_{Si<111>} = 29°$) and 83% for a photon energy of 5 keV ($\theta_{Si<111>} = 23°$). Given that the coherent flux increases inversely with the photon energy, this small reduction of brightness at the low photon energies has minimal effect on the beamline throughput.

High positional stability of the focused spot in the experimental station requires high angular stability of the beam accepted by the focusing optics. This requires high relative angular stability of the 1st with regard to the 2nd crystal of the DCM, estimated at ~ 0.1 μrad. Similar stability is required for the DMM to provide diffraction-limited resolution and positional stability of the focal spot obtained with reflective mirror optics.

Pink beam with high total power at closed gap will impinge on the DMM and the DCM. To allow operation at 20 nm spot size with diffractive optics and 50 nm spot size with reflective optics, the local thermal expansion (thermal bump) of the monochromator optics needs to be minimized. This is typically achieved by cooling with liquid nitrogen (LN2). Therefore, both LN2 cooled monochromators and the requisite LN2 pump will be procured.

4.6.3.3 Focusing Elements

The ISN instruments will use both diffractive and reflective optics to focus incident x-rays into a small probe. Diffractive optics such as zone plates (ZPs) or multilayer Laue lenses (MLLs) will serve as highest-resolution optics and will be used to focus monochromatic x-rays to a focal spot with a size of 20 nm. Reflective optics in K-B or Montel geometry will serve as achromatic high-flux optics and will be used to focus monochromatic x-rays into a focal spot with a size of 50 nm.

To achieve a diffraction-limited resolution of 20 nm, diffractive optics with smallest structures sizes of 15 nm must be used. At the same time, to achieve good focusing efficiency, diffractive optics have to be fabricated with a thickness corresponding to the interaction length of x-rays with the zone plate material, typically in the range of sub-micrometer to several micrometers. ZPs with the required outermost zone width of 15 nm are expected to provide good focusing efficiency in the energy range below 10 keV, while recent developments and R&D plans make good efficiency above 10 keV appear possible. MLLs with the required small structures are expected to provide good focusing efficiency in the energy range of 15 keV and above, but require added degrees of freedom for alignment, as compared to ZPs. Development of both technologies will inform the final decision on which high-resolution optics will be deployed. With the following notes, Table 4-16 lists relevant parameters for ZPs:

- To achieve diffraction-limited focusing, the zone number N has to be well below the inverse bandwidth of the illuminating beam. For the bandwidth of a Si <111> monochromator with $\Delta E/E$ of $1.4 \times 10\text{-}4$, this requires zone plates to have less than 6,000 zones. This is well satisfied for photon energies of above 6 keV, and can be satisfied for the energy range of 4-6 keV by requiring a zone plate diameter of not more than 350 μm, at a small loss of coherent photon flux.

- To realistically estimate the focusing efficiency of zone plates, it is assumed that two zone plates with an outermost zone width of 15 nm and a thickness of 250 nm can be fabricated. Furthermore, it is assumed that two such zone plates can be stacked within the optical nearfield, for a total effective thickness of 500 nm. At the same time, it is assumed that a zone plate with an outermost zone width of 15 nm can achieve its full theoretical efficiency. Current research plans might yield multiply stacked zone plates with an effective thickness of larger than 500 nm. On the other hand, it appears unlikely that the theoretical efficiency can be achieved. Therefore, the efficiency as presented offers a realistic estimate of what might be available once operation of the ISN beamline commences.

Table 4-16: Table of parameters of diffractive optics with a smallest structure size of 15 nm.

Energy range of operation [keV]	4 - 6	6 - 9	8 - 12	12-18	18-30
Reference energy [keV]	5	8	10	15	24
Diameter [μm]	350	235	176	118	74
Number of zones	5833	3921	2941	1960	1225
Focal length [mm]	21.18	21.35	21.35	21.35	21.35
Anticipated optic	ZP	ZP	ZP	ZP/MLL	ZP/MLL
Anticipated efficiency for two stacked zone plates with thickness 500 nm [%]	19 - 15	15 - 8	10 - 4	4-2	2-1
Anticipated efficiency for MLLs [%]				36	36

4.6.4 Beamline Physical Layout

Table 4-17 shows the major components of the ISN beamline, starting from the upstream components and progressing to the last component, the ISN instrument. The ISN beamline will be built at Sector 32 of the APS and will share a canted front end with the TXM program that is currently operating in Sector 32. To allow combination of the two programs in a canted sector, a total of three side-deflecting high-heat-load mirrors, operating at a grazing angle of 2.5 mrad, and providing a total angular separation of 15 mrad between the two branches, will be deployed. This setup provides a lateral separation of approximately 420 mm at 62 m, where the TXM could be positioned. Beamline optics and related components are laid out according to the following rationale:

1. Beam separation mirrors (ISN-M1, TXM-M1 and TXM-M2) have to be positioned as far upstream as possible to maximize the lateral position between the two partner branches in the downstream half of the beamline.
2. The beam-defining aperture (BDA) for the ISN beamline must be positioned downstream of all ISN beamline optics. Combined with 1) and the need to reserve a 2-m-long part of the FOE for fast access to the ratchet wall door at 37 m, the closest position for the BDA is at 42 m from the source.

3. To allow operation of the ISN instrument with a spatial resolution of 50 nm with K-B mirrors, the vertically focusing beamline mirror ISN-M2 must be positioned to focus the incident beam to a size of 4-5 μm. This requires positioning ISN-M2 at a position roughly 35-36.5 m from the source, corresponding to a source demagnification of 5-6x.

Furthermore, the ISN beamline will utilize the DCM for highest-resolution operation, which, accordingly, must be designed to provide highest stability. Therefore, the DCM is placed as close as possible to the ISN-M2, minimizing the power density the DCM crystals have to handle. All other beamline components are positioned as determined by ray tracing calculations and available space.

Table 4-17: Major components of the In Situ Nanoprobe beamline.

Component	Distance to center of straight section [m]	Notes
Front end exit window	N/A	Windowless front end.
Differential pumping section	25.5	
White-beam slit, ISN-WBS	26.7	Define beam size and total power for ISN mirror system.
White-beam slit, TXM-WBS	27.3	Define beam size and total power for TXM mirror system.
HHL mirror ISN-M1	29.7	Inboard deflecting high-heat-load mirror. Accepts outboard canted beam.
HHL mirror TXM-M1	31.5 33.4	Outboard deflecting high-heat-load mirror system. Consists of two consecutive horizontally deflecting mirrors.
HHL mirror ISN-M2	35.3	Up- or down-deflecting mirror. Focuses vertically on beam-defining aperture at 42.2 m. Accepts pink beam from ISN-M1.
Pink-beam slit ISN, ISN-PBS	36.5	Limits beam size and total power to ISN monochromators (ISN-DCM, ISN-DMM).
Access to ratchet wall door	36-37.8	Removable components to allow access to ratchet wall door.
Double-crystal monochromator for ISN branch, DCM-ISN	38.4	Energy selection between 4 keV and 30 keV, with bandwidth of 10^{-4}. Angular stability of ~ 0.1 μrad between 1st and 2nd crystal.
Double-multilayer monochromator for ISN branch, DMM-ISN	40.1	Energy selection between 4 keV and 30 keV, with bandwidth of 10^{-2}. Angular stability of ~ 0.1 μrad between 1st and 2nd multilayer optic.
White-beam stop, ISN branch	41	
Beam-defining aperture for ISN branch, BDA-ISN	42.2	Define the horizontal and vertical size of intermediate x-ray source. Resolution, accuracy and stability must be consistent with a smallest aperture size of ~ 4 μm.
Photon shutter, mono beam, ISN branch	43.9	Stop photon beam from entering ISN branch beamline.
Pink-beam slit TXM, TXM-PBS	44.0	Limits beam size and total power to TXM monochromator.
Photon shutter, mono beam, TXM branch	44.9	Stop photon beam from entering TXM branch beamline.
Collimator, ISN branch	46.2	
Collimator, TXM branch	47.3	
Double-crystal monochromator for TXM branch, DCM-TXM	44.9	Energy selection between 4 keV and 30 keV, with bandwidth of 10^{-4}. Angular stability of ~ 0.1 μrad between 1st and 2nd crystal.
Exit window assembly, ISN branch	66	Filter boxes, shutter, exit window for ISN branch

Component	Distance to center of straight section [m]	Notes
ISN control room	65-75, position depends on canted sector layout.	Control room will be temperature stabilized to match enclosure temperature. Must include an anteroom to provide enclosure access. Control room must provide user access to experimental station.
ISN enclosure	68-78	Enclosure must accommodate monochromatic beam. Enclosure must provide HVAC system with temperature stability of ~ 0.1 °C and low air flow speeds.
ISN instrument	72 or larger. Distance from source increases lateral coherence length and in turn working distance.	ISN instrument with high-resolution focusing optics, *in situ* environment, detectors.

4.6.4.1 Front End

To minimize unnecessary deposition of power on beamline components and supports, the total power transported into the first optical enclosure (FOE) should be limited as much as possible. Therefore, a small exit aperture is desired. The aperture needs to leave sufficient space to allow for optics alignment and to accommodate potential beam motions. We currently anticipate an exit aperture with a size of 2 × 2 mm, but a smaller size might be feasible as well.

4.6.4.2 Overall Beamline

The ISN beamline is designed to provide a range of photon energies between 4 keV and 30 keV, select a spatially coherent x-ray beam, and provide control of the lateral coherence length in horizontal and vertical direction at the ISN instrument station. Therefore, the beamline is designed with spatial filtering, with the beam-defining aperture (BDA) providing a secondary x-ray source in the horizontal and the vertical direction. To maximize the lateral coherence length in the experimental station, the BDA has been moved as far upstream as possible, under the following constraints: (i) only monochromatic beam is focused on the BDA; (ii) to maximize the separation between both sector branches, all beam splitting mirrors were positioned upstream of the BDA; and (iii) to preserve the coherent flux, a vertically focusing mirror must be positioned such that the image of the x-ray source in the vertical direction corresponds to the size of the BDA as determined by the acceptance of the vertical nanofocusing mirror system in the ISN instrument.

Figure 4-49 shows the resulting configuration of the major beamline optics in the first optical enclosure (FOE). ISN-M1 is placed at 29.7 m, ISN-M2 at 35.3 m, and the two mirrors for the TXM branch are located at 31.5 m and 33.4 m, respectively. The space between 36 m and 38 m is ideally kept free, or occupied by components that can be removed quickly to provide access to the ratchet wall doors. A beam position monitor (BPM) and a pink-beam slit (PBS) are positioned in this region. We anticipate that, during final design, TXM-M1 and TXM-M2 can be housed in one vacuum chamber, leading to a shorter double-mirror system and potentially permitting the BPM and the PBS to be moved upstream of the

ratchet wall door. The DCM and DMM for the ISN beamline are placed downstream of the ratchet wall door, at 38.4 m and 40.1 m, respectively. They will ultimately be placed as far upstream as possible, to minimize power density on the monochromator optics. The BDA is positioned at 42.2 m, providing a demagnification of the source of 5x and an intermediate source size of 4 μm (FWHM) in the vertical direction. The DCM for the TXM branch is placed at 44.9 m, where the lateral separation between canted beams is 165 mm. To allow monitoring of the beam position at beamline optics, a beam position monitor has been placed after each beamline mirror. Each monochromator is followed by a fluorescence flag for the same purpose.

Slits are required to confine the undulator beam and regulate total power to various components. A white-beam slit (WBS) for each branch is placed upstream of the relevant first mirror: at 26.7 m for the ISN branch and at 27.3 m for the TXM branch. The pink-beam slit (PBS) for the ISN branch is placed upstream of the first ISN monochromator at 36.5 m, and the PBS for the TXM branch upstream of the TXM DCM is located 44 m from the source. Beam position monitors are placed downstream of each major optical component to allow effective alignment. A removable white-beam monitor, typically a diamond screen, is placed downstream of each mirror at 30.5 m, 32.5 m, 34.3 m, and 36.2 m, respectively. A removable fluorescence flag is placed downstream of each monochromator at 38.8 m and 40.8 m, respectively, for the ISN branch, and at 45 m for the TXM branch. Figure 4-49 shows the position of all beamline components in the FOE, as outlined above. To accommodate the optics for the two branch beamlines, the FOE has to be expanded significantly, to a position 51-52 m from the source.

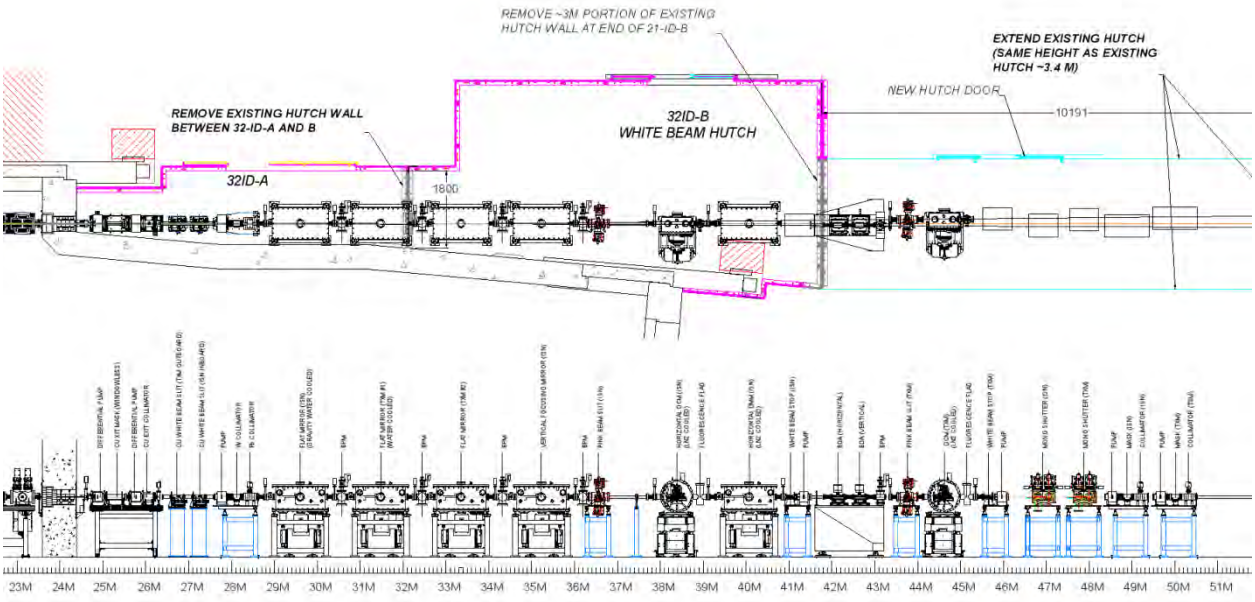

Figure 4-49: Layout of the first optical enclosure (FOE). The FOE combines mirror optics that provide beam separation between the ISN and the TXM branches; white-beam slits and pink-beam slits; a beam-defining aperture for the ISN branch; monochromators; and related masks, collimators, stops and shutters.

Figure 4-50 shows the TXM and ISN experimental stations. The ISN instrument with the exit window assembly will be placed in the existing 32-ID-C enclosure. To provide a spatial resolution of 20 nm or below, the ISN enclosure must be temperature stabilized to 0.1°C. To prevent temperature fluctuation when opening the doors to the enclosure, a temperature-stabilized control room will be built. In addition, a small anteroom will be placed between the control room and the entrance to the ISN enclosure. The anteroom serves as an airlock between the control room and the ISN enclosure, and further reduces airflow and temperature instabilities. To allow equipment to be moved into the ISN enclosure, it is planned to modify the existing enclosure by adding an angled wall to its outboard side. The TXM will be positioned in a new enclosure upstream of the existing 32-ID-C station, extending from 54 m to 65 m.

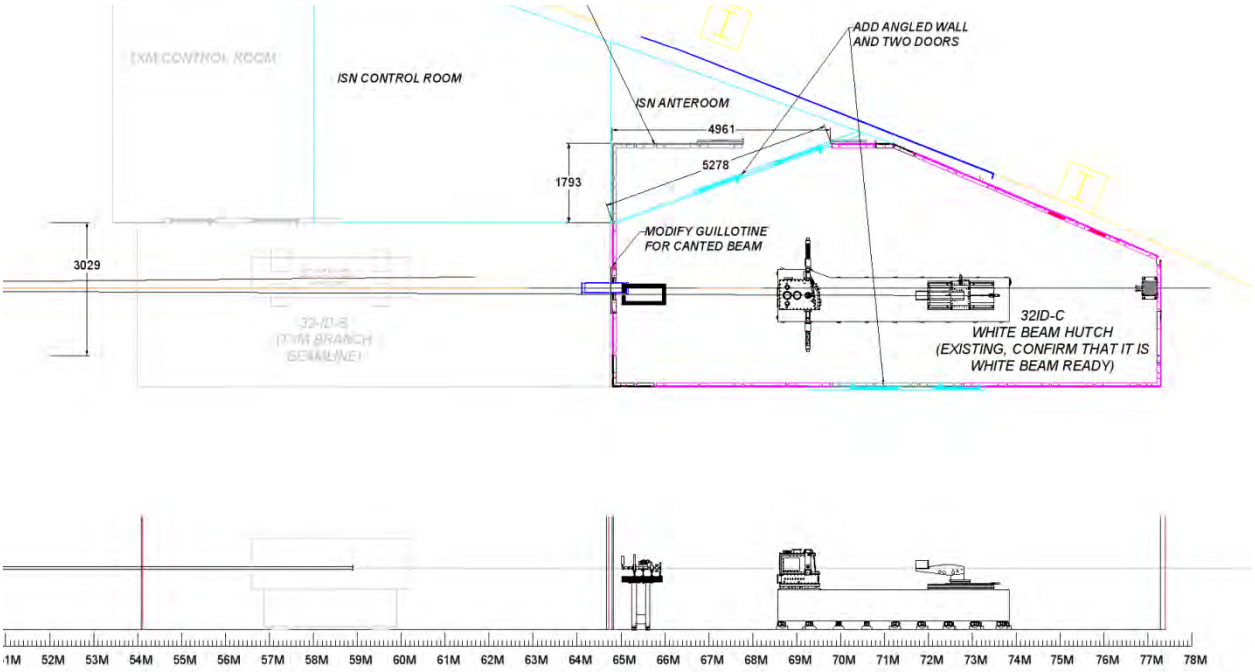

Figure 4-50: Layout of the ISN and TXM experimental stations, and the ISN control room. The ISN is located in the last enclosure of the beamline. The TXM is located in the adjacent upstream enclosure. The ISN control room is located on the outboard side of the sector, adjacent to the ISN enclosure, and separated from the enclosure by an anteroom that provides temperature stability and prevents direct air exchange between the control room and the ISN enclosure.

4.6.4.3 General Description

The ISN beamline will be sited at 32-ID (see Figure 4-51) and share the floor layout with the transmission x-ray microscope (TXM). The ISN beamline will use the outboard pointing canted undulator beam. The first ISN mirror will deflect the white undulator beam inboard, leading to a position of the ISN instrument on the inboard part of the centerline. The TXM beamline will use the inboard pointing canted undulator beam. The TXM mirror system will deflect the white undulator beam outboard, positioning the TXM instrument on the outboard side of the center line. The ISN instrument will be positioned at a position of

72-75 m from the source, in the existing 32-ID-C station. The TXM instrument will be positioned at 60-62 m from the source, in a new enclosure positioned directly upstream of the ISN enclosure.

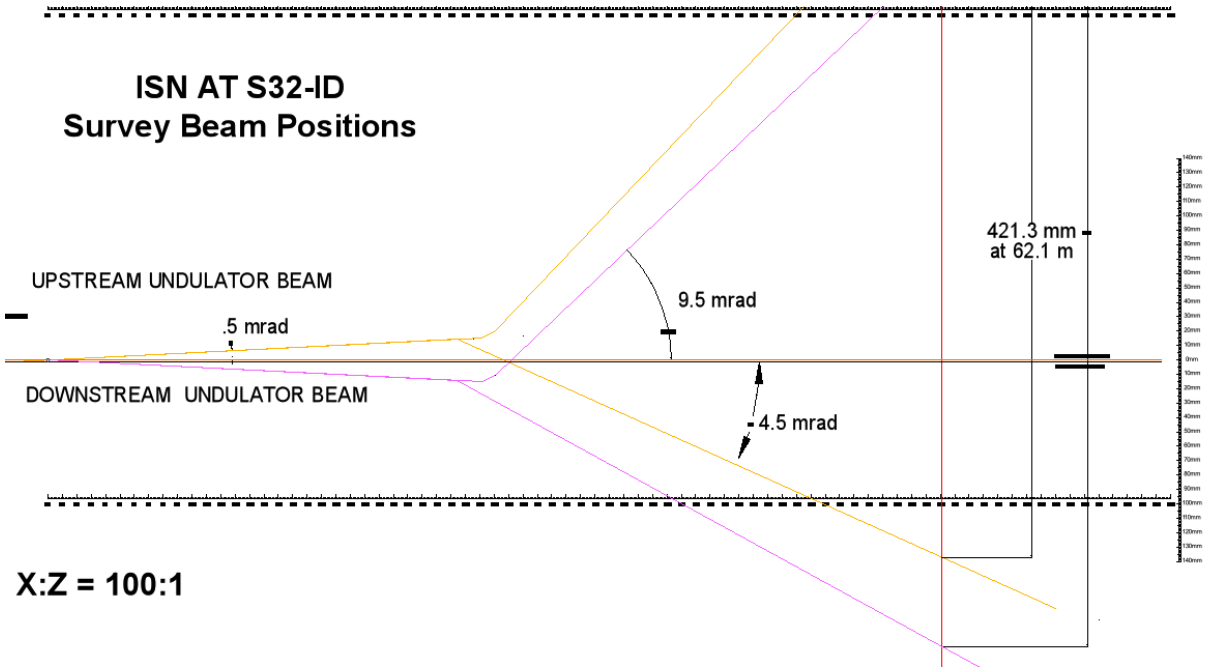

Figure 4-51: Beam separation of ISN branch and TXM branch in Sector 32. The ISN branch uses the outboard canted undulator beam, which is redirected by ISN-M1 to the inboard side of the centerline. The TXM branch uses the inboard canted undulator beam, which is redirected by TXM-M1 and M2 to the outboard side of the centerline. The lateral separation of beams at 62 m from the source is 398 mm.

4.6.4.3.1 Radiation Safety Aspects

As previously shown in the layouts in Figure 4-49 and Figure 4-50, the ISN and TXM beamlines require three enclosures, an A station for all of the beamline optics and RSS components, a B station for the TXM, and a C station for the ISN. White beam is confined to station A. Monochromatic shutters will be installed at the end of the A station, and stations B and C will receive only mono beam transported through shielded transport. All beamline shielding will conform to the APS Guidelines [52].

4.6.4.3.2 Vacuum System

The ISN beamline requires windowless operation to preserve the coherence of the undulator beam and will be designed with a windowless front end. The windowless front end and the main mirrors require ultrahigh vacuum (UHV). The water and LN2 cooling lines for mirrors and monochromators will be double-walled, which is consistent with the APS windowless beamline operation. In addition, all of the components up to the first monochromator will be designed in accordance with the APS Accelerator Ultrahigh Vacuum Guide [53].

4.6.4.3.3 Data Acquisition and Motion Control

The control system of the ISN beamline will be based on EPICS, which will provide a software interface to motion components such as motors and encoders, as well as to detectors, counters, etc. Motion control for the ISN instrument may be based on Delta Tau controllers or an alternate controller with similar capabilities. The motion controller will in turn communicate with an IOC running EPICS. The ISN will require multiple IOCs, some of which will be VME based and some of which will be PC based. Final decisions regarding the choice of controllers, EPICS IOCs, and the architecture of the data acquisition system will be made in the final design report.

The ISN instrument will acquire full fluorescence spectra from multiple energy-dispersive x-ray spectroscopy (EDS) detectors and from area detectors in step-scan, fly-scan, and tomographic data acquisition modes. Data from area detectors may be acquired at a different rate than data from EDS detectors. In addition, data in either of these modes will be acquired with scalar parameters such as temperature, gas flow, time, applied voltage, incident photon energy, etc. As such, acquisition of 4-dimensional data with full spectra (e.g., X, Y, temperature, incident photon energy) is required. The data acquisition system has to accommodate these operation modes. Details of the detector type and the related readout rates will be part of engineering discussions.

4.6.4.4 First Optics Enclosure and Infrastructure, Major Components

The first optics enclosure layout is shown in Figure 4-49. The FOE currently at 32-ID will be expanded to 52 m to accommodate all of the necessary components for the two canted beamlines.

4.6.4.4.1 Windows

The ISN beamline will be windowless. Two Si_3N_4 windows, protected from ozone by a Kapton window and flow of He gas, will be mounted on the beamline exit flange to permit x-rays to enter the ISN instrument.

4.6.4.4.2 Slits

Both the ISN and TXM lines will have white-beam slits (WBSs) in front of the first optics element, in each case a mirror system. The WBS allows minimizing the heat load to each system. These slits will be an APS standard canted-undulator design. For the same reason, pink-beam slits (PBSs) will be located upstream of monochromators to control the heat load. A beam defining aperture will be placed in the focus of the vertically focusing mirror, to allow spatial filtering in the horizontal and vertical direction.

4.6.4.4.3 Collimators

Sufficient collimation is required to provide the necessary bremsstrahlung and synchrotron radiation protection while operating the two branches independently. This will be determined by a detailed ray tracing of the final layout. Based on preliminary ray tracings, standard collimator designs will be sufficient.

4.6.4.4.4 Shutters/Stops

White beam stops will be required after each monochromator, to protect the bremsstrahlung collimators from the heat load of the incident beam. A photon shutter capable of handling the multilayer beam is located downstream of the BDA.

4.6.4.4.5 Mirrors

The ISN will use a flat horizontal-deflecting first mirror and a vertical-focusing, vertical-deflecting second mirror. The first mirror will be ~ 800 mm long, accepting a beam of ~ 2 mm. In most cases, the mirror will be illuminated along its full length to reduce the thermally induced figure error near the center. Given that the source divergence is larger in the horizontal direction, it is expected that water will provide sufficient cooling without adversely affecting the horizontal beam characteristic. Three reflective coatings (e.g., Si/Rh/Pt) will be used to provide different high-energy cutoffs and thermal management. When changing between coatings, the mirror will be translated vertically.

The second mirror also has three reflective coatings matching those of the first mirror. Ideally it can be switched between an elliptical surface for focusing onto the BDA, and a flat surface for using the vertical source directly. Investigation into whether this can be accomplished using a bendable mirror will continue. Otherwise, a polished flat and a polished elliptical surface may be fabricated next to each other. Since the x-ray phase space is nearly diffraction limited in the vertical direction, the vertical focusing property will be very sensitive to thermally induced figure error on this mirror, even though most of the heat load will be removed by the first mirror. Detailed thermal analysis will be performed to compare the performance of cryogenic versus water cooling for the second mirror.

4.6.4.4.6 Monochromators

As mentioned previously, a double-multilayer monochromator will be used for high-flux studies down to 50-nm resolution, while a double-crystal monochromator will be used for spectroscopy or high-resolution studies down to 20 nm. Both monochromators will diffract horizontally to minimize the effect of any physical- or thermal-induced distortion on the phase space of the x-ray beam. They will work in the fixed exit geometry, with a small offset of 6-10 mm. A small offset is possible because the larger offset provided by the branching mirrors should be sufficient to satisfy the bremsstrahlung shielding requirements by horizontally offset collimators. It is expected that indirect cryogenic cooling should be sufficient to handle the heat load of the pink beam, pending further thermal analysis.

Both monochromators must be designed to allow the canted beam for the TXM to pass through undisturbed. Since the monochromators will be located in the FOE about 6-10 m downstream of the branching mirrors, the lateral separation between the two canted beams is expected to be ~ 70 mm. To provide a stable illumination of the nanofocusing optics in the ISN enclosure, the angular stability of the exit beam from the monochromators should be better than 1 μrad, with the possibility of quick feedback to the second crystal/multilayer using downstream BPMs. The DCM will use a pair of Si<111> crystals to cover the 4-30 keV; the second crystal will also be cryogenically cooled to match the d-spacing of the first crystal. As for the DMM, super-polished substrates with < 1-Å roughness will be used, on which 3-4 stripes of multilayers with different d-spacings or materials will be deposited to cover various energy

ranges. Possible candidates are $MoSi_2$/Si multilayers for below 20 keV and WSi_2/Si multilayers for above 20 keV. Also, thermal analysis will be performed to determine whether cryogenic cooling is required. If it is required, possible strain built up in the multilayers due to different thermal expansions needs to be investigated.

4.6.4.4.7 Diagnostics

A fluorescence screen will be located downstream of each mirror and monochromator to provide visual feedback during alignment of the beamline optical components, as well as diagnostics once the beamline has entered operations. In addition the blades of the BDA will be fitted with beam position monitors to detect change of beam intensity and allow feedback in X and Y.

The exit window assembly in the ISN enclosure will include a fast shutter and a quadrant BPM. The latter will be used to monitor beam position within 2-4 meters of the ISN instrument.

4.6.4.4.8 *In Situ* Nanoprobe Experimental Station

The ISN instrument is located 72-75 m from the source in the ISN enclosure 32-ID-C. It will be supported on a vibration-isolated structure to minimize coupling of floor vibration. The instrument will be housed in an instrument chamber, to allow operation in a vacuum, or under inert gases.

At the core of the instrument is the nanopositioning unit that consists of an optics module, a sample module, and a reference platform that carries both modules as well as a multi-axis laser interferometer. The reference platform is made of Invar® to minimize thermally induced drifts. A laser interferometer serves as encoder and provides real-time positioning information on optics and specimens. Laser interferometer cavities and heads are mounted on the reference platform. Retro-reflectors are positioned on the optics module and the specimen module, in close proximity to the components in question. The reference platform will be mounted inside the ISN instrument chamber at three points, in a fashion that decouples it from the changes of the instrument chamber due to pressure or temperature variation. The instrument chamber also includes a mechanism for specimen change, energy-dispersive detectors, prealignment optics, viewports, and other auxiliary components. X-rays enter the instrument chamber through a Si_3N_4 window on the upstream side. A larger window will be mounted on the downstream side to allow the transmitted wavefront to propagate through. To make use of coherent diffraction techniques, a pixel array detector (PAD) is mounted downstream of the instrument chamber. The detector is mounted on a slide that moves parallel to the x-ray axis, allowing the distance between the PAD and sample to change as a function of desired scattering angle and photon energy. Figure 4-52 shows the layout of the instrument.

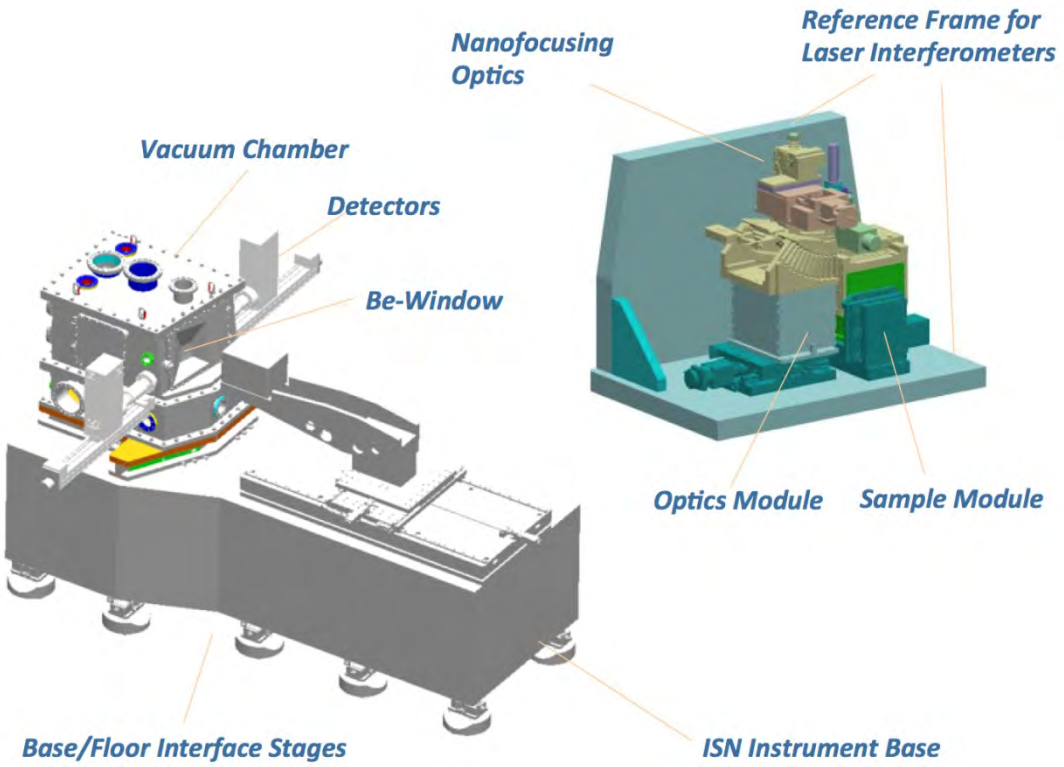

Figure 4-52: Conceptual design of the In Situ Nanoprobe instrument. The insert shows a conceptual design for the nanopositioning mechanics and laser-based encoders.

To pursue the scientific studies outlined above, environmental specimen holders are required. These holders must be consistent with highly accurate positioning, must allow exchange of gases and fluids, must provide connections for application of external fields, and must provide heating and cooling capability. Cartridge-based instrumentation will be developed that is based on a standard interface plate with proper connections and suitable for adaptation to each of the specific environmental parameters, or combinations thereof, as outlined above. For example, a cartridge for heating to high temperatures will be developed as will a cartridge for cooling. Cartridges that allow application of external fields and readback of currents, combined with flow of gases and/or fluids will also be developed. This approach will allow development of new and customized cartridges for specific experiments that may not have been proposed to date, without requiring significant modification to the ISN instrument. The approach will also allow external user groups to develop their own cartridges, and bring them to experiments. Figure 4-53 shows a concept for environmental cartridges.

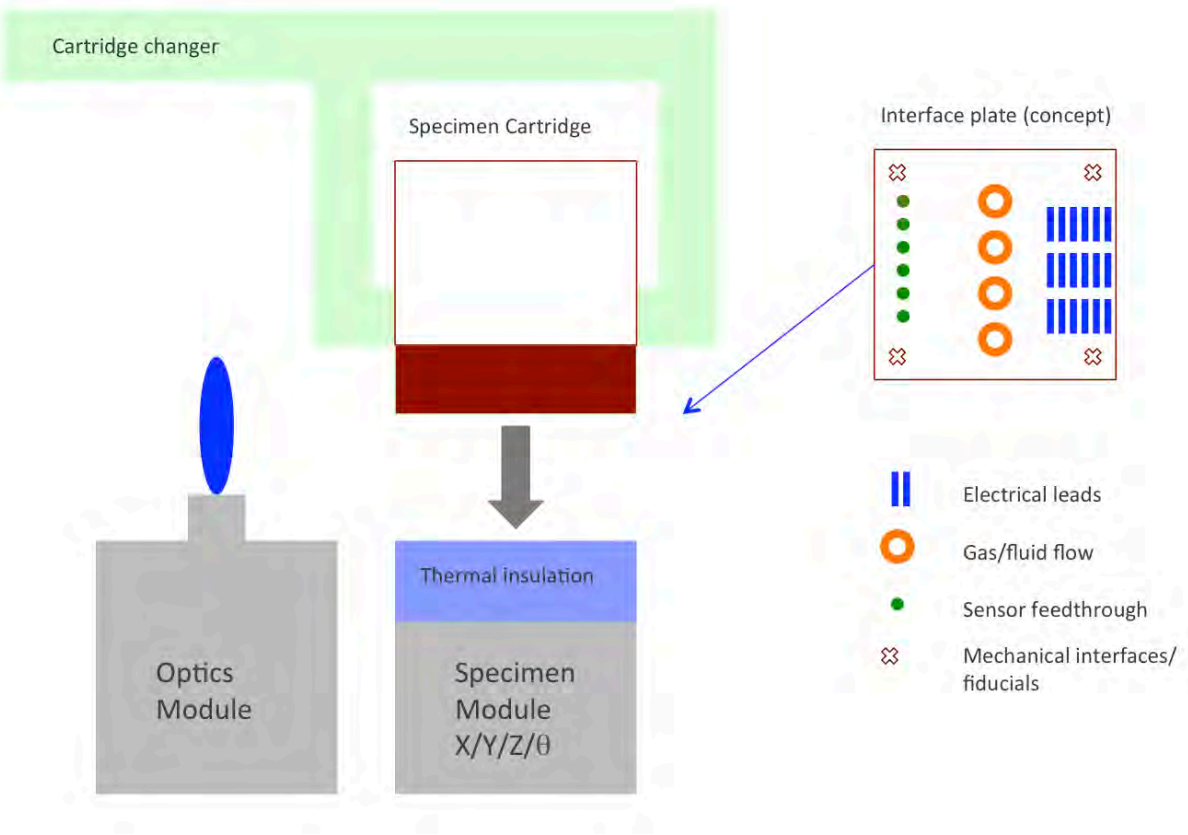

Figure 4-53: Concept for in situ specimen cartridge.

4.6.5 Additional

4.6.5.1 Conventional Facilities Requirements

Standard utilities available at the APS beamlines are required. This includes adequate power for all beamline components, control computers, and experimental needs. Temperature-stabilized water with a temperature stability of ± 0.1°C is required for cooling the mirror, while deionized water is required for cooling masks, slits, and shutters. A facility LN2 supply is required for the liquid nitrogen pump that provides coolant to the monochromators.

The ISN enclosure must be temperature stabilized to ~ 0.1°C with low speed airflow by a proper HVAC system. The control room connected with the ISN enclosure requires adequate power and high-speed network connections. Compressed He and compressed N2 with manifolds that regulate flow and switch between full and empty cylinders are required to supply gases to relevant end-station instrumentation (ion chambers, space between Kapton window and Si_3N_4 exit window, etc.).

4.7 Resonant Inelastic X-ray Scattering Beamline (RIXS)

With the advent of third-generation synchrotron radiation sources, Resonant Inelastic X-ray Scattering (RIXS) has become a very important technique to study collective electron phenomena in novel materials of great scientific and technological significance. At the APS, the RIXS program is currently one of the leading programs of its kind in the world. With its main focus on complex transition metal oxide compounds and other important electronically active materials such as graphene and novel superconductors, it has yielded many ground-breaking scientific results in its 10-year history.

Currently the RIXS program is spread over two time-shared beamlines of varying sophistication. In the context of the APS Upgrade Project, it will be consolidated at one dedicated, optimized, state-of-the-art insertion device beamline in Sector 27. Explicit goals are to optimize x-ray source parameters for this photon-hungry technique, improve the energy-resolution from the ~100 meV to the ~20 meV level or even better, and optimize throughput and momentum resolution by implementing multi-analyzer assemblies. Furthermore, new capabilities will be added including sample stages allowing access to small scattering angles, polarization control and analysis for incident and scattered photons, and a comprehensive suite of sample environments for meaningful *in situ* experimentation.

4.7.1 Research & Development

Part of the upgrade of the RIXS facility is an aggressive research and development (R&D) program aimed at developing the technology to routinely fabricate spherical sapphire analyzers (U1.02.02.02). This will be accomplished in a collaborative effort with the Crystal Optics section of the Optics Group (OPT) at the APS, which owns facilities for in-house design, fabrication, and characterization of crystal-based optical components. For the RIXS project, the following directions will be pursued:

1. Identify suitable vendors for the required materials and carry out extensive characterization of sapphire crystals using x-ray topography, double-crystal rocking curve measurements, and other suitable x-ray and optical techniques. If necessary, collaboration with the crystal growers will be initiated, providing them with characterization feedback to improve the growth techniques and processes.
2. Fabricate analyzers, including precise crystal orientation, cutting/dicing, polishing, etching, and characterizing. After fabrication, a comprehensive x-ray characterization of the fabricated analyzers is another important step for verifying the designed parameters and performance, including the strain states, the bandpass, x-ray reflectivity, and the lattice curvatures. Such information also provides important feedback for the optimization and improvement of the fabrication processes.

4.7.2 Scientific Objectives

Condensed matter physics and materials science are driven by the need to understand materials' properties, both exotic and mundane, with the ultimate goal of harnessing them in practical devices. Without exception these properties are dominated by electrons, their degrees of freedom (spin, charge, and orbital), and their interaction with the ion cores of the crystal lattice. In order to fully understand a

material it is necessary to understand the electronic ground state and the electronic excitation spectrum, which determine the material's response to dynamic perturbations, providing a direct window into the driving physics of the material.

The key for the RIXS program is the ability to provide energy-, momentum-, and polarization-resolved measurements for all relevant electronic excitations over the appropriate energy and momentum scales, and the ability to do so on extraordinarily small sample volumes, allowing the study of micron-sized crystals of the latest high-temperature superconductor, or a thin film sample undergoing photo-illumination, or a mineral under geological pressures.

Due in part to advances at the APS, the energy resolution and count rates in RIXS have improved by several orders of magnitude in recent times. As a result, an extended spectrum of condensed matter excitations have now been observed that have not been seen before, from phonons, to magnons, to orbital excitations, to charge transfer excitations and valence fluctuations. Inelastic x-ray scattering is the only technique that couples to all these excitations (neutrons do not couple to the charge, and electrons and light cannot reach the relevant momenta) and as such offers a powerful and incredibly versatile tool for understanding the materials of the twenty-first century.

In recent decades a multitude of complex oxide materials with novel phenomena of enormous scientific interest and immense technological potential have been discovered. The complex phase diagrams of many of these materials highlight the strong competition between lattice, spin, and charge degrees of freedom. Understanding the variety of interactions between these is vitally important for the understanding of such phenomena as unconventional superconductivity in cuprates, arsenides, and ruthenates; colossal magnetoresistance in manganites; the behavior of multiferroics and topological insulators. While great progress has been made in experimental and theoretical studies, most mechanisms leading to these phenomena are still poorly understood, hampering their technological and commercial exploitation.

RIXS, with its small-scattering cross section, has become viable only with the advent of third-generation synchrotron radiation sources and remains somewhat hampered by the relatively coarse energy resolutions (~100 meV) available until recently. In the context of the APS Upgrade, these shortcomings will be remedied and the resulting increased capabilities will dramatically improve the quality of information that may be extracted from a given sample with this already powerful technique.

4.7.3 Source Requirements

The source requirements for the RIXS beamline are chiefly determined by the need to access the energy at and near relevant transition metal absorption edges for a material under study.

The overall energy range necessary extends from 4.9 keV (Ti-K absorption edge) to 23 keV (Ru-K). A partial list of relevant absorption edges and emission lines is given below in Table 4-18.

Table 4-18: Partial list of transition metal absorption edges in the 4.9-keV to 23.0-keV energy range, relevant for RIXS measurements.

	Absorption Edge / Emission Line [keV]						
Element	**K 1s**	**L1 2s**	**L2 2p1/2**	**L3 2p3/2**	**Kα1**	**Kα2**	**Kβ**
Titanium Ti	4.966						
Vanadium V	5.465						
Cerium Ce				5.723			
Praseodymium Pr				5.964			
Chromium Cr	5.989						
Neodymiun Nd				6.208			
Manganese Mn	6.539						
Iron Fe	7.112				6.404	6.391	7.058
Cobalt Co	7.709						
Ytterbium Yb				8.944			
Nickel Ni	8.333				7.478	7.461	8.265
Copper Cu	8.9805						
Zink Zn	9.659						
Tantalum Ta		11.682	11.136	9.881			
Gallium Ga	10.367						
Rhenium Re		12.527	11.959	10.535			
Osmium Os		12.968	12.385	10.871			
Germanium Ge	11.103						
Iridium Ir		13.419	12.824	11.215			
Arsenic As	11.867						
Selenium Se	12.658						
Platinum Pt		13.880	13.273	11.564			
Gold Au		14.353	13.734	11.919			
Ruthenium Ru	22.117				19.279	19.150	21.657

Absorption edges and emission lines are nearly uniformly distributed within the overall energy range. Thus the most important criterion in choosing appropriate undulators for the RIXS beamline is that the delivered energy spectrum is continuous. It cannot have any gaps. Figure 4-54 shows an example of three choices of undulators available at the APS, with magnetic periods of 27, 30 and 33 mm. The lower cut-offs in energy, given an allowable minimum magnet gap of 11 mm, are 7.27 keV, 4.92 keV and 3.2keV, respectively. Clearly, the 27-mm device (blue line) has a large gap between 17 keV and 22 keV and cannot reach the lower energies listed and is therefore not suitable. The 30- and 33-mm options deliver a continuous spectrum and could reach all the energies listed. The 30-mm option, however, yields a substantially higher flux, which is critical for these flux-starved measurements. Thus, the 30-mm device is the most appropriate source for the upgraded RIXS beamline. In order to have sufficient incident photon flux available, an in-line tandem configuration of these undulators is necessary. Such a configuration is currently in use in Sector 30 and has performed very well in the context of RIXS measurements. The 30-mm devices currently installed at 30-ID will be moved to 27-ID and new undulators will be procured by the Project for 30-ID. The new IDs will be optimized to provide optimal program for the HERIX progam at 30-ID.

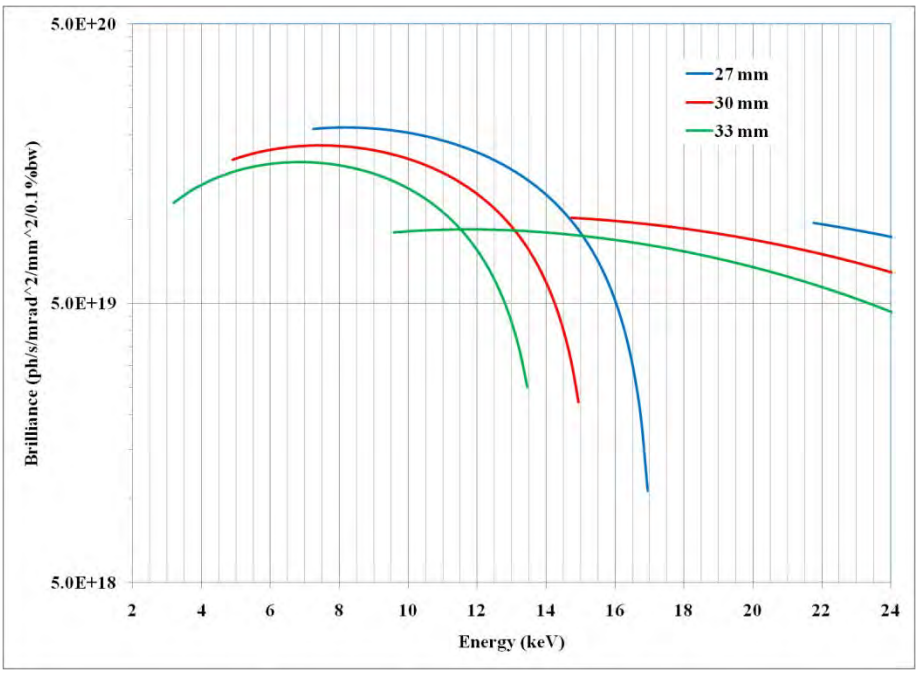

Figure 4-54: Tuning curves for the 33-mm, 30-mm, and 27-mm permanent magnet undulators (PMUs).

4.7.4 X-ray Optical Layout

The optical layout of the RIXS beamline is designed to prepare an incident x-ray beam with an energy bandpass in the meV range by a sequence of a high-heat-load monochromator and a high-resolution monochromator. The monochromatic beam is then micro-focused onto the sample at the inelastic spectrometer. Scattered radiation from the sample is captured by a single or multiple spherical-diced crystal analyzers and refocused onto a position-sensitive (strip) detector. A schematic layout of the overall RIXS beamline is shown in Figure 4-55, and the schematic sample-analyzer-detector geometry is shown in Figure 4-56.

A critical requirement for the RIXS effort at the APS is to improve the energy resolution from the current 100-200 meV to the 10-20 meV-range or better. In the optical layout four distinct contributions to the total energy resolution ΔE_{tot} can be identified, which in turn place design requirements on its components. As shown in Equation (4-1), with

$$\Delta E_{tot} = \sqrt{\Delta E_i^2 + \Delta E_s^2 + \Delta E_a^2 + \Delta E_p^2} \qquad (4\text{-}1)$$

these four contributions are:

1. The incident energy bandpass ΔE_i, which is determined by the synchrotron radiation source characteristics and the monochromators and will be addressed in section 4.7.4.1.

2. A contribution due to the x-ray footprint on the sample $\Delta E_s = E\ (s/R)\ \cot \Theta_B$. This contribution is mostly determined by the characteristics of the focusing mirrors and will be described in section 4.7.4.2.
3. The intrinsic energy resolution of the analyzer $\Delta E_a = E\ W\ \cot \Theta_B$, which will be addressed in section 4.7.4.3.
4. A geometric contribution due to the detector pitch $\Delta E_p = E\ (p/2R)\ \cot \Theta_B$. The best pixelated detectors commercially available at this point in time have a pitch of 50 µm. This number will be assumed for present resolution consideration. However, as detector development progresses, further improvement is quite possible and will be followed closely.

In the list above E means the incident photon energy, W is the angular Darwin width of the analyzer, Θ_B is the Bragg angle, s is the extension of the beam footprint on the sample projected onto the analyzer, and p and R are the detector pitch and the analyzer radius, respectively, as indicated in Figure 4-56. The inelastic spectrometer, which is currently in use at 30-ID and will be re-used on the upgraded RIXS beamline, offers a radius R between 1 m and 2 m. Other factors such as figure errors of the spherical shape might influence the overall energy resolution but are not explicitly addressed in this document.

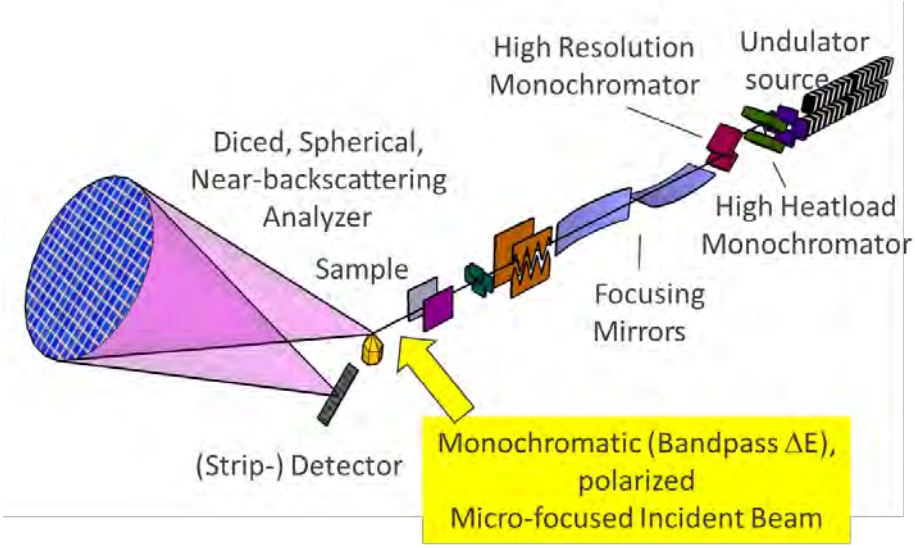

Figure 4-55: Schematic layout of the RIXS beamline.

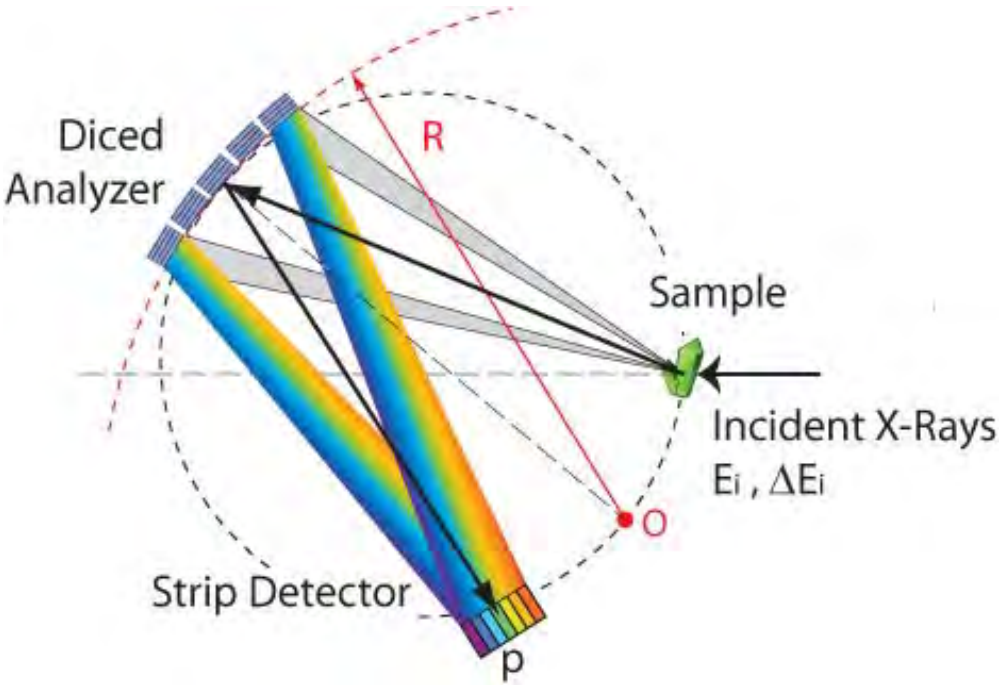

Figure 4-56: Schematic of the sample-analyzer-detector geometry.

4.7.4.1 Monochromators

A schematic layout of the monochromator sequence for the RIXS beamline is shown in Figure 4-57. The high-heat-load portion consists of a water-cooled diamond double-crystal monochromator, tunable to incident energies between 4.9 and 23 keV.

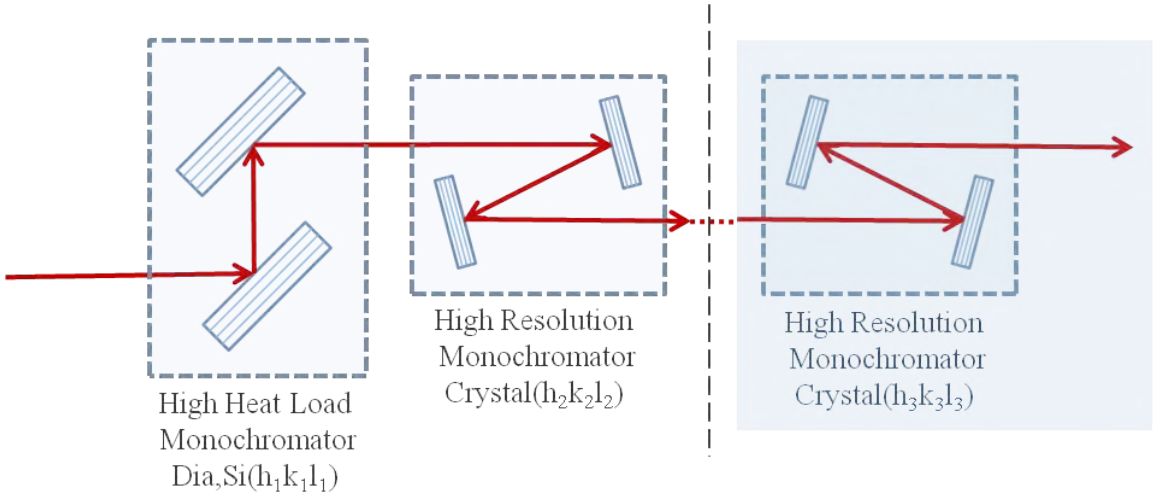

Figure 4-57: Layout of the sequence of monochromator for the RIXS facility.

The high-resolution portion can either consist of monolithic, near-backscattering, 2-bounce, or 4-bounce channel-cut crystals, which will be changed for every absorption edge or emission line energy.

Alternatively, an existing single, continuously tunable, 4-bounce device made from artificial channel-cut assemblies is available with bandpass choices of either 120 meV or 70 meV. It will be re-used for experiments requiring large throughput but less demanding resolution conditions.

4.7.4.2 Mirrors

In order to achieve the targeted overall energy resolution, the contribution due to the beam footprint on the samples needs to be better than $\Delta E_s = 10$ meV. This implies that, depending on the incident energy and Bragg angle of the analyzer, a spot size of 4-10 μm is required. Given commercially available mirror technology combined with the APS source characteristics and the envisioned beamline layout, this range of focal spot sizes is realistically attainable. However, the active length of these mirrors is limited to lengths smaller than ~ 0.6 m, or much less in some cases. Thus, to capture approximately four standard deviations of the beam footprint and retain reasonable throughput, focusing mirrors have to be as close to the x-ray source as practically achievable.

A set of dynamic-figure Kirkpatrick-Baez mirrors will be implemented for the upgraded facility. These mirrors consist of rhodium-coated Si wedges dynamically bent to the desired figure. They perform well with simple operation and are available with sub-μrad slope errors, needed to achieve sub-10-μm spot sizes.

4.7.4.3 Spherical Crystal Analyzers

A spherical analyzer for RIXS instrumentation consists of a flat wafer of an ideal crystal bonded to a glass or plastic substrate. This crystal assembly is diced into square pixels of mm-extension and bent into a spherical shape of radius R. Overall the analyzer is thus an assembly of many flat and unstrained crystallites with all surface normals pointing to a common focus. Ignoring possible deviations from a perfect spherical shape (figure errors), the intrinsic analyzer resolution ΔE_a is determined by the incident energy E, the reflection (Darwin) width W of the crystal reflection, and the Bragg angle Θ_B: $\Delta E_a = E\ W \cot \Theta_B$. It is apparent that the energy resolution is best for small reflection widths and near-backscattering conditions, where the Bragg angle is close to 90° and its cotangent approaches zero. The task is thus to identify near-backscattering crystal reflections for every absorption edge and emission line of interest, yielding the best resolution at reasonable intensities and fabricate appropriate analyzers.

In the past, silicon and germanium were the preferred choices for spherical analyzers since these materials yield nearly perfect crystals. However, with advances in crystal growth, other materials are becoming very viable, such as quartz, sapphire, and lithium niobate. While silicon and germanium have a highly symmetric, mono-atomic diamond-crystal structure, sapphire, quartz, and lithium niobate have complex unit cells of lower symmetry with multiple types of atoms. The reduced symmetry leads to more than ten times the number of available backscattering planes to match with the resonance energies. Furthermore, the larger unit cell with reduced symmetry means that most reflections tend to have weaker scattering contributions per reflecting plane, so more planes contribute to a Bragg reflection, resulting in a narrower bandwidth and better resolution. A partial set of viable reflections at various edge energies is given in Figure 4-58 for materials including silicon, germanium, sapphire, quartz, and lithium niobate. The size of the reflection marker indicates the integrated intensity of the particular reflection. It is apparent that for high-resolution analyzers in the region better than 20 meV, sapphire and lithium niobate are superior to

silicon and germanium. For lower resolution, high-throughput applications, lithium niobate would be the best choice.

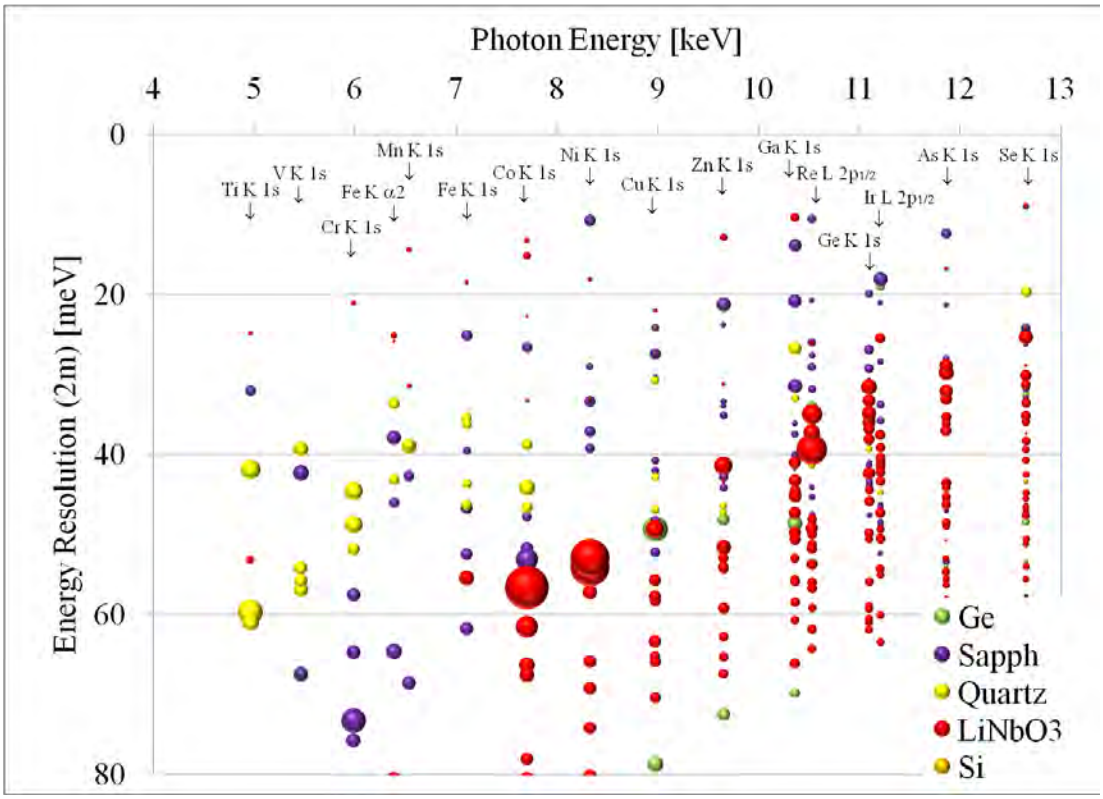

Figure 4-58: Possible analyzer near-backscattering reflections. For the various relevant energies the intrinsic energy resolution is shown. The area of the markers is proportional to the integrated reflectivity.

A comprehensive compilation of suitable analyzer reflections has been assembled in a set of tables for numerous absorption edges and emission lines of interest [54].

4.7.4.4 Alternate High-Resolution Analyzer Concept

A range of energy resolution below 10 meV is virtually inaccessible to spherical RIXS analyzers. An alternate multi-reflection analyzer system has been proposed to access this range. When fully implemented, this Si-based 3-bounce Collimation-Dispersion-Selection (CDS) analyzer system is expected to provide unprecedented energy resolution of 5-10 meV. The CDS analyzer scheme can be used for a broad class of absorption edge, including 3d, 4d, and 5d transition metals and rare earth materials. This system, shown schematically in Figure 4-59, consists of a multi-crystal CDS assembly: a collimating crystal (C) in the grazing-incidence geometry; (ii) a dispersing crystal (D); and finally (iii) a selection crystal (S). Dynamical theory calculations show that unprecedented energy resolution of ~ 5-10 meV can be achieved with high efficiency and sharp contrast for almost all the common absorption edges. Since the angular acceptance of the CDS analyzer is less than 0.2 mrad, two-dimensional multilayer Montel mirrors must be used before the CDS analyzer for collecting scattered x-rays within a sufficiently large solid angle, typically 10×10 mrad^2.

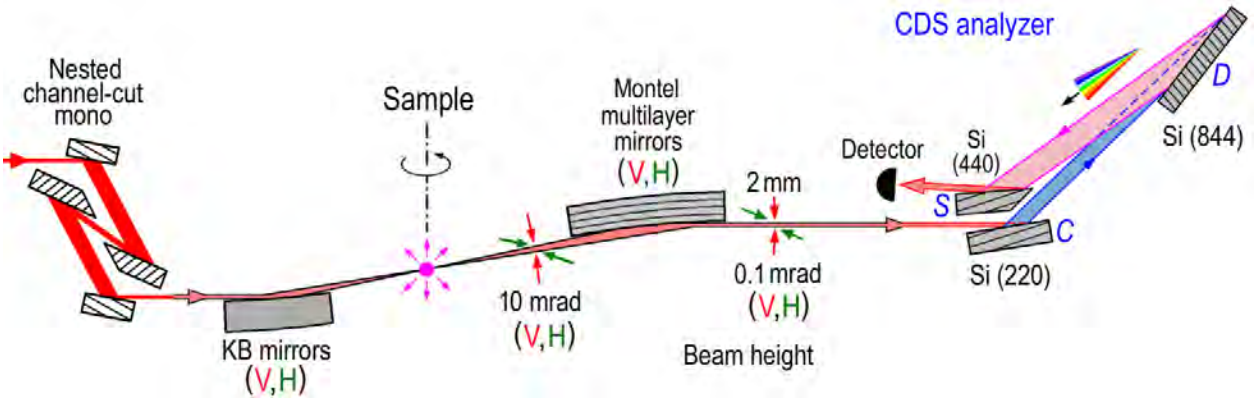

Figure 4-59: Schematic layout of an alternative high-resolution concept using a CDS analyzer combined with Montel optics.

4.7.5 Beamline Physical Layout

4.7.5.1 Overall Beamline

The RIXS beamline will be implemented at 27-ID of the APS and will consist of two back-to-back shielding enclosures, 27-ID-A and 27-ID-B, as indicated in the schematic representation in Figure 4-60 and the engineering view in Figure 4-61. The 27-ID-B enclosure is wider than the FOE and uses space normally reserved for the aisle between the ID and BM beamlines on a sector. The 27-ID-B station also extends downstream along the beamline and uses space normally reserved for access to a potential 28-BM beamline. APS management has reviewed the RIXS layout and has given permission to utilize this space [55].

The first enclosure, shown in Figure 4-62, will serve as a first optical enclosure (FOE), housing all white-beam equipment. The most downstream component is a differential pump, providing a windowless transition between the front end and the beamline, and defining the size of the entrance aperture through its intrinsic mask. The aperture size will be approximately 2.0 × 2.0 mm^2 (h × v), the actual size will be determined at a later date. The differential pump is followed by a white-beam slit and a collimator to contain bremsstrahlung radiation within an acceptable cone. The heart of the FOE will be a water-cooled, double-crystal, diamond high-heat-load monochromator, followed by beam-diagnostic devices including a beam position monitor, a fluorescent screen, and a blade. The FOE is terminated by a white-beam stop and shutter, which will allow user access to the downstream portion of the beamline while beam is present in the FOE.

The second shielding enclosure, 27-ID-B, shown in Figure 4-63, will serve as a user-accessible experimental station. It will house a set of high-resolution monochromators, focusing mirrors, and the main instrument—the inelastic spectrometer. This enclosure will be surrounded by an enclosed control room and user work space.

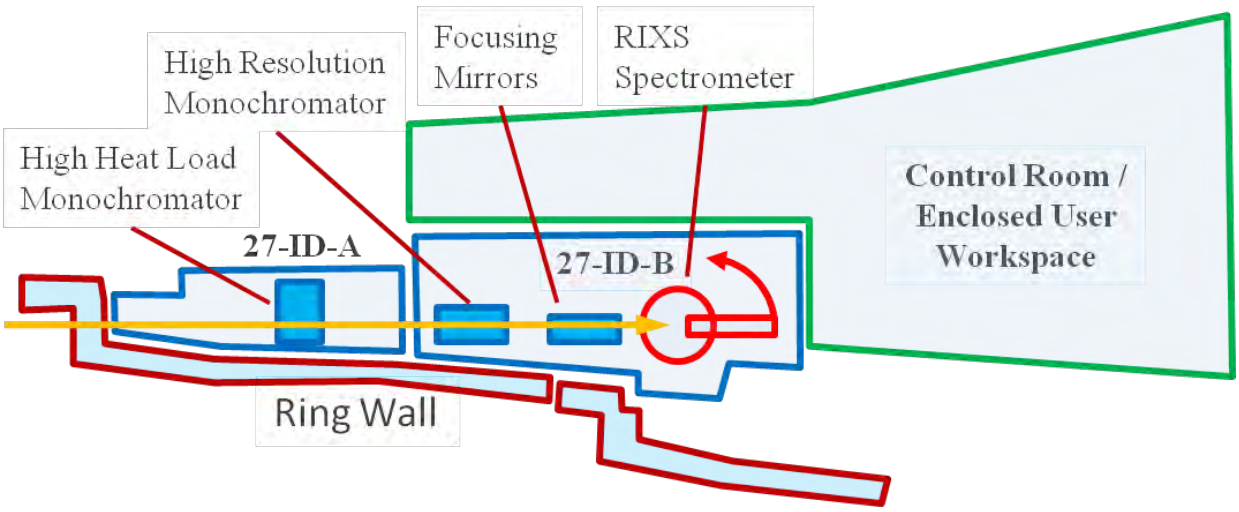

Figure 4-60: Overall schematic view of the RIXS beamline.

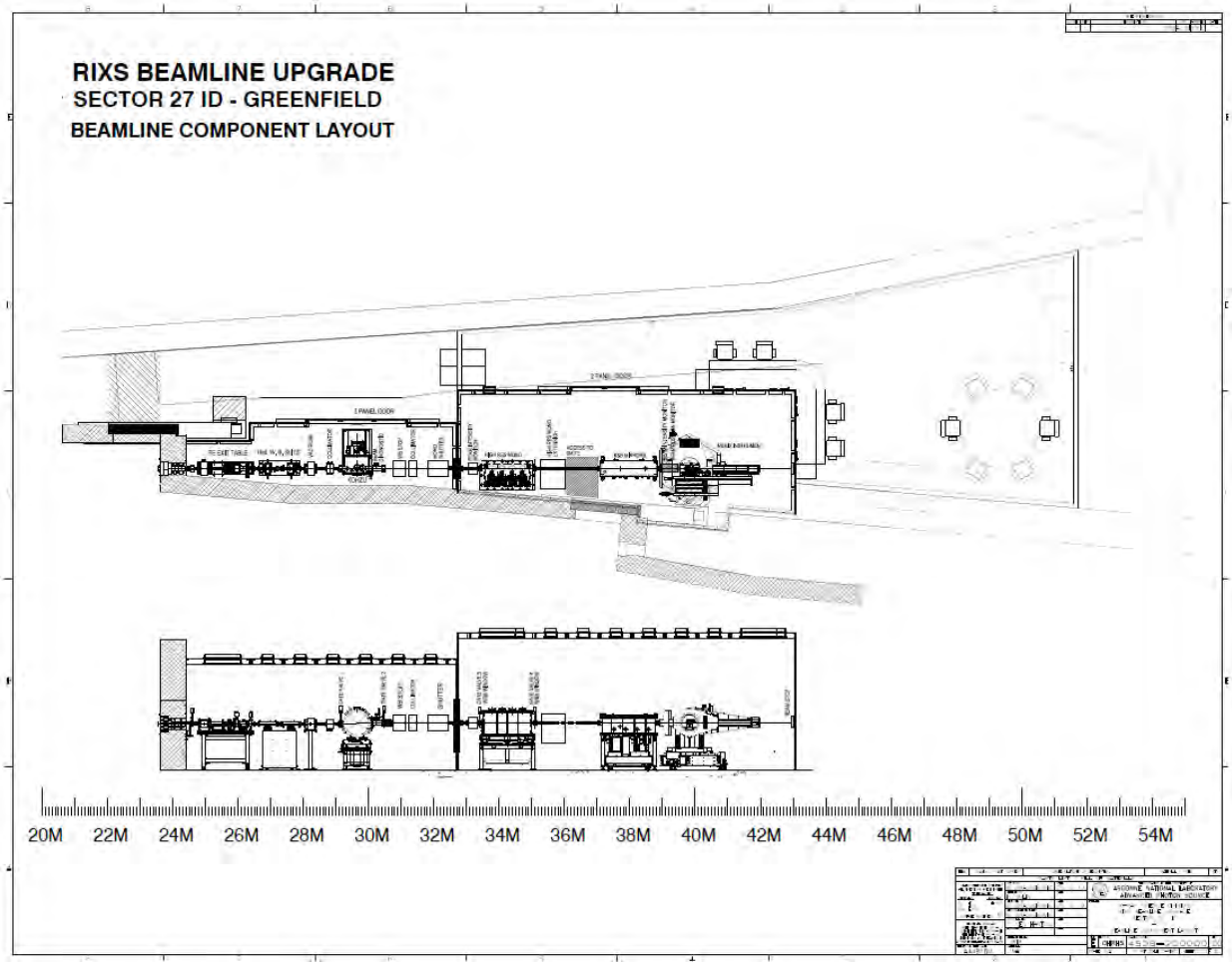

Figure 4-61: Engineering component view of the RIXS beamline.

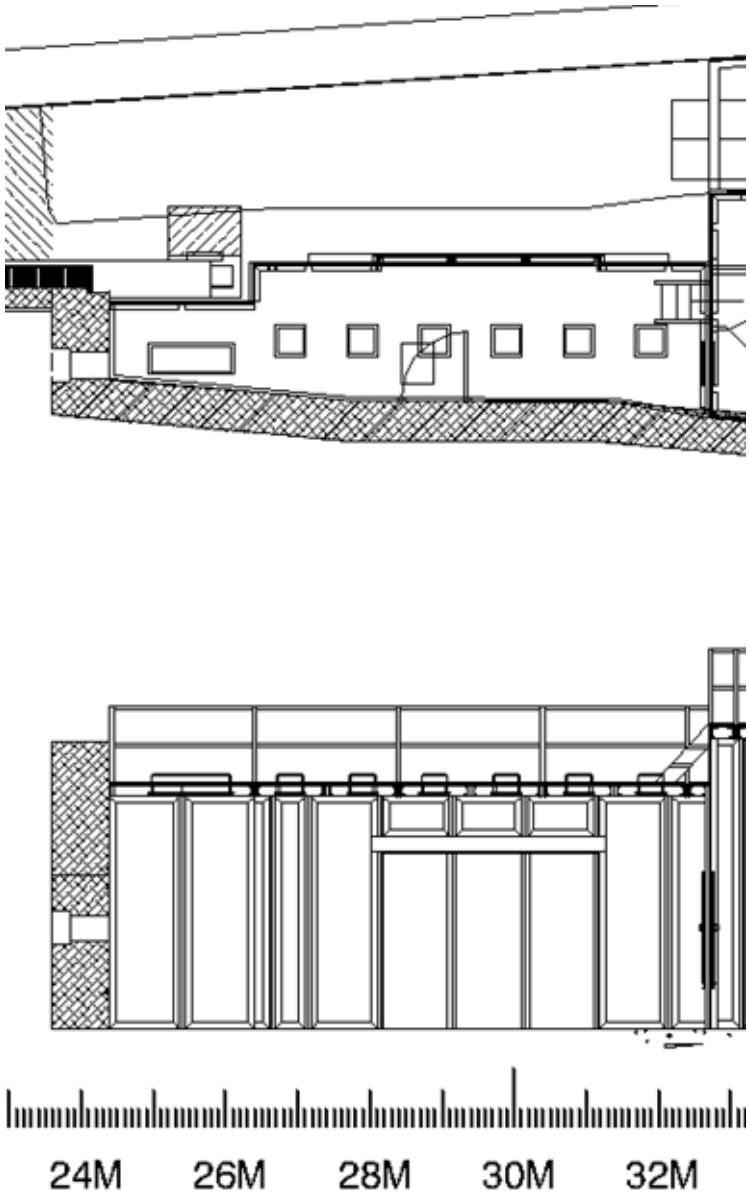

Figure 4-62: Partial engineering view of the FOE 27-ID-A.

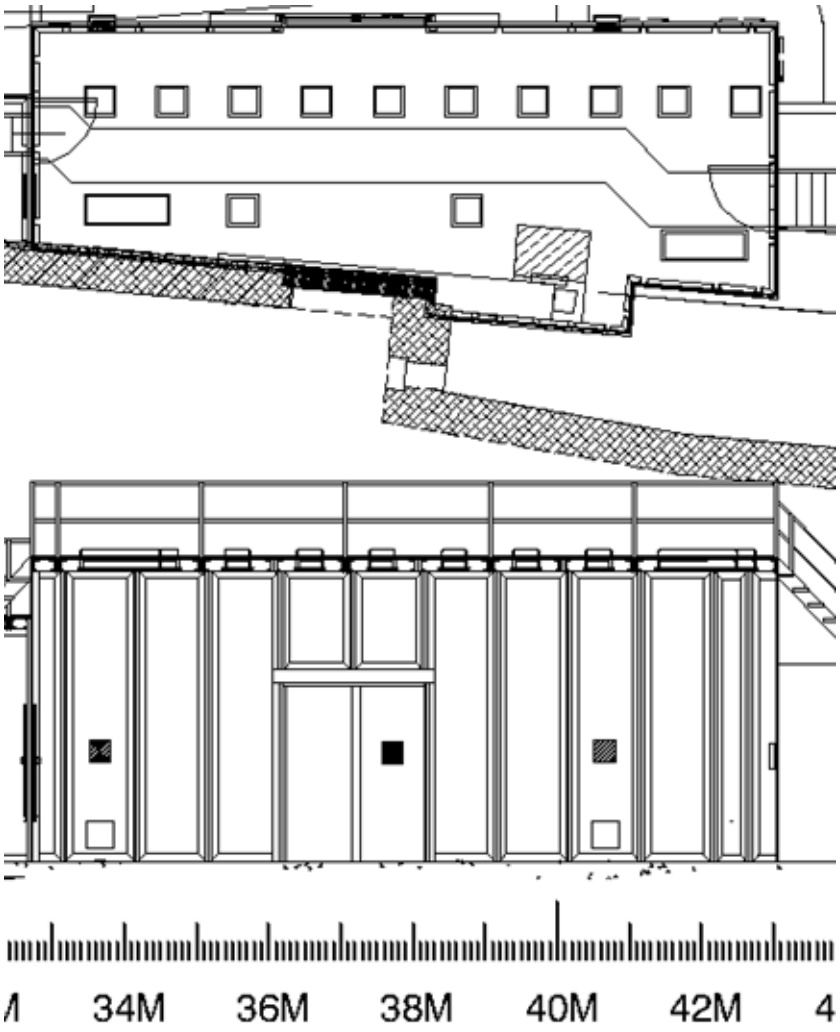

Figure 4-63: Partial view of the experimental station 27-ID-B.

4.7.5.1.1 Ray Traces

Bremsstrahlung- and synchrotron-radiation ray traces in the vertical and horizontal planes for the white-beam section of the RIXS beamline have been generated. A sample is shown in Figure 4-64.

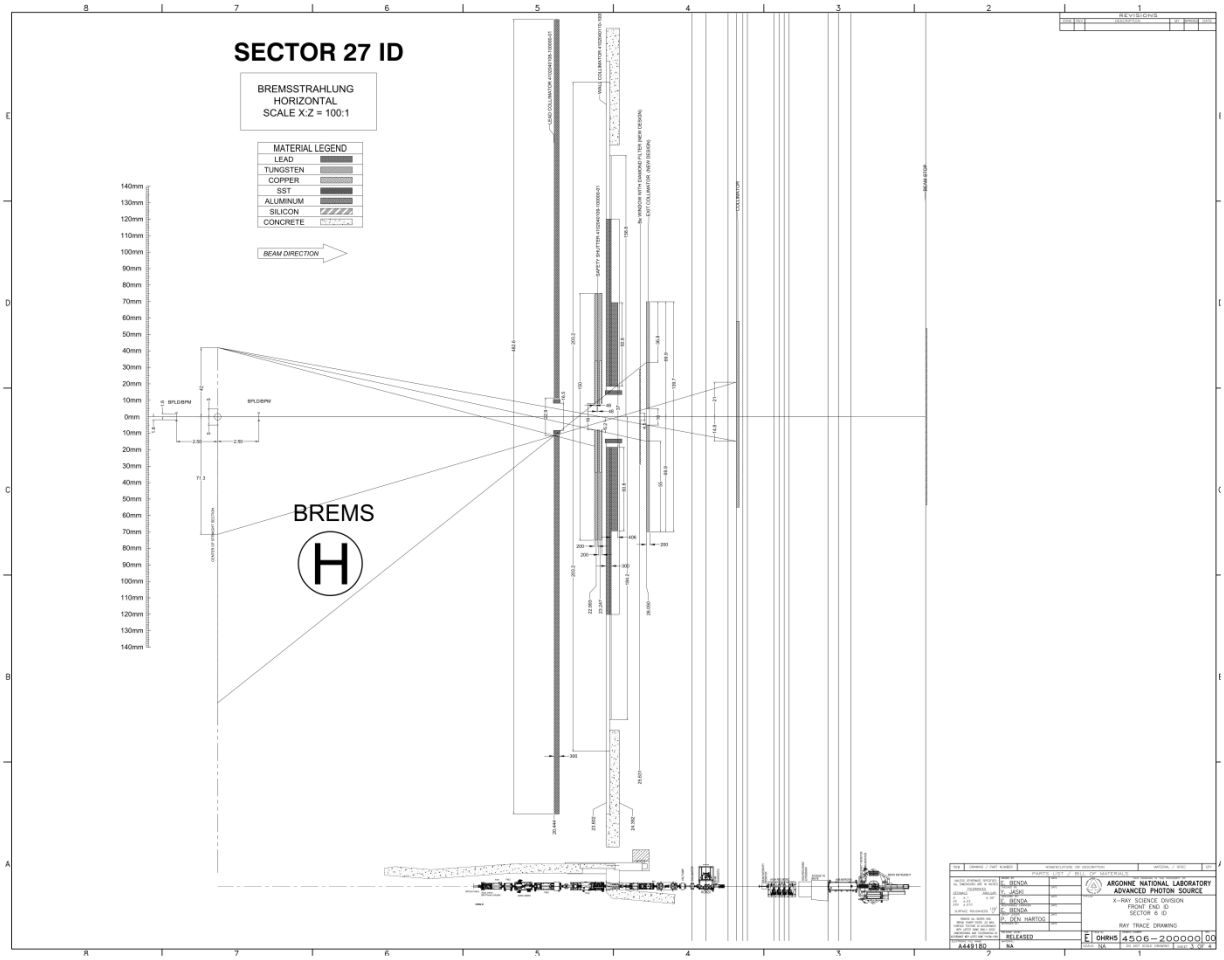

Figure 4-64: Sample of a bremsstrahlung ray-tracing drawing.

4.7.5.1.2 Radiation Safety Aspects

There will be no user operation with white beam. All user operation will be with monochromatic beam only in station B. White beam is confined to station A. There are no shielded beam transports as all stations are attached to each other.

The beamline shielding will conform to all APS standards. A photon shutter will be installed between the A and B stations, which will allow safe access to the B station even while beam is present in the A station.

4.7.5.1.3 Vacuum System

The RIXS beamline will be designed in full compliance with the APS vacuum policy. All beamline components in the FOE and up to the entrance of the high-resolution monochromator will be designed to meet ultrahigh vacuum (UHV) standards. The water cooling on the high-heat-load monochromator will be double walled to be consistent with a windowless beamline.

4.7.5.1.4 Data Acquisition and Motion Control

The data acquisition and control system of choice for the RIXS beamline is based on a combination of SPEC and EPICS. This choice is driven by the vast body of available macros and supporting software utilized in RIXS experiments.

4.7.5.2 First Optics Enclosure and Infrastructure, Major Components

The first optics enclosure (FOE), also called 27-ID-A, is a white-beam-compatible shielding enclosure, housing white-beam conditioning components including the windowless transition from the front end to the beamline, a white-beam slit, the high-heat-load double-crystal monochromator and a shutter/beam-stop assembly. The latter assembly itself consists of a white-beam stop, a bremsstrahlung collimator, and a photon shutter. The white-beam stop terminates the white-beam path near the end of the FOE; no white beam is allowed to penetrate into beamline sections further downstream. In particular, no white beam will be able to enter the experimental enclosure 27-ID-B. The photon shutter allows free user access to the downstream 27-ID-B station while x-rays are present in the FOE for thermal equilibration and stability.

4.7.5.2.1 Windows

The transition between the front end and the beamline is windowless and will be accomplished with a standard APS-designed differential pump. For normal operation a monochromatic Be window will be installed downstream of the FOE shutter and upstream of the high-resolution monochromator.

4.7.5.2.2 White-Beam Slits

The white-beam slit (WBS) is the first user-accessible beamline component following the windowless transition in the FOE. It provides a variable entrance aperture for the white beam prior to entering the high-heat-load monochromator [56]. The assembly envisioned for the RIXS beamline is in use at the APS nanoprobe beamline at 26-ID and is documented in APS Upgrade drawing # N1120301-100000 and its sub-assembly drawings. The WBS consists of two separate Glidcop® masks on motion stages that allow independent vertical and horizontal translations in a 0-5 mm range. Each mask is fitted with two tungsten knife edges mounted at right angle. Together the masks generate a near-square exit aperture of maximum dimension 5×5 mm^2. The center of this aperture can be located anywhere within the projection of the aperture of the fixed entrance mask, which is designed to accept a maximum beam size of 2.2×2.2 mm and withstand 3100 W of absorbed power with a maximum power density of 756 W/mm^2. (These values correspond to the power and power density of a beam generated by two inline Undulators A (U33) at a current of 180 mA, a gap of 10.5 mm, and at a distance of 27 m from the source.) For stability, the entire WBS assembly is mounted on a granite block as a component table.

4.7.5.2.3 Bremsstrahlung Collimators

For radiation protection, bremsstrahlung collimators contain bremsstrahlung radiation in a narrow cone around the beam centerline. According to the applicable ray tracing for the RIXS beamline, one collimator is sufficient to perform this function. It will be located within the photon shutter/white-beam

stop area. The device is a modified version of an APS standard component and consists at its core of a monolithic tungsten block with a single aperture for the monochromatic x-ray beam to pass. Engineering details of the standard component with two apertures are documented in APS Upgrade drawing 4105090405_UHEXT and applicable sub-assembly drawings (standard component for UHEXT is used for RIXS).

4.7.5.2.4 High-Heat-Load Monochromator

With regard to monochromators, the immense power load generated by two inline U30 undulators can, according to present knowledge, only be accommodated by diamond crystals that are water-cooled or, if necessary, cryogenically cooled. A unique double-crystal device of type HLD-8WM, made by KOHZU Precision Co., Ltd., is offered and in use on several existing beamlines. The monochromator is a fixed-beam offset device, with 25 mm chosen to be the vertical distance between the incident white x-ray beam and the emitted monochromatic beam. It features a high-precision main axis goniometer, providing a common rotation for the first and second crystals. Independent offset control and angular adjustments for both crystals are mounted on top of this goniometer.

Kohzu also provides the specialized crystal holders according to an APS design. They consist of a water-cooling manifold with detachable crystal holders.

4.7.5.2.5 Shutters/Stops

One white-beam stop and one monochromatic beam shutter will be utilized as the protection from synchrotron radiation at the 27-ID-B station. A modified standard high-heat-load front-end photon shutter will be used as the white-beam stop. The actuation mechanism of the photon shutter will be removed and the shutter will be permanently secured in the closed position. The elevation of the shutter assembly will be adjusted to provide passage of the monochromatic beam. The white-beam stop will be located immediately after the high-heat-load monochromator. Engineering details of the photon shutter are documented in APS Upgrade drawing 4102040105-100000 and its sub-assembly drawings. A new design of the compact monochromatic beam shutter being developed as the standard beamline component will be used to prevent monochromatic beam from entering the monochromatic enclosure 27-ID-B. The shutter will be located after the monolithic collimator and immediately before the first optical enclosure's exit guillotine.

4.7.5.2.6 Diagnostics

A set of x-ray beam position monitors will be installed in the FOE to help the accelerator control adjust the particle beam for the proper position and take-off angle within the x-ray undulator source. Beam position and angle should be reproducible and stable enough to always intercept the first monochromator crystal within a small (0.2×0.2 mm^2) area of its center and at an angle that maintains energy stability of the monochromator within its intrinsic resolution. At 13 keV of incident energy for a source fixed in position, the angular stability should thus be ~10 μrad or better; for fixed angle the source stability should be in the 20-μm range.

Downstream of the high-heat-load monochromator a further set of diagnostic tools will be implemented. These tools include a beam position monitor; a fluorescent screen; and a scannable blade to aid alignment, optimization, and operational control of the monochromatic beam as it emerges from this device.

4.7.5.3 Experimental Enclosure and Instruments

4.7.5.3.1 High-Resolution Monochromator

The MERIX spectrometer requires medium-resolution monochromatization over the energy range of 5-15 keV. Pre-monochromatization by a water-cooled double-crystal diamond <111> monochromator will produce an energy-dependent bandwidth that ranges from 0.3 eV at 5 keV to 1.2 eV at 15 keV. These bandwidths can be reduced efficiently by high-resolution monochromators. Two styles of high-resolution monochromators will be installed for different applications: constant-bandpass 4-crystal monochromators and a channel-cut monochromator.

Two constant-bandpass 4-crystal medium-resolution monochromators are currently in use at Sector 30 and will be relocated to Sector 27. Specifically, two highly efficient constant-bandwidth monochromators using an in-line (zero beam offset) design that is tunable from 5 keV to 12 keV are installed and commissioned. The existing monochromators have a 70 meV and 120 meV bandpass. The advantage of these monochromators is that they maintain a nearly constant flux at the sample over a wide range of incident energies. The implementation of these monochromators will not be changed from their current configuration.

A channel-cut monochromator will also be installed at Sector 27. Specifically, one (with a beam offset) or two (to produce a zero-beam offset) channel cuts will be installed to reduce the beam bandpass after pre-monochromatization. The implementation of this monochromator requires two rotation stages with a resolution of greater than 5 μrad. The bandpass and energy of channel-cut monochromators depends on the crystal. The crystal used to fabricate a channel cut will be chosen to match the energy resolution of other spectrometer components (such as the energy analyzer). A table of possible channel cuts and their characteristics has been generated [57]. Switching between the two monochromator options will be made by x translations of the rotation stages.

4.7.5.3.2 Focusing Mirrors

Initially the existing bimorph mirrors from beamline 30-ID-B (MERIX) will be used. For a description see [58].

Subsequently, a new mirror system will be procured in order to achieve the design goals, ideally $< 10 \times 20$ um^2 spot size and $\geq 90\%$ throughput over the applicable energy range. At this moment, the commercial system of choice is a dynamically figured K-B pair from IDT.

The mirror specifications are given in Table 4-19. Both are partially coated with Rh. They will be delivered in a vacuum-compatible configuration.

Table 4-19: Mirror specifications.

	Slope error [urad]	Surface finish [A]	Length [mm]
Vertical	<1	<1	320
Horizontal	<2	<3	500

4.7.5.3.3 RIXS Spectrometer

The core of the inelastic spectrometer is a custom-made 6-circle device currently in operation at beamline 30-ID. It will be reused in the upgraded RIXS facility and augmented by an additional high-load horizontal rotation stage to provide vertical and horizontal scattering geometries. Also, a high-precision micro-positioning system for the sample will be added. The instrument is shown schematically in Figure 4-65.

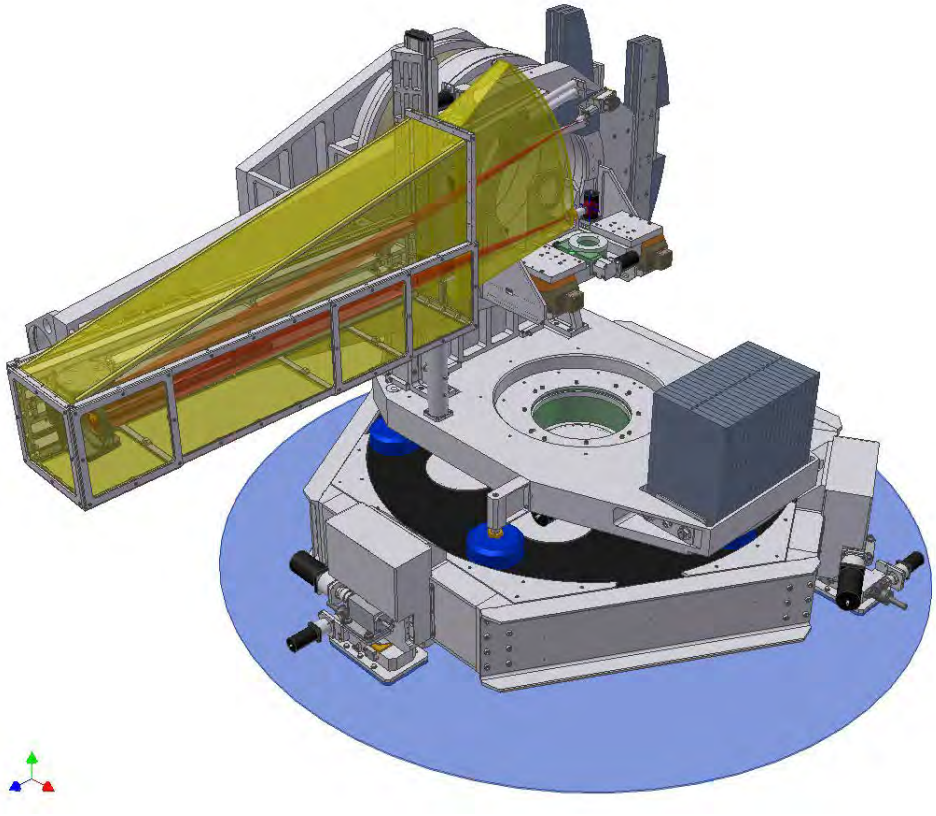

Figure 4-65: RIXS spectrometer.

4.7.5.3.4 Multi-Analyzer System

A system will be built to hold multiple spherical, diced crystal analyzers so that they can be used simultaneously and independently.

In the preliminary design shown in Figure 4-66, a frame holding nine analyzers in a square array is placed in a horizontal scattering configuration, with the center (reference) analyzer at an angle of 90° with respect to the incident beam. The sample is placed in the spectrometer circles with its detector arm in the vertical plane. The area detector and its motion stages are placed above the sample with independent support.

Each analyzer is a compact, modular unit to be placed closely side-by-side in the frame. Each is equipped with independent motorized motions to align the incident angle, the azimuthal angle and the distance from the sample.

The frame and its motion stages are placed on a column resting on the floor, independent of the spectrometer, at the required distance from the sample (2 m typical).

All the motion stages and most of the parts (except the analyzers) are expected to be commercially available. The frame will be interchangeable for experimental flexibility, to accommodate different numbers/configurations/sizes of analyzers.

The area detector could be a Pilatus-100k type initially, but to meet the energy resolution design goal, a more advanced detector with a pixel size ≤ 50 μm will be procured when it becomes commercially available.

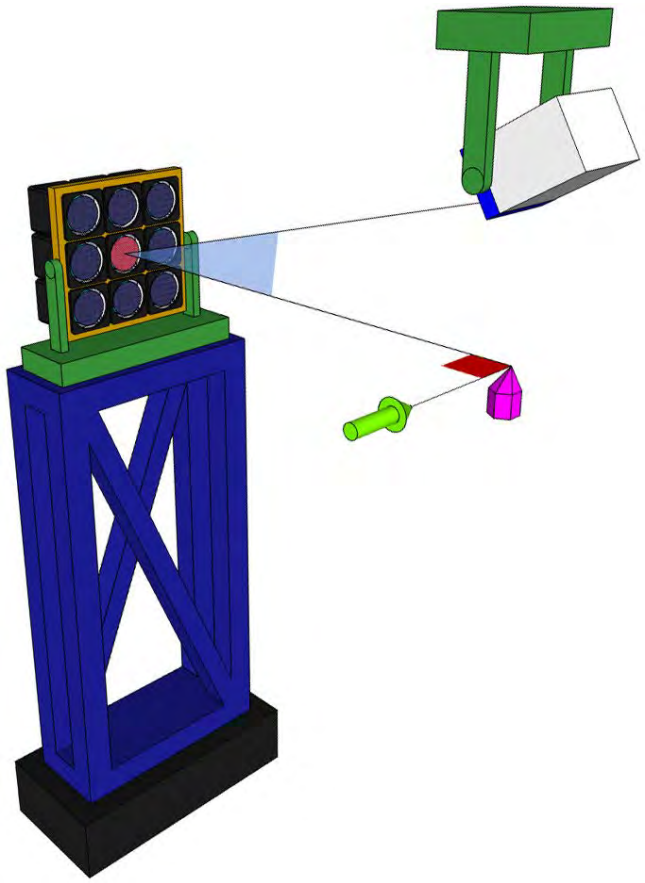

Figure 4-66: Schematic of the multi-analyzer system.

4.7.6 Alternate High-Resolution Analyzer

The alternate high-resolution analyzer assembly is shown in Figure 4-59. Here the focus is on implementing a three-bounce CDS analyzer system specifically for the Ir L3 edge at 11.215 keV. The upstream configurations of the existing beamline, including the monochromator, the K-B focusing mirrors, and the sample stage, are the same as with the spherical analyzer system. A collimating mirror is placed on the chi stage of the existing sample stage to collect scattered x-rays with 10-mrad angular acceptance. The two-dimensional multilayer mirror, i.e., Montel mirror, is the best candidate for this purpose because of it compactness and its ease of optimization. Several groups at the APS, NSLS II, and the Diamond Light Source in the UK are currently testing Montel mirrors with very promising results. Dynamical theory calculations have been carried out for the 7-meV energy resolution at 11.215 keV with 57% peak efficiency. The mechanism of the CDS analyzer involves three steps: i) The polychromatic and divergent incident beam is collected by an asymmetrically cut Si <220> "C" crystal. The incident angle is 1° and the Bragg angle is $\theta_B = 16.73°$. ii) The collimated beam is then diffracted by the dispersing Si <844> "D" crystal to form a dispersion fan. The incident angle is 15° with $\theta_B = 85.73°$. iii) Finally the selection Si <440> "S" crystal diffracts a portion of the dispersion fan from the "D" crystal to produce a narrow bandwidth. The incident angle is 67° with $\theta_B = 35.15°$. The distance between "D" and "S" is more than 0.6 m. The CDS analyzer system will be made to coexist with the spherical analyzer system. An additional stage for the "C" crystal will be installed inside the flight tank. Note that the bandwidth of the "C" crystal is about 3.8 eV and can be fixed during operation once aligned. The "D" crystal will be installed on the current analyzer holder. The "S" crystal and the detector will be installed on the current detector holder.

4.8 Magnetic Spectroscopy Hard X-rays

Beamline 4-ID-D is dedicated to variable-polarization hard x-ray spectroscopic studies of electronic and magnetic materials. Currently, this beamline shares the 4-ID sector with the soft x-ray magnetic spectroscopy program (4-ID-C), and initial plans were developed to upgrade both these beamlines in the sector. However, the Accelerator Systems Division (ASD) expressed concerns about the effects that collocating two helical insertion devices in the same sector would have on the stability of the storage ring. For this reason, current plans call for relocating the soft x-ray magnetic spectroscopy program to another sector and upgrading 4-ID-D in its current location. The primary components involved in this upgrade include:

1. installation of an APPLE-II, arbitrary polarization insertion device in the 4-ID straight to generate horizontal and vertical linear, left and right circular, and elliptical polarization states directly at the source in order to circumvent limitations of phase-retarding optics;
2. installation of ~300-mm-long Kirkpatrick-Baez (K-B) mirrors for high-pressure studies;
3. addition of fine roll adjustment to the second-crystal monochromator for dynamic control of horizontal beam position;
4. new instrumentation for high field (10 T) and high pressure (> 1 Mbar) x-ray magnetic circular dichroism (XMCD) experiments;

5. expansion of the experimental station to accommodate new instrumentation; and
6. addition of a control area enclosure.

4.8.1 Scientific Objectives

The discovery of novel electronic and magnetic materials together with a fundamental understanding of their properties is key towards enabling future technological advances. The past two decades have seen intense activity in the application of synchrotron radiation techniques to study conventional magnets composed of transition metal (TM) (3*d*) and/or rare earth (RE) (4*f*) elements. The circularly polarized x-ray source at beamline 4-ID-D, which couples a linear undulator with phase-retarding crystal optics, is well-suited for studying the properties of such conventional magnets since TM K-edges and RE $L_{2,3}$ absorption edges lie in the 5- to 10-keV energy range where these optics are most efficient. The beamline has provided atomic-level insight into the electronic interactions in a variety of complex functional magnetic systems, such as permanent magnetic [59] and giant magnetocaloric materials [60]. However, the reduced efficiency of phase retarding optics outside of this energy range has hindered the application of polarization modulated spectroscopic techniques at APS to other novel and technologically relevant magnetic materials composed of 4*d* and 5*d*, as well as 5*f*, elements, whose resonances lie outside of the 5- to 10-keV energy range. Examples of fundamental questions, which will be addressed by upgrading the 4-ID-D beamline, include:

- Does Ruthenium ferromagnetism coexist with superconductivity in layered rutheno-cuprate structures? [61, 62], (Figure 4-67).
- What is the origin of novel magnetism found in thiol-capped gold nanoparticles? [63, 64], (Figure 4-68)
- Why does adding a Pd capping layer influence the perpendicular magnetic anisotropy of FePd films? [65, 66, 67]
- Why doesn't delta-Plutonium carry a sizable net moment? [68, 69, 70]

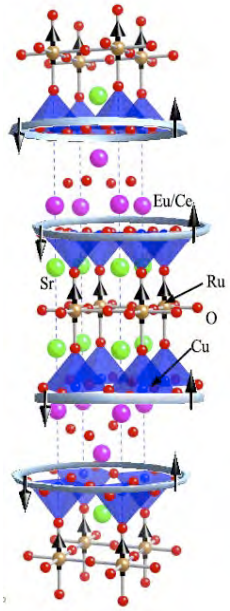

Figure 4-67: Ruthenocuprate structure with possible coexistence of Ru magnetism and superconductivity.

The element- and orbital-specificity inherent to the x-ray absorption process, coupled with the high brightness and penetrating power of hard x-rays, probe changes in valence state, orbital occupancies, hybridization, charge transfer, and electronic ordering under extreme pressures. Furthermore, when coupling high-pressure with magnetic fields, x-ray magnetic dichroism techniques can be used to yield element-specific information on spin-polarization, orbital and spin magnetization, magneto-crystalline anisotropy, and magnetic ordering at high pressures. Beamline 4-ID-D is currently the only facility in the United States for performing magnetic dichroism experiments using hard x-rays. Over the past five years, this beamline has developed cutting-edge capabilities for XAS/XMCD measurements with simultaneous control of pressure (< 0.25 Mbar), magnetic field (0.5 Tesla), and temperature (>8 K). The upgrade will significantly expand the parameter space available for these measurements (>1 Mbar, 10 T, ~2 K), thereby providing a transformational tool for the study of the electronic behavior of solids at extreme conditions.

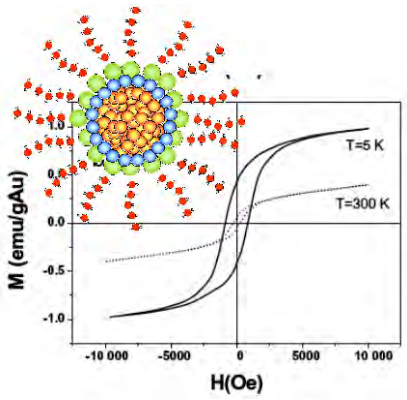

Figure 4-68: Thiol-capped Au nanoparticles displaying surface magnetism.

Manipulating electronic states in condensed matter by driving atoms closer together at extreme pressure conditions provides a route to novel electronic materials with entirely different properties, sometimes even after returning to ambient conditions [71]. Advances in high-pressure methods now allow changing inter-atomic distances in solids by up to a factor of two, with related density increases of about an order of magnitude. The resulting changes in chemical bonding give rise to new physical properties, including metallic behavior of materials with significant band gaps and the triggering of cooperative electronic phenomena such as ordering of electrons into novel magnetic, ferroelectric, and superconducting states. For example, the highest superconducting transition temperature on record, T_c=164 K, is found in mercury-copper-oxide high-temperature superconductors at 30 GPa [72]. Similarly, the ferromagnetic ordering temperature of semiconducting EuO, a promising material for spintronics, is 200 K at 15 GPa, a remarkable 130 K increase from ambient conditions [73]. Hence, the extreme pressure environment provides a knob for tuning a material's properties that is a unique tool for probing novel states of matter.

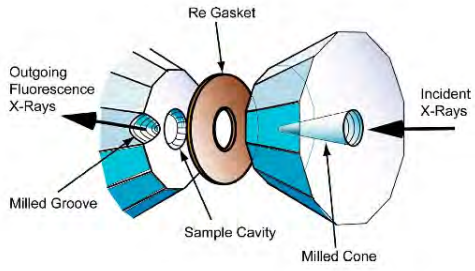

Figure 4-69: Perforated anvils reduce x-ray attenuation.

High-brightness, high-energy synchrotron radiation is ideally suited for high-pressure experimentation. The ability to penetrate diamond anvil cells, and to focus x-ray beams to micron dimensions while preserving their intensity, has provided unprecedented opportunity for high-pressure studies into the Megabar (>100 GPa) range and beyond. Although electronic and crystal structures are intimately connected, pressure-induced changes in electronic structure do not necessarily require changes in crystallographic symmetry. Hence, monitoring crystal structure and compressibility with pressure is insufficient to uncover underlying changes in electronic structure that go undetected in x-ray diffraction measurements. X-ray absorption spectroscopy (XAS) using hard x-rays is an ideal tool for *in situ* characterization of electronic structure under extreme pressure conditions. Unlike x-ray diffraction, however, XAS has been only sporadically used in high-pressure research during the last two decades [74], [75, 76]. Third-generation synchrotron sources, though, coupled with the development of novel technologies to produce perforated diamond anvils (see Figure 4-69) have provided the necessary penetration power at relevant (resonant) energies for XAS studies under high pressure. A number of recent studies have demonstrated the powerful insights that the combination of pressure, magnetic field, and low temperature can provide into the nature of magnetocalorics [77], tunable magnetic states in colossal magneto-resistive manganites (see Figure 4-70) [78] , and spintronic materials [73].

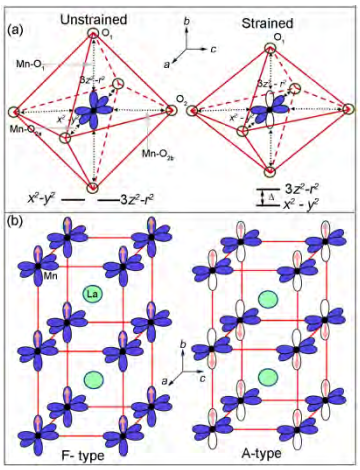

Figure 4-70: Redistribution of Mn 3d states in LaCaMnO under pressure results in the emergence of empty out-of-plane states suppressing ferromagnetic ordering and conductivity.

Although increased brightness of new neutron sources will enable extension of magnetism research to higher pressures, synchrotron-based studies of magnetism are expected to remain unchallenged for pressures above 20 GPa at least over the next decade. Similarly, superconducting quantum interference device (SQUID) magnetometry is limited to about 10 GPa, and AC susceptibility measurements are extremely challenging for detection of electronic ordering other than superconductivity. Therefore, the upgraded instrumentation at 4-ID-D is expected to be a unique resource both in the U.S. and worldwide for measurements of electronic structure and magnetism at extreme pressure conditions. Furthermore, this program nicely complements other APS Upgrade plans aimed at measuring structural and dynamic response of matter under extreme conditions.

4.8.2 Source

4.8.2.1 Spectral Requirements

The experiments described above require a fully tunable (2.7- to 25-keV) x-ray source with variable polarization, such as an APPLE-II-type insertion device. Such a device, shown in Figure 4-71, can generate circularly polarized (CP) x-rays directly at the source, circumventing the limitations of phase-retarding optics below about 5 keV (attenuation) and above 10 keV (small Bragg angles and reduced polarization). This device will enable XMCD/XMLD studies at the $L_{2,3}$ absorption edges of 4*d* elements and $M_{2,3,4,5}$ absorption edges of 5*d* and 5*f* elements in the 2.7- to 5.0-keV range, as well as the $L_{2,3}$ edges of 5*f* and 5*d* elements and the K edges of 4*d* elements in the 10- to 25-keV range, which are currently unavailable or performed inefficiently at 4-ID-D.

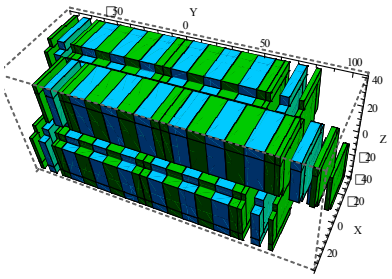

Figure 4-71: APPLE-II device in elliptical mode.

Figure 4-72 shows the expected performance for a 3.8-cm-period, 2.4-m-long APPLE-II-type device in the APS storage ring. In circular mode, the device generates CP x-rays with P_c ~1 in its first harmonic from 2.7 to 11 keV, which encompasses the $L_{2,3}$ edges of rare earths and the K-edges of first-row 3*d* transition metals. The increased flux and reduced asymmetry between incident left- and right-CP x-ray intensity relative to phase-retarder optics will result in significant improvements to data quality and reduced data acquisition time. Elliptically polarized x-rays (P_c ~0.8) can be obtained in the 10- to 25-keV range by using third and fifth harmonics. The improvements in polarized flux for various energy ranges provided by the APPLE-II device and flux density when coupled with K-B mirrors is summarized in Table 4-20. An APPLE-II-type undulator has the added benefit of not producing on-axis harmonics in circular mode, which is advantageous for high-pressure experiments where the attenuation of diamond anvils makes the measurements very sensitive to harmonic contamination. Furthermore, the reduced on-axis power in circular mode will aid in implementing a second set of monochromator crystals to mitigate beam depolarization effects incurred in the 2.7- to 2.9-keV range when using Si <111> crystals.

Table 4-20: Polarized flux density gain realized by APPLE-II coupled with new K-B focusing mirrors compared vs. phase-retarding optics and current toroidal mirror.

Energy range (keV)	**Polarized flux gain (factor) from APPLE-II**	**Polarized flux gain (factor)by focusing (P>0.3 Mbar)**	**Total flux density gain (factor)**
2.7-5	5-50	240	1200-12,000
6-10	2-10	240	480-2400
11-16	3-5	240	720-1200
17-25	Expanded energy range previously unavailable.		

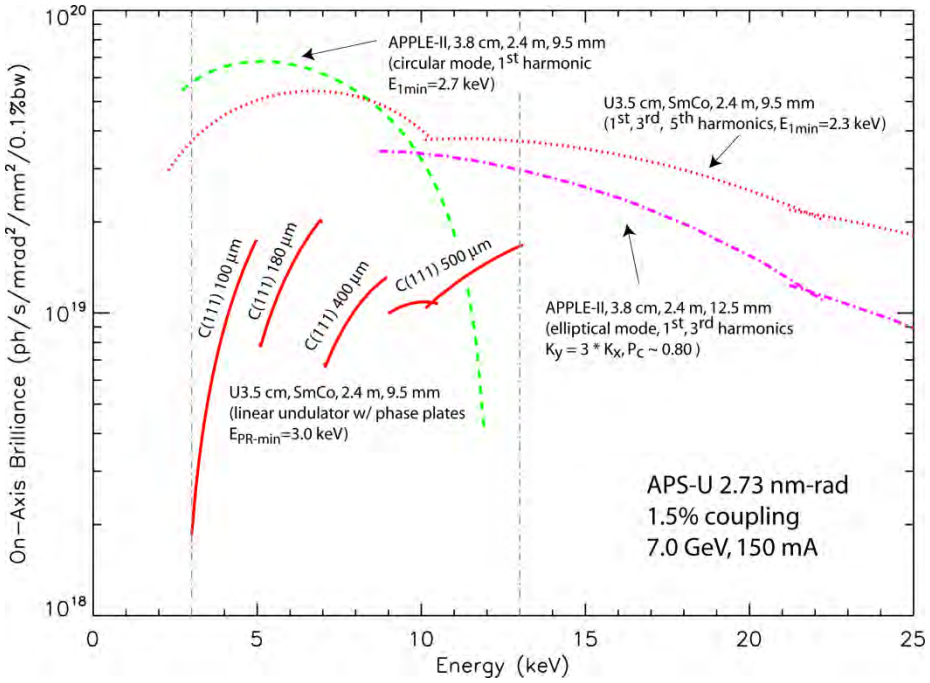

Figure 4-72: Tuning curves for APPLE-II undulator, compared with linear undulator with and without phase plates. Thickness of diamond phase plates currently used for energies between 3-13 keV is also indicated. The APPLE device covers 2.7-11 keV in circular mode and 10-25 keV in elliptical mode (Pc>82%).

4.8.3 X-ray Optical Layout

The primary optical components for this beamline are illustrated in Figure 4-73 and listed in Table 4-21. The monochromator and primary mirrors are located in the 4-ID-B station with only the K-B focusing optics located in the 4-ID-D experimental station.

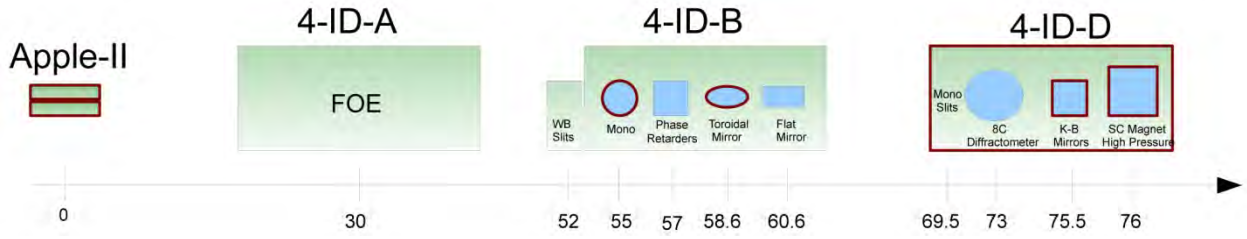

Figure 4-73: Optics and instrumentation for the 4-ID-D beamline. Components outlined in red are included in the Project scope.

Table 4-21: Beamline components for the 4-ID-D beamline.

Component	Approximate Distance to Center of Straight (m)	Notes
White-beam slits (existing)	52	Maximum beam size 3 mm (V) × 4 mm (H).
Double-crystal monochromator (minor modification)	54	Energy range 2.7 to 30 keV, cryogenically cooled Si <111>, variable offset 10-35 mm. Will be upgraded with a new stage for roll control on second crystal with PZT.
Phase retarder assembly (existing)	56	Polarization manipulation using diamond phase-retarding crystals.
Toroidal focusing mirror (new)	58	0.9 m long; vertically deflecting (upwards); adjustable meridional curvature (∞ to ~ 4.5 km); two fixed sagittal curvatures ~ 100 mm and ~ 60 mm for horizontal focus at different incidence angles (3-5 mrad); Pd coating.
Harmonic rejection mirror (existing)	60	Vertically deflecting (downwards); flat; Pd and Si coatings; 3-5 mrad incidence angles.
Monochromatic slits (existing)	68	Four independent blades with ±10 mm horizontal travel and ±75 mm vertical travel.
Psi-diffractometer (existing)	70	Existing diffractometer used for variable polarization reflectivity, diffraction, and grazing incidence absorption studies on magnetic thin films.
K-B mirror	72	300-mm-long K-B pair; Si and Pd coatings, mounted on optical table with full rotational and translational degrees of freedom.
XMCD magnet	74	10-Tesla cryogen-free superconducting magnet.

4.8.3.1 Mirrors

The current toroidal mirror on the beamline will be replaced with a new mirror with two sagittal radii to enable horizontal focusing of the beam at two different incidence angles (nominally 3 and 5 mrad). This will provide enhanced harmonic suppression without sacrificing focal spot size. In addition, this mirror will be used to generate a virtual source for the K-B mirror downstream when needed. Slope errors in the current toroidal mirror (~ 3 μrad) dictate the vertical spot size in the experimental station. This will be substantially reduced (~ x3) due to improved slope error figures expected in a new mirror (< 1 μrad) (see Figure 4-74).

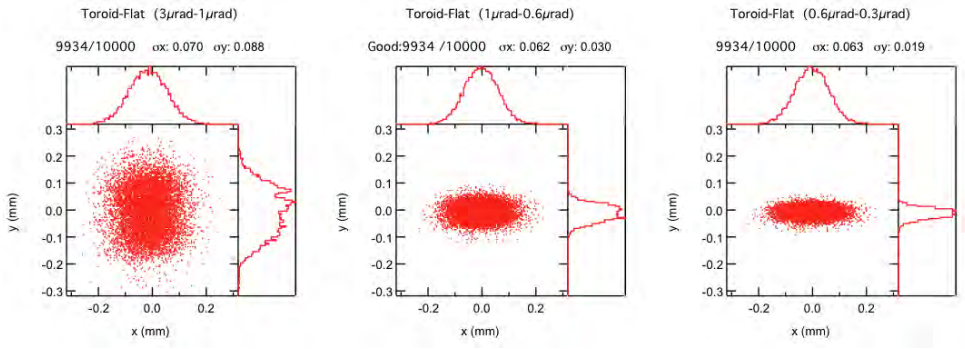

Figure 4-74: Effect of slope error reduction from 3 μrad (current mirror) to ~ 0.5 μrad (upgrade) upon focal spot size from toroidal mirror.

A K-B mirror system will be permanently installed in the 4-ID-D experimental station for focusing to < 10 × 10 μm^2 at the magnet sample position (~0.65 m working distance). This focal spot enables high-pressure absorption and emission experiments at 1 Mbar since typical sample size and gasket thickness used in transmission/emission experiments at this pressure is ~ 20-30 microns. The mirrors will be ~300 mm long and accept ~ half of the full undulator beam without a virtual source and the full undulator beam with a virtual source at ~ 68 m generated by the toroidal mirror (see Figure 4-75). The K-B mirrors will have both Pd and Si coatings for optimal harmonic rejection.

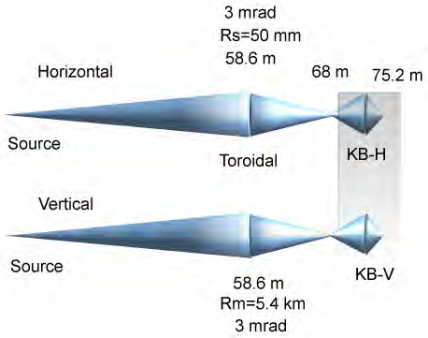

Figure 4-75: Schematic of tandem focusing using toroidal and K-B mirrors. The total demagnification is ~30 in both directions. Shaded region shows the boundaries of the expanded 4-ID-D station.

4.8.3.2 Monochromator

The current beamline Kohzu Si <111> monochromator will continue to be used for experiments. However, the second crystal stage will be modified to provide fast fine angular control of the roll angle via a piezoelectric transducer (PZT) (only coarse-angle control with a motor is currently available). The monochromator currently has coarse and fine control of the pitch angle, enabling high stability of x-ray beam vertical position (~ 1 micron) with a fast feedback loop. High-pressure experiments, however, require extreme beam stability in the horizontal direction as well; therefore, the second stage will be modified to include PZT control of roll angle with ~ ±15 arcsec angular displacement in order to implement fast feedback loops in both vertical and horizontal directions (Figure 4-76).

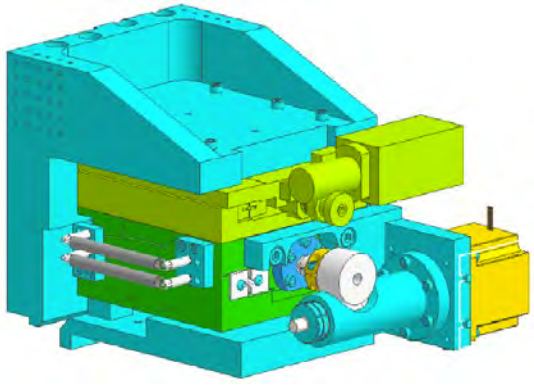

Figure 4-76: Second crystal support stage showing existing X translation and new modified fine θ_z (roll) adjustment stage.

4.8.4 Beamline Physical Layout

The physical layout of the hard x-ray magnetic spectroscopy beamline is shown in Figure 4-77. Most of the optical components for the hard x-ray beamline are located in the 4-ID-B station. The experimental station 4-ID-D will be expanded as part of the upgrade. The FOE (4-ID-A) currently contains mirrors for the soft x-ray magnetic spectroscopy beamline. Current upgrade plans envision moving this beamline to another sector and installing beam transport and collimators in this station.

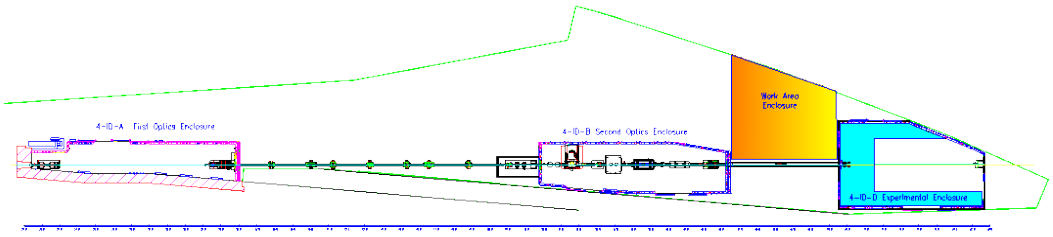

Figure 4-77: Possible layout of hard x-ray magnetic spectroscopy beamline showing the expansion of the 4-ID-D experimental station (blue) and proposed location for work area enclosure (yellow).

4.8.4.1 Front End

The current standard front end will be used for the baseline scope of the hard x-ray magnetic spectroscopy beamline upgrade. However, if a second APPLE-II undulator is added to enable fast polarization switching (this is a contingent additional scope option), a high-heat-load front end will likely need to be included, but is not part of the base scope.

4.8.4.2 Overall Beamline

The location of the existing optical enclosures (4-ID-A and 4-ID-B) along with the proposed expansion of the 4-ID-D experimental station is shown in Figure 4-77. Most of the optical components will be located in the 4-ID-B station. The location and size of the work area enclosure is approximate.

4.8.4.3 General Description

4.8.4.3.1 Radiation Safety Aspects

The existing first and second optics enclosures will be compatible with white-beam operation. The final experimental station (4-ID-D) will be commissioned for monochromatic beam only. The existing personnel safety system will be reused on the beamline.

4.8.4.3.2 Vacuum System

To minimize absorption at low energies (2.7 to ~ 4 keV), the magnetic spectroscopy beamline will be windowless through the monochromator. This requires the use of a differentially pumped transition from the front end to the first optics enclosure (FOE). Therefore, all components are designed to minimize outgassing of heavier components detrimental to the operation of the ring. This generally requires UHV-compatible components, although this condition may be relaxed if the component is sufficiently isolated from the front end and mirrors. UHV conditions are also required for the main beamline mirrors to maintain their cleanliness. The beamline design will comply with the APS beamline vacuum policy for windowless operation. Two beryllium windows will be installed downstream of the monochromator.

4.8.4.3.3 Data Acquisition and Motion Control

The current beamline control system and software, with upgrades to support new components and to replace obsolete systems, will be used. The existing system uses SPEC [79] for data acquisition with a standard APS EPICS system providing the underlying beamline control.

4.8.4.4 First Optics Enclosure and Infrastructure

The 4-ID FOE currently houses mirrors for the soft x-ray beamline in this sector. These optics will be removed and replaced with vacuum transport, leaving in place the current shutter and collimators. The scope of this task does not include moving optical components from the secondary optics enclosure (4-ID-B), but this could be revisited during the final design.

4.8.4.4.1 Windows

This beamline requires windowless operation up to the monochromator. Only two beryllium windows with a thickness of ~ 160 μm each will be used across the entire optical path in order to minimize absorption at low energies (2.7 to ~ 4.0 keV).

4.8.4.4.2 Slits

The beamline requires a water-cooled fixed aperture to minimize the heat load on the downstream components. The existing white and monochromatic beam slits will continue to be used to define the beam.

4.8.4.4.3 Collimators

Sufficient collimation is required to provide for the necessary bremsstrahlung and synchrotron radiation protection during beamline operation. The exact location of the collimators and masks will be determined when more detailed ray tracings are available after the optical layout is more developed.

4.8.4.4.4 Shutters/Stops

A white-beam shutter is required at the end of the FOE to prevent the beam from illuminating the optics further downstream. The current white-beam shutter in 4-ID-B will be converted to only accept monochromatic radiation into the D station.

4.8.4.4.5 Monochromator

The current cryogenically cooled double-crystal monochromator will remain in use with the modification of the second crystals θ_z (roll) stage for PZT (dynamic) fine control of the roll angle. This monochromator is equipped with Si <111> crystals that provide energy tenability over the entire energy range of interest. However, this crystal degrades the beam polarization at low energies (~ 2.8 keV), thus the possibility of adding alternate crystals with a larger d-spacing for this energy range is being explored.

4.8.4.4.6 Mirrors

A new toroidal mirror will be installed in the 4-ID-B station to provide better focusing and harmonic rejection than the current mirror. This mirror will improve the focal spot size obtained in the experimental station by ~ 3x, due to more optimized curvature and reduced slope errors. The toriodal mirror will be ~ 0.9 m long, with a Pd coating. The meridional curvature will be adjustable from $R_m \approx 4.5$ km to ∞. Two cylinders separated by ~ 25 mm with sagittal curvatures of $R_{s1} \approx 100$ mm and $R_{s2} \approx 50$ mm will provide horizontal focusing at different angles of incidence. The mirror will provide direct focusing at the diffractometer and also create a virtual source (at ~ 68 m) for the K-B mirrors. The incidence angle is in the 3-5 mrad range, allowing sufficient harmonic rejection below 10 keV in combination with a flat Si mirror currently at the beamline. The toroidal mirror will have slope errors of ~ 0.5 μrad, a significant improvement over the ~ 3 μrad of the current mirror. Elliptical K-B mirrors, ~ 300 mm long, with both Pd and bare Si stripes on each mirror, 2-5 mrad incidence angle, and slope errors of ~ 0.5 μrad, will be procured and installed in the 4-ID-D station for high-pressure experiments in the high-field magnet.

4.8.4.5 Experimental Station

The 4-ID-D experimental station will be dedicated to polarization-modulated spectroscopy experiments. The station will house both a diffractometer for scattering measurements (at ~ 71.6 m) and a high-field magnet for magnetic dichroism measurements in transmission and fluorescence geometries (at ~ 75 m). An expansion of this station is necessary to accommodate both these instruments (see Figure 4-77 and Figure 4-78).

4-ID-D experimental enclosure expansion: Permanent installation of the diffractometer, K-B mirrors, and high-field magnet in the 4-ID-D experimental station necessitates the expansion of the station. The preliminary design includes elongating the station ~ 2 m further upstream for additional space along the x-ray beam direction (K-B mirrors) and 1 m in each of the lateral directions (for magnet operation). Furthermore, an additional access door on the outboard wall provides more flexibility for moving ancillary equipment into the station and enables easy access to the proposed work area enclosure.

Work area enclosure: A work enclosure sufficient to house the control electronics, workstations, sample prep area, and ancillary beamline equipment required for operation is planned. A possible location and approximate size is illustrated in Figure 4-77.

4.8.4.5.1 Components

A schematic indicating the location of the instruments in the expanded 4-ID-D station is shown in Figure 4-78. The existing psi-diffractometer capable of accommodating a 2-Tesla magnet for scattering experiments will be placed at the front of the station. The K-B focusing mirrors and high-field magnet for absorption and emission studies of magnetic systems under pressure will be located in the rear portion of the station.

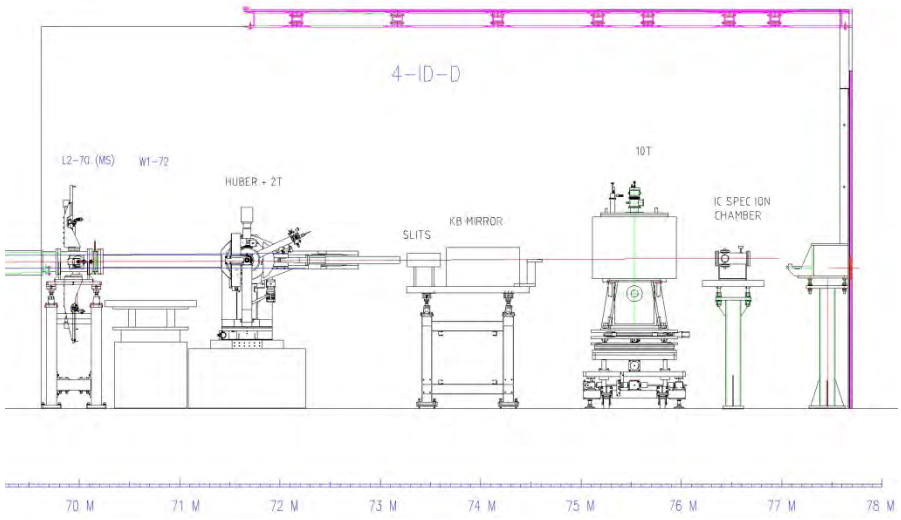

Figure 4-78: Layout of the instruments in the (expanded) 4-ID-D experimental station.

4.8.4.5.2 Instruments

Diffractometer: The existing psi-geometry diffractometer will continue to be used for variable polarization reflectivity, diffraction, and grazing-incidence absorption studies on magnetic thin films. An existing 2-Tesla magnet mounts on this diffractometer and will be used for these measurements.

High field magnet: A ~ 10-Tesla superconducting magnet will be procured as part of the upgrade for high-field XMCD measurements at both ambient and high-pressure conditions. This magnet will be cryogen free or will employ a recondenser to minimize liquid helium usage. Pulsed tube cooling

technology is being considered in the design of this magnet in order to reduce vibrations to the ~1-micron level to provide stability in high-pressure experiments.

4.9 High-Energy X-Ray Diffraction Beamlines

The high-energy x-ray diffraction (HEXD) beamlines effort is defined in U1.04.02.10 in the APS Upgrade Project's Work Breakdown Structure (WBS). Under its objective, in addition to upgrading its tunable-energy, in-line branch, beamline 1-ID will acquire dual canted undulator sources, and a fixed-energy side-branch beamline will be constructed.

The physical properties of the interaction between high-energy x-rays (>40 keV) and matter include low attenuation, small scattering angles, accessibility of large momentum transfers, and improved validity of the so-called Born approximation (i.e., single or kinematical scattering) that is almost always assumed in extracting structure from scattering data. These features, when combined with the brightness of a source like the 7-GeV APS at high x-ray energies, often make such x-rays the scattering probe of choice for interrogation of bulk material structure. Possessing a unique combination of high penetration power with high-spatial, reciprocal-space, and temporal resolution, these x-rays can be exploited to non-destructively measure phase, texture, and strain distributions under extreme environments.

Over the past several years, the 1-ID beamline has developed a number of programs for these purposes, including: (i) high-energy diffraction microscopy (HEDM), in which grain and sub-grain volumes are shape- or strain-mapped in polycrystalline aggregates, (ii) combined small- and wide-angle x-ray scattering (SAXS/WAXS), which permits collection of information over a broad range of length from the same (micron-level) volume, (iii) high-energy resonant scattering, and (iv) fluorescence. These and other techniques will be enhanced by source, optics, detector, and dedicated-instrument upgrades.

Along with a higher storage ring current, a short-period superconducting undulator (SCU) will provide an order of magnitude more flux at 1-ID than available today at high x-ray energies. The equivalent brightness increase will be exploited by short-focal-length optics setups in all stations to deliver micro-focused beams to experiments. Four experimental stations will permit optimized instruments dedicated to SAXS/WAXS, HEDM, tomography, resonant scattering, fluorescence, and investigations of surfaces and buried interfaces. Combined SAXS/WAXS enables studies of materials over micron to angstrom length scales. Similarly, near- and far-field HEDM techniques would be merged such that a single sample can be probed on multiple length scales, with application to grain growth, *in situ* deformation of metallic alloys, and stress fields of a propagating crack. Simultaneous tomographic capability can locate voids and cracks. Resonant scattering near heavy-element K-edges enables obtaining high-spatial-resolution pair distribution function measurements of interatomic structure with the added strength of element selectivity, providing insights into the structural disorder in Pt nanoparticle catalysts. The surface instrument, in combination with high-energy x-rays, will allow characterization of systems having important interfaces that lie buried deeply under their exposed surfaces.

Brief mention is made here of the other high-energy beamlines at the APS, located at 6-ID and 11-ID. 6-ID has a tunable-energy side-station D providing 50 – 120 keV. 11-ID has two fixed-energy side-stations B and C, operating mostly at 60 keV and 115 keV, respectively. 6-ID-D serves as a general purpose high-energy diffraction facility, which will eventually be decommissioned due to the designation of Sectors 5 – 7 for the short-pulse x-ray (SPX) beamlines under the APS Upgrade. The 11-ID-B station

is dedicated to pair distribution function (PDF) measurements. The 11-ID-C station enables PDF measurements as well, but also meets general high-energy diffraction requirements that can be satisfied with an area-detector. 11-ID-B and 11-ID-C will continue in these roles, with their activities not being included under the APS Upgrade scope.

4.9.1 HEXD Introduction

For many years, 1-ID has been dedicated to various materials science investigations using high-energy x-rays in the 50–130-keV range with an in-line layout of three stations: (i) A (or first optics enclosure [FOE], for optics), (ii) B (for optics and experiments), and (iii) C (for experiments). In addition to improved sources and x-ray optics, a goal of the APS Upgrade for 1-ID is to enhance efficiency and performance with dedicated and optimized instrument set-ups spread out over four experimental stations, in addition to the optics station A, which will then include the current B station via removal of the A/B separation wall. Of the four experimental stations, two (D and E) will be in-line, and two (F and G) will be on a fixed-angle side-branch. The current C station will be removed. Thus, the final configuration (Figure 4-79) will have stations A/FOE, D, E, F, and G. The station designations B and C (associated with current stations that will either be subsumed or dismantled) will not be reused to avoid terminological confusion in APS Upgrade planning, the transition phase, and even beyond when reference to past history and documentation is unavoidable in technical discussions and operations. Although the E station has been built (in fiscal year 2011) and is currently being equipped under APS operations funding, its full capability is to be reached under the APS Upgrade scope.

The in-line stations will receive a tunable 40–140 keV beam and will also be white-beam capable. The side-branch will operate at a fixed energy of approximately 70-74 keV. The two branches will receive radiation from dual canted undulator sources, one of which will be an SCU device.

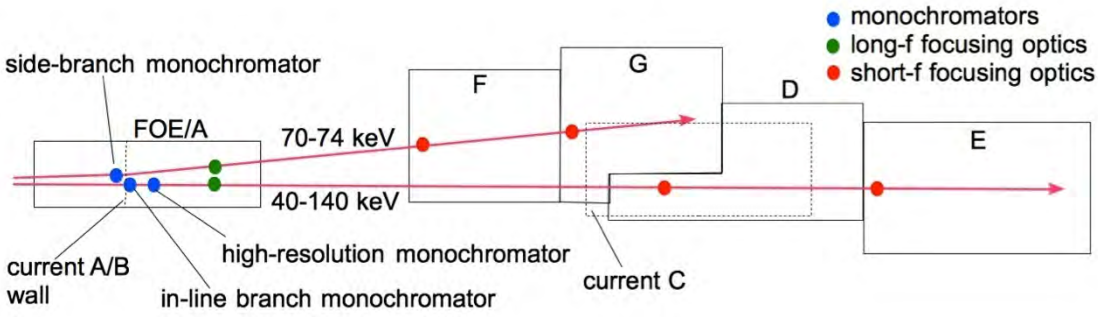

Figure 4-79: The upgraded 1-ID layout (not to scale) with locations of monochromators and focusing optics marked. Outlines of the current C station and A/B separation wall (both to be removed) are shown.

4.9.2 HEXD Scientific Programs and Scope

Presently, the C station is overburdened with too many high-energy x-ray scientific programs, essentially all the programs of 1-ID. These include SAXS/WAXS methods, the "far-field" HEDM technique, resonant scattering, and fluorescence. Only the "near-field" HEDM technique is carried out in the B

station, which also houses x-ray optics. Excessive programmatic demands on the C station, in conjunction with the numerous variations of sample environments (thermo-mechanical deformation/fatigue, high-pressure, low/high temperatures, etc.) result in continuous set-up/tear-down inefficiency that is not conducive to the continued optimization of instruments. The attempt to accommodate multiple setups has also resulted in spatial congestion that has precluded desirable features such as permanently placed short-focal-length optics near experiments.

In the upgraded 1-ID scheme, the sought-after unification of the near- and far-field HEDM instruments will be achieved within the E station, which will also contain the SAXS/WAXS capabilities. The D station will provide general purpose high-energy diffraction capability, and will include resonant scattering and fluorescence setups. The F station will offer a new program to enable high-energy surface scattering measurements of solid and liquid interfaces, as well as diffuse scattering measurements. The G station will focus on *in situ* processing and microstructural kinetics, with some scope overlapping that of the in-line E station programs, enhancing capacity to address current oversubscription (~5:1 ratio) and unabated user demand.

The planned 1-ID layout (Figure 4-79) also permits some interesting full-field imaging capabilities, whereby a sample in the A station can be imaged by x-ray lenses onto an area detector in any experimental station in either branch with large magnification. The largest magnification will occur with the imaging detector farthest away in E, achieving sample resolutions approaching 100 nm or smaller in this 40-m-long high-energy x-ray microscope.

4.9.2.1 SAXS/WAXS (E and G Stations)

Simultaneous SAXS/WAXS provides a single probe to study materials over characteristic length scales ranging from 0.1-1000 nm. SAXS/WAXS with penetrating, forward-scattered, high-energy x-rays has found a wide range of applications including nanophase evolution in supercritical environments [80], biomaterials [81], bulk-metallic glasses [82], and irradiated/nuclear materials [83, 84]. Focusing on the last application, two prominent issues that the upgrade will address are highlighted here.

The first issue is the development of more radiation-tolerant materials, for which nanostructured materials containing a large volume-fraction of interfaces are prime candidates due to their high defect-sink densities. A fundamental understanding of the controlling processes that determine the trapping effects of interfaces under irradiation, in which material swelling/voiding can occur, is needed to develop nanostructure-tailored, damage-tolerant materials. Unique understanding can be gleaned from simultaneous WAXS-diffraction (which is sensitive to the both matrix and nanoscale precipitates) and SAXS (sensitive to electron density, and thus primarily void/bubbles relative to the matrix) under thermo-mechanical processing.

The second issue is an understanding of deformation and fracture mechanisms in irradiated materials, which is of critical importance to structural integrity and lifetime prediction of nuclear reactor components. Characterization of thick specimens (several mm to cm) is critical to ensure proper materials constraint conditions, as often required by testing standards. Through the full-field imaging technique also to be available in the 1-ID upgrade, internal cracks can be visualized and then “zoomed into” with microbeam WAXS to characterize the stress/strain state, grain orientation, and local chemistry. Together, these will provide a fundamental understanding of the cracking mechanisms in irradiated materials.

Similar efforts are needed to understand degradation in Zr-based alloys (hydride formation and cracking) utilized for structural and cladding applications, and for development of next-generation reactor materials based on ceramic composite materials (e.g., SiC fiber-reinforced SiC matrix). The high-brightness x-ray beams can also be utilized to study irradiated (and non-irradiated) materials under high-pressure conditions. Such data will stringently test and refine the extensive computational models of materials behavior in these extreme environments.

4.9.2.2 Near- and Far-Field HEDM (E and G Stations)

The 1-ID upgrade will also enable transformative capabilities for HEDM measurements of polycrystalline materials. These ubiquitous materials are hierarchically structured and often subdivided by a distribution of correlated lattice defects. Modeling the performance of polycrystalline components is therefore a complex multiple length-scale problem. Grains are characterized by their crystallographic orientation and boundary topology. Individual grains and boundaries have anisotropic properties, but are constrained by their neighborhood during application/loading unless failure occurs. It is therefore crucial to be able to observe the individual states of grains and boundaries, rather than the macroscopic average, to directly reveal underlying physical principles [85]. Utilizing orientation contrast, HEDM provides the unique opportunity to probe a statistically representative number of grains in three dimensions (3-D) during thermomechanical processing, with an example of current capability shown in Figure 4-80. Grain boundary topology and stress tensors of several hundreds of grains have recently been mapped using near- and far-field HEDM, respectively. High-resolution reciprocal space mapping, or far-field HEDM, is sensitive down to the nanometer length scale and has been demonstrated to be a powerful probe of evolving dislocation structure. Other avenues to access such 3-D microstructural information include postmortem sectioning plus electron microscopy, which provides complementary information on the final states, as well as the 3-D Laue diffraction microscopy technique described under the Project's S3DD beamline capabilities (section 4.11).

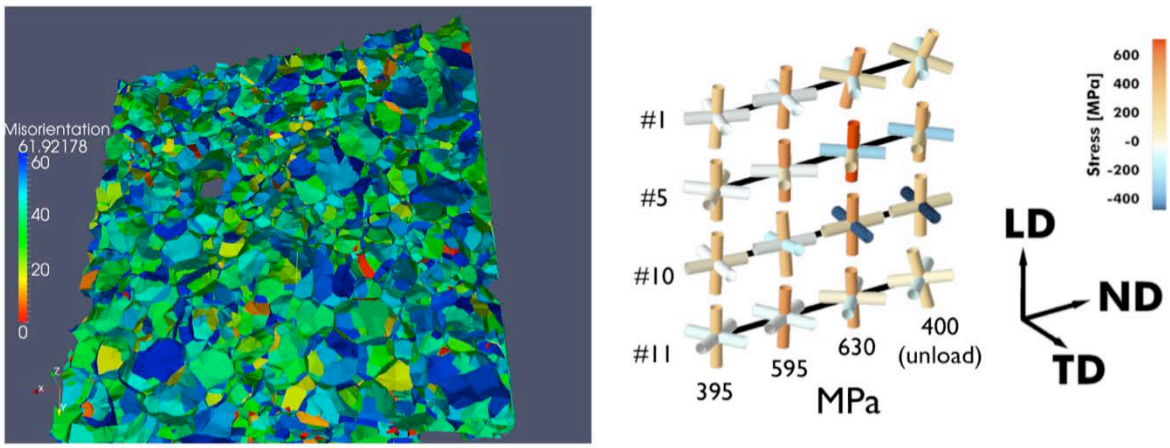

Figure 4-80: Examples of non-destructive HEDM measurements. (Left) Grain map from bulk Ni with misorientations noted and (right) principal stress triads depicting the orientation and magnitude of the principal stresses experienced by four grains within a deforming titanium polycrysalline aggregate. The macroscopic (numbers) and grain-level (color-bar) stress levels along with relevant directions are noted. Through the 1-ID upgrade, grain maps (near-field) and stresses (far-field) will be determined simultaneously.

The beamline upgrade will, for the first time, allow near- and far-field HEDM techniques to be merged such that a single sample can be interrogated on multiple length scales. Impact areas include grain growth, *in situ* deformation of metallic alloys deforming by slip and twinning on grain and sub-grain length scales, stress fields of a propagating crack, domain flipping in ferroelectrics, and variant selection of single-crystal phase transformation under high pressure. The experimental data are crucial for the validation and development of physical models such as subgrain-scale finite element calculations. 1-ID will enable the following transformative capabilities: (i) simultaneous grain-boundary topology and stress-state mapping, (ii) thermomechanical sample environments that will enable measurements under realistic conditions, and (iii) submicron beams that allow "zooming-in" on interesting features identified by the "tomographic" overview scans.

4.9.2.3 Surfaces and Buried Interfaces (F Station)

Many natural and technologically important interfaces lie buried deeply beneath their exposed surfaces. Using high-energy x-rays, the beam can penetrate centimeters of materials, making a wide variety of buried interfaces accessible for structural studies via a non-destructive, *in situ* probe with atomic-scale resolution. The new instrumentation in the F station will enable scattering techniques, such as x-ray reflectivity (XRR), crystal truncation rod (CTR) scattering, and grazing-incidence diffraction in both small- and wide-angle scattering cases (GI-SAXS and GI-WAXS), from numerous interfaces: solid-solid, solid-liquid, liquid-liquid, solid-vapor, and liquid-vapor. This capability does not currently exist in the United States and is presently available only at the European Synchrotron Radiation Facility (ESRF) beamline ID15A and the PETRA III P07 beamline.

The penetration of high-energy x-rays enables examination of samples that better match real materials under real conditions without conceding to the limitations of small sample volumes and overlayers

required when using lower energies. The F station aims to complement the tools and instrumentation utilized by the traditional surface science communities. Pioneering studies [86, 87] on ice-mineral, hydrophobic molecules-water, and Schottky contact interfaces have demonstrated some of the new material systems, questions, and possibilities that can be addressed when combining high-energy x-rays with surface science. Additionally, because the Ewald sphere flattens at high energies, it more closely matches planes in reciprocal space. This is advantageous to both the measurement of diffuse scattering from single crystals and CTR measurements of surfaces. Using large-area detectors that can collect data in sub-second times to capture large regions of reciprocal space enables reaction kinetics to be captured in systems relevant to catalysis and electrochemistry [88].

4.9.2.4 Resonant Scattering (D Station)

The unique high-resolution monochromatization optics [89] developed at 1-ID has made it the only place worldwide capable of conducting high-energy resonant scattering, particularly resonant pair distribution function (PDF) [90, 91] measurements—a capability that will be implemented with detector enhancements in the APS Upgrade. The well-known, standard PDF method is a combined diffraction and analysis technique that treats Bragg and diffuse scattering in a unified manner that is well suited for high-spatial-resolution studies of complex materials with intrinsic disorder. The PDF method's strength lies particularly in the use of high-energy x-rays (60-120 keV), which provide the improved validity of the Born approximation (i.e., single-scattering) that is almost always assumed in extracting structure from scattering data, and the accessibility to high momentum transfers, giving fine real-space atomic resolution upon Fourier inversion. This fairly routine technique provides information via a result called the "total atomic PDF," which is a weighted sum of elemental pair-correlation functions in real space, one for every pair of chemical species in the material.

At 1-ID, the high-energy PDF technique has been taken a step further by making the diffraction measurements near heavy-element *K*-edges, taking advantage of resonant (i.e., anomalous) scattering. When possible, this offers the added strength of elemental environmental selectivity by providing the differential atomic PDF that gives the distribution of distances to neighboring atoms relative to a central atom of the resonant species only, similar to the result from the extended x-ray absorption fine structure (EXAFS) method. Unlike EXAFS, which yields atomic ordering information out to 5-6 Å, the differential PDF will show such correlations up to the longest interatomic distances to which they extend. Instead of being faced with the superposition of all pair-correlations in a total PDF (which can be difficult to interpret), differential PDFs can offer unambiguous insights because the PDF is composed of fewer pair-correlations associated only with the coordination about a single element that could play a relevant role in the behavior of the material being studied. Obtaining a differential PDF involves the challenge of making a reliable subtraction of two nearly identical diffraction data sets taken in the vicinity of an atomic *K*-edge resonance whose scattering factor f' contrast or variation is relatively weak at high atomic number due to core-hole broadening and the large number of non-resonant electrons. This low contrast, combined with the specialized high-energy-resolution x-ray optics required (now uniquely available at 1-ID), has been the reason for resonant scattering at heavy element *K*-edges to be considered quite difficult, resulting in that method to be unexploited and even questioned in regard to feasibility. Although successfully conducted at 1-ID thanks to the efficient high-resolution monochromatization at the beamline, considerable enhancement of data quality in less time for these experiments will be achieved by going from the current single-element, intrinsic Ge detector to a multi-element array, as planned in the beamline upgrade.

The high-energy resonant PDF method is a valuable tool in the structural investigations of materials of technological interest with relevant intrinsic disorder and where a heavy element plays an important role. Studies of Pt- and Au-containing (78-keV and 81-keV *K*-edges, respectively) fuel cell nanoparticle catalysts are such an example, where the catalytic properties are believed to be related to the type of intrinsic disorder arising in different alloy structures, e.g., random-alloy or core-shell atomic arrangements [90].

4.9.2.5 Fluorescence (D station)

In principle, almost all elements can be identified by fluorescence lines below 25 keV without the necessity for a very-high-energy incident x-ray beam. This entails using K-lines for the lighter elements and L-lines for the heavier ones. However, detection of heavy elements by *K*-shell excitation can be attractive. The merits of the K-line fluorescence detection approach include (i) the penetration capability of the radiation both entering and leaving a thick-wall contained sample or dense host material and (ii) simpler spectra, uncomplicated by the presence of numerous overlapping peaks as are often encountered when dealing with L-lines. K-holes also have higher radiative yields, but these advantages must be weighed against lower hole-creation cross sections and the backgrounds from strong Compton scattering processes (both simple and multiple) at high energies.

An example of the application of *K*-shell fluorescence spectroscopy is the study of minority additives in high-intensity discharge lighting plasmas (lamps) [92]. Small quantities of heavy-element additives (e.g., Dy, Cs, I in Hg) play an important role in the lighting properties (efficacy and color rendering) of lamps. High-energy fluorescence is well suited to studying the distributions and concentrations of the chemical constituents of the gas systems under discharge, as they are typically contained in jackets of polycrystalline (ceramic) alumina and glass. Recently, fluorescence experiments at energies over 115 keV have been conducted to characterize actinide content (e.g., Th, U, Pu) in spent nuclear fuel and to develop instruments for more reliable nuclear safeguards applications [93]. The high-energy fluorescence program would benefit from the upgrade to the multi-element intrinsic Ge detector array, the same as the one that would also be utilized for resonant PDF studies.

4.9.3 Dual-Canted X-ray Undulator Sources for HEXD

To increase the high-energy x-ray capability and capacity at 1-ID, the configuration of dual canted undulator sources to serve two branches has been chosen. Furthermore, optimal source performance at such energies drives the selection of SCU device technology, which enables the achievement of high fields at shorter device periods. In planning for an SCU, which brings its additional cryostat space requirements, only a long straight-section (LSS, of length ~8 m) can accommodate a second device of reasonable length. However, having two SCUs is precluded by space considerations even in an LSS, particularly due to a mechanical conflict between the upstream SCU's cryostat and the 1-BM beamline's x-ray beam-pipe. This conflict also requires the SCU to be in the downstream half of the LSS. So, for its two sources, 1-ID will avail of an SCU and a permanent magnet undulator (PMU). Faced with this constraint of one SCU only, but two branches that would like to take advantage of its performance, it is necessary to consider methods of occasionally interchanging the delivery/assignment of the two undulator beams between the two branches. To this end, the capability to use monochromator optics to conduct this beam delivery interchange is planned (section 4.9.4.1). In addition, beam delivery interchange through

magnetic switching of the electron beam trajectory (i.e., switchable canting sense) has been discussed with the APS Accelerator Systems Division (ASD) and could be pursued in the future, but is not in the baseline Project scope. An important difference is that, unlike the magnetic switching approaches that will result in little or no beam motion in the experimental stations, the optics-based switching will result in much larger horizontal shifts (many cm) given by the canting angle (1 mrad) times the distance from the source (10s of meters), making it less preferable. However, adjusting the monochromators to re-steer the beams back to fixed positions might be feasible.

The SCU specified for 1-ID (referred to as SCU2) is a 1.8-cm-period device of approximately 2.3-m magnetic length (in a 3-m cryostat) with a maximum deflection parameter $K_{max} = 1.56$, corresponding to a 0.93-T peak field, giving it full spectral coverage from 40 keV to well beyond 100 keV as needed for the tunable in-line branch. However, in case its radiation is selected, due to experimental demand, for delivery to the side-branch, the in-line branch, relegated to receive radiation from the other PMU device, must still be provided with a full-spectral-coverage source. This is also judicious if the delivery of the SCU2 device were to be delayed. For these reasons, the PMU specified for 1-ID is a revolver device of two selectable periods, 2.3 cm and 2.5 cm (to fill each other's spectral gaps), of roughly 2.4-m magnetic length and $K_{max} = 1.12$ and 1.37 for the two periods, respectively. The spectral brightness of these two specified undulator systems (SCU2 and the revolver-PMU) is shown in Figure 4-81. Presently, one of the two devices at 1-ID is actually a 2.3-cm-period PMU. The other is a 3.3-cm-period PMU (i.e., a standard APS Undulator A) providing full spectral coverage at the ~10^{18} brightness level. So, relative to the sources currently at 1-ID (at 100 mA), the upgraded source SCU2 (at 150 mA) offers a brightness gain factor of 10 – 25.

The power load from the SCU2 will be considerable. At 150 mA, it will present a total power of 9.1 kW and a power density of 447 kW/mrad^2 at its highest field.

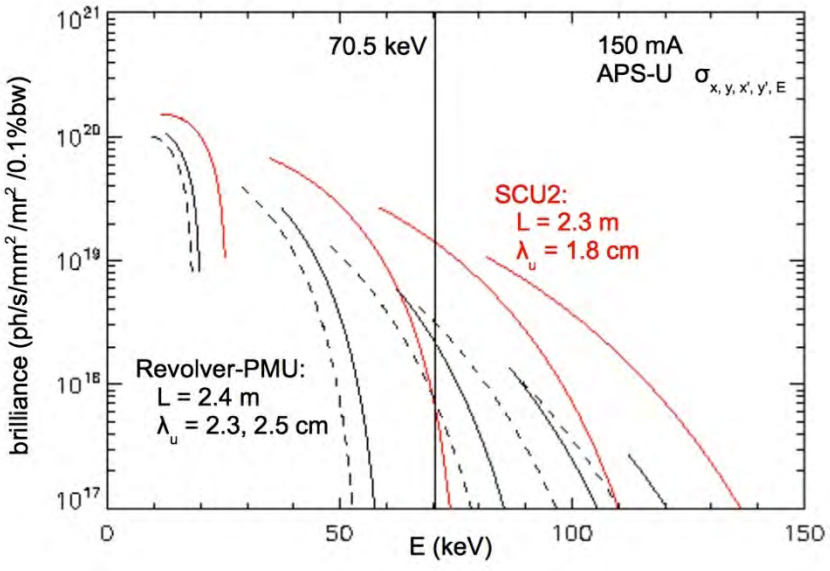

Figure 4-81: Spectral brightness performance of the requested undulator systems for 1-ID: a 1.8-cm-period SCU and a 2.3/2.5-cm-periods revolver PMU.

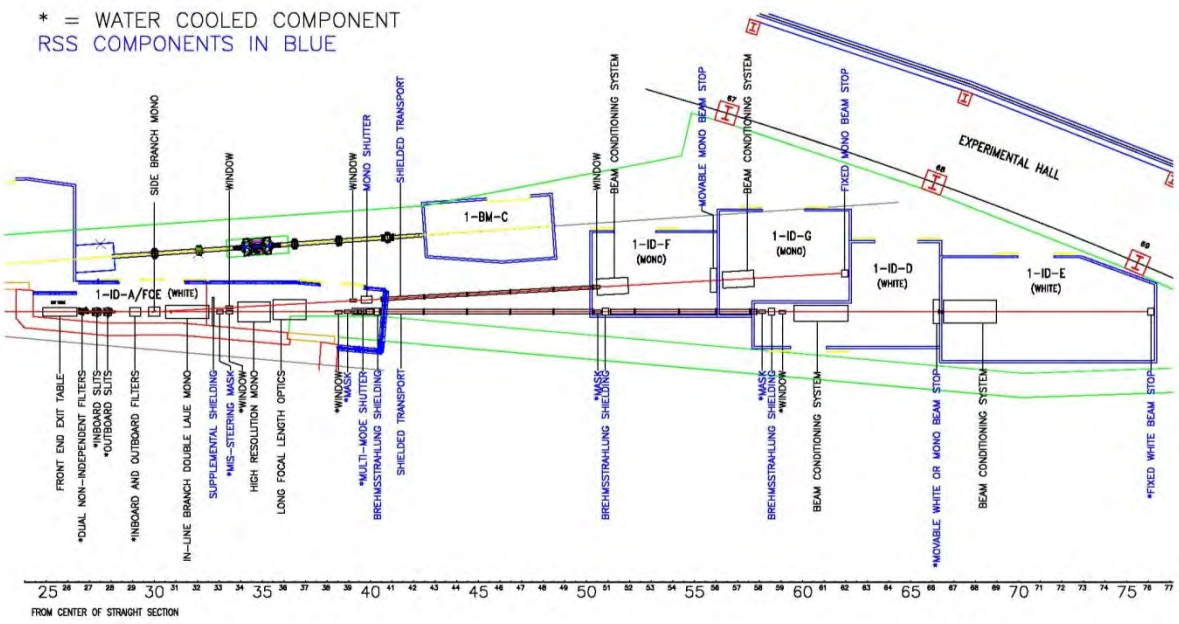

Figure 4-82: The upgraded 1-ID layout showing x-ray optics and beam-handling components, but not the specialized station instruments, which are detailed in separate figures.

4.9.4 X-ray Optics for HEXD

Monochromators and focusing (refractive) optics locations are marked in Figure 4-79 and also in the more complete (but not all-inclusive) layout in Figure 4-82, where the short-focal-length optics are incorporated in beam conditioning systems within the various experiment stations.

4.9.4.1 Monochromators

Three monochromator systems will be located in the FOE/A (Figure 4-79 and Figure 4-82). A bent double-Laue monochromator (Figure 4-83) and a bent single-Laue monochromator (Figure 4-84) will serve the in-line branch and side-branch, respectively. If needed, a high-resolution monochromator (Figure 4-85) will be utilized in addition to the bent double-Laue monochromator to achieve the higher energy resolution requirements of certain in-line branch experiments.

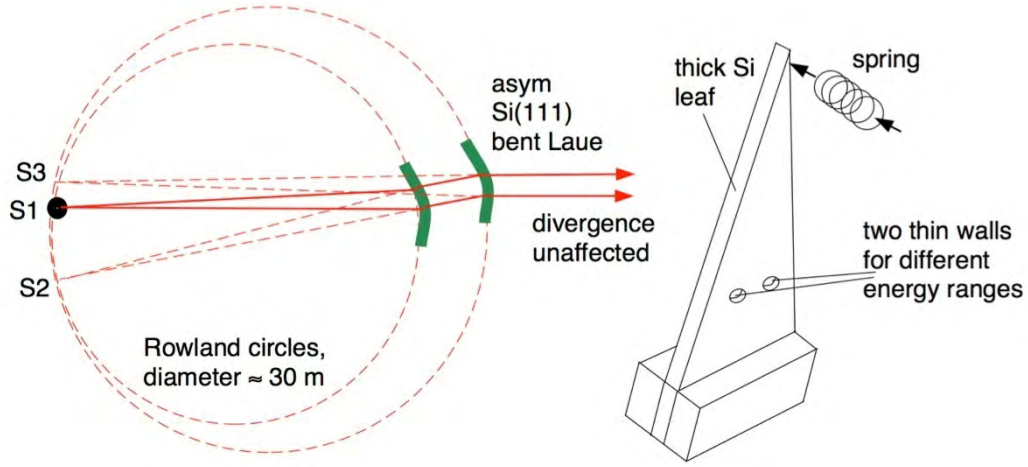

Figure 4-83: Tunable, fixed-exit monochromator (for the in-line branch stations 1-ID-D and E) consisting of two vertically diffracting, bent Laue crystals in a nested Rowland configuration. Crystals are shown with small, thinned regions that diffract the x-rays.

The familiar, conventional monochromator geometry composed of two flat, parallel crystals becomes inefficient at high x-ray energies. So, to serve the D and E stations, the in-line branch monochromator will consist of two bent, asymmetric Si<111> Laue crystals in sequential Rowland conditions (Figure 4-83), similar to what has been developed and utilized at 1-ID for the past 12 years [94] to deliver a high-flux, fully tunable, fixed-exit beam (30-35 mm vertical offset) with preserved source brightness (i.e, size and divergence), allowing efficient subsequent manipulation by additional optics. In the current arrangement, the first crystal is in a vacuum tank and cryogenically cooled, whereas the second crystal is in air. In the upgraded scheme, both crystals will be in the same vacuum tank so that the crystals can get close enough to allow the minimum energy to be reduced to 40 keV (currently 50 keV). The high end of the energy range will be 140 keV (currently 130 keV). Bender designs will also be modified. Although the overall thickness of the Laue crystals will be many millimeters for proper stiffness and heat transfer, the beam will diffract through one of two small regions thinned down to different, few-millimeter thicknesses (Figure 4-83, right panel) to suit different energy ranges. The monochromator bandwidth will be $\Delta E/E \sim 1.5 \times 10^{-3}$, which is well matched to most high-energy experiments. As done currently, the first crystal will be liquid nitrogen- (LN_2) cooled, which will be particularly important for handling the heat load of the insertion device SCU2. A compact, movable, cooled beam stop will be positioned in the tank just after the first crystal to block the transmitted white beam. This stop is intended for downstream equipment protection and is not part of the radiation safety system (RSS) for personnel protection (RSS beam-handling components are described in section 4.9.5).

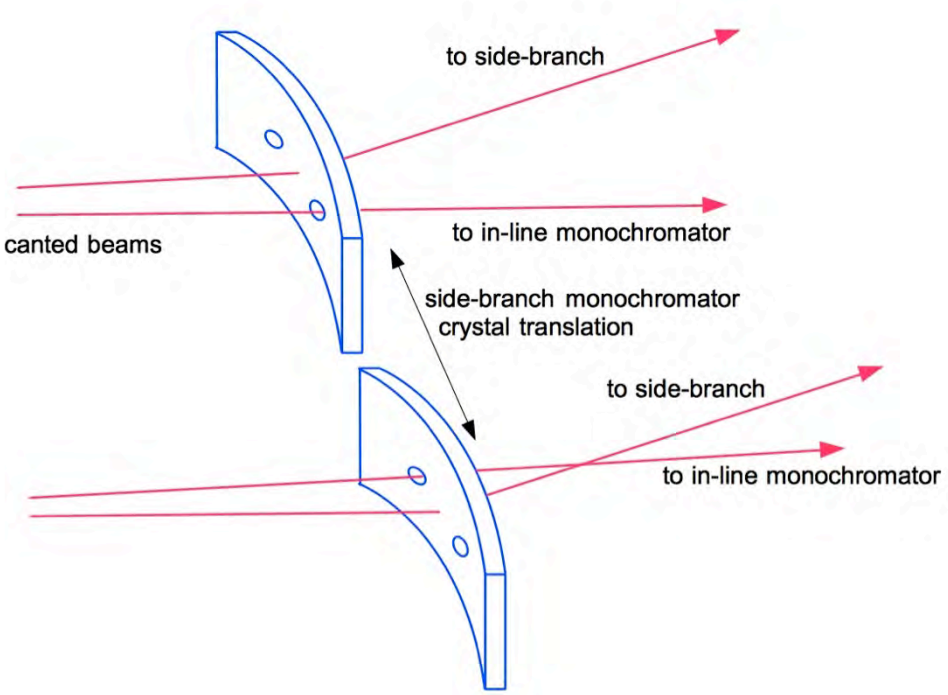

Figure 4-84: Bent single-Laue monochromator for the fixed-energy (70-74-keV) side-branch stations 1-ID-F and G. Pass-through holes enable the exchange of canted beam delivery between the two branches.

The side-branch monochromator will consist of a LN_2-cooled, single-horizontal-reflection, asymmetric Si<111> Laue crystal (Figure 4-84) in vacuum, immediately upstream of the in-line branch double-Laue monochromator. It will be bent to the Rowland condition with respect to the source to provide a fixed-energy beam of roughly 70-74 keV and $\Delta E/E \sim 1.5 \times 10^{-3}$ bandwidth to the F and G stations. As shown in Figure 4-84, pass-through holes in the crystal allow the other canted white beam to propagate unobstructed to the in-line branch monochromator. With a lateral translation of the crystal, either beam can be selected to diffract into the side-branch, letting the other beam pass through, thereby conducting an interchange in the delivery of canted beams between the two branches. Here also, a compact, movable, cooled beam-stop (non-RSS component, not shown) will be positioned in the tank just after the crystal to block the transmitted white beam.

In the optics-based canted beam delivery interchange described above, crystals of both monochromators (i.e., three crystals in all) and both compact beam stops will have to execute horizontal translations. This type of interchange will tend to have the side effect of beams in experimental stations emerging shifted horizontally (many centimeters) by the canting angle times the distance from the source. However, in the case of the side branch, the single-reflection monochromator can be easily adjusted in angle to re-steer the beam back to the same spot as an alternative option to realigning the experiment instruments to a displaced incoming beam. For the case of the in-line branch to avoid realigning the experiment, an attempt to re-steer will have to be done by tilt adjustments (about the beam axis) of one or both of its monochromator crystals, which is not as straightforward, as the required tilts turn out to be rather large—up to 1-2°. Such adjustments also result in giving the highly horizontally elongated source an effective rotation by an angle twice the crystal tilt, having consequences of enlarging the vertical size of focused

beams. For these reasons, accelerator/magnetic-based approaches to switchable canting (mentioned in section 4.9.3) are under discussion, as they offer to be more straightforward for beamline operations.

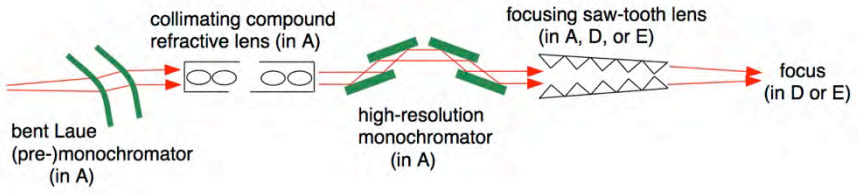

Figure 4-85: A four-reflection, high-energy-resolution monochromator for 1-ID-D and E. Refractive lenses just upstream (shown here as the cylindrical compound type) collimate the x-rays. Optionally, lenses downstream (shown here as the saw-tooth type) focus the beam.

The $\Delta E/E \sim 10^{-3}$ bandwidth delivered by the bent-crystal optics described so far will be adequate for most high-energy x-ray applications. However, certain investigations, such as high-resolution reciprocal-space measurements in far-field HEDM or resonant scattering at heavy-element *K*-edges, require higher monochromatic-energy resolution. To meet this requirement, the in-line branch will have available a high-energy-resolution monochromator (HRM) in the FOE/A that will optionally further monochromatize the beam delivered by the double-Laue system from 10^{-3} down to 10^{-4} -10^{-5} levels of energy spread over 40- 120 keV. Such an HRM, which will operate in air, has already been developed and utilized at 1-ID for many years and consists of four flat Bragg crystal reflections in a (+ - - +) dispersive configuration (Figure 4-85) [89, 95].

The upgrades to the existing HRM would include new high-angular-resolution stages, redesigned weak-link flexures for the two parallel-crystal pairs, capability of faster changing of energy and resolution, and a longer stand. When the HRM is in operation, refractive lenses placed immediately upstream of it will be set for vertical x-ray collimation in order to enhance the throughput of the low-angular-acceptance HRM. To illustrate the potential flexibility of the optics arrangements, Figure 4-85 also shows how additional focusing refractive lenses, to be discussed next, placed downstream of the HRM (in A, D, or E) can achieve a focused beam, as well as a narrow bandwidth. Such a setup has been used for high-resolution reciprocal space studies of the intra-granular strains and dislocation dynamics evolving during tensile deformation of materials [85].

4.9.4.2 Focusing Optics

Focusing in long and short focal-length configurations (i.e., low and high demagnifications, respectively) will be available in both branches using refractive lenses (Figure 4-79). Long focal lengths (f = 10 – 20 m) will provide 15- 25-μm FWHM vertical beam sizes in all four experimental stations (D, E, F, and G) using lenses placed on the long focal length optics table in A (Figure 4-82). Short focal lengths (f = 1 – 3 m) will provide few- to sub-μm FWHM vertical beam sizes in the four experiment stations utilizing lenses placed on the individual beam conditioning system (BCS) tables present at the upstream end of every station (Figure 4-82, Figure 4-86, Figure 4-87, Figure 4-89, Figure 4-91). Certain experiments might be well matched by intermediate demagnifications arising from using lenses in D to focus into E, or

the lenses in F to focus into G. Another interesting idea is to implement vertical and horizontal focusing at different demagnifications (i.e., short-*f* for horizontal, long-*f* for vertical) to achieve a more circular focal spot with high flux density gain, compensating for the elongated source. One of the salient x-ray optics aspects of the upgraded 1-ID scheme is the availability of short-focal-length optics near all instruments, which has not been practical in the current 1-ID-C station due to the overcrowding of hardware from numerous experiments being served in a single station.

Although parabolic aluminum (Al) compound refractive lenses (CRLs, cylindrical type illustrated in Figure 4-85, in the collimating location before the HRM) will be a type of lens available for use, it is saw-tooth refractive lenses (depicted in the final focusing position in Figure 4-85) that are currently of interest in the 1-ID upgrade. Considerable development and use have been made of Si and Al saw-tooth refractive lenses over the last 10 years at 1-ID to produce beams in the size range of 2-25-μm at 50-120 keV [95] [96]. Their operation is based on the principle that a pair of saw-tooth structures symmetrically inclined at grazing incidence with respect to a beam presents a parabolic projected thickness profile along the beam, as required for aberration-free focusing in one dimension, with a curvature radius determined by the inclination angles. So, in addition to being effectively parabolic, they are continuously tunable in focal length or energy by straightforward adjustment of the tilts and have no attenuation on-axis. For the fixed-energy side stations F and G, tunability can be sacrificed for the benefit of enlarged spatial-acceptance apertures by using kinoform lenses (which have lower attenuations off-axis compared to the compound or saw-tooth lenses, due to the removal of refractively inert, integer-2π phase-shifting material thicknesses) wherever possible. To advance from the current 2-μm vertical focusing capability at 1-ID to the goal of achieving just under 1-μm, some focusing research and development efforts are ongoing, but are not included in the APS Upgrade scope. As such, the actual refractive lenses will not to be obtained under the Project scope, although their manipulation systems are included in the Project scope.

The HEDM program residing in the E station will also explore alternative broadband focusing approaches to the refractive-based optics previously mentioned, namely bent Laue crystals [97] and elliptically bent multilayers [98], which will be positioned on the E-station beam-conditioning table. Laue focusing is achieved by bending a crystal in an off-Rowland geometry with the source outside of the Rowland circle. By proper choice of crystal parameters, particularly the asymmetrical cut, the crystal thickness aberration can be eliminated, achieving theoretical source-size-limited focusing in the vertical direction. Because of the off-Rowland bending with the convex side facing the source, the focusing is inherently polychromatic (broadband), requiring incident white beam onto the Laue crystal. Having such an option is one of the reasons for installing white-beam capability throughout the in-line branch all the way to the E station. One feature of this type of focusing is the rectangular-function shape of the angular divergence profile, which is beneficial for certain HEDM studies. Another anticipated advantage of Laue focusing is its significantly larger spatial acceptance as compared to refractive lenses, a feature that becomes important far from the source, as is the case for the E station. Larger spatial acceptances are also expected for elliptically bent multilayers, which can be utilized to capture and focus the horizontal, as well as vertical, undulator beam in a Kirkpatrick-Baez (K-B) geometry. To preserve the Bragg condition for a single wavelength over the elliptical profiles, the multilayers will have a meridional gradient in their bi-layer spacing. Again, delivering white beam into the E station is required to take advantage of the broad bandwidth of multilayers to capture and focus as much as possible of a full undulator harmonic.

The refractive lenses placed on the long focal length optics table in the A station will be capable of magnifying an illuminated sample placed slightly upstream of it (i.e., ~ 1 m away on the same table) onto

an area-detector in any of the four experimental stations. For the case of a detector in at the downstream end of the E station, this will provide a high-energy x-ray microscope with 40x magnification and spatial resolution far below 1 μm.

4.9.5 HEXD Beamline Layout

Having presented the x-ray optics in section 4.9.4, this section discusses the remaining layout aspects, including front end, beam-handling components; shielding; vacuum; experiment instruments; and data acquisition/control.

4.9.5.1 Front End

The upgraded 1-ID source configuration is the only one in the APS Upgrade plan to combine canted undulators in a LSS. So the front end will be unique—a long-straight-section canted-undulator front end (LSSCUFE) described in more detail in section 5.2. The design is expected to withstand the power load of two SCU2 insertion devices, one for each of the canted beams separated by 0.8-1 mrad. Although, as described in section 4.9.3, only one SCU device is planned (the other being a revolver PMU), magnetic switching of the canted beams could deliver the SCU2 radiation in either direction, requiring the LSSCUFE (and various other white-beam-handling components of the in-line branch) to accept SCU2 photons along either canting trajectory. Also, if desired, the LSSCUFE can be designed to operate at lower-than-1-mrad canting, down to 0.8 mrad. Although the current plan is to operate at 1-mrad canting, reduction to 0.8 mrad is conceivable to alleviate the magnetic field strengths required to implement the switchable canting scheme. The front-end suite of components is situated primarily before the shielding wall (in the storage ring territory), but does extend partially into the FOE/A station, occupying the front end exit table at the most upstream end (Figure 4-82).

To support routine beamline operations, an important component of the front end is the front end white-beam shutter, located upstream of the shielding wall, which will pass or block both canted white beams simultaneously but not independently. The qualifier “dual non-independent” is often utilized to describe this type of operation.

4.9.5.2 Beam-Handling Components and Radiation Safety

In discussing beam-handling components in the presence of canted beams, the description “dual non-independent” is utilized to imply that a component operates on both beams in a similar/simultaneous manner (as in the case of the front end shutter described in the previous section). If the component has the flexibility to operate on the beams separately, the term “dual independent” is utilized.

4.9.5.2.1 White-Beam Slits and Filters

Emerging from the front end, but before reaching the two white-beam monochromators, the two beams go through – in this order – dual non-independent filters, dual independent white-beam slits, and dual independent filters (Figure 4-82). The dual independent white-beam slits enable separate adjustment of the white-beam sizes for the two branches, including complete aperture closure to effectively turn off the

beam incident onto any one of the two white-beam monochromators, especially since the front end shutters are dual non-independent. As shown, the dual independent white-beam slits are two sequential, independent beam-defining systems, with each one having a pass-through aperture for the other beam.

The dual non-independent filters before the slits will be composed of light-material attenuators (e.g., carbon) on a single actuator mechanism moving them in and out of both beams. These filters will impose an overall basic level of thermal load alleviation for both branch monochromators as well as their white-beam slits. The dual independent filters after the slits will be composed of attenuator banks on two separate actuators, one for each canted beam, to enable independent additional filtering of the two beams, if needed. For example, the side branch, operating always at the same 70-74-keV energy, could accept a higher energy filter cutoff than the in-line branch which will have to operate down to 40 keV. The in-line branch, on the other hand, might occasionally need even higher attenuation to achieve a manageable heat load on the broadband focusing optics in the E station. Also, some desirable attenuator candidates for the dual independent filters can be heavier materials that will benefit from the thermal load reduction offered by the white-beam slits and dual non-independent filters placed upstream.

4.9.5.2.2 Shutters and Stops

Aside from the front end shutter operation (which affects both branches), beam delivery solely within the in-line branch is controlled by a multi-mode shutter (downstream end of A), a manually movable stop (downstream end of D), and a fixed white-beam stop (downstream end of E). The multi-mode shutter status can be in one of two modes, “white” or “monochromatic,” with remote shuttering capability in either mode. In “white-beam mode” it shutters the white beam. In “monochromatic mode” the multi-mode shutter serves as a white-beam stop while shuttering the monochromatic beam. This permits turning off the beam into D and E while preserving a stable thermal load on the in-line branch monochromator and without impacting side-branch operations.

The fixed white-beam stop is the final stop for the in-line branch, whether operating in either white or monochromatic mode. It is important to realize that both the multi-mode shutter and fixed white-beam stop must be capable of handling the simultaneous presence of two white beams in a dual non-independent fashion. The reason for this is that even though only one white beam might be physically present and interacting with these components when the in-line branch is in white-beam mode (the other white beam being stopped by the compact, cooled stop after the side-branch monochromator), both white beams exist from an RSS standpoint, because the compact movable stop (a non-RSS component) could be improperly positioned or fail.

The movable stop (downstream end of D) is a manually movable shield initially conceived to stop only monochromatic beam and hence be a simple, longitudinally low-profile, and uncooled component which is desirable given the relatively short length of D. When the moveable stop is open, it exposes a pass-through aperture (an open-air spool piece in the D/E wall) for white and monochromatic beams to go into and enable experiments in E. When slid closed, the PSS will ensure that the multi-mode shutter in A is in monochromatic mode so that white beam cannot enter D. The D station will then be available for monochromatic experiments while E will be accessible to personnel. However, if a white-beam experiment in conducted in D, the movable stop will have to be open, prohibiting access to E. To address this drawback, the possibility of a low-profile white and monochromatic beam stop is being examined. If implemented, it will also have to withstand two simultaneous white beams.

Beam delivery solely within the side-branch is controlled by a monochromatic shutter (downstream end of A), a manually movable monochromatic beam stop (downstream end of F), and a fixed monochromatic beam stop (downstream end of G). This arrangement allows (i) turning off the beam into F and G, while preserving a stable thermal load on the side-branch monochromator without impacting in-line branch operations; (ii) access to G while F is accepting beam; and (iii) a simple, low-profile F-to-G beam-handling component (a sliding shield before an open-air spool piece in the F/G wall.)

4.9.5.2.3 Windows, Transports, and Vacuum

The vacuum region of the two white-beam monochromators will extend upstream until reaching a cooled Be window on the front-end exit table and downstream to where the beams exit from the monochromator tank(s). The tank exit window flange for the in-line branch beams will have two vertically separated exit locations of Be—a cooled lower spot for the canted white beams and an uncooled higher spot for either selected monochromatic canted beam. The tank exit window flange for the side-branch beam will have a single exit spot of uncooled Be for either selected monochromatic beam.

The in-line branch white-beam transport (which passes through the F and G stations) will be evacuated going upstream until reaching the multi-mode shutter in A and will be end-capped there by a window similar to the one on the monochromator tank where the in-line branch beams exit. Another similar window will end-cap the transport vacuum at the upstream end of the D station. A portable fourth such window and evacuated x-ray flight-tube hardware will be available to extend the vacuum path all the way to the experiment in the case of white-beam or near-40-keV operation in the in-line branch. For this purpose, optional evacuated flight-tube hardware will also be available to eliminate the air gaps throughout A and D.

The side-branch mono-beam transport will be evacuated going upstream until reaching the mono-shutter in A and will be end-capped there by a window similar to the one on the monochromator tank where the side-branch beams exit. Another similar window will end-cap the transport vacuum at the upstream end of the F station.

4.9.5.2.4 Bremsstrahlung Shielding

During white-beam operation of the in-line branch, a direct line-of-sight exists from the electron source in the storage ring all the down the in-line branch. Radiation safety policies dictate that the very-high-energy (up to 7 Gev) bremsstrahlung radiation cone emitted around this line-of-sight must not escape into experiment hall floor areas accessible to personnel in the beamline vicinity. This is achieved by having collimator/mask pairs placed at spatial intervals down the line to ratchet-down the bremsstrahlung cone. These locations are expected to be at the downstream end of A, the upstream end of F, and the upstream end of D. Like some of components already discussed, the bremsstrahlung shielding components must be designed to function for the case of two simultaneous, canted white beams and sources.

4.9.5.3 D Station Instruments (In-Line Branch)

The beam conditioning system (BCS) table at the upstream end of D station (Figure 4-86) will support slits, a split-ion-chamber X-ray beam position monitor (X-BPM) to characterize beam position stability,

and refractive lenses for short (or intermediate) focal length focusing within D (or into E). A large diffractometer (reuse of a currently existing one) will be utilized for general purpose high-energy diffraction and, in particular, resonant PDF measurements, in which case a multi-element intrinsic Ge detector will be mounted on the diffractometer 2θ-arm. An alternative set of sample manipulation stages will also be available to better suit certain other types of samples/experiments, such as high-energy x-ray fluorescence. Further downstream a large GE amorphous-Si area-detector will be available and shared with the E station.

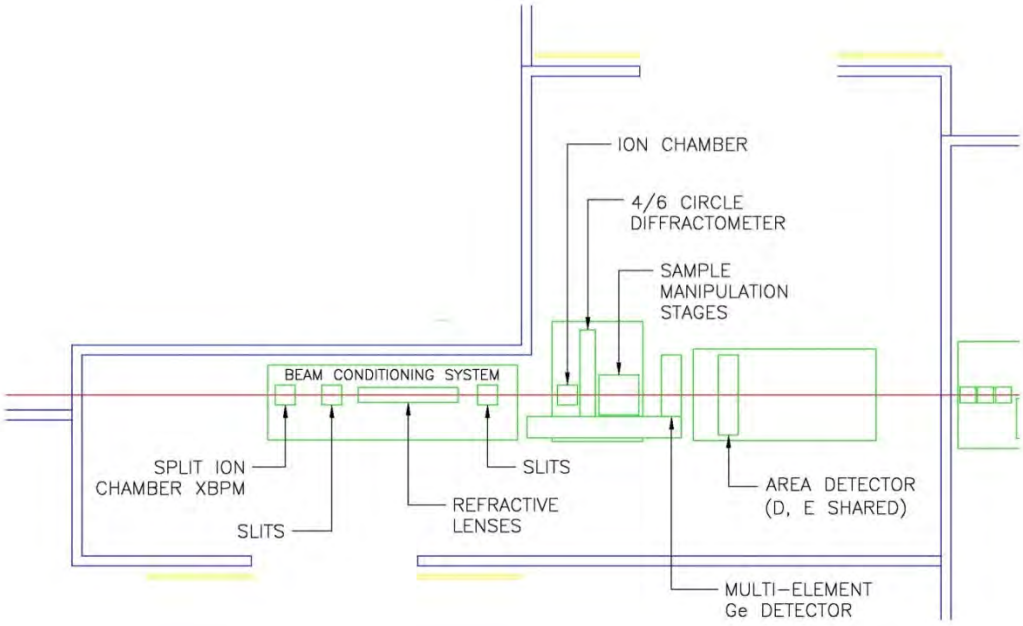

Figure 4-86: Layout plan of the in-line-branch 1-ID-D station instruments, including the beam conditioning system but excluding radiation safety components and windows.

4.9.5.4 E-Station Instruments (In-Line Branch)

Although, as mentioned earlier, the E station was built in FY2011 and will be equipped primarily from APS operations funding, the full layout is summarized here to provide a complete sense of the overall anticipated 1-ID capabilities. The BCS table at the upstream end of the E station will support similar elements as the one in the D station, with the addition of broadband focusing optics (e.g., elliptically bent multilayers) described in section 4.9.4.2. In certain cases of monochromatic focusing, D station refractive optics will be utilized in conjunction with or instead of E-station optics. A rail system will be utilized to allow easy interchange between the broadband and monochromatic (refractive-based) focusing optics. Three sample-manipulation systems (SMSs) will be employed downstream of the BCS (Figure 4-87 and Figure 4-88). The first (SMS-1) will be a 3-axis eulerian cradle, which will allow for full reciprocal space mapping. The second (SMS-2) will incorporate an air-bearing ϕ-rotation (vertical axis) with slip-ring rotary feed-throughs for high-precision 3-D mapping. The third (SMS-3) will manipulate the custom-built thermo-mechanical test frame (by MTS). SMS-1 and SMS-2 will be located on a common table allowing vertical and tilt flexibility and coupled to SMS-3 through a rail mechanism, which will allow interchange between all three systems while retaining the same sample position in absolute *xyz* coordinates.

Surrounding the SMSs will be an overhead frame on which the near-field detector, beam-stop, conical-slit system, and optical cameras can be mounted, allowing their use on any of the SMSs. Downstream will be an array of four large (far-field) area-detectors (GE amorphous-Si) arranged to provide a central hole (for the last downstream SAXS detector) and situated on large longitudinal (z) and transverse (x) translation stages. The ~2.5-m z-translation will provide user flexibility for attaining the highest momentum transfer Q-range or Q-resolution, while the x-motion will allow the array to be moved out of the diffracted beam path for use of the high-Q-resolution (very-far-field) detector. The latter will be a medium-spatial-resolution detector (e.g., Mar165 charge-couple device [CCD]) capable of large xz-translations (range ~2 m x 2 m). At the end of the station just downstream of this detector will be a SAXS detector system consisting of a beam-stop, conical attenuators, and a medium-spatial-resolution detector (e.g., ScintX).

Specific E station items that are included in the Project scope and are funded by APS Upgrade include the near-field detector, a single-panel far-field detector (shared with D station), a photon counter for knife-edge fluorescence determination of focal spot sizes, refractive lens motion stages, and conical slits for defining the longitudinal extent of diffraction gauge volumes in samples.

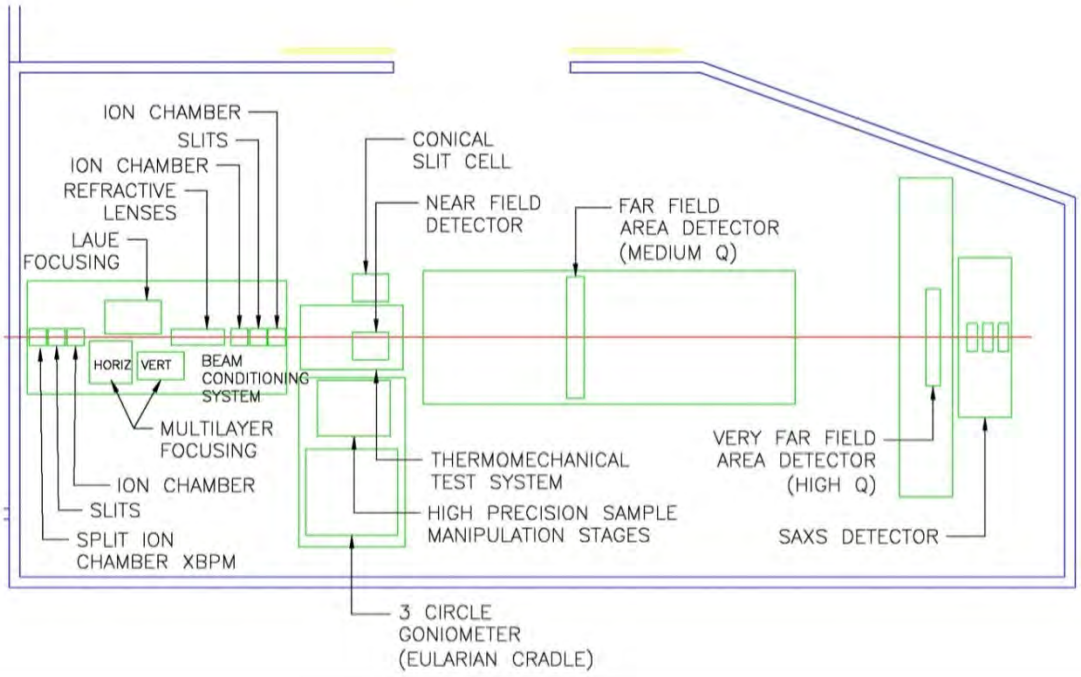

Figure 4-87: Layout plan of the in-line branch 1-ID-E station instruments, including the beam conditioning system but excluding radiation safety components and windows.

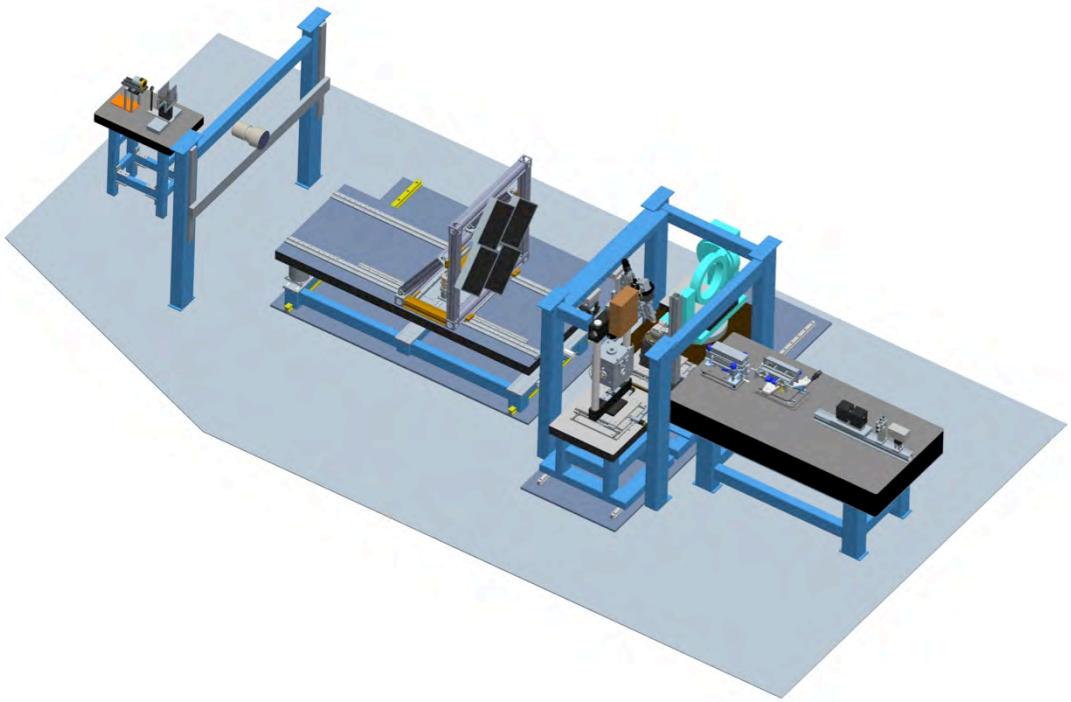

Figure 4-88: Three-dimensional equivalent of the 1-ID-E-station layout plan shown in Figure 4-87. Here, the x-ray beam enters from the right.

4.9.5.5 F-Station Instruments (Side-Branch)

X-rays entering the F station will first encounter the BCS table, as shown in Figure 4-89. Because the side-branch receives its radiation from a single, horizontal-reflection monochromator, an X-BPM will provide horizontal position monitoring to ensure a stable beam position, as well as intensity. The BCS will also include slits and short-focal-length optics to provide vertical focusing to ~1 um with the option to focus horizontally as well. Vertical focusing is critical for scattering techniques that require a grazing incidence beam. Focusing in both directions will enable the studies of samples with micron-sized features, coexistence with scanning probe instruments, and studies of materials that are susceptible to radiation damage. A horizontally-focused beam confines radiation damage to a small region of the sample and then translates it to introduce fresh material before radiation damage ensues [99]. Following the BCS is an x-ray beam-tilting system that enables studies of liquid interfaces (Figure 4-90). To study liquid-liquid and liquid-gas interfaces, the beam, focused by lenses onto the sample, must be steered out of the horizontal plane and onto the sample surface, which cannot be tilted. This will be accomplished by a bent double-Laue crystal assembly, which is very similar to the double-Laue monochromator described earlier, but instead is bent to sequential Rowland conditions with respect to the focus and uses two different crystal reflections (e.g., Si<111> and Si<220>), to obtain a non-horizontal beam (i.e., one having a vertical component in its propagation direction) [100]. By coupling both crystals into a single-tilt stage that rotates about the incident beam axis, the exit beam can be made to sweep out a cone whose vertex, into which the beam is directed, is stationary and at the sample/focus position. Such a tilt degree of freedom results in the ability to vary the incidence angle of the x-rays with respect to the surface being studied.

Because the sample remains stable by not moving, measurement techniques such as x-ray reflectivity (XRR) can acquire data rapidly in order to address dramatically reduced reaction time scales.

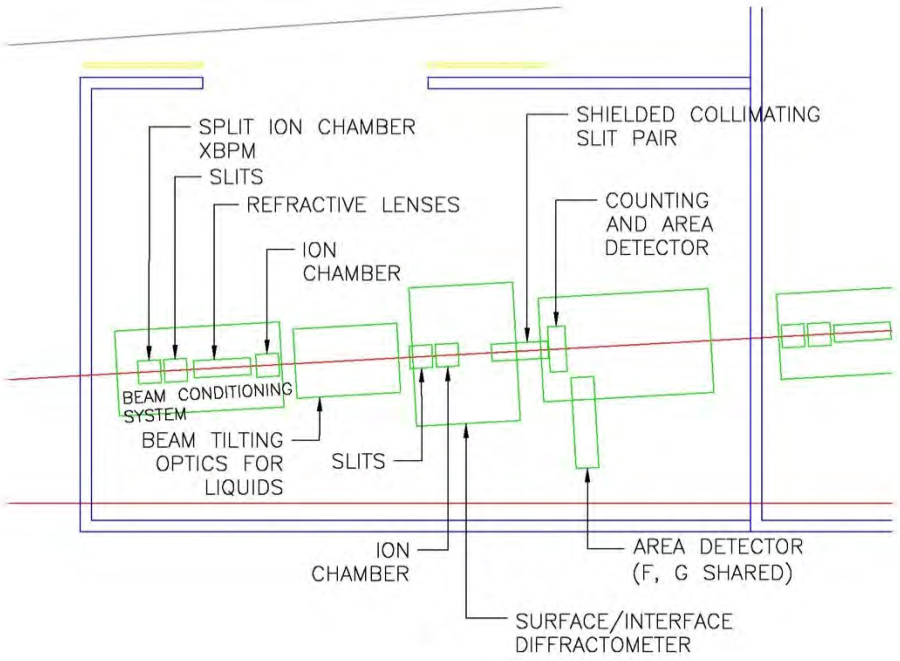

Figure 4-89: Layout plan of side-branch 1-ID-F station instruments, including the beam conditioning system but excluding radiation safety components and windows.

The sample stage (Figure 4-90) for this surface and buried interface instrument is robust and versatile, compatible with 4-circle-diffractometer scattering geometries, and capable of carrying out CTR measurements. The stage provides a 400-mm-square platform able to support 250-kg loads and suitable to host wide-ranging sample environments. With a 1-um vertically focused incident beam, position and angular stability is crucial for reliable measurements. The vertical stage must maintain ~0.1-um stability and the large underlying “swing” tilt stage must achieve the extremely small incident angles necessary for grazing-incidence geometries where scattering depth varies exponentially near the material’s critical angle.

The detector stage will accommodate a point-counting detector and also area-detectors to collect a larger region of reciprocal space. The F and G stations will share both a large-area detector (e.g., GE amorphous-silicon) and a small, structured-scintillator CCD detector (e.g., ScintX). The GE detector will be mounted on a longitudinal linear translation stage to enable flexibility when collecting wide-angle scattering data such as for powder diffraction and large sections in reciprocal space for single crystals. The smaller CCD will collect either SAXS data or to measure the specular XRR and non-specular CTR [101].

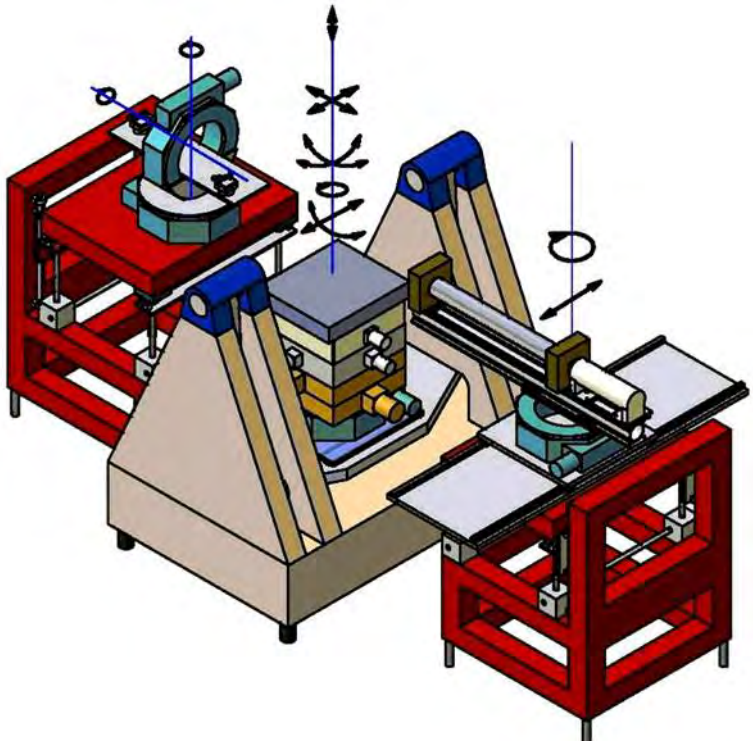

Figure 4-90: Illustration of the beam-tilting optics (for liquids), sample stages, and point-counting detector that form part of the 1-ID-F station instruments.

4.9.5.6 G-Station Instruments (Side-Branch)

At the upstream end of the G station will be a BCS table to support slits, ion chambers and one set of focusing optics (Figure 4-91). Two SMSs will be downstream, the first incorporating an air-bearing ϕ-rotation (vertical axis) for high-resolution mapping, and the second being of low-profile to allow users a large volume (~ 1 x 1 x 1 m^3) for staging complex environments. Similar to the E station, these SMSs will be combined on a rail system and will be surrounded by an overhead frame that could house a near-field detector, beam-stop, optical cameras, and spiral slit system. Downstream will be two detector stages to accommodate the shared (with F station) GE detector on ~1 m x1 m *xz*-translations and the shared ScintX detector on ~ 2 m x 2 m *xy*-translations at the downstream end of the station.

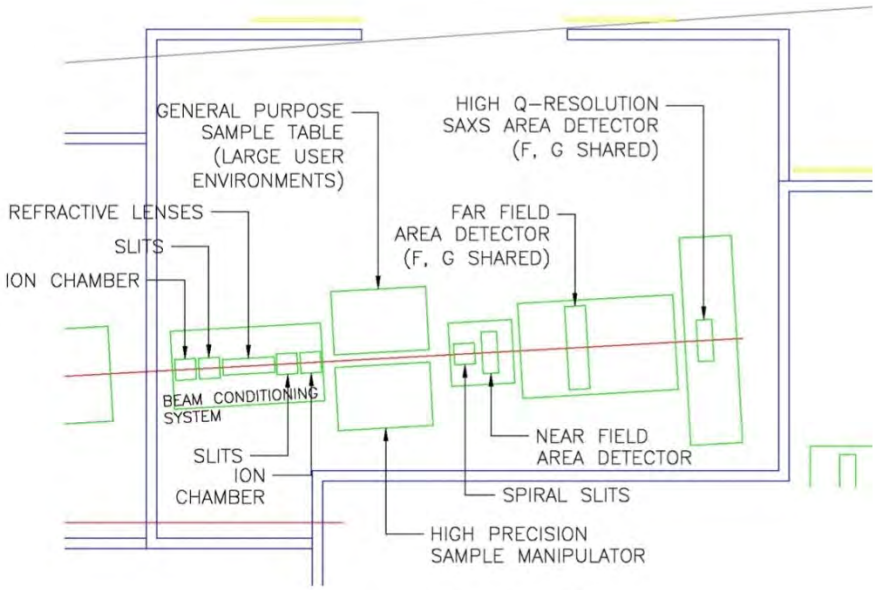

Figure 4-91: Layout plan of side-branch 1-ID-G station instruments, including the beam conditioning system but excluding radiation safety components and windows.

4.9.5.7 A High-Energy Full-Field Imaging Microscope

The 1-ID layout and optics arrangement will allow for the interesting possibility of full-field imaging. This will be accomplished by placing a specimen of interest ~1-m upstream of the lenses on the long-focal-length-optics table in A (Figure 4-82) and employing those lenses to obtain a magnified image of the specimen on an area detector in any one of the four experimental stations, reaching perhaps up to 40x in the E station with 100-nm spatial resolution. Such a setup can be developed to conduct tomographic imaging to complement HEDM measurements of ordered and deformed polycrystalline materials by seeing internal structure such as cracks, voids, and inclusions. However, there is an important operational issue that could limit this application from being frequently employed—that the experimenters' need to access to the samples in A will require closing the front-end shutter, interrupting beam delivery to the other branch as well.

4.9.5.8 Data Acquisition and Motion Control

Control of all hardware will be provided through Experimental Physics and Industrial Control Software tools using, as much as possible, components standardized by the various groups from the APS Engineering Support Division and X-Ray Science Division: Beamline Controls and Data Acquisition, Controls, Software Services, and Detectors.

4.10 X-Ray Interface Science (XIS) Beamlines

Interfacial science brings together a diverse community with interests in catalysis, oxide film growth, semiconductors, geochemistry, surface physics, corrosion, nanoscience, tribology, electrochemistry, and

the development of the next generation of energy-related technologies. One of many grand challenges in this interdisciplinary field is to understand through observation and control the organization of atoms and molecules at well-defined surfaces in complex environments. Increasingly sophisticated *in situ* x-ray methods that exploit the inherent spatial, temporal, and spectral properties of undulator radiation are being developed to meet these challenges. A dedicated X-ray Interfacial Science (XIS) facility at 28-ID of the APS will fully exploit the unique capabilities of the APS to advance our understanding of this area.

Four new beamlines, shown schematically in Figure 4-92, are proposed for this facility dedicated to interface science. These beamlines form the core of a broader development plan for a comprehensive interface science "village". The primary beamline and the first station of the first fixed-angle beamline are in the scope of Project. The second station of the first fixed-angle beamline and the other two fixed-angle beamlines are contingent additional scope (CAS). To develop a beamline design that does not preclude the CAS scope, the preliminary design of XIS includes the overall layout of the CAS stations and other beamline aspects that would be shared between stations currently in scope and CAS stations. Brief descriptions of the CAS stations are given in section 4.10.5.5.

The completed, comprehensive XIS facility will have two canted undulators producing four separate x-ray beams: one with variable energy and three with fixed angles as shown in Figure 4-93. The primary beamline will be widely tunable and will provide a flexible diffractometer instrument that will enable state-of-the-art x-ray interface scattering studies. The three fixed-angle beamlines will primarily be used at 12 keV, 20 keV, and 28 keV with use of diamond <111>, diamond <111> and Si <111> diffracting crystals, respectively. The nine planned experimental stations will house general-purpose diffractometers as well as custom-designed diffractometers to provide controlled environment and growth chambers for *in situ* real-time studies.

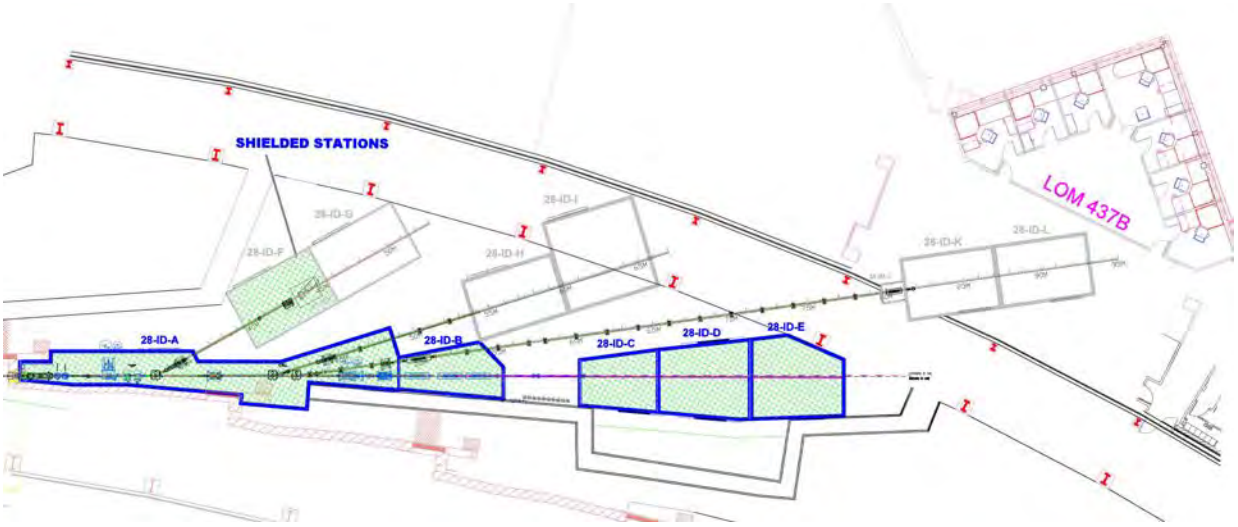

Figure 4-92: Sector layout for the XIS beamlines. Tunable experimental stations (shown blue) and fixed-angle beamline experiment stations (shown gray) complete a comprehensive interface science "village". Only the stations shown with hatched green are in the scope of the APS Upgrade Project.

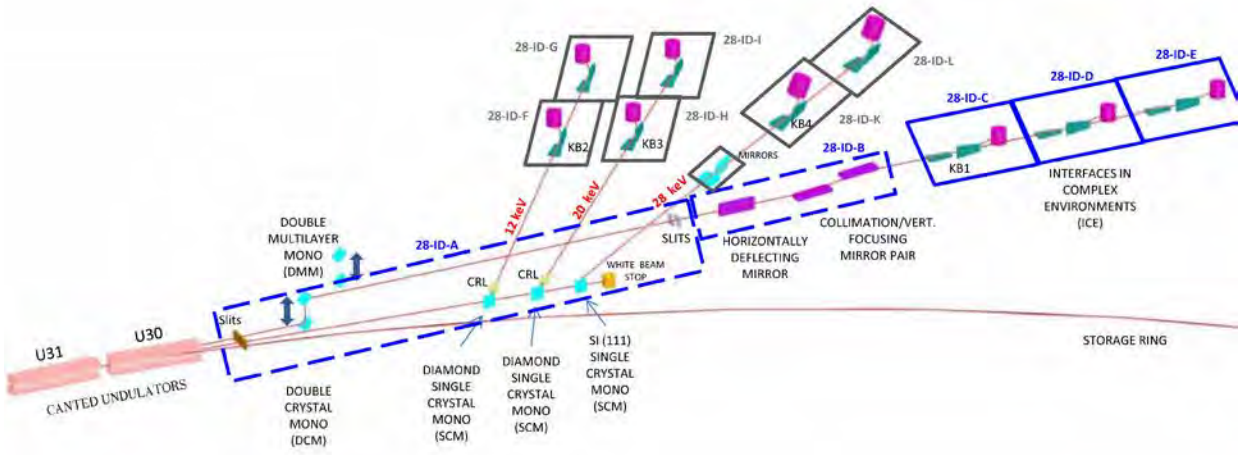

Figure 4-93: Optical schematic for the XIS sector with two undulators in canted configuration. The upstream source feeds a tunable beamline with three experiment stations. The downstream source feeds three separate and consecutive fixed-angle beamlines.

4.10.1 Scientific Objectives

Because of favorable scattering cross-sections, x-rays offer a unique opportunity to penetrate many complex environments (gas, liquid, or solid thin-film overlayers) to probe the structure and chemistry of surfaces and internal boundaries from macroscopic lengths down to the atomic level, in environments where traditional electron and other scanning probes are not applicable. High-brightness x-ray sources, such as the APS, enable these *in situ* studies, permit real-time investigations to elucidate thin-film growth mechanisms, and allow molecular-scale studies of important chemical interactions at internal boundaries utilizing scattering, diffraction, resonance and absorption, fluorescence, standing-wave, and imaging techniques.

Interfacial Reactivity in Complex Environments: Reactive interfaces are found in a broad spectrum of technical fields ranging from energy storage (e.g., batteries [102]) to electrocatalysis (e.g., fuel cells [103]), geochemistry [104], hydrogen storage, catalysis [105], and corrosion at liquid-solid /gas-solid interfaces [106, 107]. Intrinsic to each of these areas are the divergent spatial (~Å-scale to >1 μm) and temporal scales (from ~1 ps to ~1 s) [108] describing interfacial reactivity. The coupling of these disparate spatial and temporal scales can lead to unexpected complexities that are largely unexplored.

Electrochemical and Catalytic Interfaces: Understanding nanoscale mechanisms is the best way to transform a trial-and-error approach to a knowledge-based rational design approach in discovering revolutionary electrocatalysts, gas catalysts, or energy storage materials. Heterogeneous catalysis and electrocatalysis, among the energy conversion and storage processes, are pure interfacial phenomena. Therefore, the use of surface/interface x-ray techniques has been and will be critical in accelerating our understanding of nanoscale physical and chemical properties occurring at the surfaces of catalysts. This static view of catalysts dominates our understanding of them. However, recent x-ray studies point to a highly symbiotic interaction between the reactants and catalysts, where the reactants even actively modify the catalysts resulting in a significant change in catalytic activities [109].

Interfacial Geochemistry: The mineral-fluid interface is the principal site of low-temperature geochemical processes at or near Earth's surface and exerts a powerful influence on the natural geochemical cycles in our environment. Mineral-fluid interface processes effectively control the compositions of ground waters, surface waters, and to a large extent, the atmosphere. A fundamental understanding of this area is critical to the development of a predictive molecular-scale understanding of geochemical and environmental processes. Specific examples include the consequences of energy-related activities, such as subsurface CO_2 disposal by deep injection of liquid CO_2 into depleted oil and gas reservoirs, and the long-term isolation of high-level nuclear waste.

Emergent Materials' Properties at Interfaces: Interfaces are not simply the place where two materials meet, with each of them retaining its own properties. There are abrupt changes in chemical and electrostatic potentials, as well as a lattice-mismatch, that exert significant stress on the material. Ionic and electronic reconstructions can occur at the interfaces of compound semiconductor hetero structures [110] and oxides leading to the emergence of entirely new physical properties and phenomena including correlated electron behavior.

***In situ* Materials Synthesis:** There are new scientific initiatives to establish the framework needed to unite materials synthesis with *in situ* characterization, theory, and modeling in order to design and create breakthrough materials and molecules. Synthesis of new complex oxide materials are particularly promising because spatial confinement and nanoscale coupling between different epitaxial layers can result in a rich variety of physical phenomena including ferroelectricity, magnetism, multiferroicity, electronic and ionic conductivity, superconductivity, and coupled electric, magnetic, elastic, and optical properties. Whether fabricated with traditional methods or with new approaches, *in situ* time-resolved materials growth or processing x-ray studies are essential for controlling materials structure and understanding the resultant properties.

Supported Metal Nanostructures: Gaining an understanding of the behavior of materials created on the nanoscale is a new frontier in the science of materials and is important because the small size of nanoscale materials can lead to unprecedented developments in physical and chemical properties. These properties are not only fascinating from the perspective of fundamental scientific understanding, but nanostructures also present novel building blocks that can be transformative for technological applications. New electronic states [111] appear due to the quantum confinement of the conduction electrons, and this can affect the overall energetics of the nanoparticle. The interfacial energy makes a large contribution to the total energy, particularly given that the nanostructure must be supported at an interface. Interfacial effects can alter the internal structure, as well as the surface chemistry, even leading to new catalytic properties [107, 112]. Finally, all of these effects can lead to pronounced changes in the statistical mechanics and kinetic behavior of nanostructures as compared to conventional systems. Exploring these effects, which are poorly understood, will be a critical aspect of future research in nanoscience.

Scattering from Liquid Surfaces and Interfaces: Liquid interfaces are relevant to many of the energy and environmental challenges facing our nation. To address these vital needs there is currently much interest in understanding and improving processes at complex liquid interfaces. For instance, the role of interfaces in the solvent extraction of radionuclides from nuclear waste is an area of active interest. Related interfacial processes are of great importance for liquid membrane separation processes used for environmental cleanup of toxic metals. Heterogeneous chemistry at the liquid surface of sea salt aerosols controls many reactions, such as those believed responsible for depletion of ozone in the lower

troposphere at high latitudes in the spring. Monolayers of biomolecules on the surface of aqueous solutions are used to model processes such as signaling, electron transfer, and optical responses that are important for the development of biomolecular materials with novel properties. More generally, liquid interfaces provide model systems to study the self-assembly, interfacial orientation and forces, molecular interactions, and chemical reactivity of a wide range of materials. Understanding these complex processes requires x-ray surface scattering techniques because they probe molecular adsorption and ordering at the interface.

This broad range of scientific opportunities requires the development of complex experimental systems and integration with an optimally designed x-ray scattering facility. Because the demands for x-ray interfacial science capabilities are widespread, a significant effort will be made to maximize the impact of the XIS sector. The large community of users and the diversity of the envisioned specialized capabilities make it compelling to consider a large-scale facility consisting of nine experimental stations and centralized support facilities and staff.

4.10.2 Source Requirements

4.10.2.1 Spectral Requirements

The weak scattering signals from two-dimensional (2-D) interface structures require that the XIS tunable beamline has an optimized optics design and source selection. The mature XIS facility includes a large suite of instruments that exploit the x-ray brightness and hard x-ray flux of the APS. A canted undulator front end source is required to supply radiation to two independent undulator beamlines. The XIS tunable beamline requires spectral range coverage from about 4.0 to 40 keV in order to span the *K* or *L* shell absorption edges of all elements from atomic number 20 and higher. This beamline will use a 3.1-cm period undulator, which has a fully overlapping tuning curve for energies between 4.0 and 40 keV utilizing the first, third, fifth, and seventh harmonic, and provides a high-performance, brilliant source over this energy range (Figure 4-94).

The side diffracting branch beamlines use the other canted undulator source and operate at fixed angles designed for 12 keV, 20 keV and 28 keV nominal beam energy utilizing diamond <111> and Si <111> monochromator crystals. A diamond crystal as a beam splitter has been well established and it is expected that the quality of the diamond crystal will be improved even to the level of coherent scattering applications. The last branch beamline will use a Si crystal that will provide more flux than a diamond. These branch lines will utilize third and fifth harmonics as shown in Figure 4-95. It appears that a 3.1-cm (or larger) period undulator will best serve the branch line.

The choice of x-ray beam energy for the fixed-energy side branches is driven by science requirements. Liquid surface scattering, located on the first fixed-energy branch, is performed mostly using X-rays between 10-13 keV. On the other hand, most of the surface scattering experiments on the second fixed-energy branch prefer X-ray energies between 15 to 25 keV. On the third fixed-angle beamline, higher energy around 30 keV is required to allow transmission through 4 mm of quartz in the beamline windows. Using the 3rd/5th/7th harmonics of the undulator to deliver 12/20/28 keV to these fixed-angle beamlines is a compromise solution. This combination is mostly optimized for liquid surface scattering at 12 keV.

However, the brightness for the second and the third fixed-angle beamlines will be less than one can achieve from 3rd and 5th harmonics.

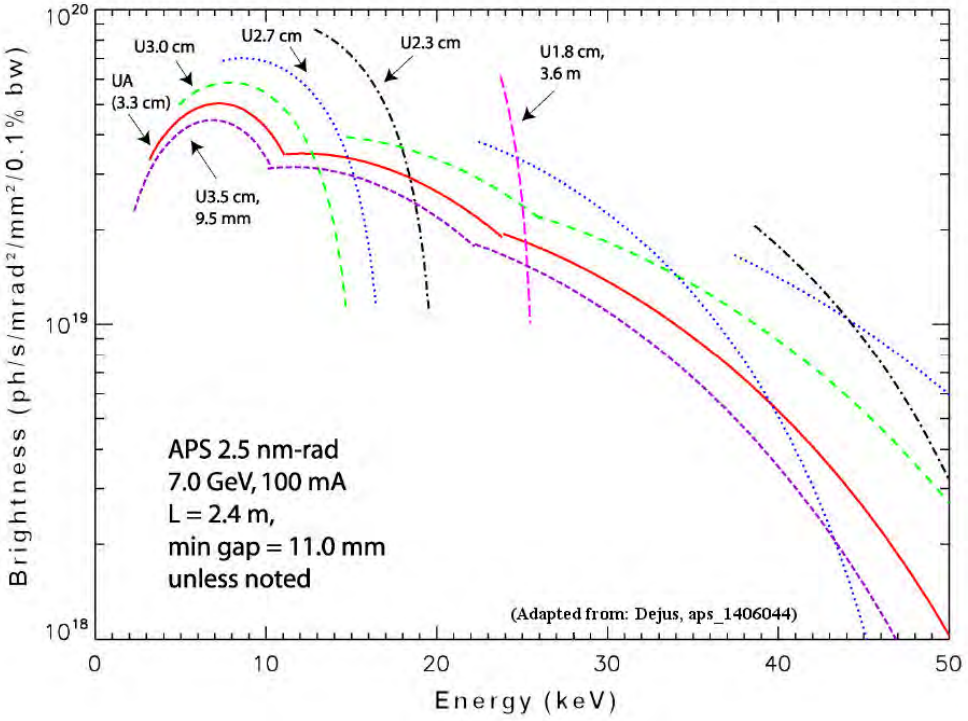

Figure 4-94: Tuning curves for various planar undulator periods at the APS.

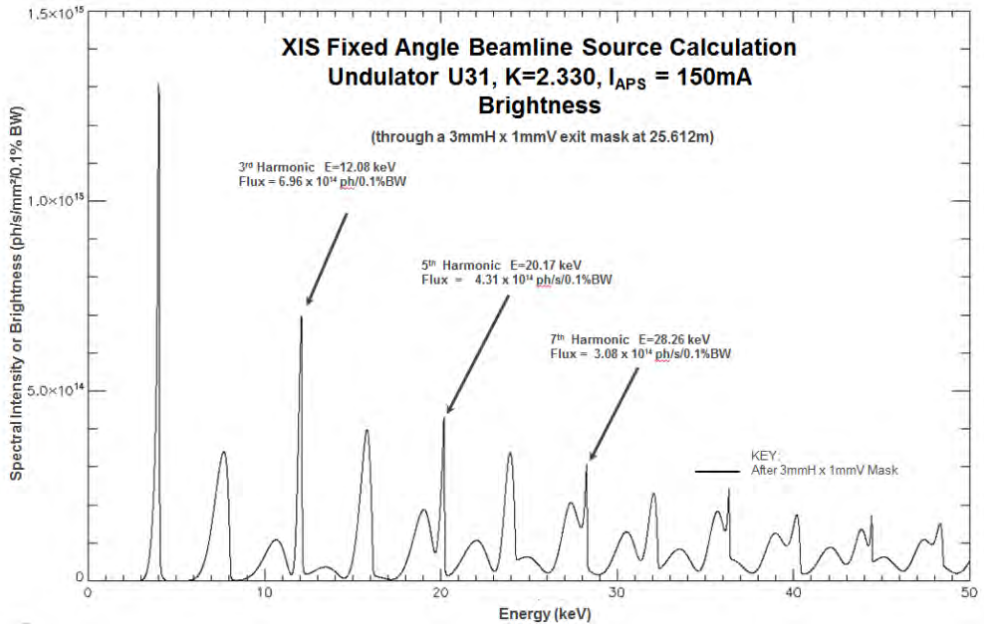

Figure 4-95: Spectral properties of undulator 3.1 at fixed K value for fixed-energy branch beamline operations.

4.10.3 X-ray Optical Layout

4.10.3.1 Tunable Beamline (4.0-40 keV)

The fully tunable beamline requires high performance over a demanding energy range. To meet the requirements of diverse scientific objectives, this beamline will use a flexible, high-performance optical design and can be operated in one of several focusing geometries as shown in Figure 4-96.

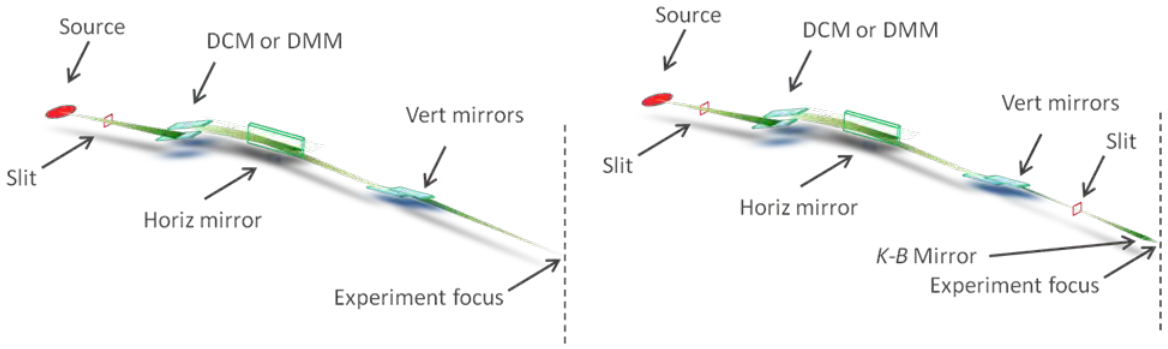

Figure 4-96: Schematic layout of the tunable beamline optical components.

The primary beamline mirrors can be set for focusing at the experiment location in any of the three enclosures with the demagnification shown in Table 4-22. This mode is often used for surface and interface diffraction experiments that require moderately small beams and high resolution. These mirrors can also be configured to collimate the beam for high angular resolution requirements. For focusing to smaller beam sizes, experiment stations will have additional focusing capability, utilizing a set of Kirkpatrick-Baez (K-B) mirrors that can be inserted as needed. For experiments such as x-ray standing wave, high collimation is required and the vertically deflecting mirror pair can be set to collimating geometry or can be removed from the beamline.

Table 4-22: Demagnification and the beam sizes, full width half maximum (FWHM). The beam sizes are estimated assuming 1 μrad figure error. The local focusing is optimized for the vertical beam sizes.

		Beamline Optics Focusing			Local K-B Mirror Focusing		
	Horiz. Demag	**Vert. Demag**	**H Beam Size (μm)**	**V Beam Size (μm)**		**H Beam Size (μm)**	**V Beam Size (μm)**
ID-C	3.4	4.1	200	90		18	4
ID-D	2.5	3.0	270	120		25	6
ID-E	2.0	2.3	330	150		35	8

4.10.3.1.1 Mirrors

To provide flexibility with regard to beam focusing or collimation, dynamically bent mirrors are used. The mirrors also provide harmonic rejection. The first mirror will use a large, horizontally deflecting surface with two material stripes. A Rh stripe will be used for energies as large as 22 keV and a Pt stripe will be used for energies up to 40 keV. The mirror meridional bend radius will be adjusted dynamically to allow horizontal focusing to any of the three experiment enclosures or to provide a horizontally collimated (parallel) beam. This mirror will be located at 49.7 m from the source and will require 2-mrad incidence. To accept the full horizontal beam of the central cone at this location will require a very long mirror length (effective length ~1.23 m). If this long mirror is prohibitively expensive or the figure cannot be as good as standard-length ones, the Project will consider a shorter length mirror (effective length ~ 0.83 m) and operate mainly at 3-mrad incidence angle. The shorter mirror would sacrifice the acceptance of the undulator central cone (the source size (HxV): 633 μm x 35 μm, the source divergence (HxV): 27 μrad x 9 μrad, all in FWHM) at high energy above 25 keV, which requires the mirror angle to be 2 mrad.

This beamline is designed to operate with vertically deflecting mirrors that improve the harmonic rejection and provide vertical focusing or collimation at the experimental locations. Dynamically bendable mirrors with four coated stripes of various materials (Si, Cr, Rh, and/or Pt) provide excellent reflectivity and harmonic rejection for two different incident angles. For example, when operated at 3.5 mrad, the mirror pair is efficient for energies up to about 22 keV. For higher energies, the mirror pair will operate as low as 2 mrad. The quantitative spectral analysis for the high reflectivity of the fundamental wavelength and harmonic rejection is shown in Figure 4-97.

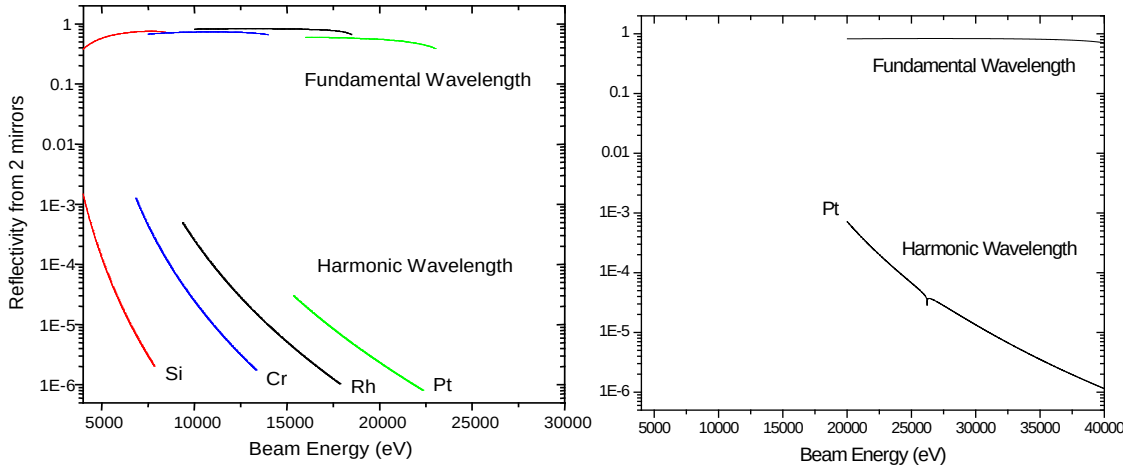

Figure 4-97: Mirror reflectivity shows that good peak throughput and harmonic rejection can be achieved over the range 4 keV-22 keV for 3.5 mrad without changing the mirror angle. Above ~22 keV, the mirrors perform well for 2.0-mrad incidence.

4.10.3.1.2 Monochromators

To select the monochromatic band pass, a cryogenically cooled Si <111> crystal pair will be used. The energy bandwidth provided by this beamline optics is well matched to the lifetime broadened core-hole width for all the *K*-shells between 4.0 and 40 keV and is substantially better than widths for the accessible *L*-shells. This is critically important for high resolution and for anomalous scattering experiments. Resonance is an important contrast mechanism often used to locate and identify atomic species at buried interfaces or at surfaces in complex liquid or gaseous environments. The monochromator will use a fixed offset design and will include robust scanning capability to facilitate resonant studies. The first, third, fifth, or seventh harmonic energies of the undulator will be used to span the operating energy range.

Because some interface science measurements are flux-limited and do not require excellent energy resolution, an additional multilayer monochromator is included in the beamline design. A pair of multilayer optics with 2-nm d-spacing (1% bandwidth) can produce an approximate 2-order-of-magnitude increase in photon flux. This dramatic enhancement in flux performance will provide significantly increased dynamic range for imaging techniques such as x-ray reflection interface microscopy (XRIM) or for studying surface kinetics/dynamics at the nanosecond time scale. If the band pass of the multilayer monochromator is too large, a post-monochromator (e.g., with Ge <111>) will be employed to cut down bandwidth.

4.10.3.1.3 Focusing Elements

Local K-B mirrors will be used for focusing the beam to a small size at the sample location. Imaging a secondary source produced by the beamline optics will permit local focusing at the sample to make the beam size as small as 18-35 μm in the horizontal direction, and between 4-8 μm in the vertical direction. Small crystalline samples or surface facets can require these small beams. This local focusing scheme will be provided by a common optimized set of K-B mirrors for the experiment stations on the tunable line.

4.10.3.2 Fixed-Angle Beamline #1 – 12-keV

Each fixed-angle beamline will operate most of the time with a fixed energy. The optical design is optimized for these fixed energies. However, flexibilities are included for operation with non-standard photon energies.

4.10.3.2.1 Compound Refractive Lenses

No mirrors are anticipated for fixed-angle beamline #1 at this time. Instead, compound refractive lenses (CRLs) will be used for collimation and focusing. A 2-D parabolic CRL with 0.5-mm radius curvature will primarily be used; all CRLs will be made of Be. The fixed-energy operation of the beamline permits use of the CRLS for focusing to any experiment location along the beamline. CRLs take up quite a small space and the cost is relatively cheaper than typical mirror systems for focusing.

The CRL focal length depends inversely on δ (decrement of index of refraction), which in turn depends on $1/E^2$. Because the focal points for 12 keV and 36 keV (λ/3) are quite different, slitting down the beam close to the focal point will accomplish some harmonic rejection. This rejection ratio is modest and on the order of 10-100. Local K-B mirrors for secondary focusing will function as harmonic rejections mirrors. Transmission through parabolic Be CRLs (radius of curvature R=0.5 mm, number of single CRLs N=12, thickness d = 30 μm) will be 72% for the upstream station.

4.10.3.2.2 Monochromators

This first fixed-angle beamline will deliver 12-keV x-rays to tandem experimental stations (ID-F and ID-G) utilizing a diamond <111> monochromator by horizontally diffracting the x-ray beam by 29.0° from the incident beam direction. This monochromator crystal must be sufficiently thin to allow high transmission of the fifth/seventh-order harmonic for use in the downstream branch beamlines. To allow 85% transmission of the 20-keV photons, the diamond crystal must be no thicker than 300 μm. The diamond monochromator crystal will be cooled with water to perform properly with the high-power beam.

4.10.3.2.3 Focusing Elements

Local K-B mirrors will be used for focusing the beam to small size at the sample location. Imaging a secondary source produced by the beamline optics will permit local focusing at the sample to make the beam size as small as 10-20 μm in the horizontal and vertical direction without losing much flux. Small crystalline samples or surface facets may require these small beams. This local focusing scheme will be provided only where when the requirement is clearly identified. A common set of small K-B mirrors will be shared between experimental stations. The dedicated mounts and control cables will be built at the stations for easy installation of the shared K-B mirrors.

4.10.4 Beamline Physical Layout

The layout for the XIS sector is shown in Figure 4-98. This assumes the XIS beamline will be located at Sector 28. The quoted locations of the beamline components are tentative.

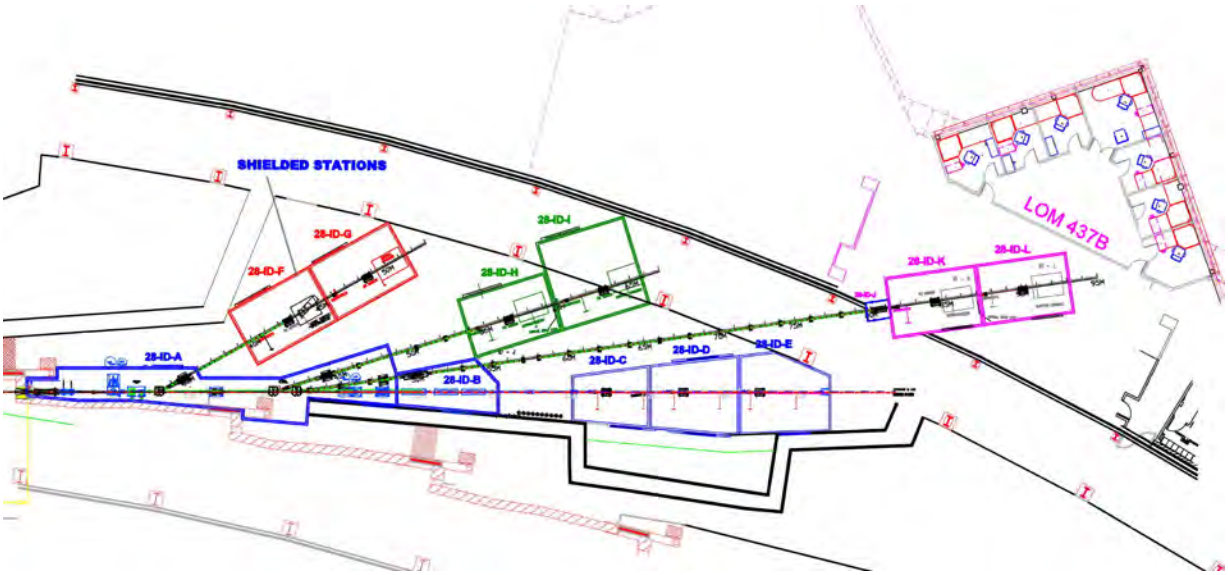

Figure 4-98: Sector layout for the XIS tunable beamline (shown in dark blue) and fixed-angle beamlines (red: branch 1, dark green; branch 2, magenta: branch 3) that complete a comprehensive interface science "village." The main (blue) XIS beamline is widely tunable from 4.0-40 keV and the fixed-angle beamlines provide 12, 20, and 28 keV beams, respectively.

4.10.4.1 Front End

A canted front end design is required for the completed XIS facility. The upstream undulator will be canted toward outboard feeding the tunable beamline.

4.10.4.2 Overall Beamline

In full operation, the overall beamline design allows four simultaneously operating experiments to be conducted while experiment preparations proceed on open stations along each branch. High capacity for experimentation and centralized support service are key to the sector mission.

4.10.4.3 General Description

There are 12 shielded stations needed to complete the XIS sector. These include 9 experimental stations on the ID port and 3 enclosures for beamline optics (a first optics enclosure plus 1 monochromatic mirror enclosure plus 1 monochromatic ministation). To permit five monochromators and independently operated shutters for the tunable and side-diffracting branch beamlines on the ID port, the Project will require an unusually large white-beam optics enclosure. The fully tunable beamline will also require separate monochromatic enclosures for the mirror assemblies.

The monochromatic experiment enclosures are each approximately 6 m L x 4 m W x 3.4 m H and will include provisions for hazardous-gas exhaust. Because the requirements of the completed XIS sector include nine experiment stations, the effective use of sector space will require planning to fully utilize the roof spaces of many or all of the enclosures. For example, whenever possible, ancillary support equipment, electronics, etc. will be located on the enclosure roofs. Because the six experiment stations on the side-diffracting branch beamlines will only accept a small bandpass at a fixed angle from the crystal monochromators, only monochromatic stations will be required.

4.10.4.3.1 Radiation Safety Aspects

Both primary and secondary bremsstrahlung radiation will be controlled and contained within the FOE, so only synchrotron radiation must be considered in the other optics and experimental stations. For this consideration, the shielding requirements include monochromatic operations with narrow bandpass optics as well as wide bandpass operations with multilayer monochromators. Only the ID-A FOE will be shielded for white-beam operations.

4.10.4.3.2 Vacuum System

The beamline and all components will be designed for ultrahigh vacuum compatibility. This assures that reliable vacuum operations can be realized and that the beamline optics will be protected from unacceptable contamination. The vacuum control and monitoring will be included in an equipment protection system.

4.10.4.3.3 Data Acquisition and Motion Control

Detectors and software development will enhance scientific productivity. Specialized 2-D detectors are required for higher resolution, throughput, sensitivity, and high-energy photons. There is demand for improved user-friendly computer software for image processing (acquisition, visualization, and post-processing) and data manipulation and analysis. The XIS beamlines will also exploit development of new algorithms for grazing-incidence small-angle x-ray scattering coherent diffractive imaging, coherent Bragg rod analyses, and other direct methods for general users. Integration of specialized gas handling with the data acquisition control is essential for safe, productive experiments with the ICE (interfaces in complex environments) instrument. Also essential similar integration of the data acquisition control software with the specialized growth chambers.

4.10.4.3.4 First Optics Enclosure and Infrastructure, Major Components

Table 4-23 lists the key components located in the FOE together with the distance from the source.

Table 4-23: FOE components.

Component	Approx. Distance from Source*
Exit Mask	25.61 m•
Window or differential pump	25.80 m•

Component	Approx. Distance from Source*
Collimator(s)	26.07 m†
White-Beam Slits – Tunable Energy Branch	26.88 m†
White-Beam Slits – Fixed-Angle Branch	27.39 m †
Cryo-Cooled Monochromator	31.35 m•
Cryo-Cooled Monochromator, (Multilayer) DMM	32.50 m•
White Beam Stop – Tunable Line	34.00 m†
X-Ray Mono-Beam Diagnostics – Tunable Energy Branch	35.60 m•
Side Branch 1 Horizontal Diffracting Monochromator	34.40 m•
[Note: Side Branch 1 Meter Marks Diverge From Tunable Branch At Horizontal Diffracting Monochromator]	
Side Branch 1 Be Window (Optional)	35.00m•
Side Branch 1 CRL Optics	35.20 m•
Side Branch 1 Beam Diagnostics	38.00 m†
Side Branch 1 Shutter	39.00 m†
Collimator(S) – Both Beamlines	38.50 m•
Collimator (Tunable Branch) & White-Beam Stop (Fixed Angle)	45.00 m•
X-Ray Diagnostics – Tunable Branch	46.00 m•
Mono Slits – Tunable Branch	47.00 m†
Monochromatic Shutter – Tunable Branch	48.10 m†
Mirror, Focusing, Monochromatic, Horizontal (In) Deflecting	49.70 m•
Mirror, Focusing, Monochromatic, Vertical (Up) Deflecting	51.80 m•
Mirror, Collimating, Monochromatic, Vert.(Down) Deflecting	53.60 m•

*Note: Components referenced with respect to 0 m at center of straight section. Distances to downstream extent (†) or optical element center (•) of the respective component. Locations are tentative.

4.10.4.3.5 Windows

A standard window assembly for a canted front end undulator beamline is required at 25.8 m to separate the beamline vacuum from the storage ring vacuum. This white beam window can be removed at the mature stage of beamline operation. Windowless operation will enhance the transmission of low energy X-rays. Additionally, for each of the fixed-angle branch beamlines, windows will be placed at the end of the branch beamline just before the experiment apparatus or diffractometer.

4.10.4.3.6 Slits

Independently operated white-beam slits are required on each of the two canted lines. A standard L-31 canted white-beam slit assembly similar to that installed in Sector 34 will allow independent selection of the radiation cone for the tunable beamline and for the fixed-angle beamline(s). The slits are located at 26.88 m and 27.39 m for the fixed-angle and tunable lines, respectively.

4.10.4.3.7 Collimators

Bremsstrahlung collimators and stops are required to safely operate the beamlines. The collimation at 26, 38.5, and 45 m will limit the required extent of the bremsstrahlung stop located near the end of the ID-A enclosure at 48.3 m.

4.10.4.3.8 Shutters/Stops

A monochromatic shutter is located at the end of the FOE at 48.1 m. It is important to design the facility such that each of the tunable and side-diffracting branch beamlines can operate independently. This requires that the FOE (ID-A) incorporate four separate shutters – one on the tunable beamline and one on each of the three side diffracting branch beamlines. Each shutter is monochromatic, designed for an undulator beamline. The sequential experiment enclosure design requires that a movable beam stop be incorporated in the downstream wall of the upstream enclosure. This will permit access to the downstream enclosure while x-rays are permitted in the upstream station.

4.10.4.3.9 Monochromators

Tunable-Branch Double-Crystal Monochromator: The monochromator will use a fixed offset design and will include robust scanning capability to facilitate resonant studies. A cryogenically cooled Si <111> crystal pair will be used. To achieve reliable operations over a wide energy range (4.0-40 keV) will require excellent mechanical design with adjustments for the translations, pitch, and roll of each crystal. Instrumentation and actuation for feedback control is required.

Tunable-Branch Double-Multilayer-Monochromator (DMM): The multilayer monochromator included in the beamline design uses a pair of multilayer optics with 2-nm d-spacing (1% bandwidth) that can produce an approximate 2 order-of-magnitude increase in photon flux. The multilayer pair will use Si substrates and be cooled cryogenically in order to address the power loading from the undulator source. The mechanical design will allow for operations between 10 keV and 40 keV. Adjustments for the translations, pitch, and roll of each multilayer are required as well as instrumentation and actuation for feedback control.

The side-diffracting monochromators are of similar design. Adjustments of the crystals for pitch and roll are required as well as instrumentation and actuation for feedback control. Each monochromator will be water or cryogenically cooled to address considerations of power loading from the undulator source.

4.10.4.3.10 Mirrors

Mirror optics are attractive as highly efficient achromatic focusing elements and will be used widely throughout the XIS sector beamlines. On all the branch lines, there will be dynamically bent mirrors along the beamline and/or in the experiment enclosures as listed in Table 4-24. Also included are the approximate location, the size of the optical components necessary to take the undulator central cone (4 x RMS size), and the bending radius required.

Table 4-24: Mirrors required for the XIS beamlines.

		Mirror	Location	Horiz. Size (mm)	Vert. Size (mm)	Minimum Bending Radius (Km)
Tunable Beamline						
		Horizontal Focusing Mirror	49.7 m	830-1250		5.9
		Vertical Focusing Mirror	51.8 m		700	5.1
		Vertical Reflecting Mirror	53.6 m		700	
	ID-C	K-B Mirror Assembly A (Shared)	62 m	200	85	(H/V) 0.2/0.15
	ID-D	K-B Mirror Assembly A (Shared)	67 m			
	ID-E	K-B Mirror Assembly A (Shared)	72 m			
Fixed-Angle Beamline #1 (12 KeV)						
	ID-F	K-B Mirror Assembly B (Shared)	43.7	185	50	(H/V) 0.2/0.15

4.10.4.3.11 Compound Refractive Lenses

Compound refractive lenses are ideally suited as focusing elements for fixed-angle beamlines operating at fixed energies because they are highly chromatic and function optimally with long focal lengths. 2-D parabolic CRLs with a 0.5-mm radius curvature and a 1.4-mm aperture will be the primary lens utilized.

Each CRL module has multiple sets of CRLs and requires linear actuators to bring sets of CRLs in and out of the beam in order to change the focusing distance depending on which station is active.

Table 4-25 shows total number of CRL elements required for the focusing condition at each experiment station. Commercially available CRLs are limited in the selection of radius of curvature. However, utilizing CRLs with 0.5-mm radius of curvature means beams can be focused close to the actual sample spots by varying number of elements.

Table 4-25: The total number of CRL elements required to focus x-rays at each station. The calculated image sizes are for the horizontal direction. The focus distance is the actual distance to the focused point from the CRL.

Energy (KeV)	Radius of Curvature (mm)	Total Number of Elements	Focal Distance (m)	Focus Distance (m)	Image Size (micron, FWHM)	Efficiency	Station	Actual Distance to Sample (m)
12	0.5	12	8.8	11.7	153	72%	F	11
12	0.5	9	11.7	17.5	243	77%	G	16.6
20	0.5	26	11.17	17.79	341	70%	H	17.2
20	0.5	17	17.08	39.7	765	78%	I	41.3

4.10.4.3.12 Diagnostics

Beamline diagnostics are required to locate and optimize the beam at various points along each beamline. On the tunable beamline, a diagnostic and feedback module will be located downstream of two monochromators to visualize the monochromatic beam and measure the flux. This flux measurement can be used for the feedback control on the second-crystal tilt. Also, on the fixed-angle lines, a diagnostic module will be located downstream of each monochromator to visualize the monochromatic beam and measure the flux. There is no need for feedback functions for these modules if a single-bounce monochromator is used. Further diagnostics will be provided at the experiment stations for monitoring of beam positions and intensities. For the fixed-angle beamlines, this beam position monitor at the experiment station can be used for the two-theta feedback of the single-bounce monochromator.

In addition to intensity monitors, such as ion chambers and beam position monitors, sets of filters and slit assemblies will be provided to further prepare the x-ray beam at each experiment station.

4.10.4.4 Experimental Station D: Instrument for Complex Environments (Tunable Beamline)

The experimental station instrumentation included in the Tunable Beamline Project is a versatile diffractometer that is equipped for interface studies in complex environments and chemistries. The ultimate goal is for these environments and chemistries to reproduce real situations such as in fuel cells and catalytic processing chambers. The basic layout of the instrument, shown in Figure 4-99, incorporates a modular architecture. The modular aspect is important because different chemistries can be highly incompatible and yet a vibrant user program requires the flexibility to rapidly switch between different environments. There are three main components to the instrument design that must be integrated together: the diffractometer, the gas and liquid handling systems, and environmental chambers. Appropriate gas/liquid monitoring and alarm systems are required to assure safe operation of the instrument.

Measurements and analysis of x-ray reflectivity and crystal truncation rods have been essential techniques for the structural studies of interfaces. This will be true for this instrument, but there are new techniques being developed. The most important techniques are coherent diffraction and diffraction imaging of surface/interface. This diffractometer will be built to satisfy the requirements of these new techniques.

The Interfaces in Complex Environments (ICE) instrument will have two independent detector arms. The first will be a high-resolution detector arm in a traditional diffractometer configuration. The second detector arm will be mounted on a support decoupled from the sample goniometers and located either on the floor or on the enclosure roof to maximize the accessible parameter space and so that it can be moved out of the way to allow easy access to the sample-chamber environment. The second detector arm will have a variable sample-to-detector distance far longer than one can change manually in a conventional diffractometer. The decoupled detector arm will enhance the stability of the sample orientation/position with respect to the upstream optics. On the other hand, a traditional detector arm, which is coupled mechanically to the sample, will be necessary when the stiffness between the detector and sample is more important, such as in diffraction imaging.

The sample and chamber mount will utilize a combination of two high-resolution goniometers to provide full 360° motion about the vertical and horizontal axes along with a high-load hexapod for sample

positioning The hexapod will handle large-sample chambers (up to 200 kg), with the ability to tilt the chambers by ±15° and translate them up to ±25-mm vertically and up to ±50-mm horizontally. The hexapod mounts to either of the high-load diffractometer circles so that it enables wide access to the sample reciprocal space. The vertical axis geometry for the goniometer circle has the benefit of the higher load capacity for the circle and the hexapod. On the other hand, the horizontal geometry allows x-ray reflectivity measurement in a large q-range. As nanomaterials have drawn more attention from the surface/interface community, the location of the sample should stay locked to the beam during the motion of diffractometer. It is desired that the locational stability be under 1μm in 1^0 of the sample rotation.

The XIS facility will provide two sample chambers for high and low x-ray energy studies, small environmental cells for heating and cooling, and a series of flow cells for surface studies in aqueous solutions. One chamber will have Be windows for ultra-high vacuum, low background, and low photon energy measurements along with provision for optical and conductivity measurements. A second chamber will have a quartz tube reaction zone for chemical reaction studies. Both chambers will have heaters for use in reducing or oxidizing atmospheres at temperatures up to 1000° C. The ICE instrument is capable of supporting a wide range of specialized environment chambers (e.g., user-supplied electrochemical cells and specialized atomic layer deposition chambers).

The sophisticated gas/liquid handling system provides a flexible choice of sample environment and computer control of gas composition so that complicated exposure sequences can be efficiently implemented. This system will have channels for either directly flowing gasses or for flow-employing bubblers. The reactive gas and bubbler channels have matched flow so that nonreactive and reactive streams can be easily switched between a vent line and a line to the chamber. Active pressure balancing between the vent and chamber lines will maintain uniform flows. The gas plumbing system will have two gas cabinets to separate incompatible chemistries for safety purposes. Permanent lines for standard gasses (Ar, He, N_2, O_2, H_2, CO) along with four channels for experiment specific gasses are planned.

A separate liquid-handling system will control the composition and flow of liquids to the solid-liquid interface cell. To facilitate the experiment procedures during many of the solid-liquid interface studies, wet chemistry lab capabilities such as a fume hood will be built close to the station. The diffractometers will be built to withstand chemical spills.

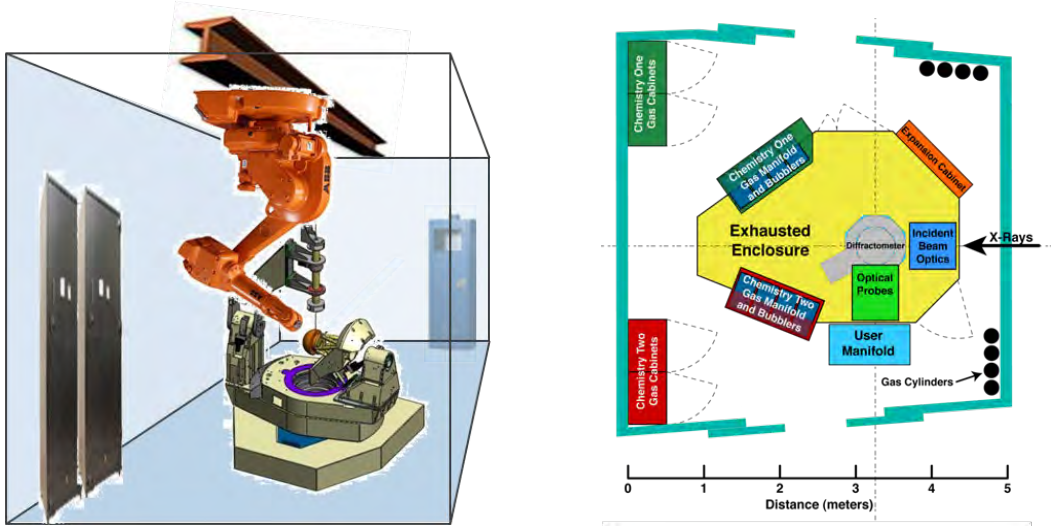

Figure 4-99: (Right) Concept for a general diffractometer with decoupled detector and sample motions for improved stability and flexibility. A decoupled detector arm, such as robotic actuation will improve area detector flexibility for studies of interfaces in complex environments. (Left) Layout of the ICE experimental station with gas/liquid handling and secondary enclosure.

4.10.4.5 Experimental Station C (Tunable Beamline): X-ray Reflection Interface Microscope

The instrumentation for the X-ray Reflection Interface Microscope will be supplied by users. It is described here for completeness. There are powerful advantages to combining reciprocal space information from x-ray scattering measurements with high-spatial resolution real-space imaging. For example, direct observations during new-materials synthesis can be used to reveal where islands nucleate (at defects or step edges) and how they grow. Imaging elementary topography in real space demonstrates the ability to probe the behavior of individual structures. This capability has been demonstrated with XRIM (Figure 4-100) [113]. XRIM is similar to traditional full-field optical and x-ray microscopes, but uses the weak, interface-sensitive, specular reflected or crystal-truncation-rod x-ray beams (with a reflectivity of $<10^{-5}$) to create an image. Since the reflectivity signal is interface specific, this leads to the ability to directly image interfacial topography and structures in *in situ* environments during growth or processing. An optimized XRIM system is being proposed by the group that invented the technique. It is anticipated that there will be a large demand for the XRIM instrument from general user societies. The XRIM is one of the techniques to take advantage of the larger energy band path from the double-multilayer monochromator. However, a post-monochromator will be used to bring down the band path from 1% to 0.1% for optimum performance.

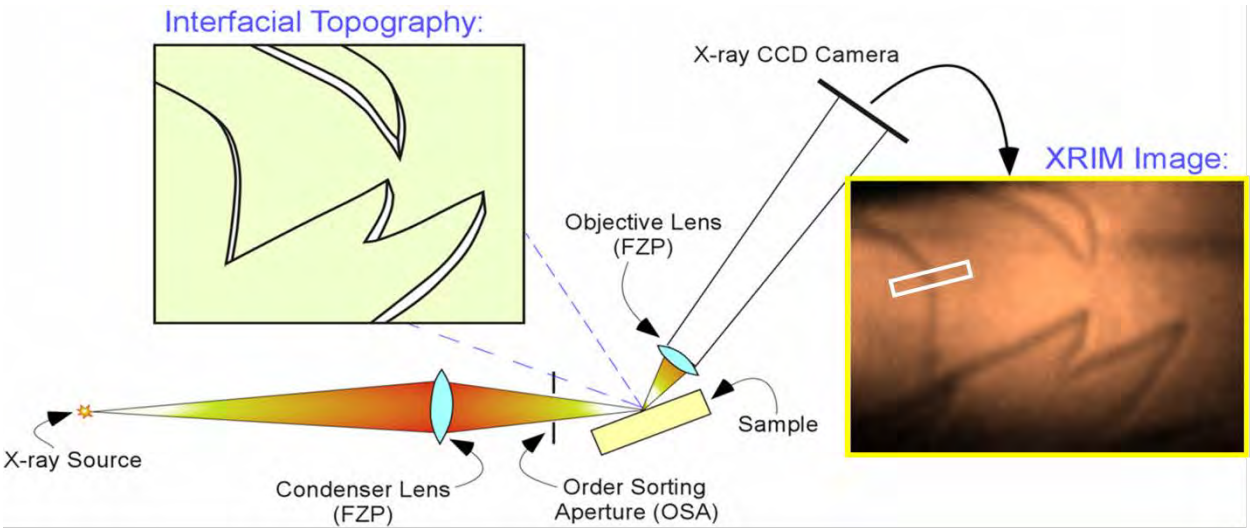

Figure 4-100: A schematic diagram for an XRIM system.

4.10.4.6 Experimental Station E: Oxide Molecular Beam Epitaxy (Tunable Beamline)

The strong candidate instrumentation to fill the third experiment station (E) on the tunable beamline is an oxide molecular beam epitaxy (MBE) system. The instrumentation for Oxide MBE will be supplied by users. It is described here for completeness. The oxide MBE community has long called for a dedicated facility and is now planning to build a fully functional MBE system (See Figure 4-101) dedicated for x-ray structural studies.

Oxides are in the midst of a renaissance. Not only have they become vital to major industries such as the semiconductor industry, but the electron interactions in many oxides give rise to incredible and poorly understood phenomena. While there are many ways to grow epitaxial oxide films, oxide MBE has the advantage of being able to prepare films of the highest quality and with unparalleled layering control at the atomic-layer level. This includes phases and perfection that are not achievable by other techniques. Such control has also been demonstrated by MBE for the synthesis of oxide superlattices with atomic-scale thickness control and abrupt interfaces, and the construction of new oxide phases with atomic layer precision. These advances in thin-film deposition technology have made it possible to customize oxide heterostructures with subnanometer precision.

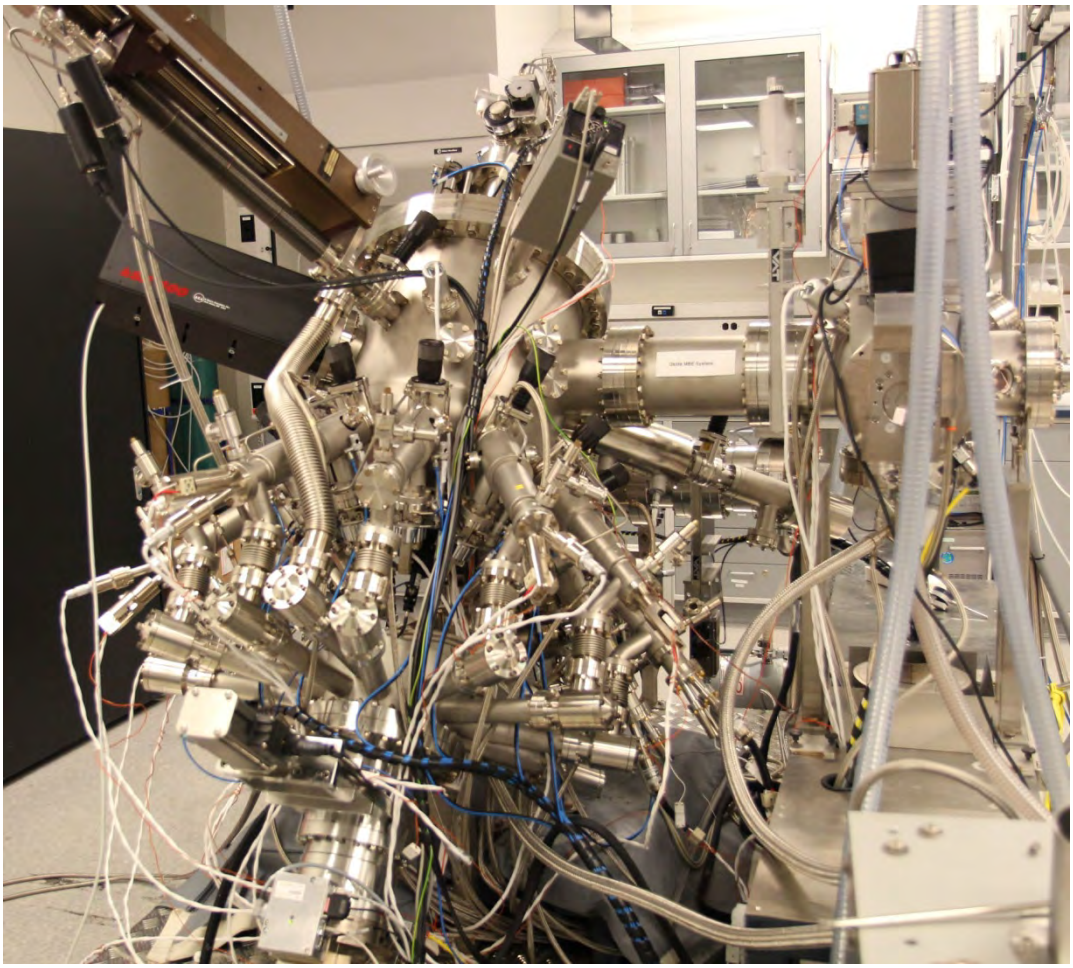

Figure 4-101: A fully fledged oxide MBE system at Argonne's Center for Nanoscale Materials.

4.10.4.7 Experimental Station F: Liquid Surface Scattering (Fixed-Angle Beamline)

The fixed-angle beamline #1 will accommodate the liquid surface scattering program. Outside the scope of the APS Upgrade, a new liquid surface scattering instrument will be provided for this experimental station.

4.10.4.8 Instruments

The proposed instruments for some of the stations were described in previous sections. The completed comprehensive XIS facility will provide a large suite of state-of-the-art instruments for XIS, spectroscopy, and microscopy. The tandem design for the experiment stations on each beamline can accommodate a general diffractometer in the upstream experimental enclosure from an operational perspective. However, a high-throughput instrument with a large user base such as PLD and oxide MBE also can be located in the upstream stations. General diffractometers will mount small, easily detachable, standardized sample environmental cells and chambers. Infrastructure will be provided for reactive gases

and corrosive liquids. Each instrument will permit high-resolution measurements and incorporate rapid-scanning features. New 2-D detectors, local focusing capabilities, and multiple detector schemes will be integrated with each instrument.

The completed comprehensive XIS sector will include nine experimental enclosures. The specific instruments and designs are expected to result from partnerships with user groups that define the science and instrument requirements and capabilities for each specialized experimental station. A possible suite of instruments is included in Table 4-26. Interfaces in Complex Environments is the only potential instrument included before that is included in the Project scope.

Table 4-26: XIS experiment stations emphasis. Note that these potential instruments are not all included in the scope of the Project.

Potential Instrument
X-ray Interface Microscopy
Interfaces in Complex Environments
X-ray Oxide Molecular Beam Epitaxy
Interface Diffraction/Scattering
Materials Synthesis (PLD/Laser MBE growth)
Interface Diffraction/Scattering for Liquid-Solid Studies
Multi-technique Ultrahigh-Vacuum Surface Chamber
Interface Diffraction/Scattering for Nanoscience
Materials Synthesis (Hybrid ALD/MBE or MOCVD)

4.10.5 Additional Information

4.10.5.1 Safety Requirements

Many experiments in the XIS sector will use toxic, corrosive, or noxious gasses that require adequate exhaust and monitoring infrastructure. Special ventilation and monitoring will be provided. Toxic gas ventilation will be installed in three groups. On the experimental floor, three experimental stations on the tunable beamlines will go on one toxic gas ventilation system and be connected to a strobic air exhaust fan mounted on the roof of the experiment hall. Another strobic exhaust fan will be used for four experimental stations on the first and second fixed-angle beamlines. All these toxic-exhaust lines will be built of stainless steel and have sound attenuation systems. The control for these exhaust systems will be connected to the existing APS Metasys system. The remaining two experimental stations on the third fixed-angle beamline will be located in the LOM and will be connected to the wet-lab exhaust system.

4.10.5.2 Conventional Facilities Requirements

The requirements for the XIS beamlines conventional facilities are common to other existing beamlines. Electricity, chilled water, distilled water, compressed air, and liquid nitrogen distribution are required. There will be multiples of gas cabinets for flammable gases. These gas cabinets will be equipped with sprinklers. The ventilation system for the toxic gasses is mentioned in the above section.

The XIS beamlines require control room spaces located near the respective experiment enclosure. Each control room will incorporate fire protection smoke detectors and sprinklers, and will conform to all Argonne requirements. Each control room will also be integrated with the APS heating, ventilation, and air conditioning system.

4.10.5.3 Vibration Isolation and Control

Mechanical-vibration conduction from the utility flows will be isolated to keep the propagation of the vibration to the optical elements and experiment instruments. This may require separate supports or damping mechanisms for utilities such as water, air, and liquid nitrogen, and will be determined during Final Design. Some of the experiment stations at the fixed-angle beamlines may house a scanning tunneling microscope or an atomic force microscope, which require more stringent vibrational and acoustical isolation.

4.10.5.4 Centralized Supporting Facilities

Analysis/preparation laboratory space is also required in the LOM adjacent to the sector. Off-line characterization and sample preparation are recognized as critical to the scientific programs for the XIS facility. Optical microscopy, STM/AFM, and *in situ* scanning electron microscopy in sample preparation chambers are considered essential. Traditional electron probes such as x-ray photoelectron spectroscopy and Auger electron spectroscopy are also needed for surface characterization. These analysis capabilities in the laboratory space will complement x-ray measurements and provide timely feedback to process-oriented experiments, thus improving the effectiveness of the facility for the synthesis and processing of new materials. The fully developed XIS facility will require support laboratory and office facilities for the staff, users, and partner-user groups that will operate the general and specialized experimental station instruments.

4.10.5.5 Contingent Additional Scope

The fixed-angle beamlines #2 and #3 are not in the baseline scope of the Project; they are described briefly here and are contingent additional scope (CAS). Additionally, the second experiment station (G) on the fixed-angle beamline #1 is contingent additional scope.

4.10.5.5.1 Fixed-Angle Beamline #2 – 20-keV [CAS]

Compound Refractive Lenses

Requirements for the focusing optics are the same as for the fixed-angle branch #1 (4.10.3.2), although the exact design of the CRLs will be different due to the difference in the location of focusing elements and the sample.

Monochromators

The fixed-angle beamline #2 monochromator diffracts a large fraction of the undulator fifth harmonic peak. A diamond <111> crystal will be employed in Bragg-diffracting geometry with a deflection angle of approximately 17.4° from the incident beam direction.

Focusing Elements

Local K-B mirrors will be used for focusing the beam to a small size at the sample location. Imaging a secondary source produced by the beamline optics will permit the local focusing at the sample to make the beam size as small as 10-50 μm in the horizontal and vertical direction without losing much flux. Small crystalline samples or surface facets may require these small beams. This local focusing scheme will be developed when the requirement is clearly identified.

4.10.5.5.2 Fixed-Angle Beamline #3 – 28-keV [CAS]

Mirrors

A pair of dynamically bent, Pt-coated K-B mirrors, located at 50 and 80.6 m, will be used to focus (or collimate) the beam and to provide adequate harmonic rejection. The mirrors will be large enough to accept the entire central cone of radiation. The location of the vertically focusing mirror is now quite close to the tandem experiment stations. These stations are located at the long distance (85 m /91 m) from the source. There are both benefits and trade-offs in putting the vertically focusing mirror close to the diffractometer. The demagnification factor increases and it produces a very small vertical beam size (20 to 50 μm). The tradeoff is increased divergence. The vertical divergence will be 70 and 140 μrad instead of 9.2 μrad for 1:1 demagnification. The divergence can be reduced by unbending the mirror and sacrificing the narrow vertical beam size. However, the enlarged divergence can be useful for some experiments. It will project the longer length of crystal truncation rods. A small, vertically reflecting steering mirror (K-B mirrors can also perform this function) will be located in each experiment station to level the beam.

Monochromators

The final side-diffracting branch beamline will deliver x-rays at approximately 8.1° from the incident beam direction. This results in 28-keV x-rays when utilizing a Si<111> monochromator and the seventh harmonic of an optimized undulator source. A single multilayer monochromator can be used in place of the crystalline Si<111>. If a multilayer monochromator with 1-nm d-spacing becomes available, 8.8-keV x-rays can be delivered to the stations. Multilayer optics is usually coated on Si and the same liquid nitrogen cooling can be used as the crystalline monochromator.

Focusing Elements

Local K-B mirrors will be utilized for focusing the beam to a small size at the sample location. Imaging a secondary source produced by the beamline optics will permit the local focusing at the sample in order to make the beam size as small as ~50 μm in the horizontal direction and less than 10 μm in the vertical direction. Small crystalline samples or surface facets might require these small beams. This local focusing scheme will be developed when the requirement is clearly identified.

4.10.5.5.3 Additional Major Components in First Optic Enclosure [CAS]

Table 4-27 lists the key components for the contingent additional scope, located in the FOE together with the distance from the source.

Table 4-27: Contingent Additional Scope FOE components.

Component	Approx. Distance from Source*
Side Branch 2 Horizontal Diffracting Monochromator	40.50 m•
[Note: Side Branch 2 Meter Marks Diverge From Tunable Branch At Horizontal Diffracting Monochromator]	
Side Branch 2 Be Window (Optional)	41.10 m•
Side Branch 2 CRL Optics	41.50 m•
Side Branch 2 Beam Diagnostics	43.70 m•
Side branch 2 Shutter	44.40 m†
Side Branch 3 Horizontal Diffracting Monochromator	42.00 m•
[Note: Side Branch 3 Meter Marks Diverge From Tunable Branch At Horizontal Diffracting Monochromator]	
Side Branch 3 Be Window (Optional)	43.15 m•
Side Branch 3 Beam Diagnostics	43.75 m•
Side Branch 3 Shutter	48.00 m†
Side Branch 3 K-B Mirrors (Horizontal Inboard Refl.)	50.00 m†
Side Branch 3 K-B Mirrors (Vertically Up Refl.)	80.56 m†

*Note: Components referenced with respect to 0 m at center of straight section. Distances to downstream extent (†) or optical element center (•) of the respective component. Locations are tentative.

4.10.5.5.4 Additional Mirrors [CAS]

Mirror optics is attractive and will be used throughout the XIS sector beamlines under the contingent additional scope. These are listed in Table 4-28.

Table 4-28: Mirrors required for the CAS portion of the XIS beamlines (CAS).

		Mirror	Location	Horiz. Size (mm)	Vert. Size (mm)	Minimum Bending Radius (Km)
Fixed-Angle Beamline #1 (12 Kev)						
	ID-G	K-B Mirror Assembly B (Shared)	49.3			
Fixed-Angle Beamline #2 (20 Kev)						
	ID-H	K-B Mirror Assembly C (Shared)	55.9	230	32	(H/V) 0.23/0.15
	ID-I	K-B Mirror Assembly C (Shared)	61.9			
Fixed-Angle Beamline #3 (28 Kev)						
		Beamline K-B Mirror	50/80.6 m	1110(840)	670	(H/V) 15.2/1.6
	ID-K	K-B Mirror Assembly D (Shared)	81.1 m	450	-	(H) 0.18
	ID-L	K-B Mirror Assembly D (Shared)	86.9 m			

4.10.5.5.5 Experimental Stations G and H (Fixed-Angle Beamline) [CAS]

Experimental station G is located at the downstream end of the first fixed-angle beamline. The strategy of the tandem station is to have a more complex instrument in the downstream station and a less complex, general purpose instrument in the upstream station. This arrangement will allow longer preparation time for the more complex downstream instrument utilizing the uninterrupted access to the experiment station.

Experimental station G will host one of the instruments provided through user partnerships. One emphasis of the XIS sector is materials synthesis. Pulsed laser desposition (PLD), atomic layer deposition, and chemical vapor deposition are some of the most popular tools for the discovery of new materials and also have a large society of general users. This type of dedicated instrument for materials synthesis will be located in experimental station G and serve the partner users and also general users.

Experimental station H is the upstream one of the tandem stations on the fixed-angle beamline #2. This is a place for a general diffractometer. A versatile diffractometer will be provided together with sets of detectors, e.g., a scintillation detector, a photon counting pixel detector such as a Pilatus-II, and a spectroscopic energy-dispersive detector.

4.10.5.5.6 Experimental Stations I, K, and L (Fixed-Angle Beamline) [CAS]

Experimental station I is the downstream experimental station among the tandem stations on the second fixed-angle beamline. It spans the boundary of the experiment floor and the hallway. For vibrational isolation, the concrete base for the station will be rebuilt. This experimental station is designed to be wider than other experimental stations to accommodate extended capability instruments including a

scanning tunneling microscope/atomic force microscope (STM/AFM). Thus, the concrete base will satisfy the requirements to achieve atomic resolution with a STM/AFM. The experimental stations K and L are outside of the experimental floor. They span between the hallway and the laboratory/office module (LOM) space. The base concrete will be rebuilt for the stability of the experimental station. There will be a small enclosure, J, just upstream of experimental station K to house a vertically focusing mirror. The site preparation will include the base for the enclosure J.

Wide-band-path x-ray beams will be also available to the experimental stations K and L through a multilayer monochromator. Real-time experiments on surfaces and interfaces are usually photon flux limited in terms of time resolution. With a 1 % band path, 2 orders of magnitude improvement of the time resolution can be expected. For example, the measurements of surface x-ray diffraction transients during PLD processes reveal that the elementary processes of interlayer transport and crystallization occur on a time scale that is faster than the microsecond range resolution used in current experiments and much faster than previously measured utilizing reflection high-energy electron diffraction and *in situ* x-ray diffraction. These results clearly illustrate that some of the most fundamental questions related to the controlled growth of materials remain unanswered and require time-resolved diagnostic tools to probe the growth surface at the shortest time scales possible. The 2 order-of-magnitude increase in the flux will extend the transient measurements below the microsecond regime and allow time-resolved scattering from individual (subnanosecond) synchrotron x-ray pulses. This will permit exploration of the underlying physics of this critical, ultra-fast phase of PLD, and will provide additional insight on the role of energetic species not just in PLD growth but in epitaxial thin-film growth in general.

Metal organic chemical vapor deposition/atomic layer deposition (MOCVD/ALD) or their hybrids require the use of quartz windows for the aggressive gasses they use. For good penetration, the 28-keV line is optimal for these techniques.

4.11 Sub-Micron 3D Diffraction (S3DD)

The Sub-Micron Three-Dimensional Diffraction (S3DD) beamline is an upgraded insertion device (ID) beamline to be developed at Sector 34. Dedicated X-ray polychromatic and monochromatic nanofocusing platforms will be constructed. Canted undulators will allow for simultaneous and independent use of microbeam diffraction and nanoscale diffraction facilities [114].

Focusing X-rays to nanometer scale requires excellent focusing optics, a significant demagnification factor (ratio of source-optics distance to optics-focus distance), and a highly stable beamline. A new optical enclosure (34-ID-F) and a new experiment enclosure (34-ID-G) will be constructed downstream of the existing microbeam diffraction enclosure (34-ID-E) [See Figure 4-103]. A nanodiffraction experiment platform utilizing both Kirkpatrick-Baez (K-B) mirror and zone plate (ZP)-based nanoprobes will be instrumented for high-resolution and three-dimensional studies of advanced materials. Technical advances in nanofocusing optics are crucial for the success of this beamline. The performance required for both K-B mirrors and zone plates will challenge the current state of the art: in optical systems, in instrument mechanical and thermal stability, and in acoustic noise and vibration isolation.

The new nanoscale diffraction beamline will take the inboard branch of the canted undulators of Sector 34, while the current microbeam diffraction beamline will be relocated to the outboard branch. Many of the components currently in use at 34-ID-E for the polychromatic microbeam diffraction instrument will

remain in place. The present microdiffraction activities at 2-ID-D will be relocated to 34-ID-G, where they will be supported by the newly developed instrumentation. The current coherent diffraction activity at 34-ID-C will no longer be supported at beamline 34-ID.

4.11.1 Scientific Objectives

The S3DD upgrade will provide users with scientific access to a suite of scanning diffraction instruments (both K-B mirror and zone-plate-based), which will be unique in the world. These instruments will use highly focused beams to measure the local lattice structure, orientation, and strain tensor with high point-to-point spatial resolution. The size of the focused x-ray beams in the two independently operated stations will range from ~50 nm to ~micron in size, enabling the match of the probe size to the fundamental scale of the materials problem with a minimum of angular divergence in order to provide the highest possible resolution in reciprocal space. The ability to easily alternate between polychromatic and tunable monochromatic diffraction modes will be another key feature unique to APS 34-ID, enabling studies of a much wider range of randomly oriented or polycrystalline “real” materials.

With improvements resulting from the S3DD upgraded capabilities, scientific progress toward a more fundamental and predictive understanding of materials processing is expected. Just as electron microscopy has revolutionized our knowledge of dislocation interactions, high-resolution and quantitative diffraction microscopy can transform our understanding to a level where macroscopic physical properties emerge from the inhomogeneous local interactions of individual defects, grains, and strain fields. By providing new insights into a wide range of exciting problems, the new instrument will have impact on research covering all branches of materials science and many other diverse fields, including high-pressure geophysics, mineralogy, and environmental science.

4.11.2 Source Requirements

34-ID has a canted configuration, and its undulator sources will be optimized for separate microbeam and nanobeam diffraction experiments. The outboard branch beamline will host the existing microdiffraction instrument with improved capabilities. A new undulator beamline, including a new optics enclosure and a new experimental station, will be built on the canted inboard branch to support a new nanoprobe platform that integrates a Laue diffraction microscope and a diffractometer for wider access to reciprocal space.

A wide-energy bandpass of >20 keV is required to fully utilize the advantages of the Laue technique. For polychromatic X-ray Laue diffraction, tapered undulator source is often used to provide the broad spectrum. However, a high-brightness monochromatic beam is also needed when the energy of a reflection is measured for absolute strain analysis or when micro/nanodiffraction analysis takes place utilizing zone plate focusing elements. So, in addition to high brightness, continuous energy tunability over the energy range 5-30 keV is essential for both undulator sources. The low limit of the spectral range will allow micro-spectroscopy, as complementary to microdiffraction, at the binding energies of most elements down to vanadium in the periodic table. The high energy limit is desired for broad access to reciprocal space for most engineering crystal materials, and matches the energy cutoff set by the mirror grazing angle of focusing optics. The current outboard line has a permanent-magnet undulator source with a period of 3.0 cm, while the inboard line has an APS Undulator A with a period of 3.3 cm [115]. Both

undulators meet the energy range requirements for micro/nano diffraction. The 3.0-cm undulator will be more appropriate because of the higher brightness for the monochromatic beam mode.

4.11.3 X-ray Optical Layout

The basic optical layout of the two branches is shown in Figure 4-102. This section describes the basic beamline layouts, with more detailed specifications for the individual components given in section 4.11.4.

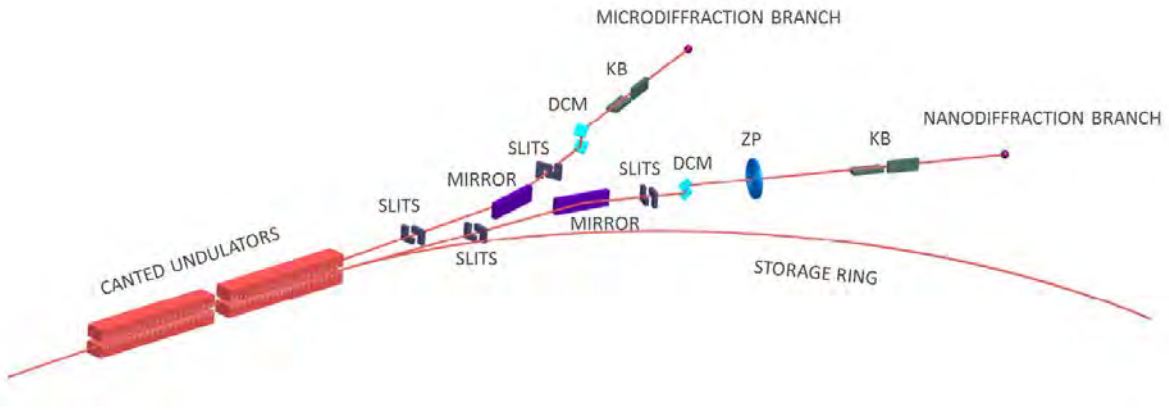

Figure 4-102: Basic optical layout of the two branch lines for microdiffraction and nanodiffraction.

Since the IDs at Sector 34 are canted by only 1 miliradian, two horizontal deflection mirrors in 34-ID-A will be used to further separate the 34-ID-E beamline from 34-ID-G beamline. The existing liquid nitrogen-cooled beam-splitting mirror, which is currently used for coherent diffraction activities on the outboard beamline, will remain for this purpose. An additional liquid nitrogen-cooled mirror will be installed on the inboard beamline in 34-ID-A to further separate the two beamlines.

A removable, small-offset Si <111> monochromator for the energy range of 5-30 keV will be installed in the optical enclosure 34-ID-D to provide monochromatic x-rays to enclosure 34-ID-E. The monochromator is designed to pass either a pink beam or a monochromatic beam through the same exit slit. The current removable microbeam monochromator in 34-ID-D will be relocated to 34-ID-F to provide monochromatic X-ray beams to the 34-ID-G nanobeam experiment enclosure.

A new K-B nanofocusing mirror system will be installed in 34-ID-G for Laue nano-diffraction measurements in either polychromatic or monochromatic mode. The system will have an initial focal spot of <100 nm and will achieve ~50 nm with further development. In addition, the zone plate-based monochromatic nanoprobe diffractometer instrument at 2-ID-D will be relocated and integrated into the 34-ID-G beamline, with upgraded focusing performance. New zone plate optics with an outer zone width of <50 nm will be installed for nanodiffraction.

4.11.3.1 Mirrors

Two horizontal reflecting mirrors will be located in first optics enclosure (FOE) 34-ID-A on each branch to further separate the canted beamlines.

The existing liquid nitrogen-cooled mirror reflects the outboard beam further outboard. The Si mirror is Pt coated for increased reflectivity up to 30 keV, and has been designed to permit the inboard synchrotron beam to pass behind the mirror. This mirror currently operates at a grazing angle of 5 mradian and reflects x-rays of energy up to 15 keV. However, this energy cutoff does not meet the 5-30-keV energy range requirement. The incident angle of the mirror will be reduced from 5 mrad down to 2.5 mrad in order to extend its energy bandpass up to 30 keV.

An additional mirror will be installed on the inboard beamline in 34-ID-A with the purpose of providing both a high-energy cutoff and further separation of the two beamlines. It will reflect the inboard beam and permit the outboard beam to pass behind the mirror. This new mirror will have a design similar to that of the existing outboard mirror, e.g., it will be liquid nitrogen-cooled and with an incidence angle of 2.5 mrad. However, the inboard mirror will have multiple coating stripes (Pt, Rh, and bare Si) that can be interchanged to optimize harmonic suppression. It is assumed that this horizontal reflecting mirror will not affect the nano-focusing performance in the vertical direction.

The two deflection mirrors in 34-ID-A plus the canted sources will provide a beamline separation of about 400 mm in 34-ID-E, thus providing adequate space for installing a shielded beam-transport pipe behind the microdiffraction facility in the E enclosure.

4.11.3.2 Monochromators

In the S3DD upgrade, each branch beamline will require a double-crystal monochromator. In the second optics enclosure (SOE), a compact pink-beam transport pipe behind the monochromator and shutter will be installed to transport the inboard branch beam. The separation of the two beamlines in the enclosure is ~330 mm, which is not sufficient to allow the current monochromator to stay. Therefore, the existing monochromator in the SOE will be relocated to the new optical enclosure 34-ID-F.

A new double-crystal monochromator is planned. This would be a removable, small-offset Si <111> monochromator for the energy range of 5.3-30 keV, to be installed in the SOE (34-ID-D) to provide monochromatic X-rays to the enclosure 34-ID-E outboard branch with an energy resolution of $\Delta E/E = 1 \times 10^{-4}$. The energy resolution is driven by the strain resolution of the Laue diffraction microscopy limited by the focusing optics. It will be satisfied by use of silicon <111> crystals as monochromator optics. The monochromator is designed to pass either a polychromatic beam or a monochromatic beam through the same exit slit. To achieve this, the beam offset in the monochromator is kept to 1 mm, which is within the dimension of the pink-beam vertical profile entering the 34-ID-E enclosure. To reduce the thermal load, a slit at the front of the water-cooled monochromator restricts the size of the incident beam in both polychromatic and monochromatic modes.

The current monochromator in 34-ID-D (to be relocated to the third optics enclosure 34-ID-F) will provide monochromatic X-ray beams to the 34-ID-G nanobeam experiment enclosure. The monochromator will be modified so that its energy range can be expanded from the current 6.8-30 keV

span to 5.3-30 keV to cover the needs of spectroscopy at an energy down to the *K*-edge of V. The expanded energy range requires a maximum incidence angle of 21.9°, which is not achievable with the existing monochromator.

4.11.3.3 Focusing Elements

Two K-B mirror systems will be located in 34-ID-E and 34-ID-G for simultaneous and independent use of the two diffraction stations for microbeam and for nanobeam experiments. In addition, the zone plate-based monochromatic nanoprobe diffractometer instrument at 2-ID-D will be integrated into 34-ID-G with upgraded focusing performance.

The beamline demagnification and focal lengths are shown in Table 4-29. Because the undulator source size in the horizontal plane is relatively large and the demagnification of focusing optics is also limited by the beamline length, slits in the FOE will be used when focal size is more important than flux. A white-beam slit at 26.8 m will be placed to control the total power in the beam and to reduce the undulator horizontal source size down to 100 μm or less for the outboard branch. A slit of the same type will be placed at 27.3 m for the inboard branch. These two slits also act to create new effective sources in the horizontal plane for the two beamline branches. In the vertical plane, the undulator source serves directly as the source.

Table 4-29: Parameters of the beamline focusing optics.

	Horiz Focal Length (mm)	**Horizontal Demag.**	**Vert. Focal Length (mm)**	**Vert. Demag.**	**Focal Size (nm)**	
					Early Goal	**Final Goal**
Microdiffraction 34-ID-E at 64 m	60	575	130	496	350	150
K-B Nanodiffraction 34-ID-G at 74 m	40	1037	80	893	100	50
ZP Nanodiffraction 34-ID-G at 71 m	50	830	50	1430	80	50

4.11.4 Beamline Physical Layout

A sector layout is shown in Figure 4-103. This assumes that both branches will be located at Sector 34. The current coherent diffraction activity at 34-ID-C will no longer be supported at 34-ID.There will be a total of five enclosures in operation as shown. The A enclosure will house front end optical components. The D and E enclosures are for the microdiffraction branch. The F and G enclosures will house the nano-diffraction branch.

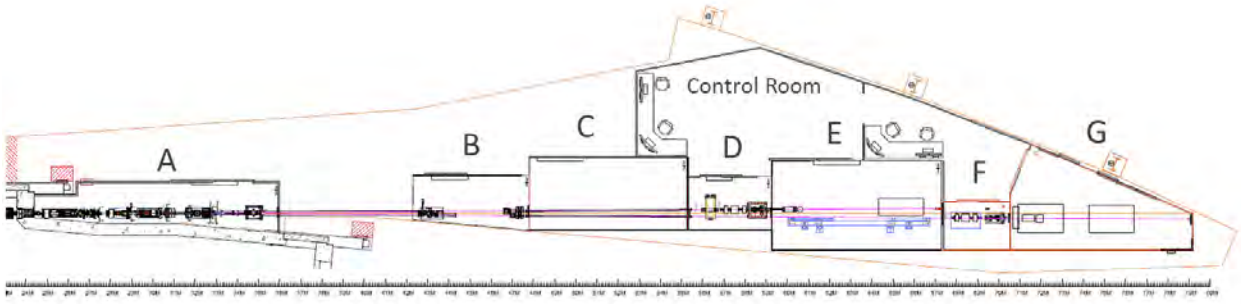

Figure 4-103: Sector 34 layout showing enclosures and main optical components. The new optical enclosure (34-ID-F) and new experiment enclosure (34-ID-G) are located at the end of the existing beamline.

4.11.4.1 Front End

The front end will be a standard canted undulator front end. The FOE, designated 34-ID-A, is home to beamline components such as slits, masks, and collimators. Two deflection mirrors are also located in this enclosure and serve to further separate the inboard and outboard beams by an additional 10 mrad.

4.11.4.2 Detailed Beamline Layout

4.11.4.2.1 General Description

The canted undulator beamline design will allow for simultaneous and independent use of the two diffraction stations for microbeam (34-ID-E) and nanobeam (34-ID-G) experiments. A dedicated, polychromatic, microbeam diffraction instrument in 34-ID-E will continue to provide routine and reliable performance based on a hard x-ray beam focused to ~300 nm. The second canted undulator will be dedicated to the 34-ID-G nanoprobe station located downstream of the current microprobe station. The K-B mirror-based polychromatic focused beam will have an initial focal spot <100 nm and will reach, with further development, ~50 nm. The zone plate-based monochromatic nanodiffraction probe will provide X-ray beams focused to ~50 nm. Table 4-30 shows the main optical components in the 34-ID beamline.

Table 4-30: Beamline components in the 34-ID beamline.

Enclosure	Component	Distance to source (m)	Notes
34-ID-A	White-Beam L-31 Slits	26.8	Outboard branch
34-ID-A	White-Beam L-31 Slits	27.3	Inboard branch
34-ID-A	Deflection Mirrors	29.6	Two liquid nitrogen cooled horizontal mirrors will be located in 34-ID-A on each branch to further separate the outboard and inboard beamlines

Enclosure	Component	Distance to source (m)	Notes
34-ID-A	Photon Mask / Beam Stop	32.1	Photon beam stop for both inboard and outboard branch synchrotron beams; it also includes apertures to limit the transports of the mirror-reflected inboard and outboard beams
34-ID-B	Beam Transports	43	The current pink-beam P9-30 integral shutter will be relocated to 34-ID-D
34-ID-C	Shielded Beam Transports	46	The current coherent diffraction activities in 34-ID-C will be relocated
34-ID-D	Small-Offset Double-Crystal Monochromator	57	New design; Si <111> monochromator for energy range of 5.3-30 keV with 1-mm vertical offset, water-cooled
34-ID-D	Pink-Beam Shutter	58	Pink-beam P9-30 integral shutter (relocated from 34-ID-B) for outboard branch 34-ID-E experiment station
34-ID-E	Exit window	60	Double beryllium windows
34-ID-E	Shielded Beam Transport Pipe	60	Small outside diameter is required to permit experiments at 34-ID-E
34-ID-E	Microdiffraction Platform	64	To be relocated to outboard branch
34-ID-F	Small-Offset Double-Crystal Monochromator	67	Relocated from 34-ID-D
34-ID-F	Pink-Beam Shutter	69	Pink-beam P9-30 integral shutter (relocated from 34-ID-D).
34-ID-G	Exit window	71	Double beryllium windows
34-ID-G	Zone Plate Based Nanodiffraction Platform	71	
34-ID-G	K-B Mirror-Based Nanodiffraction Platform	74	

4.11.4.2.2 Radiation Safety Aspects

The current 34-ID beamline includes optical enclosures 34-ID-A, 34-ID-B, and 34-ID-D, and experiment stations 34-ID-C and 34-ID-E. 34-ID-A, 34-ID-B, 34-ID-D, and 34-ID-E are white-beam enclosures while 34-ID-C is a pink-beam enclosure. The current coherent diffraction activities in 34-ID-C will be relocated to another sector. An additional pink-beam transport will be installed in 34-ID-C to provide X-ray beams to the 34-ID-E microbeam experiment enclosure. This will make 34-ID-C accessible when X-rays are present in stations E and G.

The new optical enclosure 34-ID-F and the experiment station 34-ID-G will be pink-beam enclosures. The beamline separation will be about 400 mm in 34-ID-E due to the two deflection mirrors in the FOE, plus the canted sources. A compact shielded beam-transport pipe behind the microdiffraction facility in the E enclosure will be installed.

Bremsstrahlung and synchrotron radiation ray tracings are shown in **Error! Reference source not found.**. They will follow the guidelines set out in APS document TB-7 [116] to satisfy radiation safety requirements.

4.11.4.2.3 Vacuum System

To minimize optical aberrations that could affect focusing performance and absorption at low energies, both beamlines will be compatible with windowless operation utilizing a differentially pumped transition from the front end to the FOE. All vacuums are maintained by ion pumps along the beamlines. All components will be generally ultrahigh vacuum (UHV) compatible to prevent outgassing detrimental to storage ring operation; although requirements could be relaxed if the component is sufficiently isolated from the front end. Both beamlines will comply with the APS beamline vacuum policy for windowless operation. Double beryllium windows will be installed in the end experiment stations of 34-ID-E and 34-ID-G for both branches.

The current 34-ID equipment protection system (EPS) is not supported by the APS Safety Interlocks Group. In the S3DD upgrade, standard vacuum equipment and controllers will be purchased and integrated into EPS and the Experimental Physics and Industrial Control System (EPICS).

4.11.4.2.4 Data Acquisition and Motion Control

The current motion control infrastructure of the 34-ID-E microdiffraction beamline will remain. For the new 34-ID-G nanodiffraction branch, motion control equipment will be purchased, installed, and integrated into EPICS.

The data acquisition rate can be up to 10 TB/day. Required data storage will be 300 TB for user operation for one run cycle. A cluster computer with 128 cores or more will be installed for data analysis. Horizontal Bremsstrahlung and synchrotron radiation ray tracings of 34-ID is available in the APS Upgrade drawing # U142121-100000.

4.11.4.3 First Optics Enclosure (34-ID-A) and Infrastructure, Major Components

The first optics enclosure has a standard layout as shown in Figure 4-103, with provision for the two beams from the canted undulators.

4.11.4.3.1 Windows

The current Be window assembly in the FOE is designed to separate the beamline vacuum from the front end, and is compatible with the exit mask and collimator [117].

In the S3DD upgrade, both beamlines will be windowless by utilizing a differentially pumped transition from the front end to the FOE. The current Be window assembly in the FOE will be removed. To comply with the APS beamline vacuum policy for windowless operation, final, double Be windows will be

installed in the end experimental stations of 34-ID-E and 34-ID-G for each branch. To minimize optical aberrations that could affect focusing performance, these windows must be polished.

4.11.4.3.2 Slits/Apertures

The water-cooled white-beam slit assembly is designed to permit either of the canted branch beamlines to be defined in both the vertical and horizontal direction without affecting the other branch beamline. Both beamlines will require these apertures in order to minimize the heat load on the downstream components. To effectively define both beams requires use of two slit assemblies. Because these two slits also set the secondary horizontal source size for the focusing of the microbeam and nanobeam diffraction experiments, the focus quality is partly determined by the sharpness of the slit edge. To assure a sharp source edge, a tungsten rod insert is included in these slits. Thermal analysis indicates the presence of the tungsten will not adversely affect the slit performance [118].

Two slit assemblies are located directly in front of the deflection mirrors for both branches, as indicated in section 4.11.4.2.1.

4.11.4.3.3 Collimators

Collimation is required to provide necessary bremsstrahlung and synchrotron radiation protection while operating the two branches independently. Preliminary ray tracing of the beamline layout shows all the necessary standard collimators, as indicated in section 4.11.4.2.2.

Existing exit collimator at 25 m from source [119]: The exit collimator is designed to separate and limit the extent of primary bremsstrahlung radiation for both inboard and outboard branches of the beamline. This collimator limits the extreme rays in both the horizontal and vertical directions.

Existing bremsstrahlung collimator at 29 m from source [120]: This in-vacuum collimator is designed to limit the extent of primary bremsstrahlung to reduce the size of subsequent downstream collimators and stops and limits the extreme rays in both the horizontal and vertical directions.

Existing bremsstrahlung collimator at 29 m from source [121]: This collimator is designed to function with the in-vacuum bremsstrahlung collimator [122] to provide the required lateral collimation shielding dimension; the primary bremsstrahlung is not directly incident on this collimator.

Existing bremsstrahlung collimator at 32 m from source [123]: This collimator will be modified or removed because of the addition of the inboard deflection mirror.

4.11.4.3.4 Photon Masks/Beam Stops

This component is designed as a photon beam stop for the outboard branch synchrotron beam. It also serves as a mask to limit the extent of the inboard synchrotron beam in both the horizontal and vertical directions. The assembly also includes an aperture to limit the transport of the reflected pink beam [124].

This mask/beam stop will be redesigned. The photon beam stop will be used for the both inboard and outboard branch synchrotron white beams. It should also include apertures to limit the transports of the reflected pink inboard and outboard beams.

4.11.4.3.5 Mirrors

The FOE will house two horizontally deflecting mirrors for both branches, as indicated in section 4.11.4.2.2.

The existing liquid nitrogen-cooled mirror reflects the outboard beam to the 34-ID-C coherent diffraction station, and operates at a grazing angle of 5 mrad. A simple, gravity-fed LN_2 delivery system has been used to minimize vibration that could affect focusing performance. A heat exchanger is filled by a flexible, vacuum-jacked LN_2 line that runs through a roof labyrinth to a phase separator on the roof of the FOE. The pressure in the phase separator is maintained only slightly above atmospheric, so the LN_2 is gravity-fed down. The phase separator is connected to the central APS LN_2 supply. The mirror mount system had been designed to permit the inboard synchrotron beam to pass behind the mirror. In the S3DD upgrade, this LN_2 cooling system will not remain at the 34-ID beamline for the outboard microdiffraction branch. Two new reflecting mirrors will be installed on both inboard and outboard beamlines in 34-ID-A to provide both a high-energy cut-off and further separation of the two beamlines. It will reflect one beam while permitting the other beam to pass behind the mirror by utilizing a design similar to that of the existing outboard mirror. To meet the 5-30-keV energy range requirement, the incident angle of the mirror will be reduced to 2.5 milliradians.

Because of the small acceptance of <500 μm of the incident beam, both mirrors require mirror lengths of only 200 mm. The mirrors will have RMS surface roughness of <0.1 nm and slope errors of 1-rad RMS. Mirrors will provide horizontal collimation to improve flux. Both mirrors will be made of Si with multiple coated stripes (Pt, Rh, and bare Si) that can be interchanged for optimized harmonic suppression. Pt allows operation to 30 keV; Si will be used below 13 keV for harmonic rejection; and Rh is the general purpose option covering most of the energy range below 22 keV without absorption edges.

To minimize vibration that could affect focusing performance, further discussion with vendors for an improved design is necessary. For proper cooling, thermal distortion analysis will be carried out as needed.

4.11.4.3.6 Beam Transport

Shielded pink-beam transports between 34-ID-A (FOE) and 34-ID-D (SOE) are needed for each canted beam. Currently, there is one shielded white-beam transport between FOE and SOE. This can continue to serve as beam transport for the inboard branch. Because the current coherent diffraction activities in 34-ID-C will be relocated to another sector, an additional shielded pink-beam transport between FOE and SOE will be installed for the outboard branch.

In the 34-ID-E microdiffraction experimental enclosure, a compact pink-beam transport pipe behind the microdiffraction apparatus is required to transport the nanodiffraction branch beam with minimal interference with the microdiffraction experiments. The separation of two beamlines in the E enclosure is about 400 mm.

4.11.4.3.7 Diagnostics

X-ray beam diagnostics are needed for monitoring and assessing beam stability. This will include beam position monitors on each branch.

An additional viewport will be installed to allow visual examination of the pink beam on each branch by inserting a phosphor crystal. This will facilitate the alignment of the pink beam for each branch. Because it is needed for alignment only, it could potentially be operated only with large undulator gaps to reduce heat loads.

4.11.4.4 Second Optics Enclosure (34-ID-D)

The SOE as shown in Figure 4-103 will house a new monochromator and a pink beam shutter for the outboard microdiffraction branch line.

A compact pink beam transport pipe behind the monochromator and shutter is required to transport the nanodiffraction branch beam. The separation of two beamlines in the D enclosure is about 330 mm. Because of the transport pipe, the existing monochromator together with the pink beam P9-30 integral shutter in 34-ID-D will be relocated to the new optical enclosure 34-ID-F.

4.11.4.4.1 Monochromator

A new monochromator with water cooled Si <111> double-crystals is planned (see section 4.11.3.2). This will be a removable small-offset monochromator for the energy range of 5.3 - 30 keV, to provide monochromatic X-rays to enclosure 34-ID-E outboard branch.

For Laue micro/nano-diffraction experiments, the design of the monochromator typically has several requirements: 1) energy accuracy $\Delta E/E$ is about 1×10^{-4}; 2) energy range should cover the pink beam bandpass of K-B focusing mirror optics; 3) the monochromator should be rapidly switchable between polychromatic mode and monochromatic mode for the rapid strain measurements; and 4) the focused beam position should be maintained when switching between polychromatic and monochromatic beams; and when scanning energy in monochromatic mode, the beam stability should be kept at same level as the focused beam size. To achieve the goals outlined above, a specially designed small-displacement Si <111> double-crystal monochromator will be needed.

To maintain a constant offset when the beam is cycled between polychromatic and monochromatic modes or scanned in energy, the monochromator will have a gap of 500 μm resulting in beam offset of about 1 mm. This is within the dimension of the pink beam vertical profile entering the 34-ID-E enclosure. For a monochromator with a gap G between the two crystal faces, the exit beam offset is given by: $2G\cos\theta$. For a Si <111> monochromator operating at required energy range of 5.3 keV to 30 keV, Bragg angle changes from 21.9° to 3.8°. At the highest angle, the gap of 500 μm will result in a beam displacement of 928 μm; while at the lowest angle, the beam displacement is 998 μm. The offsets remain almost fixed and are about twice of the gap G. Because the x-ray beams required for micro-focusing mirror optics are typically < 200 microns, a special step slit system can be designed to allow either polychromatic or monochromatic beam to pass through a same exit slit. This brings the total power on the first crystal of

the monochromator into the range which can be handled by water-cooled optics and the thermal distortions on the crystal do not substantially decrease the source brightness under most conditions.

A schematic drawing of the beams relative to the monochromator and slits for both polychromatic and monochromatic modes is shown in Figure 4-104.

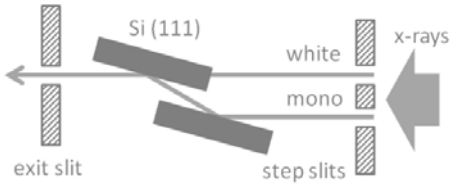

Figure 4-104: A switchable small displacement monochromator for micro/nano-diffraction beamline. In the monochromatic mode, the mono entrance slit passes a ~300 μm vertically wide beam onto the first crystal. Then the beam is reflected by the double crystals and directed onto the exit slit. In the polychromatic mode, the crystals are horizontally translated away from the incident x-rays. The pink entrance slit also accepts a 300 μm wide beam and has the same height as of the exit slit. The exit slit defines the vertical height at which either polychromatic or monochromatic beam can pass through.

Although the monochromator design illustrated in Figure 4-104 ensures that the beam exits from the same vertical aperture with or without the monochromator, there is a small angular difference between the polychromatic and monochromatic beams that exit from the final aperture. The 1 mm displacement at 57 m from source has an angular difference of ~20 microradians. This will result in a shift of the focused beam by about 5 μm when the mirror focal length is 130 mm. One solution is that the angular displacement can be corrected by heating the second crystal of the monochromator to tilt up the exit beam, so that the monochromatic beam is not only coincident but also parallel to the polychromatic beam. For a Si <111> monochromator, the temperature of the second crystal can be set at around 40°C for the monochromatic beam at 15keV, while the temperature of the first crystal remains at 22°C.

The monochromator should be close to the focusing optics for good angular stability. To improve the stability when scanning energy, the monochromator will incorporate an in-vacuum sine-bar drive mechanism for the combined pitch motion of the double crystals and a flexure-based high-stiffness weak-link mechanism for fine-tuning the pitch and roll of the second crystal [125]. It expects that an exceptionally uniform and stable beam will be delivered.

4.11.4.4.2 Slits

To reduce the thermal load, a slit at the front of the water-cooled monochromator restricts the size of the incident beam in both polychromatic and monochromatic modes. Because the acceptance of the microfocusing optics is at most 200 μm, a fixed slit is placed before the monochromator, which reduces the thermal load without affecting the usable intensities. The entrance step slits and exit slits are all water cooled, with W or Ta blades. The monochromatic beam entrance slit has a 1-mm offset with respect to the polychromatic beam entrance slit, as shown in Figure 4-104.

4.11.4.4.3 Shutters/Stops

A pink-beam shutter will be required after the monochromator in the SOE. The current pink-beam shutter in 34-ID-B could be relocated to 34-ID-D. This shutter will block the mirror-reflected beam to permit access to the 34-ID-E experiment station [126].

The current pink-beam P9-30 integral shutter in 34-ID-D, together with the existing monochromator in 34-ID-D, will be relocated to the new optical enclosure 34-ID-F.

4.11.4.5 Microdiffraction Station (34-ID-E)

The 34-ID-E station is a white-beam enclosure for the existing Laue diffraction three-dimensional microscope [127, pp. 108-111].

A non-dispersive, total-external-reflecting K-B mirror pair is used to focus either polychromatic or monochromatic x-ray beams. The primary advantage of Laue microdiffraction is the ability to determine crystalline structure without sample rotation. This is essential for submicrometer spatial resolution diffraction measurements, particularly for polycrystalline materials. In a typical experiment, the sample is rastered in the x-ray beam by a precision 3-axis stage. The Laue patterns generated at each sample position are collected by x-ray area detectors. Because of the beam penetration, the overlapped Laue patterns from each voxel along the X-ray beam must be depth resolved. This is done by a differential aperture that scans across the surface of the sample [128]. In the differential aperture technique, a highly absorbing wire is translated in submicron steps. From the depth-resolved Laue patterns, phase and orientation of the crystalline structure within each voxel can be determined. It is often possible to measure the elastic deviatoric strain tensor and/or the plastic deformation tensor. To determine full strain, reflection energies must be measured. This can be done by inserting the monochromator into the x-ray beam and tuning to the energy of the Bragg reflection.

In microdiffraction, a larger working distance is always important for real experiments. It is therefore useful to produce a low figure-error elliptical mirror to provide a longer focal length. Currently, the focused beam spot size at 34-ID-E is about 500 nm or less during routine operation. This is mainly limited by the mirror slope errors. In the S3DD upgrade, a new set of advanced K-B mirrors with ultra-low slope errors of ~0.1 μrad will be installed at 34-ID-E for microdiffraction experiments. This will bring the focal size down to <300 nm without scarifying working distance. With research and development effort on nested K-B (Montel) mirror focusing optics [129], focal size can be improved by significantly increasing the vertical demagnification. For a conventional non-extra-long beamline, the nested K-B mirror optics is a desirable goal because of its compact design with stronger demagnification and with the ability to collect larger divergences.

The detector system currently used at 34-ID-E is based on PerkinElmer amorphous Si detectors. This system provides readout capabilities of 15 frames/sec with 6 megapixels. The drawbacks of the amorphous Si detector are that it is noisier than a charge-coupled device (CCD) and it cannot collect data that require long exposures. An ideal detector system for Laue diffraction microscopy should have large solid-angle coverage, moderate pixel size, no pixel distortions, high speed, and low background. In the S3DD upgrade, advanced photon-counting detectors, e.g., Pilatus, with excellent signal-to-noise ratio and

large dynamic range are desirable. An advanced CCD with negligible pixel distortions could also be considered.

The enclosure will require upgraded temperature control to be better than 0.2° C to minimize the thermal drift of the instrument.

In the S3DD upgrade, the current Laue diffraction three-dimensional microscope will be relocated to the outboard microdiffraction branch line. A compact pink-beam transport pipe behind the microdiffraction facility will be installed to transport the nanodiffraction branch beam with separation of two beamlines about 400 mm.

4.11.4.6 Third Optics Enclosure (34-ID-F)

The third optics enclosure (TOE), as shown in Figure 4-103, will house a monochromator and a pink-beam shutter for the inboard nanodiffraction branch line. The existing monochromator together with the pink-beam P9-30 integral shutter in 34-ID-D will be relocated to this enclosure.

4.11.4.6.1 Monochromator

The existing monochromator in 34-ID-D will be relocated to the TOE in order to provide monochromatic x-ray beams to the 34-ID-G nanobeam experiment enclosure. This monochromator meets most of the requirements for the micro/naonodiffraction experiments, as outlined in section 4.11.4.4.1. It is a water cooled, Si <111>, double-crystal monochromator. It has a small offset of 1 mm with a crystal gap of 0.5 mm. A step-slit system is used for an easy switch between polychromatic and monochromatic modes.

In order to achieve the expanded energy range from the current 6.8 – 30 keV to 5.3 – 30 keV, the monochromator has to be modified. The energy range requires change of the maximum incidence angle from 16.9 degrees to 21.9 degrees. The flexure pivots used for the main theta sine-bar drive mechanism will be replaced to expand angular range.

If the modification of the existing monochromator becomes difficult, a second new monochromator can be built for the nanodiffraction branch as an alternative [CAS]. The new monochromator will have the same drive mechanism as described in section 4.11.4.4.1 with expanded energy range and improved stability when scanning energy.

4.11.4.6.2 Shutters/Stops

A pink-beam shutter will be required after the monochromator in the TOE. The shutter will block the mirror-reflected beam to permit access to the 34-ID-G experiment station. The current pink-beam P9-30 integral shutter in 34-ID-D will be relocated to the TOE [130].

4.11.4.7 Nanodiffraction Station (34-ID-G)

The 34-ID-G station is a pink-beam enclosure located on the inboard nanodiffraction branch line. It will house a nanodiffraction experiment platform utilizing both K-B mirror- and zone plate-based nanoprobes for high-resolution studies of advanced materials.

Technical advances in nanofocusing optics are crucial for the success of this beamline. The performance required for both K-B mirrors and zone plates will challenge the current state of the art in optical systems, in instrument mechanical and thermal stability, and vibration isolation. An integrated design of the two nanoprobe systems in 34-ID-G will be based on the same infrastructure. Detectors can be shared by both systems, with enhanced capabilities for a combined nanodiffraction instrument.

4.11.4.7.1 K-B Nanofocusing Mirror System

A new K-B nanofocusing mirror system will be installed in 34-ID-G for polychromatic and monochromatic Laue diffraction measurements. These ultra-precise mirrors require a figure error of better than 0.1-μrad RMS and a surface roughness of 0.1-nm RMS. These values will assure diffraction-limited two-dimensional focusing for hard x-rays below 50 nm as the ultimate goal. The mirror specs are based on current state-of-the-art mirror technologies, for example the elastic emission machining by JTEC, Inc.

Table 4-31 lists the parameters of the 34-ID-G nanofocusing K-B mirror optics, including both traditional K-B and nested K-B (Montel) configurations. These parameters are based on consideration of optimizing working distance, beamline geometrical demagnification, mirror angle, beam acceptance, and beam divergence for the needs of nanodiffraction measurements. To achieve nanofocusing on a conventional beamline of 70 m in length, the working distance will be sacrificed because of the insufficient demagnification [131]. Therefore, nested K-B mirror focusing optics can be considered for nanofocusing. The working distance could be expanded by increasing the horizontal mirror focal length. Increased beam acceptance for more photon flux and larger divergence for lowering diffraction limit are expected too. Research and development will be needed on nested K-B mirror nanofocusing.

Table 4-31: Parameters of the 34-ID-G beamline nano-focusing optics.

		Mirror Length (mm)	Working Distance (mm)	Focal Length (mm)	Demag	Glancing Angle (mrad)	Beam Acceptance (μm)	Angular Acceptance (mrad)
Sequential K-B at 73m	Vert.	50	25	80	893	3	120	1.5
	Horiz.	30		40	1037	3	60	1.5
Nested K-B at 73 m (optional)	Vert.	40	30	50	1190	3	120	2.4
	Horiz.	40		50	830	3	120	2.4

To minimize the instability of the optics, the mirror support will use a high-stiffness, high-precision flexure-based stage system with a small travel range of 0.5 mm and nanoradian multidimensional positioning resolution, utilizing orthogonally configured laminar weak-link mechanisms [127]. Figure 4-105 shows a preliminary design of the nanopositioning system for focusing mirror optics.

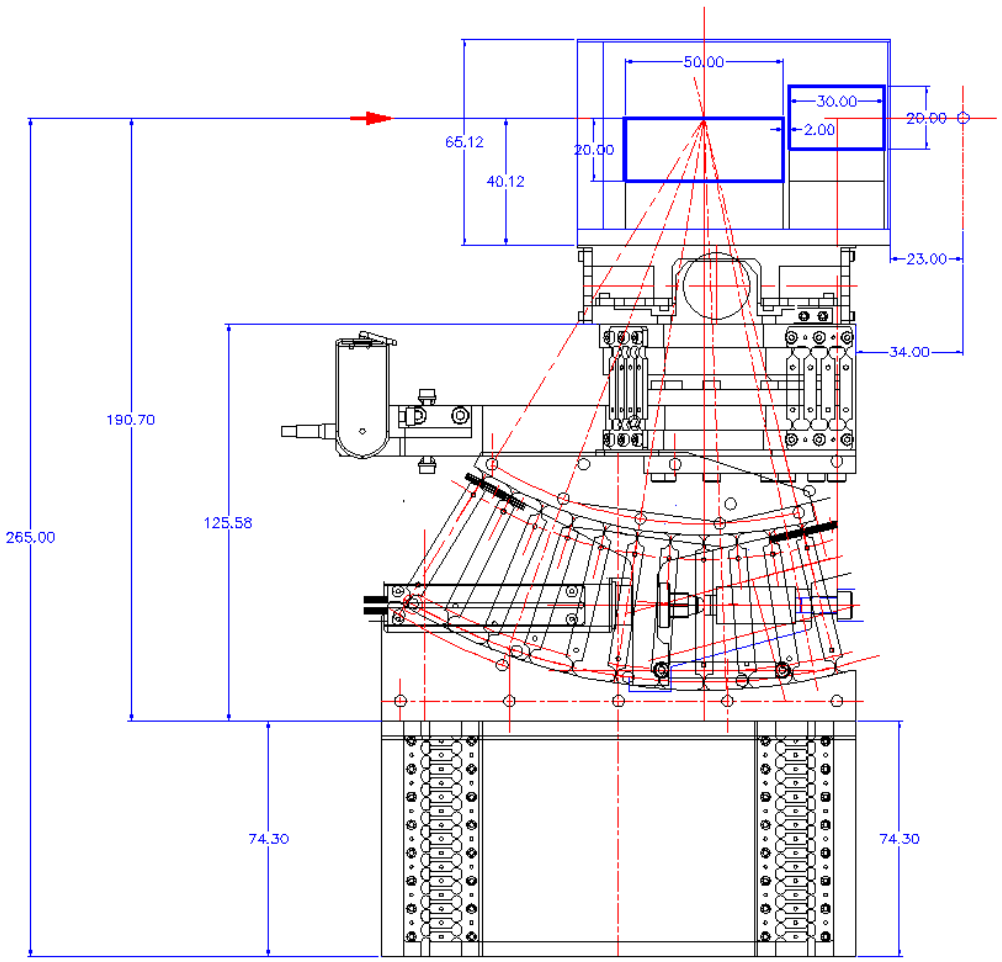

Figure 4-105: Preliminary design of the nanopositioning system for focusing mirror optics.

4.11.4.7.2 Zone Plate Nanoprobe Diffractometer

The zone plate-based monochromatic nanoprobe diffractometer instrument at 2-ID-D will be relocated to 34-ID-G with upgraded focusing performance [132]. New zone plate optics will be installed for nanodiffraction on the diffractometer platform, and related mechanical structures and sample assembly will be modified to satisfy stability and nanopositioning requirements. This instrument will permit control of the incident polarization utilizing an x-ray phase plate.

To achieve a diffraction limited resolution better than 50 nm, zone plates must have an outmost zone width less than 38 nm. As far as the focusing efficiency is concerned, zone plates must be fabricated in a proper thickness for necessary phase shift of x-rays in the composing material. For the energy range of 6 to 20 keV, gold zone plate thickness is typically in the range of several hundred nanometers to several micrometers. Zone plates with the required outermost zone width of 35 nm are expected to provide good focusing efficiency in the energy range of below 10 keV. Stacking zone plate would provide good focusing efficiency for energies up to 20 keV. Operation at higher energy depends on the success of the multilayer Laue lens development or, at a low efficiency, utilizing low-energy zone plates. The outcome

of the optics developments in the next few years will inform the final decision on which high-resolution optics will be deployed for higher energy operation.

With the following notes, Table 4-32 lists relevant parameters for zone plates:

Based on the ultimate goal of the resolution and the working space requirement for a broad range of nanodiffraction applications, an outmost zone width of 35 nm and a focal length of 50 mm were used to determine the rest parameters of zone plates.

While estimating the focusing efficiency of zone plates, it is assumed that two zone plates with an outermost zone width of 35 nm and a thickness of 600 nm can be fabricated and stacked within the optical nearfield. The focusing efficiency of zone plates is estimated as if a single zone plate having a thickness of 1.2 μm is used.

The number of zones of all the zone plates listed is far less than the maximum zones that would start to limit the bandwidth of the beam selected by a Si <111> monochromator with $\Delta E/E$ of 1×10^{-4}.

The zone plate with a focal length of 80 mm is required to accommodate special experiments in which a cryostat is needed. In this case, the attainable demagnification will not support a resolution of 50 nm. Therefore, an outermost zone width of 70 nm is used to determine other parameters of the zone plate.

Table 4-32: Parameters of diffractive optics with a smallest structure size of 35 nm.

Energy Range of Operation [keV]	6 - 9	8 - 12	8 - 12	12-18	18-30
Representative Energy [keV]	8	10	10	15	24
Diameter [μm]	221	177	142	118	74
Number of Zones	1576	1263	508	842	530
Focal Length [mm]	50	50	50	50	80
Anticipated Optics	ZP	ZP	ZP	ZP	ZP/MLL
Anticipated Efficiency of Stacking ZPs [%]	25	17	27	12	7
Anticipated Efficiency of MLL [%]					36

The existing nanodiffraction instrument at 2-ID-D is built on a Kappa diffractometer. The instability, due to a 2.5-m mechanical loop between the axis of the nanoprobe and the sample, limits the apparent beam spot size to 200 nm. To achieve 50-nm resolution, the mechanical structure of the diffractometer must be modified. A new sample assembly including goniometer and scanning stages will be installed directly on the same platform where the nanoprobe is based. Detector circles of the Kappa will be maintained in the new instrument.

4.11.4.7.3 Advanced Area Detectors

The detector system is a core part in x-ray Laue diffraction microscopy. In Laue diffraction, the energy bandpass, the reciprocal space volume of the crystal lattice unit cell, and the solid angle subtended by the detector determine the number of diffraction spots that can be observed. It is essential to have a sufficient volume of reciprocal space accessible by the detector for crystal orientation and strain tensor measurement experiments, and for nanocrystallography.

An ideal detector system for Laue diffraction microscopy should have large solid-angle coverage, moderate pixel size, no pixel distortions, high speed, and low background. While CCD detectors have low noise, their pixel distortions have significant effect on strain measurements and require grid distortion corrections. The requirements for the area detectors for the nanoscale polychromatic diffraction instrument in 34-ID-G are more stringent than those for the microbeam facility. Nanostructures provide intrinsically weak scattering signals, so the signal-to-noise performance of these area detectors is significantly more important than for many other applications.

4.11.4.7.4 Instrumentation and Infrastructure

Another challenge in nanoscale structural characterization concerns the accurate and precise manipulation of the sample. To fully exploit the nanoscale-focused beam size will require high-precision sample stages for translating and rotating samples. Although the polychromatic Laue technique does not require sample rotation to explore reciprocal space, focusing with chromatic optics, such as zone plates, will require accurate rotational control to sweep the sample reciprocal lattice through the Ewald sphere. Sub-10-nm and sub-100 nrad resolution is required for these sample manipulations.

In addition, for both types of optical systems (K-B and zone plate-based), environmental stability and control of temperature, acoustic noise, and vibrations are essential for effective nanoscale focusing and measurements. The thermal expansion coefficient of aluminum is approximately 23×10^{-6}/°C. This means that with a 0.1° change in temperature, a 100-mm-long aluminum object will have a 230-nm change in length. For invar, this will be about 12 nm. In order to minimize the thermal drift of the instrument, the environment surrounding the nanodiffraction probe should be maintained at 0.1° C. It is expected that significant engineering effort will be needed to develop a feasible design for the air and temperature control in the enclosure. Vibration stability is also very important in order to achieve the 50-nm mirror focal size, which is the ultimate goal. This requires minimization of disturbances from acoustic noise, water system, air handling system, beamline equipment noise, etc. Sub-50-nm vibration stability is desired in the experiment enclosure 34-ID-G.

Finally, beamline control hardware and software for 34-ID-F and 34-ID-G are required. Because the nanoscale Laue diffraction technique is relatively new and the software for data collection and analysis is not mature, efforts to improve this software are essential for making the best use of this capability. In addition, the collection of large volumes of area-detector images requires considerable computational and network infrastructure (see section 4.11.4.2.4).

4.11.5 Additional

4.11.5.1 Control Room

A new, enclosed control room is planned for 34-ID on the outboard side of stations 34-ID-D, E, F and G as shown in Figure 4-103. It will house workstations and some control equipment. This room will also provide a buffer to reduce or eliminate thermal exchange between the experiment stations and the APS experiment hall floor while the enclosure door is opened. With the control room enclosure, the temperature stability of both nanodiffraction and microdiffraction experimental setups can be significantly improved.

4.12 Advanced Spectroscopy and LERIX

The Advanced Spectroscopy and Lower Energy Resolution Inelastic X-ray (LERIX) beamline is a canted undulator expansion to the existing programs located at beamline 20-ID. This document assumes the upgraded program will be located at Sector 25. It consists of the Advanced Spectroscopy and LERIX (ASL) branch lines. The Advanced Spectroscopy branch line expands on the capabilities of the current Sector 20 microprobe station to optimize it for additional spectroscopy applications based on variable-resolution analysis of the sample fluorescence. The resolution will be optimized to the application. High-resolution methods, based on diffracting analyzers, will achieve 0.5- to 1.0-eV resolution with large-collection solid angles, suitable for rapid measurement of resonant and non-resonant x-ray emission spectra for determination of valence, spin, and some aspects of local electronic environment in a complementary method to the typical x-ray absorption near edge structure (XANES) analysis

The LERIX branch will support the LERIX spectrometer and the ultra-high vacuum (UHV) component of the advanced spectroscopy techniques. The LERIX-1 was the first spectrometer optimized for high-throughput, non-resonant inelastic x-ray scattering. The current LERIX-1B spectrometer is an upgrade providing improved sample handling, better low-energy capabilities, and a more flexible support frame. They both have the notable and unique feature of collecting a wide range of scattering angles simultaneously. Somewhat surprisingly, the q-dependence of the scattering has proven to be a rich source of information in many systems. The new branch line will provide variable-energy resolution to allow selection of the optimum resolution/flux trade-off for the experiment.

4.12.1 Scientific Objectives

4.12.1.1 Advanced Spectroscopy Branch

The Advanced Spectroscopy branch line will support three classes of experiments: micron-scale x-ray microprobe, x-ray absorption fine structure (XAFS) requiring the high flux and brightness of an undulator source (i.e., very dilute systems, high-pressure cells, or glancing angle measurements of thin films), and fluorescence spectroscopy using miniXS or other high-resolution spectrometers. The first two categories include most of the applications at the current microprobe station. The current station has a diverse and active set of users averaging about 20 publications per year while using about 50% of the available beam time at 20-ID. These capabilities will be retained and the enhanced beamline performance should attract additional users for the current applications and bring in a new community of users interested in fluorescence spectroscopy.

As the detection resolution is improved, fundamentally distinct variants of spectroscopic information become accessible. These include lifetime-broadening suppression, which occurs when selecting regions of individual emission channels, magnetic-state or valence-specific x-ray absorption spectroscopy (XAS) when selecting emission channels that couple directly to the spin- or charge-state of a metal ion, and the possibility of performing non-resonant and resonant x-ray emission spectroscopy (XES and RXES, respectively).

Nonresonant XES (or simply XES) is the spectral emission from the target species when the incident photon energy is at least ~100 eV above the binding energy, so that quantum mechanical coupling

between the absorption and emission processes is only weakly relevant for the emitted spectrum. That means a core hole has been formed and some electrons from a less-tightly-bound shell will decay to fill the core-level vacancy. For hard x-ray applications, with ~30% to 70% probability, this will result in the emission of a fluorescence x-ray. This process is manifestly atomic in nature, with a weak, but still sometimes useful, influence of the nearest-neighbor species. Most critically, it is important to note that XES characterizes the occupied density of states – without the complications of final-state effects – while XANES is instead sensitive to the unoccupied density of states. For example, the many Kβ features for 3d transition metals often provide unique insight into spin, valence, ligand species, and ligand bonding. Such information could be of critical importance for studies of bulk and nanophase transition metal oxide compounds used in numerous energy science applications. Unfortunately, comparatively few XANES studies at hard x-ray energies are accompanied by XES measurements with resolution comparable to the core-hole lifetimes (e.g., 0.5 - 2 eV for 3d transition metals) even though many such studies would vastly benefit from the complementary information provided by XES. This is due to the complexity, cost, and sheer physical scale of high-throughput x-ray spectrometers based on arrays of spherically-bent crystal analyzers. Recent work at the APS has demonstrated a new type of "miniature" x-ray spectrometer (miniXS) [133, 134], which overcomes many of these issues while also providing better-than-order-of-magnitude improvement in measurement times compared to existing APS apparatus. Using either the miniXS approach or a traditional spherically bent crystal analyzer (SBCA)-based system, as needed, x-ray emission spectrometers will be developed for operation from 3 to 12 keV. This energy range is of high scientific importance, as it spans the K-emission for 3d transition metals, the L-emission for lanthanides, and the M-emission for actinides.

By means of context, a technically relevant example from a recent study at 20-ID is presented in Figure 4-106 (a). In the figure, the nonresonant 3p→1s XES is shown for somewhat dilute Co species in two different states of a commercial Co-Mo catalyst used to produce ultra-low-sulfur gasoline. The performance of this catalyst is positively correlated to the cobalt sulfidation, such that mapping the location of the sulfided versus unsulfided (calcined) Co within an extrudate is of primary importance. For Co, as with all of the heavier 3d transition metals, the position of the main peak (spectroscopically designated Kβ1,3) is much more sensitive to the degree of covalency of the metal-ligand bond than to the nominal valence of the metal ion. The position of this peak then gives an unambiguously atomic fingerprint of the evolution from calcinated to sulfided Co species upon catalytic processing. Using the high-flux option at the new microprobe beamline (via a wide-bandpass monochromator) and new developments in highly efficient x-ray spectrometers, such spectra could be collected in less than 1 sec for the catalyst samples, and even more quickly for concentrated systems. Such capabilities will enable rapid two-dimensional (2-D) raster-imaging of entire XES spectra, a capability never before achieved at any hard x-ray light source. This will allow spatial imaging of information that is often very complementary to that obtained by 2-D imaging of specific XANES features, or even when collecting entire XANES spectra.

These considerations are further diversified when moving to RXES. Here, the APS convention is used and a study is designated to be RXES when the energy resolution is ~0.5 eV or poorer, as opposed to calling it resonant inelastic x-ray scattering, a designation reserved for significantly higher resolution studies of the same coupling of absorption and emission channels. The results of a recent, spectroscopically complete RXES study at 20-ID are presented in Figure 4-106 (b). In this example, the splitting of the f-orbital final states (accessible by quadrupolar transition channels) at ~5719-eV incident energy gives a clean fingerprint of the f-electron ground state properties.

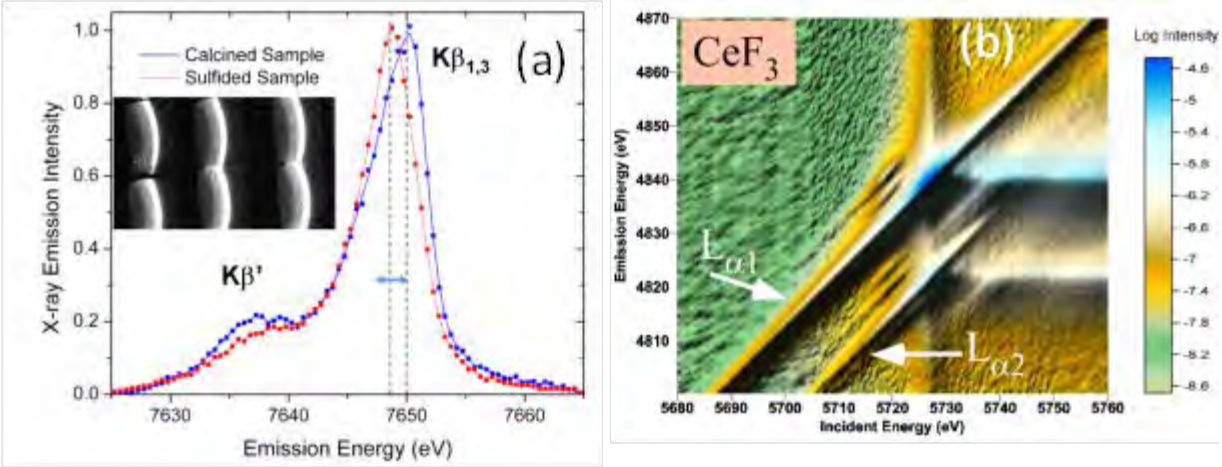

Figure 4-106: Some recent miniXS results. ***(a)*** *Non-resonant x-ray emission spectra showing the shift in the $K\beta_{1,3}$ maximum x-ray emission energy depending on the sulfided or oxidized Co bonding environment. The inset shows the XES spectrum collected from a single snapshot from the miniXS for one of the samples. The reflection from six crystals is shown.* ***(b)*** *A spectroscopically complete RXES study for the Ce Lα emission of CeF_3 using the miniXS instrument installed at 20-ID of the APS. Note the strong splitting of the pre-edge resonance at ~5719-eV incident photon energy LERIX branch*

4.12.1.2 LERIX branch

The LERIX branch will support the LERIX spectrometer for x-ray Raman studies (XRS) and upgraded UHV chambers provided by Canadian collaborators. X-ray Raman scattering, from semi-core and relatively low-lying electronic core levels, is an emergent branch of synchrotron-based science. XRS is a subset of nonresonant inelastic x-ray scattering (NIXS), which more broadly also includes the scattering from valence levels. In XRS or NIXS, a fixed-energy spectrometer and a scanning monochromator work in unison to generate energy loss spectra which, at given momentum transfer Q, provide a direct probe of the electronic excitations in the system. This technique has gone from being a curiosity, used in only a handful of studies prior to 1995, to being a central part of the plans of all third-generation light sources.

X-ray Raman spectroscopy (XRS) is a very powerful tool for examining the chemical structure and environment in light elements embedded in thick or absorbing objects [135]. It combines the power of soft x-ray spectroscopy with the *in situ* capabilities of hard x-rays. This technique has been widely used in high-pressure research to examine light elements, including hydrogen. Recent work at the APS has demonstrated that XRS is applicable to work on Li-ion batteries, providing important information about the redox chemistry through measurement of all low-energy edges in the system (i.e., the oxygen *K*-edge, transition metal *L*- and *M*-edges, and in some cases, the Li *K*-edge). In addition, it is possible to explore the momentum transfer (Q) dependence of the scattering, move beyond the dipole approximation, and access a unique combination of S(Q,ω),which cannot be observed with longer-wavelength, electromagnetic radiation [136, 137, 138, 139, 140].

The second major capability of the beamline is the UHV station. In addition to continuing to allow UHV surface XAFS studies, it will be upgraded to allow the fluorescence spectroscopy described in section 4.12.1.1 and to allow use of the advanced detectors being developed for ultra-dilute detection. This

upgrade will be carried out by Canadian collaborators and will likely be complete prior to the APS Upgrade beamline scope described here. They have also agreed to support its use by general users subject to possible restrictions on what will be allowed in the chamber. There will always be a subset of samples that will require *in situ* UHV conditions. These include kinetic studies of growing films and interfaces, the initial bonding as interfaces are formed, and air-sensitive thin films that are not amenable to capping layers.

4.12.2 Source Requirements

The Advanced Spectroscopy branch will operate over the energy range of 3.5-27 keV. As a microprobe it will require the highest brightness possible throughout this range. A canted version of an APS Undulator A (3.3-cm period) would be a good choice.

The LERIX branch will cover a similar energy range of 4-32 keV, although the majority of operations will be in the range of 9-12 keV. For the LERIX branch the most important parameter is flux rather than brightness. An Undulator A will satisfy the basic requirements. If a revolver undulator becomes available, then a 2.6-cm-period undulator could provide a significant flux increase in the 9-12 keV range. An Undulator A could be used to fill in the gaps in the spectrum from the 2.6-cm undulator.

4.12.3 X-ray Optical Layout

The basic optical layout of the two branches is shown in Figure 4-107. The two branches will be discussed separately. In this section we describe the basic beamline layouts, with more detailed specifications for the individual components given in section 4.12.4.

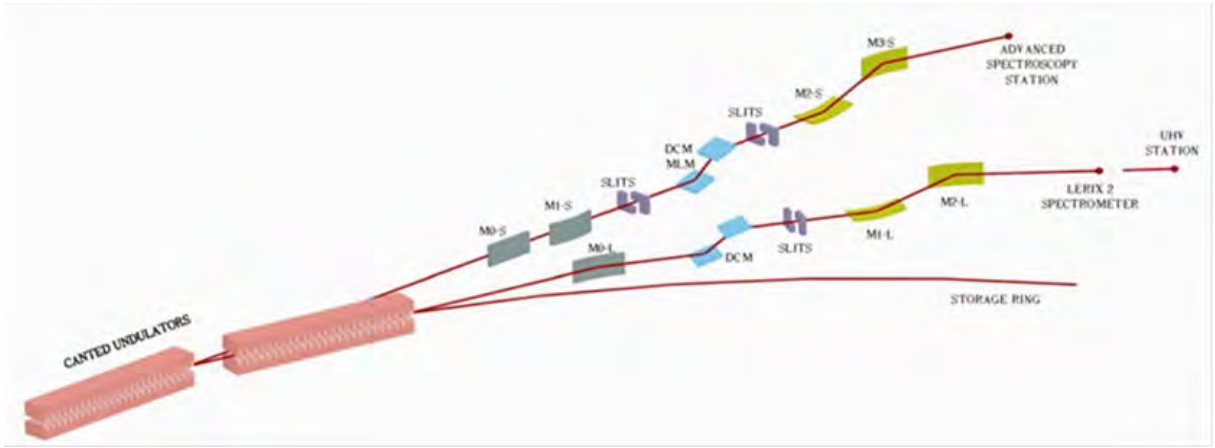

Figure 4-107: Basic optical layout of the two branch lines.

4.12.3.1 The Advanced Spectroscopy Branch

This branch will be the outboard side station. As such it will have the LERIX branch beam pipe passing nearby. To achieve a greater separation of the branches, horizontally deflecting mirrors will be used.

4.12.3.1.1 Mirrors

Two horizontally deflecting mirrors will be the first optical components. They will be located in the FOE for maximum downstream beam deflection. They will operate at about 3-mrad horizontal deflection to increase the canted beam separation by about 12 mrad. The first mirror will be flat, while the second will be bent or figured to provide a horizontal focus at the intermediate source-point defined by downstream slits. These mirrors will each have three reflecting stripes (likely bare Si, Rh, and Pt) to provide harmonic rejection and cover the operational energy range. Vertical translation is required to change the reflecting stripe utilized. To maximize the beam branch line separation, these mirrors should be as close to the source as feasible.

There are two alternative deflection schemes. The preferred is to deflect the inboard beam in the inboard direction, and the outboard beam in the outboard direction as shown in Figure 4-107. This has the disadvantage that the first outboard mirror has to be fairly thin (~20 mm) in the region of the beams to allow the second inboard beam to pass by. Since this is a horizontally deflecting mirror, gravitational bending should not be an issue and the edges of the mirror can be thicker to stiffen it for polishing. The issue is proper cooling and avoiding thermal distortions. Discussions with vendors are currently under way, and finite element analysis (FEA) calculations will be carried out as needed.

If this arrangement proves to be problematic, the alternative is to use the mirrors to cross the beams, deflecting the inboard beam outwards and the outboard beam inwards. This would allow arbitrary thickness mirrors, but reduce the total beam offset. Bremsstrahlung and synchrotron radiation ray tracing (see section 4.12.4.2.1) indicates both are feasible.

4.12.3.1.2 Monochromator

The monochromator will provide two operational modes (see section 4.12.4.4.5). The first is as a standard Si<111> monochromator with liquid nitrogen-cooled crystals and fixed exit operation. The second mode is as a multilayer monochromator with the multilayer crystals located directly upstream and downstream of the Si first crystal and second crystal, respectively. Shifting between modes will require a small vertical translation of the monochromator. For this to be feasible, the beam offset must be small (~10 mm). A small offset is possible because the large horizontal beam-offset provided by the first mirrors should allow bremsstrahlung shielding requirements to be satisfied by horizontally offset collimators. Initial ray tracing (see section 4.12.4.2.1) demonstrates the feasibility of this approach.

4.12.3.1.3 Focusing Elements

The final focusing elements will be a set of Kirkpatrick-Baez (K-B) mirrors located close to the sample. The vertical focusing mirror will image the source and provide a 2-μm vertical focus at the normal sample position. The horizontal mirror will image the intermediate focus and provide a 2-20-μm horizontal focus depending on the setting of the intermediate-focus horizontal aperture. By combining quick scanning of the sample in the vertical direction with the variable horizontal beam size, the microprobe will provide effective resolutions from 2-20 μm that can be quickly changed by the user. Both mirrors will be bendable to allow for optimization of the mirror angles for best efficiency, the ability to increase the spot

size for reduction of radiation damage, and the repositioning of the focus to accommodate *in situ* set-ups that might require a larger working distance.

4.12.3.2 LERIX Branch

The LERIX branch will provide beam into two experimental stations. The first will house the LERIX spectrometer, and the second will house two UHV chambers for *in situ* sample preparation and measurement.

4.12.3.2.1 Mirrors

The first optical element will be a horizontal-deflection collimating mirror. Ray tracing has shown that for small undulator beams a cylindrical approximation provides excellent collimation in the vertical direction. This mirror would be Rh coated and operate at approximately 2 mrad to provide an additional 4 mrad of beam separation. Rh is chosen because its L and K edges provide minimal interference within the intended operating range. To maximize the beam branch line separation at the experimental station, the mirror is placed as close to the source as feasible.

4.12.3.2.2 Monochromators

The monochromator will be a liquid nitrogen-cooled double-crystal instrument. This monochromator will use Si<111> crystals to take the primary heat load of the beam. To allow flexibility in optimizing the energy resolution there will also be a secondary monochromator preceding the K-B focusing mirrors. This will be a simple, uncooled, channel-cut Si monochromator with easily exchangeable crystals.

4.12.3.2.3 Focusing Elements

Final focusing will be provided by a pair of K-B mirrors located in the C enclosure. In the baseline scope these will be a pair of 300-mm-long mirrors currently in use at Sector 20.

4.12.4 Beamline Physical Layout

A sector layout is shown in Figure 4-108. This assumes that the beamline will be located at the unoccupied Sector 25. There will be a total of five enclosures as shown. The A and B enclosures will house optical components. The C enclosure is for the AS experimental station. The D enclosure will house the LERIX spectrometer along with its focusing mirrors, and the E enclosure will house two UHV chambers operated by the spectroscopy group's Canadian collaborators based at the Canadian Light Source.

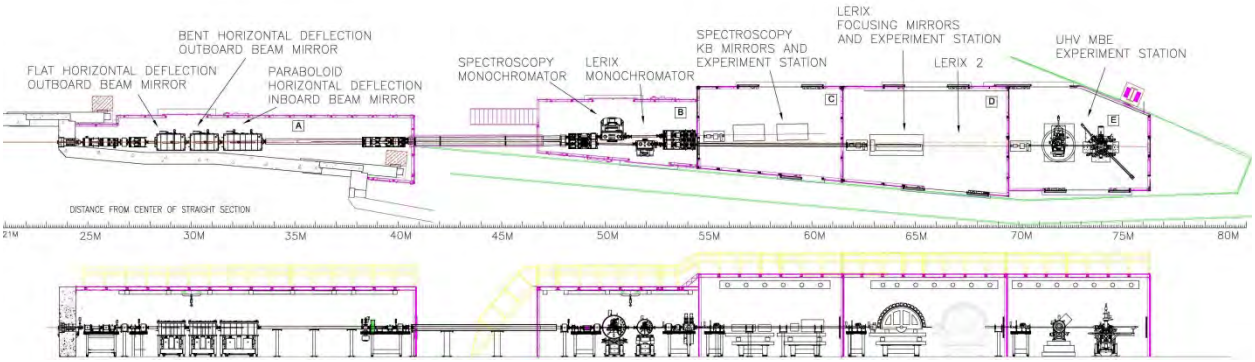

Figure 4-108: Sector layout showing enclosures and main optical components.

4.12.4.1 Front End

The front end will be a standard canted undulator front end.

4.12.4.2 General Description of Physical Layout

4.12.4.2.1 Radiation Safety Aspects

The FOE will be compatible with canted-undulator operation. The second optical enclosure will be compatible with pink beam, accepting the branch beams reflected from their deflecting mirrors. The typical mirror cutoff energy will be approximately 30 keV. The other three enclosures are for monochromatic beam. The C enclosure will accept a wide-bandpass monochromatic beam. This enclosure will also require a compact shielded beam pipe for bringing the LERIX branch beam to the D and E enclosures while access is allowed to the C enclosure. A removable beam stop between the D and E enclosures is included to allow set-up in the E enclosure while beam is brought into the D enclosure.

The horizontally deflecting mirrors satisfy the radiation safety requirements using collimators offset in the horizontal direction. Two configurations of the mirrors are under consideration, as shown in Figure 4-109; either one will satisfy radiation safety requirements, although the non-crossed-beam case provides more clearance at the experiment.

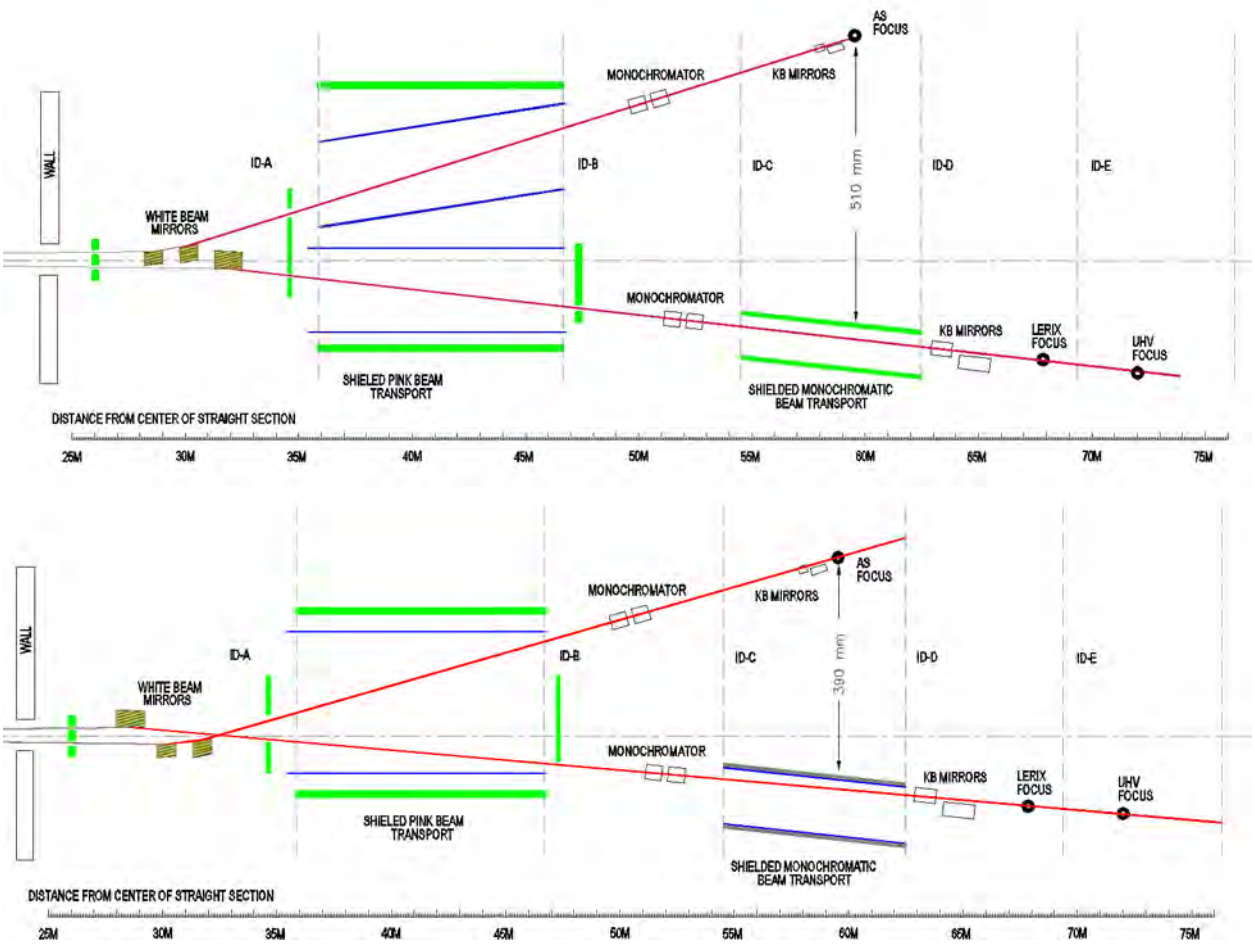

Figure 4-109: Simplified horizontal ray traces showing the required collimators/stops (vertical green lines) for the two possible mirror configurations.

4.12.4.2.2 Heat Load Considerations

The mirrors will reduce the power passed on to the downstream optics. Table 4-33 summarizes the maximum powers expected to be absorbed by various components. Of particular interest is the monochromator first-crystal performance at 150 mA. The total power from the canted undulator at 150 mA is somewhat higher than the current Sector 20 installation. The mirrors provide significant power filtering, reducing the total power. However, they absorb the higher energy x-rays that would penetrate deeply into the Si crystal and so are easier to handle. To provide a comparison of different cases, Lee et al. [141] suggested using the average power absorbed in the first 10 μm of beam path because this is the approximate diffracting region. Various cases calculated using the XOP program are shown in Table 4-33. The current Sector 20 power load is also given for comparison. Closed-gap operation will only occur for the third harmonic at 9 keV because the specifications do not call for a closed gap for the first harmonic. For the crystal the lowest energy of operation is generally the most severe and these cases are included. It has been found that the total heat load is more important than the power density, although both are a factor. In all cases, the total heat load on the first crystal will be less than the current installation at Sector 20, suggesting that the preliminary design for indirectly cooled Si crystals should be

able to handle the heat. However, for the AS branch the horizontal focusing gives rise to large average power densities exceeding 10 W/mm^2, although the total power is quite low.

The Project has initiated FEA calculations to compare these cases with the Sector 20 monochromator since it is known that the distortions there are currently acceptable. In an extreme case, it is assumed the Rh mirror can be used at the lowest energy (3.5 keV). This has a similar surface power density as the Si case, but the total absorbed power is increased to 104 W. Normally the Si stripe would be used for this case, but the potential exists for the Rh stripe to be used as well. The initial calculations used simplified models that may do not give accurate absolute distortions, but are believed to be sufficient for an initial comparison. The distortions and maximum temperature were found to be slightly smaller than for the current monochromator. Thus, it is preliminarily assumed that the heat loads should be manageable.

The maximum powerfor the mirrors is found for the Si first mirror on the AS branch. At closed gap, this will absorb 250 W over a length of about 600 mm.

Table 4-33: Power calculations for optical components. The Sector 20 first-crystal power is given for comparison. The current aperture for Sector 20 is 2.4 x 1.2mm at 31 m. The proposed apertures for the new beamlines are 2 x 1mm at 28 m.

Optical System	**Conditions**	**Total Power through Aperture**	**Absorbed Power, First Mirror**	**Absorbed Power, First Crystal**	**Absorbed Power in 10-µm Si**	**Avg. Power Density, First-Crystal Surface**
Sector 20 First Crystal	100-mA full Undulator A, 4.3 keV	244 W	No mirror	244 W	18.9 W	3.0 W/mm^2
Lerix Branch	150-mA canted Und. A, 2-mrad Rh, 9 keV	293	107	166	19.9	2.2
Lerix Branch	150-mA canted Und. A, 2-mrad Rh, 4 keV	276	91	165	20	5.0
AS Branch, Rh Mirrors	150-mA canted Und. A, two 3-mrad Rh mirrors, 9 keV	293	177	82	18.3	4.5
AS Branch, Si Mirrors	150-mA canted Und. A, two 3-mrad Si mirrors, 3.5 keV	284	235	43	16.8	10.7

4.12.4.2.3 Vacuum System

To minimize absorption at low energies, both beamlines must be compatible with windowless operation using a differentially pumped transition from the front end to the FOE. Therefore, all components must be designed to minimize outgassing of heavier components detrimental to operation of the storage ring. This generally requires UHV-compatible components, although this condition could be relaxed if the component is sufficiently isolated from the front end and mirrors. UHV conditions are also required for

the main beamline mirrors to maintain their cleanliness. Both beamlines will comply with the APS beamline vacuum policy for windowless operation.

4.12.4.2.4 Data Acquisition and Motion Control

It is planned to continue use of the current beamline control system and software, with upgrades to support new components and to replace obsolete systems. The current system uses a Labview user interface with a standard APS Experimental Physics and Industrial Control System providing the underlying beamline control. The software and controls will be upgraded to support quick scanning of the microprobe stage and the AS monochromator.

4.12.4.3 First Optics Enclosure (25-ID-A) and Infrastructure, Major Components

The first optic enclosure has a standard layout as shown in Figure 4-108 with provision for the two beams from a canted undulator. Major components are described in the following sections.

4.12.4.3.1 Windows

Both beamlines will be windowless except for the final Be window near the experiment. These windows will be polished to minimize coherence artifacts in the beam-intensity profiles.

4.12.4.3.2 Slits/Apertures

Both beamlines will require water-cooled apertures to minimize the heat load on the downstream components. These apertures are needed in front of the horizontally deflecting mirrors and the monochromators. At present, fixed size apertures are planned, but they could be variable white-beam slits if needed. The primary heat-reducing apertures will be located directly in front of the mirrors, and as indicated in section 4.12.4.2.2, a 2 x 1-mm opening will pass the entire central cone of the undulator.

4.12.4.3.3 Collimators

Sufficient collimation is required to provide the necessary bremsstrahlung and synchrotron radiation protection while operating the two branches independently. This will be determined by detailed ray tracing of the final layout. Based on preliminary ray tracing, standard collimator designs will be sufficient.

4.12.4.3.4 Shutters/Stops

White/pink-beam stops will be required after the monochromators and as necessary to protect the bremsstrahlung collimators.

4.12.4.3.5 Mirrors

The FOE will house the horizontally deflecting mirrors for both branches. For the AS branch, there will be two mirrors in series, each set at 3 mrad. Both will be water-cooled Si approximately 800-mm long. The first mirror will be flat and the second mirror will focus the beam horizontally onto an aperture in the second optics enclosure (SOE). These will have three reflecting stripes: bare Si, Rh, and Pt. Rh is the general purpose option covering most of the energy range below 22 keV without edges; Pt allows operation to 27 keV; Si will be used below 9 keV for harmonic rejection. A vertical translation is needed to switch between stripes. The mirrors will each require a meridional slope error of less than 2 μrad under the full heat load of the undulator. The radius of the second mirror will be approximately 7 km. Each mirror will require precision positioners with typical specifications as given in Table 4-34. The mirrors and positioners must be compatible with the second undulator beam passing nearby.

Table 4-34: Typical specifications for the positioning systems of the horizontal deflecting mirrors in the FOE.

Axis	Range	Precision
X (horizontal)	±5 mm	1 μm
Y(vertical)	±15 mm	5 μm
Θ (tilt or rot. about vertical axis)	-2 → 5 mrad	2 μrad
φ (yaw or rot. about horizontal axis)	±5 mrad	5 μrad
χ (roll or rot. about beam dir.)	±5 mrad	5 μrad

For the LERIX branch there will be a single side-deflecting mirror to collimate the beam. It will be paraboloidal in shape or an approximation (e.g., cylindrical) that can meet the slope error specifications. The slope error specifications will be determined by ray tracing. This mirror will collimate the beam vertically to better than 5 μrad, and additionally, the slope errors should not degrade the final focus significantly. It will operate at 2 mrad and consist of a water cooled Si substrate with a Rh coating. It will handle the full undulator power. It will also require a precision positioning system with specifications similar to those given in Table 4-34.

4.12.4.3.6 Diagnostics

There will be sufficient diagnostics to allow alignment of the mirrors. This will require retractable monitors capable of withstanding the white or pink beam downstream of the mirrors. Since they are needed for alignment only, they could potentially be operated with large undulator gaps to reduce heat loads.

4.12.4.4 Second Optics Enclosure (25-ID-B)

The second optics enclosure, as shown in Figure 4-108, will house the two branch-line monochromators, the horizontal source point for the AS K-B mirrors, and monochromatic beam shutters for the two branches.

4.12.4.4.1 Slits

This enclosure will house the horizontal source point for the K-B mirrors of the AS branch. It will require a precision set of slits capable of handling the horizontally focused pink beam. It will have precision of 2 μm, and the horizontal opening will typically be varied between 40 and 500 μm depending on the desired focal spot size. The vertical opening will only be used to control the monochromator resolution (the vertical source point is the ring), and will typically be in the range of 0.3 to 1 mm. For beam monitoring purposes, the drain current from the slit jaws will be independently measured.

4.12.4.4.2 Collimators

Sufficient collimation is required to provide the necessary bremsstrahlung and synchrotron radiation protection while operating the two branches independently. This will be determined by detailed ray tracing of the final layout.

4.12.4.4.3 Shutters/Stops

Pink-beam stops will be required after the monochromators and as necessary to protect the bremsstrahlung collimators. This enclosure will also house the monochromatic beam shutters for both branches.

4.12.4.4.4 Diagnostics

There must be sufficient diagnostics to allow alignment of the mirrors and monochromator. This will require a retractable imaging monitor in front of the AS slits capable of withstanding the pink beam downstream of the mirrors. This will be used to optimize the horizontal focus. Also included will be the capability of monitoring the drain current from the slit jaws as an online monitor of the beam position.

4.12.4.4.5 Monochromators

Advanced Spectroscopy Monochromator

The monochromator for the AS branch will be located in 25-ID-B. It will be a fixed-offset monochromator with liquid nitrogen-cooled crystals. It will be designed to allow the LERIX branch beam to pass nearby. The exact clearance will be determined by the final layout, but is expected to be at least 200 mm. It will have two crystal options. The first is Si<111> crystals. Their energy range is 3.5-27 keV (4-35° Bragg angles). A small beam-offset is used to allow use of multilayers (see below) and to enhance the stability of the monochromator. Its value will be optimized in the final design. With a beam offset of 10 mm the second crystal will be at least 80-mm long. The first crystal will be long enough to provide for proper heat transfer to the liquid nitrogen coolant.

For high-flux applications, the monochromator will have multilayers mounted directly upstream of the first crystal and downstream of the second crystal as shown in Figure 4-110. The desired energy range is approximately 7-15 keV. To maintain the 10-mm offset this would require 150-mm-long multilayers with

a d-spacing of approximately 30 Å. These would operate in the Bragg-angle range of approximately 0.5-2°. A vertical translation of the monochromator will switch between crystal options.

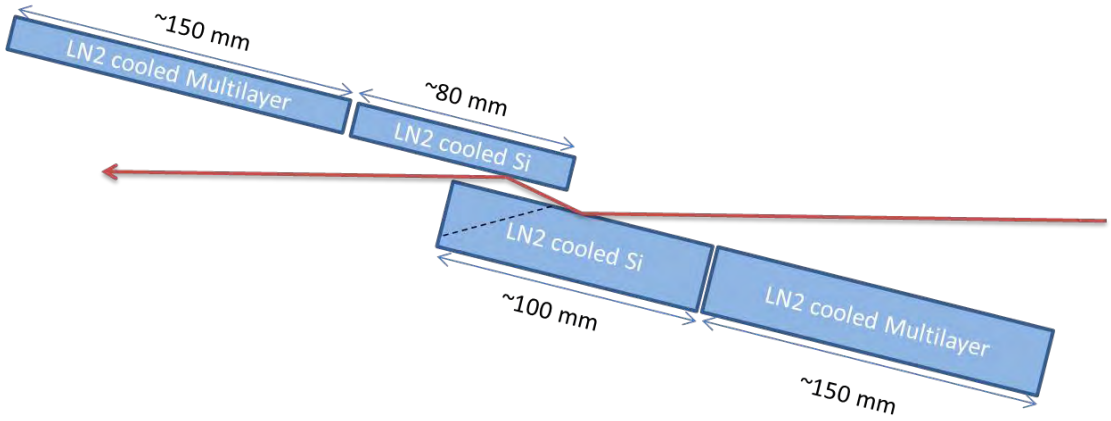

Figure 4-110: Proposed monochromator crystal arrangement with small beam offset and multilayer option. Approximate crystal sizes are shown. The first crystal must be massive for proper cooling. The first Si crystal also requires a notch (dashed line) to allow the reflected beam from the second crystal to pass when operating at large angles.

General features of the monochromator will include:

- An accurate angle-encoder located on the main rotation axis with better than
  0.5-µrad resolution and 5-µrad accuracy
- Smallest motor step of less than 1 µrad
- Scan speed of greater than 0.5°/sec
- Appropriate alignment stages to accurately align the first and second crystals; this includes some type of piezo stages for real-time feedback of the crystal alignment
- Cooling of the second crystals to less than 150 K with full ID power incident on the first crystal
- Provision for active temperature control of the second-crystal mounts to minimize alignment shifts with ID gap changes
- Vacuum compatibility to 10^{-8} torr or better.

LERIX Monochromators

The primary monochromator for the LERIX branch will be located in the 25-ID-B. It will require specifications similar to the AS monochromator, but will only need the Si<111> crystal option. Higher energy resolution will be provided by a secondary monochromator located in the LERIX station (see section 4.12.4.6.1). The operating energy is 4-32 keV (3.5-30° Bragg angles).

As discussed in section 4.12.4.2.2, operation up to 150 mA with a canted Undulator A should be possible with the current indirect crystal-cooling solution in most beamline configurations. Additional FEA thermal studies are needed to fully validate this conclusion and to validate possible upgrades to 150-mA operation with a 26-mm-period undulator or for 200-mA operation.

4.12.4.5 Advanced Spectroscopy Station (25-ID-C)

The C station is a monochromatic beam enclosure capable of handling the beam from a multilayer monochromator; it will house the AS experimental station. It will require upgraded temperature control to better than 0.5° C and facilities for handling hazardous gases. In front of the station there will be a beam monitoring and conditioning station. This will consist of beam intensity and position monitors, a fast shutter, and a set of computer controlled filters to allow adjustment of the beam intensity.

4.12.4.5.1 Experimental Station

In the base scope, the existing Sector 20 microprobe station will be used with upgraded K-B mirrors. New K-B mirrors will be designed to collect the full beam from the intermediate source point and focus to better than 20-μm horizontally and 2-μm vertically. The working distance from the end of the K-B mirror tank must be at least 15 cm. The horizontal source point is the intermediate slit and the horizontal focusing mirrors will supply a better than 2-μm focus when the intermediate slits are closed to smaller than 50 μm. This will require mirrors with slope errors less than 0.5 μrad. These mirrors will operate in the angle range of 2.5 to 5 mrad. Thus, they will be bendable.

4.12.4.5.2 Advanced Spectroscopy Detectors

The experimental station will require several types of detectors. A 4-element vortex detector, a 13-element Ge detector for higher energies, a WDX spectrometer, and a prototype polycapillary based high-resolution spectrometer are currently available. Section 4.12.5.4.1 describes some potential upgrades to this set of detectors. A limited set of miniXS spectrometers for rapid parallel detection of the emission spectrum are also available.

The miniXS spectrometers will require a large-area, Pilatus-type pixel array detector capable of detecting individual x-ray photons. A Pilatus 100K is currently being utilized. This detector is also the microdiffraction detector for microprobe applications, and for the alignment and possibly the operation of SBCAs. Area detectors from the Detector Pool should cover those rare cases when both miniXS and microdiffraction are required.

The miniXS detectors are undergoing rapid development [134]. Generally each elemental fluorescence line will require a specialized detector. Under development at Sector 20 is a modular system of diffracting crystals and apertures that can be combined with a common detector mount to allow easy shifting between fluorescence lines. Sufficient modules will be produced to cover the entire range of absorption edges for which miniXS-style detectors are appropriate. Generally this would be for energies less than about 12 keV. For higher energies, SBCAs are more appropriate, and the Project is planning appropriate alignment systems to handle one or more of such analyzers.

4.12.4.6 LERIX-2 Station (25-ID-D)

This is a monochromatic beam enclosure that will house the final focusing optics for the LERIX branch and the LERIX-2 spectrometer. At the front of enclosure there will be a secondary monochromator and a beam monitoring and conditioning station. This consists of beam intensity and position monitors, and a set of computer controlled filters to allow adjustment of the beam intensity.

4.12.4.6.1 Secondary Monochromator

The secondary monochromator will match the beamline resolution to the experiment for those cases needing resolution better than provided by Si<111> crystals. Because the beam has been collimated, the use of a secondary monochromator can be nearly as efficient as having exchangeable crystals in the primary monochromator. The only loss is due to the reflectivity of the two additional reflections, which is close to 1 for Si. This arrangement provides greater flexibility in matching the beamline resolution to that needed for the experiment and avoids the need to exchange liquid nitrogen-cooled crystals. The secondary monochromator is a simple channel-cut Si crystal mounted on an encoded high-resolution angular stage providing a smallest step of 0.5 μrad and 2-μrad accuracy. The crystals will be easily exchangeable. It is expected that Si<311> will be used for high resolution, and Si<220> for intermediate resolution.

4.12.4.6.2 K-B Focusing Mirrors

The primary focusing for the upgraded beamline will be a set of 300-mm long K-B mirrors currently in operation at Sector 20. While not optimum (see contingent additional scope section for possible improvements), they will collect the majority of the monochromatic beam and focus to a spot size of about 40 (H) x 20 (V) μm. This is a significant improvement over the current 400 x 200-μm focus.

4.12.4.7 25-ID-E Enclosure

The E station will be a monochromatic beam enclosure approximately 5 x 7 m. It will house the upgraded UHV chambers run by the spectroscopy group's Canadian collaborators.

4.12.4.7.1 UHV chambers

There will be two UHV chambers. These will be supplied by the Canadian collaborators and are not part of the APS Upgrade Project scope. They are being upgraded to support emission spectroscopy as well as surface XAFS.

4.12.5 Additional

4.12.5.1 Safety Requirements

The C, D, and E enclosures will be capable of handling hazardous gases such as hydrogen and carbon monoxide. This requires a hazardous-gas exhaust system, a hazardous-gas storage cabinet, and appropriate hazardous-gas sensors.

4.12.5.2 Conventional Facilities Requirements

A full set of cable trays connecting the enclosures and control stations are required along with liquid nitrogen lines connecting the monochromators to the liquid nitrogen pumps located outside of 25-ID-B. A standard APS water skid will be installed in the mezzanine to provide cooling water for beamline components. As discussed above, some of the enclosures will require improved temperature control. An enclosed controls area will be located near the C and D enclosures, with two rooms to service the two branches. No unusual power requirements are anticipated. The standard sector power will be sufficient.

The E enclosure will have enhanced roof fans equipped with filters to provide a cleaner environment for the UHV equipment.

4.12.5.3 Beam Transport

Between the FOE and SOE there will be shielded pink-beam transport capable of handling the two canted beams. In the C enclosure a compact monochromatic beam transport pipe will transport the LERIX branch beam with minimal interference with the AS experimental station.

4.12.5.4 Contingent Additional Scope

If additional funds become available, there are several additional upgrade components that could be applied to the experimental stations. For the AS branch this would include a new support platform with improved experimental station equipment and a number of detector upgrades. For the LERIX branch the primary additional scope will be improved focusing mirrors and enhancements to the LERIX spectrometer.

4.12.5.4.1 Advanced Spectroscopy Upgrades [CAS]

The enhanced experimental station is proposed to improve the experimental station stability, provide better sample scanning, and better support multiple detection options. It consists of two parts: a highly stable platform with entrance slit, K-B focusing mirrors, I_0 detector and cleanup aperture, precision sample stages, and transmission detector; and a second detector platform that will handle heavy detectors such as large area detectors, multiple bent-crystal analyzers, or multi-element fluorescence detectors. This will allow detectors to be moved or changed without affecting the focused beam size or position.

The stable mirror platform will have an overall horizontal (±5-mm) and vertical (±5-mm) travel to allow alignment with the incident beam. This motion will support at least 100 kg and have a resolution of 1 μm in both directions. The detector platform will also need horizontal (±25-mm) and vertical (±50-mm) travel. These motions will support at least 150 kg with a resolution of 1 μm.

The precision sample stage will provide precision linear motion of 0.2-μm resolution and handle sample loads up to 20 kg. At a minimum 3 axes of linear motion with at least 50-mm travel and 1 rotation axis are required. The need for additional motions is currently being evaluated.

The I_0 detector and cleanup aperture will be combined and mounted on a motorized mount for alignment with the beam. This mount will require two axes of linear motion, with 1-μm resolution. The mount will have sufficient motion to allow removal of the aperture from the beam during alignment operations.

The upgraded experimental station will also provide a means of optically aligning the sample to the x-ray focal-spot position along three axes. This will likely be a dual TV camera system or crossed laser beams.

Two approaches to the detectors for dilute concentrations are being considered. The same type of SBCAs as for emission spectroscopy could be used, although the tradeoff between collection solid angle and energy resolution would be different. However, it is expected that the same alignment infrastructure could be used in both cases. A second approach is the use of collimating polycapillary optics with flat crystal analyzers [142, 143]. These same optics could be used for confocal (depth dependent) mapping and reduction in background scattering. Initial tests are promising. They require a compact θ-2θ spectrometer and appropriate alignment stages to accurately (1-μm resolution) align the optic to the x-ray beam along three axes. A range of analyzer crystals will be required in order to efficiently match an energy range from 3 keV to somewhat past 20 keV. A prototype version of this detector has proven the concept, and further development is proposed to add additional, more efficient spectrometers.

For general microprobe applications a multielement Si drift detector is most appropriate. Currently, these can be purchased in 4-element configurations, although more elements may be possible in the future. As an upgrade over the single 4-element detector currently in use, a total of three 4-element detectors will be supported, mounted in a suitable mounting frame that allows an adjustable sample-to-detector distance and provides suitable collimation to suppress the scattering background. This mount will also allow the easy (possibly mechanized) addition of detector filters. A number of single element drift detectors will also be used with the SBCAs and with polycapillary analyzers.

4.12.5.4.2 LERIX Upgrades [CAS]

When looking to the future, it is important to seek experimental capabilities that further enable the ongoing transition of NIXS to a truly standard synchrotron radiation technique. The baseline beamline will be optimized for NIXS capabilities. It requires only the addition of better K-B focusing mirrors and an improved LERIX (LERIX-2) spectrometer to take full advantage of its capabilities. The new K-B mirrors will provide approximately 20% better collection efficiency. In addition, the new mirrors will be designed in conjunction with the spectrometer to allow placement closer to the sample, resulting in a smaller focal spot. This will be particularly advantageous for high-pressure studies in diamond anvil cells (DACs) where users have requested spot sizes near 10 μm.

The LERIX-2 spectrometer is an upgraded version of the LERIX-1B spectrometer with provision for better collection efficiency and improved sample handling capabilities. The goal for the upgraded system is to have at least five times the effective signal of the current LERIX-1B spectrometer, which uses 19 100-mm Si<555> analyzers located 1 m from the sample. This can be achieved by better collection solid angle, better matching of the analyzer resolution to the beamline, and better rejection of the background.

As a path to this improvement there are several possible upgrades:

1. Moving from the present Si <555> reflection to the more efficient Si <660> reflection; following work at the European Synchrotron Radiation Facility, "relief cut' analyzers will be utilized, with coarse dicing on the scale of ~3 mm to obtain a reasonable relaxation of stresses and achieve a net energy resolution that will be monochromator limited.
2. Ge <660> for improved integral reflectivity could yield more than a factor of two increase in integral reflectivity over Si <660> at equal collection solid angle. It will be important to verify that resonant Raman scattering from the Ge K-edge does not provide an untenable fluorescence background at the detectors up to operations at 10.7 keV, i.e., 1.5 keV past the elastic line.
3. SBCA with radii of curvature somewhat smaller than the 1-m standard moving to 85 cm, for example, would allow a 30% decrease in the number of analyzer modules and associated support electronics and alignment protocols with no decrease in total collection solid angle. For operation at ~10 keV, there is no obvious technical limitation to achieving "relief cut" analyzers at 85 cm or somewhat smaller that are still monochromator limited. It may be necessary to somewhat trim the analyzer collection angle in the dispersive direction to minimize Johann error contributions when working farther from backscatter.
4. Using polycapillary based coupling optics to improve the collection efficiency of an individual analyzer by several times. The confocal nature of the polycapillaries also provide very useful rejection of background scattering, an enormous benefit for small samples surrounded by containment such as in DAC's.

These improvements will instantly enable and make standard a broad range of important studies that are generally impossible, or at least prohibitively difficult, to conduct with existing facilities at the APS or elsewhere.

4.13 Magnetic Spectroscopy – Soft X-rays

The Soft X-ray Magnetic Spectroscopy (MS-S) program currently resides in Sector 4 at the Advanced Photon Source (APS) (beamline 4-ID-C) which is shared with the higher-energy magnetic spectroscopy program (beamline 4-ID-D) by using canted undulators in the 4-ID straight section. Consideration was given to upgrading this beamline at its current location (4-ID-C) however, concerns were expressed about the storage ring stability with the co-location of two helical insertion devices in the same sector (4-ID-D upgrade involves replacing the current planar with a helical device). Therefore, the baseline design for the APS Upgrade for this beamline calls for moving the MS-S beamline into a new sector, nominally 2-ID, where it will share the straight section with another beamline that uses a planar device. This is the most

conservative approach involving the least risk to the Project. If the conflict of having two helical devices in the same sector can be mitigated, an upgrade of the MS-S beamline in its current location as originally planned could still be considered. In either scenario, the major components included in the MS-S upgrade are the same, involving the following:

1. The installation of a specialized variable-polarization insertion device with fast switching capabilities (~10 Hz);
2. replacement of the beamline mirrors and monochromator to increase the available flux by two orders of magnitude;
3. installation of new focusing mirrors to provide more flexible flux densities in each experimental station;
4. installation of a new higher-field, cryogen-free magnet to expand sample environment capabilities; and
5. the addition of a control area enclosure.

4.13.1 Scientific Objectives

Since the discovery of the x-ray magnetic circular dichroism (XMCD) effect, and especially its demonstration at soft x-ray absorption edges, this technique has become an indispensable part of the suite of experimental methods needed for research in magnetic materials [144]. Its elemental, chemical, and magnetic specificity, high sensitivity, and applicability to imaging and time-resolved techniques have produced a revolution in magnetic materials research. The present state of the art in soft x-ray magnetic circular dichroism is usually achieved on helical undulator beamlines at third-generation synchrotrons, where differences in the absorption signal of ~ 10^{-3} can be observed. Such capabilities will enable the detection of magnetic moments down to 0.01 μ_B/atom and probing the magnetization in sub-monolayer thin films. While this sensitivity is quite high, many XMCD experiments have become flux- and sensitivity-limited. This is due to the fact that the most interesting new and emerging physics now involves small induced magnetic moments, buried interfaces, nanoscale structures, or very dilute systems. Therefore, either the sample volume or the intrinsic signal level has evolved to push the limit of soft x-ray dichroism at the APS and other synchrotron sources.

For example, the induced magnetic moments in doped magnetic semiconductors are ~ 0.01 μ_B/atom for doping levels of between ~2-5% [145]. However, this doping level is relatively high, and to truly understand the physics of an isolated dopant, it is essential to study samples with much lower concentrations, which are beyond the present limits of XMCD sensitivity. Furthermore, better sensitivity will provide the opportunity to study dynamics of spin-polarized carrier populations in the confined geometries of real devices (see Figure 4-111) using element-specific time-resolved magnetic imaging via x-ray photoemission electron microscopy (X-PEEM) [146]. Magnetic imaging experiments would provide information on how spin currents propagate, what electronic states are involved in their conduction, and what length scales are important for their application in real functional devices.

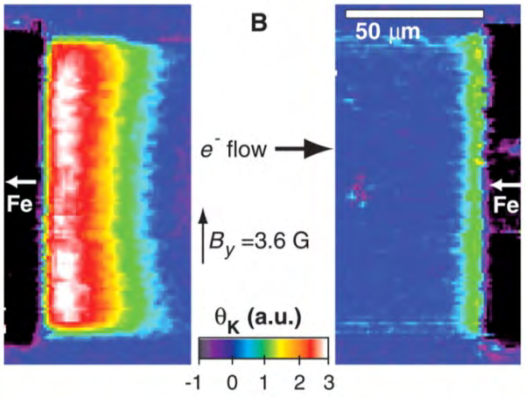

Figure 4-111: Spin accumulation in a GaAs microstructure measured by Kerr microscopy. Greater flux and sensitivity would enable XMCD and X-PEEM studies of such systems.

Other questions facing similar sensitivity limitations are the interplay between charge, magnetic, and structural order at complex oxide interfaces. Competing interactions at these interfaces can lead to new behaviors and functionalities, such as superconductivity. Probing the magnetism of such systems is difficult via conventional techniques, since a superconductor is a perfect diamagnet, frequently obscuring the signal of interest. X-ray techniques are insensitive to the diamagnetic components, making them the perfect tool for addressing such problems. Figure 4-112 shows XMCD measurements of a heterostructure consisting of superconducting $YBa_2Cu_3O_{7-x}$ and ferromagnetic $La_{0.7}Ca_{0.3}MnO_3$ [147, 148]. The magnetism of Cu and Mn can be tracked separately via XMCD, shedding light on how they coexist. However, these measurements were performed using electron yield, which only probes a single interface near the sample surface. To fully understand the behavior of this system fluorescence yield measurements probing multiple interfaces in the bulk of the sample are needed. With the low yield for fluorescence emission in this energy range, the signals are in general too noisy for the bulk-sensitive measurements of small signals. Therefore, higher flux sources and better fluorescence detectors are required for such studies.

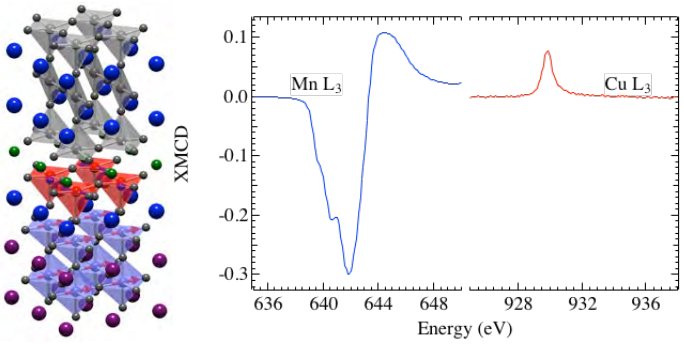

Figure 4-112: Element-resolved measurement magnetism at the interface between superconducting $YBa_2Cu_3O_{7-x}$ and ferromagnetic $La_{0.7}Ca_{0.3}MnO_3$.

Thin film and interface magnetism encompasses a wide range of fundamental scientific and technologically relevant problems. These include issues that are directly related to scaling down the dimensions such that finite size and collective effects dominate the magnetic behavior. XMCD has been

integral to the development of this field, providing information on the chemical environments as well as the spin and orbital moments of materials in reduced dimensionality. However, significantly improved sensitivity is necessary as new spintronic phenomena emerge. Figure 4-113 shows such an example of spintronic structure consisting of a thin 2-Å Fe layer between a Co/Pd multilayer and a Ta electrode. Calculations [149] suggest that the magnetism of the Fe layer can be turned on and off isothermally by applied voltage. Magnetic dichroism is the ideal technique to test these predictions and understand the role of electric fields on interfacial magnetism by quantitatively measuring the changes in the band filling and spin and orbital moments. The bottom panel in Figure 4-113 plots a recent attempt to measure this effect via XMCD fluorescence. This data took over 6 hours to collect and clearly there is not sufficient signal-to-noise to perform detailed studies of the systematic response to electric field. Improvements in the flux and sensitivity by two orders of magnitude will enable such photon-in photon-out spectroscopy experiments of buried interfaces in active device structures and dramatically increase our knowledge of electro-magnetic phenomena.

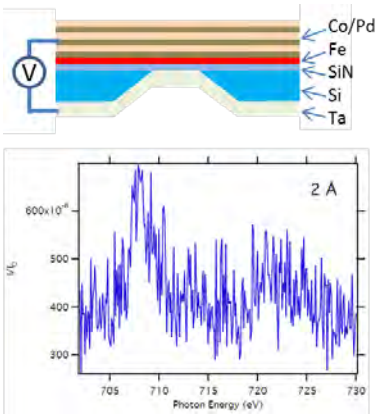

Figure 4-113: Schematic of a device structure for measuring anisotropy changes in a 2-Å Fe interfacial layer (red) along with associated Fe XMCD fluorescence data collected over 6 hours.

The above examples illustrate that x-ray based element-resolved studies have become a critical diagnostic tool, yet many effects are just barely observable with current sensitivity limits (detectable differences ~10^3), making comprehensive, systematic studies, and especially time-resolved studies, difficult to achieve. Therefore, the ability of polarized x-ray techniques to contribute similar insights into the most compelling questions of the *next* 10-15 years will be limited without substantial increases in sensitivity over the current capabilities. The upgrade of the soft x-ray magnetism beamline seeks to provide magnetic spectroscopy and imaging capabilities with a sensitivity level that is two orders of magnitude better than the current capabilities through a hundred fold increase x-ray flux (x10 in sensitivity), and faster polarization switching and lock-in detection (x10 increase in sensitivity). This improvement will enable XMCD experiments on materials with dilute magnetic dopants, ultra-small induced magnetic moments, and buried interfacial structures.

4.13.2 Source

4.13.2.1 Spectral Requirements

Tunable radiation from 0.4-2 keV will be provided to cover the absorption edges of interest for magnetic studies (nitrogen K, oxygen K, transition metal L, rare earth M, etc.). Most measurements will be conducted in the 0.5- to 1.0-keV range, thus the undulator will be optimized to provide maximum flux in this portion of the spectrum.

4.13.2.2 Other Source Requirements

The insertion device (ID) will provide variable polarization including both horizontal and vertical linear polarization and both helicities of circular light over the full spectral range with greater than 96% polarization purity in all modes. High polarization definition is necessary in order to not obscure small changes in differential measurements. Furthermore, the device will provide the ability to switch between circular modes quickly and at high repetition rates (~3-10 Hz) in order to employ lock-in detection methods and thus provide the highest sensitivity to small magnetic signals. These specifications are consistent with an electromagnetic variable polarization undulator (EMVPU) with ~ 12-cm period similar to the current device used for this beamline, but with a much improved switching rate.

4.13.3 X-ray Optical Layout

The primary optical components and experimental station instruments for the magnetic spectroscopy beamline are shown in Figure 4-114 and listed in Table 4-35. The first optics enclosure (FOE) will house two mirrors to provide power filtering and separation between the MS-S beamline and the other beamline sharing the sector. A mirror coupled with a varied line spacing monochromator will be located just downstream of the FOE for selecting and scanning the energy. K-B mirrors immediately before the experimental experimental stations will provide adjustable focusing for each instrument on the beamline. A new high-field experimental station will be procured as part of the APS Upgrade scope, and the current octopole, X-PEEM, and XPS experimental stations will be reused as they are currently configured.

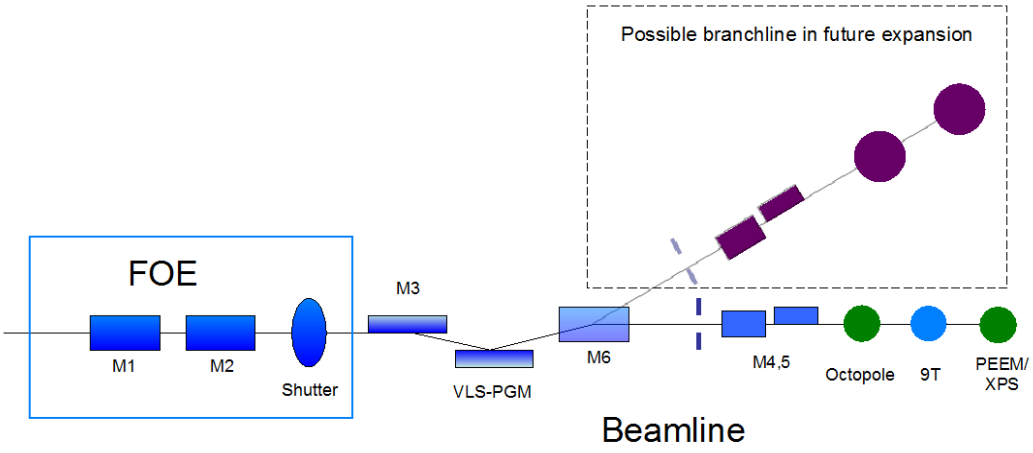

Figure 4-114: Optics and instrumentation for the enhanced soft x-ray magnetic spectroscopy beamline. Blue indicates components that will be upgraded within APS Upgrade, green are existing experimental stations that will be reused, and purple are components for a possible future expansion branch line.

Table 4-35: Beamline components for the enhanced MS-S beamline.

Component	Approximate Distance to Center of Straight (m)	Notes
Collimating aperture	27	Integrated white-beam aperture to define central cone (2 mm (V) × 3 mm (H)) from each insertion device in canted sector.
White-beam mirror (M1)	30	Flat, horizontally deflecting (outboard bounce), water cooled, ~ 300-mm Si substrate; Pd, Au, and Si coatings; 1.1° incident angle;1-Å surface roughness; and 1-mrad slope error.
Pink-beam mirror (M2)	31	Flat, horizontally deflecting (outboard bounce), water cooled, ~ 200 mm Si substrate; Pd, Au, and Si coatings; 1.5° incident angle;1-Å surface roughness; and 1-mrad slope error.
Pink-beam slits	38	Water cooled slits, ±10-mm travel on all blades.
Deflecting mirror (M3)	39	Internally water-cooled 100-mm-long mirror, variable incidence angle ~ 0.4° to 1.5°.
Variable line-spacing grating monochromator	40	Energy range 400-2000 eV; three interchangeable plane grating slots, gratings with varied line spacing from 400-1200 l/mm; ~ 0.7° to 3.0° incidence angle.
Exit slit	50	Monochromatic slits; 0- 5 mm vertical opening with 5-µm resolution.
K-B mirrors (M4,5)	55	~ 300 mm vertical and horizontal K-B pair on Si substrate; mirrors 1-Å roughness; 1-mrad slope error.
Low-field experimental station (existing)	57	Octopole electromagnet with 100-A power supplies. 1-Tesla omnidirectional magnetic field.
High field experimental station	59	9-Tesla superconducting magnet. Cryogen-free or closed-cycle recondenser.
Roll-off experimental stations (existing)	61	Position for existing X-PEEM, XPS, or user-supplied experimental stations.

4.13.3.1 Mirrors

4.13.3.1.1 White-Beam Mirror (M1)

This mirror acts as a deflector to gain additional separation between this and the other canted beamline in the sector, and as a power filter for optics downstream. The white-beam incidence angle on this optic will be approximately 1.1° in order to provide the necessary spectral reflectivity in the desired energy range. Separate coatings such as Pd, Au, and Si will be used to suppress harmonic contamination in different spectral ranges. The mirror will be ~ 300 mm long with a flat figure. Slope errors will be less than 1 µrad with 1-Å surface roughness to preserve the beam brightness and provide maximum reflectivity. The calculated power from the source coupled with 1.1° incidence angle is consistent with indirect side water cooling for mitigating the heat load on this mirror.

4.13.3.1.2 Pink-Beam Mirror (M2)

This mirror acts as a deflector to gain additional separation between this and the other canted beamline in the sector, and provides additional power reduction. The pink-beam incidence angle will be ~ 1.5°, which puts the critical cut-off energy at the upper end of the operating range of the beamline (2000 eV). The mirror will be provided with matching coatings to the M1 mirror (Pd, Au, and Si). The mirror will be ~ 200 mm long with a flat figure. Slope errors will be less than 1 µrad with 1-Å surface roughness in order to retain the beam brightness and provide the maximum reflectivity.

4.13.3.1.3 Grating Mirror (M3)

This mirror acts as a deflector (vertical; scattering down ~ 0.5° to 1.5°) onto the varied line spacing (VLS) grating monochromator to maintain a fixed exit focus for all energies. The length of the mirror will be ~ 120 mm with a flat profile and < 0.2-µrad slope errors in the meridional plane in order to preserve the energy resolution from the grating.

4.13.3.2 Monochromator

A variable line spacing monochromator is planned with three interchangeable gratings for differing energy ranges and resolutions. It will provide monochromatic x-rays with an energy resolution of $\Delta E/E = \sim 1 \times 10^{-4}$. The angle of incidence on the grating will vary from 0.7° to 3.0° resulting in a monochromatic x-ray beam inclined at ~ 1.0° angle upwards after the monochromator. The design of the monochromator will be similar to that of the intermediate energy x-ray (IEX) beamline currently being built at 29-ID. An illustration of the monochromator chamber for this beamline is shown in Figure 4-115.

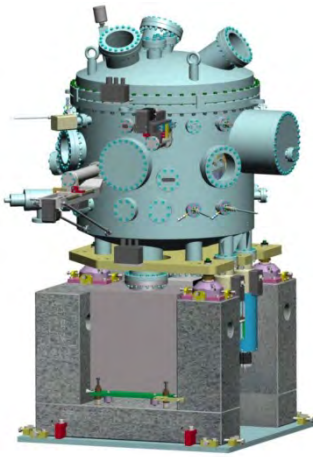

Figure 4-115: Design of a varied line spacing monochromator similar to what is expected to be installed on the upgraded soft x-ray magnetic spectroscopy beamline.

4.13.3.3 Focusing Elements

4.13.3.3.1 K-B Mirrors (M4, 5)

A K-B mirror pair will be located just upstream of the experimental experimental stations in order to provide increased flux density onto the samples (>200 times unfocused beam). These mirrors will be ~300-m long Si substrates coated with Au or Pd. They will have adjustable benders to provide variable focusing (~ 10x15 to 70x85 μm^2) into each of the experimental chambers downstream.

4.13.4 Beamline Physical Layout

A general layout of the MS-S beamline in the envisioned location in 2-ID is shown in Figure 4-116. The straight section will be canted, thus it will share the sector with another insertion device beamline and the current 2-BM bending magnet beamline. The FOE will have the mirrors to deflect the soft x-ray beamline horizontally providing separation between it and the other beamline in the sector. The monochromator will reside just downstream of the FOE and the experimental stations at ~ 60 m from the source.

Figure 4-116: General layout of the soft x-ray magnetic spectroscopy beamline in the 2-ID location being considered. Space requirements around beamline optics and experimental stations are highlighted in yellow. Approximate size and location for a control room is also shown.

4.13.4.1 Front End

The MS-S beamline will share a straight section with another hard x-ray beamline (most likely for magnetic diffraction) using a standard canted front end with a 1-mrad separation.

4.13.4.2 Overall Beamline

The location of the beamline components and infrastructure in Sector 2 is shown in Figure 4-116 above. Figure 4-117 provides a more detailed layout for the end-station instruments and control room relative to the other experimental stations in the sector. The exact location and size of the other stations is currently under development, but will account for the space requirements for the MS-S beamline outlined in section 4.13.5 and illustrated in Figure 4-116. Further, the exact size of the work area enclosure is still preliminary.

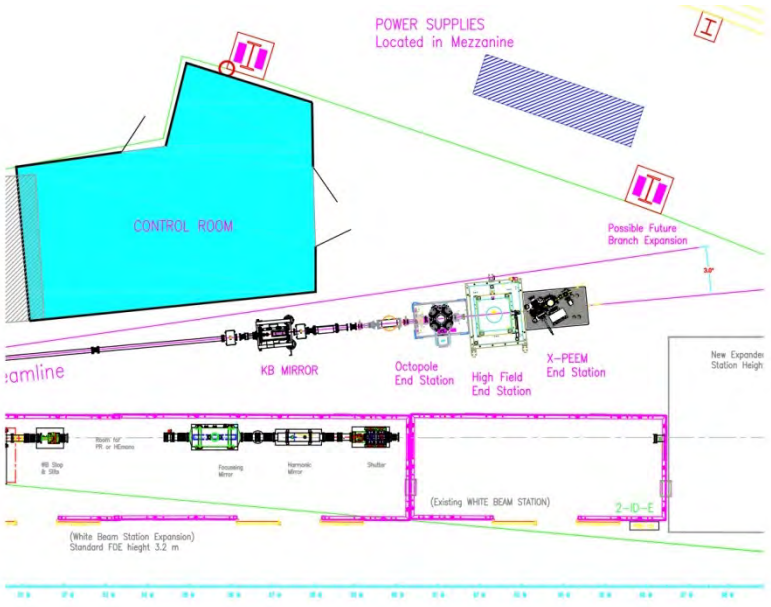

Figure 4-117: Locations of MS-S experimental stations and control room relative to potential canted partner beamline.

4.13.4.3 General Description

4.13.4.3.1 Radiation Safety Aspects

The FOE will be compatible with canted-undulator operation and white beam. The first and second mirrors for the magnetic spectroscopy beamline effectively filter out energies above ~ 2.5 keV, therefore the vacuum system of the transport and optical components outside the FOE will provide the required radiation shielding.

4.13.4.3.2 Vacuum System

To minimize absorption at low energies, the magnetic spectroscopy beamline will be compatible with windowless operation using a differentially pumped transition from the front end to the FOE. Therefore, all components are designed to minimize outgassing of heavier components detrimental to the operation of the ring. All beamline components will be designed to be UHV compatible up to the experimental experimental stations. UHV conditions are also required for the main beamline mirrors to maintain their cleanliness. The beamline design complies with the APS beamline vacuum policy for windowless operation.

4.13.4.3.3 Data Acquisition and Motion Control

The current beamline control system and software, with upgrades to support new components and to replace obsolete systems, will be used. The current system uses Python scripting with a standard APS EPICS system providing the underlying beamline control.

4.13.4.4 First Optics Enclosure and Infrastructure

The MS-S beamline requires two mirrors located in the FOE to horizontally deflect the beamline, both of which are included in the base scope of the Project. The standard-length FOE can accommodate these mirrors and provide enough beam separation for two independent shutters. Due to the limited room between the two beams, however, the FOE can only accommodate minimal optical components for the other beamline located in this sector.

4.13.4.4.1 Windows

The MS-S beamline requires windowless operation all the way through to the experimental experimental stations.

4.13.4.4.2 Slits

The beamline requires a water-cooled aperture to minimize the heat load on the downstream horizontally deflecting mirrors. A fixed-size aperture (2 mm vertical × 3 mm horizontal) is included in the base scope and will be designed to accommodate the other canted beamline in the sector.

4.13.4.4.3 Collimators

Sufficient collimation is required to provide the necessary bremsstrahlung and synchrotron radiation protection while operating the two branches independently. This will be determined using detailed ray tracing once the design is more developed.

4.13.4.4.4 Shutters/Stops

A pink-beam shutter is required at the end of the FOE to prevent the beam from illuminating the optics further downstream.

4.13.4.4.5 Mirrors

The FOE houses two horizontally deflecting mirrors for the MS-S beamline, which directs the beam outboard by ~ 5°, providing power filtering and separation from the other beamline in the sector.

4.13.4.5 Experimental Station Instruments

The beamline will have four end-station instruments dedicated to soft x-ray polarization modulated spectroscopy, three of which are shown in Figure 4-118 below. Two instruments will be permanently placed in the upstream position on the beamline for low- and high-field magnetic spectroscopy studies. Two other instruments, for X-PEEM and XPS measurements, will be interchanged in the downstream position. Only the high-field magnet will be upgraded as part of the APS Upgrade. The other instruments will be transferred as they are currently configured.

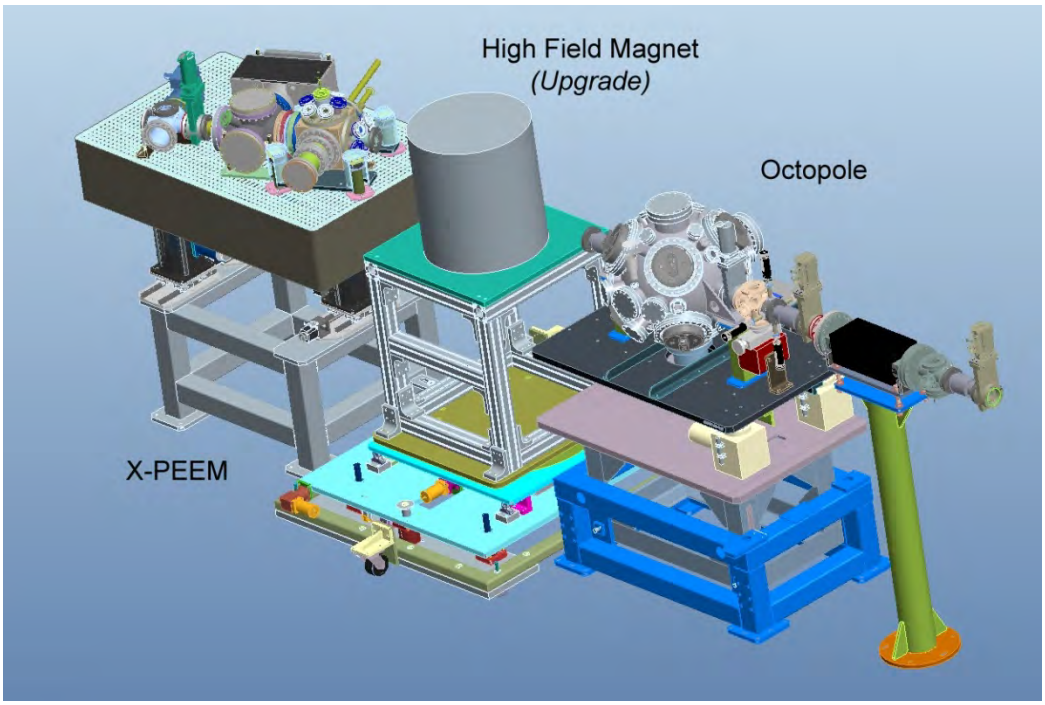

Figure 4-118: Picture of experimental experimental stations for the soft x-ray beamline. Existing octopole, new high field magnet, and existing X-PEEM instruments are shown.

4.13.4.5.1 Octopole Magnet Station (existing)

This existing instrument is an omnidirectional, eight-pole electromagnet capable of applying a ±1-T field along any direction. The magnetic poles are arranged to provide complete access to the horizontal plane for scattering measurements. The chamber is equipped with an integrated scattering detector. A liquid He cryostat provides sample temperatures of 4.2-350 K and four-axis motion (x, y, z, polar angle), with accuracies of 10 μm and 0.01°. The octopole magnet experimental station on this beamline includes a set of large electrical power supplies, which require a significant amount of floor space (~ 5 m × 2 m) within ~10 m of the experimental station to minimize the length of the electrical cabling. In the currently planned 2-ID location for this beamline, it may be possible to place these power supplies in the mechanical mezzanine, thereby preserving valuable space on the experimental hall floor.

4.13.4.5.2 High-Field Magnet Station (upgrade)

A new 9-Tesla superconducting magnet will be procured for soft x-ray spectroscopy and reflectivity studies. The magnet will be a split coil design with the magnetic field coincident with the x-ray beam (along the bore). It will be either cryogen-free or equipped with a recondenser to minimize liquid helium usage. The magnet system may be of either the warm or cold-bore type, and must be a windowless design to allow the soft x-ray beam through. The angular acceptance of the axial ports should be at least ± 10°, in order to perform XMCD studies in reflection geometry. Radial access ports (~ 40 mm) within the sample vacuum space are necessary for mounting of x-ray fluorescence and optical luminescence detectors. Separate cooling for the sample will enable studies between 2 and 325 K. Wiring on the sample cooling

stage for monitoring of electron yield signals and for moderate voltage biasing (~ 2 kV) will be incorporated into the design.

4.13.4.5.3 Photoelectron Microscopy Station (existing)

This existing instrument is an electrostatic X-PEEM used for magnetic imaging studies by using polarized absorption contrast with ~ 100-nm spatial resolution. Time-resolved imaging studies are possible by using pump-probe techniques to study domain dynamics. The instrument is equipped with a cryogenic sample stage for imaging between 25 and 325 K and has four-axis sample motion.

4.13.4.5.4 X-ray Photoemission Spectroscopy Station (existing)

This instrument is for electron spectroscopy measurements probing near-surface electronic states. This station will continue to be used for XPS experiments that take advantage of the unique polarization manipulation characteristics provided by the EVMPU.

4.13.5 Additional

Control Room: A work enclosure sufficient to house the control electronics, workstations, sample preparation area, and ancillary beamline equipment will be installed as part of the base scope. A possible location and approximate size is illustrated in Figure 4-117.

Clearance from other co-located beamline: The soft x-ray beamline optics and beamline transport extend from the end of the FOE (~ 35 m) to a distance of about 50 m. Approximately ± 0.5 m of clearance is provided on either side of the beamline along this entire distance to accommodate the various optical components. The experimental experimental stations extend another 10 m beyond the last optical components (from ~ 50 to 60 m). These instruments extend ± 1.5 m on either side of the beam, and additional room is required for access. These clearance requirements are highlighted in yellow in Figure 4-116.

4.13.5.1 Conventional Facilities Requirements

A full set of cable trays connecting the enclosures, experimental station, and control room will be installed in the sector for this beamline. As stated above, the electromagnet requires large power supplies, but the standard sector power should be sufficient.

4.14 Magnetic Diffraction (MD)

The APS Upgrade Project includes plans for constructing the Short-Pulse X-ray Imaging and Microscopy beamline (SPXIM – discussed in section 4.3) in Sector 6, adjacent to the Short Pulse X-ray Scattering and Spectroscopy (SPXSS – discussed in section 4.2) beamline in Sector 7. The siting of the SPXIM beamline on 6-ID necessitates the relocation of the programs currently using this sector. Current upgrade plans call for moving the existing Magnetic Diffraction (MD) capabilities located at beamline 6-ID-B (including existing in-field scattering) to Sector 2, where it will share the insertion device (ID) port with the

Magnetic Spectroscopy – Soft x-ray (MS-S – discussed in section 4.13) program using a canted geometry. The major components of this relocation involve the following:

1. Installation of new mirrors to provide more flexible focusing (smaller and variable spot size), and better harmonic suppression.
2. Upgrade of the current monochromator to provide enhanced beam stability.
3. Construction of a new secondary optics enclosure (SOE) to house the monochromator, mirrors, and other optics for the MD program.
4. Reconstruction of the 2-ID-D experimental station to provide sufficient room inside the station to accommodate the diffractometer and magnet from 6-ID-B.
5. Construction of enclosed control area for users with adequate background noise reduction.

In addition, considerations in the design of the beamline are being made to accommodate all or part of the proposed X-ray High-Field (XHF) beamline as a future contingent additional scope. Space will be set aside in the SOE for this purpose.

4.14.1 Scientific Objective

The scientific objective of MD is to preserve and enhance those scattering programs currently supported at 6-ID-B, exclusive of surface and interface scattering, by relocating them to another sector, 2-ID-1 as described in the Roadmap base scenario. Although labeled "Magnetic Diffraction" for convenience, these programs employ a variety of scattering techniques to investigate families of emergent materials in various extreme environments including temperature, pressure, magnetic field, and electric field. Most of these materials exhibit some form of magnetic structure, typically coupled to one or more additional degrees of freedom. The resulting phase diagrams can be quite complex, requiring multiple scattering techniques and applied fields to unambiguously sort out the magnetic, orbital, lattice, electronic, and topological structure of each phase. Below are necessarily brief synopses of a few of the results of the programs to be preserved by the relocation.

The iron pnictide superconductors and their parent compounds have been extensively studied at Sector 6. The doped compounds exhibit coexistence of magnetically ordered and superconducting phases [150], while the undoped parent compounds have subtly distinct structural and magnetic phase transitions [151]. Both x-ray resonant magnetic scattering (XRMS) and high-resolution conventional (charge) scattering have been powerful tools essential to understanding their microscopic structure. Pulsed magnetic fields up to 27.5 T have been used to detwin a sample of under-doped $Ba(Fe_{0.955}Co_{0.045})_2As_2$ and clearly demonstrate *ab*-plane magnetic anisotropy in the orthorhombic phase both above and below the spin density wave transition temperature [152].

Sector 6 has hosted several different groups studying complex oxides, which frequently contain both rare earth and transition metal species. These materials have some of the richest phase diagrams yet found. High resolution, polarization analysis, and applied fields have been essential to unraveling their intricate microscopic structures. Both bulk- and thin-film forms have been studied, with the latter including strain via substrate lattice mismatch that would otherwise fracture macroscopic crystals.

Bulk $TbMn_2O_5$ was intensively studied at 6-ID-B using both XRMS and non-resonant scattering to determine the relationship between the commensurate and incommensurate magnetic phases and the spontaneous polarization of the ferroelectric phase [153]. The origin of the ferroelectricity was found to be the atomic displacements in the commensurate phase that are driven by the magnetic ordering, and the transition to the low-temperature incommensurate phase was attributed to discommensuration due to competing frustrated magnetic orders of the Mn ions. Following the report that $HoMnO_3$ exhibited a strong magnetoelectric effect [154], attributed to Ho^{3+} order changing from antiferromagnetic to ferromagnetic upon application of an electric field, the nature of the holmium magnetism was studied with both XRMS and x-ray magnetic circular dichroism (XMCD) [155]. It was found that the holmium magnetic structure was unaffected by the application of electric fields.

While charge and orbital ordering in bulk manganites has been of great interest for many years, only recently have the surface effects been studied. Grazing incidence x-ray diffraction was used at 6-ID-B to separately measure the crystal truncation rods and the orbital order truncation rods of the cleaved surface of $La_{0.5}Sr_{1.5}MnO_4$, showing that the orbitally ordered surface is substantially rougher than the atomically smooth crystallographic surface [156]. Further measurements demonstrated the melting of the electronic surface, quite distinct from the crystallographic surface [157].

There have been a number of diffraction measurements in Sector 6 exploring different aspects of complex oxide thin films. One notable experiment discovered an in-plane structural modulation in the $La_{1/3}Sr_{2/3}MnO_3$ alloy film [158]. This modulation wavelength increased substantially in digitally synthesized films of the same average composition as did the antiferromagnetic ordering temperature, thus showing the impact of cation site ordering. X-ray structural and density functional theory studies of epitaxial $LaNiO_3$ films quantified the role of strain in oxygen octahedral rotations in these perovskite oxide films [159], and was followed by the discovery that digital synthesis of $(LaNiO_3)_m/(SrMnO_3)_n$ superlattices allows control over these rotations by varying the n/m ratio [160]. Films of $NdNiO_3$ were grown under compressive or tensile strain ($LaAlO_3$ or $SrTiO_3$ substrates, respectively) and studied with both x-ray diffraction and x-ray absorption spectroscopy [161]. The metal insulator transition was discovered to be quenched under compressive strain.

Exhibiting strong spin orbit coupling, the 5*d* transition metal oxides are believed to host a wide range of exotic magnetic phases. The bilayer iridate, $Sr_2Ir_3O_7$, was recently studied using XRMS and was found to have an easy c-axis collinear antiferromagnetic structure [162]. This is in stark contrast to the single-layer analog, Sr_2IrO_4, where the ordered phase exhibits *ab*-plane canted moments. Detailed theoretical analysis allowed the authors to ascribe the spin-flop transition to competing intra- and interplanar bond-directional pseudodipolar interactions of the effective spin orbit coupled moments. A different *5d* transition metal oxide, $NaOsO_3$, was also studied using XRMS and found to undergo a magnetically driven (Slater) metal insulator transition [163].

The in-field scattering program, recently moved from Sector 4 to Sector 6, has opened new portions of phase diagrams by adding the magnetic field variable. A recent experiment using a pulsed magnetic field to 28 T showed that the collapsed volume phase of $Ce_{0.8}La_{0.1}Th_{0.1}$ was present and unaffected by the highest applied pulsed field [164]. Since prior equilibrium in-field measurements suggest this phase is suppressed by magnetic fields, the above observation may be indicative of “sluggish dynamics” in these alloys.

Another oxide system of great importance is the quasi two-dimensional magnet $SrCu_2(BO_3)_2$. Under pressure at low temperature this system exhibits a quantum phase transition near 2 GPa, where the singlet-triplet energy gap goes to 0 [165]. Long range antiferromagnetic order appears around 4.5 GPa. This final example is actually of work done at Sector 4, but will be accommodated by MD by upgrading the beamline optics to include a toroidal mirror to provide sagittal focusing and greatly increased flux through the small aperture of a diamond anvil cell gasket.

4.14.2 Source

4.14.2.1 Spectral Requirements

Fully tunable radiation from below the uranium *M* edges (ca. 3.3 keV) to above 40 keV is required. An APS Undulator A will meet this requirement.

4.14.3 X-ray Optical Layout

The presence of MS-S on this canted sector forces several important MD beam conditioning and optical components out of the first optical enclosure (FOE) and into a newly constructed downstream second optical enclosure (SOE). These items are shown schematically in Figure 4-119. Existing components will be reused where technically feasible and cost effective. Experiment instrumentation to be reused is shown schematically in Figure 4-120. The various components, together with their relative positions, are listed in Table 4-36.

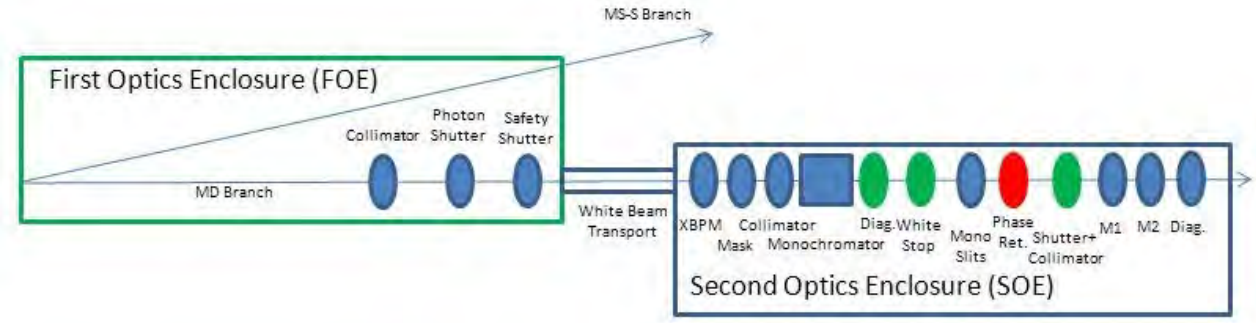

Figure 4-119: Beam conditioning and x-ray optical components for the magnetic diffraction beamline. Blue indicates elements that will be purchased new within the APS Upgrade; green indicates existing elements that may require minor modification for reuse, and red indicates items that are not part of the APS Upgrade scope but are future off-Project scope optics.

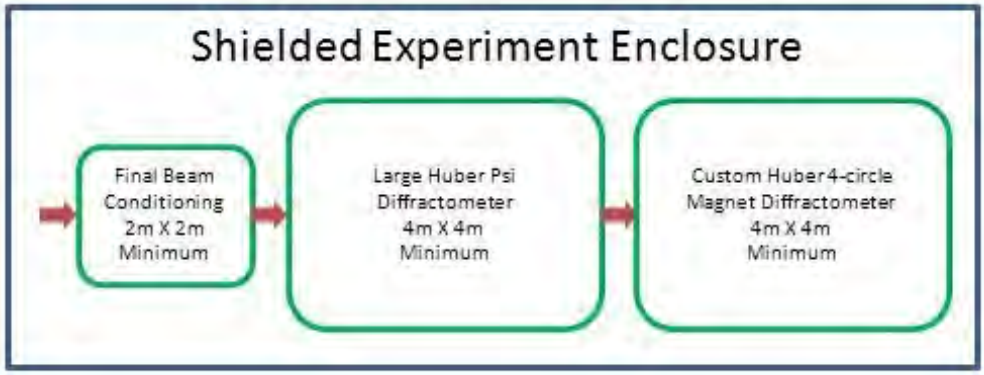

Figure 4-120: Instrumentation in experiment experimental station. All instruments currently exist. The enclosure will be purchased new within the APS Upgrade and will replace an existing enclosure that is too small.

Table 4-36: List of components for the relocated MD beamline.

Component	Approximate Distance to Center of Straight (m)	Notes
Collimating Aperture	27	Integrated white-beam aperture to define central cone (2 mm (V) x 3 mm (H)) from each ID in canted sector
Collimator	33	Type, location, and size to be determined by ray tracing
Photon Shutter	34	White-beam shutter to protect safety shutter that follows
Safety Shutter	35	Protects SOE from bremsstrahlung radiation
White Beam Transport	36 – 48	Shielded evacuated white-beam transport pipe and supports
X-ray Beam Position Monitor	48.3	For white beam position diagnostics
Mask	48.5	Further limits heat load and protects collimator that follows
Collimator	48.9	Limits bremsstrahlung cone for a small-offset monochromator
Monochromator	50	Small (variable) offset, with on-axis liquid nitrogen feedthroughs
Diagnostic Screen	51	Reuse existing, replace phosphor screen
White-Beam Stop	52	Reuse existing, new support required
Monochromatic Beam Slits	53	Defines monochromatic beam footprint on following optics
Vacuum Pipe	54	Space for future non-APS Upgrade scope optics.
Integral Shutter / Collimator	55	Reuse existing, position for minimum offset
Focusing Mirror	57	Bendable 1-m-long toroid, with two sagittal radii, 1 μm slope error, 0.1 nm roughness
Flat Beam Leveling Mirror	58	Flat 1–m-long harmonic rejection mirror to bring beam back to level, 1 μm slope error, 0.1 nm roughness
Beam Diagnostic	60	Retractable cerium doped YAG screen with camera
Final Beam Conditioning	66.5 – 68	Existing, configurable, X95 supported: slits, attenuators, Kirkpatrick-Baez mirror, ion chambers, and beam position monitor
Custom Large Huber Psi Diffractometer and Table	70	Existing heavy load diffractometer with removable Eulerian cradle and provision for heavy diffracted beam optics and detectors
Custom Horizontal Huber Diffractometer and Table	73.5	Existing locally assembled diffractometer customized to support existing superconducting magnets

4.14.3.1 Mirrors

Focusing mirror (M1): Design of the first mirror is still in development, but is currently planned to be an up-bounce bendable toroid with two sagittal radii focusing at the centers of the two diffractometers in the end experiment station. It is expected to have at least a 1-m long usable area due to the distance to the source and the desire to focus high energies. It will be specified to have minimum slope errors and roughness consistent with the current state of the art of mirror polishing and the size of the optic. Coating stripes and the possibility of a flat area between the toroidal grooves are under discussion.

Harmonic rejection / beam leveling mirror (M2): Design of the second mirror is also still under discussion, but is tentatively planned to be a down-bounce flat mirror. It is expected to have at least a 1-m long usable area due to the distance to the source and the desire to focus high energies. It will be specified to have minimum slope errors and roughness consistent with the current state of the art of mirror polishing and the size of the optic. Coating stripes and the possibility of moving the bending function from the first to the second mirror are under discussion. Detailed ray tracings for the combined mirrors will be finished before final design choices are made. Note that this second mirror, not present in the current location (Sector 6), is essential to re-level the beam for the in-field scattering program. That diffractometer table has no provision for tilting and probably cannot be added.

4.14.3.2 Monochromator

A cryogenically cooled, double-silicon, <111> crystal monochromator with a minimum offset consistent with the bremsstrahlung ray tracing delivering monochromatic beam to the experiment experimental station is required. Provision for a long, cryogenically cooled second crystal to allow beam-walk will extend the high-energy limit beyond the nominal value for the monochromator. On-axis liquid nitrogen feedthroughs are required to help reduce internal hose lengths that contribute to cryocooler pump pulsations telegraphing into the monochromatic beam. This latter phenomenon places limits on pulsed magnetic field work since the cryocooler pump frequency falls within the critical band for measurements. Reducing the monochromator's contribution to RMS beam motion to approximately 10% of the source values will require substantial off-line development time. Crystal supports and accompanying Compton shielding will need to be redesigned. The requirement of minimum offset necessarily means minimal mechanical clearances for the silicon crystals and Compton shields, placing a premium on having accurate dimensions for the monochromator crystal stages. To reduce the risks related to procuring the monochromator, the Project will plan to have the "bare" monochromator in-hand six months earlier than needed for installation so that final design adjustments of crystal supports and Compton shields can proceed from a known, measured, as-built foundation. Given the priority placed on uninterrupted ongoing APS user operations, having the monochromator fully assembled with crystals installed together with an operational cryocooler at least two months prior to installation for off-line optical vibration testing is critical.

4.14.3.3 Focusing Elements

In addition to the toroidal mirror, the provision to add an existing Kirkpatrick-Baez (K-B) mirror pair or zone plates inside the experiment experimental station, as needed, will be maintained.

4.14.4 Beamline Physical Layout

Under the current APS Upgrade Roadmap Scenario, Sector 2 will retain the existing 2-BM (bending magnet) beamline while the ID portion will be canted to support two relocated beamlines: MS-S and MD. The existing FOE will be used by the first optics for MS-S and by the masks, collimators, shutters, and stops required for radiation safety. All MD optics will be placed downstream in a new, long, white-beam SOE.

4.14.4.1 Front End

According to the APS Upgrade Roadmap Scenario plans, the MD beamline will share a straight section with the relocated MS-S beamline utilizing a standard canted front end with a 1 mrad separation.

4.14.4.2 Overall Beamline

A general layout of the MD beamline sharing Sector 2 with MS-S and the 2-BM programs is shown in Figure 4-121. Expanded views of the SOE and the experiment experimental station are shown in Figure 4-122 and Figure 4-123, respectively.

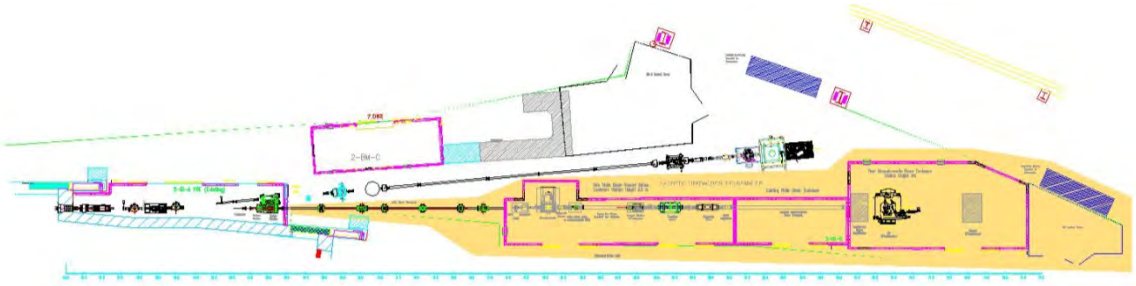

Figure 4-121: Overview sector drawing (preliminary) of the MD beamline.

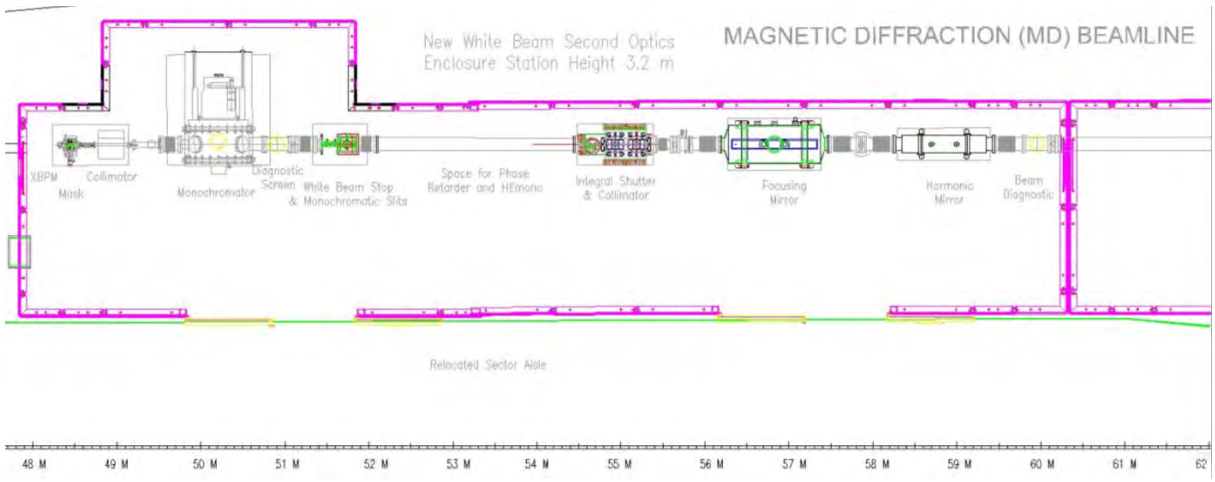

Figure 4-122: MD SOE layout (preliminary). Scale is distance to straight section center.

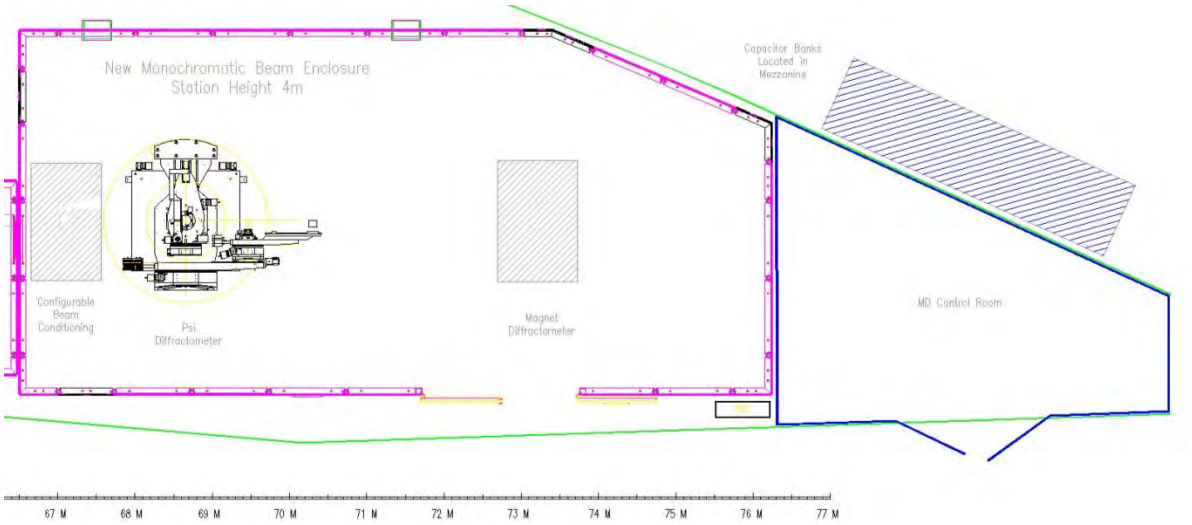

Figure 4-123: MD experiment experimental station layout (preliminary).

4.14.4.3 General Description

4.14.4.3.1 Radiation Safety Aspects

APS Technical Bulletin (TB)-44 and associated documents, as interpreted by the APS Radiation Safety Committee, will guide all radiation shielding decisions. Preliminary synchrotron and bremsstrahlung radiation ray tracings have been made and will guide the final design locations and apertures of collimators and protective masks. The monochromator is planned to have the minimum possible offset between white and monochromatic beams, which will require mask and collimator aperture sizes as small as possible consistent with passing the entire central cone from the undulator. As a canted sector, careful attention will be paid to shielding for both sources. The FOE will house white-beam and bremsstrahlung stops for the MS-S branch, and photon (white beam) and safety shutters to protect the MD branch SOE, whose shielding design will be specified to white-beam standards. Evacuated white-beam transport will carry the beam between the FOE and SOE.

4.14.4.3.2 Vacuum System

Due to the need to operate at low energies, both MS-S and MD branches will be “windowless” beamlines, sharing a common vacuum space. A differential pump is required for the transition between front end and beamline components. All beamline components will be designed to be ultra-high vacuum (UHV) compatible to minimize outgassing, especially of high-mass components. UHV conditions are especially important to minimize contamination of critical mirror optics. This beamline will comply with the APS vacuum policy for windowless operation. It is expected that the only beamline window will be the beryllium end window into the experiment station.

4.14.4.3.3 Data Acquisition and Motion Control

The existing Sector 6 controls systems and software will be reused as much as possible. Cabling will be replaced due to layout changes in the new location. The control standard is Certified Scientific Software's spec [166] using the Experimental Physics and Industrial Control System (EPICS) as the underlying software.

4.14.4.4 First Optics Enclosure and Infrastructure

The FOE is nearly taken up by components for MS-S and shutters and stops. The only modification expected is to replace the guillotines to accommodate the transition pipes specific to MS-S and MD.

4.14.4.4.1 Windows

The low-energy range of the MD beamline requires windowless operation from the source to the experiment station monochromatic beryllium exit window.

4.14.4.4.2 Slits

No white-beam slits are planned. Masks will be used to reduce the synchrotron radiation to the central cone from the undulator to protect the collimators and limit the total power to the first silicon crystal. Beam position monitors and steering corrections, requested as needed, will keep the beam on the optical axis. Precision UHV monochromatic slits will be used to define the footprint of the beam from the monochromator on the mirrors and the (contingentadditional scope) phase retarder.

4.14.4.4.3 Collimators

Collimator thickness, extents, locations, and apertures will be determined by the radiation transport calculations reported in APS TB-44 and by the detailed ray tracings that have yet to be completed.

4.14.4.4.4 Shutters / Stops

Since all of the MD optical components have been forced out of the FOE and into the SOE, a combination of an ID photon and safety shutter is required to protect the SOE. An existing monochromatic ID shutter with an integral collimator can be moved and reused to reduce costs.

4.14.4.4.5 Mirrors

The mirrors are critically important optical elements and detailed ray tracings informed by manufacturer polishing limitations and cost estimates will be used to decide the balance of focusing and harmonic rejection between the two mirrors. A key question yet to be resolved is whether or not sagittal and vertical focusing should be done by a single optic or distributed between the two mirrors.

4.14.4.5 Experimental Station Instruments

The experimental station instruments currently in 6-ID-B will be relocated to the new experiment enclosure. These instruments are a robust Huber Psi geometry diffractometer with precision positioning table and an in-house assembled magnet diffractometer made from Huber stages. Any upgrades to the magnet diffractometer will be covered under contingent additional scope activities.

4.14.5 Additional

A small enclosed work area at the end of the sector is planned as part of the base scope.

4.14.5.1 Safety Requirements

The current 6-ID-B enclosure is too small to safely house both instruments. This has caused a chronic tripping hazard. The new enclosure is large enough to mitigate this hazard. The pulsed magnets generate boil-off gas from the liquid nitrogen cooling and dissipated power. This gas will be conducted out of the experiment station. Oxygen deficiency sensors and alarms will be installed in the experimental station as required. The aisle between Sectors 2 and 3 will be relocated to accommodate the new SOE. An appropriate duck-under permitting emergency cross-sector passage will be defined.

4.14.5.2 Conventional Facilities Requirements

The existing central utility distribution core will be partially removed and supported during enclosure construction and rebuilt after construction is complete. Cable trays interconnecting the enclosures are required. Electrical power, conditioned air, fire sprinklers, and smoke sensors will be installed in the new enclosed work area. The new stations will have their electrical distribution panels and piping connected to the central utility distribution system.

4.15 Fuel Spray Dynamics (FSD) Beamline

Over the past 12 years, Argonne developed a well-respected program in high-speed measurements and visualizations of liquid sprays. This development has led to the commissioning of the 7-BM beamline, which is dedicated to time-resolved x-ray radiography and fluorescence measurements with a high flux, monochromatic beam. The installation of the Short-Pulse X-Ray source will significantly increase the size of the 7-BM x-ray source. As such, the current research program must be relocated to a new beamline. This section describes the preliminary design of the relocated beamline, termed the Fuel Spray Dynamics (FSD) beamline.

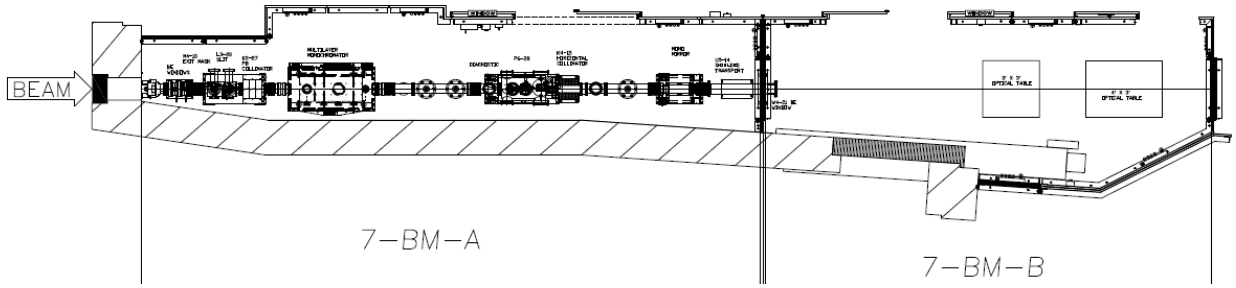

Figure 4-124: Layout of the current 7-BM.

4.15.1 FSD Scientific Program and Scope

The FSD beamline focuses on x-ray measurements of fluid dynamic systems. One of the most important applications of x-ray techniques in fluid dynamics is the measurement of spray flowfields. Liquid sprays are critical to a number of industrial applications, including fuel injection systems for a wide variety of combustion engines, inkjet printers, liquid-jet cutting tools, and paint application. For example, in automotive fuel injection, it is well established that the structure of sprays has a profound impact on fuel-air mixing, which in turn heavily influences the efficiency and pollution formation in engines. In liquid rocket applications, instabilities in spray flowfields can lead to destructive combustion instabilities, which can lead to catastrophic engine failure [167].

Computational models of spray behavior lack the predictive power needed for accurate, predictive modeling. As such, high-fidelity measurements of spray flowfields are essential, both to obtain a better understanding of spray behavior and to validate advanced spray models. High-pressure sprays are often optically dense and highly transient, which hampers the use of optical diagnostics in these flowfields [168]. Despite significant advances in diagnostics over the last 20 years, quantitative measurements in the region close to the nozzle have proven elusive [169]. For many applications, the spray is transient, requiring highly time-resolved measurements to accurately measure the spray. The lack of quantitative, time-resolved analyses of the structure and dynamics of sprays in the near-nozzle region limits the accuracy of spray modeling and creates obstacles to improving spray technology.

Unlike visible light, x-rays scatter weakly from spray droplets. As such, x-ray absorption can be used to make highly quantitative measurements of sprays with high optical density. If monochromatic x-rays are used, the analysis of the radiography measurements is straightforward and follows the form $I/I_0 = \exp(-\mu_m M)$, where I and I_0 are the transmitted and incident beam intensities, respectively, μ_m is the mass absorption coefficient, and M is the mass per unit beam area. Since μ_m can be measured accurately for the absorbing medium, the mass/area in the beam path can be easily deduced from the transmission, I/I_0.

Radiography experiments have been performed using tube-type x-ray sources for decades [170]. However, these measurements lack the sensitivity or time resolution to examine many spray flowfields [171]. With the advent of synchrotron radiation sources, extremely brilliant monochromatic x-ray beams are now available. These sources have paved the way for fast experiments of this type using monochromatic beams and achieving time resolution of 1 μs or better. The first attempts to use these powerful yet nonintrusive beams for studying fuel sprays near the injection nozzles have been extremely

successful, and many discoveries on high-pressure fuel sprays have been made. The experiments revealed quantitatively and unambiguously many characteristics of fuel sprays that were previously unknown and/or that could not be measured by any other means [172]. The existing spray radiography program is well-supported by the US Department of Energy and is recognized as a core capability of Argonne's engine research program.

The existing 7-BM beamline was recently commissioned as a dedicated facility for time-resolved radiography on a wide variety of spray flowfields [173]. Due to the installation of the Short-Pulse X-Ray source as part of the APS Upgrade, the capabilities of this beamline must be moved to a new location. In order to prevent a disruption of the existing experimental program at 7-BM, the reconstituted FSD beamline must preserve the existing experimental capabilities of the 7-BM beamline.

4.15.2 X-ray Bending Magnet Source for the FSD Beamline

The source is a standard APS bending magnet (BM).

4.15.3 X-ray Optics for the FSD Beamline

The scientific program of the FSD beamline requires a high-flux, focused, monochromatic beam for raster-scan experiments to provide quantitative, time-resolved measurements with sufficient spatial resolution. For imaging experiments, a broad, high-flux, monochromatic beam is needed. The FSD beamline will use a relatively simple optical scheme to achieve these specifications.

4.15.3.1 Monochromator

The monochromator is a custom double-multilayer design using two flat multilayer substrates (see Figure 4-125). The substrate dimensions are 90 mm (L) x 90 mm (W) x 12 mm (T), allowing a large portion of the BM fan to be intercepted. The substrates are currently coated with a uniform W/B_4C multilayer coating 100 bilayers thick with a period spacing of 23.75 Å. The reflectivity at the first Bragg angle is 68% at 7.35 keV and the delivered energy bandpass is 1.4% at 8 keV. These multilayers can, however, be easily recoated with multiple stripes of coatings of various specifications to provide greatly enhanced flexibility in energy range and resolution. As the BM radiation is horizontally uniform across the multilayers, each stripe can be used simply by using a different portion of the BM fan.

The multilayers are mounted on two independent, motorized, high-precision Kohzu stage groups to allow x-ray energy selection from 5 to 10 keV with a 35-mm vertical offset between the two multilayers. The offset is adjustable from 20 to 35 mm, though the current design of the beamline shutter and shielding limits the offset to 30-35 mm. The first multilayer element is water-cooled by direct thermal contact with a copper cooling block to prevent thermal interlayer diffusion, which would result from the heat load of the incident BM white beam. The cooling water is supplied by a gravity feed system to isolate vibrations from mechanical water pumps. The monochromator and gravity feed cooling system will be moved from 7-BM to the FSD beamline. The shielding of the FSD beamline will also be modified slightly from the existing 7-BM shielding to accommodate a 25 mm monochromatic beam offset; this will allow the monochromator to provide higher energy beams more easily.

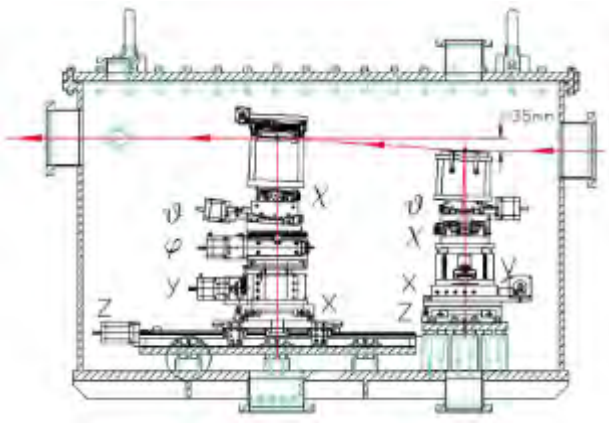

Figure 4-125: Schematic of the high-vacuum chamber and vacuum-compatible high-precision motorized stages. The x-ray beam enters the chamber from the right port and the subsequent monochromatic x-rays exit the chamber from the left vacuum port with a vertical offset.

4.15.3.2 Mirror Optics

The 7-BM-A enclosure is equipped with a 0.5 m-long platinum-coated flat mirror for harmonic rejection, though this mirror is seldom used. The FSD beamline will omit this mirror, as harmonic rejection is currently achieved with proper multilayer design and with the K-B focusing mirrors used in the experiment station.

The natural width of the unfocused BM beam is well-suited for wide-field imaging experiments. Focusing optics are needed for raster-scan measurements. Focusing is currently achieved in the experiment station using a pair of K-B mirrors commercially available from IDT. The mirrors are 300 mm long (260 mm illuminated length) Si substrates which are Rh coated. The mirrors produce a focus size of 5 x 6 μm FWHM at a working distance of 250 mm from the mirror enclosure. These mirrors will be moved from the 7-BM beamline to the FSD beamline.

4.15.4 Beamline Layout

As the scope of this work relocates an existing beamline, the layout of the new FSD beamline largely parallels that of the existing 7-BM beamline. The existing design assumes an enclosure layout identical to the existing 7-BM enclosures; the enclosure layout may change slightly depending on the layout of the adjoining ID sector. A drawing of the layout of the FSD beamline is shown in Figure 4-126.

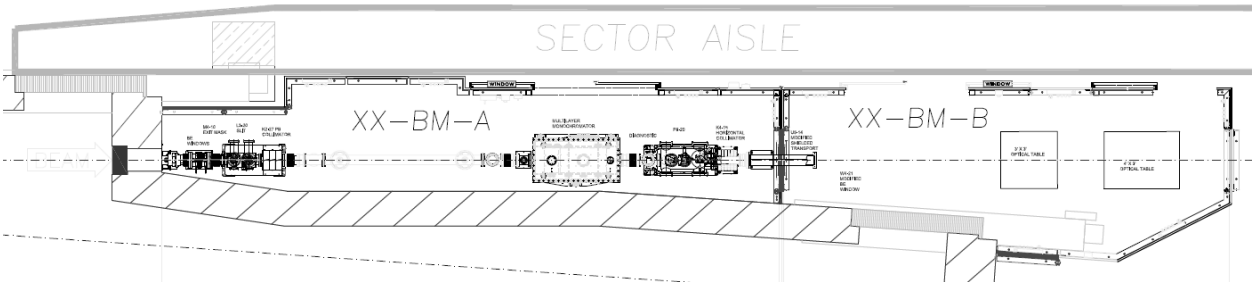

Figure 4-126: Layout of the Fuel Spray Dynamics beamline.

4.15.4.1 Front End

The front end (FE) is a standard APS bending magnet component.

4.15.4.1.1 Front End Exit Window

The FSD beamline will use a standard APS BM beryllium window assembly between the FE vacuum and the beamline vacuum. This is a water-cooled design with two 250 μm thick beryllium windows.

4.15.4.1.2 Front End Mask

The FSD beamline FE mask will be a standard copper BM FE mask. The mask will be designed to pass the a large fraction of the vertical fan of the BM white beam (7 mm) and approximately 3 mrad of the BM white beam horizontal fan. This provides sufficient protection of FOE components but provides a wide beam (100 mm horizontally) for wide-field imaging.

4.15.4.2 White-Beam Slits

The FSD beamline will be equipped with APS standard white-beam slits, which will be moved from the 7-BM beamline. The slits are capable of passing any beam size from zero to the full width admitted through the FE mask. The slits are water cooled by the APS-supplied deionized water and are monitored in the beamline equipment protection system.

4.15.4.3 Monochromator

The monochromator for the 7-BM beamline is placed 24.5 m from the x-ray source. The FSD beamline will use a different layout, with the monochromator placed 28 m from the x-ray source. Moving the monochromator downstream reduces the impact of residual multilayer slope errors or beam motions arising from the monochromator, especially for imaging experiments. It also creates space for the possible future inclusion of a water-cooled mirror for vertical collimation and/or pink-beam operations.

4.15.4.4 Shutters and Stops

The P6-28 integral shutter used at the 7-BM beamline will be reused at the FSD beamline. The P6-28 integral shutter is a modified P6-20. The mode change capability has been eliminated by removing the cylinder assembly and replacing it with rigid fixtures. The photon stop and the bremsstrahlung stop are rigidly fixed in place on the chamber housing. The water flow to the photon stop will be monitored in beamline EPS. In the 7-BM beamline, the shutter is centered 27.6 m from the x-ray source. In the FSD beamline, the shutter will be centered 29.7 m from the x-ray source to accommodate the revised location of the monochromator.

To provide adequate shielding for bremsstrahlung radiation, the 7-BM beamline contains a K2-27 exit collimator (23 m), a fixed photon stop/bremsstrahlung stop/mono shutter (P6-28) (27.7 m), and a K4-15 horizontal collimator (28.4 m). Due to the relatively long distance between the shutter and the downstream wall of the FOE, a beam transport between stations A and B (U5-12) is used. In the FSD beamline, the exit collimator will remain unchanged. The K4-15 horizontal collimator will remain immediately downstream of the shutter, now approximately 30.8 m from the source. The U5-12 shielded transport will remain in the same position as in the 7-BM beamline. In order to control the bremsstrahlung, an additional collimator is required upstream of the monochromator (27.2 m from the source). All shielding components aside from the tungsten collimator will be moved from the 7-BM beamline.

4.15.4.5 Experiment Enclosure Layout

The FOE vacuum terminates in the 7-BM-B enclosure with a single uncooled beryllium window (400 μm thickness) that contains two apertures, one for direct monochromatic beam and one for beam reflected from the existing monochromatic flat mirror. The FSD beamline will use a similar beryllium window with only a single aperture, as the monochromatic flat mirror will be removed. This window will also be designed to accommodate the proposed 25 mm monochromatic beam offset.

The experiment enclosure of the FSD beamline will contain two motorized optical tables with six degree-of-freedom motion. These tables will not be permanently mounted, providing significant flexibility in the enclosure layout depending on the needs of users. These tables are used currently at the 7-BM beamline and will be moved.

4.15.4.6 Utilities

The existing utilities of the 7-BM beamline will be replicated at the FSD beamline. These include electrical service, compressed air, and both chilled and deionized water in both enclosures. Access to the APS Liquid Nitrogen Distribution System is required for users that require large quantities of dry nitrogen for high-flow experiments. The FSD B enclosure will also be equipped with an air exhaust system to remove gases and vapors from the enclosure as needed.

4.15.4.7 Data Acquisition and Motion Control

The beamline controls will be based on the traditional VME technology that is widely deployed at the APS. The controls will be largely replicated from the existing 7-BM beamline. The FSD A station will have a full-size, 64-bit VME crate housing OMS motor controllers, serial communications, and analog-digital converters (ADCs). The FSD B station will use a 64-bit VME crate housing OMS motor controllers, serial communications, ADCs, a multichannel scaler, a timing electronics to provide accurate timing to the APS electron bunch structure. Motion control will be achieved using stepper motor technology. Two 8-channel banks of motor drivers will be required for the FSD A enclosure. Six 8-channel banks of motor drivers will be needed for the FSD B enclosure. These electronics are currently used at the 7-BM beamline and will be moved to the FSD beamline.

The time-resolved spray experiments performed at the 7-BM and FSD beamlines require proper timing to the APS storage ring timing. Timing electronics are currently fed by an optical fiber signal synchronized to the storage ring timing. A similar scheme will be used at the FSD beamline. Relatively low-speed data acquisition at the FSD beamline will be performed using VME-based electronics (scalers and ADCs). For high-speed data acquisition, oscilloscopes will be used with custom-written control software. This is the current scheme at the 7-BM beamline, and has proved flexible and effective for the high-speed measurements performed at this beamline.

4.16 Bragg Coherent Diffraction Imaging

Instrumentation for Bragg Coherent Diffraction Imaging (BCDI), currently emphasizing measurement of data in the vicinity of Bragg peaks of crystalline samples is located at beamline 34-ID-C on a canted insertion device (ID) straight section. According to the current APS Upgrade Roadmap, the BCDI instrumentation will be moved from Sector 34-ID to a newly canted sector and reside, once again, on a branch with independent control of its source at Sector 9.

In order to maintain high source demagnification with reasonable working distance, the BCDI experimental station needs to be located at the most downstream part of the sector.

4.16.1 Scientific Objectives

The existing BCDI instrumentation at 34-ID-C offers imaging of structural properties of samples at spatial resolution exceeding current x-ray optics. It can exploit a variety of contrast mechanisms within the material of interest, including electron density variation, magnetic structure and strain in a crystalline lattice, to name a few [174, 175]. The user community primarily includes researchers in the fields of materials, environmental and nano science. Some life science applications are also being explored, including chromosome and collagen structures.

4.16.2 Source Requirements

The energy range requirements of the beamline include 6-25 keV, preferably in overlapping tuning curves of an undulator. A U3.0 currently serves the BCDI instrument at Sector 34-ID and will suffice in the relocation to Sector 9.

4.16.3 X-ray Optical Layout

For the BCDI beamline, there are four critical optical components: a white-beam slit is used to reduce the heat load on the beamline optics; a pair of mirrors is required both for harmonic rejection and to achieve sufficient angular separation of the BCDI branch from the partner instrument branch; a pair of pink-beam slits, one in the first optical enclosure (FOE) and another downstream in a mini enclosure which will be used to define the beam ultimately focused onto the sample in the experiment; and a double-crystal monochromator and pink-beam-compatible shutter which will be placed in the second optical enclosure (SOE). The beamline must be pink-beam compatible throughout, as broadband Laue diffraction patterns will be acquired to determine crystallographic orientations.

4.16.4 Beamline Physical Layout

4.16.4.1 Front End

The front end will be a standard canted-undulator front end, with an exit aperture of 2 × 2 mm and a (windowless) differential pumping station.

4.16.4.2 General Description

The planned layout for the BCDI beamline partnering with the mFluor beamline (discussed in section 4.17) at Sector 9 is shown in Figure 4-127 and Figure 4-128. To increase the lateral separation between the two programs, three mirrors are used in the FOE, two deflecting outboard to the BCDI beamline and one deflecting inboard to the mFluor beamline. Two white-beam slits (one for each branch) upstream of the mirrors are used to manage thermal load onto the mirrors. Two pink-beam slits, one for each program, are located directly downstream of the respective mirrors to provide a secondary source both horizontally and vertically. The BCDI station will also have another pink-beam slit in mini enclosure PS2 (not shown in the figures) to act as an alternative secondary source to reduce the demagnification of the final objective lens for experiments requiring a larger beam spot size. Two pink-beam shutters, one for each program, are located in the third mini-enclosure PS3 just upstream of the B station (Figure 4-128).

The experimental enclosure for BCDI needs to accommodate detector arm motions of the diffractometer up to 4 meters outboard of the x-ray beam. The enclosure must also be very long, 10 meters is specified, to accommodate the use of large pixel area detectors in the forward scattering measurement geometry. The enclosure must also be pink-beam compatible to enable Laue patterns to be measured for sample alignment and multi-wavelength BCDI measurements, which are in the preliminary stages of development.

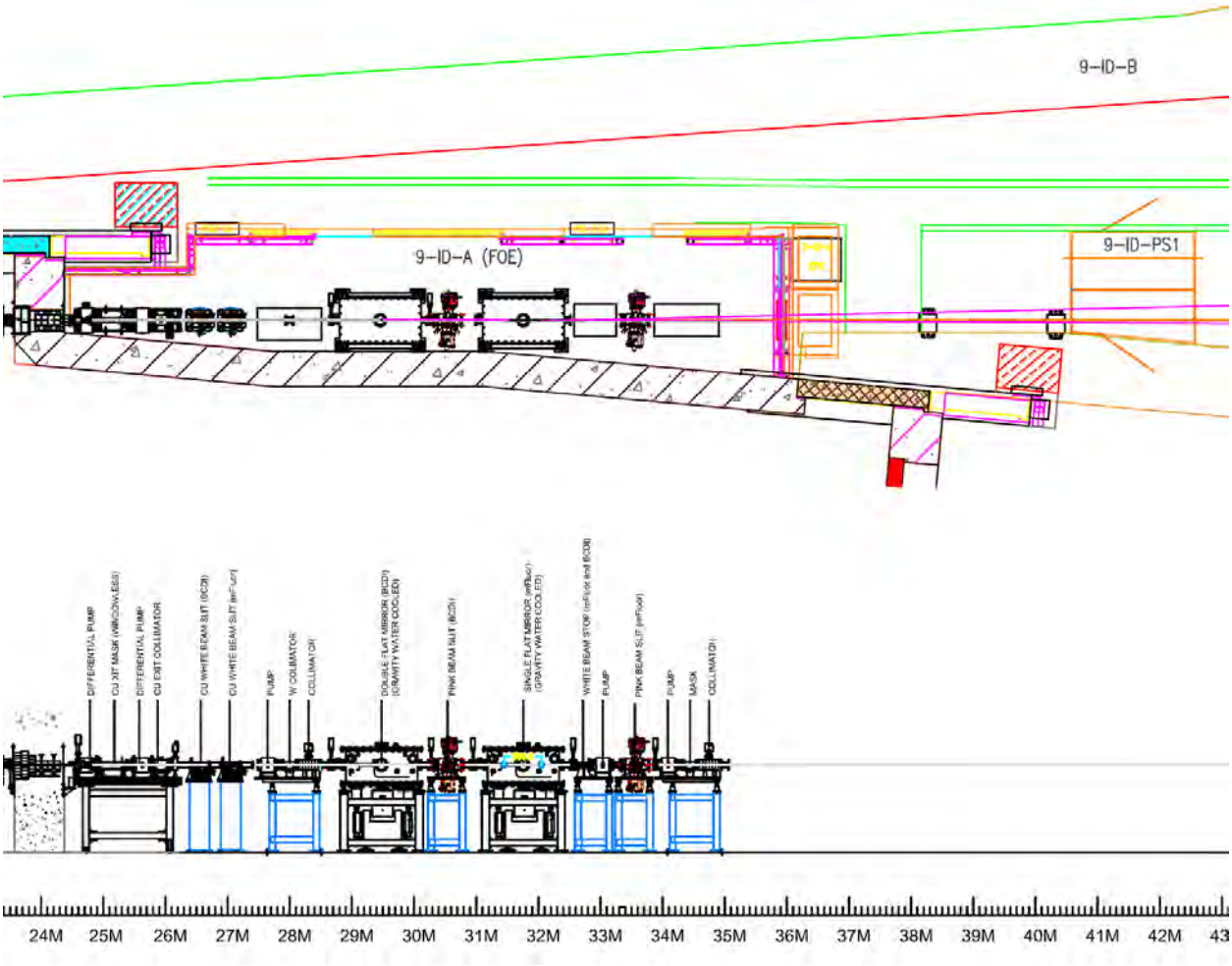

Figure 4-127: Layout of the Sector 9 FOE for the mFluor and BCDI programs.

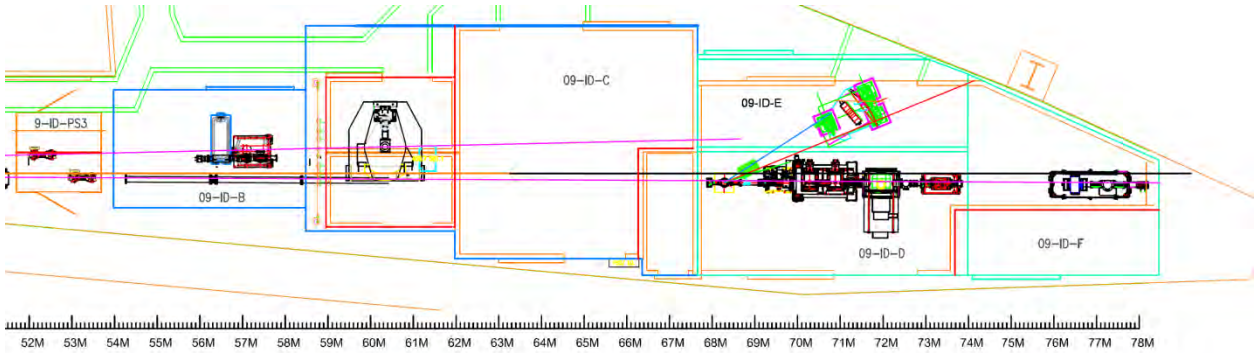

Figure 4-128: Layout of the Sector 9 enclosures for the mFluor (D, E, and F stations) and BCDI (B and C stations) programs.

4.16.4.2.1 Radiation Safety Aspects

Ensuring sufficient shielding to ensure radiation safety is heavily dependent on the design of the canted layout. As the final location of the BCDI beamline may change during Final Design, the beamline shielding cannot yet be fully determined. The design will include masks, shutters, and collimators for the canted front end and the branch beamline. Compact shielded beam transport may be needed to accommodate the partner program.

4.16.4.2.2 Vacuum System

To minimize absorption at low energies and to preserve the wavefront, the BCDI beamline will utilize a windowless front end with differential pump. This generally requires UHV compatible components in the FOE. UHV conditions are also required for the main beamline mirrors to maintain their cleanliness.

4.16.4.2.3 Data Acquisition and Motion Control

The control system of the BCDI will continue to be based on EPICS. Python is the desired scripting language. A higher-level user interface based on Python or other suitable software is required to ease day-to-day user operation. Spec (Certified Scientific) is also required for crystallographic orientation of samples and scanning for data acquisition. Motion controls related to the instrument itself will be relocated from 34-ID. A small amount of new control systems will be required in the FOE and SOE.

4.16.4.3 First Optics Enclosure and Infrastructure, Major Components

Major FOE optical components related to the BCDI beamline are a white-beam slit, pink-beam slit, and a pair of horizontally deflecting mirrors. All components must be designed to allow beam for the partner program to pass close by.

4.16.4.3.1 Slits

The BCDI beamline requires a horizontal/vertical white-beam slit to limit total power to the mirror system. A pink-beam slit immediately following the mirror system will be used to reduce the effective source size in both horizontal and vertical directions. The slit should be UHV compatible and capable of reproducible slit settings down to 20-200 μm with an accuracy of 2 μm.

An additional pink-beam-compatible slit, horizontal/vertical, is also required with identical specifications for placement in a mini enclosure: 20- to 200-μm gaps with an accuracy of 2 μm. This nearer slit will be used to reduce the demagnification of the effective source when larger focal spot sizes are needed at the experiment.

4.16.4.3.2 Collimators

Sufficient collimation is required to provide the necessary bremsstrahlung and synchrotron radiation protection while operating the branch stations independently. Collimators will be specified following identification of the final site for the beamline and the partnering program on the adjoining cant.

4.16.4.3.3 Shutters/Stops

A white beam shutter will be used upstream of the FOE to allow access to the FOE. A white beam stop will also be required downstream of the FOE flat mirrors.

4.16.4.3.4 Mirrors

Two high-heat-load mirrors are required to reject undulator harmonics, reduce heat load on downstream optics, and to provide physical separation of the two branches of the canted beamline. The BCDI beamline will use flat, water-cooled, horizontal-deflecting mirrors at ~ 30 m from the source with 3 mrad angle of incidence to reflect x-rays up to 25 keV. The mirrors will have three reflective stripes (Si/Rh/Pt) to provide good harmonic rejection across the full energy range at fixed grazing angle. Vertical translation will be used to change the reflecting stripe used. Each mirror will have an optical length of approximately 200 mm to accept up to 0.3 mm of one canted undulator beam. To preserve the coherent wave front of the beam, the slope error of the mirrors should be < 3 μrad. The mirror must be designed to allow a canted beam for the partner program to pass by undisturbed.

4.16.4.3.5 Diagnostics

Retractable diagnostics monitors capable of withstanding white beam are required downstream of the mirrors to align and monitor the beam position.

A quadrant detector will be required downstream of the mirror to sense the horizontal and vertical motions of the pink beam and may be used for the purpose of feedback.

4.16.4.4 Second Optical Enclosure

An SOE located about 50-60 m from the source will house the monochromator, beam diagnostics, and shutters for the BCDI branch. The SOE needs to be pink-beam compatible.

4.16.4.4.1 Monochromator

The BCDI instrumentation will require a small-offset vertical-diffracting water-cooled double-crystal monochromator. The design can be identical to the monochromator and mono slit assembly being designed for the S3DD beamline at Sector 34-ID (discussed in section 4.11). It covers the 6-25 keV energy range with a pair of Si<111> crystals and allows for rapid switching between pink beam and monochromatic beam, while leaving downstream optics in place.

4.16.4.4.2 Diagnostics

A retractable diagnostic monitor capable of withstanding the pink beam is required upstream of the double-crystal monochromator to align and monitor the pink-beam position.

A quadrant detector will also be required downstream of the double-crystal monochromator to sense the horizontal and vertical motions of the mono beam and may be used for the purpose of feedback.

4.16.4.4.3 Shutters

The SOE will contain a pink-beam shutter to allow access to the BCDI instrumentation enclosure independent of the partner branch on the canted sector. It will be designed to allow independent operation of the two beamlines. Pink-beam shutters in the PS3 mini-enclosure allow independent access to the SOE for each beamline of the canted sector without interruption of the partnered experiment.

4.16.4.5 Experimental Enclosure

4.16.4.5.1 Windows

Either polished Beryllium or Silicon Nitride windows will be used in the experimental enclosure to isolate the beamline vacuum from the outside world.

4.16.4.5.2 Focusing Elements

The BCDI instrumentation uses Kirkpatrick-Baez (K-B) mirrors to maximize the coherent flux upon a sample. In most cases, the spot size is limited by geometric demagnification of the source, and thus the source distance should be maximized whenever possible for optimal spot sizes. There are experiments, however, where the spot size on the sample is required to be larger. This is the reason a second set of pink-beam slits will be installed in the mini-enclosure between the FOE and the SOE. When larger focal spots are required for the experiment, the downstream slits will be closed to an appropriate size as determined by the demagnification required of larger spot sizes at the experiment without loss of coherent flux.

4.16.4.6 Control Room

A control room, ideally connected to the experimental enclosure station, is required. In addition to providing a control area for users, this will reduce air flow and temperature fluctuation when accessing the stations.

4.16.5 Additional

4.16.5.1 Conventional Facilities Requirements

Standard utilities available at the APS beamlines are required. This includes electrical power for all beamline components, control computers, and experimental equipment. Temperature-stabilized deionized water with a temperature stability of ± 0.1°C is required for cooling the mirror, slits, monochromator, and shutters. A control room with relevant power, network connections, etc., is required. Manifolds that regulate gas flow and switch between full and empty cylinders of helium and nitrogen are required to supply gases to the BCDI station.

4.16.5.2 Environmental Considerations

The temperature stability of the C station should be regulated to better than ± 0.1°C. Vibration stability is also very important for achieving high resolution, reliable measurements. The station should be located on a low-floor-vibration site, with minimal disturbances from:

- Ambient noise and user operations
- Water systems
- Air handling systems
- Other beamline equipment
- Vacuum pumping systems.

4.17 Fluorescence Microprobes (mFluor)

The Fluorescence Microprobes (mFluor) beamline is currently located at 2-ID on a non-canted front end. The facility consists of two hard x-ray fluorescence microprobes in stations 2-ID-D and 2-ID-E. The two microprobes provide submicron spatial resolution and high elemental sensitivity for diverse studies in life, environmental, materials, and nanoscience. They share a beam from two independent collinear insertion devices, with the side-branch microprobe at 2-ID-E intercepting the outboard part of the undulator beam using a beam-splitting crystal, while the in-line microprobe at 2-ID-D uses the central part of the incident beam. In the base scenario for the APS Roadmap, the mFluor beamline will share a new canted front end with a partner program, Bragg Coherent Diffractive Imaging (BCDI), at 9-ID.

Microprobes rely on being located a long distance from the source to provide the requisite source demagnification needed for achieving a submicron focus. In order to maintain a reasonable working distance, it is therefore important to locate the microprobes at the most downstream part of the sector. Additionally, this placement will minimize the effects of the astigmatic beamline layout due to different horizontal and vertical source positions.

4.17.1 Scientific Objectives

The fluorescence microprobes offer very high trace-element sensitivity (on the order of parts per million) and mapping capability at submicron resolution. They are supporting a diverse user community at 2-ID, with applications in life, environmental, materials, and nanoscience, and will continue to do so after the relocation. In addition to regular 2D elemental mappings, the microprobes can also operate in x-ray absorption near edge structure spectroscopy (XANES) and tomography (3D) mode. Single-element and multi-element energy dispersive detectors are used for detection of characteristic x-ray fluorescence radiation from the sample. Data are acquired in both step-scan and fly-scan modes, with fly-scan mode enabling the fastest scan rate. A complementary transmission image of the sample matrix is currently provided by measuring the differential phase contrast (DPC) signal using a segmented detector downstream of the sample. Under development is the use of an area detector to provide coherent diffraction imaging (ptychography) for even higher spatial resolution.

4.17.2 Source Requirements

4.17.2.1 Spectral Requirements

The in-line (2-ID-D) microprobe operates in the energy range of 5-30 keV, while the side-branch (2-ID-E) microprobe operates in the range of 7-17 keV. Currently both microprobes are served by two collinear undulators at 2-ID, a U3.3 and a U5.5, each of which is a standard 2.4-m-long device. The U3.3 is used when both microprobes operate at the same energy. If the microprobes require different energies, the in-line microprobe typically tunes the U3.3 to one energy while the side-branch microprobe tunes the U5.5 to a different energy (with a substantial reduction in flux). In the future, two independent insertion devices are required in order to maintain this ability for the instruments to operate independently.

4.17.2.2 Other Source Requirements

As defined in the APS Roadmap, the mFluor beamline will be placed at a canted sector with a standard 5-m-long straight section, and will share the sector layout with a partner program. Therefore, only a 2.5-m-long straight section will be available for the mFluor beamline compared to the current 5-m-long straight section at 2-ID, thus reducing the capabilities of the existing instruments. To maintain independent energy tuning and high brightness to each of the two microprobes throughout the required range of photon energies, two short (1.2-m-long) collinear undulators are required to be deployed as sources for the mFluor beamline in the relocation. One of the short undulators will be a U3.0 (3.0-cm period) to provide continuous coverage from 5 to 30 keV for the in-line microprobe, while the other short undulator will be a U2.7 (2.7-cm period) to cover the range from 7 to 16 keV for the side-branch microprobe in the first harmonic. In addition, on an experiment-by-experiment basis, the two microprobes can also share the beam by tuning the IDs to the same energy, thereby maximizing the incident flux.

4.17.3 X-ray Optical Layout

For the mFluor beamline, there are two critical optical components in the first optics enclosure (FOE): a high-heat-load mirror to deflect the beam inboard and a pink-beam slit to reduce the effective horizontal

source size. At ~ 60 m from the source, the outboard part of the pink beam is intercepted by a single-crystal monochromator and diffracted to the side-branch microprobe. The remaining (center) part of the beam is further conditioned by a pink-beam slit, a double-multilayer monochromator, and a double-crystal monochromator before being delivered to the in-line microprobe.

4.17.3.1 Mirrors

High-heat-load mirrors are required for higher harmonics rejection, power handling, and for providing physical separation of the two branches of a canted beamline. The mFluor beamline will use a plane, water-cooled, horizontal deflecting mirror at ~ 30 m from the source with a 2.6 mrad (0.15 deg) angle of incidence to allow reflection of x-rays up to 30 keV. The mirror will have 3 reflective stripes (Si/Rh/Pt) to provide good higher-harmonics rejection across the full energy range at a fixed grazing angle. Vertical translation of the mirror is required to change the reflecting stripe used. The mirror will have an optical length of approximately 800 mm to accept 2 mm of the canted undulator beam horizontally. To preserve the coherence of the beam, the slope error of the mirror will be < 2 μrad rms. The mirror will be designed to allow a canted beam for the partner program to pass by undisturbed.

4.17.3.2 Monochromators

There are three monochromators for the mFluor beamline, all located at about 60-65 m from the source: a single-crystal monochromator for the side-branch microprobe, plus a double-multilayer monochromator and a double-crystal monochromator for the in-line microprobe. They are described in the following sections.

4.17.3.2.1 Single-Crystal Monochromator

The side-branch microprobe is served by a horizontal diffracting water-cooled single-crystal monochromator. It uses two crystals, Si <111> and Si <220>, to cover the 7- to 17-keV energy range. The crystals are L-shaped and arranged symmetrically in the vertical direction to allow the center part of the beam to be transmitted to the in-line microprobe downstream. Vertical and horizontal translation is required to bring one of the crystals to within 300-600 microns of the beam center and direct the off-axis radiation to the side-branch microprobe. The crystals can be rotated over a limited angular range to tune the energy. As such, the side-branch microprobe is placed on an arc bearing to follow the diffracted beam from the monochromator.

4.17.3.2.2 Double-Multilayer Monochromator

Depending on the flux and the spectral bandwidth requirement, the in-line microprobe can use either a double multilayer or a double crystal monochromator. The double-multilayer monochromator is vertical diffracting and water-cooled, with an adjustable beam offset of 10-30 mm. Two highly polished substrates, each coated with 3-4 multilayer stripes with different d-spacing and material, will be used to cover the energy range from 7 to 25 keV. The d-spacing of the multilayer pair must be matched as much as possible to minimize dispersion of the beam exited from the monochromator. The selection of

multilayer is based on its ability to provide high reflectivity at a spectral bandwidth of 0.5-1.0%. Currently, WSi_2/Si and $MoSi_2$/Si multilayers are used.

4.17.3.2.3 Double-Crystal Monochromator

For high spatial resolution or spectroscopy operation, the in-line microprobe uses a vertical diffracting water-cooled double-crystal monochromator. It covers the 5- to 30-keV energy range with a pair of Si<111> crystals. The beam offset is typically about 21 mm but is adjustable between 10-30 mm. Currently thermal distortion can widen the natural rocking curve by ~ 50% at a ring current of 100 mA. In order to take advantage of higher ring current at 150 mA, it is required that the water cooling be replaced by cryogenic cooling. New indirectly cooled cryogenic crystals and a LN_2 pump is therefore required.

4.17.3.3 Focusing Elements

Both microprobes use Fresnel zone plates to focus incident x-rays to a submicron spot on the sample. In most cases, the spot size is limited by geometric demagnification of the source, and thus the source distance will be maximized whenever possible. Depending on the experimental needs, zone plates with different diameters and finest zone widths and thicknesses, are used for optimizing flux and resolution at various energies. As the technology matures, mirror reflective optics may also be considered as focusing elements.

4.17.4 Beamline Physical Layout

4.17.4.1 Front End

The front end will be a standard canted undulator front end, with an exit aperture of 2 x 2 mm and a (windowless) differential pumping station.

4.17.4.2 General Description

The layout for the mFluor beamline partnering with the Bragg coherent diffractive imaging (BCDI) beamline at Sector 9 is shown in Figure 4-129 and Figure 4-130. To increase the lateral separation between the two beamlines, three mirrors are used in the first optics enclosure (FOE), one deflecting inboard to the mFluor beamline and two deflecting outboard to the BCDI beamline. Two white-beam slits upstream of the mirrors are used to manage thermal load onto the mirrors. Two pink-beam slits, one for each beamline, are located directly downstream of the respective mirrors to provide a secondary source horizontally. Two pink-beam shutters, one for each beamline, are located in the third mini-enclosure PS3 just upstream of the B station (Figure 4-130).

BCDI will occupy the B and C stations upstream of the D, E, and F stations for the mFluor program (Figure 4-130). The D station is a second optics enclosure (SOE) that consists of: (i) a single-crystal monochromator and a mono-beam shutter for the side-branch microprobe; and (ii) a pink-beam slit, a double-multilayer monochromator, a double-crystal monochromator, beam diagnostic, and a pink-beam

shutter for the in-line microprobe. The E station will house the side-branch microprobe, while the F station will house the in-line microprobe.

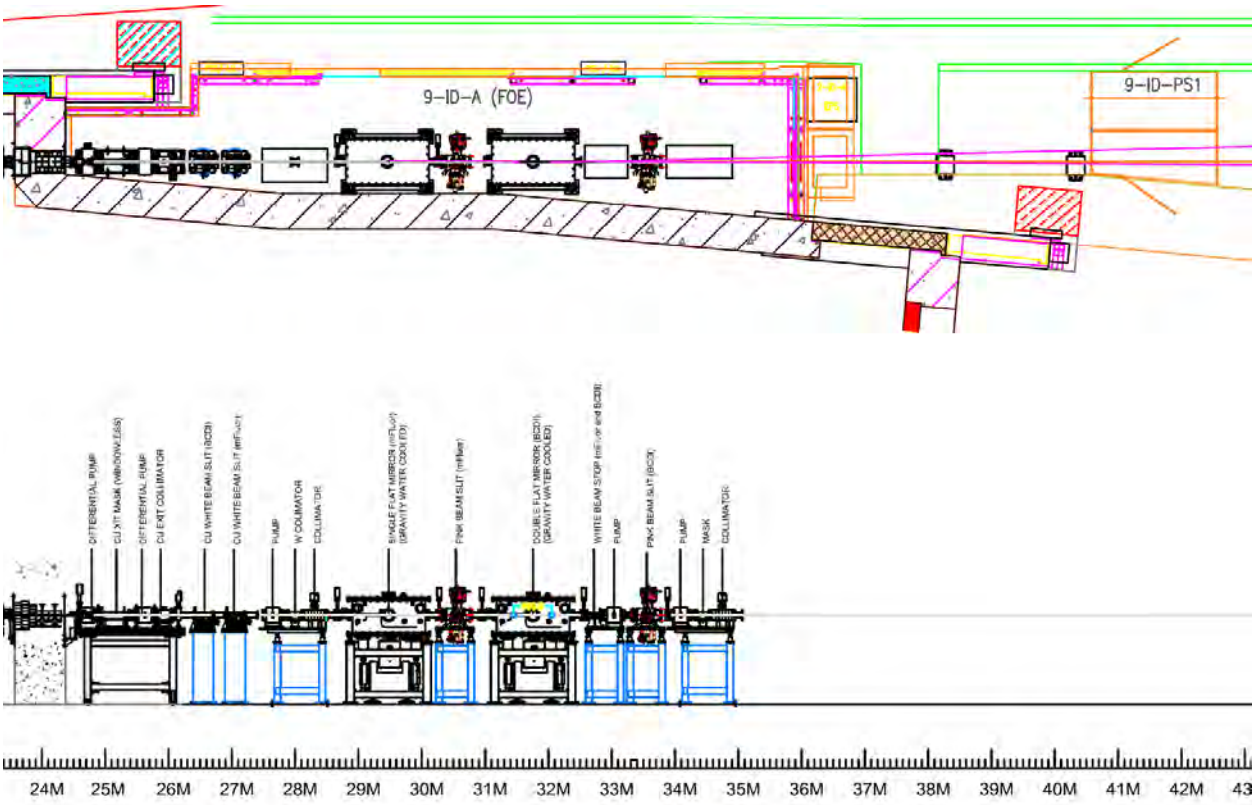

Figure 4-129: Layout of the Sector 9 FOE for the mFluor and BCDI partner program.

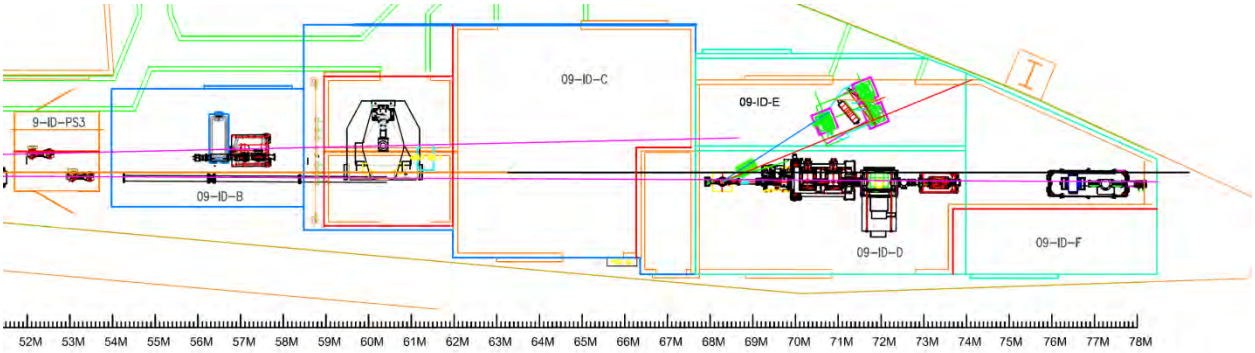

Figure 4-130: Layout of the Sector 9 enclosures for the mFluor (D, E, and F stations) and BCDI (B and C stations) partner program.

4.17.4.2.1 Radiation Safety Aspects

The radiation safety aspect sensitively depends on the design of the canted layout; this will be addressed during final design. The design will include masks, shutters, and collimators for the canted front end and

the branch beamline. The existing FOE at Sector 9 is adequate as a white-beam station. Pink-beam transport from the FOE to the D station will be needed. In particular, compact shielded pink-beam transport may be needed in the B and C stations to accommodate the experimental needs of the BCDI program. Both the D and F stations should be compatible with pink beam, while the E station should be a mono-beam enclosure.

4.17.4.2.2 Vacuum System

To minimize absorption at low energies and to preserve the beam wavefront, the mFluor beamline will utilize a windowless front end with a differential pump. This generally requires UHV-compatible components in the FOE, although this requirement can be relaxed for components further downstream. UHV conditions are also required for the mirrors in the FOE in order to maintain their cleanliness.

4.17.4.2.3 Data Acquisition and Motion Control

The control system for the mFluor beamline will continue to be based on EPICS. Python is the desired scripting language. A higher-level user interface based on Python or other suitable software is required to ease day-to-day user operation.

The mFluor microprobes will acquire full fluorescence spectra from multiple energy-dispersive detectors in both step-scan and fly-scan modes. The data acquisition system has to accommodate these operation modes. The ability to read out an area detector in the fly-scan mode is also desired. Details of the detector type and the related readout rates will be part of the final design.

4.17.4.3 First Optics Enclosure and Infrastructure, Major Components

Major FOE optical components related to the mFluor beamline are a white-beam slit, a horizontally deflecting mirror, and a pink-beam slit. All components will be designed to allow beam for the partner program to pass close by. In most cases, the horizontally deflecting mirror will be illuminated along its full length to minimize thermally induced slope errors. A pink-beam slit downstream of the mirror will clean up any beam distortion introduced by the mirror, providing a stable secondary source horizontally for downstream focusing optics.

4.17.4.3.1 Windows

The mFluor beamline will use a windowless front end. A silicon nitride or beryllium window will serve as the exit window in the experimental station.

4.17.4.3.2 Slits

The mFluor beamline requires a horizontal/vertical white-beam slit (WBS) upstream of the mirror to limit the total power incident on the mirror system. A pink-beam slit downstream of the mirror is required to reduce the effective source size horizontally. Both slits will be UHV compatible and capable of reproducible slit settings down to 20 μm with an accuracy of 2 μm.

4.17.4.3.3 Collimators

Sufficient collimation is required to provide the necessary bremsstrahlung and synchrotron radiation protection while operating the branch stations independently. Collimators will be specified following detailed layout with the partnering program at the canted sector.

4.17.4.3.4 Shutters/Stops

Shutters and stops will be specified following detailed layout with the partnering program at the canted sector. Due to limited space in the FOE, a pink shutter will be located in one of the mini-enclosures downstream of the FOE.

4.17.4.3.5 Mirrors

See section 4.17.3.1 for a physical description of the first mirror in the FOE. To increase the lateral separation between mFluor and BCDI, it is desirable to deflect the outboard undulator beam outboard and to deflect the inboard undulator beam inboard. However, this requires a large opening in the mirror substrate along its entire length in order to let the other beam passed through undisturbed. Detailed thermal analysis will be performed during final design to verify whether the performance of the mirror will be adversely affected. Until such analysis is completed, it is conservatively assumed that the outboard undulator beam will be deflected inboard and the inboard undulator beam will be deflected outboard.

4.17.4.3.6 Diagnostics

Retractable diagnostics monitors capable of withstanding white beam are required downstream of the mirror for alignment purposes.

A quadrant detector is required downstream of the mirror to sense the horizontal and vertical motions of the pink beam and may be used for the purpose of feedback.

4.17.4.4 Second Optics Enclosure

A second optics enclosure (D station) at about 60-70 m from the source will house the monochromators, slits, beam diagnostics, and shutters for the in-line and side-branch microprobe. The SOE will be pink-beam compatible.

4.17.4.4.1 Monochromators

See section 4.17.3.2.1 for a physical description of the single-crystal monochromator for the side-branch microprobe. It is expected that the single-crystal monochromator currently at the 2-ID-E station will be modified to deflect the beam outboard instead of inboard.

See section 4.17.3.2.2 for a physical description of the double-multilayer monochromator for the in-line microprobe. It is expected that the double-multilayer monochromator currently at the 2-ID-E station may be used with minimal or no modification.

See section 4.17.3.2.3 for a physical description of the double-crystal monochromator for the in-line microprobe. It is expected that the double-crystal monochromator currently at the 2-ID-E station will be modified to be cryogenically cooled instead of water cooled.

4.17.4.4.2 Slit

A pink-beam slit is required upstream of the double-multilayer monochromator to manage power load on the monochromators. The slit will be capable of reproducible slit settings down to 50 μm with an accuracy of 5 μm. It is expected that the pink-beam slit currently at the 2-ID-E station will be used with minimal or no modification.

4.17.4.4.3 Diagnostics

A retractable diagnostics monitor capable of withstanding the pink beam is required downstream of the double-crystal monochromator for alignment purpose.

A quadrant detector is also required downstream of the double-crystal monochromator to sense the horizontal and vertical motions of the mono beam and may be used for the purpose of feedback.

4.17.4.4.4 Shutters

The SOE will contain a monochromatic beam shutter for the side-branch microprobe and a pink-beam shutter for the in-line microprobe. These are designed to allow independent operation of the two microprobes. In particular, the shutter for the side-branch microprobe will be a compact design centered on the diffracted beam from the single-crystal monochromator.

4.17.4.5 E Station

The E station, on the outboard side of the SOE, will house the side-branch microprobe currently located in the 2-ID-E station. It will be a monochromatic beam enclosure. In order to follow the diffracted beam from the single-crystal monochromator, the side-branch microprobe will ride on an arc bearing centered around the crystal. Due to the addition of a mono beam shutter between the crystal and the microprobe, a new set of arc bearings with increased radii will be installed on the microprobe table.

4.17.4.6 F Station

The F station, directly downstream of the SOE, will house the in-line microprobe currently located at 2-ID-D. It will be capable of handling pink beam. The temperature stability will be regulated to better than $\pm$ 0.1 °C, and liquid nitrogen will be supplied from the facility.

4.17.4.7 Control Room

A temperature-stabilized control room, ideally connected to the E and F stations, is required. In addition to providing a control area for users, it will provide a constant temperature environment adjacent to the stations and thus reduce air flow and temperature fluctuations when accessing the stations.

4.17.5 Additional

4.17.5.1 Conventional Facilities Requirements

Standard utilities available at the APS beamlines are required. This includes adequate power for all beamline components, control computers, and experimental needs. Temperature stabilized water with a temperature stability of $\pm$ 0.1 °C is required for cooling the mirror, slits, monochromators, and shutters. A control room with relevant power, network connections, etc., is required. Compressed helium gas with manifolds that regulate flow and switch between full and empty cylinders are required to supply gases to the E and F stations.

Environmental Considerations

The temperature stability of the E and F stations will be regulated to better than $\pm$ 0.1 °C. Low vibration is also very important for achieving high resolution and taking reliable measurements. The two stations should be located on a low-floor-vibration site, with minimal disturbances from:

- Ambient noise and user operations
- Water systems
- Air handling systems
- Other beamline equipment
- Vacuum pumping systems.

4.18 General Beamline Upgrades

This component of the Project has been developed specifically to assist those operating beamlines around the ring that are not directly included in the APS Upgrade Project plans. Figure 4-131 shows the twenty-one “non-upgrade” sectors on the standard APS map. (A sector designates a 9° segment of the Experimental Hall floor space and usually contains multiple beamlines.) These active, mature, R&D producing facilities will continue to operate, uninterrupted, while the APS Upgrade, including new beamlines and beamline relocation projects, are built. The one key performance parameter (KPP) that does globally affect every research sector, upgrade or not, is the increase in ring-current from 100 mA to 150 mA.

Since the Project’s inception, it has always been the intention that no beamline will be rendered inoperable nor suffer degraded performance by changes made during the APS Upgrade Project. This

tenant has sometimes been characterized as a “do no harm” policy or even jokingly as the (politically sensitive) “no beamline left behind” policy. It is the express purpose of this General Beamline Upgrades task, to collaborate with the technical staff of each beamline to evaluate and then re-engineer, repair, or replace the at-risk optics or components around the ring.

4.18.1 High Heat Load Optics

The first beamline components under re-evaluation for increased ring current operation are the high heat load (HHL) optical elements. Historically, each APS sector was developed by independent design/build teams and chose different optical schemes depending on the science mission supported by that beamline. It is not surprising that there are a wide variety of mirrors and monochromator designs used throughout the facility, as illustrated in Figure 4-132 for diffractive optics.

Evaluating these disparate mechanical systems and the wide variety of HHL first-crystal designs, with consideration of the sources and power loads incident upon each, is one of the goals of this sub-project. Figure 4-133 presents a sampling of the wide design variety used to dissipate the power loads incident on monochromator first crystals. Except for the water-cooled Si beam splitter (F.) and water-cooled diamond crystal (H.), all of the designs rely upon liquid nitrogen-cooled silicon technology to survive the total power and power density levels produced by APS insertion devices.

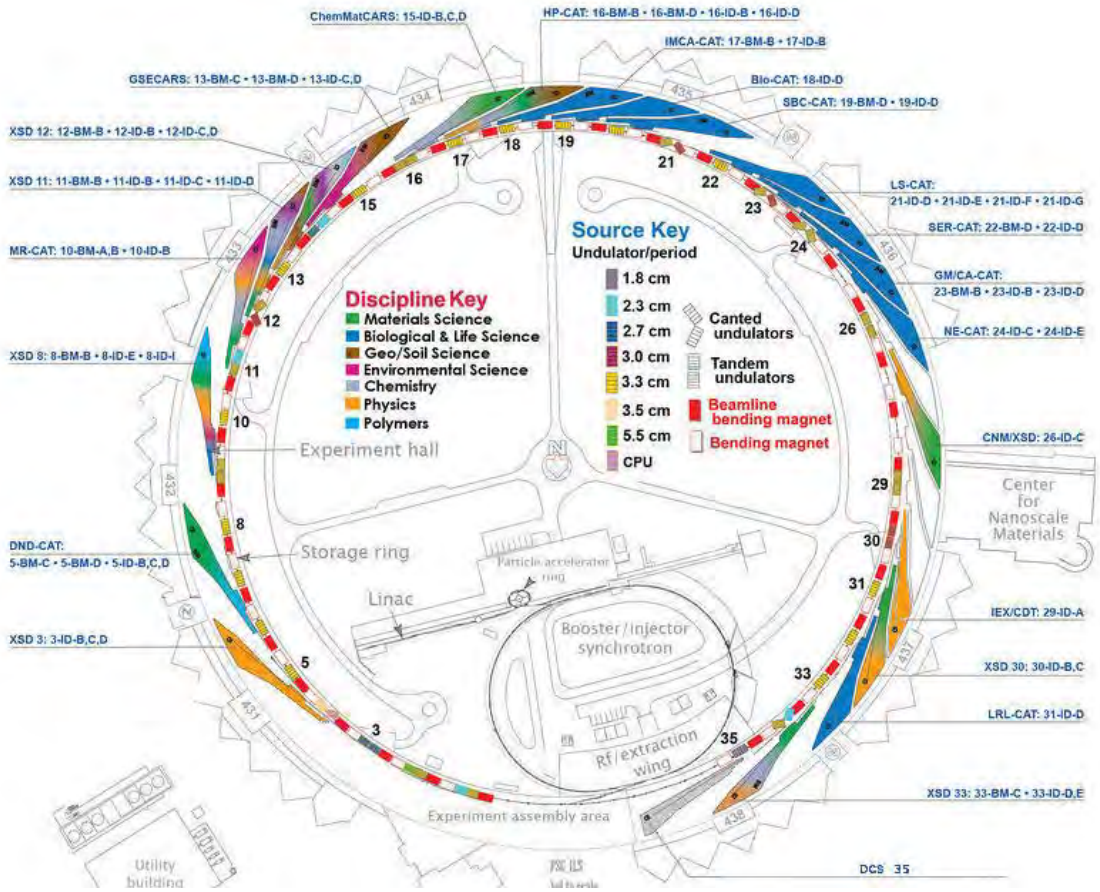

Figure 4-131: APS beamline map highlighting sectors not specifically included in the APS Upgrade plan.

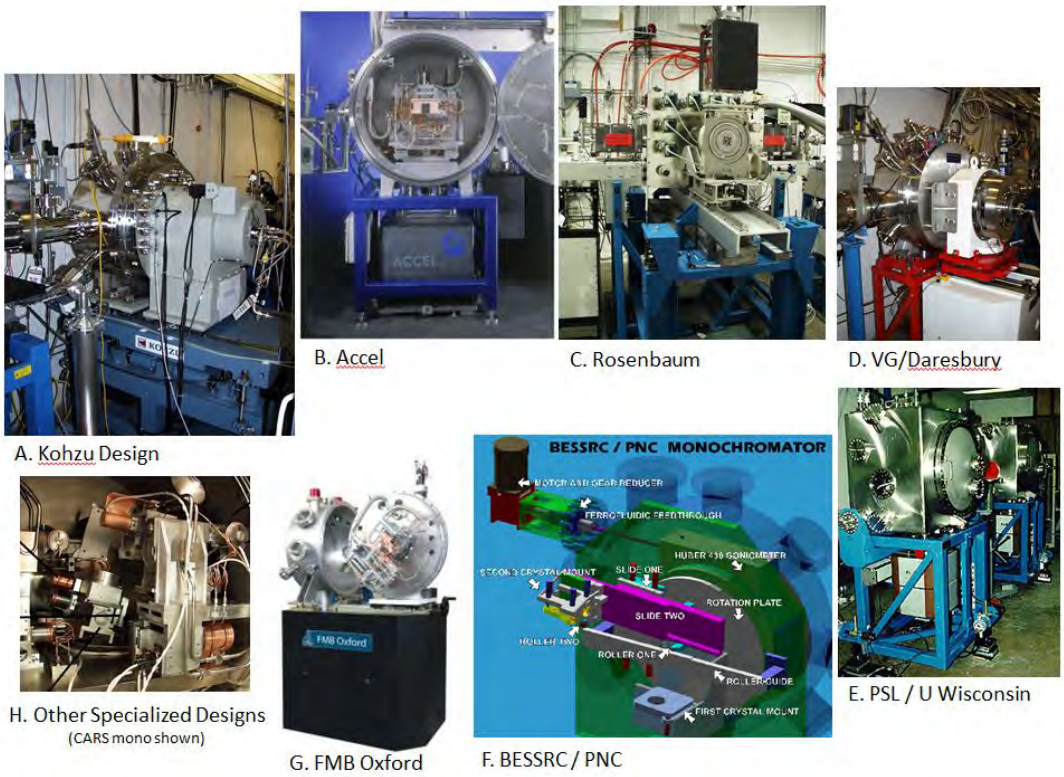

Figure 4-132: A sample of the various monochromator designs used at APS beamlines: (clockwise from top left) ***A.*** *Kohzu (commercial),* ***B.*** *ACCEL (commercial),* ***C.*** *Rosenbaum (government),* ***D.*** *Vacuum Generator/Daresbury (commercial + government),* ***E.*** *Physical Sciences Lab/University of Wisconson (commercial + university),* ***F****. Bassic Energy Sciences Synchrotron Radiation Center/Pacific Northwest Collaborative Access Team (government + university),* ***G.*** *FMB Oxford (commercial), and* ***H.*** *a representative, specialized, in-house built and designed system (University of Chicago, Consortium for Advanced Radiation Sources design shown).*

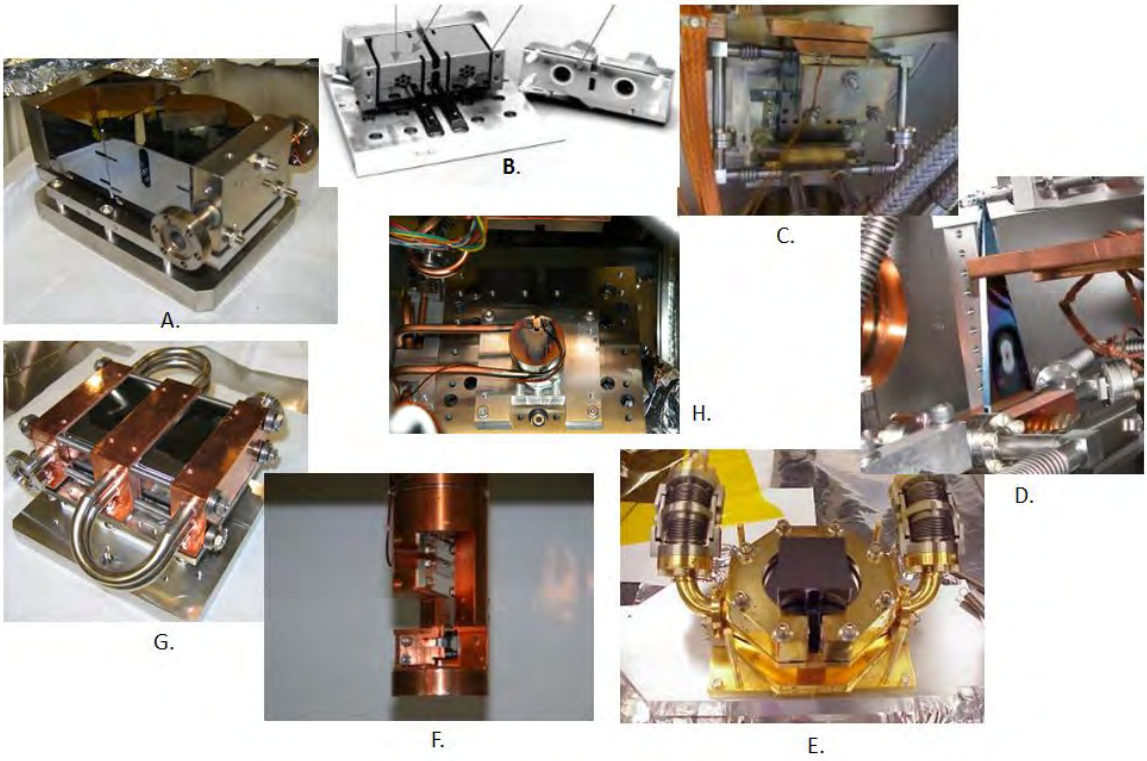

Figure 4-133: Representative sample of high-heat load-monochromator first-crystal designs. (Clockwise from top left) ***A****. Transverse flow, internally liquid-nitrogen (LN_2)-cooled Si<111> and Si<220> set;* ***B****. Longitudinal flow, internally LN_2-cooled thin-web design;* ***C****. Single transverse flow design;* ***D****. Edge LN_2-cooled bent-triangle Laue design;* ***E.*** *Fin-cooled LN_2 'hockey puck' design;* ***F.*** *Water-cooled, Si<111> knife-edge undulator beam splitter design;* ***G.*** *Side-cooled, LN_2 two-crystal design; and* ***H.*** *(center) Water-cooled, diamond<111> design.*

4.18.1.1 Optics Evaluation Strategies

For the preliminary design, the Project has identified the optical components most likely to require re-engineering for higher power operations, illustrated in Table 4-37. This table exemplifies the systematic, APS-wide, component by component process used to triage optical systems. The first two columns list the sectors and sources. The third column designates with highlighting, the beamlines using mirrors as first HHL optical elements. Mirror systems are inherently difficult to re-surface, difficult to retrofit with cooling, and difficult to replace quickly so they garner the highest priority. The beamlines that are highlighted with red boxes (Sectors 8 and 12) have mirrors are an obvious choice for early finite element analysis (FEA) evaluation. Other HHL mirrors in the system are either exempt because they fall under the APS Upgrade plans (cross-hatched cells) or are safe because they are part of newer, recently designed beamlines (Sectors 26 & 35) with 150 mA operations in the baseline design.

Table 4-37: Visual summary of first high-heat-load optical element schemes for individual APS beamlines.

Sector		Mirror 1st HHL Beamline Designs	Monochromator 1st HHL Designs				
			Diamond	Si LN2 Internal Cooled	Si LN2 Fin Cooled	Si LN2 Side Cooled	Si Water Cooled
Sector 1	ID						
Sector 2	ID						
Sector 3	ID						
Sector 4	ID						
Sector 5	ID						
Sector 6	ID						
Sector 7	ID						
Sector 8	ID						
Sector 9	ID						
Sector 10	ID						
Sector 11	ID						
Sector 12	ID						
Sector 13	ID					(2X)	
Sector 14	ID						
Sector 15	ID						
Sector 16	ID						
Sector 17	ID						
Sector 18	ID						
Sector 19	ID						
Sector 20	ID						
Sector 21	ID						
Sector 22	ID						
Sector 23	ID						
Sector 24	ID						
	ID						
	ID					(future)	
Sector 25							
Sector 26	ID						
Sector 27							
Sector 28							
Sector 29	ID						
Sector 30	ID						
Sector 31	ID						
	ID						
	ID						
Sector 32	ID						
Sector 33	ID						
Sector 34	ID						
Sector 35	ID						
		KEY:	Mirror = first optical element in the beamline				
			Water cooled diamond				
			Internally/direct cooled LN2 Silicon				
			Fin-cooled LN2 Silicon "Hockey Puck"				
			Side-Cooled LN2 Silicon (Cu block pressing Si)				
			Water cooled Silicon				
			These sectors are part of APS Upgrade				

Following the same ranking methodology, HHL monochromators were initially evaluated and, as the final 5 columns of Table 4-37 highlight, those sectors with high-power-producing sources and side-cooled or fin-cooled monochromator systems are also scheduled for early evaluation.

Guidance for choosing which x-ray optics systems are at highest risk comes from three places. First, an *ad-hoc* HHL user group has formed at the APS to discuss these problems. The members bring with them, a wealth of information and optics experience that guide this evaluation task. Second, there will be short, periodic, 150 mA operations runs, typically just prior to a scheduled shut-down, that allow users to evaluate their optical system's performance as ring current is gradually increased. The first of these high-current runs occurred on August 23, 2012 and reports are being collected and evaluated. Finally, as part of the Argonne-sponsored R&D described in section 4.18.1.3 below, verified FEA models for liquid

nitrogen cooled monochromators are being developed. Experience gained in creating these models will be directly applied to the numerous geometries found around the ring.

4.18.1.2 Optics Remediation

Remediation strategies will be individually planned in collaboration with the individual beamlines. Among the many remediation options are:

Filtering – reducing the low-energy portion of the white radiation through suitable filter materials and thicknesses. Cost index is low for this option.

Source change – in some cases, substitution of a planar undulator with a period less than the standard, Undulator A period of 33 mm, would serve the scientific purposes of the beamline while simultaneously lowering the total power load on the optical elements. Cost index is high for this option.

Mask or slit changes – most early sectors at the APS were designed to survive power loadings appropriate for a (4.5 mm × 4.5 mm) exit mask. Reducing this mask size to the new standard of 3 mm-H × 1 mm-V allows the central full width at half maximum (FWHM) cone of radiation to pass at the 25-m mark while eliminating a significant portion of the total power loading. Cost index is low for this option.

Cooling enhancements – for older optics, it may be possible to increase the cooling capability on mirrors. A combination of enhanced thermal coupling and clever cooling-plate design may solve some of the increased power loading problems. Cost index is moderate for this option. Areas of enhancement include:

- better thermal coupling by increased clamping force, different interface materials, larger transfer surface area, better side plate design, increased flow-rates, lower process-water temperatures
- addition of heat transfer enhancements to the process water hot-wall through the use of coil insert technology
- enhanced cooling plate geometry analysis. That is, current FEA models illustrate that there are excess global slope-errors induced on long mirrors by full-length side cooling without full-length mirror illumination.

4.18.1.3 Optics R&D

The HHL synchrotron community, including many APS researchers, has developed strategies for reducing the thermal-stress-induced deformations on x-ray optics. We have experimental confidence in the ability of water-cooled diamond to withstand high power loads and power densities [176]. In a similar manner, we have experimental guidance using liquid nitrogen internally cooled [177] and liquid nitrogen side-cooled [178] silicon monochromator crystals. As the confidence in FEA modeling has increased [179], the results of this modeling process have become more reliable.

Argonne has provided early R&D support for this critical area of concern, through the Laboratory Director's Research and Development (LDRD) program. The R&D program is in progress but the results, coupling measured optics response (Figure 4-134) with FEA modeling (Figure 4-135) are aiding in the construction of verified HHL FEA models. The results and experience gained in building these models will be extensively used while evaluating optical components around the facility.

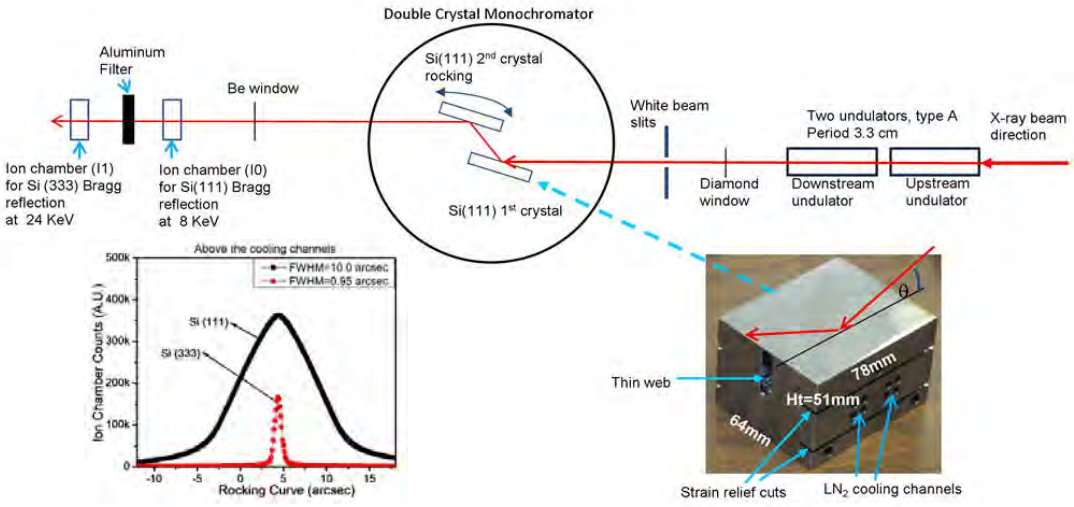

Figure 4-134: Early results. HHL monochromator first-crystal distortion measurements under dual undulator (3.3-cm period) power loading [180].

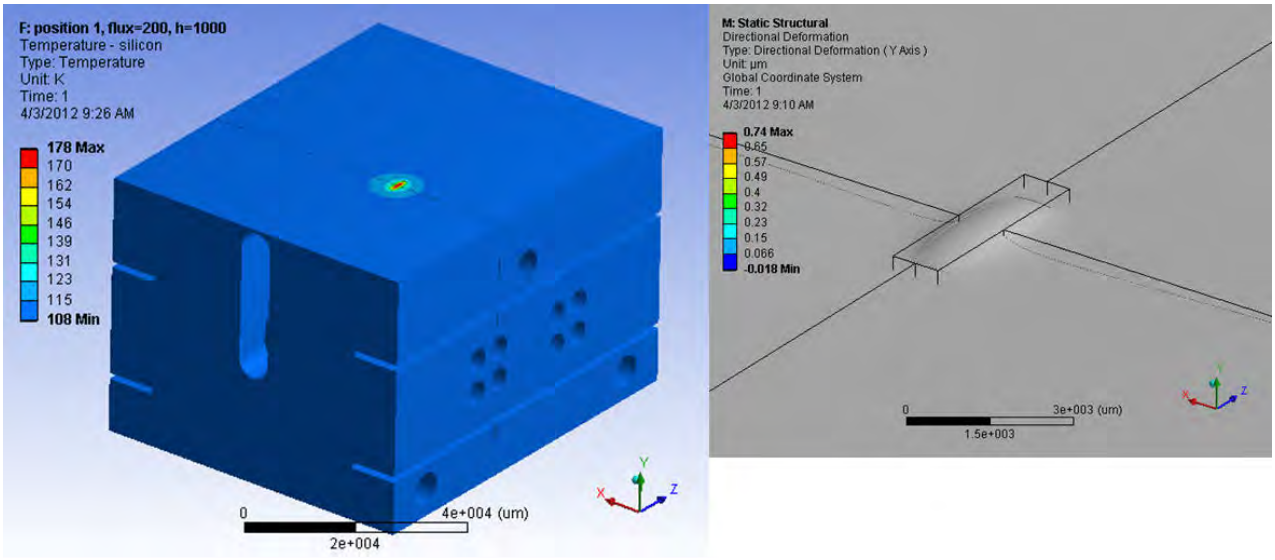

Figure 4-135: Dynamic FEA model of transverse liquid-nitrogen-cooled Si<111> HHL monochromator first crystal used in Figure 4-134 [181].

4.18.2 High-Heat-Load Components

Another critical set of beamline components under re-evaluation for increased ring current operation are the HHL absorbers. Absorbers are the generic term for the category of beamline components including all of the items listed below. They absorb unneeded x-rays, convert them into heat, and safely dispose of that heat via a cooling process-water stream. These components are further subdivided into:

Apertures – cooled copper absorbers designed to continuously remove the outer shell or corona of the radiation stream. They have fixed openings that allow a calculated, central solid-angle of radiation to pass while absorbing the surrounding synchrotron radiation halo.

Beam Limiting Apertures (BLAs) – see apertures.

Collimators – although not a HHL component, these thick tungsten apertures are included to clarify the lexicon used at the APS. Collimators are apertures for the very high energy bremsstrahlung radiation that readily passes through typical copper apertures. They absorb very little total power since they are always guarded by an upstream copper aperture. They stop the up to 7-GeV radiation present in any white beam and effectively collimate the high-energy end of the synchrotron radiation spectrum.

Filters – thin absorbers, made of various materials, typically carbon or aluminum, designed to selectively remove power from the lower energy portion of the beam.

Masks – see apertures.

Shutters – absorbers that cyclically block or unblock the entire x-ray beam including the central beam core. Shutters can include collimators or stops in their designs but, strictly speaking, shutters are the moving blocks of materials that alternately block or pass x-rays, with all spectral characteristics, at the user's command.

Slits – apertures with variable size, on demand.

Stops – absorbers that are the final component for all radiation that has not been used by other upstream components.

Windows – vacuum barriers that must incidentally survive exposure to the main radiation stream as that stream passes through them. Most often, they are made of low-Z materials such as beryllium, diamond or silicon-nitride.

As previously noted, each APS sector has historically been developed by independent design/build teams and has chosen different absorber schemes to meet the performance requirements of that beamline. It is not surprising that there are a wide variety of absorber designs used throughout the facility, as illustrated in Figure 4-136. Even though to first approximation, all are water-cooled-copper devices absorbing x-rays at shallow-to-grazing incidence angles, it is the details of the materials, cooling schemes, thermal paths, and source characteristics that make each device's behavior unique. Subsequently, it is this uniqueness that requires each component be analyzed on a case-by-case basis to determine its suitability for 150-mA or even 200-mA operation.

Fortunately, many of these absorbers are part of the carefully controlled radiation safety system (RSS) protocols and are well analyzed and documented. At this preliminary design phase, it is these documents as well as the final beamline design reports that are being culled to extract critical component information.

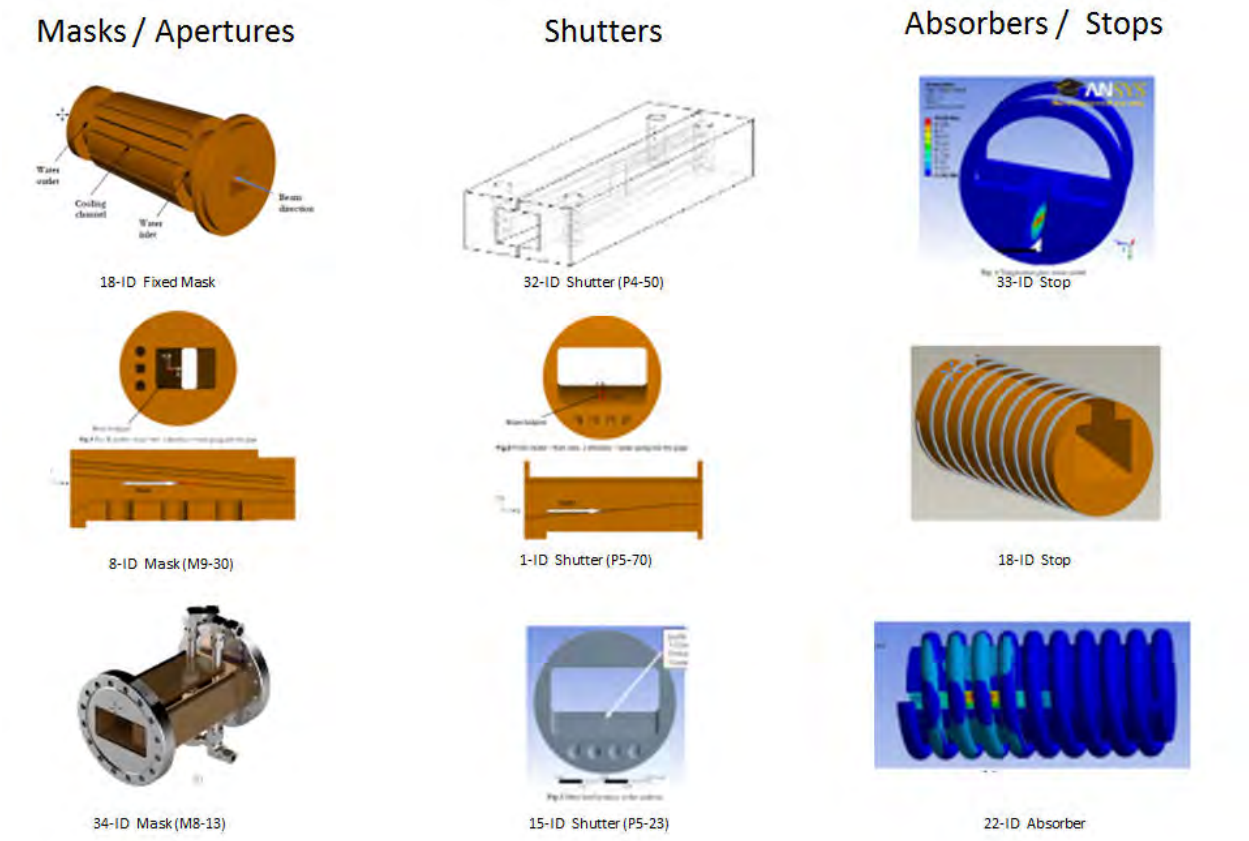

Figure 4-136: Examples of the variety of absorbers deployed in various beamlines around the APS.

4.18.2.1 Component Evaluation Strategies

An initial tabulation of results is shown in Table 4-38. An ongoing work in progress, this table illustrates the process, from component evaluation through analysis to remediation planning, that must take place for each non-APS Upgrade beamline around the ring. Each identified marginal or underperforming component must be evaluated for suitability at higher ring current. The component can be modified, retrofitted, or replaced to bring the beamline into compliance with the demands of higher current and higher power load operation.

Table 4-38: Initial tabulation of 'weak link' HHL components by beamline. Red fill highlights components selected for early analysis. Grey hatched rows indicate beamlines in the APS Upgrade Project. White rows indicate sectors supported by effort from General Beamline Upgrades.

Beamline	Weakest Link	Mask	Shutter	Stop
1ID	> 200mA		P4-70 (P2-21), Integral Shutter, P5-70 (P5-23), Integral Shutter	
2ID	< 150mA		P9-30, Photon Shutter	
3ID	< 150mA		P5-20 (P5-23), Integral Shutter	
4ID	< 150mA		P4-40, White Beam Shutter	P4-60 White Beam Stop
5ID	< 150mA		P5-20 (P5-23), Integral Shutter	
6ID	< 150mA		P5-20 (P5-23), Integral Shutter	
7BM	< 150mA	M4-10, Fixed Mask		
8ID	> 200mA	M9-30, Fixed Mask	P9-30 & P9-50, Integral Shutters	Pink Stop
9ID	< 150mA	FM103	P5-23	
10ID	150 to 200mA		P5-23 (Inverted)	
11ID	< 150mA			White Beam Stop
12ID	< 150mA	M8-11	P9-50, Photon Shutter, Pink Beam Shutter	
13ID				
14ID	> 200mA			White Beam Stop
15ID	150 to 200mA	M4-30, Fixed Mask	P5-23, Beam Stop	
16ID	< 150mA	400W & 100W Masks	Thermal Shutter	
17ID	150 to 200mA			P5-23, Beam Stop
18ID	< 150mA	Fixed Mask		White Beam Stop
19ID	< 150mA			18-ID WB Absorber.
20ID	< 150mA		P5-20 (P5-23), Integral Shutter	
21ID	150 to 200mA	IDT Mask (Inboard & Outboard)	P4-40 Shutter	Inboard White Beam Stop, K5-50, White Beam Stop, P4-60, White Beam Stop,
22ID	< 150mA			White Beam Absorber
23ID	> 200mA		Integral Beam Shutter	Integral Beam Stops (30 & 62m)
24ID	150 to 200mA			
25ID				
26ID	150 to 200mA	M26-A1, Fixed Mask, M26-A3, Pink Beam Mask	PS26-A	M26-A2, White Beam Stop
27ID				
28ID				
29ID	< 150mA	M1-20, M2-20, M1A, M2A, M3A		Beam Stop
30ID	> 200mA		P5-80 Integral Shutter	
31ID	> 200mA			P4-51 White Beam Stop
32ID	150 to 200mA		P4-50 (P4-51), Integral Shutter	P11-10, Movable Beam Stop, P12-20, Fixed Beam Stop
33ID	< 150mA	M8-30, Fixed Mask		White Beam Stop
34ID	150 to 200mA	M8-12 & M8-13	P9-30 White, Integral Shutter, P9-30 Pink, Integral Shutter	White & Pink Beam Stops
35ID	(new)			

4.18.2.2 Component Remediation

With the exception of filters and windows, all other HHL absorbers are made of high thermal conductivity copper; usually Oxygen Free High Conductivity (OFHC™), Oxygen Free Copper (OFC), or Oxygen Free Electronic (OFE) copper. All are grades in the general category of oxygen-reduced pure copper alloys denoted with unified numbering system (UNS) alloy number C01xxx. Alternately, GlidCop® (UNS-C15715), a proprietary [182] dispersion-strengthened high-conductivity copper is used due to its greatly increased strength and ability to retain that strength at temperature with only a minor loss of conductivity.

Remediation strategies will be individually planned in collaboration with the individual beamlines. These strategies can include:

- Material change from OFC to GlidCop® or cladding OFC with GlidCop®. (moderate cost)
- Retrofitting components with pre-absorbers. (low cost)
- Changing the angle of incidence by re-mounting the absorber. (low cost)
- Modifying the active strike surface. (moderate cost)
- Re-designing the cooling process-water efficiency by: i) adding inserts for increased thermal coupling, ii) decreasing the hot-wall to wet-wall distances, or iii) increasing coolant flow, among other solutions. (moderate cost).

4.18.2.3 Component R&D

Argonne has also provided early R&D support for evaluation of GlidCop® absorber material through the LDRD program. Under this program, samples of absorber material were cyclically exposed to full spectrum, white x-radiation simulating 10,000 cycles, as shown in Figure 4-137.

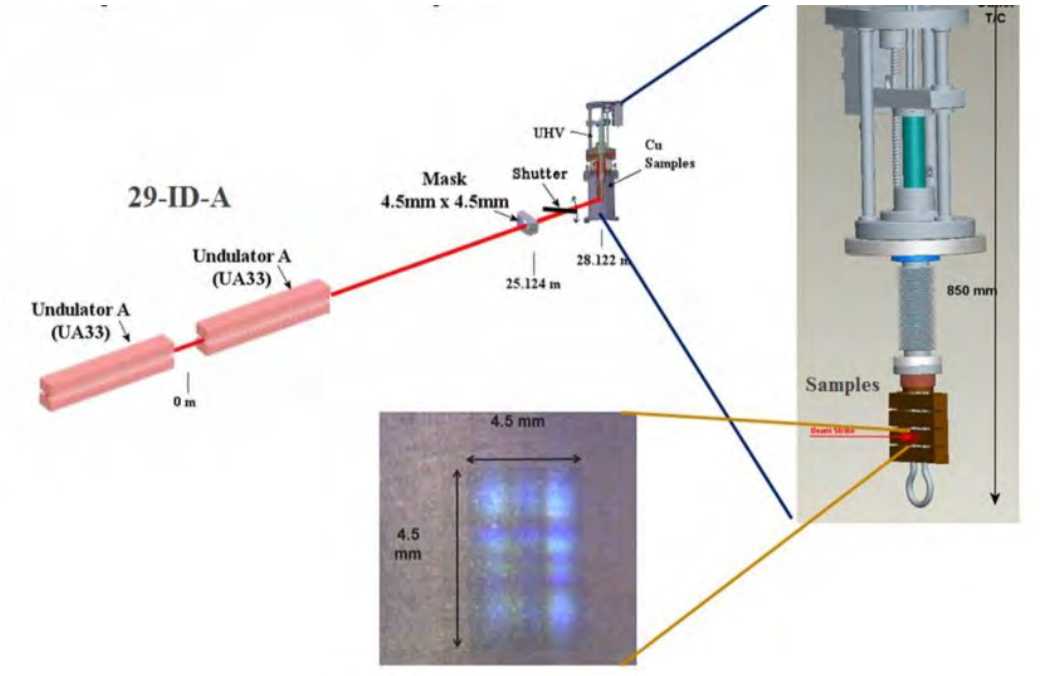

Figure 4-137: Experiment layout, white-x-ray-induced thermal fatigue studies of GlidCop® absorber materials.

The R&D program identifying the failure modes of this material over a wide range of power loadings, shown in Figure 4-138, is in progress. These results will be applied to component retrofitting and redesign FEA analyses. At this pre-publication stage, results look promising and any findings will be applied to component re-design after appropriate review.

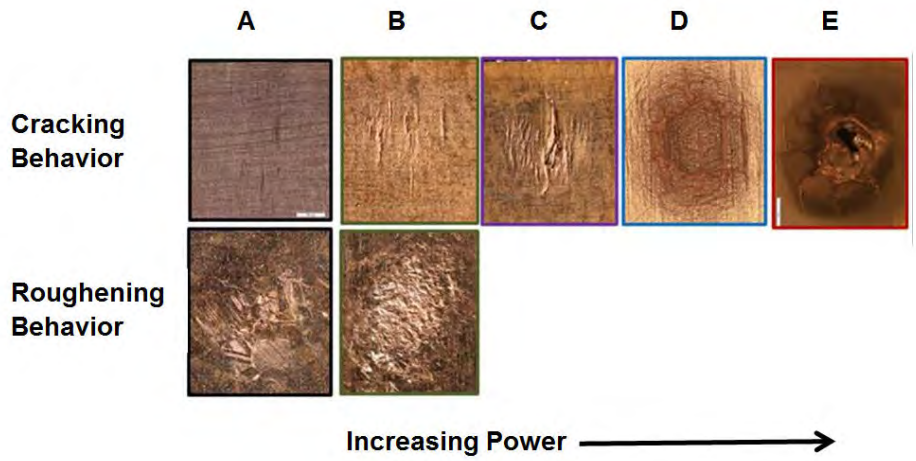

Figure 4-138: Range of GlidCop® material responses with cyclic exposure to full white spectrum synchrotron x-rays. (left to right) A) incipient to fine surface cracks, B) multiple 'cat-scratch' surface cracks, C) emergence of a dominant crack system, D) multiple major cracks plus surface heaving, E) surface melting plus major crack emergence. At low to moderate power loads, surfaces exhibit an alternate deformation mode consisting of a surface rumpling or roughening rather than cracking morphology.

4.19 Detector Development

Detectors are an enabling technology critical to the operation of the APS. Good detectors convert x-rays to electric signals with high efficiency before front-end electronics process these signals to record spatial patterns, measure energies, and record timing information required by experiments. Large synchrotron facilities like the APS have many specialized detector needs that are often not satisfied by commercially available detectors developed for medicine or industry. In addition, new and emerging detector technologies have the potential to enable new science or revolutionize existing techniques. Detector development is key to full utilization of a synchrotron source.

One field long in need of specialized detectors is the fast timing community at the APS. Beamlines using fast imaging techniques have desired an area detector capable of capturing multiple images at 6.5 MHz. Such a detector, which is not commercially available, would permit single-bunch imaging in the APS 24-bunch fill pattern.

Within the scope of the APS Upgrade, then, is development of an R&D Plan for the production of a fast area detector for the APS timing community. This section provides a brief overview of the need for fast area detectors, and discuss the study methods to be used to develop the required R&D Plan.

4.19.1 Need for Fast Area Detectors

While fast area detectors will enhance capabilities and facilitate new science around the APS ring, this section briefly discusses fast detector needs for pump-probe beamlines and the new Dynamic Compression Sector.

4.19.1.1 Pump-Probe Experiments

Detectors have long been an impediment for pump-probe experiments performed by the APS timing community. In a typical pump-probe experiment, a fast laser pulse is used to optically excite ("pump") the sample. X-ray pulses are then used to "probe" the short-lived excited state. The delay between the pump and probe pulses is varied to study the sample at differing time scales. Ideally, the time delay could be as short as consecutive x-ray pulses from the APS (153 nano-seconds). No currently available detectors are capable of taking a pair of images temporally separated by 153 ns. All available area detectors read out immediately after an exposure, requiring dead-time of several milli-seconds where the detector is not active. Even the upcoming Dectris Eiger will have a dead-time of 3 μs after an exposure and is not optimized for pump-probe experiments (private communication with Roberto Dinapoli)

Pump probe experiments are an important component of the APS Upgrade. This technique will be used at the Short Pulse X-ray facility and at the High Flux Pump Probe beamline at Sector 14. In addition, pump-probe experiments are currently conducted at Sectors 7, 11, and 14.

4.19.2 Scope and Goals of Study

WBS U1.02.02.01 will develop an R&D Plan to meet the high speed detection needs of the APS. The deliverable is a development plan, not an actual detector. The APS Detectors Group will study the beamline needs to develop specifications for needed high speed detectors, and then attempt to determine the best path to produce the required detectors on a timeframe consistent with the APS Upgrade. Development of this plan will require the following general steps:

Definition of Detector Specifications: Staff from the APS Detectors Group will meet with beamline scientists and APS users to ensure that needs are clearly understood. Key detector parameters, such as required frame rates or desired energy sensitivity will be identified. Discussions will be held with both the pump-probe and dynamic compression communities as well as other interested groups.

Investigation of Possible Development Options: The APS Detectors Group will then evaluate options for production of the required detectors. Promising detector development efforts already underway at other institutions will be evaluated and studied for possible adaptation to the APS needs. Possible collaborations with other institutions will also be explored. Each option will be evaluated according to standard project management concerns (cost, schedule, and risk). Posible collaborations will also be evaluated for social concerns and the projected APS contribution to the develoment effort.

Development of the Work Plan: Once a devleopment option is chosen, a formal resource-loaded schedule will be developed in accordance with the management practices of the APS Upgrade.

4.20 Nanofocusing Optics

4.20.1 Introduction

One of the key APS Upgrade performance parameters is to deliver x-ray optics capable of focusing hard x-rays with a photon energy of 25 keV to a spot size of 20 nm. Successful fabrication and implementation of such optics will allow the APS Upgrade to meet the specifications for the new *In Situ* Nanoprobe (ISN) beamline [section 4.6], and for the S3DD Monochromatic Nanodiffraction Probe [section 4.11]. More generally, the availability of efficient, high-resolution hard x-ray nanofocusing optics will be beneficial to hard x-ray microscopy beamlines at the Advanced Photon Source, as well as at other synchrotron facilities with hard x-ray microscopy capabilities, by filling a critical gap to high-throughput, high resolution analysis and imaging.

Currently, Fresnel zone plates (FZPs) [183, 184, 185, 186, 187, 188, 189, 190, 191, 192] appear to be the most straightforward choice, both because of their fundamental limit and because they are well-established diffractive optical elements for x-ray focusing and imaging. Using FZPs, 10 and 12 nm [184, 185] spatial resolution has been demonstrated in the soft x-ray regime and 25 nm [186] in the hard x-rays. The APS has the required expertise and access to the facilities and infrastructure to develop FZPs for high resolution in the high energy x-ray range. Developing efficient FZPs with a resolution limit of 20 nm and proper diameter will benefit not only hard x-ray scanning nanoprobes but also full field transmission microscopes. This section describes the strategy to develop advanced Fresnel zone plates that meet the APS Upgrade goal. The worldwide achievements in the relevant x-ray focusing by FZPs is described in Table 4-39.

Table 4-39: Achievements worldwide in the relevant x-ray focusing by FZPs.

Parameter	**FZP**
Typical Energy (keV)	0.2 – 25
Present Multi-keV Spot size	25 nm*
Fabrication Limit	~10 nm
Chromaticity	$f \sim 1/\lambda$
Demonstrated efficiency	6% @ 10 keV
Acceptance	~250 μm
*Achieved at APS and in collaboration with Paul Scherrer Institut (Switzerland)	

4.20.2 Fresnel Zone Plates

FZPs [183, 184, 185, 186, 187, 188, 189, 190, 191, 192] are well-established diffractive optical elements for x-ray focusing and imaging. They consist of circular diffraction gratings with radially increasing line density, and diffract incident x-rays into several diffraction orders with different focal lengths. Their diffraction-limited resolution is determined by the outermost zone width. High aspect ratio nanostructures are required to ensure both high spatial resolution and sufficient diffraction efficiency, especially for hard x-ray energies. For example, in theory, a FZP made of iridium focusing down to a spot size of 20 nm with 20% focusing efficiency at 25-keV photon energy would require an outermost zone width of 16 nm and a

thickness of about 2000 nm, thus requiring very challenging aspect ratios above 120:1. While conventional FZPs with an outermost zone width of 10 nm have been fabricated for the soft x-ray regime [184], the achieved aspect ratio was only 8:1. Recently, a zone-doubling fabrication technique [187] has been demonstrated as a very effective approach to reach higher aspect ratios. This method employs high-resolution electron beam lithography (EBL) to generate the FZP pattern in low atomic number inorganic resist, and atomic layer deposition (ALD) of high atomic number metal such as iridium or platinum. This technique, originally developed at the Paul Scherrer Institut (Switzerland), can now reliably deliver FZPs with an outermost zone width down to 20 nm and zone heights of 500-600 nm [188, 189], or aspect ratios of above 25:1 with diffraction efficiencies significantly higher than that of conventional methods (4-5% compared 0.5-1.5% at 10 keV) [193]. In addition to meeting APS Upgrade Project needs, all of the APS hard x-ray microscopy beamlines will greatly benefit from the development of zone plate optics with improved performance.

4.20.2.1 Challenges and Technical Approach

There are several approaches to achieve high-quality diffractive x-ray optics. As discussed above, zone-doubling fabrication has been shown to be a very effective way to fabricate zone plates with much higher aspect ratios than is possible with more conventional methods. The technique has recently been transferred from the Paul Scherrer Institute in Switzerland to the APS. The equipment and expert personnel in the APS Optics Group, at the Center for Nanoscale Materials (CNM), and in the Energy Systems Division (ESD), including tools for electron beam lithography for zone plate exposure and zone plate patterning using atomic layer deposition (ALD) of high atomic number metals. However, the achievable thickness is still below the aspect ratio of 100:1 required to achieve 20% efficiency at 25 keV.

One approach to achieve the challenging aspect ratios above 100:1 is by mechanically stacking multiple FZPs, as has been pioneered by the APS [191]. However, previous work required that the multiple identical zone plates be within an optical near-field distance (Figure 4-139(a)), which made stacking more than two zone plates very extremely challenging. More recently, Joan Vila Comamala of the Optics Group has proposed stacking zone plates with greater separation distances by utilizing FZPs of adapted diameters on the converging nanofocused beam (Figure 4-139(b)), and also allowing zone plates to be separated by distances corresponding to silicon wafer thicknesses so that more than two zone plates can be stacked. For example, Figure 4-140(a) compares the simulated focal spots for two stacked zone plates of 25-nm outermost zone width, at 6.2 keV, as a function of separation distance, ld, for the near-field. To stack two zone plates of equal diameter effectively, the distance required between them is below 10 μm. Crucially, the distance between the two zone plates can be relaxed significantly by tuning the diameter of the second FZP according to its downstream position [Vila-Comamala, et. al., in preparation]. For the far field simulation data shown in Figure 4-140(b), the two zone plates were designed for a separation of 25 μm, being the diameter of the FZPs of 45 μm and 44.8 μm.

A proposed solution for the methodic, precise, and reliable mechanical stacking of multiple FZPs is the utilization of microelectromechanical systems for both lateral and axial positioning. The use of microelectromechanical systems (MEMS) devices offer a path to stack multiple zone plates with the required accuracy and long-term stability, while achieving a compact and light optics system that could be deployed in x-ray microscopes much as zone plates are today. MEMS-based stacked zone plates have the potential to reach a 10-fold improvement in focusing efficiency at a photon energy of 25 keV, without

sacrificing spatial resolution. The development of these systems will be done with the combined expertise of scientists at Argonne's Center for Nanoscale Materials (CNM) and the APS.

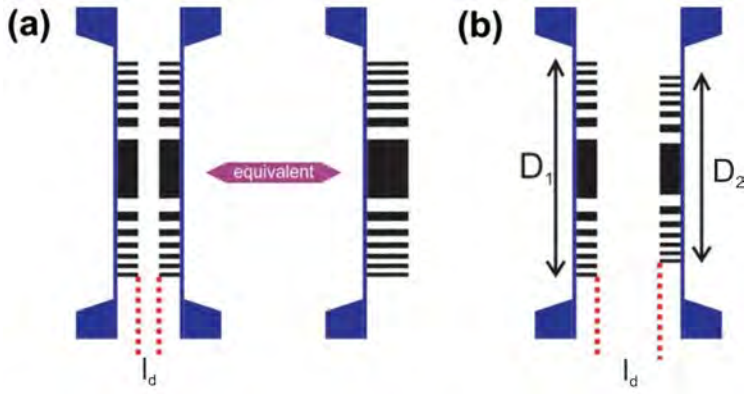

Figure 4-139: The concept of zone plate stacking. (a) The equivalency between two thin zone plates and one thick one, when the spacing is small. (b) At larger spacing a second zone plate with smaller diameter can be utilized.

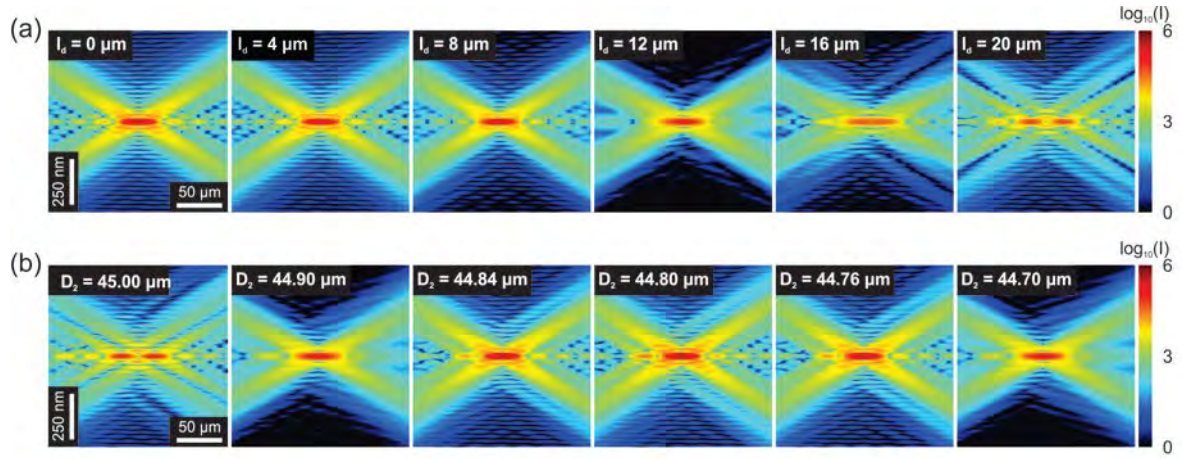

Figure 4-140: Simulated focal spots for two stacked Fresnel zone plates of 25 nm outermost zone width as a function of separation distance l_d. (a) When two zone plates of equal diameter are stacked the separation distance required between them is below 10 µm. (b) The distance between them can be relaxed by tuning the diameter of the second optic according to its downstream position; in this simulation, the two zone plates were designed for a separation distance of l_d of 25 µm, and a diameter, D_2, of 44.8 µm is required for the 2nd Fresnel zone plate.

The third very promising, but challenging approach for the fabrication of high aspect ratio FZPs is the overlay of multiple, independently exposed patterns on the same chip. This technique has been developed by the X-ray Microscopy Group at the Helmholtz-Zentrum Berlin [192] aiming for high resolution at the soft x-ray regime. The technique is challenging because a very accurate alignment is required for the consecutive electron beam lithography exposures [192]. However, the possibility of generating structures with tilted profiles by multiple overlays opens up the possibility of obtaining high diffraction efficiencies

for high diffraction order, and thus high spatial resolutions. Using the third diffraction order can reach a 20-nm focal spot using FZPs with a 48-nm outermost zone width. The electron beam lithography system (JEOL JBX-9000FS) used at the CNM has high field and overlay accuracy as needed for R&D activities in this area.

4.20.3 Infrastructure Needs

The proposed work plan requires continuous access to the nanofabrication facility and cleanrooms of the Center for Nanoscale Materials, engineering resources and regular access to beam time for the characterization of the fabricated focusing optics. The Energy Systems Division of Argonne will also be involved in the deposition processes of the fabrication of FZPs.

The stacking of FZPs using microelectromechanical systems (MEMS) will require the collaboration with the Nanofabrication Group at the CNM; the fabrication of the MEMS will be done by MEMSCAP Inc (www.memscap.com).

In summary, to meet the APS upgrade key performance parameter of 20 nm resolution at 25 keV, we will perform research and development aimed at frequency-doubled zone plates of Iridium, with an outermost zone width of 15 nm, and a goal of 500 nm thickness. We will develop stacking approaches to multiply the effective thickness of FZPs by a factor two or three. Furthermore, we will pursue MEMS-based approaches to stack several zone plates, to yield compact, high resolution zone plates with good efficiency at high energies.

4.21 Contingent Additional Scope

This section describes entire beamlines that are identified as contingent additional scope (CAS). The preliminary and final design for the CAS beamlines are in scope so that if any CAS items are brought into the project at a future date, execution of those activities will be able to commence in a timely manner. Other CAS activities that only relate to an individual beamline are discussed in the context of that beamline subsection.

4.21.1 High-Energy Tomography Beamline (HEXT)

This document details for the High Energy X-ray Tomography beamline (HEXT) Preliminary Design Report (PDR). The goal of the beamline is to be a world-class high energy micro-tomography facility using both phase and absorption contrast to provide 3D imaging of dynamic systems.

4.21.1.1 Introduction

There are three key parameters for this beamline: (1) energy range, (2) beam size, and (3) photon density ($ph/s/mm^2$) at the sample position. In x-ray projection-based tomography, the match between x-ray penetration length, set by the beam energy, and the beam size is critical, since for x-ray tomography the sample must be maintained in the image field of view for a full 0 to 180 degree rotation. The deep penetration of high-energy x-rays allows, for a given material, handling of larger samples. The HEXT

beamline will be designed to be able to handle samples up 100 mm in horizontal size in the experimental station.

4.21.1.2 Scientific Objectives

The scientific focus of the HEXT beamline is on the 3D dynamics of real-size samples. X-ray micro-tomography has proven to be a very successful technique to determine high-resolution 3D density distributions. It has been used extensively in new materials properties characterization, engineering material structural imaging, biology, highly mineralized biological tissues density distribution, and in various industrial applications. However, the highest x-ray energy at the currently available dedicated APS micro-tomography beamline (XSD 2-BM) is only 30 keV. At this energy, x-rays can penetrate less than 0.3-mm steel or 3-mm mid-crustal shear zone rock. To look at highly absorbing samples using these energies requires reducing the size of the sample, which is often not possible without compromising the experiment. High-energy tomography in the 30- to 100-keV range allows the study of new materials like high-temperature and multifunctional Ti lattice-load supporting structures, leadless ceramic chip carriers, advanced engine components, and metal-matrix composites in real size. White- and pink-beam illumination will also allow performing tomographic measurements in real operating conditions.

The goal for the HEXT beamline is to perform 3D imaging with 1-μm spatial resolution as fast as possible. Based on experience at the APS XSD 2-BM beamline, it is anticipated that it will be possible to perform full 2048^3 3D tomography in less than 1 second routinely.

4.21.1.3 Source Requirements

The key parameter of the HEXT beamline is to provide unfocused white and monochromatic x-ray beam 50 mm (H) × 5 mm (V) at the sample location in the first experiment station located immediately downstream of the optics station and 100 (H) mm × 10 (V) mm at the sample location in the experimental station. The beamline also requires as high a photon density as possible on the sample. A regular APS bending magnet source, with an inherently large horizontal spread, has proven sufficient to provide the flux required ($\sim 8 \times 10^{10}$ ph/s/mm^2) to perform tomography of dynamic systems up to 30 keV. Figure 4-141 shows the source photon density in ph/s/mm^2 at 30- and 60-m sample position for a regular APS 0.6-T BM source compared with a 1.2-T super bend (SB) source. To cover the range above 30 keV with sufficient flux to allow dynamic tomography measurements, a 1.2-T SB bending magnet source is required. A 1.2-T SB (double the present field) is possible without changing the current vacuum chamber height.

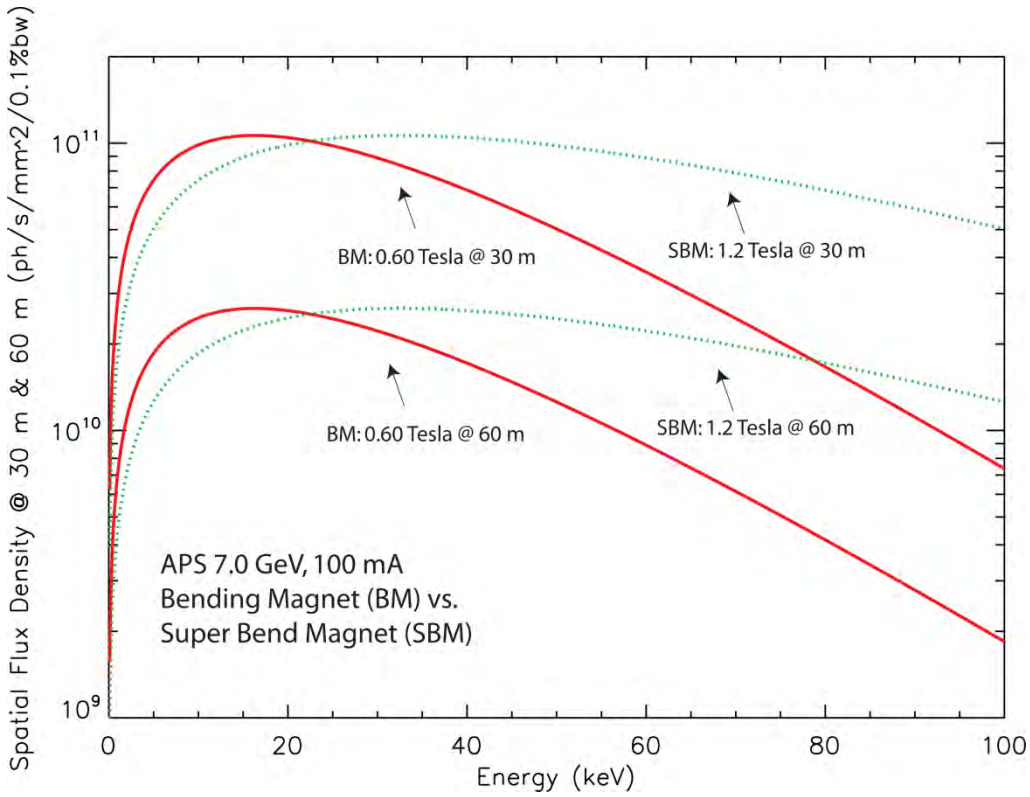

Figure 4-141: Photon density (ph/s/mm^2) at 30- and 60-m sample position for a regular APS 0.6-T BM source compared with a 1.2-T SB.

4.21.1.3.1 Spectral Requirements

In many cases, x-ray tomography does not require a high level of beam monochromaticity. Fast tomography and qualitative edge-enhancement can be achieved using broad x-ray energy radiation obtained by filtering the low-energy components, or by using a large bandwidth DMM ($\Delta E/E = 10^{-2}$), or even with white beam.

There are two basic optical schemes for the HEXT beamline to provide high-speed and high-resolution tomography: broad high-energy (white) and monochromatic beam modes. These modes will be accessible in both experiment stations.

4.21.1.3.2 X-ray Optical Layout

The HEXT bending magnet beamline receives 1.7 mrad (from the 6 mrad fan). It uses a vertical-bounce, double-crystal monochromator (DCM) or a vertical-bounce, double-multilayer monochromator (DMM). The HEXT beamline schematic optical layout is shown in Figure 4-142.

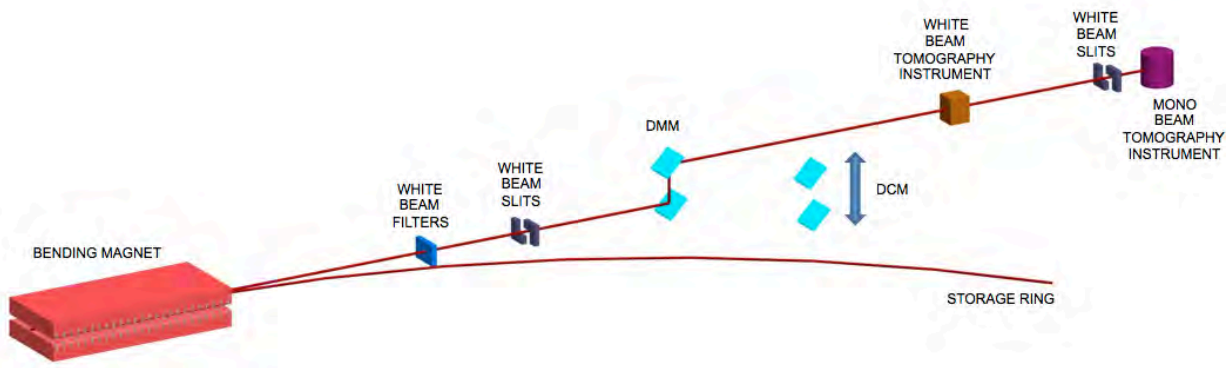

Figure 4-142: HEXT beamline schematic optical layout.

4.21.1.3.3 Monochromators

There are two vertical bounce monochromators on the HEXT beamline: double-multilayer monochromator and double-crystal monochromator.

Double-Multilayer Monochromator (DMM)

The double-multilayer monochromator system will be similar to that used at 2-BM but with a multilayer coating optimized to work in the 20- to 60-keV range at 10^{-2} bandwidth ($\Delta E/E$). Such a multilayer system is commercially available and used at ESRF's ID19 and SLS's TOMCAT beamlines. The specifications of the DMM are listed in Table 4-40.

Table 4-40: Specifications of the DMM.

Items	Specifications, TBD, or NA
Sector # and beamline	HEXT at sector TBD
Mono designation/name	Double-crystal monochromator
Incident Beam	
Source and spectrum	BM white
Limiting apertures upstream H x V (mm)	37 × 3.7 at 22.2 m
Beam power at the mono (W)	
Beam size at the mono, H x V (mm)	42.5 × 4.25
Monochromator Crystal	
Number of crystal sets	1
Substrate material and orientation	
Operating energy range (keV)	20-60
Diffraction direction: H or V	
Diffraction method: Laue or Bragg	
Mono dimension, L × W × T (mm)	
Cut angle if asymmetric crystal	
Surface specifications, e.g., for coherence/imaging	
Special features, none, thin web, mounting groove, etc.	
Cooling	
Internal or contact-cooled?	Contact cooled
Coolant preference, water, nitrogen, others	Water
Maximum desired size of the diffracted beam, H × V (mm)	
Beam stability, max allowed beam motion for >1 Hz (μm)	
Beam stability, max allowed beam motion for <1 Hz (μm)	
Miscellaneous	
Mono environment: air, He, vacuum, UHV, etc.	UHV

Double-Crystal Monochromator (DCM)

The double-crystal monochromator will be similar to that used at 1-ID with appropriate modifications for the wider bending-magnet beam and with water cooling. It will provide 30- to 100-keV energy tenability at 10^{-4} bandwidth (ΔE/E). The specifications of the DCM are listed in Table 4-41.

Table 4-41: Specifications of the DCM.

Items	Specifications, TBD, or NA
Sector # and beamline	HEXT at sector TBD
Mono designation/name	Double-crystal monochromator
Incident Beam	
Source and spectrum	BM white
Limiting apertures upstream H × V (mm)	37 × 3.7 at 22.2 m
Beam power at the mono (W)	
Beam size at the mono, H × V (mm)	45 × 4.5
Monochromator Crystal	
Number of crystal sets	1
Substrate material and orientation	
Operating energy range (keV)	30-100
Diffraction direction: H or V	
Diffraction method: Laue or Bragg	
Mono dimension, L × W × T (mm)	
Cut angle if asymmetric crystal	
Surface specifications, e.g., for coherence/imaging	
Special features, none, thin web, mounting groove, etc.	
Cooling	
Internal or contact-cooled?	Contact-cooled
Coolant preference, water, nitrogen, others	Water
Maximum desired size of the diffracted beam, H × V (mm)	
Beam stability, max allowed beam motion for >1 Hz (μm)	
Beam stability, max allowed beam motion for <1 Hz (μm)	
Miscellaneous	
Mono environment: air, He, vacuum, UHV, etc.	UHV

4.21.1.4 Beamline Physical Layout

The beamline physical layout is shown in Figure 4-143.

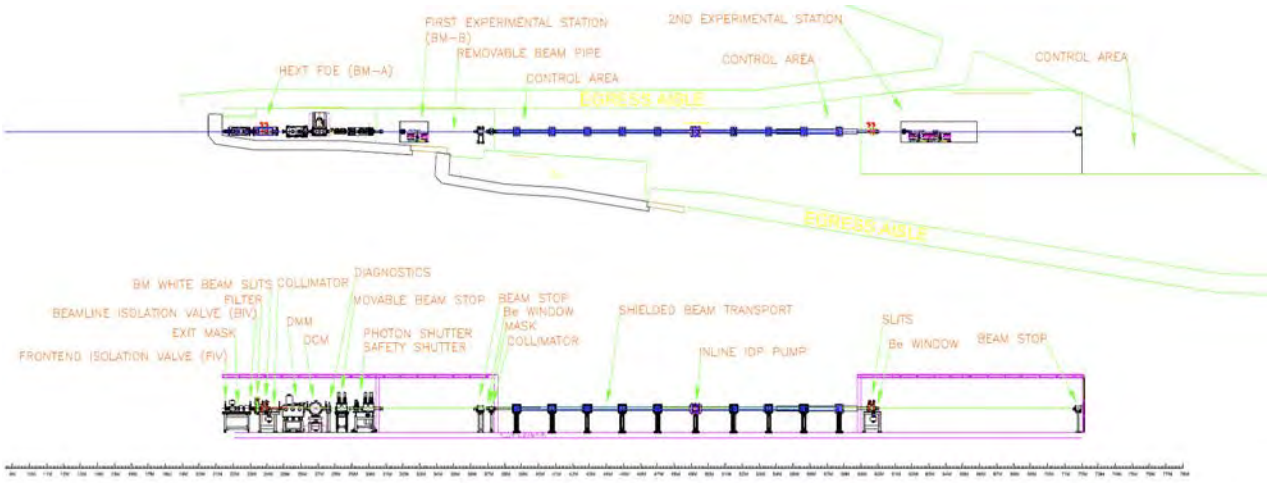

Figure 4-143: Beamline physical layout.

4.21.1.4.1 Front End, if applicable

The mask and shutters in the current bending magnet front end need be modified to accommodate higher energy from a super bend bending magnet.

4.21.1.4.2 Overall Beamline

General Description

The HEXT beamline will be constructed in phases as outlined in Table 4-42. The construction phase in which each component will be installed is indicated in the component descriptions. Components will be replaced with spool pieces during phases that precede their installation.

Table 4-42: HEXT beamline construction phases.

Phase 1	White beam to BM-A
Phase 2	White beam to BM-B
Phase 3	White beam to BM-C
Phase 4	Mono beam to BM-B and BM-C

Radiation Safety Aspects

The beamline primarily employs APS standard radiation safety system (RSS) and BLEPS components. Modifications to the standard components will be made to fit the specific need of the HEXT beamline. The associated thermal calculations will be performed. The synchrotron and bremsstrahlung ray tracing and several aspects of radiation safety of the beamline are covered in detail below.

Optics and Missteering Ray Trace: Figure 4-144.1, Figure 4-144.2, and Figure 4-144.3 are ray-trace diagrams for the synchrotron radiation of both normal beam and synchrotron radiation with missteering due to movement of the electron beam and components beyond the normal range.

Primary Bremsstrahlung Containment: Figure 4-144.4, Figure 4-144.5, and Figure 4-144.6 are ray-trace diagrams for the bremsstrahlung. This shielding is based upon 300 mm of Pb or 180 mm of W to stop the primary gas bremsstrahlung. The shielding is designed to comply with APS Policy 1-01304: Policy on Design, Installation, and Maintenance of Radiation Safety Systems.

Personnel Safety System Requirements: The components of the RSS are outlined in Figure 4-144. The operation modes are shown in Figure 4-145 below. The truth table for the personnel safety system of the HEXT beamline is outlined in Table 4-43. This table identifies the conditions that must be satisfied in order to open each shutter and permit access to each enclosure. This truth table does not identify the individual PSS components for each enclosure. These include the door switches, search buttons, shielded beam pipes, etc.

Equipment Protection System: An EPS will be designed and built for the HEXT beamline that is designed to provide standalone fail-safe equipment protection. Vacuum monitoring, vacuum integrity protection, and valve control will be performed through the EPS. Water cooling system monitoring, protection and control will also be connected through the EPS.

Ozone Mitigation: The following actions will be taken to mitigate the ozone problem:

- Keep the white beam-in-air paths to a minimum
- Make the effective evacuation volumes as small as possible
- Add a filter to absorb the low-energy photons
- Use local shielding to minimize ozone production in scattered beams
- Install an ozone monitor that produces an audible tone when the ozone concentration is above an APS-specified level
- Install a local ventilation system that vents into the experiment hall floor with filtering to reduce the ozone emission to less than 0.0017g/min
- Interlock the ozone monitor into PSS.

Vacuum System

The vacuum system includes three sections separated by Be windows: the FOE, BM-B, and beam transport sections. FOE components will be built to ultra-high vacuum specifications with no vacuum-to-coolant joints. The FOE will expect vacuum in the 10^{-9}-Torr range. BM-B is removable beam pipe. The beam transport section connects the BM-B and BM-C enclosures. In the BM-B and beam transport section, components will be built to high-vacuum specifications with no vacuum-to-coolant joints. The BM-B and beam transport section will expect vacuum in the 10^{-7}-Torr range. The APS double Be window

will be used for commissioning and will be replaced with a differential pump after the beamline is stabilized. Ion pumps will be used to pump all the beamline sections.

The beamline vacuum flow diagram is shown in Figure 4-146.

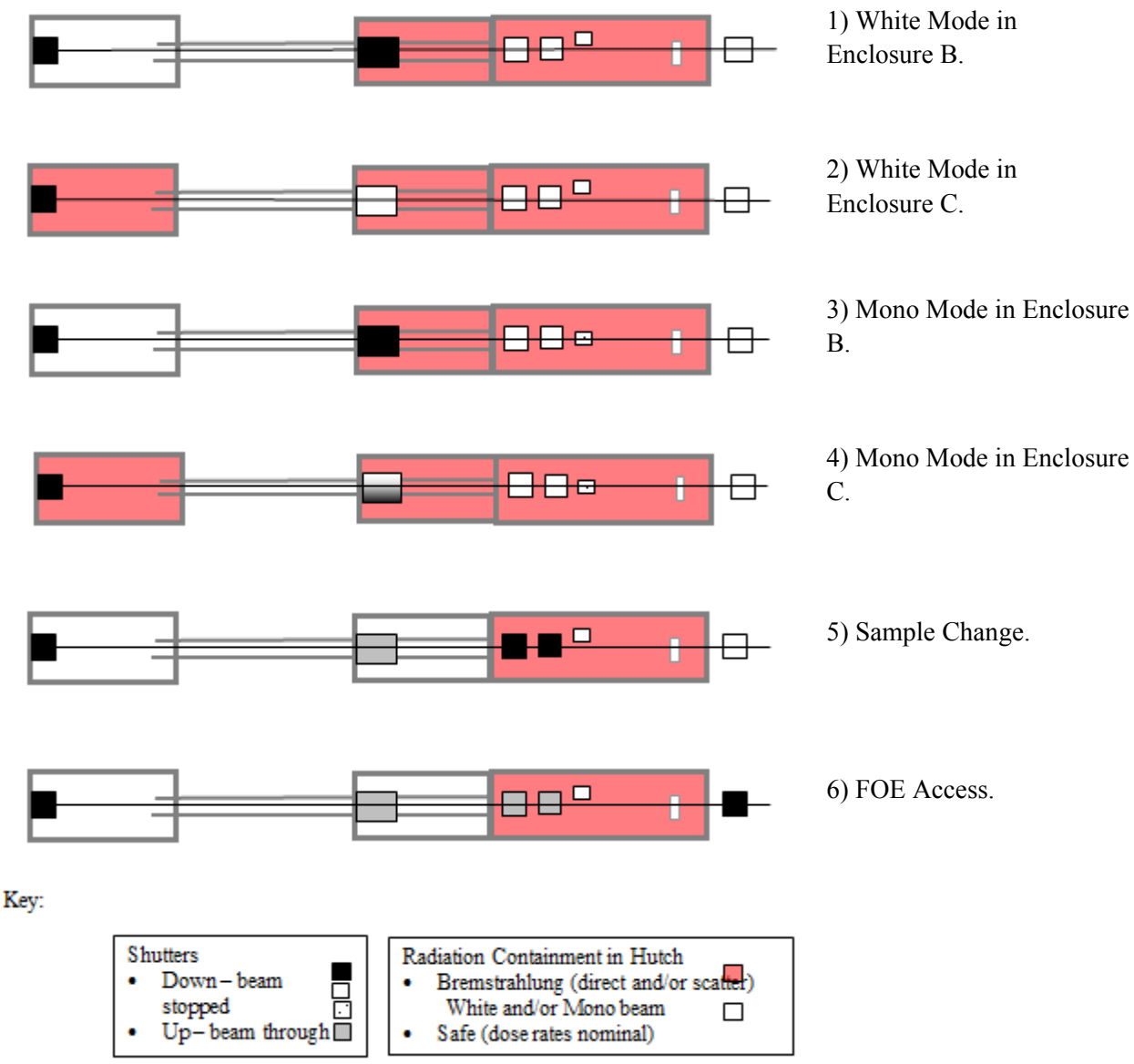

Figure 4-144: Operation modes of HEXT beamline.

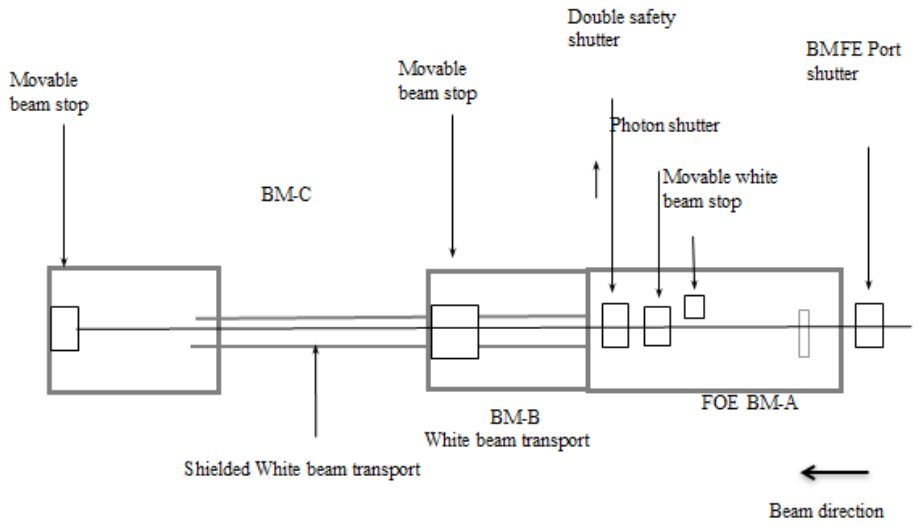

Figure 4-145: Operation modes.

Table 4-43: Truth table for the personnel safety system of the HEXT beamline.

Comp. status→ / **Beamline action ↓**	**FE shutter closed**	**FOE secure**	**Photon shutter and safety shutter closed**	**BM-B secure**	**Beam stop closed**	**BM-C secure**
Open FOE shutter*	O	T	T	X	X	X
	O	T	X	T	T	X
	O	T	X	T	X	T
Open photon shutter and safety shutter	X	X	O	T	X	T
	X	X	O	T	T	X
Open movable beam stop*	X	X	X	X	O	T
Access to FOE	T	O	X	X	X	X
Access to BM-B	X	X	T	O	X	X
Access to BM-C*	X	X	T	X	X	O
	X	X	X	X	T	O

T	True
X	Status does not matter
O	Component whose status will change with action
*	The action can be taken when either of the branch situations is satisfied

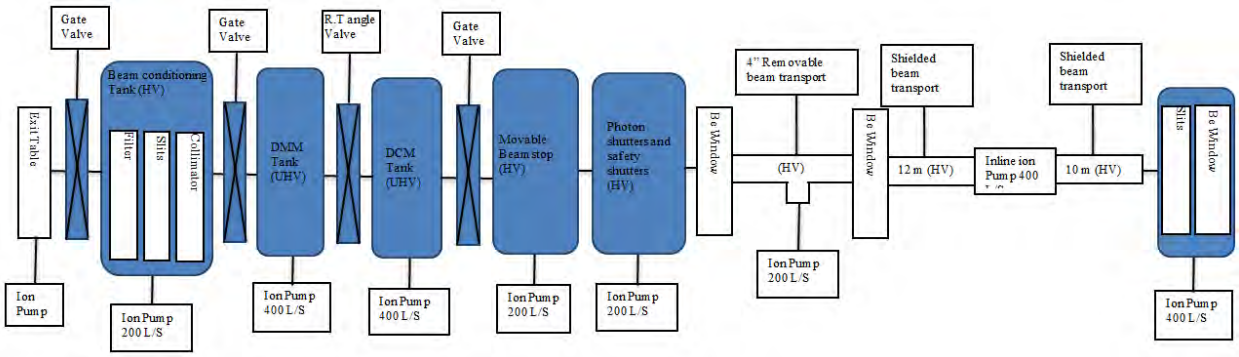

Figure 4-146: Beamline vacuum flow diagram.

Data Acquisition and Motion Control

Control of all hardware will be provided through EPICS using components as standardized by the AES BCDA, AES Controls, AES SSG, and XSD Detector groups.

4.21.1.4.3 First Optics Enclosure and Infrastructure, Major Components

The FOE (enclosure A) is approximately 2.0 m wide × 9.0 m long (15.4 m^2)) and of nominal 3.4-m height. It shares a downstream wall with enclosure B, and it is attached to the ratchet wall. The FOE has one entry consisting of a manual door paired with a pneumatically controlled door. It also includes clean and utility power, compressed air, de-ionized cooling water, and a one-ton trolley-mounted chain hoist installation.

APS Area for Front-end Be Window

This location, as described in Table 4-44, is reserved for the front-end Be window. The window will be removed after commission. A differential pump assembly will be installed after this window is removed.

Table 4-44: APS area for front-end Be window.

Distance from source (m)	21.35 – 22.2
Construction/commissioning phase	1

M3-24M Mask

This is a water-cooled mask modified from M3-24 (4102020101-240000) with aperture of 37.1 (H) mm × 3.7 (V) mm. The location and installation phase are specified in Table 4-45.

Table 4-45: M3-24M mask.

Distance from source (m)	22.1 – 22.3
Construction/commissioning phase	1

Differential Pump Assembly

This is a commercially available differential pump assembly. The location and installation phase are specified in Table 4-46.

Table 4-46: Differential pump assembly.

Distance from source (m)	22.3 – 23
Construction/commissioning phase	1

Valve

This is the 8” Viton gate valve used to isolate the beamline from the exit table. The location and installation phase are specified in Table 4-47.

Table 4-47: Valve.

Distance from source (m)	23 – 23.1
Construction/commissioning phase	1

Bellows

This is a bellows with an 8” flange. The location and installation phase are specified in Table 4-48.

Table 4-48: Bellows.

Distance from source (m)	23.1 – 23.3
Construction/commissioning phase	1

Filter

This water-cooled filter is used to place selectable foils to provide beam power from 10 keV to 100 keV in 10-keV increments. The location and installation phase are specified in Table 4-49.

Table 4-49: Filter.

Distance from source (m)	23.3 – 23.6
Construction/commissioning phase	1

White Beam Slits

This component is the generic adjustable water-cooled horizontal and vertical slits.

- Horizontal width range: two blades with –1 to 40 mm and 1 to –40 mm.
- Vertical width range: two blades with –1 to 4 mm and 1 to –4 mm.
- Power load: 300 W

The location and installation phase are specified in Table 4-50.

Table 4-50: White beam slits.

Distance from source (m)	23.6 – 24.2
Construction/commissioning phase	1

K4-21 Collimator

This is a lead collimator with an 8” flange. The location and installation phase are specified in Table 4-51.

Table 4-51: K4-21 collimator.

Distance from source (m)	24.3 – 24.7
Construction/commissioning phase	1

Valve

This is the 8” Viton gate valve used to isolate the upstream end of the double-multilayer monochromator tank. The location and installation phase are specified in Table 4-52.

Table 4-52: Valve.

Distance from source (m)	24.7 – 24.8
Construction/commissioning phase	4

Double-multilayer Monochromator

The double-multilayer monochromator is specified in Table 4-40, the location and installation phase are specified in Table 4-53.

Table 4-53: Double-multilayer monochromators.

Distance from source (m)	24.8 – 26.4
Construction/commissioning phase	4

Valve

This is the 8” Viton gate valve used to isolate the downstream end of the DMM and the upstream end of the double-crystal monochromator tank. The location and installation phase are specified in Table 4-54.

Table 4-54: Valve.

Distance from source (m)	26.4 – 26.5
Construction/commissioning phase	4

Double-crystal Monochromator

The double-crystal monochromator is specified in Table 4-41, the location and installation phase are specified in Table 4-55.

Table 4-55: Double-crystal monochromators.

Distance from source (m)	26.5 – 27.3
Construction/commissioning phase	4

Valve

This is the 8” Viton gate valve used to isolate the downstream end of the DCM tank. The location and installation phase are specified in Table 4-56.

Table 4-56: Valve.

Distance from source (m)	26.5 – 26.6
Construction/commissioning phase	4

Beam Diagnostics

This standard fluorescent screen, similar to the one installed at 2-BM, will be installed after the monochromators and used for alignment and diagnostics of the optics. The location and installation phase are specified in Table 4-57.

Table 4-57: Beam diagnostics.

Distance from source (m)	27.5
Construction/commissioning phase	1

Movable Beam Stop (Mode Switcher)

This is a dual-design movable white beam stop and W absorber. It is used to completely stop white beam and bremsstrahlung radiation at mono mode. The location and installation phase are specified in Table 4-58.

Table 4-58: Movable beam stop (mode switcher).

Distance from source (m)	28 – 28.8
Construction/commissioning phase	1

Shutter

This is a dual-design shutter that completely stops both synchrotron radiation and bremsstrahlung radiation. This shutter modifies the APS dual safety shutter. It attaches a water-cooled Glidcop plate to both tungsten absorbers. It is used to completely stop the synchrotron radiation and bremsstrahlung radiation when users need to access the BM-B and BM-C enclosures. The location and installation phase are specified in Table 4-59.

Table 4-59: Shutter.

Distance from source (m)	29 – 29.8
Construction/commissioning phase	1

4.21.1.4.4 Enclosure B and Major Components

The B enclosure is an approximately 3.0 m wide × 7.0 m long (16.8 m^2) white-beam experiment enclosure (WBEE) of nominal height that shares an upstream wall with the FOE and is attached to the ratchet wall. It has one entry consisting of a manual door paired with a pneumatically controlled door. It also includes clean and utility power, compressed air, de-ionized cooling water, and a one-ton trolley-mounted chain hoist installation.

Be Window

The standard Be window design will be a 0.25-mm Be sheet brazed to a water-cooled Cu block. The window material will be Brush Wellman SR-200-E grade. The material properties for this grade are tested and guaranteed for each beryllium sheet by Brush Wellman. The purity of the beryllium will be preferentially selected to 99.3% Be assay, with the iron and copper content each less than 300 ppm. Unless otherwise specified, all Be windows are 0.25 mm thick. The location and installation phase are specified in Table 4-60.

Table 4-60: Be window.

Distance from source (m)	30.7
Construction/commissioning phase	1

Instruments (Physical Description of Major Experimental Instruments)

The HEXT beamline will include two experiment stations: BM-B and BM-C. Both experiment stations will be white beam compatible.

Station BM-B will house the first experiment table for experiments that require the highest temporal resolution and will be able to handle samples up to 50 mm in size.

The white-beam-compatible BM-B station, approximately 7 m in length, will be located immediately downstream of the optics station BM-A. The BM-B station will house an ultrafast tomography setup and an experiment table. One manual movable beam stop will be installed close to the end of the BM-B station.

The high-energy micro-tomography beamline BM-B station will include one experiment setup designed to provide 1-µm resolution tomography data. The setup will be optimized for ultrafast and fast white-beam tomography (UF-WT and F-WT).

The system will use a detector to assure all measurements are x-ray flux limited and not detector limited. All detectors will be coupled-scintillator-screen optimized for higher efficiency at high energies, and used in 90° geometry to protect the detector from the x-rays. The UF-WT system in the BM-B station will handle samples up to 50 mm horizontal and 10 kg in weight, and will allow testing real engineering components under real operating conditions while their 3D internal morphology is monitored. The UF-WT system will use an ultrafast camera, like the Photron SA2 or the PCO.dmax, and will routinely perform tomography below 1 second.

Movable Beam Stop

This is an APS design with a water-cooled Gildcop plate and 300-mm-thick lead block to completely stop both synchrotron radiation and bremsstrahlung radiation. The purpose of this stop is to allow access to the BM-C enclosure. The location and installation phase are specified in Table 4-61.

Table 4-61: Movable beam stop.

Distance from source (m)	36.2
Construction/commissioning phase	2

Be Window

This Be window starts the beam transport from enclosure B to enclosure C. When an experiment is conducted in BM-C, a beam transport will be connect between this Be window and the Be window (discussed in section 0). The location and installation phase are specified in Table 4-62.

Table 4-62: Be window.

Distance from source (m)	36.9
Construction/commissioning phase	3

Mask

This is a water-cooled Glidcop mask with 8” flange and an aperture size of 62 (H) mm × 6.2 (V) mm. The location and installation phase are specified in Table 4-63.

Table 4-63: Mask.

Distance from source (m)	37
Construction/commissioning phase	3

Collimator

This is a tungsten collimator with a tankless design. The aperture size is 63 (H) mm × 7.2 (V) mm, and the location and installation phase are specified in Table 4-64.

Table 4-64: Collimator.

Distance from source (m)	37.1
Construction/commissioning phase	3

Shielded Beam Transport

This is a shielded beam transport with sections of 4” pipe, 6” pipe, 8” pipe, and 10” pipe. The location and installation phase are specified in Table 4-65.

Table 4-65: Shielded beam transport.

Distance from source (m)	37.5 – 59
Construction/commissioning phase	3

4.21.1.4.5 Enclosure C and Major Components

The C enclosure is a WBEE approximately 5.0 m (W) × 12.0 m (L) (59.1 m^2) of nominal 3.4-m height that shares an upstream wall with the C-MH1 SOE enclosure. It has one entry consisting of a manual door paired with a pneumatically controlled door. It also includes clean and utility power, compressed air, de-ionized cooling water, and a one-ton trolley-mounted chain hoist installation.

White Beam Slits

This component is the generic, adjustable, water-cooled horizontal and vertical slits.

- Horizontal width range: two blades with –1 to 50 mm and 1 to –50.
- Vertical width range: two blades with –1 to 5 mm and 1 to –5 mm.
- Power load: 300W

The location and installation phase are specified in Table 4-66.

Table 4-66: White beam slits.

Distance from source (m)	59.3 – 60
Construction/commissioning phase	3

Be Window

This Be window ends the beam transport to enclosure C. The location and installation phase are specified in Table 4-67.

Table 4-67: Be window.

Distance from source (m)	60
Construction/commissioning phase	3

Instruments (Physical description of major experimental instruments)

Station BM-C will be for experiments that require lower temporal resolution and will be able to handle samples up to 100 mm.

The white-beam-compatible BM-C station will be the HEXT experimental station, located as far downstream as possible on the experiment hall floor and 5 m × 13 m in size. This station will house a tomography setup optimized for high-speed high-sensitivity tomography, a second setup optimized for high-resolution high-throughput tomography, and a white-beam stop.

The high-energy micro-tomography beamline BM-B station will include three experiment setups. All three setups are designed to provide 1-μm resolution tomography data. One setup will be optimized for ultrafast and fast white-beam tomography (UF-WT and F-WT). The BM-C station will also have a fast monochromatic tomography (F-MT) and a phase-contrast-enhanced tomography (PT) system. The three systems will use different detectors to assure all measurements are x-ray flux limited and not detector limited. All detectors will be coupled-scintillator-screen optimized for higher efficiency at high energies, and used in 90° geometry to protect the detector from the x-rays.

The BM-C experiment instrumentation will focus on high-resolution and high-sensitivity measurements but will also be suitable for large-size specimens and slow dynamics. In this station, an F-WT system will be able to handle the largest samples, up to 100 mm horizontal and 20 kg in weight, to test real engineering components under real operating conditions in slow dynamics. This system will monitor the 3D internal morphology with 3D volume rates ranging from a few seconds to 1 min. The PT system, in line with the F-WT system, will provide high-sensitivity imaging.

The F-MT system will be optimized for high resolution, will operate with monochromatic beam ranging from 20 to 60 keV, and will handle samples up to 1 cm in diameter. This system will use a more sensitive/slower camera, like the PCO Edge sCMOS high-performance digital camera, and will be able to collect a full tomography data set in ≈ 1 minute.

The current detector technology allows for the F-MT to operate in a sustained mode, i.e., with a 3D volume rate of one minute. For this system, full automation for sample loading, unloading, and alignment will be added, achieving a maximum throughput of over 1,000 samples per day.

4.21.2 Short Pulse Soft X-ray Spectroscopy Beamline

The short-pulse soft x-ray spectroscopy (SPSXS) beamline is one of three beamlines to be developed in the short-pulse x-ray (SPX) facility fed by the crab cavities. Soft x-rays are generated from the chirped electron bunches passing through a bending magnet source (6-BM), resulting in an expanded vertical source size. The first optical element accepts 0.84-mrad horizontal and the full vertical fan and focuses the radiation to a vertical slit to allow selection of the pulse duration and to a horizontal slit that determines the resolution. An additional vertical slit or chopper assembly will select off-axis radiation for polarization control. At the SPX baseline radio-frequency (rf) voltage of 2 MV, a vertical slit accepting 1% of the incident radiation will produce a pulse duration of 1 ps. Photon energy selection will be accomplished with a horizontal bounce plane grating monochromator. The SPSXS beamline instrumentation will be geared toward magnetic spectroscopy in transmission, fluorescence, and reflectivity in the energy range of 200-2000 eV. An interchangeable exit slit/charge-coupled device (CCD) array assembly will provide functionality for both transmission spectroscopy in a dispersive geometry and monochromatic spectroscopy in a high-field downstream experiment chamber. The conceptual design [194] called for vertical timing and energy dispersion, resulting in a coupling between the timing and energy resolutions. In the preliminary design, horizontal energy dispersion with a horizontal entrance slit at the timing slit position is chosen to decouple these resolutions.

4.21.2.1 Research & Development

The SPSXS beamline will generate short pulses using the chirped bunches from the SPX rf cavities. Therefore, the achievable pulse duration will depend on research and development (R&D) for the accelerator modification for the SPX.

4.21.2.2 Scientific Objective

The achievable time resolution (1-100 ps) and photon energy range (200-2000 eV) of this beamline are ideally matched to the dynamics of conduction and valence electrons in solids, molecules, and atomic systems. With circular polarization control via the off-orbit beam components, the dynamics of electron spins in these systems will also be accessible. Therefore, the major science drivers for the SPSXS beamline are the study of spin and charge dynamics in novel magnetic, optical, and electronic materials. These will include magnetically-doped semiconductors, metallic systems, and strongly correlated electron systems.

One of the most promising branches of magnetism research is the integration of ferromagnetic materials with semiconductors to create the ability to generate spin-polarized carrier populations. Accomplishing this goal promises to enable new functionalities in electronic devices that use the electron spin as well as charge. This research relies heavily on the growth and characterization of metal-semiconductor heterostructures. Over the past three years, several groups have made giant strides in the electrical generation and detection of spin-polarized carriers in semiconductors using ferromagnetic contacts.

Prototypical spin transport devices based on III-V semiconductors [195, 196, 197, 198, 199] and silicon [200, 201, 202] have been demonstrated. For the most part, the basic physics of these systems remains unexplored. The development of new x-ray probes could have a major impact in two areas of this research: characterization of interfaces and spatially and time-resolved studies of spin dynamics in the system.

The microscopic origins of spin damping in ferromagnetic metals are not well understood and arebeing investigated theoretically [203, 204] no ferromagnetic metal currently exists with near-zero damping *G,* where *G* is the Gilbert damping parameter. Identification of such a low-damping metal would be an enormous advantage for many high-frequency nanoscale magnetic devices, particularly spin-torque devices (such as magnetoresistive random-access memory) because critical currents are directly proportional to *G*. [205] The much larger values of damping in metals, compared with insulators, have motivated explanations in terms of the mobile electrons: [206] electrons annihilate the long-wavelength magnons that make up precession, closing down the cone angle towards zero in spin-flip scattering. This model, known as *spin-orbit damping*, has been proposed in analogy to the slow-relaxing impurity model of insulators described in the previous paragraph. With the APS Upgrade Project, the enhanced temporal resolution (1-10 ps) will likely bring the interesting temporal scale for precession (<1 ps) into reach.

Spectacular new functional properties such as metal-insulator transitions, high-temperature superconductivity, and colossal magnetoresistance found in highly correlated oxides are caused by a strong interplay between electronic (charge, orbital, spin) and lattice degrees of freedom. This leads to various, nearly degenerate ground states and an abundance of phase transitions as a function of temperature, doping, and external fields. One of the most intriguing aspects is the formation of phases with charge/orbital order and their relationship to the materials' functionality such as electrical conductivity.

Recently, time-resolved soft x-ray resonant scattering (SXRS) experiments on the prototypical correlated electron material magnetite (Fe_3O_4) using soft x-ray pulses from the free-electron laser FLASH in Hamburg observed the ultrafast melting of the charge-orbital order, leading to the formation of a transient phase, which has not been observed in equilibrium [207]. Similar transient states have also been reported for manganites [208] and cuprates [209]. Their picosesond lifetime makes them ideal candidates to be studied in detail at the SPSXS Beamline.

Among the most important and compelling questions in magnetization dynamics is the influence of lateral structure and finite size and domain dynamics on the ground states and fundamental excitations in artificially structured nanoscale magnets. In particular, spin excitations and domain wall motion in one-dimensional (1-D) nanowires and zero-dimensional (0-D) nanodots are of interest for many magnetoelectronic devices. In nonlinear excitation regimes such as are obtained with high-field pulses or high-power laser excitation, ultrafast transient dynamics in the sub-100-ps regimes are very important to the operation of the device.

The SPSXS beamline will include an option for an instrument providing transmission x-ray microscopy (TXM) and scanning transmission x-ray microscopy (STXM) capabilities due to the higher spatial resolution limit and better collection efficiency in comparison with photoemission electron microscopy (PEEM). An approach similar to the TXM beamline at the Advanced Light Source (ALS) (TMX beamline 6.1.2 at ALS) is preferable, as this is also a bending magnet beamline. The microscope will be installed downstream of the first experimental station and will use a relatively wide-bandwidth pink

beam. Bandwidth selection will be accomplished via a zone plate monochromator with ~1% bandwidth, sufficient for resolution of the transition metal *L*2 and *L*3 edges as needed for magnetic contrast, but which will also provide high flux.

4.21.2.3 Source Requirements

Soft x-ray experiments at the SPX facility will be conducted utilizing a bending magnet source. This will limit the flux available from the beamline; but utilizing soft x-ray undulators with the chirped electron beam presents significant technical problems. Most notably, the energy dependence of the pulse duration limits the achievable performance to 8-10 ps with 2-MV acceleration [210]. With the bending magnet source, the vertically expanded source size allows a 1-ps x-ray pulse duration to be achieved using a vertical slit passing 1% of the full beam [211]. Figure 4-147 shows flux tuning curves for the APS bending magnets in the 100-2000-eV range. Across the soft x-ray range of 100-1000 eV, the flux from an APS bending magnet is approximately equal to the flux from bending magnet sources at the ALS.

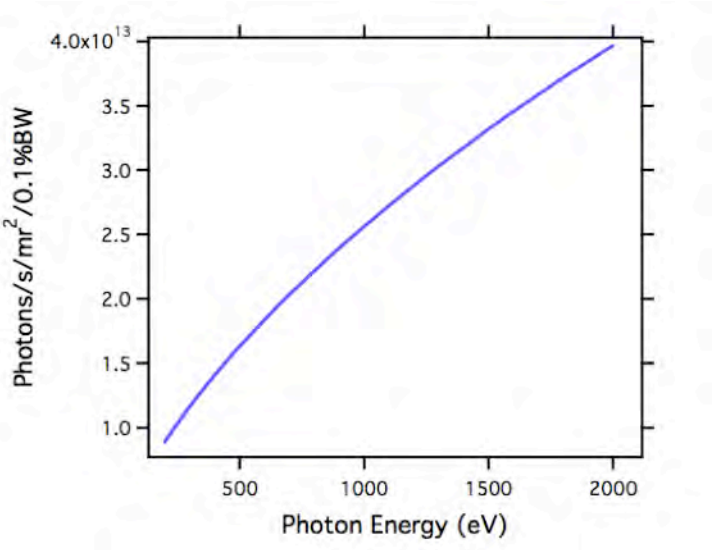

Figure 4-147: Bending magnet flux from a standard (0.6 T) APS bend.

4.21.2.3.1 Other Source Requirements

The beamline will utilize the off-axis (above and below the orbit plane) components of the bending magnet radiation to obtain left- and right-circularly polarized x-rays. This will be accomplished with a chopper placed downstream of the first focusing mirror.

An alternative scenario for improving the flux and performance of the beamline is to reduce the effective bending magnet field strength [212]. Figure 4-148 shows the vertically integrated flux for several different field strengths. A reduction of the bending magnet field from the standard 0.6 T to 0.2 T would result in a flux increase of ~50% in the photon energy range of 500-1200 eV. In addition, the height of the bending magnet radiation fan at 250 eV decreases by approximately 1/3, making it possible to use smaller apertures and smaller mirrors, and thus improving the quality of the beamline optics. While it is possible to make a separate bend magnet for the source, a lower-cost approach would be machining and shimming

the existing APS bend magnet poles to profile the field along the orbit while preserving the total bend angle and entrance/exit orbit for the entire magnet.

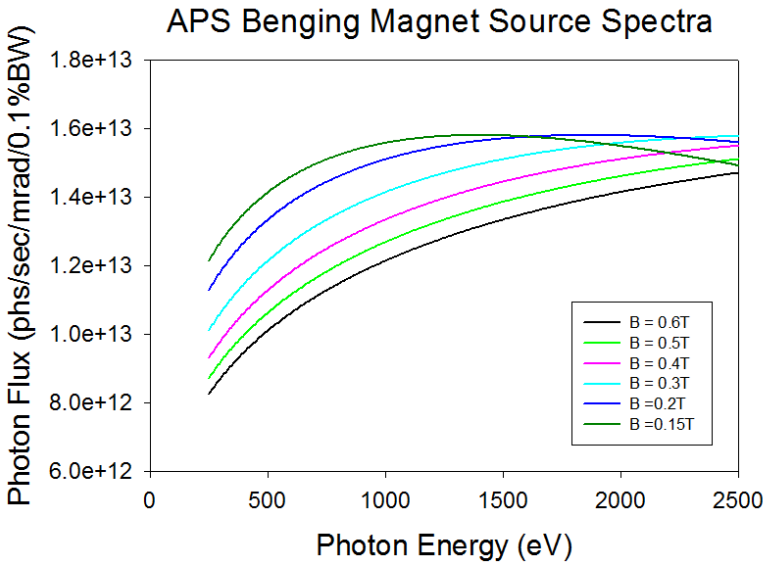

Figure 4-148: Calculated APS bending magnet source spectra for several different fields.

4.21.2.4 X-ray Optical Layout

The main consideration in the optical design of the SPSXS beamline is to maximize the flux at the experiment station with medium-energy resolving power (up to E/ΔE= 5000). As described below, this is achieved with four optical elements, all deflecting the beam in the horizontal plane. The SPSXS beamline will exploit the vertical timing dispersion inherent in the rf-chirped bending magnet source and use horizontal dispersion for photon energy selection. This requires a focusing system in the first optics enclosure (FOE) that will illuminate a horizontal slit for energy resolution selection and a vertical slit for timing resolution selection. As explained in section 4.21.2.4.1, a single horizontally deflecting ellipsoidal mirror imaging the source onto the vertical and horizontal slits has been selected. The slit assembly will be included in an experiment station for transmission spectroscopy of optically thin samples. The sample space will be immediately downstream of the slit assembly to minimize the beam size due to the divergence from the slit. The horizontal and vertical slits will be imaged by a toroidal mirror onto the exit-slit plane. A varied line spacing plane grating (VLSPG) downstream of the toroid will focus the virtual horizontal source (at the exit plane) onto a two-dimensional (2-D) area detector located at the exit-slit plane for collection of energy- and time-dependent spectra. The area detector will be interchangeable, with a horizontal exit-slit assembly for monochromatic beam operations. An ellipsoidal mirror will demagnify the exit slit onto the sample.

Figure 4-149 shows the layout of the beamline in horizontal and vertical views.

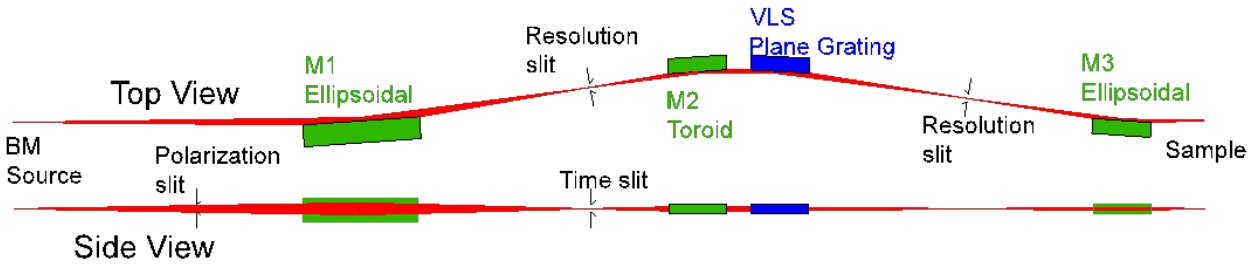

Figure 4-149: Optical layout of the SPSXS beamline showing horizontal and vertical views.

Table 4-68: Major beamline components for the SPSXS beamline.

Component	Location (m)	Notes
White-Beam Mirror (M1)	24.8	Ellipsoidal, horizontally deflecting, incidence angle 1.5°, horizontal and vertical focusing at timing slit position (34.8m), Au coated, accepts 0.84 (h) mrad
Timing and Resolution Slits	34.8	Vertical and horizontal slits defining time and energy resolution
Experimental station 1	34.9	Integrated with slit assembly; includes sample mounts and intermediate-fields electromagnet for transmission experiments
Pink-Beam Mirror (M2)	38.3	Toroidal, horizontally deflecting, incidence angle 1.5°, Au coated, provides horizontal collimation for the plane grating
Grating	38.9	Energy range 400-2000 eV; three interchangeable plane grating slots, gratings with varied line spacing from 400-1200 l/mm
Exit Slit/Camera Assembly	42.4	Interchangeable exit slit/CCD detector assembly; exit provides monochromatic light downstream; CCD array permits timing and energy dispersive spectroscopy in transmission
Refocusing Mirror (M3)	46.4	Ellipsoidal, horizontally deflecting, incidence angle 1.5°, horizontal and vertical focusing at sample position (47.4m), Au coated
Experimental station 2	47.4	5-T superconducting magnet, cryogen-free or closed cycle recondensor

4.21.2.4.1 Mirrors

A Kirkpatrick-Baez (K-B) mirror pair with elliptical cylinders is the optimal optical configuration in terms of image quality for focusing the bending magnet source onto the timing and resolution slits. However, the requirement for the minimum number of mirrors and a beam parallel to the floor at the experiment stations implies that an additional mirror with a vertical deflection if a K-B system is chosen.

Since the horizontal beam size is relatively large (110-µm RMS), a horizontally deflecting ellipsoidal with meridional RMS slope errors of ≈1 µrad is sufficient to avoid losses at the horizontal (energy) slit. A time resolution better than 1 ps can be still achieved with RMS sagittal slope errors of less than 20 µrad on the ellipsoidal due to the forgiveness factor, i.e., the angle of grazing incidence on the mirror (0.026 rad). Two mirror manufacturers have confirmed that an 800-mm-long mirror with entrance and exit arms of 24.8 m and 10.0 m, operating at a grazing angle of 1.5° can be manufactured with the required specifications. The chosen ellipsoidal mirror (M1) will collect 0.84-mrad horizontally and the full vertical fan. Note that the mirror length is determined by the acceptance of a 180-mm-long grating and the floor space constrains.

4.21.2.4.2 Entrance and Timing Slit

Two orthogonal slits will be placed at a distance of 10 m from M1. The timing slit (vertical) will select the pulse duration and will be adjustable to accept 1-10% of the incident radiation, providing pulse durations of 1-10 ps. The horizontal slit will serve as the monochromator entrance slit. In Figure 4-150, we show a SHADOW simulation of the spot size at the timing/entrance slit when the timing slit is set to accept 2 ps and the horizontal slit is fully open. The parameters of the source used in the ray tracings described in the figure are those of an APS bending magnet at 900 eV with σ_x=101 µm and a vertical beam 4.6-mm tall (corresponding to 100 ps). The ray tracings include RMS slope errors of 1 and 10 µm along the meridional and sagittal directions. The expected RMS size along the horizontal is 44 µm, whereas the value in the figure is 48 µm due to the meridional slope errors. Ray tracings performed with the above slope errors and zero height source yield a spot size with full width half maximum (FWHM) of less than 13 µm, which corresponds to a time resolution of less than 0.7 ps.

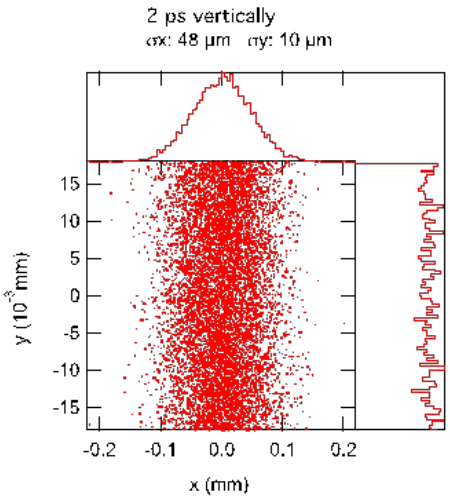

Figure 4-150: Beam profile at the timing/entrance slit assembly.

4.21.2.4.3 Monochromators

The monochromator is based on the Monk Gillieson mounting [213], in which a spherical mirror provides a collimating beam to a VLSPG. In this optical design, the energy selection is done by a simple grating rotation. The present design replaces the spherical mirror with a toroidal mirror (M2) that focuses the

beam along both directions at the exit slit. The linear, quadratic, and cubic terms on the variation of the grating line density zero the defocus, coma, and spherical aberration terms of the mirror-grating combination at a single photon energy. However, the required resolving power of ≈2000 (or even higher) can still be obtained in the full range of energies covered by one grating as shown in Figure 4-151 for a 500 lines/mm grating at its center and a 20-µm entrance slit. The ray tracings include meridional RMS slope errors of 0.5 µrad on the toroidal and 0.2 µrad on the grating. The toroidal mirror is located at 3.5-m downstream of the entrance slit and deflects the beam by 3°. The grating is located 600-mm downstream of the toroid, deflecting the beam by 4°. It should be noted that the chosen optical design also focuses the zero-order light at the exit slit. The design for a varied line spacing monochromator similar to what is expected to be installed on the SPSXS beamline is shown in Figure 4-152.

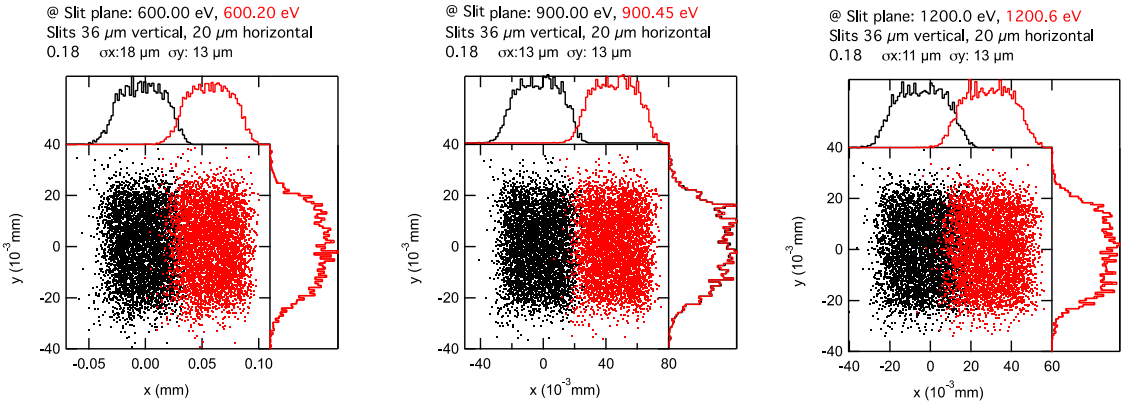

Figure 4-151: Shadow ray tracing of the monochromatic beam at the position of the monochromator exit slit showing the energy resolution performance at 600, 900, and 1200 eV. A resolving power of at least 2000 is obtained across this energy range using a grating line spacing of 500 l/mm and an entrance slit setting of 20 µm.

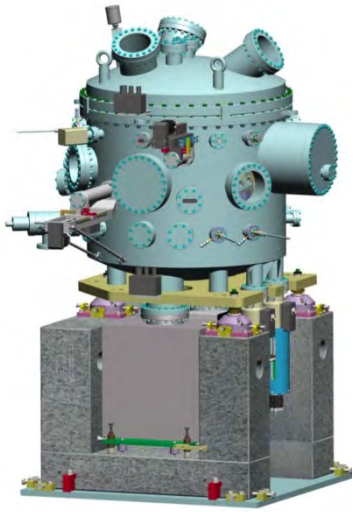

Figure 4-152: Design for a varied line spacing monochromator similar to what is expected to be installed on the short-pulse soft x-ray spectroscopy beamline.

4.21.2.4.4 Monochromator Exit Slit

A horizontal slit downstream of the VLSPG will provide energy selection of the dispersed radiation from the monochromator. This slit will be fixed-position, variable-width, and allow bandwidth selection larger than 0.02%, thus providing the required spectral resolution. The slit will be interchangeable with a vertical position-sensitive detector to allow for dispersive spectroscopy in transmission mode.

4.21.2.4.5 High-order Rejection System

For operation at the lower energy range of the beamline, second-order contamination may be a concern for certain spectroscopy experiments due to the broadband nature of the source. To mitigate this problem, a harmonic rejection system will be included. This system will consist of two vertically deflecting plane mirrors, one upward deflecting and one downward deflecting to restore a horizontal beam. The incidence angles of both mirrors will be 1.5°, and the RMS slope errors will be ~1 μrad to preserve the focus of M1. The plane mirrors will have two coating stripes to reject radiation over 500 and 1000 eV, respectively. The mirror system will be located downstream of the monochromator, before the exit slit. The exit slit, refocusing mirror (M3), and second experimental station must be translatable by ~20 mm to accommodate use of the high-order rejection mirrors.

4.21.2.4.6 Choppers

A polarization-selection chopper will be placed downstream of the first mirror. This chopper will have the capability to select the above- and below-orbit portions of the beam for polarization selection at frequencies of up to several kHz in order to provide lock-in detection ability. The chopper will be ultra-high vacuum (UHV)-compatible and capable of being withdrawn to allow the full beam to pass through. Figure 4-153 shows the polarization characteristics of the APS bending magnet beam at 250 eV, indicating the above- and below-orbit portions of the beam that provide circular polarization. The chopper will select approximately 10% of the beam between +(-)0.2 and +(-)0.4 mrad and provide ~60-70% circular polarization. Downstream from the first focusing mirror (M1), the vertical size of the beam is reduced significantly, allowing for polarization selection with a small excursion above and below the orbit plane.

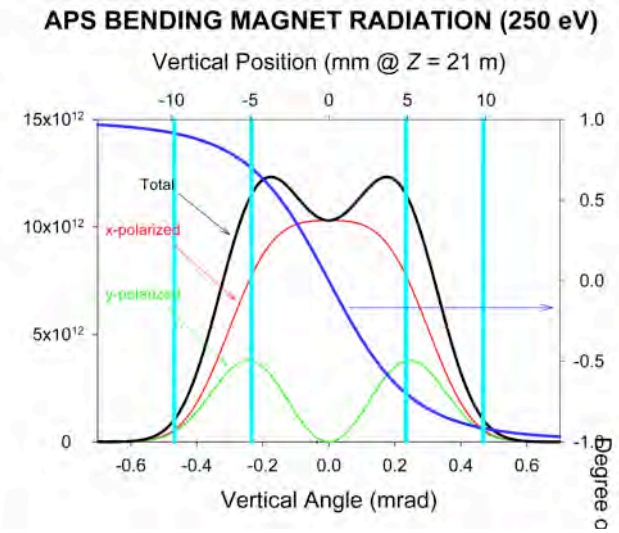

Figure 4-153: Polarization characteristics of the APS bending magnet radiation.

4.21.2.4.7 Focusing Elements

An ellipsoidal refocusing mirror (M3) will be located downstream of the monochromator exit slit. This mirror will image the exit slit plane to provide a small spot size in the second experimental station. The mirror also deflects the beam by 3°. It is located at 4 m from the slit and focuses at the sample position located 1-m downstream. The spot size will depend on the respective slit settings. Figure 4-154 shows, as an example, the ray tracings at the sample position when the energy resolution slits are set to 20 µm and the timing slit is set to 2 ps. As seen in the figure, the vertical size is comparable to the size expected from the demagnification of the 36-µm slit, 10.6 µm. The vertical profile is mainly due to the sagittal slope errors assumed on the toroid and the refocusing ellipsoidal (10-µrad RMS). Evidently, the vertical size will increase when the timing slit is opened. For 10 ps the vertical size at the sample will be 53 µm.

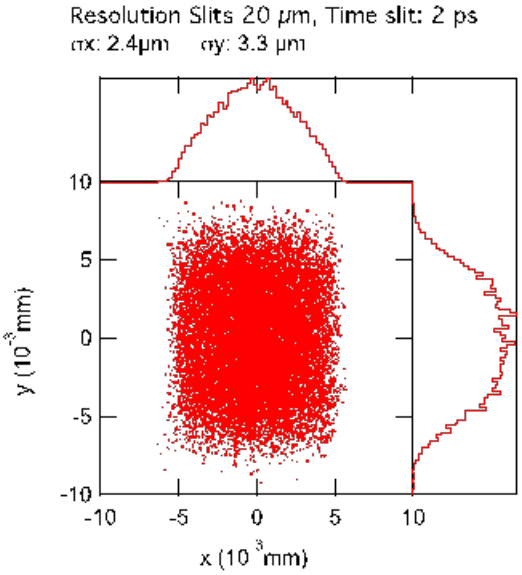

Figure 4-154: Monobeam spot size in the second experiment experimental station, at the focus of M3. The vertical dimension assumes a timing slit setting of 38 μm, which results in a pulse duration of 2 ps. The resolution slits are both set to 20 μm.

4.21.2.5 Beamline Physical Layout

The first focusing mirror (M1) will be included in the FOE (6-BM-A), followed by a pink-beam shutter. The timing/entrance slit assembly and first experimental station will be in the second white-beam enclosure (6-BM-B). The rest of the optics will be outside of the enclosures on the experiment hall floor just outboard of the 6-ID enclosures. A control room and work area will be located downstream of the beamline, near the 6-ID-C enclosure.

4.21.2.5.1 Front End, If Applicable

A modified APS front end with a 18.4-mm (H) by 14.9-mm (V) exit mask is required to allow collection of off-axis polarized radiation. With the exception of the final exit mask (FM3), no other modifications are required. This front end may be equipped with timing and beam-tilt diagnostics to ease the rf cavity operation.

4.21.2.5.2 Overall Beamline

The SPSXS beamline is one of three SPX beamlines that will occupy Sectors 6 and 7, and will use the 6-BM port. Figure 4-155 shows the layout for Sector 6, showing the beamline on the experiment hall floor next to 6-ID.

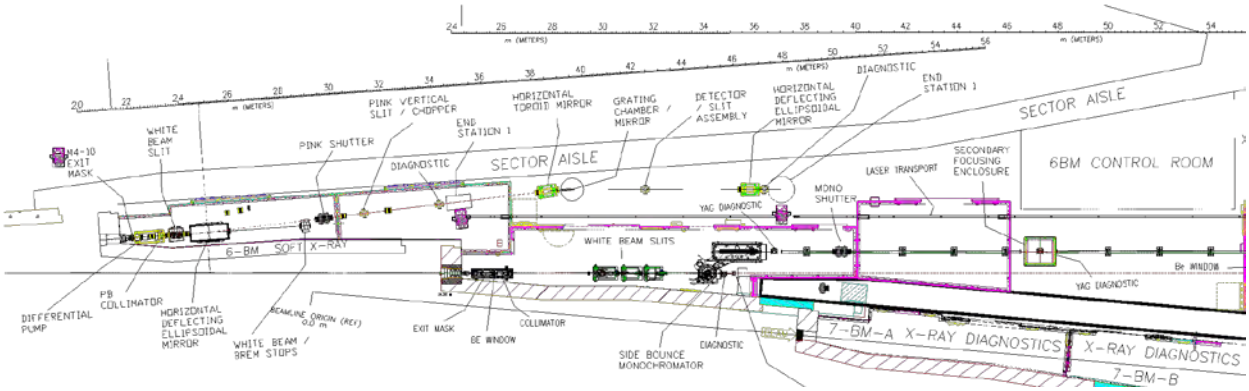

Figure 4-155: Sector 6 layout showing the SPSXS beamline.

4.21.2.5.3 General Description

The 6-BM beamline will be a horizontally-deflecting varied line spacing plane grating (VLSPG) monochromator beamline, optimized for an energy range of 200-2000 eV, and will include instrumentation for transient absorption spectroscopy in transmission, reflectivity, and fluorescence. Instrumentation appropriate for studies of magnetic materials will be required.

Radiation Safety Aspects

A new personnel safety system is required for 6-BM. In the energy range of this beamline, the vacuum chamber is sufficient to provide radiation shielding. Therefore, no enclosures or shielded transport are required for the monochromatic beam. The first three mirrors use large angular deflections (3°), collimators, and bremsstrahlung stops to eliminate scattered radiation. In addition, Au coatings will reject most of the bending magnet radiation above ~2.2 keV; therefore, shielded transport will not be necessary after these optics. This will be verified by detailed geometric and physical ray.

The present white-beam capability in the existing 6-BM-B enclosure will be kept for ease of commissioning.

Vacuum System

A new equipment protection system and vacuum controllers are required for 6-BM. Due to the windowless operation of the beamline, a differential pump is required upstream of the first mirror.

Data Acquisition and Motion Control

A new data acquisition and controls infrastructure will be required for this beamline. This will consist of standard motor drivers, input/output controllers, workstation, and Experimental physics and Industrial Control System support for the new optical components and instrumentation.

4.21.2.5.4 First Optics Enclosure and Infrastructure, Major Components

Windows

No windows can be used in the FOE, as transmission through standard Be windows is negligible in the energy range of this beamline.

Slits

A standard bending magnet beamline, water-cooled, white-beam slit assembly is adequate here, using the latest standard design.

Collimators

A collimator will be integrated after the front end to ease the bremsstrahlung shielding. Its location and aperture will be chosen following engineering ray traces.

Shutters/Stops

A shutter with a white-beam stop, bremsstrahlung stop, and pink-beam shutter will reside at the end of 6-BM-A. The beam stop and shutter will require water cooling sufficient to take the full power of the bending magnet beam. A pink-beam stop is integrated in the monochromator assembly.

Monochromators

The monochromator will be of the Monk Gillieson type [213], with horizontal dispersion and an included angle of 173° (both the mirror and the grating deflect inboard). A horizontal toroidal mirror (instead of a spherical mirror) will provide converging light at the grating. The grating tank will have 3-4 interchangeable gratings of different line spacings, allowing for flexibility in choosing energy resolution at various photon energies. The line spacing variation parameters will be chosen to provide a nearly fixed focus at the exit slit/detector assembly.

Mirrors

The first mirror (M1) is water-cooled, using a single-crystal Si substrate with optical dimensions of 800 mm x 20 mm. The first mirror will be able to absorb 110 W of power with a maximum power density of 50 mW/mm^2 from the bending magnet source when the crab cavity is off and the white beam slits are fully open.

The toroidal mirror optical dimensions are 300 mm x 10 mm and will absorb a maximum power density of 7 W. The gratings will be 1800-mm long and 10-mm wide.

The refocusing mirror (M4) will be an ellipsoid with an optical surface of approximately 200 mm × 10 mm and designed with a demagnification of 4 to the focus at the second experimental station.

All of the mirrors will have RMS surface roughness <3 Å. The ellipsoidals will have meridional and sagittal RMS slope errors better than 1.5 μrad and 15 μrad, respectively. The toroidal and grating RMS meridional slope errors will be better than 0.5 μrad and 0.2 μrad, respectively. Their sagittal RMS slope errors will be better than 3 μrad.

Miscellaneous Optics

A soft x-ray chopper will be placed downstream of M1, and before the vertical/horizontal slit assembly. The chopper will be capable of selecting the on-axis as well as the above and below orbit portions of the beam to allow full beam chopping and polarization selection at kHz frequencies. The chopper apertures will be vertical slits with variable positions above and below the orbit plane. This will allow compensation for the energy dependence of the vertical source polarization dependence.

Diagnostics

Two beam diagnostics chambers will be required to be located upstream of experimental stations 1 and 2. Each diagnostics chamber will be equipped with an isolated Au mesh for I_0 monitoring, an Au evaporator for restoration of the Au mesh surface, and a calibrated Si P-I-N diode detector (IRD AXUV-100) for quantitative beam flux measurements. Beam-defining slits will be placed downstream of the mesh/detector assembly.

4.21.2.5.5 Low-field Transmission Experimental Station

Components

This experiment chamber will be equipped with a UHV-compatible resistive electromagnet and sample cryostat. The chamber will have multiple access ports for laser pumps and detectors. The cryostat will be mounted on a 4-axis, UHV, motorized positioning stage capable of varying the sample lateral position (X,Y), height (Z), and polar angle (θ) with ranges of 10±0.01 mm, 50±0.01 mm, and 180±0.02°, respectively. The requirement on the sample Z range is to allow for multiple samples to be mounted simultaneously, and the requirement on the sample θ is to allow the beam incidence angle to be varied from grazing to normal incidence. A horizontal arc-shaped track concentric with the sample rotation axis will be required for mounting of a movable scattering detector. The design of the chamber and the electromagnet will allow for maximum access to the horizontal scattering plane, with a goal of at least 0-120°.

Instruments

This experiment station will be equipped with a 4-element Si drift-diode detector for fluorescence measurements, microchannel plate detectors for electron yield measurements, and standard electrometers and amplifiers for photocurrent measurements.

4.21.2.5.6 High-Field Spectroscopy Experimental Station

Components

The high-field transmission experimental station will consist of a UHV-compatible, superconducting, split-coil electromagnet equipped with a sample cryostat and sample interchange capability. The magnet will be cooled with either a closed-cycle He refrigerator system or a LHe recirculator. The magnet will have radial access ports for laser pump access and/or detectors. The axial ports and bore size will be sufficient to allow ±10° of access in the horizontal plane for the incident and transmitted beams. The cryostat will be mounted on a UHV, motorized positioning stage capable of varying the sample height (Z) and polar angle (θ) with ranges of 50±0.01 mm and 180±0.02°, respectively. The requirement on the sample Z range is to allow for multiple samples to be mounted simultaneously, and the requirement on the sample θ is to allow the beam incidence angle to be varied from grazing to normal incidence. The conceptual design report calls for a maximum field of 5 T and a minimum sample temperature of 4.2 K; however, a detailed cost/benefit analysis should be done to determine if better performance can be achieved within the current cost estimate of this component. The magnet chamber will be mounted on a custom table capable of Y (inboard-outboard), Z (height), and angular motions for alignment purposes.

Instruments

The primary detector for this transmission instrument will be located downstream of the monochromator. This will be a position-sensitive detector located at the focal point of the monochromator, allowing spectral data to be collected in parallel to improve throughput.

4.21.2.5.7 Additional Beamline Components

State-of-the-art detection and excitation schemes will be necessary for experiments at the SPX facilities. For SPX operation at the full repetition rate of 6.5 MHz, standard detectors are suitable. Advanced photon counting detectors, e.g., Vortex, are required at 6-BM for detection of fluorescence and scattering from dilute samples. For these photon-counting detectors, two additional features are desirable: an upper- and lower-level discriminator, and multiple, independently-gateable count registers. Complementary advanced pixelated integrating detectors with large dynamic range and fast readout are desirable for transmission spectroscopy studies, especially for the high-field experimental station.

High-repetition-rate time-resolved experiments require lasers for sample excitation with high repetition rates, tunable wavelength, fluence on the order of 1 μJ/1000 μm^2, and synchronization of better than 200 fs with respect to the x-ray pulse arrival. Two mobile fiber optic lasers with a pulse duration from 0.5 to 20 ps, and a repetition rate ranging from 50 kHz to 10 MHz, with a power of 50 W, will be available for the SPX facilities. In addition, a Ti:Sapphire laser with a 10-100-kHz repetition rate, 50-fs pulse duration, and 50 W will be housed in a new laser enclosure at Sector 6 as shown in Figure 4-30. These three new lasers will produce a broad band of laser energies from 200 nm to 10 μm using Optical Parametric Amplifier/THz converters. The technical requirements for the new lasers are discussed in the Short Pulse X-ray Imaging and Microscopy Beamline SPXIM section of this Preliminary Design Report (section 4.3). An evacuated laser-beam transport system will feed the 6-BM-B enclosure and experiment hall floor in

Sector 6 from the laser enclosure in Sector 7. The beam transport system will have beam viewing screens, power monitor, polarization control, and flip and steering mirrors to send the laser beam into a given enclosure.

4.21.2.6 Additional

4.21.2.6.1 Safety Requirements

Laser safety is key to the success of the programs on the SPSXS beamline. The laser power will be a factor of 20 higher than is currently available at 7-ID-E, so special care will be needed for beam alignment and transport.

4.21.2.6.2 Conventional Facilities Requirements

A new enclosed controls area is planned for 6-BM, on the outboard side of 6-ID-B. It will house workstations, beamline controls equipment, and sample preparation and mounting facilities.

References

[1] "Developing APS Roadmap Scenarios," 2012. [Online]. Available: http://www.aps.anl.gov/Upgrade/Forum/.

[2] A. Zholents, P. Heimann, M. Zolotorev and J. Byrd, "Generation of subpicosecond X-ray pulses using RF orbit deflection," *Nucl. Instrum. Meth. A,* vol. 425, p. 385, (1999).

[3] M. Borland, "Simulation and analysis of using deflecting cavities to produce short x-ray pulses with the Advanced Photon Source," *Phys. Rev. ST Accel. Beams ,* vol. 8, p. 074001 , 2005.

[4] L. Chen, "Probing Transient Molecular Structures In Photochemical Processes Using Laser-Initiated Time-Resolved X-Ray Absorption Spectroscopy," *Annual Review of Physical Chemistry,* vol. 56, p. 221 , (2005).

[5] C. Bressler and M. Chergui, "Molecular Structural Dynamics Probed by Ultrafast X-ray Absorption Spectroscopy,," *Annual Review of Physical Chemistry,* vol. 61, p. 263, 2010.

[6] J. Katz, X. Zhang, K. Attenkofer and e. al., "Electron Small Polarons and Their Mobility in Iron (Oxyhydr)oxide Nanoparticles," *Science,* vol. 337, p. 1200, 2012.

[7] M. Maroncelli, "The dynamics of solvation in polar liquids," *J. Mol. Liq. ,* vol. 57, p. 1–37 , 1993.

[8] E. Castner Jr., J. F. Wishart and H. Shirota, "Intermolecular dynamics, interactions, and solvation in ionic liquids," *Acc. Chem. Res.,* vol. 40, pp. 1217-1227, 2007.

[9] G. Fleming and M. H. Cho, "Chromophore-solvent dynamics," *Annu. Rev. Phys. Chem.,* vol. 47, p. 109–34, 1996.

[10] M. A. Scarpulla, O. D. Dubon, K. M. Yu, O. Monteiro, M. R. Pillai, M. J. Aziz and M. C. Ridgway, "Ferromagnetic Ga1−xMnxAs produced by ion implantation and pulsed-laser melting," *Appl. Phys. Lett. ,* vol. 82, p. 1251, 2003.

[11] Y. Y. Wu and P. D. Yang, "Melting and welding semiconductor nanowires in nanotubes," *Adv. Mater. ,* vol. 13, p. 520 , 2001.

[12] M. Hu, D. Poulikakos, C. P. Grigorpoulos and H. Pan, "Recrystallization of picosecond laser-melted ZnO nanoparticles in a liquid: A molecular dynamics study," *J. Chem. Phys. ,* vol. 132, p. 164504 , 2010.

[13] M. Trigo, J. Chen, M. P. Jiang, W. L. Mao, S. C. Riggs, M. C. Shapiro, I. R. Fisher and D. A. Reis, "Ultrafast pump-probe measurements of short small-polaron lifetimes in the mixed-valence perovskite Cs2Au2I6 under high pressures," *Phys. Rev. B ,* vol. 85, p. 081102 , 2012.

[14] H. Marciniak, M. Fiebig, M. Huth, S. Schiefer, B. Nickel, F. Selmaier and S. Lochbrunner, "Ultrafast exciton relaxation in microcrystalline pentacene films," *Phys. Rev. Lett. ,* vol. 99, p. 176402, 2007.

[15] C. Buth, R. Santra and L. Young, "Electromagnetically Induced Transparency for X-rays," *Phys. Rev. Lett.,* vol. 98, p. 253001 , 2007.

[16] T. E. Glover, M. Hertlein, S. Southworth, T. Allison, J. van Tilborg, E. Kanter, B. Krässig, H. Varma, B. Rude, R. Santra, A. Belkacem and L. Young, "Controlling X-rays with Light," *Nature Physics,* vol. 6, pp. 69-74, 2010.

[17] A. March, A. Stickrath, G. Doumy, E. Kanter, B. Kressig, S. Southworth, K. Attenkofer, C. Kurtz, L. Chen and L. Young, "Development of high-repetition-rate laser pump/x-ray probe methodologies for synchrotron facilities," *Rev. Sci. Inst.,* vol. 82, p. 073110, 2011.

[18] K. Haldrup, G. Vanko, W. Gawelda, A. Galler, G. Doumy, A. March, E. P. Kanter, A. Bordage, A. Dohn, T. van Driel, K. Kjær, H. Lemke, S. Canton, J. Uhlig, V. Sundstrom, L. Young, S. Southworth, M. Nielsen and C. Bressler, "Guest-host interactions investigated by time-resolved x-ray spectroscopies and scattering at MHz rates: solvation dynamics and photoinduced spin transition in aqueous Fe(bipy)_3^2+," *J. Phys. Chem. A,* vol. 116, pp. 9878-9887, 2012.

[19] Haeffner, Dean, "APS Upgrade Sharepoint Source Dependencies," March 2011. [Online]. Available: https://apsshare.aps.anl.gov/apsu/dependencies/Master%20Dependencies/Beamline%20Source%20Data.xlsx.

[20] M. Borland, "Elegant: A Flexible SDDS-Compliant Code for Accelerator Simulation,' APS LS-287," 2000. [Online]. Available: http://www.aps.anl.gov/Science/Publications/lsnotes/content/files/APS_1418218.pdf.

[21] T. Tanaka and H. Kitamura, "SPECTRA - a synchrotron radiation calculation code," *J. Synchrotron Radiation,* vol. 8, pp. 1221-1228, 2001.

[22] Welnak, C.; Chen, G.; Cerrina, F., "SHADOW: a synchrotron radiation and x-ray optics simulation tool.," *Nucl. Instr. and Meth. A,.,* vol. 347, p. 344, 1994.

[23] M. Sanchez del Rio, N. Canestrari, F. Jiang and F. Cerrina, "SHADOW: a new version of the synchrotron x-ray optics modelling package.," *Journal of Synchrotron Radiation,,* vol. 18, no. 5, p. 708–716, 2011.

[24] Kirkpatrick, P.; Baez, A., "Formation of optical images by x-rays," *J. Opt. Soc. Am.,* vol. 38, p. 776–774, 1948.

[25] Y. J. Wang, K.-S. Im, K. Fezzaa, W. Lee, J. Wang, P. Micheli and C. Laub, "Quantitative x-ray phase-contrast imaging of air-assisted water sprays with high Weber numbers," *Appl. Phys. Lett. ,* vol. 89, p. 151913, 2006.

[26] M. Gembicky, D. Oss, R. Fuchs and P. Coppens, "A fast mechanical shutter for submicrosecond time-resolved synchrotron experiments," *J. Synchrotron Rad.,* vol. 12, p. 665–669, 2005.

[27] T. Ejdrup, H. Lemke, K. Haldrup, T. Nielsen, D. Arms, D. Walko, A. Miceli, E. Landahl, E. Dufresne and M. Nielsen, "Picosecond Time-resolved laser pump/X-ray probe experiments using a gated single-photon-counting area detector," *J. Synchrotron Rad.,* vol. 16, pp. 387-390, 2009.

[28] G. Vanko, A. Bordage, P. Glatzel, E. Gallo, M. Rovezzi, W. Gawelda, A. Galler, C. Bressler, G. Doumy, A. March, E. Kanter, L. Young, S. Southworth, S. Canton, J. Uhlig, G. Smolentsev, V. Sundstrom, K. Haldrup, T. van Driel, M. M. Nielsen, K. S. Kjaer and H. T. Lemke, "Spin-state studies with XES and RIXS: From static to ultrafast (accepted)," *Journal of Electron Spectroscopy and Related Phenomena,* 2012.

[29] Evans, P.; Clarke, R.; Reis, D.A.; Wang, J., "APS Upgrade proposal: Short-Pulse X-ray Facility Hard X-ray Diffraction and Imaging Beamline," Argonne, IL, February 2011.

[30] D. Daranciang, M. Highland, H. D. Wen, S. M. Young, N. C. Brandt, H. Y. HWang, M. Vattilana, M. Nicoul, F. Quirin, J. Goodfellow, T. T. Qing, I. Grinberg, D. M. Fritz, M. Cammarata, D. L. Zhu, T. Lemke, D. A. Walko, E. M. Dufresne, Y. Li, J. Larsson, D. A. Reis, K. Sokolowski-Tintin, K. A. Nelson, A. M. Rappe, P. H. Fuoss, G. B. Stephenson and A. M. Lindenberg, "Ultrafast Photovoltaic Response in Ferroelectric Nanolayesr," *Phys. Rev. Lett.,* vol. 108, p. 087601, 2012.

[31] J. Jo, P. Chen, R. Sichel, S. Callori, J. Sinsheimer, E. M. Dufresne, M. Dawber and P. G. Evans, "Nanosecond Dynamics of Ferroelectric/Dielectric Superlattices," *Phys. Rev. Lett.,* vol. 107, p. 055501, 2011.

[32] P. Chen, J. Y. Jo, H. N. Lee, E. M. Dufresne, S. M. Nakhmanson and P. G. Evans, "Domain- and symmetry-transition origins of reduced nanosecond piezoelectricity in ferroelectric/dielectric superlattices," *New J. Phys.,* vol. 14, p. 013034, 2012.

[33] M. Tomes and T. Carmon, "Photonic Micro-Electromechanical Systems Vibrating at X-band (11-GHz) Rates," *Phys. Rev. Lett.,* vol. 102, p. 113601, 2009.

[34] X. K. Sun, J. J. Zheng, M. Poot, C. W. Wong and H. X. Tang, "Femtogram Doubly Clamped Nanomechanical Resonators Embedded in a High-Q Two-Dimensional Photonic Crystal Nanocavity," *Nano Lett.,* vol. 12, p. 2299, 2012.

[35] B. Ferguson and X.-C. Zhang, "Materials for terahertz science and technology," *Nature Mater.,* vol. 1, p. 26, 2002.

[36] A. G. MacPhee, M. W. Tate, C. F. Powell, Y. Yue, M. J. Renzi, A. Ercan, S. Narayanan, E. Fontes, J. Walther, J. Schaller, S. M. Gruner and J. Wang, "X-ray Imaging of Shock Waves Generated by High-Pressure Fuel Sprays," *Science ,* vol. 295, p. 1261 , 2002.

[37] M. Reyssat, J. M. Yeomans and D. Quéré, "Impalement of fakir drops," *Europhys. Lett.,,* vol. 81, p. 26006, 2008.

[38] C. Sparks, B. Borie and J. Hastings, "X-ray monochromator geometry for focusing synchrotron radiation above 10 kev," *Nuclear Instruments and Methods,* vol. 172, p. 237 – 242, 1980.

[39] P., Kirkpatrick; Baez, A., "Formation of optical images by x-rays," *J. Opt. Soc. Am.,* vol. 38, p. 776–774, 1948.

[40] V. Sajaev, "SPX Upgrade (AOP-TN-2011-012)," Advanced Photon Source, Argonne, 2011.

[41] R. Dejus, "Power distribution and front-end aperture size for an rf-deflected beam at the APS Rev. 1 (private communication)," Argonne National Lab., Argonne, 2005.

[42] S. N. Luo, B. Jensen, D. Hooks, K. Fezzaa, K. Ramos and J. Yeager, "Gas gun shock experiments with single-pulse x-ray phase contrast imaging," *Rev. Sci. Instrum.,* vol. 83, p. 073903 , 2012.

[43] "PHAROS product page from Light Conversion Ltd.," [Online]. Available: http://www.lightcon.com/products/product.php?ID=28.

[44] "See Tangerine product line," [Online]. Available: http://www.amplitude-systems.com/.

[45] "Impulse High-Average-Power Femtosecond Laser," [Online]. Available: http://www.cmxr.com/Products/LaserProducts/Impulse.html.

[46] "Legend Elite Cryo PA product page," [Online]. Available: http://www.coherent.com/Products/?1019/Legend-Elite-Cryo-PA.

[47] T. Graber, H. Brewer, Y.-S. Chen, H.-S. Cho, N. Dashdorj, R. W. Henning, I. Kosheleva, G. Macha, M. Meron, R. Pahl, Z. Ren, S. Ruan, F. Schotte, V. Srajer, P. J. Viccaro, F. Westferro, P. Anfinrud and K. Moffat, "BioCARS: a synchrotron resource for time-resolved X-ray science," *J. Synchrotron Rad.,* vol. 18, pp. 658-670, 2011.

[48] M. Wulff, A. Plech, L. Eybert, R. Randler, F. Schotte and P. Anfinrud, "The realization of sub-nanosecond pump and probe experiments at the ESRF," *Faraday Discuss.,* vol. 122, pp. 13-26, 2002.

[49] S. Nozawa, S. Adachi, J. Takahashi, R. Tazaki, L. Guerin, M. Daimon, A. Tomita, T. Sato, M. Chollet, E. Collet, H. Cailleau, S. Yamamoto, K. Tsuchiya, T. Shioya, H. Sasaki, T. Mori, K. Ichiyanagi, H. Sawa, H. Kawata and S. Koshihara, "Developing 100 ps-resolved X-ray structural analysis capabilities on beamline NW14A at the Photon Factory Advanced Ring," *J. Synchrotron Rad.,* vol. 14, p. 313–319, 2007.

[50] V. Sajaev, "Simulation of Canted Orbit in Switchable Straight-Canted Configuration," 2012.

[51] R. Dejus and S. Sasaki, "Short-Period APPLE II Undulator for Generating 12-15 keV X-Rays at the Advanced Photon Source," 2009.

[52] APS Guidelines, Technical Specifications for APS Beamline First Optics, White, and Monochromatic Beam Experimental Enclosures (410509-00002).

[53] APS Accelerator Ultrahigh Vacuum Guide, TB-16.

[54] T. Gog, D. M. Casa, A. Said, M. H. Upton, J. Kim, I. Kuzmenko, X. Huang and R. Khachatryan, "Near-Backscattering, Spherical Analyzers for RIXS: A Compilation of Viable Reflections in Si, Ge, LiNbO3, Sapphire and Quartz," in *http://www.aps.anl.gov/Sectors/Sector30/AnalyzerAtlas/AnalyzerAtlas.html*, 2012.

[55] Stevenson, Brian; Mills, Dennis, *Justification of the Design for the UPgraded RIXS Beamline in Sector 27 (APS_1432189),* https://icmsdocs.aps.anl.gov/docs/groups/aps/@apsshare/@bdl/documents/correspondence/aps_1432189.pdf , October 17, 2012.

[56] C. Benson, Y. Jaski, T. Powers and O. Schmidt, "White Beam Slits andPink Beam Slits for the Hard X-ray Nanoprobe Beamline at the Advanced Photon Source," in *AIP Conf. Proc. 879*, 2007.

[57] T. Gog, D. M. Casa, A. Said, M. H. Upton, J. Kim, I. Kuzmenko, X. Huang and R. Khachatryan, "High-Resolution Si Channel-Cut Monochromators for RIXS: A Compilation of Viable Crystal Combinations," in *http://www.aps.anl.gov/Sectors/Sector30/AnalyzerAtlas/MonoAtlas.html*, 2012.

[58] M. Ramanathan, B. Brajuskovic, D. Shu, Y. Amer, H. Sinn, Y. Shvyd'ko, C. Burns, W. Sturhahn, T. s. Toellner, E. Alp and J. Hill, "Final Design Report, Inelastic X-ray Scattering CDT, Sector 30," 2006.

[59] D. Haskel, J.C. Lang, Z. Islam, A. Cady, G. Srajer, M. van Venendaal, P. Canfield, "Atomic Origin of Magnetocrystalline Anisotropy in Nd2Fe14B," *Phys. Rev. Lett.,* vol. 95, pp. 217207-1-4, 2005.

[60] D. Haskel, Y.B. Lee, B.N. Harmon, Z. Islam, J.C. Lang, G. Srajer, Ya. Murdyk, K.A. Gschneidner, V.K. Pecharsky, "Role of Ge in Bridging Ferromagnetism in the Giant Magnetocaloric Gd5(Ge1-xSix)4 Alloys," *Phys. Rev. Lett.,* vol. 98, pp. 247205-1-4, 2007.

[61] I. Zegkinoglou, J. Strempfer, C.S. Nelson, J.P. Hill, J. Chakhalian, C. Bernhard, J.C. Lang, G. Srajer, H. Fukazawa, S.Nakatsuji, Y. Maeno, B. Keimer, "Orbital Ordering Transition in Ca2RuO4 Observed with Resonant X-Ray Diffraction," *Phys. Rev. Lett.,* vol. 95, pp. 136401-1-4, 2005.

[62] N. Souza-Neto, D. Haskel, J. Lang, O. Cmaissem, B. Dabrowski, I. Felner, "Element-specific probe of Ru magnetism and local structure in RuSr2Eu1.5Ce0.5Cu2O10," *Phys. Rev. B,* vol. 80, pp. 140414-1-4, 2009.

[63] M. Suzuki, N. Kawamura, H. Miyagawa, J. S. Garitaonandia, Y. Yamamoto, "Measurement of a Pauli and Orbital Paramagnetic State in Bulk Gold Using X-Ray Magnetic Circular Dichroism Spectroscopy," *Phys. Rev. Lett.,* vol. 108, pp. 047201-1-5, 2012.

[64] Y. Yamamoto and H. Hori, "Direct observation of the ferromagnetic spin polarization in gold nanoparticles: a review," *Rev. Adv. Mater. Sci.,* vol. 12, pp. 23-32, 2006.

[65] J. de la Venta, V. Bouzas, A. Pucci, M.A. Laguna-Marco, D. Haskel, S. G. E. te Velthuis, A. Hoffmann, J. Lal, M. Bleuel, G. Ruggeri, C. de Julian Fernandez, M. A. Garcia, "X-ray Magnetic Circular Dichroism and Small Angle Neutron Scattering Studies of Thiol Capped Gold Nanoparticles," *J. Nanosci. and Tech.,* vol. 9, pp. 6434-6438, 2009.

[66] S. S. Dhesi, G. van der Laan, H. A. Durr, M. Belakhovsky, S. Marchesini, P. Kamp, A. Marty, B. Gilles, A. Rogalev,, "Magnetocrystalline anisotropy in FePd alloys studied using transverse X-ray magnetic circular dichroism," *J. Mag. Mag. Mater.,* vol. 226, pp. 1580-1582, 2001.

[67] C. Clavero, J. R. Skuza, Y. Choi, D. Haskel, J. M. Garcia-Martin, A. Cebollada, R. A. Lukaszew, "Control of the perpendicular magnetic anisotropy of FePd films via Pd capping deposition," *Appl. Phys. Lett.,* vol. 92, pp. 162502-1-3, 2008.

[68] K. T. Moore and G. van der Laan, "Nature of the 5f states in actinide metals," *Reviews of Modern Physics,* vol. 81, pp. 235-298, 2009.

[69] G. H. Lander, M. S. S. Brooks, B. Johansson, "Orbital band magnetism in actinide intermetallics," *Phys. Rev. B,* vol. 43, pp. 13672-13675, 1991.

[70] A. B. Shick, V. Drchal, L. Havela, "Coulomb-U and magnetic-moment collapse in ∂-Pu," *Europhys. Lett.,* vol. 69, pp. 588-594, 2005.

[71] J. Wadsworth, G.W. Crabtree, R.J. Hemley, "Basic reseach needs for materials under extreme conditions," 2007.

[72] L. Gao, Y. Y. Xue, F. Chen, Q. Xiong, R. L. Meng, D. Ramirez, C. W. Chu, J. H. Eggert, H. K. Mao, "Superconductivity up to 164 K in HgBa2Cam-1CumO2m+2+δ (m=1, 2, and 3) under quasihydrostatic pressures," *Phys. Rev. B ,* vol. 50, pp. 4260-4266, 1994.

[73] N. M. Souza-Neto, D. Haskel, Y-C. Tseng, G. Lapertot, "Reentrant Valence Transition in EuO at High Pressures: Beyond the Bond-Valence Model," *Phys. Rev. Lett.,* vol. 102, pp. 057206-1-4 , 2009.

[74] O. Mathon, F. Baudelet, J.-P. Itie, S. Pasternak, A. Polian, S. Pascarelli, "XMCD under pressure at the Fe K edge on the energy-dispersive beamline of the ESRF," *J. Synch. Rad. ,* vol. 11, pp. 423-427, 2004.

[75] N. Ishimatsu, O. Shimomura, H. Maruyama, N. Kawamura, M. Suzuki, Y. Ohishi, M. Ito, S. Nasu, T. Kawakami, "Pressure-induced magnetic transition in Fe sub 4 N probed by Fe K-edge XMCD measurement," *J. Phys. Soc. Jpn.,* vol. 72, pp. 2372-2376, 2003.

[76] D. Haskel, Y.C. Tseng, J.C. Lang, S. Sinogeikin, "Instrument for x-ray magnetic circular dichroism measurements at high pressures," *Rev. Sci. Instrum.,* vol. 78, pp. 083904-1-5, 2007.

[77] Y. C. Tseng, D. Haskel, J.C. Lang, S. Sinogeikin, Y. Mudryk, V. K. Pecharsky, K. A. Gschneidner, "Effect of hydrostatic pressure upon the magnetic transitions in the Gd5(SixGe1−x)4 giant magnetocaloric compounds: X-ray magnetic circular dichroism study," *Phys. Rev. B,* vol. 76, pp. 014411-1-6, 2007.

[78] Y. Ding, D. Haskel, Y. C. Tseng, E. Kaneshita, M. van Veneendaal, J. Mitchell, S. Sinogeikin, V. Prakapenka, H.-K. Mao, "Novel Pressure-Induced Magnetic Transition in Magnetite (Fe3O4)," *Phys. Rev. Lett.,* vol. 102, pp. 237201-1-4 , 2009.

[79] [Online]. Available: www.certif.com.

[80] N. Lock, M. Bremholm, M. Christensen, J. Almer, Y. S. Chen and B. B. Iversen, "In-Situ High-Energy Synchrotron Study of Boehmite Formulation, Growth, and Phase Transformation to Alumina in Sub- and Supercitical Water," *Chemistry - a European Journal,* vol. 15, pp. 13381-13390, 2009.

[81] A. C. Deymier-Black, F. Yan, A. Singhal, J. Almer, L. C. Brinson and D. Dunand, "Evolution of Load Transfer Between Hydroxyapatite and Collagen During Creep Deformation of Bone," *Acta Biomaterialia,* vol. 8, pp. 253-261, 2012.

[82] U. K. Vempati, P. K. Valvala, M. L. Falk, J. Almer and T. C. Hufnagel, "Length-Scale Dependence of Elastic Strain from Scattering Measurements in Metallic Glasses," *Physical Review B,* vol. 85, pp. 214201-10, 2012.

[83] X. Pan, X. Wu, X. Chen, J. Almer, J. Ilavsky, D. Haeffner and J. F. Stubbins, "Lattice Strain and Damage Evolution of 9-12% Cr Ferritic/Martensitic Steel During In-Situ Tensile Test by X-Ray Diffraction and Small-Angle Scattering," *Journal of Nuclear Materials,* vol. 407, pp. 10-15, 2010.

[84] M. Kerr, M. R. Daymond, R. A. Holt and J. D. Almer, "Observation of Growth of a Precipitate at a Stress Concentration by Synchrotron X-Ray Diffraction," *Acta Materialia,* vol. 58, pp. 1578-1588, 2010.

[85] B. Jakobsen, H. F. Poulsen, U. Lienert, J. Almer, S. D. Shastri, H. O. Sorensen, C. Gundlach and W. Pantleon, "Formation and Subdivision of Deformation Structures During Plastic Deformation," *Science,* vol. 312, pp. 889-892, 2006.

[86] S. Engemann, H. Reichert, H. Dosch, J. Bilgram, V. Honkimaki and A. Snigirev, "Interfacial Melting of Ice in Contact with SiO2," *Physical Review Letters,* vol. 92, p. 205701, 2004.

[87] M. Mezger, H. Schroder, H. Reichert, S. Schramm, J. Okasinski, S. Schroder, V. Honkimaki, M. Deutch, B. M. Ocko, J. Ralston, M. Rohwerder, M. Stratmann and H. Dosch, "Molecular Layering of Fluorinated Ionic Liquids at a Charged Sapphire (0001) Surface," *Science,* vol. 322, pp. 424-428, 2008.

[88] P. Nolte, A. Stierle, N. Kasper, N. Y. Phillipp, H. Riechert, A. Ruhm, J. Okasinski, H. Dosch and S. Schroder, "Combinatorial High-Energy X-Ray Microbeam Study of the Size-Dependent Oxidation of Pd Nanoparticles on MgO(100)," *Physical Review B,* vol. 77, p. 115444, 2008.

[89] S. D. Shastri, "Combining Flat Crystals, Bent Crystals, and Compound Refractive Lenses for High-Energy X-Ray Optics," *Journal of Synchrotron Radiation,* vol. 11, pp. 150-156, 2004.

[90] V. Petkov and S. D. Shastri, "Element-Specific Structure of Materials with Intrinsic Disorder by High-Energy Resonant X-Ray Diffraction and Atomic Pair-Distribution Functions: A Study of PtPd Nanosized Catalysts," *Physical Review B,* vol. 81, pp. 165428-1-8, 2010.

[91] V. Petkov, S. M. Selbach, M.-A. Einarsrud, T. Grande and S. D. Shastri, "Melting of Bi Sublattice in Nanosized BiFeO3 Perovskite by Resonant X-Ray Diffraction," *Physical Review Letters,* vol. 105, pp. 185501-1-4, 2010.

[92] T. Nimalasuriya, J. J. Curry, C. J. Sansonetti, E. J. Ridderhof, S. D. Shastri, A. J. Flikweert, W. W. Stoffels, M. Haverlag and J. J. van der Mullen, "X-Ray Induced Fluorescence Measurement of Segregation in a DyI3-Hg Metal-Halide Lamp," *Journal of Physics D,* vol. 40, pp. 2831-2838, 2007.

[93] G. J. Havrilla, M. Collins, V. Montoya, W. T. Elam, S. D. Shastri and A. Mashayekhi, "Ultra-High-Energy X-Ray Fluorescence: A New Paradigm for Actinide Characterization of Spent Fuel," *Proceedings of the Institute of Nuclear Materials Management - 52nd Annual Meeting,* pp. A229-11, 2011.

[94] S. D. Shastri, K. Fezzaa, A. Mashayekhi, W.-K. Lee, P. B. Fernandez and P. L. Lee, "Cryogenically Cooled, Bent Double-Laue Monochromator for High Energy X-Rays (50-200 keV)," *Journal of Synchrotron Radiation,* vol. 9, pp. 317-322, 2002.

[95] S. D. Shastri, J. Almer, C. Ribbing and B. Cederstrom, "High-Energy X-Ray Optics with Silicon Saw-Tooth Refractive Lenses," *Journal of Synchrotron Radiation,* vol. 14, pp. 204-211, 2007.

[96] A. H. Said and S. D. Shastri, "Silicon Saw-Tooth Refractive Lens for High-Energy X-Rays Made Using a Diamond Saw," *Journal of Synchrotron Radiation,* vol. 17, pp. 425-427, 2010.

[97] C. Schulze, U. Lienert, M. Hanfland, M. Lorenzen and F. Zontone, "Microfocusing of Hard X-Rays with Cylindrically Bent Crystal Monochromators," *Journal of Synchrotron Radiation,* vol. 5, pp. 77-81, 1998.

[98] U. Lienert, H. F. Poulsen, V. Honkimaki, C. Schulze and O. Hignette, "A Focusing Multilayer Analyser for Local Diffraction Studies," *Journal of Synchrotron Radiation,* vol. 6, pp. 979-984, 1999.

[99] M. Mezger, H. Reichert, S. Schroder, J. Okasinski, H. Schroder, H. Dosch, D. Palms, J. Ralston and V. Honkimaki, "High-Resolution In-Situ X-Ray Study of the Hydrophobic Gap at the Water-Octadecyl-Trichlorosilane Interface," *Proceedings of the National Academy of Sciences of the USA,* vol. 103, pp. 18401-18404, 2006.

[100] V. Honkimaki, H. Reichert, J. S. Okasinski and H. Dosch, "X-Ray Optics for Liquid Surface/Interface Spectrometers," *Journal of Synchrotron Radiation,* vol. 13, pp. 426-431, 2006.

[101] P. Fenter, J. G. Catalano, C. Park and Z. Zhang, "On the Use of CCD Area-Detectors for High-Resolution Specular X-Ray Reflectivity," *Journal of Synchrotron Radiation,* vol. 13, pp. 293-303, 2006.

[102] A. J. Bard, H. D. Abruna, C. E. Chidsey, L. R. Faulkner, S. W. Feldberg, K. Itaya, M. Majda, O. Melroy and R. W. Murray, "The electrode/electrolyte interface - a status report," *J. Phys. Chem.-US,* vol. 97, no. 28, p. 7147, 1993.

[103] V. R. Stamenkovic, B. S. Mun, M. Arenz, K. J. J. Mayrhofer, C. A. Lucas, G. Wang, P. N. Ross and N. M. Markovic, "Trends in electrocatalysis on extended and nanoscale Pt-bimetallic alloy surfaces," *Nat. Mater.,* vol. 6, no. 3, p. 241, 2007.

[104] G. Brown, A. L. Foster and J. D. Ostergren, "Mineral surfaces and bioavailability of heavy metals: A molecular-scale perspective," *P. Natl. Acad. Sci. USA,* vol. 96, no. 7, p. 3388, 1999.

[105] G. Ertl and H. J.Freund, "Catalysis and surface science," *Physics Today,* vol. 52, no. 1, p. 32, 1999.

[106] C.-Y. Kim, A. A. Escuadro, P. C. Stair and M. J. Bedzyk, "Atomic-Scale View of Redox-Induced Reversible Changes to a Metal-Oxide Catalytic Surface: VOx/α-Fe2O3(0001)," *J. Phys. Chem. C,* vol. 111, no. 5, p. 1874, 2007.

[107] P. Nolte, A. Stierle, N. Y. Jin-Phillipp, N. Kasper, T. U. Schulli and H. Dosch, "Shape changes of supported Rh nanoparticles during oxidation and reduction cycles," *Science,* vol. 321, no. 5896, p. 1654, 2008.

[108] F. Ribeiro, A. VonWittenau, C. Bartholomew and G. Somorjai, "Reproducibility of turnover rates in heterogeneous metal catalysis: Compilation of data and guidelines for data analysis," *Catal. Rev.,* vol. 39, p. 49, 1997.

[109] A. Menzel, K.-C. Chang, V. Komanicky, Y. V. Tolmachev, A. V. Tkachuk, Y. S. Chu and H. You, "High-density electrosorbed carbon monoxide monolayers on Pt(111) under atmospheric pressure," *Phys. Rev. B,* vol. 75, no. 3, p. 035426, 2007.

[110] C. H. Ahn, A. Bhattacharya, M. Di Ventra, J. N. Eckstein, C. D. Frisbie, M. E. Gershenson, A. M. Goldman, I. H. Inoue, J. Mannhart, A. J. Millis, A. F. Morpurgo, D. Natelson and J.-M. Triscone, "Electrostatic modification of novel materials," *Rev. Mod. Phys.,* vol. 78, no. 4, p. 1185, 2006.

[111] D. A. Luh, T. Miller, J. J. Paggel, M. Y. Chou and T. C. Chiang, "Quantum electronic stability of atomically uniform films," *Science,* vol. 292, no. 5519, p. 1131, 2001.

[112] M. Valden, X. Lai and D. W. Goodman, "Onset of catalytic activity of gold clusters on titania with the appearance of nonmetallic properties," *Science,* vol. 1647, no. 5383, p. 281, 1998.

[113] P. Fenter, C. Park, Z. Zhang and S. Wang, "Observation of subnanometre-high surface topography with X-ray reflection phase-contrast microscopy," *Nat. Phys,* vol. 700, no. 10, p. 2, 2006.

[114] "APS Upgrade Conceptual Design Report, 4.6.4 Sub-micron 3D Diffraction Upgrade (34-ID)," 2011.

[115] "Sector 34-ID Canted Front-end Beamline Upgrade, Advanced Photon Source," 2011.

[116] N. Ipe et al., "Guide to Beamline Radiation Shielding Design at the Advanced Photon Source," TB-7, 2011.

[117] Argonne Engineering Drawing: Existing Be window assembly (4102030111-200000).

[118] Argonne Engineering Drawing: Existing white-slits assembly (4105091505-310000).

[119] Argonne Engineering Drawing: Existing exit collimator (4102030108-500000).

[120] Argonne Engineering Drawing: Existing bremsstrahlung collimator (4105090403-110000).

[121] Argonne Engineering Drawing: Existing bremsstrahlung collimater (4105090403-120000).

[122] Argonne Engineering Drawing: 4105090403-110000.

[123] Argonne Engineering Drawing: 4105090403-300100.

[124] Argonne Engineering Drawing: Existing photon mask/beam stop (4105091008-120000).

[125] D. Shu, S. Narayanan, A. Sandy, M. Sprung, C. Preissner, and J. Sullivan, "Precision Mechanical Design of an UHV-Compatible Artificial Channel-Cut X-ray Monochromator," SPIE Vol. 6665-23, 2007.

[126] Argonne Engineering Drawing: Pink-beam branch P9-30 integral shutter (DX p931me00.dwg APS_1290544).

[127] W. Liu, P. Zschack, J. Tischler, G. Ice, B. Larson (I. McNulty, C. Eyberger, B. Lai, eds.), "X-ray Laue Diffraction Microscopy in 3D at the Advanced Photon Source," in *10th International Conference on X-ray Microscopy, AIP*, 2011.

[128] B. C. Larson, Wenge Yang, G. E. Ice, J. D. Budai, J. Z. Tischler, "Three-dimensional x-ray structural microscopy with submicrometre resolution," *Nature 415,* vol. February , pp. 887-890 , 2002.

[129] Wenjun Liu, Gene E. Ice, Lahsen Assoufid, Chian Liu, Bing Shi, Ruben Khachatryan, Jun Qian, Paul Zschack, Jonathan Z. Tischler and J.-Y. Choi, "Achromatic nested Kirkpatrick–Baez mirror optics for hard X-ray nanofocusing," *J. Synchrotron Rad. ,* vol. 18, p. 575–579 , 2011.

[130] Argonne Engineering Drawing: Pink beam branch P9-30 integral shutter (DX p931me00.dwg APS_1290544).

[131] Wenjun Liu, Gene E. Ice, Jonathan Z. Tischler, Ali Khounsary, Chian Liu, Lahsen Assoufid, and Albert T. Macrander, "Short focal length Kirkpatrick-Baez mirrors for a hard x-ray nanoprobe," *Rev. Sci. Instrum,* vol. 76, no. 113701, 2005.

[132] Z. Cai, B. Lai, Y. Xiao, S. Xu, "An X-ray diffraction microscope at the Advanced Photon Source," *J. Phys.,* vol. IV, no. 17, 2003.

[133] B. Dickinson, G. T. Seidler, Z. Webb, J. Bradley, K. Nagle, S. M. Heald and R. A. Gordon, "A short working distance multiple crystal x-ray spectrometer," *Rev. Sci. Instrum.,* vol. 79, pp. 123112-1-123112-8, 2008.

[134] B. Mattern, G. Seidler, M. Haave, J. Pacold, R. Gordon, J. Planillo, J. Quintana and B. Rusthoven, "A Plastic Miniature X-ray Emission Spectrometer (miniXES) based on the Cylindrical von Hamos Geometry," *Rev. Sci. Instrum.,* vol. 83, pp. 023901-1-023901-9, 2012.

[135] U. Bergman, P. Glatzel and S. Cramer, *Microchem. J.,* vol. 71, p. 221, 2002.

[136] J. Soininen, A. Ankudinov and J. Rehr, *Phys. Rev. B,* vol. 72, p. 045136, 2005.

[137] J. Bradley, G. Seidler, G. Cooper, M. Vos, A. Hitchcock, A. Sorini, C. Schlimmer and K. Nagle, "Comparative Study of the Valence Electronic Excitations of N2 by Inelastic X-Ray and Electron Scattering," *Phys. Rev. Lett.,* vol. 105, p. 053202, 2010.

[138] T. Gog, G. T. Seidler, D. M. Casa, M. H. Upton, J. Kim, S. Stoupin, K. P. Nagle, M. Balasubramanian, R. A. Gordon, T. T. Fister, S. M. Heald, T. Toellner, J. P. Hill, D. S. Coburn, Y.-J. Kim, A. H. Said, E. E. Alp, W. Sturhahn, H. Yavas and C. A. Bu, "Momentum-resolved Resonant and Nonresonant Inelastic X-ray Scattering at the Advanced Photon Source," *Synchrotron Radiat. News,* vol. 22, no. 6, p. 12, 2009.

[139] T. T. Fister, F. D. Vila, G. T. Seidler, L. Svec, J. C. Linehan and J. O. Cross, "Local Electronic Structure of Dicarba-closo-dodecarboranes C2B10H12," *J. Am. Chem. Soc.,* vol. 130, p. 925, 2008.

[140] R. Gordon, G. Seidler, T. Fister, M. Haverkort, G. Sawatzky, A. Tanaka and T. Sham, "High multipole transitions in NIXS: Valence and hybridization in 4f systems,," *Europhys. Lett.,* vol. 81, p. 26004, 2008.

[141] W.-K. Lee, K. Fezzaa, P. Fernandez, G. Tajiri and D. Mills, "Performance limits of indirectly cryogenically cooled silicon monochromators - experimental results at the APS," *J. Synchrotron Rad.,* vol. 8, pp. 22-25, 2001.

[142] J. P. Kirkland, V. E. Kovantsev, C. M. Dozier, J. V. Gilfrich, W. M. Gibson, Q.-F. Xiao and K. Umezawa, "Wavelength-dispersive x-ray fluorescence detector," *Rev. Sci. Instrum.,* vol. 66, p. 1410, 1995.

[143] J. Szlachetko, M. Cotte, J. Morse, M. Salomé, P. Jagodzinski, J.-C. Dousse, J. Hoszowska, Y. Kayser and J. Susini, "Wavelength-dispersive spectrometer for X-ray microfluorescence analysis at the X-ray microscopy beamline ID21 (ESRF)," *J. Synchrotron Rad.,* vol. 17, pp. 400-408, 2010.

[144] G. Srajer, L.H. Lewis, S.D. Bader, A.J. Epstein, C.S. Fadley, E.E. Fullerton, A. Hoffmann, J.B. Kortright, Kannan M. Krishnan, S.A. Majetich, T.S. Rahman, C.A. Ross, M.B. Salamon, I.K. Schuller, T.C. Schulthess, J.Z. Sun, "Advances in nanomagnetism via X-ray techniques," *J. Magn. Magn. Maer.,* vol. 307, pp. 1-31, 2006.

[145] D.J. Keavney, D. Wu, J.W. Freeland, E. Johnston-Halperin, D.D. Awschalom, J. Shi, "Element Resolved Spin Configuration in Ferromagnetic Manganese-Doped Gallium Arsenide," *Phys. Rev. Lett.,* vol. 91, pp. 187203-1-4, 2003.

[146] X.M. Cheng, D.J. Keavney, "Studies of nanomagnetism using synchrotron-based x-ray photoemission electron microscopy (X-PEEM)," *Rep. Prog. Phys,* vol. 75, no. 2, pp. 026501-1-30, 2012.

[147] J. Chakhalian, J.W. Freeland, H.-U. Habermeier, G. Cristiani, G. Khaliullin, M. van Veenendaal, B. Keimer, "Orbital Reconstruction and Covalent Bonding at an Oxide Interface,," *Science,* vol. 318, pp. 1114-1117, 2007.

[148] J. Chakhalian, J.W. Freeland, G. Srajer, J. Strempfer, G. Khaliullin, J.C. Cezar, T. Charlton, R. Dalgliesh, C. Bernhard, G. Cristiani, H.-U. Habermeier, B. Keimer, "Magnetism at the interface between ferromagnetic and superconducting oxides," *Nat. Phys.,* vol. 2, no. 4, pp. 244-248, 2006.

[149] I.V. Ovchinnikov and K.L. Wang, "Theory of electric-field-controlled surface ferromagnetic transition in metals," *Phys. Rev. B,* vol. 79, no. 2, pp. 020402-1-4, 2009.

[150] D. K. Pratt, W. Tian, A. Kreyssig, J. L. Zarestky, S. Nandi, N. Ni, S. L. Bud'ko, P. C. Canfield, A. I. Goldman and R. J. McQueeney, "Coexistence of Competing and Superconducting Phases in the Underdoped Ba(Fe0.953Co0.047)2As2 Compound Using X-ray and Neutron Scattering Techniques," *Physical Review Letters,* vol. 103, p. 087001, 2009.

[151] M. G. Kim, R. M. Fernandes, A. Kreyssig, J. W. Kim, A. Thaler, S. L. Bud'ko, P. C. Canfield, R. J. McQueeney, J. Schmalian and A. I. Goldman, "Character of the structural and magnetic phase transitions in the parent and electron-doped BaFe2As2 compounds," *Physical Review B,* vol. 83, p. 134522, 2011.

[152] J. P. C. Ruff, J.-H. Chu, K.-K. Kuo, R. K. Das, H. Nojiri, I. R. Fisher and Z. Islam, "Susceptibility Anisotropy in an Iron Arsenide Superconductor Revealed by X-Ray Diffraction in Pulsed Magnetic Fields," *Physical Review Letters,* vol. 109, p. 027004, 2012.

[153] J. Koo, C. Song, J.-S. Lee, J. Park, T.-H. Jang, C.-H. Yang, J.-H. Park, Y. H. Jeong, K.-B. Lee, T. Y. Koo, Y. J. Park, J.-Y. Kim, D. Wermeille, A. I. Goldman, G. Srajer, S. Park and S.-W. Cheong, "Non-Resonant and Resonant X-Ray Scattering Studies on Multiferroic TbMn2O5," *Physical Review Letters,* vol. 99, p. 197601, 2007.

[154] T. Lottermoser, T. Lonkai, U. Amann, D. Hohlwein, J. Ihringer and M. Fiebig, "Magnetic phase control by an electric field," *Nature,* vol. 430, p. 541, 2004.

[155] S. Nandi, A. Kreyssig, L. Tan, J. W. Kim, J. Q. Yan, J. C. Lang, D. Haskel, R. J. McQueeney and A. I. Goldman, "Nature of Ho Magnetism in Multiferroic HoMnO3," *Physical Review Letters,* vol. 100, p. 217201, 2008.

[156] Y. Wakabayashi, M. H. Upton, S. Grenier, J. P. Hill, C. S. Nelson, J.-W. Kim, P. J. Ryan, A. I. Goldman, H. Zheng and J. F. Mitchell, "Surface effects on the orbital order in the single-layered manganite La0.5Sr1.5MnO4," *Nature Materials,* vol. 6, p. 972, 2007.

[157] S. B. Wilkins, X. Liu, Y. Wakabayashi, J.-W. Kim, P. J. Ryan, H. Zheng, J. F. Mitchell and J. P. Hill, "Surface melting of electronic order in La0.5Sr1.5MnO4," *Physical Review B,* vol. 84, p. 165103, 2011.

[158] S. J. May, P. J. Ryan, J. L. Robertson, J.-W. Kim, T. S. Santos, E. Karapetrova, J. L. Zarestky, X. Zhai, S. G. E. te Velthuis, J. N. Eckstein, S. D. Bader and A. Bhattacharya, "Enhanced ordering temperatures in antiferromagnetic manganite superlattices," *Nature Materials,* vol. 8, p. 892, 2009.

[159] S. J. May, J.-W. Kim, J. M. Rondinelli, E. Karapetrova, N. A. Spaldin, A. Bhattacharya and P. J. Ryan, "Quantifying octahedral rotations in strained perovskite oxide films," *Physical Review B,* vol. 82, p. 014110, 2010.

[160] S. J. May, C. R. Smith, J.-W. Kim, E. Karapetrova, A. Bhattacharya and P. J. Ryan, "Control of octahedral rotations in (LaNiO3)n/(SrMnO3)m superlattices," *Physical Review B,* vol. 83, p. 153411, 2011.

[161] J. Liu, M. Kareev, B. Gray, J. W. Kim, P. J. Ryan, B. Dabrowski, J. W. Freeland and J. Chakhalian, "Strain-mediated metal-insulator transition in epitaxial ultrathin films of NdNiO3," *Applied Physics Letters,* vol. 96, p. 233110, 2010.

[162] J. W. Kim, Y. Choi, J. Kim, J. F. Mitchell, G. Jackeli, M. Daghofer, J. van den Brink, G. Khaliullin and B. J. Kim, "Dimensionality Driven Spin-Flop Transition in Layered Iridates," *Physical Review Letters,* vol. 109, p. 037204, 2012.

[163] S. Calder, V. O. Garlea, D. F. McMorrow, M. D. Lumsden, M. B. Stone, J. C. Lang, J.-W. Kim, J. A. Schlueter, Y. G. Shi, K. Yamaura, Y. S. Sun, Y. Tsujimoto and A. D. Christianson, "Magnetically Driven Metal-Insulator Transition in NaOsO3," *Physical Review Letters,* vol. 108, p. 257209, 2012.

[164] J. P. C. Ruff, Z. Islam, R. K. Das, H. Nojiri, J. C. Cooley and C. H. Mielke, "Robust but disordered collapsed-volume phase in a cerium alloy under the application of pulsed magnetic fields," *Physical Review B,* vol. 85, p. 024104, 2012.

[165] S. Haravifard, A. Banerjee, J. C. Lang, G. Srajer, D. M. Silevitch, B. D. Gaulin, H. A. Dabkowska and T. F. Rosenbaum, "Continuous and discontinuous quantum phase transitions in a model two-dimensional magnet," *Proceedings of the National Academy of Sciences,* vol. 109, p. 2286, 2012.

[166] Certified Scientific Software, "Welcome page," [Online]. Available: http://www.certif.com/index.html.

[167] G. Sutton and O. Biblarz, Rocket Propulsion Elements, New York: Wiley, 2001.

[168] V. Sick and B. Stojkovic, "Attenuation effects on imaging diagnostics of hollow-cone sprays," *Applied Optics,* vol. 40, no. 15, pp. 2435-2442, 2001.

[169] P. Leick, R. Grzeszik, S. Arndt and S. Wissel, "Suppression of Multiple Scattering Using Structures Light Sheets - A First Assessment for Diesel and Gasoline Spray Visualization," in *24th European Conference on Liquid Atomization and Spray Systems*, Estoril, Portugal, 2011.

[170] T. Heindel, "A Review of X-Ray Flow Visualization With Applications to Multiphase Flows," *Journal of Fluids Engineering,* vol. 133, no. 7, p. 074001, 2011.

[171] E. Robert, S. Dozias, C. Cachoncinlle and J. Pouvesle, "Table-top flash X-ray diagnostics of dodecane sprays," in *23rd Annual Conference on Liquid Atomization and Spray Systems*, Brno, Czech Republic, 2010.

[172] A. G. MacPhee, M.W. Tate, C.F. Powell, Y. Yong, M.J. Renzi, A. Ercon, S. Narayanan, E. Fontes, J. Walther, J. Schaller, S.M. Gruner, J. Wang, "X-ray Imaging of Shock Waves Generated by High-Pressure Fuel Sprays," *Science,* vol. 295, p. 1261, 2002.

[173] A. Kastengren, C.F. Powell, D. Arms, E.M. Dufresne, H. Gibson and J. Wang, "The 7BM beamline at the APS: a facility for time-resolved fluid dynamics measurements," *J. Synchrotron Rad. ,* vol. 19, p. 654, 2012.

[174] Harder, Ian Robinson and Ross, "Coherent X-ray diffraction imaging of strain at the nanoscale," *Nat Mater,* vol. vol. 8, no. 4, pp. 291-298, 2009.

[175] Ashish Tripathi, Jyoti Mohanty, Sebastian H. Dietze, Oleg G. Shpyrko, Erik Shipton, Eric E. Fullerton, Sang Soo Kim, and Ian McNulty,, "Dichroic coherent diffractive imaging," *Proceedings of the National Academy of Sciences,* vol. vol. 108, no. 33, pp. 13393-13398, 2011.

[176] P. Fernandez, W. Lee, D. Mills, G. Tajiri and L. Assoufid, "Double-undulator tests of a diamond monochromator at the Advanced Photon Source," *Nuclear Instruments and Methods in Physics Research A,* vol. 459, pp. 347 - 353, 2001.

[177] W.-K. Lee, P. Fernandez and D. M. Mills, "Performance limits of direct cryogenically cooled silicon monochromators ± experimental results at the APS," *J. Synchrotron Rad.,* vol. 7, pp. 12 - 17, 2000.

[178] W.-K. Lee, K. Fezzaa, P. Fernandez, G. Tajiri and D. Mills, "Performance limits of indirectly cryogenically cooled silicon monochromators - experimental results at the APS," *J. Synchrotron Rad.,* vol. 8, pp. 22 - 25, 2001.

[179] G. Tajiri, W.-K. Lee, P. Fernandez, D. Mills, L. Assoufid and F. Amirouche, "Nonlinear thermal-distortion predictions of a silicon monochromator using the finite element method," *J. Synchrotron Rad.,* vol. 8, pp. 1140 -1148, 2001.

[180] N. Kujala, A. Macrander, M. Ramanathan, E. Dufresne, G. Navrotski, S. Marathe, L. Assoufid, D. Mills and D. Mancini, "High-Heat-Load Studies of Cryogenically Internally Cooled Silicon Double Crystal Monochromators," in *Synchrotron Radiation Instrumentation* , 2012.

[181] A. Khounsary, R. Fischer and P. Strons, "Geometry Optimization for Cryogenically Contact-Cooled Silicon Monochromators for APS Upgrade," (APS-U Internal Report), 2012.

[182] "GlidCop® is a registered trademakk of SCM Metal Products, Inc.," Research Triangle Park, NC, USA.

[183] Lai, B.; Yun, W. B.; Legnini, D.; Xiao, Y.; Chrzas, J.; Viccaro, P. J.; White, V.; Bajikar, S.; Denton, D.; Cerrina, F.; Di Fabrizio, E.; Gentili, M.; Grella, L.; Baciocchi, M., "Hard x-ray phase zone plate fabricated by lithographic techniques," *Applied Physics Letter,* vol. 61, no. 16.

[184] Holmberg, J. Reinspach, M. Lindbom, E. Chubarova, M. Bertilson, O. von Hofsten, D. Nilsson, M. Selin, D. Larsson, P. Skoglund, U. Lundström, P. Takman, U. Vogt, and H. M. Hertz, "Towards 10-nm Soft X-ray Zone Plate Fabrication," *The 10th International Conference on X-ray Microscopy, AIP Conf. Proc. 1365,* pp. 18-23, 2011.

[185] W. Chao, J. Kim, S. Rekawa, P. Fischer, and E. H. Anderson, "Demonstration of 12 nm resolution Fresnel zone plate lens based soft X-ray microscopy," *Opt. Express,* vol. 17, no. 20, p. 17669–17677, 2009.

[186] Tsung-Yu Chen, Yu-Tung Chen, Cheng-Liang Wang, Ivan M. Kempson, Wah-Keat Lee, Yong S. Chu, Y. Hwu, and G. Margaritondo, "Full-field microimaging with 8 keV X-rays achieves a spatial resolutions better than 20 nm," *Optics Express,* vol. 19, no. 21, pp. 19919-19924, 2011.

[187] K. Jefimovs, J. Vila-Comamala, T. Pilvi, J. Raabe, M. Ritala, C. David, "Zone-doubling technique to produce ultrahigh-resolution X-ray optics, Phys. Rev. Lett. 99 (2007) 264801.".

[188] J. Vila-Comamala, S. Gorelick, E. Färm, C. M. Kewish, A. Diaz, R. Barrett, V. A. Guzenko, M. Ritala, C. David, "Ultra-high resolution zone-doubled diffractive X-ray optics for the multi-keV regime," *Optics Express,* vol. 19, pp. 175-184, 2011.

[189] J. Vila-Comamala, A. Diaz, M. Guizar-Sicairos, A. Mantion, A. Menzel, C. M. Kewish, O. Bunk, C. David, "Characterization of high-resolution diffractive X-ray optics by ptychographic coherent diffractive imaging," *Optics Express,* vol. 19, pp. 21333-21344, 2011.

[190] J. Vila-Comamala, S. Gorelick, V. A. Guzenko, C. David, "3-D Nanostructuring of hydrogen silsesquioxane resist by 100 keV electron beam lithography," *J. Vac. Sci. Technol. ,* vol. B29, p. 06F301, 2011.

[191] J. Maser, B. Lai, W. Yun, S. D. Shastri, Z. Cai, W. Rodrigues, S. Xu, E.Trackhtenberg, "Near-field stacking of zone plates in the x-ray range," *Proc. of SPIE,* vol. 4783, p. 74–81, 2002.

[192] S. Werner, S. Rehbein, P. Guttman, S. Heim, G. Schneider, "Towards stacked zone plates, J. Phys.: Conf. Ser. 186 (2009) 012079.".

[193] J. Vila-Comamala, S. Gorelick, E. Färm, C. M. Kewish, A. Diaz, R. Barrett, V. A. Guzenko, M. Ritala, C. David, "Ultra-high resolution zone-doubled diffractive X-ray optics for the multi-keV regime, Optics Express 19 (2011) 175-184.".

[194] "APS Upgrade Conceptual Design Report," May 2011.

[195] X. Lou, C. Adelmann, S. A. Crooker, E. S. Garlid, J. Zhang, K. S. M. Reddy, S. D. Flexner, C. J. Palmstrøm, and P. A. Crowell, "Nat Phys," vol. 3, p. 197, 2007.

[196] C. Awo-Affouda, O. M. J. van t'Erve, G. Kioseoglou, A. T. Hanbicki, M. Holub, C. H. Li, and B. T. Jonker, *Appl. Phys. Lett.,* vol. 94, p. 102511, 2009.

[197] M. Ciorga, A. Einwanger, U. Wurstbauer, D. Schuh, W. Wegscheider, and D. Weiss, "Phys. Rev.," vol. B 79, p. 165321, 2009.

[198] S. A. Crooker, E. S. Garlid, A. N. Chantis, D. L. Smith, K. S. M. Reddy, Q. O. Hu, T. Kondo, C. J. Palmstrøm, and P. A. Crowell, "Phys. Rev.," vol. B 80, p. 041305, 2009.

[199] G. Salis, A. Fuhrer, R. R. Schlittler, L. Gross, and S. F. Alvarado, "Phys. Rev.," vol. B 81, p. 205323, 2010.

[200] I. Appelbaum, B. Q. Huang, and D. J. Monsma, "Nature," vol. 447, p. 295 , 2007.

[201] B. Huang, D. J. Monsma, and I. Appelbaum,, *Phys. Rev. Lett. ,* vol. 99, p. 177209, 2007.

[202] O. M. J. van t' Erve, A. T. Hanbicki, M. Holub, C. H. Li, C. Awo-Affouda, P. E. Thompson, and B. T. Jonker, "Appl. Phys. Lett.," vol. 91, p. 212109 , 2007.

[203] K. Gilmore, Y. U. Idzerda, and M. D. Stiles, "Phys. Rev. Lett.," vol. 99, p. 027204, 2007.

[204] M. Fahnle and D. Steiauf, "Phys. Rev.," vol. B 72, p. 064450, 2005.

[205] J. Slonczewski, J. Magn, "Magn. Mater," vol. 195, p. L261, 1999.

[206] V. Kambersk´y, "Canadian Journal of Physics," vol. 48, p. 2906, 1970.

[207] "N. Pontius, T. Kachel, C. Schüßler-Langeheine, W. Schlotter, M. Beye, F. Sorgenfrei, C. F. Chang, A. Föhlisch, W. Wurth, P. Metcalf, I. Leonov, A. Yaresko, N. Stojanovic, M. Berglund, N. Guerassimova, S. Düsterer, H. Redlin, H. A. Dürr, (submitted).".

[208] D. Polli, et al.,, "Nature Mater," vol. 6, p. 643, 2007.

[209] N. Gedik, D.-S. Yang, G. Logvenov, I. Bozovic, A. Zewail, "Science," vol. 316, p. 425, 2007.

[210] M. Borland, "Phys. Rev. ST Accel. Beams," vol. 8, p. 074001 , 2005.

[211] B.X. Yang, A.H. Lumpkin, E.C. Landahl et al., "Proc. of PAC07, p 1156," 2007. [Online]. Available: http://www.JACoW.org.

[212] B. Yang, D. Keavney, and E. Dufresne, "APS Technical Note DIAG-TN-2010-01," 2010.

[213] M. Hettrick, J. Underwood, P. Batson, and M. Eckart, "Appl. Opt.," vol. 27, p. 200, 1988.

The Advanced Photon Source, an Office of Science User Facility operated for the U.S. Department of Energy (DOE) Office of Science by Argonne National Laboratory, is supported by the DOE under Contract No. DE-AC02-06CH11357.

rev. 20121127

Advanced Photon Source Upgrade Project

Preliminary Design Report

December 2012

Chapter 5: Enabling Technical Capabilities

Table of Contents

List of Figures

List of Tables

Acronyms and Abbreviations

ADA	Americans with Disabilities Act
AES	APS Engineering Support Division
BECS	Bioexhaust Containment System
BeW	beryllium window
BIV	beamline isolation valve
BM	bending magnet
BMPS	bending magnet photon shutter
BSL	biosafety laboratory
BSL-3	biosafety level 3
CDR	Conceptual Design Report
CSI	Construction Specifications Institute
CU	canted undulator
CUFE	canted undulator front end
CVD	chemical vapor deposition
DS	Downstream
EPS	Equipment Protection System
FE	front end
FEA	finite element analysis
FEEPS	Front-End Equipment Protection System
FEV	Front end valve
FEv1.2R	Front-end version 1.2 Retrofit
FM1, FM2	first fixed mask, second fixed mask, etc.
FOE	first optical enclosure
GRID-XBPM	grazing-incidence insertion device x-ray beam position monitor
HHL	high heat load
HHLFE	high-heat-load front end

HVAC	heating, ventilation, and air conditioning
IBC	International Building Code; Institutional Biosafety Committee (section 5.3.3)
ICD	interface control document
ID	insertion device
IM1, IM2	intensity monitor 1, intensity monitor 2
LED	light-emitting diode
LN_2	liquid nitrogen
LOM	laboratory/office module
LPPS	low power photon shutter
LSSCU	long straight section canted undulator
LSSCUFE	long straight section canted undulator front end
MEP	mechanical, electrical, and plumbing
OFHC	oxygen-free high conductivity
PHC-AB	Pin hole camera – upstream top A and upstream bottom B
PHC-CD	Pin hole camera –downstream top C and downstream bottom D
PMU	permanent magnet undulator
PS, PS1, PS2	photon shutter, photon shutter 1, photon shutter 2
PSS	Personnel Safety System
PVC	polyvinyl chloride
RSS	Radiation Safety System
SCU	superconducting undulator
SPX	short-pulse x-ray
SPXCU	short-pulse x-ray canted undulator
SPXCUFE	short-pulse x-ray canted undulator front end
SR	storage ring
SS, SS1, SS2	safety shutter, safety shutter 1, safety shutter 2
SV	slow valve
UA	Undulator A
UHV	ultra-high vacuum
UL	Underwriter Laboratories, Inc.
UPS	uninterrupted power supply
US	Upstream

vM	von Mises
WBS	Work Breakdown Structure
WFI	wide-field imaging
XBPM	x-ray beam position monitor
XBPM1, XBPM2	first x-ray beam position monitor, second x-ray beam position monitor
XRF	x-ray fluorescence

5 Enabling Technical Capabilities

5.1 Overview

The Advanced Photon Source (APS) Upgrade Project covers various aspects of the current APS from the accelerator to the beamlines to infrastructure. To fully support the APS Upgrade main scope, the enabling technical capabilities section encompasses areas that will supplement the other two areas of Project scope, namely the accelerator (x-ray beam position monitors) and beamline (physical infrastructure and front ends) upgrades.

5.1.1 Front Ends

The accelerator in this context is defined as mainly the storage ring, where the electron beam orbits. A beamline is usually defined as the section where the x-ray beam travels to the experiment. The front end, in this context, is the portion of the beamline inside the storage ring enclosure; it is the first element to "see" the x-ray photon beam.

The APS storage ring has been operating at 7 GeV with 100 mA of stored beam for the past 15 years. There are 70 locations around the ring for beamlines. Of these locations, 35 are for taking a fan of bending magnet (BM) radiation and the remaining 35 are for insertion device (ID) radiation. The BM front end was designed to handle 300 mA of stored beam. The ID front ends were originally designed to handle 100 mA of stored beam from a typical undulator insertion device 2.4-m long with a 3.3-cm period. Over the past few years, newer ID front ends, capable of handling 4.8-m-long devices and higher currents of 200 mA, have been designed and installed in some locations in the storage ring. A new canted undulator (CU) front end that handles two beams separated by about 1 mrad was also designed and installed at several beamlines.

The APS Upgrade Project scope calls for operating the storage ring routinely at 150 mA and 7 GeV. This will require upgrading the existing front ends to handle the higher currents. The Project scope also involves converting some beamlines to the aforementioned canted geometry to provide two independent beams from a single location.

One goal of the Project is to enhance beam stability. One of the elements for increased beam stability is the next-generation x-ray beam position monitor (XBPM). The next-generation XBPM is a component of the front end. The recently designed high-heat-load (HHL) front end and CU front end (CUFE) have been modified to accommodate the next-generation XBPM.

The Project scope calls for replacing some of the existing front ends with either HHL front ends equipped with next-generation XBPMs or with CU front ends with next-generation XBPMs. Existing front ends

that are not affected by beamline upgrades will be retrofitted to allow for 150-mA operation. More details of the complete scope for the Project are discussed throughout this chapter.

5.1.2 Physical Infrastructure

The APS experiment hall can accommodate a maximum beamline length of ~75 m from the center of a straight section in the storage ring. Most of the beamlines end well before the sector boundary, at about 60 m from the source.

The Project scope includes building a long beamline extending to about 250 m from the source. This beamline, to be used for wide-field imaging, will be located in 20-ID and is described in Chapter 4. Construction of the long beamline requires modification to the existing APS experiment hall. In addition, an external building will be constructed to house the experiment station at 250 m from source. This beamline will traverse the experiment hall corridor, enter the laboratory/office module, and exit the APS main building. A new beam transport corridor to connect the APS building with the external building will be constructed.

All activities related to the construction of the external building, the transport corridor, and all modifications to the APS experiment hall are covered later in this chapter. Details of the construction and modification to the existing infrastructure will also be discussed later in this chapter.

5.1.3 Enabling Technical Capabilities Scope and Work Breakdown Structure

The scope for Enabling Technical Capabilities with its associated Work Breakdown Structure (WBS) is listed in Table 5-1.

Table 5-1: Enabling Technical Capabilities Scope.

WBS	PDR Section	Description	Quantity
U1.05.02	5.2	Front End Upgrades	
U1.05.02.02	5.2.1	Front End for High Heat Load Inline Undulators (HHLFE)	7
U1.05.02.03	5.2.2	Front End for Canted Undulators (CUFE)	6
U1.05.02.04	5.2.4.1	Front End for Long Straight Section Canted Undulators (LSSCUFE)	1
U1.05.02.06	5.2.3	Front End v1.2 Retrofit	7
U1.05.02.08	5.2.4.2	Front End for SPX Canted Undulators (SPXCUFE)	1
U1.05.02.11	5.2.1.3	Next Generation X-ray BPM System for HHL	7
U1.05.02.12	5.2.2.3	Next Generation X-ray BPM System for CU	6
U1.05.02.13	5.2.4	Next Generation X-ray BPM System for LSSCU	1
U1.05.02.15	5.2.4	Next Generation X-ray BPM System for SPXCU	1
U1.05.02.20	5.2.5	Front End Installations	23
U1.05.03	5.3	Site Services & Utilities	
U1.05.03.01	5.3.2	Wide Field Imaging Beamline Facility	
U1.05.03.04	5.3.3	Facility Enhancement for High Flux Pump-Probe (Sector 14)	

5.1.4 Interdependencies

The APS Upgrade has been divided into three technical areas: accelerator upgrades, beamline upgrades, and enabling technologies. The technical scopes in these three areas are discussed in Chapters 3, 4, and 5, respectively. There are numerous dependencies between the three areas. In addition, the APS is an operating facility and numerous APS Upgrade activities are dependent on APS Operations.

The dependencies between the areas are described in the Project Interface Control Documents (ICDs). The interdependencies, as and when identified, will be captured in the ICDs. To give a few examples: a front end is a prerequisite for a beamline. The specific beamline needs are taken into consideration for the choice of the front end. In addition, the front end must have the source defined by the type of ID to be installed by the accelerator upgrade. Installations of the front ends are coordinated with the APS accelerator maintenance cycles.

Construction of the external building will meet the requirements for the Wide Field Imaging (WFI) beamline. Physical infrastructure activities rely on close coordination with numerous outside entities, namely external contractors and Argonne Facilities Management & Services. All such activities will be captured in the ICDs.

5.2 Front End Upgrades

A major goal of the Project is to increase the flux and brightness of x-rays delivered by the APS. One way to do this is via higher electron beam current, which will be increased from 100 mA to 150 mA. Another goal of the Project is to improve beam stability by integrating the next-generation XBPM system into new insertion device (ID) front ends (FEs). Some programs require longer undulators, several in-line IDs, or multiple undulators in canted configuration. Such changes will significantly increase the x-ray power loads on front-end components. So, an essential enabling condition is an upgrade of those components. In this section, the upgrades of FEs will be discussed in detail.

Following the beamline Roadmap, there will be a total of 22 ID front-end upgrades. Out of the 22 FEs, 20 belong to one of the following first three types. The other two FEs are one-of-a-kind. The upgrade for ID FEs is summarized as follows:

1. **High-heat-load front end (HHLFE):** For two inline undulators; a grazing-incidence insertion device (GRID) XBPM will be integrated into this front end. The Project includes seven HHLFEs.
2. **Canted undulator front end (CUFE):** For two undulators in canted configuration; a GRID-XBPM will be integrated into the front end. The Project includes six CUFEs.
3. **Front-end version 1.2 retrofit (FEv1.2R):** For a single undulator to operate at 150 mA; certain components in the original version of the FEs will be replaced by components capable of 150-mA operation. The original XBPM will remain for these FEs. The Project includes seven FEv1.2Rs.
4. **Long straight section canted undulator front end (LSSCUFE):** This front end is specifically designed for beamline 1-ID, with a long straight section that can potentially house multiple undulators in the canted configuration. One branch will

have 1 or 2 superconducting undulators (SCUs) and another branch will have a revolver of permanent magnet undulators (PMUs). This front end will be a special version of the CUFE.

5. **Short-pulse x-ray canted undulator front end (SPXCUFE):** This front end is for a short-pulse x-ray (SPX) beamline in the canted configuration and is specially designed for beamline 6-ID. This front end is a special version of the CUFE, with one branch requiring a large vertical exit aperture.

The function of the beamline FEs is to constrain the synchrotron radiation and bremsstrahlung radiation to a defined opening angle and to provide a means of stopping and absorbing the radiation upstream of the ratchet wall in order to allow personnel access to equipment downstream in the first optical enclosure (FOE). The beamline FEs are located primarily within the storage ring (SR) enclosure. The major components of the beamline FEs are photon masks and shutters; beam-defining apertures, bremsstrahlung collimators and safety shutters; vacuum valves for machine protection and isolation; XBPMs and other beam diagnostic devices; and beryllium or chemical vapor deposition (CVD) diamond windows and filters that isolate the vacuum systems while transmitting x-rays.

The FE starts at the SR exit valve and extends to the beamline isolation valve (BIV). The usable length of the front-end area in the tunnel is about 7.6 m (24.9 ft) for the ID beamlines and 13.3 m (43.6 ft) for the bending magnet (BM) beamlines. The FE also includes the ancillary systems such as vacuum pumps and gauges; provision for residual gas analysis; utilities distribution including water, compressed air, and electrical power; the personnel safety system (PSS); and the front-end equipment protection system (FEEPS).

The HHLFE, CUFE, and FEv1.2R account for 20 out of the total 22 upgraded front ends. These front end designs have been developed beyond the preliminary design level and are described in detail below. The LSSCUFE and SPXCUFE are still in the conceptual design stage and are described briefly.

5.2.1 High-Heat-Load Front End

The original high-heat-load FE (HHLFE) was designed in 2004 for the Inelastic X-ray Scattering beamline (30-ID) and the nanoprobe beamline (26-ID). The original HHLFE design report is in the APS Integrated Content Management System as “High Heat Load Front End Design Report” [1]. The original HHLFE was equipped with two photoemission-based XBPMs, each measuring 250 mm in length. The redesign of the HHLFE is motivated by the need to fit the GRID-XBPM into the FE. The GRID-XBPM is the main component of the next-generation XBPM system and is about 1.4 m in length. To fit the GRID-XBPM into the FE, the photon shutter 1 (PS1) has to be replaced with a smaller footprint low power photon shutter (LPPS) to create the needed space. The radiation safety and operational logic changes necessitated as a result of removing the PS1 will be discussed in this Chapter.

5.2.1.1 HHLFE Design Goal

The design criteria for integrating the next-generation XBPM system into the new HHLFE are:

1. Maintain the high-heat-load capability the same as the original HHLFE.

2. Reuse the design of the photon shutter and safety shutter to maintain compatibility with the original HHLFEs, with the least possible change to components.
3. The aperture in the GRID-XBPMs will not be included in radiation safety evaluations for the front end.
4. Design around the existing components such as the photon shutter, exit mask, Be window, pump chambers to fit in the intensity monitor 1 (IM1), intensity monitor 2 (IM2), and XBPM2.
5. Modify the logic in the front-end PSS and FEEPS so they work with the low power photon shutter.

5.2.1.2 Functional Description of the New HHLFE with Next-Generation XBPM System

A comparison of the new and existing HHLFE layouts is shown in Figure 5-1. The FE begins with the storage ring exit valve, which isolates the SR vacuum from the front-end vacuum, and ends with the BIV, which isolates the FE vacuum from the beamline vacuum. The functional description of each component for the new HHLFE is as follows:

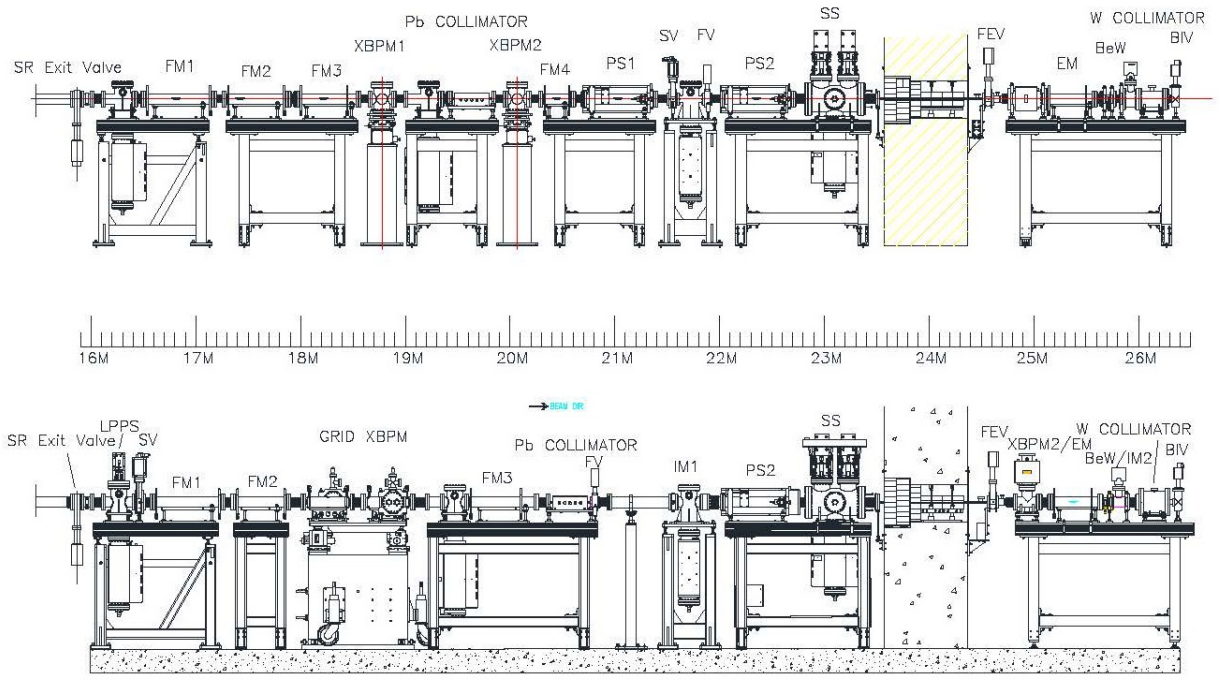

Figure 5-1: HHLFE layout comparison. The top figure is the existing HHLFE layout and the bottom figure is the new HHLFE layout with the next-generation XBPM system.

Exit valve: This is an all-metal valve and is ultra-high-vacuum (UHV) tight. It isolates the storage ring vacuum from the FE. This valve belongs to the SR vacuum control system and is in the closed position before commissioning of the FE.

Pre-mask: The function of the pre-mask is to block the dipole radiation from the downstream bending magnet such that it does not hit the uncooled flange of the first fixed mask at normal incidence. For each SR sector there are two bending magnets that bend the electron beam by 9° per sector. The radiation from the upstream "B" dipole magnet is extracted and used as the BM beamline, while the radiation from the downstream "A" dipole magnet is not used. Part of the radiation from the "A" dipole travels down the same pipe that contains the ID beam.

Low power photon shutter: The low power photon shutter (LPPS) is a new component added to the insertion device FE due to the removal of the photon shutter 1. The purpose of the LPPS is to protect the vacuum valves from the heat load from bending magnet radiation. The LPPS is a cooled copper block capable of stopping BM radiation only. It cannot withstand the heat load from the undulator beam. In normal operating condition, the LPPS is in the open position to allow the beam to pass. The open limit switches are interlocked in the FEEPS, to protect the LPPS from thermal damage due to the undulator beam.

Slow valve: The slow valve (SV) is an all-metal, remotely actuated UHV valve that seals to isolate the ring from any vacuum breach in the FE. The closing time is usually 1-2 seconds. However, it cannot accept the heat load from the photon beam and therefore has to be interlocked to close only when the beam is dumped or the LPPS is closed. Compared to the original HHLFE, the position of the SV was moved from the middle of the FE to the upstream end of the FE to provide the operational convenience described in section 5.2.1.8.

First fixed mask: The design of the first fixed mask (FM1) is unchanged compared to the original HHLFE. The FM1 is used to confine the x-ray beam and reduce the beam missteering envelope. To avoid corner stress concentration due to high power density, the FM1 only confines the beam horizontally. The vertical aperture is wide open to allow for beam passage.

Second fixed mask: The second fixed mask (FM2) is slightly changed compared to the original HHLFE FM2. The FM2 also only confines beam horizontally. The new FM2 has a larger horizontal aperture of 10.4 mm, compared to 8 mm in the original FM2. The larger exit aperture in the new FM2 allows full view of the x-ray beam by the GRID-XBPM. The new FM2 has the same beam taper angle as the original FM2, so the thermal performance is not changed. A model of the FM2 is shown in Figure 5-2.

GRID-XBPM: Refer to section 5.2.1.3 for a description of the GRID-XBPM.

Pump chamber: The pump vacuum chamber supports the ion pump for the GRID-XBPM upstream and third fixed mask (FM3) downstream. Installing the pump below the beam path occupies the least space along the beam.

Third fixed mask: The FM3 collimates the synchrotron beam in both the horizontal and vertical directions. The design is modified from the original HHLFE. The mask is essentially two vertical plates forming a V-shape. The taper angle is determined by thermal analysis. The outlet aperture can be any size without changing the taper angle. The model of the FM3 is shown in Figure 5-3.

Lead collimator: The function of the lead collimator is to reduce the bremsstrahlung cone size.

Fast valve: The fast valve (FV) is an all-metal, remotely actuated UHV valve that reduces the conductance during a vacuum breach in the beamline. The closing time is of the order of few milliseconds. The fast valve is triggered by two sensors located in the exit table and in the safety shutter. The fast valve provides the time needed fro the slow valve to close in the case of a vacuum breach. The trigger mechanism for the fast valve is an independent unit and will automatically trigger a beam dump.

Space reserved for beamline optics: About half a meter of space has been reserved for beamline use in the future, for example, for pinhole slits or other optical elements as needed.

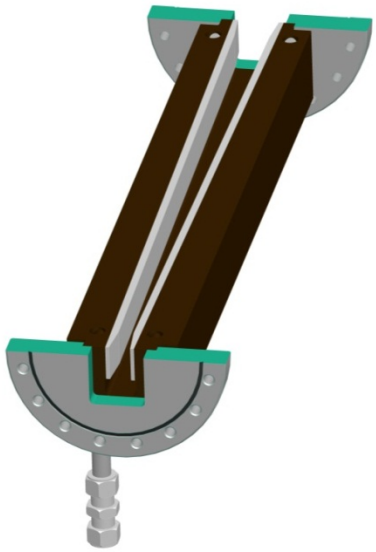

Figure 5-2: The HHLFE second fixed mask.

Figure 5-3: The HHLFE third fixed mask.

Pump Chamber/Intensity Monitor 1: The pump chamber/IM1 provides pump support and housing for the next-generation XBPM intensity monitor 1. See the next section for a description of IM1.

Photon Shutter 2: The photon shutter 2 (PS2) design is unchanged from the original HHLFE. To close the beam, PS2 pivots towards the inboard side. The photon shutter has redundant springs, with one inside the air cylinder and one outside the air cylinder to ensure that the shutter is closed in the event of lost air in the air cylinder.

Safety Shutter: The safety shutter (SS) consists of two redundant UHV-compatible tungsten block assemblies. Each block assembly is 200 mm long. When the safety shutter is closed, it blocks the bremsstrahlung radiation completely. When the safety shutter is opened, it works as a collimator for the bremsstrahlung cone. Each tungsten block assembly consists of upper and lower blocks. The lower block is fixed in the vacuum tank. The upper block is mounted on a pneumatic actuator, and in the closed position, it fits into the lower block. The SS is not cooled, so it is interlocked to PS2. In operation, the SS closes after PS2 is closed and opens before PS2 is opened.

Wall Collimator: The function of the wall collimator is to reduce the bremsstrahlung cone size.

Front End Valve: The front end exit valve (FEV) is an all-metal valve that isolates the FE components inside the ratchet wall from downstream beamline components. The FEV valve is closed for installation of the exit table.

Pump Chamber/XBPM2: The pump chamber/XBPM2 provides pump support and housing for the components of the XBPM2. Refer to section 5.2.1.3 for a description of the XBPM2.

Exit Mask: This mask defines the exit aperture of the FE. The mask design is similar to FM3; it consists of two vertical planes forming a “V” shape. The aperture can be any aperture specified by a beamline without affecting its thermal capability. The maximum exit mask horizontal aperture is 3.0 mm due to restriction from the GRID-XBPM. The maximum vertical aperture is 2.0 mm but typically 1.0 mm is sufficient.

Beryllium window (BeW)/Intensity Monitor 2: The Be window has a 0.5-mm-thick polished Be foil. It has a built-in filter holder to hold a 0.2-mm CVD diamond filter if needed for thermal protection. The downstream end of the window has a cone-shaped cut to allow scattering from the BeW to enter intensity monitor 2. See the next section for a description of IM2.

Exit Collimator: The function of the exit collimator is to cut down the size of the bremsstrahlung cone especially in the horizontal direction. The tungsten block size is enlarged compared to the original HHLFE to compensate the effect of the first lead collimator having moved downstream by 940 mm.

Beamline Isolation Valve (BIV): This is the last component in the FE. The BIV isolates the FE vacuum from the beamline vacuum. The BIV is installed regardless of whether or not the FE has a window; if the window is removed, a pump chamber will be installed in the space previously occupied by the window and a bellows.

5.2.1.3 Description of the Next-Generation XBPM System

Beam stability improvement is an important part of the Project. Improved beam stability will be supported by a new feedback system and several new/improved diagnostics, including the next-generation XBPM. The next-generation XBPM consists of four components: (1) the first grazing-incidence insertion device x-ray beam position monitor (called GRID-XBPM), (2) beam intensity monitor 1 (IM1), (3) the second XBPM (XBPM2), and (4) beam intensity monitor 2 (IM2).

5.2.1.3.1 GRID-XBPM

The XBPMs have been useful for monitoring beam-pointing angles due to their location far from the undulator source. However, the widely used, photo-emission-based XBPMs are sensitive to soft radiation generated by the bend magnets and corrector magnets upstream and downstream of the undulator sources. The steering of the electron beam through the undulator moves these background beams on the XBPM even when the undulator beam is centered at the XBPM. The movements create false readings and reduce the effectiveness of carefully designed background subtraction algorithms, especially when the undulator is at a larger gap and emits lower power.

The GRID-XBPM, however, derives the x-ray beam position from the x-ray fluorescence (XRF) footprint on the limiting apertures of the beamline by using two absorbers on the inboard and outboard sides of the beam axis, as shown in Figure 5-4. The difference in their XRF intensities gives the horizontal position readout. By combining the two optical components of the beamline, the problem of their possible misalignment from each other can be eliminated, thus allowing minimization of the aperture and the transmitted x-ray power on user optics. In addition to these advantages, the GRID-XBPM can also be implemented to measure the center-of-mass of the XRF footprint when pinhole-camera-like optics are used for vertical position and tilt readout.

The GRID-XBPM assembly is positioned downstream of FM2 and has the following design features.

1. The assembly consists of two identical vertical water-cooled absorber plates facing in opposite directions and made of GlidCop® explosion-bonded to oxygen-free high conductivity (OFHC) copper. The incidence angle of the beam to the plate is 1.0° and the total length of the active surface of each plate is 380 mm.
2. A beryllium window is used to separate the main chamber from the detector module, so the latter can be serviced without venting the FE. The design of the detector module follows normal UHV design practices. In the event of beryllium window failure, the GRID-XBPM continues to function with no impact on FE and beamline operations.
3. In the horizontal direction, the travel should be sufficient to allow decent overlap of the XBPM aperture with two edges of the FM3 so that beam-based alignment can be performed.

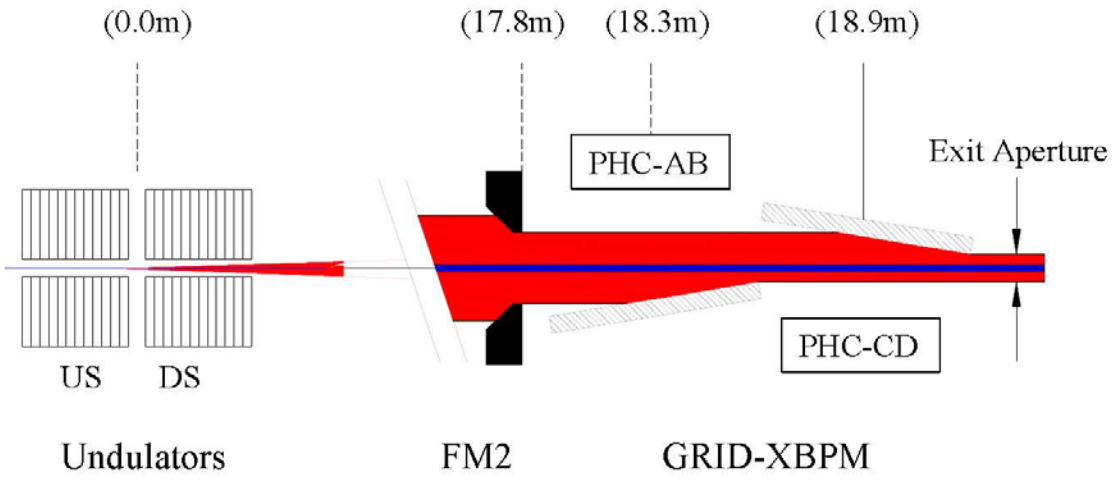

Figure 5-4: Schematic principle of the GRID-XBPM assembly (beam is from the left to the right).

4. The vertical beam positions are obtained using pinhole-camera-based center-of-mass measurements. The pinhole camera consists of one imaging aperture and a pair of photodiode modules. The imaging aperture is placed inside the main GRID-XBPM chamber. A pre-aperture with a slightly larger dimension is placed upstream of the imaging aperture to minimize the power load and thermal expansion of the imaging aperture proper. Each detector module contains two silicon photodiode assemblies with steel down-converters that read vertical positions of the undulator beam.
5. The chamber wall is made of thick OFHC copper with water-cooled channels built in. Cooling water with a constant temperature is to be used to maintain the temperature stability of the chamber. Cooling water will also be used to regulate the temperature of the XBPM support structure. Furthermore, a real-time position monitor will be used to maintain the long-term stability of the XBPM.
6. At the downstream end, the absorber is held rigidly for a well-defined exit aperture. At the upstream end, it is held on a flexure hinge so that it can expand freely without distorting the chamber.

Figure 5-5 shows the solid model of the GRID-XBPM assembly. The exploded view on the left of the figure shows the XBPM motion sensor mounting rods, which are made of Invar.

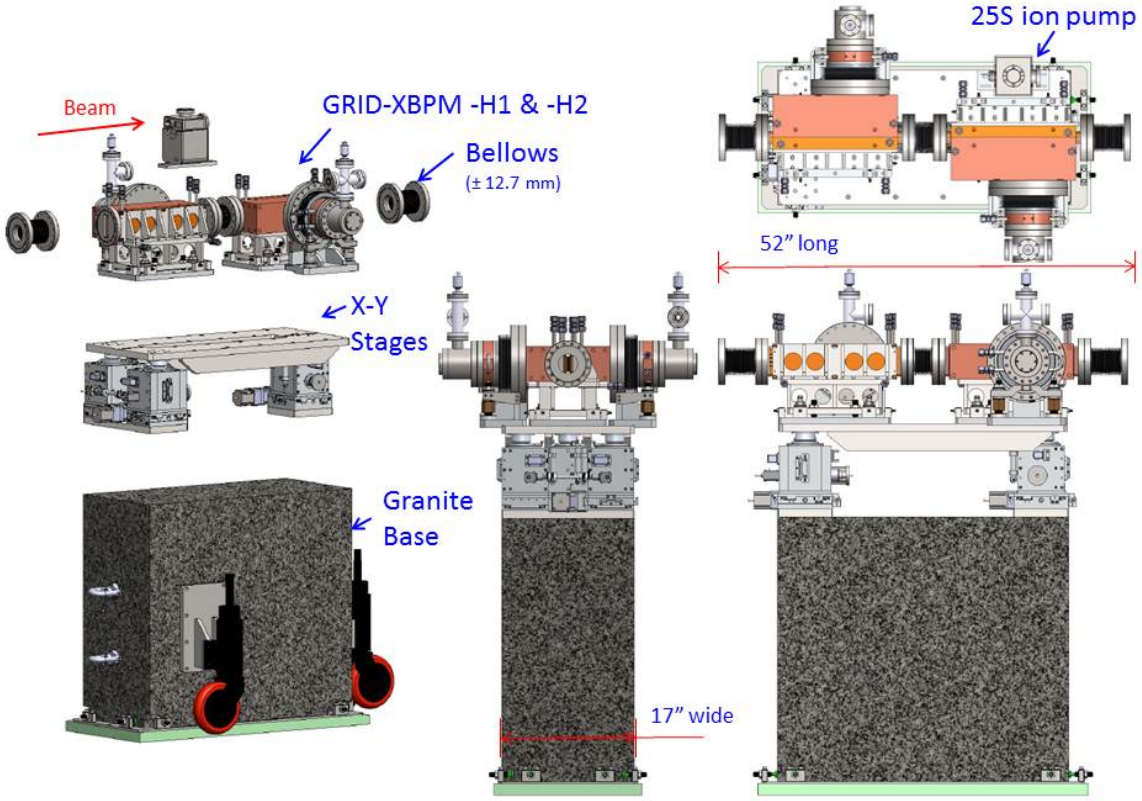

Figure 5-5: HHLFE GRID-XBPM assembly (beam is from the left to the right).

5.2.1.3.2 Intensity Monitor 1

The first beam intensity monitor (IM1) is an alignment aid inside the FE. The intensity profile of the beam can be measured using the fluorescence and Compton-scattered x-ray photons striking the surface of photon shutter 2.

The IM1 detector assembly is located inside the pump chamber just upstream of PS2, attached to internally welded stainless steel rings. Silicon pin photodiodes upstream detect fluorescence and scattered x-ray beam intensity while an aperture downstream of the photodiodes provides the image for the detector plane. The model of the IM1 is shown in Figure 5-6.

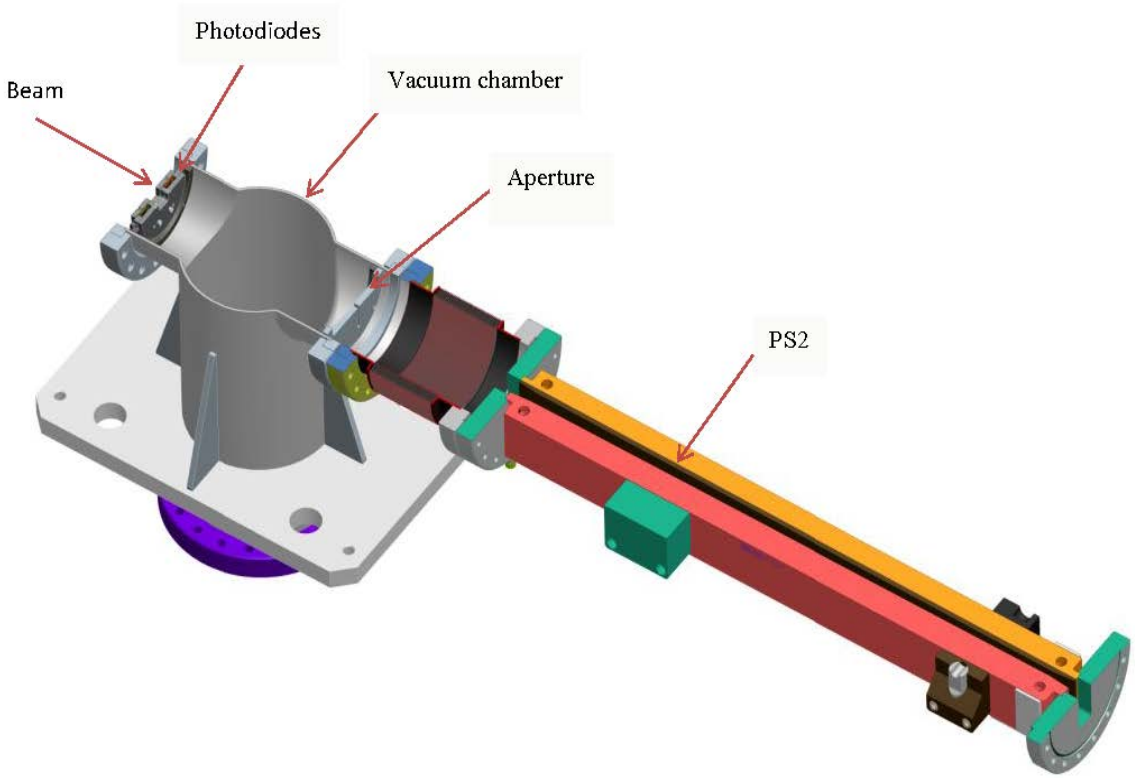

Figure 5-6: The HHLFE first intensity monitor.

5.2.1.3.3 XBPM2

The second XBPM uses fluorescence and Compton-scattering x-ray photons from the exit mask in the backward direction to measure x-ray flux. The XBPM2 assembly is located within a vacuum pump chamber at the upstream part of the exit table. Internally welded stainless steel rings inside the chamber support the photodiodes upstream and the imaging aperture downstream.

The second XPBM is based on the principle of the pinhole camera when the feedback system centers the x-ray beam at the upstream limiting aperture; the position of the projected beam spot at the downstream screen is anti-correlated with the source position. The model of the XBPM2 is shown in Figure 5-7.

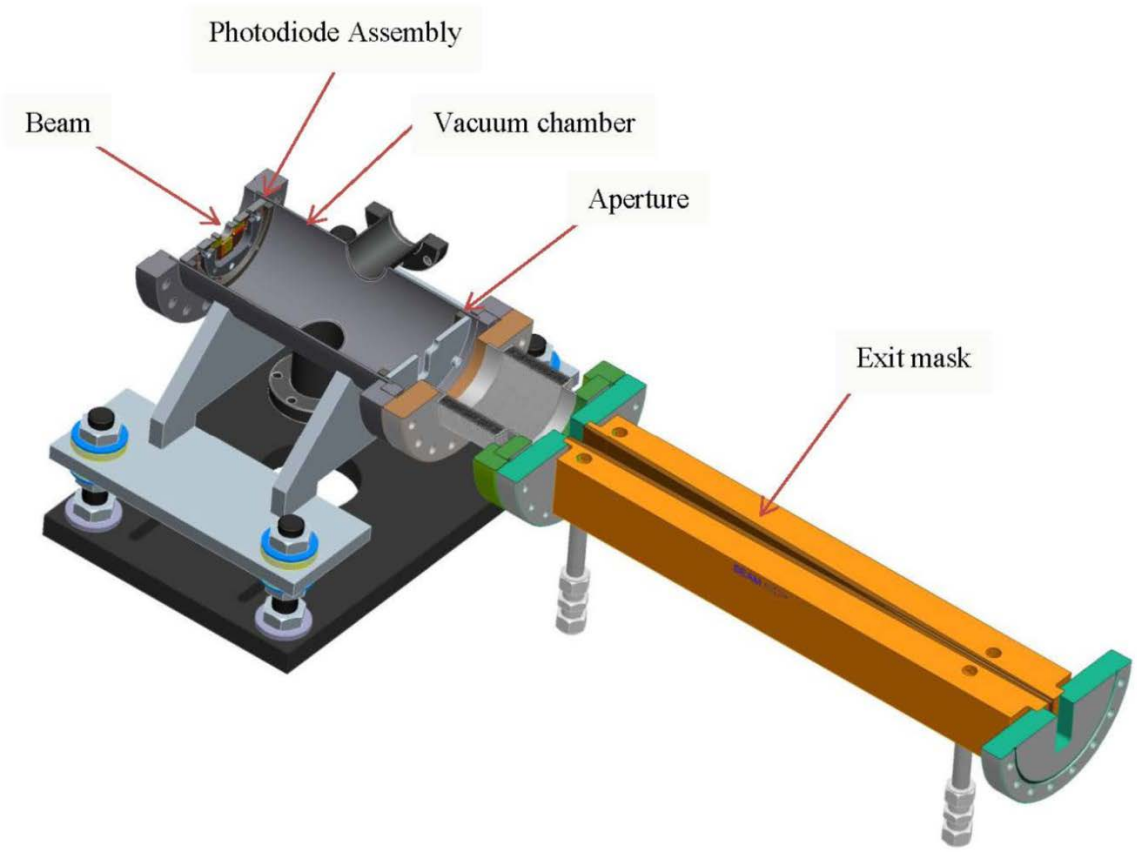

Figure 5-7: The HHLFE second x-ray beam position monitor.

5.2.1.3.4 Intensity Monitor 2 for Front End with Window

The second beam intensity monitor (IM2) is an alignment aid at the end of the FE. It is used to measure the intensity profile when the x-ray beam is scanned across the exit mask: when the x-ray beam center is pinned at GRID-XBPM, this means scanning the position of the electron beam. The center of the intensity profile is expected to coincide with the white-beam center.

The IM2 picks up its signal from forward Compton-scattered x-ray photons from the FE Be window. Photodiodes are attached inside a vacuum chamber on the downstream side of the window. To reduce multiple scattering and fluorescence from the copper and stainless steel, a cone made of aluminum will be placed inside the body of the Be window, as shown in Figure 5-8.

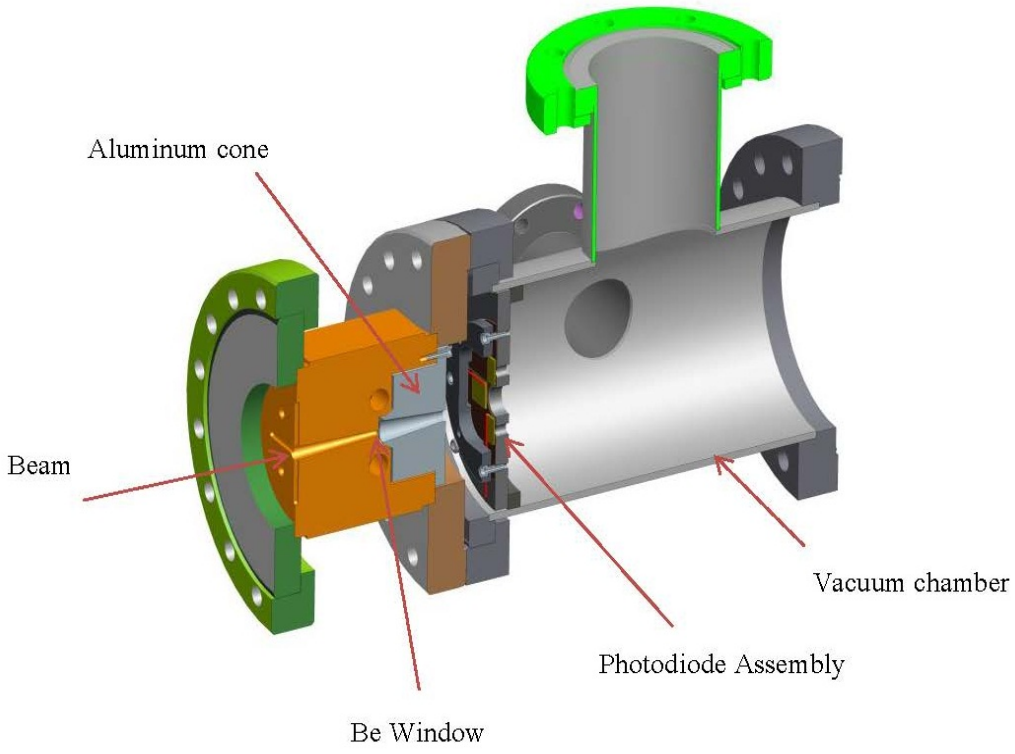

Figure 5-8: IM2 for a front end with window.

5.2.1.3.5 IM2 for Windowless Front End

The IM2 for windowless beamlines uses backward Compton-scattered x-ray photons from a diamond film target. Pin diodes are attached inside a vacuum chamber upstream of the diamond film. Because the diamond filter is in the path of the white beam, a special water-cooled mount is needed. During operations, the IM2 is minimally invasive since the diamond film could be removed from the beam via a motorized actuator. The model of the IM2-windowless is shown in Figure 5-9.

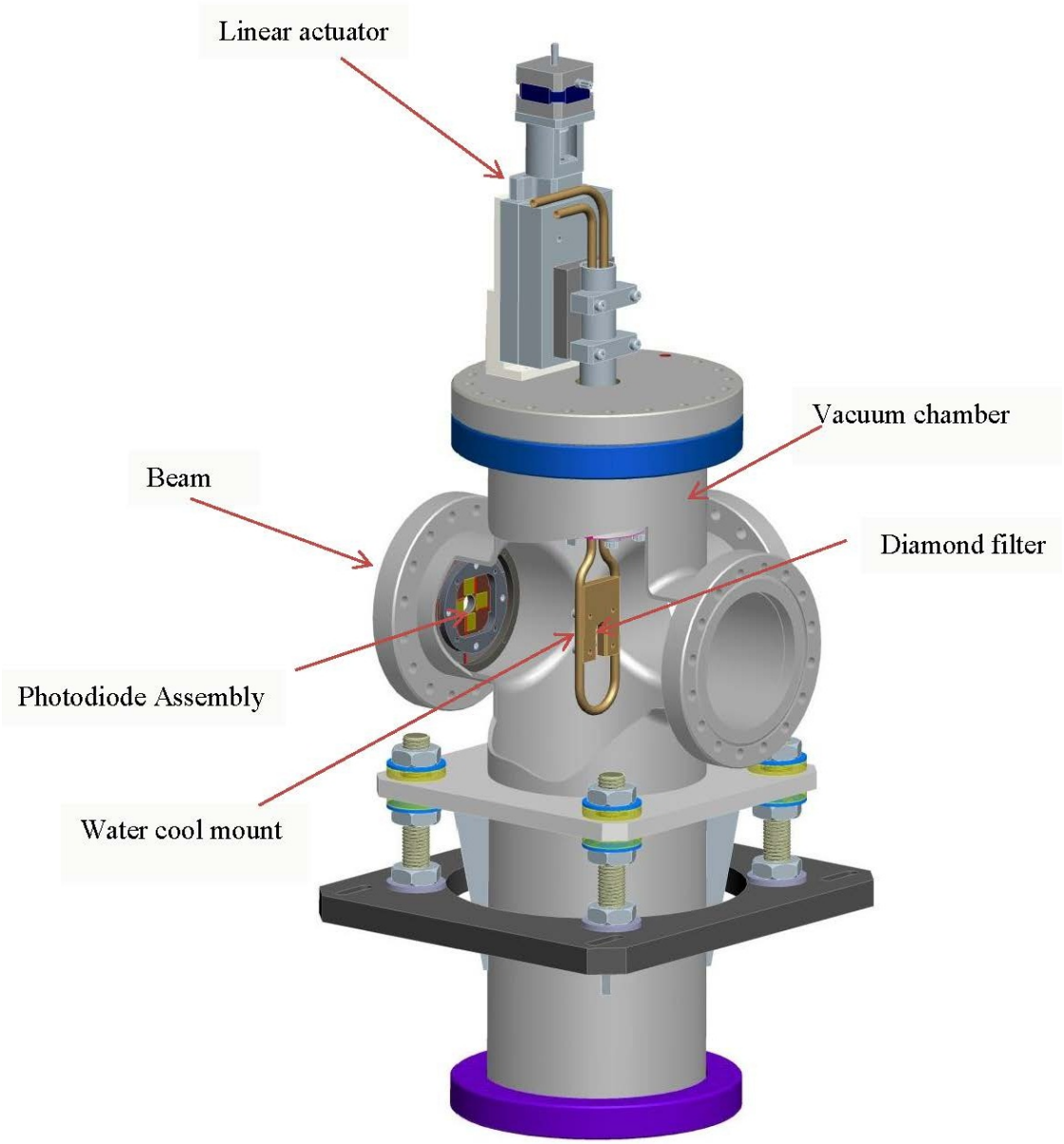

Figure 5-9: IM2 for a windowless front end.

5.2.1.4 HHLFE Aperture Table

The HHLFE aperture table is shown in Table 5-2.

Table 5-2: HHLFE Aperture Table.

Components name		Distance to Center of Straight Section (m)	Optical Aperture H × V (mm × mm)	Shielding Aperture H × V (mm × mm)	Comments
Premask		15.9 (from inlet)	36 × 26		No change
Low Power Photon Shutter		16.3			New
Slow Valve		16.5	ϕ100		Enlarged
First Fixed Mask	Inlet		38 × 47		No change
	Outlet	17.2	20 × 47		
Second Fixed Mask	Inlet		24 × 47		Changed horizontal exit aperture
	Outlet	17.9	10.4 × 47		
GRID-XBPM	Inlet		15.5 × 47		New
	Outlet	19.0	2.2 × 47		
Third Fixed Mask	Inlet		16 × 47		New
	Outlet	20.3	3.6 × 6		
Lead Collimator		20.4 (from inlet)	16.5 × 16.5	23 × 23	No change
Fast Valve		20.8	ϕ63		No change
Photon Shutter 2	Inlet		10 × 47		
	Outlet	22.7	5 × 47		No change
Safety Shutter		22.95 (from inlet)	16 × 16	16 × 16	No change
Wall Collimator		23.6 (from inlet)	27 × 17	37 × 26	No change
Front End Valve		24.6	ϕ63		No change
Exit Mask	Inlet	25.1	12 × 47		User can specify the exit size
	Outlet	25.5	3 × 1		
Be Window		25.6 (from center)	4.5 × 3.0 oblong		
Exit Collimator		26.0 (from inlet)	10.0 × 7.0	10 × 7	Larger external horizontal dimension
Beamline Isolation Valve		26.4 (from outlet)	ϕ40		No change

5.2.1.5 HHLFE Heat-Load Limit and Synchrotron Components

The heat-load-handling capability of the new HHLFE with a GRID-XBPM is the same as the original HHLFE. The HHLFE can handle the heat load from two inline undulators UA at 10.5-mm gap and 180 mA. Thermal analysis for the original FE was performed [1]. The new heat-load components are the second fixed mask and the third fixed mask. The second fixed mask does not require thermal analysis because the only modification is shortening the mask; the taper angle remains the same. The third fixed mask is new, with a horizontal incidence angle of 0.95º; thermal analysis has been performed for this mask for the heat load of two undulators UA at 10.5-mm gap and 180 mA. Three cases were analyzed with: (i) no beam missteering; (ii) vertical missteering only; and (iii) both vertical and horizontal missteering. In the missteering cases, the full beam is absorbed. The temperature and stress plots for vertical missteering are shown in Figure 5-10 and Figure 5-11, respectively. Both temperature and stress are within the APS-specified failure criteria listed in APS TB-50 [2].

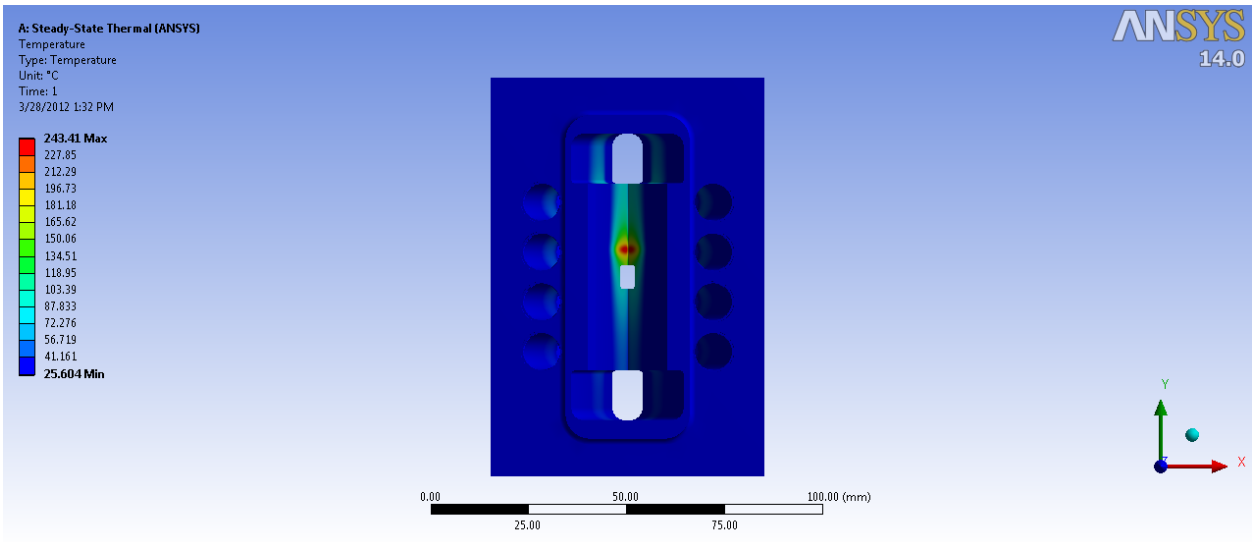

Figure 5-10: Temperature (C) of FM3 with beam vertical missteering at [0,7].

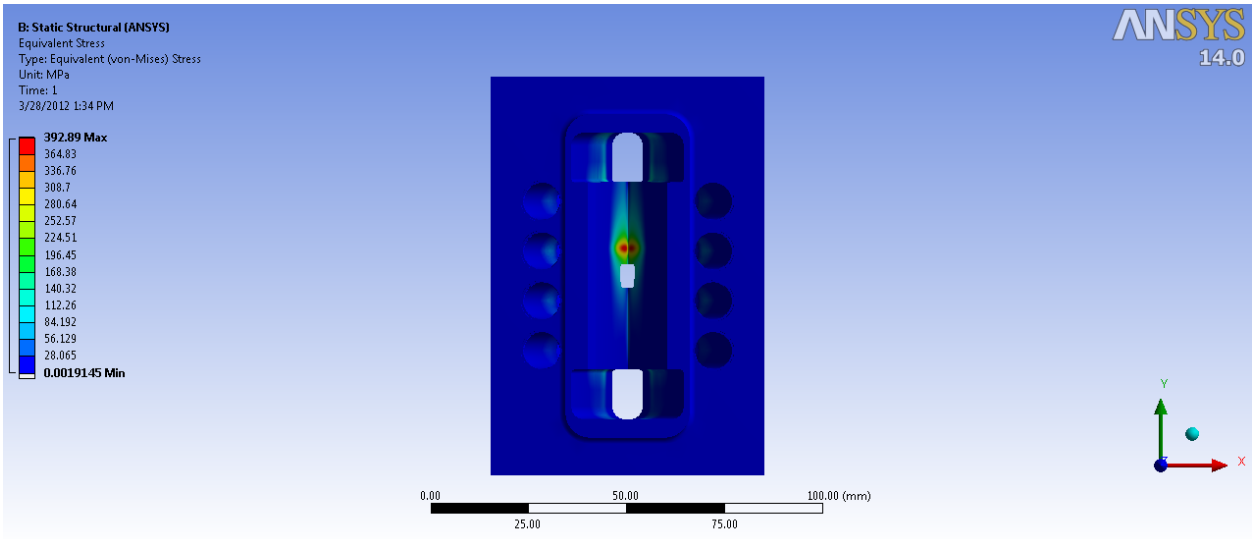

Figure 5-11: Stress (MPa) of FM3 with beam vertical missteering at [0,7].

5.2.1.6 HHLFE Shielding Components

There are four shielding components in the HHLFE: lead collimator, safety shutter, wall collimator, and exit collimator. Compared to the existing HHLFE, the only change for the shielding components in the new HHLFE is that the lead collimator was moved downstream by 940 mm. Due to this move, the exit collimator tungsten block overall horizontal size must be enlarged to ensure the distance between the extreme bremsstrahlung ray and the edge of the tungsten is at least 30 mm as specified by the APS radiation safety guidelines [3]. The diameter of the vacuum chamber was enlarged from 6 in to 8 in to accommodate the tungsten block. The new collimator is shown in Figure 5-12.

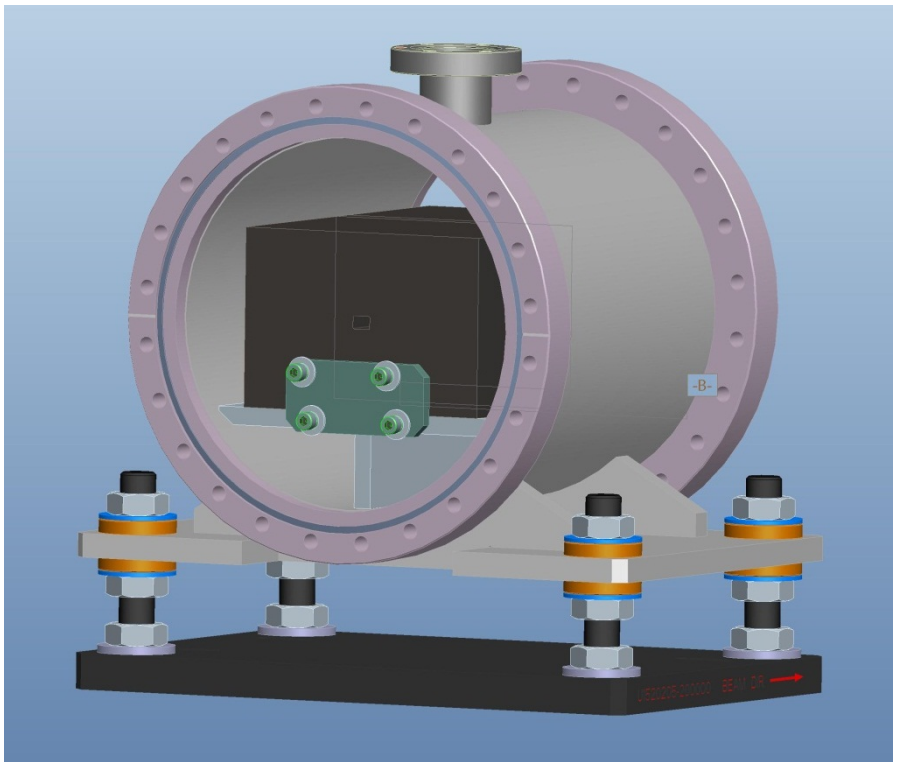

Figure 5-12: The HHLFE exit tungsten collimator.

5.2.1.7 HHLFE Exit Configuration

The HHLFE can either have a window or be windowless. Both configurations have an exit mask with a default exit aperture of 3 mm (H) × 1 mm (V) at 25.5 m. The maximum vertical exit aperture for a windowed version is 2 mm. The horizontal aperture cannot be enlarged if a GRID-XBPM is used. Users must specify the exit mask aperture size and their preference of window or windowless. For the windowed version, the Be window is 0.5 mm thick. If the vertical exit aperture is greater than 1 mm, then the Be window will have a chemical vapor deposition (CVD) diamond filter for thermal protection. The thickness of the filter is typically 0.2 mm but can be thinner or thicker depending on the ID source chosen and the exit mask aperture size. An exit collimator is provided at the FE exit table and is part of the HHLFE. The exit mask and exit collimator remain at the same location for both window and windowless configurations. Therefore, the radiation safety system (RSS) ray tracing will not change if the beamline configuration changes from window to windowless. The HHLFE ends with the BIV in both window and windowless cases.

5.2.1.8 HHLFE PSS EPS Vacuum Protection Logic

All existing APS FEs have two photon shutters (PS1 and PS2) and two safety shutters (SS1 and SS2). The safety shutters are operated in redundancy, meaning they open and close together. However, the photon shutters are not operated in redundancy; instead, PS1 is used as a backup for PS2. A shutter cluster consists of PS2, SS1, and SS2 shutters. In normal operating conditions, PS1 remains in the open position. To close the shutter, PS2 will close followed by the closure of SS1 and SS2. To open the shutter, SS1 and

SS2 will open followed by the opening of PS2. If PS2 fails to close, the PSS system will command PS1 to close resulting in the closure of the two safety shutters. As long as PS1 is functional, the storage beam will not be dumped. However, a beamline with a failed PS2 in the FE will not be able to take beam until the next maintenance period. Both the fast valve and the slow valve are located downstream of the PS1, so PS1 also provides thermal protection for the valves in case of vacuum failure downstream of the valves.

The new FE improves operational convenience in vacuum protection by moving the slow valve to the very upstream end and installing the LPPS upstream of the SV.

In the original FE, the SV is located in the middle section of the FE, downstream from the two masks (FM1 and FM2), XBPM1 and PS1. If vacuum failure occurs upstream of the SV, the stored beam must be dumped, followed by closure of the SR exit valve. Due to the SR exit valve not being protected by any cooled thermal dump for BM radiation, the storage ring cannot resume operation with the SR valve closed. To reopen the SR valve, a controlled access must take place to replace a bellows downstream of the SR valve with a BM beam dump. The section between the SR valve and the BM beam dump will be pumped down; once the vacuum reaches the ring vacuum, the SR valve will be open to resume storage ring operation. This process could take a day.

In the new FE, the SV is located at the very upstream end of the FE. In the event of vacuum failure, the FEEPS will trigger the SV to close, and the closing logic will dump the stored beam and close the LPPS and the SV. Operator intervention is necessary to open and lock the ID gap before the storage ring can resume operation. No controlled access is necessary.

5.2.2 Canted Undulator Front Ends

The original (version 1) canted undulator front end (CUFE) was designed in 2003 for APS beamlines 21-ID, 23-ID, and 24-ID. In 2009, the version 2 CUFE was designed for 12-ID and also was installed later at 13-ID, 16-ID, and 34-ID. The design changes of the CUFE from version 1 to version 2 can be summarized as follows:

1. The photon shutter was redesigned to use an air cylinder instead of bellows to open and close the shutter, thus improving reliability.
2. The support table design was changed from all-aluminum to a steel weldment base with an aluminum top in order to reduce thermal expansion due to ambient temperature change.
3. The exit collimator design was changed from external tungsten shielding with internal tungsten wedge to tungsten core with lead exterior in order to eliminate bremsstrahlung cross talk.

Both versions of the CUFE are equipped with two photoemission-based XBPMs, each measuring 250 mm in length. The CUFE can handle the heat load from two canted undulators UA at a 1-mrad canting angle, 10.5-mm gap, and 200 mA. The motivation to redesign the CUFE for the APS Upgrade is to make room for the next-generation XBPM system.

5.2.2.1 CUFE Design Goal

The new CUFE design criteria are:

1. Maintain the high-heat-load capability of the original CUFE.
2. Reuse the design of the photon shutter and safety shutter to maintain compatibility with the version 2 CUFE while trying to change as few components as possible.
3. Ensure the front end will have sufficient synchrotron beam collimation without a GRID-XBPM in place, because the aperture in the GRID-XBPM will not be counted for radiation safety.
4. Design around the existing components such as the photon shutter, exit mask, Be window, and pump chambers to fit in IM1, IM2, and the XBPM2.
5. Modify the front-end PSS and the FEEPS logic so they function with the low power photon shutter.
6. Redesign the exit table assembly so that the RSS components remain in the same position for both the window and windowless types of FE. Neither the version 1 nor the version 2 CUFE has this feature.

5.2.2.2 Functional Description of the New CUFE with the Next-Generation XBPM System

The new and existing CUFE layout comparison is shown in Figure 5-13. The layout is very similar to the HHLFE. The FE begins with the storage ring exit valve, which isolates the storage ring vacuum from the FE vacuum, and it ends with the BIV, which isolates the FE vacuum from the beamline vacuum. The functionality of all components is very similar to the HHLFE, and therefore a detailed description is not provided.

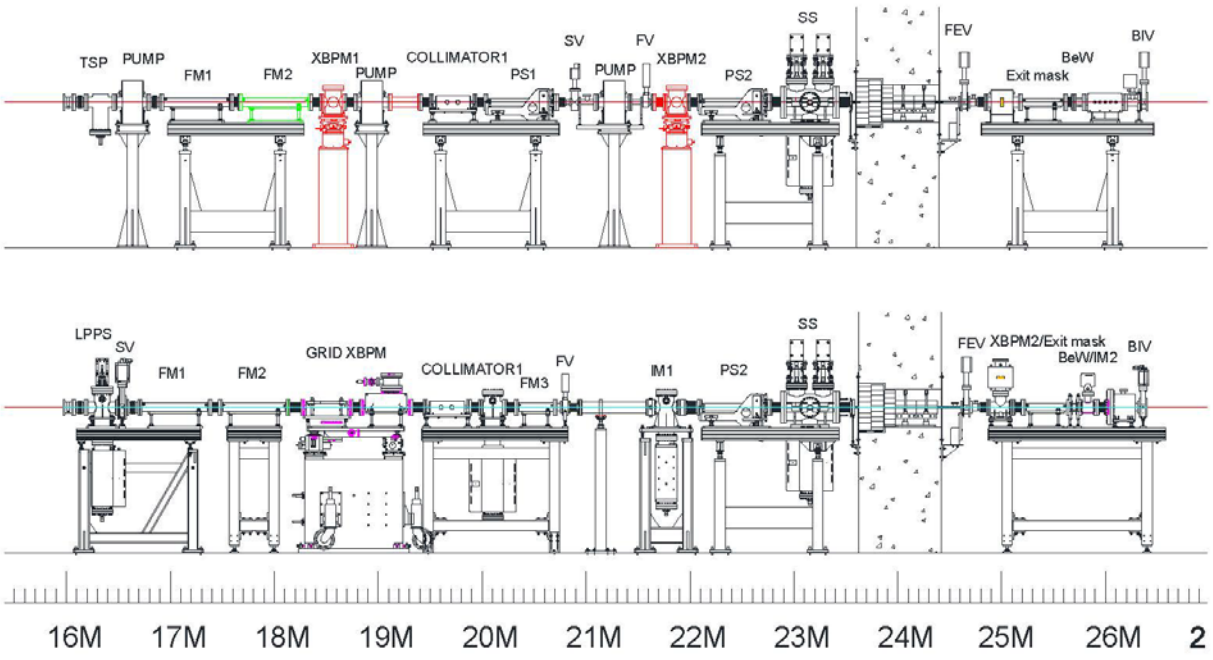

Figure 5-13: CUFE layout comparison. The top figure is the existing CUFE layout; the bottom figure is the new CUFE layout with the next-generation XBPM system. Beam direction is from left to right.

Changes to the CUFE can be summarized as follows:

1. A LPPS was added and the SV moved upstream. The slow valve diameter is enlarged because there is no upstream mask.
2. The FM2 exit aperture was enlarged. The new FM2 exit aperture will provide the GRID-XBPM with a full view of the beam.
3. Due to the FM2 exit aperture being enlarged, FM3 must be added to collimate the synchrotron beam missteering envelope both horizontally and vertically to contain the beam within the acceptance of PS2 and the exit mask.
4. A pump chamber upstream of PS2 was added to fit in IM1 for the next-generation XBPM.
5. The fast valve was moved upstream.
6. The exit collimator was redesigned to be similar to the collimator for the HHLFE with in-vacuum tungsten. The new design uses less space on the exit table along the beam direction.

5.2.2.3 Description of the Next-Generation XBPM System for the CUFE

The next generation XBPM for the CUFE consists of four components: (1) the GRID-XBPM, (2) beam intensity monitor 1, (3) the second XBPM (XBPM2), and (4) beam intensity monitor 2 (IM2).

5.2.2.3.1 GRID-XBPM

The design principles and features of the GRID-XBPM for the CUFE are similar to those for the HHLFE mentioned in section 5.2.1.3. Major differences are that the absorber plates for the CUFE are rotated by 90° (i.e., the GRID-XBPM assembly for the CUFE consists of two identical horizontal water-cooled absorber plates facing the upward and downward directions) and the incidence angle of the beam to the plate is 0.6° for the CUFE instead of 1.0° for the HHLFE. However, the total length of the GRID-XBPM assembly for the CUFE is the same as that of the HHLFE. Therefore, most components in the GRID-XBPM for the HHLFE will be used in the GRID-XBPM assembly for the CUFE. For beam position monitoring, the difference in the XRF intensities from the absorbers gives the vertical position readout. Measurements of the center-of-mass of the x-ray fluorescence footprint with pinhole-camera-like optics are used for horizontal position and tilt readout.

5.2.2.3.2 Intensity Monitor 1

The first beam intensity monitor IM1 is similar in design and principle to that used in the HHLFE, as described in section 5.2.1.3.2. Due to the presence of two canted beams, as opposed to one beam for the HHLFE, and to eliminate the crosstalk between the two canted beams, a center plate is used to separate the two signals. The model of IM1 is shown in Figure 5-14.

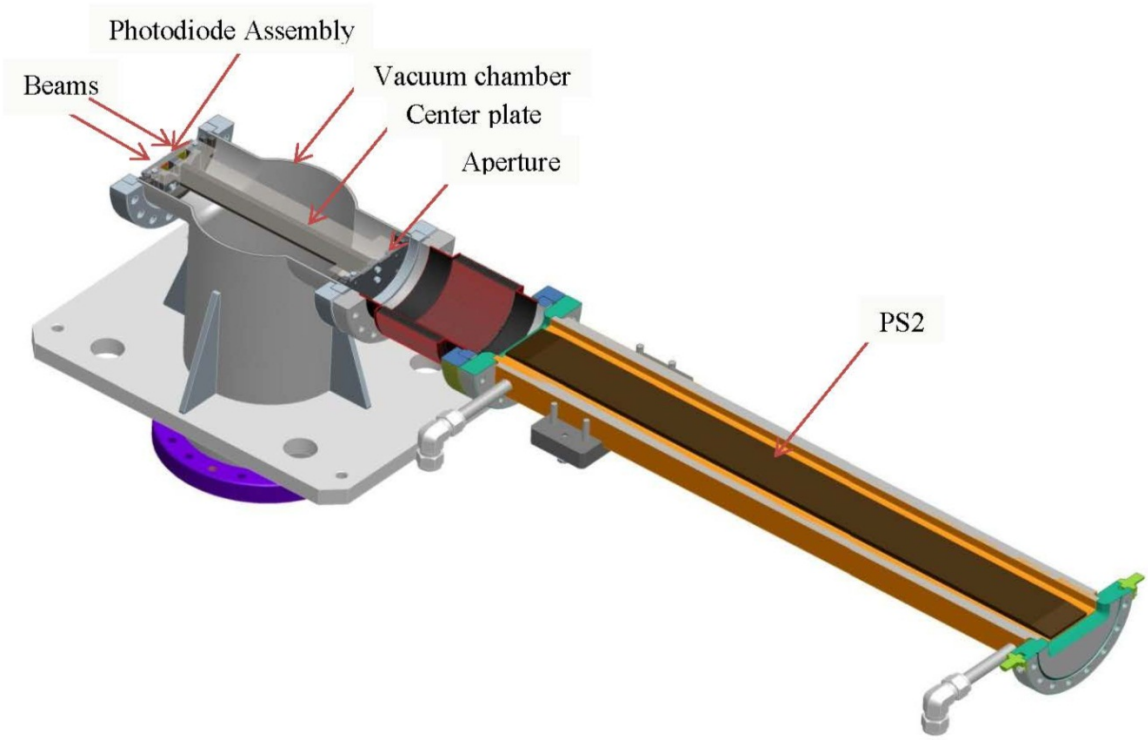

Figure 5-14: The CUFE first intensity monitor.

5.2.2.3.3 XBPM2

The second x-ray beam position monitor XBPM2 is similar in design and principle to that used in the HHLFE, as discussed in section 5.2.1.3.3. To separate the signal from the two canted beams, a center plate with top and bottom baffles is utilized. The model of the XBPM2 is shown in Figure 5-15.

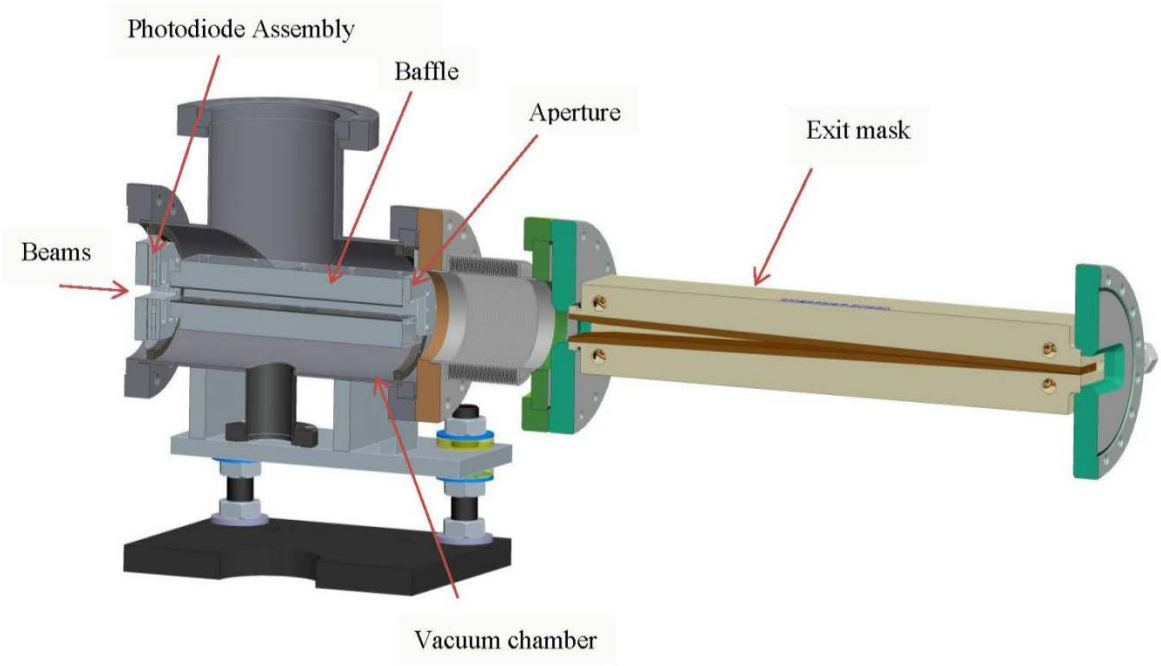

Figure 5-15: The CUFE second x-ray beam position monitor.

5.2.2.3.4 Intensity Monitor 2 for Front End with Window

The second beam intensity monitor (IM2) is similar in design and principle to that used in the HHLFE and is described in section 5.2.1.3.4. Due to the presence of two canted beams, the design is modified to eliminate the cross talk between the two beams. This is accomplished by placing a center baffle attached to the photodiode assembly. The model of IM2 is shown in Figure 5-16.

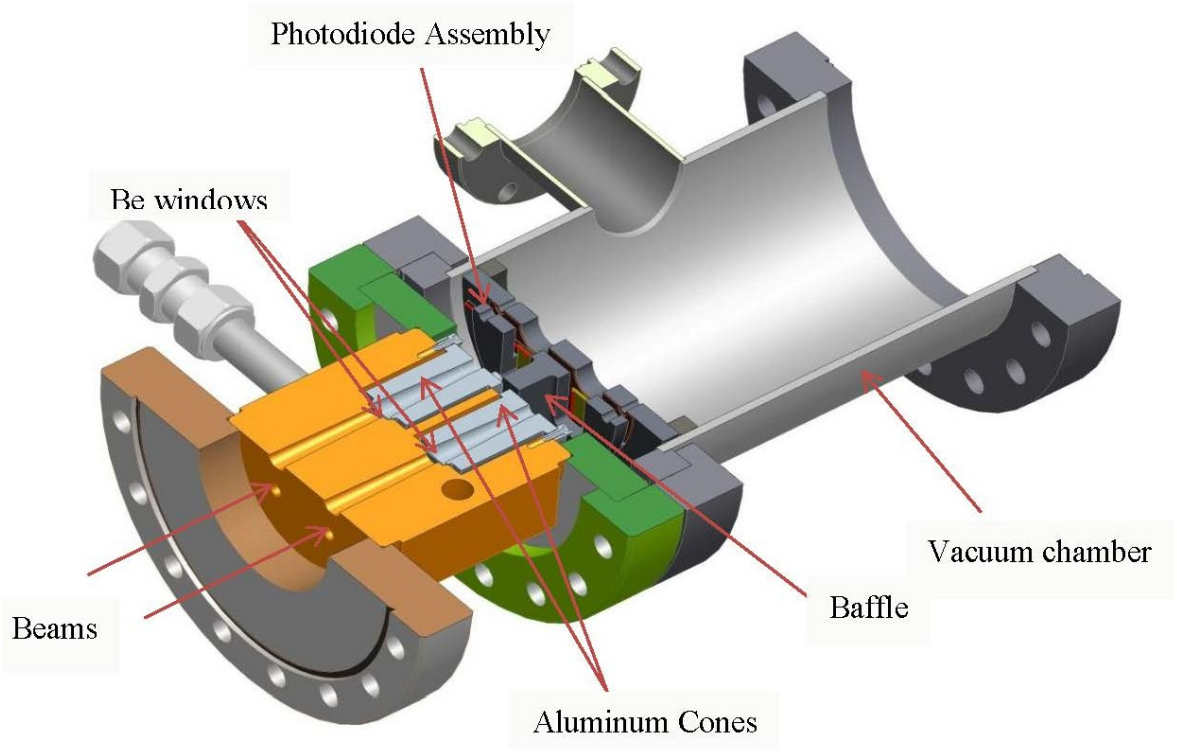

Figure 5-16: IM2 for a front end with window.

5.2.2.4 CUFE Aperture Table

The new CUFE aperture table is shown in Table 5-3.

Table 5-3: CUFE Aperture Table.

Component Name		Distance to Center of Straight Section (m)	Optical Aperture H × V (mm × mm)	Shielding Aperture H × V (mm × mm)	Comments
Premask		16.0 (from inlet)	(+32/-29) × 25		Smaller inboard aperture
Low Power Photon Shutter		16.3			New component
Slow Valve		16.5	ϕ100		
First Fixed Mask	Inlet		64 × 26		
	Outlet	17.3	40 × 14		
Second Fixed Mask	Inlet		46 × 17		
	Outlet	18.1	29.0 × 5.8		Enlarged
GRID-XBPM	Inlet	18.3	47 × 13		New component
	outlet	19.3	47 × 1.5		
Lead Collimator		19.5 (from inlet)	40 × 16	46 × 22	
Third Fixed Mask	Inlet		40 × 12		New component
	Outlet	20.8	31× 4		
Fast Valve		21.5 (from center)	50 × 35		VAT all-metal valve

Component Name		Distance to Center of Straight Section (m)	Optical Aperture H × V (mm × mm)	Shielding Aperture H × V (mm × mm)	Comments
Second Photon Shutter	Inlet	22.2	50 × 10		
	Outlet	22.8	50 × 5		
Safety Shutter		22.95 (from inlet)	50 × 16	50 × 16	
Wall Collimator		23.6 (from inlet)	47.6 × 16.8	56 × 25.4	
Front End Valve		24.6	ϕ63		VAT all-metal valve
Exit Splitter Mask	Inlet	25.1	50 × 9		
	Outlet	25.5	Dual 3 × 2 oblong		
Be Window		25.6 (from center)	Dual 4.5 × 3.0 oblong		
Exit Collimator		25.75 (from inlet)	Dual 7.0 × 6.0	Dual 7.0 × 6.0	New design
Beamline Isolation Valve		26.2 (from center)	ϕ63		VAT all-metal valve

5.2.2.5 CUFE Heat-Load Limit and Synchrotron Components

The heat-load limit of the new CUFE remains the same as the existing CUFE. The CUFE will be able to operate with 20 kW of total power and 281 kW/mrad^2 of peak power density. This power load is equivalent to two 3.3-cm-period, 2.07-m-long undulators operating at 200-mA beam current at 10.5-mm gap. For different undulators at 150-mA operation, the FE will function as long as each undulator emits less than or equal to 10 kW of total power and less than or equal to 281 kW/mrad^2 of peak power density. The FE heat-load limit is a combination of both the total power and the peak power density. It is more sensitive to the total power than to the peak power density. The peak power density can exceed the limit if the total power is substantially lower than the limit and vice versa. FEA thermal analysis must be performed on the FE if either the total power or peak power density exceeds the limit. The FE thermal handling capability depends on the two beams being separated by 1 mrad, and the interlock of the canting magnets' power supply to the storage ring beam dump being used to prevent heat-load damage to the FE in case the canted beams become collinear.

There are five RSS heat load components in the CUFE. They are the FM1, FM2, FM3, PS2, and exit mask. The FM1, PS2, and exit mask are identical to those in the existing CUFE. The new FM2 has the same inlet aperture and taper angle as the existing FM2. The exit aperture is enlarged to provide the GRID-XBPM with a full view of the beam. The thermal performance of FM2 is not changed. The FM3 is a new component added to limit beam missteering in the horizontal and cut down the beam size in the vertical. The horizontal exit aperture of the FM3 must allow the XBPM2 a full view of the beam. The vertical exit aperture of the FM3 is the same as that of PS1, which was removed and was at the same location. The FM3 provides protection for both PS2 and the exit mask.

5.2.2.6 CUFE Shielding Components

The shielding components inside the ratchet wall remain the same design and at the same location compared to the existing CUFE. The exit collimator design will be changed. The exit collimator has gone through several design changes in the existing CUFE. The existing exit collimator has a tungsten core surrounded by lead. The tungsten core is welded to the stainless steel flange to contain the vacuum. There

are two drawbacks in this design: several fabrication steps are involved in welding tungsten to the steel flange, and the hybrid tungsten/lead collimator requires 300-mm shielding material length, which occupies too much space on the exit table. So the decision is to make the exit collimator with in-vacuum tungsten and to be as compact as possible in the beam direction. The new design model is shown in Figure 5-17. The total length of the tungsten is 8 in along the beam direction; this breaks down into four blocks so that it only takes one person to lift a tungsten block during assembly of the collimator.

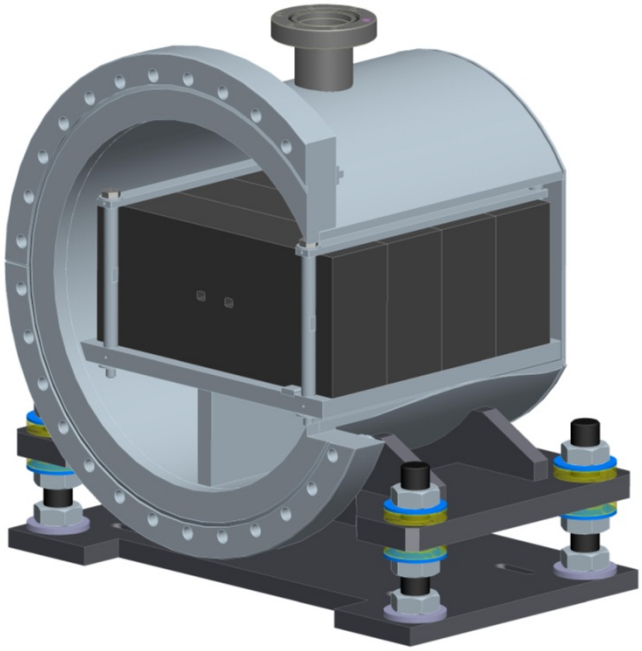

Figure 5-17: CUFE tungsten exit collimator.

5.2.2.7 CUFE Exit Configuration

There are window and windowless configurations for the CUFE. The improvement made for the new CUFE is that the RSS components remain at the same location for both the window and windowless configurations. This allows users to change from window to windowless or vice versa without having to update the ray trace drawings.

5.2.2.8 CUFE PSS FEEPS Logic

The CUFE PSS FEEPS logic is the same as for the HHLFE. To standardize the design, the LPPS table assembly is identical to that of the HHLFE. Refer to section 5.2.1.8 for details.

5.2.3 Front End Version 1.2 Retrofit

Front end version 1.2 is the original ID FE built at the start of the APS. The maximum operational beam current with one Undulator A is 130 mA. The FE has hockey-stick-style photon shutters with a thin

cooling wall. At 150 mA, the cooling wall temperature of the photon shutter will exceed the water saturation temperature at the water pressure. To operate at 150 mA, the photon shutters must be replaced. For the beamlines that only plan to use one undulator or plan to upgrade to canted undulators in the future, the current plan is to retrofit the existing FE so it can operate at 150 mA. The existing photo-emission-based XBPM will not be replaced with the next-generation XBPM system.

5.2.3.1 FEv1.2 Retrofit Design Goal

The FEv1.2 retrofit (FEv1.2R) design goal is to upgrade the original FEv1.2 heat load components to be 150-mA compatible when operating with one Undulator A (UA). The guiding principle is to retrofit the FEv1.2 at minimum cost and only upgrade the components that must be upgraded. All shielding components and XBPMs will remain unchanged and at their original locations. The details of the FEv1.2 design can be found in APS TB-5 [4].

5.2.3.2 Changes to the Existing FEv1.2

The original FEv1.2 has two photon shutters. PS1 has a beam incidence angle of 1.5° and PS2 has a beam incidence angle of 2.0°. Thermal analysis shown in APS TB-50 [2] indicates that when operating at 150 mA, both PS1 and PS2 water channels exceed the water boiling temperature at the channel-water pressure. Since the new FE logic will only use one photon shutter, the idea is to remove PS2 and move PS1 to the PS2 location. Since PS1 has a smaller incidence angle to the beam, this scenario will solve the heat load issue. The summary of the FEv1.2 thermal analysis is shown in Table 5-4.

Table 5-4: Thermal analysis of FEv1.2 components with one UA at 11-mm gap k=2.62, at 150 mA. Note: Data shown in red, and italicized, are data that exceed design criteria.

	FM1 (M1-30)	**FM2 (M2-20)**	**PS1 (P1-20)**	**PS2 (P2-20)**	**Exit Mask (L5-83)**
Distance to Source (m)	16.0	19.35	16.75	19.95	23.75
Incidence Angle	1.5° h, 1.5° v	1.5° h, 1.5° v	1.5° v	2.0° v	4.0° h, 2.0° v
Peak Surface Pd (W/mm^2)	24.2	16.5	22.1	20.7	14.6 v
T_{max} (°C)	*358.5 v*	297.1 v	*331.9*	*345.3*	273.1 v
T_{wall} (°C)	111.7 v	121.9 v	*160.5*	*171.3*	124.2 v
σ_{vm} (MPa)	539.6v , 624.5c	459.3 v	459.2	457.8	463.7v, 584.1c
Note: h stands for horizontal incidence or horizontal missteering, v stands for vertical incidence or vertical missteering, c stands for corner missteering					

Due to the FM1 exceeding multiple criteria, such as surface temperature greater than 300°C and von Mises (vM) stress that far exceeds the elastic limit, the FM1 will be replaced with a new mask at a 1.0° incidence angle. Thermal analysis of PS1 when moved to the PS2 location is shown in Table 5-5, with the temperature plot in Figure 5-18 and the von Mises stress plot in Figure 5-19.

Table 5-5: Thermal analysis of PS1 at PS2 location, 19.95 m to source at 150 mA with one UA at downstream location.

	Flow rate (gpm)	h (W/mm^2 C)	T_{max} (°C)	T_{wall} (°C)	vM Stress (MPa)
Nominal Operation	4.5	0.02	269	137	373
FEEPS Trip Limit	3.0	0.015	282	152	383
Below FEEPS Trip Limit	1.5	0.01	302	174	396

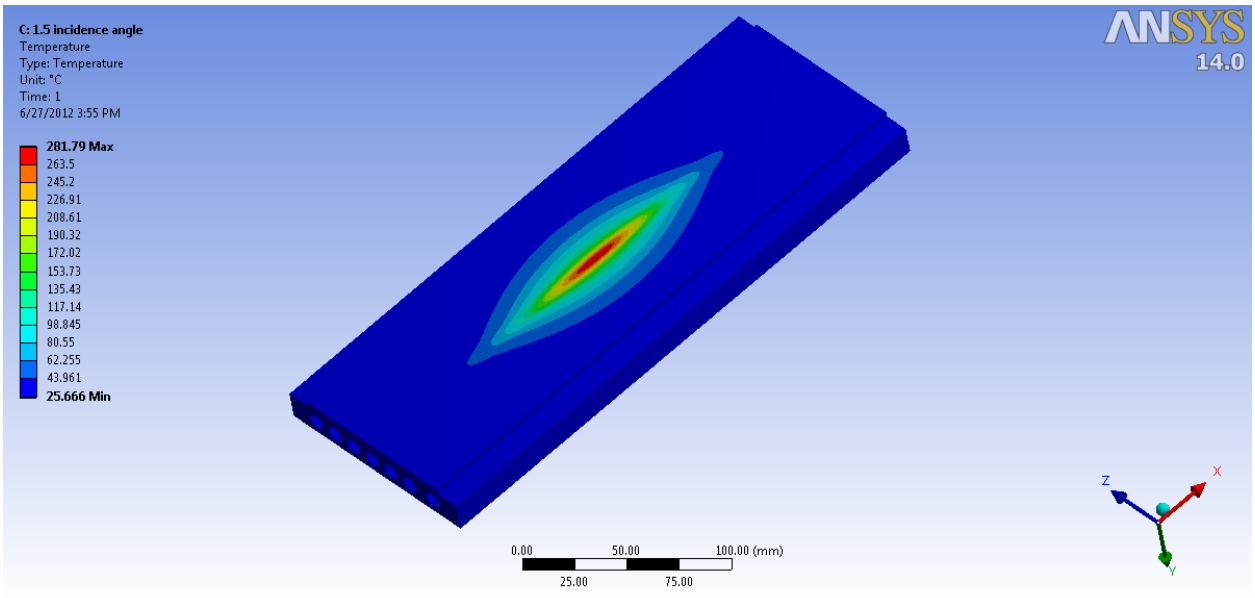

Figure 5-18: Temperature plot of PS1 at PS2 location with UA at 11-mm gap, 150 mA.

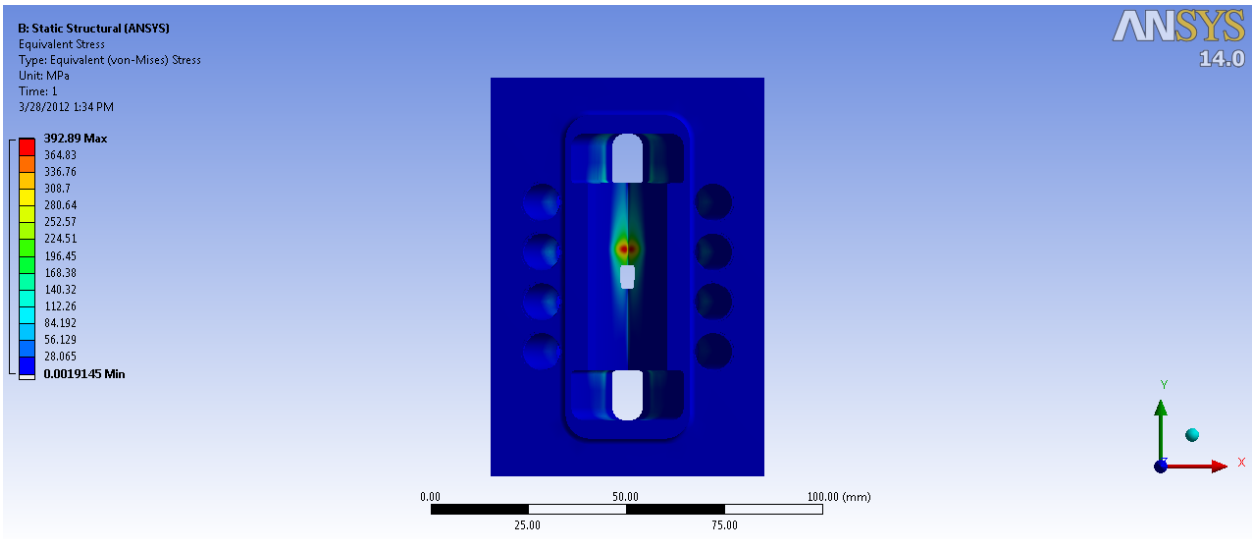

Figure 5-19: von Mises stress plot of PS1 at PS2 location with one UA at 11-mm gap at 150 mA.

5.2.3.3 FEv1.2R Layout and Aperture Table

The comparison layouts of FEv1.2 and FEv1.2R are shown in Figure 5-20, and the aperture table is shown in Table 5-6.

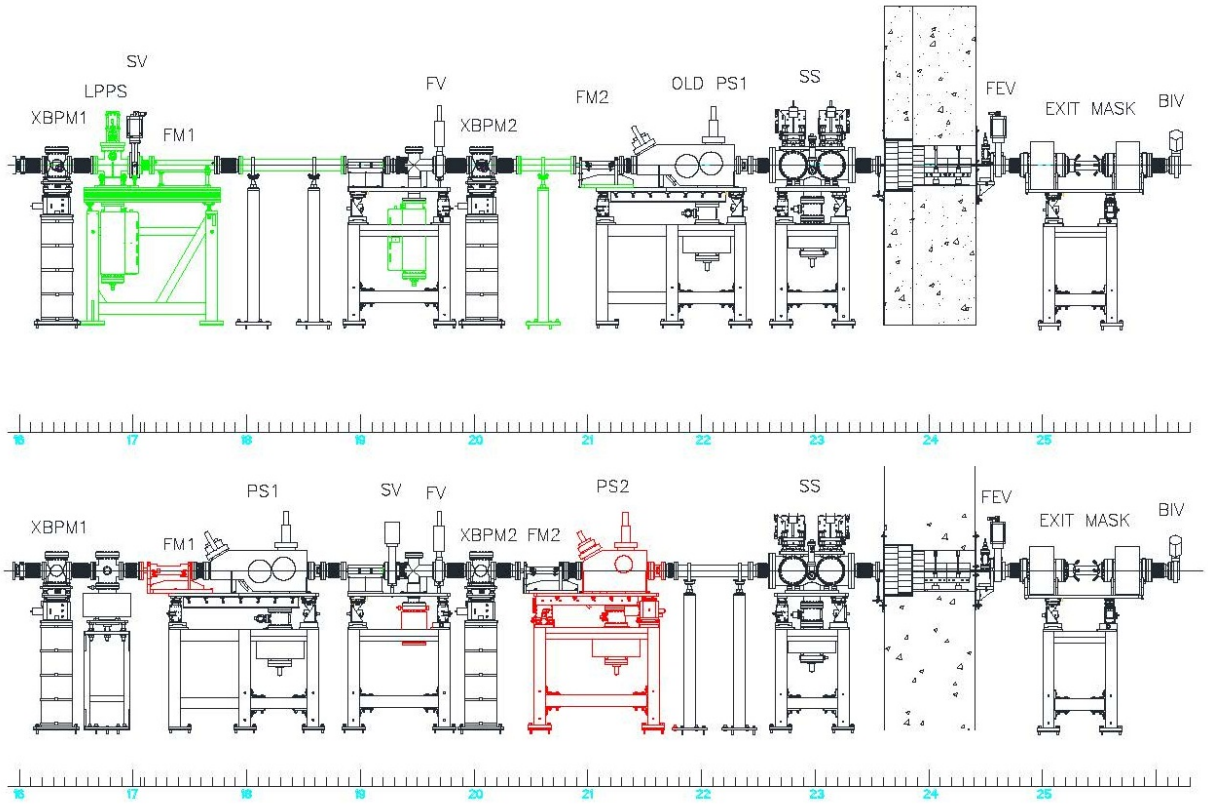

Figure 5-20: The top layout is the FEv1.2R; the bottom layout is the original FEv1.2 [5].

5.2.3.4 FEv1.2R Shielding Components

There are three shielding components in the FEv1.2: a lead collimator, a safety shutter, and a wall collimator. All three will stay in their original positions. Although there are no required changes in the shielding components designs and apertures, operations and maintenance issues are addressed. The original wall collimators were made with lead shot; over time the weight of the lead pressing on the vacuum tube has made it sag. Consequently, the wall collimator with lead shot will be replaced with lead brick at the time of the upgrade installation.

5.2.3.5 FEv1.2R Exit Table Configuration

The exit table of the FEv1.2R is unchanged compared to the FEv1.2; it has either a 3 mm × 2 mm exit mask with a BE window or a 4.5 mm × 4.5 mm windowless exit mask.

Table 5-6: FEv1.2R Aperture Table.

Component Name		Distance to Center of Straight Section (m)	Optical Aperture H × V (mm × mm)	Shielding Aperture H × V (mm × mm)	Comments
Premask		16.0	(+31/-17) × 25		Smaller inboard aperture
XBPM1		16.3	72 × 27		
Low Power Photon Shutter		16.8			New component
Slow Valve		17.0	ϕ100		
First Fixed Mask	Inlet	17.2	38 × 26		
	Outlet	17.7	20 × 10		
Lead Collimator		19.0 (from inlet)	62 × 20	68 × 26	
Fast Valve		19.8	80 × 35		
XBPM2		20.1	32 × 18		
Second Fixed Mask	Inlet	20.9	66 × 18		
	Outlet	21.2	54 × 6		
Second Photon Shutter	center	21.8			
Safety Shutter		22.66 (from inlet)	72 × 20	72 × 20	
Wall Collimator		23.6 (from inlet)	66 × 14	77 × 25.4	
Front End Valve		24.6	ϕ100		VAT all-metal valve
Exit Mask	Inlet	25.2	40 × 23.7		
	Outlet	25.5	4.5 × 4.5		
Beamline Isolation Valve		26.2 (from center)	ϕ100		VAT all-metal valve

5.2.3.6 FEv1.2R PSS EPS Logic

The LPPS shutter table is identical to the HHLFE and CUFE. The operational logic is the same as for the HHLFE; further details are provided in section 5.2.1.8.

5.2.4 Other Types of New ID Front Ends

Two additional unique FEs are included in the Project: one is the LSSCUFE for the long straight section at 1-ID, which can potentially have two superconducting undulators (SCUs) in a canted configuration; the second is the SPXCUFE for short-pulse x-ray (SPX) beam with canted undulators at 6-ID, with a regular-length straight section. Both FEs can be modified from the standard CUFE. Similarly, the next-generation XBPM for these two front ends will be based on the CU design.

5.2.4.1 LSSCUFE

The LSSCUFE is a special-case CUFE for the long straight section at 1-ID where at least one undulator for each of the two branches of the beamline is included in the scope. The optimal period length of the SCU at the downstream location is 1.8 cm.

The undulator at the upstream location has several options:

1. SCU with a 1.8-cm period
2. SCU with a 1.6-cm period
3. Revolver with PMUs

All current canted-undulator systems at the APS deliver the beamline from the upstream undulator to the outboard branch, and the beamline from the downstream undulator to the inboard branch, as shown in Figure 5-21. As discussed in section 4.9, the program for 1-ID requires that the undulator beams are switchable, meaning the upstream undulator can deliver beam to the inboard branch and the downstream undulator delivers beam to the outboard branch, and vice versa. If this switch is performed by the canting magnets adjacent to the undulator, it will result in shifting of the centerline that bisects the canting angle by about ±2 mm. This means the FE horizontal apertures must be larger if the canting angle remains at 1.0 mrad. Another possibility for switching the beam is utilizing the Decker 5-kick bump scheme [5], which will have no axis shift as shown in Figure 5-22, and is also discussed in section 4.9. However, the canting angle may need to be reduced to 0.8 mrad when using this scheme. The front end will be designed to handle either shift-axis or no-shift-axis cases. In order to use the existing CUFE shielding components, the canting angle can be no larger than 0.8 mrad with the shifting axis, and the canting angle can be 0.8 to 1.0 mrad with no axis shift.

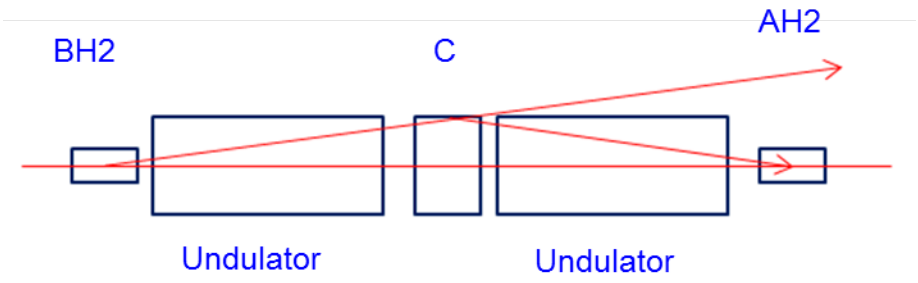

Figure 5-21: Typical canted undulator canting schematic at the APS.

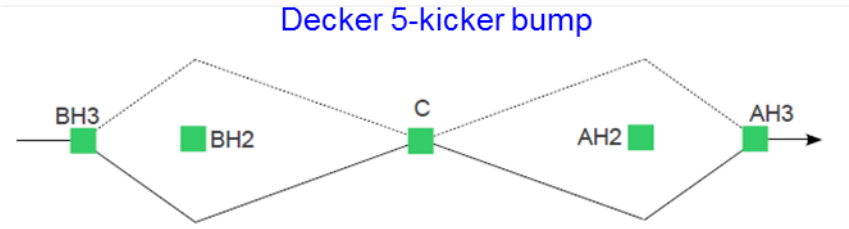

Figure 5-22: Decker 5-kick bump canted undulator canting scheme.

5.2.4.1.1 Heat Load Study

The LSSCUFE is similar to the CUFE, but with a higher heat load; studying the heat load is the key to the successful design of the LSSCUFE. The photon shutter (PS) is the most critical component in the LSSCUFE and is used as a benchmark for the heat load study. The PS1 in the CUFE has a shallower beam incidence angle and will be used as the PS2 for the LSSCUFE. The following five cases are considered with 150 mA, a heat transfer film coefficient assumed to be 0.015 W/mm^2/° C and a bulk temperature of 25.6° C.

1. Two SCUs are utilized. Upstream: 1.6-cm period, 2.3-m long, k=1.06, total power 5.4 kW, peak power density 377 kW/mrad^2; downstream: 1.8-cm period, 2.3-m long, k=1.56, total power 9.1 kW, peak power density 447 kW/mrad^2. Canting angles range from 0.5 mrad to 1 mrad in 0.1-mrad increments. This is to study the canting angle effect on photon shutter thermal performance. As the canting angle gets smaller, the two beam spots move closer together, and both the temperature and stress will be higher. The temperature and stress data are summarized in Table 5-7. There are no issues associated with operating at a 0.8-mrad angle or larger.

Table 5-7: SCU1.6 upstream and SCU1.8 downstream, temperature and stress vs. canting angle.

Undulator Canting Angle (mrad)	Maximum T (°C)	Cooling Wall T (°C)	Maximum von Mises Stress (MPa)
1.0	262.85	118.76	393.71
0.9	264.13	122	396.9
0.8	266	125.67	401.41
0.7	268.75	128.7	407.37
0.6	272.29	130.91	414.6
0.5	276.94	132.23	424.42

2. Two SCUs, both 1.8-cm period, 2.3-m long; canting angles of 0.8 mrad and 1.0 mrad. This is the worst heat-load case. Data are summarized in Table 5-8.

Table 5-8: Two SCU1.8, temperature and stress at 0.8 mrad and 1.0 mrad canting angles.

Undulator Canting Angle (mrad)	Maximum T (°C)	Cooling Wall T (°C)	Max. von Mises Stress (MPa)
1	274.29	130.76	397.87
0.8	281.41	140.51	412.4

3. For the case of 0.8 mrad, both peak temperature and wall temperature are within current failure criteria. The von Mises (vM) stress, however, slightly exceeds the current conservative criterion of 400 MPa [2]. Operation in this condition is acceptable. The temperature plot is shown in Figure 5-23.

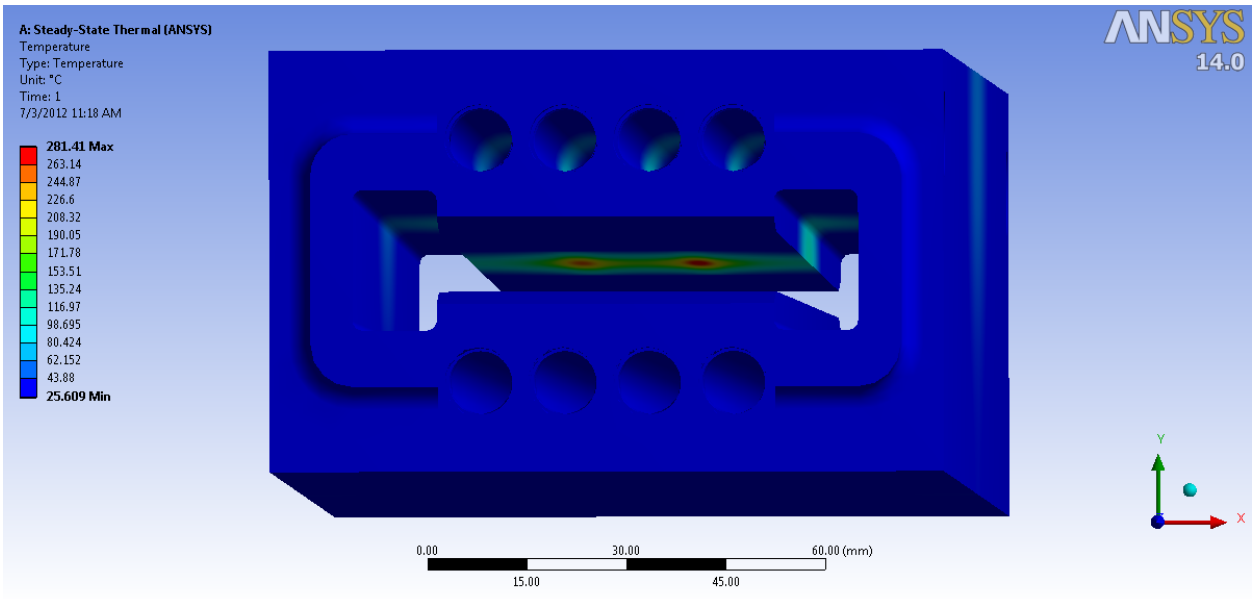

Figure 5-23: Temperature plot of LSSCUFE PS2 with two 1.8-cm-period SCUs.

4. One 1.8-cm-period SCU downstream with various lengths and one 2.4-m-long revolver PMU upstream. A 2.7-cm-period PMU is used for the calculation. This is the most practical case for 1-ID because, with the PMU upstream, the 1-BM beamline will not be blocked. To see the heat-load limit on the photon shutter, various lengths of SCUs were used for analysis. The data are summarized in Table 5-9.

Table 5-9: Temperature and stress with PMU2.7 upstream and SCU1.8 downstream. Note: data shown in red and italicized exceed the design criteria.

SCU Length (m)	Canted Angle (mrad)	Maximum T (°C)	Max. Stress (MPa)	Cooling Wall T (°C)	Total Power Absorbed (kW)
2.3	0.8	267.47	402.81	127.08	13402
2.3	1.0	263.95	394.43	119.8	13401
3.0	1.0	*331.48*	*513.11*	143.63	15952
3.3	1.0	*360.90*	*564.9*	154.01	17064

5. For SCU lengths of 3.0 and 3.3 m, both the peak temperature and peak stress exceeded current failure criteria. However, the cooling wall temperature was below the boiling water saturation temperature, and the shutter will not have catastrophic failure; instead, the failure will be due to fatigue.

5.2.4.1.2 Modification from CUFE

With either a 1.0-mrad canting angle with no axis shift, or a 0.8-mrad canting angle with axis shift, the shielding components for the LSSCUFE (except the exit collimator) are expected to be the same as the

standard CUFE. The PS1 of the current CUFE will be functional as the PS2 for the LSSCUFE. The analysis of the masks will be performed in order to determine if the masks need to be changed. If longer masks are required, there is room upstream of the IM1 chamber. Replacement of PS1 with a LPPS has made the design for higher heat load possible.

5.2.4.2 SPXCUFE

An SPXCUFE is planned for 6-ID, with an SPX canted beam. The SPXCUFE is a special case of a CUFE with a large vertical aperture for one branch to pass beam with a vertical size of up to 1 mrad. The installation of this FE is scheduled to be completed near the end of the Project; as such, the requirements for the front end are still in development. The FE will be modified from the standard CUFE, and design of the SPXCUFE is planned to start in 2014.

5.2.5 Upgrade Plan and Installation

As discussed in Chapter 1, the front-end installations can occur only during the three scheduled maintenance periods per year in order to maintain ongoing APS operations. High-heat-load FEs and FEv1.2R FEs can be installed during any shutdown period before the start of 150-mA operation. Installation of the canted undulator FE, the LSSCUFE, and the SPXCUFE must be synchronized with the specific beamline upgrade schedule. Installation planning is managed by the Project Office and is being carefully coordinated between APS Operations and the APS Upgrade Project. Two FE installations will be completed during a typical shutdown, with a maximum of three FE installations occurring in a single shutdown. In addition to the 22 ID front ends that will be installed, one BM front end will also be relocated. The cost of relocation of this BM front end is part of the Project scope.

5.3 Physical Infrastructure

5.3.1 Introduction

This section describes the APS Upgrade Project conventional facilities scope of work, which provides the building envelope, interior environment, utilities, and protection needed for the scientific devices and experiments to be housed inside such facilities. The renovation of existing building enclosures or construction of new building enclosures will be designed and built in accordance with all applicable requirements including the International Building Code (IBC 2012). All installations will be designed in a manner similar to the existing APS facility and provide the appropriate vibration, temperature, and dimensional stability in addition to the required life safety systems. The design of the conventional facilities components is coordinated with APS engineering as well as Argonne's Facilities Management and Services.

To minimize repetition, the subsections below describe the various efforts or work components associated with conventional facilities infrastructure work. More specific descriptions are given, where appropriate, in sections 5.3.2 and 5.3.3. The work associated with each component will also be broken down, when applicable, into these various disciplines or specialties:

- General trades (e.g., demolition, civil, structural, architectural, finishes).
- Mechanical (e.g., heating, ventilation, and air conditioning [HVAC], plumbing, process piping, sprinklers, temperature controls).
- Electrical (e.g., lighting, power, fire alarm, communication, telephone/ data, public announcement).

5.3.1.1 General Trades

Demolition: Removal of walls, floors, and other site objects as required for the final configuration and the rerouting or replacement of any affected mechanical, electrical, and plumbing (MEP) components.

Civil: Excavation and backfill to shape the site contours as required to place the building pads, and to achieve proper collection and routing of storm water in a fashion similar to the preexisting patterns. A portion of the excess excavation spoils will be used as structural and non-structural backfill with the balance to be disposed of outside the Laboratory (Argonne). Construction of outside sidewalks, driveways, and parking places is included to provide access for the occupants and to facilitate delivery of material.

Structural: Foundations that are a combination of spread footings and drilled piers. Framings will be made of standard-shape structural steel members and steel roof decking acting as diaphragms. Lateral load resistance will be a combination of diagonal bracing and moment connection frames.

Architectural: Drywall, 3-in horizontal insulated metal siding, integrated glass units, paint finishes, flooring, and ceiling to match or complement the existing facility, and polyvinyl chloride (PVC) roofing membrane with 5-in insulation.

5.3.1.2 Mechanical Work

Mechanical Work: This will include activities covered by Construction Specifications Institute (CSI) Divisions 15 &17 (mechanical and temperature controls). The facility will be protected with a dedicated-zone wet-pipe sprinkler system (ordinary hazard) fed from the existing underground water main, with 2-in domestic water service to the bathroom. Sprinklers in the affected existing facilities will be modified as needed. Piping (deionized water and compressed air) will be run and branched out as needed (no humidity control required). Proprietary Johnson Controls Direct Digital Controls equipment and Metasys system will be used for temperature control.

5.3.1.3 Electrical

The electrical scope of work includes provision for power devices, lighting, public announcement, smoke detection, fire alarm, grounding, lightning protection systems, and conduit for all associated terminations. Existing electrical systems in the experiment hall will be the primary source of the various electrical services.

Lighting: Lighting systems will provide light quantity sufficient to permit visual performance and light quality to control discomfort, glare, and ceiling reflections, and to satisfy architectural design aesthetic requirements. Primary goals in lighting design techniques also include occupant safety and energy conservation. Fixtures in open areas shall be continuous run, pendant-type indirect/direct fluorescent strip fixtures with T5 or light-emitting diode (LED)-type lamps. Exit and emergency lighting connected to local normal power will be provided with emergency battery packs. Emergency battery pack light fixtures or light fixture systems will be provided for emergency egress illumination as well as for illumination during transfer to and from the generator source or generator failure.

Generally lighting will be controlled via local dual technology occupancy sensors with override switches. Standardization of luminaire and lamp types will be considered wherever possible to reduce maintenance costs. In general, the Project will utilize fluorescent lighting systems or LED lighting systems with energy-efficient lamp and ballast combinations and low-brightness diffusers. Strategically arranged corridor fixtures will be unswitched for code-required emergency egress lighting, which also provides for economic night-time illumination. Means of egress “EXIT” signs are incorporated into the design and will be fitted with LED light sources. In an effort to provide lighting systems that are in harmony with energy conservation efforts, the design will incorporate (i) high-efficiency luminaires and associated diffusers; (ii) energy-saving, high-power factor, solid-state electronic ballasts with 10% maximum total harmonic distortion (THD); and (iii) automatic lighting controls including occupancy and day lighting sensors where applicable.

Power: One duplex power receptacle will be provided at 25-35-ft intervals, with one duplex receptacle for every enclosed space wall. Electrical power connections, disconnect switches, and motors starters will be provided for all mechanical equipment connections. If any abandoned raceway and cabling is encountered, it will be removed, as required by code. Reused equipment with circuitry routed in existing walls, ceilings, or floors designated to be removed will be extended or relocated with new raceways and wiring to provide original circuit continuity. Conduits in all finished areas will be routed concealed. Conduits in all unfinished areas will be routed exposed. The minimum conduit size will be ¾-in.

Communications: Two duplex voice/data outlets will be provided for each work station. Two wall voice outlets shall be provided at convenient locations.

Fire Alarm: New or modified existing fire alarm systems will be Underwriter Laboratories, Inc. (UL) listed and will function as communication, signaling, monitoring, and control systems displaying the UL label. The systems will be of a solid-state modular design to allow for future expansion with a minimum of hardware additions. The fire alarm systems will be microprocessor-based monitoring and control systems. The completed systems will incorporate multiplex wiring techniques, a central processing unit, annunciator panels, and detection and alarm devices such as smoke/heat detectors, visual signaling devices, and manual pull stations. The fire alarm detection and signaling system will be of the addressable type operating at 24-volt DC with a standby battery or uninterrupted power supply (UPS) to function for four hours during a major power failure. These systems will provide complete fire detection and alarm capabilities monitoring, manual pull stations, automatic detectors, sprinkler system water flow, and valve position indicators. In case of emergency, the fire alarm signaling devices will broadcast an audible warning as well as visual flashing indicator lights for the hearing impaired. In an alarm condition, the fire alarm system will initiate a remote alarm signal to the Laboratory Fire Department, the HVAC fan shut-down, and/or door unlocking and release, where provided.

Security: Empty boxes and conduit feeders will be provided for all security devices. Electronic identification card readers will be installed at entrance doors where required.

5.3.2 Conventional Facilities for the Wide-Field Imaging Beamline

The proposed Wide-Field Imaging (WFI) beamline extends approximately 250 m (820 ft) from the insertion device source of Sector 20-ID. It will be routed from the experiment hall to the external building through laboratory/office module (LOM) 436 followed by a beam transport/utility corridor. The new building enclosures (comprising the external building, corridor, transition to LOM 436, etc.) are designed to complement the current APS facility and provide the appropriate vibration, temperature, and dimensional stability in the external building as described in the requirements below,

5.3.2.1 Requirements for Wide-Field Imaging Facility

5.3.2.1.1 External Building to House Stations D and E

An external building is required to house the D and E stations. In addition, the building will accommodate areas for data acquisition and analysis, sample preparation, cabinets, toolboxes, and areas for users and staff. The beamline staff will work primarily in this building for a considerable period of time during a run. So, while there are no closed offices in this building, there will be working space for the staff. Because the stations are so far from the main experiment hall, the building must have the entire supporting infrastructure and equipment as is generally available in the main experiment hall. Figure 5-24 shows a preliminary layout of the remote external building.

Based on the operational requirements stated above, the size of the building will be approximately 110 ft x 40 ft x 20 ft high. The floor of the building will have the same vibrational and stability specifications as the main experiment hall in the APS. The location of the external building will be as far away from the source point as possible. The building will have the following:

1. Temperature and humidity control similar to that of the main experiment hall, preferably with a temperature stability in the E station of 0.1° C over a 24-h period; up to 0.5° C stability could be tested at first, with the option to reverse to lower threshold if it proves insufficient
2. In addition to standard entrance/exit doorways, it will have a large, typical, double-door-type entrance for delivery of large items such as monochromators
3. 120-V and 208-V three-phase electrical power with separate clean and dirty lines for 120 V
4. Emergency electrical power for the liquid nitrogen pump and ion pump for the monochromator in the D station
5. A liquid nitrogen supply line that is hooked into the central system in the experiment hall
6. Water and compressed-air supply

7. A unisex bathroom with a bathroom sink
8. A separate sink outside the bathroom for general sample preparation use
9. A vent to accommodate a chemical hood
10. A spark-proof exhaust system with 100 foot-per-minute face velocity to vent flammable and/or mildly toxic gases from the D station to the outside
11. Sprinkled-gas cabinet for flammable gases such as hydrogen
12. An eyewash less than 50 ft from the chemical hood
13. A connecting driveway to nearby road and parking for at least four passenger vehicles
14. A gas-cylinder storage yard outside the building.

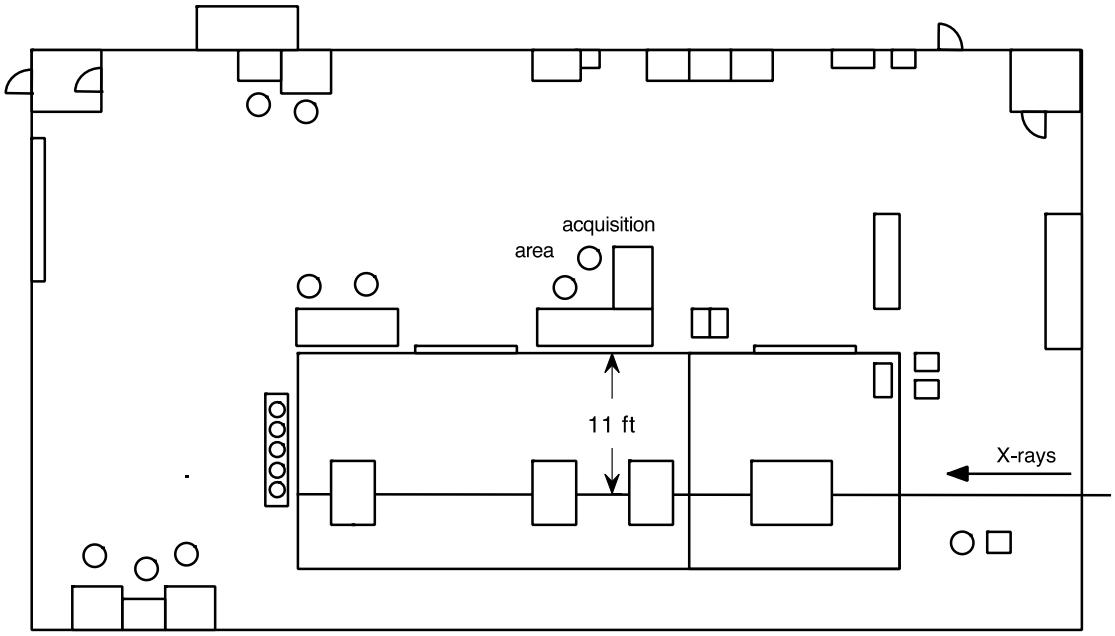

Figure 5-24: Preliminary layout of the external building.

5.3.2.1.2 Transport Corridor from Main Experiment Hall to External Building

A beam-transport corridor is required to house the shielded beam transport from the main experiment hall to the external building housing the D and E stations. The corridor will accommodate utility runs between the external building and the main experiment hall. It will also serve as a personnel walkway between the two buildings. Based on this requirement, the approximate size of the corridor is 10 ft W x 9 ft H x 450 ft L. The corridor will satisfy the following:

1. House the beam transport and associated vacuum pumps
2. Have required power to run the vacuum pumps
3. Accommodate pedestrian access to the external building to/from the main experiment hall
4. Accommodate the necessary utility runs to/from the main experiment hall.

5.3.2.2 Description of Scope of Work

Please refer to the figures below (Figure 5-25: WFI beamline layout ; Figure 5-26: WFI beamline floor plan; Figure 5-27: WFI beamline elevation views; Figure 5-28: WFI beamline structural roof plan; Figure 5-29: WFI beamline corridor cross section; Figure 5-30: WFI beamline plumbing; Figure 5-31: WFI beamline sprinkler and water; and Figure 5-32: WFI beamline external building lighting) at the end of section 5.3.3.10.

There are several distinct components to the conventional facilities aspects of the proposed WFI beamline, as listed below:

- Work inside the experiment hall building.
- Modification to LOM 436.
- Rework of support facilities (e.g., truck lock, LN_2 yard).
- Site work (parking, roadways, drainage).
- Transport beam/ utility corridor.
- External building.
- Engineering design by APS Engineering Support Division (AES) and/or outside consultants.

Infrastructure and Modifications to the Existing Facility: The construction of the WFI beamline will disrupt some existing APS buildings including the experiment hall, LOM 436, and the LOM 436 parking lot and driveway. It will require alteration to pedestrian and vehicular traffic patterns at the truck air lock and the liquid nitrogen storage area at LOM 435. As a result of the disruptions, associated reconfiguration of these facilities is included in the Project scope; however, remediation and function replacement, if needed, are not included in this scope.

5.3.2.3 Work within the Experiment Hall Building

5.3.2.3.1 General Trades

The experiment hall aisle (below the mechanical mezzanine) will be disrupted by the long beamline included in the scope of the Project. To mitigate this disruption, a portion of the beamline that crosses the aisle will be removable. A platform over the beamline is also required to provide access; it will have two sets of stairs with accessible lifts to comply with the Americans with Disabilities Act (ADA). An alternate

approach is also being considered that utilizes a ramp constructed below floor level, but this option is not included in the baseline cost and schedule.

There will be some demolition and rework of siding, trim work, support members, doors, etc., especially in the vicinity of LOM 436.

5.3.2.3.2 Mechanical

The major mechanical utilities for the WFI beamline external building and connecting corridor will be provided from the main APS utility infrastructure distribution system located in Building 400 (the APS experiment hall). These utilities will include deionized process cooling water for beamline components, compressed air, and liquid nitrogen. Building heating and cooling options include utilizing the process cooling water in conjunction with high-efficiency heat pumps, direct connection to the APS chilled and low-temperature heating water systems, or a combination of both. The final system configuration will be determined during Final Design and will be based on achieving the best value with respect to energy efficiency and capital cost.

5.3.2.3.3 Electrical

Existing lighting systems will remain as is.

Electrical power connections, disconnect switches, and motors starters will be provided for all new ADA-accessible lift equipment connections. The power will connect to and bring power from the existing 480/277 panel.

The WFI beamline extension will pass in front of an existing distribution panel TPP-X4-6, thus creating an electrical code violation. To resolve this violation, distribution panel TPP-X4-6 will be relocated to the right side of existing experiment hall column #128.

The experimental stations will receive an electrical power service panel at the external building. This electrical panel will be sourced from the existing experiment hall distribution panel TPP-X3-6, which currently supplies power to all Sector 20 beamlines. The experimental stations will also receive an emergency power panel board sourced from existing experiment hall emergency distribution panel EDP-X1-1.

5.3.2.4 Modification to LOM 436

5.3.2.4.1 General Trades

The WFI beamline will extend through both the laboratories in pentagon A and the offices in pentagon B of LOM 436. The laboratory spaces will undergo minor reconfiguration (e.g., walls, case work, doors, utilities). A double door to the experiment hall along the path of the WFI beamline will be removed. A concrete masonry wall and siding will be installed in its place. A new fire-rated double door and/or a single door with structural framing will be installed nearby. The sleeve penetration for the beamline transport will maintain the integrity of the fire rated separation.

The WFI beamline will protrude through a mechanical chase in the wall between the laboratory and corridor requiring demolition and rerouting of mechanical piping and plumbing inside the chase. On the other side of the same wall, an HVAC control panel will become inaccessible and will be relocated. Structural steel and wall framing demolition and rework will also be carried out.

Due to the extension of the beamline into the LOM, an existing suite of offices (approximately five offices and a conference room, approximately 500 sq ft) will no longer be accessible; the partition walls will be demolished along with their associated electric systems.

The existing ceiling, flooring, and HVAC distribution system will also be reworked. Because the transfer corridor springs out near the apex point of the Pentagon B office, an approximately 20-ft-long portion of the LOM skin (glass, siding, steel framing, wiring, roofing, flashing, etc.) will be demolished and reconstructed to serve as the transition area between the LOM office and the corridor.

Any additional laboratory and office space that may be required to compensate for the lost spaces is not included in the scope.

5.3.2.4.2 Mechanical

The WFI beamline beam-transport line and mechanical utilities will pass through LOM 436, cutting across an existing chemistry laboratory, building corridor, and office space and will tie into existing LOM 436 utilities. The chemistry laboratory will be reconfigured and remain an active chemistry lab; no modification to the existing HVAC or lab exhaust system will be required. The office space reconfiguration will include relocation of building zone thermostats and revision of ductwork to move existing supply air diffusers; the primary mechanical systems for this space will remain unchanged. The existing plumbing piping inside the plumbing chase will be rerouted as a part of the Project scope.

5.3.2.4.3 Electrical

The WFI beamline extension will include removal of some existing interior and exterior walls. The existing electrical systems impacted by the WFI beamline extension will be modified, rerouted, and/or removed. Existing lighting systems will largely remain as is. The existing HVAC controls panel in the Pentagon A corridor are in the path of the 20-ID beamline and will be relocated.

All new equipment installed as part of this Project in existing LOM 436 that requires power or communications circuitry connections will be connected to existing electrical systems serving LOM 436.

5.3.2.5 Rework of Support Facilities (Truck Lock, LN_2 Yard, etc.)

Guards, barriers, and other traffic control devices will be installed to protect the WFI beamline pipe from vehicles and other equipment. Lifting hoists for the removable portion of WFI beamline pipe will be installed. A branch liquid N_2 piping from the liquid N_2 yard or truck air lock will be extended to the downstream side of the WFI beamline to provide for an additional liquid N_2 fill station and to supply the WFI beamline experimental stations. This will eliminate the need to move LN_2 dewars across the WFI beamline pipe.

5.3.2.5.1 General Trades

Several adjustments to doors and aisles, e.g., signage and guard rails, will be needed to assure ease of access for delivery trucks and construction equipment.

5.3.2.5.2 Electrical

Any existing electrical systems that interfere with modifications to existing support facilities will be rerouted as needed. The specifics will be determined during Final Design.

5.3.2.6 Site Work (Parking, Roadways, Drainage)

5.3.2.6.1 General Trades

Most of the proposed WFI beamline site is either in low ground (near LOM 436) that was a wetland and is underlain by soft organic soil, or high ground (by Kearney Road). The site is also crossed by water lines and storm-water drainage systems. Significant amounts of excavation, backfill, utility rerouting, storm-water drainage structures, and moderately deep foundations will be required. Special precautions will be taken near the newly installed gas and sewer pipes for the Advanced Protein Crystallization Facility and the existing water mains.

The fire protection and potable water supply will be provided by tapping into the buried 12-in water main near the LOM 436 sidewalk or by extending the LOM 436 water system. Two small lift stations (for sanitary and lab sewer) will be installed near the external building, with force main sewer pipes taking the waste to the existing LOM 436 lift station. The external building will have retaining walls along most of its perimeter. It will also have four parking spots and a driveway for material delivery, which will also serve as an access ramp. The storm water from the site and from roof drains will be routed to flow southward to maintain the present watersheds. A nominal amount of landscaping will maintain the existing erosion control measures.

5.3.2.6.2 Mechanical

New lift stations will be needed as discussed in the above section and also described on the plumbing drawings.

5.3.2.6.3 Electrical

Additional site lighting is included in the scope of work and will be selected to match existing site lighting at the adjacent facilities. LED lighting will be considered in an effort to conserve energy. New lighting will be time-clock controlled with photocell override. New site utilities (lift station) will be served from new or existing electrical services depending on distance and power source requirements.

5.3.2.7 Transport Beam/Utility Corridor

The transport beam/utility corridor is primarily to connect the beam transport from the APS facility to the external building. In addition, the corridor is used for pedestrian traffic to travel between the external building and the rest of the APS facility. The corridor is also used to supply MEP utilities to the external building. The aisle in the transport corridor is sufficiently wide to move material in small carts between the external building and the rest of the APS facility.

5.3.2.7.1 General Trades

The transport beam/utility corridor will be approximately 9 ft wide × 10 ft high × 330 ft long with a wider transition at LOM 436. Siding on the exterior will closely match that of LOM 436, with windows on the north face (and possibly on the south face, pending cooling load analysis).

5.3.2.7.2 Mechanical

The transport beam/utility corridor will serve as the path for routing all mechanical system utility piping. Heating and cooling of the corridor will be provided by unitary heat pumps or fan coil units placed incrementally along the corridor. The corridor will be supplied with outdoor air at a ventilation rate of 0.06 cfm per sq ft of floor space. This air will be provided from each end of the corridor and exhausted at the corridor midpoint through a room-mounted exhaust ventilator.

5.3.2.7.3 Electrical

Lighting control will optimize use of natural light (introduced through windows spaced every 15 ft) to reduce overall power consumption. Lighting control concepts will be designed to respond to the environment through the use of sensors to monitor natural lighting as well as internal occupancy levels. Sensors will reduce and/or turn off the associated artificial lighting when the space is not occupied. Local overrides will be provided for specialized needs.

One wall-mounted double-duplex electrical receptacle will be provided every 25-35 ft for general power requirements along the corridor and two 4-in x 12-in-wide cable trays routed through the corridor from the new external building to the experiment hall.

5.3.2.8 External Building

The External building houses two x-ray experimental stations D and . In addition, the building will provide areas for data acquisition and analysis, sample preparation, cabinets, toolboxes, and work space for users and staff (refer to Chapter 4, section 4.5).

5.3.2.8.1 General Trades

The external building will be a rectangular high-bay building, approximately 40 ft wide × 120 ft long × 20 ft high. The finish floor is at the same level as the experiment hall building (elevation 744 ft), which

makes it 5 ft lower than the finish-grade elevation near Kearney Road. Routine access will be at the northwest entrance, which will lead into a vestibule with a 5-ft-drop stairway. A long driveway/ ramp will be located on the north side to provide ADA access and bulk-material delivery through a large double door. A unisex toilet, a janitor's closet, an emergency eye wash, and emergency shower, if determined to be necessary, will be located at the northeast corner.

5.3.2.8.2 Mechanical

The external building HVAC will consist of unitary heat pumps or fan coil units located along the perimeter wall of the building. The building will also have a single dedicated outdoor air unit for ventilation air and make-up air for enclosures and for specialty exhaust systems required for a 4-ft fume hood and gas cabinet.

Utilities needed for beamline use (e.g., process cooling water, compressed air, and liquid nitrogen) will be brought into the external building and terminated with valves for future connection by users.

5.3.2.8.3 Electrical

Lighting systems will provide light of a sufficient quantity and quality for visual performance and control discomfort, glare, and ceiling reflections, and to satisfy aesthetic requirements. Lighting control concepts will be designed with sensors in order to monitor the building's internal occupancy levels. These sensors will reduce and/or turn off the associated artificial lighting when a space is not occupied. Local overrides will be provided for specialized needs.

The new power service distribution to the external building will respond to the power requirements of the building program, with the flexibility to accommodate future space/function changes. The distribution systems will provide the reliability and flexibility required in modern facilities, with special considerations for separation of delicate equipment (e.g., computers, special system equipment) from unstable voltage/amperage load, such as motors. Secondary distribution voltage at the external building will be 480 V, 3 phase, 4 wire, plus ground. This will provide service to equipment and lighting loads and will be further transformed down to 208Y/120 V, 3 phase, 4 wire, plus ground as necessitated by the building loads and their location. Generally, this lower voltage will be utilized for receptacles, miscellaneous equipment, etc. The new secondary distribution system will be separated into the following branches:

Normal: This branch provides normal source power to the bulk of the facility load (e.g., general lighting and receptacle loads, miscellaneous equipment loads, and mechanical equipment loads) that is not essential to building or user functions; therefore, this branch is not connected to an alternate or back-up source of power, such as a generator.

Clean power: This branch provides clean power for use only with technology and critical/sensitive loads such as computers, monitors, printers, scanners, and data network electronics. The distribution system will consist of separate power panels, surge protection (two levels), branch circuits, and double-duplex (non-isolated ground) receptacles.

The new secondary distribution will utilize copper-on-phase and neutral buses with copper ground bus. Panel boards will have 25% spare loading and pole capacity, and 10% spare breakers will be provided in branch circuit panel boards. All other equipment will have 20% spares, but no spare protective devices. All dry-type transformers will be TP-1-, 150° rise-, 220° C-insulation class with 6, 2-1/2% taps. Consideration will be given for harmonic mitigating transformers or harmonic filters to handle anticipated harmonic generators throughout the building. Circuit protection will be bolt-in type molded case circuit breakers for branch circuit panel boards. Transient voltage surge suppression devices will be installed on the panel boards serving major electronic equipment load.

One wall-mounted double-duplex electrical receptacle space will be provided every 25-35 ft for general power requirements along the exterior building walls. One wall-mounted double-duplex electrical receptacle and one voice/one data outlet will be provided at desk locations. One dedicated duplex isolated-ground receptacle and one voice/one data outlet will be provided at each copier or printer location. One duplex ground fault interrupter receptacle will be provided at all sink locations.

The emergency power service distribution to the new external building is designed to provide service to equipment that could create unacceptable risk during any interruption of the normal electrical supply. The emergency power voltage at the external building will be 480 V, 3 phase, 4 wire, plus ground. This will be further transformed down to 208Y/120 V, 3-phase, 4-wire, plus ground as necessitated by the building emergency loads.

Empty conduit will be provided for wall phone locations, as will two 4-in x 12-in-wide cable trays routed from the corridor to the furthest wall at the new external building.

5.3.2.9 Miscellaneous and Other Related Work

It is anticipated that during the final design there may be addition of a monorail to handling the assembly and disassembly of the beamline. Other items like fume hoods and cabinetry are expected to be added during Final Design. These items are expected to have a minor impact on construction cost.

5.3.2.10 Engineering Design by AES and/or Outside Consultants

Efforts by APS engineers will be supplemented with outside consultants to provide specialized services, e.g., geotechnical engineering investigation, architect/engineer services, drafting support, and professional construction cost estimation.

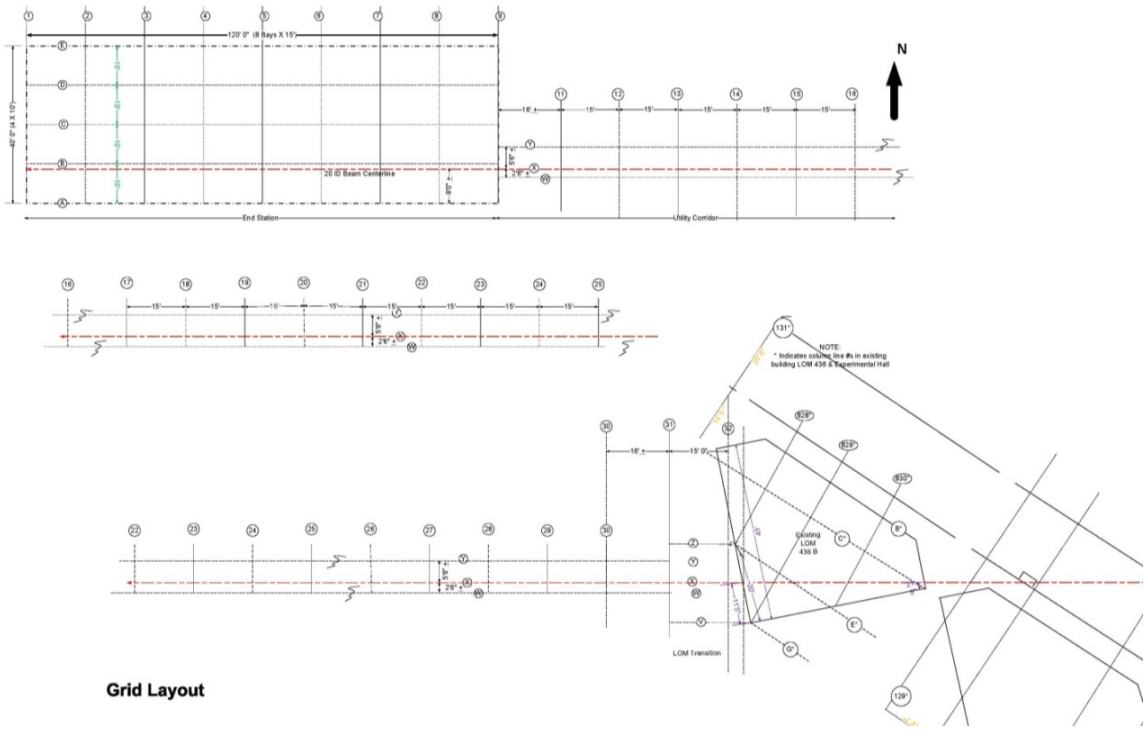

Figure 5-25: WFI beamline layout grid.

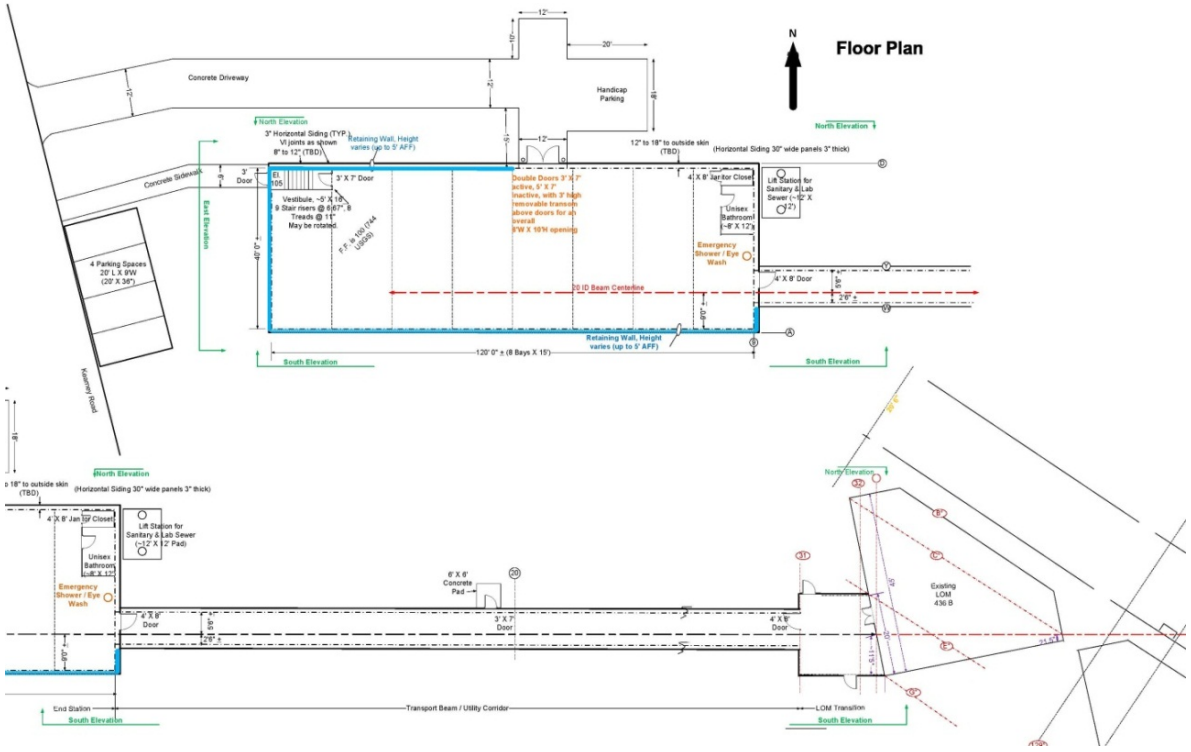

Figure 5-26: WFI beamline floor plan.

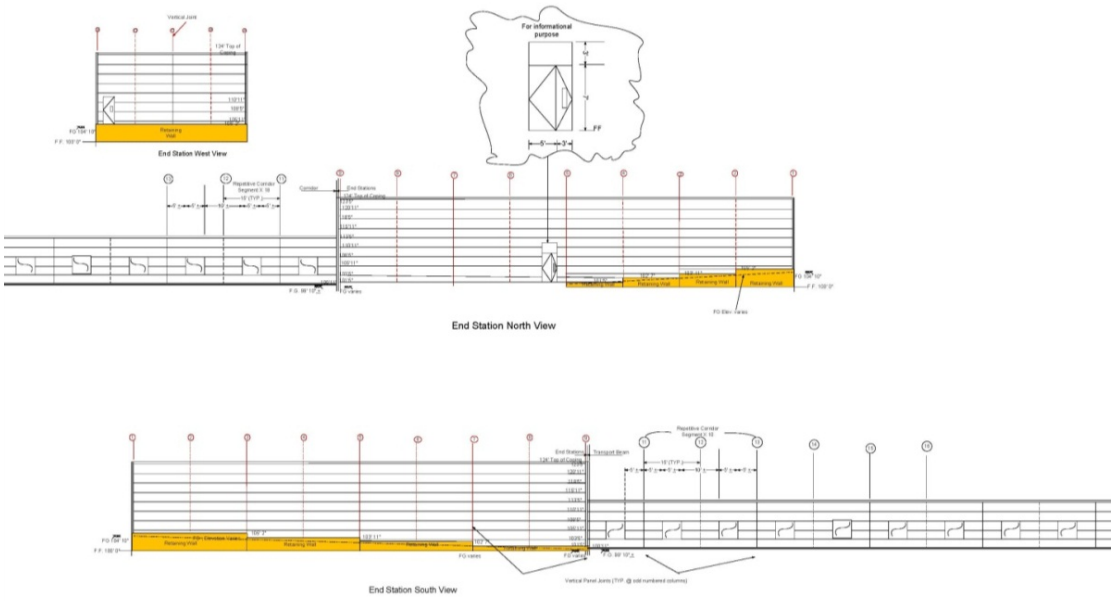

Figure 5-27: WFI beamline elevation views.

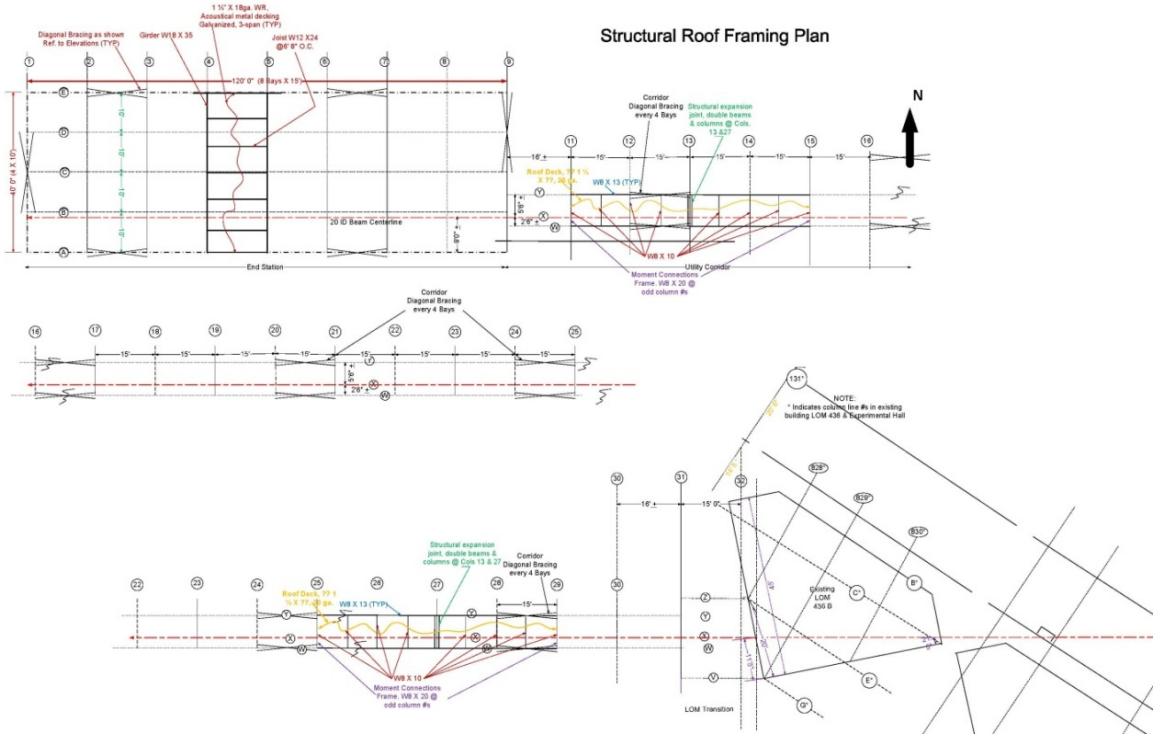

Figure 5-28: WFI beamline structural roof plan.

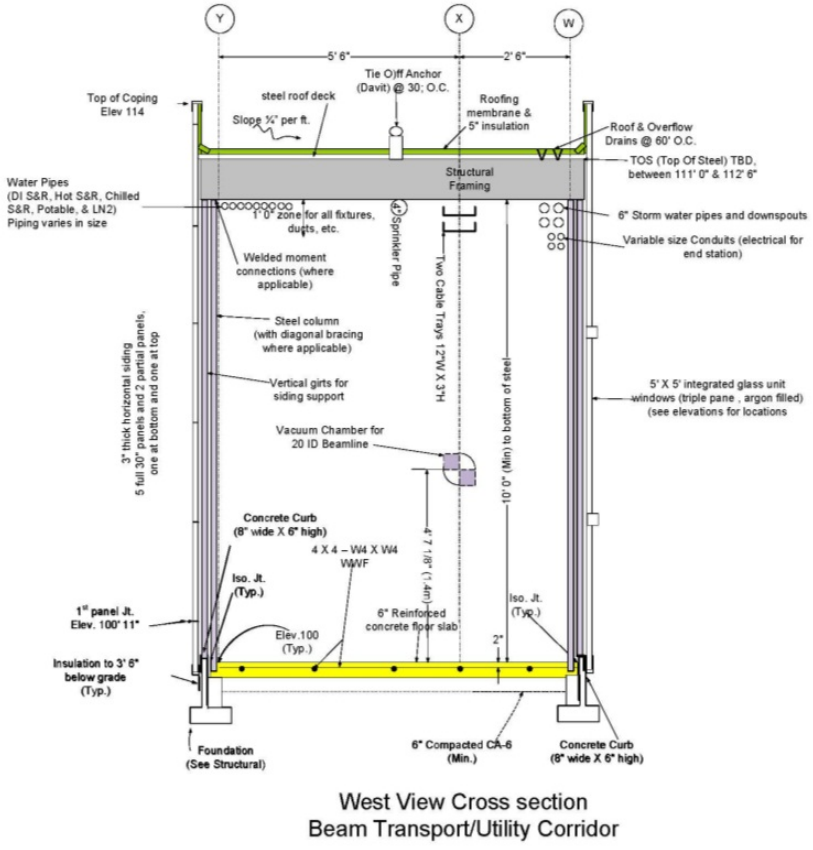

Figure 5-29: WFI beamline corridor cross section.

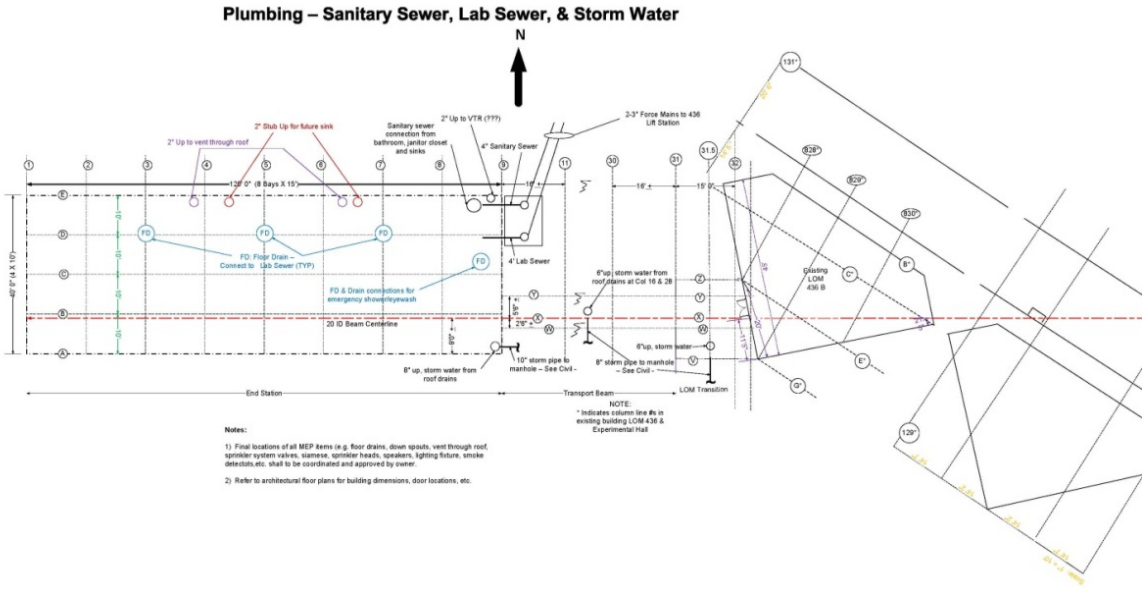

Figure 5-30: WFI beamline plumbing.

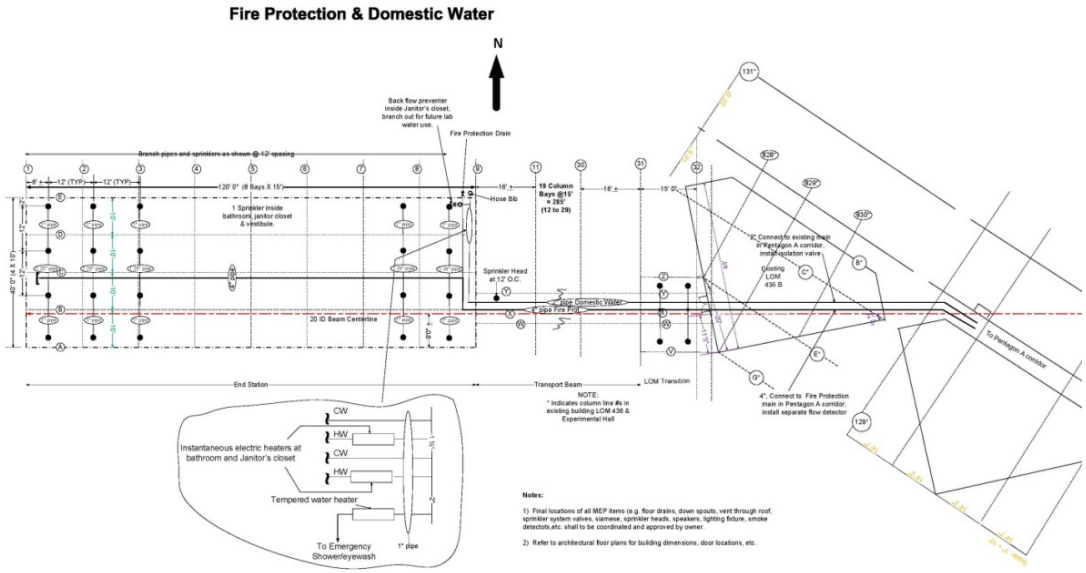

Figure 5-31: WFI beamline sprinkler and water.

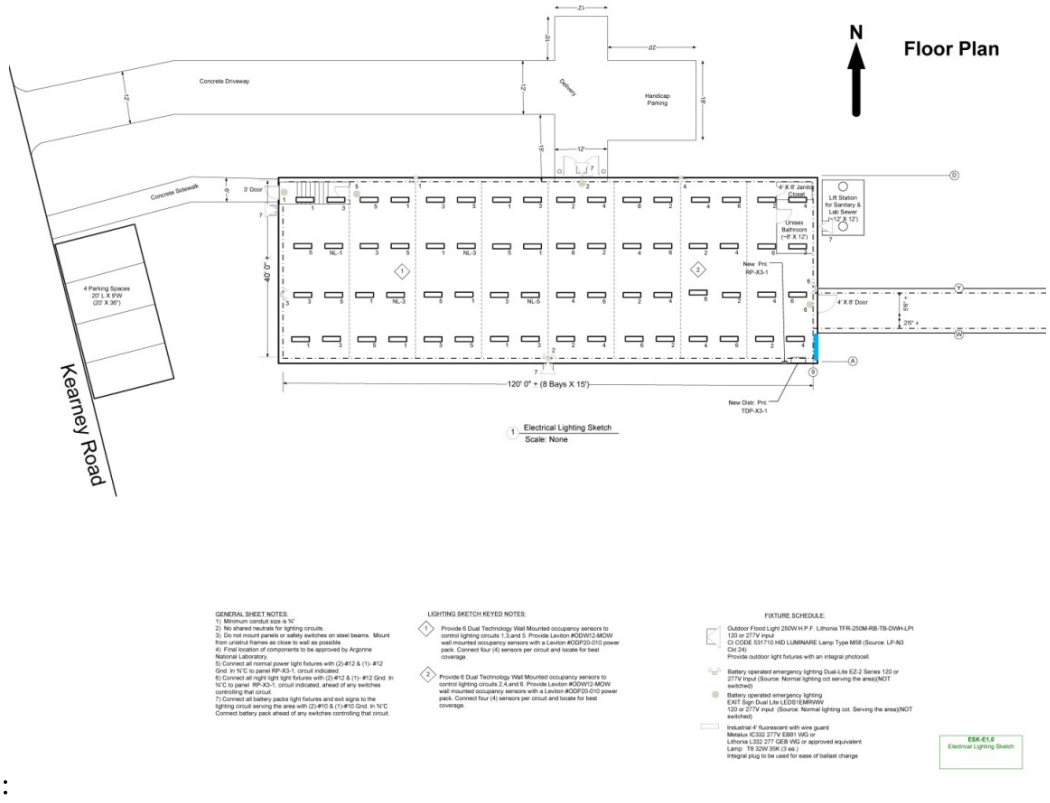

:

Figure 5-32: WFI beamline external building lighting.

5.3.3 Infrastructure Enhancement for High Flux Pump Probe Beamline at Sector 14

5.3.3.1 Requirements for Sector 14 Infrastructure Enhancements

The data acquisition area adjacent to the 14-ID-B station will be reconfigured to accommodate the new station footprint. Two doors and two walls will need to be removed and reconfigured. The entire facility, including the 14-ID-B station, will be sealed and recertified for BSL-3 use upon completion of the Project.

The deconstruction work also includes removal of some adjacent walls of the conventional facility. The construction work includes installation of associated utilities (electric, water, air), and of the APS-supplied Personnel Safety System (PSS) related equipment. The sections below describe the scope of the new conventional facilities construction, i.e., attachment of the existing control room to the new 14-ID-D enclosure, and modification of the existing conventional facility configuration and utilities to achieve BSL-3 certification. The HVAC system will be integrated into the APS building system. Before the deconstruction of 14-ID-B begins, the HVAC control electronics will be integrated into the APS environmental control system.

5.3.3.2 Description of Scope of Work

The conventional facilities work is limited only to alterations to the existing Biosafety Level 3 (BSL-3) facility, which will be modified as part of the Sector 14 upgrade. The work associated with lead-shielded work stations (enclosures) is not part of this scope; it is described in section 4.4.

Please refer to Figure 5-33: Sector 14 Layouts at the end of section 5.3.3.11.1 showing current, upgrade, and superimposed layout (floor plans).

There are several distinct components to the conventional facilities aspects of the APS Upgrade Project, as listed below:

- BSL-3 review by the Institutional Biosafety Committee (IBC).
- Temporary roof support.
- Demolition of existing walls, relocation of utilities.
- New walls, ceilings, and finishes (no enclosures).
- Mechanical/electrical/plumbing work (MEP).
- Commissioning (containment verification, test and balance, etc.).
- Engineering design by AES and/or outside consultants.
- HVAC controls, removal and replacement.

5.3.3.3 BSL-3 Review by Institutional Biosafety Committee

Any alteration to any biosafety laboratory (BSL) requires review by the Argonne Institutional Biosafety Committee (IBC). The IBC is actively engaged with the planned approach for the changes to the BSL-3 facility.

5.3.3.3.1 Mechanical

During the conceptual design of Sector 14, the IBC was consulted, and they reviewed the draft of the APS Upgrade Conceptual Design Report (CDR). During the CDR review it was noted that the new enclosure will replicate the existing BSL-3 containment and exhaust system; based on the conceptual enclosure design no changes are anticipated to the existing system or to the containment methodology. The IBC will be provided with progress reports and documents during Final Design and a formal review of the design will be conducted at approximately the 50% and 95% completion points of Final Design.

5.3.3.4 Temporary Roof Support

5.3.3.4.1 General Trades

Prior to the construction of the new experiment station, the old station has to be torn down. In addition, part of the BSL-3 facility has to be removed. During the demolition, a portion of the existing facility roof will be braced on timber or steel beams supported on floor posts until the final roof structure is in place.

5.3.3.5 Demolition of Existing Walls, Relocation of Utilities

5.3.3.5.1 General Trades

The existing wall and a portion of the roof (where the new, larger enclosure will be located) will be removed after the electrical and mechanical items have been disconnected and disassembled. The existing ceiling in the control room will be removed.

5.3.3.5.2 Mechanical

Demolition of the existing walls, ceiling, and finishes of the existing enclosure and control room will not significantly impact the existing mechanical system infrastructure. The exhaust connection to the existing enclosure will be disconnected directly above the enclosure and reconnected to the new structure. The fan coil unit in the existing enclosure will be removed and the cooling piping demolished and terminated above the enclosure for reconnection upon completion of the new structure. The existing fan coil unit that was recently installed (2010) has sufficient capacity for cooling the new enclosure and will be reused. Process cooling water will be terminated above the existing enclosure and reconnected as part of the enclosure build-out.

5.3.3.5.3 Electrical

Demolition of the existing walls, ceilings, and finishes in the existing enclosure and control room will greatly impact the existing electrical system infrastructure. This effort will include removal of some existing interior enclosure walls. Any existing electrical systems that interfere with removal of existing enclosure walls and creation of new walls will be modified as required. Any abandoned systems encountered will be removed as required by code. Reused equipment having circuitry routed in existing walls, ceilings, or floors designated to be removed will be extended or relocated with new raceways and wiring to provide original circuit continuity. Conduits in all finished areas will be routed in concealed fashion. New equipment installed as part of this project that requires power or communications circuitry connections will be connected to existing electrical systems currently serving the existing enclosure.

5.3.3.6 New Walls, Ceiling and Finishes (No Enclosures)

5.3.3.6.1 General Trades

Once the experiment station installation is complete, the BSL-3 facility has to be reconstructed. This will require installation of new permanent structural support. New walls will be constructed with gypsum-board and doors will be installed. The walls, ceiling, and flooring will be sealed and painted for BSL-3 capabilities.

5.3.3.7 Mechanical/Electrical/Plumbing Work

5.3.3.7.1 Mechanical

The HVAC equipment currently supplying the existing enclosure and control room will remain as is and will not be relocated or modified as part of this work. Some minor modification to the existing ductwork in the control room ceiling will be carried out in order to reconnect supply and return air diffusers to accommodate the new ceiling grid configuration.

5.3.3.7.2 Electrical

Lighting control concepts will be designed to respond to the environment through the use of sensors to monitor occupancy levels. Sensors will reduce and/or turn off the associated artificial lighting when the space is not occupied. Local overrides will be provided for specialized needs.

One wall-mounted double-duplex electrical receptacle will be spaced every 25 ft for general power requirements along the enclosure walls. One wall-mounted double-duplex electrical receptacle and one voice/one data outlet will be located at the desk location.

5.3.3.8 Commissioning (Containment Verification, Test and Balance, etc.)

5.3.3.8.1 Mechanical

Upon completion of construction of the new enclosure and control room, the entire Sector 14 HVAC and bioexhaust containment system (BECS) will be re-commissioned in accordance with the existing BECS commissioning plan.

5.3.3.8.2 Electrical

Electrical system commissioning is a systematic process confirming that the completed electrical systems have been installed, properly started, and consistently operated in strict accordance with the design engineers' system requirements; that all systems are complete and functioning in accordance with the design documents; and that the installing contractor has provided the owner with adequate system documentation and training.

The purpose of electrical systems commissioning is to verify the reliability of electrical power systems after installation by identifying operation problems and providing a set of baseline values for comparison with subsequent future tests. All new and existing modifications to existing electrical systems will be commissioned.

5.3.3.9 Miscellaneous and Other Related Work

This effort covers potential hoists, cabinetry, interlock hardware, and other specialty items. These are judged to have a minor impact on construction cost.

5.3.3.10 Engineering Design by AES and/or Outside Consultants

Effort by APS engineers might be supplemented by outside consultants.

5.3.3.11 HVAC Controls, Removal and Replacement

5.3.3.11.1 Mechanical

The demolition of the existing enclosure and a section of the control room will include a wall containing all the original beamline HVAC controls. These controls consist of hard-wired relays mounted on the wall and are obsolete and cannot be reused. They will be replaced by new digital controls connected to the APS Metasys temperature control system. The new controls will integrate the existing BSL-3 exhaust system, which is currently on the APS temperature control system network.

Figure 5-33: Sector 14 Layouts.

5.4 Contingent Additional Scope

The Enabling Technical Capabilities section of the WBS at this stage does not include any contingent additional scope. Enabling Technical Capabilities is a support service for both the accelerator and the beamlines. In the event that any of the scope currently identified as contingent additional scope in the beamlines or accelerator is added to the baseline scope, an evaluation will done to determine what additional scope, if any, is needed. Of specific interest is the HEXT beamline discussed in U1.04, which will require a new bending magnet front end to be procured and installed.

References

[1] Y. Jaski, "High Heat Load Front End Design Report," 2004.

[2] Y. Jaski, "Thermal Analysis of the Components of the Insertion Device Front Ends FEv1.2 and FEv1.5," TB-50, 2005.

[3] P.K. Job, "Guidelines for Beamline and Front-End Radiation Shielding Design at the Advanced Photon Source," TB-44, 2012.

[4] T. Kuzay, "Functional Description of APS Beamline Front Ends," TB-5, 1993.

[5] V. Sajaev, "Simulation of switchable canted orbit in 5-kicker bump configuration," AOP-TN-2011-030, 2011.

The Advanced Photon Source, an Office of Science User Facility operated for the U.S. Department of Energy (DOE) Office of Science by Argonne National Laboratory, is supported by the DOE under Contract No. DE-AC02-06CH11357.

rev. 20121120